Springer Link Search Log in

Download PDF

Original Article | Published: 31 July 2021

Nano-decolorization of methylene blue by *Phyllanthus reticulatus* iron nanoparticles: an eco-friendly synthesis and its antimicrobial, phytotoxicity study

Rajathirajan Siva Dharshini, Mani Poonkothai ✉, Palanisamy Srinivasan, Raja Mythili, Asad Syed, Abdallah M. Elgorban, Thangasamy Selvankumar & Woong Kim ✉

Applied Nanoscience (2021)

933 Accesses | **4** Citations | Metrics

Abstract

The present study was investigated to synthesis the iron nanoparticles (FeNPs) using the leaf extract of *Phyllanthus reticulatus*. The phytosynthesized FeNPs exhibited UV–visible absorption peaks at 229 nm and its crystalline nature was confirmed through XRD. FT-IR analysis revealed the presence of various functional groups which are responsible for the bioreduction of FeNPs. The SEM results showed that FeNPs were aggregated, irregular sphere shaped with rough surfaces and EDX spectrum recorded densely occupied iron nanoparticles region. The particle size range of the synthesized iron

PRINCIPAL
PGP College of Arts and Science
Namakkal

Applied Nanoscience
https://doi.org/10.1007/s13204-021-02002-3

ORIGINAL ARTICLE

Nano-decolorization of methylene blue by *Phyllanthus reticulatus* iron nanoparticles: an eco-friendly synthesis and its antimicrobial, phytotoxicity study

Rajathirajan Siva Dharshini[1,2] · Mani Poonkothai[1] · Palanisamy Srinivasan[3] · Raja Mythili[3] · Asad Syed[4] · Abdallah M. Elgorban[4] · Thangasamy Selvankumar[3] · Woong Kim[5]

Received: 14 May 2021 / Accepted: 19 July 2021
© King Abdulaziz City for Science and Technology 2021

Abstract

The present study was investigated to synthesis the iron nanoparticles (FeNPs) using the leaf extract of *Phyllanthus reticulatus*. The phytosynthesized FeNPs exhibited UV–visible absorption peaks at 229 nm and its crystalline nature was confirmed through XRD. FT-IR analysis revealed the presence of various functional groups which are responsible for the bioreduction of FeNPs. The SEM results showed that FeNPs were aggregated, irregular sphere shaped with rough surfaces and EDX spectrum recorded densely occupied iron nanoparticles region. The particle size range of the synthesized iron nanoparticles was 185.6 nm. The FeNPs showed potential methylene blue decolourisation activity which was visually observed by gradual colour change in the dye solution from deep blue to colorless. The control exhibited no change in coloration during exposure to sunlight and the iron nanoparticles completely disintegrated the methylene blue within 10 s in 10 mg/L methylene blue (98%), whereas the color change was decreased when the concentration of the dye increased. In addition, the phytosynthesized FeNPs exhibited extensive antibacterial and antifungal activity against the selected pathogens. Phytotoxicity assay confirms the potential of biosynthesized iron nanoparticles as a fertilizer for the growth of green gram seeds. Thus the present study leads to development of cost-effective green synthesis, reduction of toxic chemicals and its extensive applications in the biological sciences.

Keywords *Phyllanthus reticulatus* · Iron nanoparticles · Photocatalytic activity · Phytotoxic activity · Antimicrobial activity

Introduction

Synthesis, manipulation and use of nanoscale size materials and/or nanoparticles have attracted much attention due to their unique properties and applications in the field of science and technology and medicine (Praveen et al. 2018). Among, the synthesis methods, green and/or biosynthesis of metal nanoparticles gained increasing attention due to their eco-friendly, cost-effective, reproducible nature and large-scale synthesis (Sengottaiyan et al. 2016; Selvam et al. 2017; Arularasu et al. 2018; Mythili et al. 2018). Among the metal nanoparticles, iron nanoparticles (FeNPs) have been widely applied as in solar energy conversion, biomedical applications, drug delivery and also as a catalyst (Kumar and Gupta 2005). In addition, FeNPs possess strong toxicity against a broad spectrum of pathogenic bacteria and fungi (Mahmoud et al. 2011). Because of excellent properties and applications, FeNPs synthesis using bio-based materials has attracted much attention in the field of nanoscience and

✉ Mani Poonkothai
poonkothaii_zoo@avinuty.ac.in

✉ Woong Kim
elshine@knu.ac.kr

1 Department of Zoology, Avinashilingam Institute for Home Science and Higher Education for Women, Tamil Nadu, Coimbatore, India

2 Department of Genetic Engineering, Molecular Genetics Laboratory, School of Bioengineering, SRM Institute of Engineering and Technology, Kattankulathur, Kanchipuram, Chennai, Tamilnadu 603203, India

3 PG & Research Department of Biotechnology, Mahendra Arts and Science College (Autonomous), Tamil Nadu, Kalippatti, Namakkal 637501, India

4 Department of Botany and Microbiology, College of Science, King Saud University, 2455, Riyadh 11451, Saudi Arabia

5 Department of Environmental Engineering, Kyungpook National University, Daegu, South Korea

Published online: 31 July 2021

technology. Nanoparticles synthesized using plant extract resulted in the photocatalytic degradation of organic dyes which was found to be time dependent and moreover, there was no loss of activity of the nanoparticles until the reuse of particles (Goswami et al. 2018).

Biosynthesis of FeNPs has been reported using microorganisms, enzymes and plants (Devatha et al. 2016; Raj et al. 2018). Among the biological sources, plant-based materials are advantageous because, they contain higher bioactive molecules and/or secondary metabolites which can be effectively reduced and act as a capping agent for the synthesis of FeNPs (Charbgoo et al. 2017). Studies on the synthesis of FeNPs using plants have been documented by several researchers (Mohan Kumar et al. 2013; Huang et al. 2014; Wang et al. 2014), however, to date, synthesis of FeNPs using *Phyllanthus reticulatus* has not been reported.

Phyllanthus reticulatus (Poir.) (Black honey shrub) belongs to the family Euphorbiaceae is widespread in India and tropical Africa. It act as an diuretic, antidiabetic and antidiarrheal agent and reported to contain various phytochemicals such as lupeol, lupeol acetate, and stigmasterol, polyphenols, flavonoids, glycosides, tannic acid and octacosanol (Khatun et al. 2014). Since, the plant contains variety of secondary metabolites and/or bioactive molecules it could be used as biological reducing agents for FeNPs synthesis. Hence the present study is an attempt to synthesis and characterize the FeNPs using *P. reticulatus* leaf extract and to assess the photocatalytic degradation of the methylene blue, antimicrobial activity and phytotoxicity of the synthesized nanoparticle under in vitro conditions.

Materials and methods

Plant material and its extract preparation

In this present study, the fresh leaves of *P. reticulatus* were collected from Mohanur, Namakkal district, Tamil Nadu, India and were identified by Botanical Survey of India (BSI/SRC/23/2018/Tech./2873), Tamil Nadu Agricultural University, Coimbatore, Tamil Nadu, India. To remove the dust particles present on the surface of the collected leaves, they were washed with running tap water followed by deionized distilled water. The surface cleaned leaves were shade dried for a week and crushed into fine powder with the help of a suitable grinder. The powder was stored in an airtight container and kept in a cool, dark and dry place for further analysis. About 10 g of powdered leaves were dissolved with 100 ml of distilled water and boiled at 180–90 °C for 30 min. The contents were filtered through Whatman No.1 filter paper and the obtained clear filtrate was stored at 4 °C for further FeNPs synthesis.

Biobased green synthesis of iron nanoparticles

Ferrous sulphate was prepared in different concentrations (1–5 mM) and to each 1–5 ml of the leaf extract was added separately. The reaction time was varied from 0 to 10 min and the contents were incubated at room temperature. At the optimized conditions, the reduction of Fe^{+} to Fe^{0} was confirmed by the colour change of solution from yellow to black. The biosynthesized iron nanoparticles were centrifuged at 1000 rpm for 5 min to obtain the black precipitate which served as iron nanoparticles. The obtained iron nanoparticles were dissolved in 100 ml of double distilled water and stored at 4 °C for further analysis (Suruthika et al. 2020).

Characterization of FeNPs

The *Phyllanthus reticulatus*-mediated FeNPs was characterized by various spectroscopic techniques. The formation of FeNPs and the development of Surface Plasmon Resonance (SPR) peak were measured by UV–visible spectroscopy (Hitachi U2800**,** Tokyo, Japan). The morphology, size distribution and the elemental Fe of the prepared FeNPs were determined by scanning electron microscope equipped with X-ray energy dispersive spectrometer was employed (Nova, Bergenfield, USA). The FT-IR (Shimadzu8400S, Kyoto, Japan) analysis was carried out to determine the possible secondary metabolites and/or biomolecules which are involved the reduction and capping of FeNPs. X-ray diffraction (Shimadzu XRD 7000, Japan) was performed to determine the crystalline structure of FeNPs and the particle size range of the synthesized iron nanoparticles was determined using a particle size analyzer.

Photocatalytic degradation activity

Photocatalytic degradation activity of FeNPs was evaluated by the disintegration of methylene blue (MB) under sunlight irradiation. 500 mg of FeNPs were dispersed in 100 ml of distilled water. A series of screw cap tubes containing different concentrations of MB (10–50 mg/L) was taken and 1 ml of prepared FeNPs solution was added separately to the dye solutions. The experimental setup was kept over the sunlight irradiation 14 h to observe the color change of the dye. The resultant solution was monitored in the wavelength range of 680 nm in a colorimeter and the percentage dye removal was calculated by

$$\text{Dye removal (\%)} = (C_0 - C) / C_0 \times 100$$

Where C_0 is the initial concentration of dye and C is the final concentration of dye at time (Bishnoi et al. 2018).

Antimicrobial activity of synthesized iron nanoparticles

The antibacterial and antifungal activity of the synthesized FeNPs was assessed by standard agar well diffusion method (Bauer et al. 1966). The bacterial cultures, *Klebsiella pneumonia* (MTCC 432), *Shigella flexneri* (MTCC 1457), *Proteus vulgaris* (MTCC 426), *Salmonella typhi* (MTCC 531), *Vibrio cholera* (MTCC 3906), *Pseudomonas aeroginosa* (MTCC 424), *Staphylococcus aureus* (MTCC 96) and *Staphylococcus epidermidis* (MTCC 435), and fungal cultures *Aspergillus niger* (MTCC 282), *Aspergillus fumigatus* (MTCC 9657), *Aspergillus flavus* (MTCC 277) and *Trichoderma sp.* (Accession number:KX856353) were used in the present study. The selected bacterial and fungal cultures were swabbed on the Muller Hinton agar (Bacteria) and Rose Bengal Chloramphenicol agar (Fungi) plates separately. To each well 20 µl (100 µg) of the biosynthesized FeNPs, aqueous extract of *P. reticulatus* leaves and the standard antibiotics chloramphenicol (bacteria) and fluconazole (fungi) which served as positive control were added separately. The plates were then incubated at 37 °C for 24 h (bacteria) and at room temperature for 5 days (fungi). To determine the antimicrobial activity, the diameter of inhibition zone was measured and expressed in millimeter.

Phytotoxicity assay

The green gram seeds subjected for germination assay were immersed in 10% sodium hypochlorite solution for 10 min to ensure surface sterility (USEPA 1996). After surface sterilization, the seeds were soaked in distilled water (T_1), plant extract (T_2) and iron nanoparticles (T_3) suspensions for about 24 h and rinsed thrice with distilled water. The experiment was conducted in triplicates. A layer of cotton was placed on each Petri dish and 5 ml of the selected test medium was added separately. Seeds were then transferred onto the cotton layer, with ten seeds per dish and 1 cm distance between each seed. The plates were watered regularly with the selected treatment. Petri dishes were covered and placed in the dark chamber for 3 days. After 7 days of incubation, germination percentage, shoot length, root length and vigour index of the green gram seedlings were recorded (Anupama et al. 2014).

Results and discussion

Among the different concentrations of ferrous sulphate solution and plant extract used with the varying time intervals, the colour change from yellow to black was well observed immediately with 2 mM ferrous sulphate with1ml of leaf extract indicating the synthesis of iron nanoparticles (Fig. 1a). The change in the colour of the solution represented the reduction of ferrous sulphate to ferrous ions and thereby leads to the formation of FeNPs. The reaction mechanism might be due to the formation of a complex when the plant extract was added to the metal which breaks the –OH bond and forms a partial bond with the metal ion. Further there might be breakage of the partial bond and the transfer of electrons to reduce the metal ions to nanoparticles (Gottimukkala et al. 2017). Hence it is assured that biomolecules present in the leaf extract may function as reducing agent and capping agent.

UV–Vis spectral analysis (200–800 nm) of the biosynthesized FeNPs showed broad absorption peak around 229 nm (Fig. 1b). Devatha et al. (2016) observed the strong absorption peak of FeNPs at 259 nm and our results showed that strong absorption band at 229 nm. The SEM image obtained for FeNPs synthesized from *P. reticulatus* and its corresponding EDX spectrum is shown in Fig. 2. SEM images revealed that the synthesized FeNPs were aggregated and irregular sphere shape with rough surfaces. Ali et al. (2016) reported spherical-shaped irregular iron oxide particles, which might have occurred due to agglomeration and its adhesiveness, the characteristic nature of metallic nanoparticles. To further validate the FeNPs, the elemental composition was determined by EDX. The EDX spectrum showed intense peak of 10.12% for Cl, and 38.32% for O illustrating the existence of macromolecule as stabilizing agent on the surface of iron nanoparticles and also showed a strong signal of pure Fe with a weight percentage of 51.56%. The presence of Fe and O peaks indicated the formation of FeNPs.

FT-IR analysis is carried out to determine the possible secondary metabolites and/or biomolecules responsible for the reduction of Fe ions (Fig. 3a). The strong absorption band at 3367.71 and 3255.84 cm^{-1} indicated the OH stretching vibrations and the presence of alcohols and phenols (Litvin et al. 2012). The peaks at 2985.8 and 2353.16 cm^{-1} indicates the C-H stretching vibrations of alkanes and –OH stretching of amino acids. The peaks at 1639.49 and 1473.62 cm^{-1} may be assigned to the amide bond of the proteins and C=C stretching of aromatic compounds. The absorption peak in the range of 1380–1240 cm^{-1} indicates C-N stretch of aliphatic amines. It has been reported by Lin et al. (2005) that the carbonyl groups from the amino acid residues and peptides of proteins have a strong affinity to bind metals. So that protein can act as encapsulating agent and thus protect the nanoparticles from agglomeration. The amide linkages in proteins and polypeptides give well-known signature in IR region. Presence of organic groups in the FT-IR spectrum of iron oxide nanoparticles indicated that bioactive compounds from *P. reticulatus* act as capping agent and decorate the surface of prepared particles. This

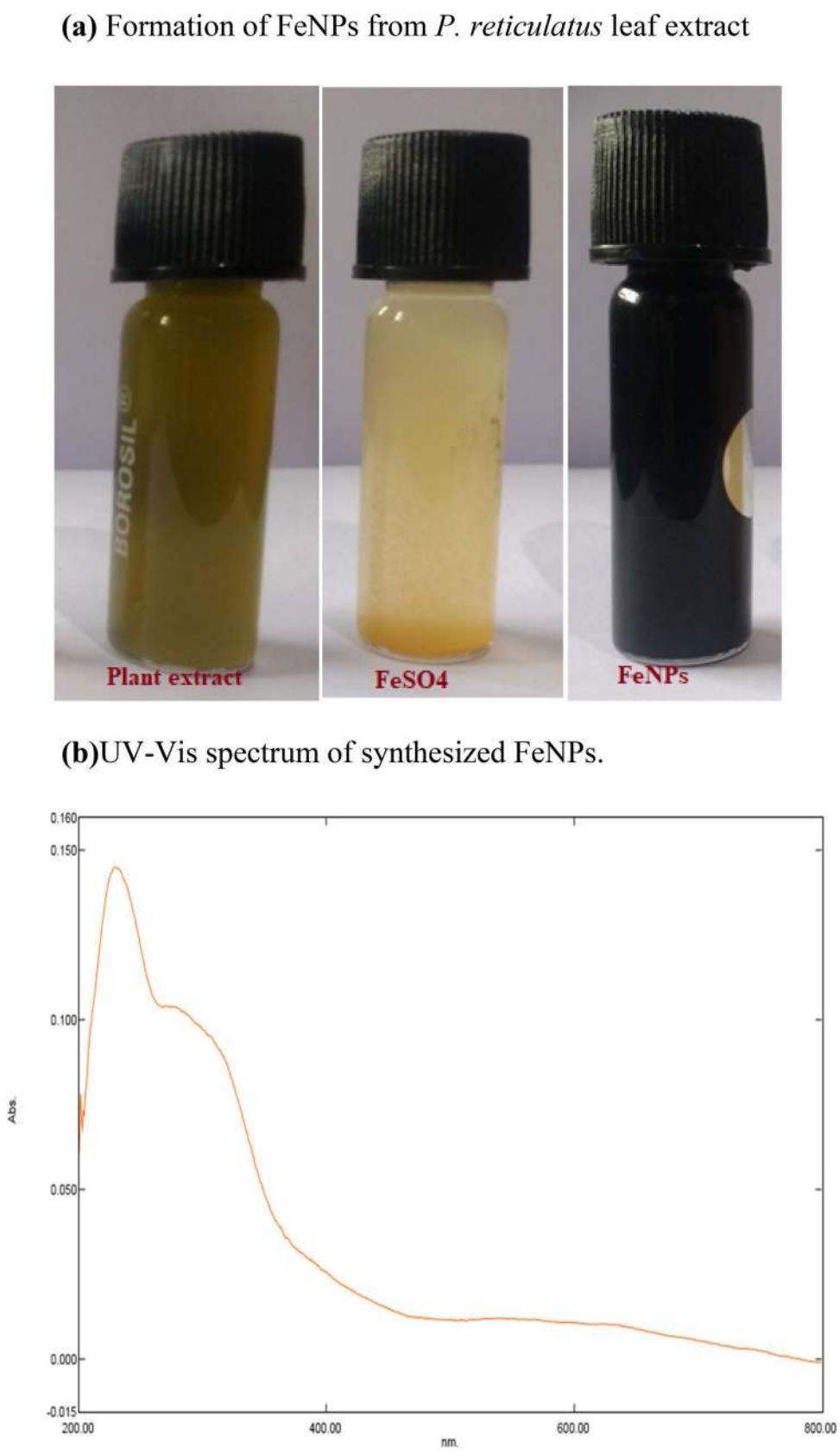


Fig. 1 **a** Formation of FeNPs from *P. reticulatus* leaf extract **b** UV–Vis spectrum of synthesized FeNPs

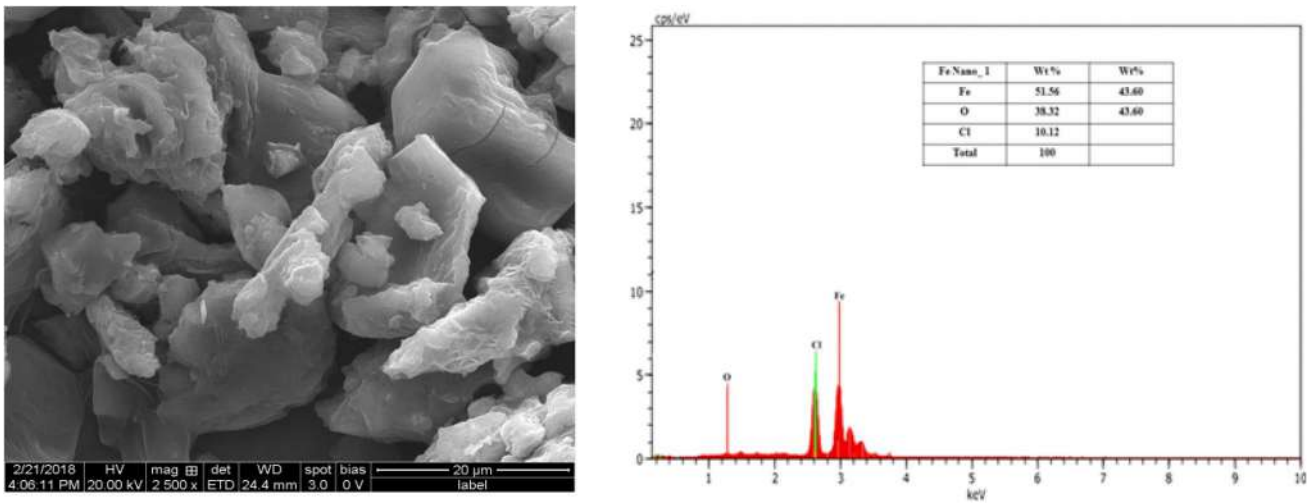


Fig. 2 SEM and EDX analysis of phytosynthesized FeNPs

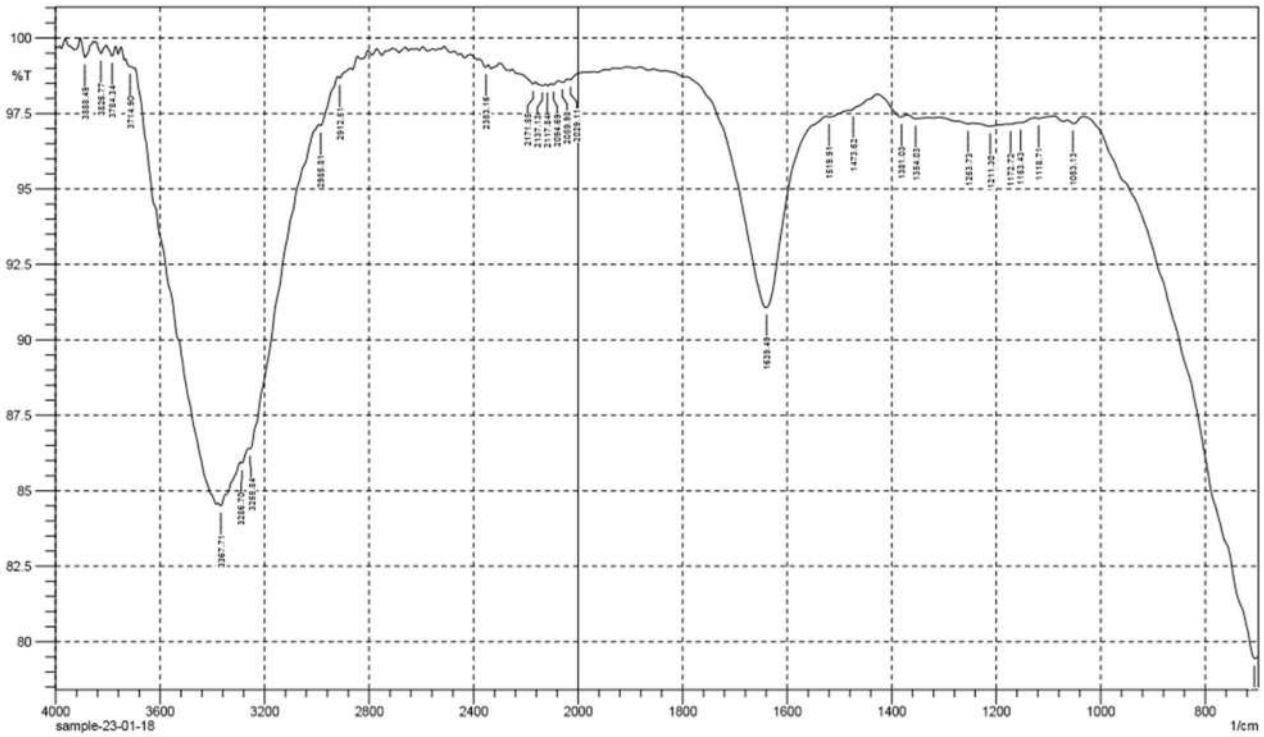
organic coating increases the chemical and colloidal stability of iron oxide nanoparticles and also can increase the biocompatibility of nanoparticles (Ebrahiminezhad et al. 2017). From the analysis of FT-IR study, it was revealed that the carbonyl group from the amino acid residue, carbohydrates and phytochemical constituents has the stronger ability to bind metal nanoparticles (capping of iron oxide nanoparticles) to prevent the agglomeration and thereby stabilize the medium. This suggests that biological molecules could possibly perform the dual function of formation and stabilization of iron oxide nanoparticles in the aqueous medium (Ali et al. 2016). Shah et al. (2015) also stated that presence of hydroxyl, carboxyl and amino functional groups may act as a precursor in metal ion reduction and also as capping agent to form the robust coating on the metal nanoparticles and leads to the colour change from yellowish brown to black.

The crystalline nature and phase composition of FeNPs were identified by X-ray diffractometer with Bragg's angle ranging from 20 to 80° within 2θ range (Fig. 3b). The XRD pattern of biosynthesized iron nanoparticles exhibit several broad Bragg's peaks corresponding to 220, 400, 422 and 440 orientations respectively indicating its crystalline nature of FeNPs.

Dynamic light scattering is a widely used technique for the determination of particle size in colloidal solution. Particle size and distribution are the major characteristics to be determined for a nanoparticles based on its saturation solubility, dissolution velocity, physical stability or even biological performance (Vishal and Agarwal 2011). The resulting particle size of iron nanoparticles exhibits the size distribution of 185.6 nm (Fig. 4). These results are consistent with the UV–Vis spectra where broadness of absorption peak is proportional with the size of the particle. Prabhakar et al. (2017) reported that *Mimosa pudica*-based iron nanoparticles showed comparatively larger size distribution of 65–230 nm.

Photocatalytic degradation of methylene blue was investigated using green-synthesized FeNPs under solar light irradiation. The degradation was visually observed by gradual change in the colour of the dye solution from deep blue to colorless (Fig. 5).The control exhibited no change in coloration during exposure to sunlight and the iron nanoparticles completely disintegrated the methylene blue within 10 s in 10 mg/L dye (98%), whereas the colour change was decreased in 20 mg/L (87%) and 30 mg/ L (66%) at 25 and 30 min of incubation, respectively. Minimum decolourisation was observed in 40 mg/L (27%) and 50 mg/L (15%) dye inoculated with 1 ml of iron nanoparticles. It has been reported that the dye degradation is associated with the breakdown of chromophoric group of the methylene blue and the transformation of dye into the low molecular weight by-products. The results are consistent with previous studies reported the degradation of methyl orange and methylene blue using FeNPs synthesized from *Amaranthus spinosus* (Garole et al. 2018).The mechanism of degradation of dye took place due to the generation of surface plasmons under resonant excitation with molecular environment (Tsibul'nikova et al. 2015). It was also described by Maji et al. (2007) that the mechanism of degradation of dye might be due to photo-absorption, electrons and holes generation, charge carriers transfer and the recombination of carrier with the dye molecules. The high surface area of iron oxide nanoparticles in the present study assists the methylene blue degradation and increase the formation of hydroxyl radicals. The results of the present study coincides with the findings of Shahwan et al. (2011) who reported 80% removal of methylene blue dye within 5 min of sunlight irradiation and the remaining concentration of dye was decolourised after

(a) FT-IR analysis of FeNPs.



(b) XRD analysis of FeNPs

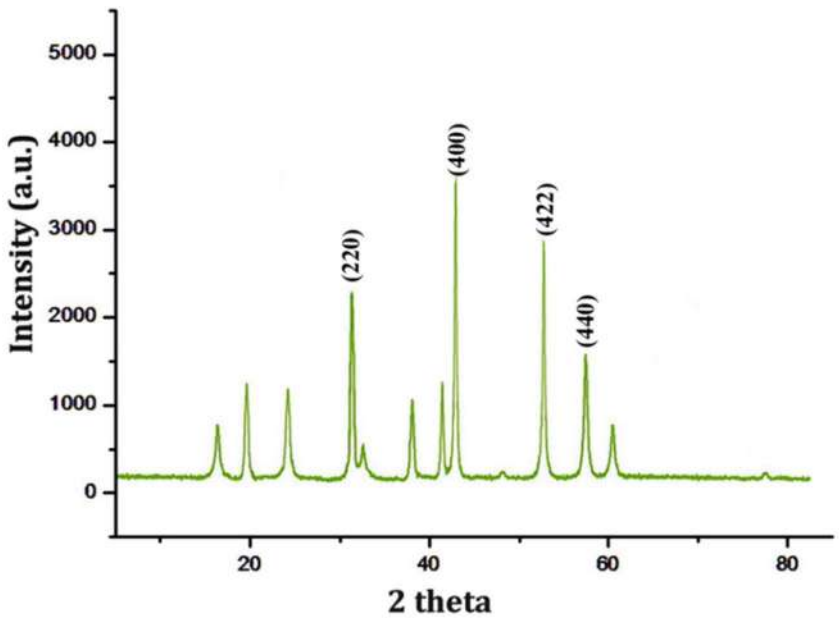


Fig. 3 **a** FT-IR analysis of FeNPs **b** XRD analysis of FeNPs

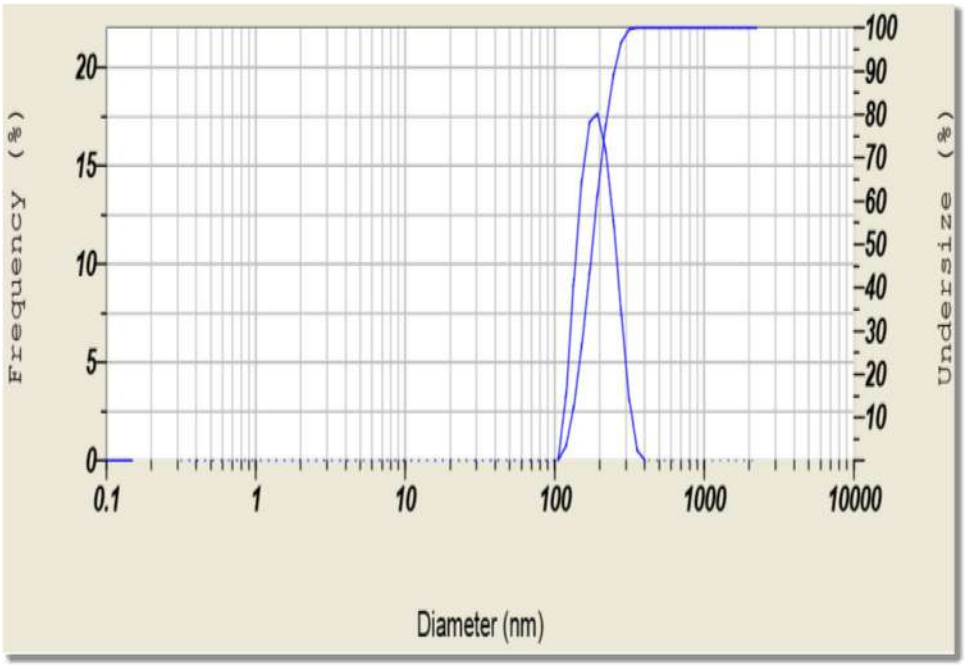


Fig. 4 Particle size of biosynthesized iron oxide nanoparticles

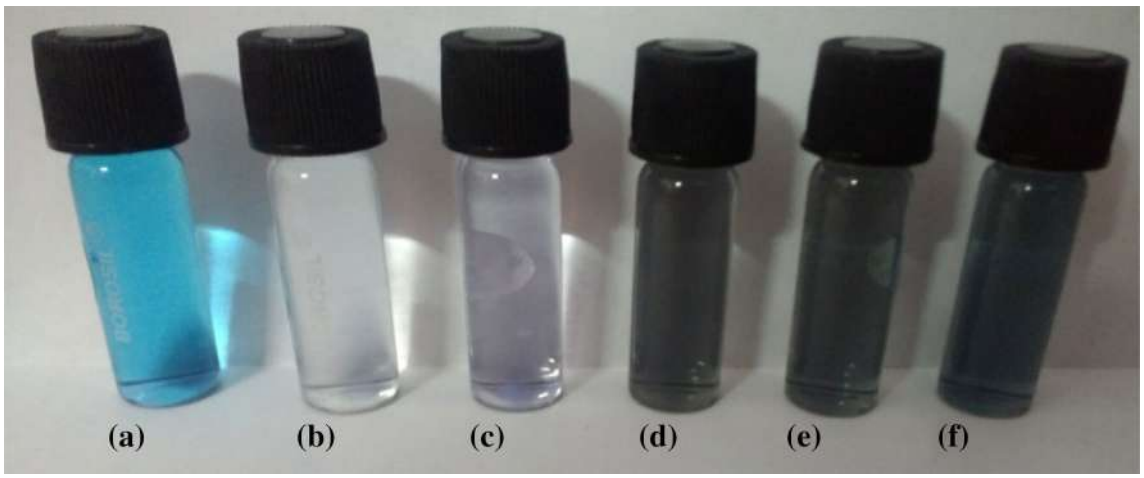


Fig. 5 Methylene blue degrading activity of FeNPs. **A**-Control (Methylene blue); **B** 10 mg/L FeNPs; **C** 20 mg/L FeNPs; **D** 30 mg/L FeNPs; **E** 40 mg/L FeNPs; and **F** 50 mg/L FeNPs

200 min under optimized conditions. Similar studies were performed using iron nanoparticles to remove malachite green by green tea leaf extract (Weng et al. 2013), indigo carmine by *Azadirachta indica* and methyl orange by benzoate supported nanoscale zerovalent iron (Chen et al. 2011). Govarthanan et al. (2021) investigated the photocatalytic degradation of methylene blue and rhodamine-B using the novel heterogeneous MoS_2@MIL-88(Fe) hybrid composite under UV irradiation.

Antibacterial activity of FeNPs was measured by the zone of inhibition for different pathogenic bacteria. The zone of inhibition of the selected bacterial isolates against FeNPs and leaf extract was compared with the standard antibiotic chloramphenicol. The FeNPs showed maximum zone of inhibition against Gram negative bacteria *P. vulgaris* (25 mm), *V. cholera* (25 mm), *S. flexneri* (23 mm), *S. typhi* (20 mm), *K. pneumoniae* (15 mm) and *P. aeruginosa* (32 mm) whereas, Gram positive *S. aureus* (15 mm) and *S. epidermis* (17 mm) exhibited minimum zone of inhibition for iron nanoparticles (Table 1). The zone of inhibition clearly indicated that the FeNPs had significant antibacterial activity against wide range of both Gram-positive and Gram-negative bacteria. It has been reported that the effect of FeNPs was mainly electrostatic attraction between

Table 1 Antibacterial activity of the biosynthesized FeNPs and leaf extract

Bacterial isolates	Zone of inhibition (mm)		
	P. reticulatus extract	FeNPs	Chloramphenicol
Gram negative bacteria			
Proteus vulgaris	10 ± 1.3	25 ± 2.4	30 ± 2.5
Vibrio chlorae	18 ± 2.1	25 ± 3.2	32 ± 2.7
Shigellaflexneri	12 ± 1.0	23 ± 2.6	36 ± 2.5
Salmonella typhi	12 ± 1.0	20 ± 1.5	32 ± 3.1
Klebsiella pneumonia	13 ± 1.5	15 ± 1.2	35 ± 3.8
Pseudomonas aeruginosa	50 ± 4.8	32 ± 3.4	42 ± 4.2
Gram positive bacteria			
Staphylococcus aureus	10 ± 1.1	15 ± 1.3	35 ± 3.4
Streptococcus epidermis	12 ± 1.7	17 ± 1.1	31 ± 3.0

positively charged FeNPs and negatively charged bacterial cell wall and this phenomena leads to the formation of reactive oxygen species (ROS) caused by cell death (Li et al. 2008; Burello and Worth 2011). The antibacterial activity was caused based on the fact that Fe ions released form iron oxide nanoparticles infused the bacterial cell membrane by attaching to the negatively charged cell wall (Ren et al. 2009; Sankar et al. 2013). Fe ions may indulge in cross linkage of nucleic acid strands by binding them with DNA of bacteria. This may lead to the disordered helical structure of DNA molecule which may be due to the denaturation of proteins and irregular of some biochemical processes in the cell, it may result the complete destruction of the bacterial cell (Yallappa et al. 2013). Ravishankar Rai and Jamuna Bai (2011) and Tong et al. (2012) reported that iron oxide nanoparticles can interact with thiol (–SH) group of the protein present on the bacterial cell wall that leads to the denaturation of surface protein along with the loss of cell membrane permeability, subsequently cause cell death. Also they act with phosphorus present inside the DNA by inactivating and inhibiting the enzyme activity leading to the death of bacteria.

The antifungal activity of the green synthesized FeNPs was compared with the standard antibiotic fluconozole. The fungicidal activity of FeNPs was found to be maximum in *Rhizopus sp.* and *Trichoderma viridae* with corresponding zone of inhibition of 31 and 30 mm, respectively. *A. fumigatus* and *A.niger* showed a zone of inhibition of 25 mm and followed by *A. flavus* (18 mm), respectively (Table 2). The zone of inhibitions on the fungal plates clearly indicated the antifungal activity of FeNPs. It has been reported that the maximum zone of inhibition depends on the concentration of FeNPs and also spore concentration produced by the corresponding fungi. Abdeen and Salahuddin (2013) have

Table 2 Antifungal activity of the biosynthesized FeNPs and leaf extract

Fungal isolates	Zone of inhibition (mm)		
	P. reticulatus extract	FeNPs	Fluconazole
Trichoderma viridae	15 ± 1.2	30 ± 2.2	40 ± 3.4
Aspergillus niger	22 ± 2.1	25 ± 2.3	30 ± 2.9
Aspergillus fumigatus	20 ± 2.0	25 ± 2.3	30 ± 2.8
Aspergillus flavus	13 ± 1.1	18 ± 1.9	20 ± 1.7

been reported that the iron nanoparticles possess promising antimicrobial activity against several human pathogens. Nehra et al. (2018) reported that the iron oxide NPs showed strong lethal effects towards the *A. niger* and *F. solani.* The broad spectrum of antibacterial and antifungal activity of the synthesized FeNPs could be used as potential antimicrobial agent in the field of clinical medicine. Similarly, zinc oxide nanoparticles were synthesized using funnel-shaped ivory flowers of *Candelabra cactus* which exhibited anticancer and antibacterial activity (Govarthanan et al. 2020).

The results of phytotoxicity assay such germination percentage, shoot length, root length and vigour index of green gram seeds grown with distilled water (T_1), *Phyllanthus reticulatus* leaf extract (T_2), and biosynthesized iron nanoparticles (T_3) were depicted in Table 3. The germination percentage was maximum T_1 (97%) followed T_3 (93%) and T_2 (90%) (Fig. 6). Similar trend was noticed in the vigour index of green gram seeds (Table 3). The values observed for the shoot lengths of green gram were 3.83, 1.54 and 3.54 cm in T_1, T_2 and T_3, respectively. The root length was heightened in T_1 (2.92 cm) followed by T_3 (1.35 cm) and T_2 (0.69 cm). Increase in the germination and seedling growth by biosynthesized iron oxide nanoparticles shows that iron with plant extract might have acted as stabilizer and proves to be non-toxic in nature. It has also been anticipated for the bioremediation of pollutants (Yavuz et al. 2006; Barrena et al. 2009). Literature also says that iron oxide nanoparticles act as non-toxic material in many fields (Ju-Nam and Lead 2008) and also perform as biostimulant and micronutrient (Liu et al. 2014).

Conclusion

Phyto-synthesis of FeNPs using *P. reticulatus* leaf extract is a cost effective, simple and eco-friendly method that excludes the hazards arising out of the use of harmful reducing and/or capping agents. The phyto-synthesized FeNPs have potential broad-spectrum of antibacterial and antifungal activity. Furthermore, the catalytic activity of FeNPs to degrade methylene blue, classic contaminant of water bodies

Table 3 Phytotoxicity assay of green gram seeds grown with different treatments

Treatments	Germination percentage	Shoot length (cm)	Root length (cm)	Vigour index
T_1	97	3.83 ± 0.24	2.92 ± 0.03	655
T_2	90	1.25 ± 0.81	0.69 ± 0.60	175
T_3	93	3.54 ± 0	1.35 ± 0.18	455

Values of Mean ± Standard Deviation

Where, T_1—Distilled water (Control), T_2—Leaf extract of *P. reticulates,* T_3—Phytosynthesised iron nanoparticles

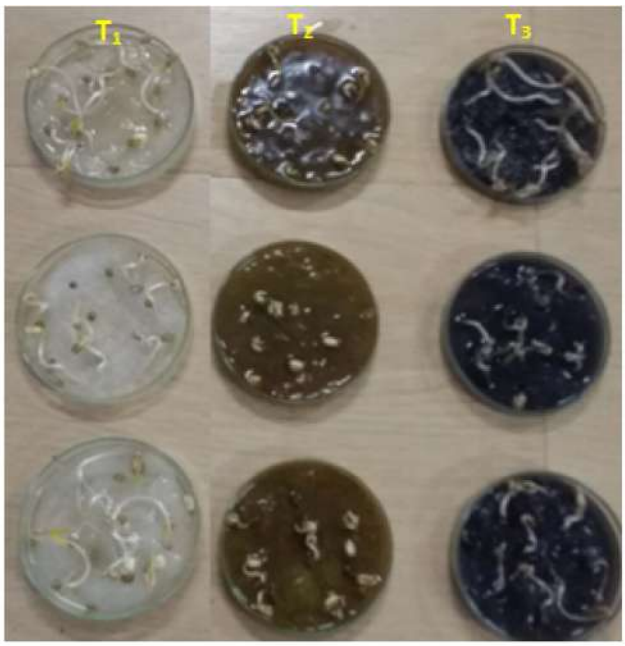


Fig. 6 Germination of green gram seeds using different treatments. T_1—Distilled water (Control), T_2—Leaf extract of *P.reticulatus,* T_3—Biosynthesised iron nanoparticles

T_1- Distilled water (Control), T_2 - Leaf extract of *P.reticulatus,* T_3- Biosynthesised iron nanoparticles

was successfully investigated. The outcome of this study may find applications in therapeutics, agriculture and textile industries.

Acknowledgements The authors acknowledge the higher authorities of Avinashilingam Institute for Home Science and Higher Education for Women, Coimbatore for providing the facilities to conduct this study. This work was partly supported by the Korea Institute of Energy Technology Evaluation and Planning (KETEP) grant funded by the Korea government (MOTIE)

(No. 20194110100100, full-scale feasibility study of the stability and efficiency improvement of a biogas production facility based on biomass from urban/living environments). The authors extend their appreciation to the Researchers Supporting Project number (RSP-2021/56), King Saud University, Riyadh, Saudi Arabia.

Declarations

Conflict of interest The authors declare that they have no conflict of interest.

References

Abdeen R, Salahuddin N (2013) Modified chitosan-clay nanocomposite as a drug delivery system intercalation and in vitro release of ibuprofen. J Chem. https://doi.org/10.1155/2013/576370

Ali A, Zafar H, Zia M et al (2016) Synthesis, characterization, applications, and challenges of iron oxide nanoparticles. Nanotechnol Sci Appl 9:49–67. https://doi.org/10.2147/NSA.S99986

Anupama N, Murali M, Jogaiah S, Amruthesh KN (2014) Crude oligossacarides from Alternaria solani with Bacillus subtilis enhance defense activity and induce resistance against early blight disease of tomato. Asian J Sci Technol 5:412–416

Arularasu MV, Anbarasu M, Poovaragan S et al (2018) Structural, optical, morphological and microbial studies on SnO_2 nanoparticles prepared by co-precipitation method. J Nanosci Nanotechnol 18:3511–3517. https://doi.org/10.1166/jnn.2018.14658

Barrena R, Casals E, Colón J et al (2009) Evaluation of the ecotoxicity of model nanoparticles. Chemosphere 75:850–857. https://doi.org/10.1016/j.chemosphere.2009.01.078

Bauer AW, Kirby WMM, Sherris JC et al (1966) Antibiotic susceptibility testing by a standardized singledisk method. Am J Clin Pathol 36:493–496

Bishnoi S, Kumar A, Selvaraj R (2018) Facile synthesis of magnetic iron oxide nanoparticles using inedible *Cynometra ramiflora* fruit extract waste and their photocatalytic degradation of methylene blue dye. Mater Res Bull 97:121–127

Burello E, Worth AP (2011) A theoretical framework for predicting the oxidative stress potential of oxide nanoparticles. Nanotoxicology 5:228–235. https://doi.org/10.3109/17435390.2010.502980

Charbgoo F, Bin AM, Darroudi M (2017) Cerium oxide nanoparticles: green synthesis and biological applications. Int J Nanomedicine 12:1401–1413

Chen C, Liu J, Liu P, Yu B (2011) Investigation of photocatalytic degradation of methyl orange by using nano-sized ZnO catalysts. Adv Chem Eng Sci 01:9–14. https://doi.org/10.4236/aces.2011.11002

Devatha CP, Kumar A, Katte SY (2016) Green synthesis of iron nanoparticles using different leaf extracts for treatment of domestic waste water. J Clean Prod 139:1425–1435. https://doi.org/10.1016/j.jclepro.2016.09.019

Ebrahiminezhad A, Taghizadeh S, Berenjian A et al (2017) Green synthesis of silver nanoparticles capped with natural carbohydrates using Ephedra intermedia. Nanosci & Nanotechnology-Asia. https://doi.org/10.2174/2210681206666161006165643

Garole VJ, Choudhary BC, Tetgure SR et al (2018) Detoxification of toxic dyes using biosynthesized iron nanoparticles by photo-Fenton processes. Int J Environ Sci Technol 15:1649–1656. https://doi.org/10.1007/s13762-017-1510-0

Goswami M, Baruah D, Das AM (2018) Green synthesis of silver nanoparticles supported on cellulose and their catalytic application in the scavenging of organic dyes. New J Chem 42(13):10868–10878

Gottimukkala KSV, Harika RP, Zamare D (2017) Green synthesis of iron nanoparticles using green tea leaves extract. J Nanomedine Biotherapeutic Discov 7(151):2

Govarthanan M, Srinivasan P, Selvankumar T et al (2020) Utilization of funnel-shaped ivory flowers of Candelabra cactus for zinc oxide nanoparticles synthesis and their in-vitro anti-cancer and antibacterial activity. Mater Lett 273:127951

Govarthanan M, Mythili R, Kim W et al (2021) Facile fabrication of (2D/2D) MoS2@MIL-88(Fe) interface-driven catalyst for efficient degradation of organic pollutants under visible light irradiation. J Hazard Mater 414:125522. https://doi.org/10.1016/j.jhazmat.2021.125522

Huang L, Weng X, Chen Z et al (2014) Green synthesis of iron nanoparticles by various tea extracts: Comparative study of the reactivity. Spectrochim Acta - Part A Mol Biomol Spectrosc 130:295–301. https://doi.org/10.1016/j.saa.2014.04.037

Ju-Nam Y, Lead JR (2008) Manufactured nanoparticles: An overview of their chemistry, interactions and potential environmental implications. Sci Total Environ 400:396–414. https://doi.org/10.1016/j.scitotenv.2008.06.042

Khatun H, Nesa L, Islam R et al (2014) Antidiabetic and antidiarrheal effects of the methanolic extract of Phyllanthus reticulatus leaves in mice. Asian Pacific J Reprod 3:121–127. https://doi.org/10.1016/S2305-0500(14)60015-4

Kumar A, Gupta M (2005) Cytotoxicity suppression and cellular uptake enhancement of surface modified magnetic nanoparticles. Biomaterials 26:1565–1573. https://doi.org/10.1016/j.biomaterials.2004.05.022

Li N, Xia T, Nel AE (2008) The role of oxidative stress in ambient particulate matter-induced lung diseases and its implications in the toxicity of engineered nanoparticles. Free Radic Biol Med 44:1689–1699. https://doi.org/10.1016/j.freeradbiomed.2008.01.028

Lin Z, Wu J, Xue R, Yang Y (2005) Spectroscopic characterization of Au3+ biosorption by waste biomass of Saccharomyces cerevisiae. Spectrochim Acta - Part A Mol Biomol Spectrosc 61:761–765. https://doi.org/10.1016/j.saa.2004.03.029

Litvin VA, Galagan RL, Minaev BF (2012) Kinetic and mechanism formation of silver nanoparticles coated by synthetic humic substances. Colloids Surfaces A Physicochem Eng Asp 414:234–243. https://doi.org/10.1016/j.colsurfa.2012.08.036

Liu X, Huang N, Li H et al (2014) Multidentate polyethylene glycol modified gold nanorods for in vivo near-infrared photothermal cancer therapy. ACS Appl Mater Interfaces 6:5657–5668. https://doi.org/10.1021/am5001823

Mahmoud AA, El-Feky GS, Kamel R, Awad GEA (2011) Chitosan/sulfobutylether-β-cyclodextrin nanoparticles as a potential approach for ocular drug delivery. Int J Pharm 413:229–236. https://doi.org/10.1016/j.ijpharm.2011.04.031

Maji SK, Pal A, Pal T, Adak A (2007) Modeling and fixed bed column adsorption of As(III) on laterite soil. Sep Purif Technol 56:284–290. https://doi.org/10.1016/j.seppur.2007.02.011

Mohan Kumar K, Mandal BK, Siva Kumar K et al (2013) Biobased green method to synthesise palladium and iron nanoparticles using Terminalia chebula aqueous extract. Spectrochim Acta - Part A Mol Biomol Spectrosc 102:128–133. https://doi.org/10.1016/j.saa.2012.10.015

Mythili R, Selvankumar T, Sudhakar C et al (2018) Utilization of market vegetable waste for silver nanoparticle synthesis and its antibacterial activity. Mater Lett 225:101–104. https://doi.org/10.1016/j.matlet.2018.04.111

Nehra P, Chauhan RP, Garg N, Verma K (2018) Antibacterial and antifungal activity of chitosan coated iron oxide nanoparticles. Br J Biomed Sci 4845:1–6. https://doi.org/10.1080/09674845.2017.1347362

Prabhakar R, Samadder SR, Jyotsana (2017) Aquatic and terrestrial weed mediated synthesis of iron nanoparticles for possible application in wastewater remediation. J Clean Prod 168:1201–1210. https://doi.org/10.1016/j.jclepro.2017.09.063

Praveen A, Lakshmi Narayana Rao G, Balakrishna B (2018) Performance and emission characteristics of a diesel engine using Calophyllum Inophyllum biodiesel blends with TiO2nanoadditives and EGR. Egypt J Pet. https://doi.org/10.1016/j.ejpe.2017.10.008

Raj S, Chand Mali S, Trivedi R (2018) Green synthesis and characterization of silver nanoparticles using Enicostemma axillare (Lam.) leaf extract. Biochem Biophys Res Commun 503:2814–2819. https://doi.org/10.1016/j.bbrc.2018.08.045

Ravishankar Rai V, Jamuna Bai A (2011) Nanoparticles and their potential application as antimicrobials, science against microbial pathogens: communicating current. research and technological advances. In: Méndez-Vilas A (ed) Formatex, Microbiology series, vol 1, no 3, pp 197–209

Ren G, Hu D, Cheng EWC et al (2009) Characterisation of copper oxide nanoparticles for antimicrobial applications. Int J Antimicrob Agents 33:587–590. https://doi.org/10.1016/j.ijantimicag.2008.12.004

Sankar R, Karthik A, Prabu A et al (2013) Origanum vulgare mediated biosynthesis of silver nanoparticles for its antibacterial and anticancer activity. Colloids Surfaces B Biointerfaces 108:80–84. https://doi.org/10.1016/j.colsurfb.2013.02.033

Selvam K, Sudhakar C, Govarthanan M et al (2017) Eco-friendly biosynthesis and characterization of silver nanoparticles using Tinospora cordifolia (Thunb.) Miers and evaluate its antibacterial, antioxidant potential. J Radiat Res Appl Sci 10:6–12. https://doi.org/10.1016/j.jrras.2016.02.005

Sengottaiyan A, Aravinthan A, Sudhakar C et al (2016) Synthesis and characterization of Solanum nigrum-mediated silver nanoparticles and its protective effect on alloxan-induced diabetic rats. J Nanostructure Chem 6:41–48. https://doi.org/10.1007/s40097-015-0178-6

Shah M, Fawcett D, Sharma S et al (2015) Green synthesis of metallic nanoparticles via biological entities. Materials 8(11):7279–7308

Shahwan T, Abu Sirriah S, Nairat M et al (2011) Green synthesis of iron nanoparticles and their application as a Fenton-like catalyst for the degradation of aqueous cationic and anionic dyes. Chem Eng J 172:258–266. https://doi.org/10.1016/j.cej.2011.05.103

Suruthika B, Poonkothai M, Lalitha P et al (2020) Synthesis of nano-silver from Navicula cincta and the evaluation of its antimicrobial activity. Micro Nano Lett 15(2):119–124. https://doi.org/10.1049/mnl.2019.0365

Tong H, Ouyang S, Bi Y et al (2012) Nano-photocatalytic materials: possibilities and challenges. Adv Mater 24:229–251. https://doi.org/10.1002/adma.201102752

Tsibul'nikova AV, Bryukhanov VV, Slezhkin VA (2015) Enhancement of singlet-triplet energy transfer between dyes in a polymer film by surface plasmons of gold nanoparticles. Russ Phys J 57:1716–1724. https://doi.org/10.1007/s11182-015-0443-7

USEPA (1996) Soil screening guidance: technical background document. Office of Emergency and Remedial Response, Washington, DC. https://doi.org/10.1016/j.materresbull.2017.08.040. EPA/540/R95/128

Vishal P, Agrawal YK (2011) Current status and advanced approaches in ocular drug delivery system. Global Trends Pharma Sci 2(2):131–148

Wang T, Jin X, Chen Z et al (2014) Science of the Total Environment Green synthesis of Fe nanoparticles using eucalyptus leaf extracts for treatment of eutrophic wastewater. Sci Total Environ 466–467:210–213. https://doi.org/10.1016/j.scitotenv.2013.07.022

Weng X, Huang L, Chen Z et al (2013) Synthesis of iron-based nanoparticles by green tea extract and their degradation of malachite. Ind Crops Prod 51:342–347. https://doi.org/10.1016/j.indcrop.2013.09.024

Yallappa S, Manjanna J, Sindhe MA et al (2013) Microwave assisted rapid synthesis and biological evaluation of stable copper nanoparticles using T. arjuna bark extract. Spectrochim Acta - Part A Mol Biomol Spectrosc 110:108–115. https://doi.org/10.1016/j.saa.2013.03.005

Yavuz H, Denizli A, Güngüneş H et al (2006) Biosorption of mercury on magnetically modified yeast cells. Sep Purif Technol 52:253–260. https://doi.org/10.1016/j.seppur.2006.05.001

Publisher's Note Springer Nature remains neutral with regard to jurisdictional claims in published maps and institutional affiliations.

Springer Link Search Log in

Original Article | Published: 25 September 2021

Biogenic production of silver nanoparticles from milk of *Capra aegagrus hircus* and mechanism of antibacterial activity on different bacteria

R. Mythili, P. Srinivasan, L. Praburaman, Mysoon M. Al-Ansari ✉, Latifah Al-Humaid, S. Vijayalakshmi & T. Selvankumar ✉

Applied Nanoscience (2021)

142 Accesses | **2** Citations | Metrics

Abstract

In the present study, we report a simple, rapid, cost-effective approach for the white synthesis of silver nanoparticles (AgNPs) using *Capra aegagrus hircus* milk. The formation of AgNPs was visually examined and further investigated using UV–visible spectrophotometer, transmission electron microscopy, scanning electron microscopy with energy dispersive X-ray, Fourier infrared spectroscopy, and X-ray diffractometer. Crystalline lattice indices of AgNPs were performed using the XRD analysis. The diffraction peaks at 2θ values of 37.7°, 46.1°, 67.4°, and 76.84° corresponding to lattice planes (111), (200), (220), and (311),

PRINCIPAL
PGP College of Arts and Science
Namakkal

Applied Nanoscience
https://doi.org/10.1007/s13204-021-02095-w

ORIGINAL ARTICLE

Biogenic production of silver nanoparticles from milk of *Capra aegagrus hircus* and mechanism of antibacterial activity on different bacteria

R. Mythili[1] · P. Srinivasan[1] · L. Praburaman[2] · Mysoon M. Al-Ansari[3] · Latifah Al-Humaid[3] · S. Vijayalakshmi[4] · T. Selvankumar[1]

Received: 27 July 2021 / Accepted: 9 September 2021
© King Abdulaziz City for Science and Technology 2021

Abstract
In the present study, we report a simple, rapid, cost-effective approach for the white synthesis of silver nanoparticles (AgNPs) using *Capra aegagrus hircus* milk. The formation of AgNPs was visually examined and further investigated using UV–visible spectrophotometer, transmission electron microscopy, scanning electron microscopy with energy dispersive X-ray, Fourier infrared spectroscopy, and X-ray diffractometer. Crystalline lattice indices of AgNPs were performed using the XRD analysis. The diffraction peaks at 2θ values of 37.7°, 46.1°, 67.4°, and 76.84° corresponding to lattice planes (111), (200), (220), and (311), respectively. The obtained AgNPs were spherical in shape with the size between 5 and 50 nm. The antibacterial activity of AgNPs against *Klebsiella* sp. (Accession Number: KC899845), and *Staphylococcus* sp. (Accession Number: KC688883) were evaluated by means of cell growth.

Keywords Antibacterial · Goat milk · Silver · Pathogens · White synthesis

Introduction

Nanoparticles are being considered as an eminent component of the widely accelerating field of nanotechnology exemplifying various real-world applications. In the realms of metal nanoparticles, silver, gold, copper, and zinc oxide have been demonstrated as phenomenon alternative therapeutic agents (Khan et al. 2021). Metallic nanoparticles have attracted considerable scientific interest due to their unique optical properties of surface plasmon resonance (SPR) and physicochemical properties (Castro et al. 2014). They are classified into different types such as carbon, metal, ceramic, polymeric, semi-conductor, and lipid-based nanoparticles, based on size, and structure properties (Thomas et al. 2015). Among them, silver nanoparticles (AgNPs) are one of the most sought after and greatly investigated metal nanoparticles.

Silver nanoparticles (AgNPs) are one of the most engineered nanoparticles used in several commercial areas, including medical devices, healthcare products, cleaning agents, food storage, packing, and textile coatings (Rolim et al. 2019). Silver nanoparticles (AgNPs) play a significant role in resolving numerous medical problems due to their chemical biocompatibility, inertness, oxidation resistance, and safe use as antibacterial activity (Carlson et al. 2008) against a variety of microorganisms (Mahmoud et al. 2021). The antimicrobial potency of silver nanoparticles increased the usage of silver nanoparticles in wound dressing, drug carriers, and in artificial implantation (Liao et al. 2019). They are also used for environmental applications because of their potent antimicrobial activity against bacteria, viruses, and fungi (Rolim et al. 2019; Ahluwalia et al. 2018).

✉ Mysoon M. Al-Ansari
myalansari@ksu.edu.sa

✉ T. Selvankumar
selvankumar75@gmail.com

[1] PG and Research Department of Biotechnology, Mahendra Arts and Science College (Autonomous), Kalippatti, Namakkal, Tamil Nadu 637501, India

[2] School of Minerals Processing and Bioengineering, Central South University, Changsha 410083, China

[3] Department of Botany and Microbiology, College of Science, King Saud University, Riyadh 11451, Saudi Arabia

[4] Food Science and Biotechnology, School of Agriculture and Life Sciences, Kangwon National University, Chuncheon, South Korea

Published online: 25 September 2021

To exploit the numerous properties of AgNPs, innovative methods of synthesis are being employed. Chemical and physical modes are widely implemented for the synthesis of AgNPs (Khan et al. 2021; Gurunathan et al. 2015). Eco-friendly green synthesis of nanoparticles is biocompatible, cost effective, less time and energy consuming and it also non toxic compared to the physical and chemical methods (Veeraraghavan et al. 2021). Accordingly, numerous biological resources are being explored for the synthesis of AgNPs including, plants (Aravinthan et al. 2015; Mythili et al. 2018; Sengottaiyan et al. 2016; Ameen et al., 2019; Sampath et al., 2021), bacteria (Ameen et al. 2020), fungi (Mukherjee et al. 2002), algae (Gopu et al., 2021; Valarmathi et al., 2020; Govarthanan et al. 2017) oilcakes (Govarthanan et al. 2016), organic compound (Govarthanan et al. 2014), and even vegetable waste (Mythili et al. 2018). So far, many studies reported for AgNPs as plant extracts, due to medical value owing to the presence of phenolic compounds (polyphenols, tannic acid, flavonoids, terpenoids), amino acids and vitamins (Ebrahiminezhad et al. 2018). But only few studies attempted the biosynthesis of AgNPs using milk and other related bioresources.

Lee et al. (2013) reported that, synthesis of AgNPs using cow milk have potential application in medical and pharmaceutical sciences. Although a wide variety of biological sources have been used to synthesize AgNPs, the use of *Capra aegagrus* (goat) milk is not common. However, there is no report on synthesis of AgNPs using goat milk. In addition, goat milk has various effects of human health considering the total solid, fat, protein, mineral, vitamins, and lactose (Turkmen et al. 2017). In particular, goat milk contains 13.2% total solids, consisting of 4.5% fat, 3.6% protein, 0.8% minerals, and 4.3% lactose (Üçüncü 2013). It has been reported that the goat milk has maximum number of conjugated linoleic acids which play an important role in stimulation of immunity, growth promotion, and prevention of diseases. The most important effect of goat milk proteins is their healing effect on cow milk allergy, the most common food allergy, which causes many deaths in infants (Turkmen 2017). The present study investigated the biological synthesis of silver nanoparticles using fresh goat milk and evaluate the antibacterial activity of the synthesized AgNPs against the human pathogens.

Materials and methods

Materials and chemicals

Silver nitrate was purchased from Sigma–Aldrich (St. Louis, MO), nutrient broth was purchased from Hi-media Laboratories Pvt. Ltd (Mumbai, India). *Capra aegagrus* milk was procured from local goat farm in Mallasamudram, Tamil Nadu, India.

Synthesis of AgNPs

AgNPs synthesis was carried out according to Lee et al. (2013). Briefly, 4 ml of goat milk was mixed with 96 ml of 1 mM silver nitrate solution. The mixture was then incubated in a rotary shaking incubator at 37 °C until the color changed to dark brown. The reaction precipitates were then filtered and centrifuged at 10,000 rpm for 15 min. the resulting AgNPs were washed with sterile water. The obtained AgNPs was freeze dried at – 80 °C and used for further characterization and antibacterial studies.

Characterization of AgNPs

The optical absorption spectra of the synthesized AgNPs were observed using UV–visible spectrophotometer (Elico-SL 164) in the range of 200–800 nm. The morphology and size of the biogenic AgNPs were determined by transmission electron microscopy (TEM, FEI Tecnai TF 20 high resolution). The presence of elemental silver in the AgNPs was analyzed by scanning electron micrograph-energy dispersive spectroscopy (SEM–EDS; Jeol JSM 6390). Fourier transform infrared (FT-IR) spectra of the AgNPs were analyzed using Perkin-Elmer FT-IR spectrophotometer (IRAffinity-1S) operated at a resolution of 4 cm^{-1}. The spectra were recorded at wavelength ranges from 500 to 4000 cm ^{1}. The structural characterization was conducted using X-ray powder diffraction (XPERT-Pro diffractometer using Cu–Ka radiation). Sample Scanning was done in the region of 2θ from 20 to 80° at 0.04°/min with a time constant of 2 s.

Antibacterial activity

The antibacterial activity against *Klebsiella* sp. (Accession Number: KC899845), and *Staphylococcus* sp. (Accession Number: KC688883) of AgNPs synthesized from goat milk was evaluated according to Govarthanan et al. (2014). Briefly, the strains cultivated in 100 mL of nutrient broth amended with different concentrations (1–5 mM) of AgNPs. The growth of the bacterial strains was indexed by measuring the optical density (at $\lambda = 600$ nm) at regular intervals (0–48 h) using spectrophotometer. The growth curve was plotted between optical density and time. The flask without AgNPs was used as a control for this experiment.



Fig. 1 Process of goat milk mediated AgNPs synthesis

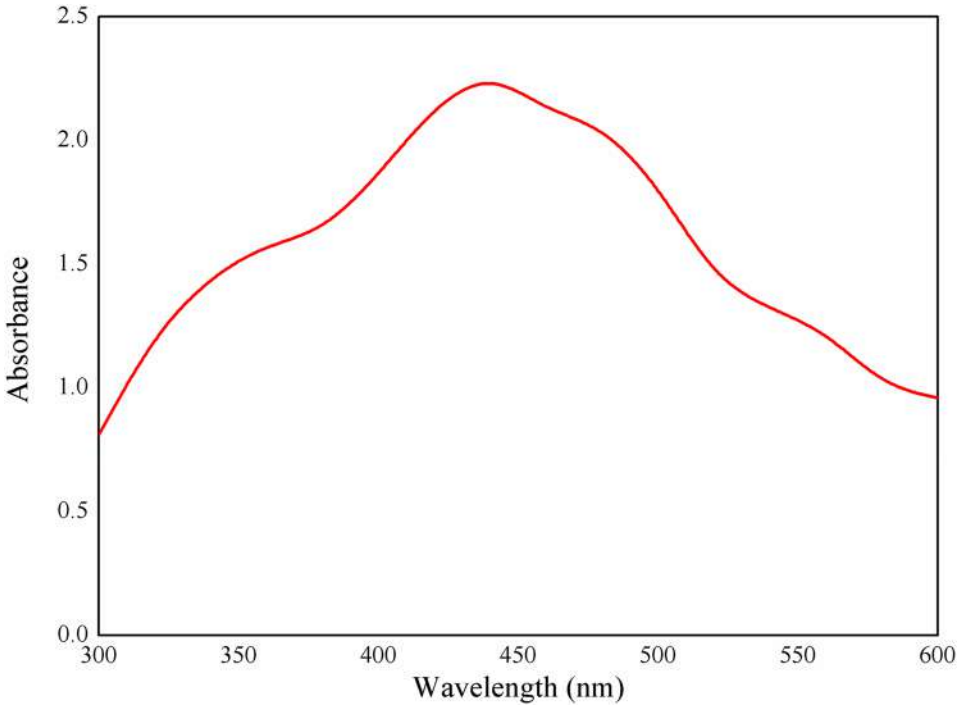


Fig. 2 Surface plasmon resonance spectra of AgNPs synthesized using goat milk

Results and discussion

Characterization of AgNPs

In the present study investigated a white chemistry milk approach-based biosynthesis of AgNPs from *Capra aegagrus* milk. The development AgNPs through the reduction of Ag^{+} into Ag^{0} ions was visually confirmed from colorless to dark brown in the flasks within 5 h. It has been reported that the proteins present in the milk could be responsible for the reduction of Ag^{+} in the mixture. The process of goat milk mediated AgNPs synthesis is shown in Fig. 1. Our previous study obtained after 8 h of reaction, the mixture turned from milky white to dark brown (Lee et al. 2013). The preliminary conformation of AgNPs synthesis was recorded by UV–Vis spectroscopy. The surface plasmon resonance (SPR) was found to be

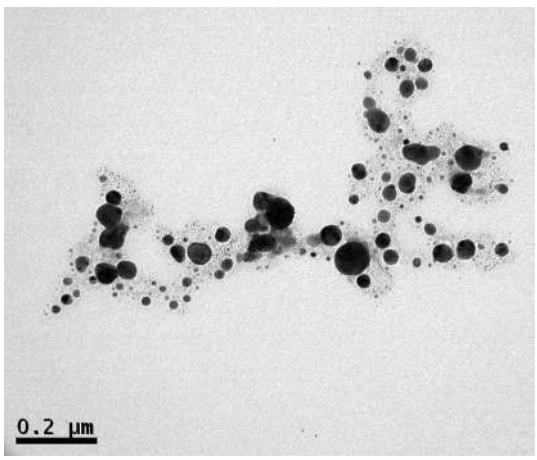


Fig. 3 TEM image of synthesized AgNPs

higher at 420 nm and its absorbance intensity increased with the increase of the incubation period (Fig. 2). The SPR at 420–450 is corresponding to the silver nanoparticles formation, according to the earlier reports (Singh et al. 2015).

The TEM images of biogenic AgNPs are shown in Fig. 3. The size of the AgNPs was in the range of 5–50 nm. The AgNPs were found to be spherical in shape, well dispersed, and homogeneous in nature. Shape is another important parameter that has an influence on the biological activity of nanomaterials. It was stated that the cellular uptake of spherical shaped nanoparticles was higher than rod-shaped (Barabadi et al. 2021). Further validate the formation of AgNPs, samples were characterized by SEM–EDS and the results are presented in Fig. 4. Strong silver peak was observed at 3 keV, which is reasonable absorption peak of AgNPs which could be the crystallites due to SPR. The results are consistent with previous studies reporting strong absorption of AgNPs approximately at 3 keV (Lee et al. 2013). The agglomerations of the particles on the surface are due to the multilayer coating of the particle leading to the formation of a few huge clusters on the surface.

FT-IR analysis involved in identifying the possible functional groups and/or secondary metabolites involved in AgNPs synthesis. Figure 5 shows the FT-IR spectra of AgNPs synthesized from goat milk. The band at 2929 cm^{-1} indicates the presence of C–H bonds of alkanes. The bands at 1662 and 1536 cm^{-1} are characteristic of amide I and amide II bands, respectively. Subsequently, intense peaks were identified at 1404 and 1028 cm^{-1}, corresponding to C=C and C–O bonds, respectively. The peak recorded at 1662 cm^{-1} could be due to the C=C stretching associated with the presence of aromatic rings, while the band around 1404 cm^{-1} could be attributed to aliphatic and aromatic groups in the plane deformation vibrations of methyl and methylene groups (Memon et al. 2018; Zhao et al. 2016).

Crystalline lattice indices of AgNPs were performed using the XRD analysis (Fig. 6). The diffraction peaks at 2θ values of 37.7°, 46.1°, 67.4°, and 76.84° corresponding to lattice planes (111), (200), (220), and (311), respectively. The observed peaks have been attributed to hexagonal phase of AgNPs (JCPDS no. 41–1402). A lot of unimportant peaks are seen owing to the bioorganic phases of crystallization that are stuck to the synthesized nano particles' surfaces. The XRD pattern strongly confirms the high crystalline nature of the biosynthesized silver nanoparticles. The similar XRD peaks were also found in the earlier studies have been observed the diffraction peaks of AgNPs at lattice planes of (111), (200), (220), and (311), respectively, (Govarthanan et al. 2016; Aravinthan et al. 2015).

Antibacterial activity

The antibacterial activity of AgNPs against *Klebsiella* sp. (Accession Number: KC899845), and *Staphylococcus* sp. (Accession Number: KC688883) was evaluated by means of cell growth. Optical density was measured

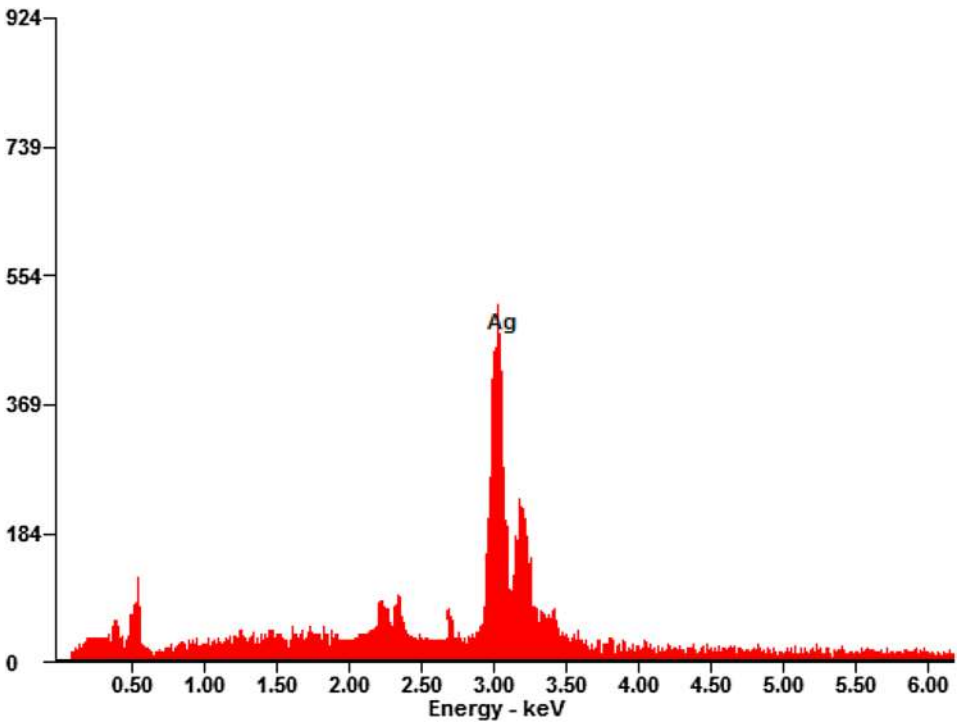


Fig. 4 SEM–EDX of AgNPs synthesized using goat milk

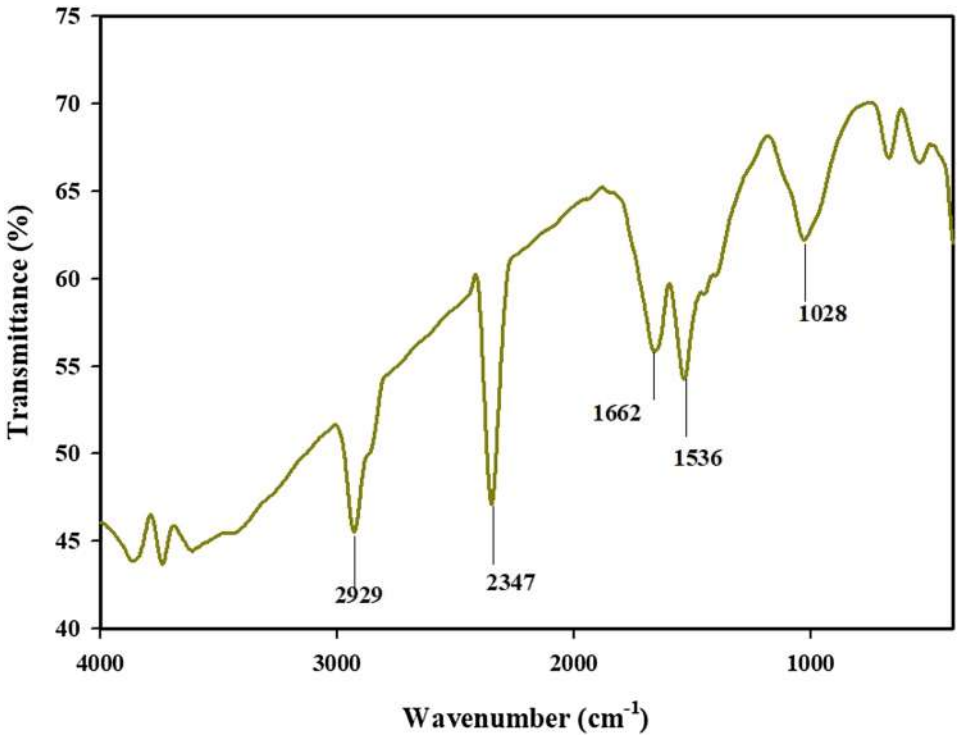


Fig. 5 FT-IR analysis of AgNPs synthesized using goat milk

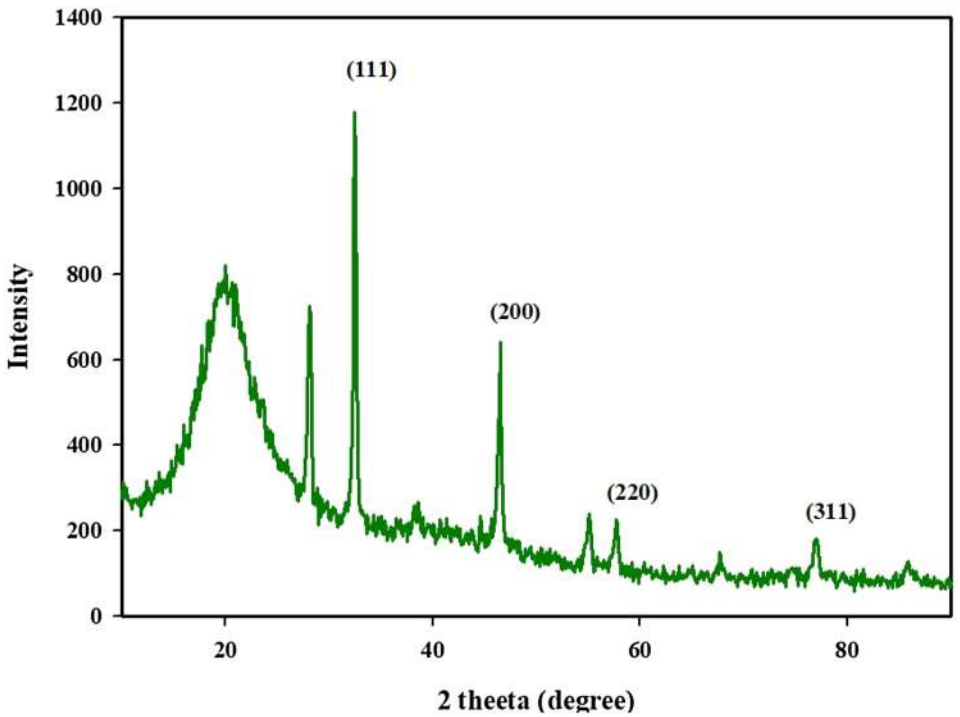


Fig. 6 XRD of goat milk mediated synthesis of AgNPs

at 600 nm and plotted as a function of time for 48 h at regular intervals with various concentrations (1–5 mM) of AgNPs (Fig. 7a and b). The results showed that the higher concentration (5 mM) of AgNPs effectively encountered the population of cell growth. As expected, the increasing concentration of AgNPs decreased the growth of bacterial population in the medium (Saxena et al. 2012).

It has previously been reported that nanoparticles with a size smaller than 20 nm can interact more easily with membrane proteins, causing maximum permeability,

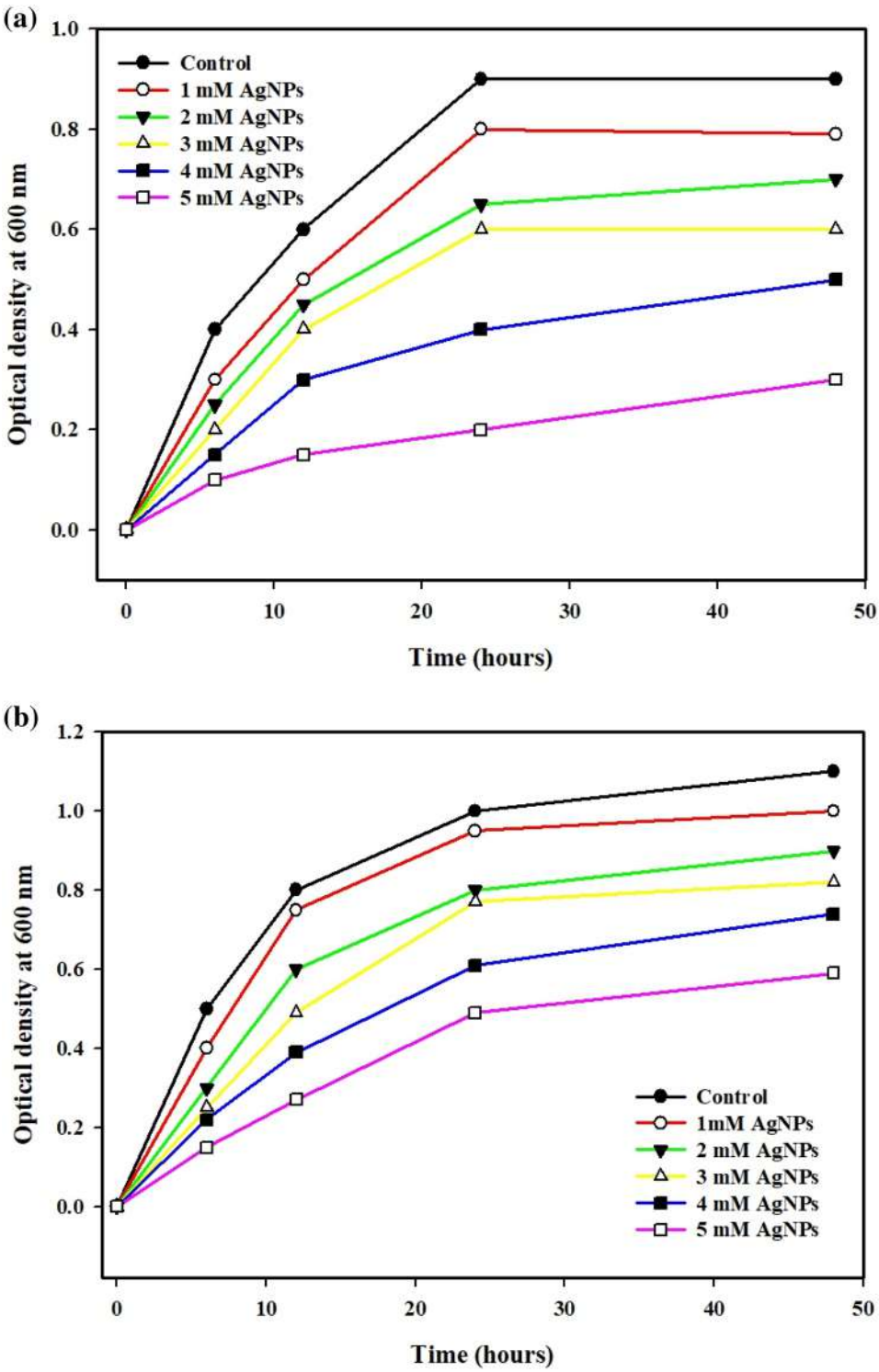


Fig. 7 **a**, **b** Antibacterial activity of AgNPs

which leads to the cell death of bacteria (Deshmukh et al. 2019). The mechanism of antibacterial activity of AgNPs remains unclear to date. Meanwhile, the mechanism of action of silver itself is by disrupting the cell membrane, causing ROS, penetration of cell membrane, and will bind to DNA and protein. However, based on existing works of literature, the principle of antibacterial mechanism of AgNPs is divided into oxidative stress, metal ion release, and non-oxidative mechanism (Sukweenadhi et al. 2021).

Conclusion

A simple one step white synthesis of AgNPs is reported along with the bio-reduction as well as biostabilization potentials of *Capra aegagrus* milk. The elemental analysis confirmed the presence of elemental silver in AgNPs. FT-IR analysis confirmed that the functional groups of goat milk have played a significant role for the bio-reduction of Ag^{+} ions into AgNPs. The antibacterial activity results clearly demonstrated that AgNPs synthesized by goat milk could be used for the treatment of disease which will cause by *Klebsiella* sp. and *Staphylococcus* sp. Thus, the white synthesized AgNPs can be used as a potential antibacterial agent in near future.

Acknowledgements The authors extend their appreciation to the Researchers Supporting Project Number (RSP-2021/228), King Saud University, Riyadh Saudi Arabia.

Declarations

Conflict of interest The authors declare that have no conflict of interests.

References

Ahluwalia V, Elumalai S, Kumar V, Kumar S, Sangwan RS (2018) Nano silver particle synthesis using *Swertia paniculata* herbal extract and its antimicrobial activity. Microb Pathog 114:402–408. https://doi.org/10.1016/j.micpath.2017.11.052

Ameen F, Srinivasan P, Selvankumar T, Kamala-Kannan S, Al Nadhari S, Almansob A, Govarthanan M (2019) Phytosynthesis of silver nanoparticles using *Mangifera indica* flower extract as bioreductant and their broad-spectrum antibacterial activity. Bioorg Chem 88:102970

Ameen F, Alyahya S, Govarthanan M, Aljahdali N, Al-Enazi N, Alsamhary K, Alharbi SA (2020) Soil bacteria *Cupriavidus* sp. mediates the extracellular synthesis of antibacterial silver nanoparticles. J Mol Struct 1202:233

Aravinthan A, Govarthanan M, Selvam K, Praburaman L, Selvankumar T, Balamurugan R, Kamala-Kannan S, Kim JH (2015) Sunroot mediated synthesis and characterization of silver nanoparticles and evaluation of its antibacterial and rat splenocyte cytotoxic effects. Int J Nanomed 10:1977. https://doi.org/10.2147/IJN.S79106

Barabadi H, Mojab F, Vahidi H, Marashi B, Talank N, Hosseini O, Saravanan O (2021) Green synthesis, characterization, antibacterial and biofilm inhibitory activity of silver nanoparticles compared to commercial silver nanoparticles. Inorg Chem Commun 129:108647. https://doi.org/10.1016/j.inoche.2021.108647

Carlson C, Hussain SM, Schrand AM, Braydich-Stolle LK, Hess KL, Jones RL, Schlager JJ (2008) Unique cellular interaction of silver nanoparticles: size-dependent generation of reactive oxygen species. J Phys Chem B 112:13608. https://doi.org/10.1021/jp712087m

Castro L, Blázquez ML, González FG, Ballester FG (2014) Mechanism and applications of metal nanoparticles prepared by bio-mediated process. Rev Adv Sci Eng 3:199. https://doi.org/10.1166/rase.2014.1064

Deshmukh SP, Patil SM, Mullani SB, Delekar SD (2019) Silver nanoparticles as an effective disinfectant: a review. Mater Sci Eng C 97:954–965. https://doi.org/10.1016/j.msec.2018.12.102

Ebrahiminezhad A, Zare-Hoseinabadi A, Sarmah AK, Taghizadeh S, Ghasemi Y, Berenjian A (2018) Plant-mediated synthesis and applications of iron nanoparticles. Mol Biotechnol 60:154–168. https://doi.org/10.1007/s12033-017-0053-4

Gopu M, Kumar P, Selvankumar T, Senthilkumar B, Sudhakar C, Govarthanan M, Selvam K (2021) Green biomimetic silver nanoparticles utilizing the red algae *Amphiroa rigida* and its potent antibacterial, cytotoxicity and larvicidal efficiency. Bioprocess Biosyst Eng 44(2):217–223

Govarthanan M, Selvankumar T, Manoharan K, Rathika R, Shanthi K, Lee KJ, Cho M, Kamala-Kannan S, Oh BT (2014) Biosynthesis and characterization of silver nanoparticles using panchakavya, an Indian traditional farming formulating agent. Int J Nanomed 9:1593–1599. https://doi.org/10.2147/IJN.S58932

Govarthanan M, Seo YS, Lee KJ, Jung IB, Ju HJ, Kim JS, Cho M, Kamala-Kannan S, Oh BT (2016) Low-cost and eco-friendly synthesis of silver nanoparticles using coconut (*Cocos nucifera*) oil cake extract and its antibacterial activity. Artif Cells Nanomed Biotechnol 44:1878–1882. https://doi.org/10.3109/21691401.2015.1111230

Govarthanan M, Selvankumar T, Mythili R, Sudhakar C, Selvam K (2017) Biosynthesis of silver nanoparticles from *Spirulina* microalgae and its antibacterial activity. Environ Sci Pollut Res 24:19459–19464. https://doi.org/10.1007/s11356-017-9772-0

Gurunathan S, Park JH, Han JW, Kim JH (2015) Comparative assessment of the apoptotic potential of silver nanoparticles synthesized by *Bacillus tequilensis* and *Calocybe indica* in MDA-MB-231 human breast cancer cells: targeting p53 for anticancer therapy. Int J Nanomed 10:4203–14022. https://doi.org/10.2147/IJN.S83953

Khan AA, Alanazi AM, Alsaif N, Wani TA, Bhat MA (2021) Pomegranate peel induced biogenic synthesis of silver nanoparticles and their multifaceted potential against intracellular pathogen and cancer. Saudi J Biol Sci. https://doi.org/10.1016/j.sjbs.2021.06.022

Lee KJ, Park SH, Govarthanan M, Wang PH, Seo YS, Cho M, Lee WH, Lee JY, Kamala-Kannan S, Oh BT (2013) Synthesis of silver nanoparticles using cow milk and their antifungal activity against phytopathogens. Mater Lett 105:128–131. https://doi.org/10.1016/j.matlet.2013.04.076

Liao C, Li Y, Tjong SC (2019) Bactericidal and cytotoxic properties of silver nanoparticles. Int J Mol Sci 20(2):449. https://doi.org/10.3390/ijms20020449

Mahmoud MG, Asker MS, Mohamed SS (2021) Facile green silver nanoparticles synthesis to promote the antibacterial activity of cellulosic fabric. J Ind Eng Chem 99:224–234. https://doi.org/10.1016/j.jiec.2021.04.030

Memon AA, Arbab AA, Patil SA, Mengal N, Sun KC, Sahito IA, Jeong SH, Kim HS (2018) Synthesis of solution processed f-CNT@Bi2S3 hybrid film coated linen fabric as a free-standing textile structured photo catalyst. Appl Catal A 566:87–95. https://doi.org/10.1016/j.apcata.2018.06.015

Mukherjee P, Senapati S, Mandal D, Ahmad A, Khan MI, Kumar R, Sastry M (2002) Extracellular synthesis of gold nanoparticles by the fungus *Fusarium oxysporium*. ChemBioChem 3:461–463. https://doi.org/10.1002/1439-7633(20020503)

Mythili R, Selvankumar T, Kamala-Kannan S, Sudhakar C, Ameen F, Sabri AA, Selvam K, Govarthan M, Kim H (2018) Utilization of vegetable waste for silver nanoparticles synthesis and its antibacterial activity. Mater Lett 225:101–104. https://doi.org/10.1016/j.matlet.2018.04.111

Rolim WR, Pelegrino MT, de Araújo LB, Ferraz LS, Costa FN, Bernardes JS, Rodigues T, Brocchi M, Seabra AB (2019) Green tea extract mediated biogenic synthesis of silver nanoparticles: characterization, cytotoxicity evaluation and antibacterial activity. Appl Surf Sci 463:66–74. https://doi.org/10.1016/j.apsusc.2018.08.203

Sampath G, Govarthanan M, Rameshkumar N, Vo DVN, Krishnan M, Sivasankar P, Kayalvizhi N (2021) Eco-friendly biosynthesis metallic silver nanoparticles using *Aeglemarmelos* (Indian bael) and its clinical and environmental applications. Appl Nanosci. https://doi.org/10.1007/s13204-021-01883-8

Saxena A, Tripathi RM, Zafar F, Singh P (2012) Green synthesis of silver nanoparticles using aqueous solution of *Ficus benghalensis* leaf extract and characterization of their antibacterial activity. Mater Lett 67:91–94. https://doi.org/10.1016/j.matlet.2011.09.038

Sengottaiyan A, Mythili R, Selvankumar T et al (2016) Green synthesis of silver nanoparticles using *Solanum indicum* L. and their antibacterial, splenocyte cytotoxic potentials. Res Chem Intermed 42:3095–3103

Singh P, Kim YJ, Singh H, Mathiyalagan R, Wang C, Yang DC (2015) Biosynthesis of anisotropic silver nanoparticles by *Bhargavaea indica* and their synergistic effect with antibiotics against pathogenic microorganisms. J Nanomater. https://doi.org/10.1155/2015/234741

Sukweenadhi J, Setiawan KI, Avanti C, Kartini K, Rupa EJ, Yang DC (2021) Scale-up of Green synthesis and characterization of silver nanoparticles using ethanol extract of *Plantago major* L. leaf and its antibacterial potential. S Afr J Chem Eng. https://doi.org/10.1016/j.sajce.2021.06.008

Thomas SC, Mishra PK, Talegaonkar S (2015) Ceramic nanoparticles: fabrication methods and applications in drug delivery. Curr Pharm Des 21(42):6165–6188

Turkmen N (2017) The nutritional value and health benefits of goat milk components. J Funct Foods. https://doi.org/10.1016/B978-0-12-809762-5.00035-8

Üçüncü M (2013) Süt ve Mamülleri Teknolojisi. Meta Basım, İzmir

Valarmathi N, Ameen F, Almansob A, Kumar P, Arunprakash S, Govarthanan M (2020) Utilization of marine seaweed *Spyridia filamentosa* for silver nanoparticles synthesis and its clinical applications. Mater Lett 263:127244

Veeraraghavan VP, Periadurai ND, Karunakaran T, Hussain S, Surapaneni KM, Jiao X (2021) Green synthesis of silver nanoparticles from aqueous extract of Scutellaria barbata and coating on the cotton fabric for antimicrobial applications and wound healing activity in fibroblast cells (L929). Saudi J Biol Sci. https://doi.org/10.1016/j.sjbs.2021.05.007

Zhao H, Hou L, Lu Y (2016) Electromagnetic interference shielding of layered linen fabric/polypyrrole/nickel (LF/PPy/Ni) composites. Mater Des 95:97–106. https://doi.org/10.1016/j.matdes.2016.01.088

Publisher's Note Springer Nature remains neutral with regard to jurisdictional claims in published maps and institutional affiliations.

ISSN 2349-5359(Online) ISSN 2454-9967(Print)

Laccase Enzyme in Nanotechnology and their Environmental Applications

Authors: P. Srinivasan, P. Thiyagarajan, R. Yuvarajan, , T. Selvankumar

https://doi.org/10.29294/IJASE.8.2.2021.2210-2218

Published: 15 Nov 2021

0

Abstract :

Laccases are ligninolytic enzyme which belongs to the blue multicopper oxidases and participates in the degradation of polymers, and band cleavage of composite aromatic compounds. At present, laccases are commercially produced form bacteria, fungi and plants. These enzymes have wide applications in paper and pulp industries, food industry, textile industry and pharmaceutical industries. Laccases also impart in soil bioremediation, removal of toxic substances like herbicides, pesticides and dye degradation. Due to the wide range purpose, industries have more attention to the isolation and identification of high laccase yielding organisms to fulfil the demand of the enzyme needs. Hence, the present review is to emphasize the properties and applications of laccase in industrial and environmental applications for the removal of

PRINCIPAL
PGP College of Arts and Science
Namakkal

REVIEW ARTICLE

Laccase Enzyme in Nanotechnology and their Environmental Applications

P. Srinivasan, P. Thiyagarajan, R. Yuvarajan, T. Selvankumar*
PG & Research Department of Biotechnology, Mahendra Arts and Science College (Autonomous), Kalippatti, Namakkal - 637501, Tamil Nadu, India

ABSTRACT: Laccases are ligninolytic enzyme which belongs to the blue multicopper oxidases and participates in the degradation of polymers, and band cleavage of composite aromatic compounds. At present, laccases are commercially produced form bacteria, fungi and plants. These enzymes have wide applications in paper and pulp industries, food industry, textile industry and pharmaceutical industries. Laccases also impart in soil bioremediation, removal of toxic substances like herbicides, pesticides and dye degradation. Due to the wide range purpose, industries have more attention to the isolation and identification of high laccase yielding organisms to fulfil the demand of the enzyme needs. Hence, the present review is to emphasize the properties and applications of laccase in industrial and environmental applications for the removal of pesticides, dye decolorization, phenols and non-phenolic degradation of environmental pollutants.

KEYWORDS: Enzymes, Environment, Immobilization, Industrial applications, Microbes, Laccase.

https://doi.org/10.29294/IJASE.8.2.2021.2210-2218 **©2021 Mahendrapublications.com, All rights reserved**

1. INTRODUCTION

Enzymes are the biocatalysts playing an important role in accelerating chemical reactions in all stages of metabolism of the living organism. The enzymes particular attention on are called substrates, and the enzyme converts the substrates into diverse molecules known as products. The microbial enzyme research has regularly been updated and increased significantly in the 21st century; studies on their screening, stability, characterization of properties, production on bench-scale to pilot-scale and their application in bio-industry have continuously progressed. Many of the enzymes from microbial sources are already being used in various industrial intermediates. Selected microorganisms including yeast, bacteria and fungi have been globally studied for the synthesis of various enzymes for commercial applications [1]. A large number of industrial need enzymes have been optimized and designed with the input of biochemical engineering, protein engineering, and metagenomics [2].

Laccases (benzenediol: oxygen oxido reductase, EC 1.10.3.2) belong to a large group of enzymes called polyphenol oxidases including multi-copper atoms in the catalytic core and are generally called multicopper oxidases. Three types of copper atoms exist in these enzymes, one of which is accountable for their distinctive blue color. Classically laccase-mediated catalysis occurs with the reduction of oxygen to water adjunct by the oxidation of the substrate. Laccase enzyme productions are broadly disseminated in higher plants and fungi and have also been found in bacteria and insects. In plants Pears, cabbages apples, potatoes and other vegetables is possessed laccase enzyme. They are used for many biocatalytic applications in various biotechnological and industrial domains which have been included biosynthesis of intermediates, improving fibers properties, energy exploitation, bio-detection, environmental protection, degradation and assimilation of synthetic dyes, printing and dyeing industry, bio-pulping in the paper industry, separation of aromatic compounds [3], and degradation of phenols compounds it causes cancer and teratogenicity which was in wastewater. Also, Laccases are used as toothpaste, detergent, soap, mouthwash and diapers in cosmetics such as deodorants for these fast-moving consumer goods, in beverage and food industry for the preparation of wine and juice stabilization characterization [4-6], in dough or baked products to increase the strength of gluten structures; in pharmaceutical industries as anesthetics, anti-inflammatory drugs, antibiotics, and sedatives; and in nanobiotechnology as nanoparticles based biosensors.

Recently, laccases enzymes are not able to exploit full growth efficiency under harsh environmental conditions. Also, wild novel strains which have been tolerated in harsh conditions and produced the highest laccase enzyme with minimum energy consumption in the process are

*Corresponding Author: selvankumar75@gmail.com
Received: 15.09.2021 **Accepted:** 16.10.2021 **Published on**: 15.11.2021

in huge advantages with higher demand. Biotechnological applications of laccase have been extended from laccase-mediator systems, which have provided the ability to oxidize non-phenolic compounds that are otherwise hard or not oxidized o reduced by the enzyme lone.

The flourishing application of laccases in declared areas would necessitate the production of maximum quantity at minimized costs. Abundant production approaches can be adopted as well as media and process optimization to accomplish enhanced process economics. At the same time, over a phrase or disparity expression of laccase in suitable host organisms *Bacillus sp.* would provide means to achieve high titers. Use of inducers such as apple pomace, yeast extract and copper could also enhance production capabilities [7]. The present review is making an effort to provide collective data on various aspects of laccase production and also describes the structure and characterization, catalytic mechanisms and application of laccase industrial and environmental applications

1.1. Sources of laccases

1.1.1. Bacteria

Laccase producing bacterial species was first discovered in rice rhizosphere and identified as *Azospirillumlipoferum*[8].Later, laccase has been identified from a broad range of bacterial species in various genera [9-25]. Bacterial laccases are more prevalent in industrial and environmental applications due to their availability, flexibility, thermostability, alkalineoptimum and radiance tolerance. Moreover, it has low redox potentials and also widely used in decolorization of dyes, bioleaching of paper and pulp industries [26, 27].

1.1.2. Fungi

Laccase production has been reported in many fungal species. The premier laccase producing fungi are *Ascomycetes* and followed by *Zygomycetes* and *Chytridiomycetes*. The genus *Ascomycetes* are phytopathogens and isolated from soil, freshwater, wood logs on degradation. The laccase enzyme producers are more prevalent in fungi than plants. Fungal laccases are noticed in together intra and extra-cellular physiological processes of pathogenesis, delignification, pigmentation, and morphogenesis [28]. Recently, researchers are focus on screening of laccase producing novel fungal wild species and researched developing higher yield stains to meet out the demands of industries. The higher yield wild fungal laccase producers are *Basidiomycete* families. The researchers are carried out on the wild strains critically and carried out the experiments on genetic material sequences; phylogenetic relationship, catalytic property, and expression regulation of laccase isozymes systems [29,30].

1.1.3. Plants

The plant laccase was first isolated from the Japanese lacquer tree *Rhusvernicifera*. They are generally spread in a wide range of upper plants. The plant laccase enzyme activities have been pragmatic in trees, apples, turnips, cabbages, potatoes and asparagus [31]. These enzyme gene families in plants are still better than fungal laccase families. For case, rice (*Oryza sativa*) found to have at slightest 22 laccase genes [32]. *Arabidopsis thaliana,* the model plant has 17 gene members in its laccase family, which play many roles in plant enlargement and progress, depend upon the mutant characterization and expression profiling [33].

1.1.4. Insects

Insect laccases are the least characteristic of all identified laccases. Insect laccases have an important role in cuticle sclerotization and melanization of the physiological functions of the insect life cycle [34-37].

1.2. Enzyme production by fermentation

The large-scale production of laccase enzyme could be achieved by fermentation processes. They are i) Submerged fermentation and ii) Solid-state fermentation.

1.2.1. Submerged fermentation

Submerged fermentation process contains the microbial growth in a liquid medium supplemented with nutrients in aerobic conditions. The manufacturing production of enzymes is mainly achieved by submerged cultivation. The perfect of nutritional and ready conditions is the first step to be intense to achieve high production. Waste and cheap raw materials from many resources are used in huge amounts can be employed in submerged cultivation. These resources have important concentrations of all the soluble elements and even inducers for laccase production [28]. The natural raw materials are the nutrient sources in submerged fermentation, which cause glutinousness nature of production medium and subsidize the production and downstream process by hampering impeller action causing obstructions consequential in restrictions of oxygen and mass transfer [33].

1.2.2. Solid-State fermentation

SSF is a suitable method for the industrial enzyme production using natural substrates such as agricultural residues because they impersonate the environmental surroundings under which the fungi grow in nature. Laccase enzyme production

makes the most of many agricultural wastes as substrates such as pearl millet, finger millet, grape seeds, grape stalks, cone, cotton stalk, barley bran, molasses and wheat bran [37]. As compared to the additional substrates, rice bran found to produce maximum laccase enzyme by SSF [18]. Solid substrate cultivation is cost-effective as well as low-cost substrates are being utilized for enzyme production. However, there are few disadvantages or limits for growing microorganisms in SSF that includes the minimal transfer of oxygen, nutrients, moisture, and temperature and pH regulation due to the absence of any established fermentor designs [26].

1.3. Optimization of enzymes production

Optimization is one of the major strategies for obtaining a maximum yield of industrial enzymes within the limiting factors. The high yield strains are subjected to optimize with various parameters for an optimal yield of products. In laccase enzyme, the high yield stains are designed with molecular cloning techniques and the improved strains are subjected to optimization of media, environmental, physical conditions and stress conditions. The industrial production of laccase enzymes is highly influenced by media components and other conditions such as temperature, pH and agitation [38]. The optimization procedure gives enough information to scale-up the fermentation process in design and optimizing of the suitable fermentation medium with medium nutrient composition, product concentration, yield and volumetric productivity for industrial applications. It has been well documented that media components and physical factors greatly influence the production of enzymes in microorganisms and their interaction plays a significant part in the biogenesis of these enzymes.

Media optimization is frequently done to retain an explicit ratio among various medium components, however, it was completely utilized by fungi or bacteria on other hand obtain a cost-effective and prevent the wastage of medium components, while metabolite yield at the closing stages of fermentation. There are many experimental strategies available for optimization of enzymes and metabolites production from microbial sources. Optimization of media compounds by fixed "one-variable-at a-time" strategy by optimization of fermentation media compounds by traditional involving changing one independent uneven on a point in time, most commonly used act in fermentation technology. This plan varies in time and costly as soon as a massive number of factors variables are measured and is unable of detecting the true most favorable, due mainly to the connections amongst the factor [39].

1.3.1.Response Surface Methodology (RSM)

RSM is a group of statistical and numerical techniques helpful for increasing, humanizing and optimizing process in which a reaction of attention is partial by some variables and the purpose is to optimize this response. RSM has important appliance in the design, advance and preparation of novel industrial enzyme yield, as well as in the development of open product design process. Processes define the most efficacies of the free variables, only or here mixture. In accumulation to analyze the special effects of the free variables, this experimental method generates a numerical model which describes the chemical compound or biochemical processes [40-43].

RSM is usually achieved by real-time testing of many factors in the limited numeral of experiments. In data, the purposeful report among the needy and the free variables can be firm by using regression investigation which also explains the significance of the variables [39].

1.3.2. Purification of laccase

Generally, plant laccases are extracted and purified from tissues. Whenever the bacteria are utilized for the laccase production, the extracellular enzyme extracted from the medium followed by the purification process. Two operations were followed for the complete down-streaming process, in which primary operation is solid/liquid medium segregation by filtration and centrifugation. This step will be followed by dewatering, which can be carried using the salting-out precipitation method with ammonium sulphate salt [44]. The second stage of enzyme purification is achieved using ion exchange and gel filtration chromatographic techniques. Purification may be a single or multi-step process. Other works include purification of laccase from *Bacillus* sp. with ethanol precipitation, Phenyl Sepharose, DEAE-Sepharose. After separation, enzyme processing is carried out through immobilization techniques.

1.3.3. Immobilization

The term 'immobilized enzymes' refers to 'enzymes physically attached to an inert assured definite area of space with preservation of their catalytic activities, and which can provide increased conflict to change in surroundings much as pH or temperature. Besides a more easily convenient handle care of the enzyme, it also substantially simplifies the manipulation with the biocatalytic reaction and the control of the preservation process [45] while enhancing the enzyme stability under both storage and

operational conditions. Immobilization provides a facile separation of the enzyme from the product [46-48], hence protein contamination of the product is minimized or avoided altogether. Apart from the easy separation of the enzyme from a mixture of sodium alginate solution with calcium chloride, enzyme immobilization (entrapment) also remarkably reduces the cost of enzyme and the enzymatic immobilized products. Insolubilization of the enzyme by attachment to a matrix also imparts several added benefits such as; restrict the freedom of movement of an enzyme from the reaction solution and value of enzyme stability against solvents, pH, temperature, contaminants and impurities. Which is also helps for the highest recovery and reuse of more active enzymes and enable their application in continuous fixed-bed operation in fermentation. It is possible to conclude that enzyme immobilization increases the productivity of the biocatalysts and enhances their features, making them more attractive for diverse applications.

1.4. Laccase Immobilization

Laccases are immobilized for various reasons including recycling, stability during the operation process, and resistance to application conditions. The factors responsible for activity improvement depend upon different factors nature of the laccase enzyme, desired method of immobilization and preparation parameters. The immobilized microbial laccases are more broadminded to high temperatures, storage and can be reused multiple times when compared with their free enzyme counterparts [49, 50]. They are also found to be more resistant to inhibitors such as NaCl. Even though there are some limitations such as reduced enzyme flexibility, and diffusion limitations, immobilization method can improve the catalytic activity of microbial laccases occasionally.

1.4.1. Magnetic metal nanoparticles

Magnetic metal nanoparticles have been utilized in enzyme immobilization because of their precise properties together with superparamagnetic, excessive surface area, huge surface-to-quantity ratio, and easy separation under outside magnetic fields [51]. Another key issue to take complete advantages of nanoparticles such as MNPs is the way to ideally modify the orientation of the enzymes on the supports. Compared to porous supports, non-porous nanoparticles have no external diffusion problems, making them more competitive especially for large scale industrial usage in solid-liquid systems (e.g., precipitated protein). The frequently utilized MNPs are iron oxides, among which superparamagnetic Fe_3O_4 nanoparticles are the most prevalent materials because they have low toxicity, good biocompatibility [32,33].

1.4.2. Preparation of magnetic nanoparticles

MNPs can be produced by physical, chemical and biological methods: (i) physical methods [45,46], such as gas-phase evidence and electron beam lithography; (ii) dripping chemical preparation methods, such as sol-gel synthesis [52], oxidation method [53,54], chemical co-precipitation, hydrothermal reactions [55], flow injection synthesis [56], electrochemical method, aerosol/vapor phase method sonochemical breakdown reactions [57], the supercritical fluid method [58], synthesis using nanoreactors [59] and (iii) microbic methods [60,61]. Since the physical and chemical nature has decisive results at the applicability of magnetic nanoparticles, comprehensive surface characterization strategies are utilized for higher expertise of the surface properties together with chemical composition, surface morphology, and spatial distribution of the functional groups.

1.4.3. Enzyme immobilization methods

Traditionally, the selection of an appropriate immobilization approach is a very crucial part of the immobilization process as it performs the largest role in determining the enzyme activity and characteristics in a selected response. Immobilization techniques can be divided into two major characterizations namely, the chemical and physical methods. Although, there are four main principal techniques used for the immobilization of enzymes specifically, Adsorption, Entrapment, Covalent and Cross-linking [53].

1.5. Applications of Laccase

In the last few decades, enzyme-like laccases have much important attention from many researchers due to their ability to highly recalcitrant environmental pollutants and oxidize both phenol, non-phenol lignin related compounds. One of the main applications of detoxification of dye-containing industrial effluents from textile and leather industries by laccases, on the other hand over pulp bioleaching, and use as a tool in the pharmacy industry and as a bioremediation agent to dirt-free up herbicides, pesticides and certain explosive in soil [58] [Fig.1]. Water purification systems laccases are also used as clean-up agents, as catalysts for the manufacture of anti-cancer drugs and even as ingredients in cosmetics. Laccases also find application in the food industry that includes beverage (fruit juice, wine and beer) processing, sugar beet pectin gelation, baking etc.

.

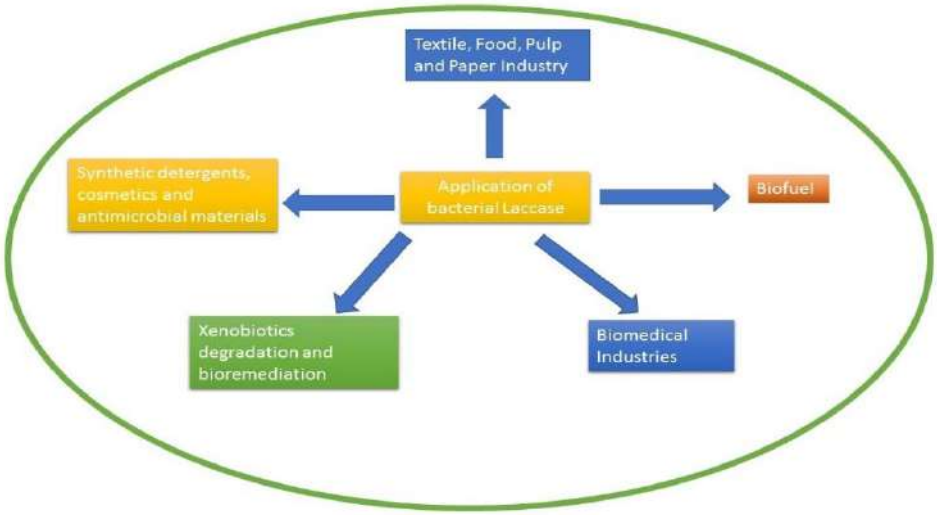


Fig.1. Applications of bacterial laccase

1.5.1. Bioremediation

The association of laccase in biodegradation was specifically because of its catalytic properties. Laccase is used for decolorizing dye residence effluents which capacity is rarely decolorized from side-to-side conventional dirt behavior foliage. The xenobiotic compound present in contaminated soil, polycyclic aromatic hydrocarbons (PAHs) in natural oil deposits and fossil fuels have been easily degraded utilizing laccase. Laccase becomes determined to be dependable for the change of 2, 4, 6-trichlorophenol to 2, 6-dichloro-1, 4-hydroquinone and 2, 6-dichloro-1, 4-benzoquinone. Laccase arbitrate system has been also used to oxidize dibenzothiophene ethyl-carbazole, carbazole, fluorine and alkenes [57, 58]. LMS has been considerably used for the oxidation of recalcitrant polycyclic aromatic hydrocarbons such as naphthalene, having two aromatic rings, and the three-ring compounds anthracene, phenanthrene and several other contaminants [54].

1.5.2. Dyedecolorization

The application of laccases in dye decolourization has enlarged in modern years and many studies have been confirmed for dye decolourization using both crude and purified forms of laccase. Some of the portion of the organic compound as redox mediators facilitate the laccase dye degrading activity and enhance its specificity to a wide range of synthetic dyes [38]. Laccases have been used for the decolorization of dyes belonging to different categories such as azo, anthraquinone, heterocyclic, triphenylmethane dyes etc. Many studies were carried for the degradation of azo dyes by microbial laccases [58].

1.5.3. Pharmaceutical Applications

The application and stability of laccases in the pharmaceutical industry have been exploited due to their specificity and bio-based nature suggested that microbial laccases may be utilized for the synthesis of the drug of anti-inflammatory, anesthetics and sedatives [45]. Pharmaceuticals and Personal Care Products (PPCPs) are detected in municipal wastewater. Laccase-catalyzed reactions are employed for the removal of PPCPs [62]. Laccase from *Myceliophthora thermophila* is used in the degradation of several anti-inflammatory drugs (diclofenac and naproxen) and estrogen hormones. Laccase from *Clitocybe maxima* exhibited anti-proliferative activity against Hep G2 and MCF-7 tumour cells [65]. Laccases are used as markers in immunological, histochemical and cytochemical assays by covalent conjugation with binding molecules.

1.5.4. Phenol removal

Removal of phenols and phenolic compounds in aqueous effluents release from industry is an important practical problem for the environment, therefore virtually all phenols are toxic and their presence in several industrial wastewaters is a health hazard [45]. The use of free laccase, tyrosinase and peroxidase, which catalyse the oxidative coupling of phenol compounds resulting in the formation of water-insoluble oligomeric and polymeric products which are then removed by sedimentation or filtration, has been proposed [48].

1.5.5. Pulp bioleaching

The major problem encountered in the pulping process is the characteristic brown color of the pulp due to the presence of residual lignin [54]. The chemical processes are usually employed in the industries for the removal of lignin and hemicelluloses from the pulp thereby the brightness of the pulp is achieved. Although the chemical treatments are an effective method to achieve this task, the high cost and related pollution harms make them unattractive [56]. In this method is the eco-friendly treatment of pulp that involves either microorganisms or their enzymes called Bioleaching. This process helps in the selective removal of lignin and hemicelluloses components without degrading cellulose. Cellulases and xylanases are the most widely used microbial enzyme for bioleaching however, the role of laccases in the process has also been elucidated in the recent year's application [57].

1.5.6. Paper industry

In the industrial preparation of the paper, the degradation and separation of lignin in wood pulp are conventionally obtained using oxygen or chlorine-based chemical oxidants. Enzymatic treatment of method like non-chlorine bleaching of pulp obtained brighter pulp with low lignin content [60]. Since wood and other soil materials are naturally degraded by biological origin, the use of lignin-degrading enzymes of laccases would provide a new alternatives approach in pulp and paper industries. Employing microbial laccase in lingo cellulosic fibers will improve the physical properties and chemical of Kraft pulp fibre products [61]. Bacterial laccases from *Streptomyces cyaneus* CECT 3335 and *Pseudomonas stutzeri*have been examined for bio-bleaching of eucalyptus kraft pulps using HOBT (Hydroxybenzotriazole) and ABTS as redox mediators.

1.5.7. Nanotechnology

The ability of laccases to catalyze electron transfer reactions without additional cofactors is being employed in biosensors. Biosensors also containing laccase have been developed for immune, histochemical and cytochemical assays used for the determination of glucose, aromatic amines and phenolic compounds. Laccases are immobilized on various substrates composed of pyrolytic graphite, ceramics supports and carbon fibres which can be used as electrodes [62]. The redox potential of laccases is also utilized in the biofuel cell to provide power for small transmitter systems. Biofuel cells do not require proton exchange membrane like in a traditional fuel cell due to the specificity of the laccase enzyme. Coupling the laccases with nanoparticles can further increase the laccase activity in the biofuel cells [63]. Laccase-based biofuel cell is also used in therapeutic applications for providing power to cells source implanted in a human body.

CONCLUSION

Laccases are highly versatile enzymes and are involved in the degradation of a range of complex and recalcitrant compounds and thus find application in an extensive range of industries. The biotechnological importance of laccases has led to a drastic boost in the demand for these enzymes and oriented the interest of scientists towards the same in recent years. The present study thus focuses on the isolation of laccase producing organisms and large-scale productions of laccases using inexpensive sources like agro-wastes. In this regard, inexpensive raw wastes will be explored for maximizing laccase production under submerged and solid-state fermentation. It is also described the optimization procedures and catalytic properties of laccase enzyme with immobilization with magnetic nanoparticles. This review also highlights the potential use of pharmaceutical applications and cleanup of environment for the removal of pesticides, dye decolourization, removal of phenolic compounds, paper and pulp industries. This review helps to understand the properties of laccase enzymes in nanotechnology for biosensor and biofuel cell development.

Acknowledgements

This work is partially supported by the Department of Biotechnology, Mahendra Arts and Science College (Autonomous), and the Department of Science and Technology, Government of India (DST-FIST sponsored—Ref. No. SR/FST/College-232/2014).

REFERENCES

[1] Pang,S., Wu, Y.,Zhang, X.,Li, B., Ouyang, J.,Ding, M., 2016. Immobilization of laccase via adsorption onto bimodal mesoporous Zr-MOF, Process Biochem. 51(2), 229–239.

[2] Chirumamilla, R.R.,Muralidhar, R., Marchant, R., Nigam, P., 2001. Improving the quality of industrially important enzymes by directed evolution, Mol Cell Biochem. 224, 159–165.

[3] Zheng, F., Cui, B.K., Wu, X.J.,Meng, G., Liu, H.X., Si, J., 2016. Immobilization of laccase onto chitosan beads to enhance its capability to degrade synthetic dyes, Int BiodeteriorBiodegrad. 110, 69–78.

[4] Surwase, S.V., Patil, S.A., Srinivas, S., Jadhav, J.P., 2016. Interaction of small molecules with fungal laccase: a surface plasmon resonance based study, Enzyme Microb

Technol., 82, 110–114.

[5] Alper, N.,Acar, J., 2004. Removal of phenolic compounds in pomegranate juices using ultra filtration and laccase-ultra filtration combinations, Food/Nahrung. 48(3), 184–187.

[6] Piacquadio, P., De Stefano, G., Sammartino, M., Sciancalepore, V., 1998. Apple juice stabilization by laccase immobilized on metal chelate regenerable carriers, IndustriedelleBevande. 27, 378–83.

[7] Zhu, M., Zhang, G.,Meng, L.,Wang, H., Gao, K., Ng, T., 2016. Purification and characterization of a white laccase with pronounced dye decolorizing ability and HIV-1 reverse transcriptase inhibitory activity from *Lepistanud,* Molecules. 21(4), 415.

[8] Givaudan, A., Effosse, A.,Faure, D., PotierP.,Bouillant, M.L., Bally, R., 1993. Polyphenol oxidase in *Azospirillumlipoferum* isolated from rice rhizosphere: evidence for laccase activity in non-motile strains of *Azospirillumlipoferum*, FEMS Microbiol Lett. 108(2), 205–210.

[9] Thakker, G. D., Evans, C. S., Koteswara Rao, K., 1992."Purification and characterization of laccase from *Monocillium indicum Saxena*, Applied Microbiology and Biotechnology, 37 (3), 321–323.

[10] BinzT.,Canevascini, G., 1997. Purification and partial characterization of the extracellular laccase from *Ophiostomanovoulmi,* Current Microbiology, 35 (5), 278–281.

[11] Edens, W. A., Goins, T. Q.,Dooley, D., Henson, J. M., 1999. Purification and characterization of a secreted laccase of *Gaeumannomycesgraminis* var. tritici, Applied and Environmental Microbiology, 65 (7), 3071–3074.

[12] FroehnerS. C., Eriksson, K. E., 1974. Purification and properties of *Neurospora crassa* laccase, Journal of Bacteriology, 120 (1), 458–465.

[13] IyerG.,Chattoo, B. B., 2003.Purification and characterization of laccase from the rice blast fungus, *Magnaporthe grisea*, FEMS Microbiology Letters, 27 (1) 121–126.

[14] Kiiskinen, L. L.,Viikari, L.,Kruus, K., 2002. Purification and characterisation of a novel laccase from the ascomycete *Melanocarpusalbomyces*, Applied Microbiology and Biotechnology, 59 (2), 198–204.

[15] MolitorisH. P., Esser, K., 1970.The phenoloxidases of the ascomycete *Podospora anserina* Properties of laccase I after further purification, Archives of Microbiology, 72 (3), 267–296.

[16] Isono, Y., Hoshino, M.,1989. Laccase-like activity of nucleoside oxidase in the presence of nucleosides. Agric Biol Chem 53, 2197-2203.

[17] Lee, Y.A., Hendson, M., Panopoulos, N.J.,Schroth, M.N., 1994. Molecular cloning, chromosomal mapping and sequence analysis of copper resistance genes from *Xanthomonas campestris* pv. juglandis: Homology with small copper proteins and multicopper oxidases, J Bacteriol, 176, 173-188

[18] Diamantidis, G.,Effosse, A.,Potier, P., Bally, R., 2000.Purification and characterization of the first bacterial laccase in the rhizospheric bacterium *Azospirillumlipoferum*, Soil Biol Biochem 32, 919-927.

[19] Solano, F.,Lucas Elio,P., Lopez SerranoD., Fernandez, E.,Sanchez Amat,A., 2001. Dimethoxyphenyl oxidase activity of different microbial blue multicopper proteins, FEMS Microbiol Lett, 204, 175-181.

[20] Hullo, M.F., Moszer, I., Danchin, A., Martin-Verstraete I., CotA of *Bacillus subtilis* is a copper-dependent laccase, J Bacteriol, 183 (2001) 5426-5430.

[21] Francis, C.A.,Tebo, B.M.,2001. *CumA* multi copper oxidase genes from diverse Mn(II)-oxidizing and non-Mn(II)-oxidizing *Pseudomonas strains*, Applied Environ Microbiol, 67, 4272-4278.

[22] Kim, C.,Lorentz, W.W.,Hoopes, J.T.,Dean, F.F., 2001.Oxidation of phenolate siderophores by the multicopper oxidase encoded by the *Escherichia coli* yacK gene, J Bacteriol, 183, 4866-4875.

[23] Fitz-Gibbon, S.T.,Ladner, H.,Kim, U.J.,Stetter, K.O.,Simon M.I., Miller, J.H., 2002. Genome sequence of the hyperthermophilic crenarchae on *Pyrobaculum aerophilum*. Proc Natl Acad Sci 99, 984-989.

[24] Cai, X., Davis, E.J., Ballif, J., Liang, M., Bushman, E.,Haroldsen, V., 2006. Mutant identification and characterization of the laccase gene family in Arabidopsis, J Exp Bot,57, 2563–2569.

[25] Turlapati, P.V., Kim, K.W., Davin, L.B.,Lewis, N.G.,2011. The laccase multigene family in Arabidopsis thaliana: towards addressing the mystery of their gene function(s). Planta 233, 439–470.

[26] Singh, G.,Bhalla, A., Kaur, P.,Capalash, N.,Sharma, P., 2011.Laccase from prokaryotes: a new source for an old enzyme, Rev Environ Sci Biotechnol. 10, 309–326.

[27] Chandra, R., Chowdhary, P.,2015. Properties of bacterial laccase and their application in bioremediation of industrial wastes, Environ Sci Process Impacts. 17, 326–342.

[28] Arora, D.S., Sharma, R.K., 2010.Ligninolytic fungal laccase and their biotechnological applications, Appl BiochemBiotechnol. 160 (6), 1760–1788.

[29] Yang, J.,Xu, X.,Yang, X.,Ye, X.,Lin, J., 2016,Cross-linked enzyme aggregates of Cerrena laccase: preparation, enhanced NaCl tolerance and decolorization of Remazol Brilliant Blue Reactive, J Taiwan Inst Chem Eng. 65, 1–7.

[30] Faraco, V., Pezzella, C., Giardina, P.,Piscitelli, A.,Vanhulle, S.,Sannia, G., 2009.Decolourization of textile dyes by the white-rot fungi *Phanerochaetechrysosporium* and *Pleurotusostreatus,* J Chem Technol Biotechnol. 84, 414–419.

[31] Madhavi, V., Lele, S.S.,2009. Laccase: properties and applications, Bioresour Technol. 4(4), 1694–1717.

[32] Huang, M.T., Lu, Y.C.,Zhang, S., Luo, F.,Yang, H., 2016. Rice (*Oryza sativa*) laccases involved in modification and detoxification of herbicides atrazine and isoproturon residues in plants, J Agric Food Chem. 64, 6397–6406.

[33] Balasubramanian, V.K., Rai, K.M.,Thu, S.W.,Hii, M.H.,Mendu, V., 2016.Genome-wide identification of multifunctional laccase gene family in cotton (*Gossypium* spp.); expression and biochemical analysis during fiber development, Sci Rep .6, 34309.

[34] Dittmer, N.T.,Kanost, M.R., 2010.Insect multicopper oxidases: diversity, properties, and physiological roles, Insect Biochem Mol Biol. 40, 179–188.

[35] Jeon, J.R., Baldrian, P., Murugesan, K.,ChangY.S., 2012. Laccase-catalysed oxidations of naturally occurring phenols: from *in vivo* biosynthetic pathways to green synthetic applications, MicrobBiotechnol. 5, 318–332.

[36] Ni, J., Tokuda, G., 2013.Lignocellulose-degrading enzymes from termites and their symbiotic microbiota, Biotechnol Adv. 31, 838–850.

[37] Cazetta ML, Celligoi MAPC, Buzato JB, Scarmino IS (2007) Fermentation of molasses by *Zymomonasmobilis*: Effects of temperature and sugar concentration on ethanol production. Bioresour Technol 98:2824–2828.

[38] Selvam, K.,Govarthanan, M.,Kamala-Kannan, S.,Govindharaju, M.,Senthilkumar, B.,Selvankumar, T., Sengottaiyan, A., 2014.Process optimization of cellulase production from alkali-treated coffee pulp and pineapple waste using *Acinetobacter* sp. TSK-MASC, RSC Adv. 4 (2014) 13045.

[39] Selvam, K., Govarthanan, M.,Senthilkumar, B.,Senbagam, D.,Selvankumar, T.,Kamala-Kannan, S.,Sudhakar, C., 2016.Optimization of protease production from surface modified coffee pulp waste and corncobs using *Bacillus* sp. by SSF, 3 Biotech. 6, 167.

[40] Selvam, K.,Selvankumar, T.,Radhika, R.,Srinivasan, P.,Sudhakar, C.,Senthilkumar, B.,Govarthanan, M., 2016. Enhanced production of amylase from *Bacillus sp*. Using groundnut shell and cassava waste as a substrate under process optimization: waste to wealth approach, Biocatal Agric iotechnol. 7, 250–256.

[41] Srinivasan, P., Selvankumar, T., Kamala–Kannan, S.,Mythili, R.,Sengottaiyan, A.,Govarthanan, M., Senthilkumar, B.,Selvam, K., 2019.Production and purification of laccase by *Bacillus* sp. using millet husks and its pesticide degradation application, 3 Biotech. 245 (9), 396.

[42] Hernandez, R. Fernandez Lafuente, 2011. Control of protein immobilization: coupling immobilization and site-directed mutagenesis to improve biocatalyst or biosensor performance, Enzyme Microb Technol. 48(2)107–122.

[43] Asuri, P.,Karajanagi, S.S.,Sellitto, E.,Kim, D.Y., Kane, R.S.,Dordick, J.S., 2006.Water-soluble carbon nanotube-enzyme conjugates as functional biocatalytic formulations, Biotechnol Bioeng. 95(5) (2006) 804–811.

[44] Sheldon, R.A., 2007.Cross-linked enzyme aggregates (CLEAs): stable and recyclable biocatalysts, Biochem Soc. 35(6), 1583–1587.

[45] Sedarati, R.,Keshavarz,T., A. Leontievsky, S. Evans, Transformation of high concentrations of chlorophenols by the white-rot basidiomycete *Trametes versicolor* immobilized on nylon mesh, Electron J Biotechn. 6(2) (2003) 104–114.

[46] Fernández-Fernández,M., Sanromán, M.A.,Moldes, D., 2013.Recent developments and applications of immobilized laccase, Biotechnol Adv. 31, 1808–1825.

[47] Asgher, M., Shahid, M.,Kamal, S.,Iqbal, H.M.N., 2014.Recent trends and valorization of immobilization strategies and ligninolytic enzymes by industrial biotechnology, J Mol Catal B Enzym. 101, 56–66.

[48] Laurent, D.,Forge, M.,Port, A.,RochC., Robic, L.,Vander Elst,R.N., 2008. Muller Magnetic iron oxide nanoparticles: synthesis, stabilization, vectorization, physicochemical

characterizations, and biological applications, Chem Rev. 108 (6), 2064–2110.

[49] Guo,X., Yuan, S.,Yang, S.,Lv, K.,Yuan, S., 2011.Mesoscale simulation on patterned core–shell nanosphere model for amphiphilic blocks copolymer, Colloid Surf A. 384, 212–218.

[50] Liu, R.,Li, D.,He, B.,Xu, X.,Sheng, M.,Lai, Y.,Wang, G.,Gu, Z., 2011.Anti-tumor drug delivery of pH-sensitive poly(ethylene glycol)-poly(L-histidine-)-poly(L-lactide) nanoparticles, J Control Release. 152, 49–56.

[51] Rishton,A., Lu, Y.,Altman, R.A.,Marley, A.C.,BianHahnes, C.,Viswanathan, R.,Xiao, G.,GallagherW.J., Parkin, S.S.P., 1997. Magnetic tunnel junctions fabricated at tenth-micron dimensions by electron beam lithography, Microelectron Eng. 35, 249–252.

[52] Mathur, S., Barth, S.,Werner, U.,Hernandez-Ramirez, F., Romano-Rodriguez, A., 2008.Chemical Vapor Growth of One-dimensional Magnetite Nanostructures, Adv Mater., 20, 1550–1554.

[53] Itoh, H.,Sugimoto, T.J., 2003.Systematic control of size, shape, structure, and magnetic properties of uniform magnetite and maghemite particles, J Colloid Interface Sci. 265, 283–295.

[54] Amemiya, Y.,Arakaki, A.,Staniland, S.S.,Tanaka, T.,Matsunaga, T., 2007.Controlled formation of magnetite crystal by partial oxidation of ferrous hydroxide in the presence of recombinant magnetotactic bacterial protein Mms6, Biomaterials. 28, 5381–5389.

[55] Vereda, F.,Rodríguez-González, B.,de Vicente,J., Hidalgo-Álvarez,R.J., 2008. Evidence of direct crystal growth and presence of hollow microspheres in magnetite particles prepared by oxidation of $Fe(OH)_2$, J Colloid Interface Sci. 318, 520–524.

[56] Chen, F.,Gao, Q.,Hong, G.,Ni, J., 2008.Synthesis and characterization of magnetite dodecahedron nanostructure by hydrothermal method, J MagnMagn Mater. 320, 1775–1780.

[57] Salazar-Alvarez, G., Muhammed, M.,Zagorodni, A.A., 2006. Novel flow injection synthesis of iron oxide nanoparticles with narrow size distribution, Chem Eng Sci. 61, 4625–4633.

[58] Dang, F., Enomoto, N.,Hojo, J.,Enpuku, K., 2009. Sonochemical synthesis of monodispersed magnetite nanoparticles by using an ethanol-water mixed solvent, UltrasonSonochem. 16, 649–654.

[59] Teng Lam,U., Mammucari, R., Suzuki, K.,Foster, N.R., 2008.Processing of Iron Oxide Nanoparticles by Supercritical Fluids, Ind Eng Chem Res 47, 599–614.

[60] Liu, J.F.,Lua, M.F.,Chaia, P.,Fua, L.,Wang, Z.L.,Cao, X.Q.,Meng, J., 2007.The magnetic and structural properties of hydrothermal-synthesized single-crystal $Sn_{1-x}Fe_xO_2$ nanograins, J MagnMagn Mater. 317, 1–7.

[61] Kumar, S., Jana, A.K.,Dhamija, I., Singla, Y., Maiti, M., 2013. Preparation, characterization and targeted delivery of serratiopeptidase immobilized on amino-functionalized magnetic nanoparticles, Eur J Pharm Biopharm. 85, 413–426.

[62] Alcalde, M. 2015.Engineering the ligninolytic enzyme consortium, Trends Biotechnol. 33 (2015) 155–162.

[63] Zheng, W.,Zhou, H.M.,Zheng, Y.F.,Wang, N., 2008. A comparative study on electrochemistry of laccase at two kinds of carbon nanotubes and its application for biofuel cell, Chem Phys Lett. 457(4–6), 381–385.

All © 2021 are reserved by International Journal of Advanced Science and Engineering. This Journal is licensed under a Creative Commons Attribution-Non Commercial-ShareAlike 3.0 Unported License.

ScienceDirect

Chemosphere
Volume 271, May 2021, 129513

Influence of biochar and EDTA on enhanced phytoremediation of lead contaminated soil by *Brassica juncea*

R. Rathika [a], P. Srinivasan [a], Jawaher Alkahtani [b], L.A. Al-Humaid [b], Mona S. Alwahibi [b], R. Mythili [a], T. Selvankumar [a]

Show more

Outline | Share | Cite

https://doi.org/10.1016/j.chemosphere.2020.129513

Get rights and content

Highlights

- Synergistic effect of biochar (BC) and EDTA to enhance phytoextraction of lead (Pb) contaminated soil investigated.
- Combined use of EDTA and biochar showed enhanced Pb uptake (60.2 mg/g).
- Pb uptake was found to be BC+EDTA (60.2 mg/g) > EDTA (23.5 mg/g) > BC (22. 0 mg/g) > control (10.0 mg/g).

Abstract

Phytoremediation technology is an eco-friendly technology for the treatment of the polluted environment. Conversely, the natural and synthetic amendments have been revealed to improve the heavy metal phytoextraction from polluted soils with hyperaccumulation and/or non-hyper accumulating plants. This study evaluated the synergistic effect of biochar (BC) and EDTA to enhance phytoextraction of heavy metal lead (Pb) from artificially polluted soil by *Brassica juncea*. The BC and EDTA amendment enhanced the growth and survival of *B. juncea* under Pb stress environment. BC and EDTA significantly increased the biomass of *B. juncea* and significantly increased the total chlorophyll content in the combined amendment of BC and EDTA (22.2 mg/g) compared to the individual amendment of BC (12.8 mg/g) and EDTA (12.2 mg/g) respectively. The combined use of EDTA and biochar showed enhanced Pb uptake (60.2 mg/g) compared to control (10.0 mg/g). The order of Pb uptake was found to be BC + EDTA (60.2 mg/g) > EDTA

PRINCIPAL
PGP College of Arts and Science
Namakkal

Chemosphere 271 (2021) 129513

Contents lists available at ScienceDirect

Chemosphere

journal homepage: www.elsevier.com/locate/chemosphere

Influence of biochar and EDTA on enhanced phytoremediation of lead contaminated soil by *Brassica juncea*

R. Rathika [a], P. Srinivasan [a], Jawaher Alkahtani [b], L.A. Al-Humaid [b], Mona S. Alwahibi [b], R. Mythili [a, **], T. Selvankumar [a, *]

[a] PG& Research Department of Biotechnology, Mahendra Arts & Science College, Kalippatti, Namakkal, 637501, Tamil Nadu, India
[b] Department of Botany and Microbiology, College of Science, King Saud University, Riyadh, 11451, Saudi Arabia

HIGHLIGHTS

- Synergistic effect of biochar (BC) and EDTA to enhance phytoextraction of lead (Pb) contaminated soil investigated.
- Combined use of EDTA and biochar showed enhanced Pb uptake (60.2 mg/g).
- Pb uptake was found to be BC+EDTA (60.2 mg/g) > EDTA (23.5 mg/g) > BC (22. 0 mg/g) > control (10.0 mg/g).

ARTICLE INFO

Article history:
Received 27 October 2020
Received in revised form
11 December 2020
Accepted 18 December 2020
Available online 31 December 2020

Handling Editor: Derek Muir

Keywords:
Antioxidant enzymes
Brassica juncea
Biochar
EDTA
Soil enzymes

ABSTRACT

Phytoremediation technology is an eco-friendly technology for the treatment of the polluted environment. Conversely, the natural and synthetic amendments have been revealed to improve the heavy metal phytoextraction from polluted soils with hyperaccumulation and/or non-hyper accumulating plants. This study evaluated the synergistic effect of biochar (BC) and EDTA to enhance phytoextraction of heavy metal lead (Pb) from artificially polluted soil by *Brassica juncea*. The BC and EDTA amendment enhanced the growth and survival of *B. juncea* under Pb stress environment. BC and EDTA significantly increased the biomass of *B. juncea* and significantly increased the total chlorophyll content in the combined amendment of BC and EDTA (22.2 mg/g) compared to the individual amendment of BC (12.8 mg/g) and EDTA (12.2 mg/g) respectively. The combined use of EDTA and biochar showed enhanced Pb uptake (60.2 mg/g) compared to control (10.0 mg/g). The order of Pb uptake was found to be BC + EDTA (60.2 mg/g) > EDTA (23.5 mg/g) > BC (22. 0 mg/g) > control (10.0 mg/g). The maximum activity of SOD (35.2 ± 1.2 U/mg), POD (47.0 ± 1.8 U/mg) and CAT (28.0 ± 1.0 U/mg) was obtained in the mixed application of EDTA and BC. The obtained results revealed that the combined use of BC and EDTA was the most advantageous option for the treatment of Pb contaminated soil as compared to individual amendments.
© 2020 Elsevier Ltd. All rights reserved.

1. Introduction

Heavy metals (HM) are trace elements, essentially required in very minute quantities for plants and animals which includes the micronutrients like cobalt (Co), copper (Cu), chromium (Cr), manganese (Mn), and Zinc (Zn); while some are non-essential and broadly cause several pollutions of soils with heavy metals (HM) due to anthropogenic activities is nowadays given a great deal of interest among scientific communities as a consequence of the harmful effects of HMs by reaching humans from plants and animals via food chain (Rinklebe et al., 2019; Ali et al., 2020). HM are exist permanent and not degradable like organic materials, hence persistent in nature (Shi et al., 2009). The sources of HM in food and associated health risks are well established (Azeh Engwa et al., 2019; Boudebbouz et al., 2020; Afonne and Ifediba, 2020). This, therefore, necessitates the remediation of soils highly polluted with HM in the view of their hazardous effects on the eco-system.

The remediation of HM in soils is a naturally occurring phenomenon where soil microorganisms and plants modify the ecological effect of HM (Park et al., 2011). However, two major scientific approaches have been employed for the removal or

* Corresponding author.
** Corresponding author.
E-mail addresses: mythi.gova@gmail.com (R. Mythili), selvankumar75@gmail.com (T. Selvankumar).

https://doi.org/10.1016/j.chemosphere.2020.129513
0045-6535/© 2020 Elsevier Ltd. All rights reserved.

extraction of HM from soil: (i) washing method and (ii) HM reduction by *in-situ* techniques, where the later technique has been used for reducing the toxicity of HMs in different soils (Shi et al., 2009). For HM remediation, various organic amendments or additives, and/or phytoremediation either alone or in combination have been intensively worked-out by researchers world-wide, and the phytoremediation approach as *in situ* HM remediation is considered as economical and environment-friendly (Shah and Daverey, 2020). Utilizing the plants of different growth forms for HM clean-up process is referred to as phytoremediation, popularly experimented to remediate polluted environment (Bian et al., 2018; Bian et al., 2019).

Phytoremediation of HMs in soils can be categorized into four major routes: (i) uptake of HM, (ii) bioaccumulation of HM, (iii) *in situ* inactivation or immobilization of HM, (iv) minimizing the bioavailability and external transport of HM, and (v) transformation of volatile forms and discharge into the atmosphere (Shah and Daverey, 2020). A variety of amendments are also applied to improve the extractability of HM along with microbial agents (Manoj et al., 2020). In this context, as an improvement option for HM remediation, biochar derived from various bio-wastes is gaining momentum (Harindintwali et al., 2020; Fan et al., 2020). Biochar – a pyrolysis product of biomass, because of its high surface area with many active sites, is used for various environmental applications especially as a soil amendment to remediate HM (He et al., 2019). The nature of raw materials used for the production of biochar and milieu of pyrolysis are the major factors influencing the attributes of biochar-metal binding apart from the soil properties when applied (Qi et al., 2017).

The biochar-HM remediation and phytoremediation occur through several mechanisms as outlined in Table 1 and the studies concerned with biochar assisted phytoremediation to show great variation in HM binding, uptake, accumulation and volatilization by the plants. Each study in this respect reports for the separate mechanism of HM-phytoremediation, it is difficult to understand the underlying mechanisms to elaborate the application to the field level.

Hence, the aim of the study investigates the synergistic effects of EDTA and biochar on phytoremediation of Pb contaminated soil. Also, the growth and phytoremediation potentials of *B. juncea* in Pb treated EDTA-BC amended soils were studied. In addition, the plant chlorophyll, lipid peroxidation activity, SOD, POD, CAT activity and soil enzyme activity were studied. Besides, the effects of EDTA and BC amendments on the antioxidant activity of *B. juncea* and soil enzymatic activities were also evaluated. This study highlights that the combined effects of BC and EDTA were the effective option for the remediation of Pb contaminated soil as compared individual amendments.

2. Materials and methods

2.1. Characterization of soil sample

The topsoil samples used in this study were collected from the campus of Mahendra Arts and Science college, Kalippatti, Tamil Nadu, India and dried in air at 37 °C, thoroughly mixed and ground. To ensure the removal of large debris to get a more homogeneous portion, the soil was separated via 1–2 mm sieve for further study. The sieved soil samples were sterilized under steam pressure for 15 min at 121 °C under 100 Pa of force and permitted become stable of the soil (Govarthanan et al., 2016). The physico-chemical nature of the study soil was estimated by using the standard methods (Gaudette et al., 1974; Helmke and Sparks, 1996; Thomas, 1996). Then the soil was unnaturally polluted with 100 mg/kg of Pb.

2.2. Biochar preparation

Neem tree wood logs were collected from the local village and air-dried, washed with double purified water to eliminate the impurities attached on the exterior of the wooden pieces and cut into small pieces (~5–10 cm) using a motorized chopper and sieved through 0.5–0.6 mm sieve and stored. Then the feedstock was pyrolyzed (5 °C/min) at 500 °C for 2 h in a muffle furnace (BF51732 BPMC-1, Thermo Scientific, USA) to get biochar. The obtained BC

Table 1
Biochar assisted remediation of heavy metals in soil.

Test soil	Source of contamination	Heavy metal(s)	Assisted remediation/Phytoremediation	Impact/Possible mechanism	Reference
Contaminated soil	Crop field soil having higher levels of Cd and Pb	Cd, Pb	By amending biochar derived from thiol-modified rice straw	Complexation of metal ions on the surface of biochar is prosperous with thiol groups; Surface complexation with Cd^{2+} and Pb^{2+} is highlighted.	Fan et al. (2020)
Agricultural top soil	Pb–Zn Mine	Pb, Cd, Cu	Co-pyrolysis biochar of rape straw and orthophosphate	Phosphate and hydroxyl groups in biochar directly formed complex with metals	Gao et al. (2020)
Purple soil from vegetable soil	Experimental	Hg	Various chemical enhancer assisted phytoremediation of Hg contaminated soil by *Oxalis corniculata*.	Sodium thiosulphate as enhancer showed potential recovery and reclaim of Hg contaminated soil by *Oxalis corniculata*. Enhancers did not affect the microbial species diversity in soil.	Liu et al. (2018)
Mine tailings	Surface soil of mine tailings	Cu, Zn, Pb, Cd, Mn, Hg	Biochar/attapulgi assisted multi-metal phytoextraction by *Solanum nigrum*.	Main system involved: cationic exchange/adsorption for attapulgite/biochar amendment.	Li et al. (2019)
Vegetation soil	Experimental	Cd	Nanoscale zerovalent iron and biochar enabled phytoremediation with *Trifolium repens*.	Optimum combination of zerovalent iron (300 mg/kg) and biochar (2.5%) improved the Cd accumulation capacity of the plant.	Zand et al. (2020)
Contaminated soil	Acidic mine waste	Al, Pb, Cu, Cr	Lemon grass (*Cymbopogon flexuosus*) waste biochar aided phytoremediation by palmarosa (*Cymbopogon martini*)	Biochar evidenced liming and immobilization of acidic mine soil and also strengthened the phytoremediation of palmarosa.	Jain et al. (2020)
Crop field soil	Experimental	Cd	Cornstalk biochar amendment for phytoremediation of Cd in *Beta vulgaris*.	Biochar (5%) enhanced the Cd accumulation in *Beta vulgaris*; Protein and pectin were the vital Cd binding sites of cell walls of *Beta vulgaris* roots.	Gu et al. (2020)
Contaminated soil	Mining	Pb, Cd, As, Zn	Biochar assisted phytoremediation with *Helianthus annuus*.	Biochar addition significantly enhanced heavy metal remediation by the plant	Jun et al. (2020)
Technosol	Former tin mine extraction site	As	Biochar-iron sulphate assisted phytoremediation of As by Salicaceae species.	The effect of biochar and iron sulphate amendment on As removal is dependent on application strata, amendment characteristics and plant species.	Simiele et al. (2020)

was further desiccated at 60 °C and stored in an air-tight container for further use.

2.3. Soil treatment and pot experiments

B. juncea L., seeds were surface decontaminated by submerging them in 95% ethyl alcohol solution for 5 min; then the seeds were sterilized into 5% sodium hypochlorite solution for 10 min, and finally rinsed with disinfected distilled water. The seeds were kept in Petri dishes filled with double distilled water and were allowed to grow at room temperature for 2–3 days. After germination, 10 seedlings were transferred to a plastic pot (22 × 26) filled with 250 g of Pb contaminated soil. The pot experiments were conducted with three replicates as follows.

(i) Control soil treated with Pb
(ii) Pb contaminated soil amended with BC (5%)
(iii) Pb contaminated soil with EDTA (100 mM)
(iv) Pb contaminated soil with BC (5%) and EDTA (100 mM).

The soil humidity was maintained at 60% of water holding capability. After 4 weeks of cultivation, the *B. juncea* plants were harvested. The roots, shoots and leaves of the *B. juncea* were washed and separated. Plant biomass and chlorophyll content were analyzed. Plant samples were dried at 70–80 °C followed by nitric acid digestion and used to investigate Pb accumulation using inductively coupled plasma mass spectrometry (ICP) (150-00191-1, Rev. A, Leemans Labs, USA). Fresh samples of *B. juncea* were used to investigate the plant biochemical parameters such as antioxidants and malondialdehyde (MDA) activity. Treated soils were collected and used to estimate the soil enzyme activities.

2.4. Determination of plant chlorophyll and lipid peroxidation activity

Chlorophyll concentrations in the fresh *B. juncea* were analyzed according to Metzner et al. (1965) and the absorbance was recorded at 480, 645 and 663 nm by UV–Vis spectrophotometer using 85% acetone as blank. The level of lipid peroxidation activity was determined by estimating MDA using thio-barbituric acid method according to Heath and Packer (1968). The optical absorbance was recorded at 532 nm and the MDA content was calculated from the extinction coefficient of 155 $mM^{-1}cm^{-1}$.

2.5. Estimation of SOD, POD and CAT activity

Superoxide dismutase (SOD) activity was determined according to Dhindsa et al. (1981) at 560 nm. Unit of SOD activity was calculated as the amount of SOD required to generate 50% inhibition of reduction of NBT. Peroxidase (POD) activity was measured according to Castillo et al. (1984) at 470 nm and POD activity was defined as an absorbance change of 0.001 U/min. Catalase (CAT) activity was estimated according to Piero et al. (1980) at 240 nm. CAR catalyzing the decomposition of 1 mmol of H_2O_2/min is calculated as one unit.

2.6. Influence of EDTA and BC on soil enzyme activity

Soil catalase was determined according to Wu et al. (2006) by $KMnO_4$ titration method and the activity was defined as in mL of 0.1 mol/L $KMnO_4$ consumed per unit weight of soil after 15 min. Urease was estimated by sodium phenol colorimetric and the activity was expressed in mg of NH^3–N per unit weight of soil after 24 h. The acid and alkaline phosphatase activities were determined by using phenylene disodium phosphate colorimetric assay and expressed as the production of p-nitrophenol (p-nitrophenol μg/(g.h)).

2.7. Statistical analysis

The experimental investigations of this study were mean values of triplicates, and the standard deviation was applied to investigate the data. The statistical analysis was carried using Microsoft excel (2010).

3. Results and discussion

3.1. Physico-chemical characteristics of the study soil and growth of B. juncea

The physico-chemical characteristics of the study soil were represented in Table 2. The soil pH (6.89) indicates that the soil was the almost neutral condition and contains 7.5% organic carbon. Lebrun et al. (2017) investigated that the application of BC and EDTA was not affected by soil pH. However, the organic carbon was slightly increased in the amended soil (data not shown). It has been reported that plant biomass is a key feature that establishes the achievement of metal phytoextraction (Praburaman et al., 2016). Also, the propensity of HMs to reduce the biomass of plants by changing the biochemical and physiological procedures are well recognized. Therefore, the influence of BC and EDTA on the biomass of *B. juncea* cultivated in Pb contaminated soil was evaluated (Fig. 1). The results designated that the addition of BC and EDTA significantly increased the biomass of *B. juncea*. The biochar alone treated plants showed 6.35 g/pot biomass however, EDTA treated pots showed 5.9 g/pot. The combination of BC and EDTA showed enhanced biomass of 10.2 g/pot. It has been observed that the combined treatment of BC and EDTA significantly increased the total biomass of the plants. The order of the increased biomass under Pb stress with the amendments was found to be BC + EDTA > BC > EDTA > control. Houben et al. (2013) identified that the biochar amendment showed higher biomass of the plants cultivated under Zn, Pb and Cd stress. It has been well reported that EDTA has been shown potential chelating agent to enhance the biomass and solubility of HMs in soil and their phytoavialability to plants (Saifullah et al., 2009). Several studies have been reported that the assistance of EDTA, non-hyperaccumulator species such as pea (Piechalak et al., 2003), corn (Hovsepyan and Greipsson, 2005), sunflower, tobacco and vetiver (Boonyappkana et al., 2005) with high biomass have been investigated for phytoextraction. However, the combination of BC and EDTA on phytoremediation of heavy metals has not been reported.

3.2. Chlorophyll and lipid peroxidation products

The EDTA and BC considerably amplified the chlorophyll content in *B. juncea.* (Fig. 2). The increase in the total chlorophyll content was observed in the combined application of BC and EDTA

Table 2
Physico-chemical properties of the soil.

Soil parameters	value
Organic matter (%)	7.5
Ca (meg/100 g)	6.25 ± 0.4
Na (meg/100 g)	56 ± 1.0
NH_4 (meg/100 g)	32.5 ± 1.5
K (meg/100 g)	38.2 ± 1.8
pH	6.89
EC (m^s/m)	0.62

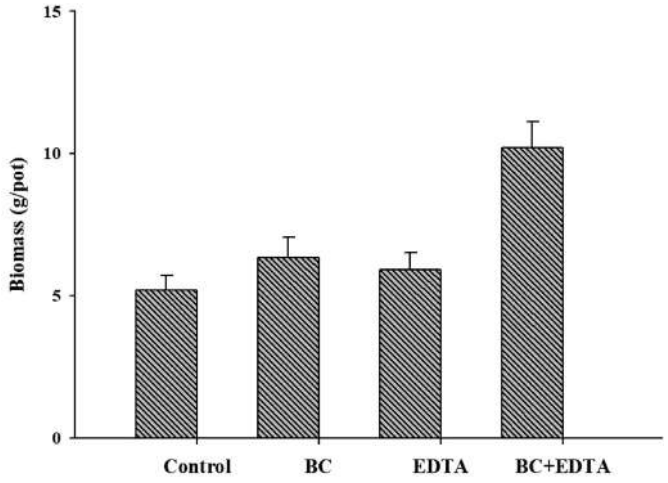


Fig. 1. Influence of BC and EDTA on the biomass of *B. juncea* cultivated in Pb contaminated soil.

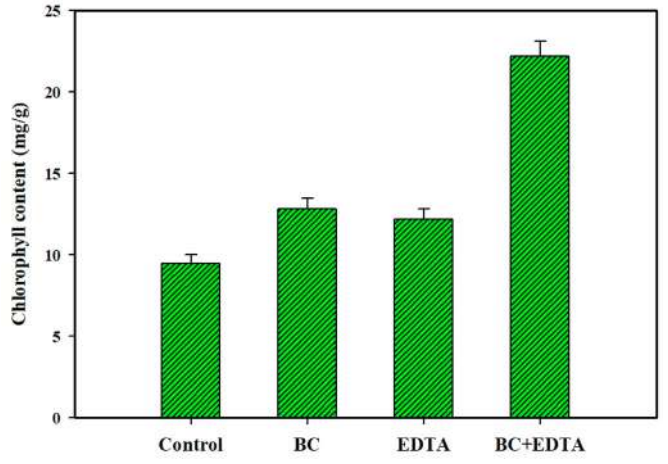


Fig. 2. Effect of BC and EDTA on total chlorophyll contents of *B. juncea* cultivated in Pb contaminated soil.

(22.2 mg/g) compared to the individual amendment of BC (12.8 mg/g) and EDTA (12.2 mg/g) respectively. The visual observations indicated that small chlorotic acne on the leaves of *B. juncea* was reported due to the effect of Pb in soil. However, Ali et al. (2020) observed that the biochar significantly abridged the pollutant stress on plants and enhanced chlorophyll content of the plants. Also, Saleem et al. (2020) observed that the EDTA plays a key role in the enhanced concentration of chlorophyll under pollutant stress environment. Increase of photosynthetic pigments by EDTA may cause additional efficient conversion of light in the photochemical reactions, leads enhancing plant growth and biomass Saleem et al., 2020. These results are reliable with our investigations by the addition of BC and EDTA significantly enhances the chlorophyll content under Pb stress environment.

Also, the effects of BC and EDTA on MDA content in Pb stressed *B.juncea* plants were also investigated. MDA is a product of lipid peroxidation caused by oxidative damage in *B. juncea*. The individual application of BC and/or EDTA extensively decreased the MDA content in the plant system (Fig. 3). Whereas, the combined application of EDTA and BC showed drastic MDA decrease compared to the individual application. Saleem et al. (2020)

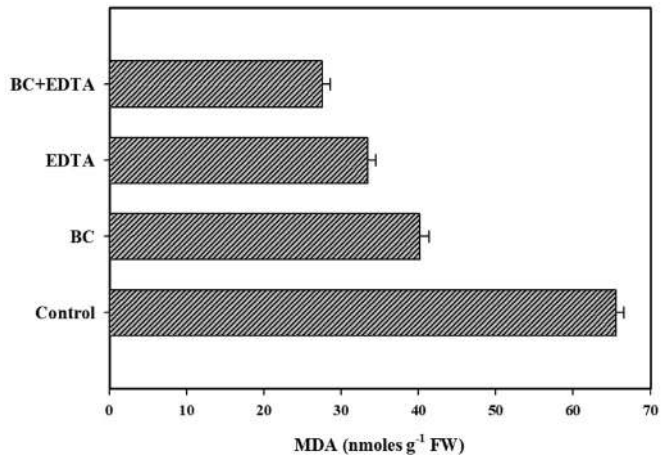


Fig. 3. Effect of BC and EDTA on lipid peroxidation (MDA) activity of *B. juncea* cultivated in Pb contaminated soil.

observed that the application of EDTA decreases the MDA content in the plant system.

3.3. Influence of EDTA and biochar on Pb uptake by B. juncea

EDTA and biochar application significantly influenced the uptake of Pb in *B. juncea* (Fig. 4). The results indicated that the individual application of EDTA (23.5 mg/g) and biochar (22.0 mg/g) significantly increased the Pb uptake by *B. juncea.* Conversely, the combination of EDTA and biochar showed enhanced Pb uptake (60.2 mg/g). The order of Pb uptake was found to be BC + EDTA (60.2 mg/g) > EDTA (23.5 mg/g) > BC (22. 0 mg/g) > control (10.0 mg/g). So far, numerous studies investigated that the application of EDTA enhances heavy metal accumulation in *B. napus* (Afshan et al., 2015) *H. annus* (Azhar et al., 2006) in the polluted soil. Ali et al. (2020) observed the enhanced Pb uptake by the addition of biochar. The findings indicated that the combination of BC and EDTA greatly influence the Pb uptake by *B. juncea.*

3.4. Influence of EDTA and biochar on plant antioxidants

The abiotic HM stress significantly influences the production of ROS, which damage the plant system. The changes in the SOD, POD

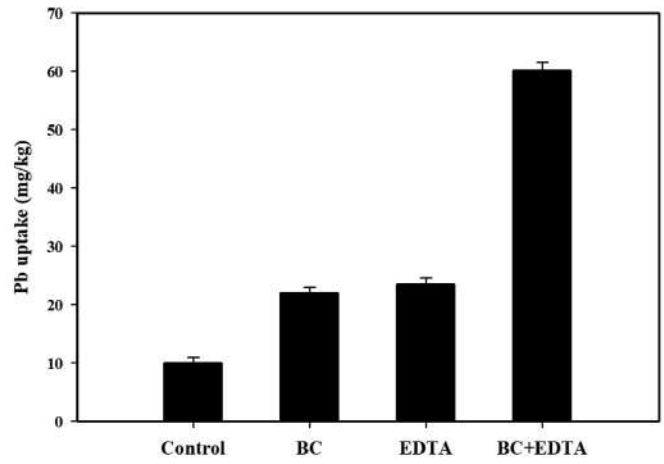


Fig. 4. Influence of BC and EDTA on Pb uptake *B. juncea* cultivated in Pb contaminated soil.

Table 3
Antioxidant enzyme activities.

Treatment groups	SOD (U/mg)	CAT (U/mg)	POD (U/mg)
Control	15.2 ± 1.0	12.12 ± 1.0	11.24 ± 1.5
BC	17 ± 1.2	14.13 ± 1.5	25.26 ± 1.2
EDTA	19.2 ± 1.0	18.4 ± 1.2	27.8 ± 1.7
BC + EDTA	35.2 ± 1.2	28.0 ± 1.0	47.0 ± 1.8

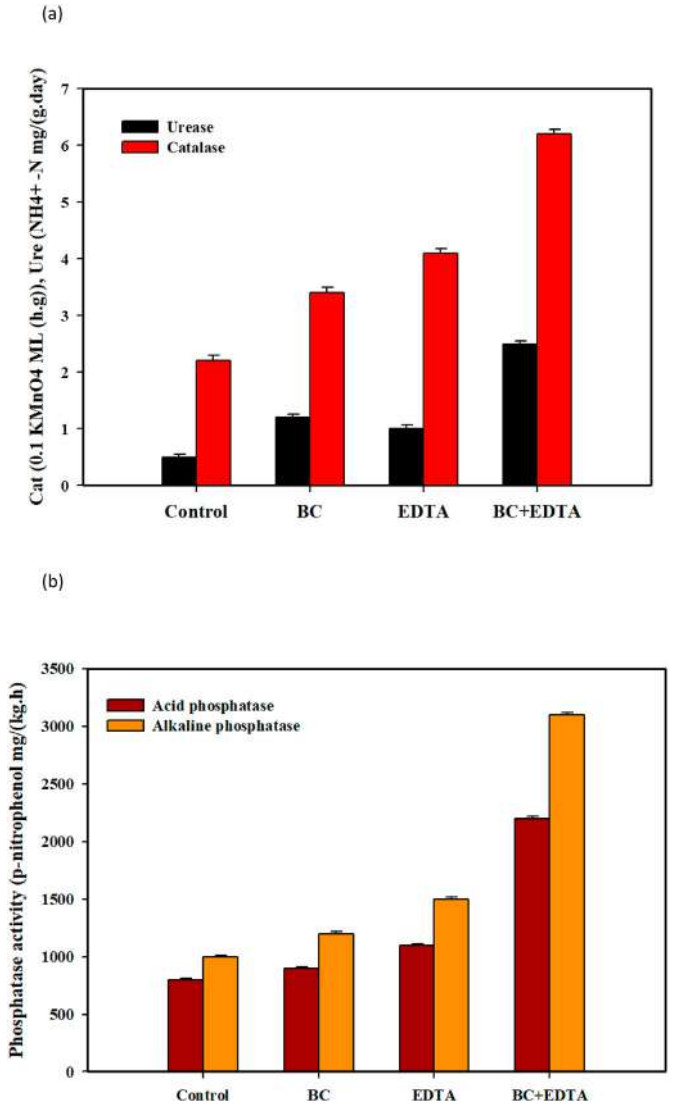


Fig. 5. Effect of BC and EDTA on soil enzyme activity, (a) urease and catalase. (b) acid and alkaline phosphatase.

and CAT activities under Pb stressed *B. juncea* following individual and/or combination of BC and EDTA were studied. SOD, POD and CAT were improved compared to the control (Table 3). The maximum activity of SOD (35.2 ± 1.2 U/mg), POD (47.0 ± 1.8 U/mg) and CAT (28.0 ± 1.0 U/mg) was obtained in the combination of EDTA and BC. Ali et al. (2020) reported a maximum increase of antioxidant enzymes in the application of biochar. It has been reported that under a stress environment, maximum antioxidant ability averts damages from the formation of reactive ROS. Furthermore, EDTA is significantly dropping the oxidative pressure created by Pb and helps the plants fight against oxidative stress and facilitate the quick revival of plants (Afshan et al., 2015). Habiba et al. (2015) reported that the EDTA enhanced antioxidants and reduced the oxidative stress by lowering MDA activity. The results are consistent with our study by increasing antioxidant enzymes and lowering MDA content in the B. *juncea* plant system.

3.5. Effect of BC and EDTA on soil enzyme activity

Soil enzymes plays a major role to make possible biochemical pathways, decomposition of natural matter and conversion, detoxification of contaminants, synthesis key products for plants and microbes and sustain soil structure (Ma et al., 2015; Gul et al., 2015). Thus, the enzyme activities were estimated and represented in Fig. 5 (a & b). The enzyme results indicated that the application of EDTA and biochar significantly increased enzyme activities than the control. The increase in phosphatase activity might liberate organophosphorus complex in soil hydrolysis for the growth of plants (Zhang et al., 2014).

4. Conclusion

The present investigation is designed to evaluate the potential of Pb phytoextraction from artificially polluted soil by *B. juncea* and investigated the influence of BC and EDTA amendments on enhanced Pb accumulation. The BC and EDTA amendment enhanced the growth and survival of *B. juncea* under Pb stress environment. BC and EDTA significantly increased the biomass of *B. juncea* and significantly increased the total chlorophyll content in the combined amendment of BC and EDTA (22.2 mg/g) compared to the individual amendment of BC (12.8 mg/g) and EDTA (12.2 mg/g) respectively. Furthermore, the decrease of Pb toxicity and oxidative stress was observed by the reduction of malondialdehyde. In light of our study, Pb in contaminated soil could be eliminating by BC and EDTA. This research provides sympathetic support for the combined application with accumulators to remediate Pb contaminated environment and proves this synergistic approach is practicable and promising.

Credit author statement

R. Rathika: Conceptualization, Methodology, Formal analysis, Data curation, Writing – original draft, review and editing, Funding acquisition. P. Srinivasan: Conceptualization, Methodology, Formal analysis, Data curation, Writing – original draft, review and editing, Funding acquisition. Jawaher Alkahtani: Conceptualization, Methodology, Formal analysis, Data curation, Writing – original draft, review and editing, Funding acquisition. L.A. Al-Humaid: Conceptualization, Methodology, Formal analysis, Data curation, Writing – original draft, review and editing, Funding acquisition. Mona S. Alwahibi: Conceptualization, Methodology, Formal analysis, Data curation, Writing – original draft, review and editing, Funding acquisition. R. Mythili: Conceptualization, Methodology, Formal analysis, Data curation, Writing – original draft, review and editing, Funding acquisition. T. Selvankumar: Conceptualization, Methodology, Formal analysis, Data curation, Writing – original draft, review and editing, Funding acquisition.

Declaration of competing interest

The authors declared that they dont have no known competing financial interests or personal relationships that could have appeared to influence the work reported in this paper.

Acknowledgements

The authors gratefully acknowledge the Deanship of Scientific

Research Deanship at King Saud University for funding this work through research group no. RG-1441-329.

References

Afonne, O.J., Ifediba, E.C., 2020. Heavy metals risks in plant foods – need to step up precautionary measures. Curr. Opin. Toxicol. 22, 1–6.

Afshan, S., Ali, S., Bharwana, S.A., Rizwan, M., Farid, M., Abbas, F., Ibrahim, M., Mehmood, M.A., Abbasi, G.H., 2015. Citric acid enhances the phytoextraction of chromium, plant growth, and photosynthesis by alleviating the oxidative damages in *Brassica napus* L. Environ. Sci. Pollut. Res. Int. 22, 11679–11689.

Ali, W., Mao, K., Zhang, H., Junaid, M., Xu, N., Rasool, A., Feng, H., Yang, Z., 2020. Comprehensive review of the basic chemical behaviours, sources, processes, and endpoints of trace element contamination in paddy soil-rice systems in rice-growing countries. J. Hazard Mater. 397, 122720.

Azeh Engwa, G., Udoka Ferdinand, P., Nweke Nwalo, F., Unachukwu, M.N., 2019. Mechanism and health effects of heavy metal toxicity in humans. In: Karcioglu, Ozgur, Arslan, Banu (Eds.), Poisoning Mod. World - New Tricks an Old Dog? Intech Open, p. 82511.

Azhar, N., Ashraf, M.Y., Hussain, M., Hussain, F., 2006. Phytoextraction of lead (Pb) by EDTA application through sunflower (*Helianthus annuus* L.) cultivation: seedling growth studies. Pakistan J. Bot. 38, 1551–1560.

Bian, F., Zhong, Z., Wu, S., Zhang, X., Yang, C., Xiong, X., 2018. Comparison of heavy metal phytoremediation in monoculture and intercropping systems of Phyllostachys praecox and Sedum plumbizincicola in polluted soil. Int. J. Phytoremediation 20, 490–498.

Bian, F., Zhong, Z., Zhang, X., Yang, C., Gai, X., 2019. Bamboo an untapped plant resource for the phytoremediation of heavy metal contaminated soils. Chemosphere 246, 125750.

Boonyapookana, B., Parkpian, P., Techapinyawat, S., DeLaune, R.D., Jugsujinda, A., 2005. Phytoaccumulation of lead by sunflower (*Helianthus annuus*), tobacco (*Nicotiana tabacum*), and vetiver (*Vetiveria zizanioides*). J Environ. Sci. Heal. 40, 117–137.

Boudebbouz, A., Boudalia, S., Bousbia, A., Habila, S., Boussadia, M.I., Gueroui, Y., 2020. Heavy metals levels in raw cow milk and health risk assessment across the globe: a systematic review. Sci. Total Environ. 141830.

Castillo, F.I., Penel, I., Reppin, H., 1984. Peroxidase release induced by ozone in sedum album leaves. Plant Physiol. 74, 846–851.

Dhindsa, R.S., Plumb-Dhindsa, P., Thorpe, T.A., 1981. Leaf senescence correlated with increased levels of membrane permeability and lipid peroxidation and decreased levels of superoxide disniutase and catalase. J. Exp. Bot. 32, 93–101.

Fan, J., Cai, C., Chi, H., Reid, B.J., Coulon, F., Zhang, Y., Hou, Y., 2020. Remediation of cadmium and lead polluted soil using thiol-modified biochar. J. Hazard Mater. 388, 122037.

Gao, R., Hu, H., Fu, Q., Li, Z., Xing, Z., Ali, U., Zhu, J., Liu, Y., 2020. Remediation of Pb, Cd, and Cu contaminated soil by co-pyrolysis biochar derived from rape straw and orthophosphate: speciation transformation, risk evaluation and mechanism inquiry. Sci. Total Environ. 730, 139119.

Govarthanan, M., Kamala-Kannan, S., Kim, S.A., Seo, Y.S., Park, J.H., Oh, B.T., 2016. Synergistic effect of chelators and *Herbaspirillum* sp. GW103 on lead phytoextraction and its induced oxidative stress in *Zea mays*. Arch Microbiol 198, 737–742.

Gu, P., Zhang, Y., Xie, H., Wei, J., Zhang, X., Huang, X., Wang, J., Lou, X., 2020. Effect of cornstalk biochar on phytoremediation of Cd-contaminated soil by *Beta vulgaris var. cicla* L. Ecotoxicol. Environ. Saf. 205, 111144.

Gul, S., Whalen, J.K., Thomas, B.W., Sachdeva, V., Deng, H., 2015. Physico-chemical properties and microbial responses in biochar-amended soils: mechanisms and future directions. Agric. Ecosyst. Environ. 206, 46–59.

Habiba, U., Ali, S., Farid, M., Shakoor, M.B., Rizwan, M., Ibrahim, M., Abbasi, G.H., Hayat, T., Ali, B., 2015. EDTA enhanced plant growth, antioxidant defense system, and phytoextraction of copper by *Brassica napus* L. Environ. Sci. Pollut. Res. 22, 1534–1544.

Harindintwali, J.D., Zhou, J., Yang, W., Gu, Q., Yu, X., 2020. Biochar-bacteria-plant partnerships: eco-solutions for tackling heavy metal pollution. Ecotoxicol. Environ. Saf. 204, 111020.

He, L., Zhong, G., Liu, Z., Dai, P.C., Brookes, J., Xu, X., 2019. Remediation of heavy metal contaminated soils by biochar: mechanisms, potential risks and applications in China. Environ. Pollut. 252, 846–855.

Heath, RL, Packer, L, 1968. Photoperoxidation in isolated chloroplasts. I. Kinetics and stoichiometry of fatty acid peroxidation. Arch. Biochem. Biophys. 125, 189–198.

Helmke, P.A., Sparks, D.L., 1996. Lithium, sodium, potassium, rubidium, and cesium. In: Sparks, D.L., et al. (Eds.), Methods of Soil Analysis: Part 3. SSSA and. ASA, Madison, WI, pp. 551–574.

Houben, D., Evrard, L., Sonnet, P., 2013. Mobility, bioavailability and pH-dependent leaching of cadmium, zinc and lead in a contaminated soil amended with biochar. Chemosphere 92, 1450–1457.

Hovsepyan, A., Greipsson, S., 2005. EDTA-enhanced phytoremediation of lead-contaminated soil by corn. J. Plant Nutr. 28, 2037–2048.

Jain, S., Khare, P., Mishra, K., Shanker, P., Singh, R.P., Singh, P., Das, R., Yadav, B.K., Saikia, Baruah, B.P., 2020. Biochar aided aromatic grass [*Cymbopogon martini* (Roxb.) Wats] vegetation: a sustainable method for stabilization of highly acidic mine waste. J. Hazard Mater. 390, 121799.

Jun, L., Wei, H., Aili, M., Juan, N., Hongyan, X., Jingsong, H., Yunhua, Z., Cuiying, P., 2020. Effect of lychee biochar on the remediation of heavy metal-contaminated soil using sunflower: a field experiment. Environ. Res. 188, 109886.

Lebrun, M., Macri, C., Miard, F., Hattab-Hambli, N., Mikael, M., Domenico, M., Sylvain, B., 2017. Effect of biochar amendments on as and Pb mobility and phytoavailability in contaminated mine technosols phytoremediated by *Salix*. J. Geochem. Explor. 182, 149–156.

Liu, Z., Wang, L., Ding, S., Xiao, H., 2018. Enhancer assisted-phytoremediation of mercury-contaminated soils by *Oxalis corniculata* L., and rhizosphere microorganism distribution of *Oxalis corniculata* L. Ecotoxicol. Environ. Saf. 160, 171–177.

Li, X., Zhang, X., Wang, X., Cui, Z., 2019. Phytoremediation of multi-metal contaminated mine tailings with *Solanum nigrum* L. and biochar/attapulgite amendments. Ecotoxicol. Environ. Saf. 180, 517–525.

Ma, S.C., Zhang, H.B., Ma, S.T., Wang, R., Wang, G.X., Shao, Y., Chun-Xi, Li, 2015. Effects of mine wastewater irrigation on activities of soil enzymes and physiological properties, heavy metal uptake and grain yield in winter wheat. Ecotoxicol. Environ. Saf. 113, 483–490.

Manoj, S.R., Karthik, C., Kadirvelu, K., Arulselvi, P.I., Shanmugasundaram, T., Bruno, B., Rajkumar, M., 2020. Understanding the molecular mechanisms for the enhanced phytoremediation of heavy metals through plant growth promoting rhizobacteria: a review. J. Environ. Manag. 254, 109779.

Metzner, H., Rau, R., Senger, H., 1965. Unter suchungen zur synchronisier barkeit einzelner pigment mangel-mutanten von Chlorella. Planta 65, 186–194.

Park, J.H., Lamb, D., Paneerselvam, P., Choppala, G., Bolan, N., Chung, J.W., 2011. Role of organic amendments on enhanced bioremediation of heavy metal(loid) contaminated soils. J. Hazard Mater. 185, 549–574.

Piechalak, A., Tomaszewska, B., Baraŀkiewicz, D., 2003. Enhancing phytoremediative ability of *Pisum sativum* by EDTA application. Phytochemistry 64, 1239–1251.

Piero, F., Lorenzo, P., Giovanni, B., 1980. Use of 3, 5-dichloro-2-hydroxybenzenesulfonic acid/4-aminophenazone chromogenic system in direct enzymic assay of uric acid in serum and urine. Clin. Chem. 26, 227–231.

Praburaman, L., Park, S.H., Cho, M., Lee, K.J., Ko, J.A., Han, S.S., Lee, S.H., Kamala-Kannan, S., Oh, B.T., 2016. Significance of diazotrophic plant growth-promoting *Herbaspirillum* sp. GW103 on phytoextraction of Pb and Zn by *Zea mays* L. Environ. Sci. Pollut. Res. 24, 3172–3180.

Qi, F., Kuppusamy, S., Naidu, R., Bolan, N.S., Ok, Y.S., Lamb, D., Li, Y., Yu, L., Semple, K.L., Wang, H., 2017. Pyrogenic carbon and its role in contaminant immobilization in soils. Crit. Rev. Environ. Sci. Technol. 47, 795–876.

Rinklebe, J., Antoniadis, V., Shaheen, S.M., Rosche, O., Altermann, M., 2019. Health risk assessment of potentially toxic elements in soils along the Central Elbe River, Germany. Environ. Int. 126, 76–88.

Saifullah, E.M., Qadir, M., Caritat, P., Tack, F.M.G., Laing, G.D., Zia, M.H., 2009. EDTA-assisted Pb phytoextraction. Chemosphere 74, 1279–1291.

Saleem, et al., 2020. Ethylenediaminetetraacetic Acid (EDTA) Mitigates the Toxic Effect of Excessive Copper Concentrations on Growth, Gaseous Exchange and Chloroplast Ultrastructure of Corchorus capsularis L. and Improves Copper Accumulation Capabilities. Plants 9 (6), 756. https://doi.org/10.3390/plants9060756.

Shah, V., Daverey, A., 2020. Phytoremediation: a multidisciplinary approach to clean up heavy metal contaminated soil. Environ. Technol. Innov. 18, 100774.

Shi, W., Shao, H., Li, H., an Shao, M., Du, S., 2009. Progress in the remediation of hazardous heavy metal-polluted soils by natural zeolite. J. Hazard Mater. 170, 1–6.

Simiele, M., Lebrun, M., Miard, F., Trupiano, D., Poupart, P., Forestier, O., Scippa, G.S., Bourgerie, S., Morabito, D., 2020. Assisted phytoremediation of a former mine soil using biochar and iron sulphate: effects on as soil immobilization and accumulation in three *Salicaceae* species. Sci. Total Environ. 710, 136203.

Thomas, G.W., 1996. Soil pH and soil acidity. In: Sparks, D.L. (Ed.), Methods of Soil Analysis, Part 3. Chemical Methods. SSSA-ASA, Madison, WI, pp. 475–490.

Wu, J.S., Lin, Q.M., Huang, Q.Y., Xiao, H.A., 2006. Determination of Soil Microbial Biomass and its Application. China Meteorological Press, [M], Beijing.

Zand, A.D., Tabrizi, A.M., Heir, A.V., 2020. Incorporation of biochar and nanomaterials to assist remediation of heavy metals in soil using plant species. Environ. Technol. Innov. 20, 101134.

Zhang, Y., Wang, X., Lu, S., Liu, D., 2014. A major root-associated acid phosphatase in Arabidopsis, AtPAP10, is regulated by both local and systemic signals under phosphate starvation. J. Exp. Bot. 65 (22), 6577–6588.

ScienceDirect

Chemosphere
Volume 264, Part 1, February 2021, 128377

Biosurfactant mediated bioelectrokinetic remediation of diesel contaminated environment

Jeevanandam Vaishnavi [a], Sandhanasamy Devanesan [b], Mohamad S. AlSalhi [b] ✉, Aruliah Rajasekar [a] ✉, Adikesavan Selvi [a], Palanisamy Srinivasan [c], Muthusamy Govarthanan [d] ✉

Show more

Outline | Share Cite

https://doi.org/10.1016/j.chemosphere.2020.128377

Get rights and content

Highlights

- *Staphylococcus epidermidis* EVR4 identified as efficient biosurfactant producing bacteria
- EVR4 degrades the nonane (C_9) to tricosane (C_{23}) completely and 85% and 47% of pentacosane and octacosane respectively
- EVR4 was found to degrade the diesel with a maximum degradation efficiency of 96% within 4 days
- The degradation efficiency was due to the synergistic role of biosurfactant and catabolic enzymes

Abstract

The present study integrated the electrokinetic (EK) with bioremediation (Bioelectrokinetic -BEK) of diesel hydrocarbon by *Staphylococcus epidermidis* EVR4. It was identified as efficient biosurfactant producing bacteria and growth parameters was optimized using response surface methodology. Upon degradation, there is a complete disappearance of peaks from nonane (C_9) to tricosane (C_{23}) and 85%, 47% of degradation of pentacosane and octacosane respectively. Marine bacterial strain, EVR4 was found to be potential to degrade the diesel with a maximum degradation efficiency of 96% within 4 d, which was due to its

PRINCIPAL
PGP College of Arts and Science
Namakkal

Chemosphere 264 (2021) 128377

Contents lists available at ScienceDirect

Chemosphere

journal homepage: www.elsevier.com/locate/chemosphere

Biosurfactant mediated bioelectrokinetic remediation of diesel contaminated environment

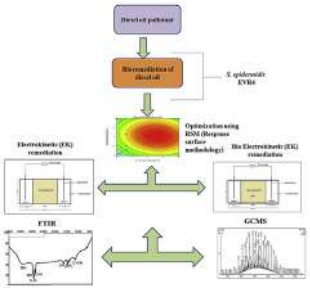
Jeevanandam Vaishnavi [a], Sandhanasamy Devanesan [b], Mohamad S. AlSalhi [b, *], Aruliah Rajasekar [a, **], Adikesavan Selvi [a], Palanisamy Srinivasan [c], Muthusamy Govarthanan [d, ***]

[a] Environmental Molecular Microbiology Research Laboratory, Department of Biotechnology, Thiruvalluvar University, Serkadu, Vellore, 632115, Tamilnadu, India
[b] Research Chair in Laser Diagnosis of Cancers, Department of Physics and Astronomy, College of Science, King Saud University, Riyadh KSA, P.O. Box -2455, Riyadh, 11451, Saudi Arabia
[c] PG & Research Department of Biotechnology, Mahendra Arts and Science College, Kalipatti, 637501, Tamil Nadu, India
[d] Department of Environmental Engineering, Kyungpook National University, Daegu, South Korea

HIGHLIGHTS

- *Staphylococcus epidermidis* EVR4 identified as efficient biosurfactant producing bacteria
- EVR4 degrades the nonane (C_9) to tricosane (C_{23}) completely and 85% and 47% of pentacosane and octacosane respectively
- EVR4 was found to degrade the diesel with a maximum degradation efficiency of 96% within 4 days
- The degradation efficiency was due to the synergistic role of biosurfactant and catabolic enzymes

GRAPHICAL ABSTRACT



ARTICLE INFO

Article history:
Received 15 July 2020
Received in revised form
6 September 2020
Accepted 15 September 2020
Available online 18 September 2020

Handling Editor: Derek Muir

Keywords:
Biodegradation
Diesel
Biosurfactant
Hydrocarbon degradation
Electrokinetic remediation

ABSTRACT

The present study integrated the electrokinetic (EK) with bioremediation (Bioelectrokinetic -BEK) of diesel hydrocarbon by *Staphylococcus epidermidis* EVR4. It was identified as efficient biosurfactant producing bacteria and growth parameters was optimized using response surface methodology. Upon degradation, there is a complete disappearance of peaks from nonane (C_9) to tricosane (C_{23}) and 85%, 47% of degradation of pentacosane and octacosane respectively. Marine bacterial strain, EVR4 was found to be potential to degrade the diesel with a maximum degradation efficiency of 96% within 4 d, which was due to its synergistic role of biosurfactant and catabolic enzymes (dehydrogenase, catalase and cytochrome C). The application of integrated BEK was an effective insitu method for the remediation of diesel contaminated soil by BEK (84%) than EK (67%). EVR4 as an effective strain can be employed for BIO-EK method to clean the diesel hydrocarbon polluted environment.

© 2020 Elsevier Ltd. All rights reserved.

* Corresponding author.
** Corresponding author.
*** Corresponding author.
E-mail addresses: malsalhi@ksu.edu.sa (M.S. AlSalhi), rajasekargood@tvu.edu.in, rajasekargood@gmail.com (A. Rajasekar), gova.muthu@gmail.com (M. Govarthanan).

https://doi.org/10.1016/j.chemosphere.2020.128377
0045-6535/© 2020 Elsevier Ltd. All rights reserved.

1. Introduction

Hydrocarbon is considered as the primary energy source and one of the major achievements made by a modern human. It is majorly used for transportation purposes throughout the world thus contributing a major cause for the environmental air/water pollution. Due to the demanding fuel need, there are many petrochemical industries flourishing all over the world. Among the hydrocarbons, diesel oil is composed of a complex mixture of alkanes and alkenes. Diesel oil is continuously reported as the major soil pollutant due to the diesel oil spillage during transportation and pipeline leakage or the leakage from the storage tanks (Hewelke et al., 2018). Oil spills occur frequently during refinery production, storage, processing, transportation, etc. Diesel oil/diesel exhaust is regarded as a potent human carcinogen (lung cancer). Diesel exhaust is the complex mixture of particles or gaseous phase of diesel oil.

Diesel oil exposure leads to eczema, blisters, and burns. Inhalation of diesel vapour causes headache, vomiting, fever, nausea and dizziness in humans (Chilcott, 2006). Physical, chemical, bioremediation, electrokinetic remediation and phytoremediation are the most common methods employed for hydrocarbon remediation (Harekrushna and Kumar 2012; Yao et al., 2012). Among other methods, bioremediation is reported as a promising, cost effective, environmental friendly approach to remediate hydrocarbon contaminated sites (Shahsavari et al., 2017). During degradation, microorganism uses hydrocarbons as a sole carbon source for their living and for their synthesis of cellular components (Coelho et al., 2015). This mechanism involves the conversion of highly toxic pollutants into less toxic form *ie.,* complex organic molecules into a simpler form which can be easily assimilated by the microbes (Coelho et al., 2015).

Hydrocarbon degrading microorganisms are ubiquitous in the marine environment and the relevant published papers of marine organisms employed towards hydrocarbon/diesel degradation are mentioned in Table 1. The major limitation of hydrocarbon biodegradation is that it takes a longer period of time, low efficiency of microbes, which makes it more difficult to remove hydrocarbons bounded to the soil (Barathi and Vasudevan, 2001; Sharma and Reddy, 2004). According to these reports, the percentage of degradation was also considerably low with a long time period. However, microbes producing surface active agents known as biosurfactants were considered to be effective in degrading hydrocarbons (Xue et al., 2019; Pi et al., 2017). It has been reported to exhibit high degradability with low toxicity and environmental friendly remediation strategy (Vijayakumar and Saravanan, 2015; Rajasekar et al., 2007a, 2007b). They were also found to be effective against extreme conditions such as pH, temperature and salinity (Pacwa-Płociniczak et al., 2011).

Along with biosurfactants, microbial enzymes also play a vital role in the biodegradation of diesel. It is reported to enhance bioremediation to several folds (Abatenh et al., 2017). But, screening of the enzymes involved in the degradation is much needed (Peixoto et al., 2011). Apart from their catabolic role, enzymes should also get adapted to the specific environmental conditions to achieve better biodegradation. Employing microbial enzymes is reported to be environmental friendly and cost effective (Karigar and Rao, 2011). These enzymes are secreted both intracellularly and extracellularly by many bacteria. So, screening of potent microbes with biosurfactant characteristics and catabolic enzyme production is of high research interest.

Electrokinetic (EK) remediation and Bioelectrokinetic (BEK) remediation is an in-situ remediation method used for soil pollutants (Yuan and Chiang, 2008). EK is a feasible method in polluted soil (Guo et al., 2014). Many studies have been reported that EK remediation effectively removes heavy metals in soil with low conductivity (Lukman et al., 2013). It is the cost effective technology to remediate different types of pollutants (Reddy, 2010). Bioelectrokinetic remediation involves the combination of biological/biotechnological remediation and electrokinetic remediation. It is more efficient than EK method due to the addition of microbes (Ma et al., 2018). EK and BEK remediation was carried out with direct current (DC), pH fluctuation was carefully monitored in BEK (Li et al., 2016) because maximum microbes do not survive in high acidic or alkaline condition (Gonzini et al., 2010). EK stimulates electroosmosis, electromigration and electrophoresis (Virkutyte et al., 2002). In low permeability soil microorganism migration will be increased (Wick et al., 2004).

The main objective of the study as follows.

- To optimizethe biosurfactant production for enhanced degradation using Response surface methodology (RSM)
- To elucidate the role of enzymes, such as, dehydrogenase, catalase and cytochrome C involved in diesel degradation
- To study the electrokinetic (EK) and bioelectrokinetic remediation (BEK)
- To characterize diesel degradation using Fourier-transform infrared spectroscopy (FT-IR) and Gas chromatography-mass spectrometry (GC-MS)
- To elucidate the probable mechanism of the degradation and to identify the degraded metabolites

2. Materials and methods

2.1. Isolation, screening, and identification of hydrocarbon degrading microorganisms

2.1.1. Sample collection

The marine sediment sample was collected from the Pichavaram mangrove forest located at Chidambaram, CuddaloreDist, TamilNadu, India (longitude 79.7955, latitude 11.4348), and the sampling site was shown in S1. The sediment sample was collected using a clean sterile container and later transported to the laboratory and stored at 4 °C.

2.1.2. Isolation and identification

Diesel degrading bacteria was isolated using Zobell marine agar (ZMA). The pH of the medium was adjusted to (pH 7.6 ± 0.2) and sterilized at 121 °C for 20 min 1 g of marine sediment sample was weighed and subjected to serial dilution using sterile marine seawater. Spread plate and pour plate technique were carried out to obtain individual colonies. Distinct colonies with dissimilar morphology were selected and cultured separately. Initially, the selected colonies were characterized by biochemical methods adopted from Bergey's manual. Molecular characterization by 16 S rRNA identification was performed as described by Bergey et al., 1994, DNA isolation protocol was carried out as mentioned in Ausubel et al., 1988. Amplification of DNA fragment was carried out using PCR. Forward primer 5′-CAGGCCTAACACATGCAAGTC-3′ and reverse primer 5′-GGCGGATGTGTACAAGGC-3'. Big dye terminator version 3.1 was used for sequencing reaction and the sequence was carried out using ABI 3130 genetic analyzer. Similar sequences are determined using BLAST through NCBI (Altschul et al., 1990). The phylogenetic tree was constructed using TREEVIEW software version 3.0.

2.2. Bacterial growth studies

The experimental study was carried out using Bushnell Haas

Table 1
List of marine organisms involved in hydrocarbon degradation from the literatures.

S.No	Marine Species	Type of hydrocarbondegradation	References	Percentage of degradation	Incubation period
1	*Alcanivorax borkumensis SK2*	Hydrocarbon/oil degrading bacteria	Kadri et al. (2018)	75%	72 h
2	*Marinobacter aquaeolei*		Huu et al. (1999)	Saturated hydrocarbons- 41% aromatic hydrocarbons- 52%	7 days
3	*Alcanivorax* sp.		Brooijmans et al. (2009)	NA	NA
4	*Oleiphilus,*				
5	*Thalassolituus,*				
6	*Marinobacter algicola DG893*				
7	*Oceanicaulis alexandrii HTCC2633*				
8	*Oleispira,*				
9	*Cycloclasticus pugetii PS-1*		Dyksterhouse et al. (1995)	NA	NA
10	*Achromobacter*	Petroleum degradation microorganis	Xue et al. (2015)	NA	NA
11	*Acinetobacter*				
12	*Alcaligenes*				
13	*Archrobacter*				
14	*Bacillus*			Aromatic hydrocarbon- 80% aliphatic hydrocarbon- 37%	
15	*Corynebacterium*				
16	*Pseudomonas*				
17	*Flavobacterium*			NA	
18	*Coryneforms*				
19	*Micrococcus*				
20	*Microbacterium*				
21	*Actinomycetes*				
22	*Nocardia*				
23	*Aureobasidium*				
24	*Candida*				
25	*Rhodotorula*				
26	*Sporobolomyces*				
27	*Aspergillus*	Petroleum degradation microorganism (Fungus)		NA	
28	*Mucor*				
29	*Fusarium*				
30	*Penicilium*				
31	*Ochrobactrum* sp. *N1*	Crude oil degradation	Bao et al. (2012)	51.1%	144 days
32	*Brevibacillusparabrevis*				
32	*Alcanivorax dieselolei*	Oil degradation	Kostka et al. (2011)	NA	NA
33	*Acinetobacter* sp				
34	*Pseudidiomarina maritime*				
35	*Marinobacter hydrocarbonoclasticus*				
36	*Vibrio hepatarius*				
37	*C. elegans*	Crude oil degradation	Cerniglia and Perry (2007)	91%	10 days
38	*Penicillium* sp.			92%	
39	*A versicolor*			NA	NA
40	*C acremonium*				

NA – not available.

(BH) media (composition g/L: $MgSO_4$-0.2, $CaCl_2$-0.02, KH_2PO_4-1.0, K_2HPO_4-1.0, NH_4—NO_3-1.0, $FeCl_3$-0.05, pH-7.0) supplemented with 1% of sterile diesel oil as a sole carbon source. Diesel oil was filter sterilized using 0.22 μm pore sized membrane filter. Diesel degrading bacteria was screened on the basis of utilization of diesel as their sole carbon source which was reflected in the respective optical density (OD) measured at 600 nm as reported in earlier studies (Borah and Yadav, 2014; Selvi et al., 2014) and to distinguish whether the bacteria is dead or alive it was cultured in a freshly prepared ZMA plate.

2.3. Screening for biosurfactant production

The isolated bacterium was screened for the production of biosurfactant by performing the standard protocol assays reported elsewhere (Parthipan et al., 2017; Thavasi et al., 2011). Tests viz., Drop collapse, oil dispersion, emulsification assay, emulsification index (E_{24}%) and BATH (bacterial adherence to hydrocarbon) assay were performed (Rosenberg, 1984).

2.4. Optimization of diesel degradation by response surface methodology (RSM)

Optimization of experimental parameters for diesel degradation process includes 3 factors of different ranges, pH (5.0—9.0), inoculum dosage (2, 4 and 6% (v/v)), diesel oil concentration (2, 4 and 6% (v/v)) were studied by RSM using Design expert statistical software (v11, Stat-Ease Inc., Minneapolis, MN,USA) approach (Selvi et al., 2015; Selvi and Aruliah, 2018). The range of each factor was fixed based on the preliminary experiments. The data analysis was carried out based on the quadratic model approach with an interaction of a single factor at a time at three different levels +1, 0 and −1. The diesel degradation (%) was fixed as a response variable, R1. The experimental design comprised of 17 runs. The validity of the model and the output responsewas analysed based on the ANOVA (Analysis of variance) results and 3D contour plots.

2.5. Biodegradation of diesel hydrocarbons

100 ml of BH medium was prepared with an optimized pH of

8.0, inoculum dosage of 4%, diesel oil concentration of 2% in a 250 ml Erlen Meyer flask and was incubated at 37 °C for 4 d in an orbital shaker. At the end of the 4th day, the residual diesel oil was extracted by shaking with an equal volume of n-hexane in a separating funnel (Adebusoye et al., 2007). The organic phase was extracted and evaporated in a hot air oven at 80 °C for 30 min. The resultant diesel oil was dissolved in n-hexane and used for characterization studies (Rajasekar et al., 2007a). Abiotic control flask containing the same components except the organism was also maintained along with the test flasks. All the experiments were carried out in duplicates.

2.6. Characterization of diesel oil degraded metabolites

2.6.1. Fourier-transform infrared (FTIR) spectroscopy

The breakdown of diesel into different new compounds can be analysed by noting the disappearance and appearance of major IR peaks in the FTIR spectra of diesel and its corresponding degraded product. After degradation, the residual diesel oil was collected following the protocol mentioned in the above section and analysed by FT-IR (Shimadzu, (Model No. 6500). The range was maintained between 4000 and 400 cm^{-1} (Rajasekar et al., 2007a).

2.6.2. Gas chromatography–mass spectrometry (GC-MS)

The degraded metabolites of diesel oil degradation were analysed using GC-MS (PerkinElmer, Clarus 680, equipped with Turbo mass software, ver 5.4.2). The residual diesel obtained after the degradation was dissolved in n-hexane. The sample was injected into the column with the injector temperature, set at 260 °C during chromatography run. Helium gas was used as a carrier at a flow rate maintained at 1.0 ml/min. The temperature was set at 60 °C–300 °C at the speed of 10 °C/min and hold at 6 min. The total run time was 32 min. The compounds were identified using National Institute of Standards and Technology (NIST) library. The diesel oil degradation was expressed in percentage on comparing with the diesel oil present in abiotic control. The percentage of diesel degradation efficiency (%) was calculated using the following formula as described by Rajasekar et al., 2008).

$$\frac{A_s \times 100}{A_c} - 100$$

A_s, sum of the area of the sample peak, A_c, Sum of the area of the abiotic control peak.

2.7. Enzyme studies

During the diesel degradation, supernatant was collected and centrifuged at 8000 rpm for 10 min and the supernatant was carefully aspirated out for dehydrogenase and catalase assay. The pellets were used to assay cytochrome C oxidase activity (Xue et al., 2017a, 2017b; Wu et al., 2016; Chandran and Das, 2012).

2.7.1. Assay of dehydrogenase activity

2 ml of supernatant was added into a separate tube containing 2 ml of tris Hcl buffer, 2 ml of glucose solution (0.1 M) and 2 ml of Triphenyl tetrazolium chloride (TTC) (0.5%) and incubated at 37 °C for 5 h. A small amount of sulphuric acid was added to stop the reaction. 5 ml of ethanol was added, shaken well and allowed to stand for 20min. The upper layer was removed to determine the dehydrogenase activity as described earlier (Xue et al., 2017; Pramila et al., 2014).

2.7.2. Assay of catalase activity

100 μl cell free broth was added into a separate tube containing 1000 μl of standard hydrogen peroxide (H_2O_2) solution. The mixture was vortexed and incubated at 37 °C for 3 min. Dichromate-acetic acid was added to stop the reaction further and the above mixture was heated to reduce dichromate in the presence of remaining H_2O_2. The remaining chromic acetate was measured at 570 nm as described earlier (Busalmen et al., 2002).

2.7.3. Assay of cytochrome C oxidase

The cell pellet was dissolved in phosphate buffer saline (pH 7.4) until the OD reached 1.0. 3 ml of the dissolved pellet was added into a separate tube containing few crystals of sodium dithionite or sodium hydrosulfite and the absorbance was measured at 554 nm as described earlier (Wen et al., 2018).

2.8. Electrokinetic study

2.8.1. Spiking of soil sample

The soil sample was collected from Serkkadu (13.0254°N, 79.2028°E), Vellore district, Tamil Nadu, India. The soil sample was air dried at room temperature and was sieved using 3 mm pore size. The soil was weighed and autoclaved at 121 °C for 20 min. The autoclaved soil was cooled at room temperature. Diesel oil was spiked into 500 g of soil at the concentration of 5 g of diesel and 20 ml of n-hexane [1:1 (v/v)], the diesel oil concentration of soil after evaporation was approximately 10 g/kg as mentioned in Song et al., (2018).

2.8.2. Electrokinetic cell setup

EK cell made of acrylic sheet with the measurement of L 10cm × W 4.0cm × H 7.0 cm and it includes DC power supply and titanium electrodes. The EK cell was divided into three equal parts by the two acrylic fritted membranes. The middle compartment was filled with spiked soil mixed with 1% bacterial pellet for BEK experiment and without bacterial serves as a control. The other two compartments are filled with electrolytes (2% NaCl). Two titanium electrodes was immersed in the electrolyte filled chamber which served as anode and cathode. Direct current (DC) power supply was used to monitor the electric current (voltage) during the experiments (Sarankumar et al., 2019) as mentioned in S2.

2.8.3. EK and BEK remediation

EK and BEK experiments were simultaneously conducted in an acrylic EK cell. The diesel oil spiked soil (EK)and 1% bacterial pellet mixed diesel spiked soil (BEK) was separately packed into a soil compartment and the electrolyte was chosen as 2% NaCl (Song et al., 2018) and it was added into anodic and cathodic compartments. The electric potential gradient of 2 V was fixed. The experiment was carried for 4 d. The electric current and pH was monitored during the incubation period. COD and TOC was further analysed to check the reduction.

2.8.4. Total organic content (TOC)

0.5 g of EK and BEK soil was weighed and transferred into a 500 ml conical flask to that 10 ml of 1 N $K_2Cr_2O_7$ was added and mixed well, 20 ml of conc. H_2SO_4 was added to the above mixture and gentle mixing was done to ensure complete contact. The content was left undisturbed for 30 min. After incubation, 200 ml of distilled water was added to it 10 ml of 85% phosphoric acid and diphenylamine indicator was added. This solution was titrated against 0.5 N ferrous ammonium sulphate. The colour is dull green at the beginning and shifts to blue and the end point is bright green colour (Mook et al., 2012).

2.8.5. Chemical oxygen demand

10 ml of cathodic electrolyte was collected from EK and BEK

remediation system to that 200 ml of distilled water was added to dilute the sample. To the reflux flask 10 ml of std potassium dichromate, 0.2 g of mercury sulphate, 0.2 g of silver sulphate and 20 ml of diluted sample was added. 30 ml of sulphuric acid was slowly added to the above mixture. The contents were then mixed and the flask was connected to the condenser of the reflux apparatus (COD digester) and reflux for 2hrs. Wait for the flask to come down to the room temperature and titrate it against ferrous ammonium sulphate using ferroin as indicator,colour change from blue green to red indicates the endpoint (Dubber and Gray, 2010).

3. Results and discussion

3.1. Isolation and identification of marine bacterial isolates

An indigenous bacterial strain, EVR4 was isolated from marine sediment samples of Pichavaram mangrove forest, Chidambaram, Cuddalore dist. Totally five diesel degrading bacteria viz., EVR3, EVR4, EVR5, EVR7 and EVR8 were isolated by culturing in Zobell marine agar (ZMA) plates. On the basis of hydrocarbon utilization, the isolate, EVR4 was chosen for further studies. Among five isolates, EVR4 colonies were white, cocci-shaped, cohesive, and raised with 1–2 mm dia in size. Further, the identification by biochemical tests showed positive for Grams staining, capsule staining, catalase, Voges-proskauer and sugar fermentation. And the negative results were observed for oxidase and methyl red. The biochemical results of all the isolates are shown in S3. The molecular analysis of 16 S rRNA was done for all the selected isolates. BLAST analysis revealed the phylogenetic relatedness of the close identity species of 100% similarity with *Staphylococcus epidermidis* strain, SRB-148 (Acc.no. MF594031.1). Hence, the EVR4 strain is identified as*Staphylococcus epidermidis*. Likewise, all other isolates were analysed by BLAST and the obtained FASTA nucleotide sequences of 16SrRNA been deposited in GenBank database with their identified names and accession numbers as follows, *Enterococcus faecium* EVR3 (Acc. No. MK377295.1), *Staphylococcus epidermidis* EVR4 (Acc. No. MK377296.1), *Vibrio alginilyticus*EVR5 (Acc, no. MK377297.1), *Bacillus foraminis*EVR7(Acc. no. MK377298.1), *Bacillus haikouensis*EVR8 (Acc. no. MK377299.1). The phylogenetic tree showing the evolutionary relationship between the closely identical bacterial species is shown in Fig. 1.

3.2. Bacterial growth studies of EVR4

The results of the effect of the growth curve of EVR4 towards diesel oil assimilation showed a standard growth curve of log phase that lasted until 66th h, after which a stationary phase was observed from the 72nd h and decline phase at 90th h at 600 nm. Growth curve analysis confirmed the assimilation ability of the strain, EVR4 as shown in S4. On further screening for the biosurfactant activity of EVR4, it showed positive results for all the screening tests (S5). The cationically charged biosurfactant was reported to attract the bacteria with anionic charge during diesel oil degradation (Ferradji et al., 2014). The exploration of biosurfactant based hydrocarbon degradation has already been reported widely (Parthipan et al., 2017). Though biosurfactant was reported to play a vital role in hydrocarbon degradation, not many reportsare available for diesel oil, in particular (Patowary et al., 2017). In the present study based on these revelations, the potentiality of the biosurfactant produced by our isolate EVR4 was explored for diesel degradation.

3.3. Optimization of experimental parameters of diesel degradation by RSM

RSM is an efficient statistical tool for the modeling of surface diagram and its contour plots with the multiple variables to predict the best result in less number of experimental trials. RSM by Box Behnken Design (BBD) was employed in the present study to optimize the experimental conditions such as pH, inoculum dosage and diesel oil concentration to favour maximum diesel degradation (Myers et al., 1995). Based on various combinations, the output

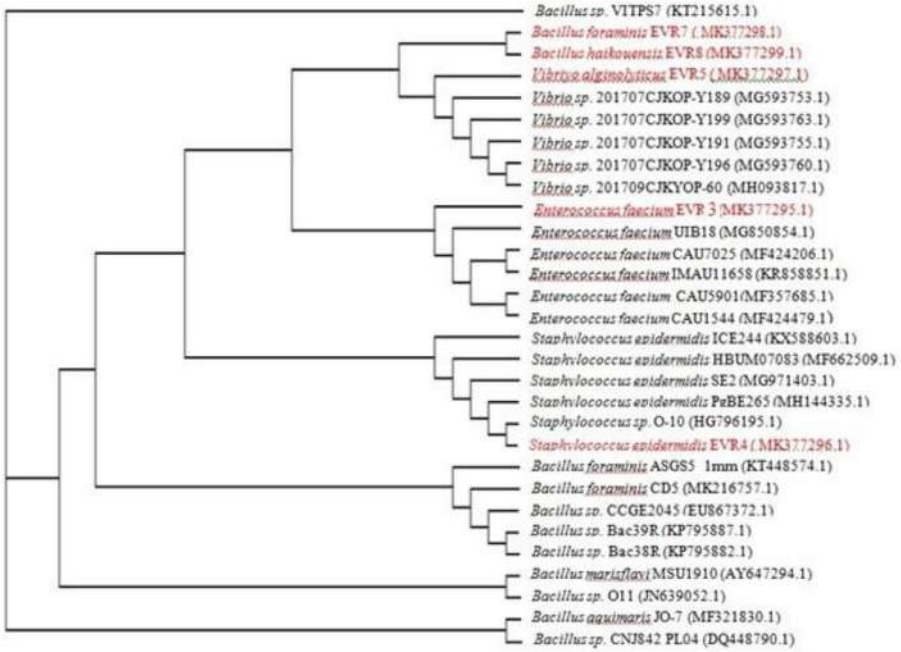


Fig. 1. Phylogenetic tree analysis of strain *Enterococcus faecium* EVR3 (MK377295.1), *Staphylococcus epidermidis* EVR4 (MK377296.1), *Vibrio alginilyticus* EVR5 (MK377297.1), *Bacillus foraminis* EVR7 (MK377298.1), *Bacillus haikouensis* EVR8 (MK377299.1) and related species. Genbank/EMBL accession numbers are included in parentheses.

response was obtained in the terms of diesel degradation percentage as shown in Fig. 2. In Fig 2a-f, the BBD model shows the 3D contour surface diagram and its contour plots. The actual and predicted values of the output response are analysed based on ANOVA in Table 2. The 3D diagram of (Fig. 2a–c) and contour plots (Fig. 2d–f) represented the optimal value of the input variable as a significant influence towards the diesel degradation either by means of dependent/independent interaction with each other. The spread of maximum red region in the contour plots inferred the significant interaction between the factors. The design comprised of 17 runs as mentioned in Table 3. The quadratic model of ANOVA showed F values of 68.13, 143.95 and 22,01 for the three responses. The significance is validated by P values, that showed <0.0001, <0.0001 and 0.0022 which was less than 0.05 in all the responses, thus indicating the model, significant. The adequate precision is used to measure the signal to noise ratio. The ratio should be greater than 4 and the adequate precision is found to be 39.080 which indicated an adequate signal. The coefficient estimate represents the expected change in response/unit change in factor value. When all other factors remaining constant. The VIF (Variance inflation factors) for pH, inoculum dosage and diesel oil concentration are found to be 1.0 which indicates the factors are orthogonal. Among the various individual factors, interaction factors and quadratic factors A (pH), B (inoculum dosage), C (Diesel oil concentration), AB, AC, BC, A^2, B^2, C^2 all were found to be significant. Based on the coded factor, equation of BBD is derived as follows,

Diesel degradation (%) = $89.40 + 1.55\,A + 2.25\,B + 0.8787C - 1.08AB - 0.6900AC - 0.8375\,BC - 7.18\,A^2 - 3.83\,B^2 - 41C^2$

The coded factor equation was used to make predictions about the response and was used to identify the relative impact of the factors. The obtained results and the statistical values were found to rely on the same accordance. Therefore, the model was found to validate the maximum diesel degradation by the strain EVR4. Optimization using RSM was already reported in other remediation studies (Selvi et al., 2015; Selvi and Aruliah, 2018). The obtained results of RSM software produced a detailed understanding of

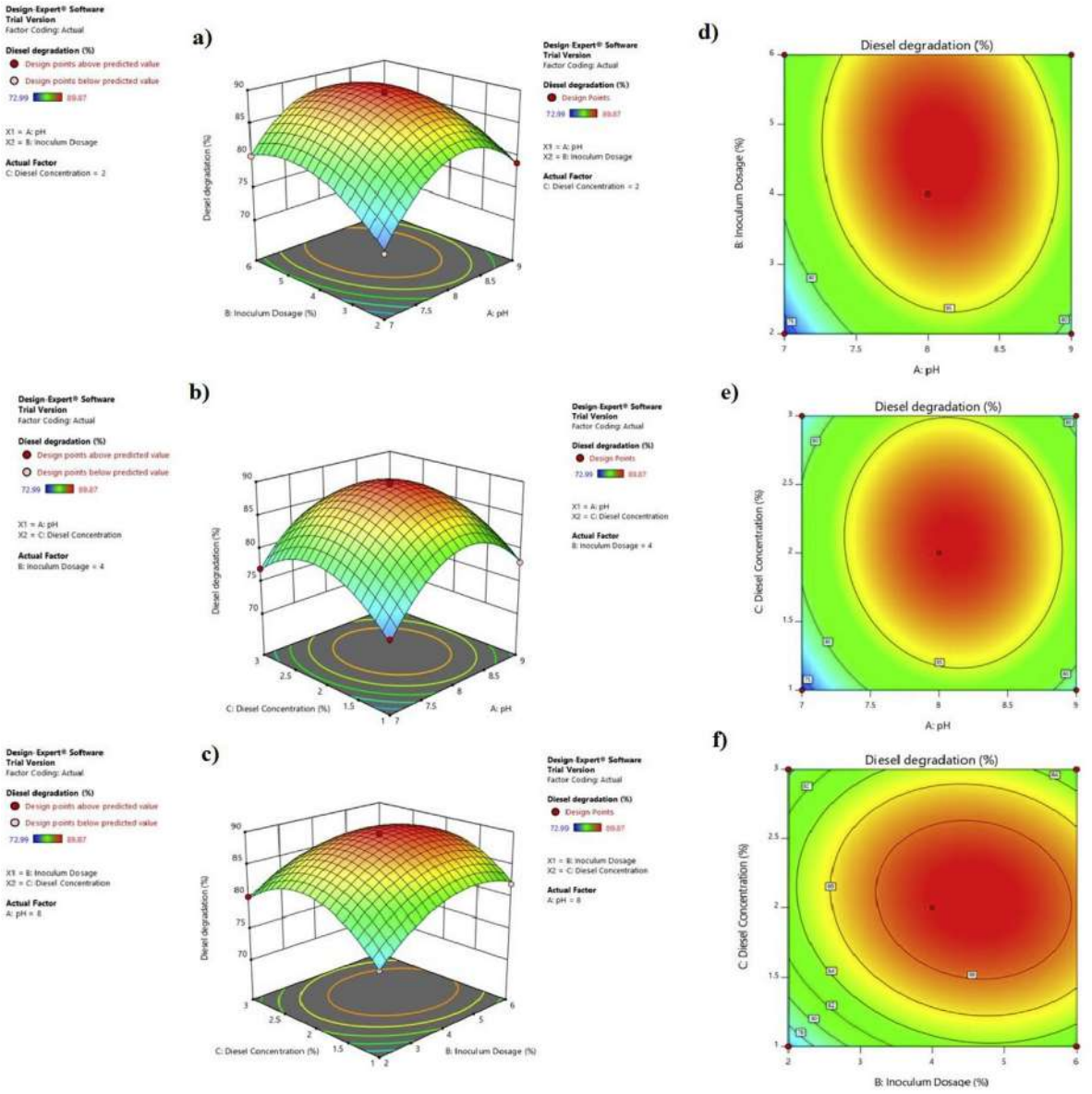


Fig. 2. The 3D surface diagram and the contour plots showing the interaction between different optimized parameters with respect to diesel degradation by *Staphylococcus epidermidis* EVR4.

various interactions between the selected factors to attain effective and maximum diesel degradation.

3.4. Fourier-transform infrared (FTIR) spectroscopy

The FTIR spectrum (Fig. 3) of uninoculated diesel oil which served as a control showed sharp peaks at 3421 cm^{-1}corresponding to O–H aromatic stretch (Rajasekar et al., 2007a, 2007b), and a strong peak at 2964 cm^{-1} belongs to O–H stretch, and at the 2931 cm^{-1} peak corresponds to C–H aliphatic alkane stretch, variable peak at 2854 cm^{-1} belongs to C–H aliphatic alkane. Medium peaks at 1458 cm^{-1} and 1382 cm^{-1} which represents the CH_2 bend and CH_3 bends (Coates, 2006; Elumalai et al., 2019). A strong peak at 1120 cm^{-1} belongs to C–OH stretch respectively (Fan et al., 2012). The FTIR spectrum of the biodegraded diesel oil with *Staphylococcus epidermidis* (EVR4) was compared with control as shown in Fig. 3b., The comparison showed disappearance of significant peaks at 2922 cm^{-1}, and 1475 cm^{-1}, thus indicating an effective degradation by EVR4. In addition, there was a formation of a new peak at 1636 cm^{-1} which corresponded to imine/oximine C═N, which may be formed due to the dehydration *ie.* removal of H_2O molecules (Ciaccia and Di Stefano, 2015). The peak at 1465 cm^{-1}corresponding to CH_2 has been completely disappeared. At the same time, there was a decrease in the intensity of the peaks at 1382 cm^{-1}, which may be due to the reduction of CH_2 to C–H (Rajasekar et al., 2007a, 2007b). Likewise, C–OH has also been found to be reduced to C–O (Revathy et al., 2015; Sharma et al., 2014). The reduced intensities and disappearance of characteristic peaks of the parent compound proved the effective biodegradation of diesel oil by EVR4 strain.

3.5. Gas chromatography-mass spectrometry analysis

On analysing the chromatogram of diesel degradation using GC-MS, it showed multiple peaks observed in the control system (Fig. 4a). Significant high intensity peaks at RT 11.91 confirmed the diesel hydrocarbon presence with the molecular formula of $C_{14}H_{30}$ (Tetradecane). On comparison with EVR4 inoculated system, most of the higher molecular weight *i. e*, corresponding to peaks at (C_9 – C_{23}) is found to be disappeared after 4 d of inoculation (Fig. 4b). The corresponding molecular weight of the degraded metabolites was mentioned in Table 4. Similar studies on hydrocarbon degradation showed that in the range C_{14}–C_{20} was consumed and utilized easily by the hydrocarbon degrading bacteria as a sole carbon source (Mishra et al., 2004; Parthipan et al., 2017). The results analysis of the degraded metabolites was extracted from NIST libraries. On calculating the biodegradation efficiency, a complete 100% of degradation of C_9H_{20}– $C_{23}H_{48}$ (Nonane, Decane, Undecane, Dodecane, Tridecane, Tetradecane, Pentadecane, Hexadecane, Heptadecane, Octadecane, Nonadecane, Eicosane, Henicosane and Tricosane) was achieved by the marine isolate *Staphylococcus epidermis*, EVR4 as shown in Table 4. In addition, Pentacosane and Octacosane compounds showed 85% and 47% degradation by EVR4. Other probable degradation products which appeared as new peaks of low intensity metabolites are reported here for the first time. The metabolites are as follows, Pentane, 2,3,3-Trimethyl (C_8H_{18}), 1-Iodo-2-Methylundecane ($C_{12}H_{25}I$), Undecane, 2,10-Dimethyl ($C_{13}H_{28}$), 1-Iodo-2-Methylundecane ($C_{12}H_{25}I$), Sulfurous Acid, 2-Propyl Tridecyl Ester ($C_{16}H_{34}O_3S$), 1H-Tetrazol-5-Amine (CH_3N_5), 2,3-Anhydro-D-Galactosan ($C_6H_8O_4$), 3-Tert-Butoxycarbonylamino-Butyric Acid ($C_9H_{17}O_4N$) were also noted after biodegradation by EVR4 (S6). The chromatogram showed the complete disappearance and reduced intensities of many significant parent peaks, thus confirming the effective degradation of biosurfactant producing EVR4. The maximum diesel degradation efficiency of 96% was noted within a short time period of 4 d, then compared to earlier studies by Rajasekar et al., 2007a, who reported on bioremediation of diesel oil degradation using *Serratia marcescens* which degraded diesel oil in 30 d with the biodegradation efficiency of 69%. Similarly, Chandran and Das (2011) too reported on *Candida tropicalis* which degraded diesel oil in 7 d with a biodegradation efficiency of 80%. Poddar et al., 2019 reported on hydrocarbon degradation using a bacterial consortium of *Enterobacter* sp., *Pantoea* sp., *Klebsiella* spp. with a degradation rate of 4.05% per day and an overall degradation rate of 16.20% in 4 d. However, our study showed the highest degradation efficiency in less number of days, thus proving the potentiality of EVR4 marine isolate.

3.6. Enzyme studies

An extracellular enzyme, dehydrogenase was reported to play a vital role in diesel oil degradation. This was evident in our study too. The measurement of dehydrogenase enzyme activity was

Table 2
ANOVA for RSM - Quadratic model –Response: percentage of diesel degradation.

Source	Sum of Squares	Df	Mean Square	F-value	p-value	
Model	520.72	9	57.86	206.10	<0.0001	Significant
A-pH	19.13	1	19.13	68.13	<0.0001	
B-Inoculum Dosage	40.41	1	40.41	143.95	<0.0001	
C-Diesel Concentration	6.18	1	6.18	22.01	0.0022	
AB	4.64	1	4.64	16.54	0.0048	
AC	1.90	1	1.90	6.78	0.0352	
BC	2.81	1	2.81	9.99	0.0159	
A^2	217.27	1	217.27	773.96	<0.0001	
B^2	61.63	1	61.63	219.55	<0.0001	
C^2	123.39	1	123.39	439.55	<0.0001	
Residual	1.97	7	0.2807			
Lack of Fit	1.53	3	0.5104	4.71	0.0844	not significant
Pure Error	0.4339	4	0.1085			
Corr. total	522.68	16				
Std. Dev.	0.5298					
Mean	81.67					
C·V. %	0.6487					
R^2	0.9962					
Adjusted R^2	0.9914					
Predicted R^2	0.9518					
Adeq Precision	39.0797					

Table 3
Data of RSM parameters for optimization and experimental design based on design expert.

Run Order	Actual Value	Predicted Value	Residual	Leverage	Internally Studentized Residuals	Externally Studentized Residuals	Cook's Distance	Influence on Fitted Value DFFITS	Standard Order
1	74.23	73.69	0.5400	0.750	2.038	2.960	1.246[1]	5.127[1]	5
2	89.25	89.40	−0.1520	0.200	−0.321	−0.299	0.003	−0.150	16
3	82.46	82.45	0.0088	0.750	0.033	0.031	0.000	0.053	12
4	72.99	73.52	−0.5312	0.750	−2.005	−2.846	1.206[1]	−4.930[1]	1
5	76.19	76.20	−0.0087	0.750	−0.033	−0.031	0.000	−0.053	9
6	78.00	78.16	−0.1625	0.750	−0.613	−0.584	0.113	−1.011	6
7	89.56	89.40	0.1580	0.200	0.333	0.311	0.003	0.156	14
8	80.00	80.17	−0.1712	0.750	−0.646	−0.617	0.125	−1.069	3
9	78.94	78.77	0.1713	0.750	0.646	0.617	0.125	1.069	2
10	76.99	76.83	0.1625	0.750	0.613	0.584	0.113	1.011	7
11	78.00	78.54	−0.5400	0.750	−2.038	−2.960	1.246[1]	−5.127[1]	8
12	82.00	82.37	−0.3688	0.750	−1.392	−1.515	0.581	−2.625[1]	10
13	80.00	79.63	0.3688	0.750	1.392	1.515	0.581	2.625[1]	11
14	89.87	89.40	0.4680	0.200	0.988	0.986	0.024	0.493	17
15	81.64	81.11	0.5313	0.750	2.005	2.846	1.206[1]	4.930[1]	4
16	89.33	89.40	−0.0720	0.200	−0.152	−0.141	0.001	−0.070	13
17	89.00	89.40	−0.4020	0.200	−0.848	−0.829	0.018	−0.415	15

found to be increased in accordance with the assimilation of diesel oil and growth characteristics of our isolate (S7). A similar study was already reported by Xue et al., 2017. The highest activity of enzyme dehydrogenase 36.13 mM min^{-1} in our study was achieved at the end of 4th day. The other enzyme, catalase too has a significance in diesel degradation as reported in previous literature (Ameen et al., 2016; Margesin et al., 2000). Catalase activities of our degradation studies were noted to be increased at the end of the incubation period with a noted value of 30.07 mM min^{-1} in accordance to the growing trend in the presence of diesel containing medium (Fig. S4). The heme protein, cytochrome C facilitates the extracellular electron transfer which helps in bioremediation (Wen et al., 2018). No study was reported earlier showing the role of cytochrome C activity in diesel degradation. In this study, cytochrome C activity assayed the diesel degradation was found to be considerably increased and achieved a maximum of 13.16 mM min^{-1} at the end of the 4th day of incubation period as shown in S7. The obtained results of enzyme assays supported the significance of their involvement in contributing to high diesel degradation in less time.

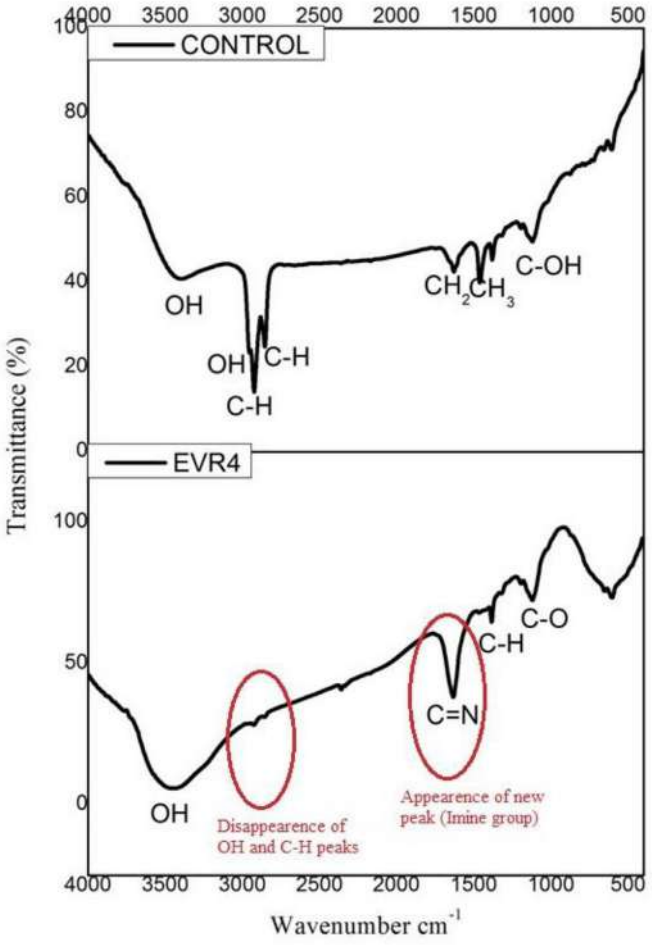


Fig. 3. FTIR spectrum of diesel degradation by *S. epidermidis* EVR4.

Based on the identification of completely degraded and partially degraded metabolites, a probable mechanism has been proposed as a flowchart as depicted in Fig. 5. As seen from the obtained degradation efficiency, the synergistic role of biosurfactants and enzymes of EVR4 are found to be responsible for the enhanced diesel degradation. The degraded metabolites are expected to breakdown to produce CO_2 and H_2O, as the final products.

Diesel oil is long chain hydrocarbons that are consumed by bacteria present in the environment by the process called bioremediation, which can be enhanced in the presence of surface active agents called biosurfactants. In addition, enzymes namely dehydrogenase, catalase and cytochrome C oxidase play a vital role in biodegradation. The biodegradation efficiency is enhanced by the biosurfactant and enzymes which results in the production of CO_2 and H_2O and thus the oxidation of hydrocarbons (O_2) occurs which is presented in Fig. 5.

3.7. EK and BEK remediation

3.7.1. Variation of pH

When the electric current is passed, the increase in H^+ ions results in a decrease in pH (anode). Whereas, an increase in the OH^- ions results in an increase in pH (Cathode) (Yuan and Chiang, 2008). According to Acar and Alshawabkeh (1993), H^+ ion dominates the electrokinetic system because it is 1.75 times greater than OH^- ions. Therefore, due to the H+and OH^- ion migration, there is a change in pH. In this study, there is a similar change in pH was monitored during EK and BEK experiments as shown in S8. Low pH was seen near the anode and high pH was seen near cathode throughout the EK and BEK experiment.

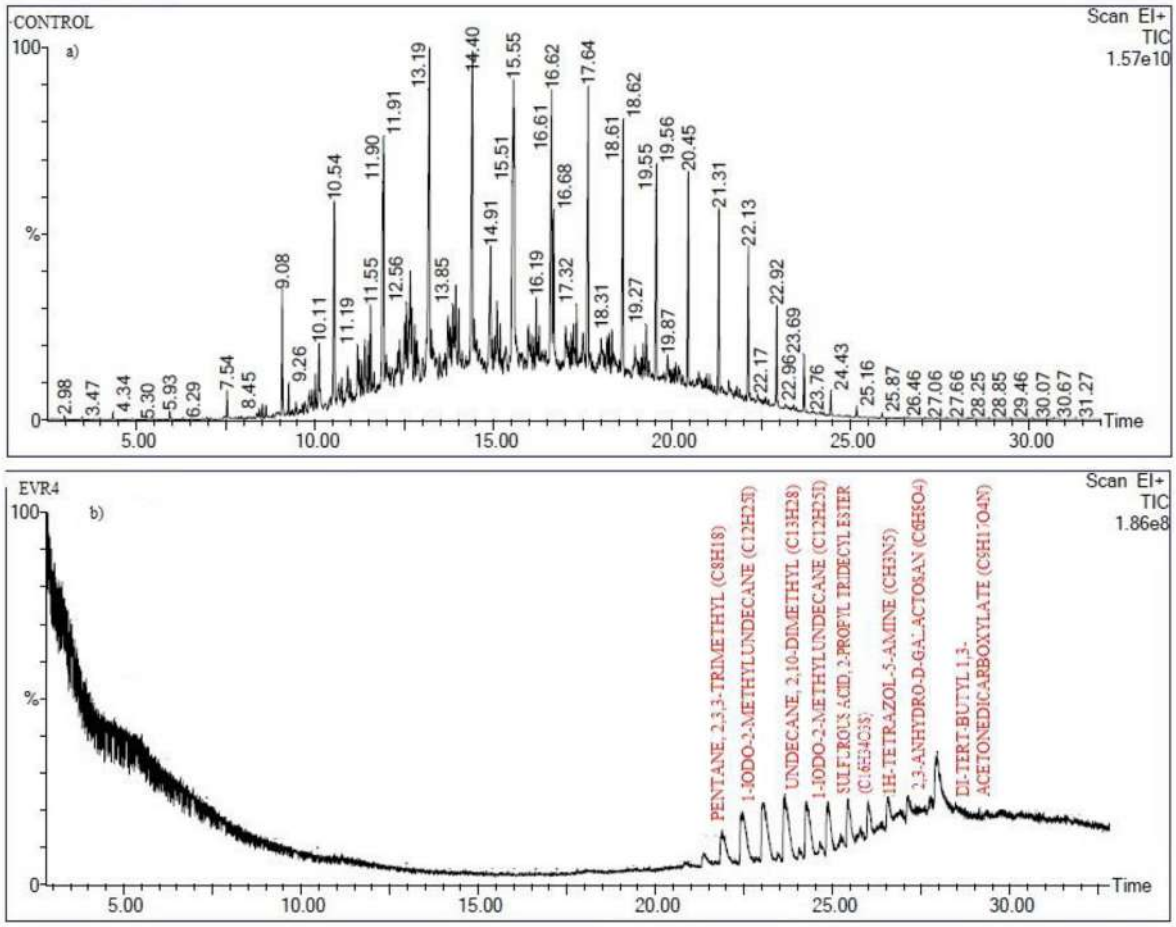


Fig. 4. GCMS spectrum of diesel degradation by *S. epidermidis* EVR4. a) Abiotic control; b) *S. epidermidis* EVR4.

Table 4
Gas chromatography–mass spectrometry (GC-MS) data for the biodegradation efficiency of diesel oil inoculated systems.

RT*	Chemical formula	Chemical name	MW*	Control RA*	EVR4 RA*	BE* (%)
4.36	C_9H_{20}	Nonane	128	49.68	0	100
5.97	$C_{10}H_{22}$	Decane	142	65.4	0	100
7.59	$C_{11}H_{24}$	Undecane	156	79.09	0	100
9.12	$C_{12}H_{26}$	Dodecane	170	80.61	0	100
10.57	$C_{13}H_{28}$	Tridecane	184	91.26	0	100
11.92	$C_{14}H_{30}$	Tetradecane	198	87.71	0	100
13.19	$C_{15}H_{32}$	Pentadecane	212	100	0	100
14.38	$C_{16}H_{34}$	Hexadecane	226	93.28	0	100
15.51	$C_{17}H_{36}$	Heptadecane	240	89.73	0	100
16.58	$C_{18}H_{38}$	Octadecane	254	88.72	0	100
17.61	$C_{19}H_{40}$	Nonadecane	268	83.65	0	100
18.58	$C_{20}H_{42}$	Eicosane	282	82.64	0	100
19.51	$C_{21}H_{44}$	Henicosane	292	81.12	0	100
20.4	$C_{23}H_{48}$	Tricosane	324	68.44	0	100
21.84	$C_{25}H_{52}$	Pentacosane	338	56.27	8.46	85
22.44	$C_{28}H_{58}$	Octacosane	394	25.35	13.44	47
Diesel degradation efficiency						96

rt$_*$- retention time, **mw**$_*$- moleular weight, **ra**$_*$- relative abudance, **be**$_*$- biodegradation efficiency.

3.7.2. Variation of current (mA)

According to Acar and Alshawabkeh (1993), the electric current across the soil is related to the mobile ions present in the soil. These mobile ions are H+and OH^- which are generated by electrolysis (Kim et al., 2005). The electric current was low in the EK experiment whereas, it was high in BEK experiments. The results were obtained in the form of mA versus hour as shown in S9. The electric current was noted to be increasing after every 10 h this may be due to the addition of electrolyte (NaCl). There is a gradual decrease after 72ndh in EK and 64thh in BEK. The maximum output was noted to be 1.01 mA/cm^2 for EK and 1.32 mA/cm^2 for the BEK experiment. The similar reports by Reddy and Cutright (2003); Wang et al., (2007) reported regarding the increase in electric current.

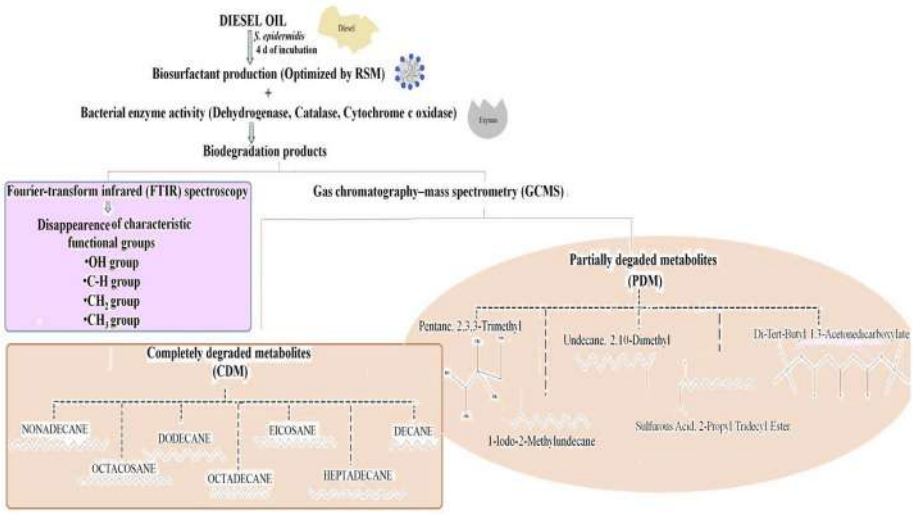


Fig. 5. Probable mechanism of diesel oil biodegradation by *Staphylococcus epidermidis* at the end of 4th day.

3.7.3. Total organic carbon (TOC)

The TOC in BEK was higher (84.9%) when compared to EK (67.4%). The maximum percentage was seen in the S5 section of soil. The S3 section of the soil has a TOC of 80.6% in BEK whereas in EK it was 63.7%. The lowest percentage of TOC was recorded in the S1 section, BEK has 73.6% and 59.9% in EK altogether BEK has a higher concentration of TOC after 4 d of treatment (S10). According to Picard and Chaouki (2017), the presence of NaCl as an electrolyte, there is more presence of chloride ions which attributes in the oxidation activity which results in the oxidation of diesel. A similar study was carried out by Song et al., (2017) the diesel oil removal from the sand matrix was coupled with the EK experiments and the maximum removal was about 1130 mg/L.

3.7.4. Chemical oxygen demand

The COD was used to measure the amount of organic compounds present in the soil. The COD level was mentioned in S11. The maximum removal percentage in EK was 67% whereas; in BEK it was 84.9%. According to Leitgib et al., (2008) available carbons and protons are utilized by the bacteria as a nutrient which reduces COD and increases the fertility of the soil.

4. Conclusion

S.epidermidis EVR4 is an effective biological agent that can be employed for diesel degradation due to the efficient production of biosurfactant and enzymes. Optimization results by RSM showed that all the factors such as pH, diesel oil concentration and inoculum concentration were found to be in good correlation towards the degradation of diesel oil. FTIR and GCMS confirm the biodegradation of diesel and the identification of degraded metabolites. In order to remove the organic content during the biodegradation process, the EK & BEK remediation was employed and shows the maximum removal of TOC (80.6%) and COD (84.9%) which increases the degradation efficiency. whereas, in biodegradation we have successfully degraded 96% diesel oil. The outcome of the study evidenced the isolate, EVR4 as an effective biological agent that can be considered to clean up the hydrocarbon contaminated sites with good degradation efficiency at less time period, compared to earlier studies.

Credit author statement

Jeevanandam Vaishnavi: Experimental work, Field collection, Writing - original draft. Sandhanasamy Devanesan: Validation, Formal analysis Mohamad S. AlSalhi: Resources, Funding acquisition. Aruliah Rajasekar: Project administration, Supervision, Validation, Writing - review & editing. Adikesavan Selvi: Software, Validation. Palanisamy Srinivasan: Visualization, Investigation. Muthusamy Govarthanan: Writing –editing, Scientific discussion.

Declaration of competing interest

The authors declare that they have no known competing financial interests or personal relationships that could have appeared to influence the work reported in this paper.

Acknowledgment

The authors are grateful to the Deanship of Scientific Research, King Saud University for funding through Vice Deanship of Scientific Research Chairs.

Appendix A. Supplementary data

Supplementary data to this article can be found online at https://doi.org/10.1016/j.chemosphere.2020.128377.

References

Abatenh, E, Gizaw, B, Tsegaye, Z, Wassie, M, 2017. The role of microorganisms in bioremediation-A review. Open Journal of Environmental Biology 2(1), 030–046.
Acar, Y.B., Alshawabkeh, A.N., 1993. Principles of electrokinetic remediation. Environ. Sci. Technol. 27 (13), 2638–2647. https://doi.org/10.1021/es00049a002.
Adebusoye, S.A., Ilori, M.O., Amund, O.O., Teniola, O.D, Olatope, S.O, 2007. Microbial degradation of petroleum hydrocarbons in a polluted tropical stream. World journal of Microbiology and Biotechnology. https://doi.org/10.1007/s11274-007-9345-3.
Altschul, S.F., Gish, W., Miller, W., Myers, E.W., Lipman, D.J., 1990. Basic local alignment search tool. J. Mol. Biol. 215 (3), 403–410. https://doi.org/10.1016/S0022-2836(05)80360-2.
Ameen, F., Moslem, M., Hadi, S., Al-Sabri, A.E., 2016. Biodegradation of diesel fuel hydrocarbons by mangrove fungi from Red Sea Coast of Saudi Arabia. Saudi J. Biol. Sci. 23 (2), 211–218. https://doi.org/10.1016/j.sjbs.2015.04.005.
Ausubel, F.M., Brent, R., Kingston, R.E., Moore, D.D., Seidelman, J.G., Struhl, K.E., 1988. Current Protocols in Molecular Biology. Wiley, New York, N.Y.
Bao, M.T., Wang, L.N., Sun, P.Y., Cao, L.X., Zou, J., Li, Y.M., 2012. Biodegradation of

crude oil using an efficient microbial consortium in a simulated marine environment. Mar. Pollut. Bull. 64 (6), 1177–1185. https://doi.org/10.1016/j.marpolbul.2012.03.020.
Barathi, S., Vasudevan, N., 2001. Utilization of petroleum hydrocarbons by Pseudomonas fluorescens isolated from a petroleum-contaminated soil. Environ. Int. 26 (5–6), 413–416. https://doi.org/10.1016/s0160-4120(01)00021-6.
Borah, D., Yadav, R.N.S., 2014. Biodegradation of diesel, crude oil, kerosene and used engine oil by a newly isolated Bacillus cereus strain DRDU1 from an automobile engine in liquid culture. Arabian J. Sci. Eng. 39 (7), 5337–5345. https://link.springer.com/article/10.1007/s13369-014-1118-3.
Bergey, D.H., Holt, J.G., Krieg, P., 1994. Bergey's Manual of Determinative Bacteriology. 1994. Williams and Wilkins, Baltimore, MD, USA.
Broojmans, R.J., Pastink, M.I., Siezen, R.J., 2009. Hydrocarbon-degrading bacteria: the oil-spill clean-up crew. Microbial biotechnology 2 (6), 587–594. https://doi.org/10.1111/j.1751-7915.2009.00151.x.
Busalmen, J.P., Vazquez, M., De Sanchez, S.R., 2002. New evidences on the catalase mechanism of microbial corrosion. Electrochim. Acta 47 (12), 1857–1865. https://doi.org/10.1016/S0013-4686(01)00899-4.
Cerniglia, C.E., Perry, J.J., 2007. Crude oil degradation by microorganisms isolated from the marine environment. ZeitschriftfürallgemeineMikrobiologie 13 (4), 299–306. https://doi.org/10.1002/jobm.3630130403.
Chandran, P., Das, N., 2011. Degradation of diesel oil by immobilized Candida tropicalis and biofilm formed on gravels. Biodegradation 22 (6), 1181–1189. https://doi.org/10.1007/s10532-011-9473-1.
Chandran, P., Das, N., 2012. Role of plasmid in diesel oil degradation by yeast species isolated from petroleum hydrocarbon-contaminated soil. Environ. Technol. 33 (6), 645–652.
Chilcott, R.P., 2006. Compendium of Chemical Hazards: Kerosene (Fuel Oil). Health Protection Agency (HPA). Chemical Hazards and Poisons Division (CHAPD HQ). Chilton, Didcot. Oxfordshire, OX11 0RQ, United Kingdom.
Ciaccia, M., Di Stefano, S., 2015. Mechanisms of imine exchange reactions in organic solvents. Org. Biomol. Chem. 13 (3), 646–654. https://doi.org/10.1039/C4OB02110J.
Coates, J., 2006. Interpretation of infrared spectra, a practical approach. Encyclopedia of analytical chemistry: applications, theory and instrumentation. https://doi.org/10.1002/9780470027318.a5606.
Coelho, L.M., Rezende, H.C., Coelho, L.M., de Sousa, P.A., Melo, D.F., Coelho, N.M., 2015. Bioremediation of polluted waters using microorganisms. In: Advances in Bioremediation of Wastewater and Polluted Soil. https://doi.org/10.5772/60770. Intech.
Dubber, D., Gray, N.F., 2010. Replacement of chemical oxygen demand (COD) with total organic carbon (TOC) for monitoring wastewater treatment performance to minimize disposal of toxic analytical waste. Journal of Environmental Science and Health Part A 45 (12), 1595–1600. https://doi.org/10.1080/10934529.2010.506116.
Dyksterhouse, S.E., Gray, J.P., Herwig, R.P., Lara, J.C., Staley, J.T., 1995. Cycloclasticuspugetii gen. nov., sp. nov., an aromatic hydrocarbon-degrading bacterium from marine sediments. Int. J. Syst. Evol. Microbiol. 45 (1), 116–123. https://doi.org/10.1099/00207713-45-1-116.
Elumalai, P., Parthipan, P., Narenkumar, J., Anandakumar, B., Madhavan, J., Oh, B.T., Rajasekar, A., 2019. Role of thermophilic bacteria (Bacillus and Geobacillus) on crude oil degradation and biocorrosion in oil reservoir environment. 3 Biotech 9 (3), 79. https://doi.org/10.1007/s13205-019-1604-0.
Fan, M., Dai, D., Huang, B., 2012. Fourier transform infrared spectroscopy for natural fibres. In Fourier transform-materials analysis. Intech. https://doi.org/10.5772/35482.
Ferradji, F.Z., Mnif, S., Badis, A., Rebbani, S., Fodil, D., Eddouaouda, K., Sayadi, S., 2014. Naphthalene and crude oil degradation by biosurfactant producing Streptomyces spp. isolated from Mitidja plain soil (North of Algeria). Int. Biodeterior. Biodegrad. 86, 300–308. https://doi.org/10.1016/j.ibiod.2013.10.003.
Gonzini, O., Plaza, A., Di Palma, L., Lobo, M.C., 2010. Electrokinetic remediation of gasoil contaminated soil enhanced by rhamnolipid. J. Appl. Electrochem. 40 (6), 1239–1248. https://doi.org/10.1007/s10800-010-0095-9.
Guo, S., Fan, R., Li, T., Hartog, N., Li, F., Yang, X., 2014. Synergistic effects of bioremediation and electrokinetics in the remediation of petroleum-contaminated soil. Chemosphere 109, 226–233. https://doi.org/10.1016/j.chemosphere.2014.02.007.
Harekrushna, S., Kumar, D.C., 2012. A review on: bioremediation. Int. J. Res. Chem. Environ. 2 (1), 13–21.
Hewelke, E., Szatyłowicz, J., Hewelke, P., Gnatowski, T., Aghalarov, R., 2018. The impact of diesel oil pollution on the hydrophobicity and CO 2 efflux of forest soils. Water, Air, Soil Pollut. 229 (2), 51. https://link.springer.com/article/10.1007/s11270-018-3720-6.
Huu, N.B., Denner, E.B., Ha, D.T., Wanner, G., Stan-Lotter, H., 1999. Marinobacter aquaeolei sp. nov., a halophilic bacterium isolated from a Vietnamese oil-producing well. Int. J. Syst. Evol. Microbiol. 49 (2), 367–375. https://doi.org/10.1099/00207713-49-2-367.
Kadri, T., Rouissi, T., Magdouli, S., Brar, S.K., Hegde, K., Khiari, Z., Daghrir, R., Lauzon, J.M., 2018. Production and characterization of novel hydrocarbon degrading enzymes from Alcanivoraxborkumensis. Int. J. Biol. Macromol. 112, 230–240. https://doi.org/10.1016/j.ijbiomac.2018.01.177.
Karigar, C.S., Rao, S.S., 2011. Role of microbial enzymes in the bioremediation of pollutants: a review. Enzym. Res. https://doi.org/10.4061/2011/805187.
Kim, S.O., Kim, W.S., Kim, K.W., 2005. Evaluation of electrokinetic remediation of arsenic-contaminated soils. Environ. Geochem. Health 27 (5–6), 443–453. https://doi.org/10.1007/s10653-005-2673-z.
Kostka, J.E., Prakash, O., Overholt, W.A., Green, S.J., Freyer, G., Canion, A., Delgardio, J., Norton, N., Hazen, T.C., Huettel, M., 2011. Hydrocarbon-degrading bacteria and the bacterial community response in Gulf of Mexico beach sands impacted by the Deepwater Horizon oil spill. Appl. Environ. Microbiol. 77 (22), 7962–7974. https://doi.org/10.1128/AEM.05402-11.
Leitgib, L., Gruiz, K., Fenyvesi, É., Balogh, G., Murányi, A., 2008. Development of an innovative soil remediation:"Cyclodextrin-enhanced combined technology". Sci. Total Environ. 392 (1), 12–21. https://doi.org/10.1016/j.scitotenv.2007.10.055.
Li, T., Wang, Y., Guo, S., Li, X., Xu, Y., Wang, Y., Li, X., 2016. Effect of polarity-reversal on electrokinetic enhanced bioremediation of Pyrene contaminated soil. Electrochim. Acta 187, 567–575. https://doi.org/10.1016/j.electacta.2015.11.097.
Lukman, S., Essa, M.H., Mu'azu, N.D., Bukhari, A., 2013. Coupled electrokinetics-adsorption technique for simultaneous removal of heavy metals and organics from saline-sodic soil. Sci. World J. https://doi.org/10.1155/2013/346910.
Ma, Y., Li, X., Mao, H., Wang, B., Wang, P., 2018. Remediation of hydrocarbon–heavy metal co-contaminated soil by electrokinetics combined with biostimulation. Chem. Eng. J. 353, 410–418. https://doi.org/10.1016/j.cej.2018.07.131.
Margesin, R., Walder, G., Schinner, F., 2000. The impact of hydrocarbon remediation (diesel oil and polycyclic aromatic hydrocarbons) on enzyme activities and microbial properties of soil. Acta Biotechnol. 20 (3-4), 313–333. https://doi.org/10.1002/abio.370200312.
Mishra, S., Sarma, P.M., Lal, B., 2004. Crude oil degradation efficiency of a recombinant Acinetobacter baumannii strain and its survival in crude oil-contaminated soil microcosm. FEMS Microbiol. Lett. 235 (2), 323–331. https://doi.org/10.1111/j.1574-6968.2004.tb09606.x.
Mook, W.T., Chakrabarti, M.H., Aroua, M.K., Khan, G.M.A., Ali, B.S., Islam, M.S., Hassan, M.A., 2012. Removal of total ammonia nitrogen (TAN), nitrate and total organic carbon (TOC) from aquaculture wastewater using electrochemical technology: a review. Desalination 285, 1–13. https://doi.org/10.1016/j.desal.2011.09.029.
Myers, R.H., Montgomery, D.C., Anderson-Cook, C.M., 1995. Response Surface Methodology. Process and Product Optimization Using Designed Experiments. John Willey & Sons. *Inc.*, New York, NY, pp. 134–174.
Pacwa-Płociniczak, M., Płaza, G.A., Piotrowska-Seget, Z., Cameotra, S.S., 2011. Environmental applications of biosurfactants: recent advances. Int. J. Mol. Sci. 12 (1), 633–654. https://doi.org/10.3390/ijms12010633.
Parthipan, P., Preetham, E., Machuca, L.L., Rahman, P.K., Murugan, K., Rajasekar, A., 2017. Biosurfactant and degradative enzymes mediated crude oil degradation by bacterium Bacillus subtilis A1. Front. Microbiol. 8, 193. https://doi.org/10.3389/fmicb.2017.00193.
Patowary, K., Patowary, R., Kalita, M.C., Deka, S., 2017. Characterization of biosurfactant produced during degradation of hydrocarbons using crude oil as sole source of carbon. Front. Microbiol. 8, 279. https://doi.org/10.3389/fmicb.2017.00279.
Peixoto, R.S., Vermelho, A.B., Rosado, A.S., 2011. Petroleum-degrading enzymes: bioremediation and new prospects. Enzym. Res. https://doi.org/10.4061/2011/475193.
Pi, Y., Bao, M., Liu, Y., Lu, T., He, R., 2017. The contribution of chemical dispersants and biosurfactants on crude oil biodegradation by Pseudomonas sp. LSH-7′. J. Clean. Prod. 153, 74–82. https://doi.org/10.1016/j.jclepro.2017.03.120.
Picard, F., Chaouki, J., 2017. NaClO/NaOH soil oxidation for the remediation of two real heavy-metal and petroleum contaminated soils. Journal of environmental chemical engineering 5 (3), 2691–2698. https://doi.org/10.1016/j.jece.2017.05.005.
Poddar, K, Sarkar, D, Sarkar, A, 2019. Construction of potential bacterial consortia for efficient hydrocarbon degradation. International Biodeterioration & Biodegradation 144. https://doi.org/10.1016/j.ibiod.2019.104770.
Pramila, M., Manikandan, S., Anju, K.S., Kannan, M.M., Hong, S., Maruthamuthu, S., Subramanian, K., 2014. Electrochemical decolorization and degradation of Turquoise Blue G (TBG) by pre-adapted petroleum degrading bacteria. Separ. Purif. Technol. 132, 719–727. https://doi.org/10.1016/j.seppur.2014.06.026.
Rajasekar, A., Babu, T.G., Maruthamuthu, S., Pandian, S.T.K., Mohanan, S., Palaniswamy, N., 2007a. Biodegradation and corrosion behaviour of Serratia marcescens ACE2 isolated from an Indian diesel-transporting pipeline. World J. Microbiol. Biotechnol. 23 (8), 1065–1074. https://link.springer.com/article/10.1007/s11274-006-9332-0.
Rajasekar, A., Babu, T.G., Pandian, S.T.K., Maruthamuthu, S., Palaniswamy, S., Rajendran, A., 2007b. Role of *Serratia marcescens* ACE2 on diesel degradation and its influence on corrosion. J. Ind. Microbiol. Biotechnol. 34, 589–598. https://doi.org/10.1007/s10295-007-0225-5.
Rajasekar, A., Maruthamuthu, S., Ting, Y.P., 2008. Electrochemical behavior of Serratia marcescens ACE2 on carbon steel API 5L-X60 in organic/aqueous phase. Ind. Eng. Chem. Res. 47 (18), 6925–6932. https://doi.org/10.1021/ie8005935.
Reddy, K., Cutright, T., 2003. Nutrient amendment for the bioremediation of a chromium-contaminated soil by electrokinetics. Energy Sources 25 (9), 931–943. https://doi.org/10.1080/00908310390221318.
Reddy, K.R., 2010. Technical challenges to in-situ remediation of polluted sites. Geotech. Geol. Eng. 28 (3), 211–221. https://doi.org/10.1007/s10706-008-9235-y.
Revathy, T., Jayasri, M.A., Suthindhiran, K., 2015. Biodegradation of PAHs by Burkholderia sp. VITRSB1 isolated from marine sediments. Sci. Tech. Rep. https://doi.org/10.1155/2015/867586, 2015.
Rosenberg, M., 1984. Bacterial adherence to hydrocarbons: a useful technique for studying cell surface hydrophobicity. FEMS (Fed. Eur. Microbiol. Soc.) Microbiol. Lett. 22 (3), 289–295.

Sarankumar, R.K., Selvi, A., Murugan, K., Rajasekar, A., 2019. Electrokinetic (EK) and bio-electrokinetic (BEK) remediation of hexavalent chromium in contaminated soil using alkalophilic bio-anolyte. Indian Geotech. J. 1–9. https://doi.org/10.1007/s40098-019-00366-6.

Selvi, A., Aruliah, R., 2018. A statistical approach of zinc remediation using acidophilic bacterium via an integrated approach of bioleaching enhanced electrokinetic remediation (BEER) technology. Chemosphere 207, 753–763. https://doi.org/10.1016/j.chemosphere.2018.05.144.

Selvi, A., Das, D., Das, N., 2015. Potentiality of yeast Candida sp. SMN04 for degradation of cefdinir, a cephalosporin antibiotic: kinetics, enzyme analysis and biodegradation pathway. Environ. Technol. 36 (24), 3112–3124. https://doi.org/10.1080/09593330.2015.1054318.

Selvi, A., Salam, J.A., Das, N., 2014. Biodegradation of cefdinir by a novel yeast strain, *Ustilago*sp. SMN03 isolated from pharmaceutical wastewater. World J. Microbiol. Biotechnol. 30, 2839–2850. https://link.springer.com/article/10.1007/s11274-014-1710-4.

Shahsavari, Esmaeil, Poi, Gregory, Aburto-Medina, Arturo, Haleyur, Nagalakshmi, Ball S., Andrew, et al., 2017. Bioremediation Approaches for Petroleum Hydrocarbon-Contaminated Environments. Enhancing Cleanup of Environmental Pollutants 21–41.

Sharma, A., Kumar, P., Rehman, M.B., 2014. Biodegradation of diesel hydrocarbon in soil by bioaugmentation of Pseudomonas aeruginosa: a laboratory scale study. Int J Environ BioremediatBiodegrad 2 (4), 202–212. https://doi.org/10.12691/ijebb-2-4-8.

Sharma, H.D., Reddy, K.R., 2004. Geoenvironmental Engineering: Site Remediation, Waste Containment, and Emerging Waste Management Technologies. John Wiley & Sons.

Song, B., Zeng, G., Gong, J., Liang, J., Xu, P., Liu, Z., Zhang, Y., Zhang, C., Cheng, M., Liu, Y., Ye, S., 2017. Evaluation methods for assessing effectiveness of in situ remediation of soil and sediment contaminated with organic pollutants and heavy metals. Environ. Int. 105, 43–55. https://doi.org/10.1016/j.envint.2017.05.001.

Song, Y., Cang, L., Fang, G., Ata-Ul-Karim, S.T., Xu, H., Zhou, D., 2018. Electrokinetic delivery of anodic in situ generated active chlorine to remediate diesel-contaminated sand. Chem. Eng. J. 337, 499–505. https://doi.org/10.1016/j.cej.2017.12.122.

Thavasi, R., Sharma, S., Jayalakshmi, S., 2011. Evaluation of screening methods for the isolation of biosurfactant producing marine bacteria. J. Petrol Environ. Biotechnol. S 1, 1–6.

Vijayakumar, S., Saravanan, V., 2015. Biosurfactants-types, sources and applications. Res. J. Microbiol. 10 (5), 181–192. https://doi.org/10.3923/jm.2015.181.192.

Virkutyte, J., Sillanpää, M., Latostenmaa, P., 2002. Electrokinetic soil remediation—critical overview. Sci. Total Environ. 289 (1–3), 97–121. https://doi.org/10.1016/S0048-9697(01)01027-0.

Wang, J.Y., Huang, X.J., Kao, J.C., Stabnikova, O., 2007. Simultaneous removal of organic contaminants and heavy metals from kaolin using an upward electrokinetic soil remediation process. J. Hazard Mater. 144 (1–2), 292–299. https://doi.org/10.1016/j.jhazmat.2006.10.026.

Wen, J., He, D., Yu, Z., Zhou, S., 2018. In situ detection of microbial c-type cytochrome based on intrinsic peroxidase-like activity using screen-printed carbon electrode. Biosens. Bioelectron. 113, 52–57. https://doi.org/10.1016/j.bios.2018.04.049.

Wick, L.Y., Mattle, P.A., Wattiau, P, Harms, H, 2004. Electrokinetic transport of PAH-degrading bacteria in model aquifers and soil. Environmental science & technology 38(17), 4596–4602. https://doi.org/10.1021/es0354420.

Wu, M., Dick, W.A., Li, W., Wang, X., Yang, Q., Wang, T., Xu, L., Zhang, M., Chen, L., 2016. Bioaugmentation and biostimulation of hydrocarbon degradation and the microbial community in a petroleum-contaminated soil. Int. Biodeterior. Biodegrad. 107, 158–164.

Xue, J., Yu, Y., Bai, Y., Wang, L., Wu, Y., 2015. Marine oil-degrading microorganisms and biodegradation process of petroleum hydrocarbon in marine environments: a review. Curr. Microbiol. 71 (2), 220–228. https://doi.org/10.1007/s00284-015-0825-7.

Xue, J., Wu, Y., Liu, Z., Li, M., Sun, X., Wang, H., Liu, B., 2017 a. Characteristic assessment of diesel-degrading bacteria immobilized on natural organic carriers in marine environment: the degradation activity and nutrient. Sci. Rep. 7 (1), 8635. https://doi.org/10.1038/s41598-017-08832-y.

Xue, J., Wu, Y., Liu, Z., Li, M., Sun, X., Wang, H., Liu, B., 2017 b. Characteristic assessment of diesel-degrading bacteria immobilized on natural organic carriers in marine environment: the degradation activity and nutrient. Sci. Rep. 7 (1), 8635.

Xue, J., Wu, Y., Shi, K., Xiao, X., Gao, Y., Li, L., Qiao, Y., 2019. Study on the degradation performance and kinetics of immobilized cells in straw-alginate beads in marine environment. Bioresour. Technol. 280, 88–94. https://doi.org/10.1016/j.biortech.2019.02.019.

Yao, Z., Li, J., Xie, H., Yu, C., 2012. Review on remediation technologies of soil contaminated by heavy metals. Procedia Environmental Sciences 16, 722–729. https://doi.org/10.1016/j.proenv.2012.10.099.

Yuan, C., Chiang, T.S., 2008. Enhancement of electrokinetic remediation of arsenic spiked soil by chemical reagents. J. Hazard Mater. 152 (1), 309–315. https://doi.org/10.1016/j.jhazmat.2007.06.099.

ScienceDirect

Materials Letters
Volume 273, 15 August 2020, 127951

Utilization of funnel-shaped ivory flowers of *Candelabra cactus* for zinc oxide nanoparticles synthesis and their in-vitro anti-cancer and antibacterial activity

M. Govarthanan [a], P. Srinivasan [b], T. Selvankumar [b], V. Janaki [c], Fahad A. Al-Misned [d], Hamed A. El-Serehy [d], Woong Kim [a], S. Kamala-Kannan [e]

Show more

Outline | Share | Cite

https://doi.org/10.1016/j.matlet.2020.127951

Get rights and content

Highlights

- Zinc oxide nanoparticles (ZnONPs) were successfully synthesized from the flower extract of *Candelabra cactus*.
- The ZnONPs are spherical in shape 20–30 nm in size.
- ZnONPs showed extensive antibacterial activity against both Gram-positive and Gram-negative bacteria.
- ZnONPs exhibited potential cytotoxic activity against MCF-7 cells.

Abstract

The present study reports an eco-friendly phytosynthesis of zinc oxide nanoparticles (ZnONPs) using *Candelabra cactus* flower extract. The structural and functional properties of the synthesized ZnONPs were examined through various instrumentation. Transmission electron microscopy analysis revealed sphere-shaped ZnONPs between 10 and 30 nm in size. The synthesized ZnONPs showed growth inhibiting activity of both Gram-positive and Gram-negative bacteria. Acridine orange ethidium bromide (AO/EB) and

PRINCIPAL
PGP College of Arts and Science
Namakkal

Materials Letters 273 (2020) 127951

Contents lists available at ScienceDirect

Materials Letters

journal homepage: www.elsevier.com/locate/mlblue

Utilization of funnel-shaped ivory flowers of *Candelabra cactus* for zinc oxide nanoparticles synthesis and their in-vitro anti-cancer and antibacterial activity

M. Govarthanan [a,*], P. Srinivasan [b], T. Selvankumar [b], V. Janaki [c], Fahad A. Al-Misned [d], Hamed A. El-Serehy [d], Woong Kim [a,*], S. Kamala-Kannan [e,*]

[a] Department of Environmental Engineering, Kyungpook National University, Daegu 41566, Republic of Korea
[b] PG & Research Department of Biotechnology, Mahendra Arts and Science College (Autonomous), Kalippatti, Namakkal 637501, Tamil Nadu, India
[c] Department of Chemistry, Sri Sarada College for Women, Salem 636 016, Tamil Nadu, India
[d] Department of Zoology, College of Science, King Saud University, Riyadh 11451, Saudi Arabia
[e] Division of Biotechnology, College of Environmental and Bioresource Sciences, Jeonbuk National University, Iksan 54596, Republic of Korea

ARTICLE INFO

Article history:
Received 3 March 2020
Received in revised form 5 May 2020
Accepted 7 May 2020
Available online 8 May 2020

Keywords:
Antibacterial
Cytotoxicity
Candelabra cactus
Flower extract
MCF-7 cells

ABSTRACT

The present study reports an eco-friendly phytosynthesis of zinc oxide nanoparticles (ZnONPs) using *Candelabra cactus* flower extract. The structural and functional properties of the synthesized ZnONPs were examined through various instrumentation. Transmission electron microscopy analysis revealed sphere-shaped ZnONPs between 10 and 30 nm in size. The synthesized ZnONPs showed growth inhibiting activity of both Gram-positive and Gram-negative bacteria. Acridine orange ethidium bromide (AO/EB) and Hoechst 33,342 staining studies revealed apoptotic bodies and chromatin condensation in the MCF-7 cancer cells.

© 2020 Elsevier B.V. All rights reserved.

1. Introduction

In recent years, metallic nanoparticles have received significant attention due to their broad physico-chemical properties, which are considerably different from the bulk materials, and their desirable applications in fields of science, technology, and medicine. Among such metallic nanoparticles, zinc oxide nanoparticles (ZnONPs) are well known due to its multifunctional, non-toxic nature with vast applications in various fields [1,2]. In addition, it has been reported that ZnONPs has been used in sunscreen lotions, ointments, bio-imaging, antimicrobial, anticancer, drug-delivery systems, dye degradation and theses multiple applications have gained significant attention to researchers [3-8]. Previously, ZnONPs are synthesized by several physico-chemical techniques such as, pulse laser deposition [9], laser ablation [10], molecular beam epitaxy [11], pyrolysis [12], sono-chemical [13] and sol–gel methods [14]. Nevertheless, these traditional physico-chemical techniques have been reported negative influence on eco-system by using potential toxic chemicals for the synthesis of ZnONPs. Thus, non-toxic biological methods have been established to reduce and/or eliminate the toxic substances used for ZnONPs synthesis.

In the biological methods, microorganisms, algae, microbial products and plants are the primary and abundant sources for ZnONPs synthesis. However, plants comprised of diverse phytochemicals and secondary metabolites which are responsible for reduction and capping of nanoparticles (NPs) compared to microorganisms and algae. Recent research papers investigated the synthesis of ZnONPs from various floras such as *Azadirachta indica* [15], *Agathosma betulina* [16], *Rhamnus virgata* [17], *Sesamum indicum* [18], *Juglans regia* [1], *Mentha pulegium* [19], and *Malus pumila* [20]. However, to the best of our familiarity, there is no study on synthesis of ZnONPs using *Candelabra cactus (Euphorbia candelabrum)* flower extracts.

E. candelabrum also known as *C. cactus*, a small succulent tree, widely distributed in African countries and some Asian countries including India. Waihenya et al. [21] reported the medicinal value of *E. candelabrum* against Newcastle disease caused by Newcastle virus. In addition, it has been reported as a potential medicine for leprosy treatment. Even though, this plant is widely distributed

* Corresponding authors.
E-mail addresses: gova.muthu@gmail.com (M. Govarthanan), elshine@knu.ac.kr (W. Kim), kannan@jbnu.ac.kr (S. Kamala-Kannan).

https://doi.org/10.1016/j.matlet.2020.127951
0167-577X/© 2020 Elsevier B.V. All rights reserved.

in southern parts of India including Tamil Nadu, there is no much utilization of this plant materials for medicinal and research applications. Hence, the present study aimed to utilize *C. cactus* flowers for ZnONPs synthesis and the present study was aimed (i) to synthesis and characterization of ZnONPs, (ii) assessing the antioxidant activity of phytosynthesized ZnONPs, (iii) evaluating the cytotoxic potential of ZnONPs against MCF-7 cell lines, and antibacterial efficiency against Gram-positive and Gram-negative bacteria.

2. Materials and methods

2.1. Flower material

Fresh flowers of *C. cactus* were collected from Kaveriyammal gardens (11.468410 N, 77.994960 W), Mallasamudram (637 503), Tamil Nadu, India and were rinsed by tap water followed by filter purified water to eliminate the dust particles attached on the surface of the flowers. About 10 g of flowers were grinded using mortar-pestle and mixed in 100 mL of double distilled water and centrifuged at 10,000 rpm for 10 min. The supernatant was used for ZnONPs synthesis.

2.2. Biosynthesis of ZnONPs

ZnONPs were synthesized according to Majeed et al. [22]. Briefly, 2 mM $Zn(NO_3)_2$ was (950 mL) mixed with 50 mL of flower extract and incubate in shaking incubator for 24 h. The production of ZnONPs was envisioned by the alteration of colourless into dark brown colour. The resulting precipitate was separated by centrifugation at 8000 × g for 10 min. The deposited pellet was washed 2–3 times with double distilled water and stored at refrigerator until use.

2.3. Characterization of ZnONPs

The optical absorption spectrum of ZnONPs was observed using UV–visible spectrophotometer (Elico-SL 164) in the range of 200–800 nm. Shape and size of the phytogenic ZnONPs were determined by Transmission electron microscopy (TEM, FEI Tecnai TF 20 high resolution). Scanning electron micrograph-energy dispersive spectra (SEM–EDS; Jeol JSM 6390) was performed to the check the elemental Zn present in the ZnONPs. A Perkin-Elmer Fourier transform infrared (FT-IR) spectrum was obtained at 4 cm^{-1} resolution between the wavelengths of 400–4000. The structural characterization was determined by X-ray powder diffraction (XPERT-Pro diffractometer using Cu-Ka radiation).

2.4. Antibacterial activity of ZnONPs

Antibacterial potential of phytosynthesized ZnONPs against *Klebsiella* sp. (Genbank Accession Number: KC899845), and *Staphylococcus* sp. (Genbank Accession Number: KC688883) was evaluated according to Solabomi et al. [23]. Briefly, the strains were

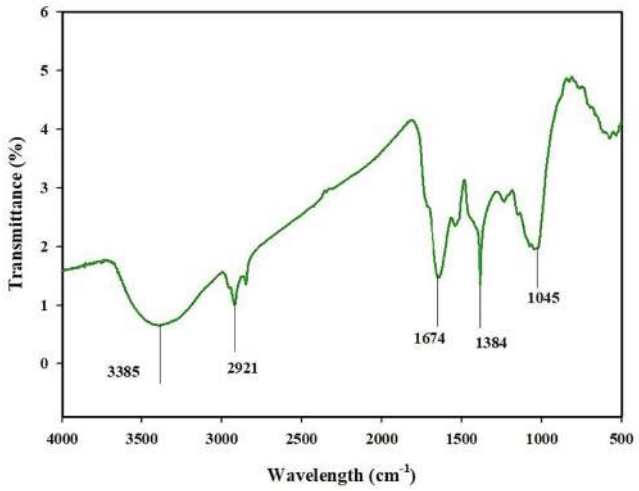


Fig. 2. FT-IR Spectrum of ZnONPs.

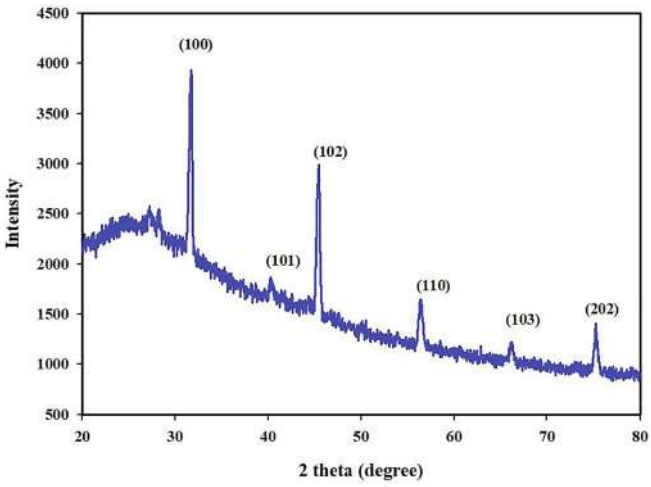


Fig. 3. XRD pattern of ZnONPs.

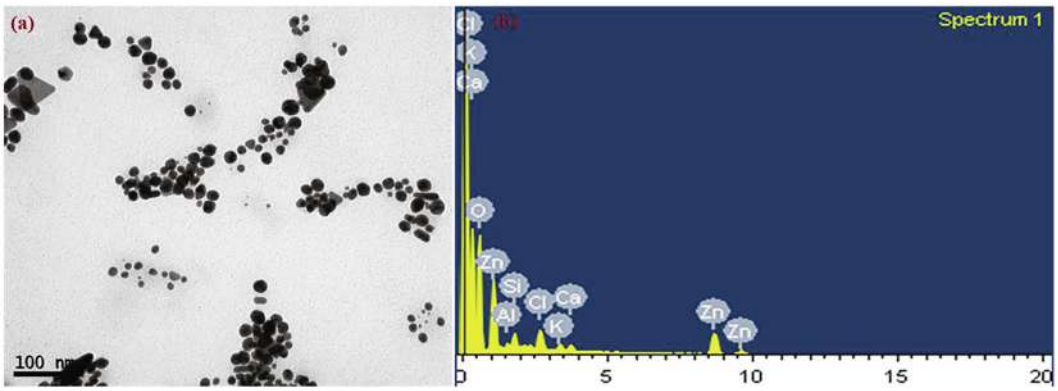


Fig. 1. **(a)** TEM image of ZnONPs synthesized from *C. cactus*, **(b)** SEM-EDS of ZnONPs.

cultivated in 100 mL of LB broth amended with 2–10 mM of ZnONPs. The bacterial population was measured at 600 nm and growth inhibition (%) was calculated by using absorption units according to Elegbede et al. [24]

2.5. Cytotoxic assay and apoptotic based staining

Cytotoxic of potentials of ZnONPs (0, 25, 50, 75 and 100 μg/mL) were analyzed by an MTT assay based on the methodology adopted by Mosmann et al. [25] after 24 h of incubation. To understand the features of apoptotic cell death, assays such as acridine orange ethidium bromide (AO/EB) and Hoechst 33,342 staining was performed, and the cells were visualized under fluorescence microscope (Accuscope, EXI-310) at a magnification of 20X.

3. Results and discussion

The flower extract of *C. cactus* was employed for the phytosynthesis of ZnONPs. Variation of colour in the reaction mixture from colourless into dark brown colour indicates the reduction of zinc nitrate. The UV–Vis spectra of the corresponding ZnONPs was observed at the wavelengths of of 350–400 nm. Previous study reported the maximum adsorption of the ZnONPs in the range of 300–350 nm [26]. TEM was used to examine the morphology and size of synthesized ZnONPs and the images showed the spherical morphology of the particles with 10–30 nm in size (Fig. 1). The EDX pattern of ZnONPs showed the presence of ZnO with the other elements such as, Cl, K, Ca, Si, Al and O. These elements may arise from the phytochemicals present in the flower extract. FT-IR

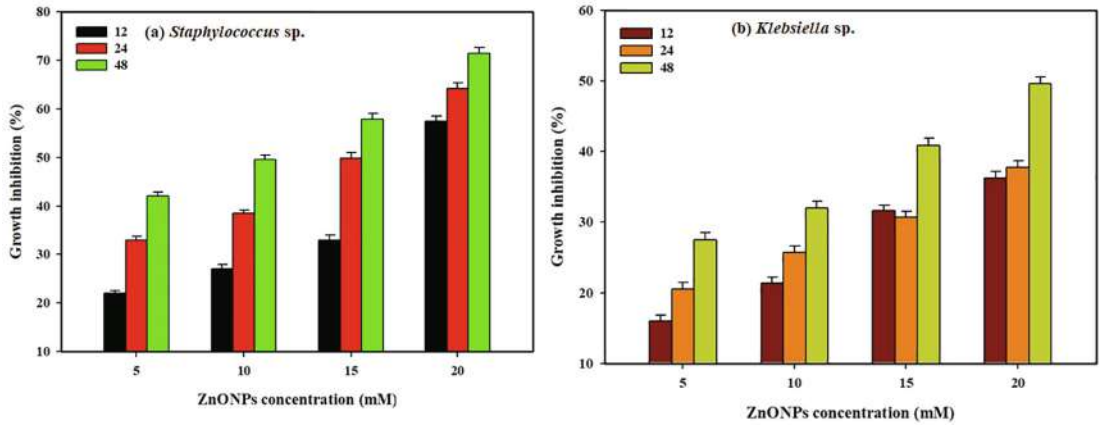


Fig. 4. Antibacterial activity of AgNPs **(a)** *Staphylococcus* sp., **(b)** *Klebsiella* sp.

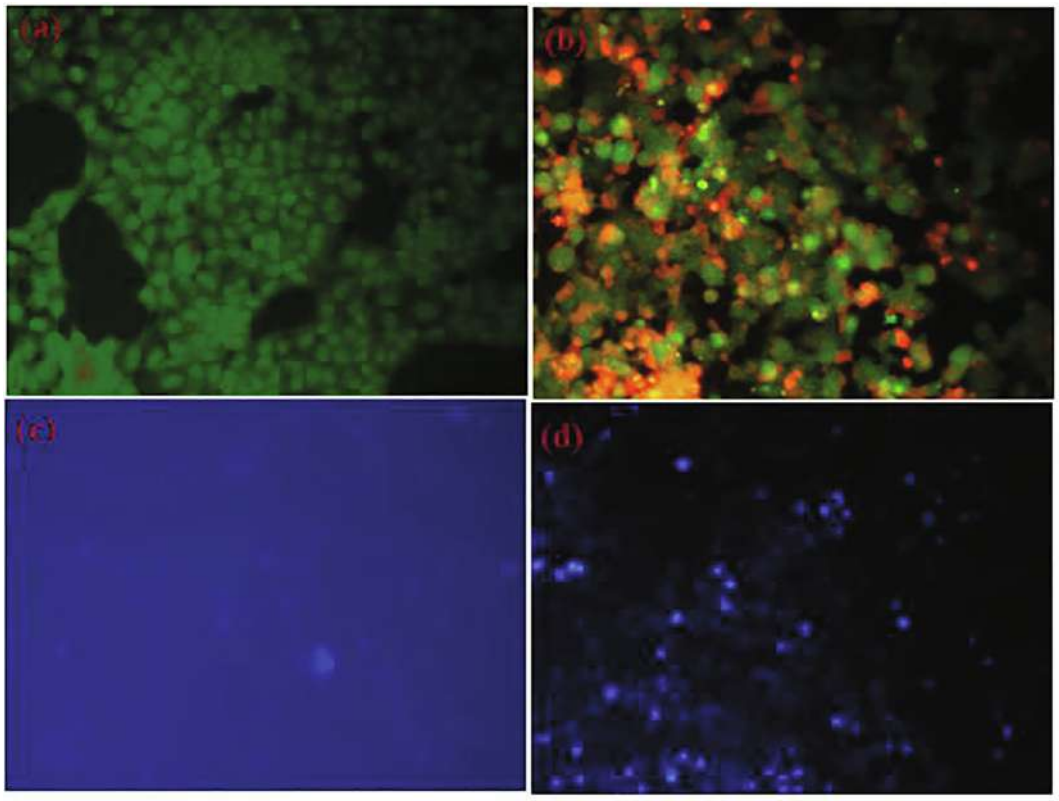


Fig. 5. Fluorescence based staining (a & b) and dual staining (c & d).

results showed a broad peak around 3385 cm^{-1} and it was attributed to the carbonyl and OH alcoholic groups of the flower extract. A sharp band at 2921 cm^{-1} was assigned to the $-CH_2$ vibrations. The moderately broad adsorption band at 1674 cm^{-1} was indicated to the presence of carbonyl group. The peaks at 1384 and 1045 cm^{-1} represents the presence of C = O and alkenes respectively. The crystalline nature of the phytosynthesized ZnONPs were confirmed by XRD analysis and the results illustrated in Fig. 2 (b). The results showed the prominent peaks corresponding to the diffraction planes of ZnONPs at (1 0 0), (1 0 1), (1 0 2), (1 1 0), (1 0 3), and (2 0 2). The highest and sharp peaks at (1 0 0) and (1 0 2) indicate the hexagonal wurtzite nature of ZnONPs reported diffraction studies standards (JCPDS 008, 82–1042) [27].

The antibacterial efficiency of ZnONPs is shown in Fig. 3. The results indicate that the photosynthesized ZnONPs inhibited the bacterial growth and the inhibition rate is directly proportional to the concentration of ZnONPs. The ZnONPs (20 mM) inhibited 71.4% of *Staphylococcus* sp. growth and 49.6% of *Klebsiella* sp. growth after 48 h of incubation (Fig. 3a and b). The results revealed that, the ZnONPs posses' strong growth inhibition rate against Gram-positive Staphylococcus sp. compared to Gram-negative *Klebsiella* sp. The anticancer potential of ZnONPs is shown in the Fig. 4. The results indicated that the viability of the MCF-7 cells was decreased according to the increasing concentration ZnONPs (25, 50, 75 and 100 μg mL^{-1}). Majeed et al. [1] reported that the cytotoxicity of ZnONPs is dose dependent and Hsin et al. [28] reported that the ZnONPs cause nuclear fragmentation, condensation, blebbing of cell membrane and apoptotic body formation. Fig. 5 shown the AO/EB staining results, normal live cells were in green color while ZnONPs treated cells were in orange color which indicates apoptotic bodies caused by chromatin condensation [29]. The results demonstrated that the ZnONPs have a better ability to pronounce apoptosis.

4. Conclusion

The present study demonstrated the synthesis of ZnONPs from *C. cactus* using a simple non-toxic greener approach. The UV–Vis spectra of the corresponding ZnONPs were observed at the wavelengths of 350–400 nm. The EDX pattern of ZnONPs showed the presence of ZnO element at 8–10 KeV. The phytosynthesized ZnONPs have exhibited attractive lethal effect with both Gram-positive and Gram-negative bacteria and potential toxic effect to the MCF-7 breast cancer cells.

CRediT authorship contribution statement

M. Govarthanan: Conceptualization, Methodology, Formal analysis, Data curation, Writing - original draft. **P. Srinivasan:** Methodology, Formal analysis. **T. Selvankumar:** Conceptualization, Formal analysis. **V. Janaki:** Methodology, Formal analysis, Writing - review & editing. **Fahad A. Al-Misned:** Writing - review & editing, Funding acquisition. **Hamed A. El-Serehy:** Writing - review & editing, Funding acquisition. **Woong Kim:** Conceptualization, Data curation, Writing - original draft, Funding acquisition. **S. Kamala-Kannan:** Conceptualization, Methodology, Writing - original draft, Funding acquisition.

Declaration of Competing Interest

The authors declare that they have no known competing financial interests or personal relationships that could have appeared to influence the work reported in this paper.

Acknowledgements

This work was supported by the Korea Institute of Energy Technology Evaluation and Planning (KETEP) grant funded by the Korea government (MOTIE) (No. 20194110100100, Full-scale feasibility study of the stability and efficiency improvement of a biogas production facility based on biomass from urban/living environments) and also supported by a National Research Foundation of Korea (NRF) grant funded from the Korean government (MSIP, South Korea) (No. 2018R1D1A1B0705004013). The authors acknowledge King Saud University, Riyadh, Saudi Arabia, for funding this research through researchers supporting project number (RSP-2019/19).

References

[1] E. Darvishi, D. Kahrizi, E. Arkan, J Mol Liq. 286 (2019) 110831.
[2] J.L. Gomez, O. Tigli, J. Mater. Sci. 48 (2013) 612–624.
[3] N. Matinise, X.G. Fuku, K. Kaviyarasu, N. Mayedwa, M. Maaza, Appl. Surf. Sci. 406 (2017) 339–347.
[4] H. Mirzaei, M. Darroudi, Ceram. Int. 43 (2017) 907–914.
[5] A.A. Bazrasshan, M. Ghaedi, S. Hajati, R. Naghiha, A. Asfaram, Ecotoxicol. Environ. Saf. 142 (2017) 330–337.
[6] E. Alipanahpour Dil, M. Ghaedi, A. Asfaram, F. Mehrabi, F. Sadeghfar, Ind. Eng. Chem. 74 (2019) 55–62.
[7] E. Alipanahpour Dil, A. Asfaram, A. Goudarzi, E. Zabihi, H. Javadian, Int. J. Biol. Macromol. 154 (2020) 528–537.
[8] S. Hameed, J. Iqbal, M. Ali, A.T. Khalil, B. Ahsan Abbasi, M. Numan, Z.K. Shinwari, Mater., Res. Express 6 (2019) 102005.
[9] M. Kawakami, A.B. Hartanto, Y. Nakata, T. Okada, Int. J. Appl. Phys. 42 (2003) 33–35.
[10] M.A. Gondal, Q.A. Drmosh, Z.H. Yamani, T.A. Saleh, Appl. Surf. Sci. 256 (2009) 298–304.
[11] X.H. Zhang, Y.C. Liu, X.H. Wang, S.J. Chen, G.R. Wang, J.Y. Zhang, X.W. Fan, J. Phys. Condens. Matter 17 (2005) 3035–3042.
[12] D. Saravanakkumar, S. Sivaranjani, K. Kaviyarasu, A. Ayeshamariam, B. Ravikumar, S. Pandiarajan, M. Maaza, J. Semicond. 39 (2018) 1–7.
[13] R.S. Yadav, P. Mishra, A.C. Pandey, Sonochem. 15 (2008) 863–868.
[14] A. Barhoum, G. Van Assche, H. Rahier, M. Fleisch, S. Bals, M.P. Delplancked, D. Bahnemann, Mater. Des. 119 (2017) 270–276.
[15] T. Bhuyan, K. Mishra, M. Khanuja, R. Prasad, A. Varma, Mat. Sci. Semicon. Proc. 32 (2015) 55–61.
[16] F.T. Thema, E. Manikandan, M.S. Dhlamini, M. Maaza, Mater. Lett. 161 (2015) 124–127.
[17] J. Iqbal, B. Ahsan Abbasi, T. Mahmood, S. Kanwal, R. Ahmad Muhammad Ashraf, J. Mole. Struct. 1189 (2019) 315–327.
[18] S. Zafar, A. Ashraf, M.U. Ijaz, S. Muzammil, M.H. Siddique, S. Afzal, R. Andleeb, K.A. Al-Ghanim, F. Al-Misned, Z. Ahmed, S. Mahboob, J. King Saud Univ. Sci. https://doi.org/10.1016/j.jksus.2019.10.017.
[19] S.S. Rad, A.M. Sani, S. Mohseni, Microb. Pathog. 131 (2019) 239–245.
[20] A. Mirza, A. Kareem, A.A. Nami, S.A. Bhat, A. Mohammad, N. Nisha, Microb. Pathog. 129 (2019) 233–241.
[21] R.K. Waihenya, M.M.A. Mtambo, G. Nkwengulila, J. Ethnopharmacol. 79 (2002) 299–304.
[22] S. Majeed, D. Mohammed, H. Muhammad, T. Mohmmed, N. Mohamad, Sustain. Chem. Pharm. 14 (2019) 100179.
[23] O. Solabomi, Y. Abdallah, M. Zhang, H. Fouad, X. Hong, E. Ibrahim, Md. Mahidul Islam Masum, A. Hossain, Artif. Cells Nanomed. Biotechnol. 47 (2019) 341–352.
[24] J.A. Elegbede, A. Lateef, M.A. Azeer, T.B. Asafa, T.A. Yekeen, I.C. Oladipo, D.A. Aina, L.S. Beukes, E.B. Gueguim-Kana, Waste Biomass Valari. (2018), https://doi.org/10.1007/s12649-018-0540-2.
[25] T. Mosmann, J. Immunol Methods 65 (1983) 55–63.
[26] A. Happy, M. Soumya, S. Venkat Kumar, S. Rajeshkumar, R. David Sheba, T. Lakshmi, V. Deepak Nallaswam, Biochem. Biophys. Rep. 17 (2019) 208–211.
[27] J. Lu, H. Ali, J. Hurh, Y. Han, I. Batjikh, E. Rupa, G. Anandapadmanaban, J. Park, D. Yang, Optics 184 (2019) 82–89.
[28] Y.H. Hsin, C.F. Chen, S. Huang, T.S. Shih, P.S. Lai, P.J. Chueh, Toxicol. Lett. 179 (2008), 139 139.
[29] F. Namvar, H.S. Rahman, R. Mohamad, J. Baharara, M. Mahdavi, E. Amini, M.S. Chartrand, S.K. Yeap, Int J. Nanomed. 9 (2014) 2479–2488.

Springer Link

Search Log in

Original Article | Published: 01 August 2020

Chlorpyrifos degradation efficiency of *Bacillus* sp. laccase immobilized on iron magnetic nanoparticles

P. Srinivasan, T. Selvankumar, Bilal Ahamad Paray, Muneeb U. Rehman, S. Kamala-Kannan, M. Govarthanan ✉, Woong Kim ✉ & K. Selvam ✉

3 Biotech **10**, Article number: 366 (2020)

454 Accesses | **15** Citations | Metrics

Abstract

The present study explored the immobilization of laccase onto iron magnetic nanoparticles (MNPs) to enhance its enzymatic properties and applications. The immobilization process was optimized using Box–Behnken design (BBD). BBD showed significance towards the quadratic model with experimental data. Maximum laccase activity recovery (99%) of the predicted model was observed at 0.75 mg/mL of laccase concentration, 200 mg/mL of MNPs, 0.3% cross linking with carbodiimide, and 3 h of cross-linking time. The magnetization activity of MNPs (8 emu/g) and the immobilized laccase with MNPs (4 emu/g) was analyzed using vibrating sample magnetometer (VSM). Maximum activity of immobilized laccase was observed at pH 7.0 and

PRINCIPAL
PGP College of Arts and Science
Namakkal

3 Biotech (2020) 10:366
https://doi.org/10.1007/s13205-020-02363-6

ORIGINAL ARTICLE

Chlorpyrifos degradation efficiency of *Bacillus* sp. laccase immobilized on iron magnetic nanoparticles

P. Srinivasan[1] · T. Selvankumar[1] · Bilal Ahamad Paray[2] · Muneeb U. Rehman[3] · S. Kamala-Kannan[4] · M. Govarthanan[5] · Woong Kim[5] · K. Selvam[1]

Received: 29 January 2020 / Accepted: 25 July 2020
© King Abdulaziz City for Science and Technology 2020

Abstract
The present study explored the immobilization of laccase onto iron magnetic nanoparticles (MNPs) to enhance its enzymatic properties and applications. The immobilization process was optimized using Box–Behnken design (BBD). BBD showed significance towards the quadratic model with experimental data. Maximum laccase activity recovery (99%) of the predicted model was observed at 0.75 mg/mL of laccase concentration, 200 mg/mL of MNPs, 0.3% cross linking with carbodiimide, and 3 h of cross-linking time. The magnetization activity of MNPs (8 emu/g) and the immobilized laccase with MNPs (4 emu/g) was analyzed using vibrating sample magnetometer (VSM). Maximum activity of immobilized laccase was observed at pH 7.0 and 55 °C. The immobilized laccase has greater stability (100 h) and significant chlorpyrifos (pesticide) degradation activity. High-performance liquid chromatography (HPLC) results confirmed the degraded metabolic products of chlorpyrifos. In all, the immobilized laccase was superior to free laccase, showing promising structural and application characteristics.

Keywords Immobilization · Laccase · Magnetic nanoparticles · Optimization · Pesticides

Introduction

Synthetic pesticides have become an inevitable part of modern agriculture, which contributes to their extensive distribution throughout the ecosystem (Kumar et al. 2018). Although the use of pesticides has contributed to better crop yields, the dispersion of their residues in the environment is disastrous to aquatic as well as to terrestrial eco systems (Li 2018; Villarreal-Chiu et al. 2017). Exposure to pesticides causes serious health problems, such as neurotoxic disorders, and can lead to death (Pereira et al. 2015; Simonelli et al. 2007). Researchers have developed a wide range of physico-chemical methods to overcome the adverse effects of pesticides on the ecosystem (Mir-Tutusaus et al. 2018; Maqbool et al. 2016). However, these physico-chemical methods are inefficient, expensive, and time consuming (Zeng et al. 2017). Thus, there is a need to develop simple, highly efficient, and environmentally sustainable processes for the removal of pesticides from the environment.

Enzymatic catalysis is considered as a simple, eco-friendly, green bioremediation method for the degradation and/or detoxification of pesticides from soil and water (Ahmed et al. 2017; Bilal et al. 2017a, b). Several studies reported that enzyme-based degradation methods have maximum degradation efficiency and stability against pH, temperature, and salinity (Kupski et al. 2019). Thus, enzyme-mediated green remediation method shave found attention as an attractive alternative to the physico-chemical methods. Among the microbial enzymes, lignolytic laccases have gained much popularity due to their

✉ M. Govarthanan
gova.muthu@gmail.com

✉ Woong Kim
elshine@knu.ac.kr

✉ K. Selvam
ksk.selvam@gmail.com

[1] PG and Research Department of Biotechnology, Mahendra Arts and Science College (Autonomous), Kalippatti, Namakkal, Tamil Nadu 637501, India

[2] Department of Zoology, College of Science, King Saud University, Riyadh 11451, Saudi Arabia

[3] Department of Clinical Pharmacy, College of Pharmacy, King Saud University, Riyadh 11452, Saudi Arabia

[4] Division of Biotechnology, College of Environmental and Bioresource Sciences, Chonbuk National University, Iksan 54596, Republic of Korea

[5] Department of Environmental Engineering, Kyungpook National University, Daegu 41566, Republic of Korea

Published online: 01 August 2020

wide range of substrate and environmental applications (Bilal et al. 2019; Bilal et al. 2017a, b).

Microbial laccases (E.C. 1.10.3.2) are lignolytic multi-copper containing monomeric extra-cellular glycoproteins that originate from various bacteria, fungi, and plants, and are abundant in nature. Because of their wide distribution and abundance, laccases have been widely applied in food, paper and pulp, and textile industries (Gursharan et al. 2019; Nandhini et al. 2019; Jordan et al. 2018; Bilal et al. 2017a). Several studies reported the laccase-mediated bioremediation of a wide range of pollutants including aromatics, xenobiotics, and phenolics (Vera et al. 2019; Antecka et al. 2018; Zdarta et al. 2018; Zeng et al. 2017). Recent studies have addressed the improvement of laccase efficiency, through its immobilization, for the bioremediation of different groups of environmental contaminants (Bilal et al. 2019). Additionally, it has been reported that immobilization enhances the enzyme's properties (Chen et al. 2016) and increases its stability (Lai et al. 2019).

The immobilization of enzymes onto nanopolymers and nanoparticles has received great interest because of the small size of the enzyme carrier materials, which is known to improve the efficiency of the immobilized enzymes (Govarthanan et al. 2020). Magnetic nanoparticles represent materials with required magnetic properties mostly used for environmental applications. Magnetic iron oxide nanoparticles (MNPs) are inexpensive to produce and exhibit sufficient physical and chemical stability, in addition to being biocompatible and environmentally safe. MNPs also confer specific applications like magnetic separation and pesticide and dye degradation (Laurent et al. 2008; Gupta and Gupta 2005). Of the several types of nanoparticles, MNPs are potential candidates for enzyme immobilization due to their low toxicity and ease of recovery. Amin et al. (2016) and Dyla et al. (2003) reported that enzyme immobilized on MNPs showed enhanced activity and stability. Also, immobilized laccase enzyme has been reported to degrade a wide range of dyes such as Direct Blue 78, Acid Blue 225, Reactive Red 195, Acid Blue 74, and Phenol Red (Jořenek and Zajoncova 2015) and pesticides (Das et al. 2020). Thus, the present study was aimed to (i) synthesize MNPs for laccase immobilization, (ii) optimize immobilization efficiency, (iii) compare the laccase properties before and after immobilization, (iv) characterize the enzyme immobilized onto the MNPs, and (v) evaluate pesticide removal by the immobilized laccase.

Materials and methods

Materials

Laccase from *Bacillus* sp., (Accession number: MF957300) (Srinivasan et al. 2019), carbodiimide, and 2, 2-azino-bis (3-ethylbenzothiazoline-6-sulfonic acid) (ABTS) were purchased from Hi-Media (Mumbai, India). Chlorpyrifos (20% EC) was obtained from Agro-Service Center, Mallasamudram, Tamil Nadu, and India.

Preparation of MNPs

MNPs (Fe_3O_4) were prepared by co-precipitating Fe^{2+} and Fe^{3+} ions. Briefly, ferric and ferrous chlorides were dissolved in a 2:1 molar ratio in water, and chemical precipitation was achieved at 25–30 °C under vigorous mixing by adding 28% NH_4OH solution. The resultant precipitate was heated at 100 °C for 15 min and washed three times with water and once with anhydrous ethanol. The particles were dried for 24 h (Govarthanan et al. 2020; Selvam et al. 2016) for further use.

Optimization of laccase immobilization

The purified MNPs (5 mg/mL) were suspended in 20 mL of acetate buffer solution (pH 4.0) with a designed amount of laccase solution (0.75 mg/mL) and the immobilization process was performed in a shaking incubator at 37 °C for 30–50 min. After incubation, the supernatant was collected for further studies. In addition, to explore the optimal immobilization conditions, the response surface methodology (RSM) based on Box–Behnken design (BBD) was adopted using the Design Expert software (9.0.0.7 trial version). Four factors [enzyme concentration, magnetic nanoparticle concentration, cross-linking (carbodiimide %), and cross-linking time] were optimized for immobilization. The results were assessed by applying the coefficient of determination (R^2), analysis of variance, and response plots. RSM was employed with the most widely used second-order polynomial equation developed to fit the experimental results and to identify the relevant model terms:

$$Y = \beta 0 \Sigma \beta iXi + \Sigma \beta iXi\beta ij + \Sigma XiXj, \quad (1)$$

where Y is the predicted response, $\beta 0$, βi, and βij are the constant regression coefficients of the model, and Xi and Xj represent independent variables.

Characterization of MNPs

The morphology of the MNPs and their elemental composition before and after laccase cross-linking were evaluated using a scanning electron microscope coupled with an energy-dispersive spectroscope (SEM–EDS; Jeol JSM 6390). The functional groups of the MNPs and immobilized laccase were analyzed using Fourier-Transform infrared spectroscopy (FT-IR, Nicolet iS5, Thermo). The magnetic of the synthesized nanoparticles were studied using a vibrating

sample magnetometer (VSM, Lake Shore, Westerville, OH, USA) at room temperature.

Determination of free enzyme and immobilized laccase activity

Free enzyme and immobilized laccase activity was determined according to Wolfenden and Wilson (1982) using ABTS (2, 2′-azino-bis (3-ethylbenzothiazoline-6-sulphonic acid) as substrate. One unit of laccase activity was defined as the amount of required enzyme to oxidize one µmol of ABTS per min under the assay conditions.

Effect of pH, temperature, and storage time on the stability of immobilized laccase

The effect of pH on free and immobilized laccase activity was analyzed by measuring the reaction at different pH levels (5–11). The effects of incubation temperature on free and immobilized laccase activities were determined by performing the reaction temperature ranging at 40–80 °C. The stabilities of free and immobilized laccase were determined after storage in phosphate buffer (0.02 mol/L, pH 7.0) at 4 °C for 100 h. Retained activities were measured as described above, and the activity of each preparation was expressed as a percentage of its retained activity compared to its initial activity.

Degradation of pesticide by immobilized MNPs' laccase

The pesticide degradation ability of immobilized laccase was tested according to Das et al. (2017) with minor modifications. Briefly, 20 mg of immobilized laccase was mixed with 100 mL of chlorpyrifos (Tricel) at a final concentration of 1000 mg/L. The reaction mixer was incubated in a shaking incubator at 300 rpm for 18 h. After the incubation, 10 mL of sample was collected and extracted with hexane in a 1:1 ratio and stored in amber colored bottles for high-performance liquid chromatography (HPLC, LC-20AD, Shimadzu, Tokyo, Japan) analysis according to Srinivasan et al. (2019).

Statistical analysis

All the experiments presented in this study were mean values of three replicates, and standard deviations were used to analyze the data. Effect of pH, temperature, and storage time on the stability of immobilized laccase results were subjected to two-way analysis of variance (ANOVA) using SPSS software v 12 (Chicago, USA).

Results and discussion

Optimization of the conditions for laccase immobilization

The laccase immobilization process is influenced by several biotic (laccase concentration) and abiotic factors (pH, temperature, incubation time) (Liu et al. 2012). Thus, BBD was designed to determine the optimal conditions for the immobilization of laccase. The BBD model is shown in Table 1. The BBD based on the analysis of variance of the quadratic regression model demonstrated high significance (Table 2). The significance of the model was further validated by the Fisher's F test with a very low probability value (F value = 397.82). Values of 'Probability > F' (0.0500) indicate that the model was significant. The predicted R^2 (0.9856) and adjusted R^2 (0.9950) values for optimal conditions were in reasonable agreement with the value of R^2 (0.9856), which is closer to 1.0, indicating better fit of the model in the experimental data. There is only a 0.01% probability that a model F value could occur because of noise. The model was further validated by sequential model sum of squares, lack of fit tests, and model summary statistics. The 3D plots generated showed significant relationship among enzyme concentration, MNPs' concentration, cross-linking (carbodiimide %), and cross-linking time (Fig. 1). The model predicted a maximum laccase activity recovery of 99% for an enzyme concentration of 0.75 mg/mL, MNPs concentration of 200 mg/mL, cross linking with carbodiimide at 0.3%, and a cross-linking time of 3 h. The predicted model values were in good agreement with the values measured in these experiments, mitigating the validity of the response model and the necessity for optimal conditions. The graphs highlighted the parts played by the variables for the production of laccase. The coefficients of the regression equation were calculated, and the following regression equation was obtained:

$$\begin{aligned} Y = {} & 99.00 + 6.58A + 6.92B + 7.75C + 2.58D \\ & + 0.25AB - 1.25AC - 1.25AD + 2.75BC \\ & - 0.2500\,BD + 3.75CD - 17.21A^2 \\ & - 12.21B^2 - 12.46C^2 - 7.96D^2 - 7.96, \end{aligned} \quad (2)$$

where Y is laccase activity, A is enzyme concentration, B is the cross-linked MNPs concentration (carbodiimide %), and D is the cross-linking time. High degrees of similarity of experimental values were observed, reflecting the precision and applicability of RSM to optimize enzyme immobilization (Soozanipour et al. 2015; Halim et al. 2009; Krishna et al. 2001). Our results are in agreement with earlier studies that reported laccase concentration and immobilization

Table 1 Box–Behnken design for the variables and the experimental observed responses

Run	Factor 1 A: Enzyme conc mg/mL	Factor 2 B: MNPs conc mg/mL	Factor 3 C: Cross linking (carbodiamide) %	Factor 4 D: Time course of cross linking h	Response 1 Enzyme activity %
1	0.75	200	0.3	3	99
2	0.75	300	0.1	3	70
3	0.75	100	0.3	1	68
4	0.75	200	0.3	3	99
5	0.75	200	0.3	3	99
6	0.5	200	0.1	3	54
7	0.75	100	0.3	5	74
8	0.75	100	0.1	3	62
9	0.75	200	0.1	5	69
10	0.5	100	0.3	3	57
11	0.75	200	0.3	3	99
12	0.5	200	0.3	1	63
13	0.5	200	0.5	3	71
14	1	100	0.3	3	70
15	0.75	200	0.3	3	99
16	0.75	300	0.3	5	89
17	1	200	0.5	3	82
18	1	200	0.3	5	82
19	1	200	0.3	1	78
20	0.75	200	0.5	1	81
21	0.75	200	0.5	5	92
22	0.75	200	0.1	1	73
23	0.5	300	0.3	3	69
24	0.75	100	0.5	3	73
25	1	200	0.1	3	70
26	1	300	0.3	3	83
27	0.5	200	0.3	5	72
28	0.75	300	0.3	1	84
29	0.75	300	0.5	3	92

time to remarkably influence the immobilization of laccase (Wen et al. 2019; Huang et al. 2017; Zheng et al. 2016; Lin et al. 2007).

Characterization studies

The morphologies of MNPs and laccase immobilized MNPs are shown in the SEM images (Fig. 2a–d). Figure 2a shows the undamaged structure of the MNPs, which consisted of homogeneous particles. The corresponding energy-dispersive spectroscopic (EDS) analysis confirmed the presence of Fe in their elemental composition (Fig. 2b). Figure 2c shows the etching appearance of MNPs in which the integrated particles (laccase) were visually damaged and the appearance of enlarged inter lamellar spaces. The corresponding EDS analysis confirmed the presence of Fe in the elemental composition of the nanoparticles (Fig. 2d). The results are consistent with a previous study reporting the immobilization of laccase on bentonite materials (Wen et al. 2019). The presence of elemental Fe in the spectra of enzyme immobilized magnetic iron particles confirmed the enzyme cross-linking over the nanoparticles. Similar observations were also reported by Das et al. (2020) and confirmed the contribution of Fe signals by the laccase enzymes.

The FT-IR spectra of the MNPs and immobilized laccase are shown in Fig. 3a. The broad bands of the MNPs (3417.86/cm) and immobilized laccase (3035.96/cm and 2679.72/cm) can be attributed to the stretching vibration of the O–H groups. The bands at 2912.51, 1338, and 1012/cm of the MNPs and immobilized laccase are due to aromatic and aliphatic C–H stretching. The small peaks at 1498.69/cm and 804.32/cm are ascribed to the C=O-stretching vibration in aldehyde groups and to the formation of C=N in the immobilization reaction. The small bands at 1012/cm are

Table 2 Analysis of variance (ANOVA) for the response surface quadratic model

Source	Sum of squares	df	Mean square	*F* value	*p* value	
Model	4906.49	14	350.46	397.82	**< 0.0000**	**significant**
A-Enzyme conc	520.08	1	520.08	590.36	< 0.0001	
B-MNPs conc	574.08	1	574.08	651.66	< 0.0001	
C-Cross linking (carbodiamide)	720.75	1	720.75	818.15	< 0.0001	
D-Time course of cross linking	80.08	1	80.08	90.91	< 0.0001	
AB	0.2500	1	0.2500	0.2838	0.6026	
AC	6.25	1	6.25	7.09	0.0185	
AD	6.25	1	6.25	7.09	0.0185	
BC	30.25	1	30.25	34.34	< 0.0001	
BD	0.2500	1	0.2500	0.2838	0.6026	
CD	56.25	1	56.25	63.85	< 0.0001	
A^2	1920.82	1	1920.82	2180.39	< 0.0001	
B^2	966.77	1	966.77	1097.41	< 0.0001	
C^2	1006.77	1	1006.77	1142.82	< 0.0001	
D^2	410.82	1	410.82	466.34	**< 0.0000**	**significant**
Residual	12.33	14	0.8810	–	–	
Lack of fit	12.33	10	1.23	–	–	
Pure error	0.0000	4	0.0000	–	–	
Cor total	4918.83	28				

attributed to the C–O–C absorption peaks. The FT-IR results are consistent with the previous studies that reported the immobilization of laccase using Fe and Kaolini nanoparticles (Jiang et al. 2018; Ztrk et al. 2008; Lin et al. 2007). The variations in the stretching vibrations of the MNPs and immobilized laccase indicate buffer interference which was used during the immobilization process. A decrease in vibration bands attributed to groups of the enzyme probably due to low amount of immobilized enzyme was observed; FT-IR could not detect it (Fortes et al. 2017).

The magnetic properties of MNPs and immobilized laccase were investigated by VSM measurements (Fig. 3b). The results clearly indicated that the magnetization of MNPs was about approximately 8 EMU/g and that of the immobilized laccase with MNPs was nearly 4 EMU/g. A reduction in magnetic strength by 50% might be due to the surface modification of MNPs by elemental Fe. The magnetic strength observed in the present study is high when compared to the results of Kalkan et al. (2011) and Mahdavi et al. (2013), who reported ten times higher magnetic strength. The oxidation of magnetite particles into maghemite could be the possible reason for the reduction in the magnetic strength of the material (Mahdavi et al. 2013). The observed results confirm that the MNPs are super-magnetic at room temperature owing to the lack of magnetic hysteresis and exhibit a high magnetic responsiveness for use in magnetic separation (Lin et al. 2017; Wang et al. 2013).

Effect of pH, temperature, and storage time on the stability of the immobilized laccase

It has been reported that immobilized laccase shows enhanced enzymatic activity in comparison with free laccase (Wu et al. 2019). The optimum pH conditions (pH 5–10) of the free laccase and immobilized laccase are shown in Fig. 4a. The results indicate that the activity of both free and immobilized laccase is high at pH 7.0. However, when the pH of the solution reached basic conditions (pH 8–10), the immobilized laccase showed higher activity than the free laccase. It has been reported that the interaction of laccase molecules with the amino groups of MNPs causes more stable activity than the free laccase (Chen et al. 2016).

Expectedly, the immobilized laccase showed activity at a wide range of temperature (40–80 °C) than the free laccase (Fig. 4b). Both free and immobilized laccase showed maximum activity at 50 °C. There was no significant difference in the activity of the enzymes at 50 °C. However, when the temperature was increased to 60 °C, the immobilized laccase showed a minor decrease in activity. However, at the same temperature, free laccase showed a marked decrease in activity. In addition, the immobilized laccase maintained over 55% of its activity in the range of 55–80 °C. Statistical analysis showed that the free enzyme and immobilized laccase activity significantly ($p < 0.5$) differed in pH, temperature, and storage time.

It has been observed that the immobilization increased the steadiness of the laccase enzyme to alterations in pH and temperature. The shift in pH might be due to the variations

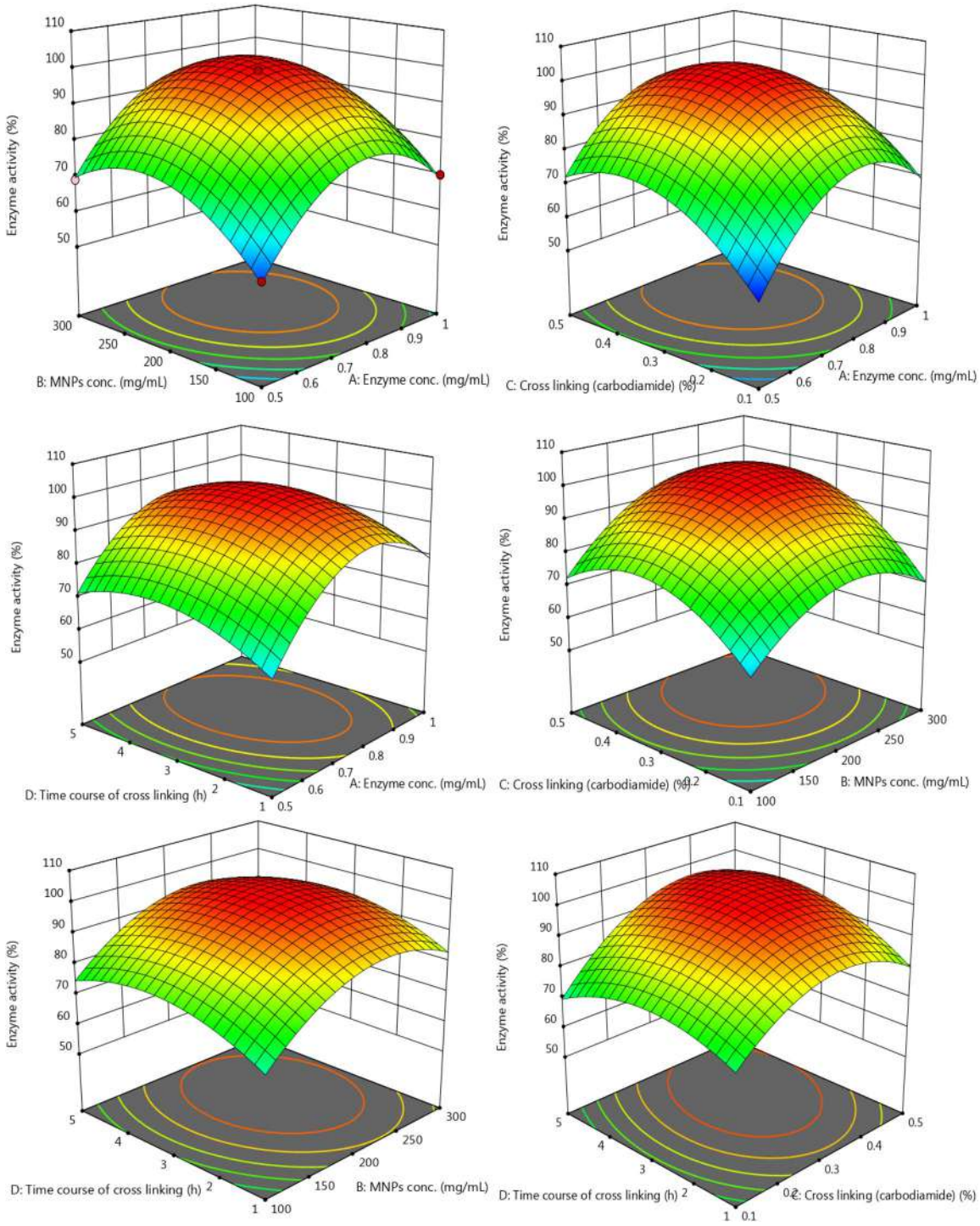


Fig. 1 Response 3-D plots of laccase immobilization magnetic nanoparticles under BBD optimized conditions

in the enzyme during covalent bond development leading to changes in the microenvironment of the laccase enzyme (Chiou and Wu 2004; Das et al. 2020). It has been reported that the occurrence of chemical transformation in the enzymes during temperature variations might be the reason for the shift in enzyme activity of free and immobilized enzymes (Kunamneni et al. 2008). Ramírez-Montoya et al. (2015) reported that the support material might have caused hindrances and diffusion limitations for the enzymes which could have also been the reason for the changes in the free and immobilized enzymes. The maximum activity range of immobilized enzyme than the free enzyme indicates

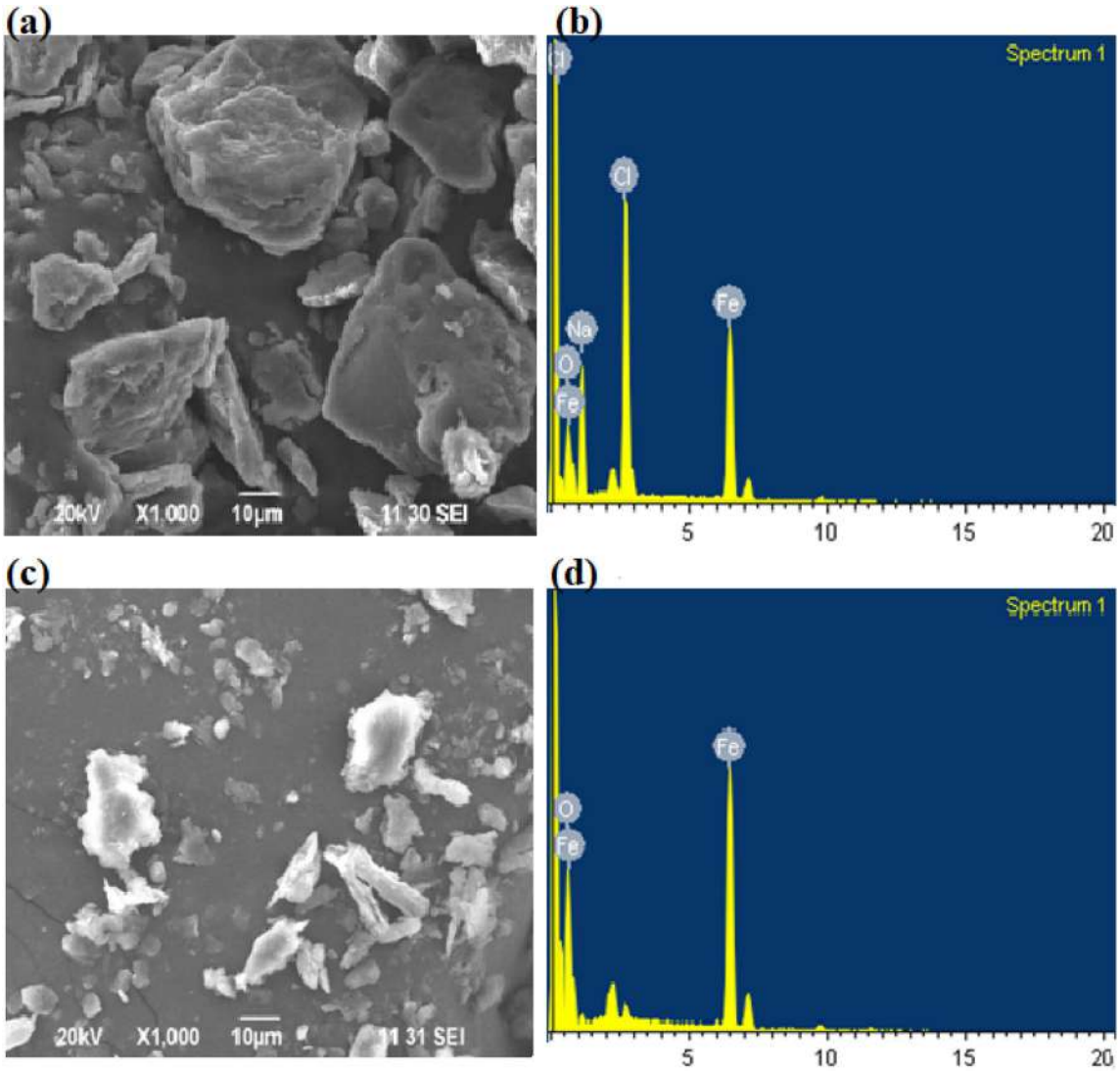


Fig. 2 SEM images of and related EDS of (**a**, **b**) MNPs before immobilization and (**c**, **d**) MNPs-Lac after immobilization

its resistance to the alkaline changes that occurred in the medium (Quiroga et al. 2011).

The immobilized laccase retained 80% of its activity after storing for 100 h, while the activity of the free laccase was only 30% over the same period (Fig. 4c). These results showed that immobilized laccase presented a better storage stability compared to its free enzyme form. This drop in activity over time can be caused by conformational changes in the enzyme during the immobilization, which enhanced the stability of the immobilized laccase. It can also be due to conformational changes in the enzyme tertiary structure during the storage period (Fortes et al. 2017). Recent studies reported that the loss of immobilized laccase activity was smaller due to the relatively stable micro environment that prevented laccase in activation (Wu et al. 2019). Arsalan and Younus (2018) reported that the covalent bonding immobilization method provided greater stability than the adsorption methods.

Pesticide degradation studies

The chlorpyrifos degradation products were identified by the HPLC analysis. Our previous study reported the chlorpyrifos degrading ability of free laccase (Srinivasan

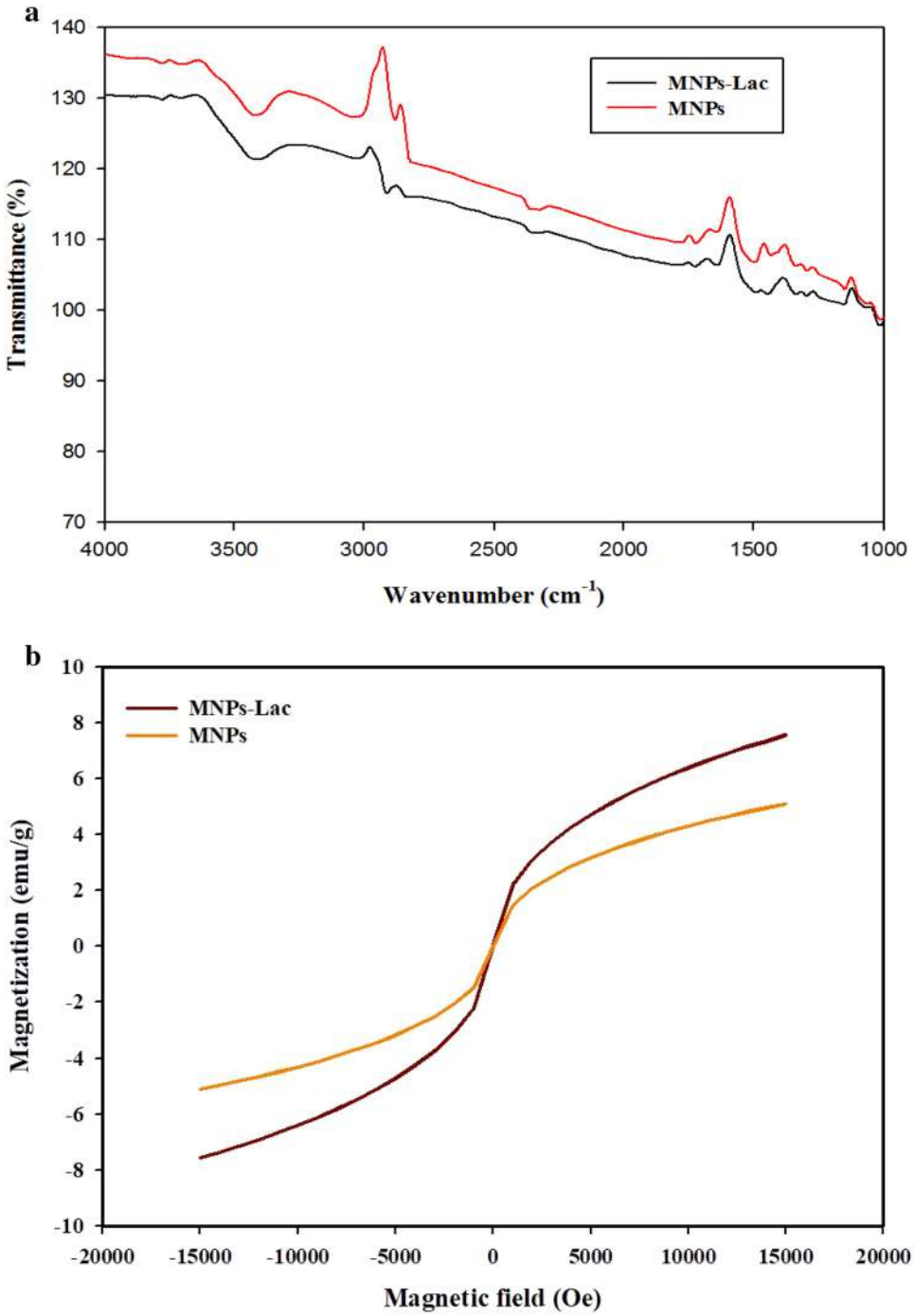


Fig. 3 **a** FT-IR spectra of MNPs before immobilization and MNPs-Lac after immobilization. **b** VSM image of MNPs before and after immobilization

et al. 2019). Hence, in this work, we tested the chlorpyrifos degradation ability of immobilized laccase, and the corresponding HPLC chromatogram is shown in Fig. 5. The immobilized laccase-mediated chlorpyrifos degradation showed dominant peak at a retention time of approximately 2.810 min, and the control showed a peak at 2.302 min (Srinivasan et al. 2019). The laccase-mediated degradation showed only two metabolic peaks. However, the immobilized laccase showed four major soluble peaks at retention times of approximately 2.810, 2.962, 4.425, and 4.760 min. The results clearly indicated that the immobilized laccase degrades chlorpyrifos more effectively than the free laccase. Based on these results, it is suggested that the immobilized laccase is capable of greater chlorpyrifos degradation.

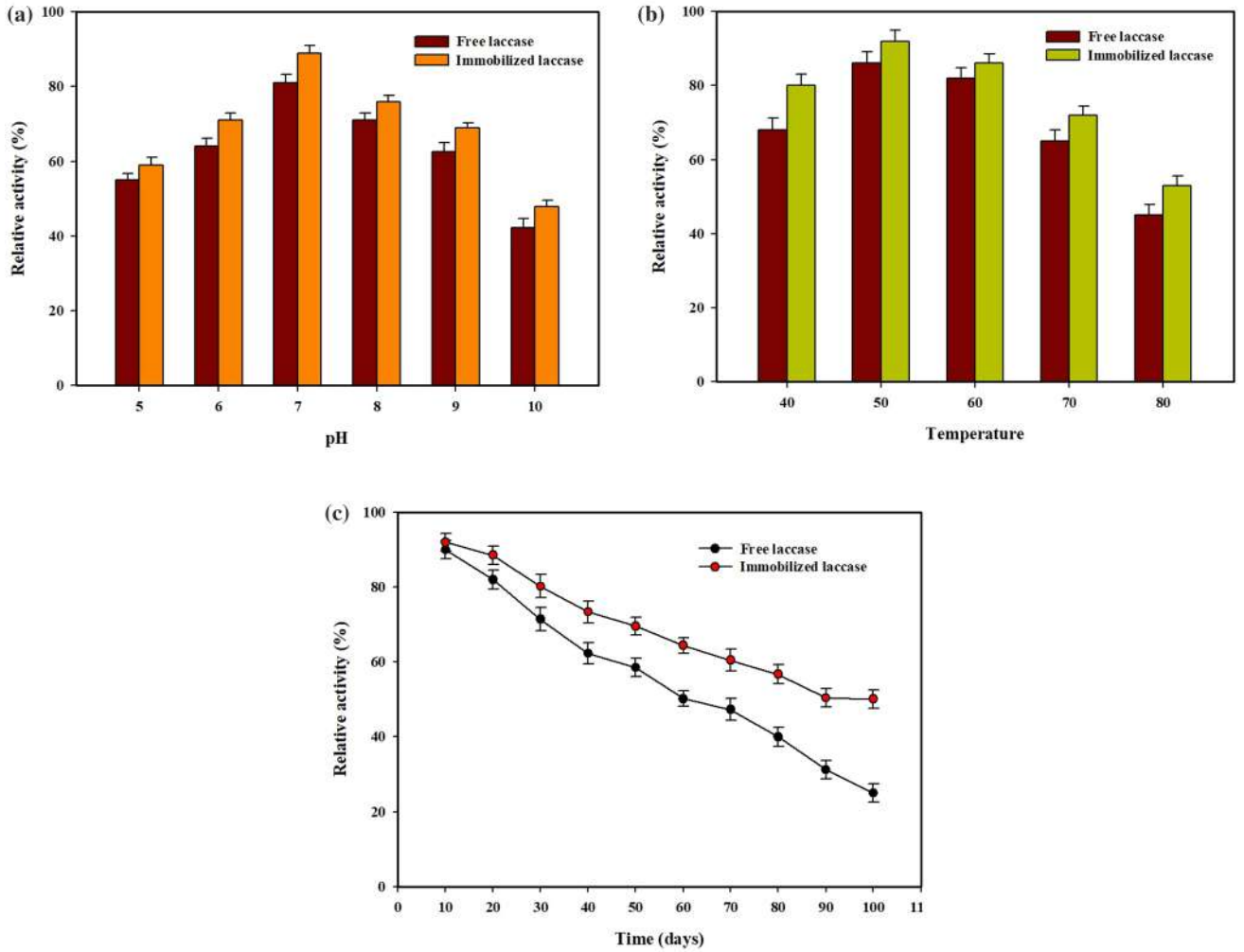


Fig. 4 Effect of pH **a** temperature **b** and stability **c** of the immobilized laccase and free enzyme activity

Conclusion

This study demonstrates that MNPs are a resourceful candidate for the immobilization of the enzyme laccase. The immobilization of laccase was confirmed by various structural characterization methods such as SEM and FT-IR. VSM analysis showed strong magnetic property of the immobilized laccase. The immobilized laccase displayed adequate enzymatic activity, including enhanced tolerance towards alkaline pH, high temperature, and storage stability up to 100 h. In addition, the immobilized laccase showed potential pesticide biodegradation activity. Hence, it is suggested that the immobilized laccase could be used as a potential candidate for biodegradation of pesticides in contaminated soil and/or water.

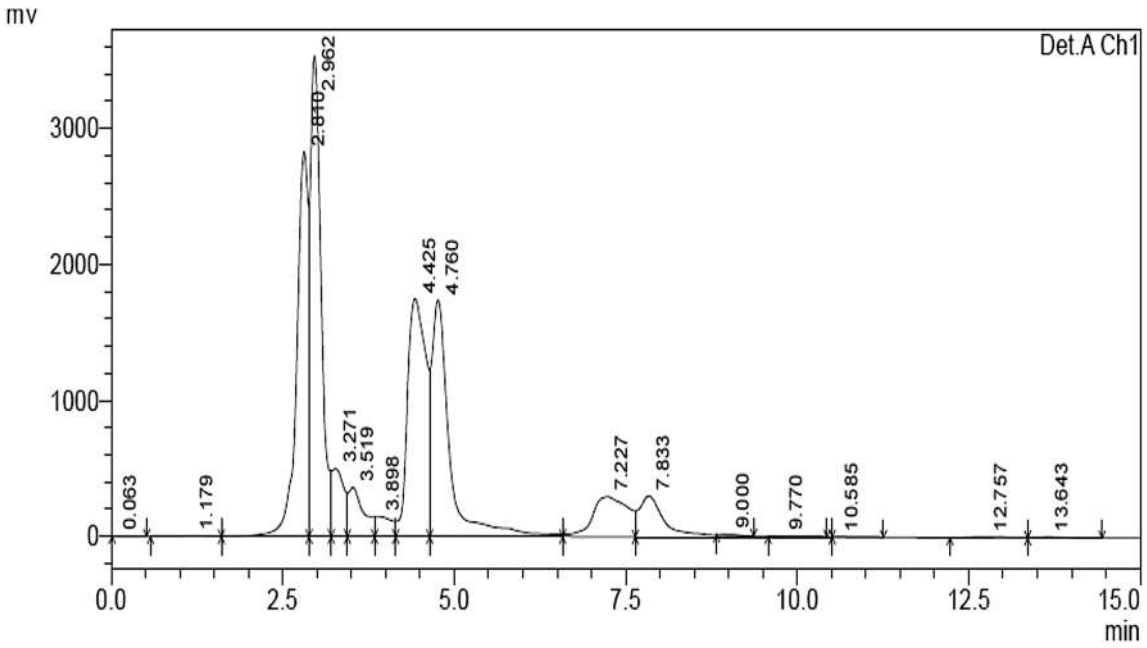


Fig. 5 HPLC chromatogram of chlorpyrifos degradation by MNPs-Lac

Acknowledgements This research is partially supported by the PG & Research Department of Biotechnology, Mahendra Arts and Science College (Autonomous), and the Department of Science and Technology, Government of India (DST-FIST sponsored-Ref. No. SR/ FST/ College-232/2014). This research was supported by Kyungpook National University Bokhyeon Research Fund, 2017. This study was supported by Researchers Supporting Project number (RSP-2020/144), King Saud University, Riyadh, Saudi Arabia.

Compliance with ethical standards

Conflict of interest The authors declare that they have no conflict of interest.

References

Ahmed I, Iqbal HM, Dhama K (2017) Enzyme-based biodegradation of hazardous pollutants an overview. J Exp Biol Agric Sci 5:402–411

Amin F, Nawaz H, Muhammad B, Bilal M (2016) Improvement of activity, thermo-stability and fruit juice clarification characteristics of fungal exo-polygalacturonase. Int J Biol Macromol. https://doi.org/10.1016/j.ijbiomac.2016.10.086

Antecka K, Zdarta J, Siwińska-Stefańska K, Sztuk G, Jankowska E, Oleskowicz-Popiel P, Jesionowski T (2018) Synergistic degradation of dye wastewaters using binary or ternary oxide systems with immobilized laccase. Catalysts 8:402

Arsalan A, Younus H (2018) Enzymes and nanoparticles: modulation of enzymatic activity via nanoparticles. Int J Biol Macromol 118:1833–1847

Bilal M, Asgher M, Hafiz MN, Hu H, Wang W, Zhang X (2017a) Bio-catalytic performance and dye-based industrial pollutants degradation potential of agarose-immobilized MnP using a Packed Bed Reactor System. Int J Biol Macromol 102:582–590

Bilal M, Asgher M, Parra-Saldivar R, Hu H, Wang W, Zhang X, Iqbal HM (2017b) Immobilized ligninolytic enzymes: an innovative and environmental responsive technology to tackle dye-based industrial pollutant a review. Sci Total Environ 576:646–659

Bilal M, Rasheed T, Zhao Y, Iqbal HM (2019) Agarose chitosan hydrogel immobilized horseradish peroxidase with sustainable bio-catalytic and dye degradation properties. Int J Biol Macromol 124:742–749

Chen YY, Stemple B, Kumar M, Wei N (2016) Cell surface display fungal laccase as a renewable biocatalyst for degradation of persistent micro pollutants bisphenol A and sulfamethoxazole. Environ Sci Technol 50:8799–8808

Chiou SH, Wu WT (2004) Immobilization of *Candida rugosa* lipase on chitosan with activation of the hydroxyl groups. Biomaterials 25:197–204

Das A, Singh J, Yogalakshmi KN (2017) Laccase immobilized magnetic iron nanoparticles: fabrications and its performance evaluation in chlorpyrifos degradation. Int Biodeterior Biodegrad 117:183–189

Das A, Jaswal V, Yogalakshmi KN (2020) Degradation of chlorpyrifos in soil using laccase immobilized iron oxide nanoparticles and their competent role in deterring the mobility of chlorpyrifos. Chemosphere 246:125676

Dyal A, Loos KM, Noto M, Chang SW, Spagnoli C, Shafi KVPM, Ulman A, Cowman M, Gross RA (2003) Activity of *Candida rugosa*lipase immobilized on g-Fe_2O_3 magnetic nanoparticles. J Am Chem Soc 125:1684–1685

Fortes C, Daniel-da-Silva AL, Xavier MRB, Tavares PM (2017) Optimization of enzyme immobilization on functionalized magnetic nanoparticles for laccase biocatalytic reactions. Chem Eng Process 117:1–8

Govarthanan M, Jeon C-H, Jeon Y-H, Kwon J-H, Bae H, Kim W (2020) Non-toxic nano approach for wastewater treatment using *Chlorella vulgaris* exopolysaccharides immobilized in iron-magnetic nanoparticles. Int J Biol Macromol 162:1241–1249

Gupta AK, Gupta M (2005) Synthesis and surface engineering of iron oxide nanoparticles for biomedical applications. Biomaterials 26:3995–4021

Gursharan S, Satinderpal K, Madhu K, Shailendramar K (2019) Biobleaching for pulp and paper industry in India: emerging enzyme technology. Biocatal Agric Biotechnol 17:558–565

Halim SFA, Kamaruddin AH, Fernando WJN (2009) Continuous biosynthesis of biodiesel from waste cooking palm oil in a packed bed reactor: optimization using response surface methodology (RSM) and mass transfer studies. Bioresour Technol 100:710–716

Huang D, Liu L, Zeng G, Xu P, Huang C, Deng L, Wang R, Wan J (2017) The effects of rice straw biochar on indigenous microbial community and enzymes activity in heavy metal contaminated sediment. Chemosphere 174:545–553

Jiang C, Yin L, Wen X, Du C, Wu L, Long Y, Liu Y, Ma Y, Yin Q, Zhou Z, Pan H (2018) Micro plastics in sediment and surface water of west dongting lake and south dongting lake: abundance, source and composition. Int J Environ Res Public Health 15:2164

Jořenek M, Zajoncová L (2015) Immobilization of laccase on magnetic carriers and its use in decolorization of dyes. Chem. Biochem Eng 29:457–466

Jordan C, Ahmed E, Cerasela Z (2018) Industrial applications of enzymes: recent advances, techniques, and outlooks. Catalysts 8:238

Kalkan NA, Aksoy S, Aksoy EA, Hasirci N (2011) Preparation of chitosan-coated magnetite nanoparticles and application for immobilization of laccase. J Appl Polym Sci 123:707–716

Krishna SH, Sattur AP, Karanth NG (2001) Lipase catalyzed synthesis of isoamyl isobutyrate optimization using a central composite rotatable design. Process Biochem 37:9–16

Kumar S, Kaushik G, Dar M, Nimesh S, Opez-chuken U, Villarreal-chiu JF (2018) Microbial degradation of organophosphate pesticides: a review. Pedosphere 28:190–208

Kunamneni A, Plou FJ, Ballesteros A, Alcalde M (2008) Laccases and their applications: a patent review. Recent Pat Biotechnol 2:10–24

Kupski L, Salcedo GM, Caldas SS, Souza TD, Furlong EB, Primel EG (2019) Optimization of a laccase-mediator system with natural redox-mediating compounds for pesticide removal. Environ Sci Pollut Res 26:5131–5139

Lai C, Zhang M, Li B, Huang D, Zeng G, Qin L, Liu X, Yi H, Cheng M, Li L, Chen Z, Chen L (2019) Fabrication of CuS/BiVO4 (0 4 0) binary hetero junction photo catalysts with enhanced photo catalytic activity for ciprofloxacin degradation and mechanism insight. Chem Eng J 358:891–902

Laurent S, Forge D, Port M, Roch A, Robic C, Vander Elst L, Muller RN (2008) Magnetic iron oxide nanoparticles: Synthesis, stabilization, vectorization, physicochemical characterizations, and biological applications. Chem Rev 108:2064–2110

Li Z (2018) Health risk characterization of maximum legal exposures for persistent organic pollutant (POP) pesticides in residential soil: an analysis. J Environ Manag 205:163–173

Lin D, Pan B, Zhu L, Xing B (2007) Characterization and phenanthrene sorption of tea leaf powders. J Agric Food Chem 55:5718–5724

Lin J, Wen Q, Chen S, Le X, Zhou X, Huang L (2017) Synthesis of amine-functionalized Fe_3O_4@C nanoparticles for laccase immobilization. Int J Biol Macromol 96:377–383

Liu Y, Zeng Z, Zeng G, Tang L, Pang Y, Li Z, Liu C, Lei X, Wua M, Ren P, Liu Z, Chen M, Xie G (2012) Immobilization of laccase on magnetic bimodal mesoporous carbon and the application in the removal of phenolic compounds. Bioresour Technol 115:21–26

Mahdavi M, Ahmad MB, Haron J, MdNamvar F, Nadi B, Rahman MZ, Amin J (2013) Synthesis, surface modification and characterization of biocompatible magnetic iron oxide nanoparticles for biomedical applications. Molecules 18:7533–7548

Maqbool Z, Hussain S, Imran M, Mahmood F, Shahzad T, Ahmed Z, Muzammil S (2016) Perspectives of using fungi as bioresource for bioremediation of pesticides in the environment: a critical review. Environ Sci Pollut Res 23:16904–16925

Mir-Tutusaus JA, Baccar R, Caminal G, Sarrà M (2018) Can white-rot fungi be a real wastewater treatment alternative for organic micro pollutants removal? A review. Water Res 138:137–151

Nandhini NT, Rajeshkumar S, Mythili R (2019) The possible mechanism of eco-friendly synthesized nanoparticles on hazardous dyes degradation. Biocatal Agric Biotechnol 19:10113

Pereira LC, Souza AO, Bernardes MFF, Pazin M, Tasso MJ, Pereira PH, Dorta DJ (2015) A perspective on the potential risks of emerging contaminants to human and environmental health. Environ Sci Pollut Res 22:13800–13823

Quiroga E, Illanes CO, Ochoa NA, Barberis S (2011) Performance improvement of araujia in, a cystein phytoprotease, by immobilization within calcium alginate beads. Process Biochem 46:1029–1034

Ramírez-Montoya LA, Hernandez-Montoya V, Montes Moran MA, Jauregui Rincon J, Cervantes FJ (2015) Decolorization of dyes with different molecular properties using free and immobilized laccases from *Trametes versicolor*. J Mol Liq 212:3037

Selvam K, Govarthanan M, Senbagam D, Kamala Kannan S, Senthilkumar B, Selvankumar T (2016) Activity and stability of bacterial cellulase immobilized on magnetic nanoparticles. Chin J Catal 37:1891–1898

Simonelli A, Basilicata P, Miraglia N, Castiglia L, Guadagni R, Acampora A, Sannolo N (2007) Analytical method validation for the evaluation of cutaneous occupational exposure to different chemical classes of pesticides. J Chromatogr B 860:26–33

Soozanipour A, Taheri kafrani A, LandaraniIsfahani A (2015) Covalent attachment of xylanase on functionalized magnetic nanoparticles and determination of its activity and stability. Chem Eng J 270:235–243

Srinivasan P, Selvankumar T, Kamala-Kannan S, Mythili R, Sengottaiyan A, Govarthanan M, Senthilkumar B, Selvam K (2019) Production and purification of laccase by *Bacillus* sp. using millet husks and its pesticide degradation application. 3 Biotech 9:396

Vera M, Nyanhongo GS, Pellis A, Rivas BL, Guebitz GM (2019) Immobilization of *Myceliophthora thermophila* laccase on poly (glycidyl methacrylate) microspheres enhances the degradation of azinphos-methyl. J Appl Polym Sci 136:47417

Villarreal-Chiu JF, Acosta-Cortes AG, Kumar S, Kaushik G (2017) Biological limitations on glyphosate biodegradation. In: Singh R, Kumar S (eds) Green technologies and environmental sustainability, 9th edn. Springer, Cham, pp 179–201

Wang J, Zhao G, Li Y, Liu X, Hou P (2013) Reversible immobilization of glucoamylase onto magnetic chitosan nanocarriers. Appl Microbiol Biotechnol 97:681–692

Wen X, Du C, Wan J, Zeng G, Huang D, Yin L, Deng R, Tan S, Zhang J (2019) Immobilizing laccase on kaolinite and its application in treatment of malachite green effluent with the coexistence of Cd (Π). Chemosphere 217:843–850

Wu E, Li Y, Huang Q, Yang Z, Wei A, Qi Hu (2019) Laccase immobilization on amino functionalized magnetic metal organic framework for phenolic compound removal. Chemosphere 233:327–335

Zdarta J, Meyer AS, Jesionowski T, Pinelo M (2018) Developments in support materials for immobilization of oxidoreductases: a comprehensive review. Adv Colloid Interface Sci 258:1–20

Zeng S, Qin X, Xia L (2017) Degradation of the herbicide isoproturon by laccase mediator systems. Biochem Eng J 119:92–100

Zheng F, Cui BK, Wu XJ, Meng G, Liu HX, Si J (2016) Immobilization of laccase onto chitosan beads to enhance its capability to degrade synthetic dyes. Int Biodeterior Biodegrad 110:69–78

Ztrk N, Tabak A, Akgl S, Denizli A (2008) Reversible immobilization of catalase by using a novel bentonite-cysteine (Bent-Cys) micro composites affinity sorbents. Colloid Surf Physicochem Eng Asp 322:148–154

ISSN 2349-8259(Online) ISSN 2454-9967(Print)

Phytochemical 6-Gingerol A promising Drug of choice for COVID-19

Authors: Thirumalaisamy Rathinavel, Murugan Palanisamy, Srinivasan Palanisamy, Arjunan Subramanian, Selvankumar Thangaswamy

https://doi.org/10.29294/IJASE.6.4.2020.1482-1489

Published: 15 May 2020

0

Abstract :

Recently, a novel corona virus (COVID-19), identified as one of the acute respiratory syndrome corona virus (SARS CoV-2) and emerged as a pandemic disease in Asia and European countries in 2020. The World Health Organization (WHO) has declared the current outbreak as a global public health crisis. Due to the variability in the amino acid and amino acid sequences, it does not develop suitable vaccines against the viral proteins. Hence, the inhibitor to be developed against the viral proteins of the corona virus is a promising idea to develop structure-based drugs from the photochemical compounds. Here, the novel drug was identified and well studied against the viral receptors by using the molecular docking technique. Phytocompound 6-gingerol possesses excellent drug likeliness with zero violations and very good pharmacokinetic properties, with the highest

PRINCIPAL
PGP College of Arts and Science
Namakkal

ACADEMIA
Accelerating the world's research.

Phytochemical 6-Gingerol -A promising Drug of choice for COVID-19

International Journal of Advanced Science and Engineering (IJASE)

International Journal of Advanced Science and Engineering

Cite this paper

Downloaded from Academia.edu

Get the citation in MLA, APA, or Chicago styles

Related papers

Download a PDF Pack of the best related papers



Identification of Anti-Diabetic Phytocompounds from Ficus racemosa and its Validation thro...
International Journal of Advanced Science and Engineering (IJASE)

Andrographolide As a Potential Inhibitor of SARS CoV 2 Main Protease An In Silico Approach
jerrine joseph, Sukanth Kumar

Identification of Dietary Molecules as Therapeutic Agents to Combat COVID-19 Using Molecular Docki...
Tariq J Faridi

RESEARCH ARTICLE

Phytochemical 6-Gingerol – A promising Drug of choice for COVID-19

Thirumalaisamy Rathinavel[1], Murugan Palanisamy[2], Srinivasan Palanisamy[1], Arjunan Subramanian*[1], Selvankumar Thangaswamy*[1]

[1]Department of Biotechnology, Mahendra Arts & Science College (Autonomous), Namakkal (Dt) -637 501, Tamil Nadu, India
[2]Nichi Asia Life Sciences Sdn Bhd, Kota Damansara, Malaysia

ABSTRACT: Recently, a novel corona virus (COVID-19), identified as one of the acute respiratory syndrome corona virus (SARS CoV-2) and emerged as a pandemic disease in Asia and European countries in 2020. The World Health Organization (WHO) has declared the current outbreak as a global public health crisis. Due to the variability in the amino acid and amino acid sequences, it does not develop suitable vaccines against the viral proteins. Hence, the inhibitor to be developed against the viral proteins of the corona virus is a promising idea to develop structure-based drugs from the photochemical compounds. Here, the novel drug was identified and well studied against the viral receptors by using the molecular docking technique. Phytocompound 6-gingerol possesses excellent drug likeliness with zero violations and very good pharmacokinetic properties with the highest binding affinity ranging from -2.8764 KJ/mol to -15.7591 KJ/mol with various COVID-19 viral protein targets. Our study reveals that 6-gingerol from ginger could act as a promising drug of choice to treat COVID-19.

KEYWORDS: SARS-CoV-2; COVID-19; 6-Gingerol, corona virus; respiratory infection.

https://doi.org/10.29294/IJASE.6.4.2020.1482-1489 **© 2020 Mahendrapublications.com, All rights reserved**

1. INTRODUCTION

Corona virus is the group of viruses that have a crown-like appearance when viewed under the electronic microscope. Corona viruses cause respiratory tract infections in humans, which can cause a wide range of illnesses from the mild common cold to lethal SARS and MERS. There are no vaccines and anti-viral drugs are available yet to treat corona viral infections. Corona virus possesses positive sense single-stranded enveloped RNA as their genetic material. The genome of corona virus is the largest group among the viruses is host specific which is based on the receptor specificity of their S-Protein. It is an enveloped virus that is made up of glycoprotein.

In December 2019, the novel corona virus (2019-nCoV or SARS CoV-2), cause corona virus disease 2019 (COVID-19) in humans, was an outbreak in Wuhan, China. The epidemic disease of SARS CoV-2 in Wuhan has occurred human to human transmission among close contacts, which becomes emerged as a pandemic disease from January 2020 spread through international travelers across the different countries and enters almost all the countries except few of them. As of 10th April 2020, there have been over 1.6 million cases with over 0.1 million deaths for the COVID-19 outbreak worldwide [1] However, there are currently no effective medications against SARS CoV-2. Several national and international research groups are working on the development of vaccines to prevent and treat the SARS CoV-2, but effective vaccines are not available yet. There is an urgent need for the development of effective prevention and treatment strategies for SARS CoV-2 outbreak. Indian people are consuming Indian traditional medicinal herb extract and Indian spices to boost the immune system to fight COVID -19.

Ginger (*Zingiber officinale*) is the herbaceous plant native to South Asia belonging to the family of Zingiberaceae. The characteristic pungent flavor of the ginger rhizome is used extensively in foods and beverages [2]. Ginger is a common Indian spice and traditional medicinal plants have important pharmacologic activities such as antibacterial, antiviral, anti-hypertensive, antioxidant, analgesic and antipyretic properties [3]. Ginger has been proved to be effective on various viruses [4-8]. Ginger rhizome possesses several outstanding bioactive non-volatile phenolic compounds such as gingerols, paradols, shogaols, and zingerones [9]. Ginger is one of the best choices of bioactive Phyto-compound in traditional medicine in Ayurvedic, Chinese and Unani systems to treat different diseases in ancient times.

6-gingerol is a bioactive phenolic phytocompound found in the fresh ginger rhizome. 6-gingerol is a promising drug candidate to treat various diseases associated with inflammation,

**Corresponding Authors: pavima08@gmail.com & selvankumar75@gmail.com*
Received: 18.01.2020 **Accepted:** 21.03.2020 **Published on**: 18.04.2020

cancer, and viral disease. Fresh ginger possesses anti-viral activity against human respiratory syncytial virus due to the presence of bioactive phenolic phytocompound 6-gingerol [10]. Hence, the present study aims to examine phytocompound 6-gingerol from the ginger plant (*Zingiber officinale*) that could act as a promising drug against COVID-19 proteins and screened through *in silico* approach.

MATERIALS AND METHOD

1.1. Ligand generation

The 2D structure of *Zingiber officinale* phytocompound 6-gingerol (CID 442793) was retrieved from Pubchem, a database of chemical molecules [11]. The retrieved 2D SDF file format of 6-gingerol was submitted to "Online SMILES convertor and Structure file generator" [12] and converted into 3D SDF format.

1.2. Drug Likeliness and Absorption, Distribution, Metabolism, Extraction and Toxicity [ADME] Calculations

Swiss ADME online server was used to calculate Drug Likeliness parameters. Drug likeliness of the phytocompounds gingerol was examined based on Violations of the following rules such as Lipinski, Ghose, Veber, Egan, and Muegge. Pharmacokinetic properties of phytocompounds gingerol were screened by preADMET is a web-based application to determine the pharmacological efficiency of phytocompounds. PreADMET predicts the various parameters associated with ADME and toxicity behavior of phytocompounds.

1.3. Preparation of Receptor and its Binding Site

Novel corona viral (SARS-CoV-2 or COVID-19) Proteases, Spike protein, RNA binding protein, N-terminal RNA binding domain are the key viral molecules involved in attachment and replication and reproduction of viral particle in the human host cells. These Protein target molecules served as a novel target to inhibit the viral lifecycle in human host cells. Three-dimensional structures of SARS CoV-2 nine molecules of main proteases (5R7Y, 5R80, 5R81, 5R83, 5R84, 6LU7, 6LVN, 6M03, 6Y84), one spike protein (6VSB), one RNA binding protein (6W4B) and one N-terminal binding domain (6M3M) was retrieved from RCSB PDB database (https://www.rcsb.org/) [13].To determine the binding affinities between the ligand and receptor, the amino acids with the binding pockets were predicted at the Q-site finder server [14].

1.4. Flexible docking

The generated gingerol SDF structures were docked with the predicted binding site of all selected protein target binding site by using teaching version of FlexX [15] with following parameters i) default general docking information ii) base placement using triangle matching, iii) scoring of full score contribution and threshold of 0.70 iv) Chemical parameters of clash handling values for protein-ligand clashes with maximum allowed overlap volume of 2.9 A03 and intra-ligand clashes with clash factor of 0.6 and considering the hydrogen in internal clash tests. v) Default docking details values of 200 for both the maximum number of solutions per iteration and a maximum number of solutions per fragmentation.

1.5. Prediction of ligand-receptor interactions

The interactions of phytocompound gingerol with twelve SARS CoV-2 proteins targets in the docked complex were analyzed by the pose-view of LeadIT [16]. 2D and 3D pose view of SARS COV-2 protein target-phytocompound gingerol was generated and analyzed using LeadIT.

1.6. Density Functional Theory DFT Analysis

DFT calculation for phytocompound gingerol was performed using Gaussian 09 software. DFT used to calculate HOMO–LUMO orbital providing energy gap between highest occupied molecular orbital (HOMO) and lowest unoccupied molecular orbital (LUMO) providing high and low electron density regions on the compounds.

2. RESULT AND DISCUSSION

2.1. Drug Likeliness and ADME Calculation

Drug likeliness calculation for phytocompound gingerol was made in Swiss ADME server and revealed that 6-gingerol possess a molecular weight of 294.39 g/mol, the number of hydrogen bond acceptor and donor are 4 & 6 respectively. Gingerol also possess excellent TPSA(topological polar surface area), lipophilicities (iLog P) and water solubility (Log S ESOL) values of 66.76, 3.48 & -2.96 respectively which proved there are nil (zero) violations for drug likeliness rules such as Lipinski, Ghose, Veber, Egan, and Muegge essential for better drug likeliness properties

ADME property of gingerol calculated by preADMET web-based application revealed that very good pharmacokinetic properties such as absorption, bioavailability and distribution parameters of 6-gingerol such as HIA 86.75%, the pure water solubility of 0.3460 mg/ml, 100% plasma protein binding, which are tabulated and presented in Table 1.

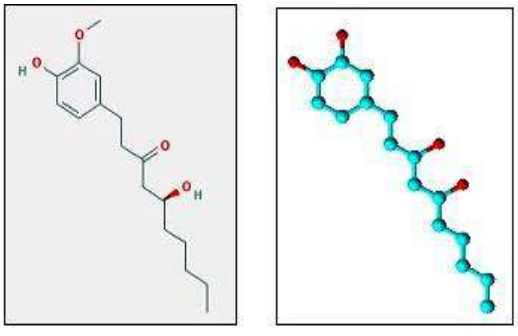


Figure 1- 2D & 3D structures of 6-Gingerol

Table 1 - ADME properties of 6-gingerol from ginger plant

ABSORPTION	
Human intestinal absorption (HIA, %)	86.75456
Caco-2 cell permeability (nm/sec)	13.5496
MDCK cell permeability (nm/sec)	0.627041
skin permeability (logKp, cm/hour)	-2.36594
BIOAVAILABILITY	
Buffer solubility (mg/ml)	0.7135
Pure water solubility (mg/ml)	0.3460
DISTRIBUTION	
Plasma protein binding (%)	100
Blood-brain barrier penetration	0.69481

2.2. Docking Study

Different COVID-19 target proteins (proteases, spike protein, RNA binding protein) and their docking score and 3D pose with 6-gingerol are presented in Table 2 and their detailed molecular interaction between them is tabulated and presented in Table 3 & Figure 2.

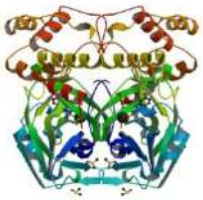
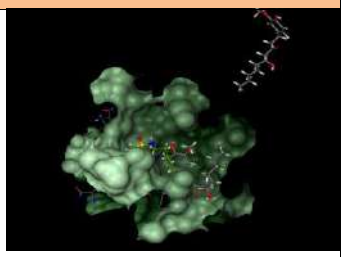
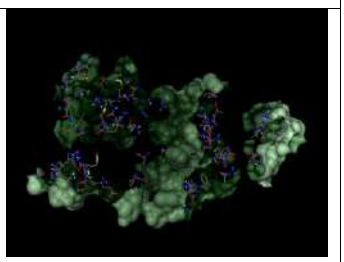
The results of a flexible docking study by flexX software between COVID-19 viral targets and gingerol was exhibit the binding affinity and docking score ranging from -2.8764 KJ/mol to -15.7591 KJ/mol. Gingerol exhibit the highest binding affinity (-15.7591 KJ/mol) with 5R7Y COVID-19 main protease essential for replication and reproduction of SARS Cov-2. Corona Viral protease 5R7Y residues such as His 164, Glu166, Thr190, Gln192 from hydrogen-bonded interaction with phytocompound gingerol, it also forms form non bonded interaction with the residues of His164, Met 165, Glu166, Leu167, Pro168, Arg188, Gln189, Thr190.

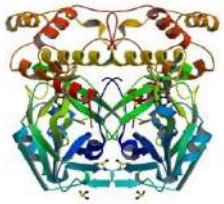
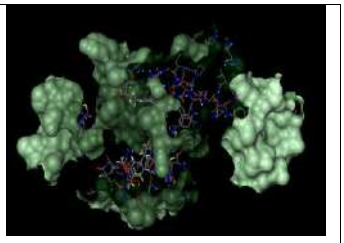
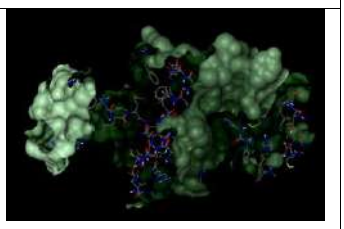
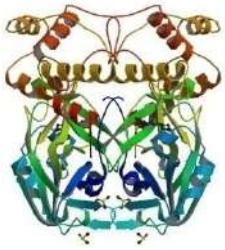
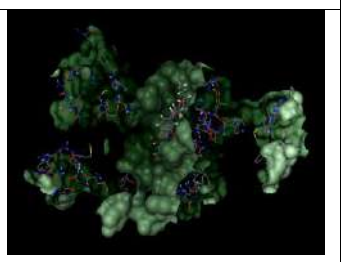
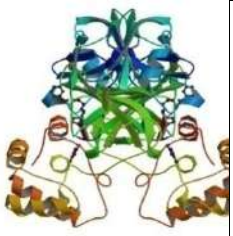
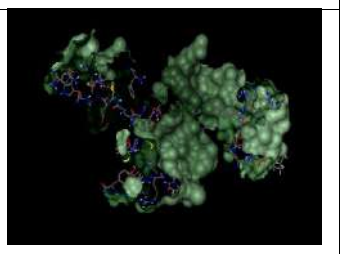
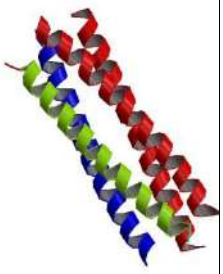
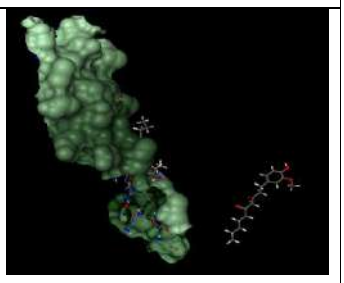
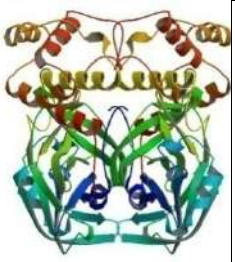
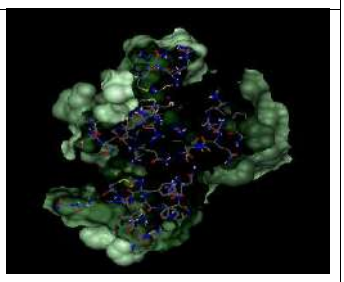
Gingerol exhibits binding affinity of -11.4082 KJ/mol, -12.9523 KJ/mol and -12.8835 KJ/mol with COVID-19 viral RNA binding protein (6W4B), N-Terminal RNA Binding Protein (6VSB), Spike glycoprotein (6M3M) respectively. Molecular interaction between COVID-19 viral spike glycoprotein with Gingerol forms hydrogen-bonded interaction with Glu63, Arg89, Thr92, Asp129 residues and form non bonded interaction with Glu63, Lys66, Arg89, Thr92, Leu168, Pro169 residues of COVID-19 spike glycol protein.

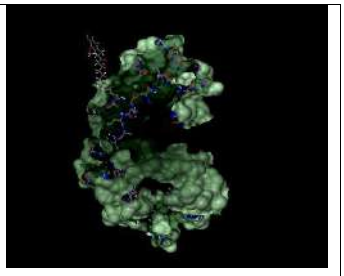
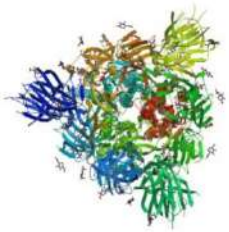
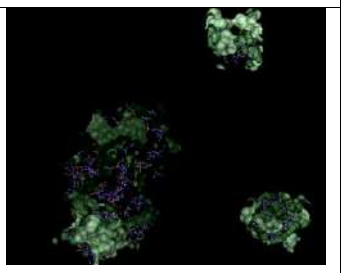
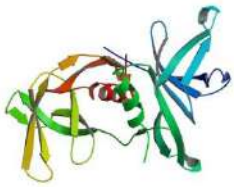
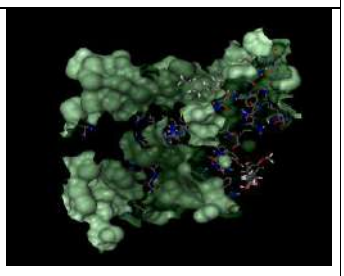
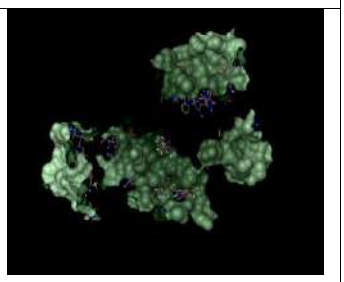
Molecular interaction between COVID-19 viral RNA binding protein with Gingerol makes hydrogen bonded interaction with Val42, Pro58, Ser60, Thr68 residues and form non bonded interaction with Arg40, Phe41, Val42, Phe57, Pro58, Lys59, Ser60, Ile66, Thr68, Ile92 residues of COVID-19 spike glycol protein.

The previous study reported that several phytocompounds of flavonoids and phenolic substances possess antiviral activities [17-19] especially 6-gingerol possess antiviral activities. Siti Khaerunnisa et al. [20] reported that 6-gingerol binds with the COVID-19 main protease active sites with the binding affinity of -5.40 K.Cal/mol.

Table 2 . COVID-19 Proteins Targets and its 3D Docking Pose with 6-gingerol

S.No	COVID-19 Protein Targets	Details	Protein 3D Structure	Docking Score (KJ/mol)	Docking
1	5R7Y	Crystal Structure of COVID-19 main protease in complex with Z45617795		-15.7591	
2	5R80	Crystal Structure of COVID-19 main protease in complex with Z18197050		-7.0885	

3	5R81	Crystal Structure of COVID-19 main protease in complex with Z1367324110		-8.2021	
4	5R83	Crystal Structure of COVID-19 main protease in complex with Z44592329		-7.4778	
5	5R84	Crystal Structure of COVID-19 main protease in complex with Z31792168		-9.5168	
6	6LU7	COVID-19 main protease in complex with an inhibitor N3		-2.8764	
7	6LVN	Structure of the 2019-nCoV HR2 Domain		-4.5961	
8	6M03	The crystal structure of COVID-19 main protease in apo form		-8.6837	

9	6M3M	SARS-CoV-2 nucleocapsid protein N-terminal RNA binding domain		-12.9523	
10	6VSB	Prefusion 2019-nCoV spike glycoprotein with a single receptor-binding domain up		-12.8835	
11	6W4B	Nsp9 RNA binding protein of SARS CoV-2		-11.4082	
12	6Y84	SARS-CoV-2 main protease with unliganded active site (2019-nCoV, coronavirus disease 2019, COVID-19)		-9.7625	

2.3. DFT Study

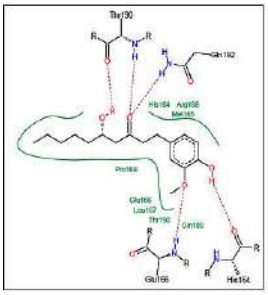
DFT study is used to explain the accurate structural and electronic properties of phytocompounds. The electronic distribution phytocompound 6-gingerol could provide a clear picture of SARS CoV-2 protein-gingerol interactions, which will be useful to explore the inhibition potentials of the phytocompound 6-gingerol. HOMO and LUMO orbital energies of 6-gingerol are shown in Figures 3 & 4. The calculated various HOMO-LUMO orbital energies are presented in Table 4.

The localization of HOMO and LUMO orbitals in the compound is very important in intermolecular interactions with SARS CoV-2 protein targets. 6-gingerol (-0.20606eV, 0.10303eV, and 9.3187eV) showed more stability and biological activity as it shows less energy gap, low hardness, and more softness. Thus the DFT calculations performed here better evidence highest binding affinity of 6-gingerol with SARS CoV-2 protein targets in molecular docking.

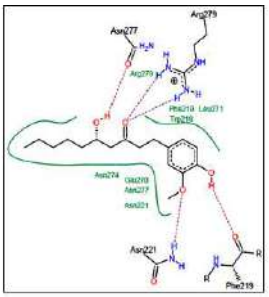
Similar comparative DFT study of phytochemical constituents of present in the bark extract of *Ficus racemosa* β-Amyrin (-0.06277eV, 0.031385eV and 31.86235eV) showed more stability and biological activity as it shows less energy gap, low hardness, and more softness followed by Betulinic acid (-0.23987eV, 0.119935eV and 8.33784eV) and Stigmasterol (-0.26925 eV, 0.134625 eV and 7.42804 eV) [21]. It was possible to characterize the compounds as well as their characteristics of electron donor/electron acceptor compared with other biological properties of the phytocompound by DFT analysis.

Table 3 .Molecular interaction of 6-gingerol with different COVID-19 Protein targets

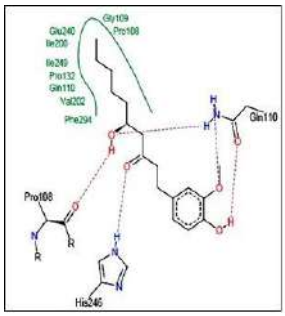
S.No.	COVID-19 Proteins Target PDB CODE	Gingerol and COVID-19 Target Protein Interactions	
		Hydrogen-Bonded Interactions	Non-Bonded Interactions
1	5R7Y	His 164, Glu166, Thr190, Gln192	His 164, Met 165, Glu166, Leu167, Pro168, Arg188, Gln 189, Thr190
2	5R80	Phe 219, Asn 221, Asn 277, Arg 279	Trp218,Trp219, Asn221, Glu270, Leu271, Asn274, Asn277, Arg279
3	5R81	Asp295,Arg298,Gln299,Thr304	Met6, Phe8,Pro9, Ile152, Tyr154, Arg298, Val 303, Thr304
4	5R83	Thr25, His41, Ser46, Gly143	-
5	5R84	Pro108,Gln110,His246	Pro108,Gly109,Gln110,Pro132, Ile200,Val202,Glu240,Ile249, Phe294
6	6LU7	Glu270,Gly275,Arg279	Phe223,Glu270,Leu271,Asn274
7	6LVN	Gln13,Asn20,Lys24	Gln13,Ile16,Asn20,Ala23,Lys24,Asn27
8	6M03	Gln110,Thr111,Phe294	Phe8,Gln110,Asn151,Phe294,Arg298,Val303
9	6M3M	Glu63, Arg89, Thr92, Asp129	Glu63, Lys66, Arg89, Thr92, Leu168, Pro169
10	6VSB	Gln773, Gln954, Ile1013, Arg1019	Glu773, Gln954, Ile1013, Arg1014, Glu1017, Arg1019
11	6W4B	Val42, Pro58, Ser60, Thr68	Arg40, Phe41, Val42, Phe57, Pro58, Lys59, Ser60, Ile66, Thr68, Ile92
12	6Y84	Met6, Ile152, Tyr154	Met6, Phe8, Pro9, Ile152, Tyr154, Arg298, Gln298, Val303, Thr304



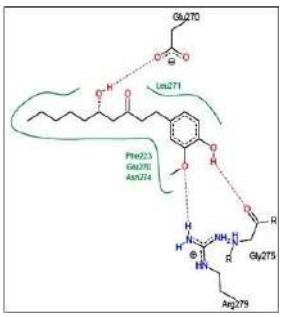
(a)



(b)



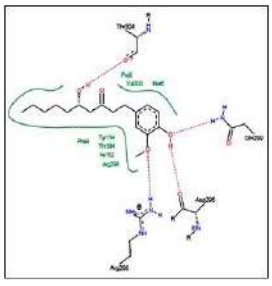
(e)



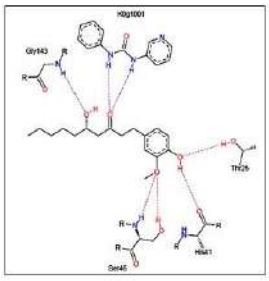
(f)

Figure 2 – Interaction plot for 6-Gingerol with COVID-19 Protein Targets (a-l)
a).Interaction of Gingerol with 5R7Y (-15.7591 KJ/mol) b).Interaction of Gingerol with 5R80 (-7.0885 KJ/mol)

e).Interaction of Gingerol with 5R84 (9.5168KJ/mol)
f).Interaction of Gingerol with 6LU7 (-2.8764KJ/mol)

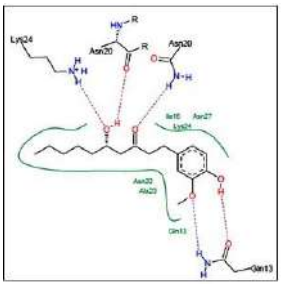


(C)

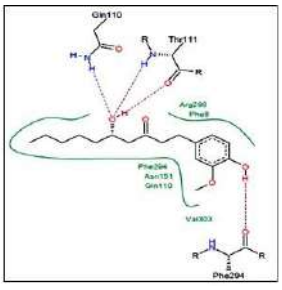


(d)

C).Interaction of Gingerol with with 5R81 (-8.2021KJ/mol)
d).Interaction of Gingerol with with 5R83 (-7.4778KJ/mol)

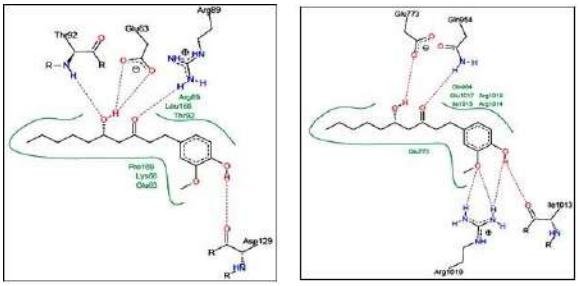


(g)



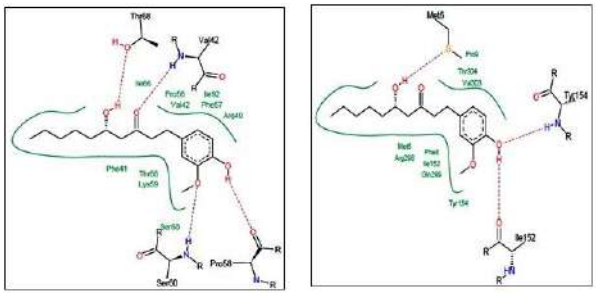
(h)

g).Interaction of Gingerol with 6LVN (-4.5961KJ/mol)
h).Interaction of Gingerol with 6M03 (-8.6837 KJ/mol)



(i) **(j)**

(i)Interaction of Gingerol with 6M3M (-12.9523 KJ/mol)
(j)Interaction of Gingerol with 6VSB (-12.8835KJ/mol)



(k) **(l)**

(k)Interaction of Gingerol with 6W4B (-11.4082 KJ/mol)
(l)Interaction of Gingerol with 6Y84 (-9.7625 KJ/mol

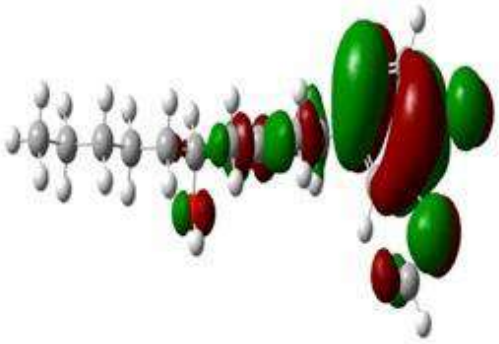


Figure 3 . HOMO orbital energy for 6-Gingerol

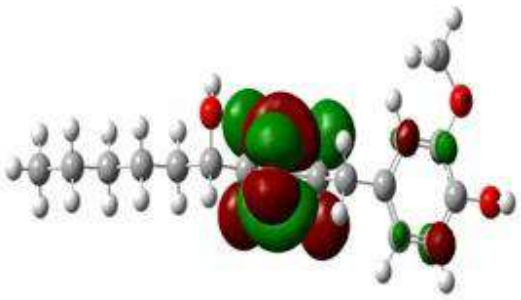


Figure 4.LUMO orbital energy for 6-Gingerol

3. CONCLUSION

The present study was attempted to prove that phytocompound 6-gingerol from *Zingiber officinale* acts as a promising drug to treat COVID-19. 6-Gingerol possesses excellent drug likeliness parameters with zero violations of different rules and very good ADME pharmacokinetic properties. Finally, 6-gingerol proves anti-viral efficiency against SARS CoV-2 by showing the highest binding affinity and interaction with multiple targets of COVID-19 including Viral proteases, RNA binding protein, Spike protein. DFT study finally evidences the reason behind the highest binding affinity between 6-gingerol and COVID-19 protein targets. The present study proves that 6-gingerol from the ginger plant could be served as a promising drug to treat the novel COVID-19.

Acknowledgments

This work is partially supported by the PG & Research Department of Biotechnology, Mahendra Arts and Science College (Autonomous), and the Department of Science and Technology, Government of India (DST-FIST sponsored - Ref. No. SR/FST/College-232/2014).

Compound	HOMO	LUMO	Energy Gap	Ionization potential(IE)(eV)	Electron affinity (EA(eV)	Electro negativity (χ)(eV)	Electro chemical potential (μ)(eV)	Hardness (η) (eV)	Softness (σ)(eV)
6-Gingerol	-0.21034	-0.00428	-0.20606	0.21034	0.00428	0.10731	-0.10731	0.10303	9.3187

Table.4. HOMO LUMO Orbital Energies for 6-Gingerol through DFT calculations

REFERENCES

[1] Worldometer is a provider of global COVID-19 statistics for a wide audience of caring people around the world. https://www.worldometers.info/ coronavirus/
[2] Govindarajan VS. 1982. Ginger—chemistry, technology & quality evaluation: parts I & II, Crit. Rev. Food Sci. Nutr. 17 (1-96): 189–258 (CRC).
[3] Hara MO, Kiefer D, Farrell K, Kemper K.1998. A review of 12 commonly used medicinal herbs, Arch. Family Med. 7:523–536.

[4] Chrubasik S, Pittler MH, Roufogalis BD. 2005. *Zingiberis rhizoma*: a comprehensive review on the ginger effect and efficacy profiles.Phytomedicine12:684–701.

[5] Denyer CV, Jackson P, Loakes DM, Ellis MR, Young DA. 1994. Isolation of anti -rhinoviral sesquiterpenes from ginger (*Zingiber officinale*). Journal of Natural Products 57:658–662.

[6] Koch C, Reichling J, Schneele J, Schnitzler P. 2008. Inhibitory effect of essential oils against herpes simplex virus type 2. Phytomedicine 15:71–78.

[7] Schnitzler P, Koch C, Reichling J. 2007. Susceptibility of drug-resistant clinical herpes simplex virus type1 strains to essential oils of ginger, thyme, hyssop, and sandalwood. Antimicrobial Agents and Chemotherapy. 51:1859–1862.

[8] Sookkongwaree K, Geitmann M, Roengsumran S, Petsom A, Danielson UH. 2006. Inhibition of viral proteases by Zingiberaceae extracts and flavones isolated from Kaempferia parviflora. Pharmazie. 61:717–721.

[9] Langner E, Greifenberg S, and Gruenwald J. 1998. "Ginger: history and use," Advances in Therapy. 15(1):25–44.

[10] Jung San Chang, Kuo Chih Wang, Chia Feng Yeh , Den En Shieh , Lien Chai Chiang. 2013. Fresh ginger (Zingiberofficinale) has anti-viral activity against human respiratory syncytial virus in human respiratory tract celllines, Journal of Ethnopharmacology 145: 146–151

[11] Kim S, Chen J, Cheng T et al. PubChem 2019 update: improved access to chemical data. *Nucleic Acids Res*. 2019;47(D1):D1102–D1109. doi:10.1093/nar/gky1033

[12] Weininger D. 1988. SMILES, a chemical language and information system. Introduction to methodology and encoding rules, J Chem. Inf. Comput. Sci., 28:31–36

[13] Berman HM, Westbrook J, Feng Z, Gilliland G, Bhat TN, Weissig H, Shindyalov IN, Bourne PE. 2000. The protein data bank, Nucl Acids Res, 28:235–242.

[14] Laurie AT, Jackson RM. 2005. Q-SiteFinder: an energy-based method for the prediction of protein-ligand binding sites, Bioinformatics, 21:1908–1916.

[15] Rarey M, Kramer B, Lengauer T, Klebe G. 1996 A fast flexible docking method using an incremental construction algorithm, J Mol Biol, 261: 470-89

[16] Stierand K, Maab P, Rarey M. 2006. Molecular Complexes at a Glance: Automated Generation of two-dimensional Complex Diagrams, Bioinformatics, 22: 1710-1716

[17] Zakaryan H, Arabyan E, Oo A, and Zandi K. 2017. "Flavonoids: promising natural compounds against viral infections," Arch. Virol., 162(9):2539–2551. doi: 10.1007/s00705-017-3417-y.

[18] Thayil, Seema M, and Thyagarajan SP. 2016. Pa-9: A flavonoid extracted from plectranthus amboinicus inhibits HIV-1 protease, Int. J. Pharmacogn. Phytochem. Res., 8 (6):1020–1024.

[19] Jo S, Kim S, Shin DH, and Kim MS. 2020. Inhibition of SARS-CoV 3CL protease by flavonoids, J. Enzyme Inhib. Med. Chem. 35(1):145–151. doi: 10.1080/14756366.2019.1690480.

[20] Siti Khaerunnisa, Hendra Kurniawan, Rizki Awaluddin, Suhartati Suhartati, Soetjipto Soetjipto. 2020. Potential Inhibitor of COVID-19 Main Protease (Mpro) from Several Medicinal Plant Compounds by Molecular Docking Study. Preprints. doi: 10.20944/preprints202003.0226.v1.

[21] Thirumalaisamy Rathinavel, Subramanian Ammashi, Selvankumar Thangaswamy and Gnanendra Shanmugam. 2019. Identification of Anti-Diabetic Phytocompounds from *Ficus racemosa* and its Validation through *In Silico* Molecular Modeling. Int. J. Adv. Sci. Eng. 5(4):1085-1098.

All © 2020 are reserved by International Journal of Advanced Science and Engineering. This Journal is licensed under a Creative Commons Attribution-Non Commercial-ShareAlike 3.0 Unported License.

ScienceDirect

Chemosphere
Volume 243, March 2020, 125389

Significance of allochthonous brackish water *Halomonas* sp. on biodegradation of low and high molecular weight polycyclic aromatic hydrocarbons

M. Govarthanan [a], Ashraf YZ. Khalifa [b, c], S. Kamala-Kannan [e], P. Srinivasan [d], T. Selvankumar [d], K. Selvam [d], Woong Kim [a]

Show more

Outline | Share | Cite

https://doi.org/10.1016/j.chemosphere.2019.125389

Get rights and content

Referred to by M. Govarthanan, Ashraf YZ. Khalifa, S. Kamala Kannan, P. Srinivasan, T. Selvankumar, K. Selvam, Woong Kim
Corrigendum to "Significance of allochthonous brackish water *Halomonas* sp. on biodegradation of low and hi...
Chemosphere, Volume 274, July 2021, Pages 130509

Download PDF

Highlights

- PAHs degrading *Halomonas* sp. isolated from brackish water.
- *Halomonas* sp. RM was found capable of biodegradation of low and high molecular weight PAHs.
- Various process optimizing factors on biodegradation of PAHS were discussed.
- Low and high molecular weight PAHs biodegradation was enhanced by addition of sucrose at pH 7.0 with 4% salinity.

PRINCIPAL
PGP College of Arts and Science
Namakkal

Abstract

The present study is aimed to isolate and identify polycyclic aromatic hydrocarbons (PAHs) degrading bacteria from brackish water and to assess the biodegradation efficiency against low and high molecular

Chemosphere 243 (2020) 125389

Contents lists available at ScienceDirect

Chemosphere

journal homepage: www.elsevier.com/locate/chemosphere

Significance of allochthonous brackish water *Halomonas* sp. on biodegradation of low and high molecular weight polycyclic aromatic hydrocarbons

M. Govarthanan [a, *], Ashraf YZ. Khalifa [b, c], S. Kamala-Kannan [e], P. Srinivasan [d], T. Selvankumar [d], K. Selvam [d], Woong Kim [a, **]

[a] Department of Environmental Engineering, Kyungpook National University, Daegu, 41566, Republic of Korea
[b] Biological Sciences Department, College of Science, King Faisal University, Saudi Arabia
[c] Botany and Microbiology Department, Faculty of Science, University of Beni-Suef, Beni-Suef, Egypt
[d] PG& Research Department of Biotechnology, Mahendra Arts and Science College (Autonomous), Kalippatti, Namakkal, 637501, Tamil Nadu, India
[e] Division of Biotechnology, College of Environmental and Bioresource Sciences, Chonbuk National University, Iksan, 54596, Republic of Korea

HIGHLIGHTS

- PAHs degrading *Halomonas* sp. isolated from brackish water.
- *Halomonas* sp. RM was found capable of biodegradation of low and high molecular weight PAHs.
- Various process optimizing factors on biodegradation of PAHS were discussed.
- Low and high molecular weight PAHs biodegradation was enhanced by addition of sucrose at pH 7.0 with 4% salinity.

ARTICLE INFO

Article history:
Received 22 October 2019
Received in revised form
11 November 2019
Accepted 14 November 2019
Available online 18 November 2019

Handling Editor: T Cutright

Keywords:
Biodegradation
Halomonas sp.
Phenanthrene
Phyrene
Salinity

ABSTRACT

The present study is aimed to isolate and identify polycyclic aromatic hydrocarbons (PAHs) degrading bacteria from brackish water and to assess the biodegradation efficiency against low and high molecular weight PAHs. Among 15 isolates, the isolate designated as RM effectively degraded 100 mg/L of phenanthrene (Phe) (67.0%), pyrene (Pyr) (63.0%), naphthalene (NaP) (60.0%), and benzo [a]pyrene (BaP) (58.0%) after 7 days of incubation. Carbon sources, pH, and salinity of the culture medium were optimized to enhance the growth and PAHs biodegradation of the isolate RM. Sucrose was found to be an excellent carbon source to enhance PAHs biodegradation (Phe, 75.0; Pyr, 68.5; NaP, 62.5; and BaP, 59.5%). Furthermore, the isolate showed enhanced degradation at pH 7.0 and 4% salinity. The isolate RM was identified as *Halomonas* sp. based on partial 16S rDNA gene sequence analysis. The results indicated that the isolate RM (i.e., *Halomonas* sp.) has the potential to be used in remediation of oil spills in the marine ecosystem.

© 2019 Elsevier Ltd. All rights reserved.

1. Introduction

Polycyclic aromatic hydrocarbons (PAHs) are a group of organic compounds with two or more benzene-rings arranged in a linear, angular, or a cluster structure (Li et al., 2014; Chen et al., 2015). PAHs are one of the most common pollutants in the soil and/or water environment and have become a matter of urgency due to their negative impacts on human health (Zeng et al., 2010; Kuppusamy et al., 2016; Zhao et al., 2017). PAHs mostly originate from anthropogenic activities including accidental spilling of hydrocarbons and incomplete combustion of fossil fuels (Chen et al., 2015). Low solubility, elevated stability, and hydrophobic nature of PAHs cause dysfunction in soil biodiversity by altering microbial population, soil fertility, and impairing water quality (Nwoko, 2014). Significant accumulation of PAHs in the soil and their subsequential migration into the aquatic system have led to chronic

* Corresponding author.
** Corresponding author.
E-mail addresses: gova.muthu@gmail.com (M. Govarthanan), elshine@knu.ac.kr (W. Kim).

https://doi.org/10.1016/j.chemosphere.2019.125389
0045-6535/© 2019 Elsevier Ltd. All rights reserved.

exposure, which is associated with cancerous diseases in humans and aquatic animals and enhanced mutagenicity of soil and/or sediments (Qi et al., 2017). Negative clinical effects of PAHs, ubiquitous migration into the soil and/or water stream, and elimination of these contaminants are of great research interest (Dong et al., 2016; Schneider et al., 2016; Alrumman et al., 2016).

Several studies have reported the use of physico-chemical methods (e.g., volatilization, photo-oxidation, and chemical oxidation) for the removal of PAHs in soil (Zhao et al., 2008). However, these physico-chemical practices are environmentally aggressive, cost-intensive, and disruptive towards soil quality and fertility (Khan et al., 2000; Gan et al., 2009). Thus, it is necessary to eliminate PAHs from the environment without adverse impacts. Biological treatment, especially bioremediation using microorganisms, is a cost-effective, efficient, and eco-friendly method for PAHs removal from contaminated soil and/or water (Kuppusamy et al., 2016). Several attempts have been made for PAHs biodegradation using microorganisms belonging to the genus *Pseudomonas* (El-Naas et al., 2009), *Rhodococcus* (Martinkova et al., 2009), *Sphingomonas* (Miguel et al., 2009), *Stenotrophomonas* (Juhasz et al., 2000), and *Mycobacterium* (Kim et al., 2005). However, compared with neutrophilic microorganisms, halophilic microorganisms have received greater attention from environmental researchers, because they secrete metabolites that can work in extreme environmental conditions (Ali et al., 2013, 2016).

Halophilic bacteria are frequently being isolated from hypersaline habitats and can grow in vitro at a high salt concentration (Ali et al., 2016). Among halophilic bacteria, *Halomonas* sp. has been shown to grow under different environmental conditions, and is multi-metal resistant (Govarthanan et al., 2017). Further, *Halomonas* sp. can utilize a wide range of readily available substrates as energy sources for its rapid growth (Ali et al., 2016). To date, most studies have reported on PAHs-degrading bacteria isolated from PAHs-contaminated soil. However, little is known about bacteria isolated from the brackish water environment, a buffering zone of sea and inland water. The environmental characteristics of brackish water force microorganisms to thrive under high salt conditions with their diverse biological functions and productivity (Kamala-Kannan and Krishnamoorthy, 2006). Thus, the objectives of this study were as follows: (i) isolation, identification, and screening of PAHs degrading bacteria from brackish water, and (ii) assessing the influence of different carbon sources, NaCl, and pH on PAHs biodegradation.

2. Materials and methods

2.1. Chemicals

Phenanthrene (Phe), pyrene (Pyr), naphthalene (NaP), and benzo [a]pyrene (BaP) were purchased from Sigma-Aldrich (St. Louis, MO, USA). All other chemicals used were of reagent grade with high purity.

2.2. Isolation of PAHs degrading bacteria

Brackish water sample (~1–2 m depth) was collected from Pichavaram mangrove (11°23′–11°30′ and 79°45′–79°50′), Tamil Nadu, India, using sterile polyethylene bottles and transported on ice to the laboratory. The collected water sample was processed within 10 h. Enrichment cultures were prepared by adding 10 mL of water sample into a 250 mL Erlenmeyer flask containing 100 mL of minimal medium (MM) composed of (per liter) 0.4 g K_2HPO_4, 0.2 mg $MgSO_4 \cdot 2H_2O$, 20 mg $CaCl_2 \cdot 2H_2O$, 10 mg $FeSO_4 \cdot 7H_2O$, 0.6 g Na_2HPO_4, 20 mg $MnSO_4 \cdot H_2O$, and 1 g NH_4NO_3 supplemented individually with 100 mg/L of Phe, Pyr, NaP, and BaP. The flasks were incubated in a shaking incubator (250 rpm) at 27 ± 2 °C for 7 days. The subsequent enrichment cultures were serially diluted and plated on M9 agar medium with the corresponding PAHs as vapor phase (Megharaj et al., 1997). After incubation, bacterial growth was observed on the agar surface of each plate. Well grown bacterial colonies were purified and stored at 4 °C for further degradation assays. Based on the screening isolate RM was selected for further identification and degradation study.

2.3. Identification of PAHs degrading bacteria

Bacterial DNA was extracted using the QIAGEN (Valencia, CA, USA) DNA isolation kit, and its concentration was determined using a Nanodrop spectrophotometer (NanoDrop 2000; Shimadzu, Japan). Bacterial universal primer-27f (5′-AGAGTTTGATCCTGGCTCAG-3′) and −1492r (5′-CCCCGTCAATTCATTTGAGTTT-3′) were used to amplify the 16S rRNA gene sequences at 94 °C (5 min) followed by 35 cycles at 94 °C (1 min), 49 °C (2 min), and 72 °C (2 min) with a final extension temperature of 72 °C for 7 min. The amplified polymerase chain reaction (PCR) product was purified using the QIAGEN PCR (Valencia, CA, USA) purification kit and sequenced using an automated ABI PRISM 3700 sequencer (Foster City, CA, USA). The obtained 16S rRNA sequence was compared to available sequences in the database using the NCBI BLAST program (http://www.ncbi.nlm.nih.gov/BLAST). A phylogenetic tree was constructed using the neighbour-joining distance method with Mega software version 6.0.

2.4. Effect of PAHs on isolate growth

Effect of Phe, Pyr, NaP, and BaP on RM growth was performed in batch experiments. Briefly, the isolate RM was grown in LB medium for 3 days were harvested, washed, and resuspended in MM medium (A_{600}, 0.6). The resuspension was (10 mL) inoculated into 250 mL Erlenmeyer flasks containing 100 mL of MM and incubated in a shaking incubator (200 rpm) for 24 h at 27 ± 2 °C. Further, 100 mg/L of Phe, Pyr, NaP and BaP were added individually into the culture flasks at the late exponential phase, and incubated in dark conditions in 200 rpm (1–7 days) at 27 ± 2 °C. Bacterial growth was determined by measuring the optical density (600 nm) (UV-1800, Shimadzu, Kyoto, Japan) at predetermined time intervals (1–7 days). All the experiments were performed in triplicates and mean values were reported. Growth of the isolate without PAHs was used as a control for this experiment.

2.5. Effect of different carbon sources on PAHs biodegradation

Five different carbon sources, including glucose, galactose, fructose, maltose, and sucrose were added individually into MM medium at a concentration of 1.5%. The isolate grown in LB medium for 3 days were harvested, washed, and resuspended in MM medium (A_{600}, 0.6) and the resuspension was used as an inoculum (10 mL) for this experiment. The inoculated flasks were incubated in a shaking incubator (200 rpm) for 7 days at 27 ± 2 °C. Samples were withdrawn at pre-determined time intervals and PAHs degradation efficiency of the culture was determined using gas chromatography - mass spectrometry (GC-MS, Shimadzu, Kyoto, Japan). Briefly, an equal volume of hexane was mixed with the sample and centrifuged at 10,000 rpm for 10 min. The organic layer of the sample was carefully separated and used for GC-MS analysis according to Govarthanan et al. (2017).

2.6. Effect of pH on PAHs biodegradation

Batch experiments were performed to study the effect of pH on PAHs biodegradation. Briefly, 100 mg/L Phe, Pyr, NaP, and BaP were mixed with 100 mL of MM containing 3% inoculums. The pH of the culture medium was adjusted to 5–10. The flasks were incubated in a shaking incubator (200 rpm) at 27 ± 2 °C for 7 days. Samples were withdrawn at predetermined time intervals and PAHs concentrations in the samples were determined using GC-MS.

2.7. Effect of NaCl on PAHs biodegradation

The effect of NaCl on biodegradation of PAHs was performed in batch experiments. Briefly, NaCl (1–10%) was added individually to MM bottles containing Phe, Pyr, Nap, and Bap, and the bottles were incubated in a shaking incubator (200 rpm) at 27 ± 2 °C for 7 days. Samples were withdrawn at fixed time intervals and PAHs concentrations in the samples were analyzed using GC-MS.

2.8. Statistical analysis

All the results presented in this study were mean values of three replicates of experiments, and standard deviations were used to analyse the data. Statistical analysis was performed using Microsoft El-Naas et al., 2009.

3. Results and discussion

3.1. Isolation and identification of PAHs-degrading bacteria

Fifteen morphologically different bacterial isolates were obtained from the brackish water sample of Pichavaram mangrove. Based on the PAHs-degrading index five bacterial isolates designated as RM, RM1, RM2, RM3, and RM4 were chosen for further studies. Among the five isolates, the isolate RM degraded multiple PAHs. Thus, the biodegradation efficiency of the isolate RM was further investigated. Morphological and biochemical characteristics of the isolate RM is represented in Table 1. PCR amplification of 16S rDNA resulted in a predicted 1.4 kb amplicon, and the sequences exhibited 98% identity with *Halomonas* sp. X29 (KM974782). The partial 16S rDNA of the isolate RM was deposited in GenBank (Accession Number: MH330005). A phylogenetic tree was derived using the partial 16S rDNA sequences of the isolate *Halomonas* sp. RM with existing sequences in NCBI and the result of this study are shown in Fig. 1, indicating that the isolate RM and *Halomonas* sp. were in the same cluster. Furthermore, several studies have reported PAHs-degrading bacteria from PAHs-contaminated sites (Potin et al., 2004; Zhao et al., 2009; Kuppusamy et al., 2016), which belonged to the genus *Paenibacillus, Pseudomonas, Mycobacterium* (Zeng et al., 2010), *Cupriavidus* (Kuppusamy et al., 2016), *Haemophilus,* and *Rhodococcus* (Haritash and Kaushik, 2009). However, to the best of our knowledge, *Halomonas* sp. isolated from brackish water that is able to degrade low and high molecular weight PAHs has yet to be reported.

Table 1
Morphology and Biochemical characteristics of the isolate *Halomonas* sp. RM

Test	Result
Morphology	
Gram staining	-
Shape	rod
Motility	+
Catalase	+
Oxidase	+
Aerobic	+
Anaerobic	+
PAHs degradation efficiency	
Phenanthrene (Phe)	+
Pyrene (Pyr)	+
Naphthalene (NaP)	+
Benzo [a]pyrene (BaP)	+

+ = Positive, − = Negative.

3.2. Increased growth of Halomonas sp. RM on different PAHs

The growth of *Halomonas* sp. RM in the presence of different PAHs at an initial concentration of 100 mg/L was determined, as measured at an optical density at 600 nm and the results are shown in Fig. 2a. The time-course *Halomonas* sp. RM growth indicated that the isolate was capable of utilizing both low (Phe, Pyr, and NaP) and high (BaP) molecular weight PAHs for growth. It has been reported that successful biodegradation of PAHs depends on the survival of microorganisms in the presence of PAHs. Therefore, cell density was measured in the presence of Phe, Pyr, NaP, and BaP to observe *Halomonas* growth after inoculation, which showed significantly increasing OD values over time. This may be due to successful adaptation of the isolate in the PAHs environment, which was evident from the increase in PAHs degradation.

Concurrently, the biodegradation efficiency of the isolate was analyzed for each PAH and presented in Fig. 2b. The result showed enhanced biodegradation of each target PAHs with increased growth of *Halomonas* sp. RM after 7-day incubation. The order of PAHs biodegradation was Phe (67%) > Pyr (63%) > NaP (60%) > BaP (58%). By contrast, the biodegradation rate of most bacteria reported in the literature was found to be below 50%, even after 10-day incubation (Machín-Ramírez et al., 2010; Song et al., 2011; Thavamani et al., 2012). It has been established that biodegradation of complex PAHs occurs in a stepwise process to reduce the number

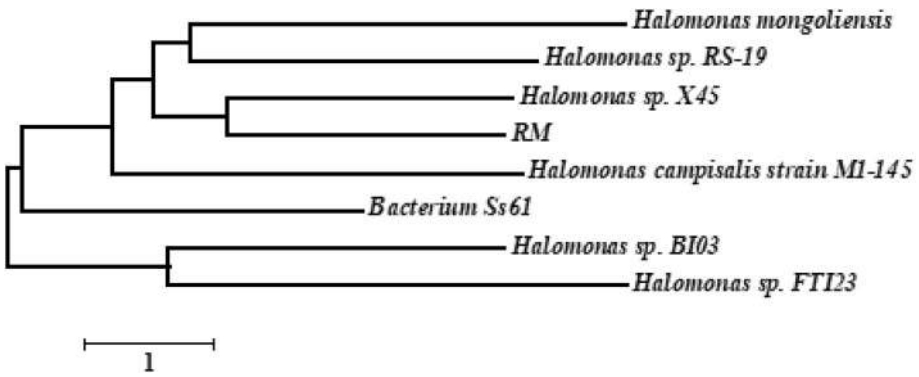


Fig. 1. Phylogenetic tree of *Halomonas* sp. is constructed based on 16S rDNA sequences using neighbour-joining method.

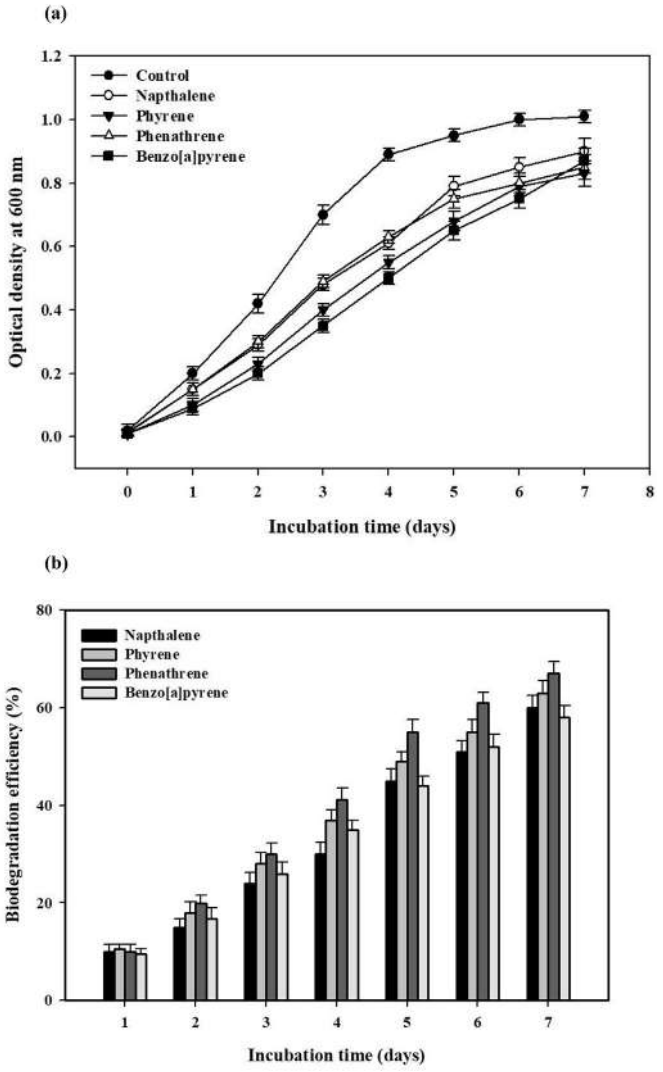


Fig. 2. (a). Growth (optical density at 66 nm), and (b) PAHs degradation potential of *Halomonas* sp. RM exposed to 100 mg/L of PAHs.

of aromatic rings (Nzila, 2018). The isolate *Halomonas* sp. RM showed ~58% biodegradation efficiency for a high molecular weight PAH (i.e., BaP). Further, this isolate could also effectively degrade (>60%) low molecular weight PAHs (i.e., Phe, Pyr, and NaP).

3.3. Sucrose as a carbon source enhances PAHs degradation

In general, the microorganisms require favorable growth conditions (e.g., carbon sources, nutrients, temperature, pH, salinity) which strongly influences their growth. Carbon source fed to the growth medium is considered to be as a key factor for the growth curve and metabolism of PAHs degrading bacteria. Thus, carbon sources were supplied to enhance the bacterial activity in a series of batch experiments to identify the effect of different carbon sources (i.e., glucose, galactose, fructose, maltose, and sucrose) on PAHs biodegradation by *Halomonas* sp. RM (Fig. 3). Higher degradation efficiency of PAHs (Phe, 75.0; Pyr, 68.5; NaP, 62.5; and BaP, 59.5%) was observed in flasks containing sucrose as a carbon source. However, minimum degradation of PAHs (Phe, 52.0; Pyr, 48.7; NaP, 46.8; and BaP, 42.5%) was observed in fructose amended flasks. Therefore, isolate *Halomonas* sp. RM utilized sucrose to enhance degradation of Phe, Pyr, NaP and BaP.

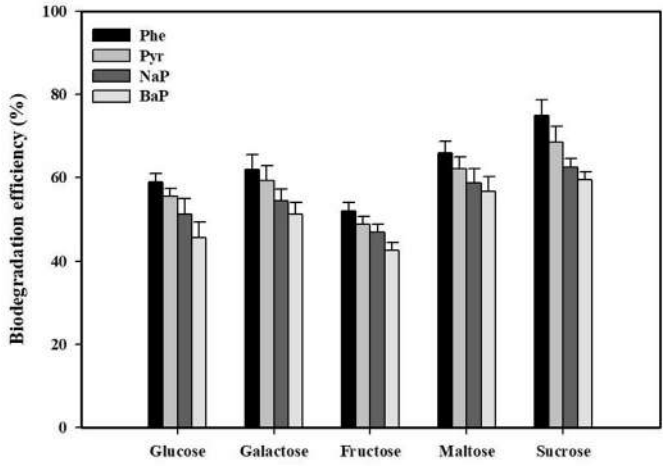


Fig. 3. Effect of carbon sources on PAHs biodegradation.

3.4. pH affects PAHs biodegradation efficiently

pH of a medium can affect the bacterial activity possibly through altering the enzymatic activity and nutrient solubility, which eventually leads to effective biodegradation (lin et al., 2010). Thus, pH is one of the most important factors for PAHs biodegradation in the culture medium. The isolate *Halomonas* sp. RM effectively degraded PAHs at pH ranging from 5 to 10 (Fig. 4). Maximum biodegradation was observed at pH 7.0 (Phe, 72.0; Pyr, 67.5; NaP, 64.5; and BaP, 59.5%). However, even at pH 5.0 (Phe, 58.0; Pyr, 55; NaP, 51; and BaP, 45%) and pH 6.0 (Phe, 60.0; Pyr, 57.0; NaP, 47.0; and BaP, 40.5%), moderate degradation of PAHs was observed. The results are consistent with previous studies that reported bacterial PAHs biodegradation at neutral pH (Thavamani et al., 2012; Kuppusamy et al., 2016).

3.5. Salinity impacts PAHs biodegradation

The effect of salinity on biodegradation of Phe, Pyr, NaP and BaP was tested at 1–10% NaCl, and the result is presented in Fig. 5. Maximum degradation of PAHs was observed at 4% NaCl (Phe, 74.5; Pyr, 70.2; NaP, 67.2; and BaP, 62.2%). However, moderate

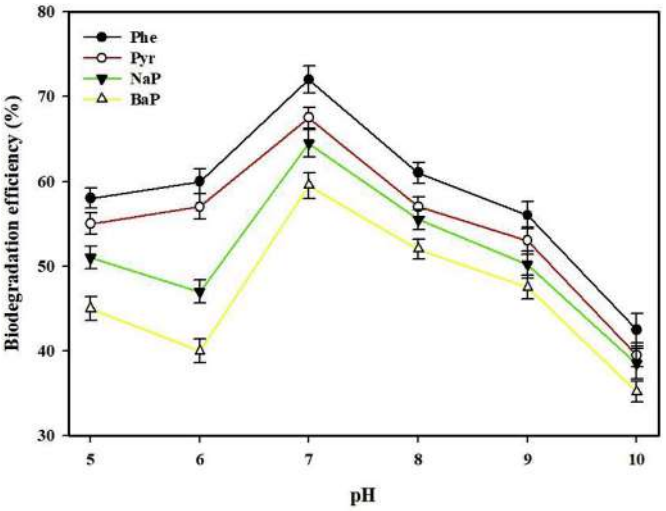


Fig. 4. Effect of pH on PAHs biodegradation.

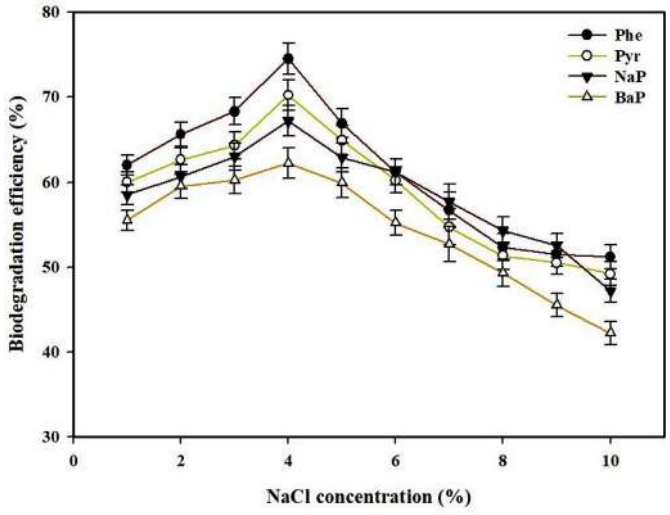


Fig. 5. Effect of salinity on PAHs biodegradation.

degradation rates were observed at 1, 2, 3, 5 and 6% NaCl (Fig. 5). The degradation rate declined as the NaCl concentration increased from 7 to 10%. Feng et al. (2012) reported that *Martelella* sp. AD-3 degraded 100% of phenanthrene (200 mg/L) at 3% salinity. However, our isolate showed its maximum degradation efficiency at 4% NaCl. Thus, this study indicates that the growth of *Halomonas* sp. RM required a minimal salt concentration for their growth (4%) to enhance removal of PAHs.

4. Conclusion

In this study, the *Halomonas* sp. RM was isolated from brackish water demonstrated biodegradation of Phe, Pyr, NaP and BaP within a wide range of pH, carbon sources and salinity. Isolate RM showed ~58% biodegradation efficiency for the high molecular weight PAH (i.e., BaP) and also effectively degrade (>60%) low molecular weight PAHs, i.e., Phe, Pyr and NaP. Further, optimization of the carbon sources, pH, and salinity of the culture conditions enhanced the degradation process. As a result, maximum degradation was found with sucrose as the carbon source and at pH 7.0 and 4% salinity. Therefore, the *Halomonas* sp. RM could be used for bioremediation of water and/or soil systems contaminated with multiple PAHs.

Declaration of competing interest

The authors declare that they don't have any conflict of interest.

Acknowledgements

This work was supported by a National Research Foundation of Korea (NRF) grant funded from the Korean government (MSIP, South Korea) (No. 2017R1A4A1015628; No. 2018R1D1A1B07050040), and partly supported by the Korea Institute of Energy Technology Evaluation and Planning (KETEP) grant funded by the Korea government (MOTIE) (No. 20194110100100, Full-scale feasibility study of the stability and efficiency improvement of a biogas production facility based on biomass from urban/living environments). The author Ashraf Y Z Khalifa acknowledges the Deanship of Scientific Research at King Faisal University, Saudi Arabia sponsor id: 501100004686, for the financial support under Nasher track (Grant No. 186140).

Appendix A. Supplementary data

Supplementary data to this article can be found online at https://doi.org/10.1016/j.chemosphere.2019.125389.

Author contributions

All authors conceived the Study, MG, designed and performed the experiment, collected data, analyzed data and wrote the draft manuscript. AYZ Khalifa contributed data analysis and revisions. SKK contributed experiment design, data analysis and revision. PS, TS and KS contributed isolation of the microorganisms from the brackish water. W. Kim contributed experiment design, data analysis, and revision. All authors commented on the manuscript.

References

Ali, I., Kanhayuwa, L., Rachdawong, S., Rakshit, S.K., 2013. Identification, phylogenetic analysis and characterization of obligate halophilic fungi isolated from a man-made solar saltern in Phetchaburi province, Thailand. Ann. Microbiol. 63, 887–895.

Ali, I., Prasongsuk, S., Akbar, A., Aslam, M., Lotrakul, P., Punnapayak, H., Rakshit, S.K., 2016. Hypersaline habitats and halophilic microorganisms. Maejo Int. J. Sci. Technol. 10, 330–345.

Alrumman, S.A., Hesham, A.L., Alamri, S.A., 2016. Isolation, fingerprinting and genetic identification of indigenous PAHs degrading bacteria from oil-polluted soils. J. Environ. Biol. 37, 75–81.

Chen, M., Xu, P., Zeng, G., Yang, C., Huang, D., Zhang, J., 2015. Bioremediation of soils contaminated with polycyclic aromatic hydrocarbons, petroleum, pesticides, chlorophenols and heavy metals by composting: applications, microbes and future research needs. Biotechnol. Adv. 33, 745–755.

Dong, D.M., Liu, X.X., Hua, X.Y., Guo, Z.Y., Li, L.F., Zhang, L.W., Xie, Y.J., 2016. Sedimentary record of polycyclic aromatic hydrocarbons in Songhua River, China. Environ. Earth Sci 75, 508–515.

El-Naas, M.H., Al-Muhtaseb, S.A., Makhlouf, S., 2009. Biodegradation of phenol by *Pseudomonas putida* immobilized in polyvinyl alcohol (PVA) gel. J. Hazard Mater. 164, 720–725.

Feng, T.C., Cui, C.Z., Dong, F., Feng, Y.Y., Liu, Y.D., Yang, X.M., 2012. Phenanthrene biodegradation by halophilic *Martelella* sp. AD-3. J. Appl. Microbiol. 113, 779–789.

Gan, S., Lau, E.V., Ng, H.K., 2009. Remediation of soils contaminated with polycyclic aromatic hydrocarbons (PAHs). J. Hazard Mater. 172, 532–549.

Govarthanan, M., Fuzisawa, S., Hosogai, T., Chang, Y.C., 2017. Biodegradation of aliphatic and aromatic hydrocarbons using the filamentous fungus *Penicillium* sp. CHY-2 and characterization of its manganese peroxidase activity. RSC Adv. 7, 20716.

Haritash, A., Kaushik, C., 2009. Biodegradation aspects of polycyclic aromatic hydrocarbons (PAHs): a review. J. Hazard Mater. 169, 1–15.

Juhasz, A.L., Stanley, G.A., Britz, M.L., 2000. Microbial degradation and detoxification of high molecular weight polycyclic aromatic hydrocarbons by *Stenotrophomonas maltophilia* strain VUN 10,003. Lett. Appl. Microbiol. 30, 396–401.

Kamala-Kannan, S., Krishnamoorthy, R., 2006. Isolation of mercury resistant bacteria and influence of abiotic factors on bioavailability of mercury—a case study in Pulicat Lake north of Chennai, south east India. Sci. Total Environ. 367, 341–353.

Khan, A.G., Kuek, C., Chaudhry, T.M., Khoo, C.S., Hayes, W.J., 2000. Role of plants, mycorrhizae and phytochelators in heavy metal contaminated land remediation. Chemosphere 41, 197–207.

Kim, Y.H., Freeman, J.P., Moody, J.D., Engesser, K.H., Cerniglia, C.E., 2005. Effects of pH on the degradation of phenanthrene and pyrene by *Mycobacterium vanbaalenii* PYR-1. Appl. Microbiol. Biotechnol. 67, 275–285.

Kuppusamy, S., Thavamani, P., Megharaj, M., Lee, Y.B., Naidu, R., 2016. Polyaromatic hydrocarbon (PAH) degradation potential of a new acid tolerant, diazotrophic P-solubilizing and heavy metal resistant bacterium *Cupriavidus* sp. MTS-7 isolated from long-term mixed contaminated soil. Chemosphere 162, 31–39.

Li, H., Qu, R., Li, C., Guo, W., Han, X., He, F., Ma, Y., Xing, B., 2014. Selective removal of Polycyclic aromatic hydrocarbons (PAHs) from soil washing effluents using biochars produced at different pyrolytic temperatures. Bioresour. Technol. 163, 193–198.

Machín-Ramírez, C., Morales, D., Martínez-Morales, F., Okoh, A.I., Trejo-Hernández, M.R., 2010. Benzo[a]pyrene removal by axenic- and co-cultures of some bacterial and fungal strains. Int. Biodeterior. Biodegrad. 64, 538–544.

Martinkova, L., Uhnakova, B., Patek, M., Nešvera, J., Křen, V., 2009. Biodegradation potential of the genus *Rhodococcus*. Environ. Int. 35, 162–177.

Megharaj, M., Wittich, R., Blasco, R., Pieper, D., Timmis, K., 1997. Superior survival and degradation of dibenzo-p-dioxin and dibenzofuran in soil by soil-adapted *Sphingomonas* sp. strain RW1. Appl. Microbiol. Biotechnol. 48, 109–114.

Miguel, V.S., Peinado, C., Catalina, F., Abrusci, C., 2009. Bioremediation of naphthalene in water by *Sphingomonas paucimobilis* using new biodegradable surfactants based on poly (-caprolactone). Int. Biodeterior. Biodegrad. 63, 217–223.

Nwoko, C.O., 2014. Effect of *Arbuscular Mycorrhizal* (AM) fungi on the physiological performance of *Phaseolus vulgaris* grown under crude oil contaminated soil. J. Geosci. Environ. Prot. 2, 9–14.

Nzila, A., 2018. Biodegradation of high-molecular-weight polycyclic aromatic hydrocarbons under anaerobic conditions: overview of studies, proposed pathways and future perspectives. Environ.Pollu. 239, 788–802.

Potin, O., Veignie, E., Rafin, C., 2004. Biodegradation of polycyclic aromatic hydrocarbons (PAHs) by *Cladosporium sphaerospermum* isolated from an aged PAH contaminated soil. FEMS Microbiol. Ecol. 51, 71–78.

Qi, Y.B., Wang, C.H., Yuan, C., Lun, Z.M., Zheng, C.G., 2017. Removal capacities of polycyclic aromatic hydrocarbons (PAHs) by a newly isolated strain from oil field produced water. Int. J. Environ. Res. Public Health 14, 215.

Schneider, I.L., Teixeira, E.C., Agudelo-Castañeda, D.M., Silva, G., Balzaretti, N., Braga, M.F., Oliveira, L.F., 2016. FTIR analysis and evaluation of carcinogenic and mutagenic risks of nitro-polycyclic aromatic hydrocarbons in PM1.0. Sci. Total Environ. 541, 1151–1160.

Song, X., Xu, Y., Li, G., Zhang, Y., Huang, T., Hu, Z., 2011. Isolation, characterization of Rhodococcus sp. P14 capable of degrading high-molecular-weight polycyclic aromatic hydrocarbons and aliphatic hydrocarbons. Mar. Pollut. Bull. 62, 2122–2128.

Thavamani, P., Megharaj, M., Naidu, R., 2012. Bioremediation of high molecular weight polyaromatic hydrocarbons co-contaminated with metals in liquid and soil slurries by metal tolerant PAHs degrading bacterial consortium. Biodegradation 23, 823–835.

Zeng, J., Lin, X., Zhang, J., Li, X., 2010. Isolation of polycyclic aromatic hydrocarbons (PAHs)-degrading *Mycobacteriums* pp. and the degradation in soil. J. Hazard Mater. 183, 718–723.

Zhao, H.P., Wang, L., Ren, J.R., Li, Z., Li, M., Gao, H.W., 2008. Isolation and characterization of phenanthrene-degrading strains *Sphingomonas* sp. ZP1 and *Tistrella* sp. ZP5. J. Hazard Mater. 152, 1293–1300.

Zhao, H.P., Wu, Q.S., Wang, L., Zhao, X.T., Gao, H.W., 2009. Degradation of phenanthrene by bacterial strain isolated from soil in oil refinery fields in Shanghai China. J. Hazard Mater. 164, 863–869.

Zhao, O., Zhang, X., Dong Feng, S., Zhang, L.X., Shi, W., Yang, Z., Miao Chen, M., Dan Fang, X., 2017. Starch-enhanced degradation of HMW PAHs by *Fusarium* sp. in an aged polluted soil from a coal mining area. Chemosphere 174, 774–780.

ScienceDirect

Chemosphere
Volume 243, March 2020, 125327

Effect of citric acid and vermi-wash on growth and metal accumulation of *Sorghum bicolor* cultivated in lead and nickel contaminated soil

R. Rathika [a], Ashraf.Y.Z. Khalifa [b, c], P. Srinivasan [a], L. Praburaman [d], S. Kamala-Kannan [e], T. Selvankumar [a] ✉, Woong Kim [f] ✉, M. Govarthanan [f] ✉

Show more

Outline | Share | Cite

https://doi.org/10.1016/j.chemosphere.2019.125327

Get rights and content

Referred to by M. Govarthanan, Ashraf YZ. Khalifa, S. Kamala Kannan, P. Srinivasan, T. Selvankumar, K. Selvam, Woong Kim
Corrigendum to "Significance of allochthonous brackish water *Halomonas* sp. on biodegradation of low and hi...
Chemosphere, Volume 274, July 2021, Pages 130509

Download PDF

Highlights

- The biomass of the *S. bicolor* has been enhanced by the addition of VW (24, and 26%) and CA (11, and 9%) in Pb and Ni contaminated soil respectively.
- The shoot anatomic structure showed an accumulation of Pb and Ni were positively impacted by the amendment of VW and CA.
- VW showed enhanced antioxidant enzymes activity (140, 125 and 152 u/mg of CAT, SOD and POD).
- Pb contaminated soil treated with VW showed enhanced Rubisco activity of 1.49 U/ml, whereas, CA treatment showed 1.23 u/ml of Rubisco.

Abstract

P.G.P. COLLEGE OF ARTS & SCIENCE NAMAKKAL 637 206

PRINCIPAL
PGP College of Arts and Science
Namakkal

Chemosphere 243 (2020) 125327

Contents lists available at ScienceDirect

Chemosphere

journal homepage: www.elsevier.com/locate/chemosphere

Effect of citric acid and vermi-wash on growth and metal accumulation of *Sorghum bicolor* cultivated in lead and nickel contaminated soil

R. Rathika [a], Ashraf.Y.Z. Khalifa [b, c], P. Srinivasan [a], L. Praburaman [d], S. Kamala-Kannan [e], T. Selvankumar [a, **], Woong Kim [f, ***], M. Govarthanan [f, *]

[a] PG & Research Department of Biotechnology, Mahendra Arts and Science College (Autonomous), Kalippatti, Namakkal, 637501, Tamil Nadu, India
[b] Biological Sciences Department, College of Science, King Faisal University, Saudi Arabia
[c] Botany and Microbiology Department, Faculty of Science, University of Beni-Suef, Beni-Suef, Egypt
[d] School of Mineral Processing and Bio Engineering, Central South University, 932 South Lushan, Hunan, 410083, PR China
[e] Division of Biotechnology, College of Environmental and Bioresource Sciences, Chonbuk National University, Iksan, 54596, South Korea
[f] Department of Environmental Engineering, Kyungpook National University, Daegu, 41566, Republic of Korea

HIGHLIGHTS

- The biomass of the *S. bicolor* has been enhanced by the addition of VW (24, and 26%) and CA (11, and 9%) in Pb and Ni contaminated soil respectively.
- The shoot anatomic structure showed an accumulation of Pb and Ni were positively impacted by the amendment of VW and CA.
- VW showed enhanced antioxidant enzymes activity (140, 125 and 152 u/mg of CAT, SOD and POD).
- Pb contaminated soil treated with VW showed enhanced Rubisco activity of 1.49 U/ml, whereas, CA treatment showed 1.23 u/ml of Rubisco.

ARTICLE INFO

Article history:
Received 17 September 2019
Received in revised form
31 October 2019
Accepted 5 November 2019
Available online 8 November 2019

Handling Editor: T Cutright

Keywords:
Antioxidant
Citric acid
Rubisco
Sorghum bicolor
Vermi-wash

ABSTRACT

The aim of the present study is to assess the influence of vermi-wash (VW) and citric acid (CA) on *Sorghum bicolor* growth and phytoaccumulation of lead (Pb) and nickel (Ni) contaminated soil. The biomass of the *S. bicolor* has been enhanced by the addition of VW (24 and 26%) and CA (11 and 9%) in Pb and Ni contaminated soil, respectively. The VW treatment showed enhanced shoot and root lengths and chlorophyll concentrations compared to CA. The shoot anatomic structure showed an accumulation of Pb and Ni were positively impacted by the amendment of VW and CA. In addition, VW treatment showed enhanced antioxidant enzymes activity (140, 125 and 152 U/mg of CAT, SOD and POD). Further, the plants grown in Pb contaminated soil treated with VW showed enhanced Rubisco activity of 1.49 U/ml, whereas, CA treatment showed 1.23 U/ml of Rubisco. It has been observed that the VW showed as a potential chelator as well as plant beneficial formulation for the enhanced phyto-remediation of Pb and Ni.

© 2019 Elsevier Ltd. All rights reserved.

1. Introduction

Soil and/or water contamination has been a serious problem worldwide, due to population explosion, rapid industrialization and lack of funds for pollution control and renewal of the environment (Patil et al., 2016; Yılmaz, 2016). Heavy metals, the most hazardous environmental contaminants, are natural elements that could be supplied to soils by atmospheric deposition, agricultural practices such as the application of fertilizer, pesticide and municipal wastes such as composts, and sewage sludge (Abou Elwafa et al., 2019). For instance, lead (Pb), and nickel (Ni) cause morphological, physiological or biochemical harmful effects on living organisms (Signa et al., 2017). In plants, they decrease seedling development, root elongation, transpiration, chlorophyll

* Corresponding author.
** Corresponding author.
*** Corresponding author.;
E-mail addresses: selvankumar75@gmail.com (T. Selvankumar), elshine@knu.ac.kr (W. Kim), gova.muthu@gmail.com (M. Govarthanan).

https://doi.org/10.1016/j.chemosphere.2019.125327
0045-6535/© 2019 Elsevier Ltd. All rights reserved.

production, cell division and eventually plant growth (Maestri et al., 2010; Pourrut et al., 2011; Krzeslowska et al., 2016). Although low concentrations of Ni have several roles in enhancing plant growth and metabolism, high concentrations pose harmful effects (Parlak, 2016; Gautam et al., 2017). Similarly, small quantities of these metals are essential for human health, though in higher concentrations they become toxic, affecting brain, kidney, lungs, liver and other important organs. Moreover, long-term exposure to them can cause physical, muscular and neurological degenerative processes, and even cancer (Jarup, 2003; Álvarez Mateos et al., 2019).

Numerous soil remediation technologies such as biomineralization, bioleaching, biotransformation have been developed to eliminate metals and obtained some satisfactory results (Govarthanan et al., 2013, 2014, 2015). However, more cost-effectiveness soil remediation techniques are still necessary to practical application and with high study-worthy (Chang et al., 2019). Phytoremediation refers to the use of green plants and their related microbiota, soil amendments, and agronomic techniques to eliminate, comprise, or reduce harmful environmental contaminants (Li et al., 2019). However, several factors such as growth rate of plants, reduced biomass, phytotoxicity of metals, geochemistry of the contaminated soil, biotic and abiotic stress in plants, and limited uptake of metals hinder the efficiency of such mechanisms (Praburaman et al., 2015).

Recently, the use of specific chelating agents and plant growth-promoting rhizobacteria (PGPR) to increase the solubility and metal accumulation in plants (assisted phytoextraction) is receiving significant attention (Meers et al., 2008a, 2008b, Evangelou et al., 2007; Murakami et al., 2007; Shakoor et al., 2014). Metal's mobility and solubsility in the soil are most important for their bioavailability. For this purpose, different chelating agents have been used to enhance metal solubility in the soil (Ehsan et al., 2014). In addition, the use of chelating agents increases the resistance of a plant to drought stress and accumulation of metals in the plant (Guo et al., 2019). Numerous studies suggested that the addition of chelating agents, such as diethylene triamine penta acetic acid (DTPA) and ethylenediamine tetraacetic acid (EDTA) and *N*-(2-hydro- xyethyl)-ethylene diamine tri acetic acid (HEDTA) and organic chelates such as citric acid may enhance metal mobility and bioavailability (Sinhal et al., 2010; Szczygłowska et al., 2011; Bareen, 2012; ; Chigbo and Batty, 2013). Synthetic chelators are capable of phytoextraction but cause groundwater contamination and are non-biodegradable (Anwer et al., 2012; Bareen, 2012). Furthermore, negative effects of synthetic chelators have been reported to increase toxicity of metals to plants and soil microorganisms (Tandy et al., 2006; Evangelou et al., 2007).

It has been reported that synthetic chelating agents should be replaced by biodegradable low molecular weight citric acid (CA) to alter the chemical nature of metals, bioavailability and to improve the phytoremediation of metals (Al Mahmud et al., 2018). Due to its eco-friendly nature, easily biodegradable and non-toxic properties, CA has been applied as an amendment for the betterment of phytoextraction of various metals (Anwer et al., 2012). Several studies reported that CA has a role in enhancing the phytoremediation of various metals by increasing metal mobilization and solubility and also effective against metal-induced oxidative stress by enhancing the activity of key enzymes involved in antioxidative defense system (Gao et al., 2010; Freitas et al., 2013; Al Mahmud et al., 2018). In addition, recent studies have also indicated the effect of vermicompost and its by-products on enhanced phytoremediation. Abbasi et al. (2015) reported that the effect of vermicompost on *Eichhornia* sp. growth along with a comprehensive comparison of the physicochemical parameters, stability analysis, and micro and macronutrient changes. However, based on our knowledge, there is no report on the use of vermi-wash (VM) on effect of plants cultivated metal contaminated soils.

VW, a vermicompost extract, brown-colored liquid obtained by washing the vermicompost system. It contains amino acids, vitamins, plant growth-promoting hormones, nitrogen, potassium, zinc, calcium (Aghamohammadi et al., 2016). Several studies applied VW as a potential bio-fertilizer, pesticide to enhance the growth and productivity of crops. Thus, the objectives of the study were to assess the effect of CA and VW on (i) growth, biomass, antioxidants, chlorophyll and Rubisco protein levels of *S. bicolor* grown in metal contaminated soil, and (ii) Pb and Ni phytoaccumulation rate of *S. bicolor* grown in metal contaminated soil.

2. Materials and methods

2.1. Soil sample

Garden soil (0–30 cm topsoil) used in the experiments was collected from the Biotechnology block (11.510610 N, 78.034411 W), Mahendra Arts and Science College, Namakkal, Tamil Nadu, India. The different physicochemical characteristics such as, pH, electrical conductivity (EC), organic carbon (OC), water holding capacity (WHC), nitrogen (N), phosphorus (P), sodium (Na), potassium (P) of the soil sample were analyzed according to Govarthanan et al. (2014). The soil sample was air-dried and sieved through a 2 mm metal sieve to remove the stones and other coarse components of the soil and autoclaved for 20 min at 121 °C for 15 min. The sterilized soil was artificially contaminated with 100 mg/kg of Pb and Ni individually, whereas control soil was prepared without any metal contamination. The metal solutions were mixed with the soil samples and stabilized for 3–4 weeks. The moisture content of the soil samples were maintained at 60–70% using double distilled water.

2.2. Pot experiments

S. bicolor seeds were purchased from the local agricultural training center in Mallasamudram, Tamil Nadu, India. The seeds were surface sterilized with 2% NaOCl washed several times with distilled water and soaked (24–48 h) in distilled water at room temperature for germination. The germinated seedlings were transplanted into plastic pot (8 cm in diameter with 10 cm height) filled with 500 g of soil contaminated with Pb and Ni respectively. The pots were maintained under fixed incubation conditions of 10 h photoperiod, 26 °C with 60–65% of humidity. After 5–7 days of seedlings adaptation, the pots were treated with 10 ml of VM and 10 ml of (10 mM) CA respectively. However, the control pot was treated with 10 ml of distilled water. After 30 days, the plants were harvested and the root system was cleaned with tap water followed by distilled water. The shoot and root lengths were recorded. The dry weights of shoot and roots are recorded as biomass of the plant. The Pb and Ni concentration in the samples were determined using atomic absorption spectroscopy (AAS) (Thermo Scientific™ iCE™ 3500).

2.3. Biochemical assays

The antioxidant enzymes such as catalase (CAT), superoxide dismutase (SOD) and peroxidase (POX) were assayed according to the methods developed by Chance and Maehly (1955). The chlorophyll concentrations of the plants were measured according to Porra (2002). Protein and proline concentrations were estimated by the methods of Lowry et al. (1951) and Bates et al. (1973) respectively.

2.4. Microscopic observation of shoot structure of S. bicolor

After 1 month treatment with CA and VW, the shoot thin-section of the *S. bicolor* was prepared and stained with basic strain safranin and fast green. After washing with water, the sections were observed under an inverted phase-contrast microscope (Olympus- Magnus, Trinocular Microscope) and photographed to check the accumulation of Pb and Ni on the shoots of *S. bicolor.*

2.5. Estimation of Rubisco protein

Rubisco protein was isolated from the leaves of *S. bicolor* grown in Pb and Ni contaminated soils according to Wang et al., 1992. The activity of the isolated Rubisco was spectrophotochemically spectrophotometrically determined at 340 nm according to Racker (1962). The enzyme unit was calculated as one unit of enzyme was defined as the amount of enzyme-producing 1 M of RuBP per min.

Table 1
Physico-chemical properties of soil.

Parameter	value
pH	7.3
EC (ds/m)	2.69
Organic matter (%)	14.75 ± 1.23
Na (meg/100 g)	36.5 ± 1.21
K (meg/100 g)	49.5 ± 1.91
NH_4 (meg/100 g)	51.3 ± 2.1

3. Results and discussion

3.1. Characterization of soil sample and effect of VW, CA on biomass and morphological changes of S. bicolor

The texture of the study soil was sandy loam with a neutral pH of 7.25. The EC and OC of the soil were approximately 2.69 (ds/m) and 14.75 ± 1.23% respectively (Table 1). The pH of the soil was neutral with moderate EC. The AAS results revealed that trace amount (less than 1%) of heavy metals including Pb and Ni were present in the soil but the concentrations were below the detectable limit. The effects of VW and CA on morphology of *S. bicolor* cultivated in the Pb and Ni contaminated soils are represented in Fig. 1. The biomass of CA and VW treated *S. bicolor* plants were significantly increased when compared with the control plants. CA treated plants showed 24, and 26% of increased biomass in Pb and Ni amended soils, whereas, VW treated plants showed 11 and 9% increased in Pb and Ni amended soils. (Fig. 2). Compared to control, CA treated plants showed 3 and 5 cm of increased shoot and root length cultivated Pb and Ni contaminated soils, whereas, VW treated plants showed 6 and 8 cm of increased shoot and length compared to CA cultivated

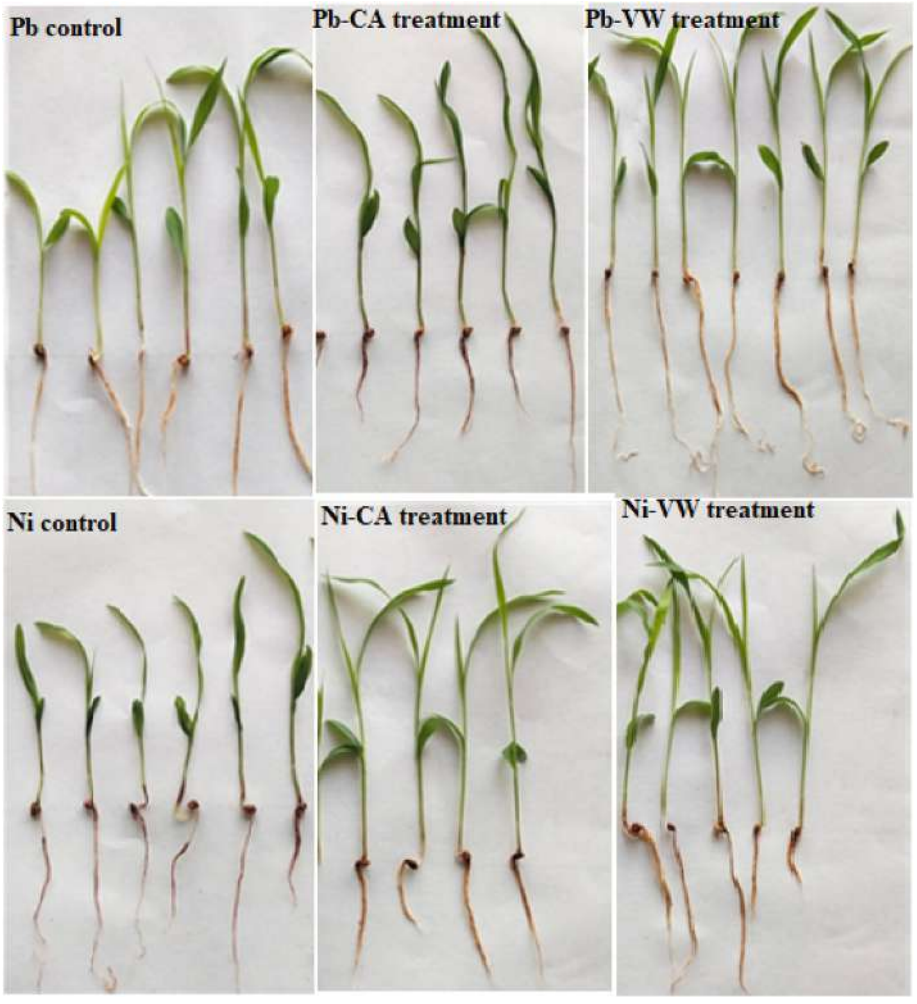


Fig. 1. Effects of VW and CA on the morphology of *S. bicolor* cultivated in the Pb and Ni amended soil.

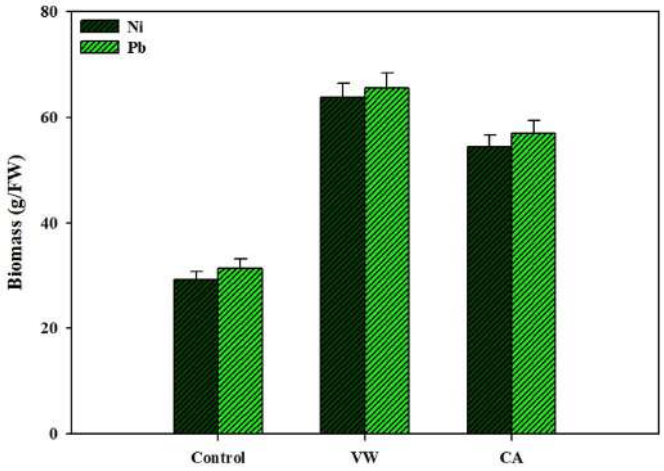


Fig. 2. Influence of VW and CA on the biomass of *S. bicolor* cultivated in the Pb and Ni amended soil.

with Pb and Ni contaminated soil respectively (Table 2). Statistical analysis showed significant differences ($P < 0.05$) for biomass, shoot length and root length in CA and VW treatments. The biomass and plant growth results indicated that the addition of VW improved the growth characteristics as well as amelioration of Pb and Ni toxicity symptoms in *S. bicolor.*

The difference in the biomass and growth rate of *S. bicolor* between CA and VW was due to the presence of essential nutrients such as nitrogen, phosphorus, and potassium in VW (Majumdar et al., 2018). Jiang et al. (2012) reported that high biomass, elevated levels of metals in shoot and root parts of the plants could be more successful practice of phytoremediation. Han et al. (2018) reported that the addition of CA and other synthetic organic acids in the heavy metals contaminated soils could alleviate the toxicity on particular plant to a certain extent as well as beneficial to the growth of plants. However, the CA and other organic acids have only limited nutrient source for the plant compared to VW (Suthar et al., 2014).

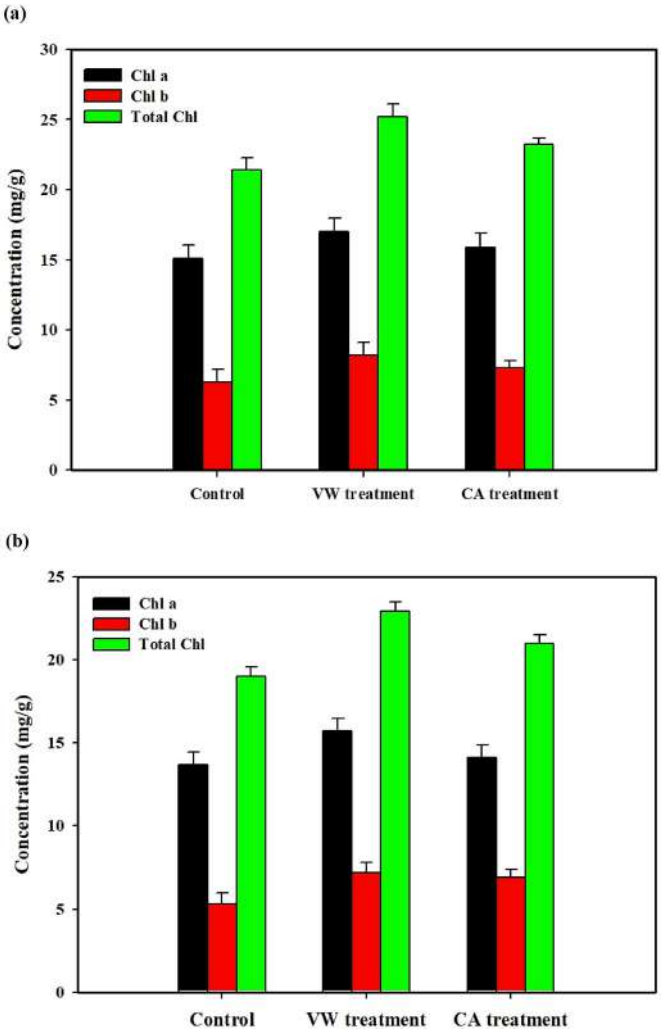


Fig. 3. (a,b). Chlorophyll concentrations of *S. bicolor* treated with VW and CA cultivated in the Pb and Ni amended soil.

3.2. Effect of VW and CA on chlorophyll concentration of the plants cultivated in Pb and Ni contaminated soil

The effect of VW and CA on the chlorophyll concentration of the plants was investigated and represented in Fig. 3 (a and b). VW significantly increased chlorophyll concentrations of the plants cultivated in Pb and Ni contaminated soil. VW treatment showed maximum total chlorophylls concentration (25.2 and 22.9 mg/g) compared to CA treated plants (23.2 and 21.0 mg/g) in Pb and Ni contaminated soils. Ehsan et al. (2014) found that the addition of CA significantly increased total chlorophyll concentration of *Brassica napus* cultivated with cadmium contaminated soil. Aghamohammadi et al. (2016) reported that VW enhances the chlorophyll contents of the plants by increasing photosynthetic pigments.

3.3. Influence of VW and CA on antioxidant enzymes of S. bicolor

It has been reported that the tolerance of plants to heavy metals stress is associated with the induction of antioxidant enzymes. Thus, the antioxidant activity of the VW and CA treated *S. bicolor* cultivated in Pb and Ni soil was investigated. Accordingly, CAT, SOD, and POX enzymes were analyzed and the results presented in Fig. 4 (a and b). The results showed differences in enzyme activities between the control, as well as between plants grown in a Pb and Ni-contaminated soils treated with VW and CA. The VW treated plants showed an increased concentration of enzyme activities compared to CA in Pb and Ni contaminated soils. The plants grown in Pb soil treated with VW showed 140, 125 and 152 u/mg of CAT, SOD and POD activity. However, plants grown Ni contaminated soil treated with VW showed increased CAT, SOD and POD activities (135, 130

Table 2
Effect of VW and CA on shoot and root lengths of *Sorghum bicolor* cultivated in the Pb and Ni contaminated soil.

Sample	Control		CA treated		CA treated	
	Pb	Ni	Pb	Ni	Pb	Ni
Root length (cm)	2.5 ± 0.1	2.7 ± 0.2	3.0 ± 0.2	3.4 ± 0.2	6.3 ± 0.2	6.5 ± 0.2
Shoot length (cm)	7.2 ± 0.4	7.7 ± 0.3	9.3 ± 0.2	9.7 ± 0.1	11.2 ± 0.2	11.8 ± 0.2

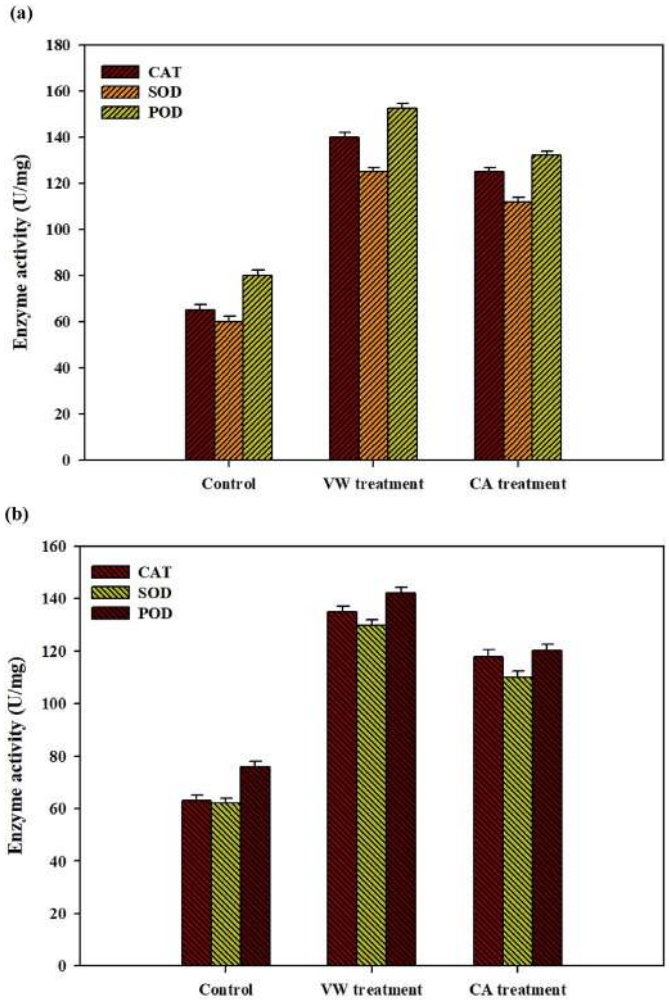


Fig. 4. Effects of VW and CA on antioxidant enzymes of *S. bicolor* cultivated in the Pb and Ni amended soil.

and 142 U/mg) respectively. The results indicated that there is no significant difference in the antioxidant enzymes level of VW treated *S. bicolor* plants irrespective of metals. On the other hand, the CA treatment showed 125, 112 and 132 U/mg of CAT, SOD, and POD in plants of Pb contaminated soils and 118, 110 and 120 U/mg of CAT, SOD, and POD in plants of Ni contaminated soil respectively. The order of antioxidant enzyme activity in plants was found to be VW > CA > control in both Pb and Ni contaminated soil. Ehsan et al. (2014) reported that the addition of citric acid significantly increases the SOD and POD activities in *B. napus* cultivated with cadmium contaminated soil. It has been confirmed that the CA scavenges oxidative stress by the increase of H_2O_2 production and enhanced the increased activity of antioxidant enzymes as well as protected plants from oxidative stress (Najeeb et al., 2009).

3.4. Anatomical observation of shoot section of S. bicolor treated VW and CA

A three mesophyll cell of the shoots within the upper and lower epidermis was found in both VW and CA treatment. The results indicated that the Pb and Ni not affected the VW and CA treated shoot mesophyll cells of *S. bicolor*. These results are consistent with the previous study reported the positive impact of organic acids on the root and leaf structure of *Iris halophila* cultivated in Pb mine soil

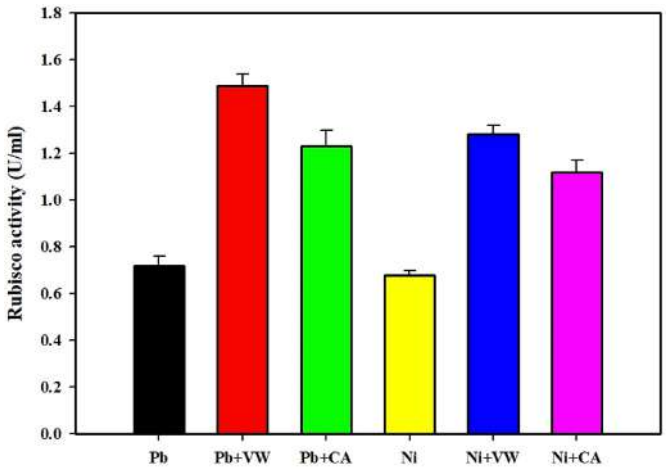


Fig. 5. Effects of VW and CA on the activity of Rubisco in leaves of *S. bicolor* cultivated in the Pb and Ni amended soil.

(Han et al., 2018). It has been reported that the heavy metal stress can reduce plant growth, cause physiological and metabolical disorders, and damage of root, shoot, leaf, and even death. Han et al. (2018) reported that some of organic acids alleviate the metal cytotoxicity to the plant system.

3.5. Rubisco activity on VW and CA treated plants

Rubisco protein estimation has been performed and the results were presented in Fig. 5. The results indicated that the enhanced activity of Rubisco was found in the plants (grown in Pb and Ni contaminated soil) treated with both VW and CA. In particular, the plants grown in Pb contaminated soil treated with VW showed the enhanced activity of 1.49 U/ml, whereas, CA treatment showed 1.23 U/ml of Rubisco. Both the treatments showed higher activity than the control (0.72 U/ml). Arena et al. (2017) reported that the *Cynara cardunculus* grown in Pb contaminated soil showed enhanced Rubisco activity compared to untreated plants. It has been reported that the photosynthetic enzyme concentrations decrease in metal treated sensitive plants, whereas tolerant species adopt heavy metal stress by enhancing Rubisco activity. In this study, the addition of VW neutralizes the Pb and Ni in soil lead to enhanced Rubisco activity.

4. Conclusion

The results clearly indicated that the VW amendment increased biomass, shoot and root lengths, chlorophyll concentrations, antioxidant enzymes, and Rubisco proteins of plants cultivated in Pb and Ni contaminated soil compared to CA. Therefore, the present study suggested that the VW could be used as a potential chelator for phyto-accumulation of heavy metals, as well as growth-promoting formulation. Hence, the VW could be replaced the CA for the enhanced phytoremediation of heavy metals.

Declaration of competing interest

The authors declared that they dont have no known competing financial interests or personal relationships that could have appeared to influence the work reported in this paper. Any conflict of interest in this manuscript.

Acknowledgments

This work is supported by the Department of Biotechnology, Mahendra Arts and Science College (Autonomous), and UGC-SERO Minor project F.No.:4-4/2015. The author Ashraf acknowledges the Deanship of Scientific Research at King Faisal University, for the financial support under Nasher track (Grant No. 186140). This work was supported by a National Research Foundation of Korea (NRF) grant funded from the Korean government (MSIP, South Korea) (No. 2017R1A4A1015628; No. 2018R1D1A1B07050040), and partly supported by the Korea Institute of Energy Technology Evaluation and Planning (KETEP) grant funded by the Korea government (MOTIE) (No. 20194110100100, Full-scale feasibility study of the stability and efficiency improvement of a biogas production facility based on biomass from urban/living environments).

Appendix A. Supplementary data

Supplementary data to this article can be found online at https://doi.org/10.1016/j.chemosphere.2019.125327.

References

Abbasi, S.A., Nayeem-Shah, M., Abbasi, T., 2015. Vermicomposting of phytomass: limitations of the past approaches and the emerging directions. J. Clean. Prod. 93, 103–114.

Abou Elwafa, S.F., Amin, A.E.E.A.Z., Shehzad, T., 2019. Genetic mapping and transcriptional profiling of phytoremediation and heavy metals responsive genes in sorghum. Ecotoxicol. Environ. Safe 173, 366–372.

Aghamohammadi, Z., Etesami, H., Ali, H.A., 2016. Vermiwash allows reduced application rates of acaricide azocyclotin for the control of two spotted spider mite, *Tetranychus urticae* Koch, on bean plant (*Phaseolus vulgaris* L.). Ecol. Eng. 93, 234–241.

Al Mahmud, J., Hasanuzzaman, M., Nahar, K., Bhuyan, M.B., Fujita, M., 2018. Insights into citric acid-induced cadmium tolerance and phytoremediation in *Brassica juncea* L.: coordinated functions of metal chelation, antioxidant defense and glyoxalase systems. Ecotoxicol. Environ. Safe. 147, 990–1001.

Álvarez Mateos, P., Alés Álvarez, F.J., García Martín, J.F., 2019. Phytoremediation of highly contaminated mining soils by *Jatropha curcas* L. and production of catalytic carbons from the generated biomass. J. Environ. Manag. 231, 886–895.

Anwer, S., Ashraf, M.Y., Hussain, M., Ashraf, M., Jamil, A., 2012. Citric acid mediated phytoextraction of cadmium by Maize (*Zea Mays* L.). Pak. J. Bot. 44, 1831–1836.

Arena, C., Figlioli, F., Sorrentino, M.C., Izzo, L.G., Capozzi, F., Giordano, S., Spagnuolo, V., 2017. Ultrastructural, protein and photosynthetic alterations induced by Pb and Cd in *Cynara cardunculus* L. and its potential for phytoremediation. Ecotoxicol. Environ. Safe. 145, 83–89.

Bareen, F.E., 2012. Chelate assisted phytoextraction using oil seed *brassicas*. Environ. Pollut. 21, 289–311.

Bates, L.S., Waldren, R.P., Teare, I.D., 1973. Rapid determination of free proline for water stress studies. Plant Soil 39, 205–207.

Chance, B., Maehly, A.C., 1955. Assay of catalase and peroxidase. Methods Enzymol. 2, 764–775.

Chang, J.H., Dong, C.D., Shen, S.Y., 2019. The lead contaminated land treated by the circulation enhanced electro kinetics and phytoremediation in field scale. J. Hazard Mater. 368, 894–898.

Chigbo, C., Batty, L., 2013. Effect of EDTA and citric acid on phytoremediation of Cr-B [a] P-co-contaminated soil. Environ. Sci. Pollut. Res. 1–9.

Ehsan, S., Ali, S., Noureen, S., Mahmood, K., Farid, M., Ishaque, W., Shakoor, M.B., Rizwan, M., 2014. Citric acid assisted phytoremediation of cadmium by *Brassica napus* L. Ecotoxicol. Environ. safe 106, 164–172.

Evangelou, M.W.H., Ebel, M., Schaeffer, A., 2007. Chelate assisted phytoextraction of heavy metals from soil. Effect, mechanism, toxicity, and fate of chelating agents. Chemosphere 68, 989–1003.

Freitas, E.V., Nascimento, C.W., Souza, A., Silva, F.B., 2013. Citric acid-assisted phytoextraction of lead: a field experiment. Chemosphere 92, 213–217.

Gao, Y., Miao, C., Mao, L., Zhou, P., Jin, Z., Shi, W., 2010. Improvement of phytoextraction and antioxidative defense in *Solanum nigrum* under cadmium stress by application of cadmium resistant strain and citric acid. J. Hazard Mater. 181, 771–777.

Gautam, S., Rathoure, A.K., Chhabra, A., Pandey, S.N., 2017. Effects of nickel and zinc on biochemical parameters in plants a review. Octa. J. Environ. Res. 5, 8.

Govarthanan, M., Lee, G.W., Park, J.H., Kim, J.S., Lim, S.S., Seo, S.K., Cho, M., Myung, H., Kamala-Kannan, S., Oh, B.T., 2014. Bioleaching characteristics, influencing factors of Cu solubilization and survival of Herbaspirillum sp. GW103 in Cu contaminated mine soil. Chemosphere 109, 42–48.

Govarthanan, M., Lee, K.J., Cho, M., Kim, J.S., Kamala-Kannan, S., Oh, B.T., 2013. Significance of autochthonous Bacillus sp. KK1 on biomineralization of lead in mine tailings. Chemosphere 90, 2267–2272.

Govarthanan, M., Park, S.H., Park, Y.J., Krishnamurthy, R.R., Lee, S.H., Lovanh, N., Kamala-Kannan, S., Oh, B.T., 2015. Lead biotransformation potential of allochthonous Bacillus sp. SKK11 with sesame oil cake extract in mine soil. RSC Adv. 5, 54564–54570.

Guo, D., Ali, A., Ren, C., Li, R., Lahori, A.H., Xiao, R., Zhang, Z., Zhang, Z., 2019. EDTA and organic acids assisted phytoextraction of Cd and Zn from a smelter contaminated soil by potherb mustard (*Brassica juncea, Coss*) and evaluation of its bioindicators. Ecotoxicol. Environ. Saf. 167, 396, 03.

Han, Y., Zhang, L., Gu, J., Zhao, J., Fu, J., 2018. Citric acid and EDTA on the growth, photosynthetic properties and heavy metal accumulation of *Iris halophila* cultivated in Pb mine tailings. Biodeterior. Biodegrad. 128, 15–21.

Jarup, L., 2003. Hazards of heavy metal contamination. Br. Med. Bull. 68, 167–182.

Jiang, Z.F., Huang, S.Z., Han, Y.L., Zhao, J.Z., Fu, J.J., 2012. Physiological response of Cu and Cu mine tailing remediation of *Paulownia fortunei* (Seem) Hemsl. Ecotoxicology 21, 579–767.

Krzeslowska, M., Rabeda, I., Basinska, A., Lewandowski, M., Mellerowicz, E.J., Napieralska, A., Samardakiewicz, S., Wozny, A., 2016. Pectinous cell wall thickenings formation - a common defense strategy of plants to cope with Pb. Environ. Pollut. 214, 354–361.

Li, X., Wang, X., Chen, Y., Yang, X., Cui, Z., 2019. Optimization of combined phytoremediation for heavy metal contaminated mine tailings by a field-scale orthogonal experiment. Ecotoxicol. Environ. safe 168, 1–8.

Lowry, O.H., Rosenbrough, N.J., Farr, A.L., Randall, R.J., 1951. Protein measurement with the folin phenol reagent. J. Biol. Chem. 193, 265–275.

Maestri, E., Marmiroli, M., Visioli, G., Marmiroli, N., 2010. Metal tolerance and hyperaccumulation: costs and tradeoffs between traits and environment. Environ. Exp. Bot. 68, 1–13.

Majumdar, A., Barla, A., Upadhyay, K., Ghosh, D., Chaudhuri, P., Srivastava, S., Bose, S., 2018. Vermiremediation of metal(loid)s via *Eichornia crassipes* phytomass extraction: a sustainable technique for plant amelioration. Environ. Manag. 220, 118–125.

Meers, E., Tack, F.M.G., Van Slycken, S., Ruttens, A., Du Laing, G., Vangronsveld, J., Verloo, M.G., 2008a. Chemically assisted phytoextraction: a review of potential soil amendments for increasing plant uptake of heavy metals. Int. J. Phytoremediation 10, 390–414.

Meers, E., Tack, F.M.G., Verloo, M.G., 2008b. Degradability of ethylenediamine disuccinic acid (EDDS) in metal contaminated soils implications for its use soil remediation. Chemosphere 70, 358–363.

Murakami, M., Ae, N., Ishikawa, S., 2007. Phytoextraction of cadmium by rice (*Oryza sativa* L.), soybean (*Glycinemax (L.)*Merr.), and maize (*Zea mays* L.). Environ. Pollut. 145, 96–103.

Najeeb, U., Xu, L., Ali, S., Jilani, G., Gong, H.J., Shen, W.Q., Zhou, W.J., 2009. Citric acid enhances the phytoextraction of manganese and plant growth by alleviating the ultrastructural damages in *Juncus effusus* L. J. Hazard Mater. 170, 1156–1163.

Parlak, K.U., 2016. Effect of nickel on growth and biochemical characteristics of wheat (*Triticum aestivum* L.) seedlings. NJAS - Wageningen J. Life Sci. 76, 1–5.

Patil, S.S., Kar, A., Mohapatra, D., 2016. Stabilization of rice bran using microwave: process optimization and storage studies. Food Bioprod. Process. 99, 204–211.

Pourrut, B., Shahid, M., Dumat, C., Winterton, P., Pinelli, E., 2011. Lead uptake, toxicity, and detoxification in plants. Rev. Environ. Contam. Toxicol. 213, 113–136.

Praburaman, L., Park, J.H., Govarthanan, M., Selvankumar, T., Oh, S.G., Jang, J.S., Cho, M., Kamala-Kannan, S., Oh, B.T., 2015. Impact of an organic formulation (panchakavya) on the bioleaching of copper and lead in contaminated mine soil. Chemosphere 138, 127–132.

Racker, E., 1962. Ribulose diphosphate carboxylase from spinach leaves: ribulose diphosphate + CO2 + H2O fi 2 3-P-glycerate. Methods Enzymol. 5, 266–270.

Shakoor, M.B., Ali, S., Hameed, A., Farid, M., Hussain, S., Yasmeen, T., Najeeb, U., Bharwana, S.A., Abbasi, G.H., 2014. Citric acid improves lead (Pb) phytoextraction in *Brassica napus* L. by mitigating Pb induced morphological and biochemical damages. Ecotoxicol. Environ. Safe 109, 38–47.

Signa, A., Mazzola, R., Leonardo, D., Vizzini, S., 2017. Element-specific behavior and sediment properties modulate transfer and bioaccumulation of trace elements in a highly-contaminated area (Augusta Bay, Central Mediterranean Sea). Chemosphere 187, 230–239.

Sinhal, V.K., Srivastava, A., Singh, V.P., 2010. EDTA and citric acid mediated phytoextraction of Zn, Cu, Pb and Cd through marigold (*Tagete serecta*). J. Environ. Biol. 31, 255–259.

Suthar, S., Sajwan, P., Kapil Kumar, P., 2014. Vermi remediation of heavy metals in waste water sludge from paper and pulp industry using earthworm *Eisenia fetida*. Ecotoxicol. Environ. Safe 109, 177–184.

Szczygłowska, M., Piekarska, A., Konieczka, P., Namiesnik, J., 2011. Use of *Brassica* plants in the phytoremediation and biofumigation processes. Int. J. Mol. Sci. 12, 7760–7771.

Tandy, S., Schulin, R., Nowack, B., 2006. Uptake of metals during chelant assisted phytoextraction with EDDS related to the solubilized metal concentration. Environ. Sci. Technol. 40, 2753–2758.

Wang, Z.Y., Snyder, G.W., Esau, B.D., Portis Jr., A.R., Ogren, W.L., 1992. Species-dependent variation in the interaction of substrate bound ribulose-1,5-bisphosphate carboxylase/oxygenase (rubisco) and rubisco activase. Plant Physiol 100, 1858–1862.

Yılmaz, N., 2016. Middle infrared stabilization of individual rice bran milling fractions. Food Chem. 190, 179–185.

Springer Link Search Log in

Short Reports | Published: 11 October 2019

Production and purification of laccase by *Bacillus* sp. using millet husks and its pesticide degradation application

P. Srinivasan, T. Selvankumar, S. Kamala-Kannan, R. Mythili, A. Sengottaiyan, M. Govarthanan ✉, B. Senthilkumar & K. Selvam ✉

3 Biotech **9**, Article number: 396 (2019)

424 Accesses | **13** Citations | Metrics

Abstract

Lignocellulosic agricultural bi-products, pearl millet (PM) and finger millet (FM) husks, were used for the production of laccase using *Bacillus* sp. PS under solid-state fermentation (SSF). Abiotic variables such as substrate (PM, FM) concentration (1–5%), incubation time (24–96 h) and pH (5–10) were optimized using Response surface methodology (RSM) to maximize the laccase production. The predicted model showed maximum laccase activity of 402 U/mL appearing after 96 h of incubation with PM 2.0 g/L and FM 1.5 g/L at pH 7.0. Single protein band on sodium dodecyl sulfate polyacrylamide gel electrophoresis (SDS-PAGE) confirmed homogeneity of the laccase with a molecular weight of 63–75 kDa. The partially purified laccase effectively degraded the

P.G.P. COLLEGE OF ARTS & SCIENCE NAMAKKAL 637 206.

PRINCIPAL
PGP College of Arts and Science
Namakkal

3 Biotech (2019) 9:396
https://doi.org/10.1007/s13205-019-1900-8

SHORT REPORTS

Production and purification of laccase by *Bacillus* sp. using millet husks and its pesticide degradation application

P. Srinivasan[1] · T. Selvankumar[1] · S. Kamala-Kannan[2] · R. Mythili[1] · A. Sengottaiyan[1] · M. Govarthanan[1] · B. Senthilkumar[3] · K. Selvam[1]

Received: 11 June 2019 / Accepted: 16 September 2019
© King Abdulaziz City for Science and Technology 2019

Abstract

Lignocellulosic agricultural bi-products, pearl millet (PM) and finger millet (FM) husks, were used for the production of laccase using *Bacillus* sp. PS under solid-state fermentation (SSF). Abiotic variables such as substrate (PM, FM) concentration (1–5%), incubation time (24–96 h) and pH (5–10) were optimized using Response surface methodology (RSM) to maximize the laccase production. The predicted model showed maximum laccase activity of 402 U/mL appearing after 96 h of incubation with PM 2.0 g/L and FM 1.5 g/L at pH 7.0. Single protein band on sodium dodecyl sulfate polyacrylamide gel electrophoresis (SDS-PAGE) confirmed homogeneity of the laccase with a molecular weight of 63–75 kDa. The partially purified laccase effectively degraded the pesticides (Tricel, 71.8 ± 3.5 and Phoskill 77.3 ± 3.4%) within 5 days of incubation (40 °C) in pH 7.0. The pesticide degradation was further confirmed by high-performance liquid chromatography (HPLC) and the chromatograms showed the single dominant peaks at retention time 2.482 (tricel) and 2.608 (phoskill) min, respectively. Pesticide-degrading laccase was produced by *Bacillus* sp. PS under SSF reveals the utilization of low-cost bi-substrates for enhanced laccase production.

Keywords *Bacillus* sp. · Finger millet · Pearl millet · Laccase · Phoskill · Tricel

Introduction

Pesticides are widely used in modern agriculture to control pests and crop losses, and to increase commodity, yield and quality. It has been reported that ~ 80% of crop yields have been lost when pesticides are not used (Zhou et al. 2015). However, reckless an irrelevant use of pesticides has contributed to the global pesticide pollution. Pesticides used in agriculture, in addition to contaminating the environment, tend to accumulate in biological organisms, biomagnify across the food chain, and cause several disorders to the biotic communities in the ecosystem (Pizzul et al. 2009). The clinical disorder associated with pesticide exposures includes cancer, birth deformities, memory loss, respiratory issues, etc. in both human and animal systems (Upadhyay et al. 2016). Thus, it is important to remediate pesticide-contaminated soil/water.

Numerous physical and chemical methods have been reported for the removal of pesticides from contaminated soil or water. Although these conventional methods were reported as being effective, they are not without shortcomings. Thus, researchers are exploring an eco-friendly and in-expensive technology to alleviate pesticide pollution in the contaminated environment. Several studies have reported that the microorganisms present in the soil degrade the pesticides through enzymatic oxidation, reduction, and hydrolysis mechanisms (Amitai et al. 1998; Eduardo et al. 2003). Thus, the present study focuses on the use of soil microorganisms in pesticide degradation.

✉ M. Govarthanan
gova.muthu@gmail.com

✉ K. Selvam
ksk.selvam@gmail.com

[1] PG and Research Department of Biotechnology, Mahendra Arts and Science College (Autonomous), Kalippatti, Namakkal, Tamil Nadu 637501, India

[2] Division of Biotechnology, College of Environmental and Bioresource Sciences, Chonbuk National University, Iksan 570752, South Korea

[3] Department of Medical Microbiology, College of Health and Medical Sciences, Haramaya University, P.O.Box 235, Harar, Ethiopia

Published online: 11 October 2019

Laccase (EC 1.10.3.2, Benzenediol: oxygen oxidoreductase), a multi-copper oxidase enzyme, catalyzes a wide range of reactions involving organic and inorganic substrates (Wang et al. 2017; Sharma et al. 2017; Jaya Mary et al. 2018), such as oxidation of phenolic derivatives, polymerization of monomers and polymer degradation (Rodriguez Couto and Toca Herrera 2006). High catalytic capacity and low substrate specificity enhance the enzyme's applications in industries (paper, pulp, textile, petrochemical), bioremediation, medicine and nano-sciences (Kuddus et al. 2013; Garlapati et al. 2019).

Laccases are produced by bacteria (Chauhan et al. 2017), fungi (Dhiman and Shirkot 2015) and cyanobacteria (Demissie and Kumar 2014). Among the various sources, bacterial laccases have high stability at elevated temperature and pH compared to fungal and plant laccases (Margot et al. 2013). In addition, bacterial laccases have broad substrate specificity and are cost-effective (Lu and Miyakoshi 2012). In recent years, agro-industrial wastes have gained increasing attention due to their low costs, alleviation of environmental toxicity, vast quantity and the potential to convert waste into different high value-added products (Wolfenden and Wilson 1982). Several studies report using single agro-industrial wastes for the production of laccases (Laemmli 1970). However, the use of bi-substrate combination for enhanced laccase production has not been reported in the literature.

In this study, a combination of PM and FM husks was used for the production of laccase. The PM and FM are the one of the important agricultural commodities in the sampling site. Moreover, these agricultural bi-products are easily available at agro-industries. The millets grew rapidly, within a short period of time and the husks were accumulated from the farm fields. These husks are among the millions of tons of agro-industrial wastes seeking ways of eco-friendly utilization (Karimi et al. 2016). The easy renewability, biodegradability, and cost-effectiveness of these millets attract possible utilization of value-added products. Thus, the present study uses millet husks for the production of laccase. Thus, the aim of this study is to (1) isolate and identify laccase-producing bacteria from soil, (2) optimize laccase production using agro-industrial wastes (PM and FM husks), (3) purify and characterize laccase, and (4) assess the pesticide degradation potentials of laccase.

Materials and methods

Isolation and identification of laccase-producing bacteria

Soil samples were collected from dye effluents stream at Pallipalaiyam (Latitude: 11°23′22.79″N, Longitude: 77°44′20.99″E), Tamil Nadu, India. The collected soil samples were immediately transferred to laboratory for further studies. The isolation of bacteria from soil was carried out according to Govarthanan et al. (2016). Briefly, after appropriate serial dilutions, the growth of bacterial isolates was enriched by incubating with nutrient agar medium at 35 ± 2 °C for 24–36 h. The pure cultures were obtained from continuous streaking methods and were stored at 4 °C. The pure cultures were screened for laccase activity using plate method. Briefly, the cultures were spotted on nutrient agar plates amended with 5 mM guaiacol and plates were incubated at 35 ± 2 °C for 24–36 h. The formation of reddish brown color around the bacterial colonies indicated laccase production.

Genomic DNA was extracted using QIAGEN (CA, USA) DNA extraction kit according to manufacturer's instruction. Amplification of 16S rDNA gene was performed using universal primers 27 f (5′ AGA GTT TGA TCA TGG CTC AG 3′) and 1492 r (5′ CAC GGA TCC TAC GGG TAC CTT GTT ACG ACT T 3′). The purified PCR products were sequenced in an automated ABI PRISM 3700 sequencer (USA) and the obtained sequences were compared using the BLAST search. The neighboring bacterial strain and the percentage of similarity were obtained from BLAST match. Phylogenetic tree was constructed using mega software based on neighbor-joining method.

Substrate pretreatment and characterization using scanning electron microscopy, Fourier-transform infrared spectroscopy

Pearl millet and FM were obtained from local farm field at Mallasamudaram, Tamil Nadu, India, and chopped into small pieces. The chopped PM and FM were washed with tap water and dried at 60 °C for 12–24 h and grounded into 10–20 mm mean particles. Table 1 shows the chemical composition of PM and FM. The PM and FM were soaked in sodium hydroxide (1% w/v) solution with a solid–to-liquid ratio of 1:10 at 121 °C for 30 min. The NaOH-treated PM and FM were thoroughly washed with sterile distilled water to remove traces of base followed by drying at 50 °C (Liu et al. 2016; Selvam et al. 2016a, b; Guo et al. 2017; Sharma et al. 2018). The dried and pretreated PM and FM were used for characterization and fermentation studies. Scanning electron microscopy (SEM, Jeol JSM 6390, USA) was used to examine the morphological modifications of PM and FM before and after the NaOH pretreatment operating with high vacuum at 10 kV. The changes in the functional groups of control and pretreated substrates were analyzed using Fourier-transform infrared spectroscopy (Shimadzu IRAffinity-1 Spectrometer, USA).

Table 1 Chemical composition of pearl millet (PM) and finger millet (FM)

S.no.	Chemicals	Composition (mg/100 g)		References
		PM	FM	
1.	Moisture	11.27±0.17	5.58±0.21	Audu et al. (2018)
2.	Crude fat	6.42±0.11	7.94±0.06	Kumar and Chauha (1993)
3.	Ash content	2.05±0.05	2.51±0.11	Azhari et al. (2017)
4.	Crude protein	9.48±1.26	8.42±0.05	
5.	Crude fiber	1.30±0.005	2.51±0.06	
6.	Carbohydrate	69.57±0.04	73.32±0.23	

Solid-state fermentation, enzyme assay and protein estimation

Solid-state fermentation was carried out in 100 ml Erlenmeyer flasks containing the pretreated PM and FM and were vigorously mixed, moistened (70%) using distilled water and autoclaved at 121 °C for 15 min. After sterilization, the flasks were cooled and inoculated with 5 mL of isolated bacteria carrying 10^8 cells mL^{-1} (0.8 OD at 600 nm) as a seed culture under aseptic condition. The flasks were incubated under conditions stated in Box-Behnken design (BBD). Laccase activity was determined according to Wolfenden and Wilson (1982) using ABTS (2, 2′-azino-bis (3-ethylbenzothiazoline-6-sulphonic acid) as substrate. Protein concentration was estimated according to the method described by Lowry et al. (1951) using bovine serum albumin as the standard.

Optimization of laccase production

Box-Behnken design was employed for screening of significant factors which influence the laccase production under SSF. Four factors were screened including PM and FM concentrations (1–5%), incubation time (24–96 h) and pH (5–10). The design consisted of 46 trials and the independent process variables were studied at 3 different levels (Table 2). Second-order polynomial coefficient equation was developed to fit the experimental results for identifying the model terms. The general form of the second-order polynomial Eq. (1) is

$$Y = \beta_0 + \sum \beta_i X_i + \sum \beta_{ii} X_i^2 + \sum \beta_{ij} X_i X_j, \quad (1)$$

where Y is the predicted response (laccase production), $x_i x_j$ are input variables which influence the response laccase production; β_0, offset term; β_i linear coefficient; β_{ii} quadratic coefficient and β_{ij} is interaction coefficient. Statistical analysis of the BBD was evaluated using analysis of variance (ANOVA), correlation and coefficient determination (R, R^2). Designing the experiments and statistical analysis of this study were performed using Design-Expert statistical software (Version 11.0, Stat-Ease Inc., and Minneapolis, USA). All the experiments were carried out in triplicates.

Partial purification and sodium dodecyl sulfate polyacrylamide gel electrophoresis

The crude laccase was precipitated with ammonium sulfate at a final concentration of 80% (w/v) and incubated for 5 h at 4 °C. After incubation, the precipitate was centrifuged at 17,000 *g* for 20 min and re-suspended with 100 mM sodium acetate buffer and dialyzed against the same buffer for 12 h. The resulting super natant was used for SDS-PAGE. The molecular mass of the partially purified laccase was determined using SDS-PAGE according to Laemmli (1970).

Effect of pH and temperature on partially purified laccase activity

The optimum pH of partially purified laccase activity was determined by measuring the enzyme activities at pH 4–9 using ABTS as substrate. Briefly, laccase was equilibrated with 50 mM sodium citrate buffer (pH 4–6) and 50 mM sodium phosphate buffer (pH 6–8). The optimum temperature for laccase activity was studied by incubating the reaction mixture at different temperatures (30–80 °C). The residual laccase was measured with time by standard assay conditions (Selvam et al. 2014, 2016a, b).

Degradation of pesticides by laccase and residual analysis by HPLC

Tricel (chlorpyrifos) and phoskill were used for degradation experiments, which are commonly used by farmers in India. These pesticides were obtained from local agricultural extension centre at Mallasamudram, Tamil Nadu, India. Batch experiments were carried out according to Jin et al. (2016) with minor modifications. Briefly, 20 mg/L of pesticides were mixed with the buffer solutions (citric acid-dibasic sodium phosphate buffers) and incubated in dark room at 30 °C for 5 days. The samples were collected at predetermined time intervals and the pesticide concentration (Delcour et al. 2015) was determined using

Table 2 Box–Behnken design for the variables and the experimentally observed responses

Run	A: pH	B: temperature (°C)	C: pearl millet (g/l)	D: finger millet (g/l)	Laccase enzyme activity (U/ml)
1	7	40	2	1.5	402
2	6	55	2	0.5	221
3	7	40	2	1.5	402
4	8	40	3	1.5	252
5	7	40	2	1.5	402
6	4	40	1	1.5	240
7	4	55	2	1.5	202
8	8	40	2	2.5	234
9	8	40	2	0.5	228
10	7	40	2	1.5	402
11	6	40	2	0.5	276
12	6	40	3	0.5	233
13	6	25	2	1.5	232
14	6	25	2	2.5	223
15	7	40	2	1.5	402
16	4	40	2	1.5	226
17	4	40	2	1.5	219
18	6	40	3	1.5	256
19	6	25	1	1.5	236
20	6	40	1	0.5	251
21	4	40	3	1.5	228
22	6	40	2	2.5	269
23	8	25	2	1.5	125
24	6	55	2	1.5	231
25	8	40	1	1.5	244
26	6	25	2	0.5	220
27	4	40	2	2.5	229
28	7	40	2	1.5	402
29	8	40	2	1.5	291
30	6	55	2	1.5	238
31	6	40	1	1.5	298
32	6	55	3	1.5	246
33	4	40	2	0.5	228
34	8	55	2	1.5	225
35	6	55	1	1.5	244
36	7	40	2	1.5	402
37	6	25	2	1.5	244
38	8	40	2	1.5	236
39	6	25	2	1.5	258
40	6	40	1	2.5	261
41	6	40	2	2.5	270
42	6	40	2	0.5	253
43	6	40	3	2.5	276
44	6	40	1	1.5	273
45	4	25	2	1.5	240
46	6	40	3	1.5	256

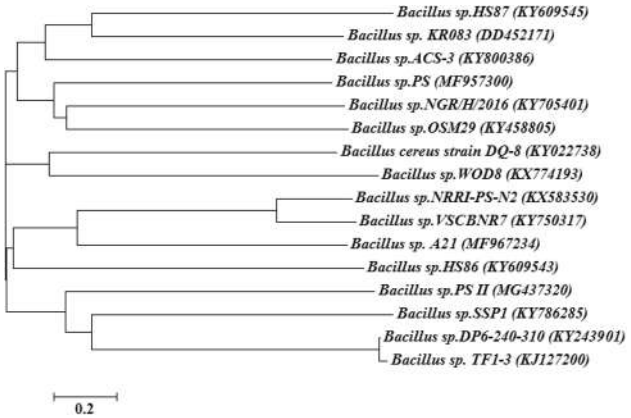


Fig. 1 16S rDNA-based phylogenetic analysis of *Bacillus* sp. strain PS. The Phylogenetic tree was constructed by the neighbor-joining method using MEGA, version 6 (Selvankumar et al. 2017). The scale bar shows 0.2 nucleotide exchanges per nucleotide

HPLC (LC-20AD, Shimadzu, and Tokyo, Japan). The reaction mixture without laccase was used as a control for this experiment. All the analyses were carried out in triplicates.

Results and discussion

Isolation and identification of laccase-producing bacteria

A total of seven different bacterial strains were isolated from the soil samples collected at Pallipalayam (Latitude: 11°23′22.79″N, Longitude: 77°44′20.99″E) Tamil Nadu, India. Among the seven isolates, one isolate designated as PS produced reddish brown color on the Nutrient agar plate. Thus, the isolate PS was identified and used for further studies. The 16S rRNA sequence of the selected isolate PS showed closest similarity (93%) with *Bacillus* sp. strain NGRH (GenBank Accession No. KX583530) available in NCBI database. The partial 16S RNA gene of the isolate PS was submitted in NCBI with GenBank accession number MF957300. Figure 1 shows the phylogenetic relationship of the isolate PS with other *Bacillus* sp. Recent study reported the production of the laccase using variety of fungi (Binod et al. 2012). However, limited studies made an attempt for the laccase production using *Bacillus* sp. (Zhao et al. 2012). Narayanan et al. (2015) reported that the production of laccase from *Bacillus subtilis* using agro-residues. However, there is no report on potential laccase-producing *Bacillus* sp. isolated from dye effluent streams utilizing PM and FM husks as a potential substrates.

Substrate pretreatment and its characterization using SEM and FT-IR

Several studies reported that substrate pretreatment modifies or loosens the structure of cell wall, causes delignification of hemicelluloses and lignin, and improves enzyme production (Liu et al. 2016; Selvam et al. 2016a, b; Guo et al. 2017; Sharma et al. 2018). Thus, the PM and FM were pretreated using NaOH and the micrographs were depicted in (Fig. 2a–d). Before NaOH treatment, PM and FM surfaces were smooth and rigid in nature which was hard for the bacterial system to colonize on the surface of the substrates. However, NaOH pretreatment could obliterate the linkages of inter-units and functional groups which cause the disruption of cell wall and lignin structure of the substrates as well as increased surface area to make more availability and accessibility.

The functional group changes before and after pretreatment of substrates were analyzed using FT-IR. Figure 3a shows the FT-IR spectra of PM before and after NaOH treatment and Fig. 3b shows the spectrum of FM. The significant reductions in the intensity of some peaks were observed for the PM after NaOH pretreatment, such as lignin peaks at 1551.80 and 1644.36 cm^{-1} (Fig. 3a). The near absence of this peak indicates the removal of lignin content through NaOH pretreatment. Similarly, lignin peaks at 1421.60 and 1321.30 cm^{-1} were significantly reduced in NaOH-pretreated FM (Fig. 3b). Both PM and FM NaOH-treated substrates have large band at 3555.92, 3410.29 and 2935.78 $cm^{-1}$and they are assigned as the O–H stretching of hydrogen bonds and C–H bonds. These bands are responsive to characteristic features of cellulose.

Optimization of laccase production using BBD

BBD was applied to identify the optimal conditions for the enhanced production of laccase. Table 3 represents the experimental design. ANOVA of the quadratic regression showed the significant model terms and it was evidenced that the Fisher's *F* test had a very high probability value (*F* value = 5.37). Values of 'Prob > *F*' (0.0001) indicate that the term of the model was significant. The Model *F* value of 5.37 implies that the model was significant. There was only a 0.01% chance that a model *F* value could occur due to noise. The predicted R^2 (0.4130) and adjusted R^2 (0.5760) values for laccase production were in reasonable agreement with the value of R^2 (0.4130), which is closer to 1.0, that indicates the better fitness of the model in the experimental data.

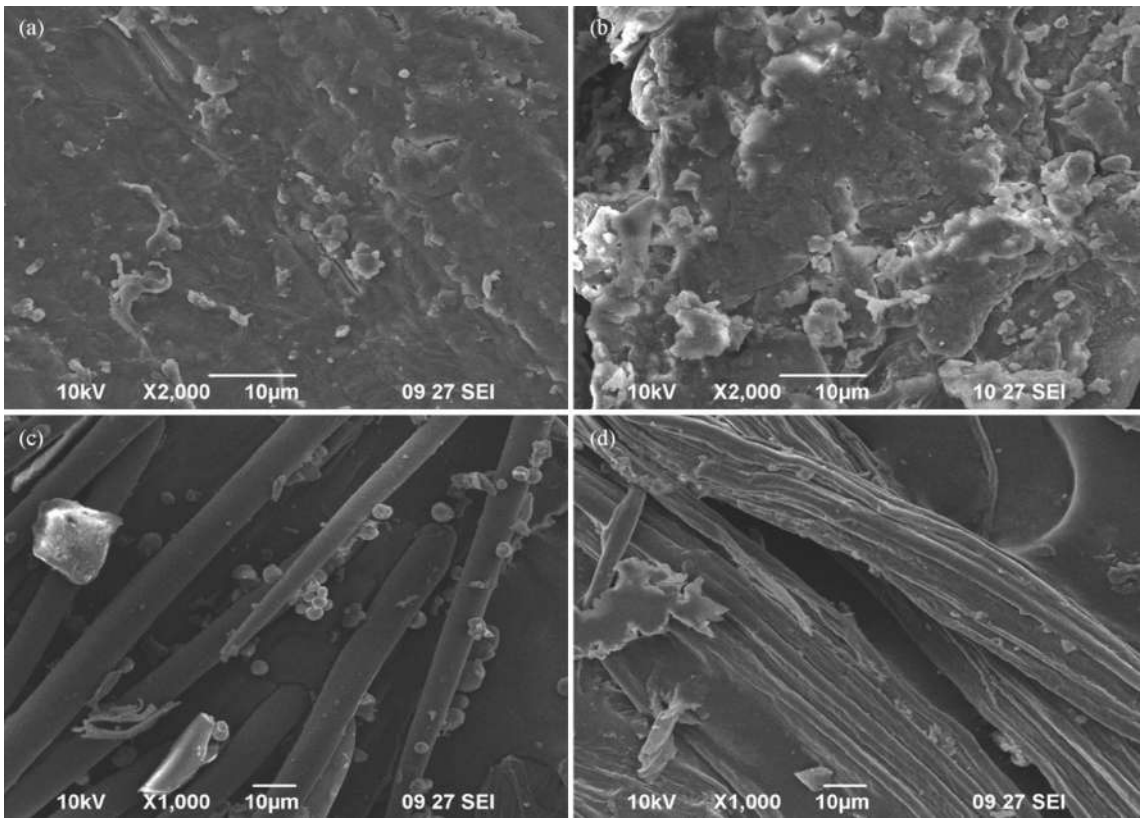


Fig. 2 **a**–**d** Surface morphology of substrates, **a** control and **b** NaOH-pretreated pearl millet (PM), **c** control and **d** NaOH-pretreated finger millet (FM)

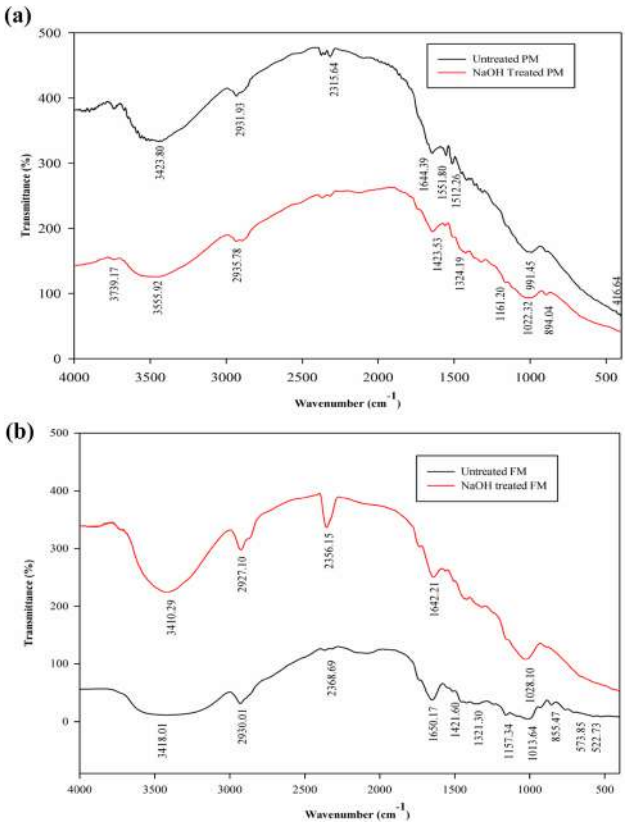


Fig. 3 Fourier-transform infrared spectra of **a** control and NaOH-pretreated pearl millet (PM), **b** control and NaOH-pretreated finger millet (FM)

The 3D plots, a graphical representation, generated (Fig. 4) explain the optimum levels of the variables that were obtained by BBD. The model was predicted with a maximum laccase activity of 402 U/mL appearing after 96 h cultivation with PM 2.0 g/L, FM 1.5 g/L of substrates at pH 7.0. The results were consistent with previous study reporting the maximum laccase (345 U/mL) production by *Bacillus subtilis* (Narayanan et al. 2015). However, our results showed the production of high amount of laccase with the presence of bi-substrate combination. The predicted model was validated and experiments were conducted using these optimal conditions. The predicted model values were in good agreement with the values measured in these experiments, thus mitigating the validity of the response model with the necessity for optimal conditions. The graphs highlighted the roles played by the variables in the production of laccase. The coefficients of the regression equation were calculated from the following regression equation:

$$Y = 365.91 + 12.25A + 7.59B - 7.22C + 4:15D + 34.50AB + 5.00AC + 1.25AD + 13:36BC - 2.41BD + 8.25CD - 77.96A^2 - 95.65B^2 - 57.55C^2 - 65.23D^2, \quad (2)$$

Table 3 Analysis of variance (ANOVA) for the response surface quadratic model

Source	Sum of squares	df	Mean square	*F* value	*p* value
Model	1.300E + 05	14	9289.21	5.37	**< 0.0001**
A-pH	2506.92	1	2506.92	1.45	0.2379
B-temperature	783.77	1	783.77	0.4528	0.5060
C-pearl millet	742.98	1	742.98	0.4292	0.5172
D-finger millet	244.90	1	244.90	0.1415	0.7094
AB	4761.00	1	4761.00	2.75	0.1073
AC	100.00	1	100.00	0.0578	0.8116
AD	6.25	1	6.25	0.0036	0.9525
BC	480.95	1	480.95	0.2778	0.6019
BD	15.50	1	15.50	0.0090	0.9252
CD	272.25	1	272.25	0.1573	0.6944
A^2	49,127.36	1	49,127.36	28.38	<0.0001
B^2	73,252.31	1	73,252.31	42.32	<0.0001
C^2	27,737.94	1	27,737.94	16.02	0.0004
D^2	36,057.23	1	36,057.23	20.83	<0.0001
Residual	53,662.83	31	1731.06	–	–
Lack of fit	51,185.16	16	3199.07	19.37	**< 0.0001**
Pure error	2477.67	15	165.18	–	–
Cor total	1.837E + 05	45	–	–	–

Significance values are in bold

where *Y* stands for laccase activity, *A* is pH, *B* is incubation time, *C* is PM and *D* is FM.

Purification of laccase

The crude laccase was partially purified with 80% saturation in ammonium sulfate precipitation. The crude enzyme showed maximum laccase activity of 100 U/mL, and the dialyzed samples showed 210 U/mL. Simultaneously, 13.45 mg/mL of protein was obtained from partially purified laccase. Sodium dodecyl sulfate polyacrylamide gel electrophoresis was carried out to determine the molecular weight of the produced laccase from *Bacillus* sp. utilizing PM and FM as substrates. The results revealed the presence of laccase ~ 63–75 kDa (Fig. 5). The results are consistent with previous studies that reported the range of molecular weight of the laccase (Narayanan et al. 2015).

Effect of pH and temperature on laccase activity

The optimum pH of the purified laccase activity was studied in the range of pH 4–9 and the results are depicted in (Fig. 6a). The maximum activity (93.5%) of the enzyme was observed at pH 7 and considerable activity was observed

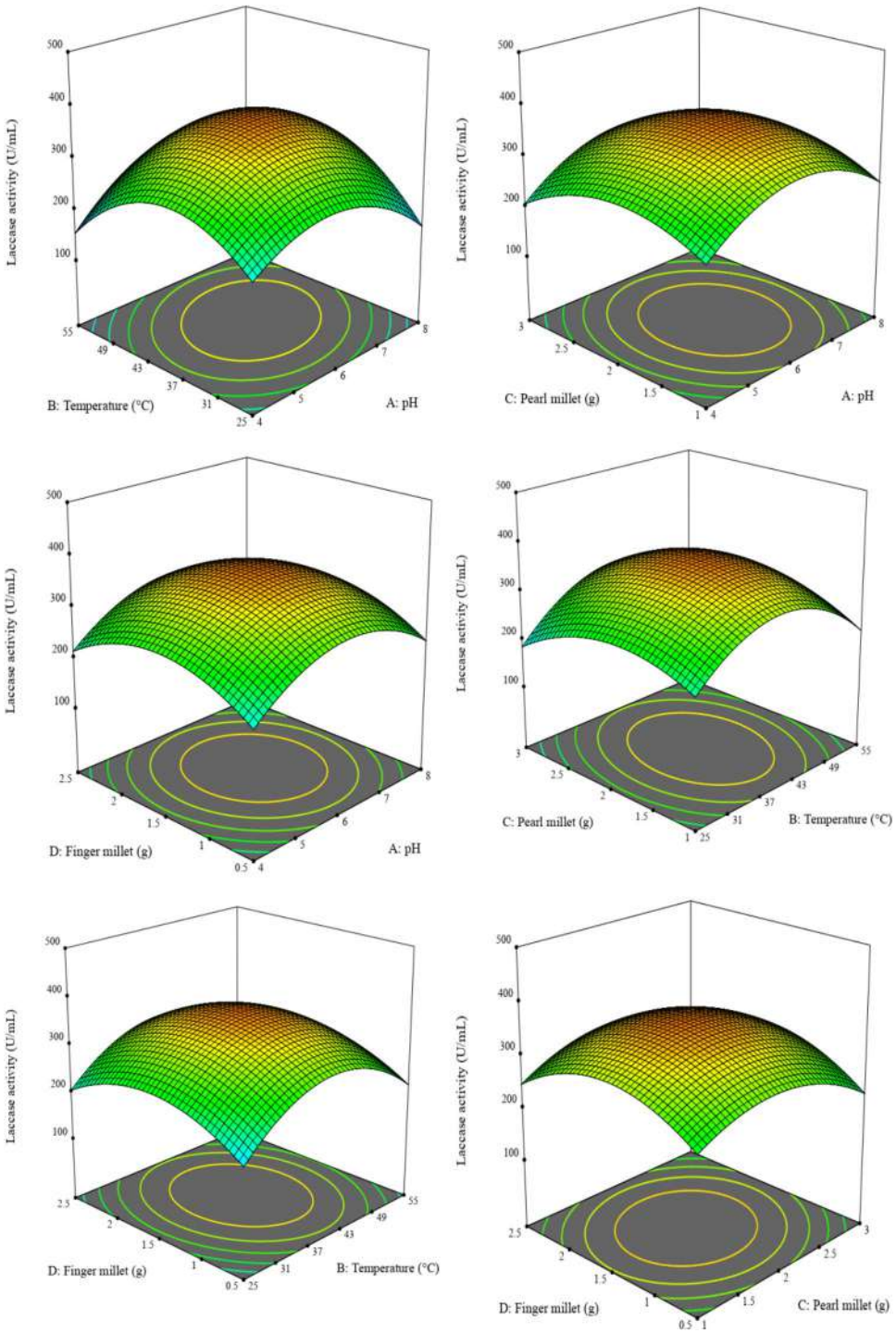


Fig. 4 Response 3D plots of laccase production under BBD optimized conditions with pH, cultivation time, and concentration of pearl millet (PM) and finger millet (FM) as fixed variables

at pH 6 (84%) and 8 (88%). However, the enzyme activity was decreased to less than 60% at high acidic and alkaline pH. Thus, it was concluded that the extracted laccase showed activity in wider pH range (pH 6–8). The results were consistent with previous study reported that the laccase extracted *B. subtilis* MTCC 2414 and *Bacillus* sp. PC-3 exhibited good activity at wide range of pH (Narayanan et al. 2015; Sonica et al. 2015).

The optimum temperature of the purified laccase activity was observed at 40 °C (Fig. 6b). However, a gradual decrease in the enzyme activity was observed with increase in the temperature and it could be due to the denaturation of proteins. The results are in agreement with previous study reported the optimum laccase activity at 40 °C (Mishra and Srivastava 2016; Chauhan et al. 2017). The results indicate the applicability of laccase at different pH and temperature.

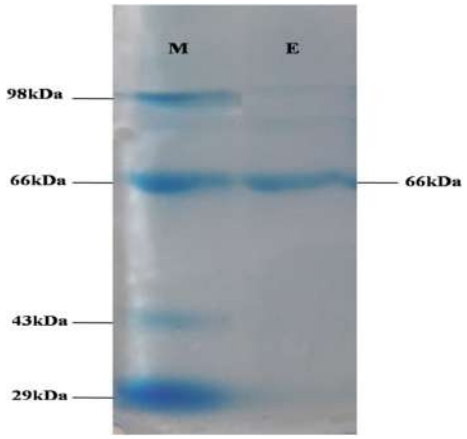


Fig. 5 SDS-PAGE electrophoresis image of partially purified laccase produced by *Bacillus* sp

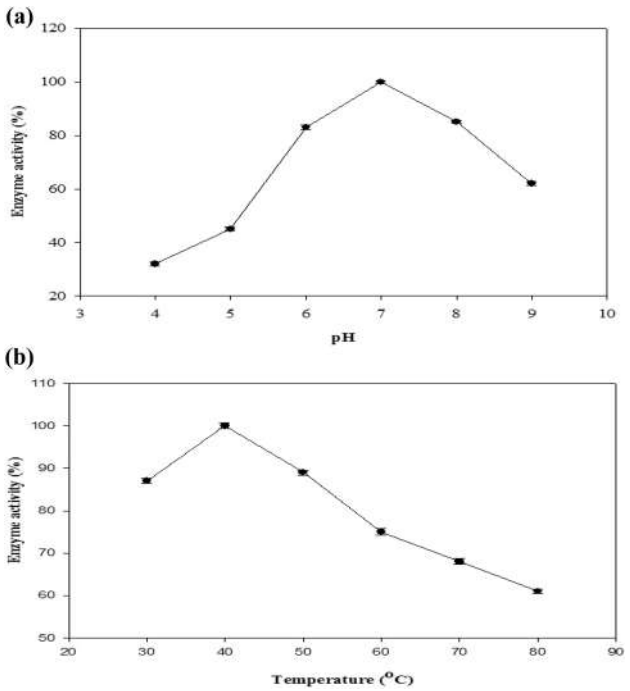


Fig. 6 Activity of partially purified laccase at pH between 4 and 9 (**a**) and temperatures between 30 and 80 °C (**b**)

Degradation of pesticides by laccase and residual analysis through HPLC

High-performance liquid chromatography analysis was performed to determine the residual pesticides and their degradation products. The time course degradation study shows (Fig. 7a–d) that the maximum degradation (Tricel 71.8 ± 3.5 and Phoskill 77.3 ± 3.4%) was observed at day 5. However, minimum degradation of tricel (10.4 ± 2.1%) and phoskill (11.3 ± 2.0%) was observed on the very first day. A gradual increase in the tricel and phoskill degradation was observed according to the incubation time. The results are consistent with previous study that reports increased degradation by increasing the incubation period (Kim et al. 2017). Jin et al. (2016) observed the maximum degradation of chlorpyrifos (~ 80%) after 8 days of incubation. However, our study achieved that 71.8% of tricel (chlorpyrifos) within 5 days of incubation.

The residual analyses of the pesticides were determined using HPLC. The results have been compared with their controls (without laccase). Both the controls (tricel and phoskill) showed the single dominant peaks at a retention time of 2.482 (tricel), 2.608 (phoskill) min, respectively. The control chromatograms did not show any absolute peaks. However, the laccase-treated chromatograms showed their solute peaks at retention time at 5.027 (tricel-laccase treated) and 4.051 (phoskill-laccase treated) min, respectively. The results indicated that the removal of tricel and phoskill was due to biodegradation, not biosorption or any other mechanisms. Fungal laccases showed high activity at the slightly alkaline pH values (7–8) as well as tolerance to high NaCl (> 1 M) concentrations (Molina Guijarro et al. 2009). The degradation of toxic pesticides by *Bacillus* sp. suggests the potential alternative to the fungal laccases in the degradation of pollutants in the ecosystem.

Conclusions

The present study reveals that FM and PM husks could be used as the combined substrates for enhanced laccase production by *Bacillus* sp. PS in SSF. The maximum laccase activity (402 U/mL) was achieved after 96 h of cultivation with PM 2.0 g/L, FM 1.5 g/L of substrates at pH 7.0. The partially purified laccase exhibited a molecular mass of 63–75 kDa and optimum pH 7.0 and optimum temperature 40 °C. In addition, the enzyme demonstrated the effective degradation of tricel (71.8%) and phoskill (77.3%) pesticides. Meshophilic and neutral pH characteristics of the laccase from *Bacillus* sp. PS indicate its applicability in a variety of industrial process as well as decontamination of the pesticide that pollutes soil.

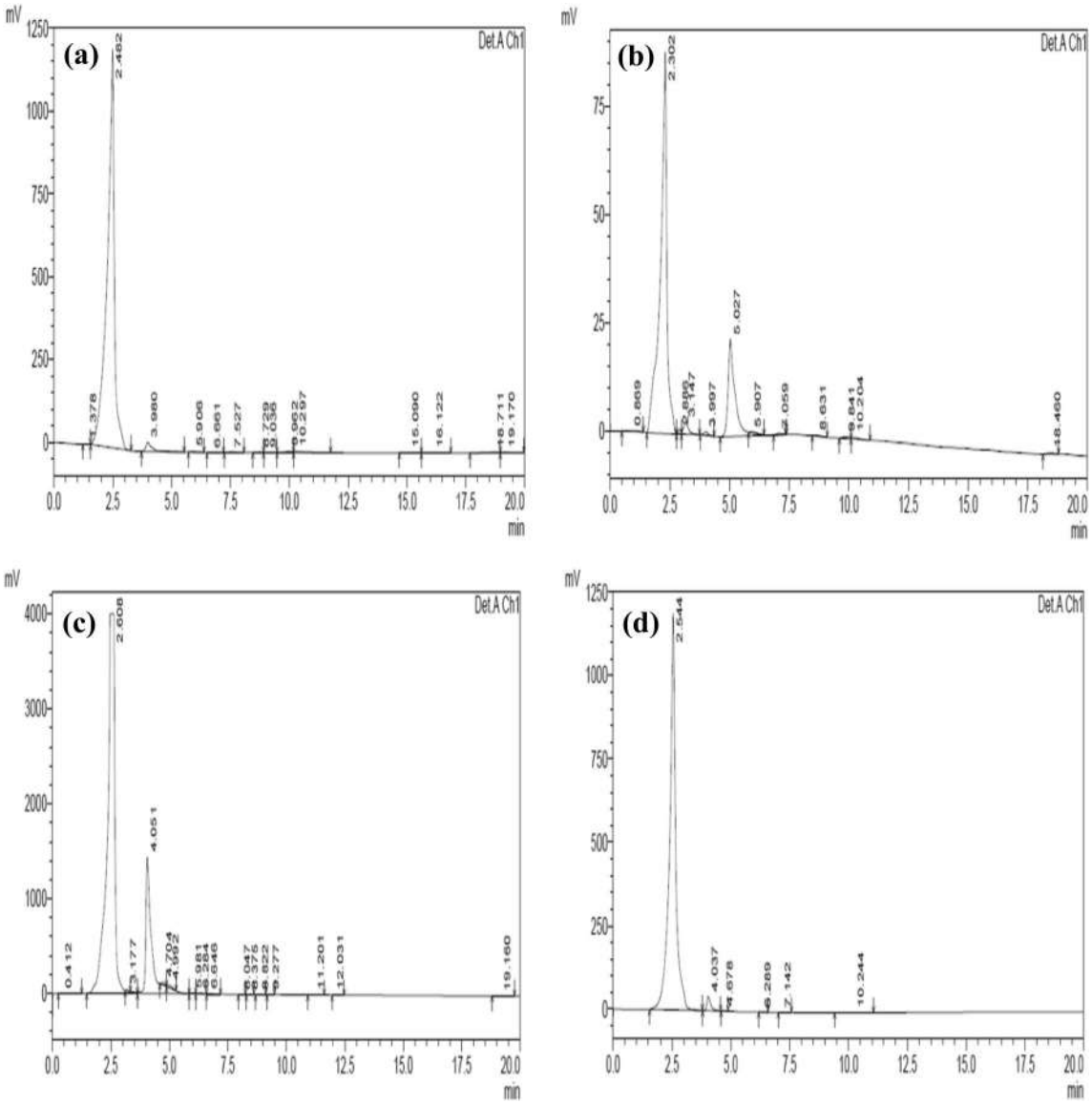


Fig. 7 HPLC chromatograms of **a** control phoskill, **b** laccase-mediated degradation of phoskill, **c** tricel control, **d** laccase-mediated degradation of tricel. Significant peaks were observed with control and degraded samples and compared with the literatures

Acknowledgements This work is partially supported by the Department of Biotechnology, Mahendra Arts and Science College (Autonomous), and the Department of Science and Technology, Government of India (DST-FIST sponsored—Ref. No. SR/FST/College-232/2014).

Compliance with ethical standards

Conflict of interest The authors declare that they do not have any conflict of interest.

References

Amitai G, Adani R, Sod-Moriah G, Rabinovitz I, Vincze A, Leader H, Chefetz B, Leibovitz-Persky L, Friesem D, Hadar Y (1998) Oxidative biodegradation of phosphorothiolates by fungal laccase. FEBS Lett 438:195–200

Audu SS, Ehanwo AA, Aremu MO, Tukura BW, Ambo AI, Usman A (2018) Chemical composition of finger millet (*Eleusine coracana*). Trends Food Sci Tech 3(2):905–908

Azhari AMN, Adiamo OQ, Awad RM, Babiker EE (2017) Changes in chemical composition and total energy as affected by fermentation and/or cooking of pearl millet flour supplemented with Moringa or fenugreek seeds flour. Food Res Int 24(4):1562–1570

Binod P, Satyanagalakshmi K, Sindhu R, Janu KU, Sukumaran RK, Pandey A (2012) Dilute acid pretreatment and enzymatic saccharification of sugarcane tops for bioethanol production. Renew Energy 37:109–116

Chauhan PS, Goradia B, Saxena A (2017) Bacterial laccase: recent update on production, properties and industrial applications. 3 Biotech 7:323

Delcour I, Spanoghe P, Uyttendaele M (2015) Literature review: impact of climate change on pesticide use. Food Res Int 68:7–15

Demissie AG, Kumar A (2014) Production and partial purification of laccase produced by *Bacillus* species isolated from contaminated soil. Int J Emerg Tech Adv Eng 4:17862–17869

Dhiman K, Shirkot P (2015) Bioprospecting and molecular characterization of laccase producing bacteria from paper mills of himachal pradesh. Sect B Biol Sci 85:4

Eduardo T, Bustos-Jaimes I, Le Sylvie B (2003) Potential use of oxidative enzymes for the detoxification of organic pollutants. Appl Catal B Environ 46:1–15

Garlapati D, Chandrasekaran M, Devanesan A, Mathimani T, Pugazhendhi A (2019) Role of cyanobacteria in agricultural and industrial sectors: an outlook on economically important byproducts. Appl Microbiol Biotechnol 103(12):4709–4721

Govarthanan M, Mythili R, Selvankumar T, Kamala-Kannan S, Rajasekar A, Chang Young-Cheol (2016) Bioremediation of heavy metals using an endophytic bacterium *Paenibacillus* sp. RM isolated from the roots of *Tridax procumbens*. 3 Biotech 6:242

Guo H, Lin C, Wang S, Jiang D, Zheng B, Liu Y, Qin W (2017) Characterization of a novel laccase producing *Bacillus* sp. A4 and its application in *Miscanthus* degradation. Bio Resour 12:4776–4794

Jaya Mary J, Karthik C, Smita GR, Kumar S, Prabakar D, Kadirvelu K, Pugazhendhi A (2018) Biological approaches to tackle heavy metal pollution: a survey of literature. J Environ Manage 217:56–70

Jin XH, Heo PS, Hong JS, Kim NJ, Kim YY (2016) Supplementation of dried mealworm (*Tenebrio molitor* larva) on growth performance, nutrient digestibility and blood profiles in weaning pigs. Asian Aust J Anim Sci 29:979–986

Karimi K, Mohammad J, Taherzadeh A (2016) A critical review on analysis in pretreatment of lignocelluloses: degree of polymerization, adsorption/desorption, and accessibility. Bioresour Technol 230:348–356

Kim TH, Kim JS, Sunwoo C, Lee YY (2017) Pretreatment of corn stover by aqueous ammonia. Bioresour Technol 90:39–47

Kuddus M, Joseph B, Ramteke PW (2013) Bacterial laccase: recent update on production, properties and industrial applications. Biocatal Agric Biotechnol 2:333–338

Kumar A, Chauha BM (1993) Chemical composition and utilization of pearl millet sprouts. Mol Nutr Food Res 37(4):356–363

Laemmli UK (1970) Cleavage of structural proteins during the assembly of the head of *Bacteriophage* T4. Nature 227:680–685

Liu J, Tan L, Wang J, Wang Z, Ni H, Li L (2016) Complete biodegradation of chlorpyrifos by engineered *Pseudomonas putida* cells expressing surface immobilized laccases. Chemosphere 157:200–207

Lowry OH, Rosebrough NJ, Farr AL, Randall RJ (1951) Protein measurement with the folin phenol reagent. J Biol Chem 193:265–275

Lu R, Miyakoshi T (2012) Studies on acetone powder and purified rhus laccase immobilized on zirconium chloride for oxidation of phenols. Enzyme Res 8:375309

Margot J, Granier CB, Maillard J, Blánquez P, Barry DA, Holliger C (2013) Bacterial versus fungal laccase: potential for micropollutant degradation. AMB Express 3:6

Mishra SK, Srivastava SK (2016) Production of extracellular laccase from bacterial strain *Bacillus subtilis* MTCC 1039 using different parameter. Biosci Biotech Res 13(3):1645–1650

Molina Guijarro JM, Pérez J, Muñoz Dorado J, Guillén F, Moya R, Hernández M, Arias ME (2009) Detoxification of azo dyes by a novel pH versatile, salt resistant laccase from *Streptomyces ipomoea*. Int Microbiol 12(1):13–21

Narayanan PM, Jackson B, Raj AJ, Sevanan M (2015) Production of extracellular laccase from *Bacillus subtilis* MTCC 2414 using agro residues as a potential substrate. Biochem Res Int 1:9–18

Pizzul L, Pilar Castillo M, Stenstcom J (2009) Degradation of glyphosate and other pesticides by ligninolytic enzymes. Biodegradation 20:751–759

Rodriguez Couto S, Toca Herrera JL (2006) Industrial and biotechnological applications of laccases: a review. Biotechnol Adv 24:500–513

Selvam K, Govarthanan M, Kamala-Kannan S, Govindharaju M, Senthilkumar B, Selvankumar T, Sengottaiyan A (2014) Process optimization of cellulase production from alkali-treated coffee pulp and pineapple waste using *Acinetobacter* sp. TSK-MASC. RSC Adv 4:13045

Selvam K, Selvankumar T, Radhika R, Srinivasan P, Sudhakar C, Senthilkumar B, Govarthanan M (2016a) Enhanced production of amylase from *Bacillus sp*. Using groundnut shell and cassava waste as a substrate under process optimization: waste to wealth approach. Biocatal Agric Biotechnol 7:250–256

Selvam K, Govarthanan M, Senthilkumar B, Senbagam D, Selvankumar T, Kamala-Kannan S, Sudhakar C (2016b) Optimization of protease production from surface modified coffee pulp waste and corncobs using *Bacillus* sp. by SSF. 3 Biotech 6:167

Selvankumar T, Radhika R, Mythili R, Arunprakash S, Srinivasan P, Govarthanan M, Kim Hyunook (2017) Isolation, identification and characterization of arsenic transforming exogenous endophytic *Citrobacter* sp. RPT from roots of *Pteris vittata*. 3 Biotech 7:264

Sharma N, Kalra KL, Oberoi HS, Bansal S (2017) Optimization of fermentation parameters for production of ethanol from kinnow waste and banana peels by simultaneous saccharification and fermentation. Indian J Microbiol 47:310–316

Sharma V, Ayothiraman S, Dhakshinamoorthy V (2018) Production of highly thermo–tolerant laccase from novel thermophilic bacterium *Bacillus* sp. PC–3 and its application in functionalization of chitosan film. J Biosci Bioeng 127(6):672–678

Sonica S, Prince S, Nancy G, Prakram S, Chauhan P, Naveen G (2015) An extracellular thermo alkali stable laccase from *Bacillus tequilensis* SN4, with a potential to biobleach softwood pulp. 3 Biotech 5:175–185

Upadhyay P, Shrivastava R, Agrawal PK (2016) Bioprospecting and biotechnological applications of fungal laccase. 3 Biotech 6:1–12

Wang Z, Denisi M, Vaida P, Chen B, Moshammerf K, Mohamed YS, Wang HS, Sioudh S, Rajih MA, Hooinghausi KK, Hansenf N, Dagautj P, Leone SR, Mani Sarathya S (2017) New insights into the low temperature oxidation of 2–methylhexane. Proc Combust Inst 36:373–382

Wolfenden RS, Wilson RL (1982) Radicalcations as reference chromogens in the kinetic studies of one–electron transfer reactions: pulse radiolysis studies of 2, 2′–azinobis–(3–ethylbenzthiazoline–6–sulphonate). J Chem Soc Perkin Trans 2:805–812

Zhao D, Zhang X, Cui D, Zhao M (2012) Characterization of a novel white laccase from the *Deuteromycete* fungus *Myrothecium verrucaria* NF05 and its decolourisation of dyes. PLoS ONE 7:38817

Zhou N, Li D, Wu S, He S, Chen Y, Bai Y, Zhou M, He J, Wang C (2015) Acceleration effect of sodium selenite on yeast growth and fermentative capability. J Gen Appl Microbiol 61:27–30

ScienceDirect

Bioorganic Chemistry
Volume 88, July 2019, 102970

Short communication

Phytosynthesis of silver nanoparticles using *Mangifera indica* flower extract as bioreductant and their broad-spectrum antibacterial activity

Fuad Ameen [a], P. Srinivasan [b], T. Selvankumar [b], S. Kamala-Kannan [c], S. Al Nadhari [d], A. Almansob [a], T. Dawoud [a], M. Govarthanan [e]

Show more

Outline | Share Cite

https://doi.org/10.1016/j.bioorg.2019.102970

Get rights and content

Highlights

- Silver nanoparticles were synthesized successfully using Mango flower extract.
- This method is rapid, simple and cost effective.
- Structural and optical analysis revealed the nature of AgNPs.
- The AgNPs effectively inhibit the growth of broad-spectrum of antibacterial activity.

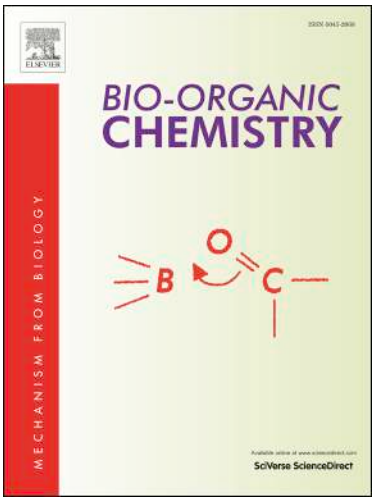
Abstract

The present study focused on the evaluation of antibacterial property of silver nanoparticles (AgNPs) synthesized using mango flower extract. The morphology of the synthesized AgNPs was observed under transmission electron microscopy and the particles have shown spherical shape in the range of 10–20 nm. X-ray powder diffraction analysis confirmed the crystalline nature of the AgNPs. The atomic percentage of the Ag element in the nanoparticles was about 7.58% which is greater than the other elements present in the sample. The AgNPs showed extensive lethal effect on both Gram-positive (*Staphylococcus* sp.) and Gram-negative (*Klebsiella* sp., *Pantoea agglomerans*, and *Rahnella* sp.) bacteria. The extensive lethal effect of AgNPs

P.G. COLLEGE OF ARTS & SCIENCE NAMAKKAL 637 206

PRINCIPAL
PGP College of Arts and Science
Namakkal

Accepted Manuscript



Phytosynthesis of silver nanoparticles using *Mangifera indica* flower extract as bioreductant and its broad-spectrum antibacterial activity

Fuad Ameen, P. Srinivasan, T. Selvankumar, S. Kamala-Kannan, S. Al Nadhari, A. Almansob, T. Dawoud, M. Govarthanan

PII: S0045-2068(19)30391-8
DOI: https://doi.org/10.1016/j.bioorg.2019.102970
Article Number: 102970
Reference: YBIOO 102970

To appear in: *Bioorganic Chemistry*

Received Date: 13 March 2019
Revised Date: 26 April 2019
Accepted Date: 30 April 2019

Please cite this article as: F. Ameen, P. Srinivasan, T. Selvankumar, S. Kamala-Kannan, S. Al Nadhari, A. Almansob, T. Dawoud, M. Govarthanan, Phytosynthesis of silver nanoparticles using *Mangifera indica* flower extract as bioreductant and its broad-spectrum antibacterial activity, *Bioorganic Chemistry* (2019), doi: https://doi.org/10.1016/j.bioorg.2019.102970

This is a PDF file of an unedited manuscript that has been accepted for publication. As a service to our customers we are providing this early version of the manuscript. The manuscript will undergo copyediting, typesetting, and review of the resulting proof before it is published in its final form. Please note that during the production process errors may be discovered which could affect the content, and all legal disclaimers that apply to the journal pertain.

ACCEPTED MANUSCRIPT

Phytosynthesis of silver nanoparticles using *Mangifera indica* flower extract as bioreductant and its broad-spectrum antibacterial activity

Fuad Ameen[1], P. Srinivasan[2], T. Selvankumar[2], S. Kamala-Kannan[3], S. Al Nadhari[4], A. Almansob[1], T. Dawoud[1], M. Govarthanan[5]*,

[1]Department of Botany and Microbiology, College of Science, King Saud University, Riyadh 11451, Saudi Arabia

[2]PG & Research Department of Biotechnology, Mahendra Arts and Science College (Autonomous), Kalippatti, Namakkal - 637501, Tamil Nadu, India

[3]Division of Biotechnology, College of Environmental and Bioresource Sciences, Chonbuk National University, Iksan - 54596, South Korea

[4]Department of plant protection, College of Agriculture, King Saud University, Riyadh, Saudi Arabia.

[5]Department of Environmental Engineering, University of Seoul, Seoul 02504, South Korea

*Corresponding author: M. Govarthanan, E-mail: gova.muthu@gmail.com; ORCID iD: https://orcid.org/0000-0001-8725-3059

ACCEPTED MANUSCRIPT

Abstract

The present study focused on the evaluation of antibacterial property of silver nanoparticles (AgNPs) synthesized using mango flower extract. The morphology of the synthesized AgNPs was observed under transmission electron microscopy and the particles have shown spherical shape in the range of 10-20 nm. X-ray powder diffraction analysis confirmed the crystalline nature of the AgNPs. The atomic percentage of the Ag element in the nanoparticles was about 7.58% which is greater than the other elements present in the sample. The AgNPs showed extensive lethal effect on both Gram-positive (*Staphylococcus* sp.) and Gram negative (*Klebsiella* sp*., Pantoea agglomerans,* and *Rahnella* sp.) bacteria. The extensive lethal effect of AgNPs against clinically important pathogens demonstrated that the mango flower mediated AgNPs could be applied as potential antibacterial agent to control the bacterial population in the respective industries.

Keywords: *Antibacterial; Bacterial infections; Broad-spectrum; Mango flower; Silver nanoparticles*

ACCEPTED MANUSCRIPT

1. Introduction

Bacterial contaminations remain as a one of the most severe issues in medical devices, water treatment and food industries [1]. Both Gram-positive and Gram-negative bacteria are the common contaminants and cause diseases in human beings [2, 3]. Several antibacterial agents are available in the market to control bacterial contaminations in various products. However, these available antibacterial agents have numerous drawbacks such as, reduced solubility, high cost, toxicity and side effects [4]. Thus, there is much interest to investigate safe and effective antibacterial compounds [5], [6]. Currently, in several products, such as in disinfectants, the active substance used is metal nanoparticles, silver nanoparticles being one of the most efficient against pathogenic bacteria [7]. Silver nanoparticles (AgNPs) synthesis has gained much attention because they potentially offer a solution to overcome bacterial contaminations and/or infections in an effective and safe approach.

Several physico-chemical routes, including electro-chemical [8], photochemical [9], and radiation methods [10] are commonly used to produce AgNPs. These methods, however, have disadvantages due to environmental contamination or toxic residues in the nanoparticles [11]. Therefore, new environmentally friendly techniques, which use biological organisms to mediate the nanoparticle synthesis, are still searched.

Efficient biological substrates used in the production of AgNPs are various, for instance, plant extracts [12], [13], microorganisms [14], algae [15], panchakavya [16], oilcake [17], vegetable waste [18], seaweed [19], enzymes [20], and metabolites of arthropods [21]. It has been generally suggested that plant based materials are promising substrates for the AgNPs synthesis because the process is simple to scale up [22].

ACCEPTED MANUSCRIPT

Mango (*Mangifera indica* L.) is an important tropical and sub-tropical crop belonging to the *Anacardiaceae* family [23], [24]. The leaves of this native South-Asian species have various properties, including antidiabetic, antimicrobial and anti-inflammatory activities [25]. AgNPs have been successfully synthesized using mango peel [26] and leaves [27]. Mango flowers have not been reported for their efficiency of AgNPs synthesis and its broad-spectrum antibacterial activity. Hence, the study aimed (i) to produce AgNPs using a mango flower extract, (ii) to characterize the biosynthesized AgNPs using various spectroscopic techniques, and (iii) to measure their antibacterial property.

2. Methods

2.1. Plant material

Analytical grade chemicals were used, $AgNO_3$ was purchased from Sigma-Aldrich Chemicals (USA). Fresh and healthy flowers of *M. indica* were collected from Mallasamudram, Tamil Nadu, India. The collected flowers were first rinsed with running tap water and then with autoclaved water until no dust particles remained. The flowers (25 g) were mixed with autoclaved water (250 ml), grinded using a juicer, filtered through Whatman No.1 filter paper and stored at 4˚C for the AgNPs synthesis.

2.2. AgNPs biosynthesis

AgNPs synthesis was carried out as described in Govarthanan et al. [15]. An aliquot of 4 ml of the prepared extract was mixed with 96 ml of $AgNO_3$ (1 mM) and mixed with vigorous magnetic stirring for 30 min until the color change from pink to brown indicated the synthesis. The mixture was centrifuged at 3000 rpm for 15 min, the pellet was dispersed in double-distilled water and dried in lyophilizer to be used for further studies.

2.3. Spectroscopic characterization

ACCEPTED MANUSCRIPT

The formation AgNPs were initially screened by UV–vis spectrophotometer (Elico-SL 164) at 400-800 nm. The purity and the crystalline nature of the AgNPs were determined using X-ray powder diffraction (XRD, XPERT-Pro diffractometer using Cu-Ka radiation) by scanning the region of 2θ from 10 to 80° at 0.04°/min with a time constant of 2 s. The functional groups of the AgNPs were recorded using a Fourier transform infrared spectroscopy (FT-IR) (Perkin-Elmer FT-IR spectrophotometer, IR Affinity-1S), diffuse reflectance mode, resolution 4 particles cm^{-1} in KBr pellets. The AgNPs were analysed for the morphology and size using transmission electron microscopy (TEM, FEI Tecnai TF 20 high resolution) and for the elemental composition using a scanning electron microscopy coupled with energy-dispersive spectroscopy (SEM–EDS; Jeol JSM 6390).

2.4. Antibacterial activity

Four human pathogenic bacterial strains, namely *Pantoea agglomerans* (Accession Number: KR296735), *Rahnella* sp. (Accession Number: KX656894), *Staphylococcus* sp. (Accession Number: KC688883), *Klebsiella sp.* (Accession Number: KC899845) were used to study the antibacterial activity of the AgNPs according to Govarthanan et al. [16]. The pathogens were cultured in nutrient broths with different AgNPs concentrations (2.5, 5, 7.5 and 10 mM). At regular intervals (0–48 h), the bacterial growth was observed using an UV-vis spectrophotometer at 600 nm. The inhibition of the growth was calculated as a percentage according to Elegbede et al. [28] as follows:

$$\% \text{ Growth inhibition} = \{(\text{Absorbance}_{control} - \text{Absorbance}_{Test}) / \text{Absorbance}_{control}\} \times 100\%$$

3. Results and discussion

The green synthesis of AgNPs using plants as a bioreductants has attracted over other biological sources, because plants are more suitable for a large-scale synthesis. In this study, a mango flower extract was used. The formation of AgNPs was confirmed by the color change

ACCEPTED MANUSCRIPT

of pink to brown and the UV-Visible spectroscopy analysis (Fig.1). A characteristic absorption peak was observed around 450 nm, which is attributed to the surface plasmon resonance (SPR) of AgNPs [29], [30].

The TEM image shows the spherical shape of the AnNPs, the size ranging from 10 to 20 nm (Fig 2a). Fig. 2(b) shows the SEM-EDS pattern of AgNPs. The atomic percentage of Ag was 7.58 % (Table 1). This is greater than the other elements present in the sample. The sharp peak at ~3 keV confirms the presence of elemental silver in its pure form and consistent with previous reports using other biological materials [31].

The secondary metabolites responsible for the AgNPs synthesis were revealed by FT-IR spectrum that showed a small peak at 3734 cm^{-1} assigned to ―OH stretching vibrations (Fig 3). The peak at 2950 cm^{-1} indicated the presence of alkane ―CH stretching. The band at 2350 cm^{-1} could be assigned to the aliphatic C―H stretching vibration. The peaks at 1530, 1030 and 690 cm^{-1} correspond to the C―O and N=O stretches of the ester, and to nitro groups, respectively. As indicated by the FT-IR analysis, the phyto-chemicals, such as alkaloids, flavonoids, amino acids and proteins seem to be responsible for the synthesis of AgNPs. These functional groups play an important role in the stability and capping of the AgNPs. Ajitha et al. [32] reported that polyphenols and other secondary metabolites present in the plant extract mediate the reduction of Ag ions and the presence of Ag –O groups on the surface of AgNPs. Guan et al. [12] reported that the biosynthesized AgNPs are in the form of a face-centered cubic crystal nature. This form was indicated by the XRD spectrum of the AgNPs that showed strong diffraction peaks corresponding to 111, 200, 220 and 311 sets of lattice planes (Fig. 4).

The AgNPs showed antibacterial activity against Gram-negative bacteria *Klebsiella* sp., *P.*

ACCEPTED MANUSCRIPT

agglomerans, and *Rahnella* sp. at 10 mM of AgNPs (Fig. 5). The calculated inhibition percentages were 65.9 %, 62.1%, and 51.4%, respectively (Fig. 5). Statistical analysis showed significant differences ($P < 0.05$) were observed in the different AgNPs concentration groups. Lateef et al. [33] observed that *Petiveria alliacea* L. leaf extract mediated AgNPs inhibited 100 % of the growth of Gram-negative *Klebsiella pneumonia* and Gram-positive *Staphylococcus aureus*. However, their used a relatively high concentration compared to us, 150 mM of AgNPs. In our studies, 10 mM AgNPs inhibited Gram-positive *Staphylococcus* sp. 39.4%. The inhibitory capabilities of AgNPs has been associated with the initiation of the attack on the cell wall resulting in the leakage of the cytoplasmic content and ultimately leading to the cell death [28]. Several other mechanisms have been reported. The formation of reactive oxygen species (ROS), sulph-hydryl group bonding between Ag^{+} ions, denaturation of bacterial proteins and cell wall damage also lead to lethal conditions [31], [34].

4. Conclusion

We investigated an eco-friendly, simple and rapid green way to the synthesize AgNPs using an extract derived from mango flowers. The resulted AgNPs were spherical in shape with diameter of 10-20 nm. The lethal effect of the AgNPs on clinically important bacterial strains was observed; *P. agglomerans*, *Rahnella* sp., *Staphylococcus* sp., and *Klebsiella* sp were inhibited by the AgNPs. This study explores the use mango flower extract in the AgNPs synthesis towards broad-spectrum of antibacterial applications in the field of clinical microbiology.

Conflicts of interest statement

The authors declared that there are no conflicts of interest.

Acknowledgement

ACCEPTED MANUSCRIPT

This paper was supported by the Deanship of Scientific Research at the King Saud University for funding the research (Research group NO (RGP-1438-029).

References

[1] N. Talebian, M. Doudi, M. Kheiri, The anti-adherence and bactericidal activity of sol–gel derived nickel oxide nanostructure films: solvent effect, J. Sol-Gel. Sci. Technol. 69 (2014) 177–182.

[2] M. Jahan, R.A. Holley, Transfer of antibiotic resistance from *Enterococcus faecium* of fermented meat origin to *Listeria monocytogenes* and *Listeria innocua*, Lett. Appl. Microbiol. 62 (2016) 304–310.

[3] E.R. Wyrsch, P. Roy Chowdhury, T.A. Chapman, I.G. Charles, J.M. Hammond, S.P. Djordjevic, Genomic microbial epidemiology is needed to comprehend the global problem of antibiotic resistance and to improve pathogen diagnosis, Front. Microbiol. 7 (2016) 843.

[4] O.I. Parisi, L. Scrivano, M.S. Sinicropi, F. Puoc, Polymeric nanoparticles constructs as devices for antibacterial therapy, Curr. Opin. Pharmacol. 36 (2017) 72–77.

[5] M. Rai, A. Yadav, A. Gade, Silver nanoparticles as a new generation of antimicrobials, Biotechnol. Adv. 27 (2009) 76–83.

[6] Y. Cui, Y.Y. Zhao, Y. Tian, W. Zhang, X. Y. Lu, X. Y. Jiang, The molecular mechanism of action of bactericidal gold nanoparticles on *Escherichia coli,* Biomaterials, 33 (2012) 2327–2333.

[7] A. Balamurugan, G. Balossier, D. Laurent-Maquin, S. Pina, A. H. S. Rebelo, J. Faure, J. M. F. Ferreira, An in vitro biological and anti-bacterial study on a sol-gel derived silver-incorporated bioglass system, Dent. Mater. 24 (2008) 1343–1351.

[8] B. Yin, H. Ma, S. Wang, S. Chen, Electrochemical synthesis of silver nanoparticles under protection of poly (N-vinylpyrrolidone), J. Phys. Chem. B. 107 (2003) 8898–8904.

ACCEPTED MANUSCRIPT

[9] A. Callegari, D. Tonti, M. Chergui, Photochemically grown silver nanoparticles with wavelength-controlled size and shape, Nano Lett. 3 (2003) 1565–1568.

[10] N.M. Dimitrijevic, D.M. Bartels, C.D. Jonah, K. Takahashi, T. Rajh, Radiolytically induced formation and optical absorption spectra of colloidal silver nanoparticles in supercritical ethane, J. Phys. Chem. B. 105 (2001) 954–959.

[11] K. J. Lee, S. H. Park, M. Govarthanan, P. H. Wang, Y. S. Seo, M. Cho, W. H. Lee, J. Y. Lee, S. Kamala-Kannan, B.T. Oh, Synthesis of silver nanoparticles using cow milk and their antifungal activity against phytopathogens, Mater. Lett. 105 (2013) 128–131.

[12] Q. Guan, C. Xia, W. Li, Bio-friendly controllable synthesis of silver nanoparticles and their enhanced antibacterial property. Catal. Today. 327 (2019) 196-202.

[13] M. Behravan, A. H. Panahi, A. Naghizadeh, M. Ziaee, R. Mahdavi, A. Mirzapour, Facile green synthesis of silver nanoparticles using *Berberis vulgaris* leaf and root aqueous extract and its antibacterial activity, Int. J. Biol. Macromol. 124 (2019) 148–154.

[14] S. V. Otari, R. M. Patil, N. H. Nadaf, S. J. Ghosh, S. H. Pawar, Green synthesis of silver nanoparticles by microorganism using organic pollutant: its antimicrobial and catalytic application, Environ Sci Pollut Res. 21 (2014) 1503–1513.

[15] M. Govarthanan, T. Selvankumar, R. Mythili, C. Sudhakar, K. Selvam, Biosynthesis of silver nanoparticles from *Spirulina* microalgae and its antibacterial activity, Environ Sci Pollut Res. 24 (2017) 19459–19464.

[16] M. Govarthanan, T. Selvankumar, K. Manoharan, R. Rathika, K. Shanthi, K. J. Lee, M. Cho S. Kamala-Kannan, B.T. Oh, Biosynthesis and characterization of silver nanoparticles using panchakavya, an Indian traditional farming formulating agent, Int J Nanomedicine 9 (2014) 1593–1599.

[17] M. Govarthanan, Y. S. Seo, K. J. Lee, I. B. Jung, H. J. Ju, J. S. Kim, M. Cho, S. Kamala-

ACCEPTED MANUSCRIPT

Kannan, B.T. Oh, Low-cost and eco-friendly synthesis of silver nanoparticles using coconut (*Cocos nucifera*) oil cake extract and its antibacterial activity, Artif Cells Nanomed Biotechnol 44 (2016) 1878–1882.

[18] R. Mythili, T. Selvankumar, S. Kamala-Kannan, C. Sudhakar, F. Ameen, A. A. Sabri, K. Selvam, M. Govarthanan, H. Kim, Utilization of Vegetable waste for silver nanoparticles synthesis and its antibacterial activity, Mater. Lett. 225 (2018) 101–104.

[19] R. Manikandan, R. Anjali, M. Beulaja, N.M. Prabhu, A. Koodalingam, G. Saiprasad, M. Arumugam, Synthesis, characterization, anti-proliferative and wound healing activities of silver nanoparticles synthesized from *Caulerpa scalpelliformis.* Process Biochem. 79 (2019) 135–141.

[20] A. Lateef, I. A. Adelere, E. B. Gueguim-Kana, T. B. Asafa, L. S. Beukes, Green synthesis of silver nanoparticles using keratinase obtained from a strain of *Bacillus safensis* LAU 13, Int. Nano Lett. 5 (2015) 29–35.

[21] A**.** Lateef, S.A. Oladejo, M.A. Azeez, T.B. Asafa, A. Akinboro, I.C. Oladipo, E.B. Gueguim-Kana, L.S. Beukes, Cobweb as novel biomaterial for the green and eco-friendly synthesis of silver nanoparticles, Appl. Nanosci. 6 (2016) 863–874.

[22] M. F. Zayed, W. H. Eisa, A. A. Shabaka, *Malva parviflora* extract assisted green synthesis of silver nanoparticles, Spectrochim. Acta A. 98 (2012) 423–428.

[23] J. C. Barreto, M. T. S. Trevisan, W. E. Hull, G. Erben, E. S. de Brito, B. Pfundstein, G. Würtele, B. Spiegelhalder, R. W. Owen, Characterization and quantitation of polyphenolic compounds in bark, kernel, leaves, and peel of mango (*Mangifera indica* L.), J. Agric. Food Chem. 56 (2008) 5599–5610.

[24] J. Pan, X. Yi, S. Zhang, J. Cheng, Y. Wang, C. Liu, X. He, Bioactive phenolics from mango leaves (*Mangifera indica* L.), Ind. Crop. Prod. 111 (2018) 400–406.

ACCEPTED MANUSCRIPT

[25] Y.S. Lin, S.S. Lee, Flavonol glycosides with α-glucosidase inhibitory activities and new flavone C-diosides from the leaves of *Machilus konishii*, Helv. Chim. Acta. 97 (2014) 1672–1682.

[26] N. Yang, W. H. Li, Mango peel extract mediated novel route for synthesis of silver nanoparticles and antibacterial application of silver nanoparticles loaded onto non-woven fabrics, Ind. Crop. Prod. 48 (2013) 81–88.

[27] D. Sundeep, T. Vijaya Kumar, P. S. Subba Rao, R. V. S. S. N. Ravikumar, A. Gopala Krishna, Green synthesis and characterization of Ag nanoparticles from *Mangifera indica* leaves for dental restoration and antibacterial applications, Prog. Biomater. 6 (2017) 57–66.

[28] J. A. Elegbede,· A. Lateef,· M. A. Azeez,· T. B. Asafa,· T. A. Yekeen, I. C. Oladipo, D. A. Aina, L. S. Beukes, E. B. Gueguim-Kana, Biofabrication of gold nanoparticles using xylanases through valorization of corncob by *Aspergillus niger* and *Trichoderma longibrachiatum*: Antimicrobial, antioxidant, anticoagulant and thrombolytic activities. Waste and Biomass Valorization, https://doi.org/10.1007/s12649-018-0540-2.

[29] P. Velmurugan, M. Cho, S. S. Lim, S. K. Seo, H. Myung, K. S. Bang, S. Sivakumar, M. Cho, B.T. Oh, Phytosynthesis of silver nanoparticles by *Prunus yedoensis* leaf extract and their antimicrobial activity, Mater. Lett. 138 (2015) 272–275.

[30] A. Aravinthan, M. Govarthanan, K. Selvam, et al., Sunroot mediated synthesis and characterization of silver nanoparticles and evaluation of its antibacterial and rat splenocyte cytotoxic effects, Int. J. Nanomed. 10 (2015) 1977–1983.

[31] M. Gomathi, P. V. Rajkumar, A. Prakasam, K. Ravichandran, Green synthesis of silver nanoparticles using *Datura stramonium* leaf extract and assessment of their antibacterial activity, Resource-Efficient Technologies, 3 (2017) 280–284.

ACCEPTED MANUSCRIPT

[32] B. Ajitha, Y.A.K. Reddy, P.S. Reddy, Green synthesis and characterization of silver nanoparticles using *Lantana camara* leaf extract, Mater. Sci. Eng. C. 49 (2015) 373–381.

[33] A. Lateef, B. I. Folarin, S.M. Oladejo, P.O. Akinola, L.S. Beukes, E.B. Gueguim-Kana, Characterization, antimicrobial, antioxidant, and anticoagulant activities of silver nanoparticles synthesized from *Petiveria alliacea* L. leaf extract. Prep. Biochem. Biotechnol. doi: 10.1080/10826068.2018.1479864.

[34] R. S. Patil, M. R. Kokate, S. S. Kolekar, Bioinspired synthesis of highly stabilized silver nanoparticles using *Ocimum tenuiflorum* leaf extract and their antibacterial activity, Spectrochim. Acta Mol. Biomol. Spectrosc. 91 (2012) 234–238.

Figure legends

Fig. 1. UV-Vis spectroscopy analysis of AgNPs

Fig. 2 (a). TEM image of bigenic AgNPs (b) EDS of AgNPs obtained from flower extract of *Mangifera indica*

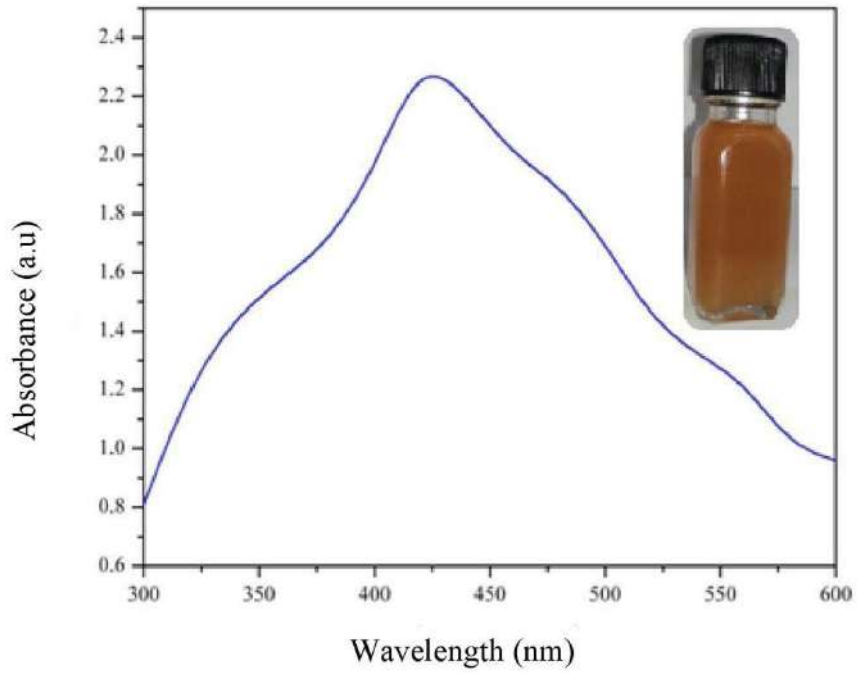
Fig. 3. FT-IR spectra of *purified* AgNPs.

Fig. 4. X-Ray Diffraction of AgNPs obtained from *Mangifera indica* flower extract.

Fig. 5. Antibacterial activity of synthesized AgNPs, (a) *Klebsiella* sp., (b) *P. agglomerans*, (c) *Rahnella* sp., and (d) *Staphylococcus* sp.

ACCEPTED MANUSCRIPT

Fig.1



ACCEPTED MANUSCRIPT

ACCEPTED MANUSCRIPT

Fig. 2 (a)

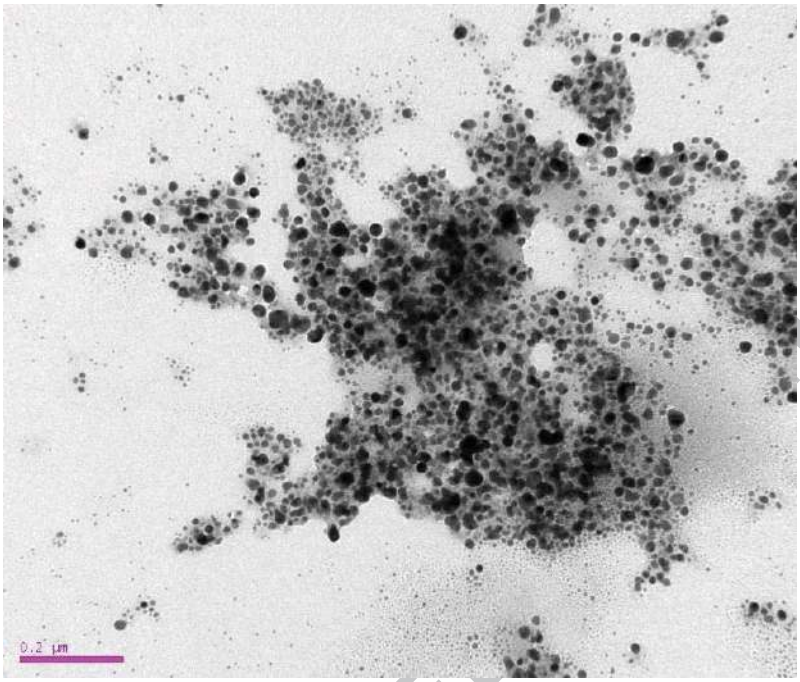


Fig. 2 (b)

ACCEPTED MANUSCRIPT

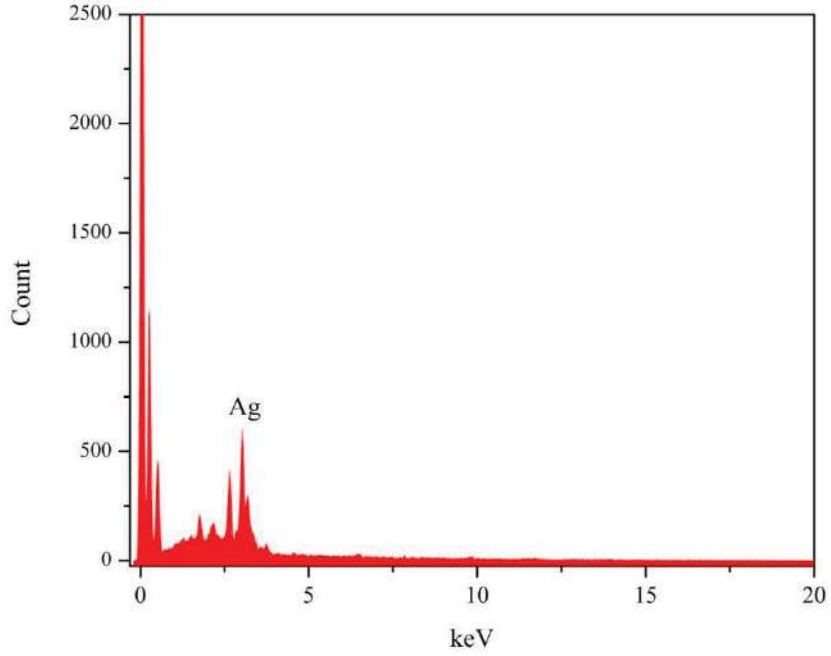

Count
keV
Ag
2500
2000
1500
1000
500
0
0
5
10
15
20

Fig. 3

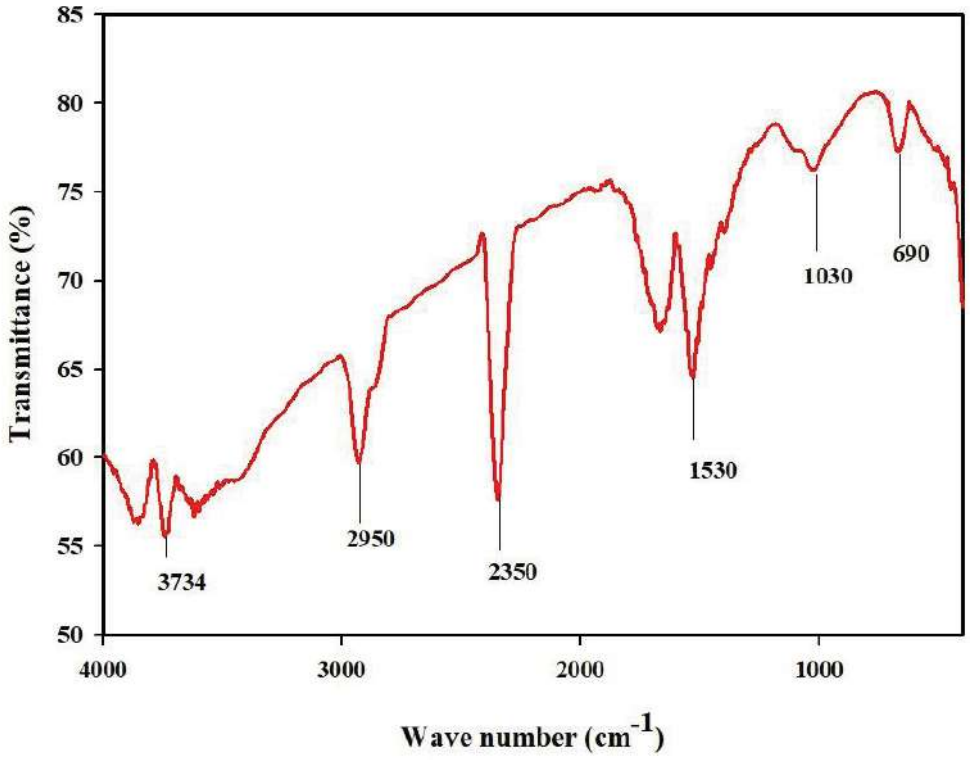

Transmittance (%)
Wave number (cm-1)
3734
2950
2350
1530
1030
690
85
80
75
70
65
60
55
50
4000
3000
2000
1000

Fig. 4

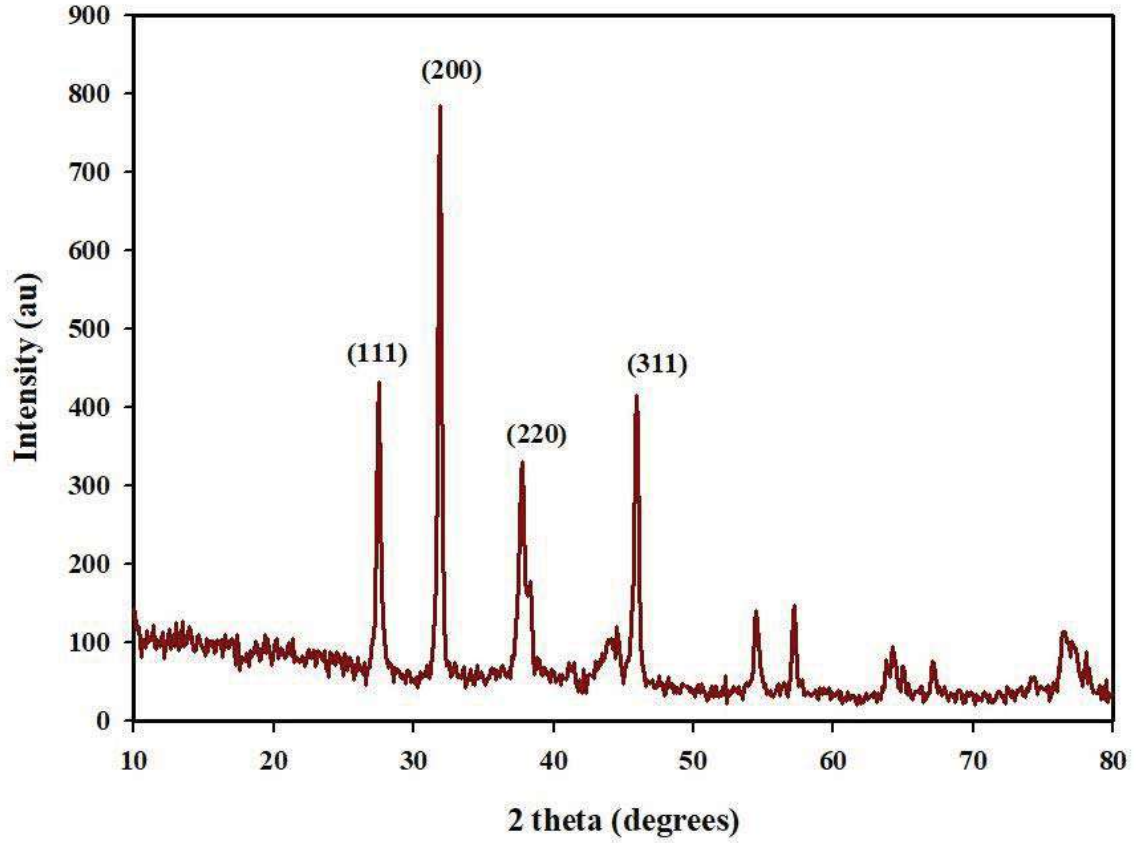
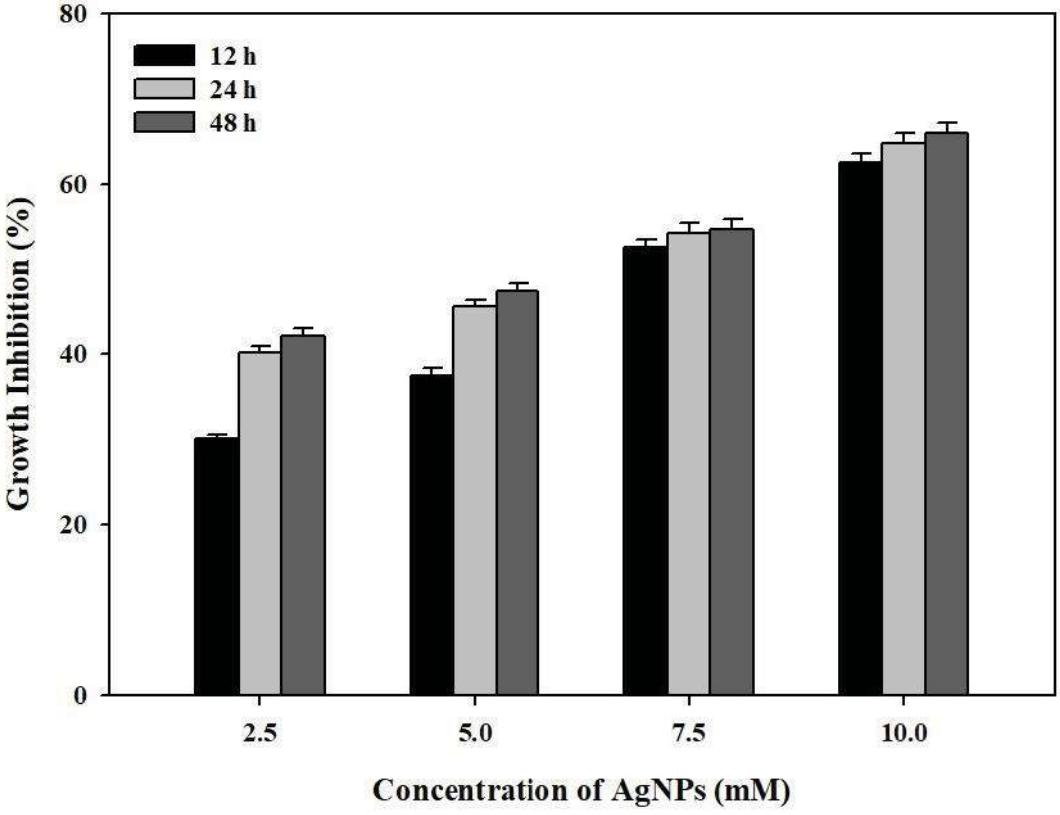
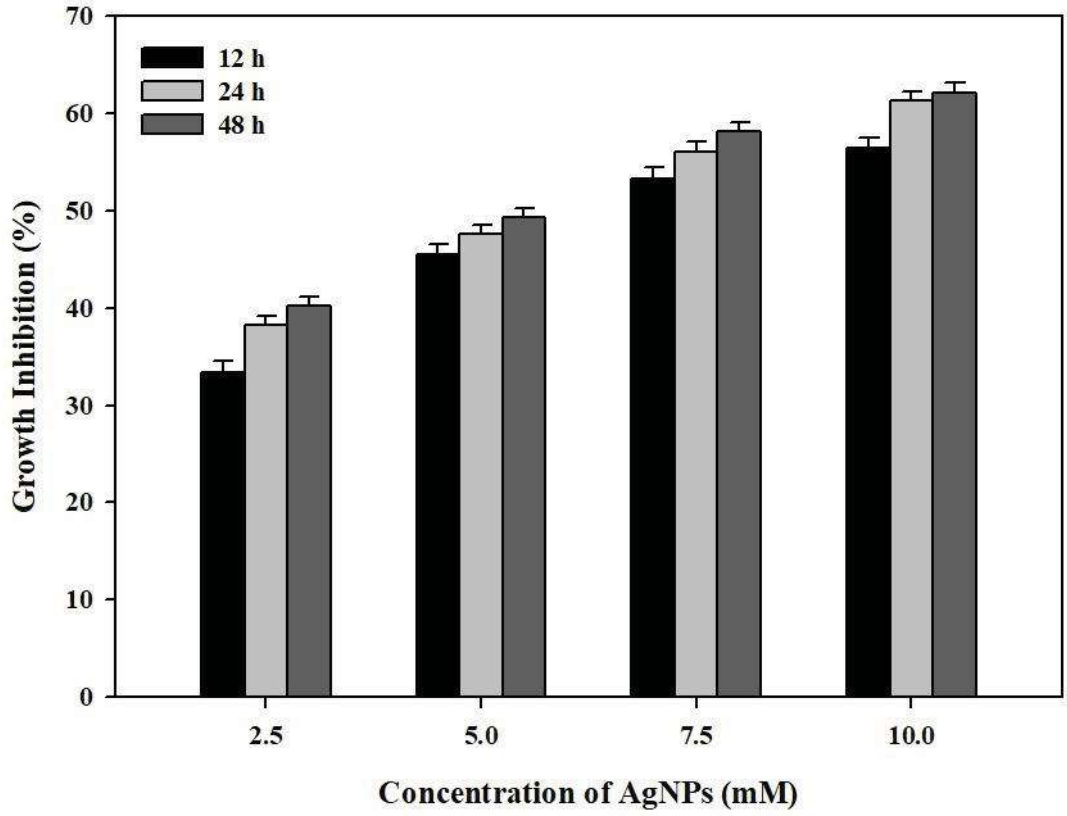


Fig. 5 (a) ***Klebsiella*** **sp.**

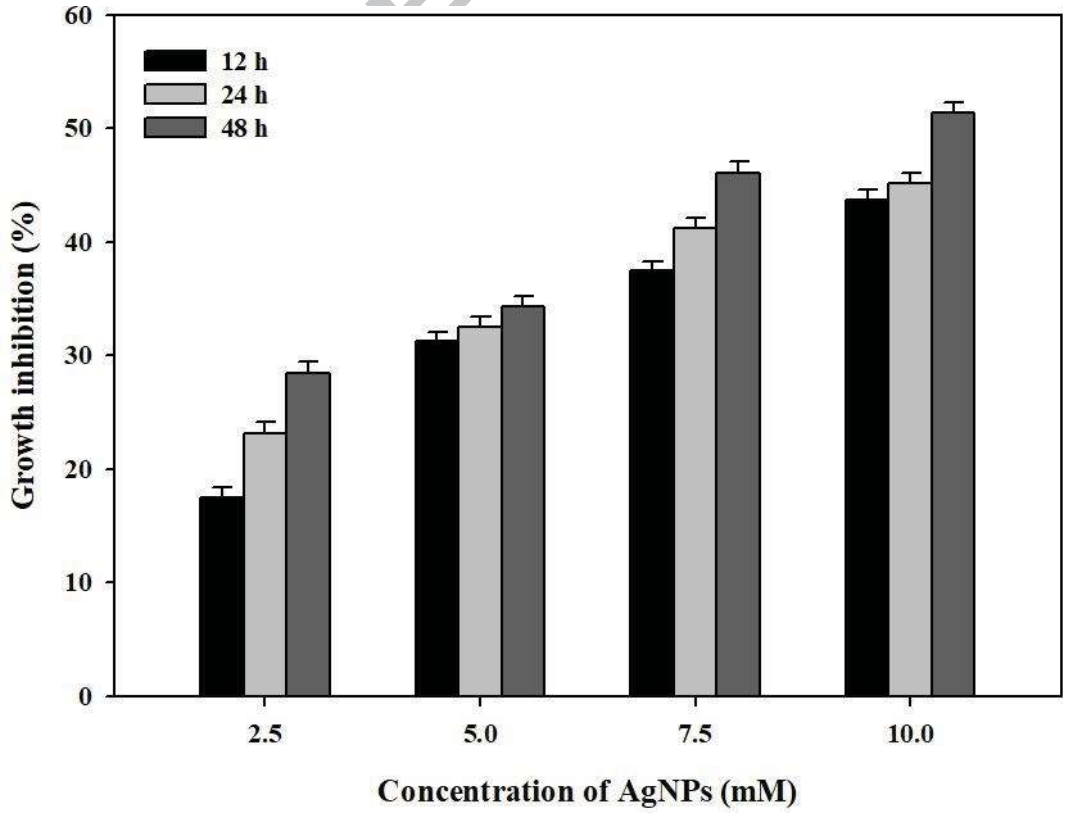


ACCEPTED MANUSCRIPT

(b) ***P. agglomerans***



(c) ***Rahnella*** **sp.**



ACCEPTED MANUSCRIPT

(d) *Staphylococcus* sp.

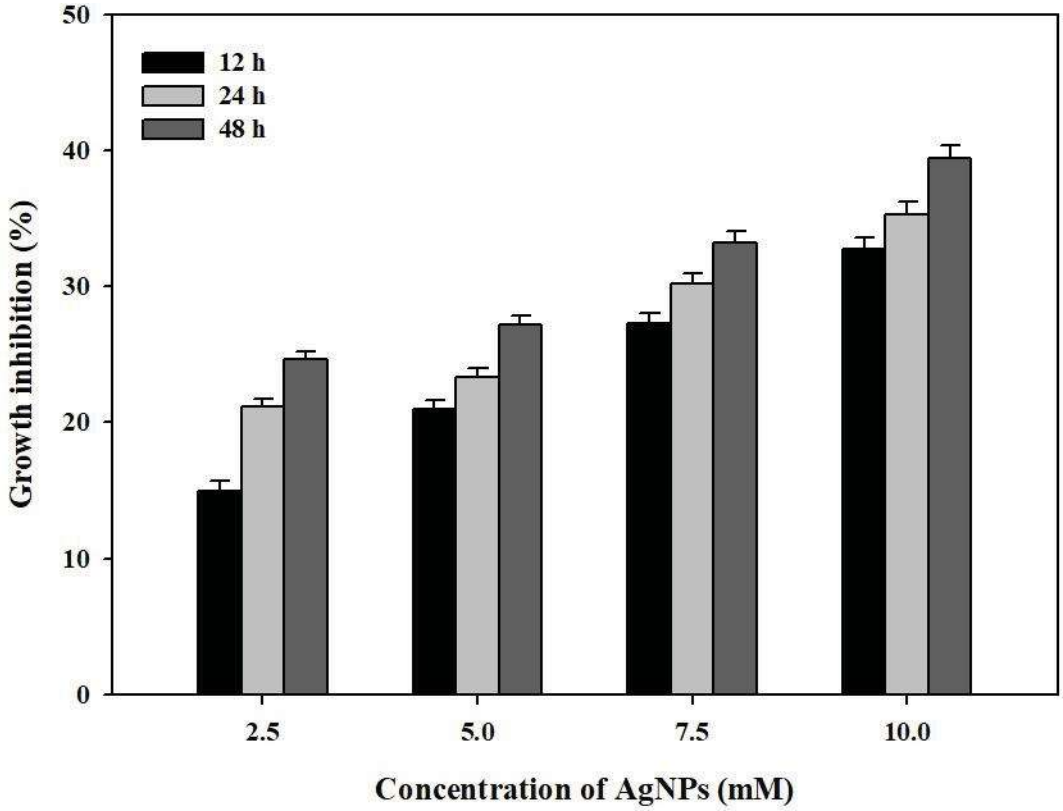


Table 1. Percentage of elements present in the synthesized AgNPs

S.No	Element	weight (%)	Atomic %
1	O K	2.35	84.04
2	Si K	0.41	2.78
3	Ci K	0.64	5.60
4	Ag L	2.00	7.58

ACCEPTED

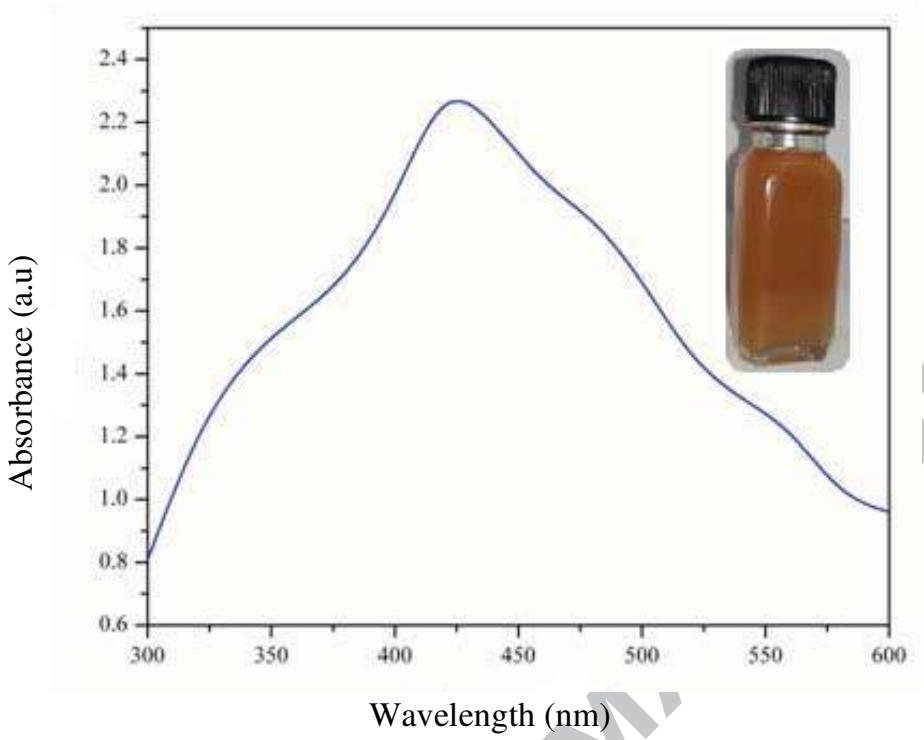
ACCEPTED MANUSCRIPT

Highlights

- Silver nanoparticles were synthesized successfully using Mango flower extract
- This method is rapid, simple and cost effective
- Structural and optical analysis revealed the nature of AgNPs
- The AgNPs effectively inhibit the growth of broad-spectrum of antibacterial activity

ACCEPTED MANUSCRIPT

ACCEPTED MANUSCRIPT



ACCEPTED MANUSCRIPT

Springer Link Search Log in

Original Paper | Published: 03 December 2018

Biogreen remediation of chromium-contaminated soil using *Pseudomonas* sp. (RPT) and neem (*Azadirachta indica*) oil cake

M. Govarthanan, T. Selvankumar, R. Mythili, P. Srinivasan, F. Ameen, S. A. AlYahya & S. Kamala-Kannan

International Journal of Environmental Science and Technology **16**, 4595–4600 (2019)

363 Accesses | **16** Citations | Metrics

Abstract

The prospective of indigenous *Pseudomonas* sp. (RPT) and neem oil cake for enhanced removal of chromium (Cr) from contaminated soil microcosm was explored in this study. The bacteria were isolated from Cr-contaminated soil and identified as *Pseudomonas* sp. based on partial 16S rDNA sequencing. The isolate RPT showed high Cr(VI) tolerance (1000 mg/l) and removal rate (64.4%) in batch experiments. Transmission electron microscopy observation showed that the isolate effectively precipitated the Cr both intra- and extracellularly. Microcosm studies revealed that neem oil cake amendment (7.5% w/v) enhanced Cr(VI) removal (82%) from contaminated soil. Furthermore, soil enzyme activities were increased in

PRINCIPAL
PGP College of Arts and Science
Namakkal

International Journal of Environmental Science and Technology
https://doi.org/10.1007/s13762-018-2136-6

ORIGINAL PAPER

Biogreen remediation of chromium-contaminated soil using *Pseudomonas* sp. (RPT) and neem (*Azadirachta indica*) oil cake

M. Govarthanan[1,2] · T. Selvankumar[2] · R. Mythili[2] · P. Srinivasan[2] · F. Ameen[3] · S. A. AlYahya[4] · S. Kamala-Kannan[5]

Received: 17 July 2018 / Revised: 13 November 2018 / Accepted: 26 November 2018
© Islamic Azad University (IAU) 2018

Abstract

The prospective of indigenous *Pseudomonas* sp. (RPT) and neem oil cake for enhanced removal of chromium (Cr) from contaminated soil microcosm was explored in this study. The bacteria were isolated from Cr-contaminated soil and identified as *Pseudomonas* sp. based on partial 16S rDNA sequencing. The isolate RPT showed high Cr(VI) tolerance (1000 mg/l) and removal rate (64.4%) in batch experiments. Transmission electron microscopy observation showed that the isolate effectively precipitated the Cr both intra- and extracellularly. Microcosm studies revealed that neem oil cake amendment (7.5% w/v) enhanced Cr(VI) removal (82%) from contaminated soil. Furthermore, soil enzyme activities were increased in the biostimulated soil. The obtained results indicated that the application of neem oil cake along with indigenous Cr(VI)-resistant bacteria could inspire the bioremediation of Cr(VI)-contaminated soil field scale.

Keywords Chromium · Neem oil cake · *Pseudomonas* sp. · Remediation · Soil

Introduction

Metals originating from metallurgical industries, mines and/or ores are a serious environmental issue as it contaminates both soil and water. The continuous accumulation of metals in the soil and water streams causes biological disorders in humans and other living organisms (Govarthanan et al. 2018; Rieger et al. 2018). With the various metals that contaminate the ecosystem, chromium (Cr) has a special place because of its wide applications in various industries.

Chromium sulfate is the commonly used tanning agent in tanneries. Ranipet (Vellore, Tamil Nadu, India) is well known for tanneries. It is reported that nearly 240 tanneries are located in this area and that they release approximately 220,000 tons of solid waste into the soil (Sundaramoorthy et al. 2016). Under certain circumstances, the trivalent chromium salts (Cr(III)) present in the solid wastes get oxidized into hexavalent chromium salts (Cr(VI)), a highly toxic form. Thus, soil and surface water system in this area are heavily polluted with Cr(III) and Cr(VI). However, only limited attempts have been made to remove and/or reduce Cr(VI) from the contaminated surface soils. Therefore, there is an immediate need to develop simple and eco-friendly methods for the removal of Cr from contaminated soils.

Recently, various technologies (physicochemical methods) have been developed with the goal of reducing Cr pollution in the contaminated ecosystem. Although physicochemical methods have been applied in practice, these methods carry several disadvantages (Ali et al. 2011; Ok et al. 2011; Saravanan et al. 2013a, b, 2015; Robati et al. 2016). Bioremediation is considered as a simple, inexpensive and eco-friendly technology that uses biotic communities for the remediation of contaminated soils. Microorganisms are primarily used, in bioremediation, to degrade or

Editorial responsibility: M. Abbaspour.

✉ S. Kamala-Kannan
kannan@jbnu.ac.kr

1 Department of Environmental Engineering, University of Seoul, Seoul 02504, South Korea

2 PG and Research Department of Biotechnology, Mahendra Arts and Science College (Autonomous), Kalippatti, Namakkal, Tamil Nadu 637501, India

3 Department of Botany and Microbiology, College of Science, King Saud University, Riyadh 11451, Saudi Arabia

4 National Centre for Biotechnology, King Abdulaziz City for Science and Technology (KACST), P.O. Box 6086, Riyadh 11442, Saudi Arabia

5 Division of Biotechnology, College of Environmental and Bioresource Sciences, Chonbuk National University, Iksan 54596, South Korea

detoxify the pollutants into harmless and less toxic forms (Wu et al. 2010; Govarthanan et al. 2013; Selvankumar et al. 2017). Metal-resistant bacteria play an important role in the removal of metals; however, the removal process is affected by several biotic and abiotic factors. It has been reported that many bacterial strains have the ability to survive in Cr-polluted soil because of their ability to cause metal efflux, DNA methylation, metal biotransformation and enzymatic reduction (Nies 2003). Bacterial reduction in Cr(VI) to Cr(III) is an interesting mechanism that can be considered as an effective chromate remediation system. Several bacterial strains belonging to the genus *Bacillus*, *Arthrobacter*, *Brucella*, *Microbacterium*, *Corynebacterium* and *Pseudomonas* have been reported to have chromium resistance/reduction mechanisms (Pattanapipitpaisal et al. 2001; Viti et al. 2003; Megharaj et al. 2003; Thacker et al. 2007; Zheng et al. 2015).

It has been confirmed that the bioremediation process is primarily influenced by physicochemical properties of the soil and the environmental conditions (Suja et al. 2014). The deficiency of nutrients in the contaminated soil reduced the growth rate of bacteria, which in turn limits the removal of metals in the entire bioremediation process. Because of the limited availability of synthetic nutrients and their expensive nature, agricultural by-products or agro-industrial wastes with bulk nutrients are considered as a choice to revive the microbial population in the contaminated soil (Brierley et al. 2002). The use of agricultural by-products has been considered as a promising method to enhance the bacterial population in contaminated soils and, thus, for the effective green bioremediation of metals. In this respect, neem (*Azadirachta indica*) oil cake was used in this study. However, the application of neem oil cake as a bacterial stimulant in the bioremediation of Cr is not yet reported. Thus, it is important to assess the indigenous Cr-resistant bacteria for the bioremediation of Cr-contaminated sites of Ranipet. Therefore, the objectives of the present study were (1) to isolate Cr-resistant indigenous bacteria from the polluted soils of Ranipet and (2) to develop active bacterial formulation using neem oil cake for enhancing Cr removal from contaminated soils.

Materials and methods

Materials

Nutrient agar (NA) and Luria–Bertani (LB) agar were procured from Hi-Media (Mumbai, India). All other chemicals used in this experiment were of analytical grade (Sigma, USA, and Hi-Media, India).

Soil sample, bacteria isolation and minimal inhibitory concentration

Soil samples (10 cm depth) were collected from the study area with sterile containers, and directly transferred to the laboratory. The total metal content in the soil was measured according to Loring and Rantala (1992). Physicochemical properties of the soil were measured by using standard methods (Gaudette et al. 1974; Helmke and Sparks 1996; Thomas 1996). Soil samples were serially diluted, and 0.1 ml of the appropriate dilution was plated onto NA plates using spread plate technique. The plates were incubated at 26 ± 2 °C for 24–48 h and observed for the bacterial growth. The pure cultures were stored at 4 °C for further study. The minimal inhibitory concentrations (MICs) of the isolates were determined by agar dilution method (Kamala-Kannan et al. 2007).

Identification of Cr-resistant bacteria

The identification of the isolate was carried out using 16S rRNA method according to Govarthanan et al. (2015) using the universal bacterial primers 27f and 907r, and the sequences were compared using the BLAST program (http://www.ncbi.nlmnih.gov/BLAST) for the identification of the isolate.

Cr(VI) removal potential of the isolate and TEM analysis

Ten milliliters of inoculum was aseptically inoculated into 100 ml of LB broth amended with increasing concentrations (100, 200, 500 and 1000 mg/l) of Cr and incubated in a shaking incubator (250 rpm) at 28 °C for 48 h. The culture aliquots of RPT were collected at predetermined time intervals (0, 12, 24, 36 and 48 h) and centrifuged, and the remaining Cr(VI) in the supernatants were measured using UV–Vis spectrophotometer (Chai et al. 2009). The bacterial pellets collected at 48 h were examined under TEM (FEI Tecnai G2 20 high resolution) to visualize the metal precipitates present in cells. The LB medium without bacteria inoculation served as a control for this experiment.

Neem oil cake extracts preparation

Neem oil cake (NOC) was procured from a local market at Mallasamudram, Tamil Nadu, India. The NOC extract was prepared according to Govarthanan et al. (2015). Raw NOC was used for the soil microcosm studies.

Effect of media on Cr removal

To observe the influence of nutrients on Cr removal, batch experiments were carried out with different culture media such as LB broth, NB and NOC extract. Briefly, log-phase

Table 1 Treatment conditions of soil microcosms

S. no	Microcosms	Treatment	Description
1	Control	Untreated soil	Cr-contaminated soil placed in the tray without any treatment
2	A	Bioaugmentation	Cr-contaminated soil with Cr-resistant *Pseudomonas* sp. (RPT)
3	B	Biostimulation with 5% NOC	Cr-contaminated soil with Cr-resistant *Pseudomonas* sp. (RPT) amended with 2.5% of NOC

culture of the isolate RPT was aseptically inoculated into 100 ml of medium (LB, NB or NOC extract) supplemented with 500 mg/l of Cr, and the flasks were incubated in an orbital shaker (200 rpm) at 28 °C for 48 h. Samples were collected at prescribed incubation period and analyzed for the total Cr concentration using inductively coupled plasma mass spectrometry (ICP, Leemans Labs, USA).

Soil microcosm

Cr-contaminated soils collected near tannery processing units were air-dried and sieved through a 0.4-cm sieve. Microcosm studies were carried out in plastic trays (bottom layer, 300 g of gravel; middle layer, 400 g of sand; and the top layer, 300 g of Cr-contaminated soil), and different sets of experiments were carried for bioaugmentation and biostimulation (Table 1). Soil humidity was adjusted with sterile distilled water to reach the final moisture content of 45% (v/w). NOC was mixed with the contaminated soil before it was placed in the microcosm. The bacterial inoculum (10^8 cells/ml) (100 ml) was evenly applied on the surface of the contaminated soils, and the experimental set without bacterial inoculum served as control. The trays were incubated at room temperature for 15 days, and Cr(VI) content in the soil was determined by 1, 5-diphenyl carbazide (DPC) method after alkaline digestion of the soil. The experiments were performed in triplicate, and mean values was considered.

Estimation of soil enzymes activities after microcosms

Urease activity of the soil was estimated according to the protocol established by Kandeler (1996). Dehydrogenase, alkaline phosphatase (Tabatabai 1994), amylase (Galstyan 1965), invertase (Ill et al. 1989) and soil cellulase activity was measured according to Kelley and Rodriguez-Kabana (1975). Three replications were carried out for all the experiments.

Results and discussion

Soil properties

The physicochemical properties of the Cr-contaminated soil are represented in Table 2. The results showed that the soil contains 10.2% of organic matter and the total Cr content in the soil was 1000 ± 5.2 (mg/kg). The results were consistent with previous studies reporting the concentrations of Cr in the study area (Jeyasingh and Philip 2005; Jeyasingh et al. 2010).

Table 2 Physicochemical properties of mine soil

Parameters	Values
Organic matter (%)	10.2
Ca (meq/100 g^{-1})	7.25
Na (meq/100 g^{-1})	15
NH_4 (meq/100 g^{-1})	43.5
K (meq/100 g^{-1})	21.7
pH	8.5
EC (m^{s}/m)	0.64
Total Cr (mg/kg)	1000

Identification and MIC of the isolate

Four Cr-resistant bacterial strains were isolated from the collected soil samples, and the isolates were designated as RPT, RPT1, RPT2 and RPT3. To evaluate their resistance against Cr, the bacterial growth was continuously monitored in plates amended with Cr (100–1000 mg/l). Among the isolates, RPT showed maximum Cr resistance (1000 mg/l) in the agar plates. Thus, the isolate RPT was chosen for further characterization and Cr removal studies. The 16S rDNA sequence of this strain showed 99% identity with *Pseudomonas* sp. The partial 16S rDNA of the isolate RPT was deposited in GenBank (Accession Number: KX348781). The results are in agreement with previous studies reporting chromium resistance in *Pseudomonas* sp. isolated from metal-contaminated soils and water (Ozturk et al. 2012; Christl et al. 2012; Mahmood et al. 2015; Huang et al. 2016).

Cr(VI) removal potential of *Pseudomonas* sp. RPT

Cr(VI) removal ability of the isolate RPT was evaluated at different initial concentrations, and the results are presented in Fig. 1 along with control. The results indicated that the Cr(VI) removal by the isolate RPT was relatively less during the first 12 h of incubation, whereas the removal rate gradually increased with the increase in incubation time and reached

maximum (64.4%) after 36 h of incubation. Nearly 23% of Cr(VI) removal was observed at an initial concentration of 100 mg/l after 24 h of incubation. Furthermore, the results confirmed the viability of the isolate RPT at higher concentration (500–1000 mg/l) and that it removed 30–46% of Cr(VI) after 48 h of incubation. The metal-contaminated environmental stress might have induced the isolate to develop an effective detoxification mechanism to survive in the adverse condition (Bader et al. 1999; Jeyasingh and Philip 2005).

Effect of media on Cr removal

The influences of nutrients on Cr removal by the isolate RPT are shown in Fig. 2. The results indicated that maximum Cr removal (64.4%) was observed in NOC extract followed by LB and NB. Thus, in the present study, NOC was used as a biostimulating agent in microcosm studies. Several studies reported that the microorganisms may utilize the organic compounds as an energy source to tolerate metal stress (Liu et al. 2004; Das et al. 2014; Govarthanan et al. 2014).

TEM analysis

TEM image of the isolate RPT is shown in Fig. 3. Cr particles were visible as dark granules on the inside and/or the surface of the bacterial cells. The results indicated that the isolate RPT removed and/or decreased Cr toxicity by both intracellular accumulation and extracellular reduction. Ozturk et al. (2012) reported that *Pseudomonas aeuroginosa* removed Cr(VI) by both intracellular accumulation and reduction.

Soil microcosm studies

The Cr(VI) removal efficiency of the isolate RPT in contaminated soil was evaluated, and the results are shown in Fig. 4. The results showed that the removal of Cr(VI) in the control soil was very less (5.2%), while in *Pseudomonas* sp. (RPT)-treated soil the removal rate significantly increased to 62%. The increased Cr(VI) removal rate in bioaugumented soil

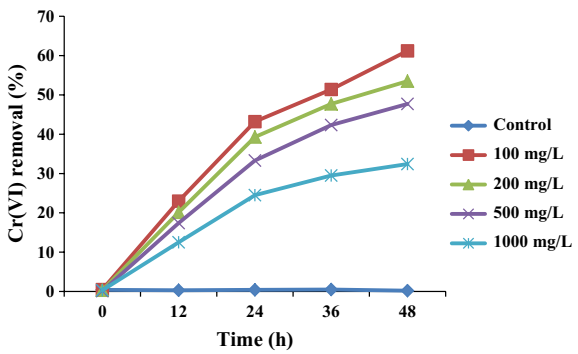


Fig. 1 Chromium removal potential of the isolate *Pseudomonas* sp. RPT

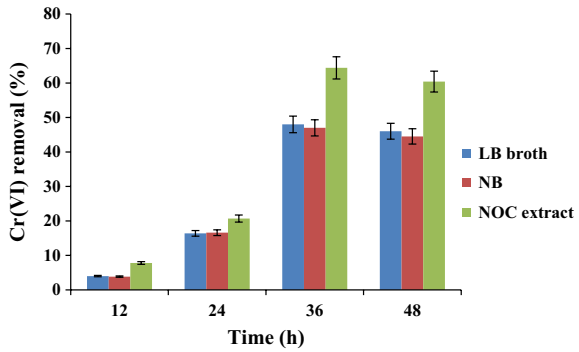


Fig. 2 Optimization of chromium removal using different media. Error bars indicate standard deviation of means. (*NOC* neem oil cake extract, *LB* Luria–Bertani broth, *NB* nutrient broth)

might be due to the activity of the isolate RPT and its metabolites. This was supported by the results from TEM analysis where extracellular metal precipitates were observed on the surface of the bacteria (Fig. 3).

The Cr(VI) removal activity by the isolate RPT was further evaluated in NOC-amended soil, and the results are shown in Fig. 4. Soil treated with 2.5% NOC showed 68% Cr(VI) removal, and it increased to 74% in soils amended with 5% NOC. The removal rate further increased to 82.7% in 7.5% NOC-amended soil. However, the removal rate was significantly decreased in the soil amended with 10% NOC. The study clearly evidenced that the Cr(VI) removal rate was increased in the presence of NOC and it could be due to an increase in microbial population in the contaminated soil. The result was consistent with the previous study reporting that the Cr removal rate of *Aspergillus niger* was increased in compost-amended soil (Srivastava and Thakur 2006). The biostimulating agents not only decontaminated the soils, but also

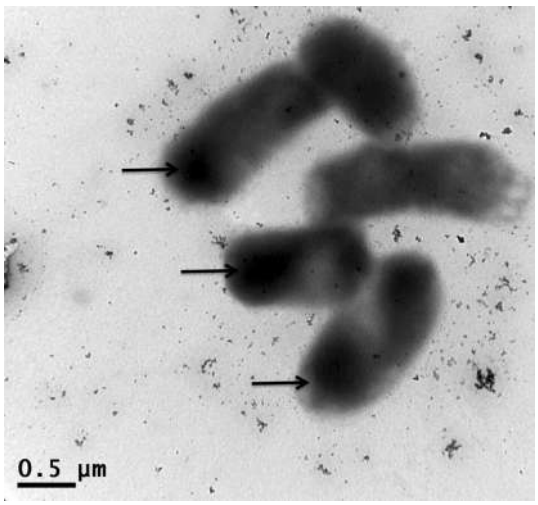


Fig. 3 Transmission electron micrograph of the isolate RPT showing Cr precipitates. (Arrows indicate the dark granules of Cr)

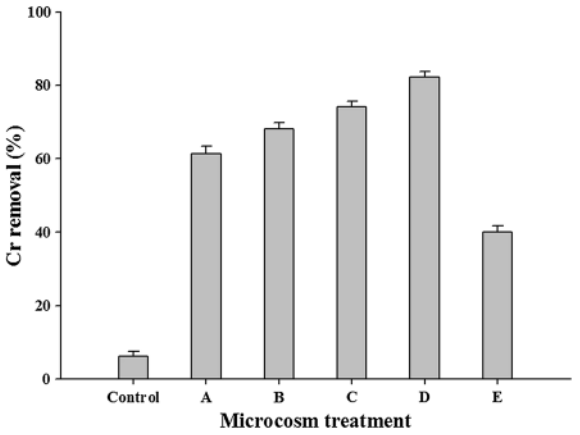


Fig. 4 Cr(VI) removal in microcosm studies. Error bars indicate standard deviation of means. *A* Bioaugmentation, *B* biostimulation with 2.5% NOC, *C* biostimulation with 5% NOC, *D* biostimulation with 7.5% NOC, *E* biostimulation with 10% NOC

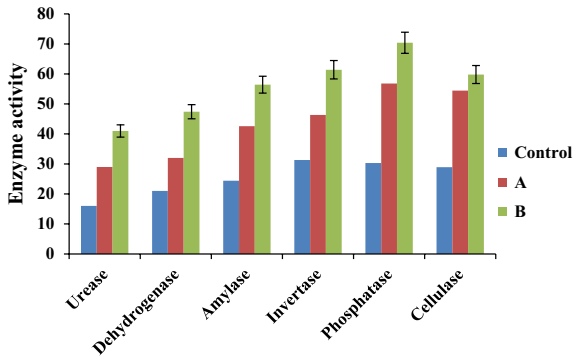


Fig. 5 Enzyme activities in soil microcosms. A marked increase in enzyme activity was observed in bioremediated soil microcosms

increased the fertility of soils as evidenced in the increased soil enzyme concentration.

Soil enzyme activities

The enzyme activity of the control, bioaugumented and biostimulated soils is shown in Fig. 5. Increased enzyme activities were found in bioaugumented and biostimulated soils. The enzyme results confirmed that the presence of oil cake can increase the growth and activity of the *Pseudomonas* sp. (RPT) in Cr-contaminated soils. The results are in agreement with Balasubramanian et al. (1972) reporting the relationship between the amendments, microbial population and soil enzyme activity.

Conclusion

To the best of our knowledge, this is the first study to report the application of neem oil cake as a biostimulating agent in Cr-contaminated soils with indigenous *Pseudomonas* sp. (RPT). The application of the neem oil cake enhanced the microbial population in the contaminated soil and, thus, caused the effective removal of Cr(VI). About 82.7% of Cr(VI) was successfully removed in Cr-contaminated soil after 15 days of incubation with 7.5% NOC. The application of NOC not only increased the Cr(VI) removal rate but also improved the soil metabolic activity, as illustrated by the extracellular enzymes in bioremediated soils. These findings can be further exploited for the possible utilization of NOC with the selected indigenous strain for the bioremediation of Cr(VI)-contaminated environment.

Acknowledgement This paper was supported by research funds of Chonbuk National University in 2017. The authors (Fuad Ameen & Sami A. AlYahya) are very grateful to the Localization and Development Technology Platform for the Infectious Diseases Surveillance and the Detection Project at Kind Abdulaziz City for Science and Technology.

Compliance with ethical standards

Conflict of interest The authors declare that they do not have any conflict of interest.

References

Ali I, Khan TA, Asim M (2011) Removal of arsenic from water by electrocoagulation and electrodialysis techniques. Sep Purif Rev 40:25–42

Bader JL, Gonzalez G, Goodell PC, Ali A, Pillai SD (1999) Chromium resistant bacterial populations from a site heavily contaminated with hexavalent chromium. Water Air Soil Pollut 109:263–274

Balasubramanian A, Siddaramappa R, Rangaswami G (1972) Effect of organic manuring on the activities of the enzymes hydrolyzing sucrose and urea and on soil aggregation. Plant Soil 37:319–328

Brierley CL, Briggs AP, Mular AL, Halbe DN, Barret DJ (2002) Mineral processing plant design, practice and control. Society of Mining Engineers, Littleton, Colo, pp 1540–1568

Chai L, Huang S, Yang Z, Peng B, Huang Y, Chen Y (2009) Cr(VI) remediation by indigenous bacteria in soils contaminated by chromium-containing slag. J Hazard Mater 167:516–522

Christl M, Imseng E, Tatti J, Frommer C, Viti L, Giovannetti R (2012) Aerobic reduction of chromium (VI) by *Pseudomonas corrugata* 28: influence of metabolism and fate of reduced chromium. Geomicrobiol J 29:173–185

Das S, Mishra J, Das SK, Pandey S, Rao DS, Chakraborty A, Sudarshan M, Das N, Thatoi H (2014) Investigation on mechanism of Cr(VI) reduction and removal by *Bacillus amyloliquefaciens*, a novel chromate tolerant bacterium isolated from chromite mine soil. Chemosphere 96:112–121

Galstyan AS (1965) A method of determining the activity of the hydrolytic enzymes in soil. Sov Soil Sci 2:170–175

Gaudette HE, Flight WR, Toner L, Folger DW (1974) An inexpensive titration method for the determination of organic carbon in recent sediments. J Sediment Res 44:249–253

Govarthanan M, Lee KJ, Cho M, Kim JS, Kamala-Kannan S, Oh BT (2013) Significance of autochthonous *Bacillus* sp. KK1 on biomineralization of lead in mine tailings. Chemosphere 90:2267–2272

Govarthanan M, Lee GW, Park JH, Kim JS, Lim SS, Seo SK, Cho M, Myung H, Kamala-Kannan S, Oh BT (2014) Bioleaching characteristics, influencing factors of Cu solubilisation and survival of *Herbaspirillum* sp. GW103 in Cu contaminated mine soil. Chemosphere 109:42–48

Govarthanan M, Park SH, Park YJ, Myung H, Krishnamurthy RR, Lee SH, Kamala-Kannan S, Oh BT (2015) Lead biotransformation potential of allochthonous *Bacillus* sp. SKK11 with sesame oil cake extract in mine soil. RSC Adv 5:54564–54570

Govarthanan M, Mythili R, Selvankumar T, Kamala-Kannan S, Kim H (2018) Myco-phytoremediation of arsenic and lead contaminated soils by *Helianthus annuus* and wood rot fungi, *Trichoderma* sp. isolated from decayed wood. Ecotoxicol Environ Saf 151:279–284

Helmke PA, Sparks DL (1996) Lithium, sodium, potassium, rubidium, and cesium. Methods Soil Anal 3:551–574

Huang H, Wu K, Khan A, Jiang Y, Ling Z, Liu P, Chen Y, Tao X, Li X (2016) A novel *Pseudomonas gessardii* strain LZ-E simultaneously degrades naphthalene and reduces hexavalent chromium. Bioresour Technol 207:370–378

Ill FG, Clausen CA, Highley TA (1989) Adaptation of the Nelson–Somogyi reducing sugar assay to a microassay using microtiter plates. Anal Biochem 182:197–199

Jeyasingh J, Philip L (2005) Bioremediation of chromium contaminated soil: optimization of operating parameters under laboratory conditions. J Hazard Mater 118:113–120

Jeyasingh J, Somasundaram V, Philip L, Murty Bhallamudi S (2010) Bioremediation of Cr(VI) contaminated soil/sludge: experimental studies and development of a management model. Chem Eng J 160:556–564

Kamala-Kannan S, Lee KJ, Krishnamoorthy R, Purusothaman A, Shanthi K, Rao NR (2007) Aerobic chromate reducing *Bacillus cereus* isolated from the heavy metal contaminated Ennore Creek sediment, north of Chennai, Tamil Nadu, south east India. Res J Microbiol 2:133–140

Kandeler E (1996) Urease activity by colorimetric technique. Methods in soil biology. Springer, New York, pp 171–174

Kelley WD, Rodriguez-Kabana R (1975) Effects of potassium azide on soil microbial populations and soil enzymatic activities. Can J Microbiol 21:565–570

Liu YG, Xu WH, Zeng GM, Tang CF, Li CF (2004) Experimental study on reduction by *Pseudomonas aeuroginosa*. J Environ Sci 16:797–801

Loring DH, Rantala RTT (1992) Manual for the geochemical analysis of marine sediments and suspended particulate matter. Earth-Sci Rev 32:235–283

Mahmood S, Khalid A, Arshad M, Ahmad R (2015) Effect of trace metals and electron shuttle on simultaneous reduction of reactive black-5 azo dye and hexavalent chromium in liquid medium by *Pseudomonas* sp. Chemosphere 138:895–900

Megharaj M, Avudainayagam S, Naidu R (2003) Toxicity of hexavalent chromium and its reduction by bacteria isolated from soil contaminated with tannery waste. Curr Microbiol 47:51–54

Nies DH (2003) Efflux-mediated heavy metal resistance in prokaryotes. FEMS Microbiol Rev 27:313–339

Ok YS, Kim SC, Kim DK, Skousen JG, Lee JS, Cheong YW, Kim SJ, Yang JE (2011) Ameliorants to immobilize Cd in rice paddy soils contaminated by abandoned metal mines in Korea. Environ Geochem Health 33:23–30

Ozturk S, Kaya T, Aslim B, Tan S (2012) Removal and reduction of chromium by *Pseudomonas* sp. and their correlation to rhamnolipid production. J Hazard Mater 231:64–69

Pattanapipitpaisal P, Brown NL, Macaskie LE (2001) Chromate reduction and 16S rRNA identification of bacteria isolated from a Cr(VI)-contaminated site. Appl Microbiol Biotechnol 57:257–261

Rieger A, Sax C, Bauert T, Wackerlin C, Ernst KM (2018) Chemical chiral pollution: impact on the society and science and need of the regulations in the 21st century. Chirality 30:402–406

Robati D, Mirza B, Rajabi M, Moradi O, Gupta VK (2016) Removal of hazardous dyes-BR 12 and methyl orange using graphene oxide as an adsorbent from aqueous phase. J Colloid Interface Sci 284:687–697

Saravanan R, Joicy S, Gupta VK, Narayanan V, Stephen A (2013a) Visible light induced degradation of methylene blue using CeO_2/V_2O_5 and CeO_2/CuO catalysts. Mater Sci Eng C 33:4725–4731

Saravanan R, Karthikeyan N, Gupta VK, Thirumal E, Stephen A (2013b) ZnO/Ag nanocomposite: an efficient catalyst for degradation studies of textile effluents under visible light. Mater Sci Eng C 33:2235–2244

Saravanan R, Mansoob Khan M, Gupta VK, Mosquera E, Gracia F, Narayanan V, Stephen A (2015) ZnO/Ag/CdO nanocomposite for visible light-induced photocatalytic degradation of industrial textile effluents. J Colloid Interface Sci 452:126–133

Selvankumar T, Radhika R, Mythili R, Arunprakash S, Srinivasan P, Govarthanan M, Kim M (2017) Isolation identification and characterization of arsenic transforming exogenous endophytic *Citrobacter* sp. RPT from roots of *Pterisvittata*. 3 Biotech 7:264

Srivastava S, Thakur IS (2006) Evaluation of bioremediation and detoxification potentiality of *Aspergillus niger* for removal of hexavalent chromium in soil microcosm. Soil Biol Biochem 38:1904–1911

Suja F, Rahim F, Taha MR, Hambali N, Razali MR, Khali A, Hamzah A (2014) Effects of local microbial bioaugmentation and biostimulation on the bioremediation of total petroleum hydrocarbons (TPH) in crude oil contaminated soil based on laboratory and field observations. Int Biodeterior Biodegrad 90:115–122

Sundaramoorthy B, Thiagarajan K, Mohan S, Mohan S, Rajendra Rao P, Ramamoorthy S, Chandrasekaran R (2016) Biomass characterization and phylogenetic analysis of microalgae isolated from estuaries: role in phycoremediation of tannery effluent. Algal Res 14:92–99

Tabatabai MA (1994) Soil enzymes. In: Weaver RW, Angel JS, Bottomley PS (eds) Methods of soil analysis, part 2—microbiological and biochemical properties. Book series no. 5. Soil Science Society of America, SSSA, Madison, pp 775–833

Thacker U, Parikh R, Shouche Y, Madamwar D (2007) Reduction of chromate by cell-free extract of *Brucella* sp. isolated from Cr(VI) contaminated sites. Bioresour Technol 98:1541–1547

Thomas GW (1996) Soil pH and soil acidity. In: Sparks DL (ed) Methods of soil analysis. Part 3. Chemical methods. SSSA-ASA, Madison, pp 475–490

Viti C, Pace A, Giovannetti L (2003) Characterization of Cr(VI) resistant bacteria isolated from chromium contaminated soil by tannery activity. Curr Microbiol 46:1–5

Wu G, Kang H, Zhang X, Shao H, Chu L, Ruan C (2010) A critical review on the bio-removal of hazardous heavy metals from contaminated soils: issues, progress, eco-environmental concerns and opportunities. J Hazard Mater 174:1–8

Zheng Z, Li Y, Zhang X, Liu P, Ren J, Wu G, Zhang Y, Chen Y, Li X (2015) A *Bacillus subtilis* strain can reduce hexavalent chromium to trivalent and an *nfrA* gene is involved. Int Biodeterior Biodegrad 97:90–96

ScienceDirect

International Journal of Biological Macromolecules
Volume 131, 15 June 2019, Pages 74-80

Effect of blue light on growth and exopolysaccharides production in phototrophic *Rhodobacter* sp. BT18 isolated from brackish water

M. Govarthanan [a], S. Kamala-Kannan [b, 1], T. Selvankumar [c], R. Mythili [c], P. Srinivasan [c], H. Kim [a]

Show more

Outline | Share | Cite

https://doi.org/10.1016/j.ijbiomac.2019.03.049

Get rights and content

Abstract

Rhodobacter sp. BT18, a phototrophic salt-resistant bacterium, was isolated from brackish water and screened for the production of exopolysaccharides (EPS). The effect of different light sources on the growth of *Rhodobacter* sp. BT18 was investigated. The effect on the growth order was found to be blue > white > green > red > yellow > dark. Based on Box-Behnken design, the studied variables (pH 7.0, 35 °C, and 30% of sucrose concentration under 60 h of incubation with blue light illumination) were found to be ideal for the maximum production of EPS (582.5 mg/L). Scanning electron microscopy images revealed the porous nature of EPS. Fourier transform spectroscopy and X-ray diffraction were applied to study the functional groups and the crystalline nature of the EPS, respectively. The emulsification index of the EPS was >75% and the maximum flocculating activity was about 75.4% at 30 mg/L concentration of EPS. In addition, EPS showed effective arsenic (64%) and lead (51%) chelating activities in liquid solutions. The multiple environmental applications of the EPS produced by *Rhodobacter* sp. BT18 make it be a promising alternative for emulsification, flocculation and metal removal in various industries.

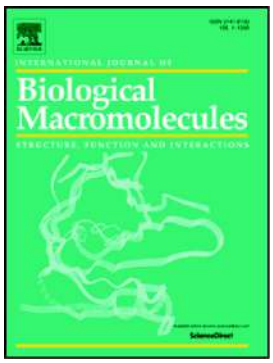
Previous Next

Keywords

Blue light; Emulsification; Exopolysaccharides; Flocculation; *Rhodobacter*

PRINCIPAL
PGP College of Arts and Science
Namakkal

Accepted Manuscript



Effect of blue light on growth and exopolysaccharides production in phototrophic Rhodobacter sp. BT18 isolated from brackish water

M. Govarthanan, S. Kamala-Kannan, T. Selvankumar, R. Mythili, P. Srinivasan, H. Kim

PII: S0141-8130(19)30412-X
DOI: https://doi.org/10.1016/j.ijbiomac.2019.03.049
Reference: BIOMAC 11879

To appear in: *International Journal of Biological Macromolecules*

Received date: 17 January 2019
Revised date: 6 March 2019
Accepted date: 6 March 2019

Please cite this article as: M. Govarthanan, S. Kamala-Kannan, T. Selvankumar, et al., Effect of blue light on growth and exopolysaccharides production in phototrophic Rhodobacter sp. BT18 isolated from brackish water, International Journal of Biological Macromolecules, https://doi.org/10.1016/j.ijbiomac.2019.03.049

This is a PDF file of an unedited manuscript that has been accepted for publication. As a service to our customers we are providing this early version of the manuscript. The manuscript will undergo copyediting, typesetting, and review of the resulting proof before it is published in its final form. Please note that during the production process errors may be discovered which could affect the content, and all legal disclaimers that apply to the journal pertain.

ACCEPTED MANUSCRIPT

Effect of blue light on growth and exopolysaccharides production in phototrophic *Rhodobacter* sp. BT18 isolated from brackish water

M. Govarthanan[1]*♣, S. Kamala-Kannan[2♣], T. Selvankumar[3], R. Mythili[3], P. Srinivasan[3], H. Kim[1*]

[1]Department of Environmental Engineering, University of Seoul, Seoul 02504, South Korea.

[2]Division of Biotechnology, Advanced Institute of Environment and Bioscience, College of Environmental and Bioresource Sciences, Chonbuk National University, Iksan 54596, South Korea.

[3]PG & Research Department of Biotechnology, Mahendra Arts and Science College (Autonomous), Kalippatti, Namakkal - 637501, Tamil Nadu, India.

♣The first two authors equally contributed in this work

*Corresponding author: M. Govarthanan, E-mail: gova.muthu@gmail.com; H. Kim, E-mail: h_kim@uos.ac.kr

ACCEPTED MANUSCRIPT

Abstract

Rhodobacter sp. BT18, a phototrophic salt-resistant bacterium, was isolated from brackish water and screened for the production of exopolysaccharides (EPS). The effect of different light sources on the growth of *Rhodobacter* sp. BT18 was investigated. The effect on the growth order was found to be blue > white > green > red > yellow > dark. Based on Box-Behnken design, the studied variables (pH 7.0, 35 °C, and 30% of sucrose concentration under 60 h of incubation with blue light illumination) were found to be ideal for the maximum production of EPS (582.5 mg/L). Scanning electron microscopy images revealed the porous nature of EPS. Fourier transform spectroscopy and X-ray diffraction were applied to study the functional groups and the crystalline nature of the EPS, respectively. The emulsification index of the EPS was > 75% and the maximum flocculating activity was about 75.4% at 30 mg/L concentration of EPS. In addition, EPS showed effective arsenic (64%) and lead (51%) chelating activities in liquid solutions. The multiple environmental applications of the EPS produced by *Rhodobacter* sp. BT18 make it be a promising alternative for emulsification, flocculation and metal removal in various industries.

Keywords: *Blue light; Emulsification; Exopolysaccharides; Flocculation Rhodobacter*

ACCEPTED MANUSCRIPT

1. Introduction

Bacterial exopolysaccharides (EPS) are extracellular biopolymers that are linear and/or branched sugar molecules composed of heterogeneous monomers coupled with glycosidic bonds (Govarthanan et al., 2015). Due to their viscosity, high emulsification, gelling nature (Priyanka et al., 2015), they find extensive applications in food, pharmaceutical and agricultural applications (Fretias et al., 2011; Amjres et al., 2015). Owing to the wide range of industrial applications and unique structural properties, bacterial EPS are gaining increased attention and are gradually becoming economically competitive with synthetic and other biopolymers produced by plants and algae (Rehm, 2009; Nicolaus et al., 2010; Carrion et al., 2015). Bacterial EPS have been found to be highly water soluble, stable, and rheological. They have emulsifying properties and are effective across a wide range of pH and temperature (Kumar and mody 2009).

Several studies have reported the production of EPS by bacteria including *Pseudomonas* sp. (Carrion et al., 2015), *Bacillus* sp. (Han et al., 2015; Malick et al., 2017), *Rhodothermus marinus* (Sardari et al., 2017), *Leuconostoc mesenteroides* (Xing et al., 2018), and *Halomonas* sp. (Govarthanan et al., 2015; Amjres et al., 2015). However, Bacteria from extreme environments have gained increased attention due to their special metabolic pathways and defensive mechanisms that enable them to withstand the harsh conditions (Carrion et al., 2015). Numerous studies have reported the EPS production by bacteria isolated from soil and water; however, there is no report on EPS produced by bacteria from brackish water environment, a buffering zone of sea and inland water.

Rhodobacter sp. is a gram-negative, phototrophic non-sulphur purple bacterium widely distributed across seas, rivers and lakes (Mujahid et al., 2011). It grows under both anaerobic and aerobic conditions with several metabolic pathways depending on the growth

ACCEPTED MANUSCRIPT

environment (Calvano et al., 2014). Several studies have reported the environmental applications of *Rhodobacter* sp. including bioremediation of heavy metals and polyaromatic hydrocarbons (Fonti et al., 2015; Li et al., 2016; Peng et al., 2018). It has been reported that the growth of phototrophic bacterium is greatly influenced by several physico-chemical parameters, such as light source, light intensity, temperature, pH, and available carbon sources present in the cultivation medium. Among all other parameters, light source greatly affects the cell growth, and metabolic pathways of the phototrophic bacterium (Kuo et al., 2012). Therefore, the present study investigated the effect of blue light on the growth and metabolic activity of phototrophic bacterium. From this perspective, this study was designed (i) to isolate and identify the phototrophic *Rhodobacter* sp. from brackish water, (ii) to evaluate the influence of different light sources on the growth of *Rhodobacter* sp., (iii) to screen for EPS production, and analyze the effect of different sources of light and carbon, pH, and temperature of the growth medium on EPS production (iv) and to assess the flocculating, emulsifying and metal chelation activity of the *Rhodobacter* sp. BT18 EPS.

2. Materials and methods

2.1. Isolation of EPS-producing phototrophic bacteria

Brackish water sample (~1 to 2 m depth) was collected from Pichavaram mangrove (11°23′–11°30′ and 79°45′–79°50′), Tamil Nadu, India, using sterile serum bottles and transported on ice to the laboratory. The enrichment cultures were prepared by adding 10 mL of water sample into a 250 mL Erlenmeyer flask containing 100 mL of Biebel and Pfennig's (PNB) medium supplemented with 3 g/L pyruvate (Biebel, 1983). The flasks were incubated in a shaking incubator (250 rpm) at 30 ± 2˚C for 2 days. The subsequent enrichment cultures were serially diluted and plated on the PNB agar medium. Isolated colonies were purified and stored at 4°C for further EPS production.

ACCEPTED MANUSCRIPT

2.2. Identification of EPS-producing phototrophic bacteria

Genomic DNA was extracted from the pure culture according to the method described by Sambrook and Russell (2001) and the isolated DNA was used as a template for PCR. The 16s rRNA gene of the isolate was amplified by using universal primer-27f (5′-AGAGTTTGATCCTGGCTCAG-3′) and -1492r (5′-CCCCGTCAATTCATTTGAGTTT-3′). The amplicons were purified using QIAGEN PCR (Valencia, CA, USA) purification kit and sequenced using ABI PRISM 3700 sequencer (Foster City, CA, USA). The obtained 16S rRNA sequence was compared with the available sequences in the database using NCBI BLAST program (http://www.ncbi.nlm.nih.gov/BLAST). A phylogenetic tree was constructed using the neighbor-joining distance method by Mega software version 6.0.

2.3. Effect of different light source on growth of *Rhodobacter* sp. BT18

Effect of different light sources on *Rhodobacter* sp. BT18 growth was investigated by carrying out batch experiments. Briefly, the flasks were covered with blue (~470 nm), green (~500 nm), yellow (~550 nm), red (~600 nm), and white papers (light source was not covered by any color paper). Flasks covered with black color cloth served as a control. All the flasks were kept in an incubator installed with an illuminated light source (Philips T8 Master TL-D T8 16 Watt 830 (Warm White) for 24 h at 30 ± 2°C. After appropriate incubation, the optical density of the cell suspension was measured at 805 nm (Kuo et al., 2012) using a UV-Vis spectrophotometer. Based on the effect of lights on the growth of *Rhodobacter* sp. BT18, blue light was used for further incubation for the enhanced production of EPS in the optimization studies.

2.4. EPS production

ACCEPTED MANUSCRIPT

The production of EPS by the isolate *Rhodobacter* sp. BT18 was carried out by flask fermentation using slight modification of the simple culture medium (SCM) (pH 7) composed of KH_2PO_4, 0.5 g/L; ammonium acetate, 0.5 g/L; $MgSO_4.7H_2O$, 9.4 g/L; NaC1, 0.4 g/L; $CaC1_2.2H_2O$, 0.1 g/L; yeast extract, 1 g/L; ferrous citrate, 0.005 g/L; glucose, 5 g/L (Cohen-Bazire et al. 1957; Ye et al., 2013). The isolate BT18 (10^8 cells/mL (0.8 OD) at 600 nm) was inoculated into 100 mL of SCM and incubated in a shaking incubator at 150 rpm at 30 ± 2˚C for 24 h. After the incubation, the cells were separated from SCM by centrifuging at 10000 rpm for 15 min at 4 °C. The resulting supernatant was precipitated overnight at 4 °C by the addition of ethanol (6 volumes of 100% ethanol). The precipitated EPS were recovered by centrifuging at 10000 rpm for 15 min at 4 °C. The crude EPS were dissolved in sterile distilled water and dialysed with Millipore membranes to remove excess salts and other compounds of the culture medium to obtain pure EPS. The purified EPS were freeze-dried for further characterization and application studies.

2.5. Optimization of EPS production

Four independent variables, pH (5-8), temperature (30-40 °C), sucrose concentration (10-50%), and blue light exposure time (24-96 h), were employed in this study and the experiments were designed by using a design expert software (Design Expert, version 10.0). The subsequent EPS production rate was evaluated by coefficient determination (R^2), ANOVA and response surface plots. A second-order polynomial equation was developed to fit the data from the experimental investigations:

$$Y = \beta_0 + \sum \beta_i X_i + \sum \beta_{ii} X_i^2 + \sum \beta_{ij} X_i X_j$$

ACCEPTED MANUSCRIPT

where Y is the predicted response; β_0, β_i, β_{ii}, β_{ij} are the fixed regression coefficients of the model; and X_i and X_j represent the independent variables.

2.6. Characterization of EPS produced by *Rhodobacter* sp. BT18

The functional groups present in the EPS were determined by using Fourier transformed infrared (FT-IR) spectroscopy (Perkin-Elmer, Norwalk, USA). An infrared spectrum of t he EPS was recorded using the KBr method in the range of 4000-400/cm. The porous nature and surface morphology of the EPS were examined by scanning electron microscopy (SEM; JEOL-64000, JEOL, Tokyo, Japan). The crystalline nature of the EPS was determined by using an X-ray diffractometer (Rigaku, Tokyo, Japan).

2.7. Emulsification activity of EPS

The emulsifying activity of EPS produced by *Rhodobacter* sp. BT18 was analyzed according to the method described by Cooper and Goldenberg (1987). Briefly, 5 mL of EPS solution and 5 mL of selected hydrophobic substrates (xylene, vaseline, coconut oil, and peanut oil) were vigorously mixed with a vortex mixer and incubated at room temperature for 24 h. Tween 80 was used as the control in this experiment. The emulsifying activity of the EPS was expressed as a percentage of total height occupied by the emulsification after 1 h and 24 h (Amjres et al., 2015).

2.8. Flocculating activity of EPS

To determine the flocculating nature of the EPS, the batch assay was performed according to Prasertsan et al. (2006) with a minor modification. Briefly, 0.5 ml of EPS solution (10, 20, 30, 50 and 50 mg/L) was mixed with 1.5 ml of $CaCl_2$ solution (pH 7.0) and 8 ml of kaolin clay

ACCEPTED MANUSCRIPT

suspension (pH 7.0). The assay mixture was stirred with a magnetic stirrer for 2 min and incubated at room temperature for 5 min. Sterile distilled water was used as a control for this experiment. Flocculating activity was measured by optical absorbance at 550 nm and calculated as the % of activity.

$$\text{Flocculating activity} = [(OD_{control} - OD_{test})/OD_{control}] \times 100$$

2.9. Heavy metal chelating activity of EPS

The heavy metal chelating property of EPS was estimated against different concentrations (50, 100, 150 and 200 mg/L) of arsenic and lead. Briefly, 1% of EPS was mixed with metal solutions, incubated at room temperature for 1 h, and filtered using a glass filter. The precipitates present in the glass filter was carefully digested with nitric acid and the metal concentration in the sample was measured using inductively coupled plasma mass spectrometry (Agilent 4500, Agilent Technologies, Palo Alto, CA, USA).

3. Results and discussion

3.1. Identification of isolate BT18

Morphologically, three different bacterial colonies were observed in the PNB agar plates and the isolates were designated as BT17, BT18, and BT19. Of the three isolates, only BT18 produced EPS. Thus, the isolate BT18 was chosen for further studies. Based on 16S rDNA sequencing, the isolate was identified as *Rhodobacter* sp. (96.0% identity with *Rhodobacter* sp. YS18 (Accession No: LN879886)). The partial 16S rDNA of the isolate BT18 was deposited in GenBank (Accession Number: MK116466). Figure 1 shows the phylogenetic relationship of the *Rhodobacter* sp. BT18. Several studies reported that the EPS producer

ACCEPTED MANUSCRIPT

belongs to the genera *Bacillus, Pseudomonas, Halomonas* etc. (Han et al., 2015; Carrion et al., 2015; Govarthanan et al., 2015). However, EPS producing phototrophic *Rhodobacter* sp. has not been reported. To the best of our knowledge, this is the first report on the EPS-producing *Rhodobacter* sp. BT18.

3.2. Growth of *Rhodobacter* sp. BT18 under different light conditions

Light is an important factor for the growth of photosynthetic microorganisms. Thus, the growth of *Rhodobacter* sp. BT18 under different lights was investigated and the results are reported in Fig. 2. The batch experiments were performed under different light sources (blue (~470 nm), green (~500 nm), yellow (~550 nm), red (~600 nm), white, and darkness). The results clearly indicated that the best light source for the growth of *Rhodobacter* sp. BT18 was blue light at 470 nm. The order of the bacterial growth under the different light sources was blue > white > green > red > yellow > dark. The minimum growth of the isolate BT18 was observed in the flasks exposed to the yellow light. Kuo et al. (2012) reported that the enhanced growth of photosynthetic *Rhodopseudomonas palustris* was found to be under the blue light emitting diode (LED-Blue) at approximate wavelength of 470 nm. Katsuda et al. (2004) reported that enhanced cell growth was observed under the blue light with short wavelength of 380-470 nm. Based on the growth studies, the blue color light was used for the optimization of the EPS production.

3.3. Response surface optimization of EPS production and ANNOVA

The effect of abiotic factors, pH (5-8), temperature (30-40°C), sucrose concentration (10-50%), light (blue) exposure time (24-96 h), and EPS yield was investigated using BBD.

ACCEPTED MANUSCRIPT

Based on the experimental design, the maximum EPS yield (582.5 mg/L) was obtained at pH 7.0, 35 °C, and 30% of sucrose concentration under 60 h of incubation with blue light illumination. Xing et al. (2018) reported that the addition of sucrose into the growth medium enhanced the production of EPS by *Leuconostoc mesenteroides*. The optimization study revealed that the blue color light and sucrose concentration in the growth medium significantly affect the EPS production in the fermentation system.

The BBD experimental design and the experimental results of the EPS production are presented in Table 1. An ANOVA test for the EPS production was performed to make sure the significance of the model terms. The test result for the quadratic model (Eq. 1) was highly significant, as evident from the Fisher's F-test ($p < 0.005$). The predicted R^2 and adjusted R^2 values were close to 1.0, indicating the model well fitted the experimental data. In addition, sequential model sum of squares, lack of fit tests and model summary statistics further supported the significance and adequacy of the model (Table 2). Three dimensional plots provided in Fig. 3 graphically represent the regression equations and were used to visualize the relationship between the response and experimental levels of each variable to determine optimum EPS production.

3.4. Characterization of EPS

SEM images showed the smooth and porous structure of the EPS (Fig.4). It has been reported that the porous nature of EPS is important for the water holding capacity (Shukla et al., 2011). The FT-IR spectra of the EPS showed many peaks from 3370-745/cm (Fig.5 a). A broad absorption peak at 3370/cm indicated the presence of a high level of O-H stretching of hydroxyls confirming the presence of polysaccharides. The sharp peaks at 2930 and 2850/cm was assigned to the C-H stretching vibrations of the polysaccharide materials. The absorption

ACCEPTED MANUSCRIPT

peaks at 1750 and 1680/cm indicate the amide and carboxyl groups, respectively. The intense peaks at 1450 and 1165/cm are assigned to be the C-O, C-O-C stretching of carbohydrates. The adoption peak at 745/cm indicates the glycosidic linkage of exopolysaccharides. The results are consistent with previous studies reporting the FTIR characterization of EPS (Kanmani et al., 2011; Sun et al., 2009; Wang et al., 2008; Saravanan et al., 2016).

XRD analysis was carried out to identify the amorphous nature of the EPS (Fig.5 b). The XRD spectra showed diffraction peaks at 31.6, 43.5, 45.3 and 50.8 °C, which indicate the crystalline structure of the EPS. The results are consistent with the previous studies reporting the crystalline nature of the EPS produced from *Bacillus licherniformis* (Singh et al., 2011), micro-algae (Mishra et al., 2011), and *Leuconostoc lactis* (Saravanan et al., 2016).

3.5. Emulsifying activity of EPS

The emulsifying activity is the most important feature of bacterial EPS. In our study, the EPS produced by the isolate *Rhodobacter* sp. BT18 showed a high emulsification activity against tested hydrophobic substrates compared to the Tween 80 (Table 3). The emulsification index of the EPS was > 75% for all the substrates (xylene, vaseline, coconut oil, peanut oil, and sunflower oil). Sunflower oil showed the maximum emulsification of 92.3%. Priyanka et al. (2015) reported that the EPS produced by *Rhizobium* sp. PRIM-18 emulsified 96% of sunflower oil. Lower emulsifications were seen in the case of xylene (75.5%) and vaseline (77.3%). Coconut oil (87.3%) and peanut oil (84.6%) too were considerably emulsified. The results indicated that the EPS was more efficient than the control Tween 80, which is an alternate to the chemical surfactants, and could be used in drug delivery systems for

ACCEPTED MANUSCRIPT

lipophilic bioactive systems. The highest emulsification activity of the oils (coconut, peanut and sunflower oil) suggested that the EPS could be used as a potential surfactant for oil spill remediation. In addition, the high xylene emulsification ability of EPS could be utilized for enhanced removal of xylene from the ecosystem.

3.6. Flocculating activity of EPS

The flocculating activity of the EPS produced by *Rhodobacter* sp. BT18 was studied with various concentrations of the EPS (Fig. 6). The results showed that the maximum flocculating activity of about 75.4% was observed at 30 mg/L concentration of the EPS. The flocculating activity gradually increased with increase in the concentration of EPS from 10-30 mg/L and decreased to 25.5 and 20.2 % at 40 mg/L and 50 mg/L, respectively. It has been reported that the dosage of EPS and the size of floc were related to each other. The kaolin particles in the reaction mixture around the EPS might aid in the increasing flocculation at lower concentrations. At higher concentrations that excessive amount of EPS may oversaturate the binding sites of the kaolin particles resulting in lower flocculating activity (Yoki et al., 1997; Prasertsan et al., 2006). Lee et al. (1995) observed that both deficiency and abundance of EPS and kaolin clay negatively affected the flocculating activity.

3.7. Metal chelation property of EPS

The EPS showed effective As and Pb chelation activities. About 64% of As and 51 % of Pb chelation was observed for 100 mg/L of As and Pb, respectively (Fig.7). Increase in As and Pb concentration confirmed the chelation activity. It has been reported that the hydroxyl and carbonyl groups of polysaccharides could be responsible for As and Pb chelation (Shuhong et

ACCEPTED MANUSCRIPT

al., 2014). The metal-chelating property of the EPS could open new avenues for the bioremediation of heavy metals from water.

4. Conclusion

In this study, a new phototrophic bacterium, *Rhodobacter* sp. BT18 was isolated from brackish water and the optimal conditions for its EPS production and the structural characteristics of the produced EPS were investigated. The maximum EPS yield (582.5 mg/L) was obtained under the condition of pH 7.0, 35 °C, and 30% of sucrose concentration, and 60 h of incubation under the blue light illumination. To the best of our knowledge, the EPS production by *Rhodobacter* sp. under different light sources has never been reported in the literature. The EPS showed potential emulsification, flocculation and metal chelating activities.

Acknowledgement

Financial support from the Korea Institute of Energy Technology Evaluation and Planning (KETEP) (Grand # 20172010000780) is appreciated. This paper was also supported by research funds of Chonbuk National University in 2017.

References

Amjres, H., Béjar, V., Quesada, E., Carranza, D., Abrini, J., Sinquin, C., Ratiskol, J., Colliec-Jouault, S., Llamas, I. (2015). Characterization of haloglycan, an exopolysaccharide produced by *Halomonas stenophila* HK30. *International Journal of Biological Macromolecules,* 72, 117–124.

ACCEPTED MANUSCRIPT

Biebl, H., & Pfennig, N., (1981). Isolation of members of the family *Rhodospirillaceae*. In: Starr, M., Stolp, H., Tru per Balows, H., Schlegel, A., editors. The prokaryotes SE e 14. Springer Berlin Heidelberg, 267–73.

Calvano, C. D., Italiano, F., Catucci, L., Agostiano, A., Cataldi, T. R., Palmisano, F., Trotta, M. (2014). The lipidome of the photosynthetic bacterium *Rhodobacter sphaeroides* R26 is affected by cobalt and chromate ions stress. *International Journal on the Role of Metal Ions in Biology, Biochemistry and Medicine,* 27, 65–73.

Carrion, O., Delgado, L., Mercade, E. (2015). New emulsifying and cryoprotective exopolysaccharide from Antarctic *Pseudomonas* sp. ID1. *Carbohydrate Polymers,* 117, 1028–1034.

Cohen Bazire, G., Sistrom, W. R., Stanier, R. Y. (1957). Kinetic studies of pigment synthesis by non-sulfur purple bacteria. *Journal of Cellular and Comparative Physiology,* 49, 25–68.

Cooper, D. G., & Goldenberg, B. G. (1987). Surface-Active Agents from Two *Bacillus* Species. *Applied and Environmental Microbiology,* 53, 224–229.

Fonti, V., Beolchini, F., Rocchetti, L., Dell Anno, A. (2015). Bioremediation of contaminated marine sediments can enhance metal mobility due to changes of bacterial diversity. *Water Research,* 68, 637–650.

Freitas, F., Alves, V. D., Reis, M. A. M. (2011). Advances in bacterial exopolysaccharides: From production to biotechnological applications. *Trends in Biotechnology,* 29(8), 388–398.

Govarthanan, M., Shim, J., Praburaman, L., Kim, S. A., Oh, B. T. (2016). Isolation of an exopolysaccharide producing heavy metal resistant *Halomonas* sp. MG. *Archives of Microbiology,* 198, 205–209.

ACCEPTED MANUSCRIPT

Han, Y., Liu, E., Liu, L., Zhang, B., Wang, Y., Gui, M., Wu, R., Li, P. (2015). Rheological, emulsifying and thermostability properties of two exopolysaccharides produced by *Bacillus amyloliquefaciens* LPL061. *Carbohydrate Polymers*, 115, 230–237.

Kanmani, P., Satish kumar, R., Yuvaraj, N., Paari, K.A., Pattukumar, V., Arul, V. (2011). Production and purification of a novel exopolysaccharide from lactic acid bacterium *Streptococcus phocae* PI80 and its functional characteristics activity in vitro. *Bioresource Technology,* 102,

Katsuda, T., Lababpour, A., Shimahara, K., Katoh, S. (2004). Astaxanthin production by *Haematococcus pluvialis* under illumination with LEDs. *Enzyme and Microbial Technology,* 35(1): S81–S86.

Kumar, A. S., & Mody, K. (2009). Microbial exopolysaccharides: Variety and potential applications. In H. A. R. Bernd (Ed.), Microbial production of biopolymers and polymer. Precursors-Applications and perspectives (pp. 229–255). Norfolk, UK: Caister Academic Press. ISBN: 978-1-904455-36-3

Kuo, F. S., Chien, Y. H., Chen, C. J. (2012). Effects of light sources on growth and carotenoid content of photosynthetic bacteria *Rhodopseudomonas palustris*. *Bioresource Technology*, 113, 315–318.

Lee, S., Lee, H., Jang, S. O., Lee, K. L. (1995). Microbial flocculant from *Arcuadendron* sp. TS-49. *Biotechnology Letters*, 17 (1), 95–100.

Li, X., Peng, W., Jia, Y., Lu, L., Fan, W. (2016). Bioremediation of lead contaminated soil with *Rhodobacter sphaeroides*. *Chemosphere*, 156, 228–235.

Malick, A., Khodaei, N., Benkerroum, N., Karboune, S. (2017). Production of exopolysaccharides by selected *Bacillus* strains: Optimization of media composition to maximize the yield and structural characterization. *International Journal of*

ACCEPTED MANUSCRIPT

Biological Macromolecules, 102, 539–549.

Mishra, A., Kavita, K., Jha, B. (2011). Characterization of extracellular polymeric substances produced by micro-algae *Dunaliella salina*. *Carbohydrate Polymers,* 83, 852–857.

Mujahid, M. D., Sasikala, C. H., Ramana, C. H. V. (2011). Production of indole-3-acetic acid and related indole derivatives from L-tryptophan by *Rubrivivax benzoatilyticus JA2*. *Applied Microbiology and Biotechnology,* 89, 1001–1008.

Nicolaus, B., Kambourova, M., Oner, E. T. (2010). Exopolysaccharides from extremophiles: From fundamentals to biotechnology. *Environmental Technology,* 31(10), 1145–1158.

Peng, W., Li, X., Song, J., Jiang, W., Liu, Y., Fan, W. (2018). Bioremediation of cadmium- and zinc contaminated soil using *Rhodobacter sphaeroides*. *Chemosphere,* 197, 33–41.

Prasertsan, P., Dermlim, W., Doelle, H., Kennedy, J. F. (2006). Screening, characterization and Flocculating property of carbohydrate polymer from newly isolated *Enterobacter cloac* WD7. *Carbohydrate Polymers,* 66:289–297.

Priyanka, P., Arun, A.B., Ashwini, P., Rekha, P. D. (2015). Versatile properties of an exopolysaccharide R-PS18 produced by *Rhizobium* sp. PRIM-18. *Carbohydrate Polymers,* 126, 215–221.

Rehm, B. H. A. (2009). Microbial production of biopolymers and polymer precursors: Applications and perspectives. Norfolk: Caister Academic Press

Sambrook, J., & Russell, D.W., (2001). Molecular cloning: a laboratory manual. 3rd ed. Cold Spring Harbor, NY: Cold Spring Harbor Laboratory Press.

ACCEPTED MANUSCRIPT

Saravanan, C., Shetty, P. K. H. (2016). Isolation and characterization of exopolysaccharide from *Leuconostoclactis* KC117496 isolated from idli batter. *International Journal of Biological Macromolecules,* 90, 100–106.

Sardari, R. R. R., Kulcinskaja, E., Ron, E. Y. C., Björnsdóttir, S., Friðjónsson, O. H., Hreggviðsson, G. O., Karlsson, E. N. (2017). Evaluation of the production of exopolysaccharides by two strains of the thermophilic bacterium *Rhodothermus marinus*. *Carbohydrate Polymers,* 156, 1–8.

Shuhong, Y., Meiping, Z., Hong, Y., Han, W., Shan, X., Yan, L. (2014). Biosorption of Cu2+, Pb2+ and Cr6+ by a novel exopolysaccharide from *Arthrobacter* sp-5. *Carbohydrate Polymers,* 101, 50–56.

Shukla, R., Shukla, S., Bivolarski, V., Iliev, I., Ivanova, I., Goyal, A. (2011). Structural Characterization of Insoluble Dextran Produced by *Leuconostoc mesenteroides* NRRL B-1149 in the Presence of Maltose. *Food Technology and Biotechnology,* 49, 291–296.

Singh, R. P., Shukla, M. K., Mishra, A., Kumari, P., Reddy, C. R. K., Jha, B. (2011). Isolation and characterization of exopolysaccharides from seaweed associated bacteria *Bacillus licheniformis*. *Carbohydrate Polymers,* 84, 1019–1026.

Sun, H.M., Mao, W.J., Chen, Y., Guo, S.D., Li, H.Y., Qi, X.H., Chen, Y.L., Xu, J. (2009). Diversity of Bioactive polysaccharide originated from marine, *Carbohydrate Polymers*, 78, 117–124.

Wang, Y., Ahmed, Z., Feng, W., Li, C., Song, S. (2008). Physicochemical properties of exopolysaccharide produced by *Lactobacillus kefiranofaciens* ZW3 isolated from Tibet kefir. *International Journal of Biological Macromolecules,* 43, 283–288.

ACCEPTED MANUSCRIPT

Xing, H., Du, R., Zhao, F., Han, Y., Xiao, H., Zhou, Z. (2018). Optimization, chain conformation and characterization of exopolysaccharide isolated from *Leuconostoc mesenteroides* DRP105. *International Journal of Biological Macromolecules*, 112, 1208–1216.

Ye, J. Y., Liu, T., Chen, Y., Liao, Q., Wang, Z. K., Chen, G. C. (2013). Effect of AI crude extract on PHB accumulation and hydrogen photoproduction in *Rhodobacter sphaeroides*. *International Journal of Hydrogen Energy*, 38, 15770–15776.

Yokoi, H., Yoshida, T., Mori, S., Hirose, J., Hayashi, S., Takasaki, Y. (1997). Biopolymer flocculant produced by an *Enterobacter* sp. *Biotechnology Letters*, 19, 569–573.

Figure legends

Fig. 1. 16S rDNA based phylogenetic analysis of *Rhodobacter* sp. BT18. The phylogenetic tree constructed by the neighbor-joining method showing the position of isolate *Rhodobacter* sp. BT18.

Fig. 2. Effect of different light sources on the growth of *Rhodobacter* sp. BT18.

Fig. 3. Response surface 3-D plots of EPS yield under the BBD optimized conditions.

Fig. 4. SEM micrographs of the EPS produced by Rhodobacter sp. BT18.

Fig. 5 (a) FT-IR and **(b)** XRD of EPS

Fig. 6. Flocculating activity of EPS

Fig. 7. Metal chelating property of EPS.

ACCEPTED MANUSCRIPT

Experiment	pH	Temp. (°C)	Sucrose (%)	Incubation with LB (h)	EPS yield (mg/L)
1	7.0	35	10	96	420.0
2	7.0	35	30	60	474.5
3	7.5	30	30	60	392.3
4	6.5	35	30	24	110.1
5	7.0	35	30	60	473.5
6	7.0	30	30	24	128.9
7	7.5	35	30	24	134.5
8	7.5	35	30	96	169.5
9	7.5	35	50	60	375.6
10	7.0	35	30	60	475.5
11	6.5	35	30	96	135.7
12	7.0	35	10	60	129.9
13	7.0	35	30	60	580.8
14	7.0	40	10	60	320.5
15	7.0	40	30	96	360.6
16	7.0	35	50	24	148.9
17	7.0	30	30	96	420.5
18	7.5	35	10	60	440.5
19	7.0	35	50	96	410.0
20	7.0	40	50	60	245.5
21	7.0	35	10	24	120.6
22	7.0	30	50	60	142.0
23	7.0	35	30	60	582.5
24	6.5	30	30	60	229.8
25	7.5	40	30	60	386.5
26	7.0	30	10	60	312.5
27	6.5	40	30	60	100.2
28	6.5	35	50	60	102.4
29	7.0	40	30	24	200.5

Table 1. Experimental design

ACCEPTED MANUSCRIPT

Table 2. ANOVA

Source of variation	Sum of Squares	Degrees of freedom	Mean squares	*F* value	*p*-value
Model	5.445E+05	14	38892.44	4.08	0.0064[a]
A	99144.63	1	99144.63	10.39	0.0061
B	12.40	1	12.40	0.0013	0.9717
C	8512.01	1	8512.01	0.8921	0.3609
D	95899.38	1	95899.38	10.05	0.0068
AB	3831.61	1	3831.61	0.4016	0.5365
AC	349.69	1	349.69	0.0366	0.8509
AD	22.33	1	22.33	0.0023	0.9621
BC	2280.06	1	2280.06	0.2390	0.6325
BD	4323.06	1	4323.06	0.4531	0.5118
CD	366.72	1	366.72	0.0384	0.8474
A^2	1.824E+05	1	1.824E+05	19.12	0.0006
B^2	66303.57	1	66303.57	6.95	0.0196
C^2	78526.33	1	78526.33	8.23	0.0124
D^2	1.683E+05	1	1.683E+05	17.64	0.0009
Residual	1.336E+05	14	9541.93	-------	-----
Lack of fit	1.198E+05	10	11.980.62	3.48	0.1205
Pure error	13780.79	4	3445.20	-----	---------
Core total	6.781E +05	28	----------	------	---------

ACCEPTED MANUSCRIPT

ACCEPTED MANUSCRIPT

Table 3. Emulsifying activity of EPS produced by *Rhodobacter* sp. BT18 against the tested hydrophobic substrates

Hydrophobic substrates	Emulsifying activity (%)	
	***Rhodobacter* sp. BT18**	**Control (Tween 80)**
Coconut oil	87.3 ± 3.0	54.4 ± 2.0
Peanut oil	84.6 ± 2.6	49.9 ± 3.3
Xylene	75.5 ± 4.2	25.4 ± 2.4
Vaseline	77.3 ± 3.2	31.4 ± 1.9
Sunflower oil	92.3 ± 1.7	57.5 ± 2.5

ACCEPTED MANUSCRIPT

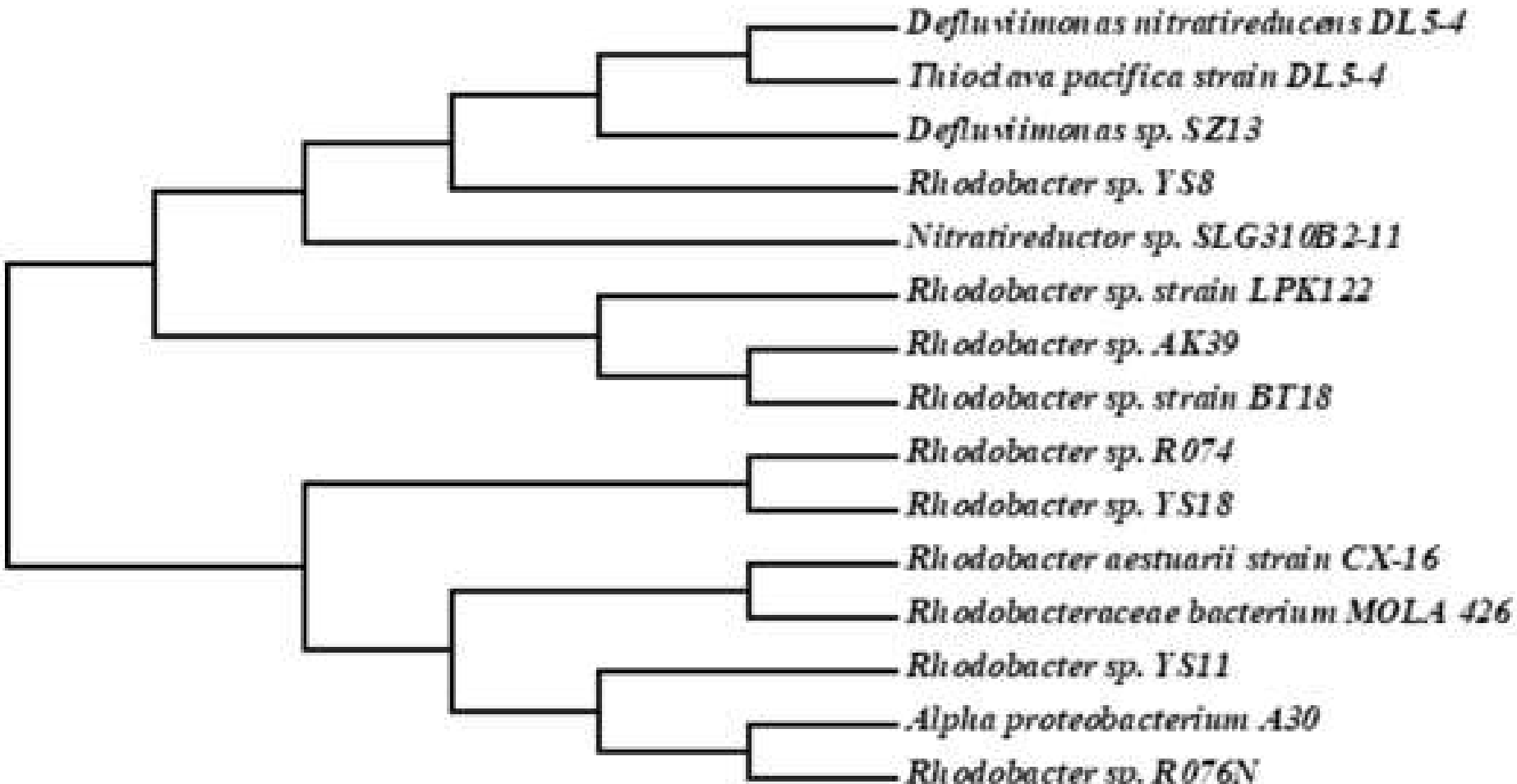

Defluviimonas nitratireducens DL5-4
Thiocdava pacifica strain DL5-4
Defluviimonas sp. SZ13
Rhodobacter sp. YS8
Nitratireductor sp. SLG310B2-11
Rhodobacter sp. strain LPK122
Rhodobacter sp. AK39
Rhodobacter sp. strain BT18
Rhodobacter sp. R074
Rhodobacter sp. YS18
Rhodobacter aestuarii strain CX-16
Rhodobacteraceae bacterium MOLA 426
Rhodobacter sp. YS11
Alpha proteobacterium A30
Rhodobacter sp. R076N

Figure 1

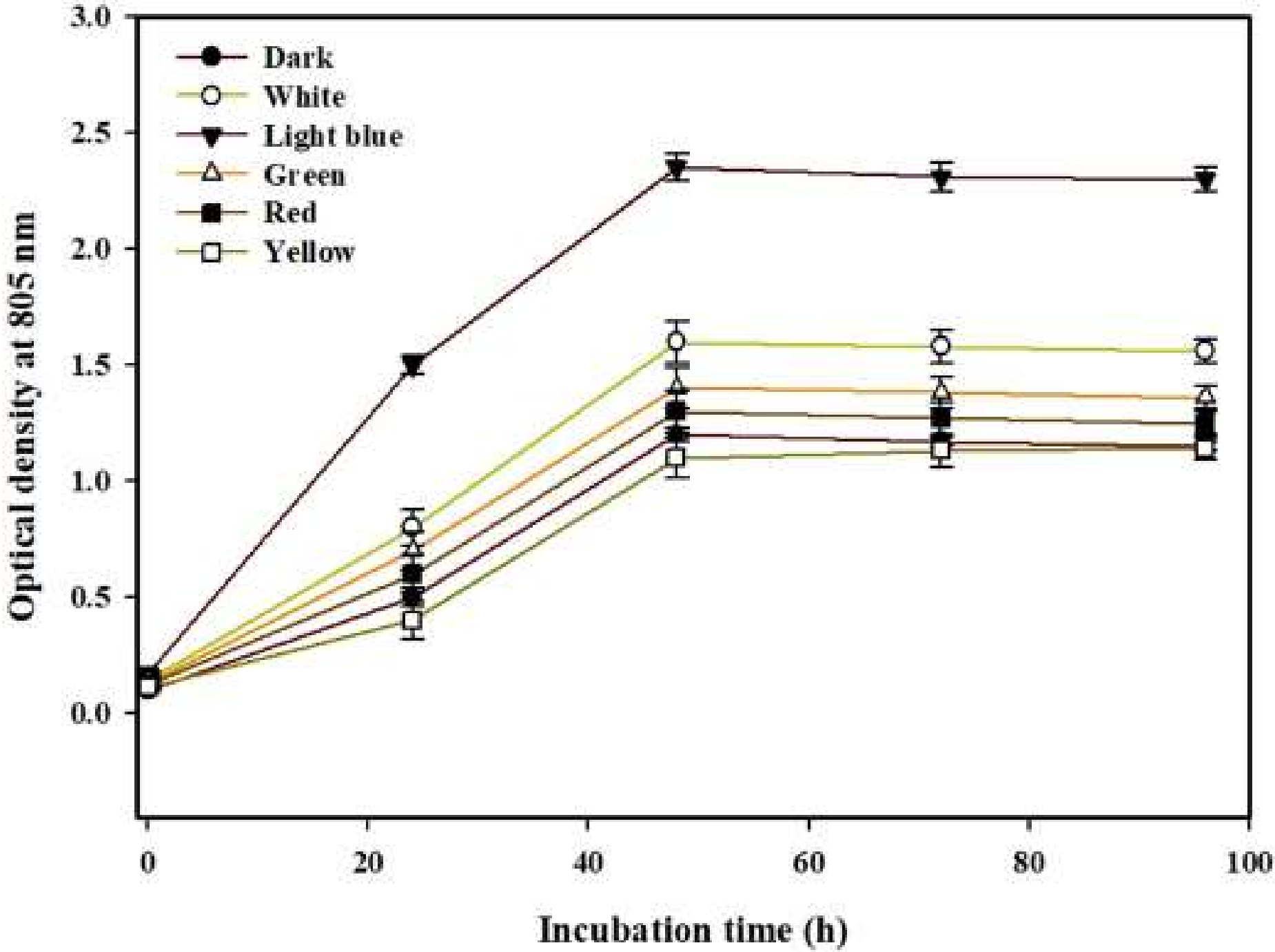

Dark
White
Light blue
Green
Red
Yellow
Optical density at 805 nm
3.0
2.5
2.0
1.5
1.0
0.5
0.0
0
20
40
60
80
100
Incubation time (h)

Figure 2

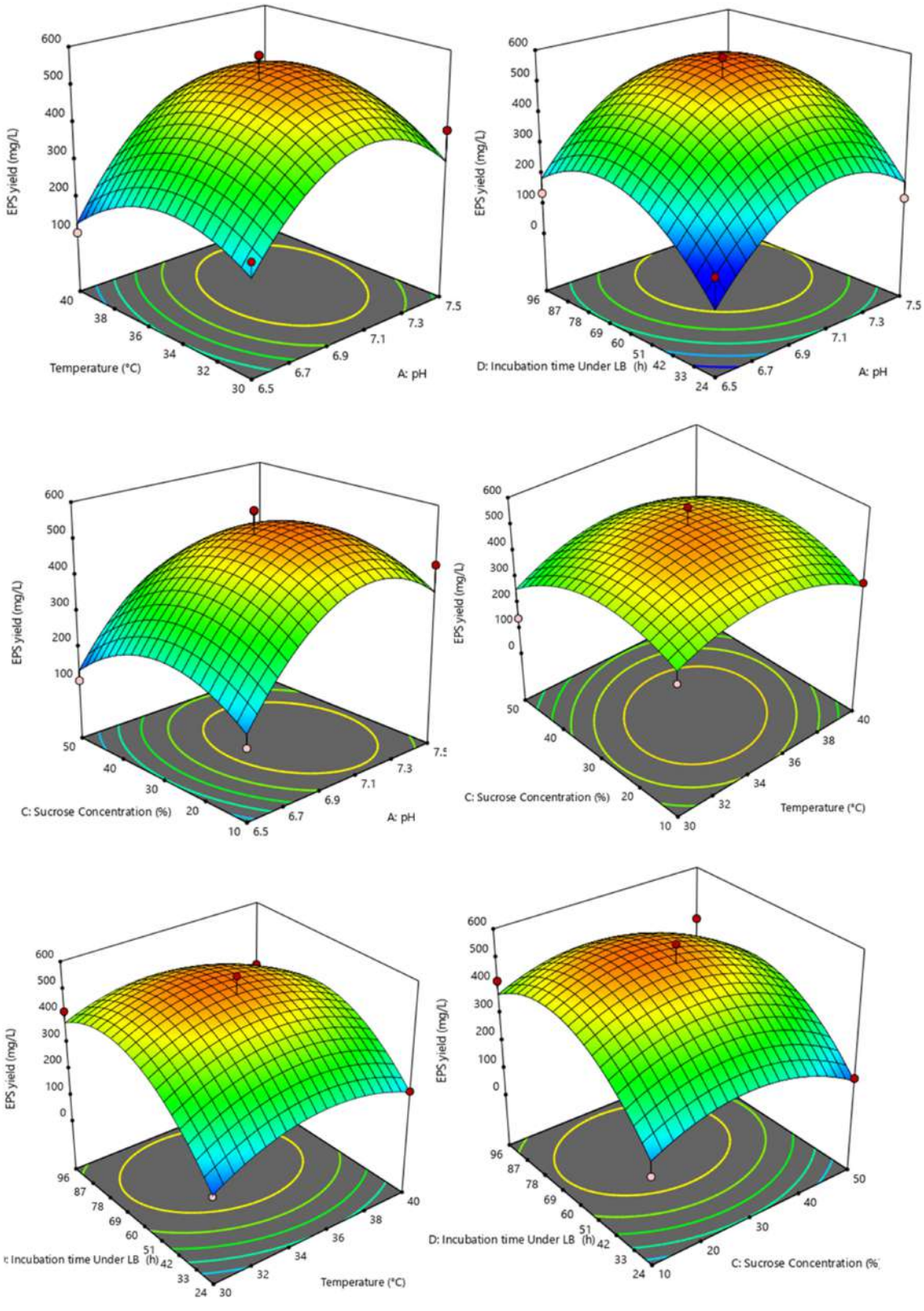

EPS yield (mg/L)
600
500
400
300
200
100
0
Temperature (°C)
40
38
36
34
32
30
A: pH
6.5
6.7
6.9
7.1
7.3
7.5
D: Incubation time Under LB (h)
96
87
78
69
60
51
42
33
24
C: Sucrose Concentration (%)
50
40
30
20
10

Figure 3

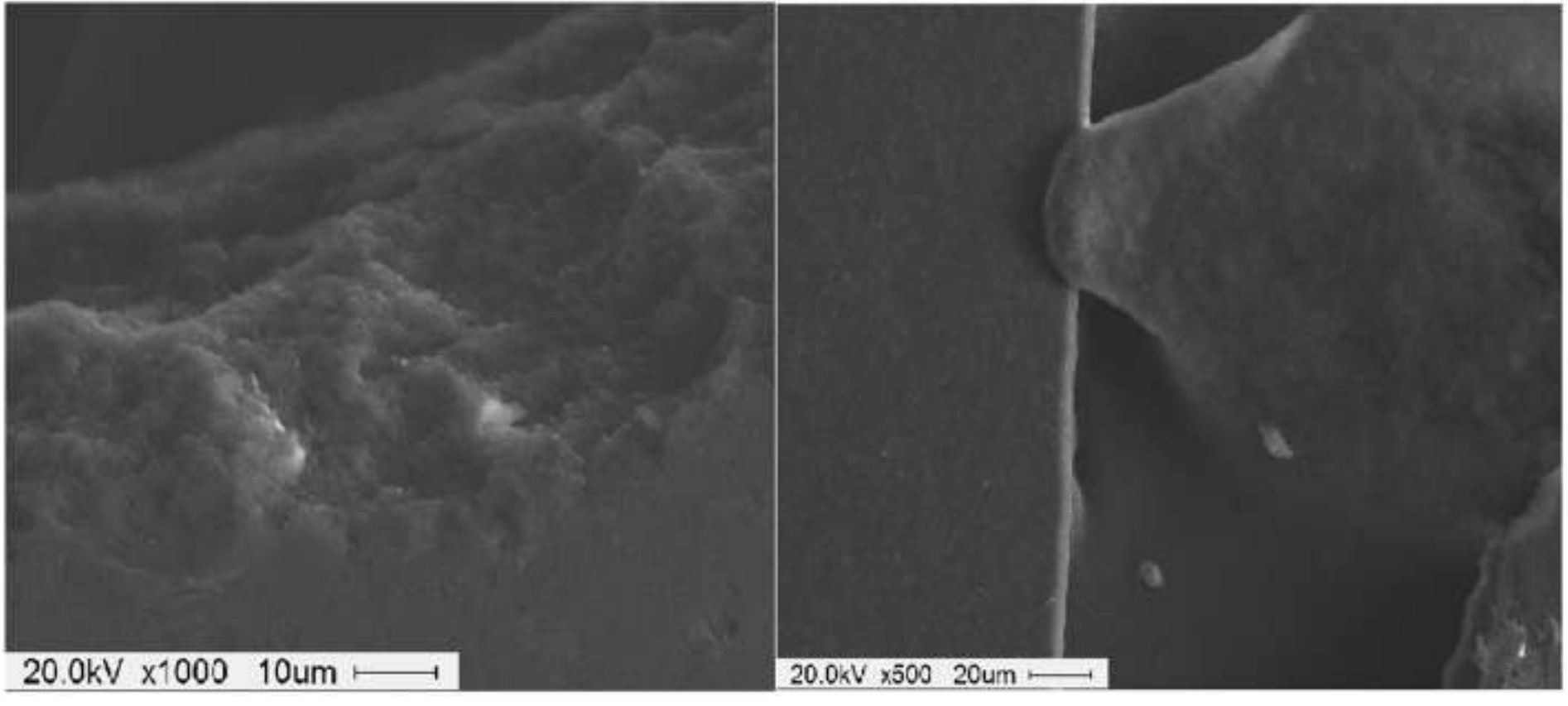


Figure 4

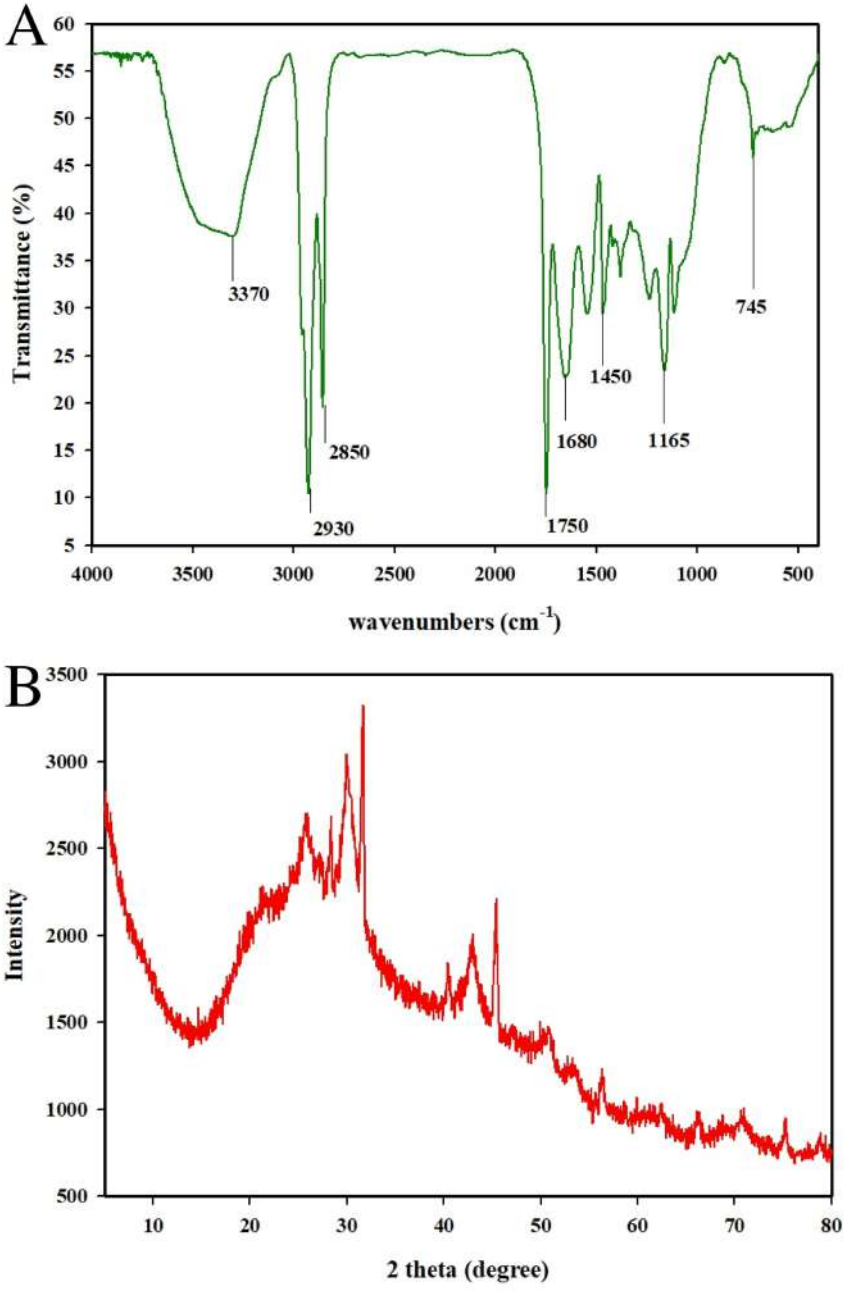

A
Transmittance (%)
wavenumbers (cm-1)
3370
2930
2850
1750
1680
1450
1165
745
B
Intensity
2 theta (degree)

Figure 5

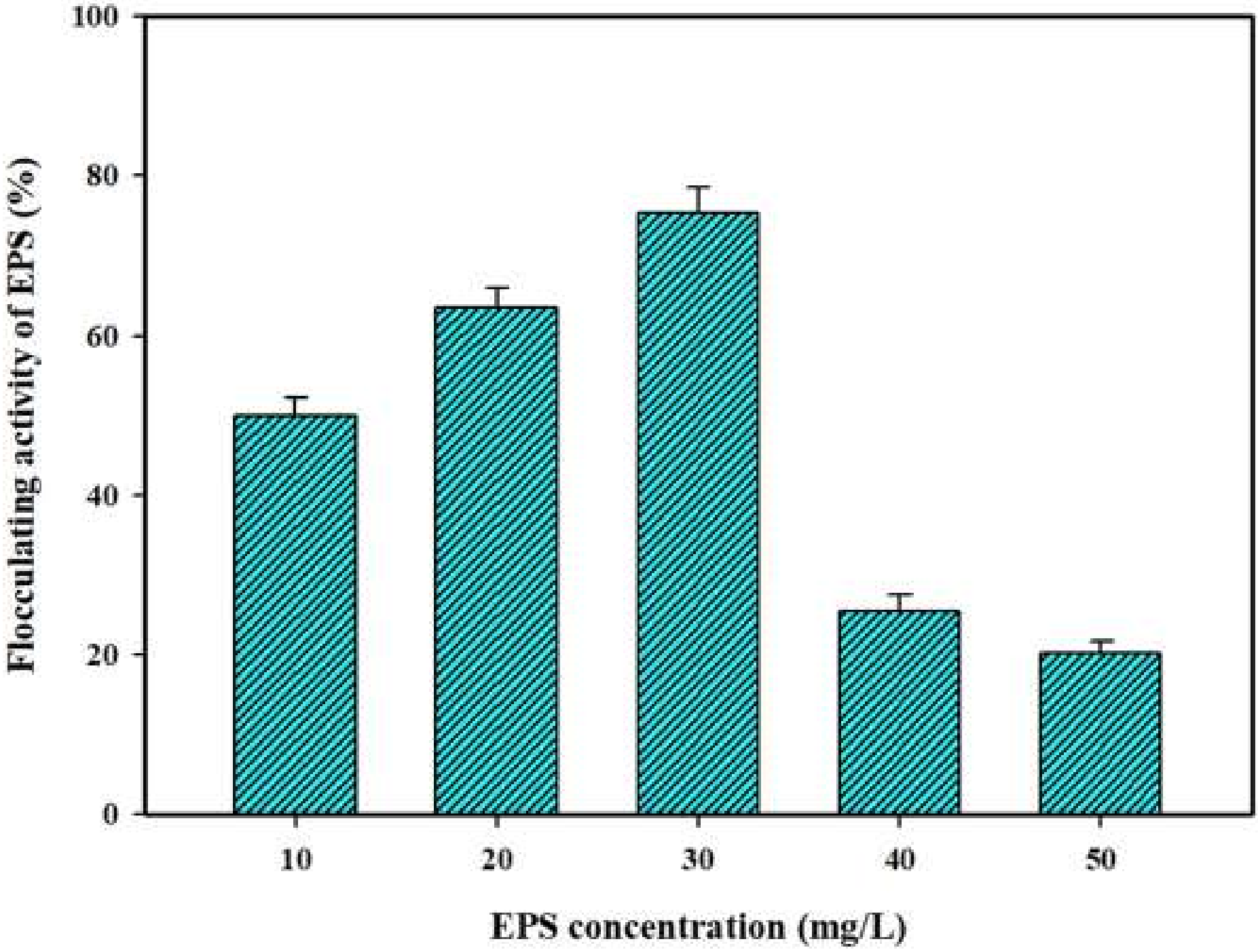

100
80
60
40
20
0
Flocculating activity of EPS (%)
10
20
30
40
50
EPS concentration (mg/L)

Figure 6

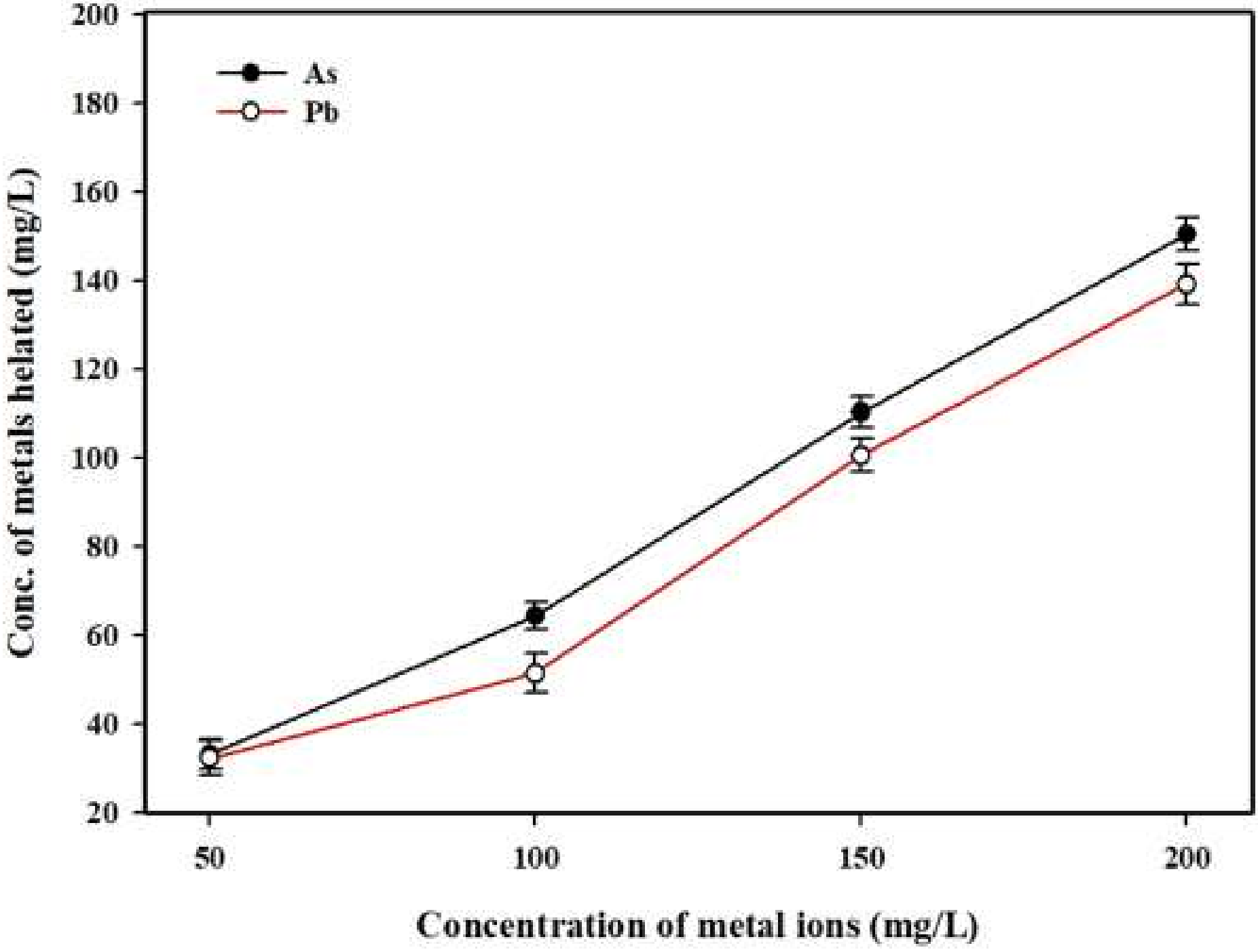

As
Pb
Conc. of metals helated (mg/L)
200
180
160
140
120
100
80
60
40
20
50
100
150
200
Concentration of metal ions (mg/L)

Figure 7

ScienceDirect

Ecotoxicology and Environmental Safety
Volume 174, 15 June 2019, Pages 699-705

In-vitro bio-mineralization of arsenic and lead from aqueous solution and soil by wood rot fungus, *Trichoderma* sp.

M. Govarthanan [a], R. Mythili [b], S. Kamala-Kannan [c], T. Selvankumar [b], P. Srinivasan [b], H. Kim [a]

Show more

Outline | Share | Cite

https://doi.org/10.1016/j.ecoenv.2019.03.034

Get rights and content

Highlights

- Wood rot fungal-mediated biomineralization of arsenic and lead in aqueous solution and soil was characterized.
- The microbiologically induced calcite precipitation was characterized using XRD and FT-IR.
- Maximum metal removal was optimized by BBD design Sequential extraction of metals revealed that the carbonate fraction of As and Pb was increase to 46.4% and 42.4% in bioremediated soil.

Abstract

In the present study, we investigated the role of calcite, i.e., microbiologically-induced precipitate by ureolytic *Trichoderma* sp. MG, in remediation of soils contaminated with arsenic (As) and lead (Pb). The fungus tolerates high concentrations of As (500 mg/L) and Pb (650 mg/L). The effects of three factors, i.e., urea concentration, $CaCl_2$ concentration and pH, on urease production and bio-mineralization of As and Pb were investigated using Box-Behnken design. The maximum urease production (920 U/mL) and metal removal efficiency (68% and 59% for Pb and AS, respectively) were observed in the medium containing urea of 300 mM and $CaCl_2$ of 75 mM at pH 9.0. Fourier transform infrared spectroscopy result revealed the formation of metal carbonates by the isolate MG. Sequential extraction of metals revealed that the

PGP College of Arts and Science
Namakkal

Ecotoxicology and Environmental Safety 174 (2019) 699–705

Contents lists available at ScienceDirect

Ecotoxicology and Environmental Safety

journal homepage: www.elsevier.com/locate/ecoenv

In-vitro bio-mineralization of arsenic and lead from aqueous solution and soil by wood rot fungus, *Trichoderma* sp.

M. Govarthanan[a,*], R. Mythili[b], S. Kamala-Kannan[c], T. Selvankumar[b], P. Srinivasan[b], H. Kim[a,*]

[a] Department of Environmental Engineering, University of Seoul, Seoul 02504, South Korea
[b] PG & Research Department of Biotechnology, Mahendra Arts and Science College (Autonomous), Kalippatti, Namakkal 637501, Tamil Nadu, India
[c] Division of Biotechnology, Advanced Institute of Environment and Bioscience, College of Environmental and Bioresource Sciences, Chonbuk National University, Iksan 54596, South Korea

ARTICLE INFO

Keywords:
Bio-mineralization
Calcite
Carbonate bound
Sequential extraction
Urease

ABSTRACT

In the present study, we investigated the role of calcite, i.e., microbiologically-induced precipitate by ureolytic *Trichoderma* sp. MG, in remediation of soils contaminated with arsenic (As) and lead (Pb). The fungus tolerates high concentrations of As (500 mg/L) and Pb (650 mg/L). The effects of three factors, i.e., urea concentration, $CaCl_2$ concentration and pH, on urease production and bio-mineralization of As and Pb were investigated using Box-Behnken design. The maximum urease production (920 U/mL) and metal removal efficiency (68% and 59% for Pb and AS, respectively) were observed in the medium containing urea of 300 mM and $CaCl_2$ of 75 mM at pH 9.0. Fourier transform infrared spectroscopy result revealed the formation of metal carbonates by the isolate MG. Sequential extraction of metals revealed that the carbonate fractions of As and Pb were increased to 46.4% and 42.4% in bioremediated soil, whereas in control they were 35.5% and 32.5%, respectively. The X-ray powder diffraction result further confirmed the role of calcite precipitate in bioremediation of As- and Pb-contaminated soils. The results points out that the microbiologically-induced calcite precipitation is a feasible, eco-friendly technology for the bioremediation of As- and Pb-contaminated sites.

1. Introduction

Arsenic (As) and lead (Pb) are well-known metals, primarily produced by mining, metal manufacturers, and human activities including modern industrial operations, and agricultural practices (Donahoe et al., 2004; Wang and Mulligan, 2006). The soil and/or water containing As and Pb pose(s) a serious threat to both the ecosystem and human health because of their high toxicity and difficulties in treatment (Hseu et al., 2010). The toxicity of the metals is associated with many kinds of human diseases including malfunctions of liver, heart, central nervous system, and kidney, skin and lung tumours, and cardiovascular disease (Dopp et al., 2004, 2010). Hence, a technology to efficiently remove As and Pb from contaminated soil and water has attracted increased attention worldwide.

The physico-chemical practices commonly applied for removal of As and Pb are ion exchange, chemical precipitation, electrochemical treatment, and reverse osmosis (Zhang et al., 2017). However, the applicability of these methods is limited because of their high cost, time demand and potential generation of secondary wastes (Cui et al., 2017). Recently, biological remediation of As and Pb is considered as a promising alternative due to its environmental friendliness and cost effectiveness (Govarthanan et al., 2010; Selvankumar et al., 2017). It has been well established that microorganisms can remediate As and Pb in soils through different routes such as intra and/or extra-cellular accumulation (Brookshaw et al., 2012), biosorption (Azarpira and Mahdavi, 2016; Balarak et al., 2016; Bazrafshan et al., 2017), bio-mineralization (Govarthanan et al., 2010), and chelation by producing organic acids (Gadd et al., 2012). However, the effectiveness of bioremediation of As and Pb varies depending on microbial sensitivity to soil redox potentials and/or valence state of metals (Qian et al., 2017).

Microbiologically-induced calcite precipitation (MICP) is a widely known in-situ bioremediation method, where metal-resistant microbes immobilize toxic metals in the form of minerals (Zhu and Dittrich, 2016). Recent progress in the science of MICP in bio-geological formations has shaped the interest of bioremediation researchers worldwide (Dhami et al., 2017). The precipitation of target metal compounds with calcium carbonate and its dominant derivatives (i.e., calcites) is mediated by a variety of bacteria, fungi, algae, and protista, thus, this mechanism is preferably defined as bio-mineralization and/or MICP (Gadd, 2010; Qian et al., 2015). Among the microorganisms, fungi have

* Corresponding authors.
E-mail addresses: gova.muthu@gmail.com (M. Govarthanan), h_kim@uos.ac.kr (H. Kim).

https://doi.org/10.1016/j.ecoenv.2019.03.034
Received 25 September 2018; Received in revised form 6 March 2019; Accepted 7 March 2019
0147-6513/ © 2019 Elsevier Inc. All rights reserved.

higher biomass and resistance to metals compared to bacteria and algae; thus, fungi could be the potential candidate for MICP in the treatment of As- and Pb-contaminated soils (Kumari et al., 2015).

Recent studies have reported the *Trichoderma* sp. could survive under As-stress conditions in the mode of biotransformation and speciation (Su et al., 2010, 2017). Most of the studies reported that *Trichoderma* sp. can remediate single metal by MICP (Su et al., 2015). Resistance to more than one metal would be advantageous in clean-up of multi-metal-contaminated soils. To the best of our knowledge, no study has been performed in the past on bioremediation of As- and Pb-contaminated soils based on calcite precipitation mediated by *Trichoderma* sp. Recently, we successfully isolated As- and Pb-resistant *Trichoderma* sp. MG from decayed wood. Hence, the present study deals (i) screening of the isolate, *Trichoderma* sp. MG, for ureolytic activity, (ii) assessing the potential of the isolate MG to immobilize As and Pb via MICP under optimized physico-chemical conditions using the Box-Behnken design (BBD), (iii) evaluating different fractions of As and Pb in bioremediated soils to better understand the interaction between the isolate MG and metals, and (iv) confirming the MICP process by applying Fourier transform infrared spectrpscopy (FT-IR) and X-ray diffraction (XRD) characterization for the bioremediated soils.

2. Materials and methods

2.1. Fungal strain

The isolation and identification of the isolate MG, and minimal inhibitory concentration of As and Pb for the fungal strain were reported in our previous study (Govarthanan et al., 2018).

2.2. Screening of ureolytic activity of isolate MG

The isolate MG was screened for urease activity using the Christensen's urea agar medium (Christensen, 1946). Briefly, well grown fungal discs (10 mm diameter) were transferred to the Christensen's urea agar and the plates were incubated at 26 ± 2 °C for 8–16 d. After incubation, the color change in the medium indicates the ureolytic activity of the isolate.

2.3. Optimization of urease activity and enhanced removal of As and Pb using Response surface methodology (RSM)

The BBD-based response surface methodology (RSM) was used to optimize the pH, urea, and $CaCl_2$ concentrations for enhanced production of urease and removal of As and Pb from soils. In brief, batch experiments were performed in 250 mL bottles containing 100 mL of mineral-precipitating media (MPM1) (Dhami et al., 2017) with different concentrations of urea (100–500 mM), $CaCl_2$ (50–100 mM), and pH (6 − 9). Metal solutions (100 mg/L) were carefully injected into the bottles after sterilization. Later, five discs of the isolate MG was aseptically inoculated into each bottle and incubated in a rotary shaker at 27 °C for 14 d. A total of 17 runs were executed to determine the optimal process factors; tests for As and Pb removal and urease activity were carried out according to the actual experimental design matrix. The result was analyzed by applying ANOVA and response plots. For RSM, the most widely used second-order polynomial equation was developed to fit the experimental result and identify the relevant model parameters.

$$Y = ß_0 + \sum ß_j X_i + \sum ß_j X_i^2 + \sum ß_{ij} X_i X_j \quad (1)$$

where Y is the predicted response; $ß_0$, $ß_i$, and $ß_{ij}$ are the coefficients of the regression model; and X_i and X_j represent independent variables.

The urease activity of the *Trichoderma* sp. was determined by measuring the amount of ammonia released from urea during the phenol-hypochlorite assay (Natarajan, 1995). One unit of urease activity was defined as the amount of enzyme liberating 1 μmol NH_3 from urea per minute. As and Pb concentrations in the samples were analyzed using inductive coupled plasma-mass spectroscopy (ICP-MS).

2.4. Characterization of fungal biomass using FT-IR

At the end of bioremediation experiments, the *Trichoderma* biomass was collected, washed several times with sterile distilled water, and dried for 24–48 h in a freeze dryer. The dried fungal biomass was analyzed by using FT-IR, and the spectrum was obtained using the KBr method on a Perkin-Elmer FT-IR spectrophotometer (Norwalk, VA, USA) in the region of 4000–400 cm^{-1}.

2.5. Bio-mineralization of As- and Pb-contaminated soil by Trichoderma sp

Soil samples were collected from a depth of 20 cm, air-dried, sieved to < 2 mm, sterilized at 120 °C for 70 min (four consecutive days), and dried in an oven at 40 °C for a week. Two different groups of experiments were performed for the bioremediation studies: bio-mineralization and control experiments. Bio-mineralization experiments were performed with the following matrix: 10 g of soil in 100 mg kg^{-1} of As or Pb in MPM1 + 10 discs of *Trichoderma* culture + 300 mM urea and 75 mM $CaCl_2$ solution. On the other hand, control experiments were performed with the following matrix: 10 g of soil in 100 mg kg^{-1} of As or Pb in MPM1. The flasks were incubated in a rotary shaker (180 rpm) at room temperature for 14 d. After incubation, the samples were dried at 60 °C for 48 h and used for metal sequential extraction studies. The exchangeable (F1), carbonate (F2), iron and manganese oxide-bound (F3), organic-bound (F4), and residual fractions (F5) of As and Pb in the soil samples were determined according to Song et al. (2009).

2.6. X-ray diffraction investigation of soil

The soil samples were analyzed by XRD to identify the metal crystals produced by *Trichoderma* sp. The XRD analysis was carried out according to Govarthanan et al. (2010).

2.7. Statistical analysis

The optimization experiments were performed using a statistical software Design Expert (Version 6.0, Stat-Ease Inc., Minneapolis, USA). The effective variables for the enhanced bio-mineralization were studied with response surface methodology (RSM) Box-Behnken design (BBD). By using the optimal BBD, the points of the bio-mineralization experiments that will reduce the error in the estimated co-efficient of the response model will be selected. An ANOVA test for urease production, As and Pb removal were performed to ensure a good model.

3. Results and discussion

3.1. Screening of ureolytic activity of isolate MG

The formation of pink color around the mycelia plug in Christensen's urea agar medium plate indicates the ureolytic activity of the isolate MG. The urea agar base was supplemented with sterile urea. Phenol red was added in the urea agar medium as a pH indicator. The urea hydrolysis will increase the pH of the medium to render it alkaline, resulting in development of pink color. The alkaline pH indicates the production of ammonia (Christensen, 1946; Li et al., 2015).

3.2. Response surface optimization of urease production, As and Pb removal

The effect of bioremediation factors such as concentrations of urea and $CaCl_2$, and pH on urease production and removal of As and Pb was investigated using the BBD (Fig. 1). Based on the experimental design, the maximum urease production (920 U/mL) and high metal removal

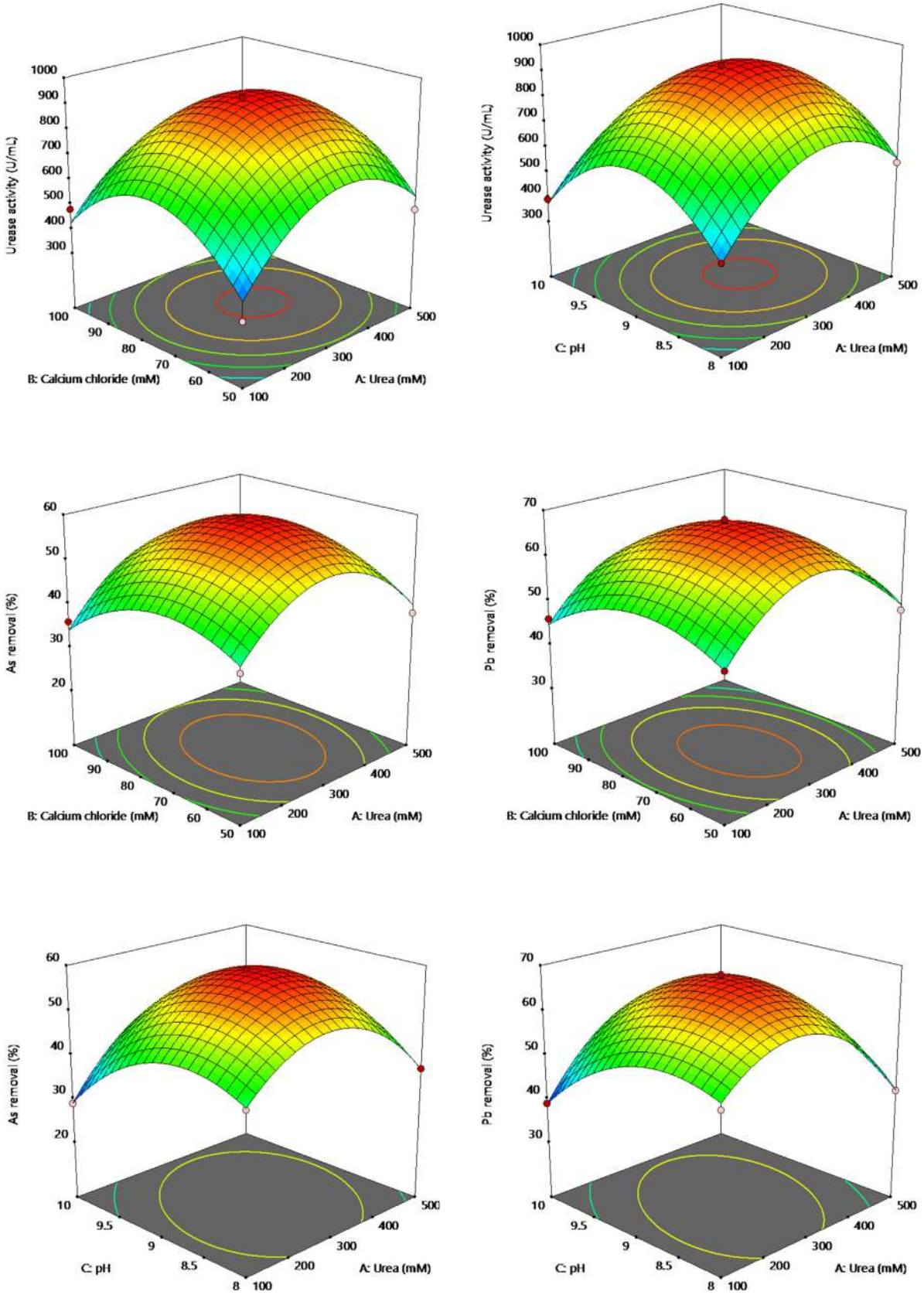


Fig. 1. Response surface 3-D plots of urease production, As and Pb removal by the isolate *Trichoderma* sp. MG.

efficiencies (68% for Pb and 59% for As) were observed at the experimental condition of 300 mM of urea and 75 mM of $CaCl_2$ at pH 9.0. However, much lower urease production (390 U/mL) and metal-removal efficiencies (39.0% for Pb and 29% for As) were achieved at 100 mM of urea and 75 mM of $CaCl_2$ at pH 10. The result showed that the metal removal was directly proportional to the amount of urease

produced. The maximum metal removal efficiency of ~60% was observed along with high urease production, while the minimum efficiency of 30% was along with low urease production. The MICP process had a positive effect on the removal of As and Pb by urease production. The different removal efficiencies by the isolate *Trichoderma* sp. MG for Pb (68.0%) and As (59%) might be due to different physiological adaptation mechanisms and metal tolerance mechanisms. Several studies have reported the varying toxicity tolerance of fungal isolates to different metals (Gonzalez-Chavez et al., 2002; Balamurugan and Schaffner, 2006). The MICP process depends on the microorganisms modifying their local environment to create an appropriate physico-chemical condition for the precipitation of metals (Gadd et al., 2010, 2012). Li et al. (2014) demonstrated that the urease-positive fungus, *Neurospora crassa* has the ability to precipitate metal carbonates when it is incubated in urea-amended media, suggesting that metal remediation or recovery by fungi is a promising method.

Li et al. (2015) reported that the media amended with urea and $CaCl_2$ involve precipitation of metals by the fungus, *M. gramineum*. Several studies have reported the concentration of available calcium sources significantly affect the microbial growth and carbonate precipitation (Gorospe et al., 2013; Li et al., 2013). It was reported that $CaCl_2$ could induce the growth of *Aspergillus* sp. UF3 and calcite precipitation under Pb stress (Dhami et al., 2017). Regarding the pH, a rather high pH is preferable; Achal et al. (2012) reported that the best pH would be 9.2 for the bio-mediated precipitation of most heavy metals. In short, the literature and the result from this study demonstrate that the optimization of physico-chemical conditions for the metal remediation or recovery by fungi would be a promising method.

3.3. ANOVA test for urease production and enhanced As and Pb removal

The BBD experimental design and results of urease production and As and Pb removal obtained from each run are presented in Table 1. The results were analyzed and the responses were generated. An ANOVA test for urease production and As and Pb removal designs was performed to ensure a good model. The test result for the quadratic regression model (Eq. (1)) exhibits that it is highly significant, as evident from the Fisher's F-test ($p < 0.005$). There was only a 0.01% chance that a model F-value could occur due to noise. The lack of fit values of urease production 146.04, As removal 36.25, and Pb removal 17.92 implies that lack of fit is also significant. There are only a 0.02%, 0.23%, and 0.88% chance that lack of fit F-value could occur due to noise respectively. The predicted R^2 and adjusted R^2 values were in reasonable agreement with the value of R^2, which is closer to 1.0, indicating the better fitness of the model in the experimental data. In addition, sequential model sum of squares, lack of fit tests and model summary statistics further supported the significance and adequacy of the model (Table 2). Three dimensional plots provided in Fig. 1 graphically represent the regression equations and were used to visualize the relationship between the response and experimental levels of each variable and the type of interaction between the variables to determine the optimum urease production and As and Pb removal efficiencies. The coefficients of all the regression equations were determined to obtain the followings.

Table 1
Box-Behnken design and response result values of urease production, As and Pb removal.

Run	Urea (mM)	$CaCl_2$ (mM)	pH	Urease (U/mL)	As (%)	Pb (%)
1	500	100.0	9.0	620.0	42.0	44.0
2	500	75.0	8.0	540.0	37.0	42.0
3	300	75.0	9.0	920.0	59.0	67.0
4	300	50.0	8.0	520.0	45.0	55.0
5	100	100.0	9.0	480.0	36.0	46.0
6	300	75.0	9.0	900.0	58.0	67.0
7	500	50.0	9.0	480.0	38.0	48.0
8	100	75.0	10.0	390.0	29.0	39.0
9	300	75.0	9.0	920.0	59.0	68.0
10	500	75.0	10.0	490.0	41.0	51.0
11	100	50.0	9.0	320.0	39.0	49.0
12	300	100.0	10.0	340.0	34.0	44.0
13	100	75.0	8.0	420.0	42.0	52.0
14	300	100.0	8.0	440.0	44.0	54.0
15	300	75.0	9.0	920.0	59.0	67.0
16	300	75.0	9.0	920.0	59.0	67.0
17	300	50.0	10.0	480.0	45.0	55.0

Table 2
ANOVA for response surface quadratic model of urease production, As and Pb removal.

Source of variation	Sum of squares	Degrees of freedom	Mean squares	*F* value	*p*-value
Model	7.774E+ 05	9	86382.42	17.10	0.0006[a]
A	33800.00	1	33800.00	335.11	< 0.0001
B	800.00	1	800.00	309.08	< 0.0001
C	6050.00	1	6050.00	312.97	< 0.0001
AB	100.00	1	100.00	88.13	< 0.0001
AC	100.00	1	100.00	87.71	< 0.0001
BC	900.00	1	900.00	3.34	0.1102
A^2	1.910E+ 05	1	1.910E+ 05	16.79	0.0046
B^2	2.189E+ 05	1	2.189E+ 05	29.42	0.0010
C^2	2.486E+ 05	1	2.486E+ 05	28.20	0.0011
Residual	35370.00	7	5052.86	—	—
Lack of fit	35050.00	3	11683.33	531.93	< 0.0001
Pure error	320.00	4	80	—	—
Core total	8.128E + 05	16	—	—	—

$$\text{Urease activity}(\text{U mL}^{-1}) = 916.00 + 65.00\,A + 10.00\,B - 27.50\,C - 5.00\,AB - 5.00\,AC - 5.00\,BC - 213.00\,A^2 - 228.00\,B^2 - 243\,C^2 \quad (2)$$

$$\text{As removal efficiency}(\%) = 58.80 + 1.50\,A - 1.37\,B - 2.38\,C + 1.75\,AB + 4.25\,AC - 2.50\,BC - 12.40\,A^2 - 7.65\,B^2 - 9.15\,C^2 \quad (3)$$

$$\text{Pb removal efficiency}(\%) = 67.20 - 0.1250\,A - 2.37\,B - 1.75\,C - 0.2500\,AB + 5.50\,AC - 2.50\,BC - 13.23\,A^2 - 7.22\,B^2 - 7.97\,C^2 \quad (4)$$

where A, B and C are the coded terms used in this experiment and represent urea (mM) and $CaCl_2$ concentration (mM) and pH (unit), respectively. The effect of process variables on the response factors are shown in 3D plots. The normality assumption of the response model was checked by obtaining a normal probability plot of the residuals. Equality of variance was checked by plotting residuals against the treatments and the treatment averages, (fitted values), and inspecting the spread in the residuals (Supplementary Fig. 1–3). The results indicated that the developed statistical model is appropriate and the assumptions associated with the ANOVA model are not violated.

3.4. FT-IR analysis

The As and Pb removal mechanism of *Trichoderma* sp. MG in MPM1 was analyzed using FT-IR. Fig. 2 showed the absorption pattern of As group. The sharp peaks at 1554, 1394 cm^{-1} could be the C–O stretching of the COOH groups. The absorption peaks at 1074 and 762 cm^{-1} are attributed to hydroxyl ethers, amines, and amides, respectively (Li et al., 2015). Fig. 3 shows the absorption pattern of Pb treatment group. The bands observed at 3475 and 2934 cm^{-1} were assigned to the C − H, O − H, and N − H stretching vibrations of COOH groups. The sharp absorption peaks at 1753 and 991 cm^{-1} could be due to the N–H stretching of primary secondary amines and amides (Qian et al., 2017; Li et al., 2015). The FT-IR results revealed that the carboxyl, alkanes, and amide groups served as the preliminary molecules for the

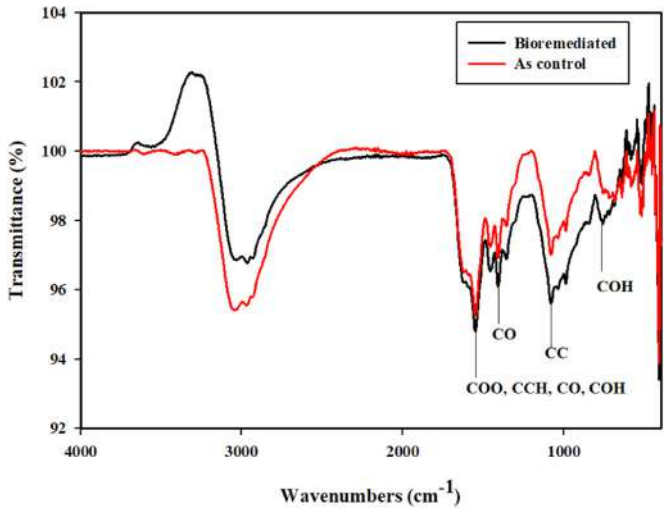


Fig. 2. FT-IR spectrum of *Trichoderma* sp. MG grown in As-containing media with and without urea and $CaCl_2$.

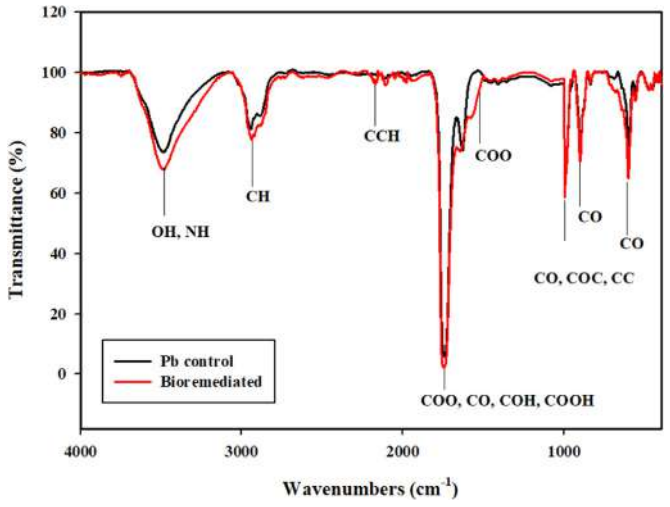


Fig. 3. FT-IR spectrum of *Trichoderma* sp. MG grown in Pb-containing media with and without urea and $CaCl_2$.

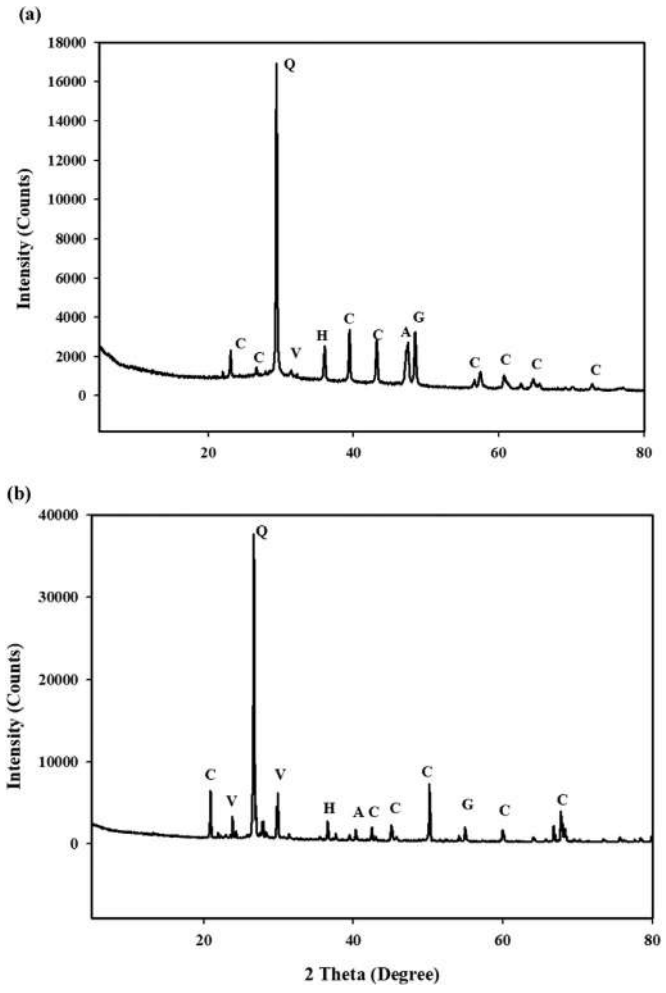


Fig. 5. X-ray diffractogram of bio-mineralized soils (a) As contaminated soil, (b) Pb contaminated soils (C-calcite, H-halite, Q-quartz, V-vaterite, A-aragonite).

subsequent precipitation of As and Pb.

3.5. Sequential extraction

A methodology to sequentially extract As and Pb was adopted to provide a comprehensive knowledge of the availability of As and Pb

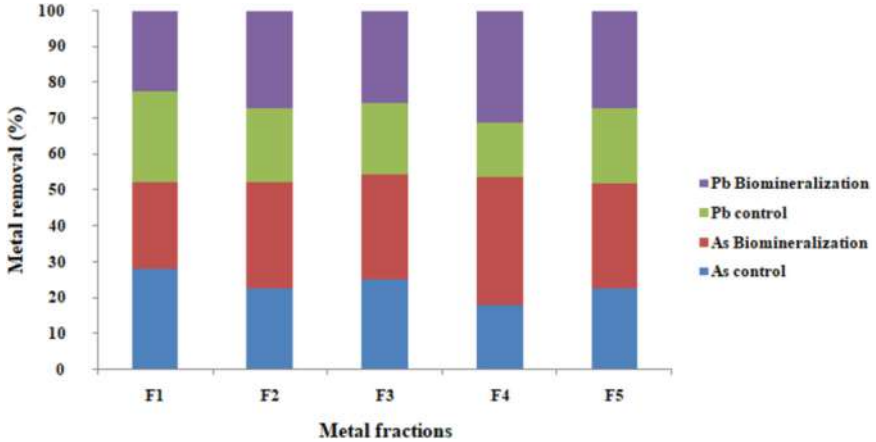


Fig. 4. Distribution of As and Pb fractions in control and bio-mineralized soils (F1- exchangeable fraction, F2- carbonate fraction, F3- iron and manganese oxide-bound fraction, F4- organic-bound fraction, and F5-residual fraction).

and their interaction with carbonates biologically formed in contaminated soils. The order of As and Pb distribution were F2 > F1 > F4 > F3 > F5. F1 for As and Pb (As bio-mineralization group: 27.6% and Pb bio-mineralization group: 25.6%) was lower than the respective control group (As control: 32.5% and Pb control: 29.5%). This result indicates that the isolate *Trichoderma* sp. MG could transform the bio-available metals into non-bio-available forms. The significantly decreased F1 value indicates that the bioaccumulation and biomagnifications of metals are prevented in the metal-contaminated soils. The results are consistent with previous studies reporting a significant reduction in exchangeable fraction of metals after bioaugmentation (Achal et al., 2012; Qian et al., 2017). However, a considerable increase in the carbonate fraction (F2) was observed in the As (46.4%) and Pb (42.4%) bioremediated soils, whereas for the control soils, it was 35.5% and 32.5%, respectively (Fig. 4). The increased distribution of carbonate-bound As and Pb was due to the induced carbonate precipitation. The results corroborate with the studies by Qian et al. (2017) and Govarthanan et al. (2013), reporting a significant increase in the carbonate fraction of metals (F2) after bioaugmentation.

The distribution of Fe-Mn oxide fraction was not altered significantly in control (As: 14.5, Pb: 11.5%) and bioremediated soils (As; 16.8% and Pb 14.8%). It might be due to the unavailability of Fe-Mn fractions (F3) of As and Pb to the isolate MG. The results are consistent with a previous study reporting that bioaugmentation did not significantly reduce the Fe-Mn oxide fraction of metals (Qian et al., 2017). F4 of As and Pb were significantly altered in the bioremediated soil (As 24.4% and Pb21.4%). The increased F4 values could be due to biosorption to the fungal mycelia biomass. The increased residual fraction (F5) was observed in bioremediated (As: 28.9, Pb: 26.9%) soils compared to the control soils (As: 22.6, 20.6%) respectively. The observed results indicated the efficiency of *Trichoderma* Sp. MG on bio-mineralization of As and Pb in contaminated soil.

3.6. XRD of soil

The result from sequential metal extractions might not be sufficient enough to confirm the role of carbonate precipitation and mineral formation. Thus, detailed XRD patterns of the bioremediated soils were investigated and the results are shown in Fig. 5. Accordingly, the XRD results showed the formation of various minerals such as, calcite, aragonite, halite, and quartz. Many calcite peaks could be observed in the bioremediated soils (Fig. 5(a), (b)). Alexandratos et al. (2007) reported that oxy-anions of the metals may substitute for the carbonate group in the calcite structure formation. It has been suggested that the calcite peaks could be due to the indirect action of urease. Qian et al. (2017) reported that the formation of calcite peaks during bio-mineralization induced by fungal degradation of urea.

4. Conclusion

In this study, the mechanism of As and Pb bio-mineralization by the isolate, *Trichoderma* sp. MG and the optimal physico-chemical conditions were determined in both aqueous solution and soil. The isolate, *Trichoderma* sp. MG could effectively immobilize As and Pb in the contaminated soils. The fungal-mediated carbonates and minerals were identified by FT-IR analysis and XRD. The MICP-associated removal of As and Pb by *Trichoderma* sp. MG presented in this paper is an eco-friendly and cost-effective bioremediation technique to clean up the soil contaminated by the heavy metals.

Acknowledgments

This research was financially supported by Korea Ministry of Environment (Project No: 2015001790002), which is greatly appreciated. This paper was also supported by research funds of Chonbuk National University in 2017.

Appendix A. Supporting information

Supplementary data associated with this article can be found in the online version at doi:10.1016/j.ecoenv.2019.03.034.

References

Achal, V., Pan, X., Zhang, D., Fu, Q.L., 2012. Biomineralization based remediation of As (III) contaminated soil by *Sporosarcina ginsengisoli*. J. Hazard. Mater. 201–202, 178–184.
Alexandratos, V.G., Elzinga, E.J., Reeder, R.J., 2007. Arsenate uptake by calcite: macroscopic and spectroscopic characterization of adsorption and incorporation mechanisms. Geochim. Cosmochim. Acta 71, 4172–4187.
Azarpira, H., Mahdavi, Y., 2016. Removal of Cd(II) by adsorption on agricultural waste biomass. Pharma Chem. 8 (12), 61–67.
Balamurugan, K., Schaffner, W., 2006. Copper homeostasis in eukaryotes: teetering on a tightrope. Biochim. Biophys. Acta (BBA) − Mol. Cell Res. 1763, 737–746.
Balarak, D., Joghataei, A., Azarpira, H., Mostafapour, F.K., 2016. Isotherms and thermodynamics of CD (II) ion removal by adsorption onto *Azolla filiculoides*. Int. J. Pharm. Technol. 8 (3), 15780–15788.
Bazrafshan, E., Sobhanikia, M., Mostafapour, F.K., Kamani, H., 2017. Chromium biosorption from aqueous environments by mucilaginous seeds of *Cydonia oblonga*: kinetic and thermodynamic studies. Glob. Nest J. 19 (2), 269–277.
Brookshaw, D.R., Pattrick, R.A.D., Lloyd, J.R., Vaughan, D.J., 2012. Microbial effects on mineral–radionuclide interactions and radionuclide solid-phase capture processes. Mineral. Mag. 76, 777–806.
Christensen, W.B., 1946. Urea decomposition as a means of differentiating *Proteus* and *Paracolon* cultures from each other and from *Salmonella* and *Shigella* types. J. Bacteriol. 52, 461–466.
Cui, Z., Zhang, X., Yang, H., Sun, L., 2017. Bioremediation of heavy metal pollution utilizing composite microbial agent of *Mucorcircinelloides, Actinomucor* sp. and *Mortierella* sp. J. Environ. Chem. Eng. 5, 3616–3621.
Dhami, N.K., Christelle Quirin, M.E., Mukherjee, A., 2017. Carbonate biomineralization and heavy metal remediation by calcifying fungi isolated from karstic caves. Ecol. Eng. 103, 106–117.
Donahoe, J., D'Imperio, S., Jackson, C., Inskeep, W., McDermott, T., 2004. Arsenite-oxidizing *Hydro genobaculum* strain isolated from an acid–sulfate–chloride geothermal spring in Yellow stone National Park. Appl. Environ. Microbiol. 70, 1865–1868.
Dopp, E., Hartmann, L.M., Florea, A.M., Von Recklinghausen, U., Piper, R., Shokouhi, B., Rettenmeier, A.W., Hirner, A.V., Obe, G., 2004. Uptake of inorganic and organic derivatives of arsenic associated with induced cytotoxic and genotoxic effects in Chinese hamster ovary (CHO) cells. Toxicol. Appl. Pharmacol. 201, 156–165.
Dopp, E., Kligerman, A.D., Diaz-Bone, R., 2010. Organo arsenicals, Uptake metabolism, and toxicity. Met. Ions Life Sci. 7, 231–265.
Gadd, G.M., 2010. Metals, minerals and microbes: geomicrobiology and bioremediation. Microbiology 156, 609–643.
Gadd, G.M., Rhee, Y.J., Stephenson, K., Wei, Z., 2012. Geomycology: metals, actinides and biominerals. Environ. Microbiol. Rep. 4, 270–296.
Gonzalez-Chavez, C., D'Haen, J., Vangronsveld, J., Dodd, J.C., 2002. Copper sorption and accumulation by the extra radical mycelium of different *Glomus* spp. (arbuscular mycorrhizal fungi) isolated from the same polluted soil. Plant Soil 240, 287–297.
Gorospe, C.M., Han, S.H., Kim, S.G., et al., 2013. Effects of different calcium salts on calcium carbonate crystal formation by *Sporosarcina pasteurii* KCTC 3558. Biotechnol. Bioprocess Eng. 18, 903–908.
Govarthanan, M., Lee, K.J., Cho, M., Kim, J.S., Kamala-Kannan, S., Oh, B.T., 2013. Significance of autochthonous *Bacillus* sp. KK1 on biomineralization of lead in mine tailings. Chemosphere 90, 2267–2272.
Govarthanan, M., Mythili, R., Selvankumar, T., Kamala-Kannan, S., Kim, H., 2018. Mycophytoremediation of arsenic- and lead- contaminated soils by *Helianthus annuus* and wood rot fungi, *Trichoderma* sp. isolated from decayed wood. Ecotoxicol. Environ. Saf. 151, 279–284.
Govarthanan, M., Park, S.H., Park, Y.J., et al., 2010. Lead biotransformation potential of allochthonous *Bacillus* sp. SKK11 with sesame oil cake extract in mine soil. RSC Adv. 5, 54564–54570.
Hseu, Z.Y., Shaw-Wei, S.U., Lai, H.Y., Guo, H.Y., Chen, T.C., Chen, Z.S., 2010. Remediation techniques and heavy metal uptake by different rice varieties in metal-contaminated soils of Taiwan: new aspects for food safety regulation and sustainable agriculture. Soil. Sci. Plant Nutr. 56, 31–52.
Kumari, D., Pan, X., Achal, V., et al., 2015. Multiple metal-resistant bacteria and fungi from acidic copper mine tailings of Xinjiang. China Environ. Earth Sci. 74, 3113–3121.
Li, Q., Csetenyi, L., Gadd, G.M., 2014. Biomineralization of metal carbonates by *Neurospora crassa*. Environ. Sci. Technol. 48, 14409–14416.
Li, Q., Csetenyi, L., Paton, G.I., Gadd, G.M., 2015. $CaCO_3$ and $SrCO_3$ bioprecipitation by fungi isolated from calcareous soil. Environ. Microbiol. 17, 3082–3097.
Li, W., Chen, W.S., Zhou, P.P., Cao, L., Yu, L.J., 2013. Influence of initial pH on the precipitation and crystal morphology of calcium carbonate induced by microbial carbonic anhydrase. Colloids Surf. B 102, 281–287.
Natarajan, K.R., 1995. Kinetic study of the enzyme urease from Dolichos biflorus. J. Chem. Educ. 72, 556–557.
Qian, X., Fang, C., Huang, M., Achal, V., 2017. Characterization of fungal-mediated carbonate precipitation in the biomineralization of chromate and lead from an aqueous solution and soil. J. Clean. Prod. 164, 198–208.
Qian, X.Y., Zhang, Q., Wilkinson, S., Achal, V., 2015. Cleaning of historic monuments:

looking beyond the conventional approach? J. Clean. Prod. 101, 180–181.
Selvankumar, T., Radhika, R., Mythili, R., Arunprakash, S., Srinivasan, P., Govarthanan, M., Kim, H., 2017. Isolation identification and characterization of arsenic transforming exogenous endophytic *Citrobacter* sp. RPT from roots of *Pteris vittata*. 3 Biotech 7, 264.
Song, Y.C., Sivakumar, S., Nguyen, T.T., Kim, S.H., Kim, B.G., 2009. The immobilization of heavy metals in biosolids using phosphate amendments – comparison of EPA (6010 and 3051) and selective sequential extraction methods. J. Hazard. Mater. 167, 1033–1037.
Su, S., Zeng, X., Bai, L., Williams, P.N., Wang, Y., Zhang, L., Wu, C., 2017. Inoculating chlamydospores of *Trichoderma asperellum* SM-12F1 changes arsenic availability and enzyme activity in soils and improves water spinach growth. Chemosphere 175, 497–504.
Su, S., Zeng, X., Feng, Q., et al., 2015. Demethylation of arsenic limits its volatilization in fungi. Environ. Pollut. 204, 141–144.
Su, S.M., Zeng, X.B., Bai, lY., Jiang, X.L., Li, L.F., 2010. Bioaccumulation and biovolatilization of pentavalent arsenic by *Penicillium janthinellum, Fusarium oxysporum,* and *Trichoderma asperellum* under laboratory conditions. Curr. Microbiol. 61, 261–266.
Wang, S., Mulligan, C.N., 2006. Occurrence of arsenic contamination in Canada: sources, behaviour and distribution. Sci. Total Environ. 366, 701–721.
Zhang, H., Ma, D., Qiu, R., Tang, Y., Du, C., 2017. Non-thermal plasma technology for organic contaminated soil remediation: a review. Chem. Eng. J. 313, 157–170.
Zhu, T., Dittrich, M., 2016. Carbonate precipitation through microbial activities in natural environment, and their potential in biotechnology: a review. Front. Bioeng. Biotechnol. 4, 4.

ScienceDirect

Journal of Molecular Liquids
Volume 262, 15 July 2018, Pages 318-321

Short Communication

Biogenic synthesis, characterization and antibacterial activity of gold nanoparticles synthesised from vegetable waste

R. Mythili [a], T. Selvankumar [a], P. Srinivasan [a], A. Sengottaiyan [a], J. Sabastinraj [b], Fuad Ameen [c], Ahmed Al-Sabri [c], S. Kamala-Kannan [d], M. Govarthanan [a, e] ✉, H. Kim [e] ✉

Show more

Outline | Share Cite

https://doi.org/10.1016/j.molliq.2018.04.087 Get rights and content

Highlights

- The study assessed green vegetable waste mediated synthesis of gold nanoparticles.
- AuNPs synthesis is simple, cost-effective and utilizing the market green vegetable waste as a substrate.
- It is an actual green method and utilizes green waste as a reducing agent.
- The biosynthesised AuNPs showed bactericidal activity against *Klebsiella* sp., and *Staphylococcus* sp.

Abstract

In this study, we report the potential use of market vegetable waste for the synthesis of gold nanoparticles (AuNPs). The AuNPs were synthesised using a green method without using any harmful chemical. The AuNPs obtained from vegetable wastes were characterised by UV– vis spectroscopy, transmission electron microscopy, scanning electron microscopy energy dispersive spectroscopy, X-ray diffraction, and Fourier transform-infrared spectroscopic (FT-IR) analysis. The particles size for the green synthesised AuNPs from vegetable waste were ranged from 10 to 70 nm. The AuNPs showed significant antibacterial activity against

P.G.P. COLLEGE OF ARTS & SCIENCE NAMAKKAL 637 206

PRINCIPAL
PGP College of Arts and Science
Namakkal

Journal of Molecular Liquids 262 (2018) 318–321

Contents lists available at ScienceDirect

Journal of Molecular Liquids

journal homepage: www.elsevier.com/locate/molliq

Short Communication

Biogenic synthesis, characterization and antibacterial activity of gold nanoparticles synthesised from vegetable waste

R. Mythili [a], T. Selvankumar [a], P. Srinivasan [a], A. Sengottaiyan [a], J. Sabastinraj [b], Fuad Ameen [c], Ahmed Al-Sabri [c], S. Kamala-Kannan [d], M. Govarthanan [a,e,*], H. Kim [e,**]

[a] PG & Research Department of Biotechnology, Mahendra Arts and Science College (Autonomous), Kalippatti, Namakkal 637501, Tamil Nadu, India
[b] Department of Biotechnology, Jamal Mohamed College (Autonomous), Tiruchirapalli 620020, Tamil Nadu, India
[c] Department of Botany and Microbiology, College of Science, King Saud University, Riyadh 11451, Saudi Arabia
[d] Division of Biotechnology, Advanced Institute of Environment and Bioscience, College of Environmental and Bioresource Sciences, Chonbuk National University, Iksan 570 752, Republic of Korea
[e] Department of Environmental Engineering, University of Seoul, Seoul, Republic of Korea

ARTICLE INFO

Article history:
Received 26 February 2018
Received in revised form 13 April 2018
Accepted 16 April 2018
Available online 17 April 2018

Keywords:
Antibacterial
Characterization
Gold nanoparticles
Green synthesis
Vegetable waste

ABSTRACT

In this study, we report the potential use of market vegetable waste for the synthesis of gold nanoparticles (AuNPs). The AuNPs were synthesised using a green method without using any harmful chemical. The AuNPs obtained from vegetable wastes were characterised by UV– vis spectroscopy, transmission electron microscopy, scanning electron microscopy energy dispersive spectroscopy, X-ray diffraction, and Fourier transform-infrared spectroscopic (FT-IR) analysis. The particles size for the green synthesised AuNPs from vegetable waste were ranged from 10 to 70 nm. The AuNPs showed significant antibacterial activity against clinical pathogens. Hence, this attempt has shown a great potential for utilizing market vegetable waste as a bio-reductant for the synthesis of AuNPs.

© 2018 Elsevier B.V. All rights reserved.

1. Introduction

Gold nanoparticles (AuNPs) are some of the most extensively studied nanomaterial in the field of nano biotechnology. AuNPs have attracted wide attention due to their potential applications in catalysis [1], antimicrobial [2], anticancer [3], drug delivery [4], and agriculture [5]. The AuNPs can be easily synthesised and show high chemical as well as thermal stability [6]. The conventional physico-chemical methods attempted over the past several years for AuNPs synthesis are electrochemical [7], photochemical [8], sono-chemical [9] and microwave assisted processes [10]. However, all these physico-chemical methods are complex, cost-intensive, and pressure-required and use toxic chemicals that can harm the human and the eco-system [11]. Currently, the use of biological materials for the synthesis of AuNPs has become a popular alternative. In particular, plants and plant based wastes have been successfully used for the production of AuNPs. Several studies have reported on the synthesis of AuNPs using plants [12–14]. To the best of our knowledge, the use of market vegetable waste has not been reported so far, for AuNPs synthesis.

In recent years, waste management represents an important challenge in agricultural industries and markets. It demands an integrated approach in the context of reuse for the production of value-added products. India is the largest consumer of vegetable and produces tons of vegetables wastes annually. Such estimates for the worldwide consumption of vegetable are several folds higher. The vegetable wastes were usually discarded in vegetable markets. The vegetables are mainly composed of phytochemicals and many natural polysaccharides. Thus, the use of market vegetable waste attracted for the synthesis of AuNPs.

In the present study, market vegetable wastes were used for the production of AuNPs. The synthesised AuNPs structures have been characterised by using standard spectrochemical methods. In addition, antibacterial activity of the AuNPs has also been investigated.

2. Materials and methods

2.1. Chemicals

Gold (III) chloride hydrate ($HAuCl_4$) was purchased from Sigma-Aldrich (St Louis, MO, USA). All other chemicals were analytical grade and purchased from Hi-Media Laboratories, Mumbai, India.

* Correspondence to: M. Govarthanan, Department of Energy and Environmental System Engineering, University of Seoul, Republic of Korea.
** Corresponding author.
E-mail addresses: gova.muthu@gmail.com (M. Govarthanan), h_kim@uos.ac.kr (H. Kim).

https://doi.org/10.1016/j.molliq.2018.04.087
0167-7322/© 2018 Elsevier B.V. All rights reserved.

2.2. Vegetable waste collection

Vegetable waste was collected from a waste disposal yard of a vegetable market (Wednesday Market), Mallasamudram (11.4939° latitude and 78.0295° longitude), India. The trading of vegetables in this city was approximately 2–5 tons/week. The 1–2 tons quantity of vegetables trading produces a huge quantity of wastes in the form of discarded vegetables, fresh skins of vegetables, fresh/damaged leaves etc. The fresh vegetable waste was collected in plastic bags and brought to the laboratory.

2.3. AuNPs synthesis

The vegetable waste was washed thoroughly with tap water and double-distilled water until no impurities remained. The mixed vegetable waste (200 g) were separated and added to 1000 mL of sterile double-distilled water and crushed using a mortar and pestle. The extract was filtered through Whatman No.1 filter paper and stored at 4 °C for further experiments. The vegetable waste extract (4 mL) was added to 96 mL of 1 mM $HAuCl_4$ solution and incubated in an orbital shaker for 12–24 h. The production of AuNPs was visually observed by a colour change from yellow to dark red.

2.4. Characterization of AuNPs

The optical absorption spectra of the synthesised AuNPs were observed using UV–vis spectrophotometer (Elico-SL 164). The surface morphology and size of the AuNPs were measured using transmission electron microscopy (TEM, FEI Tecnai TF 20 high resolution). The elemental composition of the AuNPs was confirmed by scanning electron micrograph-energy dispersive spectroscopy (SEM–EDS; Jeol JSM 6390). Fourier transform-infrared spectra (FT-IR) of AuNPs were obtained with a Perkin-Elmer FT-IR spectrophotometer (IRAffinity-1S) in the diffuse reflectance mode at a resolution of 4 particles cm^{-1} in KBr pellets. X-ray powder diffraction was used to determine the crystalline nature of the samples (XPERT-Pro diffractometer using Cu-Ka radiation). Scanning was done in the region of 2θ from 10° to 80° at 0.04°/min with a time constant of 2 s.

2.5. Antibacterial activity

The antibacterial activity of the AuNPs was assessed by the well diffusion method using two different clinical pathogenic bacteria, namely, *Klebsiella* sp. (Accession Number: KC899845), and *Staphylococcus* sp. (Accession Number: KC688883). The pure cultures of the bacteria were grown in nutrient agar media. Briefly, four different concentrations of (25, 50, 75 and 100 μg/mL) AuNPs were loaded on to the wells of the petridishes inoculated with *Klebsiella* sp. and *Staphylococcus* sp., individually. The antibiotic ampicillin (1mg/mL), was used as a positive control. The plates were incubated at 37 °C for 12–24 h and the zones of inhibition around the wells were measured manually.

3. Results and discussion

Recently, several studies have reported on the synthesis of AuNPs using environment friendly and renewable sources. In these adopted methodologies, abundant of plants and its products were utilized to generate AuNPs. In the present study, a simple and facile method was developed to synthesize AuNPs using market vegetable waste extract and chloroauric acid solution. The vegetable waste extract was mixed with chloroauric acid metal salt solution and the bio reduction of the Au^{+} into AuNPs was observed at 37 °C for 12–24 h. The colour change was monitored from yellow to dark red indicating production of AuNPs.

The AuNPs synthesised from vegetable waste was examined by UV–Vis spectroscopy in the range of 200–800 nm. Expectedly, a characteristic absorption peak was observed around 530 nm, which is attributed to the surface plasmon resonance of AuNPs. The excitation of the surface plasmon resonance of AuNPs could be responsible for the colour change in the reaction mixture. The observed results are consistent with a previous study which reported similar colour change in the reaction mixture [15]. The morphological structure and size of the AuNPs were shown in Fig. 1. The TEM image of AuNPs obtained from vegetable waste extract exhibit spherical and triangle shapes and particles size was found in the average range of 10–70 nm. Noruzi et al. [16] reported the spherical and triangle nature of the AuNPs obtained from *Rosa hybrid* petal extract with an average size of 10 nm. The particles were present mostly in aggregates. The size of the AuNPs was mainly depending on the physico-chemical properties of the reaction mixture such as, pH, temperature and reactant concentration [17].

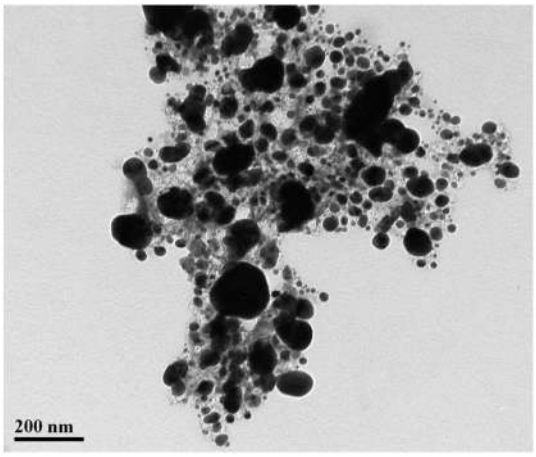


Fig. 1. (a) TEM image of AuNPs synthesised from vegetable waste extract.

Fig. 2 shows the EDS spectrum of the vegetable waste extract mediated synthesized AuNPs. The strongest peak at ~2 keV confirmed the presence of elemental gold in its pure form. Furthermore, the EDS pattern of AuNPs also consists of O and C with small amounts. The O and C peaks may be developed from the phytochemicals of the vegetable waste. The crystalline character of the synthesised AuNPs was determined by the XRD analysis. Fig. 3 shows the XRD pattern of AuNPs obtained from vegetable waste extract. The XRD pattern exhibited four different diffraction peaks (111, 200, 220 and 311) at 2θ. The reflection peak (111) is more intense than other reflection peaks (200), (220), and (311). These results are in agreement with the previous studies reported that the cubic nature of AuNPs [14,17,18].

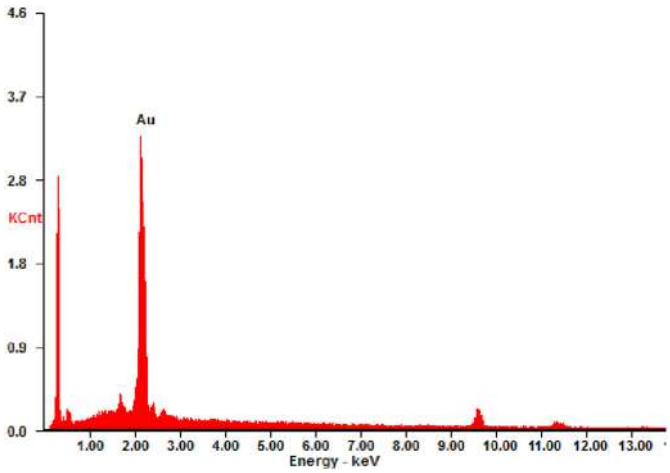


Fig. 2. SEM-EDX spectrum of AuNPs.

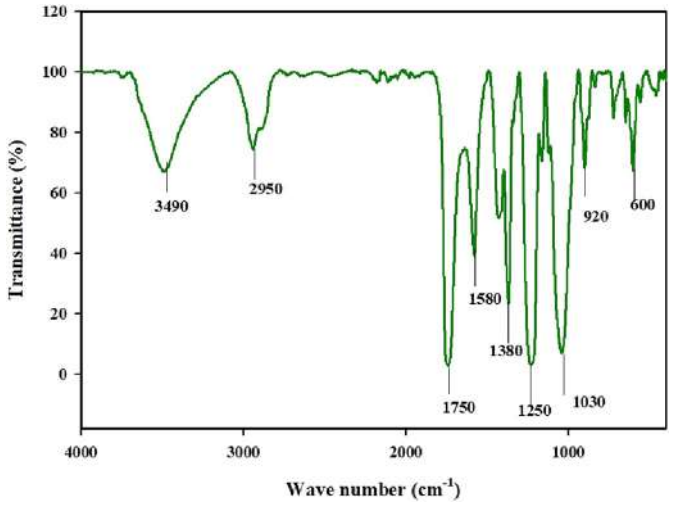


Fig. 3. FTIR spectrum of AuNPs obtained from vegetable waste extract.

The potential phytochemicals responsible for the bio-reduction and the stabilization of AuNPs can be determined by the FT-IR analysis. Fig. 4 shows the FTIR spectra of AuNPs synthesised from vegetable waste extract. The AuNPs show prominent peaks at 3490, 2950, 1780, 1580, 1380, 1250, 1030, 920, and 600 cm^{-1}, respectively. The peak at 1380 cm^{-1} was assigned to the symmetrical stretch of the carboxyl group. The peak at 1250 cm^{-1} indicated acetyl group of molecules present in the AuNPs. The peaks at 1030 and 920 cm^{-1} were due to the C—O stretching vibrations of ether and alcohol groups respectively. The peak at 600 cm^{-1} in the spectra of AuNPs corresponds to C—C groups of aromatic rings and C—O stretching of carboxyl groups of proteins. The strong adsorption bands at 3490 and 2950 cm^{-1} are characteristic stretching vibrations of O—H and C—H groups respectively [17,19]. The FT-IR results indicate the possible role of phytochemicals in capping and stabilizing the AuNPs.

Gold nanoparticles are extensively used in various value-added products as antibacterial agent to fight against the infectious microorganisms. Antibacterial activity of AuNPs was observed against *Klebsiella* sp. (Accession Number: KC899845), and *Staphylococcus* sp. (Accession Number: KC688883) and the results are shown in Fig. 5. The antibacterial activity of four different concentrations of AuNPs (25, 50, 75 and 100 μg/mL) and its representative zones of inhibition around the wells were observed respectively. The antibacterial activity of AuNPs is consistent with previous reports on that of AuNPs synthesised from plant extracts

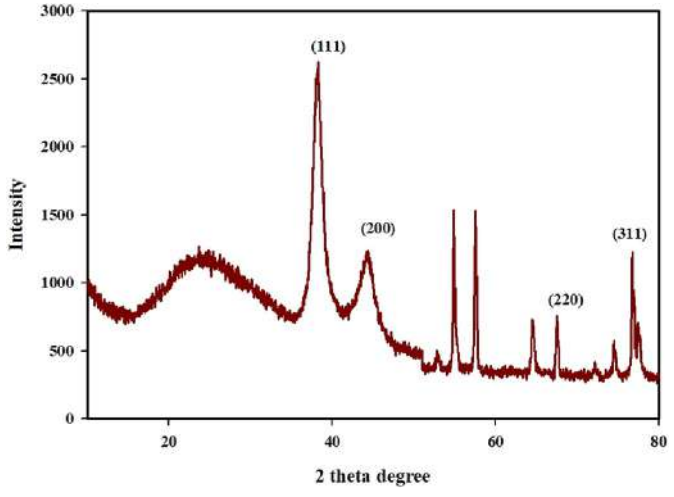


Fig. 4. XRD spectrum of AuNPs obtained from vegetable waste extract.

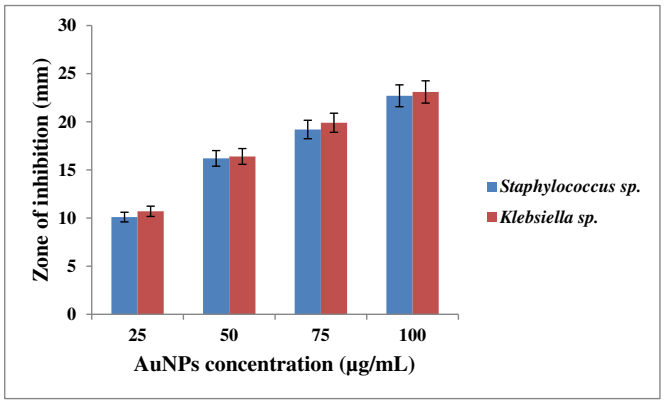


Fig. 5. Bactericidal activity of AuNPs.

[20]. The obtained results indicated that the AuNPs synthesised using market vegetable waste effectively inhibited the growth of tested pathogens. This ideal characteristics of the AuNPs makes them as a potential candidate for developing both narrow-spectrum and broad-spectrum antibacterial agent.

4. Conclusion

In conclusion, market vegetable waste could be used as an efficient biological substrate for the rapid and consistent synthesis of AuNPs. This simple, low cost, non-toxic, and abundantly available market vegetable waste could be used as an efficient alternative to the other biological materials. Such waste materials for synthesising AuNPs will be an advantage since the biological waste materials can be potentially converted into value-added nanomaterials. This study might open ways to explore utilization of other naturally available biological wastes for the synthesis of nanoparticles.

Conflict of interest

The authors declare that they don't have any conflict of interest.

Acknowledgement

The authors (Fuad Ameen and Ahmed Al-Sabri) extended their appreciation to the Deanship of Scientific Research at King Saud University for funding this work through research group NO (RGP-1438-029). H. Kim is financially supported by the Korea Environmental Industry and Technology Institute (Project no. 2015001790002), which is greatly appreciated.

References

[1] S.A. Aromal, D. Philip, Green synthesis of gold nanoparticles using *Trigonella foenum-graecum* and its size-dependent catalytic activity, Spectrochim. Acta A 97 (2012) 1–5.
[2] N. Dorosti, F. Jamshidi, Plant-mediated gold nanoparticles by *Dracocephalum kotschyi* as anticholin esterase agent: synthesis, characterization, and evaluation of anticancer and antibacterial activity, J. Appl. Biomed. 14 (2016) 235–245.
[3] S. Rajeshkumar, Anticancer activity of eco-friendly gold nanoparticles against lung and liver cancer cells, J. Eng. Biotech. 14 (2016) 195–202.
[4] M. Ghorbani, H. Hamishehkar, Redox and pH-responsive gold nanoparticles as a new platform for simultaneous triple anti-cancer drugs targeting, Int. J. Pharm. 520 (2017) 126–138.
[5] W. Mahakham, P. Theerakulpisut, S. Maensiri, S. Phumying, A.K. Sarmah, Environmentally benign synthesis of phytochemicals-capped gold nanoparticles as nanopriming agent for promoting maize seed germination, Sci. Total Environ. 573 (2016) 1089–1102.
[6] M. Noruzi, Biosynthesis of gold nanoparticles using plant extracts, Bioprocess Biosyst. Eng. 38 (2015) 1–14.
[7] Y. Hu, Y. Song, Y. Wang, J. Di, Electrochemical synthesis of gold nanoparticles onto indium tin oxide glass and application in biosensors, Thin Solid Films 519 (2011) 6605–6609.

[8] P.R. Teixeira, M.S. Santos, A.L.G. Silva, S.N. Báo, R.B. Azevedo, M.J.A. Sales, L.G. Paterno, Photochemically-assisted synthesis of non-toxic and biocompatible gold nanoparticles, Colloids Surf., B 148 (2016) 317–323.
[9] N.S.M. Yusof, M. Ashok kumar, Sonochemical synthesis of gold nanoparticles by using high intensity focused ultrasound, ChemPhysChem 16 (2015) 775–781.
[10] S.K. Seol, D. Kim, S. Jung, Y. Hwu, Microwave synthesis of gold nanoparticles: effect of applied microwave power and solution pH, Mater. Chem. Phys. 131 (2011) 331–335.
[11] C. Balalakshmi, K. Gopinath, M. Govindarajan, R. Lokesh, A. Arumugam, N.S. Alharbi, S. Kadaikunnan, J.M. Khaled, G. Benelli, Green synthesis of gold nanoparticles using a cheap *Sphaeranthus indicus* extract: impact on plant cells and the aquatic crustacean *Artemia nauplii*, J. Photochem. Photobiol. B 173 (2017) 598–605.
[12] K. Gopinath, K.S. Venkatesh, R. Ilangovan, K. Sankaranarayanan, A. Arumugam, Green synthesis of gold nanoparticles from leaf extract of *Terminalia arjuna*, for the enhanced mitotic cell division and pollen germination activity, Ind. Crop. Prod. 50 (2013) (2013) 737–742.
[13] P. Balashanmugam, P. Durai, M.D. Balakumaran, P.V. Kalaichelvan, Phytosynthesized gold nanoparticles from *C. roxburghii* DC. leaf and their toxic effects on normal and cancer cell lines, J. Photochem. Photobiol. B 165 (2016) 163–173.
[14] A. Aravinthan, S. Kamala-Kannan, M. Govarthanan, J.H. Kim, Accumulation of biosynthesized gold nanoparticles and its impact on various organs of Sprague Dawley rats: a systematic study, Toxicol. Res. 5 (2016) 1530.
[15] V.P.N. Sanna, G. Dessì, P. Manconi, A. Mariani, S. Dedola, M. Rassu, C. Crosio, C. Iaccarino, M. Sechi, Single-step green synthesis and characterization of gold conjugated polyphenol nanoparticles with antioxidant and biological activities, Int. J. Nanomedicine 9 (2014) 17.
[16] M. Noruzi, D. Zare, K. Khoshnevisan, D. Davoodi, Rapid green synthesis of gold nanoparticles using *Rosa hybrida* petal extract at room temperature, Spectrochim. Acta A 79 (2011) 1461–1465.
[17] P. Velmurugan, M. Cho, S.M. Lee, J.H. Park, K.J. Lee, H. Myung, B.T. Oh, Phytocrystallization of silver and gold by *Erigeron annuus* (L.) Pers flower extract and catalytic potential of synthesized and commercial nano silver immobilized on sodium alginate hydrogel, J. Saudi Chem. Soc. 20 (2016) 313–320.
[18] J. Zha, C. Dong, X. Wang, X. Zhang, X. Xiao, X. Yang, Green synthesis and characterization of monodisperse gold nanoparticles using *Ginkgo Biloba* leaf extract, Optik 144 (2017) 511–521.
[19] J. Yu, D. Xu, H.N. Guan, C. Wang, L.K. Huang, D.F. Chi, Facile one-step green synthesis of gold nanoparticles using *Citrus maxima* aqueous extracts and its catalytic activity, Mater. Lett. 166 (2016) 110–112.
[20] A. Bankar, B. Joshi, A. Ravi Kumar, S. Zinjarde, Banana peel extract mediated synthesis of gold nanoparticles, Colloids Surf., B 80 (2010) 45–50.

ScienceDirect

Biocatalysis and Agricultural Biotechnology
Volume 13, January 2018, Pages 95-104

Molecular modeling and docking of protease from *Bacillus* sp. for the keratin degradation

Selvam Kandasamy [a, b], Senbagam Duraisamy [c], Sudhakar Chinnappan [b], Senthilkumar Balakrishnan [a, d] ✉, Selvankumar Thangasamy [b] ✉, Govarthanan Muthusamy [e], Sengottaiyan Arumugam [b], Srinivasan Palanisamy [b]

Show more

Share Cite

https://doi.org/10.1016/j.bcab.2017.11.016 Get rights and content

Abstract

In this present study, the 3D structure of protease from Bacillus sp. was modeled by using modeler 9v9. The generated structure was accessed for geometrical errors and energy stability using RAMPAGE, VERFIY 3D, ERRAT and PROSA. The proteolytic nature of this modeled protease was determined by docking studies using FlexX. The kertinolytic activity was revealed by using polysacchadire sub units such as arabinose, rhamnose, galactose, and glucose; aminopeptidase activity was revealed by using amino acids like methionine, leucine, rivastigmine and also by protease inhibitor like N-carbobenzyloxy-L-alanine and 4-amidino phenyl methanesulfonyl flurode. The docking studies showed that Asp160 and Try246 residues were mainly involved in binding of all the compounds and other important amino acid residues such as His85, Asp97, Glu131, Asp160, Glu131, Glu132, Asp160, Tyr246, and His247 were involved in hydrogen bonding with the substrates. These studies also determined the substrate recognition pattern and the development of suitable protease can potentially enhance its applications in keratin degradation.

Introduction

Proteases are proteolytic enzymes that catalyze the breakdown of proteins by hydrolysis of peptide bonds. Proteolytic enzymes are ubiquitous in existence, it is being found in all living organisms, and is crucial for cell growth and differentiation. In accordance with global enzyme sales of industrial enzymes, protease accounts for 60–64% and constitutes to be a largest product segment of industrial enzymes (Annamalai et al., 2014, Ch, 2007, Satbir and Bijender Kumar, 2014, Selvam et al., 2016, Shankar et al., 2011). The serine alkaline proteases are one of the most important groups of industrial enzymes. They account for

P.G. COLLEGE OF ARTS & SCIENCE NAMAKKAL 637 206

PRINCIPAL
PGP College of Arts and Science
Namakkal

Biocatalysis and Agricultural Biotechnology 13 (2018) 95–104

Contents lists available at ScienceDirect

Biocatalysis and Agricultural Biotechnology

journal homepage: www.elsevier.com/locate/bab

Molecular modeling and docking of protease from *Bacillus* sp. for the keratin degradation

Selvam Kandasamy[a,b], Senbagam Duraisamy[c], Sudhakar Chinnappan[b], Senthilkumar Balakrishnan[a,d,*], Selvankumar Thangasamy[b,**], Govarthanan Muthusamy[e], Sengottaiyan Arumugam[b], Srinivasan Palanisamy[b]

[a] Centre for Biotechnology, Muthayammal College of Arts and Science, Rasipuram, Namakkal 637 408, Tamil Nadu, India
[b] Department of Biotechnology, Mahendra Arts and Science College (Autonomous), Kalippatti, Namakkal 637501, Tamil Nadu, India
[c] Department of Marine Biotechnology, Bharathidasan University,Tiruchirappalli 620 024, Tamil Nadu, India
[d] Department of Medical Microbiology, College of Health and Medical Sciences, Haramaya University, P.O. Box 235, Harar, Ethiopia
[e] Department of Energy and Environmental System Engineering, University of Seoul, Seoul, Republic of Korea

ARTICLE INFO

Keywords:
Protease
Bacillus sp.
Kertinolytic activity
3D modeling
Molecular docking

ABSTRACT

In this present study, the 3D structure of protease from *Bacillus* sp. was modeled by using modeler 9v9. The generated structure was accessed for geometrical errors and energy stability using RAMPAGE, VERFIY 3D, ERRAT and PROSA. The proteolytic nature of this modeled protease was determined by docking studies using FlexX. The kertinolytic activity was revealed by using polysacchadire sub units such as arabinose, rhamnose, galactose, and glucose; aminopeptidase activity was revealed by using amino acids like methionine, leucine, rivastigmine and also by protease inhibitor like N-carbobenzyloxy-L-alanine and 4-amidino phenyl methanesulfonyl flurode. The docking studies showed that Asp160 and Try246 residues were mainly involved in binding of all the compounds and other important amino acid residues such as His85, Asp97, Glu131, Asp160, Glu131, Glu132, Asp160, Tyr246, and His247 were involved in hydrogen bonding with the substrates. These studies also determined the substrate recognition pattern and the development of suitable protease can potentially enhance its applications in keratin degradation.

1. Introduction

Proteases are proteolytic enzymes that catalyze the breakdown of proteins by hydrolysis of peptide bonds. Proteolytic enzymes are ubiquitous in existence, it is being found in all living organisms, and is crucial for cell growth and differentiation. In accordance with global enzyme sales of industrial enzymes, protease accounts for 60–64% and constitutes to be a largest product segment of industrial enzymes (Ch, 2007; Shankar et al., 2011; Annamalai et al., 2014; Satbir and Bijender Kumar, 2014; Selvam et al., 2016). The serine alkaline proteases are one of the most important groups of industrial enzymes. They account for approximately 35% of the total microbial enzyme sales (Bhunia et al., 2012). The proteases are highly valuable commercial enzymes as various applications in food, pharmaceutical, detergent and dairy industries (Gupta et al., 2002; Vellard, 2003; Reddy et al., 2006; Ribitscha et al., 2010; Bhunia and Dey, 2012; Bhunia et al., 2013). Several *Bacillus* sp. like *B. cereus* (Prakash et al., 2014), *Bacillus licheniformis* (Lin et al., 2015), *Bacillus megaterium* (Asker et al., 2013), *B. stearothermophilus* (Sookkheo et al., 2000), *Bacillus mojavensis* (Haddar et al., 2009), *Bacillus pumilus* (Jaouadi et al., 2008) and *B. subtilis* (Maruthiah et al., 2013) were involved in production of a wide variety of extracellular enzymes, including proteases.

The molecular docking approach can be used to model the interaction between the molecule and a protein at the atomic level, which allow us to characterize the behavior of molecules in the binding site of target proteins as well as to elucidate fundamental biochemical processes (Marrone et al., 1997; Huang and Zou, 2010; Ezat et al., 2014). An important type of molecular docking is protein-ligand docking because of its therapeutic applications in modern structure-based drug design. A disadvantage of these methods is their dependence on the molecular data sets used to perform regression analyses and fitting. Protein 3D structure is major pre-requisite for understanding the function and evolutionary relationship. Various studies have reported the potential in silicon application of homology or comparative

* Corresponding author at: Department of Medical Microbiology, College of Health and Medical Sciences, Haramaya University, P.O. Box 235, Harar, Ethiopia
** Corresponding author at: Department of Biotechnology, Mahendra Arts and Science College (Autonomous), Kalippatti, Namakkal 637501, Tamil Nadu, India
E-mail addresses: nbsenthilkumar@gmail.com (S. Balakrishnan), t_selvankumar@yahoo.com (S. Thangasamy).

https://doi.org/10.1016/j.bcab.2017.11.016
Received 25 August 2017; Received in revised form 20 November 2017; Accepted 29 November 2017
Available online 05 December 2017
1878-8181/ © 2017 Elsevier Ltd. All rights reserved.



Fig. 1. Dehairing activity of goat skin before (A) and after treatment (B).

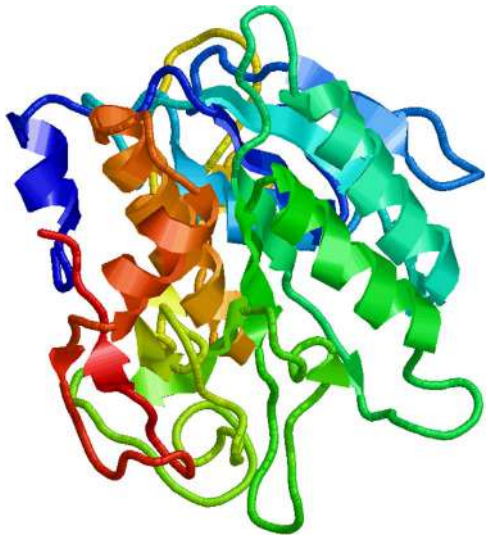


Fig. 2. Ribbon diagrams of the modeled protease showing α- Helices, β- strands, and loop.

modeling and *de novo* modeling in predicting the 3D structures and evolutionary relationship (Dalton and Jackson, 2007) using deduced amino acid sequences (Berg et al., 2002; Kalyaanamoorthy and Chen, 2014). Moreover, the stereo-chemical property of the proteins provides fundamental understanding on the stereo-chemistry of the polypeptide backbone. It has been established that Ramachandran map is a powerful computational tool to validate the stereo-chemistry of the protein structures (Ramachandran et al., 1963). ProSA is a diagnostic tool that is based on the statistical analysis of all available protein structures (Wiederstein and Sipplm, 2007), ERRAT is a program for verifying protein structures determined by crystallography (MacArthur et al., 1994).

In the present study an attempt has been made to understand the binding efficiency of the modeled protease from *Bacillus* sp. and three different substrates by molecular docking studies. The proteolytic activity was revealed by using polysacchadire sub units such as arabinose, rhamnose, galactose, and glucose; keratinolytic activity reveled by using methionine, leucine, rivastigmine and also by aminopeptidase like N-carbobenzyloxy-L-alanine and 4-amidino phenyl methanesulfonyl flurode.

2. Materials and methods

2.1. Keratin degrating activity of protease

The purified protease enzyme (previously reported Selvam et al. (2016) was applied at 1% concentration of two piece goat skin (2.5 cm × 2.5 cm), presoaked in tap water from flesh side and kept at ambient temperature (27 ± 2 °C) in a dry place. Loosening of hair and epidermis were observed by mechanical means at an hourly interval. The skin pieces were then virtually analyzed for dehairing activity as described by Sudhir et al. (2010).

2.2. Target sequence

The 3D structures of the protease from *Bacillus* sp. is not available in PDB database, thus the homologous sequences for building the 3D structure was searched against PDB using NCBI-BlastP (basic local alignment search tool) (Altschul et al., 1990; Mulukala et al., 2013). The most homologous sequence obtained was considered as the potential template structure for homology modeling. The atomic co-ordinate file of the template structure was obtained from the PDB (Berman et al., 2000).

2.3. Homology modeling and model evaluation

The atomic coordinate file of the template structure along with target and template final sequence alignment file was used to build the model using the automated homology modeling tool MODELER 9v9 (Eswar et al., 2006; Webb and Sali, 2014). The bundles of model that are randomly generated from the starting structure were calculated and the best model with the least Root Mean Square Deviation (RMSD) value was selected by superimposing the model with its template (Maiti et al., 2004). This model was used for further analysis after subjecting it for energy minimization using GROMOS of Swiss PDB viewer (Walter et al., 1999). The quality of the generated protein structure model was

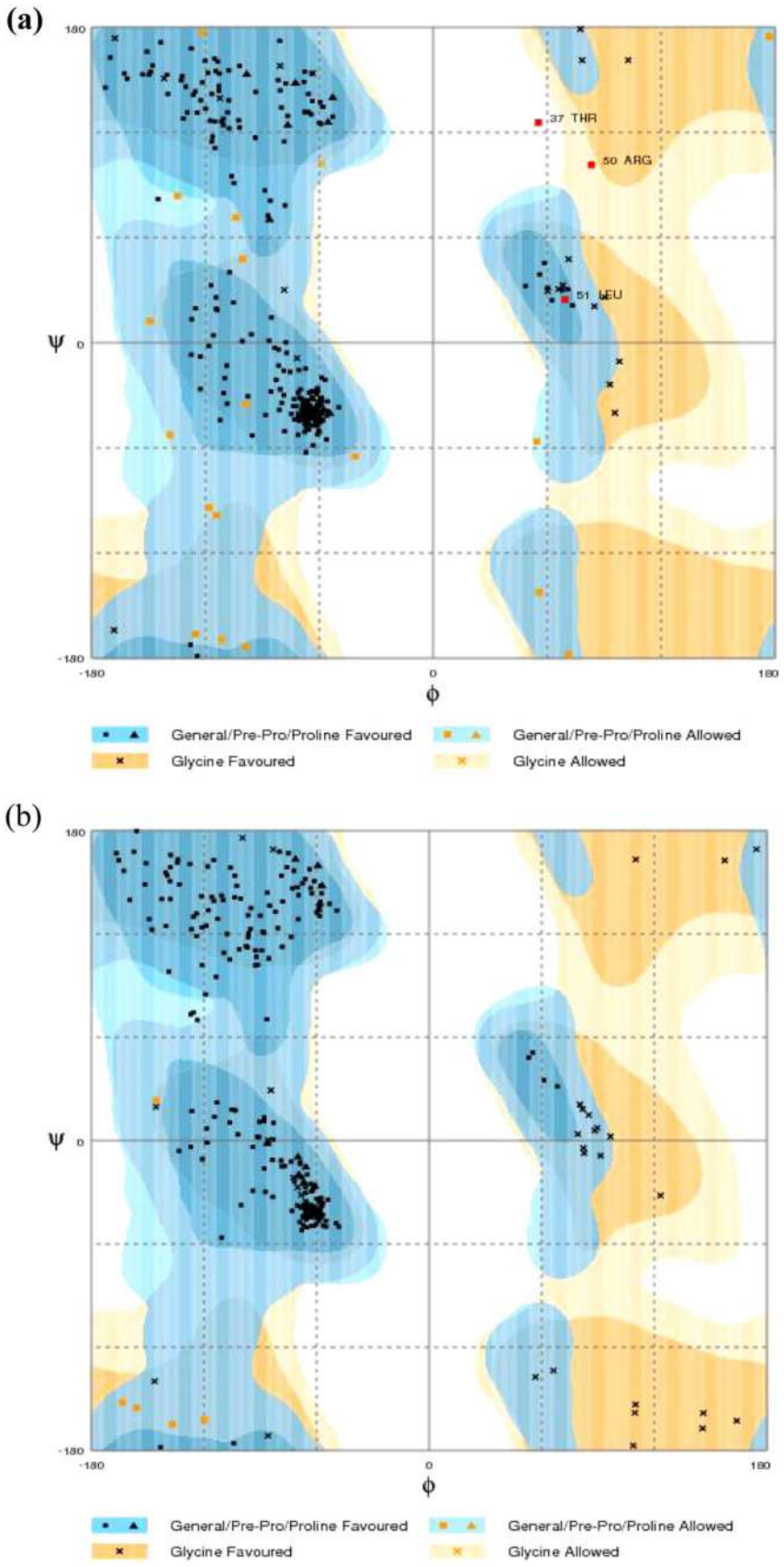


Fig. 3. Ramachandran plot (a) modeled protease, (b) template obtained by RAMPAGE, (Supplementary material) (c) model overall quality factor, (d) template overall quality factor evaluated by ERRAT, (e) Black dot in plot showing the −6.14 z-score of predicted model, (f) template showing the −9.64 z-score predicted by PROSA.

Table 1
Evaluation results of Model, template by PROCHECK, VERIFY3D, ERRAT and PROSA.

Proteins	PROCHECK				VERIFY 3D	ERRAT	PROSA
	Most favored regions	Additional Allowed regions	Generally allowed regions	Disallowed regions	3D-ID Score	Quality Factor	Z-score
Model	93.0%	6.0%	1.0%	1.0%	100.00%	85.749	−6.14
Template	98.1%	1.9%	0%	0%	100%	89.49	−9.64

Table 2
Pockets and descriptors have been calculated for XPRO.

Name	Volume [Å³]	Surface [Å²]	Lipo surface [Å²]	Depth [Å]	Drug Score
P0	1097.34	1248.97	726.55	20.62	0.80
P1	596.22	995.00	657.63	13.59	0.71
P2	179.58	324.99	274.09	10.78	0.41
P3	153.47	348.58	237.53	7.98	0.25
P4	149.18	180.83	137.21	8.13	0.28
P5	136.26	302.72	119.36	7.61	0.18
P6	117.06	201.10	99.57	8.10	0.20
P7	109.44	189.06	115.99	7.39	0.20

assessed by checking the stereo chemical parameters using RAMPAGE (Lovell et al., 2002), PROSA (Sippl, 1993; Wiederstein and Sipplm, 2007), Verfiy 3D (Bowie et al., 1991; Luthy et al., 1992) and ERRAT (Colovos and Yeates, 1993; MacArthur et al., 1994) at SAVES server (http://nihserver.mbi.ucla.edu/SAVES).

2.4. Prediction of substrate binding site

To determine the binding affinities between three categories like keratinase, aminopeptidase and proteolytic activity. The modeled protease from *Bacillus* sp. by docking with proteolytic activity was revealed by using polysacchadire sub units such as arabinose, rhamnose, galactose, and glucose; keratinolytic activity reveled by using methionine, leucine, rivastigmine and also by aminopeptidase like N-carbobenzyloxy-L-alanine and 4-amidino phenyl methanesulfonyl flurode respectively from the amino acids in the binding site of the developed was predicted by submitting the structure to DoGSiteScorer: Active Site Prediction and Analysis Server (Volkamer et al., 2012).

2.5. Ligand design

The 2D structures of the arabinose, rhamnose, galactose, glucose; Methionine, Leucine, Rivastigmine, N-carbobenzyloxy-L-alanine and 4-amidino phenyl methanesulfonyl flurode compounds were drawn in ACD-Chemsketch version 11 (2006) and their SMILES notation was obtained. The 3D structures were obtained and converted into SDF files by using 'Online SMILES convertor and Structure file generator' server (Weininger, 1988).

2.6. Substrates for molecular docking studies

The 3D structures of substrates like arabinose, rhamnose, galactose, glucose; methionine, leucine, rivastigmine, N-carbobenzyloxy-L-alanine and 4-amidino phenyl methanesulfonyl flurode were docked with the binding sites of modeled protease from *Bacillus* sp. by using FlexX (Rarey et al., 1996). The various parameters like default general docking information, base placement using triangle matching, scoring of full score contribution and threshold of 0, 30 and No score

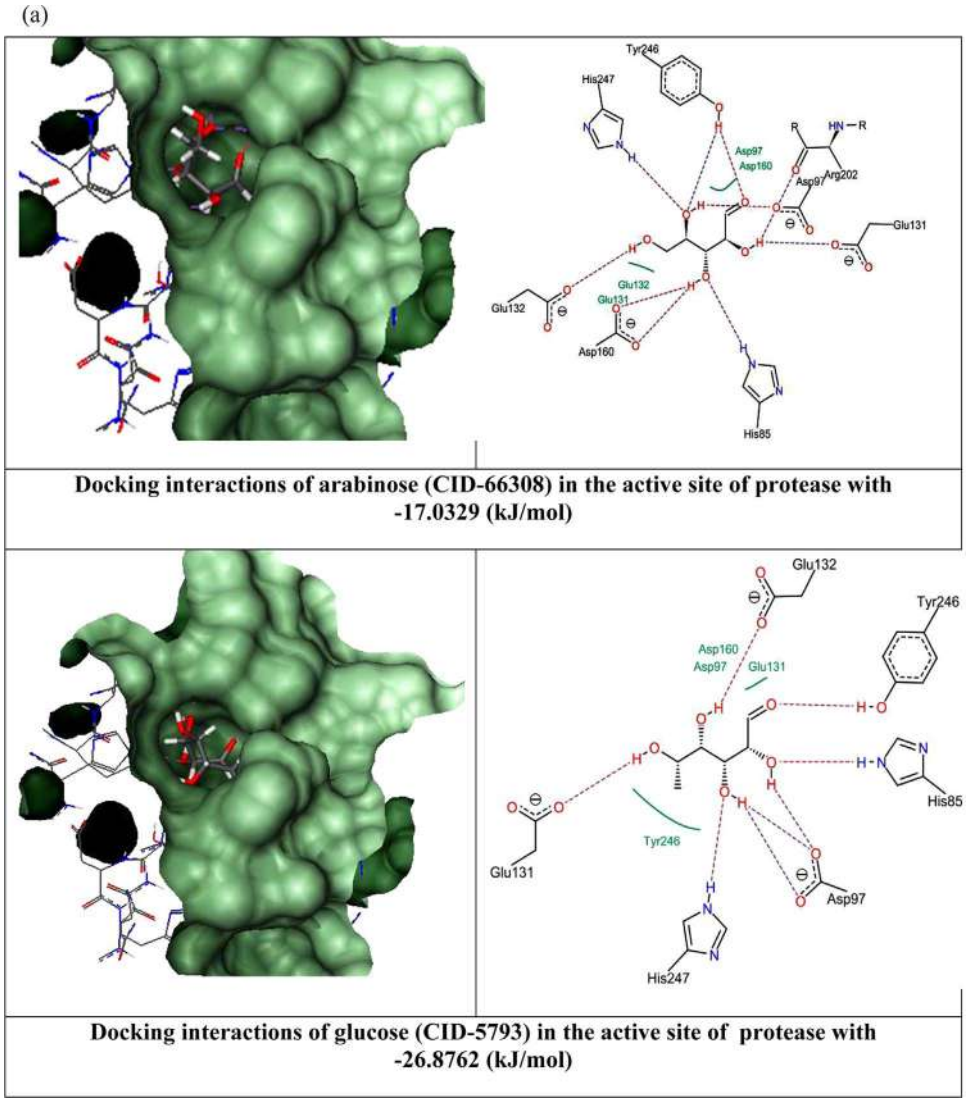


Fig. 4. Molecular docking (a) Docking interactions of polysaccharide subunits for keratinolytic activity, (b) Docking interactions of Amino acids for aminopepditase activity, (c) Docking interactions for protease inhibitors.

contribution and threshold of 0, 70. Chemical parameters of clash handling values for protein ligand clashes with maximum allowed overlap volume of 2.9 A^{03} and intra-ligand clashes with clash factor of 0.6 and considering the hydrogen in internal clash tests. Default docking details values of 200 for both the maximum number of solutions per iteration and maximum number of solutions per fragmentation.

2.7. Prediction of ligand and receptor interactions

The interactions between arabinose, rhamnose, galactose, glucose, methionine, leucine, rivastigmine, N-carbobenzyloxy-L-alanine and 4-amidino phenyl methanesulfonyl flurode and protease from *Bacillus* sp. as docked complex were analyzed by the pose-view of LeadIT (Stierand et al., 2006).

3. Results and discussion

3.1. Kertinolytic activity

Kertinolytic process has been gaining importance as an alternative chemical methodology in present day scenario as this process is significant in the reduction of toxicity in addition to improvement of leather quality (Sivasubramanian et al., 2008). However, most of the proteases reported so far were unsuitable for dehairing purpose because of the associated collagen Kertinolytic activity (Huang et al., 2003). Proteases possessing keratinolytic activity but lacking collagenolytic activity are having the great demand in the leather industry for the depilating process (Zambare et al., 2007). They selectively degrade the soft keratin tissue in the follicle, thereby pulling out intact hairs without affecting tensile strength of the leather (Thanikaivelan et al., 2004). Kertinolytic result showed that hairs from goat skin could be removed very easily 24 h post incubation of goat skin with alkaline protease as compared to skin treated with buffer only (control) confirming the Kertinolytic potency of this protease (Fig. 1).

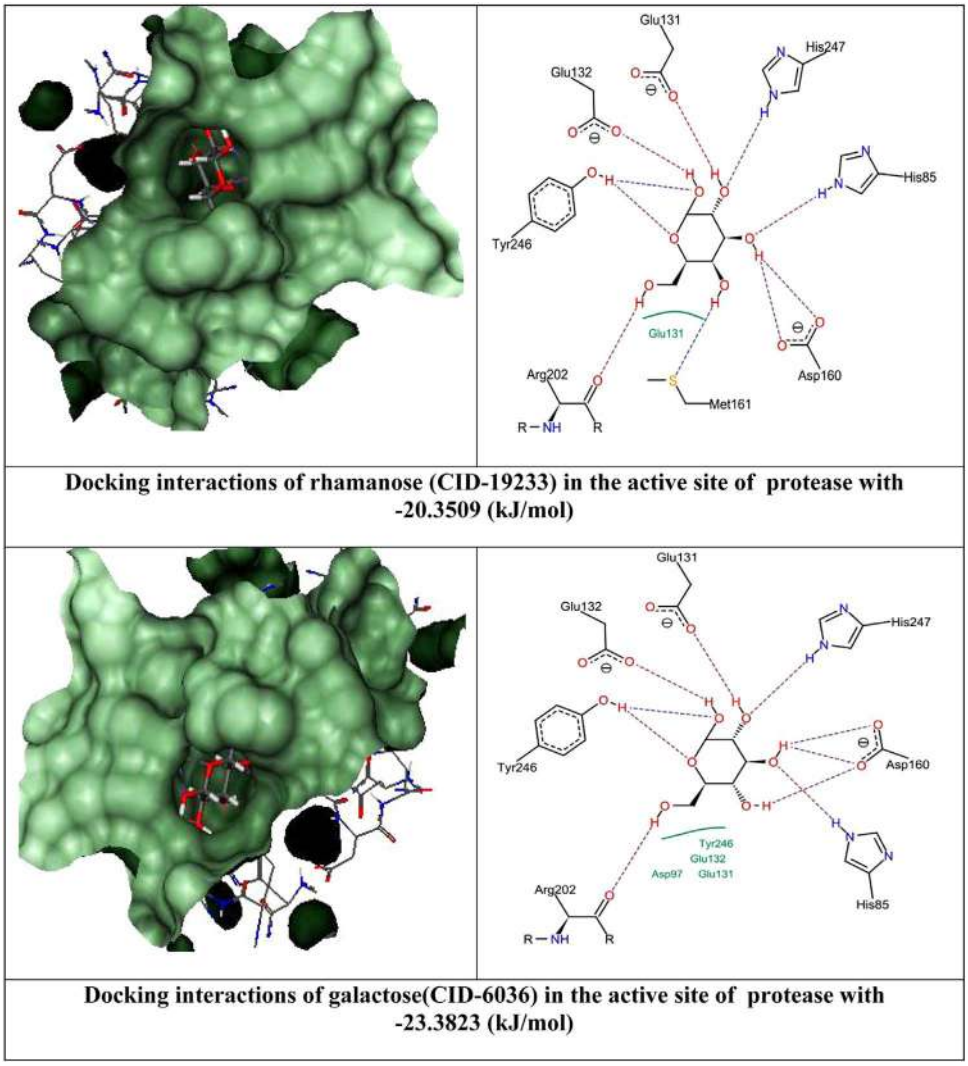


Fig. 4. (*continued*)

3.2. Sequence analysis and potential template for homology modeling

The BLASTP search for target sequences of protease from *Bacillus* sp. against PDB database resulted that crystal structure of protease from the structure of a serine protease from *Bacillus lentus subtilisin* (PDB ID: 1gci_A chain) as the most homologous with the sequence identity of 65%, at an E-value cut-off of 1e-02.

3.3. Homology modeling

The sequences of protease from *Bacillus* sp. and Co-ordinate files 1gci_A chain was used as inputs to build the initial model using MODELER 9v9, a bundle model was developed by using random generation and by applying spatial resistance. The modeled structure of protease from *Bacillus* sp. was shown in cartoon representation with group color using rasmol visualization tool (Fig. 2).

3.4. Model assessment

The quality of the generated protein structure was assessed by the overall stereo-chemical parameters by RAMPAGE, PROSA; Verfiy3D and ERRAT of SAVES server. The Ramachandran plot of the generated protease model from *Bacillus* sp. was analyzed and considered as the best model based on the number of residues plotted in most favored and additionally allowed regions. The percentage of residues plotted in the most favorable regions, additionally allowed regions, generously allowed regions and disallowed regions of Ramachandran plot for the model was given in the Fig. 3a, b and Table 1. Further the overall quality factor and compatibility of an atomic model (3D) with amino acid sequence (1D) for the model was observed as −6.14 for PROSA (Fig. 3. c, d Supplementary Material), 100.00% for Verify3D and 85.749 for ERRAT (Fig. 3. e, f Supplementary Material). The results of Ramachandran plot, RAMPAGE, PROSA, ERRAT and Verify-3D confirms that the generated model were reliable and of good quality.

3.5. Binding site prediction

The modeled protease from *Bacillus* sp. was submitted to DoGSiteScorer: active site prediction and analysis server and obtained the possible binding sites. Among the predicted binding sites, the catalytic site (Table 2) is considered based on the ligands in the template structures were also observed in the same region and the same sites were used for the further docking studies.

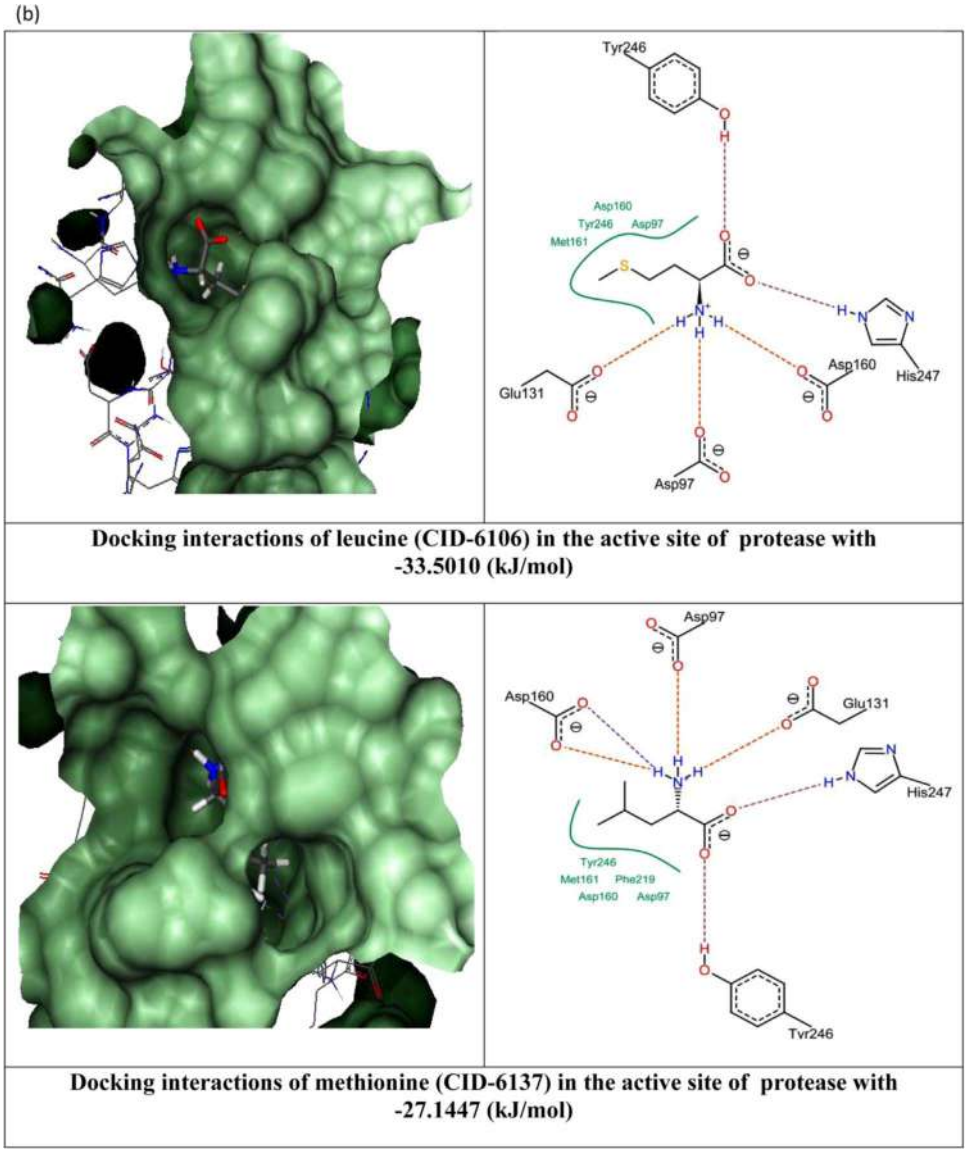


Fig. 4. (*continued*)

3.6. Molecular docking studies

The docking complex and the interactions of polysaccharide sub units, such as arabinose, rhamnose, galactose, and glucose used to determine the keratinolytic activity. The aminopeptidase activity was determined by docking the amino acids like, methionine, leucine. The protease inhibitors such as N-carbobenzyloxy-L-alanine and 4-amidino phenyl methanesulfonyl flurode were docked to understand the proteolytic activity of the predicted Protease model from *Bacillus* sp. The docking interactions between the binding site residues and the compounds with their respective binding score were given in Fig. 4a–c and Table 3.

3.6.1. Docking of polysaccharide subunits for keratinolytic activity

The docking interactions of the arabinose within the catalytic site of modeled protease from *Bacillus* sp. with dock score of −17.0329 kJ/mol supported that the arabinose is bounded by the means of 9 H bonds favored by His85, Asp97, Glu131, Glu132, Asp160 Asp160, Tyr246, and His247. This interaction is also favored by the means of hydrophobic interactions (Non-bonded) by Asp97, Glu131, Glu132, and Asp160 residues. The interactions of rhamnose is favored by His85, Asp97, Glu131, Glu132, Asp160, Tyr246, His247 by forming H bonds and the amino acids Asp97, Glu131, Asp160 and Try246 contributed the hydrophobic the interactions with the dock score of −20.3509 kJ/mol. The galactose is found to be docked with −23.3823 kJ/mol supported by His85, Glu131, Asp160, Met161, Tyr246, and His247 by H bonds and non bonded interactions by Glu131. The interaction of glucose is supported by His85, Glu131, Glu132, Asp160, Arg202, Tyr246, His247 and the non bonded interactions by Asp97, Glu131, Glu132 and Try246 with dock score of −26.8762 kJ/mol (Fig. 4.a). The early studies observed that arabinose efficiently binds with tyrosinase for inhibition activity. The binding between arabinose and tyrosinase is given in terms of dock score −26.28 kcal/moland the interaction is favored by histidine, aspargine and methioine (Hu et al., 2012).

3.6.2. Docking of amino acids for aminopepditase activity

The interactions of Methionine is favored by Asp97, Glu132, Tyr246, and His247 by forming H bonds and the amino acids Asp97, Asp160 and Try246 contributed the hydrophobic the interactions with the dock score of −27.1447 kJ/mol. The Leucine is found to be docked with −33.5010 kJ/mol supported by Asp97, Glu131, Asp160, Tyr246, and His247 by H bonds and non bonded interactions by Asp97, Asp160,

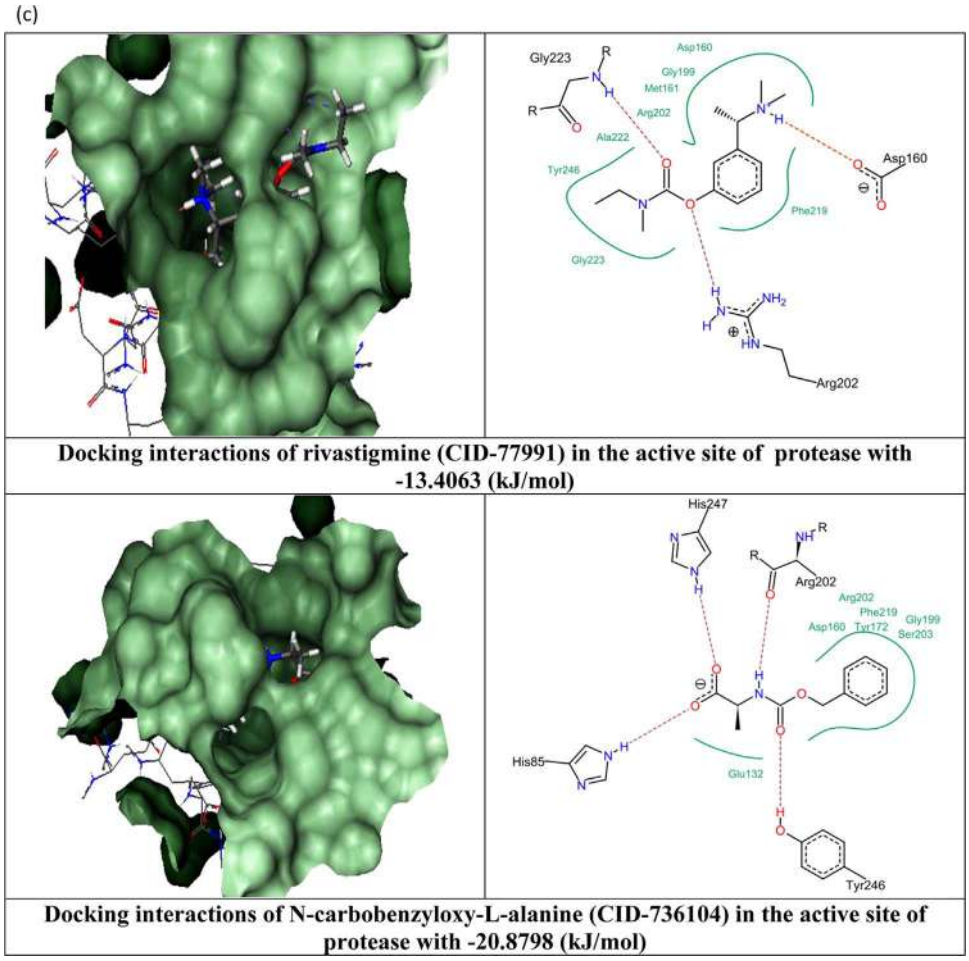


Fig. 4. (*continued*)

Met161, Phe219, and Try246. The interaction of Rivastigmine is supported by Asp160, Arg202, Gly233 and the non bonded interactions by Asp160, Met161, Gly199, Arg202, Ser203, Phe219, Ala222, Gly223, and Try246 with dock score of −13.4063 kJ/mol (Fig. 4.b). Similarly, the fibrinolytic activity of aminopeptidase from *Pseudomonas aeruginosa* through cloning studies and also explored the catalytic triad for aminopeptidase activity through docking studies. Their results showed that substrates binding are facilitated by the scaffold consisting of glutamic acid, serine and histidine (Sharma et al., 2013).

3.6.3. Docking interaction for protease activities

The interactions of N-carbobenzyloxy-L-alanine is favored by His85, Arg202, Try246 and His247 by forming H bonds and the amino acids Glu132, Asp160, Try147, Gly199, Arg202, Ser203, and Phe219 contributed the hydrophobic the interactions with the dock score of −20.8798 kJ/mol. The 4-amidino phenyl methanesulfonyl flurode is found to be docked with −29.1501 kJ/mol supported by Asp97, Glu132, Tyr172, and Hoh1010 by H bonds and non bonded interactions by Asp97, Asp160, Met161, Arg202, Ser203, Phe219, and Try246. The interaction of 3,4-dichloroisocoumine is supported by His85, His247 and the non bonded interactions by Glu131, Glu132, Asp160, Arg202, Met161, Phe219, Try246 and His246 with dock score of −13.1883 kJ/mol (Fig. 4.c). It is observed that the amino acids Try246 and His247 in the catalytic site enhanced the binding of most compounds by the formation of H bonds. Interestingly, it is observed that Asp160 and Try246 were found to contribute the h bond formation with most of the compounds, which signifies that these residues might play an essential role in the degradation pathway as enzymatic hydrolysis. Similarly reported the serine protease inhibitor namely phenyl methyl sulfonyl fluoride efficiently bound in the predicted binding site of keratinase enzyme from *Bacillus licheniformis* and the interaction of PMSF is favored by glycine residues. Where as in our study, it is observed that the interaction of PMSF, 3,4-dichloro isocoumarine and N-carbobenzyloxy-L-alanine revealed that the substrates efficiently bound with significant docking scores and the interactions are favored by Tyrosine, Histidine and Aspartic acid. Further out study envisages that the enzymatic hydrolysis activity of protease can be efficiently enhanced by modifying the residues in the catalytic site which can give better yield and maintains the cost of production (Jayalakshmi et al., 2011).

4. Conclusion

The results of this study, the substrate specificity of protease were determined by molecular studies. The degradation of goat skin keratin, and could be used to characterize the substrate specificity of proteases. The 3D model of predicted protease from *Bacillus* sp. was generated by using homology modeling approach. The modeled protease structure was accessed for stereo chemical quality using RAMPAGE, VERFIY 3D, ERRAT and PROSA. The docking studies with the dock score showed Polysaccharide subunits for keratinolytic activity against galactose −23.3823 kJ/mol, aminopeptidase activity against leucine −33.5010 (kJ/mol), and protease inhibitor against 3,4-dichloro isocoumarine −29.1501 (kJ/mol), respectively. This work determined the substrate recognition pattern and the development of suitable protease can potentially enhance its applications in many industrial sectors.

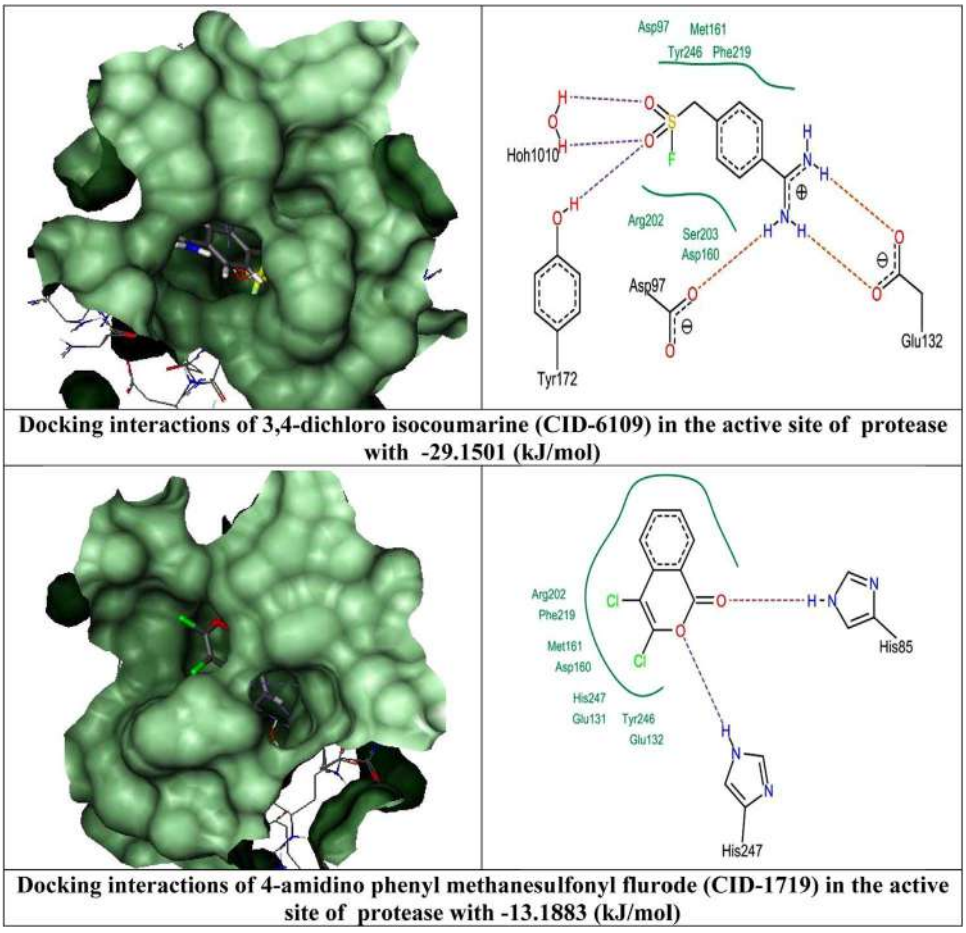


Fig. 4. (*continued*)

Table 3
Docking complex and interactions of amino acids within the catalytic site of modeled protease from *Bacillus* sp.

CID-66308	CID-19233	CID-6036	CID-5793	CID-6137	CID-6106	CID-77991	CID-736104	CID-1719	CID-1609
*His85	*His85	*His85	*His85	–	–	–	*His85	–	*His85
*Asp97	*Asp97	–	–	*Asp97	*Asp97	–	–	*Asp97	–
Asp97	Asp97	–	Asp97	Asp97	Asp97	–	–	Asp97	–
*Glu131	*Glu131	*Glu131	*Glu131	–	*Glu131	–	–	–	–
Glu131	Glu131	Glu131	Glu131	–	–	–	–	–	Glu131
*Glu132	*Glu132	*Glu132	*Glu132	*Glu132	–	–	–	*Glu132	–
Glu132	–	–	Glu132	–	–	–	Glu132	–	Glu132
*Asp160	–	*Asp160	*Asp160	*Asp160	*Asp160	*Asp160	–	–	–
Asp160	Asp160	–	–	Asp160	Asp160	Asp160	Asp160	Asp160	Asp160
–	–	*Met161	–	–	–	*Gly223	–	–	Arg202
–	–	–	–	Met161	Met161	Met161	–	Met161	Met161
–	–	–	–	–	–	–	–	*Try172	–
–	–	–	–	–	–	–	Try172	–	–
–	–	–	–	–	–	Gly199	Gly199	–	–
*Arg202	–	*Arg202	*Arg202	–	–	*Arg202	*Arg202	–	–
–	–	–	–	–	–	Arg202	Arg202	Arg202	–
–	–	–	–	–	–	–	Ser203	Ser203	–
–	–	–	–	–	Phe219	Phe219	Phe219	Phe219	Phe219
–	–	–	–	–	–	Ala222	–	–	–
–	–	–	–	–	–	Gly223	–	–	–
*Try246	*Try246	*Try246	*Try246	*Try246	*Try246	–	*Try246	–	–
–	Try246	–	Try 246	Try246	Try246	Try246	–	Try246	Try246
*His247	*His247	*His247	*His247	*His247	*His247	–	*His247	–	*His247
–	–	–	–	–	–	–	–	–	His247
–	–	–	–	–	–	–	–	*Hoh1010	–
−17.0329	**−20.3509**	**−23.3823**	**−26.8762**	**−27.1447**	**−33.5010**	**−13.4063**	**−20.8798**	**−29.1501**	**−13.1883**

*Hbond residues.
Hydrophobic residues.

Appendix A. Supplementary material

Supplementary data associated with this article can be found in the online version at http://dx.doi.org/10.1016/j.bcab.2017.11.016.

References

ACD/ChemSketch Freeware, version 11, 2006. Advanced Chemistry Development, Inc., Toronto, ON, Canada, ⟨www.acdlabs.com⟩.

Altschul, S.F., Gish, W., Miller, W., Myers, E.W., Lipman, D.J., 1990. Basic local alignment search tool. J. Mol. Biol. 215, 403–410.

Annamalai, N., Rajeswari, M.V., Sahu, S.K., Balasubramanian, T., 2014. Purification and characterization of solvent stable, alkaline protease from *Bacillus firmus* cas 7 by microbial conversion of marine wastes and molecular mechanism underlying solvent stability. Process Biochem. 49, 1012–1019.

Asker, M.M., Mahmoud, M.G., El Shebwy, K., Abd el Aziz, M.S., 2013. Purification and characterization of two thermostable protease fractions from *Bacillus megaterium*. J. Genet. Eng. Biotechnol. 11, 103–109.

Berg, J.M., Tymoczko, J.L., Stryer, L., 2002. The amino acid sequence of a protein determines its three-dimensional structure. In: Freeman, W.H. (Ed.), Biochemistry, Section 3.6, New York.

Berman, H.M., Westbrook, J., Feng, Z., Gilliland, G., Bhat, T.N., Weissig, H., Shindyalov, I.N., Bourne, P.E., 2000. The protein data bank. Nucleic Acids Res. 28, 235–242.

Bhunia, B., Basak, B., Dey, A., 2012. A review on production of serine alkaline protease by *Bacillus* spp. J. Biochem Tech. 3, 448–457.

Bhunia, B., Dey, A., 2012. Statistical approach for optimization of physiochemical requirements on alkaline protease production from *Bacillus licheniformis* NCIM-204. Enzym. Res. 905804.

Bhunia, B., Basak, B., Bhattacharya, P., Mandal, T., Dey, A., 2013. Effect of pH and temperature on stability and kinetics of novel extracellular serine alkaline protease (70 kDa). Int J. Biol. Macromol. 54, 1–8.

Bowie, J.U., Luthy, R., Eisenberg, D., 1991. A method to identify protein sequences that fold into a known three-dimensional structure. Science 253, 164–170.

Ch, W.H., 2007. Optimization of extracellular alkaline protease production from species of *Bacillus*. J. Ind. Microbiol. Biotechnol. 34, 241–245.

Colovos, C., Yeates, T.O., 1993. Verification of protein structures: patterns of nonbonded atomic interactions. Protein Sci. 2, 1511–1519.

Dalton, J.A.R., Jackson, R.M., 2007. An evaluation of automated homology modeling methods at low target template sequence similarity. Bioinformatics 23, 1901–1908.

Eswar, N., Marti-Renom, M.A., Webb, B., Madhusudhan, M.S., Eramian, D., Shen, M., Pieper, U., Sali, A., 2006. Comparative Protein Structure Modeling with MODELLER: Current Protocols in Bioinformatics. John Wiley and Sons, Inc, pp. 5.6.1–5.6.30.

Ezat, A.A., El-Bialy, N.S., Mostafa, H.I.A., Ibrahim, M.A., 2014. Molecular docking investigation of the binding interactions of macrocyclic inhibitors with HCV NS3 protease and its mutants (R155K, D168A and A156V). Protein J. 33, 32–47.

Gupta, R., Beg, Q., Khan, S., Chauhan, B., 2002. An overview on fermentation, downstream processing and properties of microbial alkaline proteases. Appl. Microbiol. Biotechnol. 60, 381–395.

Haddar, A., Agrebi, R., Bougatef, A., Hmidet, N., Sellami-Kamoun, A., Nasri, M., 2009. Two detergent stable alkaline serineproteases from *Bacillus mojavensis* A21: purification, characterization and potential application as a laundry detergent additive. Bioresour. Technol. 100, 3366–3373.

Hu, W.J., Yan, L., Park, D., Jeong, H.O., Chung, H.Y., Yang, J.M., Ye, Z.M., Qian, G.Y., 2012. Kinetic, structural and molecular docking studies on the inhibition of tyrosinase induced by arabinose. Int. J. Biol. Macromolec. 50 (3), 694–700.

Huang, Q., Peng, Y., Li, X., 2003. Purification and characterization of extracellular alkaline serine protease with dehairing function from *Bacillus pumilis*. Curr. Microbiol. 43, 169–173.

Huang, S.Y., Zou, X., 2010. Advances and challenges in proteinligand docking. Int. J. Mol. Sci. 11, 3016–3034.

Jaouadi, B., Ellouz-Chaabouni, S., Rhimi, M., Bejar, S., 2008. Biochemical and molecular characterization of a detergentstable serine alkaline protease from *Bacillus pumilus* CBS with high catalytic efficiency. Biochimie 90, 1291–1305.

Jayalakshmi, P., Krishnamoorthy, G., kumar, Ramesh, Sivaman, P., 2011. Docking conformation of Bacillus licheniformis keratinase enzyme and PMSF ligand T. Drug Invent. Today 3 (8), 200–202.

Kalyaanamoorthy, S., Chen, Y.P.P., 2014. Modelling and enhanced molecular dynamics to steer structure-based drug discovery. Prog. Biophys. Mol. Biol. 114, 123–136.

Lin, S., Zhang, M., Liu, J., Jones, G.S., 2015. Construction and application of recombinant strain for the production of an alkaline protease from *Bacillus licheniformis*. J. Biosci. Bioeng. 119, 284–288.

Lovell, S.C., Davis, I.W., Arendall III, W.B., de Bakker, P.I.W., Word, J.M., Prisant, M.G., Richardson, J.S., Richardson, D.C., 2002. Structure validation by Calpha geometry: phi, psi and Cbeta deviation. Proteins Struct. Funct. Genet. 50, 437–450.

Luthy, R., Bowie, J.U., Eisenberg, D., 1992. Assessment of protein models with three-dimensional profiles. Nature 356 (6364), 83–85.

MacArthur, M.W., Laskowski, R.A., Thornton, J.M., 1994. Knowledge-based validation of protein structure coordinates derived by X-ray crystallography and NMR spectroscopy. Curr. Opin. Struct. Biol. 4, 731–737.

Maiti, R., Van Domselaar, G.H., Zhang, H., Wishart, D.S., 2004. Super- pose: a simple server for sophisticated structural superposition. Nucleic Acids Res. 32 (1), W590–W594.

Marrone, T.J., Briggs, J.M., McCammon, 1997. Structure-based drug design. Annu. Rev. Pharmacol. Toxicol. 37, 71–90.

Maruthiah, T., Esakkiraj, P., Prabakaran, G., Palavesam, A., Immanuel, G., 2013. Purification and characterization of moderately halophilic alkaline serine protease from marine Bacillus subtilis AP-MSU 6. Biocatal. Agric. Biotechnol. 2, 116–119.

Mulukala, N.S.K., Gunda, S.K., Shaik, M., 2013. Comparative modeling of Rab6 proteins: identification of key residues and their interactions with guanine nucleotides. J. Mol. Model. 19, 1891–1900.

Prakash, S., Ramasubburayan, R., Iyapparaj, P., Sankaralingam, S., Palavesam, A., Immanuel, G., 2014. Optimization and partial purification of a protease produced by selected bacterial strains grown on trash fish meal substrate and its antagonistic property against bacterial pathogens. Biocatal. Agric. Biotechnol. 3, 288–295.

Ramachandran, G.N., Ramakrishnan, C., Sasisekharan, V., 1963. Stereo-chemistry of polypeptide chain conformations. J. Mol. Biol. 7, 95–99.

Rarey, M., Kramer, B., Lengauer, T., Klebe, G., 1996. A fast, flexible docking method using an incremental construction algorithm. J. Mol. Biol. 261, 470–489.

Reddy, Ch, S., Vijayasarathy, K., Srinivas, E., Sastry, G.M., Sastry, G.N., 2006. Homology modeling of membrane proteins: a critical assessment. Comp. Biol. Chem. 30 (2), 20–26.

Ribitscha, D., Karla, W., Birner-Gruenbergera, R., Grubera, K., Eiteljoerg, I., Remlera, P., 2010. C-terminal truncation of a metagenome derived detergent protease for effective expression in *E. coli*. J. Biotechnol. 150, 408–416.

Satbir, S., Bijender Kumar, B., 2014. Medium optimization for enhanced production of protease with industrially desirable attributes from *Bacillus subtilis* K-1. Chem. Eng. Commun. http://dx.doi.org/10.1080/00986445.2014.900052.

Selvam, K., Govarthanan, M., Senthilkumar, B., Senbagam, D., Selvankumar, T., Kamala-Kannan, S., Sudhakar, C., 2016. Optimization of protease production from surface-modified coffee pulp waste and corncobs using *Bacillus* sp. by SSF 3. Biotech 6 (2), 167.

Shankar, S., Rao, M., Seeta Laxman, R., 2011. Purification and characterization of an alkaline protease by a new strain of *Beauveria* sp. Process Biochem. 46 (2), 579–585.

Sharma, R., Verma, V.V., Gupta, R., 2013. Functional characterization of an extracellular keratinolytic protease, Ker AP from *Pseudomonas aeruginosa* KS-1: a putative aminopeptidase with PA domain. J. Mol. Catal. B Enzym. 91, 8–16.

Sippl, M.J., 1993. Recognition of errors in three-dimensional structures of proteins. Proteins 17, 355–362.

Sivasubramanian, S., Murali Manohar, B., Rajaram, A., Puvanakrishna, R., 2008. Eco-friendly lime and sulfide free enzymatic dehairing of skins and hides using a bacterial alkaline protease. Chemosphere 70, 1015–1024.

Sookkheo, B., Sinchaikul, S., Phutrakul, S., Chen, S.T., 2000. Purification and characterization of the highly thermostable proteases from *Bacillus stearothermophilus* TLS33. Protein Expr. Purif. 20, 142–151.

Stierand, K., Maab, P., Rarey, M., 2006. Molecular complexes at a glance: automated generation of two-dimensional complex diagrams. Bioinformatics 22, 1710–1716.

Sudhir, K., Rai, Ashis, K., Mukherjee, 2010. Statistical optimization of production, purification and industrial application of alaundry detergent and organic solvent-stable subtilisin-like serine protease (Alzwiprase) from *Bacillus subtilis* DM-04. Biochem. Eng. J. 48, 173–180.

Thanikaivelan, P., Rao, J.R., Nair, B.U., Ramasami, T., 2004. Progress and recent trends in biotechnological methods for leather processing. Trends Biotechnol. 22, 181–188.

Vellard, M., 2003. The enzyme as drug: application of enzymes as pharmaceuticals. Curr. Opin. Biotechnol. 14, 444–450.

Volkamer, A., Kuhn, D., Grombacher, T., Rippmann, F., Rarey, M., 2012. Combining global and local measures for strucure-based druggability predictions. J. Chem. Inf. Model 52, 360–372.

Walter, R.P., Scott, P.H., Hunenberger, I.G., Tironi, A.E., Mark, S.R., Billeter, J.F., Torda, A.E., Huber, T., Kruger, P., van Gunsteren, W.F., 1999. The GROMOS biomolecular simulation program package. J. Phys. Chem. A 103 (19), 3596–3607.

Webb, B., Sali, A., 2014. Comparative Protein Structure Modeling using Modeller. Current Protocols in Bioinformatics. John Wiley and Sons, Inc, pp. 5.6.1–5.6.32.

Weininger, D., 1988. SMILES, a chemical language and information system. Introd. Methodol. encoding rules. J. Chem. Inf. Model. 28, 31–36.

Wiederstein, M., Sipplm, M.J., 2007. ProSA-web: interactive web service for the recognition of errors in three-dimensional structures of proteins. Nucleic Acids Res. 35, W407–W410.

Zambare, V.P., Nilegaonkar, S.S., Kanekar, P.P., 2007. Production of an alkaline protease by Bacillus cereus MCM B-326 and its application as a dehairing agent. World J. Microbiol. Biotechnol. 23, 1569–1574.

Springer Link

Search Log in

Download PDF

Short Reports | Open Access | Published: 26 July 2017

Isolation, identification and characterization of arsenic transforming exogenous endophytic *Citrobacter* sp. RPT from roots of *Pteris vittata*

T. Selvankumar, R. Radhika, R. Mythili, S. Arunprakash, P. Srinivasan, M. Govarthanan ✉ & Hyunook Kim ✉

3 Biotech **7**, Article number: 264 (2017)

2065 Accesses | **15** Citations | **2** Altmetric | Metrics

Abstract

The aim of the present study was to assess the arsenic (As) transformation potential of endophytic bacteria isolated from roots of *Pteris vittata* plant. The endophytic bacterium was tested for minimal inhibitory concentration (MIC) against As. The endophytic strain RPT exhibited the highest resistance to As(V) (400 mg/l). Phylogenetic analysis of the 16S rRNA sequence suggested that strain RPT was a member of genus *Citrobacter*. The As transformation assay revealed As(III) oxidation and As(V) reduction potential of *Citrobacter* sp. RPT. The As resistance mechanism was further confirmed by amplification of *arsC* and *aoxB* genes. The growth

P.G.P. COLLEGE OF ARTS & SCIENCE NAMAKKAL 637 206

PRINCIPAL
PGP College of Arts and Science
Namakkal

3 Biotech (2017)7:264
DOI 10.1007/s13205-017-0901-8

SHORT REPORTS

Isolation, identification and characterization of arsenic transforming exogenous endophytic *Citrobacter* sp. RPT from roots of *Pteris vittata*

T. Selvankumar[1] · R. Radhika[1] · R. Mythili[1] · S. Arunprakash[2] · P. Srinivasan[1] · M. Govarthanan[1,3] · Hyunook Kim[3]

Received: 8 November 2016 / Accepted: 19 July 2017
© Springer-Verlag GmbH Germany 2017

Abstract The aim of the present study was to assess the arsenic (As) transformation potential of endophytic bacteria isolated from roots of *Pteris vittata* plant. The endophytic bacterium was tested for minimal inhibitory concentration (MIC) against As. The endophytic strain RPT exhibited the highest resistance to As(V) (400 mg/l). Phylogenetic analysis of the 16S rRNA sequence suggested that strain RPT was a member of genus *Citrobacter*. The As transformation assay revealed As(III) oxidation and As(V) reduction potential of *Citrobacter* sp. RPT. The As resistance mechanism was further confirmed by amplification of *arsC* and *aoxB* genes. The growth kinetics of strain RPT was altered slightly in the presence of different concentration (100–400 mg/l) of As stress. Temperature and pH influenced the As removal rate. The maximum As removal was observed at pH 7.0 (74%) and 37 °C (70.9%). The results suggest that strain RPT can survive under the As stress and has been identified as a potential candidate for application in bioremediation of As in contaminated environments.

Keywords Arsenic · Transformation · Bioremediation · *Pteris vittata* · *Citrobacter*

Introduction

Arsenic (As) contamination in environment is a major problem in all over the modern industrialized world. It has received increasing attention due to its carcinogenic impacts on human health. Mining and metallurgical activities lead to As pollution in the environment (Zhu et al. 2014). Due to negative clinical effects of As contamination to humans warrants urgent issue for mitigation and sustainable environmental management. Several physical and chemical techniques have been developed for mitigation of As pollution from soil and water (Yuan and Chiang 2007; Fu and Wang 2011). Although the physico-chemical methods have extensive removal application, the high cost solid and liquid waste generation from the remediation process causes unsustainable environment (Tiwari et al. 2016). Therefore, it is necessary to expand the remediation process to reduce its effects on ecosystem.

Bioremediation is a promising technology to remove As from contaminated soil and water, which is cost-effective and eco-friendly compared to physico-chemical methods (Govarthanan et al. 2013, 2015a). Microorganisms are primarily used in the bioremediation to degrade or detoxify the As into harmless and less toxic forms. Several microbial processes involve the removal of As in soil and water, including oxidation, reduction, adsorption and microbe-mediated electron transfer (Diesel et al. 2009; Guo et al. 2015). Generally As is toxic to microorganisms; however, several microorganisms gain the energy for rapid growth by metabolizing the As (Oremland and Stolz 2003, 2005). The As-resistant microorganisms utilize the As derivatives

✉ M. Govarthanan
gova.muthu@gmail.com

✉ Hyunook Kim
h_kim@uos.ac.kr

[1] PG and Research Department of Biotechnology, Mahendra Arts and Science College (Autonomous), Kalippatti, Namakkal, Tamil Nadu 637501, India

[2] Department of Botany, Arignar Anna Government Arts College, Namakkal, Tamil Nadu 637002, India

[3] Department of Energy and Environmental System Engineering, University of Seoul, Seoul, Republic of Korea

Published online: 26 July 2017

as an electron donor and/or electron receptors during the As detoxification process (Johnson et al. 2003). Several studies have reported the role of microorganisms in the transformation of As in aqueous systems (Pepi et al. 2007; Chang et al. 2008; Lievremont et al. 2009; Mirza et al. 2014).

Microbial detoxification of As mainly occurs in two ways, such as oxidation and reduction. It has been established that the bacteria reduce the As(V) to As(III) inside the cells through the *ars* operon mechanism and exclude As(III) by As(III) efflux pump. However, microbial As(III) oxidation has been described either as a detoxification mechanism or energy source for chemolithoauthotrophic bacteria (Santini et al. 2000). So far most endophytic bacteria isolated from *P. vittata* are capable of either As(V) reduction or As(III) oxidation have been isolated from As contaminated soil/water (Stolz and Oremland 1999; Stolz et al. 2002). However, to our knowledge, there is no report on the endophytic Gram-negative coliform bacterium *Citrobacter* sp. isolated from *P. vittata* grown in non-polluted soil that is able to reduce As(V).

Fern *Pteris vittata* L. is a native and widespread paleotropic As hyperaccumulator, considered the suitable candidate plant for the phytoremediation of As-contaminated soil (Ma et al. 2001). Its rapid growth, large biomass, wide and extensive root system, as well as a wide geographic distribution, justify the successful application of As remediation (Danh et al. 2014). However, the endophytic bacterial population in the roots of *P. vittata* from non-polluted soil has not been reported. Hence, the objectives of this study were (1) to isolate As-resistant endophytic bacteria from roots of *Pteris vittata* (2) to evaluate minimal inhibitory concentration of As, (3) to screen As transformation and oxidation and reduction assay, and (4) to optimize experimental variables, such as pH and temperature for enhanced As removal.

Materials and methods

Isolation of arsenic resistant endophytic bacteria from *Pteris vittata*

Healthy *Pteris vittata* plants were collected from Kolli Hills, part of the Eastern Ghats of Tamil Nadu, India. The site is located at 11.2485° latitude and a 78.3387° longitude ranges about 1000–1300 m in height. The collected *Pteris vittata* plant sample was washed with tap water followed by several rinses with sterile water (Govarthanan et al. 2016). The washed plant was dissected into roots and stems with a sterile scalpel. The root samples were surface sterilised with 95% ethanol and 3% hypochlorite solution for 2–3 min. The surface sterilised root samples were again washed several times in sterile water to remove the sterilization agents. The sterilised root tissue (1 g fresh weight) was ground in a mortar and pestle with 5 ml saline (0.85% NaCl). The saline suspension was serially diluted and plated using the spread plate technique onto Nutrient Agar (Hi-Media, India) plates. The plates were incubated at 35 ± 2 °C for 48 h and observed for bacterial growth on the agar surface. Morphologically distinct colonies were purified and stored at 4 °C for further studies.

Minimal inhibitory concentration of As

Arsenic tolerance levels of the isolates were assessed by agar-dilution method according to Kamala-Kannan and Krishnamurthy (2006). Briefly, the isolates were inoculated in nutrient agar plates containing different concentrations of As ranging from 50 to 400 mg/l. The plates were incubated overnight at 35 °C and observed for bacterial growth. The lowest concentration of the metal that completely inhibited the growth of the bacteria was considered as the minimal inhibitory concentration (MIC). Arsenic metal salts were added to the nutrient agar after autoclaving and cooling to 50 °C from filter-sterilised stock solutions.

Screening of arsenic transformation assay

Arsenite to As(V) transforming potential of the isolate was performed as described by Simeonova et al. (2004). Briefly, the isolate pre-grown on As(V) and As(III) nutrient agar plates were flooded with 0.1 M $AgNO_3$. In the presence As(III) in the medium was detected by a bright yellow precipitate formation. Negative test was represented by white colour formation (Tiwari et al. 2016).

Genomic DNA extraction and identification of As-resistant bacteria

DNA was extracted from the potential isolate RPT using QIAGEN (CA, USA) DNA extraction kit, and its concentration was determined using a UV–Vis spectrophotometer (NanoDrop 2000). Fragments of 16S rRNA were amplified using universal primers 27f (5′-AGAGTTTGATCCTGGC TCAG-3′) and 1492r (5′-CCCCGTCAATTCATTTGA GTTT-3′). The PCR product was purified using a QIAGEN PCR purification kit and sequenced using an automated ABI PRISM 3700 sequencer (USA). The obtained 16S rRNA sequence was compared against the available sequence database using BLAST program in NCBI website. The phylogenetic tree was constructed using neighbour-joining distance method by software Mega 6.0.

Effect of As on bacteria growth

Five millilitres of the mid-log phase cultures (10^8 cells/mL) of the isolate grown individually in nutrient broth is supplemented with different concentrations of As (100–400 mg/l). The flasks were incubated in a shaking incubator (200 rpm) at 37 °C, and the growth was measured at different time intervals according to the increase in optical density at 600 nm in a UV–Vis spectrophotometer (Shimadzu, Kyoto, Japan). Cultures grown in the absence of As were used as a control (Govarthanan et al. 2015b).

Amplification of As-resistant genes

The As transporting gene *arsC* was amplified using the primers amlt42-F (5′-TCG CGT AAT ACG CTG GAG AT-3′), and amlt376-R (5′-ACT TTC TCG CCG TCT TCC TT-3′) (Sun et al. 2004). The PCR conditions for the amplification were initial denaturation at 95 °C for 5 min, 35 cycles at 95 °C for 45 s, 57 °C for 1 min, 72 °C for 2 min and a final extension step of 72 °C for 7 min. Arsenic oxidizing gene *aoxB* was amplified using the primers 69-F (5′-TGY ATY GTN GGN TGY GGN TAY MA-3′) and 1374-R (5′-TAN CCY TCY TGR TGN CCN CC-3′) (Rhine et al. 2006).

Removal of As at different pH and temperature conditions

The effect of pH on the removal of As was determined at various pH levels ranging from 6 to 9. In brief, 10 ml of the bacterial suspension was aseptically inoculated into 250 ml Erlenmeyer flasks containing 100 ml of As (initial metal concentration 50 mg/l). The flasks were incubated in a shaking incubator (200 rpm) at 37 °C and the samples were collected after 48 h of incubation. The samples were centrifuged (10,000 rpm for 5 min), filtered (0.22 µm) and analysed for the residual heavy metal concentration using atomic adsorption spectroscopy (AAS) (Thermo Scientific™ iCE™ 3500). Similarly, the effect of temperature was measured by incubating the flasks at different temperatures (30, 35, 37 and 40 °C). Flask without bacteria was used as a control for this experiment. All the experiments were repeated for three times and each sample was tested in triplicate.

Results and discussion

The As-resistant mechanism of the endophytic isolate *Citrobacter* sp. RPT isolated from roots of *P. vittata* grown in unpolluted soil was investigated in this present study. A total of three morphologically different endophytes were isolated. The isolated endophytes were further tested for As resistance by determining its minimal inhibitory concentration. The minimal inhibitory concentration of the As showed that the isolate RPT exhibited maximum resistance to As (400 mg/l). The other two isolates showed inadequate resistance to the As. Based on the minimal inhibitory concentration results, the isolate RPT was selected for further As resistance characterization studies. Morphological and 16S rRNA gene sequencing was carried out to identify the isolate. The 16S rRNA sequence of this strain showed 99% identity with *Citrobacter* sp. The partial 16S rRNA of the isolate RPT was deposited in GenBank (Accession no.: KX348779). A phylogenetic tree was derived from the partial 16S rRNA sequences of the isolate *Citrobacter* sp. RPT with existing sequences in the NCBI database, and the results are shown in Fig. 1. Several studies reported the As resistance mechanism of the endophytes isolated from *P. vittata* (Xu et al. 2014, 2016). However, there is no information about arsenic resistant endophytic *Citrobacter* sp. isolated from the roots of *P. vittata.*

The isolate RPT was further screened by silver nitrate assay on LB agar plates. Silver nitrate assay is aimed to check the As(III) to As(V) and As(V) to As(III) transformation ability of the isolate RPT. The quantitative reaction between AgNO3 and As(III) or As(V) results in the formation of coloured precipitates on the LB agar plates. The reaction between $AgNO_3$ with AsO_3 (AsIII) plates showed that the yellow precipitation on the LB plates. Whereas, the reaction between AsO_4^{3-} with $AgNO_3$ showed the brownish precipitation on the surface of the LB agar plates (Simeonova et al. 2004; Tiwari et al. 2016). The As transformation assay results indicated that the isolate RPT is able to oxidize As(III) and reduce As(V). The growth rate of the isolate RPT was evaluated in LB (1/4 strength) broth supplemented with different concentrations (100 and 400 mg/l) of As. The results (Fig. 2) indicate that the growth rate of the strain RPT decreases with increasing concentrations of As. The results are in agreement with previous studies reported the growth rate of As-resistant *Herbaspirillum* sp. GW103 was decreased by the increasing concentration of As in batch experiments (Govarthanan et al. 2015b). It is suggested that the direct exposure of the strain RPT to As and limited nutrient availability in the LB broth might have reduced the growth rate of the organism.

The strain RPT was screened for *arsC*, *aoxB* genes reported in the As oxidizing and reducing bacteria. Visible *arsC* band was clearly observed on the agarose gel surface, which indicates the presence of As transporting (arsenate reductase) in the strain RPT. The arsenate reductase gene arsC is the most important genes in association with As(III) oxidation and

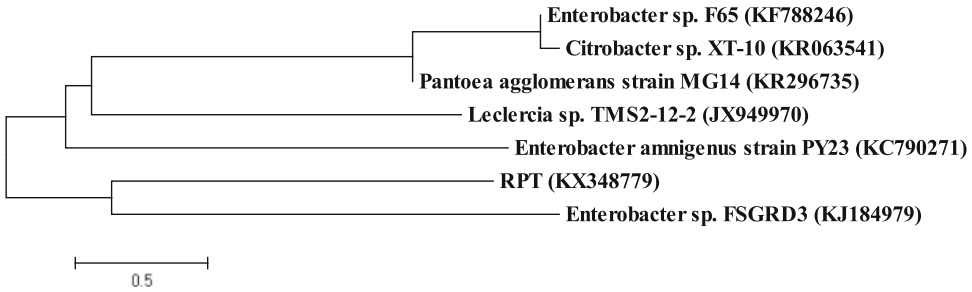


Fig. 1 A neighbour-joining tree constructed using Mega 6.0 showing the phylogenetic relationship of 16S rRNA sequence of isolated strain *Citrobacter* sp. RPT from closely related sequences from GenBank. Accession numbers at the GenBank of National Centre for Biotechnology Information (NCBI) are shown in *parenthesis*

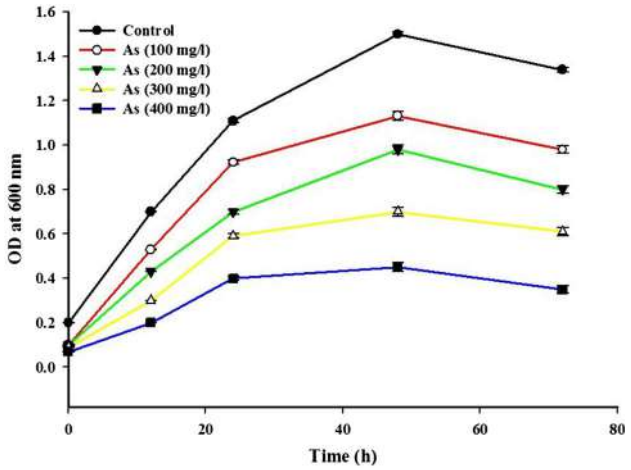


Fig. 2 Growth kinetics of *Citrobacter* sp. RPT using As at different concentrations (100–400 mg/l)

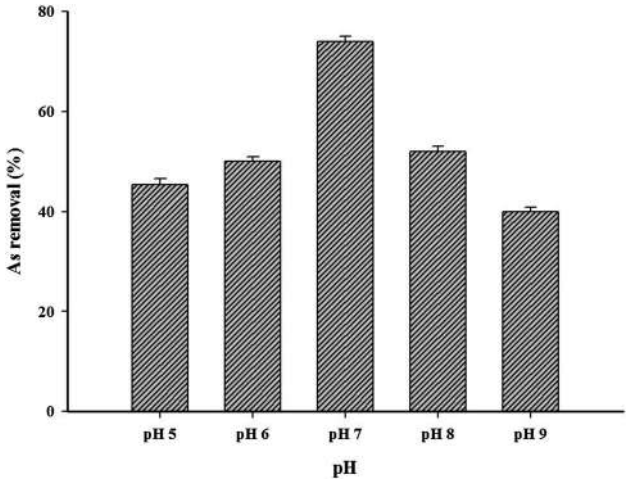


Fig. 3 Influence of pH on As removal by the isolate *Citrobacter* sp. RPT

As(V) reduction in soils by microbes (Han et al. 2017). For most bacteria, arsC-mediated As(V) reduction, followed by As(III) efflux to the external environment, is an important mechanism for As detoxification (Bhattacharjee and Rosen 2007). However, As detoxification in some bacteria is associated with As(III) oxidation by converting As(III) to less toxic As(V) (Stolz et al. 2010). No visible *aoxB* band was observed on the gel, which indicates that the strain RPT may harbour another type of As oxidizing protein or the primers (69-F and 1374-R) were inappropriate for the amplification of the *aoxB* gene present in the strain RPT.

Arsenic removal efficiency of the strain *Citrobacter* RPT at different pH levels was assessed and the results are presented in Fig. 3. The highest rate of As removal (74%) showed at pH 7.0, whereas the average levels of As removal showed at pH 5.0 (45.3%), pH 6.0 (50%), pH 8.0 (52%) and pH 9.0 (40%). It has been reported that in acidic pH, association of hydronium ions with the cell surface creates reduction of negative charge intensity on the bacterial cell wall results in the reduction or inhibition of the binding of metal ions (Khalid et al. 2011). Fourest et al. (1994) reported that the functional groups on the bacteria may become positively charged and may not interact with the metal ions at acidic pH. The decreased removal rate at alkaline pH can be attributed to the growth response of the isolate under pH stress. The limited growth of isolates at alkaline pH reduces the overall uptake of metals (Guo et al. 2010). The As removal efficiency of *Citrobacter* sp. RPT was tested with different temperature conditions, as temperature is an important parameter in biological oxidation and/or reduction of As, and the results are presented in Fig. 4. The results showed that the removal of As increased with increasing temperature up to 37 °C (70.9%), but the removal efficiency of As decreased slightly at 40 °C (25.3.9%). The biological removal of metals was highly influenced by temperature (Zhou et al. 2013). The results from this study indicated that pH and temperature play a major role in the survival of and As removal potential of the *Citrobacter* sp. RPT. The bioremediation rate of living metal-resistant bacteria should be strongly dependent on the population of cells at optimal growth conditions (Guo et al. 2010).

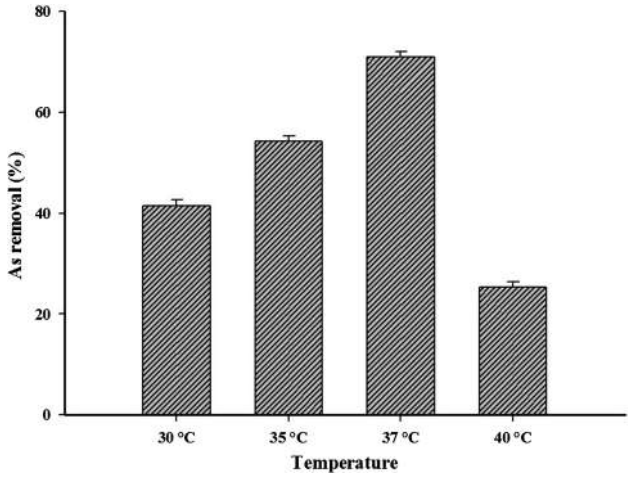


Fig. 4 Influence of temperature on As removal by the isolate *Citrobacter* sp. RPT

Conclusion

The endophytic bacteria *Citrobacter* sp. RPT isolated from *P. vittata* showed a significant resistance to As. The strain RPT grew in culture media with high As concentration (400 mg/l) under 37 °C at pH 7.0. The strain had ability to both As(III) oxidation and As(V) reduction. Bioremediation studies with batch experiments showed that the isolate RPT caused high removal of As (74%) at pH 7.0 and (70.9%) at 37 °C. The obtained results suggested that the exogenous endophytic bacteria would affect the As transformation in As-contaminated systems, and play a major role in the mitigation of As in the ecosystem.

Acknowledgements Dr. Muthusamy Govarthanan and Prof. Hyunook Kim were supported by the Korea Institute of Energy Technology Evaluation and Planning (KETEP) and the Ministry of Trade, Industry and Energy (MOTIE) of the Republic of Korea (no. 20153010091980).

Compliance with ethical standards

Conflict of interest The authors declare that they have no conflict of interest.

References

Bhattacharjee H, Rosen BP (2007) Arsenic metabolism in prokaryotic and eukaryotic microbes. In: Nies DH, Silver S (eds) Molecular microbiology of heavy metals. Springer, Germany, pp 371–406

Chang JS, Kim YH, Kim KW (2008) The ars genotype characterization of arsenic resistant bacteria from arsenic-contaminated gold–silver mines in the Republic of Korea. Appl Microbiol Biotechnol 80:155–165

Danh LT, Truong P, Mammucari R, Foster N (2014) A critical review of the As uptake mechanisms and phytoremediation potential of *Pteris vittata*. Int J Phytoremediat 16:429–453

Diesel E, Schreiber M, van der Meer JR (2009) Development of bacteria based bioassays for arsenic detection in natural waters. Anal Bioanal Chem 394:687–693

Fourest E, Canal C, Roux JC (1994) Improvement of heavy metal biosorption by mycelial dead biomasses (*Rhizopus arrhizus, Mucor miehei and Penicillium chrysogenum*): pH control and cationic activation. FEMS Microbiol Rev 14:325–332

Fu F, Wang Q (2011) Removal of heavy metal ions from wastewaters: a review. J Environ Manag 92:407–418

Govarthanan M, Lee KJ, Cho M, Kim JS, Kamala-Kannan S, Oh BT (2013) Significance of autochthonous *Bacillus* sp. KK1 on biomineralization of lead in mine tailings. Chemosphere 90:2267–2272

Govarthanan M, Lee SM, Kamala-Kannan S, Oh BT (2015a) Characterization, real-time quantification and in silico modeling of arsenate reductase (arsC) genes in arsenic resistant *Herbaspirillum* sp. GW103. Res Microbiol 166:196–204

Govarthanan M, Park SH, Park YJ, Myung H, Krishnamurthy RR, Lee SH, Lovanh N, Kamala-Kannan S, Oh BT (2015a) Lead biotransformation potential of allochthonous *Bacillus* sp. SKK11 with sesame oil cake extract in mine soil. RSC Adv 5:54564

Govarthanan M, Mythili R, Selvankumar T, Kamala-Kannan S, Rajasekar A, Chang YC (2016) Bioremediation of heavy metals using an endophytic bacterium Paenibacillus sp. RM isolated from the roots of *Tridax procumbens.* 3. Biotech 6:242

Guo H, Luo S, Chen L, Xiao X, Xi Q, Wei W, Zeng G, Liu C, Wan Y, Chen J, He Y (2010) Bioremediation of heavy metals by growing hyperaccumulaor endophytic bacterium *Bacillus* sp. L14. Bioresour Technol 101:8599–8605

Guo H, Liu Z, Ding S, Hao C, Xiu W, Hou W (2015) Arsenate reduction and mobilization in the presence of indigenous aerobic bacteria obtained from high arsenic aquifers of the Hetao basin, Inner Mongolia. Environ Pollut 203:50–59

Han YH, Fu JW, Xiang P, Cao Y, Rathinasabapathi B, Chen Y, Maa LQ (2017) Arsenic and phosphate rock impacted the abundance and diversity of bacterial arsenic oxidase and reductase genes in rhizosphere of As-hyperaccumulator *Pteris vittata*. J Hazard Mater 321:146–153

Johnson DB, Okibe N, Roberto FF (2003) Novel thermo-acidophilic bacteria isolated from geothermal sites in Yellowstone National Park: physiological and phylogenetic characteristics. Arch Microbiol 180:60–68

Kamala-Kannan S, Krishnamoorthy R (2006) Isolation of mercury resistant bacteria and influence of abiotic factors on bioavailability of mercury—a case study in Pulicat Lake north of Chennai, south east India. Sci Total Environ 367:341–353

Khalid A, Hussein Sedky HA, Hassan JHJ (2011) Potential capacity of *Beauveria bassiana* and *Metarhizium anisopliae* in the biosorption of $Cd2^{+}$ and $Pb2^{+}$. J Gen Appl Microbiol 57:347–355

Lievremont D, Bertin PN, Lett MC (2009) Arsenic in contaminated waters: biogeochemical cycle, microbial metabolism and biotreatment processes. Biochimie 91:1229–1237

Ma LQ, Komar KM, Tu C, Zhang W, Cai Y, Kennelley ED (2001) A fern that hyperaccumulates arsenic: a hardy, versatile, fast-growing plant helps to remove arsenic from contaminated soils. Nature 409:579

Mirza BS, Muruganandam S, Meng XY, Sorensen DL, Dupont RR, McLean JE (2014) Arsenic(V) reduction in relation to iron(III) transformation and molecular characterization of the structural and functional microbial community in sediments of a basin-fill aquifer in Northern Utah. Appl Environ Microbiol 80:3198–3208

Oremland RS, Stolz JF (2003) The ecology of arsenic. Science 300:939–944

Oremland RS, Stolz JF (2005) Arsenic, microbes and contaminated aquifers. Trends Microbiol 13:45–49

Pepi M, Volterrani M, Renzi M, Marvasi M, Gasperini S, Franchi E, Focardi SE (2007) Arsenic-resistant bacteria isolated from contaminated sediments of the Orbetello Lagoon, Italy, and their characterization. J Appl Microbiol 103:2299–2308

Rhine ED, Phelps CD, Young LY (2006) Anaerobic arsenic oxidation by novel denitrifying isolates. Environ Microbiol 8:899–908

Santini JM, Sly LI, Schnagl RD, Schnag RD, Macy JM (2000) A new chemolithoautotrophic arsenite-oxidizing bacterium isolated from a gold mine: phylogenetic, physiological, and preliminary biochemical studies. Appl Environ Microbiol 66:92–97

Simeonova DD, Lievremont D, Lagarde F, Muller DAE, Groudeva VI, Lett MC (2004) Microplate screening assay for the detection of arsenite-oxidizing and arsenate-reducing bacteria. FEMS Microbiol Lett 237:249–253

Stolz JF, Oremland RS (1999) Bacterial respiration of arsenic and selenium. FEMS Microbiol Rev 23:615–627

Stolz JF, Basu P, Oremland RS (2002) Microbial transformation of elements: the case of arsenic and selenium. Int Microbiol 5:207

Stolz JF, Basu P, Oremland RS (2010) Microbial arsenic metabolism: new twists on an old poison. Microbe 5:53–59

Sun Y, Polishchuk EA, Radoja U, Cullen WR (2004) Identification and quantification of arsC genes in environmental samples by using real-time PCR. J Microbiol Methods 58(3):335–349

Tiwari S, Sarangi BK, Thul ST (2016) Identification of arsenic resistant endophytic bacteria from *Pteris vittata* roots and characterization for arsenic remediation application. J Environ Manag 180:359–365

Xu JY, Li HB, Liang S, Luo J, Ma LQ (2014) Arsenic enhanced plant growth and altered rhizosphere characteristics of hyperaccumulator *Pteris vittata*. Environ Pollut 194:105–111

Xu JY, Han YH, Chen Y, Zhu LJ, Ma LQ (2016) Arsenic transformation and plant growth promotion characteristics of As-resistant endophytic bacteria from As-hyperaccumulator *Pteris vittata*. Chemosphere 144:1233–1240

Yuan C, Chiang TS (2007) The mechanisms of arsenic removal from soil by electrokinetic process coupled with iron permeable reaction barrier. Chemosphere 67:1533–1542

Zhou Q, Chen Y, Yang M, Li W, Deng L (2013) Enhanced bioremediation of heavy metal from effluent by sulfate-reducing bacteria with copper–iron bimetallic particles support. Bioresour Technol 136:413–417

Zhu YG, Yoshinaga M, Zhao FJ, Rosen BP (2014) Earth abides arsenic bio transformations. Annu Rev Earth PlSc 42:443–467

ScienceDirect

Biocatalysis and Agricultural Biotechnology
Volume 7, July 2016, Pages 250-256

Enhanced production of amylase from *Bacillus* sp. using groundnut shell and cassava waste as a substrate under process optimization: Waste to wealth approach

Kandasamy Selvam [a, 1], Thangasamy Selvankumar [b, 1], Radhika Rajiniganth [b], Palanisamy Srinivasan [b], Chinnappan Sudhakar [b], Balakrishanan Senthilkumar [a, c], Muthusamy Govarthanan [b, d]

Show more

Share Cite

https://doi.org/10.1016/j.bcab.2016.06.013

Get rights and content

Abstract

The consumption of bi-substrates (groundnut shell and cassava waste) in order to produce an amylase enzyme by Bacillus sp. using solid stated fermentation was carried out by applying Box-Behnken design (BBD). Initial pH, incubation time, concentrations of groundnut shell (GNS) and cassava waste (CW) variables were generated for each fermentation conditions of the *Bacillus* sp. to optimize the amylase production. Maximum yield of amylase (866 U/mL) was achieved by *Bacillus* sp. at the favorable conditions of the fermentation; 60 h, pH 7.0, 2 g/L GNS and 2 g/L CW. It was revealed that the combination of bi-substrates might be used in industries to produce high amount of value added amylase.

Introduction

Amylases are a group of hydrolases that can specifically cleave the α-glycosidic linkage in starch. Two important groups of amylases are glucoamylase and α-amylase. Glucoamylase (glucan 1,4-α-glucosidase) produces single glucose units from non reducing ends of amylose and amylopectin (Anto et al., 2006), whereas, α-amylases (4-α-D-glucan glucanohydrolase) are extracellular enzymes that randomly cleave the 1,4- α-d-glucosidic linkage between adjacent glucose units inside the linear amylose chain (Pandey et al., 2005, Castro et al., 2010). Amylases are among the most important enzymes in the global market because of their potential applications in a number of industrial processes such as food, pharmaceuticals, cosmetics, textile and paper industries (Sahnoun et al., 2015). Although they can be derived from different sources,

P.G.P. COLLEGE OF ARTS & SCIENCE NAMAKKAL 637 206

PRINCIPAL
PGP College of Arts and Science
Namakkal

ResearchGate

See discussions, stats, and author profiles for this publication at: https://www.researchgate.net/publication/304621703

Enhanced production of amylase from Bacillus sp. using groundnut shell and cassava waste as a substrate under process...

Article *in* Biocatalysis and Agricultural Biotechnology · June 2016

DOI: 10.1016/j.bcab.2016.06.013

CITATION
1

READS
51

7 authors, including:



Kandasamy Selvam
Sengunthar Arts and Science college
18 PUBLICATIONS **40** CITATIONS
SEE PROFILE



Selvankumar Thangaswamy
Mahendra Arts & Science College
34 PUBLICATIONS **66** CITATIONS
SEE PROFILE



Senthilkumar Balakrishnan
Haramaya University
59 PUBLICATIONS **187** CITATIONS
SEE PROFILE



Govarthanan Muthusamy
Muroran Institute of Technology
49 PUBLICATIONS **165** CITATIONS
SEE PROFILE

Some of the authors of this publication are also working on these related projects:



Multi drug resistant bacteria View project

All content following this page was uploaded by Govarthanan Muthusamy on 18 July 2016.

The user has requested enhancement of the downloaded file. All in-text references underlined in blue are added to the original document and are linked to publications on ResearchGate, letting you access and read them immediately.

Biocatalysis and Agricultural Biotechnology 7 (2016) 250–256

Contents lists available at ScienceDirect

Biocatalysis and Agricultural Biotechnology

journal homepage: www.elsevier.com/locate/bab

Enhanced production of amylase from *Bacillus* sp. using groundnut shell and cassava waste as a substrate under process optimization: Waste to wealth approach

Kandasamy Selvam [a,1], Thangasamy Selvankumar [b,1], Radhika Rajiniganth [b], Palanisamy Srinivasan [b], Chinnappan Sudhakar [b], Balakrishanan Senthilkumar [a,c], Muthusamy Govarthanan [b,d,*]

[a] Centre for Biotechnology, Muthayammal College of Arts and Science, Rasipuram, Namakkal 637408, Tamil Nadu, India
[b] PG and Research Department of Biotechnology, Mahendra Arts and Science College (Autonomous), Kalippatti, Namakkal 637501, Tamil Nadu, India
[c] Department of Medical Microbiology, College of Health and Medical Sciences, Haramaya University, P.O. Box 235, Harar, Ethiopia
[d] Department of Applied Sciences, College of Environmental Technology, Muroran Institute of Technology, 27-1 Mizumoto, Muroran, Hokkaido 050-8585, Japan

ARTICLE INFO

Article history:
Received 30 April 2016
Received in revised form
27 June 2016
Accepted 29 June 2016
Available online 30 June 2016

Keywords:
Amylase
Groundnut shell
Cassava waste
BBD

ABSTRACT

The consumption of bi-substrates (groundnut shell and cassava waste) in order to produce an amylase enzyme by *Bacillus* sp. using solid stated fermentation was carried out by applying Box-Behnken design (BBD). Initial pH, incubation time, concentrations of groundnut shell (GNS) and cassava waste (CW) variables were generated for each fermentation conditions of the *Bacillus* sp. to optimize the amylase production. Maximum yield of amylase (866 U/mL) was achieved by *Bacillus* sp. at the favorable conditions of the fermentation; 60 h, pH 7.0, 2 g/L GNS and 2 g/L CW. It was revealed that the combination of bi-substrates might be used in industries to produce high amount of value added amylase.

© 2016 Elsevier Ltd. All rights reserved.

1. Introduction

Amylases are a group of hydrolases that can specifically cleave the α-glycosidic linkage in starch. Two important groups of amylases are glucoamylase and α-amylase. Glucoamylase (glucan 1,4-α-glucosidase) produces single glucose units from non reducing ends of amylose and amylopectin (Anto et al., 2006), whereas, α-amylases (4-α-D-glucan glucanohydrolase) are extracellular enzymes that randomly cleave the 1,4- α-d-glucosidic linkage between adjacent glucose units inside the linear amylose chain (Pandey et al., 2005; Castro et al., 2010). Amylases are among the most important enzymes in the global market because of their potential applications in a number of industrial processes such as food, pharmaceuticals, cosmetics, textile and paper industries (Sahnoun et al., 2015). Although they can be derived from different sources, including microorganisms, plants and animals, microbial enzymes generally meet industrial demands (Pandey et al., 2005; Bozic et al., 2011). Amylase was excellently produced through microbial fermentation by *Bacillus* sp. (Benkiar et al., 2013; Anh et al., 2015).

Solid state fermentation (SSF) gained much interest during the past recent years and considered as an economical alternative for enzyme production and application (Pandey et al., 2002; Selvankumar et al., 2010; Govarthanan et al., 2014; Govarthanan et al., 2015). Response surface methodology (RSM) is a widely accepted statistical approach for modeling and analysis of problems, in which a response is influenced by several variables for the production of industrially important biomolecules and secondary metabolites (Govarthanan et al., 2014). BBD is a method applied in the optimization of medium constituents and other critical variables responsible for the production of biomolecules (Deepak et al., 2008; Selvam et al., 2014).

Agro-industrial residues are generally considered for the suitable substrates for the production of value-added products (Rosales et al., 2007; Selvankumar et al., 2011). Cassava (*Manihot esculenta*) is a root crop largely grown in tropical countries such as Asia. Because of its rich starch content, it is used for human consumption, animal feed and starch extraction. It has also contained the protein, lipid, lignocellulosic fibers and sugars (Teixeira et al., 2009). The cassava waste (CW) can be biotechnologically

* Corresponding author at: Department of Applied Sciences, College of Environmental Technology, Muroran Institute of Technology, 27-1 Mizumoto, Muroran, Hokkaido 050-8585, Japan.
E-mail address: gova.muthu@gmail.com (M. Govarthanan).
[1] The first two authors equally contributed to this work.

http://dx.doi.org/10.1016/j.bcab.2016.06.013
1878-8181/© 2016 Elsevier Ltd. All rights reserved.

converted into various value-added products to maximize the effective utilization (Pandey et al., 2000). Industrial development for the utilization of CW has been reviewed bioconversion of CW into protein, biomolecules, organic acids, and food compounds etc. (Soccol and Vandenberghe, 2003). Groundnut is a crop widely grown in tropics and subtropical region. It has high oil content. Groundnuts are the most important cereal in the world market because of its oily nature. It is used for human consumption, animal feed and mainly oil extraction. Groundnut shell (GNS) is an agro industrial waste involving in the production of various value-added products. So this bi-substrate combination contribute the synergistic effect should be useful technology for production of high quantity of amylase.

The aim of the present study is to investigate the enhanced production of amylase from *Bacillus* sp. BT MASC 1 under SSF using inexpensive and abundantly available GNS and CW bi-substrate combination.

2. Materials and methods

2.1. Isolation and screening of amylase producing bacterium

Soil samples were collected from sago industrial waste disposal site in Salem, Tamil Nadu, India. The serially diluted soil suspension (0.1 mL) was plated using the spread-plate technique onto starch agar (Hi-Media Pvt Ltd, Mumbai, India) composed of (g/L) peptone, 5.0; meat extract, 3.0; starch, 2.0; and agar, 20.0. The plates were incubated at 30 °C and observed the clear zone around the colonies after 24 h.

2.2. 16S rRNA amplification and phylogenetic analysis

Genomic DNA was extracted according to Sambrook and Russell (2001). The partial 16S rRNA gene was amplified using universal primers 27f (5′AGAGTTTGATCCTGGCTCAG3′) and 907r (5′ CCCCGTCAATTCATTTGAGTTT3′). The amplicon was purified (QIAGEN, CA, USA) and sequencing using ABI PRISM (Model 3700, CA, and USA). The sequences were compared using BLAST (NCBI) for the identification of the isolate. Phylogenetic analysis was performed using Neighbor-Joining method in CLC WORKBENCH 6 software (CLC bio, MA, USA).

2.3. Substrate pretreatment

GNS was procured from MPK oil mill at Mallasamudram (637503), Tamil Nadu, India and CW was collected from local sago industry located at Vennandur (637505), Tamil Nadu, India. The substrates (50 g) were soaked individually in 1% NaOH or 1% H_2SO_4, solution at the ratio of 1:10 (solid:liquid) for 2 h at room temperature (Kumar and Wyman, 2009; Irfan et al., 2011; Sindhu et al., 2011). Alkali and acid pretreated substrates were then washed with distilled water and neutralized to around pH 7 and base followed by drying.

2.4. Scanning electron microscopy of the pretreated substrate

Samples of untreated and treated GNS and CW were oven-dried at 50 °C for 1 h and thick layers were supported in the sample holder fixed on a carbon ribbon. This assembly was kept in vacuum-desiccators until the analysis. The SEM Jeol JSM 6390 model was used for observing the GNS and CW fibers in both treated and untreated samples.

2.5. Solid state fermentation

Five grams of the GNS and CW were put in Erlenmeyer flasks and moistened (60–70%) with ultrapure purified water. The contents were vigorously mixed, and the flasks were autoclaved at 121 °C for 15 min. After sterilization the flasks were cooled to 50 °C and inoculated with 3 mL of *Bacillus* sp. BT MASC 1 isolate carrying 10^8 cells/mL (0.8 OD at 600 nm) as a seed culture under aseptic condition. The contents of the flasks were well mixed and incubated at 36 ± 1 °C for 96 h.

2.6. Statistical optimization of amylase production

RSM coupled with Box-Behnken design (BBD) was established using Design Expert software (9.0.0.7 trial version). Four factors, namely, GNS, CW, pH and incubation time, were optimized for enhanced amylase production using the isolate *Bacillus* sp. BT MASC 1 under SSF. Based on BBD, the factors were analyzed at two levels: -1, for low level, and $+1$, for high level. A total of 29 runs was performed to optimize the process parameters, and experiments were carried out in accorder to the experimental design matrix. The results were assessed by applying the coefficient of determination (R^2), analysis of variance (ANOVA) and response plots. Employing RSM, the most widely used second-order polynomial equation developed to fit the experimental results and identify the relevant model terms

$$Y = ß_0 \Sigma ßiXi + \Sigma ßiXi ßij + \Sigma XiXj \quad (1)$$

where Y is the predicted response; ß0, ßi, and ßij are constant regression coefficients of the model; and Xi and Xj represent independent variables. The contour and 3D plot was used to understand the interaction of different factors and to predict optimum conditions for amylase production. The optimal values of the experimental conditions were obtained by solving the regression equation and analyzing the response surface plot.

2.7. Extraction of amylase

Amylase was extracted by mixing 50 mL of 0.1 M phosphate buffer (pH 7) with the whole solid substrate and shake on a rotary shaker at 250 rpm for 30 min. The buffer containing the enzyme was separated from the solid substrate through filter paper. The filtrate was centrifuged at 4000 rpm for 20 min. The clear brown supernatant was used as the enzyme source for the enzyme assay analysis.

2.8. Enzyme assay

Amylase activity was determined by the procedure of Bernfeld using soluble starch as a substrate (Bernfeld, 1955). The reaction mixture containing 200 µL of 1% substrate (soluble starch) (w/v) in 300 µL 0.1 M phosphate buffer (pH 7) and 150 µL of enzyme solution was incubated at 37 °C for 30 min. The reaction was stopped by adding 400 µL of 3,5-dinitrosalicylic (DNS) acid solution followed by heating in a boiling water bath for 5 min and cooling at room temperature. Then, distilled water was added until the solution volume was 12 mL. Absorbance of each solution was measured at 480 nm using a UV-Visible spectrophotometer. The initial reading was prepared by boiling the enzyme solution first in the hot water bath for 20 min to denature the enzyme protein structure.

2.9. Ammonium sulfate precipitation

Ammonium sulfate was added to the crude culture supernatant to 40% saturation at 4 °C and left over for 2 h. After that, the

precipitate was recovered by centrifugation at 10,000 rpm for 20 min at 4 °C and dissolved in a minimum volume of 50 mM phosphate buffer (pH 7.4) and dialyzed overnight against 10 mM phosphate buffer (Sundararajan et al., 2011).

2.10. Protein determination

Total protein concentration was determined by the method as described by Lowry et al. (1951). Bovine serum albumin was used as a standard.

2.11. Effect of pH on enzyme activity and stability

The optimum pH was determined by incubating the assay reaction mixture in buffers sodium acetate (pH 4 and 5), sodium phosphate (pH 6 and 7), Tris–HCl (pH 8 and 9), and glycine–NaOH (pH 10). To determine the stability of enzyme, the enzyme was pre-incubated in the same buffer systems utilized for enzyme activity for 60 min at 4 °C. The enzyme activity in the standard reaction mixture was taken as a control (Samie et al., 2012). The residual activity was assayed by standard DNS method.

2.12. Effect of temperature on enzyme activity and stability

The activity of enzyme at different temperature was determined by incubating the reaction mixture at a temperature ranging from 30 to 70 °C in 50 mM phosphate buffer pH 7. Thermal stability of enzyme was examined by incubating the enzyme at 30–70 °C in 50 mM phosphate buffer pH 7 for 60 min and followed by determining residual activity under standard assay conditions. The non-heated enzyme was considered as a control (Samie et al., 2012). The residual activity was assayed by standard DNS method.

2.13. Software and data analysis

The results of the experimental design were analyzed and interpreted using Design Expert Version 9.0.0.7 trail version (Stat-Ease Inc., USA) statistical software.

3. Results and discussion

3.1. Isolation, screening and identification of amylase producing bacteria

Soil collected from the CW disposal site was used for the isolation of amylase producing bacteria on starch agar medium. Totally five different isolates showed amylase activity upon primary screening using starch agar medium. Only one isolate showed high amylase activity. The potential isolate was identified by morphological and 16S rRNA sequencing. BLAST was performed for obtaining sequences in order to find out homology with the sequence in GenBank in which 100% similarity was found with *Bacillus cereus* strain ZK2 (GenBank:JQ773351.1). The sequence was deposited in the NCBI nucleotide sequence repository with accession number KJ438150.1. The phylogenetic tree based on the 16S rRNA sequence comparison indicating the position of strain *Bacillus* sp. BT MASC 1 (Fig. 1).

3.2. Characterization of pretreated substrates using SEM

Fig. 2 shows the untreated GNS (A), NaOH-treated GNS (B), Acid-treated GNS (C) and untreated CW (D), NaOH-treated CW (E), Acid-treated CW (F). It can be observed that the surface of the untreated GNS and CW has a layer of substances, mostly composed of fibers residue (Carta et al., 1999). From Fig. 2(B and E), the alkali NaOH-treatment eliminated most of the surface substances, which resulted a smoother morphological surface compare with control and acid treated substrates. It could be suggested that the detachment of fibers and other substances on the surfaces of substrates using NaOH pre-treatment might have better penetration of microbes and increase the utilization of the fibers nutrients by *Bacillus* sp. BT MASC 1, especially the carbon contents as a major source of the growth, thus yield higher production of amylase.

3.3. Optimization of amylase production by using BBD

The application of modern statistical models to optimize physicochemical components of the cultural conditions has been increased in the current industrial biotechnology, because of its universal applicability and suitability. The BBD was applied to identify the optimal conditions for the enhanced production of amylase enzyme. The experimental design is presented in Table 1. ANOVA of the quadratic regression model (Table 2) exhibits that it was a highly significant model, as was evident from the Fisher's *F*-test with a very high probability value (*F value* = 28.13). Values of 'Prob > F' (0.0001) indicate that the term of the model was significant. The Model F-value of 28.13 implies that the model was significant. There was only a 0.01% chance that a model F-value could occur due to noise. The predicted R^2 (0.8023) and adjusted R^2 (0.9314) values for amylase production were in reasonable agreement with the value of R^2 (0.8023), which is closer to 1.0, indicating the better fitness of the model in the experimental data.

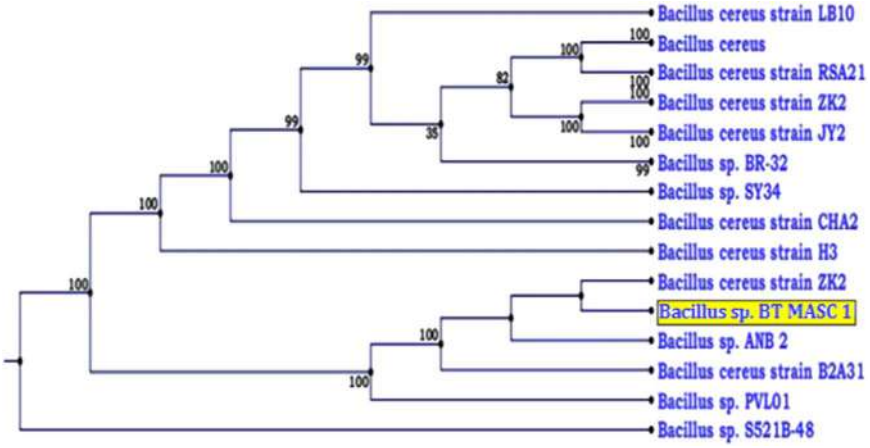


Fig. 1. 16S rRNA based phylogenetic analysis of *Bacillus* sp. BT MASC 1. Bootstrap values and scale bar depicting substitution rate per site are indicated. The phylogenetic tree constructed by the neighbor-joining method showing the position of isolate *Bacillus* sp. BT MASC 1.

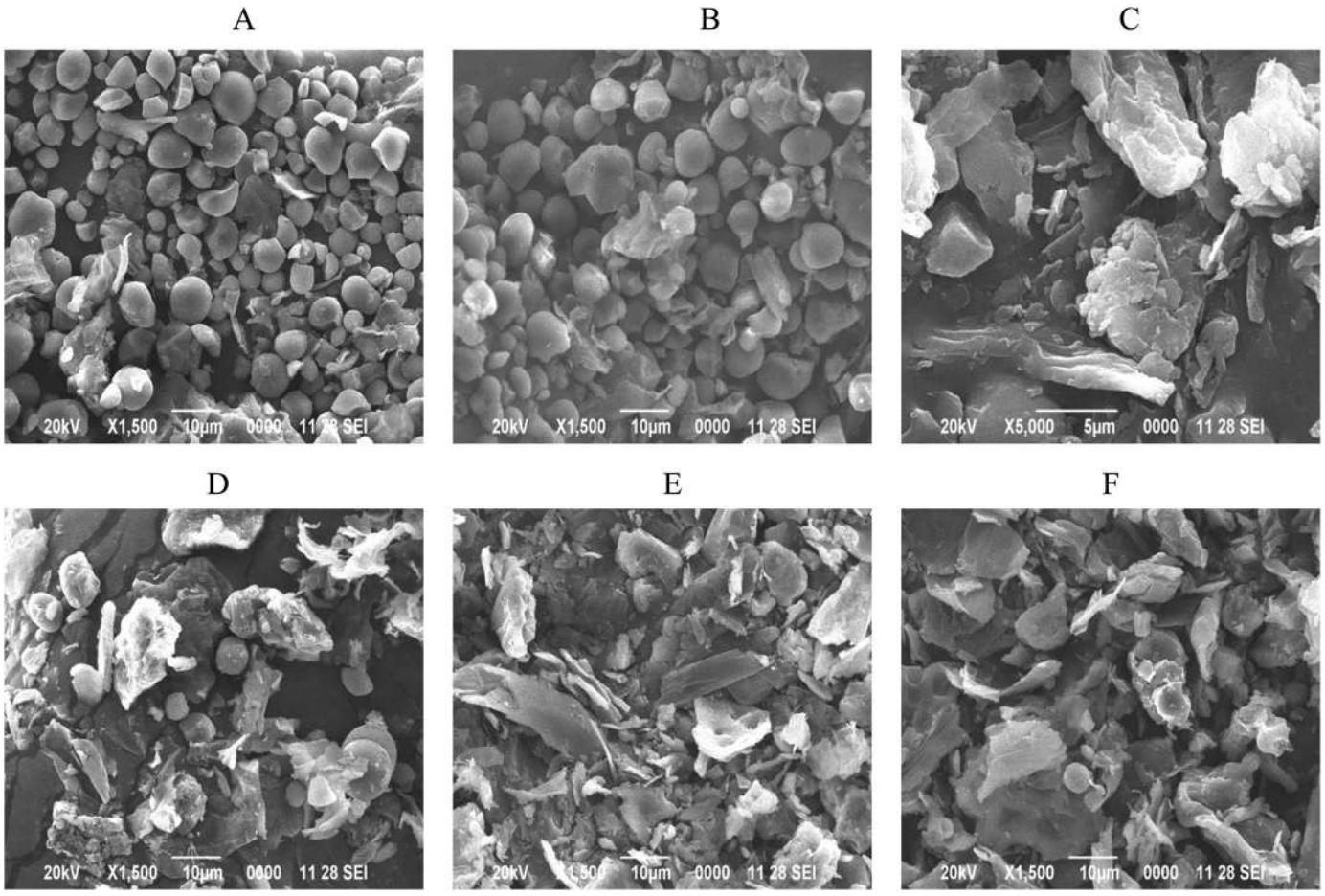


Fig. 2. Scanning Electron Microscopy (SEM) of the substrates (a) Untreated GNS (b) GNS pretreated with NaOH (c) GNS pretreated with H_2SO_4 (d) Untreated CW (e) CW pretreated with NaOH (F) CW pretreated with H_2SO_4.

Table 1
Box–Behnken design for the variables and the experimental observed responses.

Run	Groundnut shell (g)	Cassava waste (g)	pH	Incubation time (h)	Amylase activity U/mL
1	2	2	7	60	864
2	3	2	9	60	493
3	2	2	7	60	865
4	1	2	7	96	765
5	2	2	7	60	865
6	2	1	5	60	458
7	2	2	7	60	864
8	3	3	7	60	862
9	2	3	7	24	740
10	1	3	7	60	620
11	3	2	7	24	530
12	3	2	5	60	450
13	2	2	7	60	863
14	3	2	7	96	820
15	2	1	7	96	836
16	1	1	7	60	866
17	2	2	5	96	490
18	2	2	9	24	470
19	2	2	9	96	520
20	2	1	9	60	520
21	2	3	9	60	540
22	1	2	9	60	540
23	2	3	5	60	530
24	2	3	7	96	835
25	2	2	5	24	487
26	1	2	5	60	477
27	3	1	7	60	570
28	1	2	7	24	602
29	2	1	7	24	600

Table 2
Analysis of variance (ANOVA) for the response surface quadratic model.

Source	Sum of squares	df	Mean Square	F Value	p-value Prob > F
Model	7.222E+005	14	51,583.70	27.83	< ***0.0001***
A- Groundnut shell	1386.75	1	1386.75	0.75	0.4016
B- Cassava Waste	7154.08	1	7154.08	3.86	0.0696
C- pH	3040.08	1	3040.08	1.64	0.2211
D-Incubation Time	58,380.75	1	58,380.75	31.50	< 0.0001
AB	68,121.00	1	68,121.00	36.76	< 0.0001
AC	100.00	1	100.00	0.054	0.8197
AD	4032.25	1	4032.25	2.18	0.1623
BC	676.00	1	676.00	0.36	0.5555
BD	4970.25	1	4970.25	2.68	0.1238
CD	552.25	1	552.25	0.30	0.5937
A^2	56,423.81	1	56,423.81	30.45	< 0.0001
B^2	13,438.49	1	13,438.49	7.25	0.0175
C^2	5.598E+005	1	5.598E+005	302.06	< 0.0001
D^2	40,243.38	1	40,243.38	21.72	0.0004
Residual	25,944.97	14	1853.21	–	–
Lack of Fit	25,942.17	10	2594.22	3706.02	< ***0.0001***
Pure Error	2.80	4	0.70	–	–
Cor Total	7.481E+005	28	–	–	–

The model for amylase production by SSF, three different tests, namely, the sequential model sum of squares, lack of fit tests and model summary statistics were carried out in the present study.

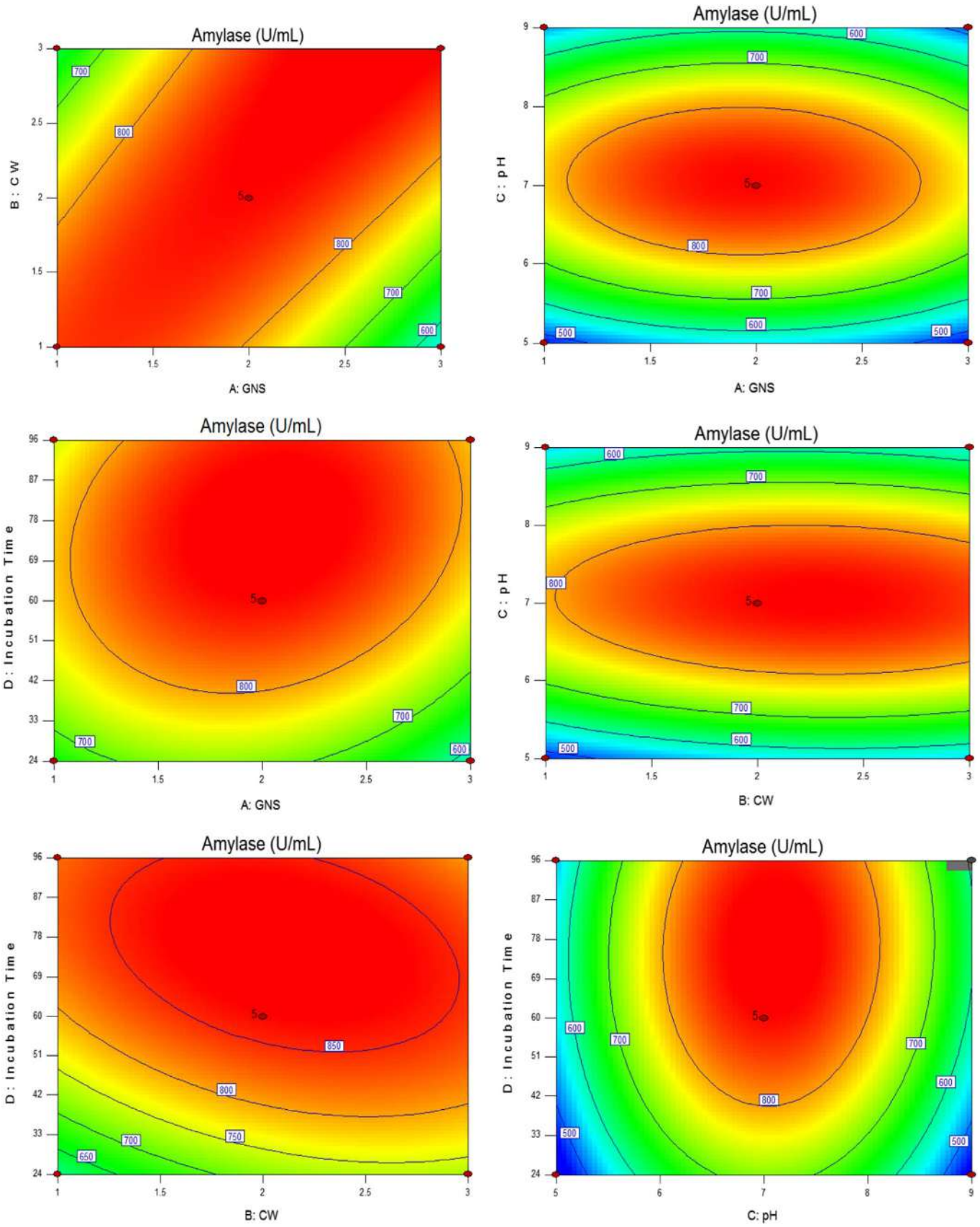


Fig. 3. Contour plots of the combined effects of two variables on amylase production by *Bacillus* sp. BT MASC 1.

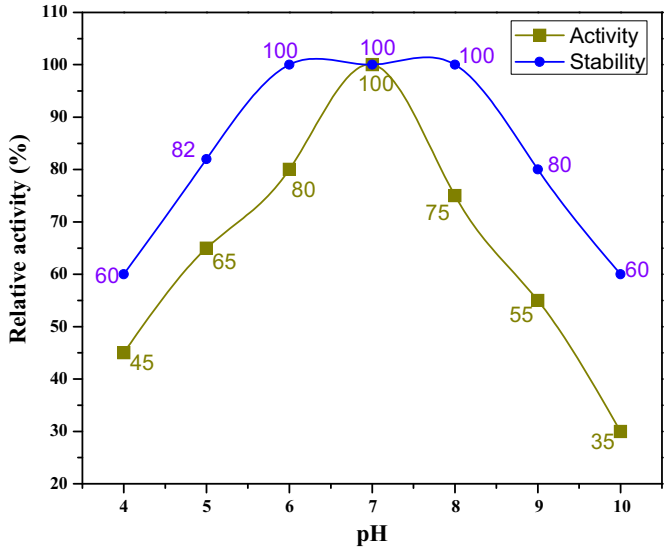


Fig. 4. Effect of temperature on activity of purified amylase of *Bacillus* sp. BT MASC 1.

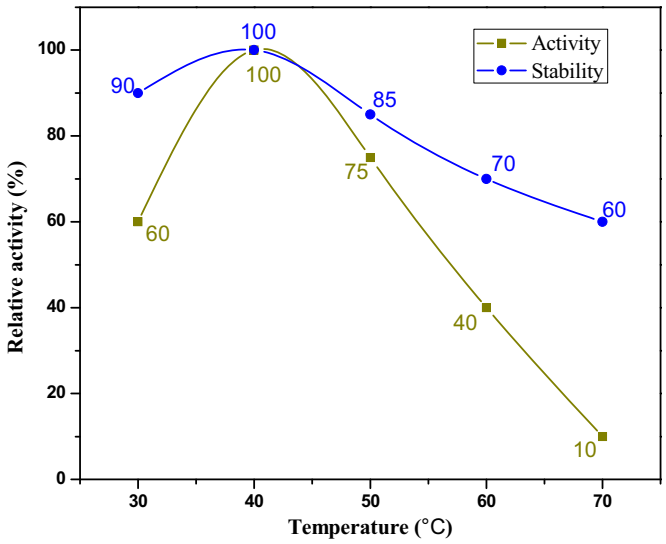


Fig. 5. Effect of pH on activity of purified amylase of *Bacillus* sp. BT MASC 1.

The contour and 3-D plots a graphical representation was generated (Fig. 3). The results demonstrate that there was a significant relation of GNS, CW, pH and incubation time for amylase production. The optimum levels of the variables were obtained by using BBD. The model predicted a maximum amylase activity of 866 U/mL appearing after 60 h cultivation with GNS 2.0 g/L, CW 2.0 g/L of substrates in pH 7. Bhange et al. (2016) reported that the amylase production was obtained from 4.61 to 27.9 U/mL by SSF using rape seed cake. However, our results showed high amount of amylase production with the presence bisubstrate combination. Predicted model was validated and experiments were conducted using these optimal conditions. The predicted model values were in good agreement with the values measured in these experiments, thus mitigating the validity of the response model and the necessity for optimal conditions. The graphs highlighted the roles played by the variables in the production of amylase.

The coefficients of the regression equation was calculated and the following regression equation was obtained.

$$Y = 863.40 - 12.08A + 23.08B + 16.17C + 70.00D + 134.50AB - 5.00AC + 31.75AD - 13.00BC - 35.25BD + 11.00CD - 91.41A^2 - 43.66B^2 - 294.28C^2 - 79.28D^2 \quad (2)$$

where Y stands for amylase activity, A is GNS, B is CW, C is pH, D is incubation time. A high degree of similarity of experimental values was observed, thus reflecting the precision and applicability of RSM to optimize the process for amylase production. Optimization of fermentation conditions for the production of amylase showed the progress the rate of production economics and it is also an attractive technology.

3.4. Effect of pH on enzyme activity and stability

The purified amylase enzyme was subjected to find the optimal activity conditions. The effect of the pH on the enzyme activity and stability was shown in Fig. 4. The optimal activity was observed at pH 7. The enzyme showed 60% of maximal activity between pH 6 and 8. The stability of the partially purified amylase exhibited at pH 6–8. Bhange et al. (2016) reported that the amylase enzyme stability level is maximum pH 6–10.

3.5. Effect of temperature on enzyme activity and stability

The effect of the temperature on enzyme activity was shown in Fig. 5. Although the enzyme was active at temperature range from 30 to 70 °C, the optimum temperature for enzyme activity was found to be at 40 °C. At least 10% of the activity were detectable at temperature between 30 and 70 °C. Thermal stability of enzyme determined at temperature range 30–70 °C. There were still up to 60% activity remaining after pre-incubation for 1 h in all samples.

4. Conclusions

In the present study, we have isolated *Bacillus* sp. BT MASC 1 from the CW disposal site and investigated the optimal media components for highest amylase production. Pretreatment of the substrate plays a pivotal role in enzyme production due to the increased accessibility of nutrients to the bacteria hindered by a thick hard layer of substrate. Optimization of process parameters is a prerequisite to enhance the yield, which is very helpful in large-scale production. Optimization of the fermentation conditions for the maximization of amylase production 866 U/mL was achieved at pH 7, after 60 h incubation with 2 g/L of GNS and 2 g/L of CW.

References

Anh, D.B.Q., Mi, N.T.T., Huy, D.N.A., Hung, P.V., 2015. Isolation and optimization of growth condition of *Bacillus* sp. from fermented shrimp paste for high fibrinolytic enzyme production. Arab. J. Sci. Eng. 40, 23–28.

Anto, H., Trivedi, U.B., Patel, K.C., 2006. Glucoamylase production by solid state fermentation using rice flake manufacturing waste products as substrate. Bioresour. Technol. 97 (10), 1161–1166.

Benkiar, A., Nadia, Z.J., Badis, A., Rebzani, F., Soraya, B.T., Rekik, H., Naili, B., Ferradji, F.Z., Bejar, S., Jaouadi, B., 2013. Biochemical and molecular characterization of a thermo and detergent-stable alkaline serine keratinolytic protease from *Bacillus circulans* strain DZ100 for detergent formulations and feather- biodegradation process. Int. Biodeterior. Biodegrad. 83, 129–138.

Bernfeld, P., 1955. Amylases, α and β. In: Methods in enzymology, Academic Press, New York.

Bhange, K., Chaturvedi, V., Bhatta, R., 2016. Simultaneous production of detergent stable keratinolytic protease, amylase and biosurfactant by *Bacillus subtilis* PF1 using agro industrial waste. Biotechnol. Rep. 10, 94–104.

Bozic, N., Ruiz, J., Lopez-Santin, J., Vujei, Z., 2011. Production and properties of the highly efficient raw starch digesting -amylase from a *Bacillus licheniformis* ATCC 9945a. Biochem. Eng. J. 53, 203–209.

Carta, F.S., Soccol, C.R., Ramos, L.P., Fontana, J.D., 1999. Production of fumaric acid by

fermentation of enzymatic hydrolysates derived from cassava bagasse. Bioresour. Technol. 68, 23–28.
Castro, A.M., Carvalho, D.F., Freire, D.M.G., Castilho, L.R., 2010. Economic analysis of the production of amylases and other hydrolases by *Aspergillus awamori* in solid state fermentation of babassucake. Enzym. Res. 1, 9.
Deepak, V., Kalishwaralal, K., Ramkumarpandian, S., Venkatesh Babu, S., Senthilkumar, S.R., Sangiliyandi, G., 2008. Optimization of media composition for nattokinase production by *Bacillus subtilis* using response surface methodology. Bioresour. Technol. 99, 8170–8174.
Govarthanan, M., Park, S.H., Kim, J.W., Lee, K.J., Cho, M., Kamala-Kannan, S., Oh, B.T., 2014. Statistical optimization of alkaline protease production from Brackish Environment *Bacillus* sp. SKK11 by SSF using horse gram husk. Prep. Biochem. Biotechnol. 44, 119–131.
Govarthanan, M., Selvankumar, T., Selvam, K., Sudhakar, C., Aroulmoji, Vincent, Kamala-Kannan, S., 2015. Response surface methodology based optimization of keratinase production from alkali-treated feather waste and horn waste using *Bacillus* sp. MG-MASC-BT. J. Ind. Eng. Chem. 27, 25–30.
Irfan, M., Gulsher, M., Abbas, S., Syed, Q., Nadeem, M., Baig, S., 2011. Effect of various pretreatment conditions on enzymatic saccharification. Songklanakarin J. Sci. Technol. 33 (4), 397–404.
Kumar, R., Wyman, C.E., 2009. Effects of cellulase and xylanase enzymes on the deconstruction of solids from pretreatment of poplar by leading technologies. Biotechnol. Prog. 25, 302–314.
Lowry, O.H., Rosebrough, N.J., Farr, A.L., Randall, R.J., 1951. Protein measurement with the Folin phenol reagent. J. Biol. Chem. 193, 265–275.
Pandey, A., Soccol, C.R., Mitchell, D.A., 2000. New developments in solid state fermentation: I-bioprocess and products. Process Biochem. 35, 1135–1169.
Pandey, A., Soccol, C.R., Nigam, P., Brand, D., Moha, R., Roussos, S., 2002. Biotechnological potential of coffee pulp and coffee husk for bioprocesses. Biochem. Eng. J. 6, 153–162.
Pandey, C., Webb, C.R., Soccol, C., 2005. Larroche, Enzyme Technology. Asiatech Publishers, Inc., New Delhi, p. 197.
Rosales, E., Couto, R.S., Sanroman, M.A., 2007. Increased laccase production by *Trametes hirsuta* grown on ground orange peelings. Enzym. Microb. Technol. 40, 1286.
Sahnoun, M., Kriaa, M., Elgharbi, F., Ayadi, D., Bejar, S., Kammoun, R., 2015. Aspergillus oryzae S2 α-amylase production under solid state fermentation: optimization of culture conditions. Int. J. Biol. Macromol. 75, 73–80.
Sambrook, J., Russell, D., 2001. Molecular Cloning: A Laboratory Manual, 3rd ed. Cold Spring Harbor Laboratory Press, Cold Spring Harbour, NY.
Samie, N., Noghabi, K.A., Gharegozloo, Z., Zahiri, H.S., Ahmadian, G., Sharafi, H., Behrozi, R., Vali, H., 2012. Psycrophilic α- amylase from *Aeromonas veronii* NS07 isolated from farm soil. Process Biochem., 1381–1387.
Selvam, K., Govarthanan, M., Kamala-Kannan, S., Govindharaju, M., Senthilkumar, B., Selvankumar, T., Sengottaiyan, A., 2014. Process optimization of cellulase production from alkali-treated coffee pulp and pineapple waste using *Acinetobacter* sp. TSK-MASC. RSC Adv. 4, 13045.
Selvankumar, T., Govarthanan, M., Govindaraju, M., 2010. Production of extracellular α-amylase enzyme by *Bacillus amyloliquefaciens* using coffee pulp waste as a substrate. Biotech. Ind. J. 4 (3), 156–159.
Selvankumar, T., Govarthanan1, M., Govindaraju, M., 2011. Endoglucanase production by *Bacillus amyloliquefaciens* using coffee pulp as substrate in solid state fermentation. Int. J. Pharma Bio Sci. 2 (3), 355–362.
Sindhu, R., Kuttiraja, M., Binod, P., Janu, K.U., Sukumaran, R.K., Pandey, A., 2011. Dilute acid pretreatment and enzymatic saccharification of sugarcane tops for bioethanol production. Bioresour. Technol. 102, 10915–10921.
Soccol, C.R., Vandenberghe, L.P.S., 2003. Overview of solid-state fermentation in Brazil. Biochem. Eng. J. 13, 205–219.
Sundararajan, S., Kannan, C.N., Chittibabu, S., 2011. Alkaline protease from *Bacillus cereus* VITSN04: potential application as a dehairing agent. J. Biosci. Bioeng. 111, 128–133.
Teixeira, E.M., Pasquini, D., Curvelo, A.A.S., Corradini, E., Belgacem, M.N., Dufresne, A., 2009. Cassava bagasse cellulose nanofibrils reinforced thermoplastic cassava starch. Carbohydr. Polym. 78, 422–431.

View publication stats

Springer Link Search Log in

Download PDF

Original Research | Open Access |
Published: 11 November 2015

Synthesis and characterization of *Solanum nigrum*-mediated silver nanoparticles and its protective effect on alloxan-induced diabetic rats

Arumugam Sengottaiyan, Adithan Aravinthan, Chinnapan Sudhakar, Kandasamy Selvam, Palanisamy Srinivasan, Muthusamy Govarthanan, Koildhasan Manoharan & Thangaswamy Selvankumar

Journal of Nanostructure in Chemistry **6**, 41–48 (2016)

3876 Accesses | **43** Citations | Metrics

Abstract

Solanum nigrum, a medicinal plant, traditionally used in treating diabetes mellitus. In this study, we used the leaf extract of the plant to synthesize silver nanoparticles (AgNPs), as a proposition to treat alloxan-induced diabetic rats. The phytosynthesised AgNPs were analyzed using UV–visible and Fourier transform infra-red spectroscopy for their functional groups. Transmission electron microscopy revealed that, the synthesized particles are found to be 4–25 nm in size. Monodispersed and spherical nature of synthesized AgNPs were shown by scanning electron

P.G.P. COLLEGE OF ARTS & SCIENCE NAMAKKAL 637 206

PRINCIPAL
PGP College of Arts and Science
Namakkal

J Nanostruct Chem (2016) 6:41–48
DOI 10.1007/s40097-015-0178-6

ORIGINAL RESEARCH

Synthesis and characterization of *Solanum nigrum*-mediated silver nanoparticles and its protective effect on alloxan-induced diabetic rats

Arumugam Sengottaiyan[1] · Adithan Aravinthan[2] · Chinnapan Sudhakar[1] · Kandasamy Selvam[1] · Palanisamy Srinivasan[1] · Muthusamy Govarthanan[1,3] · Koildhasan Manoharan[4] · Thangaswamy Selvankumar[1]

Received: 2 August 2015 / Accepted: 26 September 2015 / Published online: 11 November 2015
© The Author(s) 2015. This article is published with open access at Springerlink.com

Abstract *Solanum nigrum*, a medicinal plant, traditionally used in treating diabetes mellitus. In this study, we used the leaf extract of the plant to synthesize silver nanoparticles (AgNPs), as a proposition to treat alloxan-induced diabetic rats. The phytosynthesised AgNPs were analyzed using UV–visible and Fourier transform infra-red spectroscopy for their functional groups. Transmission electron microscopy revealed that, the synthesized particles are found to be 4–25 nm in size. Monodispersed and spherical nature of synthesized AgNPs were shown by scanning electron microscope and the presence of Ag in the AgNPs was confirmed by energy dispersive spectrum. The phytosynthesised AgNPs were evaluated for its antidiabetic activity in alloxan-induced diabetic rats. AgNPs-treated diabetic rats found to be significantly improved the dyslipidemic condition as seen in the diabetic control. Furthermore, it also reduced the blood glucose level over the period of treatment. The improvement in body weight was also found to be evidence for *S. nigrum* extract-mediated AgNPs as a potential antidiabetic agent against alloxan-induced diabetic rats.

Keywords Diabetes mellitus · *Solanum nigrum* · Silver nanoparticles · Alloxan · Animal model

✉ Arumugam Sengottaiyan
sengottaibiotech@rediffmail.com

✉ Muthusamy Govarthanan
gova.muthu@gmail.com

✉ Thangaswamy Selvankumar
t_selvankumar@yahoo.com

[1] Department of Biotechnology, Mahendra Arts and Science College (Autonomous), Kalippatti, Namakkal, Tamil Nadu 637501, India

[2] College of Veterinary Medicine, Biosafety Research Institute, Chonbuk National University, Iksan 570-752, South Korea

[3] Division of Biotechnology, Advanced Institute of Environment and Bioscience, College of Environmental and Bioresource Sciences, Chonbuk National University, Iksan 570-752, South Korea

[4] Raja Duraisingam Government Arts and Science College, Sivagangai, Tamil Nadu, India

Introduction

Diabetes mellitus (DM) is a group of syndromes characterized by hyperglycemia; altered metabolism of lipids, carbohydrates, and proteins; and an increased risk of complications from vascular disease that affects 10 % of the population [1, 2]. Despite, the availability and extensive utilization of hypoglycemic agents, diabetes and the related complications continue to be major health concerned worldwide [3]. According to International Diabetic Federation the estimated diabetes prevalence in 2010 has risen to 285 million, representing 6.4 % of the world's adult population, with a prediction that by 2030, the number of people with diabetes will have risen to 438 million, with this alarming concern, India has been declared as the "Diabetic capital of world". Currently 40.9 million people in India suffering from diabetes and by 2030 there would be 79.44 million diabetics in India alone. It is also estimated that by the year 2030, diabetes is likely to be the seventh leading cause of death, accounting 3.3 % of total deaths in the world [4].

Owing to the progressive nature of the disease, an improved treatment strategy is required, which includes, the discovery of new drugs [5]. In addition, drug treatment, is not completely successful with diabetes and there is a compelling need for better prevention and treatment

strategies [6]. Nevertheless, traditionally people have been using many plants to treat diabetes empirically despite the lack of safety and efficacy [7]. At this juncture, it is necessary to test the herbal medicine as an alternative to synthetic agent [8].

In the search of new opportunities for treatment of DM, the current study has focused on the efficacy of *S. nigrum.* The plants belong to the Solanaceae family, are considered as poisonous to human, however, *S. nigrum* is an edible plant and possesses antioxidant and hepatoprotective activity [9]. Furthermore, many parts of this plant are used as a traditional medicine. Despite, it has been used as an antidiabetic agent in traditional medicine, it lacks scientific evidence [10]. In addition, this is the first of its kind reporting the efficiency of *S. nigrum*-mediated AgNPS as an anti-hyperglycemic agent.

Since, the last decade the applications of AgNPs have been increasing rapidly in various fields. Originally, the silver metal was used as an anti-microbial agent, later in the 1990's it has been used in the medicinal field as silver colloids to treat various diseases [11]. AgNPs are usually a cluster of particles ranging between 1 and 100 nm in size and they exhibit new properties based on their size, distribution and morphology [12]. Nanoparticles are becoming the focus of intensive research, due to their wide range of applications in areas such as catalysis, optics, antimicrobials, and biomaterial production [13, 14].

Various approaches have been used for the synthesis of AgNPs. The phytosynthesis approach has many advantages over chemical, physical, and microbial synthesis [15–18], as there is no need of the elaborated process of culturing and maintaining the cell, hazardous chemicals and high-energy requirements.

In the present study, we have characterized the *S. nigrum* leaf extract-mediated AgNPs and assessed it, as an antidiabetic agent in alloxan-induced diabetic rat model.

Materials and methods

Collection of plants

The *S. nigrum* plant material was collected from Erode District, Tamil Nadu, India and authenticated by Dr. S. ArunPrakash, Department of Botany, Government Arts College, Namakkal, Tamil Nadu, India.

Preparation of aqueous extract

The leaves of the plants collected were washed and air dried in shade at room temperature for 7 days. The air dried plants were pulverized in an electric grinder and sieved using mesh to obtain uniform size for further study. The extraction process was carried out with the help of Soxhlet apparatus. Fifteen grams of dry powder were subjected to soxhlet extraction with 300 mL methanol, the extraction was repeated up to 10 cycles at 45 °C to ensure the complete recovery.

Synthesis of AgNPs

AgNPs synthesis was carried out according to Aravinthan et al. [19]. Briefly, 4 mL of the aqueous extract was mixed with 96 mL of 1 mM $AgNO_3$ solution and the resulting greenish white mixture was incubated for 8 h in a rotary shaker (200 rpm) at 26 °C. Reduction of Ag^+ ions to Ag nanocrystals was monitored by a change in color of the reaction mixture from greenish white to dark brown [19].

Characterization of AgNPs

Surface Plasmon resonance (SPR) bands of the synthesized AgNPs were characterized using UV–Vis spectroscopy (Shimadzu UV-2450) in the range of 200–600 nm. Morphological analysis and the crystalline nature of the particles were investigated by transmission electron microscopy (TEM) using FEI Tecnai TF 20 high-resolution TEM instrument operated at an accelerating voltage of 200 kV [20]. The characterization of the synthesized AgNPs was conducted with X-ray diffractometer (XPERT-Pro diffractometer using Cu K_α radiation), operated at 2θ from 30 to 80° at 0.041°/min with a time constant of 2 s. AgNPs synthesis and the elemental composition were further confirmed by SEM–EDS (SEM–EDS; JEOL-64000, Japan). The chemical characterization of changes in the surface and surface composition was performed by Fourier transform infrared spectroscopy (Shimadzu) within the mid IR region of frequency 4000–400 cm^{-1} [19].

Induction of diabetes

Diabetes was induced in male Wistar albino rats aged more than 8 weeks (140–160 g body weight) by single intraperitoneal administration of alloxan (single dose of 200 mg/kg body weight). Within 48 h after alloxan administration, blood glucose concentrations were measured via tail clip sampling. Animals with a blood glucose concentration 200 mg/dL were considered to be diabetic [21].

Toxicity assessment in rat

Acute toxicity test on AgNPs was performed in experimental rats with a graded dose levels of AgNPs (10 and 20 mg/kg body weight) [22]. The rats were observed continuously for 2 h for behavioral, neurological and

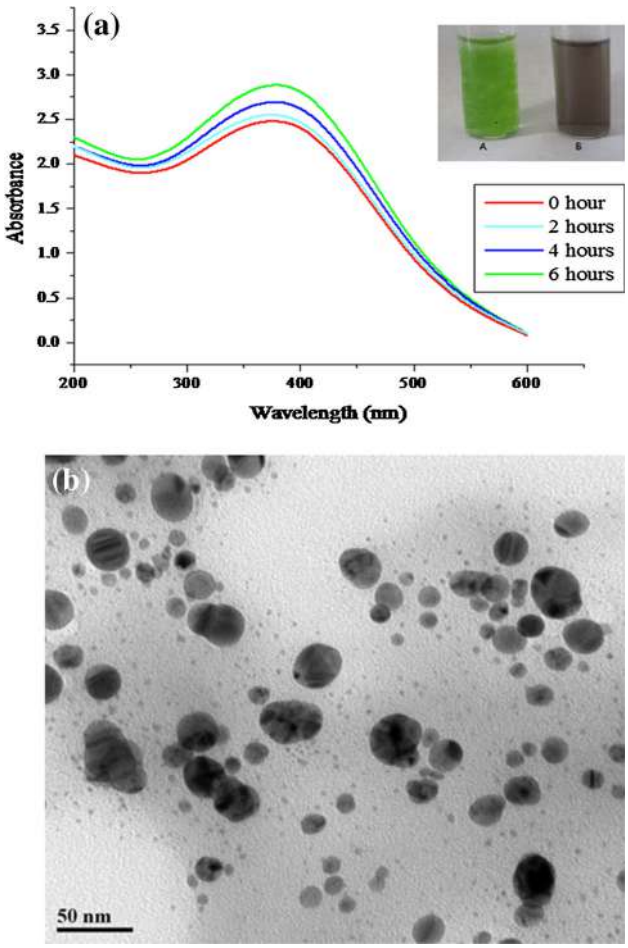


Fig. 1 **a** UV–visible spectrum of green synthesized AgNPs at different time intervals, showed peak at 420 nm. **b** TEM image of AgNPs

autonomic profiles and after a period of 24 and 72 h for any lethality or death. Further experiments were carried out using 10 mg/kg body weight AgNPs.

Experimental design

The animals were divided into five groups and each group consisted of 5 rats. Group I: Untreated normal rats; (Normal control, received only distilled water) Group II: Diabetic control, alloxan 200 mg/kg single dose, received no treatment; Group III: Diabetic rats, received glibenclamide 0.5 mg/kg for 21 days; Group IV: Diabetic rats, received *S. nigrum* Methanol extract 10 mg/kg for 21 days; Group V: Diabetic rats, received phytosynthesised AgNPs 10 mg/kg for 21 days.

Oral glucose tolerance test

The oral glucose tolerance test was performed after 21 days administration of AgNPs and plant extract to the respective groups. The rats were fasted overnight, and 2 g/kg glucose was administered orally and the blood was collected from the tail vein prior and the post administration of glucose at 0,30,60,90, and 120 min and fasting blood glucose level was measured using a glucometer (Accu-Chek, Roche Diagnostic, Manheim, Germany).

Biochemical analysis

Blood samples were collected by retro orbital puncture and centrifuged at $1000\times g$ for 15 min and the collected serum was stored at -80 °C until analysis. Total cholesterol and Triglycerides were estimated using (Biovision, Milpitas, CA, USA) kit as manufacture's instruction.

Statistical analysis

All the data were expressed as mean ± SD, and the statistical significance between the groups was analyzed using one-way ANOVA followed by Tukey's post hoc test. If $P \leq 0.05$ were considered significant.

Results and discussion

Synthesis and characterization of AgNPs

The *S. nigrum* leaf extract was mixed in the aqueous solution of the silver ion complex, and became yellowish brown due to the reduction of silver ion, indicating the completion of the reaction. Similar changes in color have also been reported earlier [23, 24]. The AgNps exhibit yellowish brown color in aqueous solution owing to excitation of surface plasmon vibrations in AgNPs [25, 26]. The plant leaf extract known to posses many active compounds such as, sugar [27] caffeine and theophylline [28] and antioxidants [29] are reported to involve in the formation of AgNPs. As *S. nigrum* also contains high antioxidants, we speculate this AgNPs formation due to the presence of high amount of antioxidants in the extract [9]. The Fig. 1a represents the absorbance spectrum of AgNPs formed at various times (0, 2, 4, 6 h) and the maximum absorption peak was observed in the range of 370–420 nm. It is reported that the absorption spectrum of spherical AgNPs present at 420 nm, and maximum absorption peak shift towards the blue region directly correlates with smaller particle size, and providing the clue for the size of the synthesized nanoparticle in the range of ≤25 nm [30]. Figure 1b shows a representative TEM image of phytosynthesized AgNPs. The AgNPs were seen to be spherical and monodispersed with the size range of 4–25 nm. This result is well agreed with the UV–Vis spectra result, in which the maximum peak shifts towards the blue region (λ

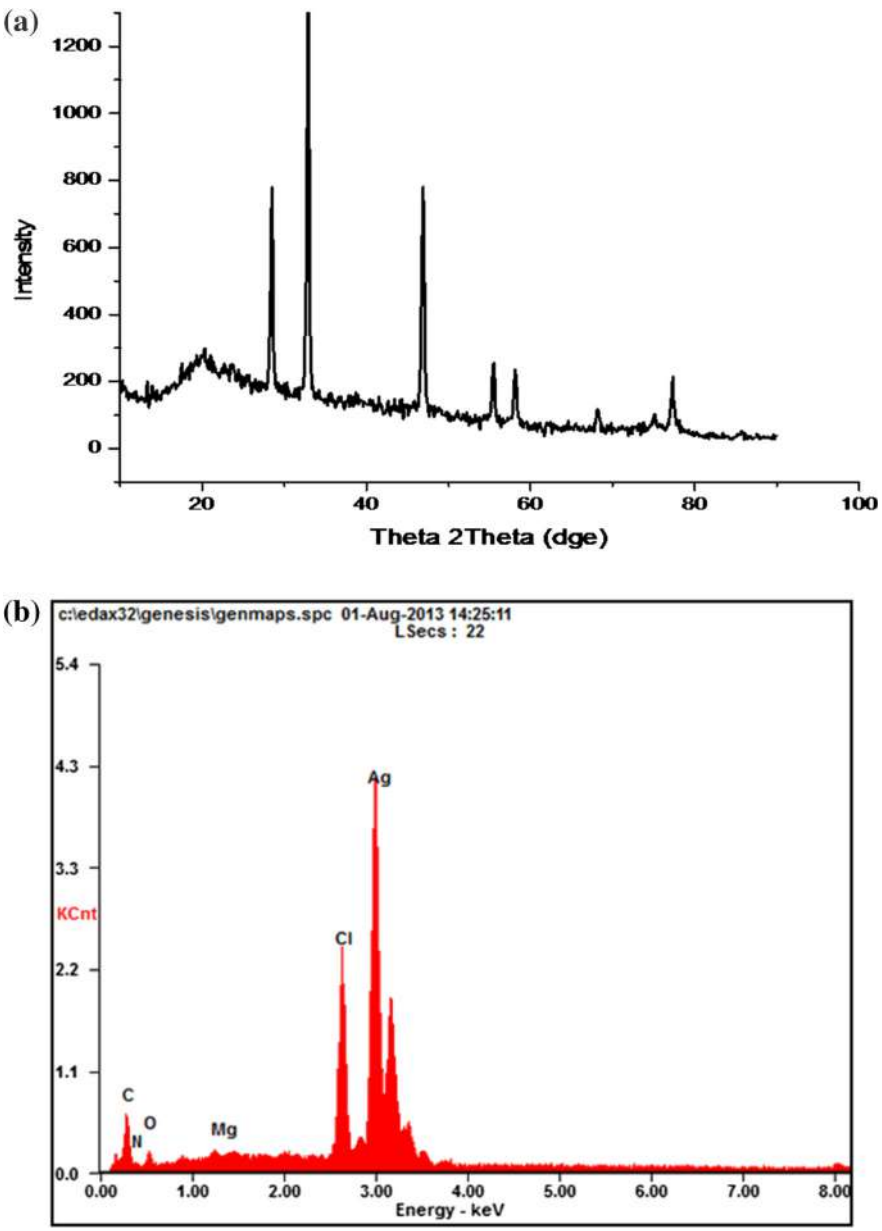


Fig. 2 **a** X-ray diffraction for crystalline nature of *S. nigrum* leaf extract-mediated silver nanoparticles. **b** SEM EDX spectrum of AgNPs, after formation of AgNPs with different X-ray emission peaks labeled

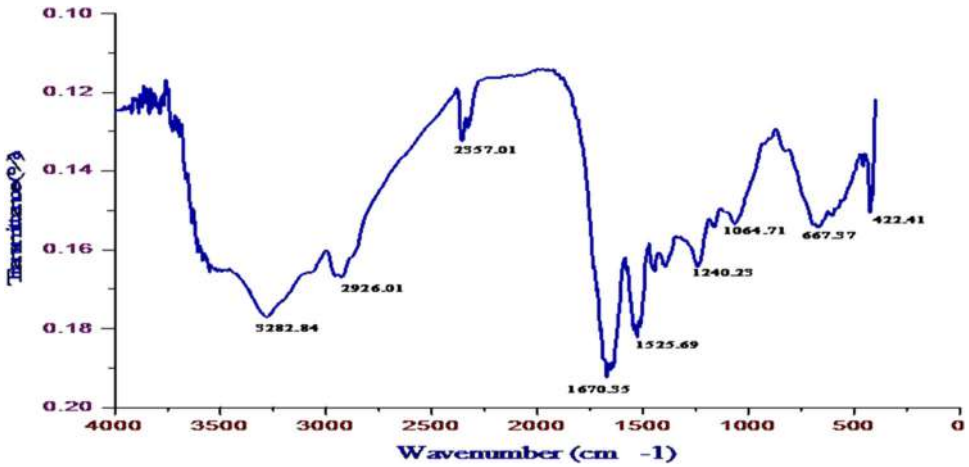


Fig. 3 FTIR spectrum of phytosynthesized AgNPs

max at 420 nm), and providing the direct evidence for size [30].

The crystalline nature of the silver nanoparticles of *S. nigrum*, the XRD analysis was undertaken, Fig. 2a revealing six peaks at degree (2θ) 10.00, 11.51, 12.00, 27.75, 32.15, and 45.94 corresponding to six diffraction facets of silver. The broadening of X-ray peaks observed can be attributed to the organic content of leaf extract. Analysis of AgNPs through Energy dispersive X-ray (EDX) spectrometers confirmed the presence of elemental silver signal at 3 keV along (Fig. 2b) with other weak signals corresponding to oxygen and carbon, which could have essentially derived from the plant extract and consistent with previous studies [31, 32]. FTIR measurement was carried out to identify the possible biomolecules in *S. nigrum* leaf extract responsible for capping leading to efficient stabilization of the silver nanoparticles (Fig. 3). The IR spectrum of silver nanoparticles manifests prominent absorption bands located at 3282, 2926, 2357, 1670, 1523, 1240, 1064, 667, and 422.41 cm^{-1}. The bands seen

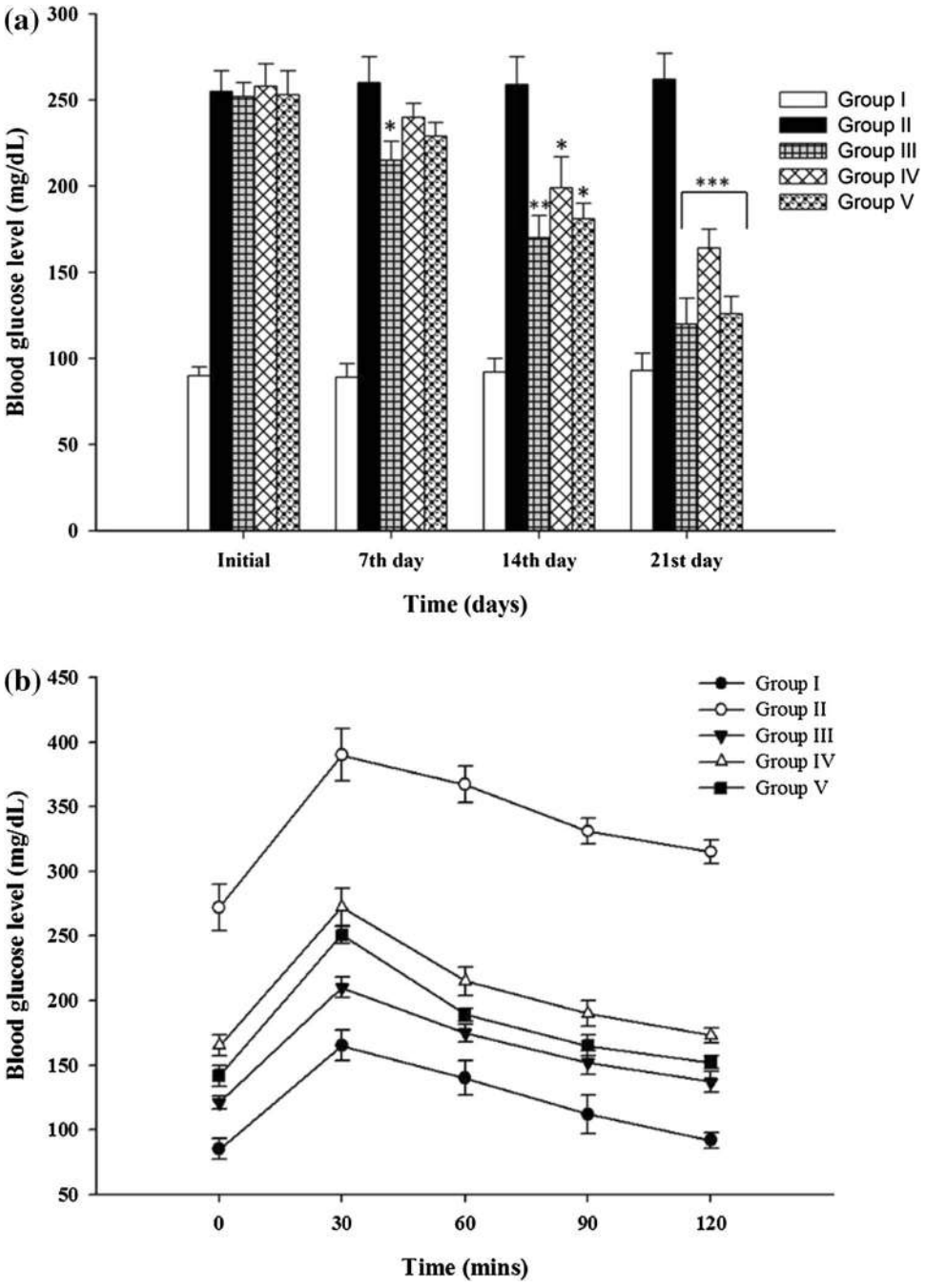


Fig. 4 **a** Effect of oral administration of *S. nigrum* leaf extract and AgNPs at a dose of 10 mg/kg, in Blood glucose level of alloxan-induced diabetic rats before and after treatment. *Each column* represents mean ± SD for five rats. $*P < 0.05$; $**P < 0.01$; $***P < 0.001$ different from diabetic control. **b** Effect of *S. nigrum* leaf extract and AgNPs in oral glucose tolerance test after 21 days of treatment. *Each column* represents mean ± SD ($n = 5$). All the values were found to be statistically significant compared to diabetic control at $*P < 0.05$

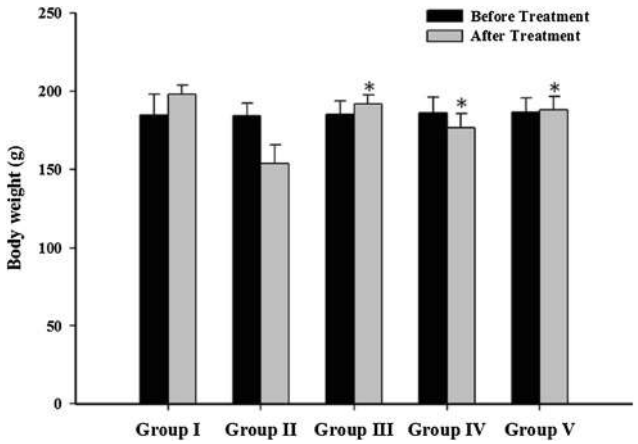


Fig. 5 Effect of methanolic extract of *S. nigrum* and AgNPs on body weight before and after treatment. *Each column* represents mean ± SD ($n = 5$). All the values were found to be significant when compared to diabetic control at $^{*}P < 0.05$

in 3282 and 2926 cm^{-1} represent the stretching vibrations of primary and secondary amines, respectively. The peak at 2357 could be attributed to H bonded OH stretching of a secondary metabolites present in the extract which might act as a reducing agent to synthesize AgNPs [33].

The antidiabetic activity of phytosynthesized AgNPs

An acute toxicity study revealed the non-toxic nature of the methanolic extract and green synthesized AgNPs. The rats treated with different doses of *S. nigrum* did not show any drug-induced physical signs of toxicity during the whole experimental period, and no deaths were observed. Based on the acute toxicity studies, with a varying concentration (10, 20 mg/kg) of AgNPs, 10 mg/kg body weight was fixed as an optimal concentration, and thus used in the treatment of alloxan-induced diabetic rats.

The blood glucose level of each group has been estimated during the course of treatment (Fig. 4a), to evaluate anti-hyperglycemic effect of plant extract and phytosynthesized AgNPs. At 14 and 21 days the treated groups (extract/AgNPs) pronouncedly decrease the blood glucose level compared to that of diabetic control (Group II). AgNPs were shown to have reduced blood glucose level higher than plant extract alone. On the other hand glibenclamide-treated groups significantly reduced the blood glucose level throughout the period of treatment compared to group II, IV and V.

The glucose tolerance level of *S. nigrum* leaf extract-mediated AgNPs-treated group was evaluated in diabetic rats (Fig. 4b), by estimating its efficacy in reducing hyperglycemic condition in blood followed an administration of glucose orally, and compared it with standard drug (Glibenclamide 0.5 mg/kg). The phytosynthesized AgNPs-treated animals shown to have a significant improvement in lowering blood glucose compared to Group II. Among the treated groups the efficiency of compounds in lowering the blood glucose level over a period of 2 h has followed with an order, group III > group V > group IV. Phytosynthesized AgNPs treatment is shown to improve the blood glucose level which is comparable to glibenclamide-treated groups. Alloxan-induced diabetic rat model has been widely used in several studies [34, 35]. In addition, the mode of action of alloxan is well documented [36]. In the treatment of diabetes, blood glucose concentration is considered as a routine and major biochemical marker to monitor the improvement in the disease condition, the results obtained for blood glucose concentration of treated groups showed a smaller total area

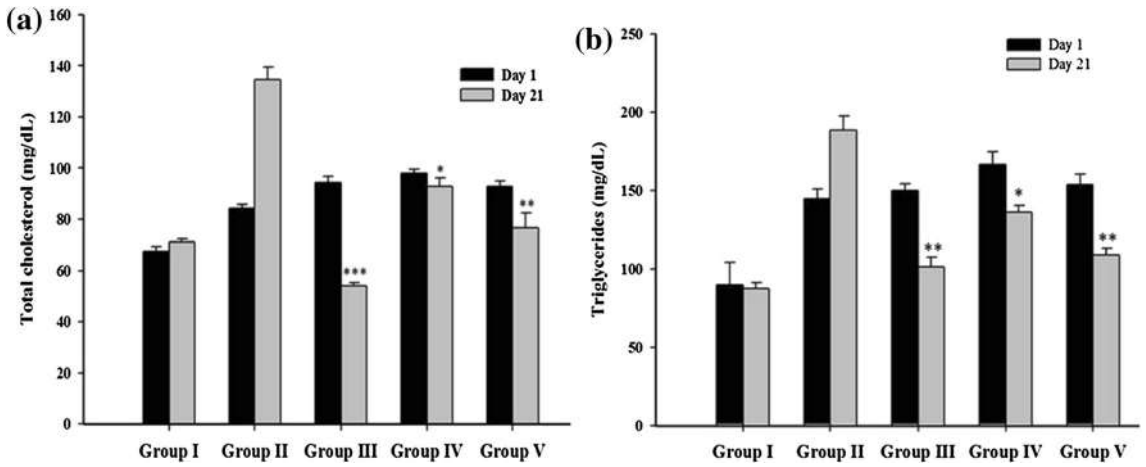


Fig. 6 **a** Effect of oral administration of methanolic extract of *S. nigrum* and AgNPs on serum cholesterol. **b** Triglycerides level before and after treatment. All the values were found to be significant with diabetic control at $^{*}P < 0.05$; $^{**}P < 0.01$; $^{***}P < 0.001$

under the curve which is significantly lesser than the diabetic control group, and these findings are in accordance with previous research [36]. Figure 5 demonstrates the level of changes in body weight of experimental rats at before and after treatment. Weight loss is one of the major syndrome associated with diabetes, probably due to muscle wasting [37]. In our study the diabetic-induced rat group (Group II) showed significant weight loss (Fig. 5) Compared to group I (Normal control). The total cholesterol (TC) and triglycerides (TG) levels were also elevated in diabetic rats (Fig. 6a, b). It is well documented that DM tends to reduce body weight as a result of increased muscle wasting, dehydration, and fat catabolism. Whereas, the treatment with plant extract as well as phytosynthesized AgNPs significantly improved the body weight loss. The TC and TG levels were retrieved comparable to normal group over a period of 21 days administration of AgNPs, the mechanism of preventing the muscle loss could probably attribute to reversal of antagonism [38].

Conclusion

In this present study, AgNPs were rapidly synthesized using aqueous leaf extract of *S. nigrum* as a bio-reductant. The efficacy of phytosynthesized AgNPs as an anti-hyperlipidemic agent has been evaluated. This study revealed that the AgNPs are found to be safe and environmentally friendly, hence, these AgNPs can be considered in treating diabetes associated syndrome.

Open Access This article is distributed under the terms of the Creative Commons Attribution 4.0 International License (http://creativecommons.org/licenses/by/4.0/), which permits unrestricted use, distribution, and reproduction in any medium, provided you give appropriate credit to the original author(s) and the source, provide a link to the Creative Commons license, and indicate if changes were made.

References

1. Alvin, C.P., David Allesio, D.D.: Endocrine pancreas and pharmacotherapy of diabetes mellitus and hypoglycaemia. In: Brunton, L., Chabner, B., Knollman, B. (eds.) Goodman and Gilman's the Pharmacological Basis of Therapeutics, 12th edn, p. 1237. McGraw-Hill, New York (2011)
2. Foster, D.W.: Diabetes Mellitus Harrison's Principles of Internal Medicine, pp. 1979–1981. McGraw Hill, USA (1994)
3. El-Amrani, F., Rhallab, A., Alaoui, T., El-Badaoui, K., Chaki, S.: Hypoglycaemic effect of *Thymelaea hirsuta* in normal and streptozotocin-induced diabetic rats. J. Med. Plants Res. **3**(9), 625–629 (2009)
4. Singh, U., Kochhar, A., Singh, S.: Blood glucose lowering potential of some herbal plants. J. Med. Plants Res. **5**(19), 4691–4695 (2011)
5. Modi, P.: Diabetes beyond insulin: review of new drugs for treatment of diabetes mellitus. Curr. Drug Discov. Technol. **4**, 39–47 (2007)
6. Baynes, J.W., Thorpe, S.R.: The role of oxidative stress in diabetic complications. Endocrinol. J. **3**, 277–284 (1996)
7. Alarcon-Aguilara, F.J., Roman-Ramos, R., Perez-Gutierrez, S., Aguilar-Contreras, A., Contreras-Webar, C.C., Felores-Saenz, J.L.: Study of the anti-hyperglycemic effect of plants used as antidiabetics. J. Ethnopharmacol. **61**, 101–110 (1998)
8. Grover, J.K., Yadav, S., Vats, V.: Medicinal plants of India with antidiabetic potential. J. Ethanopharmacol. **81**, 81–100 (2002)
9. Jain, R., Sharma, A., Gupta, S., Sarethy, I.P., Gabrani, R.: *Solanum nigrum*: current perspectives on therapeutic properties. Altern. Med. Rev. **6**, 78–85 (2011)
10. Sohrabipour, S., Kharazmi, F., Soltani, N., Kamalinejad, M.: Effect of the administration of *Solanum nigrum* fruit on blood glucose, lipid profiles, and sensitivity of the vascular mesenteric bed to phenylephrine in streptozotocin-induced diabetic rats. Med. Sci. Monit. Basic Res. **19**, 133–140 (2013)
11. Kenneth, K.Y., Liu, X.: Silver nanoparticles—the real "silver bulltet" in clinical medicine? Med. Chem. Comm. **1**, 125–131 (2010)
12. Satyavani, K., Gurudeeban, S., Ramanathan, T., Balasubramanian, T.: Biomedical potential of silver nanoparticles synthesized from calli cells of *Citrullus colocynthis* (L.). Schrad. J. Nanobiotechnol. **9**, 43 (2011)
13. Kalimuthu, K., Babu, R.S., Venkataraman, D., Bilal, M., Gurunathan, S.: Biosynthesis of silver nanocrystals by *Bacillus licheniformis*. Colloid Surf. B. **65**, 150–153 (2008)
14. Smitha, S.L., Nissamudeen, K.M., Philip, D., Gopchandran, K.G.: Studies on surface plasmon resonance and photoluminescence of silver nanoparticles. Spectrochim. Acta Mol. Biomol. Spectros. **71**, 186–190 (2008)
15. Liu, Y.C., Lin, L.H.: New pathway for the synthesis of ultrafine silver nanoparticles from bulk silver substrates in aqueous solution by sonoelectrochemical methods. Electrochem. Commun. **6**, 78–86 (2004)
16. Bae, C.H., Nam, S.H., Park, S.M.: Formation of silver nanoparticles by laser ablation of a silver target in NaCl solution. Appl. Surf. Sci. **197**, 628–634 (2002)
17. Basavaraja, S., Balaji, D.F., Lagashetty, A., Rajasab, A.H., Venkataraman, A.: Extracellular biosynthesis of silver nanoparticles using the fungus *Fusarium semitectum*. Mater. Res. Bull. **43**, 1164–1170 (2008)
18. Jha, A.K., Prasad, K.: Green synthesis of silver nanoparticles using Cycas leaf. Int. J. Green Nanotechnol.: Phys. Chem. **1**, 110–117 (2010)
19. Aravinthan, A., Govarthanan, M., Selvam, K., et al.: Sunroot mediated synthesis and characterization of silver nanoparticles and evaluation of its antibacterial and rat splenocyte cytotoxic effects. Int. J. Nanomed. **10**, 1977–1983 (2015)
20. Mukunthan, K.S., Elumalai, E.K., Patel, T.N., Murty, V.R.: *Catharanthus roseus*: a natural source for the synthesis of silver nanoparticles. Asian Pac. J. Trop. Biomed. **1**(4), 270–274 (2011)
21. Tanquilut, N.C., Tanquilut, M.A.C., Torres, E.B., Rosario, J.C., Reyes, B.A.S.: Hypoglycemic effect of *Lagerstroemia speciosa* (L.) Pers. on alloxan-induced diabetic mice. J. Med. Plants Res. **3**, 1066–1071 (2009)
22. Ghosh, M.N.: Fundamentals of Experimental Pharmacology, 2nd edn, pp. 153–158. Scientific Book Agency, Culcutta (1984)
23. Singhal, G., Bhavesh, R., Kasariya, K., Sharma, A.R., Singh, R.P.: Biosynthesis of silver nanoparticles using *Ocimum sanctum* (Tulsi) leaf extract and screening its antimicrobial activity. J. Nanoparticle Res. **13**, 2981–2988 (2011)
24. Banerjee, P., Satapathy, M., Mukhopahaya, A., Das, P.: Leaf extract mediated green synthesis of silver nanoparticles from widely available Indian plants: synthesis, characterization, antimicrobial property and toxicity analysis. Bioresour. Bioprocess. **1**, 3 (2014)

25. Maiti, S., Barman, G., Konar, L.J.: Synthesis of silver nanoparticles having different morphologies and its application in estimation of chlorpyrifos. Adv. Sci. Focus. **1**, 145–150 (2013)
26. Barman, G., Samanta, A., Maiti, S., Konar, L.J.: Detection of Cu^{+2} ion by the synthesis of bio-mass-silver nanoparticle nanocomposite. Int. J. Sci. Eng. Res. **6**, 1086–1097 (2014)
27. Shankar, S.S., Rai, A., Ahmad, A., Sastry, M.: Rapid synthesis of Au, Ag, and bimetallic Au core–Ag shell nanoparticles using Neem (*Azadirachta indica*) leaf broth. J. Colloid Interface Sci. **275**, 496–502 (2004)
28. Krishnaraj, C., Jagan, E.G., Rajasekar, S., Selvakumar, P., Kalaichelvan, P.T., Mohan, N.: Synthesis of silver nanoparticles using *Acalypha indica* leaf extracts and its antibacterial activity against water borne pathogens. Colloids Surf. B **76**, 50–56 (2010)
29. Ramteke, C., Chakrabarti, T., Saranki, B.K., Pandey, R.A.: Synthesis of silver nanoparticles from the aqueous extract of leaves of *Ocimum sanctum* for enhanced antibacterial activity. J. Chem. (2013). doi:10.1155/2013/278925
30. Martinez-Castanon, G.A., Nino-Martinez, N., Martinez-Gutierrez, F., Martinez-Mendoza, J.R., Ruiz, F.: Synthesis and antibacterial activity of silver nanoparticles with different sizes. J. Nanopart. Res. **10**, 1343–1348 (2008)
31. Govarthanan, M., Selvankumar, T., Manoharan, K., et al.: Biosynthesis and characterization of silver nanoparticles using panchakavya, an Indian traditional farming formulating agent. Int. J. Nanomed. **9**, 1593–1599 (2014)
32. Lee, K.J., Park, S.H., Govarthanan, M., et al.: Synthesis of silver nanoparticles using cow milk and their antifungal activity against phytopathogens. Mater. Lett. **105**, 128–131 (2013)
33. Dubey, S.P., Lahtinen, M., Särkkä, H., Sillanpää, M.: Bioprospective of *Sorbus aucuparia* leaf extract in development of silver and gold nanocolloids. Colloids Surf. B **80**, 26–33 (2010)
34. Attanayake, A.P., Jayatilaka, K.A.P.W., Pathirana, C., Mudduwa, L.K.B.: Study of antihyperglycaemic activity of medicinal plant extracts in alloxan induced diabetic rats. Anc. Sci. Life **32**, 193–198 (2013)
35. Ragini, V., Prasad, K.V., Bharathi, K.: Antidiabetic activity of *Shorea tumbuggaia* rox. Int. J. Innov. Pharm. Res. **2**, 113–121 (2011)
36. Fröde, T.S., Medeiros, Y.S.: Animal models to test drugs with potential antidiabetic activity. J. Ethnopharmacol. **115**, 173–183 (2008)
37. Swanston-Flatt, S.K., Day, C., Bailey, C.J., Flatt, P.R.: Traditional plant treatment for diabetes: studies in normal and streptozotocin diabetic mice. Diabetologia **33**, 462–464 (1990)
38. Whitton, P.D., Hems, D.A.: Glycogen synthesis in perfused liver of streptozotocin diabetic rats. Biochem. J. **21**, 150–153 (1975)

5:18 researchgate.net/publi
ResearchGate Join for free Login

Article PDF Available

Optimization of Xylanase Production from Aspergillus Flavus in Solid State Fermentation Using Agricultural Waste as a Substrate

December 2017 · International Journal of Advances in Interdisciplinary Research 4(3)
DOI:10.29191/ijaidr.2017.4.3.06

Authors:

Tamilmani Periasamy

Kalaivani Aiyasamy

Margret Rosaland Fathima

Mary George

Show all 6 authors

P.G. & R. COLLEGE OF ARTS & SCIENCE NAMAKKAL 637 204

Citations 2

International Journal of Advances in Interdisciplinary Research Vol. 4 Issue 3 Pages: 29-34 ISSN 2348 0696
Periasamy et al. 2017

Original Research Article Open Access

OPTIMIZATION OF XYLANASE PRODUCTION FROM *Aspergillus flavus* IN SOLID STATE FERMENTATION USING AGRICULTURAL WASTE AS A SUBSTRATE

***Tamilmani Periasamy[1], Kalaivani Aiyasamy[1], Margret Rosaland Fathima Mary George[1], Thirumalaisamy Rathinavel[2,3] and Malathi Ramasamy[1]**

[1]Department of Biochemistry, PGP College of Arts and Science, Namakkal-637207, Tamil Nadu, India

[2]Department of Biotechnology, Mahendra Arts & Science College (Autonomous), Namakkal- 637501,Tamil Nadu, India.

[3]Department of Biochemistry, Rajah Serfoji Government College (Autonomous), Thanjavur– 613005, TamilNadu, India..

Abstract

In the present study an attempt was made to optimize the cultural conditions using agricultural substrate for xylanase production by *Aspergillus flavus* in solid state fermentation process. The optimization of cultural conditions such as optimal temperature, pH and inoculam size was studied and best choice for agricultural substrate among rice bran, wheat bran, and soya bran substrates in solid state fermentation for xylanase production has been investigated. Among three different agricultural substrates rice bran shows the maximum enzyme activity of 162.0±3.0 unit /ml. The enzyme assay was carried out at different temperatures and pH which shows maximum enzyme activity of 172.0±4.1 units /ml in wheat bran at 32°C and pH 8 produce the maximum enzyme activity in soya bran 183.0±5.1 units /ml respectively. Optimization of inoculum size for xylanase production shows 140 spores/ ml that is 184.0±2.8 units /ml in wheat bran used as the substrate. With this studies the optimized culture medium for the production of the enzyme and to get the maximum enzymatic activity with the optimized temperature32°C, pH 8, substrate wheat bran and the inoculmn size of 140 spores/ml shows the maximum enzyme activity of 190±3.1units /ml.

Keywords *Aspergillus flavus, fermented vegetables, wheat bran, rice bran and soya bran*

INTRODUCTION

Enzymes are biological catalysts produced by all living things. Xylanase (E.C 3.2.1.8) is the enzyme which degrades beta-1, 4 xylan by cleaving beta-1, 4 glycosidic linkages thus forming usable products such as xylose, xylobiose like xylooligosaccharides [1 & 2]. In annual plants and hardwoods, xylan is the most abundant non-cellulosic polysaccharide which accounts for 20-35% of the total dry weight in biomass [3]. Xylanases can be produced by bacteria and fungi in both liquid culture and solid culture. The production of microbial xylanases is preferred over plant and animal sources, because of their availability, structural stability and easy genetic manipulation [4]. The enzyme named xylanase deconstructs plant structural material by breaking down hemicellulose, a major component of the plant cell wall. Plant cell walls are necessary to prevent dehydration and maintain physical integrity. They also act as a physical barrier to attack by plant pathogens. In nature, some plant consumers or pathogens use xylanase to digest or attack plants. Many microorganisms produce xylanase, but mammals do not. Some herbivorous insects and crustaceans also produce xylanase.

Filamentous fungi are useful producer of xylanases from the industrial point of view. The reasons many fold - they are non pathogenic, capable of producing high levels of extra cellular enzymes and they can be cultivated very easily. In the textile and paper industries, it is important to be able to obtain xylanases free of cellulose activity, as it is necessary to extract hemicellulose from the natural fibers, without damaging the cellulose.

Xylanase and xylan are little used in the pharmaceutical industry. Xylanases are sometimes added in combination with a complex of enzymes (hemicellulases, proteases and others) as a dietary supplement or to treat poor digestion, but few medicinal products can be found with this formulation. Hydrolytic products of xylan, such as β-D-xylopyranosyl residues, can be converted into combustible liquids (ethanol), solvents and artificial

Address Correspondence @ Tamilmani Periasamy, Head cum Assistant Professor, Department of Biochemistry, PGP College of Arts and Science, Namakkal (Dt.) -637 207, Tamil Nadu, India. Phone - 97868 20779, Email Id- tamilmanip@yahoo.co.in

low-calorie sweeteners. A variety of commercial products containing xylitol, such as chewing gum, can be found on the market. Although the enzymatic hydrolysis of xylan is a promising method of obtaining β-D-xylopyranosyl units, at present commercial xylitol is produced on a large scale by chemical catalysis. This is considered a high-cost process, mainly because the xylose has to be purified.

MATERIALS AND METHODS

Collection of samples

Fermented vegetables (Tomato, Cabbage) from vegetable market in Namakkal were collected using pre- sterilized polythene bag. Precautionary measures were taken to minimize the contamination. The sample was taken for isolating xylanase producing fungi.

Isolation and Identification of fungi

The fermented vegetables was suspended in sterile distilled water and serially diluted 1 gm of the fermented vegetable sample was transferred into the flask 1containing 9 ml of water. It gives the dilution 1:10 i.e. 10^{-1}.Then it was shake for five minutes gently with a stirrer to get spore suspension. 1.0 ml spore suspension was transferred from 10^{-1} dilution into flask 2 containing 90 ml distilled water to get dilution 10^{-2} and then mixed it gently. Similarly 1ml of spore suspension was serially transferred from 10^{-2} dilution into flask 3 containing 90 ml water to get the final dilution of 10^{-3} and mixed it gently. 1ml of suspension was aseptically poured from 10^{-3} dilution to Czapek's dox agar media plates. The plates were gently rotated so as to spread the suspension on medium. The plates were incubated at 25^{0}C for 4-5 days. For identification of fungi lacto phenol and cotton blue stain was used also called as mounting fluid. The slides were observed under microscope and fungi were identified by using standard reference manuals by wet mount preparation. *Fungal* isolates were preserved on Czapek's dox agar plates as pure culture for further studies [5].

Secondary screening

Isolated colony from the preliminary screening was cultured in liquid Media (Czapek's dox broth) in Erlenmeyer flasks. After incubation on a rotary shaker (28°C, 180 rpm) for 6 days, the culture broth was filtered using Whatmann No. 1 filter paper and the supernatant was collected for assay and xylanase production. Its ability to produce xylanase enzyme was further confirmed by Congo red test by growing *isolates* on oat spelt xylan agar plates. After incubation plate was treated with Congo red and washed with 1 M NaCl .

Mycelial dry weight

Mycelial dry biomass was collected on a pre-weighed Whatmann No.5 filter paper, dried to a constant weight at 60°C and reweighed. The difference in weight denoted the mycelial growth of fungus.

Spore count in the cell suspension Haemocytometer

Spore suspension were Pipetted out of approximately 9 microliters (this volume will vary slightly with the brand of hemacytometer) of the cell suspension into one of the two counting chambers. The spores were counted [5].

Enzyme extraction

Czapek's dox broth was autoclaved (15 min at 121°C) and then inoculated with a spore suspension of 106 spores/ml. After mixing, the flasks were incubated at 28 °C for four days. After incubation, 3 g of the homogenized fermented substrate were suspended in 30 mL of NaCl solution (0.9 %), containing Tween 80 (0.1 %) and stirred at 120 rpm in a shaker for 5 min. Solids were filtered under vacuum through Whatman no. 1 filter paper and the filtrate was used as the enzymatic crude extract.

Enzyme assay

Xylanase activity was assayed using 1 % xylan in 0.05 M citrate buffer (pH=5.3), according to the method of Bailey *et al.* The release of reducing sugars was determined using the 3,5-dinitrosalicylic acid (DNS) method [6] with a xylose standard curve. One unit (IU) of enzyme activity was defined as the amount of enzyme required to liberate 1 μmol of reducing sugars per minute. The reaction mixture contained 0.5 ml of substrate solution of 0.25 g of xylan wetted with 2ml 95% ethanol and 22.5ml of distilled water in a beaker and covered with aluminium foil and boiled to dissolve on hot plate at 100^{0}C for 10 min and made up the volume to 25ml with distilled water. To this solution, 0.1 ml of the culture filtered supernatant crude enzyme and 1ml sodium acetate buffer was added. The mixture was incubated at 40°C in water bath with shaking for 15 min. Released reducing sugar was measured using 3, 5-dinitrosalicylic acid and glucose as standard. Color was developed by boiling in water bath for 5 min and read, using spectrophotometer at 540 nm.

Characterization of xylanase production

The optimization of the growth conditions was

COLLEGE OF ARTS NAMAKKAL 637 206

carried out based on the stepwise modification of the substrate using in the Xylanase production. The effect of various substrates which rice bran, wheat bran and soya bran. The cultivation was carried out at ambient temperature (28±30 °C) for 6 days.

The effect of agitation

The effect of agitation was carried out at agitation rate at 160 rpm in a shaker incubator at 37°C, and xylanase production was studied [7].

The effect of pH

The optimum pH for enzyme activity was determined by carrying out the enzyme assay at different pH levels (5, 6, 7, and 8). The effects of incubation period were evaluated with 24 hrs interval by checking the enzyme activity and the agitation rate at 160 rpm [7].

Effect of temperature on Enzyme activity

The effect of cultivation temperature on the enzyme production was examined at different temperatures. For estimation of optimum temperature, the enzyme assay was carried out at different temperatures (28°C, 32°C, 37°C, 40°C) and the agitation rate at 160 rpm [7].

Optimization of inoculum size

Optimization of inoculum size for xylanase production was carried out by adding approximately 100 to 150 spores (the spore count carried out by Haemocytometer) of isolated fungi to 9 ml of sterile water blank. This suspension was serially diluted 1ml of the diluted sample from each dilution was transferred to sterile media and incubated at 28°C ± 2°C for 5-7 days. Optimizations of growth conditions for xylanase production by Aspergillus isolated colony in Czapek's dox broth before and after optimization for the above parameters were also carried out by Statistical Analysis .All the above readings obtained at 540 nm absorbance was subjected.

Statistical Analysis

The data obtained after experimentation was statistically evaluated using ANOVA at significance level of $p < 0.05$ by using computer based program SPSS.

RESULTS AND DISCUSSION

The aim of present study is to synthesize xylanase enzyme by utilizing indigenous agricultural wastes by products like wheat bran, soya bran and rice bran as Substrate (carbon source) for the fungus *Aspergillus flavus* to carry out the solid state fermentation. The culture conditions were optimized to achieve highest xylanase activity. The crud extract of the culture initially shows the results of enzyme activity 38.0±4.0 Unit/ml. Agricultural waste materials/by products like wheat bran, corn cobs, sugar cane bagass , rice husk, rice straw and oat straw have been used by many scientists for xylanase synthesis [7-11].

Enzyme activity

During the study, the fungus *Aspergillus flavus* produced maximum enzyme activity at 162.0±3.0 unit/ml on wheat bran (Table 1) used as the substrate that is supported by earlier reported result obtained higher yields of the enzyme when *Aspergillus flavus* was grown on wheat bran. The results are also in conformity with those of earlier study report [12] that is highest enzyme activity (1845U/g) on wheat bran when used mutant strain *A.niger* GCBMX-45 for enhanced xylanase production. Similar earlier work [13] was conducted to find out the potential of *A. niger* A3 for the production of xylanase in solid state fermentation.

Table 1. Enzyme activity on different substrate used in culture medium

S. No	Different substrate	Enzyme activity (units /ml)
1	Rice bran	98.0±8.2
2	Wheat bran	162.0±3.0
3	Soya bran	161.0±2.3

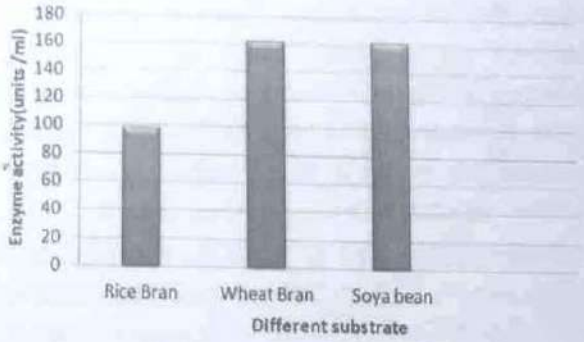


Figure 1. Xylanase enzyme activity on different substrate

Optimization of pH

The time scale production of the xylanase by *Aspergillus flavus* at four different pH levels of the culture medium. pH 8 (Table 2) shows the maximum activity in wheat bran and soya bran 182.0±4.8 and 182.0±5.1 units /ml respectively. The similar study line with *A.niger* was carried out by for optimal pH

condition for xylanase production [7].

Table 2: Effect of different pH in culture medium on Enzyme activity

S. No	pH	Enzyme activity(units /ml)		
		Rice bran	Wheat bran	Soya bran
1	5	111.0±3.1	152.0±6.0	112.0±2.0
2	6	102.0±4.1	182.0±4.8	112.0±5.3
3	7	113.0±1.2	163.0±3.4	158.0±3.2
4	8	116.0±3.0	172.0±2.1	183.0±5.1

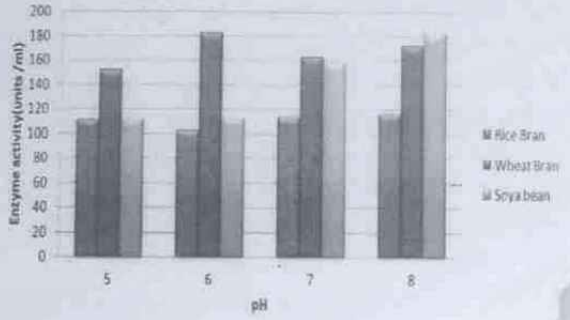


Figure 2. Xylanase enzyme activity on different pH

Optimization of Temperature

For identification of optimum temperature, the enzyme assay was carried out at different temperatures (28°C,32°C,37°C,40°C) in this studies the maximum activity recorded in 32°C of 172.0±4.1 units /ml (Table 3) in wheat bran when compared to the other substrates. It has already been observed that *A. niger* being mesophillic organism grew best at 30°C therefore, resulted higher yields of xylanase. The findings of the present study are in line with those of earlier reported results [14 & 15] described that *A. flavus* exhibits maximum xylanolytic activities at 30°C. Likewise maximum xylanase production at 30°C reported by earlier findings [16 & 17]. but in the case of the present findings the optimum temperature recorded as 32°C

Optimization of innoculam size

It was found that the increase in inoculums size resulted in a rapid increase in xylanase production. Optimization of inoculum size for xylanase production was carried out by adding approximately 110 to 140 spores of *fungi* to 9 ml of sterile water. The activity was calculated and the 140 spores/ml produces maximal activity, 184.0±2.8 units /ml (Table 4) in wheat bran.

Table 3: Effect of different temperature in culture medium on Enzyme activity

S. No	Temp	Enzyme activity(units /ml)		
		Rice bran	Wheat bran	Soya bran
1	28°C	111.0±1.0	141.0±3.0	101.0±8.0
2	32°C	102.0±3.1	172.0±4.1	113.0±6.1
3	37°C	113.0±2.2	143.0±3.4	143.0±2.0
4	40°C	102.0±2.0	132.0±2.6	100.0±4.3

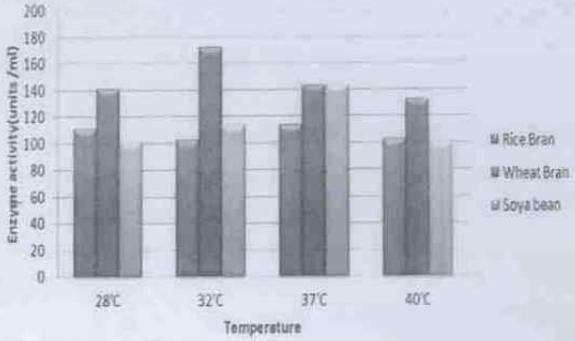


Figure 3. Xylanase enzyme activity on different temperature

Table 4: Effect of Optimization of inoculum size on Enzyme activity

S. No	A. flavus spores	Enzyme activity(units /ml)		
		Rice bran	Wheat bran	Soya bran
1	110	114.0±4.1	153.0±2.0	120.0±1.0
2	120	114.0±5.3	165.0±1.5	121.0±5.0
3	130	116.0±4.2	182.0±2.3	121.0±2.2
4	140	116.0±3.1	184.0±2.8	175.0±3.1

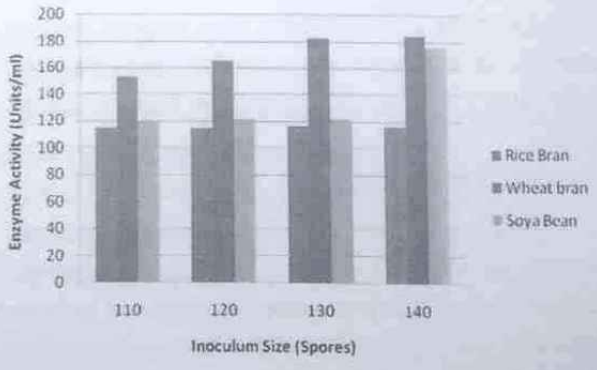


Figure 4: Xylanase enzyme activity on optimization of inoculums size

Optimization of production medium

Optimization of production medium was carried out by *Aspergillus flavus* with three different brans and similar observation was report [18] showed that maximum enzyme production and declination was achieved much faster due to the rapid degradation of substrate as a consequence of rapid growth. Nevertheless, the degradable products were used up by biomass to enhance xylanase production later in the fermentation process.

Table 5: Enzyme Assay on Optimized Production Medium

Production medium	Optimization
Spores of *A.flavus*	140
Substrate	wheat bran
Temperature	32°C
pH	8
Enzyme Activity (units /ml)	190±3.1

CONCLUSION

The results of present reveals that optimization of culture condition is very helpful to produce xylanase enzyme using cheaply available agro residual substrate such as wheat bran, rice bran and soya bran in solid state fermentation process. In this the study wheat bran supplemented optimized media was cost-effective when compared to media containing other substrate. The present study demonstrated using agricultural waste to produce higher levels of xylanase. Wheat bran is an inexpensive by product which contains a lot of xylan. Therefore, it is one the most popular components of complex media for xylanase production when compared to rice bran and soya bran. Xylanase can be used in the food and beverage, feed stock improvement, kraft pulp bleaching, in poultry industry, de-inking of newspaper and agricultural waste degradation. In the present study concluded that the *Aspergillus flavus* isolate had the capability of production of the xylanase enzyme in the large scale which was especially grown in the culture medium supplemented with the wheat bran.

REFERENCES

[1] Bernier R, Desrochers M, Jurasek L, Paice MG (1983) Isolation and characterization of a xylanase from *Bacillus subtilis*. Applied and Environmental Microbiology, 46(2): 511-514.

[2] Chakrit T, Khin LK, Khanok R (2006) Purification of xylanase from alkaliphilic *Bacillus sp.* K-8 by using corn Corn husk column. Process Biochemistry, 41(12): 2441-2445.

[3] Elegir G, Szakacs M, Jeffries TW (1994) Purification, characterization and substrate specificities of multiple xylanases from *Streptomyces sp.* strain B-12-2. Applied and Environmental Microbiology, 60(7): 2609-2615.

[4] Bilgrami KS, Pandy AK (1992) In E. S. K. Jain (Ed.), Industry and fermentation in introduction to biotechnology (pp. 149-165).

[5] Montenecourt BS, Eveileigh DE (1977) Preparation of mutants of Trichoderma reesei with enhanced cellulase production. Appl Environ Microbiol. 34, 777-784.

[6] Miller GL (1959) Use of di-nitrosalicylic acid reagent for determination of reducing sugar. *Anal. Chem.* 31: 426-428.

[7] Bakri Y, Jacques P, Thonart P (2003) Xylanase production by Penicillium canescens 10–10c in solid-state fermentation Applied Biochemistry and Biotechnology, 105-108, 737-747.

[8] Siedenberg D, Gerlach SR, Schugerl K, Guiseppin MLF, Hunik J (1998) Production of xylanases by *Aspergillus awamori* on complex medium in stirred tank an airlift tower loop reactors. J. Biotechnol. 56(3): 205-216.

[9] Christov LP, Szakacs G, Balakrishnan (1999) Production, partial characterization and use of fungal cellulase-free xylanases. Process Biochem. 34: 511–517.

[10] Gawande PV, Kamat MY (1999) Production of *Aspergillus* xylanase by lignocellulosic waste fermentaion and its application. J. Appl. Microbiol. 87: 511–519.

[11] Haq I, Khan A, Butt WA, Ali S and Qadeer MA (2002) Effect of carbon and nitrogen sources on xylanase production by mutant strain of *Aspergillus niger* GCBMX-45. J. Biol. Sci. 2(2): 143-144.

[12] Gokhale DV, Puntambekar US, Deobagkar DN (1986) Xylanase and β-xylosidase production by Aspergillus niger, Biotech. Lett. 8: 137.

[13] Cai JM, Ke W, Jie Z, Ruipen R (1998) Production, properties and application of xylanase from *Aspergillus niger*. A 3 Ann. N.Y. Acad. Sal. 864: 214-218.

[14] Duenas R, Tengerdy RP, Giutierrez-Corria M (1995) Cellulase production by mixed fungi in solid substrate fermentation bagasse. Biotechnol. Lett. 8(5): 206-210.

[15] Ali S, Haq I, Qadeer MA, Iqbal J (2002) Production of citric acid by *Aspergillus niger* using cane

molasses in a stirred fermentor. Electron J. Biotechnol. 5(3): 258-271.

[16] Chen H, Jiang Z, Gaigin L, Zizheng Y, Shuzheng Z (1999) Screening of acidic xylanase producing strain and studies on its enzyme production condition. Acta Microbiologica Sinica, 39(4):350-354

[17] Gouda MK (2000) Purification and partial characterization of cellulose free xylanase produced in solid state and submerged fermentation by *Aspergillus tamarii*. Adv. Food Sci. 22(1/2): 31-37

18] Raimbault, Alazard D (1980) M. Culture method to study fungal growth in solid fermentation. Eur. J. Appl. Microbiol. Biotechnol. 9: 199-209.

Galley Proof

Citation: Tamilmani Periasamy, Kalaivani Aiyasamy, Margret Rosaland Fathima Mary George, Thirumalaisamy Rathinavel and Malathi Ramasamy (2017) Optimization of Xylanase Production from Aspergillus flavus in Solid State Fermentation using Agricultural Waste as a Substrate, Int J Adv Interdis Res, 4 (3): 29-34 .

Received: Aug 08, 2017 | **Revised:** Sep 15, 2017 | **Accepted:** Sep 16, 2017 | **Published:** Sep 30, 2017

License : Periasamy T et al, (2017). This is an open-access article distributed under the terms of the Creative Commons Attribution License, which permits unrestricted use, distribution, and reproduction in any medium, provided the original author and source are credited.

PRINCIPAL
PGP College of Arts and Science
Namakkal

5:13

Natural Product Research ›
Formerly Natural Product Letters
Volume 32, 2018 - Issue 24

176 Views | 13 CrossRef citations to date | 0 Altmetric

Short Communication

Anti obese potential of *Cucurbita maxima* seeds oil: effect on lipid profile and histoarchitecture in high fat diet induced obese rats

A. Kalaivani, V. V. Sathibabu Uddandrao, P. Brahmanaidu, Ganapathy Saravanan, P. R. Nivedha, P. Tamilmani, K. Swapna & **Sasikumar Vadivukkarasi** ...show less

Pages 2950-2953 | Received 04 Sep 2017, Accepted 22 Sep 2017, Published online: 19 Oct 2017

Download citation
https://doi.org/10.1080/14786419.2017.1389939
Check for updates

P.G.P. COLLEGE OF ARTS & SCIENCE NAMAKKAL

Full Article — Showing
Figures & data ›
References ›
Supplemental ›
Citations ›
Metrics ›

Natural Product Research
Formerly Natural Product Letters

ISSN: 1478-6419 (Print) 1478-6427 (Online) Journal homepage: http://www.tandfonline.com/loi/gnpl20

Anti obese potential of Cucurbita maxima seeds oil: effect on lipid profile and histoarchitecture in high fat diet induced obese rats

A. Kalaivani, V. V. Sathibabu Uddandrao, P. Brahmanaidu, Ganapathy Saravanan, P. R. Nivedha, P. Tamilmani, K. Swapna & Sasikumar Vadivukkarasi

To cite this article: A. Kalaivani, V. V. Sathibabu Uddandrao, P. Brahmanaidu, Ganapathy Saravanan, P. R. Nivedha, P. Tamilmani, K. Swapna & Sasikumar Vadivukkarasi (2017): Anti obese potential of Cucurbita maxima seeds oil: effect on lipid profile and histoarchitecture in high fat diet induced obese rats, Natural Product Research, DOI: 10.1080/14786419.2017.1389939

To link to this article: http://dx.doi.org/10.1080/14786419.2017.1389939

View supplementary material

Published online: 19 Oct 2017.

Submit your article to this journal

Article views: 4

View related articles

View Crossmark data

P.G.P. COLLEGE OF SCIENCE NAMAKKAL 637 206

Full Terms & Conditions of access and use can be found at
http://www.tandfonline.com/action/journalInformation?journalCode=gnpl20

NATURAL PRODUCT RESEARCH, 2017
https://doi.org/10.1080/14786419.2017.1389939

Taylor & Francis
Taylor & Francis Group

SHORT COMMUNICATION

Check for updates

Anti obese potential of *Cucurbita maxima* seeds oil: effect on lipid profile and histoarchitecture in high fat diet induced obese rats

A. Kalaivani[a,c#], V. V. Sathibabu Uddandrao[a#], P. Brahmanaidu[b], Ganapathy Saravanan[a], P. R. Nivedha[a], P. Tamilmani[c], K. Swapna[a] and Sasikumar Vadivukkarasi[a]

[a]Department of Biochemistry, Centre for Biological Sciences, K. S. Rangasamy College of Arts and Science (Autonomous), Tiruchengode, India; [b]Department of Biotechnology, Vikrama Simhapuri University, Nellore, India; [c]Department of Biochemistry, PGP College of Art and Science, Namakkal, India

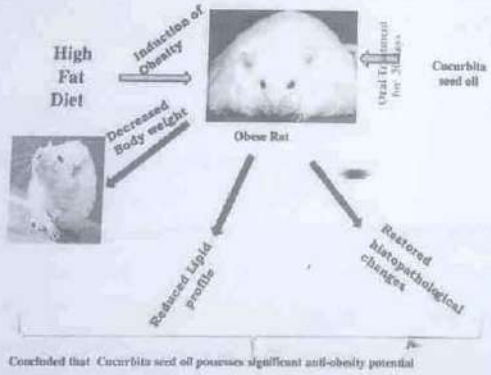
Downloaded by [180.215.122.237] at 04:43 21 October 2017

ABSTRACT

In this study, we made an attempt to evaluate the potential of *Cucurbita maxima* seeds oil (CSO) against high-fat diet (HFD)-induced obesity in rats. We investigated the effect of CSO (100 mg/kg body weight) supplementation over 30 days on the changes of HFD-induced obese rats in body weight, biochemical parameters and lipid profile as well as investigated the effects of CSO on the histopathological changes. Oral administration with CSO revealed significant diminution in body weight gain, glucose and insulin levels, which altered the activity of lipid profile and restored the pathological alterations. It demonstrated that CSO had considerably altered these parameters when evaluated with HFD control rats. In conclusion, this study established that CSO prevents the HFD-induced obesity by altering the markers important to lipid metabolism.

ARTICLE HISTORY
Received 4 September 2017
Accepted 22 September 2017

KEYWORDS
Cucurbita seed oil; obesity; metabolic disorders; lipid metabolism; high-fat diet



CONTACT Sasikumar Vadivukkarasi vadivusasi16@gmail.com, s.vadivukkarasi@ksrcas.edu
[#]Equally contributed to this work.
Supplemental data for this article can be accessed at https://doi.org/10.1080/14786419.2017.1389939.

© 2017 UK Limited, trading as Taylor & Francis Group

P.G.P. COLLEGE OF ARTS & SCIENCE NAMAKKAL

1. Introduction

Obesity is a chronic metabolic disorder caused due to an imbalance between energy intake and expenditure (Bays et al. 2009). It is however, broadly established that obesity results from a chronic imbalance between energy intake and consumption. The addition of extra calories in the diet induces fat accumulation, leading to overweight and obesity (Fried et al. 2008). It is controllable by various approaches, including traditional medications, pharmaceutical drugs, and surgery. Of these presently, the exploitation of medicinal plants is gradually being more popular and is preferable to conservative chemotherapeutic methods (Kazemipoor et al. 2012). Furthermore, specific phytochemical constituents present in medicinal plants may assist in adaptable weight and body fat through modification of metabolic pathways at the molecular level, which are responsible for signalling adipogenesis and lipolysis (Nawrocki and Scherer 2005).

Pumpkin (*Cucurbita maxima*) of the Cucurbitaceae family is extensively cultivated and utilized in many countries around the world (Lami et al. 2011). The oil from the pumpkin seed is claimed to be useful in the management of various disorders (Nkosi et al. 2006). However, till date there is no report of anti-obesity capability of these seeds; hence the present study was designed to evaluate the anti-obesity potentiality of *Cucurbita maxima* seeds oil (CSO) against high-fat diet (HFD)-induced obesity in rats.

2. Results and discussion

Diet-induced obesity (DIO) in animals has several characteristics similar to human obesity and signs of DIO are body weight composition, insulin resistance, dyslipidemia and impaired glucose tolerance (Naidu et al. 2016). In the present study, improved body weight and fat were found in HFD-fed rats. Inclusion of CSO showed a more noteworthy lessening in body weight development compared to that of HFD-fed control rats and the control of body weight gain may be due to a number of mechanisms including unusual food assimilation or decreased body energy storage and also the reduction in body weight gain (Duiyan et al. 2013).

Table S1 shows the body weight, level of plasma glucose, plasma insulin and insulin resistance in control and experimental obese rats. The body weights, levels of blood glucose were increased in obese rats and significant decline was observed in the plasma insulin levels, and there were momentous increases in insulin resistance in the HFD induced obese rats compared with the control rats. Administration of CSO or Orlistat tended to normalise the body weight, levels of plasma insulin and insulin resistance. In this study, HFD treatment to animals inveterate the nature of obesity as evidenced by escalating body weight, hyperglycaemic condition and enhanced insulin resistance. This is in line with earlier reports (Naidu et al. 2016). Under physiological circumstances, insulin inhibits lipolysis and enhances lipogenesis (Saltiel and Kahn 2001) which are principal to improved circulating levels of glucose and lipids resulting in impaired glucose-enthused insulin secretion (Brahmanaidu et al. 2017). Oral administration of CSO considerably lowered plasma glucose, insulin level and insulin resistance in treated rats compared to HFD control rats. CSO encourages insulin sensitivity by lowering insulin resistance, and reduces body weight gain and glucose level in obese animals possibly by reducing free fatty acids or regulating cell energy metabolism (Boissonneault 2009).

Downloaded by [180.215.122.237] at 04:43 21 October 2017

NAMAKKAL 637 206

Table S2 shows the levels of lipid profile in control and HFD-induced obese rats correspondingly. The level of plasma lipids was considerably enhanced in experimental obese rats compared to the normal rats. Oral treatment with CSO or Orlistat significantly ($p < 0.05$) decreased the concentrations of plasma lipids in obese rats nearly to the normal level. Superior lipogenesis is sturdily connected with obesity, insulin resistance and type-2 diabetes (Brahmanaidu et al. 2016; Uddandrao Sathibabu et al. 2016). In the current study, dyslipidaemic changes like elevated TC, LDL and TGs, and turned-down plasma level of HDL has been observed. Rise of TGs was because of dietary cholesterol that appears to decrease unsaturated fat oxidation, which resulted in long-lasting the levels of plasma and hepatic TGs and the extreme accumulation of TGs in the lipid stores. Noticeable TC levels reinforce the danger of mounting coronary heart disease by uplifting LDL. In addition, high HDL is cooperative in transporting excess cholesterol to the liver for emanation in the bile (Garjani et al. 2009). Oral administration of CSO considerably lowered TC, TGs and LDL levels in plasma of rats with HFD-induced obesity.

The histopathological observations in control and HFD-induced obese rats are depicted in Figure S1. The group of control rats that were administrated normal diet showed liver parenchyma with preserved lobular architectures and normal plates of hepatocytes. Normal morphology of central vein and portal triads made out. No evidence of any inflammatory changes or malignancy was observed (Figure S1(A)). Hepatocytes showed significant steatosis, apoptosis and swelling of parenchyma and also fat accumulation was observed in the livers of HFD-fed rats (Figure S1(B)). Interestingly, treatment with CSO and Orlistat reduced most of the pathological alterations induced by HFD in rats (Figure S1(C) and (D)). These observations can suggest that CSO is one of the promising natural remedy for improving pathological alterations caused by the obesity.

3. Conclusion

In conclusion, these results recommended that dietary supplementation of CSO possibly will hold back the augmentation in body weight and fat percentage in HFD induced obese rats. CSO administration also restored the histopathological alteration in HFD rats. This study suggests that CSO has therapeutic potential for the management of obesity and hyperlipidaemia.

Acknowledgements

The authors thank K.S.R. College of Technology, Tiruchengode, Tamilnadu, India for providing facilities to do animal studies and also express heartfelt thanks to the management of K. S. Rangasamy College of Arts and Science (Autonomous), Tiruchengode, Tamilnadu for their support and encouragement.

Disclosure statement

No potential conflict of interest was reported by the authors.

References

Bays H, Blonde L, Rosenson R. 2009. Adiposopathy: how do diet, exercise and weight loss drug therapies improve metabolic disease in overweight patients? Expert Rev Cardio Ther. 4(6):871–895.
Boissonneault GA. 2009. Obesity: the current treatment protocols. JAAPA. 22:18–19.

Downloaded by [180.215.122.237] at 04:43 21 October 2017

Naidu PB, Uddandrao S, Naik RR, Suresh P, Meriga B, Begum MS, Saravanan G. 2016. Ameliorative potential of gingerol: promising modulation of inflammatory factors and lipid marker enzymes expressions in HFD induced obesity in rats. Mol and Cell Endoc. 419:139–147.

Brahmanaidu P, Sathibabu Uddandrao VV, Pothani S, Naik RR, Begum MS, Varatharaju C, Saravanan G. 2016. Effects of S-allylcysteine on biomarkers of polyol pathway in experimental type II diabetes in rats. Can J of Diab. 40:442–448.

Brahmanaidu P, Sathibabu Uddandrao VV, Sasikumar V, Naik RR, Pothani S, Begum MS, Varatharaju G, Meriga B, Kalaivani A, Saravanan K. 2017. Reversal of endothelial dysfunction in aorta of streptozotocinnicotinamide-induced type-2 diabetic rats by S-Allylcysteine. Mol Cel Bioc. 432(1–2):25–32. doi:10.1007/s11010-017-2994-0

Duiyan J, Xua Y, Mei X. 2013. Antiobesity and lipid lowering effects of theaflavins on high-fat diet induced obese rats. J of fun foods. 5:1142–1150.

Fried M, Hainer V, Basdevant A, Buchwald H, Dietel M. 2008. Interdisciplinary European guidelines on surgery for severe obesity. Rozhl Chir. 87:468–476.

Garjani A, Fathiazad F, Zakheri A, Akbari NA, Azarmie Y. 2009. The effect of total extract of *Securigera securidaca* L. seeds on serum lipid profiles, antioxidant status, and vascular function in hypercholesterolemic rats. J Ethnopharmacol. 126:525–532.

Kazemipoor M, Radzi M, Cordell GA, Yaze I. 2012. Safety, efficacy and metabolism of traditional medicinal plants in the management of obesity: a review. Int J of Chem Engi and Appli. 3(4):288–292.

Lami AA, Barakat R, Hamed M. 2011. The antiatherogenic, renal protective and immunomodulatory effects of purslane, pumpkin and flax seeds on hypercholesterolemic rats. North Ame J of Med Sci. 3(9):351–357.

Nawrocki AR, Scherer PE. 2005. Keynote review: the adipocyte as a drug discovery target. Drug Discov Today 10:1219–1230.

Nkosi CZ, Opoku AR, Terblanche SE. 2006. Antioxidative effects of pumpkin seed (*Cucurbita pepo*) protein isolate in CCl4-Induced liver injury in low-protein fed rats. Phytother Res. 20:935–940.

Saltiel AR, Kahn CR. 2001. Insulin signalling and the regulation of glucose and lipid metabolism. Nature. 414:799–806.

Uddandrao Sathibabu VV, Brahmanaidu P, Saravanan G. 2016. Therapeutical perspectives of S-allylcysteine: effect on diabetes and other disorders in animal models. Cardiovasc Hematol Agents Med Chem. 14:1–7. doi:10.2174/1871525714666160418114120.

PRINCIPAL
PGP College of Arts and Science
Namakkal

Downloaded by [180.215.122.237] at 04:43 21 October 2017

5:16

www.researchgate.net

ResearchGate Join for free Lo

Article PDF Available

Obesity-alleviating potential of asiatic acid and its effects on ACC1, UCP2, a CPT1 mRNA expression in high fat die induced obese Sprague–Dawley rats

Springer

May 2018 · Molecular and Cellular Biochemistry 442(4)

DOI:10.1007/s11010-017-3199-2

Authors:

P. Rameshreddy





V. V. Sathibabu Uddandrao



Brahmanaidu Parim
National Animal Resource Facility for Biomedical

S. Vadivukkarasi



Ramavat Ravindarnaik
ICMR-National Animal Resource Facility For Biom

26

5:16



Ramavat Ravindarnaik
ICMR-National Animal Resource Facility For Biom...

Pothani Suresh

K. Swapna

A. Kalaivani

Parimi Parvathi

P. Tamilmani

Ganapathy Saravanan
K.S.R. College of Arts and Science

Hide

Citations 35

Reads 271

Recommendations 3

Learn more about stats on ResearchGate

Download full-text PDF

Obesity-alleviating potential of asiatic acid and its effects on *ACC1*, *UCP2*, and *CPT1* mRNA expression in high fat diet-induced obese Sprague–Dawley rats

P. Rameshreddy[1] · V. V. Sathibabu Uddandrao[1] · Parim Brahmanaidu[2] · S. Vadivukkarasi[1] · Ramavat Ravindarnaik[3] · Pothani Suresh[3] · K. Swapna[1] · A. Kalaivani[1,4] · Parimi Parvathi[2] · P. Tamilmani[4] · Ganapathy Saravanan[1]

Received: 17 July 2017 / Accepted: 6 October 2017
© Springer Science+Business Media, LLC 2017

Abstract The present study evaluated the effects of asiatic acid (AA), a pentacyclic triterpenoid from *Centella asiatica* on lipid metabolism parameters in a rat model of obesity induced using a high fat diet (HFD) for 42 days. AA (20 mg/kg body weight [BW]) was administered orally once daily for 42 days, and an orlistat-treated group of rats (10 mg/kg BW) was included for comparison. Changes in BW, blood glucose levels, insulin resistance and leptin, adiponectin, amylase, and lipase levels in the blood; lipid profiles of plasma; liver antioxidants levels; and acetyl CoA carboxylase(ACC), uncoupling protein-2 (UCP2), and carnitine palmitoyltransferase-1 (CPT1) mRNA expression were observed in the experimental rats. Our results revealed that AA (20 mg/kg BW), similar to orlistat, reduced the increase in BW; increased bone mineral contents and bone mineral densities; reduced blood glucose levels, insulin resistance, leptin, plasma lipid levels; increased adiponectin, amylase, lipase levels in the blood; showed antioxidant activity; and altered mRNA expression of lipid metabolism-related genes, including ACC, UCP 2, and CPT 1, in the HFD-fed rats. From these results, we concluded that AA possesses significant anti-obesity potential through the suppression of BW gain, lipid lowering action, development of insulin and leptin sensitivity, antioxidant activity, and increased mRNA expression of lipid metabolism-related genes.

P. Rameshreddy, V. V. Sathibabu Uddandrao, and Parim Brahmanaidu have contributed equally to this work.

✉ Ganapathy Saravanan
sarabioc@gmail.com

1 Department of Biochemistry, Centre for Biological Sciences, K. S. Rangasamy College of Arts and Science (Autonomous), Namakkal Dt, Tiruchengode, Tamil Nadu 637215, India

2 Department of Biotechnology, Vikrama Simhapuri University, Nellore, Andhra Pradesh 524003, India

3 National Centre for Laboratory Animal Sciences, National Institute of Nutrition, Hyderabad 500007, India

4 Department of Biochemistry, PGP College of Art and Science, Namakkal, Tamil Nadu 637207, India

COLLEGE OF ARTS & SCIENCE NAMAKKAL P.G.P.

Published online: 09 October 2017

See discussions, stats, and author profiles for this publication at: https://www.researchgate.net/publication/320289265

Obesity-alleviating potential of asiatic acid and its effects on ACC1, UCP2, and CPT1 mRNA expression in high fat diet-induced ....

Article in Molecular and Cellular Biochemistry · October 2017
DOI: 10.1007/s11010-017-3199-2

CITATION
1

READS
18

11 authors, including:



V. V. Sathibabu Uddandrao
K.S.R. College of Arts and Science
26 PUBLICATIONS **36** CITATIONS
SEE PROFILE



Brahmanaidu Parim
National Animal Resource Facility for Biome...
38 PUBLICATIONS **128** CITATIONS
SEE PROFILE



Ramavat Ravindarnaik
National Institute of Nutrition , Hyderabad
19 PUBLICATIONS **59** CITATIONS
SEE PROFILE



Ganapathy Saravanan
K.S.R. College of Arts and Science
38 PUBLICATIONS **231** CITATIONS
SEE PROFILE

Some of the authors of this publication are also working on these related projects:

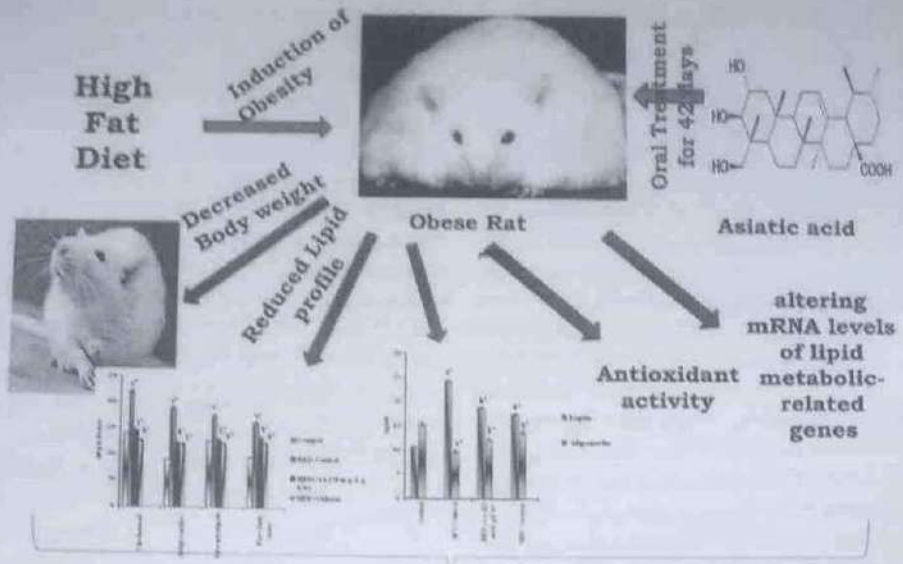
Project Diabetic cardiomyopathy View project

Project Derivation and transplantation of corneal cells View project



All content following this page was uploaded by V. V. Sathibabu Uddandrao on 26 October 2017.

Graphical Abstract



Keywords Asiatic acid · High fat diet · Lipid · Antioxidants · Metabolic disorders · Obesity

Introduction

The obesity epidemic is widespread. The prevalence and incidence of obesity are escalating worldwide in developing and developed countries, adversely affecting both men and women of different ages [1]. Obesity increases the risk of various diseases including type 2 diabetes, hypertension, hyperlipidemia, and cardiovascular diseases [2]. It is characterized by an anomalous or unnecessary fat accumulation attributable to an imbalance between energy intake and energy expenditure [3]. The etiology of obesity is dissimilar. However, the root cause is an energy discrepancy in which more calories are consumed than expended.

Numerous therapeutic interventions are available for the treatment of obesity, including low calorie diets, increased physical activity, behavioral treatments, pharmacological interventions, and bariatric surgery. However, these interventions generally have limited efficacy and safety [4]. Pharmacotherapy for obesity treatment has advanced remarkably in recent times. Along with lifestyle modifications, a reduction in supplement assimilation, and identification of groups of drugs that influence lipid assembly and utilization will be suitable for developing treatments for obesity. The drugs that are presently permitted for obesity by the US Food and Drug Administration (FDA) include orlistat, diethylpropion, and phendimetrazine, of which only orlistat is accepted for long-term use [5]. Currently, the market for anti-obesity drugs is growing rapidly, but the available drugs cannot meet the market demand. Hence, identifying novel anti-obesity drugs to alleviate obesity is necessary [6]. Epidemiological studies have recommended the use of phytoconstituents that can reduce the risk of diabetes, cardiovascular diseases, and obesity [7], thus suggesting that the consumption of asiatic acid may be beneficial for the treatment of metabolic diseases.

Asiatic acid (AA) is a triterpene found abundantly in *Centella asiatica* (L.), a perennial herbaceous creeper of the Apiaceae family [8]. It possesses an extensive array of biological functions including antioxidant, hepatoprotective, and anti-inflammatory activities [9]. Furthermore, AA exhibits antidiabetic properties by enhancing plasma levels of insulin, reducing blood glucose levels, and adjusting the status of the lipid-metabolizing enzymes [10]. It is also reported to prevent lipid peroxidation and improves the antioxidant status in rats with streptozotocin-induced diabetes [11]. However, no information pertaining to the anti-obesity effects of AA is available. Therefore, the purpose of the present study is to appraise the anti-obesity potential of AA in HFD-fed rat model.

P.G.P. COLLEGE OF ARTS & SCIENCE NAMAKKAL 637 206

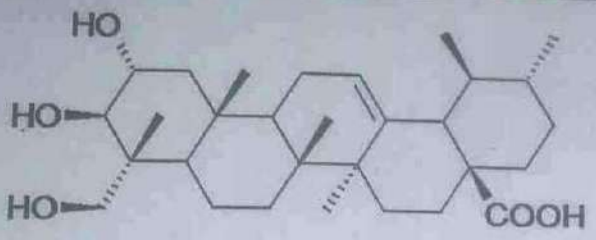


Fig. 1 Structure of the Asiatic acid (2α, 3β, 23-trihydroxyurs-12-en-28-oic acid)

Materials and methods

Chemicals

AA (2α, 3β, 23-trihydroxyurs-12-en-28-oic acid; Fig. 1) and orlistat (04139 Sigma) were purchased from Sigma-Aldrich (St. Louis, Missouri, USA). Fasting blood glucose kits and insulin kits were procured from Stanbio Laboratory USA, Bio-Merieux, RCS, Lyon, France. All the reagents used in the experiments were analytical grade reagents of the highest purity.

Animals

Male Sprague–Dawley rats were obtained from Department of Biochemistry, Muthyammal College of Arts and Science, Rasipuram, Namakkal District, Tamilnadu, India. The experimental rats were maintained under standard laboratory conditions (temperature: 22 ± 2 °C; humidity: 40–60%) and were permitted food and water ad libitum. The rats, initially weighing 180–200 g, were divided into four groups of six each ($n = 6$). All procedures involving laboratory animals were in accordance with the institutional animal ethical committee of Muthyammal College of Arts and Science (Approval No: IAEC/MCAS/05/2016).

High fat diet formula

A normal diet (ND) and HFD were procured from the National Center for Laboratory Animal Sciences, National Institute of Nutrition, Hyderabad, India (Table 1). The normal control rats were fed with standard rodent chow pellet diet according to AIN-93 guidelines, whereas the other three groups of rats were fed with HFD throughout the experiment.

Table 1 Composition of the normal and high fat diet (in grams per kilogram diet)

Ingredients	Normal diet	High fat diet
Casein	200.0	200.0
Starch	615.0	150.0
Sucrose	–	150.0
Corn oil	80.0	–
Beef tallow	–	400.0
Cellulose	50.0	50.0
Vitamin–mineral premix	50.0	50.0
DL-methionine	3.0	3.0
Choline chloride	2.0	2.0

Experimental design

Group 1 ND control group (Control).
Group 2 HFD group (HFD control).
Group 3 HFD rats orally treated with AA (20 mg/kg BW) in a vehicle solution for 42 days [10].
Group 4 HFD rats orally treated with orlistat (10 mg/kg BW) in a vehicle solution for 42 days [12].

Measurement of body weight

The BW and the total amount of food consumption (data not shown) of each rat were measured. Toward the end of the experiment, blood was collected from overnight fasted anesthetized animals by using retro-orbital puncture method. Blood was collected in anticoagulant-coated vials and allowed to stand for 15 min at room temperature. The plasma was separated by centrifugation at 2500 rpm for 15 min. At the end of the experimental period, the rats were fasted overnight, anesthetized, and sacrificed by cervical decapitation.

Blood glucose and insulin levels and insulin resistance

Plasma glucose was estimated using standard kits (Cat No 1060-500, Stanbio laboratory, USA). The plasma level of insulin was determined using kits from Bio-Merieux, RCS, Lyon, France. The insulin resistance index was evaluated by substituting the fasting serum insulin and plasma glucose levels in the following homeostasis model assessment (HOMA) formula: HOMA = fasting serum insulin (mU/L) × fasting plasma glucose (mM)/22.5.

Oral glucose tolerance test (OGTT)

OGTT was performed toward the end of the experiment; after overnight fasting, glucose was administered orogastrically at a dose of 2.0 g/kg BW and blood samples were collected at 0, 30, 60, and 120 min, and the blood glucose levels were evaluated.

P.G.P. COLLEGE OF ARTS & SCIENCE NAMAKKAL 637 206

Determination of biochemical profiles

Blood samples were centrifuged at 4000 rpm/min for 10 min to separate the plasma for lipid profile analysis and stored at −20 °C until further use. Liver tissues were weighed and rinsed in ice-cold saline. A 10% tissue homogenate was prepared using 0.025 M Tris–HCl buffer, pH 7.5. After centrifugation at 2000 rpm for 10 min, the clear supernatant was used for further biochemical assays. The plasma levels of low-density lipoprotein cholesterol (LDL-C), high-density lipoprotein cholesterol (HDL-C), triglycerides (TGs), total cholesterol (TC) by enzymatic colorimetric methods using kits (Nicholas Piramal India Ltd., Mumbai, India). Plasma amylase (cat. no. 84, Labtest® Minas Gerais, Brazil) and lipase (BioClin®, Minas Gerais, Brazil) were analyzed using the commercial kits. Plasma leptin and adiponectin (Crystal Chem, Downers Grove, IL, USA) was measured by enzyme-linked immunosorbent assay (ELISA) performed in duplicate and was expressed in ng mL^{-1}.

Liver antioxidant analysis

The liver was excised and rinsed in ice-cold normal saline and then in an ice-cold 10% KCl solution, blotted, dried, and weighed. A 10% w/v homogenate was prepared in the ice-cold KCl solution and centrifuged at 2000 rpm for 10 min at 4 °C. The supernatant thus obtained was used for the estimation of the levels of antioxidants. The level of thiobarbituric acid reactive substances (TBARS) and glutathione (GSH), the activities of superoxide dismutase (SOD), catalase (CAT), and glutathione peroxidase (GPx) in tissue were quantified using commercially available kits, purchased from Cayman Chemical Company, USA, following the manufacturer's instructions.

RT- PCR analysis

Total RNA was isolated from the liver tissue of the rats by using a combination of proteinase K, buffer component, RNX-Plus reagent, and high temperature according to the manufacturer's instructions. For cDNA synthesis, random hexamer (1 µL), Oligo (dT) (1 µL), and dNTP (1 µL) were used. Then, 10 µL RNA was added to each tube for 5 min at 65 °C and immediately placed at 4 °C. The other mixture, containing nuclease-free water (4.5 µL), M-MuLV 10× buffer (2 µL), and M-MuLV 200 U/µl (0.5 µL), was prepared in an Eppendorf tube, and added to the first tube. Final reaction volume was 20 µL and the next run duration was 60 min at 42 °C with the primers. The sequences of the primers were as follows: UCP 2, forward 5TAAAGCAGTTCTACA CCAAGGG-3 and reverse 5'CGAAGGCAGAAGTGAAGT GG-3,CPT-1,forward 5'TAGGACAGGCAGAAAATTGC3' and reverse 5CAGTAGGAGCCGATTCAAAA-3, ACC 1, forward F 5TCTATTCGGGGTGACTTTC3' and reverse 5' CTATCAGTCTGTCCAGCCC3. The housekeeping gene β-actin was used for normalization.

Western blot analysis

The liver of the rats were collected and lysed using a bead beater and centrifuged at 7000 rpm for 15 min at 4 °C. The suspension samples were collected, and 20 µL of each sample was loaded on a 6% sodium dodecyl sulfate gel and run for the HFD and treated groups (AA and orlistat). The gels were transferred from bands to polyvinylidene fluoride membrane using trans turbo gel transfer equipment. The primary antibodies anti-ACC (Ser79), anti-UCP 2 (ab67241), and anti CPT 1 (ab53532) were added, and the membrane developed blots which were analyzed using ChemiDoc equipment (ChemiDoc™, Bio-Rad Laboratories, Inc.).

Histopathological studies

Harvested liver tissues from the sacrificed animals were fixed in 10% neutral-buffered formalin solution, dehydrated in ethanol, and embedded in paraffin. Then, 5-µm thick sections were prepared using a rotary microtome and stained with hematoxylin and eosin dye for microscopic observations.

Statistical analysis

One-way ANOVA was used, and the results were expressed as mean ± standard deviation (SD). The least significant difference (LSD) test was also performed. The level of statistical significance was set at $p < 0.05$.

Results

Figure 2 depicts the changes in BW in the control and HFD groups during the experiment. The BW of the HFD group was significantly ($p < 0.05$) higher than that of the normal control group because of HFD intake for 42 days. The groups treated with orally administered AA (20 mg/kg BW) or orlistat exhibited a significantly ($p < 0.05$) lower increase in BW than the HFD control group did.

Table 2 depicts the levels of plasma glucose, plasma insulin, and insulin resistance in the control and experimental obese rats. A significant ($p < 0.05$) increase was observed in the levels of plasma glucose, plasma insulin, and insulin resistance in the HFD-fed rats. Oral supplementation of AA (20 mg/kg BW) or orlistat tended to bring the levels of blood glucose and plasma insulin toward near normal levels.

Figure 3 presents the level of oral glucose tolerance in the control and experimental obese rats. In the control rats,

COLLEGE OF ARTS & SCIENCE NAMAKKAL 637 206 P.G.P.

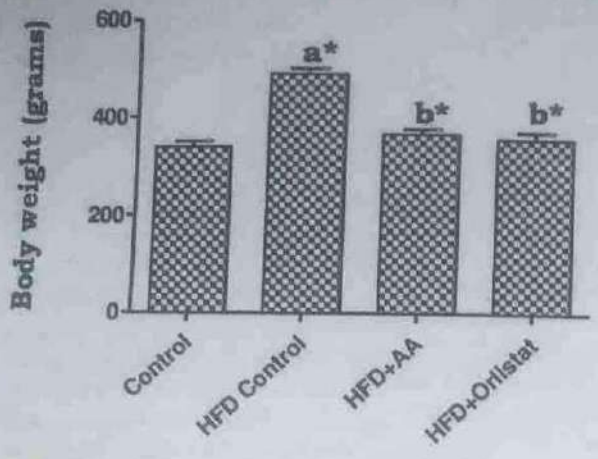


Fig. 2 Effect of AA on body weights of the control and experimental animals. Values are expressed as Mean ± SD for 6 animals in each group. Values are statistically significant at $^{*}p < 0.05$. [a]Significantly different from control. [b]Significantly different from HFD control

a significant increase was observed in the blood glucose level, and it reached the maximum value at 30 min after glucose load. Then, the levels declined to near basal levels at 120 min. However, in the HFD-induced obese rats, the blood glucose levels were at the maximum value even beyond 60 min after glucose load and remained high over the next 90 min. Oral administration of AA (20 mg/kg BW) or orlistat to obese rats resulted in a significant reduction in the blood glucose levels at 90 min compared with the HFD control rats.

Figure 4 depicts the levels of leptin and adiponectin in the control and experimental obese rats. A significant ($p < 0.05$) increase in leptin levels and decrease in adiponectin levels were observed in the HFD-induced obese rats compared with the control rats. Oral administration of AA (20 mg/kg BW) or orlistat reduced the levels of leptin and adiponectin to near normal levels.

The activities of amylase and pancreatic lipase of the normal and experimental obese rats are depicted in Fig. 5. The HFD-fed rats exhibited a significant increase ($p < 0.05$) in the activities of amylase and pancreatic lipases. Oral administration of AA (20 mg/kg BW) or orlistat to obese rats significantly reduced the activity of amylase and pancreatic lipase.

Figure 6 presents the lipid profiles of the control and HFD-induced obese rats. The levels of plasma and liver lipids were significantly higher in the experimental obese rats than in the normal rats. Oral administration of AA (20 mg/kg BW) or orlistat significantly ($p < 0.05$) reduced

Table 2 Effect of AA on the level of plasma glucose, plasma insulin, and insulin resistance in control and experimental obese rats

Group	Plasma glucose (mg dl^{-1})	Insulin (μU ml^{-1})	Insulin resistance
Normal control	80.24 ± 9.36	2.9 ± 0.89	5.1 ± 0.79
HFD control	167.36 ± 10.78[a*]	9.3 ± 1.67[a*]	8.5 ± 1.04[a*]
HFD + AA	119.32 ± 9.99[b*]	5.3 ± 0.49[b*]	5.8 ± 0.69[b*]
HFD + Orlistat	114.89 ± 10.23[b*]	4.7 ± 0.79[b*]	4.6 ± 0.77[b*]

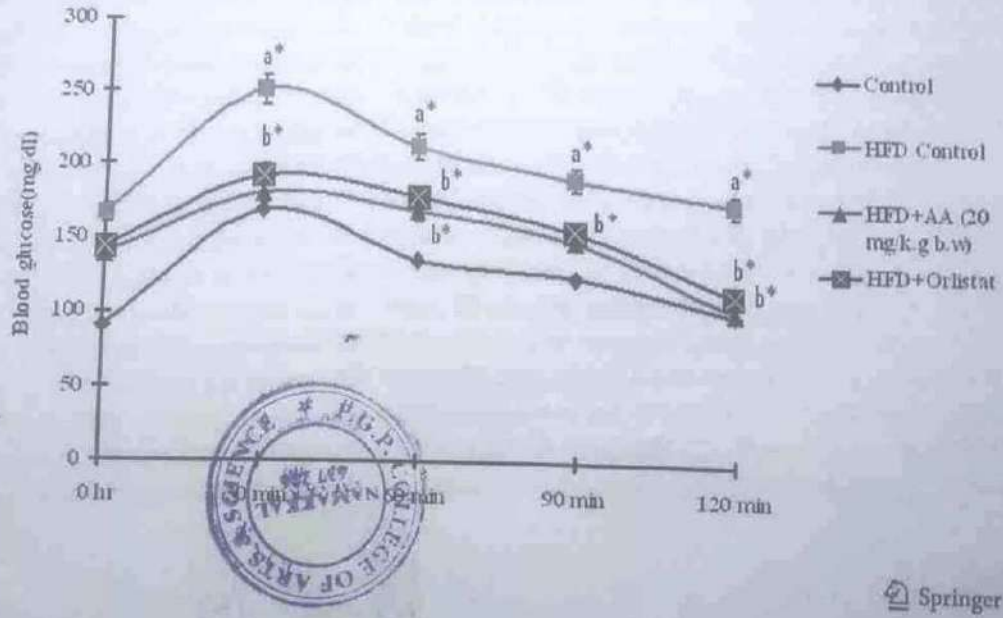
Values are expressed as Mean ± SD for 6 animals in each group

Values are statistically significant at $^{*}p < 0.05$

[a]Significantly different from control

[b]Significantly different from HFD control

Fig. 3 Effect of AA on Oral glucose tolerance test (OGTT) in control and experimental rats. Values are expressed as Mean ± SD for 6 animals in each group. Values are statistically significant at $^{*}p < 0.05$. [a]Significantly different from control. [b]Significantly different from HFD control



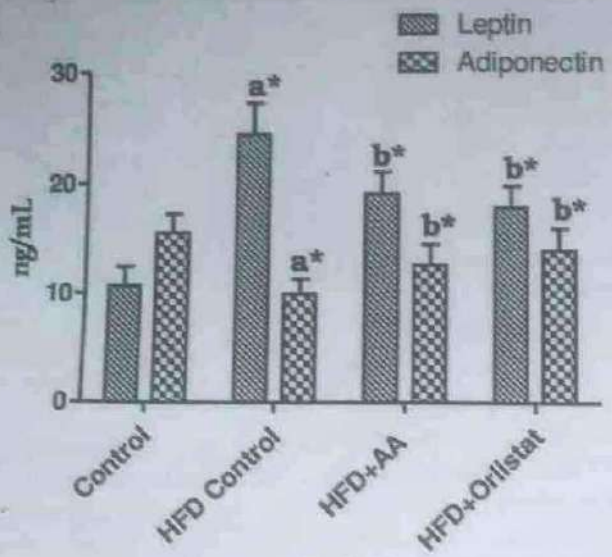


Fig. 4 Effect of AA on the level of leptin and adiponectin in control and experimental obese rats. Values are expressed as Mean ± SD for 6 animals in each group. Values are statistically significant at $^{*}p < 0.05$. [a]Significantly different from control. [b]Significantly different from HFD control

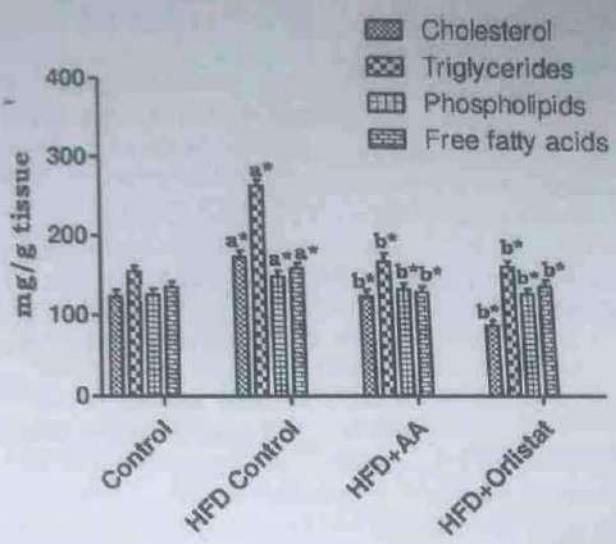


Fig. 6 Effect of AA on the levels of lipid profile in control and HFD-induced obese rats. Values are expressed as Mean ± SD for 6 animals in each group. Values are statistically significant at $^{*}p < 0.05$. [a]Significantly different from control. [b]Significantly different from HFD control

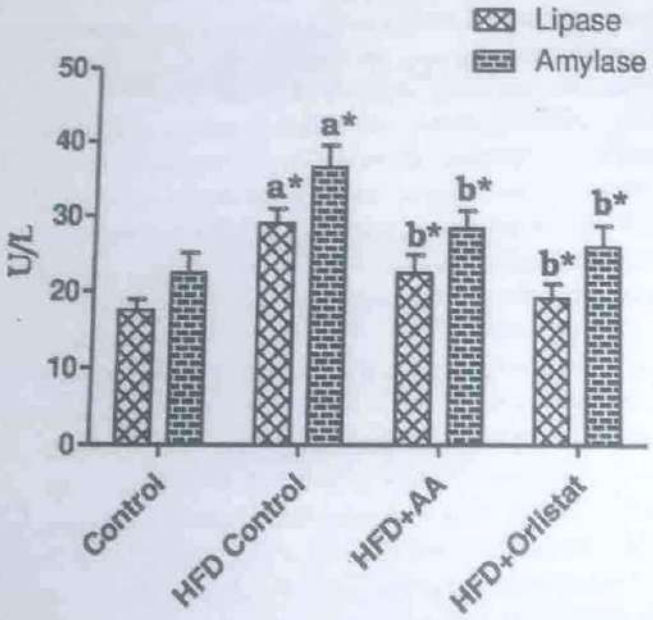


Fig. 5 Effect of AA the activities of the amylase and pancreatic lipase of normal and experimental obese rats. Values are expressed as Mean ± SD for 6 animals in each group. Values are statistically significant at $^{*}p < 0.05$. [a]Significantly different from control. [b]Significantly different from HFD control

the levels of plasma and liver lipids in obese rats to near normal levels.

Table 3 lists the levels of TBARS and activities of GSH, SOD, CAT, and GPx in the livers of the control and HFD-induced experimental obese rats. A considerable decrease in the activities of GSH, SOD, CAT, and GPx and a concomitant increase in the level of TBARS were observed in the HFD-induced experimental obese rats. Treatment with AA or orlistat considerably increased the activities of SOD, CAT, and GPx and reduced the levels of TBARS in livers of treated animals.

Figure 7 and a depicts the mRNA levels of CPT 1, UCP 2 and ACC 1 in the tissues of the control and experimental obese rats. Significantly ($p < 0.05$) lower levels of CPT 1 and UCP 2 mRNA and a concomitant increase in the levels of ACC 1 mRNA were observed in the tissues of the HFD control rats compared with the normal control rats. AA (20 mg/kg BW) or orlistat administration (oral) significantly ($p < 0.05$) increased the activity of CPT 1 and UCP 2 and reduced the activity of ACC 1 in the tissues of the treated obese rats. Figure 7b depicts the expression of the proteins CPT 1, UCP 2, and ACC 1 in the tissues of the control and experimental obese rats. Western blot analysis of these proteins revealed that the alterations in protein expression were normalized after treatment with AA or orlistat, and these results were supported by mRNA expression studies.

The group of ND-fed control rats exhibited normal histological architecture (Fig. 8a). Significant hepatic steatosis was observed along with severe swelling of the hepatic cells. Fat accumulation was observed in the livers of the HFD-fed rats (Fig. 8b). Treatment with AA or orlistat resulted in the prevention of hepatic fat deposition in hepatocytes and,

Table 3 Effect of AA on the level of antioxidants profile in control and experimental obese rats

	Control	HFD	HFD + AA	HFD + Orlistat
TBARS (mM/100 g tissue)	25.37 ± 1.89	50.42 ± 2.67^{a*}	29.90 ± 2.01^{b*}	26.74 ± 1.99^{b*}
GSH (mg/100 mg tissue)	9.87 ± 1.01	3.89 ± 1.36^{a*}	8.05 ± 1.90^{b*}	8.74 ± 1.68^{b*}
SOD (U/mg protein)	8.56 ± 1.67	4.12 ± 1.78^{a*}	7.53 ± 1.89^{b*}	8.01 ± 1.45^{b*}
CAT (U/mg protein)	16.67 ± 2.03	9.12 ± 2.67^{a*}	14.97 ± 1.90^{b*}	15.47 ± 1.36^{b*}
GPx (U/mg protein)	12.90 ± 1.61	7.67 ± 1.22^{a*}	11.76 ± 1.56^{b*}	11.99 ± 1.78^{b*}

Values are expressed as Mean ± SD for 6 animals in each group

Values are statistically significant at $^{*}p < 0.05$

[a]Significantly different from control

[b]Significantly different from HFD control

reduced most of the pathological alterations induced by HFD in the rats (Fig. 8c, d).

Discussion

Diet-induced obesity (DIO) in animals shares many features with human obesity; hence, it is widely used to identify medicinal foods for alleviating obesity. Prolonged feeding with fat-enriched diets increases in the BW in liable rats in the range of 10–20% compared with standard chow-fed controls. Although HFDs produced from animals and plant fats do not exhibit consistent differences because of fat-type effects, some authors have described obesity resistance and less hypertrophy of visceral fat pads when diets produced from fish oil are used. According to the literature, semi-purified diets with a fat content of 40% produced using animal fats and plant oils that contain ω-6/ω-9 fatty acid cause insulin resistance and obesity, whereas diets with large amounts of ω-3-fatty acids do not. However, given the plethora of dietary regimes described in the literature, characterizing a single all encompassing HF diet composition is difficult. Furthermore, diets theoretically composed of identical fat types might yield diverse results because of inherent differences among the primary fat sources and among various diet preparation methods [13].

The signs of DIO are insulin resistance, changes in body weight composition, impaired glucose tolerance, and abnormal levels of lipids [2]. In the present study, increased BW and fat were observed in HFD-fed rats. Long-term HFD intake results in increased bodyweight and plasma comorbidity factors [14]. These effects might occur because of the consumption of an energy-rich diet in the form of saturated fats (lard) and its accretion in different body fat pads [15], thus leading to an excessive development of the adipose tissue. Furthermore, the ratio of calorie ingestion to energy utilization determines the bodyweight. In this study, HFD provided a total energy content of 17.03 kJg^{-1}. Thus, compared with the ND, the HFD was hypercaloric. The HFD contained less carbohydrate but more lipids than the ND, with a net energy difference of 4.37 $kJ\ g^{-1}$. Comparable effects have been reported in previous animal studies in which obesity was induced using high-fat rodent diets having similar sources of fat as the HFD in the current study and a similar experimental length to the current study [2]. The HFD-fed rats treated with AA exhibited a significantly lower BW increase than the HFD control rats did. In the present study, AA apparently did not suppress feeding in the HFD-fed rats (data not shown). Hence, the AA-induced weight loss involves a mechanism that is independent of hypophagia. The relatively low BW gain may be caused by numerous mechanisms including unusual food assimilation, decreased body energy storage, and the reduction in the degree of BW gain [14].

The supplementation of an HFD for a period of 30 days caused hyperglycemia, as shown by the increased levels of plasma glucose, plasma insulin, and insulin resistance [16]. In the current study, the HFD with 58% calories as fat, caused insulin resistance in rats over a short period of time. Therefore, HFD intake for a period of 30 days causes insulin resistance syndrome and increased BW (obesity), hypertriglyceridemia, and mild hyperglycemia [17]. HFD-fed rats may be susceptible to insulin resistance because the receptor cells are blocked by fat deposits; consequently, diabetes becomes evident. In the present study, we found that the HFD-fed rats clearly exhibited hyperglycemia in the presence of similar amounts of plasma insulin concentrations as the normal controls. These rats also exhibited the persistence of insulin resistance. In the present study, a significant increase in the fasting blood levels of glucose and insulin, insulin resistance, and BW gain was observed in the HFD-fed rats compared with the normal control rats. This effect might be due to HFD intake [17]. Moderate hepatic and muscular uptake of glucose caused hyperlipidemia because of increased fat mobilization from the adipose tissue and resistance to the anti-lipolytic action of insulin. Impaired insulin function is related to an excessive intake of lipids. Although HFDs have been reported to induce insulin resistance through

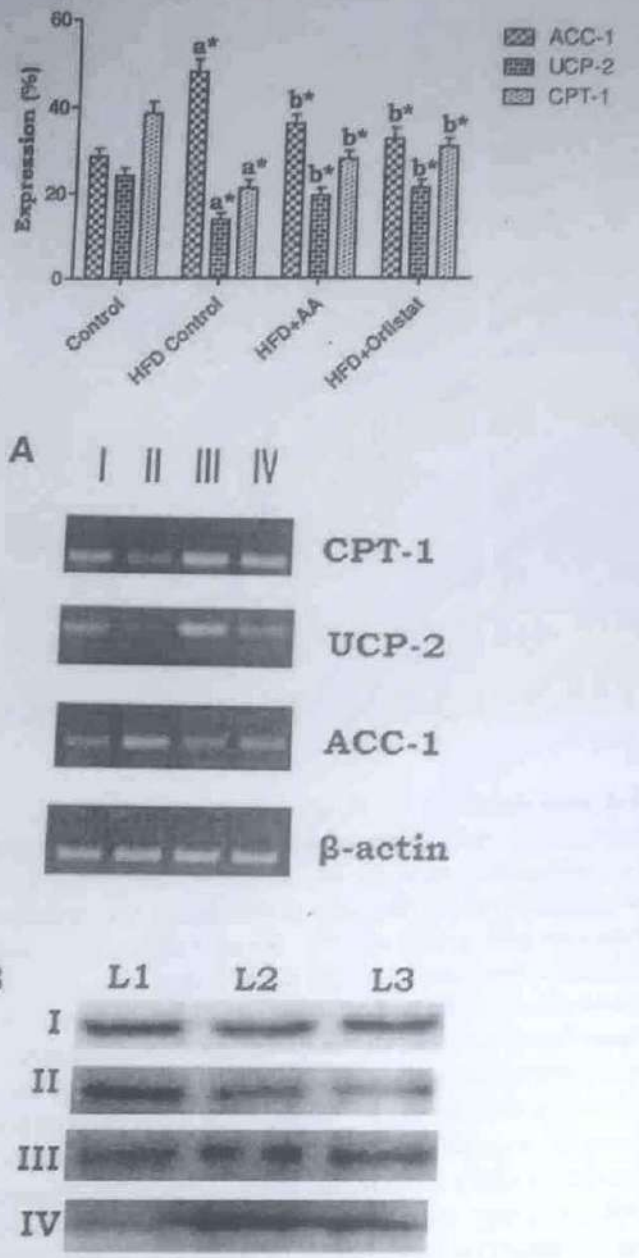


Fig. 7 Effect of AA on the mRNA levels of CPT-1, UCP-2, and ACC-1 in tissues of control and experimental obese rats. a CPT-1, UCP-2, and ACC-1 mRNA expressions. Values are expressed as Mean ± SD for 6 animals in each group. Values are statistically significant at $^{*}p < 0.05$. [a]Significantly different from control. [b]Significantly different from HFD control. b Western blot analysis of CPT-1, UCP-2, and ACC-1 protein expressions in control and experimental groups. I: Normal control; II: HFD control; III: HFD + AA; IV: HFD + Orlistat. L1: ACC; L2: UCP 2; L3: CPT 1

different mechanisms, the resistance is mainly considered to involve the Randle or glucose–fatty acid cycle [18].

HFD supplementation is demonstrated by increased TG and TC levels. Accordingly, a variation in lipid profiles can be used as an index of obesity. In the present study, HFD intake increased the lipid profile in the experimental obese rats. In addition, the modifications in the lipid profile induced by HFD might involve lipolysis, intestinal fat absorption, and the activation of gastric lipases. High TC levels increase the risk of coronary heart disease. A high LDL-C level is a risk factor for coronary heart disease, whereas a high HDL-C level facilitates the transport of excess cholesterol to the liver for excretion in the bile [19]. The increase in TG level caused by dietary cholesterol was shown to reduce fatty acid oxidation, which in turn increases the levels of hepatic and plasma triglycerol [20].

Obesity is accountable for the escalating occurrence of metabolic disease. In the body, the adipose tissue is a key site of energy storage and is crucial for energy homeostasis [15]. It is well known that insulin can ultimately stimulate leptin secretion during the metabolism of nutrients, particularly during glucose utilization in adipocytes. Hyperlipidemia, hyperglycemia, insulin resistance, impaired glucose metabolism, distinctive visceral adiposity, hyperinsulinemia, and decreased bone mineral concentration and bone mineral density are the common characteristics of DIO in rodents. In the present study, HFD treatment to the experimental animals confirmed obesity as evidenced by the increased BW, hyperglycemic condition, and increased insulin resistance [21]. Under physiological conditions, insulin enhances lipogenesis and inhibits lipolysis leading to increased circulating levels of glucose and lipids, thus resulting in impaired glucose-stimulated insulin secretion [22]. HFD is intimately associated with the development of obesity by active adipocytes; HFD results when the adipocytes incorporate glucose and free fatty acids (FFAs) to synthesize and accumulate TG to store energy [23]. In the present study, we observed that AA treatment reduced plasma insulin level, suggesting that AA could improve insulin resistance in the experimental animals. AA promotes insulin sensitivity, thus lowering insulin resistance and reducing glucose levels in obese rats, perhaps by controling the cell energy metabolism or reducing the storage of FFAs. Evidence substantiates that AA considerably lowered blood glucose levels in rats with streptozocin-induced diabetes where asiatic acid preserved β-cell death and promoted their proliferation [24]. Furthermore, administration of AA significantly improved glucose homeostasis in a metabolic syndrome such as diabetes [11].

The adipose tissue is the primary site of fat accumulation. Accumulation of excessive fat in the adipocytes is the fundamental observable symptom for obesity. Adipose tissue secretes numerous adipokines including leptin, adiponectin, resistin, visfatin, tumor necrosis factor, and interleukin-6 which participate in energy regulation [25]. Leptin and adiponectin secreted by adipocytes are believed to play prominent roles in controling metabolic homeostasis. Reduced plasma adiponectin levels were observed in obese animals and, the low levels was positively connected

P.G.P. COLLEGE OF ARTS & SCIENCE NAMAKKAL 637 206

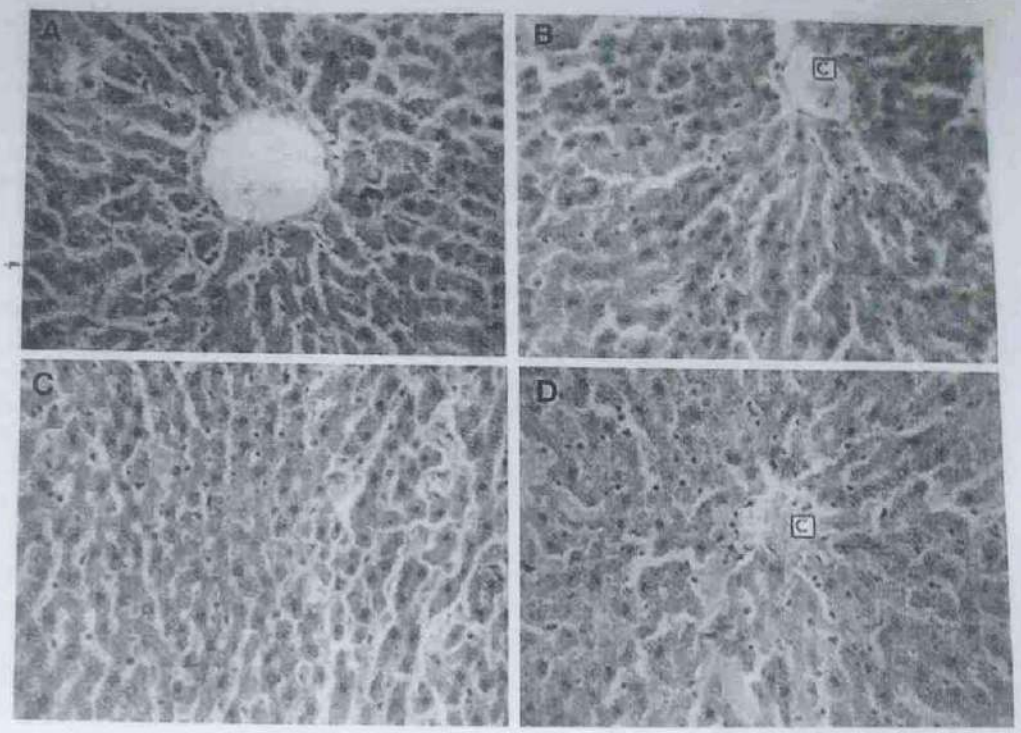


Fig. 8 Effect of AA in Liver of control and experimental obese rats. **a** (*Normal Control*) Rats administrated normal diet showed normal histological architecture; H&E, X40. **b** (*HFD Control*): Hepatic steatosis was observed along with severe swelling in hepatic cells and also fat accumulation was observed in the livers of HFD-fed rats; H&E, X40. **c** (*HFD + AA*), **d** (*HFD + Orlistat*) Treatment with AA and Orlistat reduced most of the pathological alterations induced by HFD in rats; H&E, X40

to HDL-C levels [1]. Leptin, a circulating fat-derived protein produced by the fat tissue, plays a fundamental role in controlling BW by restraining food intake and improving energy consumption. Leptin resistance is a feature of DIO, in which the blood leptin levels diminish and do not respond to target tissues (example, fat tissue, muscles, liver, and hypothalamus). Adipocytes secrete leptin in direct proportion to adipose tissue mass as well as nutritional status [26], where as adiponectin is inversely correlated with body mass [27]. During the development of obesity, elevated levels of leptin and concomitantly decreased levels of adiponectin are observed [27, 28]. Leptin secretion is positively interrelated with the extent of the TG stores in adipocytes [29]. In the present study, increased leptin and decreased adiponectin levels were observed in the plasma of HFD control group compared with the control group. Treatment with AA lowered leptin and enhanced adiponectin in the plasma of the experimental rats. A few polyphenols have been reported to affect lipid catabolism and diminish insulin resistance which are fundamental to obesity [30]. These observations suggest that the decreased leptin and increased adiponectin levels after AA supplementation may have ameliorated insulin resistance in obese rats, thus resulting in decreased plasma lipid levels and weight loss [31].

Amylase and lipase, the key catalysts in carbohydrate and lipid metabolism, are the focus for developing medication outlines for treatment of some metabolic disorders. Pancreatic lipase, the principal lipolytic enzyme secreted from the pancreas, hydrolyzes dietary fat into fatty acid and 2-monoacylglycerol. Inhibition of this digestive enzyme is accordingly useful in the treatment of overweight patients [1]. α-amylase, one of the key digestive compounds discharged from the pancreas and salivary organs, is included in hydrolytic process of starch [32]. Because dietary lipids and sugars constitute the major source of undesirable calories, the hindrance of fat and carbohydrate digestion is a novel methodology for reducing fat absorption. Activating lipase or inhibiting pancreatic lipase would have an anti-obesity effect. Lowered pancreatic amylase discharge reduces the assimilation of carbohydrates by suppressing their processing, thus resulting in decreased energy intake [33]. Various exploratory reports have reported that α-amylase inhibitors, most of which are extricated from plants, can reduce postprandial hyperglycemia, thus regulating abnormal glucose metabolism and countering metabolic disorders [34]. In the present study, pancreatic lipase and amylase levels increased in HFD-induced obese rats. Oral supplementation of AA inhibited the activity of pancreatic lipase and α-amylase in the treated rats compared with HFD control rats. The minimized levels of pancreatic amylase and lipase may represent a component that impedes the assimilation and ingestion of starches and lipids, which in turn, can reduce the caloric admission in AA-treated HFD-fed obese rats, to enhance weight reduction.

Obesity, particularly abdominal obesity, is an independent risk factor that increases cardiovascular disease risk and overall mortality and warrants medical attention [35]. The HFD-induced obese rats exhibited anomalies in

COLLEGE OF ARTS & SCIENCE NAMAKKAL P.G.P.

plasma and tissue biomarkers that mimic the commencement of a group of metabolic risks including abnormalities in lipid profile. HFD-induced obesity is associated with increasing levels of TGs, very low-density lipoproteins (VLDLs), TC, phospholipids (PLs), FFAs, and a decrease in plasma levels of HDL [36]. In the present study, lipid-level abnormalities such as elevated TGs, VLDLs, TC, PL, FFA, and LDL, and reduced plasma levels of HDL were observed. These findings was supported by Park et al. [37]. During the fed state, elevation of chylomicrons is a typical element which causes an increase in the levels of TC, TGs, and endogenous VLDL generation. The increased release of FFAs from fat tissue to different tissues increases, primarily to the liver during obesity [38], and it might be because of the increment of leptin resistance. The increase in the level of TGs was because of dietary cholesterol that had appeared to reduce unsaturated fat oxidation, which thus expanded the levels of hepatic and plasma TG and caused the excessive accumulation of TGs in the lipid stores [2]. The elevated level of phospholipids in this present study was probably due to the elevated levels of FFA and TC that can enhance the production of PLs. The elevated PL level in the present study may be because of the elevated levels of FFA [36] and an increase in cholesterol levels that can support the generation of phospholipids. High TC levels intensify the risk of coronary heart disease by increasing LDL-C levels. However, high HDL-C levels facilitate the transport of surplus cholesterol to the liver for excretion in the form of bile [39]. Oral supplementation of AA significantly lowered the levels of TC, TGs, FFAs, and PLs in both serum and liver and the LDL-C levels in the serum of the rats with HFD-induced obesity. Yongqi et al. [40] reported that supplementation of phytoconstituents to fed animals leads to a hypolipidemic state by reducing cholesterol absorption and secretion from the intestine, which leads to the reduced availability of FFAs to the liver. Our finding is consistent with this report.

The liver is considered one of the vital metabolic organs in the body, regulating and maintaining lipid homeostasis. Insulin deficit causes various disturbances in regulatory and metabolic processes [35], which in turn cause accumulation of lipids in the liver. In obesity, the liver stores excess amounts of fatty acids and after esterification with glycerol phosphate, the fatty acids are deposited as TG. This leads to a reduction in insulin-mediated metabolic activity and can cause diabetes, which ensues in metabolic syndrome [41]. The increase in the liver cholesterol levels of obese rats observed in our study could be due to decreased removal of cholesterol from the extra hepatic tissues by HDL cholesterol and also increased cholesterogenesis [19]. Treatment of obese rats with AA and orlistat showed a decrease in the liver cholesterol and TG levels. This may be due to enhanced clearance and also the decreased production of the major transporters of endogenously synthesized cholesterol and triglycerides; thus, AA exhibited hepatoprotective effects.

Oxidative damage in cells is invariably associated with disturbances in multiple non-enzymatic and enzymatic antioxidant protection systems present in the cells [42]. Enzymatic antioxidants such as CAT, GPx, and SOD synergistically prevent lipid peroxidation and scavenge reactive oxygen species. SOD, the natural antioxidant enzyme in cells, plays a crucial role in oxygen defense metabolism by intercepting and reducing the superoxide radical to hydrogen peroxide [43]. CAT, a heme-containing omnipresent enzyme, is well known to be involved in the detoxification of high hydrogen peroxide concentrations and defending the tissues from highly reactive hydroxyl radicals. GPx, a selenium-containing tetrameric glycoprotein, occurs in high concentrations in cells. It detoxifies hydrogen peroxide into molecular oxygen and water through the oxidation of reduced GSH [44]. GPx has been revealed to be a significant adaptive response to a state of prolonged peroxidative stress [45]. Previous studies have demonstrated that through obesity induced by HFD, enzymatic antioxidant levels were noticeably reduced. In the current study, lower hepatic GPx, CAT, and SOD activities were observed in HFD-fed rats than in the control rats. This is consistent with the results of Brahmanaidu et al. [46], who demonstrated relatively low levels of antioxidant enzymes in HFD-fed animals which might result from high production of free radicals. Administration of AA significantly enhanced GPx, SOD, and CAT activities and diminished TBARS [47] levels in HFD-fed rats. This finding indicates the potential of AA as an effectual inhibitor of the oxidative stress induced by HFD.

Obesity is connected with lipid accretion not only in the adipose tissues but also in non-adipose tissues, such as the liver and skeletal muscles [48]. Skeletal muscles are the chief sites of fatty acid catabolism and abnormal fat accumulation in the skeletal muscle causes metabolic disorders including overweight. CPT 1 and UCP 2 act as the rate-limiting enzyme for β-oxidation and main regulator of thermogenesis, respectively [49]. ACC 1 is the first and rate-limiting enzyme in the peroxisomal β-oxidation pathway [50]. Fatty acids are transformed to acetyl CoA through mitochondrial oxidation. Fatty acid oxidation is inhibited by dephosphorylated AMPK. PPARγ is known to be activated by SREBP1c, which leads to reduced FFA oxidation [51, 52]. In the present study, the elevated expression of ACC 1 and concomitantly reduced expression of CPT 1 and UCP 2 were observed in HFD-induced obese rats. Oral administration of AA altered the expression of ACC 1, CPT 1, and UCP 2 to near normal. These results were also supported by the western blot analysis results. Moreover, AA restored the PPAR-γ downstream genes CPT 1 and UCP 2, contributing systematically to energy catabolism. Thus, the findings imply that treatment with AA can reduce DIO by

promoting lipid oxidation through activation of PPAR-γ and its downstream genes.

In the present study, the histopathological examinations of the livers of HFD-fed rats revealed microvesicular steatosis in the hepatocytes. Notably, treatment with AA and orlistat reduced most of the pathological alterations induced by HFDs in rats because it reduced hepatic lipid accumulation, which resulted from both decreased lipogenesis and increased fatty acid oxidation. Therefore, AA has potential therapeutic use as a nutraceutical ingredient for the prevention of obesity and hyperlipidemia.

In conclusion, our results suggest that dietary supplementation of asiatic acid extracted from *C. asiatica* considerably reduces the increase in BW and fat percentage in HFD-induced obese rats by altering lipid metabolic markers. Hence, these results strongly suggest that asiatic acid has therapeutic potential for the management of obesity and hyperlipidemia and for the prevention of cardiovascular diseases.

Acknowledgements The authors thank Muthyammal College of Arts and Science, Rasipuram, Tamilnadu, India, for providing facilities to do animal studies and also express heartfelt thanks to the management of K. S. Rangasamy College of Arts and Science, Tiruchengode, Tamilnadu, for their support and encouragement.

Compliance with ethical standards

Conflict of interest The authors declare no conflict of interest.

Ethical approval All procedures involving laboratory animals were in accordance with the guidelines of Committee for the purpose of control and supervision of experiments on animals (CPCSEA), Government of India, and institutional animal ethical committee of Muthyammal College of Arts and Science (Approval No: IAEC/MCAS/05/2016).

References

1. Despres JP (2012) Body fat distribution and risk of cardiovascular disease: an update. Circulation 126:1301–1313
2. Saravanan G, Ponmurugan P, Deepa MA, Senthilkumar B (2014) Anti-obesity action of gingerol: effect on lipid profile, insulin, leptin, amylase and lipase in male obese rats induced by a high-fat diet. J Sci Food Agric 94:2972–2977
3. Ferranti S, Mozaffarian D (2008) The perfect storm: obesity, adipocyte dysfunction, and metabolic consequences. Clin Chem 54:6945–6955
4. Jindal A, Brietzke S, Sowers JR (2012) Obesity and the cardiorenal metabolic syndrome: therapeutic modalities and their efficacy in improving cardiovascular and renal risk factors. Car Ren Med 2(4):314–327
5. George M, Rajaram M, Shanmugam E (2014) New and emerging drug molecules against obesity. J Cardiovasc Pharmacol Ther 19(1):65–76
6. Colagiuri S (2010) Diabesity: therapeutic options. Diabetes Obes Metab 12:463–473
7. Kishino E, Ito T, Fujita K, Kiuchi Y (2006) A mixture of the Salacia reticulata (Kotala himbutu) aqueous extract and cyclodextrin reduces the accumulation of visceral fat mass in mice and rats with high-fat diet-induced obesity. J Nutr 136:433–439
8. Zhao Y, Shu P, Zhang Y, Lin L (2014) Effect of Centella asiatica on oxidative stress and lipid metabolism in hyperlipidemic animal models. Oxid Med Cell Longev 154:1–7
9. Huang SS, Chiu CS, Chen HJ, Hou WC, Sheu MJ, Lin YC, Shie PH, Huang GJ (2011) Antinociceptive activities and the mechanisms of anti-inflammation of asiatic acid in mice. Evid Based Complement Altern Med. doi:10.1155/2011/895857
10. Ramachandran V, Saravanan R, Senthilraja P (2014) Antidiabetic and antihyperlipidemic activity of asiatic acid in diabetic rats, role of HMG CoA: in vivo and in silico approaches. Phytomed 212:225–232
11. Ramachandran V, Saravanan R (2013) Asiatic acid prevents lipid peroxidation and improves antioxidant status in rats with streptozotocin-induced diabetes. J Funct Foods 5:1077–1087
12. Ji W, Zhao M, Wang M, Yan W, Liu Y, Ren S (2017) Effects of canagliflozin on weight loss in high-fat diet-induced obese mice. PLoS ONE 12(6): e0179960. http://doi.org.ololo.sci-hub.cc/10.1371/journal.pone.0179960
13. Buettner R, Schölmerich J, Bollheimer LC (2007) High-fat diets: modeling the metabolic disorders of human obesity in rodents. Obesity 15:798–808
14. Naidu PB, Uddandrao VS, Naik RR, Suresh P, Meriga B, Begum MS, Pandiyan R, Saravanan G (2016) Ameliorative potential of gingerol: promising modulation of inflammatory factors and lipid marker enzymes expressions in HFD induced obesity in rats. Mol Cell Endocrinol 419:139–147
15. Oben J, Kuate D, Agbor G, Momo C, Talla X (2006) The use of a Cissus quadrangularis formulation in the management of weight loss and metabolic syndrome. Lip Heal Dis 5:24
16. Srinivasan K, Patole PS, Kaul CL, Ramarao P (2004) Reversal of glucose intolerance by pioglitazone in high-fat diet fed rats. Exp Clin Pharmacol 26:327–333
17. Naidu PB, Ponmurugan P, Begum MS, Mohan K, Meriga B, Naik RR, Saravanan G (2015) Diosgenin reorganises hyperglycaemia and distorted tissue lipid profile in high-fat diet–streptozotocin-induced diabetic rats. J Sci Food Agric 95:3177–3182
18. Randle PJ, Garland PB, Hales CN, Newsholme EA (1963) The glucose fatty-acid cycle. Its role in insulin sensitivity andmetabolic disturbances in diabetes mellitus. Lancet 1:785–789
19. Saravanan G, Ponmurugan P (2012) Ameliorative potential of S-allylcysteine: effect on lipid profile and changes in tissue fattyacid composition in experimental diabetes. Exp Toxicol Pathol 64:639–644
20. Fungwe TV, Cagen LM, Cook GA (1993) Dietary cholesterol stimulated hepatic biosynthesis of triglyceride and reduces oxidation of fatty acids in the rat. J Lipid Res 34:933–941
21. Kim Y, Park T (2008) Genes are differentially expressed in the epididymal fat of rats rendered obese by a high-fat diet. Nutr Res 28:414–422
22. Zhou CJ, SongHuang JQ (2013) Sweet tea leaves extract improves leptin resistance in diet-induced obese rats. J Ethnopharm 145:386–392
23. Manuel TV, Sam JB (2007) Role of dietary so y protein in obesity. Int J Med Sci 4:72–82
24. Liu J, He T, Lu Q, Shang J, Sun H, Zhang L (2010) Asiatic acid preserves β cell mass and mitigates hyperglycemia in streptozocin-induced diabetic rats. Diabetes Metab Res Rev 26:448–454
25. Garg A (2006) Adipose tissue dysfunction in obesity and lipodystrophy. Clin Cornerstone 8:7–13
26. Cnop M, Landchild MJ, Vidal J, Havel PJ, Knowles NG, Carr DR (2002) The concurrent accumulation of intra-abdominal and subcutaneous fat explains the association between

COLLEGE OF ARTS & SCIENCE NAMAKKAL 637 206.

insulin resistance and plasma leptin concentrations. Diabetes 51:1005–1015
27. Arita Y, Kihara S, Ouchi N (1999) Paradoxical decrease of an adipose-specific protein, adiponectin in obesity. Biochem Biophys Res Commun 257:79–83
28. Kamohara S, Burcelin R, Halaas JL, Friedman JM, Charron MJ (1997) Acute stimulation of glucose metabolism in mice by leptin treatment. Nature 389:374–377
29. Staiger H, Haring HU (2005) Adipocytokines: fat-derived humoral mediators of metabolic homeostasis. Exp Clin Endocrinol Diabetes 113:67–79
30. Crozier A, Jaganath IB, Clifford MN (2009) Dietary phenolics: chemistry, bioavailability and effects on health. Nat Prod Rep 26:1001–1043
31. Ono Y, Hattori E, Fukaya Y, Imai S, Ohizumi Y (2006) Anti-obesity effect of Nelumbo nucifera leaves extract in mice and rats. J Ethnopharm 106:238–244
32. Nakajima K, Muneyuki T, Munakata H (2011) Revisiting the cardiometabolic relevance of serum amylase. BMC Res Not 4:419
33. Tundis R, Loizzo MR, Menichini F (2010) Natural products as alpha-amylase and alpha-glucosidase inhibitors and their hypoglycaemic potential in the treatment of diabetes: an update. Mini Rev Med Chem 10:315–331
34. Layer P, Rizza RA, Zinsmeister AR, Carlson GL, DiMagno EP (1986) Effect of a purified amylase inhibitor on carbohydrate tolerance in normal subjects and patients with diabetes mellitus. Mayo Clin Proce 61:442–447
35. Naidu PN, Uddandrao VS, Sasikumar V, Naik RR, Pothani S, Begum MS, Varatharaju C, Meriga B, Kalaivani A, Saravanan G (2017) Reversal of endothelial dysfunction in aorta of streptozotocinnicotinamide-induced type-2 diabetic rats by S-Allylcysteine. Mol Cell Biochem. doi:10.1007/s11010-017-2994-0
36. Jin D, Xua Y, Mei X (2013) Antiobesity and lipid lowering effects of theaflavins on high-fat diet induced obese rats. J Funct Foods 5:1142–1150
37. Park Y, Storkson JM, Liu W, Albright J, Cook ME, Pariza MW (2004) Structure–activity relationship of conjugated linoleic acid and its cognates in inhibiting heparin-releasable lipoprotein lipase and glycerol release from fully differentiated 3T3-L1 adipocytes. J Nutr Biochem 15:561–569
38. Torre-Villalvazo I, Tovar AR, Ramos-Barragan VE, Cerbon-Cervantes MA, Torres N (2008) Soy protein ameliorates metabolic abnormalities in liver and adipose tissue of rats fed a high fat diet. J Nutr 138:462–468
39. Garjani A, Fathiazad F, Zakheri A, Akbari NA, Azarmie Y (2009) The effect of total extract of Securigera securidaca L. seeds on serum lipid profiles, antioxidant status, and vascular function in hypercholesterolemic rats. J Ethnopharm 126:525–532
40. Yongqi G, Guanzhong W, Xin S, Hongxia Y, Juan Z (2009) Antiobesity action of a daidzein derivative on male obese mice induced by a high-fat diet. Nutr Res 29:656–663
41. Moller DE (2001) New drug targets for type 2 diabetes and the metabolic syndrome: a review. Nature 414:821–827
42. Uddandrao VS, Brahmanaidu P, Saravanan G (2016) Therapeutical perspectives of S-allylcysteine: effect on diabetes and other disorders in animal models. Car Hem Age Med Chem. doi:10.2174/1871525714666160418114120
43. Winterbourn CC (1995) Concerted antioxidant activity of glutathione and superoxide dismutase. In: Packer L, Fuchs J (eds) Biothiols in health and disease. Marcel Dekker Inc, New York, pp 117–134
44. Saravanan G, Ponmurugan P (2011) Ameliorative potential of S-allylcysteine on oxidative stress in STZ induced diabetic rats. Chem Biol Interact 189:100–106
45. Uddandrao VS, Brahmanaidu P, Meriga B, Saravanan G (2016) The potential role of S-allylcysteine as antioxidant against various disorders in animal models. Oxid Antioxid Med Sci 5(3):79–86
46. Naidu PB, Harishankar N, Meriga B, Pothana S, Sajjalaguddam RR (2015) Effects of Piper nigrum extracts: Restorative perspectives of high-fat diet-induced changes on lipid profile, body composition, and hormones in Sprague-Dawley rats. Pharm Biol 53(9):1318–1328
47. Naidu PB, Uddandrao VS, Pothani S, Naik RR, Begum MS, Varatharaju C, Pandiyan R, Saravanan G (2016) Effects of S-allylcysteine on biomarkers of polyol pathway in experimental type II diabetes in rats. Can J Diabetes 40:442–448
48. Van Herpen NA, Schrauwen-Hinderling VB (2008) Lipid accumulation in non-adipose tissue and lipotoxicity. Physiol Behav 94:231–241
49. Harbilas D, Braulta A, Valleranda D (2012) Populus balsamifera L. (Salicaceae) mitigates the development of obesity and improves insulin sensitivity in a diet-induced obese mouse model. J Ethnopharm 141:1012–1020
50. Wanga LJ, Zhang HW, Zhoua JY (2014) Betaine attenuates hepatic steatosis by reducing methylation of the MTTP promoter and elevating genomic methylation in mice fed a high-fat diet. J Nutr Biochem 25:329–336
51. Andrews ZB, Erion DM, Beiler R, Choi CS, Shulman GI, Horvath TL (2010) Uncoupling protein-2 decreases the lipogenic actions of ghrelin. Endocrinology 151:2078–2086
52. Ferre P, Foufelle F (2010) Hepatic steatosis: a role for de novo lipogenesis and the transcription factor SREBP-1c. Diabetes Obes Metab 12:83–92

COLLEGE OF ARTS & SCIENCE NAMAKKAL 637 206 P.G.P.
PRINCIPAL
PGP College of Arts and Science
Namakkal

4:51 • www.tandfonline.com

Log in | Register

Archives of Physiology and Biochemistry >
The Journal of Metabolic Diseases
Latest Articles

100 Views | 6 CrossRef citations to date | 0 Altmetric

ORIGINAL ARTICLE

Biochanin A attenuates obesity cardiomyopathy in rats by inhibiting oxidative stress and inflammation through the Nrf-2 pathway

Jansy Isabella Rani A, V. V. Sathibabu Uddandrao, Sangeethadevi G, Saravanan G, Chandrasekaran P, Sengottuvelu S, Tamilmani P, Sethumathi P P & S. Vadivukkarasi ...show less

Received 17 Aug 2020, Accepted 05 Jan 2021, Published online: 20 Jan 2021

Download citation
https://doi.org/10.1080/13813455.2021.1874017

Check for updates

Full Article Showing

Figures & data >

References >

P.G.P. COLLEGE OF ARTS & SCIENCE NAMAKKAL

ARCHIVES OF PHYSIOLOGY AND BIOCHEMISTRY
https://doi.org/10.1080/13813455.2021.1874017

Taylor & Francis
Taylor & Francis Group

ORIGINAL ARTICLE

Biochanin A attenuates obesity cardiomyopathy in rats by inhibiting oxidative stress and inflammation through the Nrf-2 pathway

Jansy Isabella Rani A[a,b*], V. V. Sathibabu Uddandrao[a*], Sangeethadevi G[a,b*], Saravanan G[a*], Chandrasekaran P[a], Sengottuvelu S[c], Tamilmani P[d], Sethumathi P P[a,c] and S. Vadivukkarasi[a]

[a]Centre for Biological Sciences, Department of Biochemistry, K.S. Rangasamy College of Arts and Science (Autonomous), Tiruchengode, India; [b]Department of Biochemistry, Vellalar College for Women (Autonomous), Erode, India; [c]Department of Pharmacology, Nandha College of Pharmacy, Erode, India; [d]Department of Biochemistry, PGP College of Arts and Science, Namakkal, India

ABSTRACT

Objective: In the present study, we evaluated the effect of biochanin A (BCA) on high-fat diet (HFD)-induced obesity cardiomyopathy.

Methods: BCA (10 mg/kg body weight) was administered to HFD-induced obese rats for 30 days, and its effect on anthropometrical, morphological, plasma cardiac, and inflammatory biomarkers, along with cardiac lipid profiles was assessed.

Results: Supplementation of HFD to rats significantly increased body mass index, obesity index parameters, and cardiac lipid profile along with notable oxidative stress and inflammation. Additionally, BCA treatment in obese rats demonstrated a superior therapeutic action by restoring the altered parameters to almost normal levels. Simultaneously, BCA increased the activities and mRNA expressions of enzymatic antioxidants by upregulating the Nrf-2 pathway and inhibiting the NF-κB cascade.

Conclusion: BCA may attenuate obesity and its associated cardiomyopathy by suppressing oxidative stress and inflammation through activation of the Nrf-2 pathway and inhibition of NF-κB activation.

ARTICLE HISTORY
Received 17 August 2020
Revised 21 December 2020
Accepted 5 January 2021
Published online 18 January 2021

KEYWORDS
Obesity; obesity cardiomyopathy; Biochanin-A; oxidative stress; inflammation; Nrf-2 pathway

Introduction

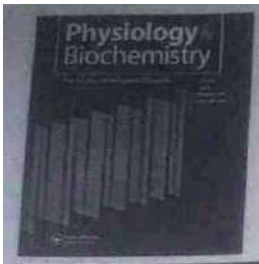
Obesity is a clinical state characterised by excess body fat deposition to such an extent that it results in unfavourable health outcomes and leads to increased health problems (Balaji *et al.* 2017). Obesity is a global epidemic, and its prevalence is increasing due to the overconsumption of high-fat diet (HFD) (Ng *et al.* 2014). Studies have reported a linear correlation between weight gain and the amount of fat ingested by animals and humans (Hariri and Thibault 2010, Uddandrao *et al.* 2020). Obesity is strongly associated with cardiovascular diseases (CVDs) and diabetes. Furthermore, obesity leads to structural and functional changes in the heart, which if untreated, lead to heart failure (Leger *et al.* 2018). On the other hand, obesity-related hyperglycaemia and insulin resistance are linked to inflammation and oxidative stress (Sathibabu Uddandrao *et al.* 2019), which affect the blood vessels and induce endothelial dysfunction (Brahmanaidu *et al.* 2017).

Wong and Marwick (2007) demonstrated that obesity is strongly associated with functional and structural cardiac alterations in experimental models. These alterations are referred to as "obesity cardiomyopathy". The possible contributors to obesity cardiomyopathy include inflammation, oxidative stress, hypertrophy, excess adiposity, fibrosis, and altered cardiac metabolism (Cavalera *et al.* 2014). Inflammation and oxidative stress play a significant role in the progression of obesity-associated complications and CVDs. Obesity has also been characterised as an inflammatory state. Chronic low-grade inflammation and oxidative stress play vital roles in the pathogenesis of obesity-induced cardiomyopathy (Taube *et al.* 2012). Circulating free fatty acids (FFAs) in obesity can lead to persistent inflammation, insulin resistance, and CVDs. FFAs can also increase the expression of pro-inflammatory cytokines and increase cellular oxidative stress (Zeng *et al.* 2015). In experimental models, the oxidative stress along with inflammation in organs such as the heart can result in apoptosis, hypertrophy, and fibrosis (Alpert 2001).

Nuclear factor erythroid 2-related factor 2 (Nrf-2) is a highly conserved pro-survival transcription factor that upregulates the expressions of many genes, including enzymes that scavenge reactive oxygen species (ROS) and those with antioxidant properties, involved in cellular flexibility (Sathibabu Uddandrao *et al.* 2018). The Nrf-2 signalling pathway is an effective strategy to counteract oxidative injury and inflammation (Kobayashi *et al.* 2016, Márton *et al.* 2018). Each obesity treatment plan includes lifestyle modifications and medications. Although the pharmacological treatment has advantages, it is often associated with weight regain after discontinuation of medication, adverse effects, and has the potential for abuse (Wilson 2013). Complementary and traditional medications used in Asia are now increasingly used worldwide. When conventional medications fail to

CONTACT S. Vadivukkarasi vadivusasi16@gmail.com Centre for Biological Sciences, Department of Biochemistry, K. S. Rangasamy College of Arts and Science (Autonomous), Namakkal District, Tiruchengode, Tamilnadu 637215, India
*These authors are equally contributed to this study.

© 2021 Informa UK Limited, trading as Taylor & Francis Group



Archives of Physiology and Biochemistry
The Journal of Metabolic Diseases

ISSN: (Print) (Online) Journal homepage: https://www.tandfonline.com/loi/larp20

Biochanin A attenuates obesity cardiomyopathy in rats by inhibiting oxidative stress and inflammation through the Nrf-2 pathway

Jansy Isabella Rani A , V. V. Sathibabu Uddandrao , Sangeethadevi G , Saravanan G , Chandrasekaran P , Sengottuvelu S , Tamilmani P , Sethumathi P P & S. Vadivukkarasi

To cite this article: Jansy Isabella Rani A , V. V. Sathibabu Uddandrao , Sangeethadevi G , Saravanan G , Chandrasekaran P , Sengottuvelu S , Tamilmani P , Sethumathi P P & S. Vadivukkarasi (2021): Biochanin A attenuates obesity cardiomyopathy in rats by inhibiting oxidative stress and inflammation through the Nrf-2 pathway, Archives of Physiology and Biochemistry, DOI: 10.1080/13813455.2021.1874017

To link to this article: https://doi.org/10.1080/13813455.2021.1874017

Published online: 20 Jan 2021.

Submit your article to this journal

View related articles

View Crossmark data



Full Terms & Conditions of access and use can be found at
https://www.tandfonline.com/action/journalInformation?journalCode=larp20

safely and efficaciously treat obesity, many individuals seek alternative options such as herbal medicine (de Freitas Junior and de Almeida 2017). Biochanin A (BCA) is a natural compound that is predominantly found in soy, chickpea, peanuts, alfalfa sprouts, and red clover. It is chemically known as O-methylated isoflavonoid and has several benefits, which include the anti-obesity action by regulating the trace element metabolism in HFD-induced obesity, as demonstrated in our previous study (Antony Rathinasamy *et al.* 2020). However, no supporting evidence for the effect of BCA on obesity-induced cardiomyopathy is available. Therefore, in the present study, we evaluated the effect of BCA on cardiac oxidative stress and inflammation through regulation of the Nrf-2 pathway in HFD-induced obese rats.

Materials and methods

Chemicals

BCA was purchased from Sigma Chemical Company (St. Louis, MO, USA).

Animals

We have taken male Wistar albino rats weighing at 180–200 g and aged at 8–12 weeks for this study and housed independently at standard laboratory conditions as described by earlier (Antony Rathinasamy *et al.* 2020). After initial adaptation, the animals were categorised in to four groups for the study. The protocol of this study was approved by the IAEC (Institutional Animal Ethical Committee), Nandha College of Pharmacy, Erode, Tamil Nadu, India (Ref. No: NCP/IAEC/2018–19/16).

Induction of obesity

Normal diet was prepared according to AIN-93 guidelines with all the recommended macro and micronutrients (Brahma Naidu *et al.* 2016) in sterile condition and fed to the Group I (Normal control) with water, *ad libitum*. HFD composition was prepared as described by Sathibabu Uddandrao *et al.* (2019) prepared at NIN (National Institute of Nutrition), Hyderabad, India, as per nutrition guidelines. Obese groups (Group-II to Group-IV) initially were fed with HFD for 15 weeks to induce the obesity (20 g daily) then the HFD rats supplemented with BCA (Group III) and Lorcaserin (Group IV) for the period of 30 days with respective doses once per day. Lorcaserin, a well-known anti-obesity drug, facilitated sustained weight loss without increasing the rate of major cardiovascular events in a high-risk population of overweight or obese patients (Bohula *et al.* 2018). Thus, the therapeutic effect of BCA was compared with lorcaserin.

Experimental protocol

The rats were divided into four groups of six animals each.

Group I: Normal control rats received 0.9% saline (2mL/kg/BW) orally for 30 days.

Group II: HFD control rats received 0.9% saline (2mL/kg/BW) orally for 30 days.

Group III: HFD control rats orally supplemented with BCA (10mg/kg BW/once per day) for 30 days (Antony Rathinasamy *et al.* 2020).

Group IV: HFD control rats orally supplemented with Lorcaserin (10mg/kg BW/once per day) for 30 days (Antony Rathinasamy *et al.* 2020).

Assessment of body weight, food and water intake

At the end of the experiment, body weight of the rats was measured and average weight in the group calculated. During the experimental period, total amount of food and water consumption per day was recorded.

Anthropometrical measurements

At the end of the experimental period, rats were fasted overnight and the AC (abdominal circumference), TC (thoracic circumference), body length were measured in anaesthized rats. The body mass index (BMI) (Novelli *et al.* 2007) was measured by considering body length and body weight.

Morphological parameters to measure obesity

After termination of experimental period, morphological parameters such as WHR (waist-hip ratio), adiposity index = (sum of the weights of white adipose tissue (WAT) of perirenal, retroperitoneal WAT, and epididymal WAT divided by body weight × 100), obesity index = (body weight of rat/nasoanal length (mm) × 104) were measured (Singh and Krishan 2010).

Plasma cardiac biomarkers

At the end of the experimental period, from the overnight fasted anaesthetised rats blood was collected by retro orbital sinus puncture method. Plasma cardiac markers such as aspartate aminotransferase (AST), alanine aminotransferase (ALT), creatine kinase-MB isoenzyme (CK-MB) and lactate dehydrogenase (LDH) were measured as per standard protocols.

Plasma inflammatory biomarkers

The plasma inflammatory biomarkers namely C-reactive protein (CRP) measured by using kit supplied by AbCam, MA,USA (catalog number ab99995) and homocysteine concentrations were measured by using automated immunoassay analyser (IMMULITE 2000 XPi, Siemens, USA) and fibrinogen levels was measured as per standard manufacturer's protocol by using SPINREACT Kits, Spain (catalog number 1709211).

Cardiac lipid profile

In brief, heart tissues were homogenised in lipid extraction buffer prepared with 5 volume isopropanol, 2 volume water and 2 volumes of Triton X-100. After vigorously vortexing, the homogenates were centrifuged 5 min at 14,000 rpm. Supernatants were collected to examine the levels of cholesterol, free fatty acids (FFA), triglycerides (TG) and phospholipids (PL) (BioAssay Systems).

Determination of lipid peroxidation and sodium potassium ATPase activity in heart

Lipid peroxidation in heart was determined as described by Ohkawa *et al.* (1979), and sodium potassium ATPase activity (Na^+/K^+-ATPase) was measured in heart tissue, method reported by Bonting (1970).

Determination of antioxidant enzymes in heart tissue

The heart tissue was homogenised with phosphate buffered saline (PBS) at a pH of 7.0 to measure antioxidant biomarkers in heart namely glutathione, glutathione peroxidase (GPx), glutathione reductase (GR), glutathione-S-transferase (GST), superoxide dismutase (SOD) and catalase (CAT) were measured as standard protocols as described by Saravanan *et al.* (2013).

Table 1. Primer sequences for RT-PCR analysis.

Gene	Sequence
Nrf-2	F 5′-GAGAGCCCAGTCTTCATTGC-3′ R 5′-TGCTCAATGTCCTGTTGCAT-3′
HO-1	5′-TTCTACCTGTTCGAGCATGTGG-3′ 5′-TGTTAGCATGGAGCCAGCCT-3′
SOD	F5′-CATTCCATCATTGGCCGTACT-3′ R5′-CCACCTTTGCCCAAGTCATC-3′
CAT	F5′-GTACAGGCCGGCTCTCACA-3′ R5′-ACCCGTGCTTTACAGGTTAGCT-3′
TNF-α	F5′-ATG TGG AAC TGG CAG AGG AG-3′ R5′-AGA AGA GGC TGA GGC ACA GA-3′
NF-κB	F 5′- ACCTTTGCTGGAAACACACC-3′ R 5′-ATGGCCTCGGAAGTTTCTTT-3′
β-actin	F 5′-ACCTTCAACACCCCAGCCATGTACG-3′ R 5′-CTGATCCACATCTGCTGGAAGGTGG-3′

RT-PCR analysis for Nrf-2, antioxidant and inflammatory markers

The heart tissues were harvested from rats. Frozen tissues were thawed and homogenised and total RNA was extracted using Trizol reagent (Invitrogen, Carlsbad, CA, USA) according to the manufacturer's instructions and reverse transcribed to attain cDNA using DNA synthesis kit (Applied Biosystems, Foster City, USA). 20 ng of cDNA was taken for semi-quantitative PCR. The PCR amplification was performed for 38 cycles using the following cycling conditions: 30 s of denaturation at 94 °C, 30 s of annealing at 59 °C and 1 min of extension at 72 °C, with the primers. The sequences of the primers of Nrf-2, haem oxygenase 1 (HO-1), SOD, CAT, TNF-α and NF-κB are presented in Table 1. The housekeeping gene β-actin was used for normalisation.

Statistical analysis

Data were expressed as mean ± S.D, $n = 6$ and evaluated using one-way analysis of variance (ANOVA) and least significant difference (LSD) test with the aid of SPSS/10.0 software. Statistical significance was defined as p values less than .01 and .05.

Results

Figure 1 depicts the effect of BCA on body weight and food and water intake in control and experimental animals. Body weight and consumption of food were significantly higher in the HFD-induced obese rats than in the normal control rats. Contrarily, BCA or lorcaserin supplementation in obese rats significantly decreased their body weight ($p < .05$, .01) (Figure 1(A)) and food (Figure 1(B)) and water intake (Figure 1(C)) ($p < .01$), compared with the untreated obese rats.

Thoracic circumference (TC) and abdominal circumference (AC) were significantly higher in the obese rats than in the normal control rats ($p < .05$, .01). Simultaneously, significant reduction in the TC and AC ($p < .05$, .01) was observed in obese rats treated with BCA as compared with the obese control rats (Figure 2(A and B)). The body mass index (BMI) in the obese rats was significantly higher than in the normal

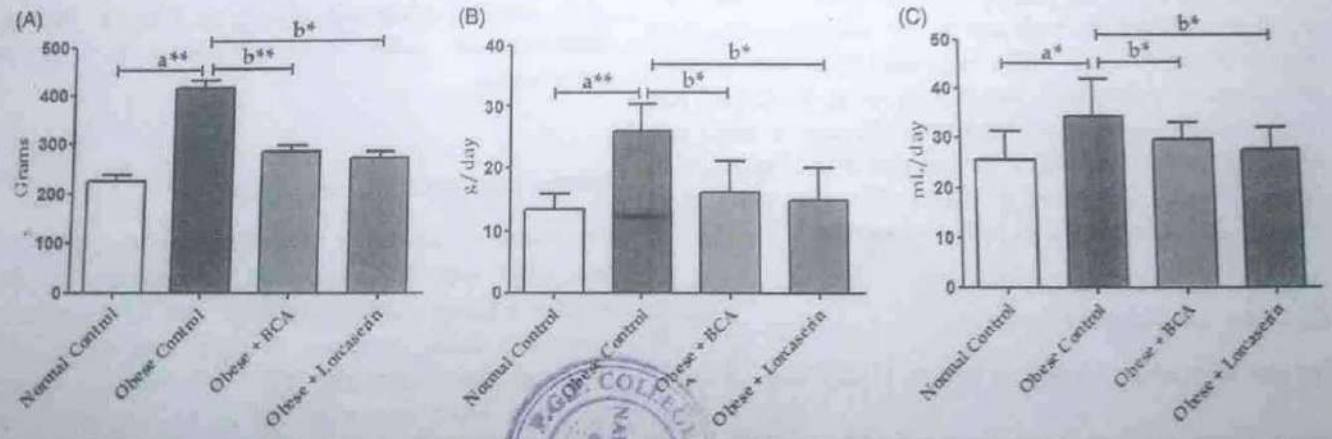


Figure 1. Effect of Biochanin A on (A) body weight, (B) food and (C) water intake in control and experimental obese rats. Values are mean ± SD, $n = 6$, Values are statistically significant at $^*p < .05$, $^{**}p < .01$, [a]significantly different from normal control, [b]significantly different from obese control.

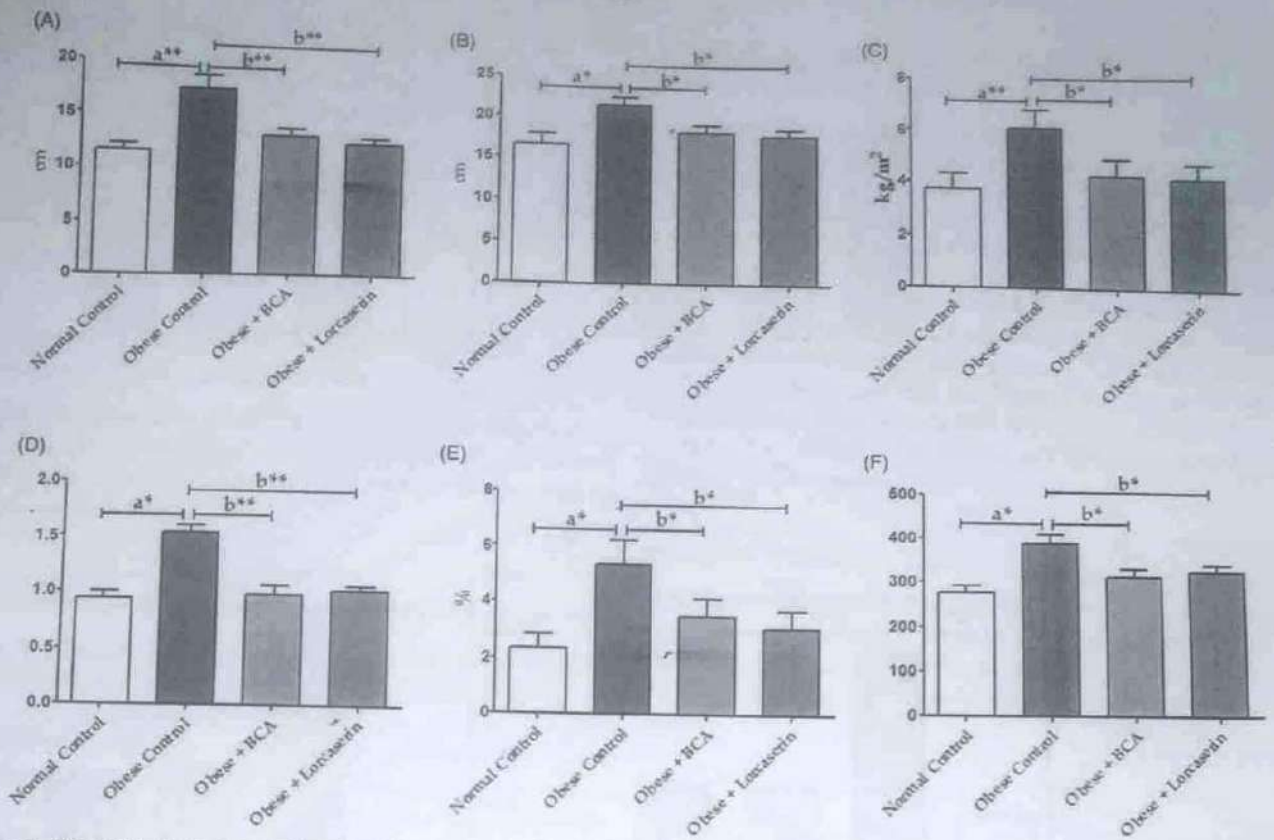


Figure 2. Effect of Biochanin A on anthropometrical measurements (A) AC (abdominal circumference), (B) TC (thoracic circumference), (C) BMI (body mass index), (D) WHR (waist-hip ratio), (E) adiposity index and (F) obesity index in control and experimental obese rats. Values are mean ± SD, $n = 6$, Values are statistically significant at $^{*}p < .05$, $^{**}p < .01$, [a]significantly different from normal control, [b]significantly different from obese control.

control rats ($p < .01$). Conversely, we observed a significant decrease in the BMI of obese rats supplemented with BCA compared with the obese control rats (Figure 2(C)).

Figure 2(D)–F illustrates the influence of BCA on morphological parameters in the control and HFD-induced obese rats. The waist–hip ratio (WHR) (Figure 2(D)), adiposity index (Figure 2(E)), and obesity index (Figure 2(F)) in HFD-induced obese rats were significantly higher than in the rats supplemented with normal diet ($p < .05, .01$). However, BCA or lorcaserin supplementation for 30 days in the obese rats significantly attenuated their WHR, obesity index, and adiposity index, as compared with the HFD-alone controls.

Figure 3 demonstrates the levels of plasma cardiac biomarkers in the control and obese rats. Plasma levels of aspartate transferase (AST), alanine transferase (ALT), creatine kinase-MB (CK-MB), and lactate dehydrogenase (LDH) were notably elevated in the obese rats ($p < .05$) as compared with the normal controls ($p < .01$). However, BCA or lorcaserin treatment exhibited a significant reduction in plasma levels of AST (Figure 3(A)), ALT (Figure 3(B)), CK-MB (Figure 3(C)), and LDH (Figure 3(D)), as compared with the HFD-alone control.

Figure 4 illustrates the plasma levels of inflammatory biomarkers in the control and experimental rats. We observed a significant increase in the levels of c-reactive protein (CRP), fibrinogen, and homocysteine in the obese rats as compared with the normal control rats. On the other hand, BCA or lorcaserin supplementation in the obese rats was found to significantly decrease ($p < .05, .01$) the levels of CRP (Figure 4(A)), fibrinogen (Figure 4(B)), and homocysteine (Figure 4(C)), when compared with the vehicle-treated obese rats.

Figure 5 represents the cardiac lipid profiles in the control and experimental obese rats. The HFD-induced obese rats demonstrated a significant increase in the levels of cholesterol, FFAs, and triglycerides (TGs) and a concomitant decrease in the phospholipid (PL) level, compared with the normal diet-fed rats. However, BCA or lorcaserin supplementation in the obese rats significantly decreased ($p < .05, .01$) the levels of cholesterol (Figure 5(A)), FFA (Figure 5(B)), and TG (Figure 5(C)) and simultaneously increased the PL level (Figure 5(D)).

Figure 6 illustrates the levels of heart lipid peroxidation and Na^+/K^+-ATPase activity in the control and experimental animals. The lipid peroxidation level was significantly increased (Figure 6(A)) and Na^+/K^+-ATPase activity was significantly decreased (Figure 6(B)) in the heart tissues of the HFD-induced obese rats, when compared with the normal control rats. On the other hand, BCA or lorcaserin supplementation in the HFD-induced obese rats significantly ($p < .05, .01$) restored the altered levels to a near normal value.

Figure 7 illustrates that the levels of antioxidant markers such as glutathione (Figure 7(A)), glutathione peroxidase (GPx) (Figure 7(B)), glutathione reductase (GR) (Figure 7(C)), glutathione S-transferase (GST) (Figure 7(D)), superoxide

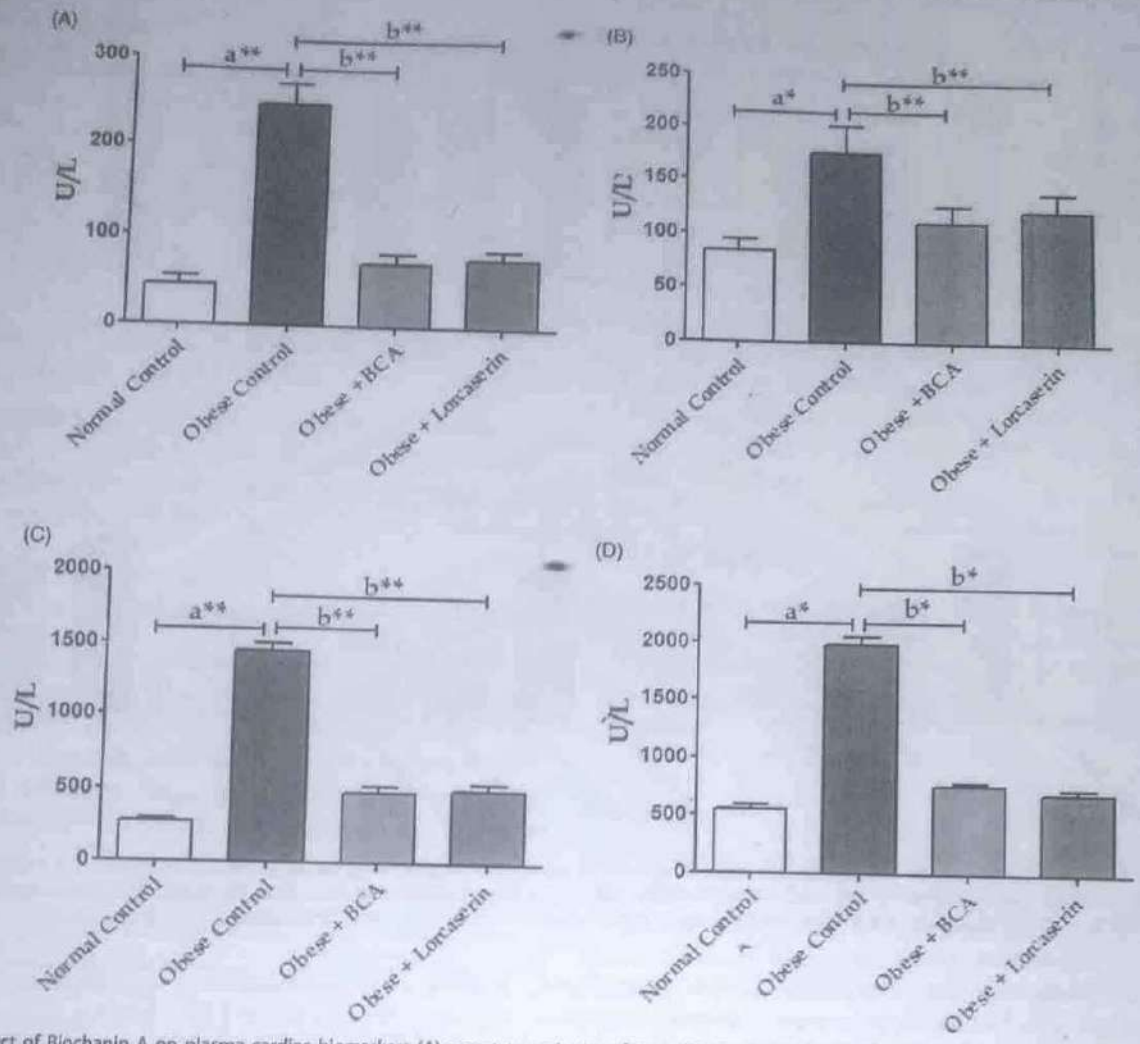


Figure 3. Effect of Biochanin A on plasma cardiac biomarkers (A) aspartate aminotransferase, (B) alanine aminotransferase, (C) creatine kinase-MB isoenzyme and (D) lactate dehydrogenase in control and experimental obese rats. Values are mean ± SD, $n = 6$, Values are statistically significant at $^{*}p < .05$, $^{**}p < .01$, [a]significantly different from normal control, [b]significantly different from obese control.

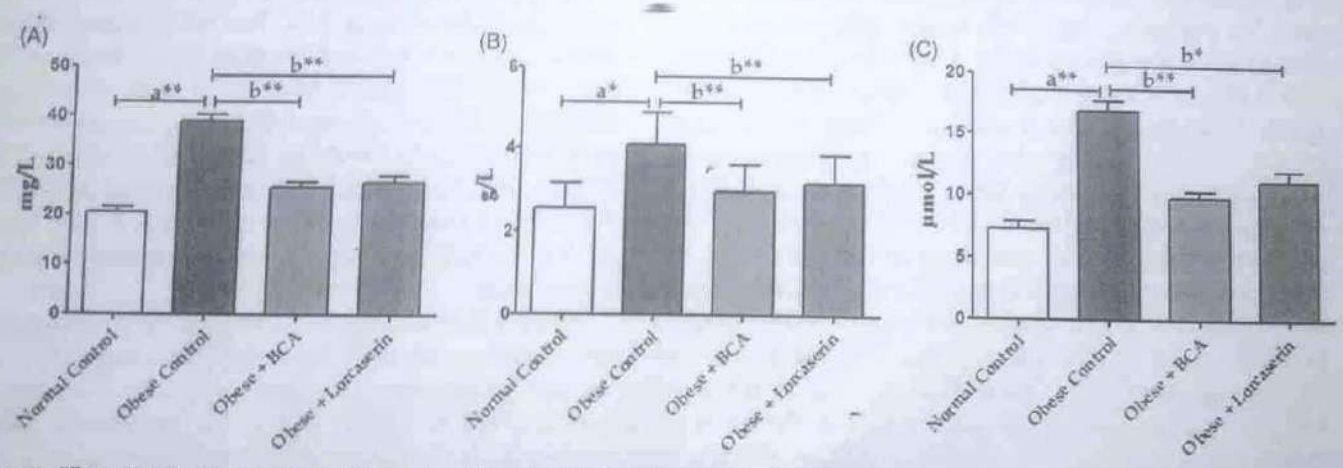


Figure 4. Effect of Biochanin A on plasma inflammatory biomarkers (A) C-reactive protein, (B) fibrinogen and (C) homocysteine in control and experimental obese rats. Values are mean ± SD, $n = 6$, Values are statistically significant at $^{*}p < .05$, $^{**}p < .01$, [a]significantly different from normal control, [b]significantly different from obese control.

dismutase (SOD) (Figure 7(E)), and catalase (CAT) (Figure 7(F)) were significantly decreased in the obese rats, when compared with the rats fed on a normal diet ($p < .05$, .01). BCA or lorcaserin supplementation for 30 days in HFD-induced obese rats restored the altered activities of enzymes close to the normal.

Figure 8(A–F) illustrates the effect of BCA on the mRNA expressions of Nrf-2, oxidative, and inflammatory markers in

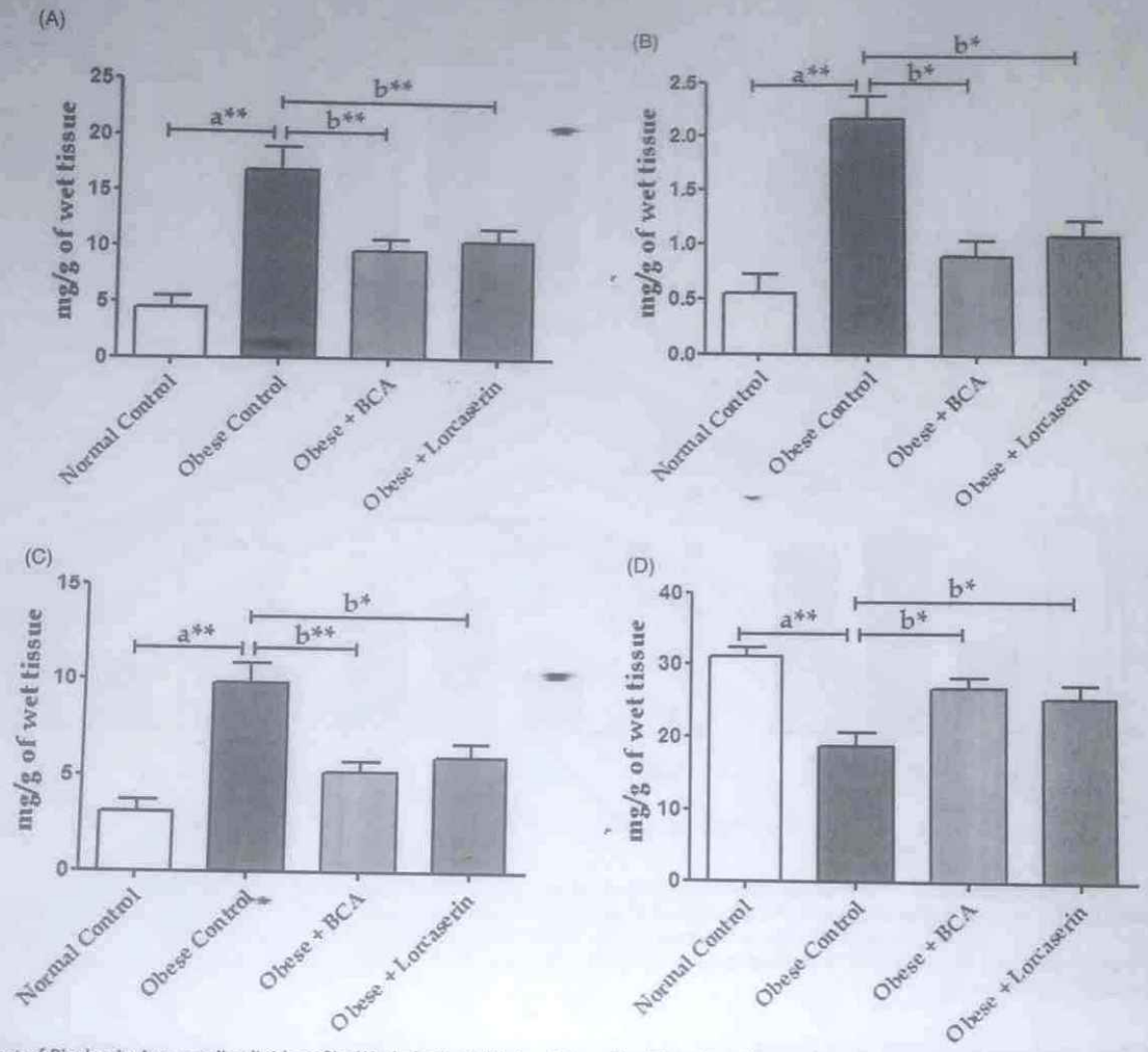


Figure 5. Effect of Biochanin A on cardiac lipid profile (A) cholesterol, (B) free fatty acids, (C) triglycerides and (D) phospholipids in control and experimental obes rats. Values are mean ± SD, $n = 6$, Values are statistically significant at $^{*}p < .05$, $^{**}p < .01$, [a]significantly different from normal control, [b]significantly different fro obese control.

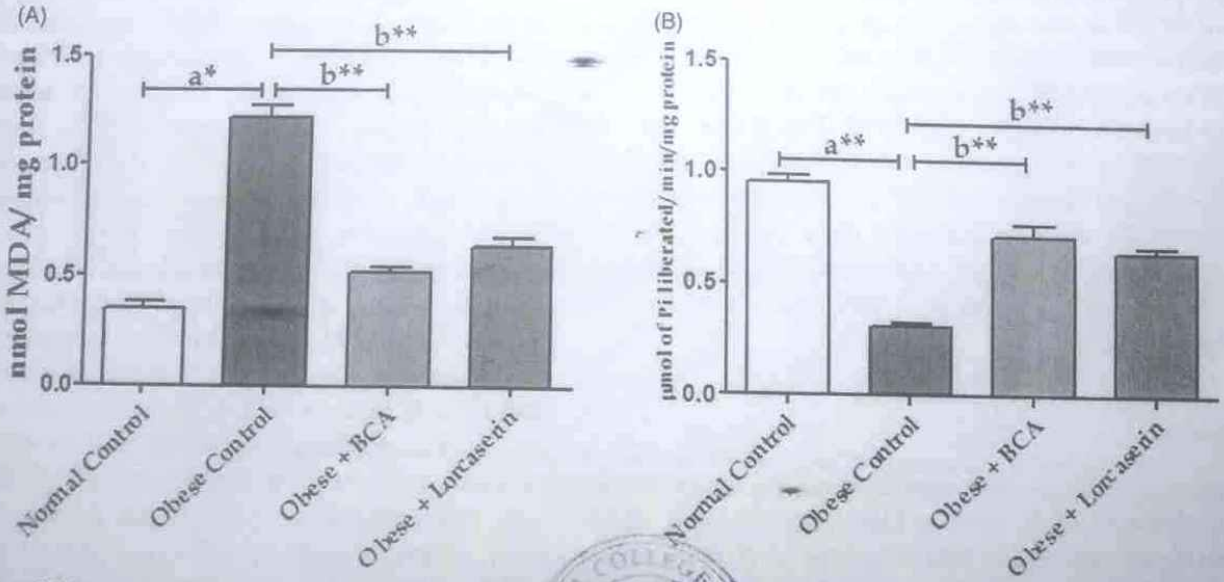


Figure 6. Effect of Biochanin A on (A) lipid peroxidation and (B) Na^{+}/K^{+}-ATPase activity of heart in control and experimental obese rats. Values are mean ± S $n = 6$, Values are statistically significant at $^{*}p < .05$, $^{**}p < .01$, [a]Significantly different from normal control, [b]Significantly different from obese control.

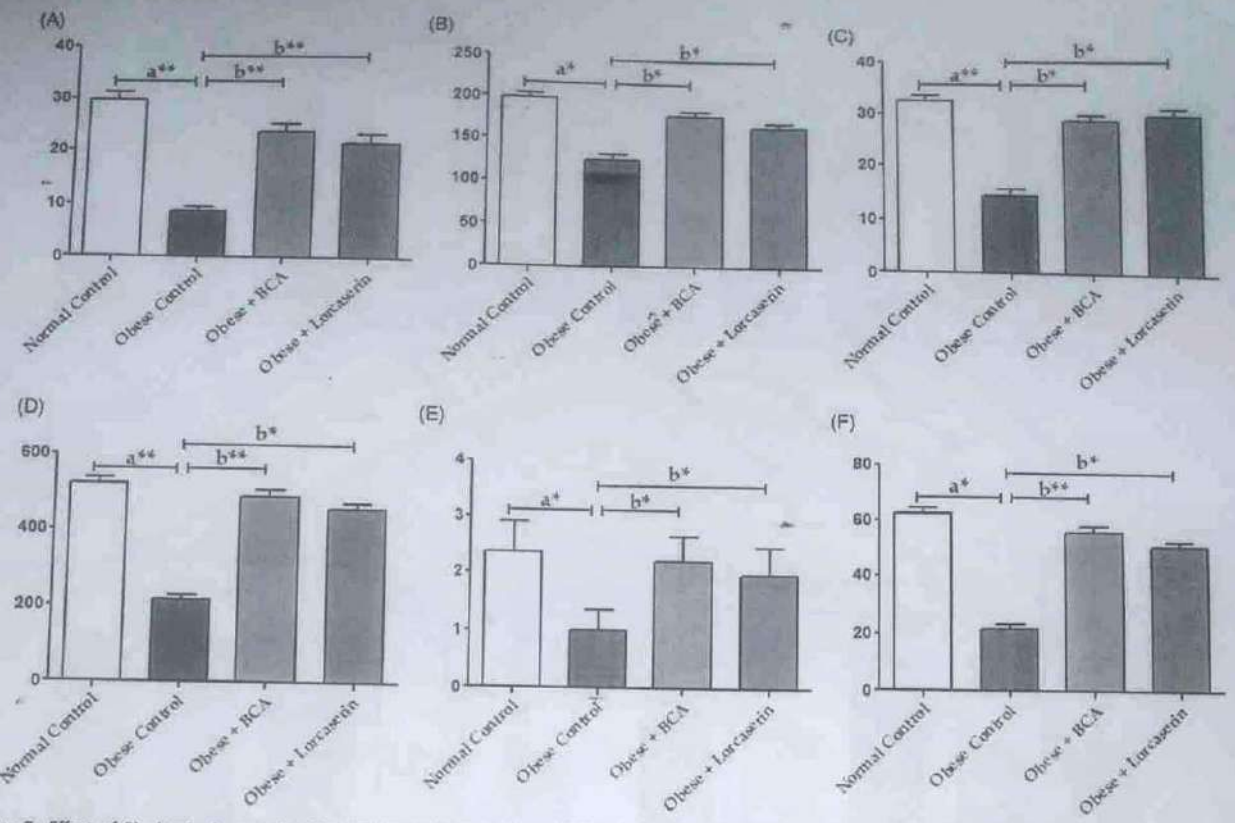


Figure 7. Effect of Biochanin A on antioxidant markers (A) glutathione, (B) GPx (glutathione peroxidase), (C) GR (glutathione reductase), (D) GST (glutathione-S-transferase), (E) SOD (superoxide dismutase) and (F) CAT (catalase) in control and experimental obese rats. Values are mean ± SD, $n = 6$, Values are statistically significant at $^{*}p < .05$, $^{**}p < .01$, [a]Significantly different from normal control, [b]Significantly different from obese control. Units: Glutathione: µmol of phosphorus liberated/min/mg protein; GPx, GR: nmol NADPH oxidized/min/mg of protein; GST: nmol CDNB conjugate formed/min/mg protein; SOD: IU/mg protein; CAT: nmol H_2O_2-consumed/min/mg protein.

the control and experimental obese rats. The reverse transcription-polymerase chain reaction assay revealed a significant reduction ($p < .05$, .01) in mRNA expressions of Nrf-2, haem oxygenase-1 (HO-1), SOD, and CAT and a concomitant increase in the expressions of tumour necrosis factor-α (TNF-α) and NF-κB in the obese rats, when compared with the rats fed on a normal diet. However, BCA or lorcaserin supplementation significantly upregulated the expression of Nrf-2 (Figure 8(A)), HO-1 (Figure 8(B)), SOD (Figure 8(C)), and CAT (Figure 8(D)) and suppressed the mRNA levels of TNF-α (Figure 8(E)) and NF-κB (Figure 8(F)) in the HFD-induced rats, compared with the vehicle-treated obese rats ($p < .01$, .05). Therefore, the present study revealed that BCA significantly activates the Nrf-2 pathway and concomitantly inhibits the NF-κB pathway.

Discussion

Obesity is associated with cardiometabolic complications such as diabetes, dyslipidaemia, high blood pressure, coronary vein illness, stroke, and mortality (Bray *et al.* 2018). Edible fat is one of the most significant risk factors for CVDs; elevated cholesterol and saturated fat diets increase the risk of atherosclerosis (McNamara 2000). Chronic oxidative stress and inflammation have been implicated in the pathophysiology of obesity-associated CVD (Fernandez-Sanchez *et al.* 2011). Uncontrolled production of provocative cytokines and ROS due to hyperlipidaemia weakens the customary cell capacity and induces cell apoptosis in various tissues, including the heart (Wende *et al.* 2012). Therefore, due to the potential roles of oxidative stress and inflammation in CVDs, molecules with antioxidant and anti-inflammatory properties can improve the efficiency of remedial interventions for obesity and HFD-induced CVD. Thus, the present study was designed to evaluate the effect of BCA on the suppression of oxidative stress and inflammation through the Nrf-2 pathway.

The present study established that HFD supplementation-induced obesity in rats is associated with increased body weight, BMI, TC, AC, adiposity index, and obesity index. The HFD-induced obese control rats weighed more than the normal controls because HFD is one of the risk factors for obesity (Brahma Naidu *et al.* 2016). HFD is calorically dense, palatable, and addictive (Woods and Seeley 2002). In the current study, parameters such as the food and water intake, body weight, BMI, WHR, adiposity index, and obesity index were used to evaluate obesity. Both AC and TC were elevated in the obese control rats. Additionally, the BMI was considerably augmented in the HFD-induced obese rats, compared with the normal control group rats. These results

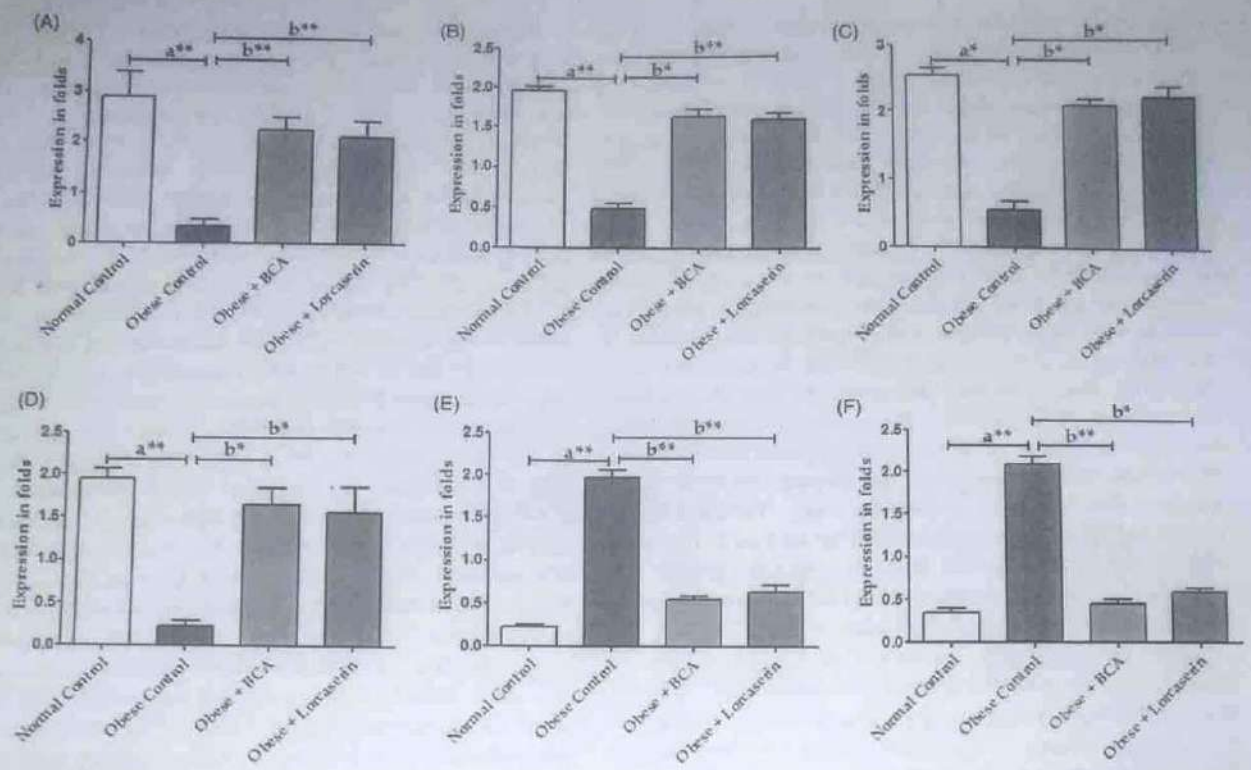


Figure 8. Effect of Biochanin A on mRNA expressions of Nrf-2, oxidative and inflammatory markers in control and experimental obese rats. (A) Nrf-2 (nuclear factor erythroid 2-related factor 2), (B) HO-1 (haem oxygenase 1), (C) SOD (superoxide dismutase), (D) CAT (catalase), (E) TNF-α (tumour necrosis factor-α) and (F) NF-κB (nuclear factor kappa light chain enhancer of activated B cells). Values are mean ± SD, $n = 6$, Values are statistically significant at $^{*}p < .05$, $^{**}p < .01$, ^{a}Significantly different from normal control, ^{b}Significantly different from obese control.

are concurrent with the findings of Novelli *et al.* (2007), who stated that the HFD induces the accumulation of fat in the thoracic and abdominal regions (Novelli *et al.* 2007). The finding confirms that the observed increase in body weight, WHR, adiposity index, and obesity index is due to the consumption of too much food and adipose tissue accumulation. The BMI has been proved to be a simple consistent estimate of body fat and obesity in rats (Novelli *et al.* 2007). Rodrigues *et al.* (2012) established the correlation of the BMI with daily lipid intake and fat accumulation. On the other hand, the observed decrease in anthropometric measures in the obese rats following BCA or lorcaserin supplementation may be due to the reserve of dietetic lipid consumption. Studies have demonstrated that the addition of medicinal plant extracts or its isolated compounds is associated with condensed energy mandatory for lipid and protein biosynthesis foremost to inferior growth performance and nutrient exploitation (Brahma Naidu *et al.* 2016, Kalaivani *et al.* 2019). Therefore, BCA may have the capability of diminishing body lipid and consequently retaining energy (Antony Rathinasamy *et al.* 2020).

In both the experimental animal and human models, obesity is associated with functional and structural changes in the heart (Redondo Useros *et al.* 2019) that include cardiac remodelling such as cardiac fibrosis, cardiac hypertrophy, and subclinical destruction of the diastolic and left ventricular systolic function (Csige *et al.* 2018). When the tissue is damaged, the macromolecular enzymes are leaked because of their tissue specificity and catalytic activity. Subsequently, in the obese rats, the levels of marker enzymes such as AST, ALT, CK-MB, and LDH in plasma were increased, which confirms myocardial necrosis and leakage of the marker enzymes from the cardiac tissues to blood (Saravanan *et al.* 2013). The liberation of cellular enzymes is a non-specific alteration in the plasma membrane integrity and permeability resulting from the β-adrenergic stimulation. The plasma LDH and CK-MB levels were significantly increased in the HFD-induced obese rats, which represents structural and functional modifications in the cardiac tissues and are indicative of disruption of the cell membrane integrity (Mohamed *et al.* 2014). The discharge of LDH and CK-MB from the damaged heart membranes denotes obesity-induced necrosis of myocardium. Similarly, increased LDH and CK-MB levels were observed in the obese rats, and these levels were restored with BCA or lorcaserin treatment. These findings are concurrent with those of Mohamed *et al.* (2014).

Data indicate that obesity is linked to a low-grade chronic inflammation, as evidenced by the increased levels of pro-inflammatory cytokines and related factors such as CRP, homocysteine, and fibrinogen (Esser *et al.* 2014). Hyperhomocysteinemia, as a powerful pro-inflammatory factor, may accelerate the progress of atherosclerosis (McCully 2005). Moreover, the augmented risk of vascular sickness from the increased homocysteine level is similar to that of

other major CVDs in HFD-indueed obesity (Chang *et al.* 2012). Fibrinogen plays a significant role in haemostasis, thrombosis, and inflammation and is capable of stimulating the development of atherosclerotic plaques through different mechanisms (Zhou *et al.* 2013). CRP is a sensitive reactant protein that is rapidly released from the heart when provoked by interleukin-6 during inflammation, cell infection, or injury. The serum CRP level might increase during acute myocardial infarction and is a precious extrapolative marker of the ischaemic heart disease (Kim *et al.* 2019). Similarly, augmented levels of plasma pro-inflammatory biomarkers such as CRP, homocysteine, and fibrinogen were present in the obese rats. This finding is mirrored by an earlier study (Kim *et al.* 2013). The data demonstrated that obesity leads to inflammation, which encourages cardiomyopathy. Martinez-Martinez *et al.* (2014) established an essential function of pro-inflammatory state by directly inducing hypertrophy, fibrosis, and eventually, the contractility in myocardial injury. Interestingly, BCA or lorcaserin treatment inhibits the increase in the levels of pro-inflammatory biomarkers. The anti-inflammatory effect of BCA was related to its cardioprotective efficacy (Govindasami *et al.* 2020).

Lipids are significant controllers of the heart function because of their role in membrane structure, cell signalling, and transport. They also serve as a substrate for β-oxidation for providing energy in the mitochondria (Lim and Bodmer 2011). Cardiac lipotoxicity involves not only an excess accumulation of intramyocellular TG in the heart but also the changes in lipid classes and the FFA profile. Accordingly, the development of active lipid mediators increases, which influences the cardiac function and metabolism, partly by permitting the expansion of cardiac fibrosis, an imperative provider to heart muscle dysfunction (Marín-Royo *et al.* 2019). Furthermore, the HFD-induced cardiac cholesterol levels indicate that HFD may cause myocardial necrosis through excessive cholesterol accumulation within cardiac tissues. Normal cells are protected from excessive cholesterol accumulation through different processes such as cholesterol synthesis, deluge, and efflux (Li *et al.* 2017), which might be undermined by different pathophysiological conditions. FFAs are responsible for the synthesis of physiologically vital substrates through oxidation. However, high concentrations of FFAs have been demonstrated to be a risk factor for CVD (Sun *et al.* 2012). Cardiomyocytes produce up to 70% of their vital requirements through the β-oxidation of FFAs (Oliver 2006). Increased cardiovascular FFA levels are harmful to the heart in several ways (Seo *et al.* 2017). Due to their amphiphilic and cleanser-like properties, FFAs can disrupt ion channels and membrane integrity and uncouple mitochondrial enzymes, thus diminishing the productivity of the respiratory cycle and decreasing the contractile capacity of the heart. PLs are crucial for the accurate localisation, capacity of the key mitochondrial enzymes, and myocardial contractility and suitability simultaneously (Marín-Royo *et al.* 2018). The changed heart lipid profiles were re-established to normal after treatment with BCA for 30 days, suggesting the anti-hyperlipidimic potential of BCA (Antony Rathinasamy *et al.* 2020).

Obesity is associated with a high risk of heart failure, which is indicated by the increased oxidative stress, chronic inflammation, and linked cardiometabolic changes (Yazici and Sezer 2017). Na^+/K^+-ATPase is a membrane protein that accounts for the active transport of Na^+ and K^+ ions across the plasma membranes in most advanced eukaryotes (Kaplan 2002). A decline in the cardiac Na^+/K^+-ATPase concentration or protein activity can reduce the cardiac contractility in experimental animals and has been recognised in patients with CVD (Liu *et al.* 2012). Decreased levels of Na^+/K^+-ATPase were observed in the HFD-induced rats, and these levels were restored with BCA treatment. In experimental studies, obesity is linked with reduction in the antioxidant capacity of either tissues or plasma or both (Olusi 2002). GSH constitutes the first-line protection against free radicals and is also accountable for the continuance of protein thiols. It acts as a substrate for GST and GPx (Brahma Naidu *et al.* 2016). Our results demonstrated that the GSH content was exhausted in the obese rats and was restored after BCA supplementation. Antioxidant enzymes such as GPx, CAT, and SOD can hunt ROS and free radicals or turn off their synthesis (Sathibabu Uddandrao *et al.* 2018, 2019). In the present study, the GPx, GR, and GST activities in the obese control rats were considerably diminished, whereas those in the obese rats supplemented with BCA or lorcaserin were notably increased in the heart. A report suggests that antioxidants can amend the cholesterol absorption and enhance the antioxidant status (Kalaivani *et al.* 2020). Rameshreddy *et al.* (2018) revealed that hyperlipidaemia decreases the potency of the antioxidant defence system in obese rats. Consequently, we hypothesise the probable explanation for the anti-obesity efficacy of BCA through the prevention of oxidative stress in obese rats.

Nrf-2 was revealed to function as an antioxidant controller in CVD and is associated with oxidative damage (Sathibabu Uddandrao *et al.* 2018). Under regular conditions, Nrf-2 is coupled with Keap1 in the cytoplasm, and the Nrf-2-Keap1 complex ensures deprivation of Nrf-2 to preserve the intracellular Nrf-2 level (Kansanen *et al.* 2013). When exposed to increasing cellular oxidants, Nrf-2 disconnects from Keap1 and translocates to the nucleus, where it combines with an antioxidant response element and initiates transcription of antioxidant genes (Suzuki and Yamamoto 2015). These genes encode various cardioprotective proteins such as HO-1, CAT, and SOD. Nrf-2 is a well-distinguished redox-sensitive transcription factor. Commencement of Nrf-2 leads to upregulation of antioxidant protective genes, which play a crucial role in coordinating antioxidant defences and in sustaining redox homeostasis. Consequently, Nrf-2 upregulation may be an efficient approach to defend the heart from obesity cardiomyopathy. Studies have demonstrated that the Nrf-2 controls the expression of phase II detoxifying enzymes, including NAD(P)H quinone oxidoreductase 1, NADPH, GR, HO-1, and antioxidant genes, that defend cells from diverse injuries through their anti-inflammatory effects, thus regulating the disease pathway (Chen *et al.* 2006). Some reports have established that HO-1 and its metabolites have momentous anti-inflammatory effects arbitrated by Nrf-2. Increase in HO-1

expression, which is interceded by activated Nrf-2, leads to the reserve of NF-κB signalling. Several pro-inflammatory cytokines are produced when NF-κB is activated by oxidative stress. Additionally, pro-inflammatory oxidative stress leads to additional activation of NF-κB and cytokine overproduction. Nrf-2 pathway activation is shown to play a significant function in disrupting this cycle (Ahmed *et al.* 2017). Similarly, our findings indicate that the antioxidant effects of BCA against HFD-induced cardiomyopathy are mediated through the activation of Nrf-2 and its target genes such as HO-1, CAT, and SOD. On the other hand, BCA supplementation reduces NF-κB inflammatory cascades, as revealed by decreased NF-κB and TNF-α expressions. Therefore, the cardioprotective effect of BCA against HFD-induced cardiac inflammation could be due to the diminished expressions of cytokines and mediators. These findings suggest that in response to oxidative stress and inflammatory stimuli, upregulation of Nrf-2 signalling inhibits the overproduction of free radicals and pro-inflammatory cytokines as well as restrains the NF-κB activation.

Conclusions

BCA supplementation may reduce the CVD risk. BCA improves cardiomyopathy and decreases inflammation and oxidative stress through the anti-inflammatory and antioxidant effects on activation of the cardiac Nrf-2 pathway and inhibition of NF-κB. Because of the cardioprotective role of BCA, it could serve as the future therapeutic intervention for obesity-induced cardiomyopathy.

Acknowledgements

The authors thank Nandha college of Pharmacy, Erode, Tamilnadu, India, for providing facilities to perform the animal studies and the management of K.S. Rangasamy College of Arts and Science (Autonomous), Tiruchengode, Tamilnadu, for their support and encouragement.

Disclosure statement

No potential conflict of interest was reported by the author(s).

Data availability statement

The data that support the findings of this study are available on request from the corresponding author, S. Vadivukkarasi.

References

Ahmed, S.M., *et al.*, 2017. Nrf2 signaling pathway: pivotal roles in inflammation. *Biochimica et Biophysica Acta. Molecular basis of disease*, 1863 (2), 585–597.

Alpert, M.A., 2001. Obesity cardiomyopathy: pathophysiology and evolution of the clinical syndrome. *The American journal of the medical sciences*, 321 (4), 225–236.

Antony Rathinasamy, J.I.R., *et al.*, 2020. Antiobesity effect of Biochanin-A: effect on trace element metabolism in high fat diet-induced obesity in rats. *Cardiovascular & hematological agents in medicinal chemistry*, 18 (1), 21–30.

Balaji, M., *et al.*, 2017. Antiobesity potential of Piperonal: promising modulation of body composition, lipid profiles and obesogenic marker expression in HFD-induced obese rats. *Nutrition & metabolism*, 14, 72.

Bohula, E.A., *et al.*, 2018. Cardiovascular safety of lorcaserin in overweight or obese patients. *New England journal of medicine*, 379 (12), 1107–1117.

Bonting, S. L., 1970. Sodium potassium activated adenosine triphosphatase and cation transport. *In:* Bitler E.E. ed. *Membrane and ion transport*. Vol-1. London: Interscience Wiley, 257–263.

Brahma Naidu, P., *et al.*, 2016. Ameliorative potential of gingerol: promising modulation of inflammatory factors and lipid marker enzymes expressions in HFD induced obesity in rats. *Molecular and cellular endocrinology*, 419, 139–147.

Brahmanaidu, P., *et al.*, 2017. Reversal of endothelial dysfunction in aorta of streptozotocin-nicotinamide-induced type-2 diabetic rats by S-Allylcysteine. *Molecular and cellular biochemistry*, 432 (1–2), 25–32.

Bray, G.A., *et al.*, 2018. The science of obesity management: an endocrine society scientific statement. *Endocrine reviews*, 39 (2), 79–132.

Cavalera, M., Wang, J., and Frangogiannis, N.G., 2014. Obesity, metabolic dysfunction, and cardiac fibrosis: pathophysiological pathways, molecular mechanisms, and therapeutic opportunities. *Translational research: the journal of laboratory and clinical medicine*, 164 (4), 323–335.

Chang, X.X., *et al.*, 2012. The effects of berberine on hyperhomocysteinemia and hyperlipidemia in rats fed with a long-term high-fat diet. *Lipids in health and disease*, 11, 86.

Chen, X.L., *et al.*, 2006. Activation of Nrf2/ARE pathway protects endothelial cells from oxidant injury and inhibits inflammatory gene expression. *American journal of physiology: heart and circulatory physiology*, 290, 1862–1870.

Csige, I., *et al.*, 2018. The impact of obesity on the cardiovascular system. *Journal of Diabetes Research*, 2018, 3407306.

de Freitas Junior, L.M., and de Almeida, E.B., Jr., 2017. Medicinal plants for the treatment of obesity: ethnopharmacological approach and chemical and biological studies. *American Journal of Translational Research*, 9 (5), 2050–2064.

Esser, N., *et al.*, 2014. Inflammation as a link between obesity, metabolic syndrome and type 2 diabetes. *Diabetes Research and Clinical Practice*, 105 (2), 141–150.

Fernandez-Sanchez, A., *et al.*, 2011. Inflammation, oxidative stress, and obesity. *International Journal of Molecular Sciences*, 12, 3117–3132.

Govindasami, S., *et al.*, 2020. Therapeutic potential of biochanin-A against isoproterenol -induced myocardial infarction in rats. *Cardiovascular & Hematological Agents in Medicinal Chemistry*, 18 (1), 31–36.

Hariri, N., and Thibault, L., 2010. High-fat diet-induced obesity in animal models. *Nutrition Research Reviews*, 23 (2), 270–299.

Kalaivani, A., *et al.*, 2019. Reversal of high fat diet-induced obesity through modulating lipid metabolic enzymes and inflammatory markers expressions in rats. *Archives of Physiology and Biochemistry*, 125 (3), 228–234.

Kalaivani, A., *et al.*, 2020., Attenuation of obesity-associated oxidative stress by cucurbita maxima seed oil in high fat diet-induced obese rats. In: Tappia P., Ramjiawan B., Dhalla N. eds. *Pathophysiology of obesity-induced health complications. Advances in biochemistry in health and disease 19*. Cham: Springer.

Kansanen, E., *et al.*, 2013. The keap1-nrf2 pathway: mechanisms of activation and dysregulation in cancer. *Redox Biology*, 1, 45–49.

Kaplan, J.H., 2002. Biochemistry of Na,K-ATPase. *Annual Review of Biochemistry*, 71, 511–535.

Kim, E.N., *et al.*, 2019. High serum CRP influences myocardial miRNA profiles in ischemia-reperfusion injury of rat heart. *PLoS One*, 14 (5), e0216610.

Kim, M.S., *et al.*, 2013. Regulation of diet-induced adipose tissue and systemic inflammation by salicylates and pioglitazone. *PLoS One*, 8 (12), e82847.

Kobayashi, E.H., *et al.*, 2016. Nrf2 suppresses macrophage inflammatory response by blocking proinflammatory cytokine transcription. *Nature Communications*, 7, 11624.

Leger, T., *et al.*, 2018. Dietary canolol protects the heart against the deleterious effects induced by the association of rapeseed oil, vitamin E

and coenzyme Q10 in the context of a high-fat diet. *Nutrition & Metabolism*, 15, 15.

Li, C.H., *et al.*, 2017. Puerarin promotes ABCA1-mediated cholesterol efflux and decreases cellular lipid accumulation in THP-1 macrophages. *European Journal of Pharmacology*, 811, 74–86.

Lim, H.Y., and Bodmer, R., 2011. Phospholipid homeostasis and lipotoxic cardiomyopathy: a matter of balance. *Fly*, 5 (3), 234–236.

Liu, C., *et al.*, 2012. Reduction of Na/K-ATPase potentiates marinobufagenin-induced cardiac dysfunction and myocyte apoptosis. *The journal of biological chemistry*, 287 (20), 16390–16398.

Marín-Royo, G., *et al.*, 2018. Inhibition of galectin-3 ameliorates the consequences of cardiac lipotoxicity in a rat model of diet-induced obesity. *Disease models & mechanisms*, 11, 032086. https://doi.org/10.1242/dmm.032086.

Marín-Royo, G., *et al.*, 2019. The impact of cardiac lipotoxicity on cardiac function and mirnas signature in obese and non-obese rats with myocardial infarction. *Scientific reports*, 9 (1), 444.

Martinez-Martinez, E., *et al.*, 2014. Leptin induces cardiac fibrosis through galectin-3, mTOR and oxidative stress: potential role in obesity. *Journal of hypertension*, 32, 1104–1114.

Mártón, M., *et al.*, 2018. NRF2-regulated cell cycle arrest at early stage of oxidative stress response mechanism. *PLoS one*, 13 (11), e0207949.

McCully, K.S., 2005. Hyperhomocysteinemia and arteriosclerosis: historical perspectives. *Clinical chemistry and laboratory medicine*, 43 (10), 980–986.

McNamara, D.J., 2000. Dietary cholesterol and atherosclerosis. *Biochimica et Biophysica Acta (BBA) – Molecular and cell biology of lipids*, 1529 (1–3), 310–320.

Mohamed, A.R., El-Hadidy, W.F., and Mannaa, H.F., 2014. Assessment of the prophylactic role of aspirin and/or clopidogrel on experimentally induced acute myocardial infarction in hypercholesterolemic rats. *Drugs in R&D*, 14 (4), 233–239.

Naidu, P.B., *et al.*, 2016. Effects of S-allylcysteine on biomarkers of the polyol pathway in rats with type 2 diabetes. *Canadian journal of diabetes*, 40 (5), 442–448.

Ng, M., *et al.*, 2014. Global, regional, and national prevalence of overweight and obesity in children and adults during 1980-2013: a systematic analysis for the Global Burden of Disease Study 2013. *Lancet*, 384 (9945), 766–781.

Novelli, E.L., *et al.*, 2007. Anthropometrical parameters and markers of obesity in rats. *Laboratory animals*, 41 (1), 111–119.

Ohkawa, H., Ohishi, N., and Yagi, K., 1979. Assay for lipid peroxides in animal tissues by thiobarbituric acid reaction. *Analytical biochemistry*, 95 (2), 351–358.

Oliver, M.F., 2006. Sudden cardiac death: the lost fatty acid hypothesis. *QJM: monthly journal of the association of physicians*, 99 (10), 701–709.

Olusi, S.O., 2002. Obesity is an independent risk factor for plasma lipid peroxidation and depletion of erythrocyte cytoprotectic enzymes in humans. *International journal of obesity*, 26 (9), 1159–1164.

Rameshreddy, P., *et al.*, 2018. Obesity-alleviating potential of asiatic acid and its effects on ACC1, UCP2, and CPT1 mRNA expression in high fat diet-induced obese Sprague-Dawley rats. *Molecular and cellular biochemistry*, 442 (1–2), 143–154.

Redondo Useros, N., *et al.*, 2019. 2-OHOA supplementation reduced adiposity and improved cardiometabolic risk to a greater extent than n-3 PUFA in obese mice. *Obesity research & clinical practice*, 13 (6), 579–585.

Rodrigues, A., *et al.*, 2012. Food intake, body mass index and body fat mass in elderly. *Asian journal of clinical nutrition*, 4 (3), 107–115.

Saravanan, G., *et al.*, 2013. Cardioprotective activity of *Amaranthus viridis* Linn: effect on serum marker enzymes, cardiac troponin and antioxidant system in experimental myocardial infarcted rats. *International journal of cardiology*, 165 (3), 494–498.

Sathibabu Uddandrao, V.V., *et al.*, 2018. Beneficial role of some natural products to attenuate the diabetic cardiomyopathy through Nrf2 pathway in cell culture and animal models. *Cardiovascular toxicology*, 18 (3), 199–205.

Sathibabu Uddandrao, V.V., *et al.*, 2019. Restorative potentiality of S-allylcysteine against diabetic nephropathy through attenuation of oxidative stress and inflammation in streptozotocin-nicotinamide-induced diabetic rats. *European journal of nutrition*, 58 (6), 2425–2437.

Sathibabu Uddandrao, V.V., Brahmanaidu, P., and Saravanan, G., 2018. Therapeutical perspectives of S-allylcysteine: effect on diabetes and other disorders in animal models. *Cardiovascular & hematological agents in medicinal chemistry*, 15 (2), 71–77.

Seo, W.K., *et al.*, 2017. Free fatty ok, acid l. associated with thrombogenicity in cardioembolic stroke. *Cerebrovascular diseases*, 44 (3–4), 160–168.,

Singh, R., and Krishan, P., 2010. Modulation of impact of high fat diet in pathological and physiological left ventricular cardiac hypertrophy by fluvastatin. *Biomedicine & pharmacotherapy = biomedecine & pharmacotherapie*, 64 (3), 147–153.

Sun, X., *et al.*, 2012. High free fatty acids level related with cardiac dysfunction in obese rats. *Diabetes research and clinical practice*, 95 (2), 251–259.

Suzuki, T., and Yamamoto, M., 2015. Molecular basis of the keap1-nrf2 system. *Free radical biology & medicine*, 88 (Pt B), 93–100.

Taube, A., *et al.*, 2012. Inflammation and metabolic dysfunction: links to cardiovascular diseases. *American journal of physiology: heart and circulatory physiology*, 302, 2148–2165.

Uddandrao, V.V.S., *et al.*, 2020. Antiobesity efficacy of asiatic acid: down-regulation of adipogenic and inflammatory processes in high fat diet induced obese rats. *Archives of physiology and biochemistry*, 126 (5), 453–462.

Wende, A.R., Symons, J.D., and Abel, E.D., 2012. Mechanisms of lipotoxicity in the cardiovascular system. *Current hypertension reports*, 14 (6), 517–531.

Wilson, C., 2013. Obesity: finding weight loss strategies that work in primary care. *Nature reviews. endocrinology*, 9 (3), 126–130.

Wong, C., and Marwick, T.H., 2007. Obesity cardiomyopathy: pathogenesis and pathophysiology. *Nature clinical practice. Cardiovascular medicine*, 4 (8), 436–443.

Woods, S.C., and Seeley, R.J., 2002. Understanding the physiology of obesity: review of recent developments in obesity research. *International journal of obesity*, 26 (S4), S8–S10.

Yazici, D., and Sezer, H., 2017. Insulin resistance, obesity and lipotoxicity. *Advances in experimental medicine and biology*, 960, 277–304.

Zeng, C., *et al.*, 2015. Curcumin protects hearts from FFA-induced injury by activating Nrf2 and inactivating NF-κB both *in vitro* and *in vivo*. *Journal of molecular and cellular cardiology*, 79, 1–12.

Zhou, B., *et al.*, 2013. Fibrinogen facilitates atherosclerotic formation in Sprague-Dawley rats: a rodent model of atherosclerosis. *Experimental and therapeutic medicine*, 5 (3), 730–734.

P.G.P. COLLEGE OF ARTS & SCIENCE NAMAKKAL 637 001

PRINCIPAL
PGP College of Arts and Science
Namakkal

5:29

www.semanticscholar.org

Corpus ID: 202618619

Free radical scavenging activity of Moringa oleifera seed ethanolic extract

P. Tamilmani, A. Kalaivani, R. Malathi • Published 2018

Moringa oleifera seed is one of the best known naturalized species of the Moringaceae family found in Asian countries. In the present study, we investigated the antioxidant and free radical...

Expand

[PDF] Aujpb.Com

Save

Alert

Share This Paper

Abstract

Figures and Tables

86 References

Related Papers



Australian Journal of Pharmaceutical Biology
ISSN Number (2209-5276)
Volume 1; Issue 2; September 2018

Original Article

Free radical scavenging activity of *Moringa oleifera* seed ethanolic extract

P. Tamilmani*, A. Kalaivani, R. Malathi

Department of Biochemistry, PGP College of Arts and Science, Namakkal, Tamil Nadu, India

ABSTRACT

Moringa oleifera seed is one of the best known naturalized species of the Moringaceae family found in Asian countries. In the present study, we investigated the antioxidant and free radical scavenging activities of ethanolic extract of *M. oleifera* seed by *in vitro* antioxidant. The antioxidant and free radical scavenging activities were used to determine 2,2-diphenylpicrylhydrazyl, nitric oxide (NO) scavenging effect, superoxide anion scavenging activity, and total antioxidant activity using spectrophotometer methods, respectively. Ethanolic extract of *M. oleifera* seed was found to have an excellent radical scavenging effect, as well as *M. oleifera* seed extract, showed remarkable inhibition of superoxide anion formation in a dose-dependent manner. Furthermore, *M. oleifera* results were reviled to inhibit NO generation and enhance antioxidant activity. Thus, the results suggested that the ethanolic extract *M. oleifera* seed is a potential source of natural antioxidant and serves as an effective free radical scavenger and inhibitor. Hence, *M. oleifera* seed might be a good plant-based pharmaceutical product for several diseases caused by free radicals.

Keywords: Antifungal, antimicrobial activity, antioxidant, free radical scavenger, *Moringa oleifera*

Submitted: 06 September 2018, Accepted: 20 September 2018, Published: 30 September 2018

INTRODUCTION

The beneficial medicinal effects of plant materials typically result from the combinations of secondary products present in the plant that the medicinal actions of plants are unique to particular plant species or groups are consistent with this concept as the combinations of secondary products in a particular plant are often taxonomically distinct (Kaufman *et al*., 1999). Ecological function of secondary products may have some bearing on potential medicinal effects for humans. The search for new molecules, nowadays, has taken a slightly different route where the science of ethnobotany and ethnopharmacognosy is being used as a guide to lead the chemist toward different sources and classes of compounds (Gurib-Fakim, 2006). Plant-derived natural products hold great promise for the discovery and development of new pharmaceuticals (McChesney *et al*., 2007). Since ancient times, medicinal plants have been harvested from the wild (Castle, 2014). In many rural communities, traditional medicine (TM) is still viewed as the mainstay of primary health-care systems (He, 2015) due to its effectiveness, cultural preference, or absence of modern alternatives (Patwardhan and Patwardhan, 2005; Barboza *et al*., 2009).

Phytochemical constituents are the basic source for the establishment of several pharmaceutical industries. The constituents present in a plant play a significant role in the identification of crude drug. The knowledge of bioactive compounds of these medicinal plants could be especially needed in designing new, safe, and effective formulations of nutriceuticals and phytotherapeutics for humans containing medicinal parts of these plants. Thus, the phytochemical screening is very important in identifying new sources of therapeutically and industrially important compounds such as alkaloids, flavonoids, phenolic compounds, saponins, steroids, tannins, and terpenoids. All the phytochemical components detected were known to support bioactive activities in medicinal plants (Edeoga *et al*., 2005). The past few decades have seen increasing scientific interest in both growth of plant tissue culture and the commercial development of this

Address for correspondence: P. Tamilmani, Department of Biochemistry, PGP College of Arts and Science, Namakkal, Tamil Nadu, India. Phone: +91-9786820779. E-mail: tamilmanip@yahoo.com/tamilp15@gmail.com

technology as a means of producing valuable phytochemicals. *In vitro* studies are highly instrumental in selecting a drug for a particular disease and also in getting the preliminary evidence to proceed for further *in vivo* pharmacological research (Chandrakala *et al.*, 2013).

Antioxidants are the chemical substances which prevent the free radicals damage in the body. Oxidative stress caused by reactive oxygen species (ROS) is associated with the pathogenesis of a numerous dreaded chronic diseases such as diabetes, cancer, atherosclerosis, coronary artery diseases, and other degenerative diseases (Husain *et al.*, 2012). Antioxidants constitute one of the several defense systems used to neutralize pro-oxidants. Since pro-oxidants and antioxidants are found ubiquitously in nature, pro-oxidant and antioxidant effects of individual compounds or mixtures have received much attention in scientific research. Antioxidants are very important in biological systems. They are known to possess anti-inflammatory, anticardiovascular disease, and anticancer properties (Kool *et al.*, 2007). Antioxidants may act as free radical scavengers, reducing agents, chelating agents for transition metals, quenchers of singlet oxygen molecules, and/or activators of antioxidative defense enzyme systems to suppress the radical damages in biological systems (Nickavar *et al.*, 2008).

To protect against damage by ROS, all biological systems have evolved complex antioxidant mechanisms. These are composed of low molecular weight compounds (such as glutathione and Vitamin E) and 24 enzymes such as catalase, superoxide dismutase, or glutathione peroxidase (Rial and Zardoya, 2009). Natural antioxidants present in the plants scavenge harmful free radicals from our body. Free radical is any species capable of independent existence that contains one or more unpaired electrons which react with other molecule by taking or giving electrons, and involved in many pathological conditions (Madhavi *et. al*, 1996; Halliwell, 2005). Free radical is a chemical compound which contains an unpaired electron spinning on the peripheral layer around the nucleus.

However, almost all organisms are protected from free radical attack by resistance mechanisms such as a defending antioxidant system that declines the rate of free radical formation, and another system to produce chain-breaking antioxidants that scavenge and stabilize free radicals. When free radical manufacturing rate exceeds the capability of the antioxidant defense mechanisms, considerable tissue injury occurs (Yehye *et al.*, 2015). Therefore, antioxidants having free radical scavenging activities may have some great significance in the prevention and therapeutics of free radical aided diseases.

An antioxidant is a molecule capable of slowing or preventing the oxidation of other molecules. They may protect cells from damage caused by unstable molecules known as free radicals. Antioxidants terminate these chain reactions by removing free radical intermediates and inhibit other oxidation reactions by being oxidized themselves. Free radicals are fundamentals to any biochemical process and represent an essential part of aerobic life and metabolism. Majority of the diseases are mainly linked to oxidative stress due to free radicals (Gutteridgde, 1995). Our body is rich in endogenous antioxidants, the substances that have the ability to stop free radical formation or limit the damage they cause (Tomas–Barberan and Robin, 1997). The effectiveness of current used exogenous antioxidants arises most probably from the increase of the endogenous free radical scavengers as enzymes (superoxide dismutase and selenium-dependent glutathione peroxidase), vitamins (alpha-tocopherol and ascorbic acid). Many plants have been also found to possess free radical scavenging activity (polyphenols, alkaloids, and terpenoids). Low levels of one or more of the essential antioxidants have been shown to be associated with many disorders including cancer, inflammation, atherosclerosis, coronary heart disease, and diabetes (Pandey and Rizvi, 2009).

Infectious diseases are the leading cause of death throughout the world. Antibiotic resistance has become a global concern. The clinical effectiveness of many existing antibiotics is being threatened by the emergence of multidrug- resistant pathogen. Many infectious diseases have been known to be treated with herbal remedies throughout the history of mankind. Natural products, either as pure compounds or as standardized plant extracts, provide unlimited opportunities for new drug leads due to the unmatched availability of chemical diversity (Cos *et al.*, 2006). There is an incessant and urgent need to discover new antimicrobial compounds with diverse chemical structures and novel mechanisms of action for new and re-emerging infectious diseases. Therefore, researchers are increasingly turning their attention to folk medicine, looking for new leads to develop better drugs against microbial infections. The escalating failure of chemotherapeutics and antibiotic resistance exhibited by pathogenic microbial infectious agents has led to the screening of several medicinal plants for their potential antimicrobial activity (Cotter *et al.*, 2013).

India is a varietal emporium of medicinal plants and is one of the richest countries in the world in regard to genetic resources of medicinal plants. It exhibits a wide range in topography and climate, which has a bearing its vegetation and floristic composition. Moreover, the agro-climatic conditions are conductive for introducing and domesticating new exotic plant varieties (Chanda and Kaneria, 2011).

In recent years, secondary plant metabolites (phytochemicals), previously with unknown pharmacological activities, have been comprehensively investigated as a source of medicinal agents (Cragg and Newman, 2013). Thus, it is anticipated that phytochemicals with adequate antibacterial

efficiency will be used for the treatment of bacterial infections. The potential for developing antimicrobials from higher plants appears rewarding as it will lead to the development of a phytomedicine to act against microbes (Hussain and Gorsi, 2004).

Plant-based antimicrobials have enormous therapeutic potential as they can serve the purpose with lesser side effects that are often associated with synthetic antimicrobials (Cowan, 1999). Sustained further exploration of plant-derived antimicrobials is needed today. Medicinal plants continue to be an important therapeutic aid for alleviating the ailments of humankind. The search for eternal health, longevity, for remedies to relieve pain and discomfort drove an early man to explore his immediate natural surroundings. This is used to produce many plant and animal products, minerals and the development of a variety of therapeutic agents (Suryawanshi and Patel, 2011). Today, there is a renewed interest in TM and an increasing demand for more drugs from plant sources. This revival of curiosity in plant described drugs is mainly due to the current widespread belief that the "green medicine" is safe and is more dependable than the costly synthetic drugs, many of which have undesirable side effects (Kataria *et al.*, 2011).

Moringa oleifera is one of the best known naturalized species of the Moringaceae family (Anwar *et al.*, 2007). It is native to India, Pakistan, Bangladesh, and Afghanistan, utilized by ancient Romans, Greeks, and Egyptians; now distributed in many countries of the tropics and subtropics (Asante *et al.*, 2014). The species *M. oleifera* is known worldwide by several popular names such as moringa, drumstick tree, horseradish tree, and ben oil tree. It is commonly called "*murungai*" in Tamil. *M. oleifera* is an extremely valued plant, dispersed in many countries of the tropics and subtropics. It has an extraordinary range of medicinal uses with high nutritive value. Different parts of this plant contain a sketch of important minerals and are a good source of protein, various phenolics, vitamins, β-carotene, and amino acids (Anwar *et. al.*, 2007). The Moringa plant offers a rich and exceptional combination of zeatin, kaempferol, quercetin, and many other phytochemicals. It is very significant for its medicinal value. Numerous parts of the plant such as the roots, seed, bark, leaves, fruit, and immature pods, flowers act as cardiac and circulatory drugs, possess antitumor (Jung, 2014; Krishnamurthy *et al.*, 2015), antipyretic, antiulcer, anti-inflammatory, and antiepileptic (Pal *et. al.*, 1995). Other chief medicinal properties of the plant include antispasmodic (Caceres *et. al.*, 1992), diuretic, antihypertensive (Attakpa *et al.*, 2017), cholesterol lowering (Sagum *et. al.*, 2014), hepatoprotective, antioxidant, antidiabetic (Paliwal *et al.*, [2011], Vongsak *et. al.*, 2013; Divi *et al.*, 2012), antibacterial, and antifungal activities (Patel *et al.*, 2014).

MATERIALS AND METHODS

Plant

Dried seeds of *M. oleifera* were collected from the country local shop. The plant was authenticated by the plant anatomy research center, Chennai, Tamil Nadu, India.

Preparation of the Plant Extract

The dried seeds of *M. oleifera* were manually de-coated, and naked seeds were grinded to powder. 10 g of the powdered seed was soaked in 100 ml of distilled water, and 100 g of the powdered seed was soaked in 400 ml 80% ethanol. Mixtures were continuously shaken at 200 rpm for 24 h. Filtrate was collected by filtration of the mixtures through Whatman filter paper. Exhaustive extraction was done by repeating extraction procedure another two times, and crude extracts were pooled together. Ethanol was evaporated from pooled ethanolic extract using rotary evaporator, and the crude water and ethanolic extracts were freeze-dried.

2,2-Diphenylpicrylhydrazyl (DPPH) Assay

The free radical quenching capacity of *M. oleifera* seed ethanolic extract was determined by the method involving the bleaching of stable DPPH (Hatano *et al.*, 1989). A reaction mixture containing methanol, DPPH (10 mM, 30 µl) and 100 µl of various concentrations of *M. oleifera* seed ethanolic extract (100–500 µg/ml) was allowed to stand at room temperature for 30 min before mixing with redistilled distilled water (1 ml) and toluene (3 ml). The solution was then centrifuged, and the absorbance of the upper phase was read at 517 nm against a blank without *M. oleifera* seed ethanolic extract, prepared and processed as described above. Vitamin C served as standard and compared with the extract. The free radical scavenging activity was calculated as given below.

$$\text{Radical scavenging } (\%) = \frac{\{\text{Control-Sample}\}}{\text{Control}} \times 100$$

The results were expressed as percentage inhibited/mg of extract.

Nitric oxide (NO-) scavenging effect

According to the method of Marcocci *et al.* (1994), sodium nitroprusside (SNP, 5 mM) was dissolved in phosphate buffered saline and this was mixed with different concentrations of *M. oleifera* seed ethanolic extract (100, 200, 300, 400, and 500 µg/ml) dissolved in 50 mM of phosphate buffer, before being incubated at 25°C for 150 min. The amount of NO^- produced by SNP was measured by Griess reagent (1%) (sulfanilamide in 5% phosphoric acid and 0.1% N- 15- naphthyl ethylenediamine dihydrochloride in distilled water). 0.5 ml of the incubation mixture was mixed with the same volume of Griess reagent. The absorbance of the mixture was read at

550 nm. Vitamin C served as standard and compared with the extract. The percentage of inhibition per each concentration of the extract was calculated as given below.

$$\text{Radical scavenging } (\%) = \frac{\{\text{Control-Sample}\}}{\text{Control}} \times 100$$

The results were expressed as % inhibited/mg of extract.

Superoxide Anion Scavenging Activity

Measurement of superoxide anion scavenging activity of *M. oleifera* seed ethanolic extract was based on the method described by Liu *et al.* (1997) with slight modifications of Gulcin *et al.* (2003).

Reagents

1. Tris–HCl buffer: 16 mM, pH 8.0
2. Nitroblue tetrazolium (NBT): 50 µM
3. Phenazine methosulfate (PMS): 10 µM
4. NADH: 78 µM.

Superoxide anions were chemically generated in a mixture of PMS and NADH. The reaction was quantified by coupling superoxide generation to the reduction of NBT. In this experiment, the superoxide radicals were generated in 3 ml of Tris–HCl buffer (16 mM, pH 8.0) containing 1 ml of NBT (50 µM) solution, 1 ml of NADH (78 µM) solution, and 1ml of various concentrations (100, 200, 300, 400, and 500 µg/ml) of *M. oleifera* seed ethanolic extract was mixed. The reaction was started by adding 1 ml of PMS solution (10 µM) to the mixture. The reaction mixture was incubated at 25°C for 5 min, and the absorbance at 560 nm in a spectrophotometer was measured.

Total Antioxidant Activity

The total antioxidant activity of *M. oleifera* seed ethanolic extract was determined according to ferric thiocyanate method of Mitsuda *et al.* (1967) and Osawa and Namiki (1981) with slight modification according to Kikuzaki and Nakatani (1993). Vitamin E was used as a standard. The results were expressed as percentage inhibited/µg of *M. oleifera* seed ethanolic extract.

Antibacterial Activity

M. oleifera seed ethanolic extract was subjected for antimicrobial activity by the disc diffusion method against both Gram-positive and Gram-negative organisms, by the method of Carson and Riley (1995).

Gram-positive organisms

1. *Staphylococcus aureus* (ATCC 9144)
2. *Staphylococcus epidermidis* (ATCC 155)
3. *Micrococcus luteus* (ATCC 4698)
4. *Bacillus cereus* (ATCC 11778).

Gram-negative organisms

1. *Escherichia coli* (ATCC 25922)
2. *Pseudomonas aeruginosa* (ATCC 1688)
3. *Klebsiella pneumonia* (ATCC 11298).

Nutrient Agar Medium (Pharmacopoeia of India, 1985)

- Beef extract – 10 g
- Peptone – 10 g
- Sodium chloride – 5 g
- Agar – 1.2%
- Distilled water to 1 L.

All the ingredients in distilled water were dissolved by gentle heat. pH of the medium was adjusted to 8.0–8.4 with 5 M sodium hydroxide and boiled for 10 min then filtered. The filtrate was adjusted to pH 7.2 and sterilized by maintaining at 115°C for 30 min.

Procedure

The sterilized (autoclaved at 120°C for 30 min) medium (40°C–50°C) was inoculated with the suspension of the various microorganisms and poured into Petri dishes to give a depth of 3–4 mm. Various (250, 500, and 750 µg/ml) concentrations of *M. oleifera* seed ethanolic extract are prepared in methanol separately. Sterile discs (made from Whatman filter paper pre-sterilized in UV lamp) dipped in the specified concentration of the extracts and standard (ciprofloxacin, 100 µg/ml). The impregnated discs are allowed to dry. The dried discs were placed on the surface of agar plates. A disc dipped in methanol and dried was used as a control.

The plates were left for 1 h at room temperature and incubated at 37°C for 18 h. The diameter of the zone of inhibition of extracts and standard were measured.

Antifungal Activity

M. oleifera seed ethanolic extract was screened for antifungal activity by disc diffusion method against following organisms as described by Carson and Riley (1995).

1. *Aspergillus niger* (ATCC 9029)
2. *Aspergillus fumigatus* (ATCC 46645)
3. *Candida albicans* (ATCC 10231).

Sabouraud dextrose agar medium was used for the study.

Sabouraud Dextrose Agar Media

- Mycological peptone - 10 g
- Dextrose - 40 g
- Agar - 15 g
- Distilled water - 1 L.

Procedure

Suspension of microorganisms was added to sterile Sabouraud dextrose agar medium at 45°C, and the mixture was transferred to sterile Petri dishes and allowed to solidify. Sterile discs dipped in various concentrations (50, 100, and 250 µg/ml) of *M. oleifera* seed ethanolic extract was placed on the surface of agar plates. A dried disc was used as a control.

The plates were used for 1 h at room temperature and incubated at 37°C for 18 h. The diameter of the zone of inhibition of extract was measured.

Statistical Analysis

Experimental results were mean±SD of three parallel measurements. Analysis of variance was performed by ANOVA procedures (SPSS 9.0 for Windows). Significant differences between means were determined by Duncan's Multiple Range tests. $P > 0.05$ was regarded as significant and $P > 0.01$ very significant.

RESULTS

DPPH Radical Scavenging Activity of *M. oleifera* Seed Extract

The antioxidant activity of *M. oleifera* seed extract is performed using the DPPH method, and the results are presented in Figure 1. From the result, it was found that *M. oleifera* seed extract showed excellent antioxidant activity in a dose-dependent manner at various concentrations such as 100, 200, 300, 400, and 500 µg/mL. Interestingly, the *M. oleifera* seed extract exhibits nearly 50% excellent radical scavenging activity at the concentration of 235 µg/mL when compared with the standard Vitamin C.

Superoxide Scavenging Activity of *M. oleifera* Seed Extract

Figure 2 depicts the inhibitory effect of *M. oleifera* seed extract on the superoxide anion formation. The scavenging effects of *M. oleifera* seed extract on the superoxide anion formation were examined at five different concentrations (100, 200, 300, 400, and 500 µg/mL). *M. oleifera* seed extract showed remarkable inhibition of superoxide anion formation in a dose-dependent manner, and maximum inhibitions of superoxide were observed at the concentration of 330 µg/mL and were comparable with Vitamin C.

Nitricoxide Scavenging Activity of *M. oleifera* Seed Extract

The results of the nitric oxide scavenging activity of *M. oleifera* seed extract are presented in Figure 3. It was found that the NO were significantly scavenged by the *M. oleifera* seed extract at various concentrations such as 100, 200, 300, 400, and 500 µg/mL with the remarkable inhibition of NO generation

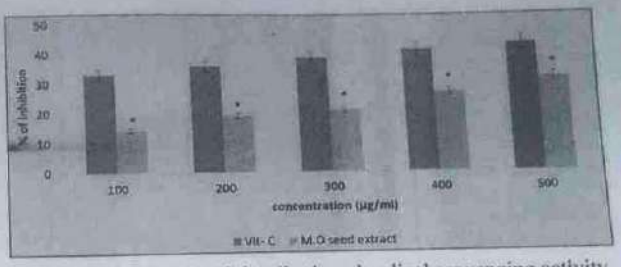


Figure 1: 2,2-Diphenylpicrylhydrazyl radical scavenging activity of *Moringa oleifera* seed extract. Values are mean ± SD of six parallel measurements. *$P > 0.05$ when compared against control. Vitamin C means Vitamin C

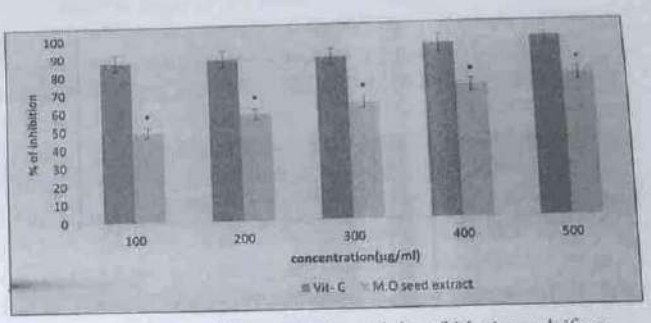


Figure 2: Superoxide scavenging activity of *Moringa oleifera* seed extract. Values are mean ± SD of six parallel measurements. *$P > 0.05$ when compared against control. Vitamin C means Vitamin C

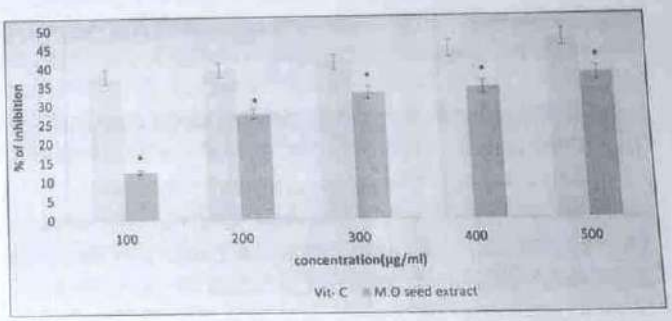


Figure 3: Nitric oxide scavenging activity of *Moringa oleifera* seed extract. Values are mean ± SD of six parallel measurements. *$P > 0.05$ when compared against control. Vitamin C means Vitamin C

observed at the concentration of 365µg/mL when compared with Vitamin C.

Total Antioxidant Activity by FTC Method

The total antioxidant activity of *M. oleifera* seed ethanolic extract by FTC method is presented in Table 1. The results revealed that the *M. oleifera* seed ethanolic extract markedly inhibited the oxidation of linoleic acid for 5 days with nearly 50% of inhibition when compared to the standard Vitamin E and the results were found to be statistically significant and were comparable to control.

Table 1: Total antioxidant activity of *Moringa oleifera* seed extract by FTC method

Days	Control	% of inhibition of vitamin C	% of inhibition of *Moringa oleifera* seed extract
Day 1	0.04±0.001	0.082±0.020#	0.610±0.004#
Day 2	0.14±0.002	0.130±0.007#	0.093±0.007#
Day 3	0.25±0.001	0.195±0.005#	0.192±0.002#
Day 4	1.67±0.010	0.270±0.006#	0.245±0.003#
Day 5	5.31±0.020	0.530±0.002#	0.496±0.004#

Values are mean ± SD of six parallel measurements. #$P>0.05$ when compared against control

Antibacterial Activity of *M. oleifera* Seed Ethanolic Extract

Antibacterial activity of aqueous extracts of *M. oleifera* seed ethanolic extract at different concentrations (50, 100, and 150 µg/ml) against both Gram-positive and Gram-negative bacteria on comparison with standard antibacterial drug ciprofloxacin was shown in Table 2. The activity of the plant extract was assessed by the formation of a zone of inhibition. The present study showed that the aqueous extracts of *M. oleifera* seed ethanolic extract had interesting activity against both Gram-positive and Gram-negative bacteria. The plant extract proved to be active against five out of five Gram-positive bacteria such as *S. aureus, Staphylococcus epidermis, M. luteus, B. cereus,* and *Bacillus subtilis.* The antibacterial effect of these extracts was found to be comparable to the antibacterial activity exhibited by conventional antibacterial drug ciprofloxacin (5 µg/ml). Gram-negative bacterial strains such as *E. coli, Pseudomonas aeuruginosa* and *K. pneumonia* is used for this study [Figure 4].

Antifungal Activity of *M. oleifera* Seed Ethanolic Extract

Antifungal activity of aqueous extracts of *Amaranthus tristis* at different concentrations (50, 100, and 150 µg/ml) against *A. niger* and *Aspergillus fumigates* is shown in Table 2. The activity of the plant extract was assessed by the formation of zone of inhibition. The results showed that the *M. oleifera* seed ethanolic extract has the capacity to inhibit the growth of the above mentioned fungal organisms by disc diffusion method. The antifungal activity of the extract at 100 µg/disc was found to be almost equal to that of standard antifungal drug ketoconazole (50 µg/disc). The results are discussed in tabular columns.

Table 2: Antimicrobial activity of *Moringa oleifera* seed extract

Name of the organism	Zone of inhibition			
Gram-positive organism	Standard	50 µl	100 µl	150 µl
Staphylococcus aureus	32	22	27	30
Staphylococcus epidermis	29	14	17	20
Micrococcus luteus	29	15	18	20
Bacillus cereus	29	16	18	21
Bacillus subtilis	29	15	18	22
Gram-negative organism				
Escherichia coli	32	19	23	27
Klebsiella pneumonia	30	21	24	28
Pseudomonas aeruginosa	30	16	19	22
Fungus				
Aspergillus niger	30	16	19	22
Aspergillus fumigatus	31	17	21	24

DISCUSSION

Plants can manufacture many different types of secondary metabolites, which have been subsequently exploited by humans due to their beneficial role in a diverse array of applications. Secondary metabolites are mainly responsible for the medicinal activity of plant species (Zwenger and Basu, 2008). The curative properties of medicinal plants are perhaps due to the presence of various secondary metabolites such as alkaloids, flavonoids, glycosides, phenols, saponins, and sterols. Microorganism seed ethanolic extract has revealed the presence of triterpenoids, steroids, glycosides, alkaloids, flavonoids, tannins, carbohydrate, and amino acids. These secondary metabolites are reported to have many biological and therapeutic properties (Vishnu *et al.*, 2013; Benedec *et al.*, 2013; Charalampos *et al.*, 2013; Narender *et al.*, 2012), so this species is expected to have many medicinal uses.

These compounds also can be correlated with the medicinal potential of the plant. Most natural compounds are derived from primary metabolites such as amino acids, carbohydrates, and fatty acids and are generally categorized as secondary metabolites. Secondary metabolites are considered products of primary metabolism but not involved in the metabolic activity (Pal, 2007). The phenolic compounds are present in most widely distributed in the plant kingdom (Hossian *et al.*, 2013). Mainly, the phenolic and flavonoids compounds extracted from the leaves samples antibiotics activity of the plant leaf extract (Subhadra *et al.*, 2014).

The phytochemical screening demonstrated the presence of different types of phytocompounds such as alkaloids, saponins,

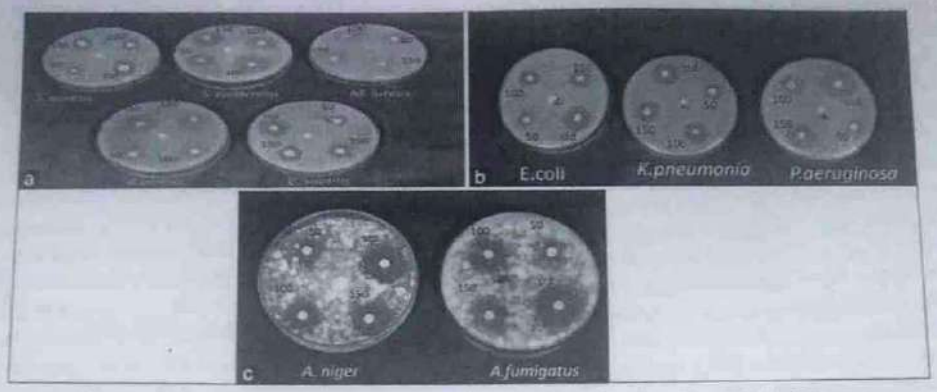


Figure 4: (a-c) Gram-positive organism, (b) Gram-negative bacteria, and (c) *Fungus*

flavonoids, steroids, and tannins which could be responsible for the various pharmacological properties. Phytochemical constituents such as tannins, flavonoids, alkaloids, and several other aromatic compounds or secondary metabolites of plants serve as a defense mechanism against predation by many microorganism, insects, and herbivores. The curative properties of medicinal plants are perhaps due to the presence of various secondary metabolites such as alkaloids, flavonoids, glycosides, phenols, saponins, and steroids (Anubha and Handa, 2013). Tannins natural tendency to ward off microbes makes them good candidates for treating fungal and yeast infections. These compounds served as natural antibiotics, which help the body to fight infections and microbial invasion. The biological functions of flavonoids apart from its antioxidant properties include protection against allergies; inflammation, free radicals, platelet aggregation, microbes, ulcers, hepatoxins, viruses, and tumors (Barkatullah *et al.*, 2013). Cardiac glycosides content was found in methanol extract. Cardiac glycosides have been used for over two centuries as a stimulant in case of cardiac failure (Aiyegoro and Okoh, 2009). The major chemical substances of interest in the earlier reports have been the alkaloids and steroidal sapogenins (saponins); however, other diverse groups of naturally occurring phytochemicals such as flavonoids, tannins, unsaturated sterols, triterpenoids, and essential oils also have been reported (Doughari, 2012).

The concentration of antioxidant compounds is needed to decrease the DPPH$^{\cdot}$ radicals by IC_{50}, which is a parameter widely used to estimate the antioxidant activity (Krishna *et al.*, 2013). DPPH$^{\cdot}$ is a stable free radical, and that can accept an electron or hydrogen radical to become a stable diamagnetic molecule (Bijaya and Bikash, 2013). A freshly prepared DPPH$^{\cdot}$ solution is of deep purple color with an absorption maximum at 517 nm, and in the presence of an antioxidant, this color disappears due to quenching of DPPH$^{\cdot}$ free radicals and converting them into a colorless product 2, 2-dipenyl-1-picryl hydrazine (Sumathy *et al.*, 2013). Hence, DPPH$^{\cdot}$ is usually used as a substance to evaluate the antioxidant activity (Shah *et al.*, 2013). In the present study, the extracts had significant scavenging effects on the DPPH$^{\cdot}$ radical which was increasing with the increase in the concentration. Similar trend of DPPH$^{\cdot}$ free radical scavenging activity was already documented well (Vishnu *et al.*, 2013; Thambiraj and Paulsamy, 2012). Scavenging activity of DPPH radical was found to rise with increasing concentration of the extracts. In addition, it has been determined that the antioxidant effect of plant products is mainly due to radical scavenging activity of phenolic compounds such as flavonoids, polyphenols, and tannins (Dai and Mumper, 2010). The antioxidant activity of phenolic compounds is mainly due to their oxidation-reduction properties, which can play an important role in adsorbing and neutralizing free radicals, reducing singlet and triplet oxygen, or decomposing peroxides (Ghasemzadeh *et al.*, 2010). The oxidative injury now appears as the fundamental mechanism causing a number of human neurologic and other disorders such as autoimmune pathologies, inflammation, viral infections, and digestive system disorders including gastrointestinal inflammation and ulcer (Ashley *et al.*, 2012). The present results suggest that all the tested plant extracts have moderate to potent antioxidant activity.

The reducing power of the extracts may serve as a significant indicator of its potential antioxidant activity (Oliveira *et al.*, 2008). In this assay, the yellow color of the test solution changes to various shades of green and blue, depending on the reducing power of the test specimen. The presence of reductones, which have been shown to be an impart antioxidant action by breaking the free radical chain by donating a hydrogen atom. The presence of reductones (i.e., antioxidants) in the sample extracts might cause the reduction of Fe^{3+}/ferric cyanide complex to ferrous form which can be monitored by spectrophotometrically at 700 nm (Nair *et al.*, 2012). The reducing power increased with the increase in the extract concentrations. This may be served as a significant indicator of its potential antioxidant activity. Hence, this study presumed that the ethanol extract of *M. oleifera* seed may have high amount of reductones

and hence the antioxidant property. The NO radicals play an important role in inducing an inflammatory response, and their toxicity multiplies only when they react with superoxide anion radicals to form peroxynitrite, which damages biomolecules such as proteins, lipids, and nucleic acids (Fridovich, 1978; Rengarajan *et al.*, 2014). NO is generated when SNP reacts with oxygen to form nitrite. Incubation with ethanol extract of *M. oleifera* seed inhibits nitrite formation by competing with oxygen to react with NO directly. In the present study, the ethanol extract of *M. oleifera* seed was active, and it might act as a very potent and novel therapeutic agent for scavenging NO. Superoxide is a well-known free radical of all oxygen-derived species (Gillis, 1997). It is the first intermediate in the sequential univalent reduction of oxygen that leads to the formation of hydrogen peroxide. Superoxide radical is unique in that it can lead to the formation of many other reactive species, including hydroxyl free radical, hydrogen peroxide, and perhydroxyl radicals (Valko *et al.*, 2007). It induces oxidative damage in lipids, proteins, and DNA (Pieta, 2000). The most important source of superoxide is oxidative enzymes, among which xanthine oxidase and NADPH/NADH oxidase are the most effective sources. On the other hand, it is also produced in the extracellular fluid by macrophages during phagocytosis in the inflammatory phase of diseased conditions (Monboisse *et al.*, 1983). In the present study, incubation with ethanol extract of *M. oleifera* seed results in a decrease of absorbance, which indicates the consumption of superoxide anion in the reaction mixture. The decreases in absorbance level of the present investigation may be due to the antioxidant activity of ethanol extract of *M. oleifera* seed.

In addition, the total antioxidant activity of ethanol extract of *M. oleifera* seed was measured by the FTC method. The FTC method was used to measure the amount of peroxide at the beginning of lipid peroxidation, in which peroxide react with ferrous chloride and form ferric ions (Zahin *et al.*, 2009). In the present investigation ethanol extract of *M. oleifera* seed showed low absorbance values, which indicate a high level of antioxidant activity. The endpoint of the FTC method indicates the presence of antioxidant activity of ethanol extract of *M. oleifera* seed which inevitably proves that ethanol extract of *M. oleifera* seed has excellent antioxidant activity *in vitro*.

Plants are important source of potentially useful structures for the development of new chemotherapeutic agents. The first step toward this goal is the *in vitro* antibacterial activity assay (Zain *et al.*, 2012). Many reports are available on the antiviral, antibacterial, antifungal, anthelmintic, anti-molluscal, and anti-inflammatory properties of plants (Gomathi *et al.*, 2017). Some of these observations have helped in identifying the active principle responsible for such activities and in the developing drugs for the therapeutic use in human beings. However, not many reports are available on the exploitation of antifungal or antibacterial property of plants for developing commercial formulations for applications in crop protection. The various phytochemical compounds detected are known to have beneficial importance in medicinal sciences. For instance, flavonoids have been referred to as nature's biological response modifiers, due to their inherent ability to modify the body's reaction to allergies and virus and they showed their anti-allergic, anti-inflammatory, antimicrobial, and anticancer activities (Mansuri *et al.*, 2014). Plant steroids are known to be important for their cardiotonic activities and also possess insecticidal and antimicrobial properties. They are also used in nutrition, herbal medicine, and cosmetics (Maobe *et al.*, 2013). Tannins were reported to exhibit antiviral, antibacterial, and antitumor activities. It was also reported that certain tannins were able to inhibit HIV replication selectively and were also used as a diuretic (Kaur and Poonam, 2014). Saponin is used as mild detergents and in intracellular histochemical staining. It is also used to allow antibody access in intracellular proteins. In medicine, it is used in hypercholesterolemia, hyperglycemia, antioxidant, anticancer, anti-inflammatory, weight loss, etc. It is also known to have antifungal properties (Mujeeb *et al.*, 2014). The results shows the ethanol extract exhibited antibacterial activity against all the tested strain viz. *E. coli*, *Pseudomonas aeuruginosa* and *K. pneumonia* [Table 2].

The extracts of higher plants can be very good source of antibiotics (Saleem *et al.*, 2010) against various bacterial pathogens. Plant having antimicrobial compounds have enormous therapeutic potential as they can act without any side effect as often found with synthetic antimicrobial products. Most antimicrobial medicinal plant is more effective against Gram-positive than Gram-negative bacteria (Viera *et al.*, 2010). However, our current findings show a remarkable activity against Gram-negative bacteria including multi-resistant Gram-negative strains. The antimicrobial activity of the ethanol extract of *M. oleifera* seed may be due to tannins and other phenolic constituents. *M. oleifera* is known to be very rich in protein, vitamins, β-carotene, amino acids, and various phenolics (Anwar *et al.*, 2007). Furthermore, zeatin, quercetin, β-sitosterol, caffeoylquinic acid and kaempferol, and other polyphenols were isolated from *M. oleifera* leaves (Igado *et al.*, 2017). Tannins are considered nutritionally undesirable because they precipitate proteins, inhibit the digestive enzyme and affect the absorption of vitamins and minerals. However, some kinds of tannins can reduce the mutagenicity of a number of mutagens and display anticarcinogenic, antimicrobial, and antioxidant activities (Sagbas *et al.*, 2015).

The result obtained in this study suggests a potential application of *M. oleifera* seed extract for the treatment of skin wounds, typhoid, and further investigations should be conducted to explore their applications. Other medicinal plants containing phenolic compounds, including tannins, as major constituents are used topically for care and repair of skin wounds (Mujeeb

et al., 2014). The advantage of the use of topical antimicrobials is their ability to deliver high local concentrations of antibiotic irrespective of vascular supply. Further benefits include the absence of adverse systemic effects, and a low incidence of resistance (Benucci *et al.*, 2014).

CONCLUSION

The ethanolic extract of *M. oleifera* seed excellently exhibited different levels of antioxidant activity in all the *in vitro* models employed and also the results revealed that the ethanolic extract of *M. oleifera seed* had significant antioxidant activity through quenching various free radicals. The free radical scavenging property exhibited by ethanolic extract of *M. oleifera seed* may be one of the mechanisms by which this drug is useful as a foodstuff and as well as usefulness against free radical-mediated diseases. Furthermore, ethanolic extract of *M. oleifera* seed has great potential as an antimicrobial agent against microorganisms and then can be used in the treatment of infectious diseases caused by resistant microorganisms. The demonstration of a broad spectrum of antibacterial activity may help to discover new chemical classes of antibiotic substances that could serve as selective agents for infectious disease, chemotherapy, and control.

REFERENCES

Aiyegoro, O. A., & Okoh, A. I. (2009). Phytochemical screening and polyphenolic antioxidant activity of aqueous crude leaf extract of *Helichrysum pedunculatum*. *International Journal of Molecular Sciences*, 10(11), 4990-5001.

Anubha, S. S. S., & Handa, S. S. (2013). Hepatoprotective activity of *Apium Graveolens* and *Hygrophila Auriculata* against paracetamol and thioacetamide intoxication in rats. *Journal of Ethnopharmacology*, 49, 119-126.

Anwar, F., Latif, S., Ashraf, M., & Gilani, A. H. (2007). *Moringa oleifera*: A food plant with multiple medicinal uses. *Phytotherapy Research*, 21(1), 17-25.

Asante, I. L., Nasare, D., Tom-Dery, K., & Ochire-Boadu, K. B. K. (2014). Nutrient composition of *Moringa oleifera* leaves from two agro ecological zones in Ghana. *African J. Plant*, 8, 65-71.

Ashley, N. T., Weil, Z. M., & Nelson, R. J. (2012). Inflammation: Mechanisms, costs, and natural variation. *Annual Review of Ecology, Evolution, and Systematics*, 43, 385-406.

Attakpa, E. S., Chabi, N. W., Bertin, G. A., Ategbo, J. M., Seri, B., & Khan, N. A. (2017). *Moringa oleifera*-rich diet and T-cell calcium signaling in hypertensive rats. *Physiological research*, 66(5), 753-767.

Barboza, G. E., Cantero, J. J., Núñez, C., Pacciaroni, A., & Ariza Espinar, L. (2009). Medicinal plants: A general review and a phytochemical and ethnopharmacological screening of the native Argentine Flora. *Kurtziana*, 34(1-2), 7-365.

Barkatullah, B. B., Ibrar, M., Ali, N., & Muhammad, N. (2013). Antispasmodic potential of leaves, barks and fruits of *Zanthoxylum armatum* DC. *African Journal of Pharmacy and Pharmacology*, 7(13), 685-693.

Benedec, D., Vlase, L., Oniga, I., Mot, A. C., Damian, G., & Hanganu, D. (2013). Polyphenolic composition, antioxidant and antibacterial activities for two Romanian subspecies of *Achillea distans* Waldst. et Kit. ex Wild. Molecules, 18, 8725-8739.

Benucci, I., Elena, C., Katia, L., & Marco, E. (2016). Inhibitory effect of ethanol, sulphur dioxide and proanthocyanidinic tannins on lysozyme antimicrobial activity in model wine. *LWT-Food Science and Technology*, 73, 320-325.

Bijaya, L. M., & Bikash, B. (2013). Antioxidant capacity and phenolics content of some Nepalese medicinal plants. *American Journal of Plant Sciences*, 4, 1660-1665.

Caceres, A., Saravia, A., Rizzo, S., Zabala, L., De Leon, E., & Nave, F. (1992). Pharmacologie properties of *Moringa oleifera*. 2: Screening for antispasmodic, antiinflammatory and diuretic activity. *Journal of Ethnopharmacology*, 36(3), 233-237.

Carson, C. F., & Riley, T. V. (1995). Antimicrobial activity of the major components of the essential oil of *Melaleuca alternifolia*. *Journal of Applied Microbiology*, 78(3), 264-269.

Castle, L. M., Leopold, S., Craft, R., & Kindscher, K. (2014). Ranking tool created for medicinal plants at risk of being overharvested in the wild. *Ethnobiology Letters*, 5, 77-88.

Chanda, S., & Kaneria, M. (2011). Indian nutraceutical plant leaves as a potential source of natural antimicrobial agents. *Science Against Microbial Pathogens: Communicating Current Research and Technological Advances*, 2, 1251-1259.

Chandrakala, S., Mallikarjuna, K., & Reddy, C. S. (2013). *In vitro* pharmacological investigations of *Biophytum sensitivum* callus extract: Lack of potent activities. *Journal of Pharmaceutical Negative Results*, 4(1), 60.

Charalampos, P., Konstantina, L., Olga, K. M., Panagiotis, Z., & Vassileia, J. S. (2013). Antioxidant capacity of selected plant extracts and their essential oils. *Antioxidants*, 2, 11-22.

Cos, P., Vlietinck, A. J., Berghe, D. V., & Maes, L. (2006). Anti-infective potential of natural products: How to develop a stronger *in vitro* 'proof-of-concept'. *Journal of Ethnopharmacology*, 106(3), 290-302.

Cotter, P. D., Ross, R. P., & Hill, C. (2013). Bacteriocins-a viable alternative to antibiotics?. *Nature Reviews Microbiology*, 11(2), 95-105.

Cowan, M. M. (1999). Plant products as antimicrobial agents. *Clinical Microbiology Reviews*, 12(4), 564-582.

Cragg, G. M., & Newman, D. J. (2013). Natural products: A continuing source of novel drug leads. *Biochimica et Biophysica Acta (BBA)-General Subjects*, 1830(6), 3670-3695.

Dai, J., & Mumper, R. J. (2010). Plant phenolics: Extraction, analysis and their antioxidant and anticancer properties. *Molecules*, 15(10), 7313-7352.

Divi, S. M., Bellamkonda, R. A. M. E., & Dasireddy, S. K. (2012). Evaluation of antidiabetic and antihyperlipedemic potential of aqueous extract of *Moringa oleifera* in fructose fed insulin resistant and STZ induced diabetic wistar rats: A comparative study. *Asian Journal Pharmaceutical and Clinical Research*, 5(1), 67-72.

Doughari, J. H. (2012). Phytochemicals: Extraction methods, basic structures and mode of action as potential chemotherapeutic agents. In: *Phytochemicals-A Global Perspective of their Role in Nutrition and Health*. New York: InTech.

Edeoga, H. O., Okwa, D. E., & Mbaebie, B. O. (2005). Phytochemical constituents of some Nigerian medicinal plants. *The African*

Journal of Biotechnology; 4(7), 685-688.

Fridovich, I. (1978). The biology of oxygen radicals. *Science*, 201, 875-880.

Ghasemzadeh, A., Jaafar, H. Z., & Rahmat, A. (2010). Antioxidant activities, total phenolics and flavonoids content in two varieties of Malaysia young ginger (*Zingiber officinale* Roscoe). *Molecules*, 15(6), 4324-4333.

Gillis, C. N. (1997). *Panax ginseng* pharmacology: A NO link. *Biochemical Pharmacology*, 54, 1-8.

Gomathi, S., Ambikapathy, V., & Panneerselvam, A. (2017). Antimicrobial activity of some medical plants against *Pythium debaryanum* (Hesse). *Journal of Microbiology and Biotechnology Research*, 1(2), 8-13.

Gulcin, I., Uguz, M. T., Oktay, M., Beydemir, S., & Kufrevioglu, O. I. (2003) Antioxidant and antimicrobial activites of *Tenerium polium* L. *Journal of Food Technology*, 1, 9-17.

Gurib-Fakim, A. (2006). Medicinal plants: Traditions of yesterday and drugs of tomorrow. *Molecular Aspects of Medicine*, 27, 1-93.

Gutteridgde, J. M. C. (1995). Free radicals in disease processes: A complication of cause and consequence. *Free Radical Research Communications*, 19, 141-158.

Halliwell, B. (2005). *Free Radicals and Other Reactive Species in Disease*. Singapore: *eLS*.

Hatano, T., Edamatsu, R., Mori, A., Fujita, Y., & Yasuhara, E. (1989). Effect of interaction of tannins with co-exixting substances. VI. Effects of tannins and related polyphenols on superoxide anion radical and on DPPH radical. *Chemical and Pharmaceutical Bulletin*, 37, 2016-2021.

He, K. (2015). Traditional Chinese and Thai medicine in a comparative perspective. *Complementary Therapies in Medicine*, 23(6), 821-826.

Hossian, A. M., Al-Raqmi, S. A. K., Al-Mijizy, H. Z., Weli, M. A., & Al-Riyami, Q. (2013). Study of total phenol, flavonoids contents and phytochemical screening of various leaves crude extracts of locally grown *Thymus vulgaris*. *Asian Pacific Journal of Tropical Biomedicine*, 3(9), 705-710.

Husain, N., Kumar, A., & Radicals, F. (2012). Reactive oxygen species and natural antioxidants: A review. *Advanced Biomedical Research*, 17(1), 24-38.

Hussain, M. A., & Gorsi, M. S. (2004). Antimicrobial activity of *Nerium oleander* Linn. *Asian Journal of Plant Sciences*. 3(2), 177-80.

Igado, O. O., Jan, G., Mario, R. T., Ezgi, E. B., Foluso, A. A., Ulrike, H., Helga, S., & James, O. O. (2017). Isolation of a novel compound (MIMO2) from the methanolic extract of *Moringa oleifera* leaves: Protective effects against vanadium-induced cytotoxity. *Drug and Chemical Toxicology*, 2017, 1-10.

Jung, I. L. (2014). Soluble extract from *Moringa oleifera* leaves with a new anticancer activity. *PloS one*, 9(4), e95492.

Kataria, S., Bhardwaj, S., & Middha, A. (2011). Standardization of medicinal plant materials. *International Journal of Research in Ayurveda and Pharmacy*, 2(4), 100-104.

Kaufman, P. B., Cseke, L. J., Warber, S., Duke, J. A., & Brielmann, H. L. (1999). *Natural Products from Plants*. Boca Raton, FL: CRC Press.

Kaur, S., & Poonam, M. (2014). Study of total phenolic and flavonoid content, antioxidant activity and antimicrobial properties of medicinal plants. *Journal Microbiology Experience*, 1, 1-6.

Kikuzaki, H., & Nakatani, N. (1993). Antioxidant effects of some ginger constituents. *Journal of Food Science*, 58, 1407-1410.

Kool, J., Sebastiaan, M., Liempd, V., Harmsen, S., Schenk, T., Irth, H., Commandeur, J. N. M., & Vermeulen, N. P. E. (2007). An on-line post-column detection system for the detection of reactive-oxygen-species-producing compounds and antioxidants in mixtures. *Analytical and Bio Analytical Chemistry*, 388, 871-879.

Krishna, T. M., Shiva, D., Keerthi, D., Nandini, A., Aswaq, A., & Reddy, T. (2013). *In vitro* evaluation of antioxidant properties of *Cucumis melo* L. Extracts of leaves and fruit. *International Journal of Pharma and Bio Sciences*, 4(1), 705-712.

Krishnamurthy, P. T., Vardarajalu, A., Wadhwani, A., & Patel, V. (2015). Identification and characterization of a potent anticancer fraction from the leaf extracts of *Moringa oleifera* L. *Indian Journal of Experimental Biology*, 53, 98-103.

Liu, F., Oovi, V. F. C., & Chang, S.T. (1997). Free radical scavenging activity of mushroom polysaccharide extracts. *Life Science*, 60, 763-777.

Madhavi, D. L., Deshpande, S. S., & Sulunkhe, D. K. (1996). *Food Antioxidant: Technological, Toxicological and Health Perspectives*. New york: Marcel Dekker.

Mansuri, M. L., Parihar, P., Solanki, I., & Parihar, M. S. (2014). Flavonoids in modulation of cell survival signalling pathways. *Genes and nutrition*, 9(3), 400.

Maobe, M. A., Gatebe, E., Gitu, L., & Rotich, H. (2013). Preliminary phytochemical screening of eight selected medicinal herbs used for the treatment of diabetes, malaria and pneumonia in Kisii region, Southwest Kenya. *European Journal of Applied Sciences*, 5(10), 1-6.

Marcocci, L., Pecker, L., Sakaki, A., & Albert, M. (1994). Antioxidant action of *Gingko biloba* extract (EGb 761). *Methods in Enzymology*, 234, 462-475.

McChesney, J. D., Venkataraman, S. K., & Henri, J. T. (2007). Plant natural products: Back to the future or into extinction? *Journal of Phytochemistry*, 68, 2015-2022.

Mitsuda, H., Yasumoto, K., & Iwani, K. (1967). Antioxidant activity of indole compounds during the autoxidation of linoleic acid. *Eiyo to Shoduryo*, 19, 210.

Monboisse, J. C., Braquet, P., & Borel, J. P. (1983). Non-enzymatic degradation of acid-soluble calf skin collagen by superoxide ion: Protective effect of flvonoids. *Biochemistry and Pharmacology*, 32, 53-58.

Mujeeb, F., Preeti, B., & Neelam, P. (2014). Phytochemical evaluation, antimicrobial activity, and determination of bioactive components from leaves of *Aegle marmelos*. *BioMed Research International*, 2014, 1-11.

Nair, V. D., Paneerselvam, R., & Gopi, R. (2012). Studies on methanolic extract of *Rawolfia* species from Southern Western Ghats of India – *In vitro* antioxidant properties, characterization of nutrients and phytochemicals. *Industrial Crops and Products*, 39, 17-25.

Narender, P. D., Ganga, R., Sambasiva, E., Mallikarjuna, T., & Praneeth, V. S. (2012). Quantification of phytochemical constituents and *in vitro* antioxidant activity of *Mesua ferrea* leaves. *Asian Pacific Journal of Tropical Biomedicine*, 2(2), S539-S542.

Nickavar, B., Alinaghi, A., & Kamalinejad, M. (2008). Evaluation of the antioxidant properties of five *Mentha* species. *International Journal of Production Research*, 7, 203-209.

Oliveira, I., Sousa, A., Ferreira, I., Bento, A., Estevinho, L., &

P.G. COLLEGE OF ARTS & SCIENCE NAMAKKAL 637 002

Pereira, J. A. (2008). Total phenols, antioxidant potential and antimicrobial activity of walnut (*Juglans regia* L.) green husks. *Food and Chemical Toxicology*, 46, 2326-2331.

Osawa, T., & Namiki, M. (1981). A novel type of antioxidant isolated from leaf wax of eucalyptus leaves *Agricultural and Biological Chemistry*, 45, 735-740.

Pal, A. (2007). *Biotechnology: Secondary Metabolites: Plants and Microbes*. Portland: Science Publishers. p. 70.

Pal, S. K., Mukherjee, P. K., & Saha, B. P. (1995). Studies on the antiulcer activity of *Moringa oleifera* leaf extract on gastric ulcer models in rats. *Phytotherapy Research*, 9(6), 463-465.

Paliwal, R., Sharma, V., & Sharma, S. H. (2011). Hepatoprotective and antioxidant potential of *Moringa oleifera* pods against DMBA-induced hepatocarcinogenesis in male mice. *International Journal of Drug Development and Research*, 3(2), 263-275.

Pandey, K. B., & Rizvi, S. I. (2009). Plant polyphenols as dietary antioxidants in human health and disease. *Oxidative Medicine and Cellular Longevity*, 2(5), 270-278.

Patel, P. L., Patel, T. A., Patel, A., Desai, S., & Meshram, D. Y. (2014). Phytochemical analysis and antifungal activity of *Moringa oleifera*. *International Journal of Pharmacy and Pharmaceutical Sciences*, 6(5), 144-147.

Patel, P., Bhalodia, Y., Gohil, T., Malavia, S., & Devmurari, V. (2011). *In vitro* antioxidant activity of ethanolic extract of *Azadirachta Indica* leaves. *Journal of Advances in Pharmacy and Healthcare Research*, 1(3), 22-27.

Patwardhan, B., & Partwardhan, A. (2005). Traditional Medicine: Modern Approach for Affordable Global Health. Geneva: World Health Organization, 1-172.

Pieta, P. G. (2006). Flavanoids as antioxidants. *Journal of Natural Products*, 63, 1035-1042.

Rengarajan, T., Rajendran, P., Nandakumar, N., Balasubramanian, M. P., & Nishigaki, I. (2014). Free radical scavenging and antioxidant activity of D-pinitol against 7, 12 dimethylbenz (a) anthracene induced breast cancer in sprague dawley rats. *Asian Pacific Journal of Tropical Disease*, 4(5), 384-390.

Rial, E., & Zardoya, R. (2009). Oxidative stress, hermogenesis and evolution of uncoupling proteins – Mini review. *Journal of Biological Chemistry*, 8, 58.

Sagbas, S., Nahit, A., & Nurettin, S. (2015). Modified biofunctional p (tannic acid) microgels and their antimicrobial activity. *Applied Surface Science*, 354, 306-313.

Sagum, R. S., Mallillin, A. C., Trinidad, T. P., de Leon, M. P., Borlagdan, M. P., Cid, K. B. B., & Alcantara, J. D. S. (2014). Changes in glucose and lipid profile after consumption of malunggay (*Moringa oleifera*) leaves products in humans with moderately raised serum glucose and cholesterol levels. *Food and Public Health*, 4(4), 200-203.

Saleem, M., Nazir, M., Ali, M. S., Hussain, H., Lee, Y. S., Riaz, N., & Jabbar, A. (2010). Antimicrobial natural products: An update on future antibiotic drug candidates. *Natural Product Reports*, 27(2), 238-254.

Shah, N. A., Khan, M. R., Ahmad, B., Noureen, F., Rashid, U., & Khan, R. A. (2013). Investigation on flavonoid composition and anti–free radical potential of *Sida cordata*. *BMC Complementary and Alternative Medicine*, 13, 276-288.

Subhadra, D. V., Gopal, R. M., & Uma, M. M. (2014). Preliminary phytochemical screening of various extracts of *Valeriana wallichii* root. *Sky Journal of Biochemistry Research*, 3(9), 80-85.

Sumathy, R., Sankaranarayanan, S., Bama, P., Ramachandran, J., Vijayalakshmi, M., & Deecaraman, M. (2013). Antioxidant and antihemolytic activity of flavonoids extract from fruit peel of *Punica granatum*. Asian Journal of Pharmaceutical and Clinical Research, 6(2), 211-214.

Thambiraj, J., & Paulsamy, S. (2012). *In vitro* antioxidant potential of methanol extract of the medicinal plant, *Acacia caesia* (L.) Wild. *Asian Pacific Journal of Tropical Biomedicine*, 2(2), S732-S736.

Tomas–Barberan, F. A., & Robins, R. J. (1997). *Phytochemistry of Fruits and Vegetables*. Oxford, New York: Caledon Press.

Valko, M., Leibfritz, D., Moncol, J., Cronin, M. T., Mazur, M., & Telser, J. (2007). Free radicals and antioxidants in normal physiological functions and human disease. *The International Journal of Biochemistry and Cell Biology*, 39(1), 44-84.

Viera, G. H. F., Mourão, J. A., Ângelo, Â. M., Costa, R. A., & Vieira, R. H. S. D. (2010). Antibacterial effect (*in vitro*) of *Moringa oleifera* and *Annona muricata* against gram positive and gram negative bacteria. *Revista do Instituto de Medicina Tropical de São Paulo*, 52(3), 129-132.

Vishnu, R., Nisha, R., Jamuna, S., & Paulsamy, S. (2013). Quantification of total phenolics and flavonoids and evaluation of in vitro antioxidant properties of methanolic leaf extract of *Tarenna asiatica* - An endemic medicinal plant species of Maruthamali hills, Western Ghats, Tami Nadu. *Journal of Plant Science and Research*, 2(2), 196-204.

Vongsak, B., Sithisarn, P., Mangmool, S., Thongpraditchote, S., Wongkrajang, Y., & Gritsanapan, W. (2013). Maximizing total phenolics, total flavonoids contents and antioxidant activity of *Moringa oleifera* leaf extract by the appropriate extraction method. *Industrial Crops and Products*, 44, 566-571.

Yehye, W. A., Rahman, N. A., Ariffin, A., Hamid, S. B. A., Alhadi, A. A., Kadir, F. A., & Yaeghoobi, M. (2015). Understanding the chemistry behind the antioxidant activities of butylated hydroxytoluene (BHT): A review. *European Journal of Medicinal Chemistry*, 101, 295-312.

Zahin, M., Aqil, F., & Ahmad, I. (2009). The *in vitro* antioxidant activity and total phenolic content of four Indian medicinal plants. *International Journal of Pharmacy and Pharmaceutical Sciences*, 1(1), 88-95.

Zain, M. E., Awaad, A. S., Al-Outhman, M. R., & El-Meligy, R. M. (2012). Antimicrobial activities of Saudi Arabian desert plants. *Phytopharmacology*, 2(1), 106-113.

Zwenger, S., & Basu, C. (2008). Plant terpenoids: Applications and future potentials. *Biotechnology and Molecular Biology Reviews*, 3, 1-7.

This work is licensed under a Creative Commons Attribution Non-Commercial 4.0 International License.

PRINCIPAL
PGP College of Arts and Science
Namakkal

4:55 ... 187-Apr-2781.pdf

Genetic Determinants Responsible for Multi ... Resistance of *Salmonella spp.* isolated from Poult... Meat and HIV Infected Patients in Tamilnadu, Indi...

Prakash B[1*]., Tamilmani P[2]., Vinoth Kumar V[3]., Gayathri VR[4]., Yashicka JV[4]

[1] *Department of Biochemistry, PGP College of Arts & Science, Namakkal, Tamilnadu, India*

[2] *Department of Biochemistry, PGP College of Arts & Science, Namakkal, Tamilnadu, India*

[3] *Department of Biochemistry, Sree Narayana Guru College, Coimbatore, Tamilnadu, India*

[4] *Department of Biotechnology, Vivekanandha College of Arts & Science for Women, Namakkal, Tamilnadu, India*

tract : **Tracking antimicrobial resistance among animal and human isolated bacteria is essential to educate pul icy on the suitable use of antimicrobial agents in animal and human medication, 200 *Salmonella spp* were isola m both animal and clinical samples. Antimicrobial activity of all the isolates was analysed. Chicken meat isolates greatest antimicrobial content among them. In this study shows, the plasmid profiles were also not similar for b es of isolates. From the overall result, no compatible relationship was observed between clinical and meat isola ring the analysis of antibacterial susceptibility, virulence gene and plasmid profile, no correlation was obser ween the isolates. However, these observations support the possibility that chicken meat indirectly might be one of ential sources of antibiotic-resistant Salmonella infections in human.**

words: ***Salmonella spp.*** **Poultry meat, Clinical isolates**

I. Introduction

Poultry products, and chicken, in particular, continue to be a favorite element of t man diet since they can be used for both their meat and their eggs. However, chickens can source of several bacterial and viral-related diseases and infections due to the varic thogenic organisms they carry. Coming to the common diseases by poultry, Salmonellosis : most talked. *Salmonella* poisoning, or Salmonellosis, is probably the most common bacter liction that humans can get by eating chicken meat or eggs that have been contaminated w s bacterium. Especially, HIV patients are prone to get this, due to their we munogenicity. Salmonellosis is characterized by high fever, abdominal cramping a rrhea, and it is especially dangerous when it affects young children, the elderly or peo th compromised immune systems like AIDS. We have chosen the Namakkal distri milnadu as the site for the research. Especially in Namakkal District produces about 65% : egg output of Tamil Nadu. The additional benefit of choosing the district is that t ncerned district is not only well known for its poultry and dairy industries, it also ranks in t) position for holding many HIV patients. Previous researches have shown that isolates of t *monella spp.* often possess resistance to various antibiotics, since they pass their virul nes even to other unrelated organisms. Thus, the purpose of this work was to study t netic determinants responsible for the resistance of *Salmonella* isolated from animals as w hospitalized HIV patients.

P.G.P. COLLEGE OF ARTS & SCIENCE NAMAKKAL 637 204

dian University https://doi.org/10.37896/jxu14.4/187 ISSN No...

Journal of Xidian University https://doi.org/10.37896/jxu14.4/187 ISSN No:1001-2400

Genetic Determinants Responsible for Multiple Drug Resistance of *Salmonella spp.* isolated from Poultry Meat and HIV Infected Patients in Tamilnadu, India

Prakash B[1*]., Tamilmani P[2]., Vinoth Kumar V[3]., Gayathri VR[4]., Yashicka JV[4]

[1] *Department of Biotechnology, Vels Institute of Science, Technology and Advanced Studies, Chennai, Tamil Nadu, India*

[2] *Department of Biochemistry, PGP College of Arts & Science, Namakkal, Tamilnadu, India*

[3] *Department of Biochemistry, Sree Narayana Guru College, Coimbatore, Tamilnadu, India*

[4] *Department of Biotechnology, Vivekanandha College of Arts & Science for Women, Namakkal, Tamilnadu, India*

Abstract : **Tracking antimicrobial resistance among animal and human isolated bacteria is essential to educate public policy on the suitable use of antimicrobial agents in animal and human medication, 200 *Salmonella spp* were isolated from both animal and clinical samples. Antimicrobial activity of all the isolates was analysed. Chicken meat isolates has the greatest antimicrobial content among them. In this study shows, the plasmid profiles were also not similar for both types of isolates. From the overall result, no compatible relationship was observed between clinical and meat isolates. During the analysis of antibacterial susceptibility, virulence gene and plasmid profile, no correlation was observed between the isolates. However, these observations support the possibility that chicken meat indirectly might be one of the potential sources of antibiotic-resistant Salmonella infections in human.**

Keywords: ***Salmonella spp.*** **Poultry meat, Clinical isolates**

I. Introduction

Poultry products, and chicken, in particular, continue to be a favorite element of the human diet since they can be used for both their meat and their eggs. However, chickens can be a source of several bacterial and viral-related diseases and infections due to the various pathogenic organisms they carry. Coming to the common diseases by poultry, Salmonellosis is the most talked. *Salmonella* poisoning, or Salmonellosis, is probably the most common bacterial affliction that humans can get by eating chicken meat or eggs that have been contaminated with this bacterium. Especially, HIV patients are prone to get this, due to their weak immunogenicity. Salmonellosis is characterized by high fever, abdominal cramping and diarrhea, and it is especially dangerous when it affects young children, the elderly or people with compromised immune systems like AIDS. We have chosen the Namakkal district, Tamilnadu as the site for the research. Especially in Namakkal District produces about 65% of the egg output of Tamil Nadu. The additional benefit of choosing the district is that the concerned district is not only well known for its poultry and dairy industries, it also ranks in the top position for holding many HIV patients. Previous researches have shown that isolates of this *salmonella spp.* often possess resistance to various antibiotics, since they pass their virulent genes even to other unrelated organisms. Thus, the purpose of this work was to study the genetic determinants responsible for the resistance of *Salmonella* isolated from animals as well as hospitalized HIV patients.



II. MATERIALS AND METHODS

A. Sampling Sites

Poultry meat samples were collected from different poultry markets in Tamilnadu and Clinical samples of HIV patients possessing salmonellosis were collected from all over Tamilnadu (India).

B. Bacteriological analysis

Biochemical profile and the staining results were noted for the isolated colonies of *Salmonella spp.*, from both meat and human.

C. Antibiogram pattern of S.typhimurium

Our *S.typhimurium* isolates from both meat and human were checked for their respective antibiotic profiles against the following antibiotic discs: Gentamicin (10µg), Trimethoprim (5µg), Nalidixic acid (30µg), Ciprofloxacin (5µg), Cephotaxime (30µg), Imipenem (10µg), Colistin (10µg), Ceftazidim (30µg), Amoxicillin (30µg), Ampicillin (10µg), Chloramphenicol (30µg), Streptomicin (10µg) and Tetracycline (30µg).

D. Identification of MDR Salmonella typhimurium

The Multidrug-resistant *S. typhimurium* from both meat and human sample was identified separately by measuring their zone of inhibition per CLSI standard chart for *Enterobacteriaceae*. The isolates that showed resistance against three or more antibiotics were considered as MDR *S. Typhimurium*.

E. Phytochemical Analysis

The plants and plant parts of *Mangifera indica* were collected from in and around the Namakkal area. The collected plants were repeatedly washed in distilled water to remove adherent materials. Seed kernel of *M. indica* was our concern, which was separated, shade dried then mechanically powdered. The dried powder was stored separately in an airtight container before extraction.

F. Preparation of plant extracts

The powdered seed kernel was subjected to the successive Soxhlet extraction method using methanol and chloroform as the solvents. The extracts of respective solvents obtained were concentrated to dryness in a rotary flash evaporator under reduced pressure and controlled temperature and stored at 4^0C in the refrigerator until further use.

G. Antibacterial assay

The antibacterial assay was performed by agar well diffusion method for both the *S. typhimurium* isolates from meat and human sample respectively using the same procedure. The overnight culture was prepared by inoculating in 2 ml Nutrient broth with 2-3 colonies of each organism taken from nutrient agar. Broths were incubated overnight at 37^0C and from this 100µl of suspension was transferred on to the Petri plates (2 plates for each isolate) containing 20 ml of solidified NA and then the suspension was spread evenly on the medium to get a uniform lawn of bacteria. Four wells of 6 mm diameter were made at the 4 corners of the plates. The seed kernal extracts of two different solvents were loaded to the wells by using 100µl micropipette (100 mg/ml) in four different plates. Such that, each *S. typhimurium* isolate of meat and human sample are tested against both chloroform and methanol extract obtained from the seed kernel of *M. indica*. The plates were incubated at 37^0C for 24 hours. The antibacterial activity was determined by the recording zone of inhibition formed around the well. Kanamycin, nalidixc acid and Novabiocin at 100µg/ml were used as positive control and DMSO was used as a negative control.

H. Determination of biofilm formation

The solid medium of brain heart infusion broth (BHI) supplemented with 5% sucrose and Congo red was prepared (Mathur *et al.*, (2006). The medium was composed of BHI, sucrose, agar and congo red stain. Congo red was prepared as a concentrated aqueous solution and autoclaved at 121°C for 15 minutes, separately from other medium constituents and was then added to the agar which had cooled to 55°C. The isolates from both human and meat samples were streaked on Congo red plate and incubated at 37°C for 48 hours.

I. Isolation of Plasmid DNA

The MDR *S. typhimurium* cultures obtained from both meat and human were grown overnight at 37°C in Luria Bertani broth (50ml) containing antibiotic (30µg/ml) for the isolation of their plasmids. The same procedure was followed for both the cultures. The 1.5 ml of each culture was taken in Eppendorf tubes and centrifuged at 12,000 rpm for 10 min to collect the cell pellets. Then, 100µl of ice-cold suspension buffer solution I was used to the resuspended pellet and gently vortexed and kept on ice for 5minutes followed by the addition of 200 µl of freshly prepared alkaline lysis solution II and mixed by inverting the tubes for several times and allowed to keep on ice for 5 minutes. Neutralizing solution III (3M) of 150µl was added and kept on ice for 5 minutes. The supernatant was recovered by spin down at 12,000rpm for 10 minutes and resuspended in 500µl of solution IV (Phenol: Chloroform mixture) and mixed gently by inverting the tubes several times and kept at room temperature for 2 minutes. After centrifugation for 5 minutes at 12,000 rpm, the supernatant was discarded. The 300µl of 70% ethanol was added to the pellet and centrifuged at 12,000rpm for 10 minutes. The pellet containing the plasmid DNA was air-dried and dissolved in 20µl TE buffer. Furtherly, the isolated plasmids from the MDR *S. typhimurium* of both the meat and human samples were observed by Agarose Gel Electrophoresis.

J. Plasmid curing

The tubes were incubated at 37°C for 24 hrs. After the incubation, the isolates were inoculated again in sterile nutrient broth and incubated further for 24 hrs. The cured isolates were checked for antibiotic sensitivity.

K. Transconjugation

To determine if the resistance was transferable, a transconjugation experiment was performed. Both isolates of CTXm gene harbouring *Salmonella typhimurium* was used as donors and *E.coli* (cef^r) as the recipient in transconjugation experiments. The organisms were inoculated into 4 ml of Luria-Bertani (LB) broth (Difco, Detroit, Mich.) and incubated for 20 hours at 35°C with shaking. Both organisms are mixed with *E.coli* (cef^r) at a proportion of 1:2, The 24 hrs old cultures of both the isolates were grown in sterile nutrient broth containing various chemical agents viz, acridine orange (100 mcg/ ml) and 2% SDS. incubated for 4 hours at 35°C with shaking. After centrifugation for 5 minutes at 4000 rpm, the precipitate was mixed with 1 ml distilled water and inoculated onto MacConkey agar plates containing 2 µg of cefotaxime per millilitre. The same procedure was followed for both the *Salmonella typhimurium* isolates from meat and human. Transparent colonies were selected from the agar plates and inoculated into MacConkey agar again for activation. Plasmid electrophoresis was further analyzed.

Monitoring antimicrobial resistance trends among bacteria isolated from food, animals, and humans is necessary to inform public policy regarding the appropriate use of antimicrobial agents in veterinary and human medicine (Cummings *et al*. 2013). Some studies conducted in Nigeria also indicated the considerable prevalence of *Salmonella* both in veterinary and clinical samples (Jegadeesh *et al*., 2010; Fasure *et al*. 2012; Prakash *et al*., 2012, Ogunleye *et al*. 2013; Yemisi *et al*., (2014). In the present study, 200 isolates of *Salmonella spp.* were observed from clinical and chicken meat samples in around Namakkal area. Among them, chicken meat has the highest antimicrobial resistance patterns than clinical isolates.

In this study, high levels of resistance were found to Cotrimaxzole, Tetracycline, and Gentamycin 60%, 35%, and 40%, respectively. A comparative study in India, Nigeria, reported a high frequency (87%) of reduced susceptibility to CIP among the chicken isolates and a high frequency of resistance to TET (93%), NA (81%), and sulfamethoxazole (87%), while resistance to chloramphenicol, sulfamethoxazole, trimethoprim, and AMP ranged from 36% to 59% for the human isolates (Fashae *et al*. 2010). In the previous study in India, Yemisi *et al*., (2014) also observed the highest resistance isolates of *Salmonella* spp from clinical and animal sources.

High level of resistance to NA 45 (22.5%) as observed in this study, particularly from food animal, reaffirms the importance of the need for strengthening collaboration between veterinary and public health sectors on appropriate detection and reporting of zoonotic foodborne pathogens (Adesiji and Fagbami, 2006).

In the present study, all isolates were subjected to biofilm formation. Among both isolates, 78% of chicken meat isolates were the capacity to producing the biofilm formation. Compare to clinical isolates the biofilm formation is too high in Chicken meat isolates.

In the present study, transconjugation process was carried out with cefotaxime resistance isolates of *S.typhimurium*. They were transconjugated with non-ESBL producing and non-lactose fermenting E. coli that were susceptible to extended-spectrum cefotaxime. 20% of meat isolates have transferred the resistance to the recipient, whereas 40% of clinical isolates have transferred the resistance gene to a recipient.

According to Gilbert *et al* (2002), the resistance of microbial biofilms to a wide variety of antimicrobial agents is related with the organization of bacterial cells inside the polymer matrix, which hinders the penetration of antimicrobial agents into the biofilm. In the present study, most of biofilm-producing isolates were resistant to most of the antibiotics. This result was correlated to previous studies of Sereno *et al* 2011. Furthermore, plasmid profile was carried out for both isolates. The plasmid profiles were not similar for both types of isolates.

The present study underlines the unique problem of plasmid-mediated resistance, which has created a therapeutic challenge for Clinicians and Microbiologists. Hence, urgently need new ways to deal with pathogens, especially MDR and Biofilm producing isolates. One of the studies by Prakash *et al* (2012)., confirmed that the biofilm-producing isolates always had the highest tolerance towards antibiotics and additionally, isolates that are capable of producing a strong biofilm layer resisted any kind of antibiotics. Against the backdrop of this information, our investigation was focused on biological derivatives, because the biological nature of these compounds involves reduced side effects compared to conventional chemical agents. This study was considered to evaluate the antibacterial potential of plant extracts against *Salmonella* isolates. If the biological derivatives available, plants are considered a popular, costless, easily cultivate and suitable option for dealing with pathogenic isolates.

Among the potential sources of new agents, plants have long been investigated. Because which contain many bioactive compounds that can be interested in therapeutic. In this way, our goal was inhibition of *Salmonella* isolates by the seed kernel of *Mangifera indica*. The results revealed that the Methanol extracts of *M. indica* possess good antibacterial activity than chloroform extract. As methanol is a highly polar solvent, it shows very little difference in their extractive abilities. The zone of inhibition was ranged from 10 mm to 21 mm. Different concentration was used for this susceptibility study when using 125µg of extract, the best inhibition was observed. A Similar study was attempted by Al-Shwayeh *et al.*, 2000. They were noted the antimicrobial activity of the seed extract of *M. indica* against *E.coli*. Amgad *et al.*, 2012 noted 17mm zone of inhibition against clinical isolate of *E.coli*. Furthermore, MIC was also detected by broth dilution method. Among the different concentrations, 18 µg and 65 µg were MIC against *Salmonella* isolates.

From the overall result, no compatible relationship was observed between clinical and meat isolates. During the analysis of antibacterial susceptibility, virulence gene and plasmid profile, no correlation was observed between the isolates. But still, as far as Griffith's transformation principle is concerned, there are chances for the dead strain which could transform into a virulent one. Hence, there are chances for the *salmonella* spp., (killed while cooking the meat) to retain its virulence though the well-cooked meat is consumed. However, these observations support the possibility that chicken meat might be one of the potential sources of antibiotic-resistant *Salmonella* infections in human. Presently, the prevalence and MDR patterns of *Salmonella* isolated from retail chicken meat were different depending on the brands of chicken meat produced by different integrated broiler operations.

The retail chicken meats used in the present study were individually packaged at the end of the slaughter line, it is considered that the *Salmonella* profiles of each brand were directly associated with those of the corresponding integrated broiler operation. In addition, considering that similar MDR patterns of *Salmonella* isolates from each brand were consistently found over the 3 month sampling period, these consistent MDR patterns may be associated with the antibiotic usage pattern of the particular integrated company as feed additive and therapeutics and cross-contamination within integrated broiler operations (Kim *et al.*, 2007; Lee *et al.*, 2007).

ACKNOWLEDGEMENT

My Sincere thanks to UGC-South Eastern Regional Office (SERO, Government of India) Hyderabad for the research grant.

REFERENCE

[1]. Adesiji YO, Fagbami AH. Epidemiology of bacterial zoonosis in Nigeria. Niger. J. Health Biomed. Sci. 2006; 5:20–25.

[2]. Al-Swayeh OA, Futter LE, Clifford RH, Moore PK. Nitroparacetamol exhibits anti-inflammatory and antinociceptive activity. Br J Pharmacol 2000; 130:1453-6.

[3]. T Mathur, S Singhal, S Khan, DJ Upadhyay, T Fatma, A Rattan. Detection of Biofilm Formation

[4]. among the Clinical Isolates of Staphylococci: An Evaluation of Three Different Screening Methods. Indian Journal of Medical Microbiology, (2006) 24 (1):25-9.

[5]. Amgad A. Awad El-Gied., Martin R. P. Joseph., Ismail M. Mahmoud., Abdelkareem M., Ahmad M. Al akami., Mohamed E. Hamid. Antimicrobial Activities of Seed Extracts of Mango *(Mangifera indica L.)* 2012.

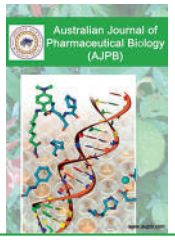
[6]. Cummings K.J., Aprea V.A., Altier, C. (2013). Antimicrobial resistance trends among Escherichia

[7]. coli isolates obtained from dairy cattle in the northeastern United States, 2004-2011. Foodborne Pathog Dis. 2014 Jan;11(1):61-7. doi: 10.1089/fpd.2013.1605. Epub 2013 Oct 17.
[8]. Fashae, K., Ogunsola, F., Aarestrup, F. M. and Hendriksen, R. S. (2010). Antimicrobial susceptibility and serovars of *Salmonella* from chickens and humans in Ibadan, Nigeria. J. Infect. Dev. Countries 4: 484-494.
[9]. Fasure, A. K., Deji-Agboola, A. M. and Akinyemi, K. O. (2012). Antimicrobial resistance patterns and emerging fluoroquinolone-resistant *Salmonella* isolates from poultry and asymptomatic poultry workers. Afr. J. Microbiol. Res. 6: 2610-2615.
[10]. Gilbert P, Allison DG, McBain AJ. Biofilms in vitro and in vivo: do singular mechanisms imply. Journal of Applied Microbiology Symposium Supplement 2002;92(1):98–110.
[11]. Hernández A, Sánchez MB, Martínez JL. Quinolone resistance: much more than predicted[J]. Front Microbiol, 2011, 2(22): 22.
[12]. Jegadeesh kumar D, Saritha V, Moorthy K, Suresh Kumar BT. Prevalence, antibiotic resistance and RAPD analysis of food isolates of *Salmonella* species. Int J Biol Tech 2010; 1:50-55.
[13]. Ogunleye AO, Ajuwape ATP. Adetosoye AI, Carlson SA. Characterization of *Salmonella enterica Ituri* isolated from diseased poultry in Nigeria. Afr. J. Biotechnol. 2013; 12:21–25.
[14]. Sereno MJ, Druziani JT, Gallego J, Bonatto CB, Bersot LS. Prevalência de *Salmonella spp.* em carcaças de frango na região Oeste do Estado do Paraná e Perfil de resistência a antimicrobianos. Resumos Evento da Iniciação científica; Evento de Iniciação em Desenvolvimento Tecnológico e Inovação; 2013; Curitiba, Paraná. Brasil: Fundação Araucária; 2011. p.505.
[15]. Yemisi, O. A., Vijaya, K. D. and Indran, K. (2014). Antimicrobial Resistant Genes Associated with *Salmonella* spp Isolated from Human, Poultry and Seafood Sources. Journal of Food Science and Nutrition 2(4): 436-442.
[16]. Prakash, B., Mathew, L. P., Narendrababu. R., Perumal, P., Geandeal, M. A. And Jagathesh, P. Identification of Biofilm and Extended-Spectrum B- Lactamases (ESBL) producing isolate of *Klebsiella Pneumonia* from Tamilnadu. Journal of Cell and Tissue Research Vol. 14(2) 4405-4408 (2014); ISSN: 0973-0028; E-ISSN: 0974-0910.
[17]. Lee, Y. J., H. J. Kim, C. K. Park, K. S. Kim, D. H. Bae, M. S. Kang, J. K. Cho, A. R. Kim, J. W. Kim, and B. H. Kim. 2007. Characterization of *Salmonella* spp. isolated from an integrated broiler chicken operation in Korea. J. Vet. Med. Sci. 69:399–404.
[18]. Kim, A., Y. J. Lee, M. S. Kang, S. I. Kwag, and J. K. Cho. 2007. Dissemination and tracking of *Salmonella* spp. in integrated broiler operation. J. Vet. Sci. 8:155–161.

PRINCIPAL
PGP College of Arts and Science
Namakkal

Australian Journal of Pharmaceutical Biology

ISSN Number (2209-5276)
Volume 1; Issue 2; September 2018



Original Article

Cytotoxic effect of *Moringa oleifera* seed ethanolic extract on human hepatocellular carcinoma cells (HepG2)

P. Tamilmani*, R. Malathi, A. Kalaivani

Department of Biochemistry, PGP College of Arts and Science, Namakkal, Tamil Nadu, India

ABSTRACT

In this study we evaluate the Ethanolic extract of Moringa oleifera seed were screened in vitro cytotoxicity effects and reduced glutathione (GSH) levels on HepG2 cell lines. The cytotoxic effects were assessed by 3-(4,5-dimethylthiazol-2-yl)-2,5-diphenyltetrazolium bromide (MTT) assay; however, the HepG2 cells were treated with ethanolic extract of *M. oleifera* seed at various concentrations (100, 200, 300, 400, and 500 µg/mL) and incubated for 24 h, 48 h, and 72 h, respectively. Furthermore, reduced GSH levels were determined by spectrophotometry. The cytotoxic effects assessed by MTT assay indicated that the ethanolic extract of *M. oleifera* seed exhibited a significant cytotoxic effect as well as depletion of GSH content was observed in HepG2 cells. Further, from the results, we observed *M. oleifera* seed extract to treat various cancer cell lines.

Keywords: Glutathione, HepG2 cells, *Moringa oleifera*, MTT assay

Submitted: 10 August 2018, Accepted: 21 September 2018, **Published:** 30 September 2018

INTRODUCTION

Natural products are known to play an important role in both drug discovery and chemical biology. In fact, many of the current drugs are made up of either naturally or chemically occurring molecules which have structures that are fully or partly derived from natural motifs. Natural antimicrobials can be derived from barks, stems, leaves, flowers, and fruits of plants, various animal tissues, or microorganisms (Nair and Chanda, 2007). Although some therapeutic benefits can be traced to specific plant compounds, many herbs contain dozens of active constituents, which together coalesce to give the plant its therapeutic values. Infectious diseases are the leading cause of death throughout the world. Antibiotic resistance has become a global concern. The clinical effectiveness of many existing antibiotics is being threatened by the emergence of multidrug-resistant pathogen. Many infectious diseases have been known to be treated with herbal remedies throughout the history of mankind. Natural products, either as pure compounds or as standardized plant extracts, provide unlimited opportunities for new drug leads because of the unmatched availability of chemical diversity (Cos *et al*., 2006). There is an incessant and urgent need to discover new antimicrobial compounds with diverse chemical structures and novel mechanisms of action for new and re-emerging infectious diseases. Therefore, researchers are increasingly turning their attention to folk medicine, looking for new leads to develop better drugs against microbial infections. The escalating failure of chemotherapeutics and antibiotic resistance exhibited by pathogenic microbial infectious agents has led to the screening of several medicinal plants for their potential antimicrobial activity (Cotter *et al*., 2013).

India is a varietal emporium of medicinal plants and is one of the richest countries in the world in regard to genetic resources of medicinal plants. It exhibits a wide range in topography and climate, which has a bearing its vegetation and floristic composition. Moreover, the agro-climatic conditions are conducive for introducing and domesticating new exotic plant varieties (Chanda and Kaneria, 2011). In recent years, secondary plant metabolites (phytochemicals), previously with unknown pharmacological activities, have

Address for correspondence: P. Tamilmani, Department of Biochemistry, PGP College of Arts and Science, Namakkal, Tamil Nadu, India. Phone: +91-8778897778. E-mail: malathirbc@gmail.com

been comprehensively investigated as a source of medicinal agents (Cragg and Newman, 2013). Thus, it is anticipated that phytochemicals with adequate antibacterial efficiency will be used for the treatment of bacterial infections. The potential for developing antimicrobials from higher plants appears rewarding as it will lead to the development of a phytomedicine to act against microbes (Hussain and Gorsi, 2004).

Any part of the plant may contain active components, for example, the roots of the *ginseng* plant contain saponins and essential oils, while eucalyptus leaves are harvested for essential oils and tannins (Woolf, 2003). Considering the aforementioned, it is assumed that the need of the hour is to search for new antimicrobials and antioxidants with this in mind; in this present work, the seed of *Moringa oleifera* is screened for their potential antioxidant and antimicrobial activity, where there is a paucity of information regarding its antioxidant potential and antimicrobial efficacy. Ahmed *et al.* (2015) suggested that seed essential oil from *M. oleifera* has potent cytotoxic activities against different cancer cell lines (HeLa, HepG2, MCF-7, CACO-2, and L929). Furthermore, the extracted phytochemicals from *M. oleifera* seeds, fractionated ethanolic extract, and cytotoxicity of the extracts and fractions on MCF7 and MCF 10A were showed that HFCEE (IC_{50} = 130 µg/ml) has antiproliferative effect on MCF7 breast cancer cell with insignificant cytotoxicity to MCF 10A normal breast cell (Adebayoa *et al.,* 2017).

M. oleifera parts are being employed for the treatment of different ailments in the indigenous system of medicine, particularly in South Asia (Anwar *et. al*., 2007). In addition, *M. oleifera* seeds possess water purifying powers by flocculating Gram-positive and Gram-negative bacterial cells (Kawo *et al.,* 2009). *M. oleifera* seeds can also be used as a less expensive bioabsorbent for the removal of heavy metals (Sharma *et al.,* 2006).

Precise components used for Moringa oleifera preparations are hypotensive, anticancerous and others including 4-(4'-O-acetyl-α-L-rhamnopyranosyloxy)benzyl isothiocyanate (Abrams *et al*., 1993), 4-(α-L-rhamnopyranosyloxy) benzyl isothiocy-anate. Abuye *et. al*., (1999), pterygospermin (Anderson *et al*., 1986), benzyl isothiocyanate (Anwar *et al*., 2003), and 4-(α-L-rhamnopyranosyloxy) benzyl glucosinolate (Asres, 1995). While these compounds are comparatively unique to the *Moringa* family, it is also rich in a quantity of vitamins and minerals as well as other more commonly predictable phytochemicals such as the carotenoids (including β-carotene or pro-Vitamin A). The seeds of *M. oleifera* can be consumed fresh, pounded, roasted, or pressed into sweet, non-desiccating oil. The aqueous extract of mature seeds is effective in clarifying turbid and wastewater in tropical countries (Jahn, 1998). The seeds of this plant are one of the best natural coagulants that have been discovered so far and the crushed seeds are viable replacement for synthetic coagulants (Kalogo *et al*., 2000). *Moringa* seeds are obtainable locally at a fraction of the cost of alum in many countries; they are simple to use and cheap to maintain (Jahn, 1998; Ndabigengesere and Narasiah, 1998). They have been used in the treatment of hard water, and the efficiency of *M. oleifera* seeds in hardness removal increases with increasing dosing (Muyibi and Evison, 1995).

Therefore, this study sought to investigate the *in vitro* antioxidant and cytotoxicity properties of ethanolic extract of *M. oleifera* seed.

MATERIALS AND METHODS

Chemicals

Dulbecco's modified eagle medium (DMEM) F-12 HAM nutrient medium, sodium bicarbonate, and trypsin-ethylenediaminetetraacetic acid (EDTA) were purchased from Biochrome, Germany, and antibiotic/antimycotic solution and fetal bovine serum (FBS) were purchased from GIBCO, Invitrogen, USA. All other chemicals including solvents were of high purity and analytical grade marketed by Glaxo Laboratories, Mumbai, and Sisco Research Laboratories Pvt., Ltd., Mumbai, India.

Cell Culture Reagents

DMEM F-12 HAM nutrient medium

15.6 g DMEM and 1.5 g sodium bicarbonate were dissolved in 900 ml of sterile Milli Q water. To this solution, 10 ml of antibiotic-antimycotic solution were added, pH was adjusted to 7.4 using NaOH, and final volume was made up to 1 L with Milli Q water. Then, the medium was sterile filtered (using 0.22 micron) and stored at 4°C.

Growth medium (DMEM F-12 HAM with 10% FBS)

100 ml of growth medium was prepared by adding 10 ml FBS in 90 ml (DMEM) F-12 HAM and stored in a sterile container at 4°C.

Phosphate buffer saline (PBS pH 7.4)

0.63 g of sodium phosphate monobasic (NaH_2PO_4) and 4.5 g of sodium chloride (NaCl) were dissolved in 500 ml of sterile Milli Q water, and pH was adjusted to 7.4 with NaOH, sterile filtered (0.22 micron), and stored in refrigerator.

Hanks' balanced salt solution (HBSS)

9.8 g of HBSS and 350 mg of sodium bicarbonate were dissolved in 900 ml of sterile Milli Q water. To this solution, 5 ml of antibiotic-antimycotic solution was added and the final volume was made up to 1 L with Milli Q water. Then, the medium was sterile filtered (using 0.22 micron) and stored at 4°C.

Cell Culture

Human HepG2 cells were procured from the National Centre for Cell Sciences, Pune. The cells were grown in T-75 culture

flasks containing DMEM F-12 HAM supplemented with 10% FBS.

Passaging the Cells

On reaching confluence, the medium from T-75 culture flask was aspirated, rinsed with 2 ml of HBSS, and aspirated quickly; then, 5 ml of trypsin-EDTA solution was added and kept at room temperature (in the laminar hood) for 40 s. Then, trypsin-EDTA solution was aspirated quickly and the flask was kept at 37°C in CO_2 incubator for 3 min and tapped gently over the flask for complete detachment of cells from the surface of the flask. The cells were then gently resuspended in fresh growth medium and transferred to sterile T-75 flasks, and the volume of the medium was made up to 10 ml with growth medium.

Cell Viability Assay

3-(4,5-dimethylthiazol-2-yl)-2,5-diphenyltetrazolium bromide (MTT) method was performed as described by Cardile *et al*. (2004). The viability of the cells was assessed by MTT assay, which is based on the reduction of MTT by the mitochondrial dehydrogenase of intact cells to a purple formazan product. Cells were seeded in 96-well microplates (1×10^4 cells/well in 180 µl medium) and routinely cultured in a humidified incubator at 37°C in 5% CO_2 for 24 h. *M. oleifera* seed ethanolic extract was added in serial concentrations such as 100, 200, 300, 400, and 500 µg and incubated for 24 h. Then, the medium was discarded and 30 µl of MTT dye solution (0.5 mg/ml in PBS) was added to every well and re-incubated for 4 h. After removing untransformed MTT reagent, 100 µl of DMSO was added to dissolve the formed formazan crystals. Amount of formazan was determined by measuring the absorbance at 540 nm using an ELISA plate reader.

Estimation of Glutathione (GSH)

Reduced GSH was determined by the method of Moron *et al*. (1979). 5% TCA was added to HepG2 cell lines (1×10^6 cells). The precipitate was removed by centrifugation. To an aliquot of the supernatant, 2 ml of DTNB was added to make a final volume to 3 ml. The absorbance was read at 412 nm against a blank containing TCA instead of sample. Aliquots of the standard solution were treated similarly. The amount of GSH was expressed as n moles/1×10^6 cells.

Statistical Analysis

Experimental results were mean±SD of three parallel measurements. Analysis of variance was performed by ANOVA procedures (SPSS 9.0 for Windows). Significant differences between means were determined by Duncan's Multiple Range tests. $P > 0.05$ was considered as statistically significant and $P > 0.01$ very significant.

RESULTS

MTT Assay

The cytotoxic effect of *M. oleifera* seed ethanolic extract on HepG2 cells was performed by the MTT method, which is reliable to detect the proliferation of cells. The results of the MTT assay are presented in Figure 1. The results clearly confirm that the exposure of *M. oleifera* seed ethanolic extract at different concentrations such as 100, 200, 300, 400, and 500 µg/ml for 24, 48, and 72 h resulted in a decrease of cell proliferation in a dose-dependent manner.

There is an extreme decrease in HepG2 cell proliferation which was observed at 226 µg and 354 µg, respectively. It exhibits 47.3% reduced cell viability at 354 µg, and the viability of cell was decreased more than 52% (cell proliferation) at 226 µg. All the measurements were repeated at least 3 times.

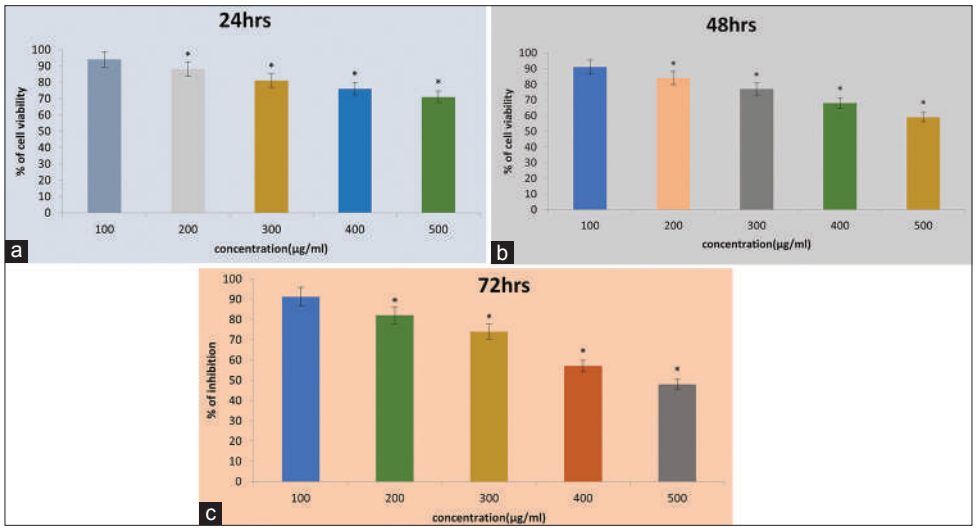


Figure 1: (a-c) Effect of *Moringa oleifera* seed extract on cytotoxicity of HepG2 cells. Values are expressed as mean ± SD. *$P < 0.05$

Reduced GSH Content

The levels of GSH content in control and *M. oleifera* seed ethanolic extract-treated HepG2 cells were determined, and the results are presented in Figure 2. From the present study, it is inferred that a significant ($P < 0.001$) depletion of GSH content was observed in *M. oleifera* seed ethanolic extract treated at the concentration of 226 and354 µg when compared to the control cells are represented in Figure 3.

DISCUSSION

In vitro cytotoxicity was measured by two methods, i.e. MTT assay which detected the level of succinate dehydrogenase within the mitochondria and the lactate dehydrogenase (LDH) assay which determined the release of LDH as an indicator of cell membrane damage (Senthilkumar *et al*., 2010). In the present investigation, the cytotoxic effects of *M. oleifera* seed extract on HepG2 cells were tested by the MTT method, which is reliable to detect the proliferation of cells. MTT assay is a non-radioactive, fast, and economical assay widely used to quantify cell viability and proliferation. MTT is a yellow water-soluble tetrazolium salt. Metabolically active cells are able to convert the dye to water-insoluble dark blue formazan by reductive cleavage of the tetrazolium ring. The reduction of MTT is proportional to the number of active mitochondria in the live cells (Prasanna *et al*., 2009). From the present study, the percentage of inhibition was reduced periodically in *M. oleifera* seed extract-treated cells. *M. oleifera* seed extract inhibits above 50% of the cell population at the concentration of 226 µg for 72 h in HepG2 cells. This clearly indicated that *M. oleifera* seed extract strongly inhibits the HepG2 cells in culture and exhibits its cytotoxic nature. The cytotoxic property of the extract may be due to the antioxidant activities of the phenolics the samples contain. Our observations are consistent with several past works that have linked the antioxidant activities of phenolic compounds to their antiproliferative effects on various cancer cells (Diogo *et al*., 2009; Goel *et al*., 2008; Sa *et al*., 2010; Saeidnia and Abdollahi, 2013). Recently, Adebayoa et al. (2017) reported that the cytotoxic potential of Moringa oleifera seed extract in MCF-7 cells through inhibiting the cell concentration by dose dependent manner.

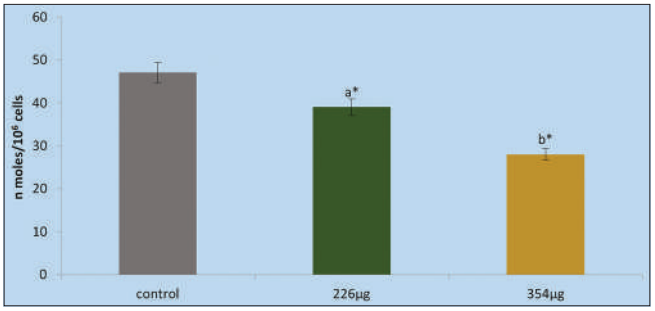


Figure 2: The levels of glutathione in control and *Moringa oleifera* seed extract-treated HepG2 cells. Human HepG2 were incubated for 24 h with *Moringa oleifera* seed extract. Values are expressed as mean ± SD; $n = 6$. HepG2: [a]226 µg of *M. oleifera* seed extract compared with control, [b]354 µg of *M. oleifera* seed extract compared with control *$P < 0.05$

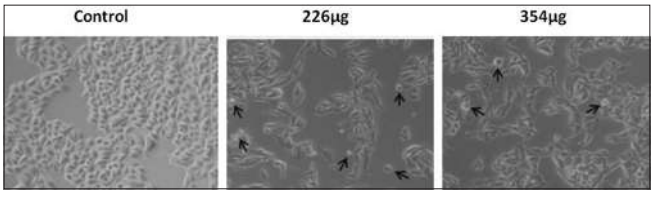


Figure 3: The morphology of HepG2 cells under phase contrast, after 48 h incubation. Arrows indicate rounded and detaching cells

Involvement of intracellular redox status as a key mediator of apoptosis has been well established in many cancer cell lines. Reduced GSH, most abundant cellular thiol and the major determinant of cellular redox equilibrium, has been shown to be an important factor in apoptosis. GSH contributes to an extraordinary range of metabolic process including the maintenance of intracellular redox status and plays an important role in the detoxification of intracellular H_2O_2, lipid peroxides, and also in the metabolism of exogenously derived compounds, mutagens, and carcinogens. Depletion of intracellular GSH renders the cancer cells more sensitive to apoptotic agents.

Nandakumar *et al*. (2011) are of the opinion that the inhibition of GSH synthesis or modulation of GSH storages in tumors to reduce anticancer drugs resistance may comprise a novel anticancer strategy. The GSH levels were significantly lower when compared to control cells. Cellular GSH plays an important role in protection against oxidative stress-induced injury. Depletion of GSH levels has been shown to enhance th susceptibility to oxidative stress-induced cytotoxicity. This result was consistent with *M. oleifera* leaf extracts (Luqman *et al*., 2011). The depletion of endogenous GSH sensitized the cells to *M. oleifera* seed ethanolic extract treatment and thereby increased the apoptotic cells, thus suggesting inactivation by the formation of GSH conjugate.

CONCLUSION

With the evidence of antibacterial and antifungal activities of the extracts of preparations under study, it can be rationally suggested that further work needs to be done to identify the chemical natures of the active principles as well as their modes of actions on bacterial cells and their roles in diseases curing. The MTT and GSH assays clearly confirmed that the cytotoxic effect and reduction of active species in HepG2 cells. The preliminary finding reveals that the *M. oleifera* seed extract has potential free radical scavengers which show its antioxidant

nature of the extracts. Further studies are needed with these plants under study to characterize and elucidate the structure of the bioactive compounds of these plants for industrial drug formulation and to purify proteins from these plants which may act as a drug for the treatment of various diseases.

REFERENCES

Abrams, B., Duncan, D., & Hertz-Piccioto, I. (1993). A prospective study of dietary intake and acquired immune deficiency syndrome in HIV-sero-positive homosexual men. *Journal of Acquired Immune Deficiency Syndrome*, 8, 949-958.

Abuye, C., Omwega, A. M., & Imungi, J. K. (1999). Familial tendency and dietary association of goitre in Gamo-Gofa, Ethiopia. *East African Medical Journal,* 76, 447-451.

Adebayoa, I. A., Arsada, H., & Samianb, M. R. (2017). Antiproliferative effect on breast cancer (MCF7) of *Moringa oleifera* seed extracts. *African Journal of Traditional Complementary and Alternative Medicine* 14(2), 282-287.

Ahmed, E. E., Sharaf-Eldin, M. A., & Wadaan, M. (2015). *In vitro* evaluation of cytotoxic activities of essential oil from *Moringa oleifera* seeds on HeLa, HepG2, MCF-7, CACO-2 and L929 cell lines. *Asian Pacific Journal of Cancer Prevention,* 16, 4671-4675.

Anderson, D. M, Bell, P. C., McDougall, F. J., Gill, M. C. & McNab, C. G. (1986). The gum exudates from *Chloroxylon swietenia*, *Sclerocarya caffra*, *Azadirachta indica* and *Moringa oleifera*. *Phytochemistry*, 25(1), 247-249.

Anwar, F., & Bhanger, M. I. (2003). Analytical characterization of *Moringa oleifera* seed oil grown in temperate regions of Pakistan. *Journal of Agricultural and Food Chemistry*, 51, 6558-6563.

Anwar, F., Latif, S., Ashraf, M., & Gilani, A. H. (2007). *Moringa oleifera*: A food plant with multiple medicinal uses. *Phytotherapy Research*, 21(1), 17-25.

Asres, K. (1995). The major constituents of the acetone fraction of Ethiopian *Moringa stenopetala* leaves. *Mansoura Journal of Pharmacological Science*, 11(1), 55-64.

Cardile, V., Renis, M., Scifo, C., Lombardo, L., Gulino, R., Mancari, B., & Panico, A. (2004). Behaviour of the new asbestos amphibole fluorendenitein different lung cell systems. *International Journal of Biochemistry and Cell Biology,* 36, 849-860.

Chanda, S., & Kaneria, M. (2011). Indian nutraceutical plant leaves as a potential source of natural antimicrobial agents. *Science Against Microbial Pathogens: Communicating Current Research and Technological Advances*, 2, 1251-1259.

Cos, P., Vlietinck, A. J., Berghe, D. V., & Maes, L. (2006). Anti-infective potential of natural products: How to develop a stronger *in vitro* 'proof-of-concept'. *Journal of Ethnopharmacology*, 106(3), 290-302.

Cotter, P. D., Ross, R. P., & Hill, C. (2013). Bacteriocins-a viable alternative to antibiotics? *Nature Reviews Microbiology*, 11(2), 95-105.

Cragg, G. M., & Newman, D. J. (2013). Natural products: A continuing source of novel drug leads. *Biochimica et Biophysica Acta (BBA)-General Subjects*, 1830(6), 3670-3695.

Diogo, C. V., Félix, L., Vilela, S., Burgeiro, A., Barbosa, I. A., Carvalho, M. J., Oliveira, P. J., & Peixoto, F. P. (2009). Mitochondrial toxicity of the phyotochemicals daphnetoxin and daphnoretin–relevance for possible anticancer application. *Toxicology in Vitro*, 23(5), 772-779.

Goel, A., Kunnumakkara, A. B., & Aggarwal, B. B. (2008). Curcumin as-curecumin: From kitchen to clinic. *Biochemical Pharmacology*, 75(4), 787-809.

Hussain, M. A., & Gorsi, M. S. (2004). Antimicrobial activity of *Nerium oleander* Linn. *Asian Journal of Plant Science*, 3(2), 177-80.

Jahn, S. A. (1988). Using *Moringa oleifera* seeds as coagulant in developing countries. *Journal of the American Water Works Association*, 6, 43-50.

Kalogo, Y., Rosillon, F., Hammes, F., & Verstraete, W. (2000). Effect of a water extract of *Moringa oleifera* seeds on the hydrolytic microbial species diversity of a UASB reactor treating domestic wastewater. *Letters in Applied Microbiology*, 31, 259-64.

Kawo, A., Abdullahi, B., Halilu, A., Gaiya, Z., Dabai, M., & Dakare, M. (2009). Preliminary phytochemical screening, proximate and elemental composition of *Moringa oleifera* lam seed powder. *Bayero Journal of Pure and Applied Sciences*, 2(1), 96-100.

Luqman, S., Srivastava, S., Kumar, R., Maurya, A. K., & Chanda, D. (2011). Experimental assessment of *Moringa oleifera* leaf and fruit for its antistress, antioxidant, and scavenging potential using *in vitro* and *in vivo* assays. *Evidence-Based Complementary and Alternative Medicine*, 2012, 519084.

Moron, M. S., Depierre, J. W., & Mannervik, B. (1979). Levels of glutathione reductase and glutathione-S-transferase activities in rat lung and liver. *Biochimica et Biophysica Acta,* 582, 67-78.

Muyibi, S. A., & Evison, L. M. (1995). *Moringa oleifera* seeds for softening hard water. *Water Research*, 29, 1099-1105.

Nair, R., & Chanda, S. (2007). Antibacterial activities of some medicinal plants of the Western region of India. *Turkish Journal of Biology*, 31(4), 231-236.

Nandakumar, N., Rengarajan, T., Haribabu, L., Perumal, S., & Balasubramanian, M. P. (2011). Effect of flavonone hesperidin on the apoptosis of human mammary carcinoma cell line MCF - 7. *Biomedicine and Preventive Nutrition,* 1(3), 207-215.

Ndabigengesere, A., & Narasiah, C. (1998). Quality of water treated by coagulation using *Moringa oleifera* seed. *Water Research*, 32, 781-791.

Prasanna, R., Harish, C. C., Pichai, R., Sakthisekaran, D. & Gunasekaran. P. (2009). Anti-cancer effect of *Cassia auriculata* leaf extract *in vitro* through cell cycle arrest and induction of apoptosis in human breast and larynx cancer cell lines. *Cell Biology International,* 33(2), 127–134.

Sa, G., Das, T., Banerjee, S., & Chakraborty, J. (2010). Curcumin: From exotic spice to modern anticancer drug. *Al Ameen Journal of Medical Science*, 3, 21-37.

Saeidnia, S., & Abdollahi, M. (2013). Antioxidants: Friends or foe in prevention or treatment of cancer: The debate of the century. *Toxicology and Applied Pharmacology*, 271(1), 49-63.

Senthilkumar, K., Elumalai, P., Arunkumar, R., Banudevi, S., Gunadharini, N. D., Sharmila, G., Selvakumar, K. & Arunakaran, J. (2010). Quercetin regulates insulin like growth factor signaling and induces intrinsic and extrinsic pathway mediated apoptosis in androgen independent prostate cancer cells (PC-3). *Molecular and Cellular Biochemistry,* 344(1-2), 173-184.

Sharma, P., Kumari, P., Srivastava, M. M., & Srivastava, S. (2006). Removal of cadmium from aqueous system by shelled *Moringa oleifera* Lam. seed powder. *Bioresource Technology*, 97(2), 299-305.

Woolf, A. D. (2003). Herbal remedies and children: Do they work? Are they harmful? *Pediatrics*, 112(Supplement 1), 240-246.

This work is licensed under a Creative Commons Attribution Non-Commercial 4.0 International License.

Purakala

ISSN:0971-2143

Vol-31-Issue-41-May -2020

(UGC Care Journal)

Enhanced DNA cleavage and biopotencial properties of new Schiff base mixed-ligand complexes of Co(II), Ni(II), Cu(II) and Mn(II) derived from Isatin

T. Sujeshwari [1], E. Akila [2] & P. Maheswaran [3*]

[1] Research Scholar, Department of Chemistry, P.G.P college of Arts and science, Namakkal.

[2] Department of Chemistry, Sri Sarada College for women (Autonomous), Salem-16.

[3] Principal and Head, Department of Chemistry, P.G.P college of Arts and science, Namakkal*

ABSTRACT

Background: *Transition metal complexes have been used widely by many bioinorganic chemists for developing active transition metal anticancer complexes with better efficiency. The interaction of transition metal complexes with DNA has beena subject of passionate research in the field of bioinorganic chemistry.* ***Objective:*** *To synthesize a new Schiff base ligand (1-Methyl-4-nitro-benzene(2-imino-1,2-dihydro-indol-3-ylidene)-(4-nitro-phenyl)-amine) by the condensation reaction between isatin and p-nitroaniline and Its Co(II), Ni(II), Cu(II) and Mn(II) complexes were prepared by the interaction of the Schiff base ligand with metal(II) chloride.* ***Method:*** *They were characterized by elemental analysis, IR, ^1H NMR, EPR, UV–Vis, magnetic susceptibility measurements and conductivity measurements. DNA cleavage activity by the complexes was performed by gel electrophoresis method. The Schiff base and its complexes have been screened for their antibacterial (Staphylococcus aureus, Escherichia coli, Bacillus subtilis and Klebsila Pneumonia.).* ***Result:*** *All the synthesized complexes have distorted octahedral geometry and the coordination of ligand to metal complexes confirmed by IR spectral studies .* ***Conclusion:*** *In all the biological studies, metal complexes show better activity than the ligands.*

Keywords: Schiff base, Metal(II) complexes, DNA cleavage, Antimicrobial activity

INTRODUCTION

The Schiff base ligands are well known due to their extensive range of applications in industrial and pharmaceutical fields [1]. Some Schiff base ligands derived from istain derivatives and their copper(II) complexes have also been shown to inhibit growth of tumor. These studies have exposed that complexation of metals to Schiff base ligands enhance the biopotentials of the ligands. Many reports are obtainable for the preparation and properties of above metal complexes as they mimic metalloproteins [2]. In adding up, the reports of Schiff base and their metal complexes have emerged more in recent times.

In recent years, the binding studies of transition metal complexes have turn into an significant field in the growth of DNA molecular probes and chemotherapeutics. Metal complexes such as Cobalt, Nickel, Copper and Manganese with N-containing ligands have shown outstanding cleavage activities [3]. There is a considerable literature supporting the

P.G.P. COLLEGE OF ARTS & SCIENCE NAMAKKAL 637 104

Copyright © 2020Authors

ISSN:0971-2143
Vol-31-Issue-41-May -2020
Purakala (UGC Care Journ

function of artificial DNA cleaving agents in biotechnology; structural studies of nucleic acids or development of new drugs. Transition metal complexes can interact with DNA during covalent binding, electrostatic interactions, groove binding or intercalation. Compounds showing the properties of effectual binding as well as cleaving double stranded DNA under physiological conditions are of immense importance since these could be used as diagnostic agents in medicinal and genomic research.

Although Schiff bases containing a N donor atoms have efficient biological activity, the studies based on 1-Methyl-4-nitro-benzene(2-imino-1,2-dihydro-indol-3-ylidene)-(4-nitro-phenyl)-amine Schiff base chemistry are less extensive. Our laboratory has been presently involved in exploring this chemistry [4]. Bearing all the above facts in mind, and as a part of our progressing research, herein the synthesis of Schiff base ligand (1-Methyl-4-nitro-benzene(2-imino-1,2-dihydro-indol-3-ylidene)-(4-nitro-phenyl)-amine) and its Co(II), Ni(II), Cu(II) and Mn(II) complexes has been reported. In order to investigate the coordination mode of ligand, the complexes of Co(II), Ni(II), Cu(II) and Mn(II) have been characterized by UV–Vis, IR, and ^{1}H NMR studies. The antimicrobial and cleavage properties of the Schiff base ligand (1-Methyl-4-nitro-benzene(2-imino-1,2-dihydro-indol-3-ylidene)-(4-nitro-phenyl)-amine) and its complexes have also been investigated.

MATERIALS AND METHODS

The chemicals used in this work viz., isatin, p-nitroaniline, 2, 2′ bipyridyl, acetic acid and Tris–HCl buffer were of Merck grade. The AR grade of metal salts $CoCl_2.6H_2O$, $NiCl_2.6H_2O$, $CuCl_2.2H_2O$ and $MnCl_2$.$5H_2O$ were used. Commercial solvents were distilled and then used for the preparation of ligand and its complexes

Carbon, hydrogen and nitrogen analyses of the complexes were carried out on a CHN analyzer. Carlo Erba Model 1108. The infrared spectra (4000–200 cm^{-1} KBr disks) of the samples were recorded on a Perkin–Elmer FT-IR-8300 spectrophotometer. The electronic absorbance spectra in the 200–800 nm were recorded on Double beam spectrometer Cyber lab between 200 – 800 nm. ^{1}H NMR spectra of ligand were recorded on Bruker Spectrometer at 400 MHZ in DMSO. The chemical shifts are given in PPM, using Tetramethylsilane (TMS) as the internal reference. Magnetic susceptibility measurements were carried out by employ the Gouy method at room temperature on powder sample of the complexes using $CuSO_4.5H_2O$ as calibrant. The metal contents of the complexes were determined according to the literature method [5].

DNA cleavage activity

Gel electrophoresis

The DNA cleavage of supercoiled pUC18DNA promoted by metal complex was proceeded by addition of reaction mixture (40µl). The reaction mixture (40µl) containing pUC18DNA, 50mM Tris-HCl, pH 7.4, 50 mm NaCl, 10 mM H_2O_2 added in a different volume, followed by adding Millipore water for final volume. Then the mixed solutions were incubated at 37° C for 1 hr. They checked by agarose electrophoresis methods [6].

Antibacterial activity

The antibacterial screening effects of the Schiff base ligand and their corresponding Co(II), Ni(II), Cu(II) and Mn(II) complexes were tested against four bacterial strains namely

COLLEGE OF ARTS & SCIENCE NAMAKKAL 637 206
Copyright © 2020Authors

Bacillus subtilis, Staphylococcus aureus, Klebsilla pneumonia and Escherichia coli by disc diffusion method, using nutrient agar medium. The compounds were dissolved in DMF. The plates were incubated aerobically at 37 °C for 24 hours and the antimicrobial activity was assess by measuring the inhibition of microbial development around the well. This method involves the experience of the zone inhibition toward the diffusion of micro-organism on agar plate [7].

Synthesis of Schiff base ligand (1-Methyl-4-nitro-benzene(2-imino-1,2-dihydro-indol-3-ylidene)-(4-nitro-phenyl)-amine)

The Schiff base ligand was synthesized by adding Isatin (1 mM) in 20 ml of ethanol, p- nitroaniline (2 mM) in 20 ml of ethanol. The mixture was refluxed for 2-3 hrs. Then solution of the ligand was kept for slow evaporation and yellow colored precipitate was collected and dried in air [8].

Synthesis of Schiff base metal complexes

The ethanolic solution of synthesized ligand (1 mM) was added dropwise stirring to an ethanolic solution of the metal chloride (1 mM) (Metal = Cu(II), Co(II), Ni(II) and Mn(II)) with constant stirring and followed by an ethanolic solution of 2, 2′ bipyridyl is added and the mixture was boiled under reflux for 3-5 hrs. Then, the volume of the reaction mixture was reduced by evaporation. The precipitated complexes were filtered off, washed with ethanol and then dried in vacuuo [9].

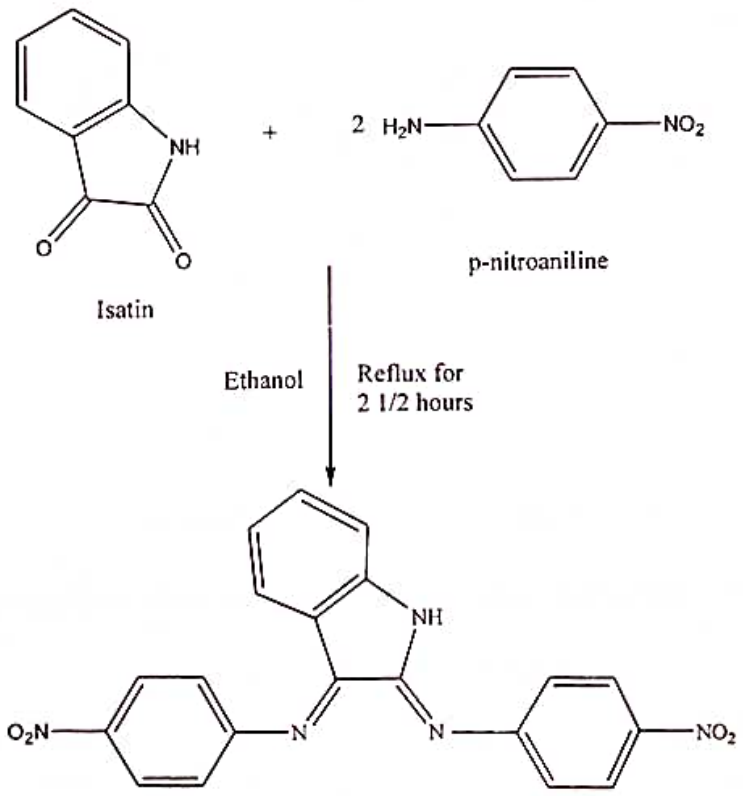


Fig.1. Synthesis of Schiff base ligand

P.G.P. COLLEGE OF ARTS & SCIENCE NAMAKKAL 637 206

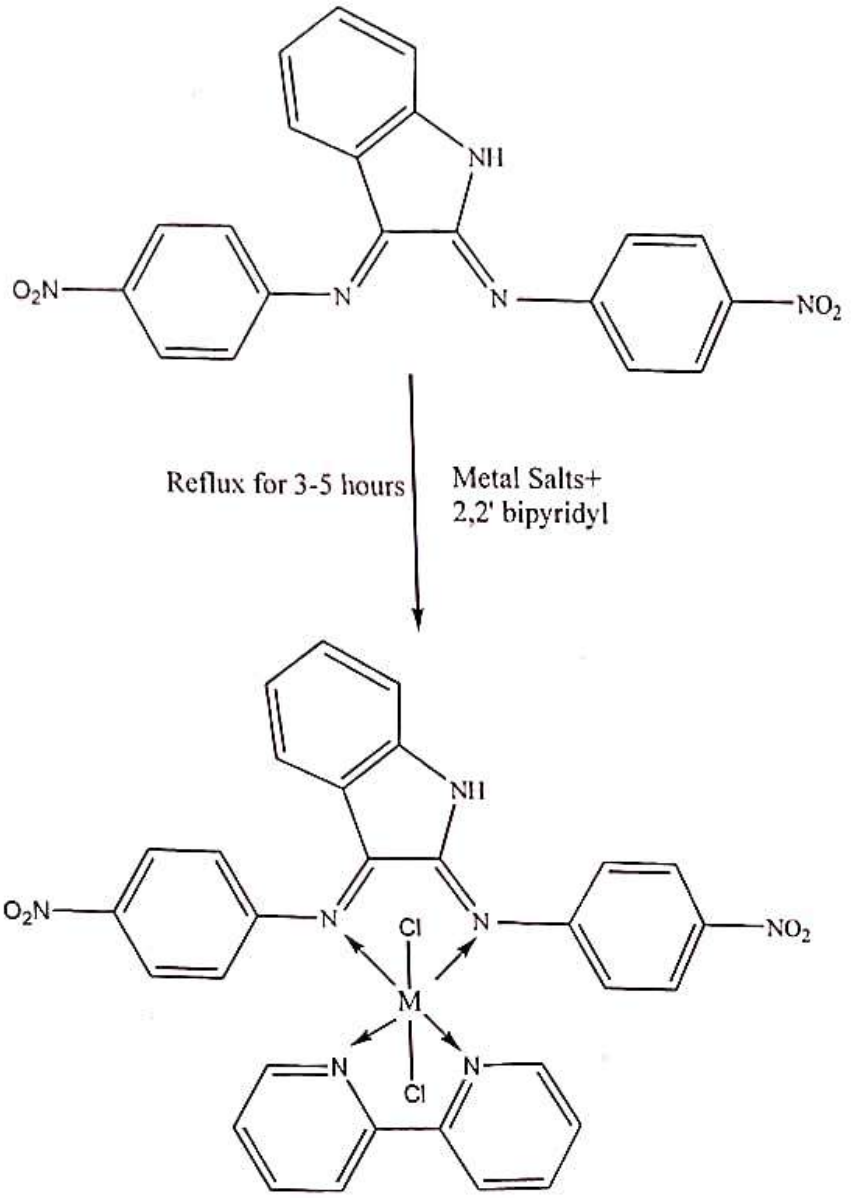
Copyright © 2020Authors

ISSN:0971-2143

Purakala

Vol-31-Issue-41-May -2020

(UGC Care Journal)



M=Cu(II), Ni(II), Co(II) and Mn(II)

Fig.2. Synthesis of Mononuclear Schiff base Metal(II) complexes

RESULTS AND DISCUSSION

Physicochemical properties of the synthesized compounds

The ligand was prepared by refluxing an appropriate amount of isatin and p-nitroaniline in 1:2 molar ratio and the complexes were formed with the metal salts and ligand in the ratio of 1:1:1. All the complexes show 1:1:1 metal– ligand stoichiometry. They

P.G.P. COLLEGE OF ARTS & SCIENCE NAMAKKAL 637 206

Copyright © 2020Authors

ISSN.0971-2143

Vol-31-Issue-41-May -2020

are non-hygroscopic, decomposed above 200 °C and possess good keeping qualities. The molar conductance values in DMF (Table 1) reveal the non-electrolytic nature of the complexes [10].

Electronic spectra and magnetic properties of metal(II) complexes

The electronic spectra were recorded in DMF solution and data are given in the Table 1. The ligand exhibits absorption bands in UV–Vis region around 340 and 364 nm. The first band below 340 nm is assigned to $\pi \rightarrow \pi^*$ transition. Another band observed at 364 nm is assigned to $n \rightarrow \pi^*$ transition originating from the amide or imine function of the Schiff base ligand [11].

The magnetic moment value (1.90 B.M.) for $[CuL_1L_2]$ as well as the broad band in its electronic spectrum centered at 505 and 604 nm, assigned to $^2B_{1g} \rightarrow {}^2E_{1g}$ and $^2B_{1g} \rightarrow {}^2A_{1g}$ transitions suggested a distorted octahedral geometry around the copper(II) ion. However, the band observed at 365 nm was probably due to a ligand-metal charge transfer transition.

The Ni(II) complex reported here is high spin with a room temperature magnetic moment value of 3.12 B.M. which is in the normal range observed for octahedral Ni(II) complexes. This indicates that, the Ni(II) complex is possibly octahedral. The electronic spectrum of Ni(II) complex displayed three bands at 446, 578 and 625 nm, assigned to $^3A_{2g}(F) \rightarrow {}^3T_2g(F)$, $^3A_{2g}(F) \rightarrow {}^3T_1g(F)$ and $^3A_{2g}(F) \rightarrow {}^3T_1g(P)$ d–d transitions, respectively. The spectrum also showed a band at 365 nm, attributed to ligand to metal charge transfer transition.

The measured magnetic moment value (3.60 B.M.) of the Co(II) complex was lower than spin-only value (3.87 B.M.) and also lower than the value reported for complex have octahedral geometry . The electronic spectrum of $[Co\ L_1L_2]$ showed broad bands at 464, 595 and 625 nm which are assigned to $^4T_1g(F) \rightarrow {}^4T_{2g}(F)$, $^4T_1g(F) \rightarrow {}^4A_{2g}(F)$ and $^4T_1g(F) \rightarrow {}^4T_{2g}(P)$ transitions, respectively, in around the cobalt(II) ion. A moderately intense peak observed at 365 nm is also due to ligand to metal charge transfer transition.

The electronic spectra of Mn(II) complexes show the absorption bands in the range 694, 555 and 522 nm. These absorption bands may be assigned to the $^6A_1g \rightarrow {}^4A_1g$, $^6A_1g \rightarrow {}^4A_2g$, and $^6A_1g \rightarrow {}^4Eg$, ^4A_1g transitions, respectively. These bands suggest that the complexes possess an octahedral geometry. The Mn(II) complex show magnetic moments is 5.92 B.M. at room temperature corresponding to five unpaired electrons which suggest octahedral geometry. In the spectra of the Schiff base iigand, the absorption band observed at 281-294 nm were assigned to intra-ligand $\pi \rightarrow \pi^*$ transition and the band at 342-390 nm were assigned due to $n \rightarrow \pi^*$ transition associated with the azomethine chromophore (-C=N).

Molar conductivity

With a view to study the electrolytic nature of the mononuclear metal complexes, their molar conductivities were measured in DMF at 10^{-3} M. The molar conductivity values of all the complexes are in the range 4.1–7.9 $ohm^{-1}\ cm^2\ mol^{-1}$ (shown in Table 1), which is in agreement with the non-electrolytic nature of the complexes.

Table 1:Electronic absorption spectral data of metal(II) complexes at 300 K.

Complex	λmax (nm)	Band assignments	Geometry	Magnetic moment (B.M.)	Molar conductance $ohm^{-1}\ cm^2$

Copyright © 2020Authors

P.G.P. COLLEGE OF ARTS & SCIENCE NAMAKKAL 637 206

ISSN:0971-2143
Vol-31-Issue-41-May -2020
Purakala (UGC Care Journal)

					mol^{-1}
$[CuL_1L_2]$	340 365 505 604	INCT LMCT $^2B_{1g} \rightarrow {}^2E_{1g}$ $^2B_{1g} \rightarrow {}^2A_{1g}$	Distorted octahedral	1.90	6.6
$[NiL_1L_2]$	352 365 446 578 625	INCT LMCT $^3A_{2g}(F) \rightarrow {}^3T_2g(F)$, $^3A_{2g}(F) \rightarrow {}^3T_1g(F)$ $^3A_{2g}(F) \rightarrow {}^3T_{1g}(P)$		3.12	5.7
$[CoL_1L_2]$	355 365 464 595 625	INCT LMCT $^4T_{1g}(F) \rightarrow {}^4T_{2g}(F)$, $^4T_{1g}(F) \rightarrow {}^4A_{2g}(F)$ $^4T_{1g}(F) \rightarrow {}^4T_{2g}(P)$		3.60	7.6
$[MnL_1L_2]$	290 365 522 555 694	INCT LMCT $^6A_1g \rightarrow {}^4A_1g$, $^6A_1g \rightarrow {}^4A_2g$, $^6A_1g \rightarrow {}^4Eg, {}^4A_1g$		5.92	8.2

Infrared spectra of the ligand and its metal(II) complexes

The IR spectra give valuable information about the coordinating sites of Schiff base ligand which has been previously discussed by Raman et al . The IR spectra of the complexes were compared with that of the free ligand to decide the change that may have taken place throughout the complexation. A comparative study of the IR spectra of ligand and its metal complexes divulge that certain peaks are general and therefore, only significant peaks, which have also shifted or have recently appeared, are discussed. Table 2 shows that ν(C-O) and ν (C=N) modes occur at 1224-1332 cm^{-1} and 1595-1620 cm^{-1} correspondingly. The shifting of (C-O) towards higher frequency as compared to the ligand (1224 cm^{-1}) is due to the conversion of hydrogen bonded structure into a covalent metal bonded structure. Lowering of (C=N) in the complexes as compared to the ligand (1620 cm^{-1}) is due to reduction of double bond nature of carbon-nitrogen bond of the azomethine group. Metal-ligand bond is further confirmed by the appearance of a medium intensity band in the range 444-468, cm^{-1} in the spectra of the complexes assigned to stretching frequencies of (M-N) bond formation respectively [12].

Table 2: Infrared Spectroscopic Data of the Schiff Base Ligand and its mononuclear metal complex

Compounds	(C=N) (cm^{-1})	(C-O) (cm^{-1})	(M–N) (cm^{-1})

Copyright © 2020Authors
P.G.P. COLLEGE OF ARTS & SCIENCE NAMAKKAL 637 206

ISSN:0971-2143

Vol-31-Issue-41-May -2020

Ligand	1620	1244	--
$[CuL_1L_2]$	1605	1288	460
$[NiL_1L_2]$	1609	1320	454
$[CoL_1L_2]$	1595	1332	468
$[MnL_1L_2]$	1600	1324	444

^{1}H NMR spectra

The ^{1}H NMR spectra of Schiff base was recorded in DMSO- d_6 at room temperature. Three different type of protons were identified i) characteristic resonance due to azomethine proton in the Schiff base appears at 8.227 ppm was observed and ii) the other signals in the region 6.24–7.72 ppm exhibits due to aromatic protons. All these observations support the infrared conclusions.

EPR spectra

The EPR spectra of complexes give information of significance in studying the metal ion surroundings. The EPR spectra of the Cu(II) Schiff base complex recorded on powder samples with room temperature, on X-band at frequency 9.3 GHz under the magnetic field strength 4000 G.

The EPR spectrum of the Cu(II) Schiff base complex (Figure 2) complexes show a broad signal with g_{iso} at 1.9998 which is consistent with an octahedral geometry [13].

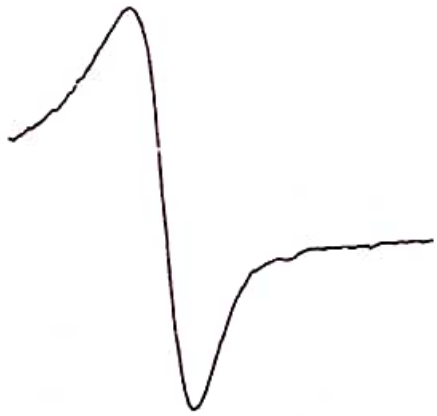


Fig. 3. EPR spectra of Cu(II) Schiff base complex

Chemical nuclease activity

There has been substantial attention in DNA cleavage reactions that are initiated by transition metal complexes. The release of metal ion to the helix, in nearby generating oxygen

P.G.P. COLLEGE OF ARTS & SCIENCE NAMAKKAL 637 206

Copyright © 2020Authors

ISSN:0971-2143
Vol-31-Issue-41-May -2020
Purakala (UGC Care Journ

or hydroxide radicals, yields a proficient DNA cleavage reaction. In order to consider the chemical nuclease activities of the Co(II), Ni(II), Cu(II) and Mn(II) complexes for DNA strand scission, pUC18DNA was incubated with all the above metal(II) complexes under the reaction conditions. The cleavage reaction can be monitored by gel electrophoresis. When circular pUC18DNA is subjected to electrophoresis, comparatively fast migration will be observed for the intact supercoiled form (Form I). If scission occurs on one strand (nicking), the supercoiled form will relax to produce a slower-moving nicked form (Form II). If both strands are cleaved, a linear form (Form III) that migrates between Form I and Form II will be generated.

The chemical nuclease activities of the four complexes have been studied using supercoiled pUC18DNA plasmid DNA as a substrate in a medium of 50 mM Tris–HCl/ NaCl buffer (pH = 7.2) in the presence of hydrogen peroxide under physiological conditions. There was no DNA-cleavage observed for the controls in which either in the absence of hydrogen peroxide with DNA or in the presence of hydrogen peroxide with DNA (Lanes 1 and 2). In Fig. 4, all the complexes were found to exhibit nuclease activity in the presence of hydrogen peroxide as reducing agent (Lanes 3–6). The dissimilar DNA-cleavage efficiency of the complexes may be due to the diverse binding affinity of the complexes to DNA. The nuclease effectiveness of the complexes is known to depend on the reducing agent used for initiating the DNA cleavage [14].

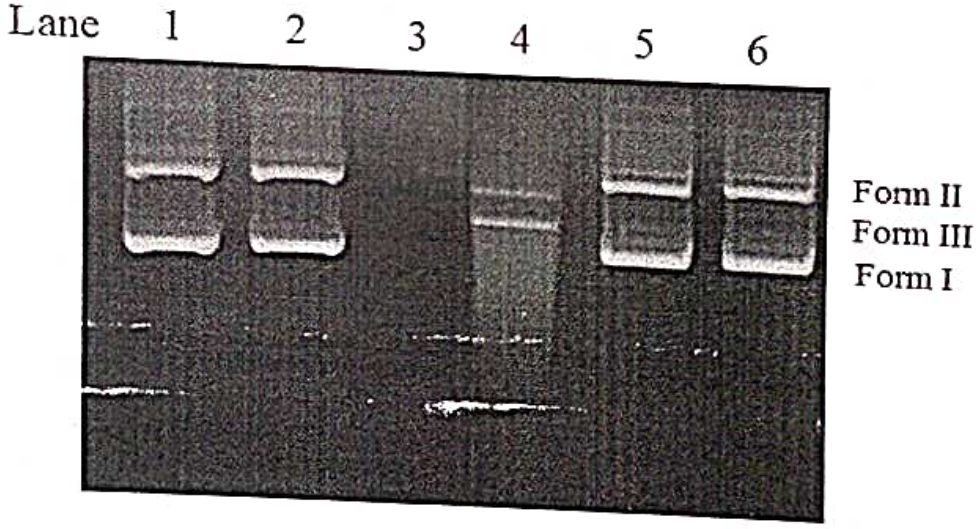


Fig. 4. Changes in the agarose gel electrophoretic pattern of pUC18DNA induced by H_2O_2 and metal complexes. Lane 1-DNA alone; Lane 2- DNA alone + H_2O_2; Lane 3-DNA + Cu complex + H_2O_2; Lane 4-DNA + Ni complex+ H_2O_2; Lane5-DNA + Co complex Lane 6-DNA+ Mn complex H_2O_2.

Antibacterial activity

Biological activity of the ligand and a series of its metal complexes [Cu(II), Ni(II), Co(II) and Mn(II)] were screened for anti-bacterial activity against *Staphylococcus aureus, Escherichia coli, Bacillus subtilis and Klebsilla pneumonia* by using disc-agar diffusion method (Figure 5). The results indicate that the complexes show more activity and the ligand

P.G.P. COLLEGE OF ARTS & SCIENCE NAMAKKAL 637 206
Copyright © 2020Authors

have less activity against same microorganisms under identical experimental conditions. This would suggest that the chelation could facilitate the ability of a complex to cross a cell membrane and can be explained by Tweedy's chelation theory. Chelation considerably reduces the polarity of the metal ion because of partial sharing of its positive charge with donor groups and possible electron delocalization over the whole chelate ring. Such a chelation could enhance the lipophilic character of the central metal atom, which subsequently favors its permeation through the lipid layer of the cell membrane. The copper(II) complex shows higher anti-fungal activity than other complexes. The variation in the effectiveness of different compounds against different organisms depends either on the impermeability of the cells of the microbes or on differences in ribosome of microbial cells [15].

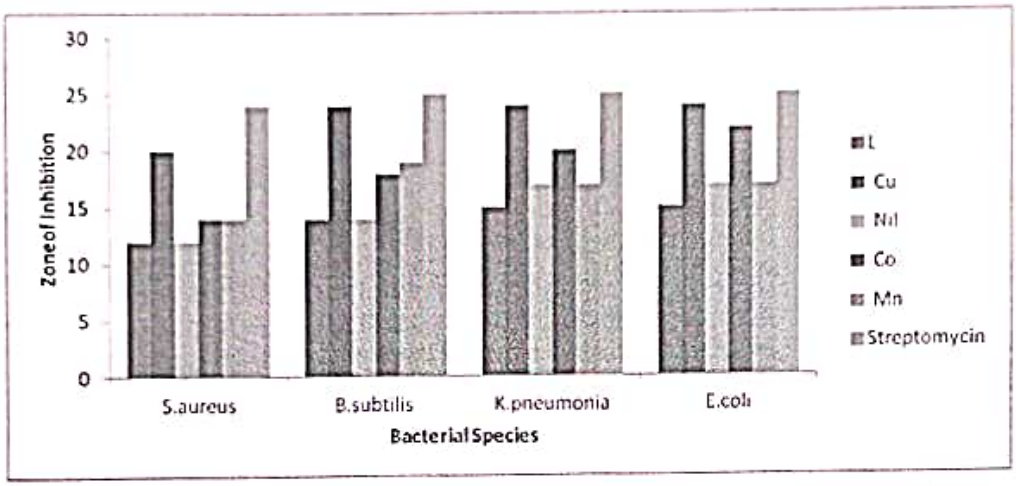


Fig. 5: Antibacterial activity of Schiff base ligand and its mononuclear Schiff base metal complexes against Bacterial Strains

CONCLUSION

The present paper reports on the synthesis, spectral characterization and their electronic absorption spectra of Schiff base ligand and its metal complexes. The synthetic procedure in this work resulted in the formation of complexes in the molar ratio (1:1:1) ($M:L_1:L_2$), respectively. In these complexes, the bidentate Schiff base ligand is coordinated to metal ion through the azomethine-nitrogen atoms. The present study reveals that distorted octahedral geometry around Co(II), Ni(II), Cu(II) and Mn(II) complexes The conductance value show that all the metal complexes are non-electrolytes in nature. Noticeably, metal complexes have been found to promote cleavage of plasmid pUC18DNA from the supercoiled Form I to the open circular Form II or the linear Form III in the presence of H_2O_2. These findings clearly point out that transition metal based complexes have many possible practical applications, like the growth of nucleic acid molecular probes and new therapeutic reagents for diseases. The results of antimicrobial activity show that the metal complexes exhibit antimicrobial properties and it is significant to note that they show enhanced inhibitory activity compared to the parent ligand under identical experimental conditions. But the ligand and metal complexes have low activity as compared to standard drugs.

P.G.P. COLLEGE OF ARTS & SCIENCE NAMAKKAL 637 206

Copyright © 2020Authors

Purakala (UGC Care Jou

DECLARATIONS

Acknowledgments

The author is indebted to Supervisor for his constant encouragement and support. STIC Cochin, St. Joseph College, Trichy and Progen lab , Salem are gratefully acknowledged for providing instrumental facilities.

Conflict of interests

The authors declare that they have no conflict of interest

References:

[1] Akila, E., Usharani, M., et al. "Tetradentate-Arm Schiff base Derived from the Condensation Reaction of 3, 3′-dihydroxybenzidine, glyoxal/ diacetyl and 2-aminophenol: Designing, Structural Elucidation and Properties of their Binuclear Metal(II) Complexes" Arabian. J. Chem, http://dx.doi.org/10.1016/j.arabjc.2013.11.031.

[2] Ren S, Wang R, et al. "Synthesis, biological evaluation, and quantitative structure-activity relationship analysis of new Schiff bases of hydroxysemicarbazide as potential antitumor agents" J. Med. Chem 2002; 45: 410.

[3] Akila. E, Usharani.M et al. " Spectral, Magnetic, Biocidal Screening and DNA Cleavage Studies Of Binuclear Metal(II) Complexes of Tetracoordinate Schiff Base Ligand of 3, 3′-Dihydroxybenzidine" International Journal of Recent Scientific Research 2013; 4(10): 1497-1503.

[4] Sima J, "Mechanism of Photoredox Reactions of Iron(III)Complexes Containing Salen-type Ligands" Crao. Chem. Acta 2001; 74: 593.

[5] E. Akila, M. Usharani et al. " Design, synthesis and interpretation of binuclear schiff base metal complexes and their application; antibacterial activity" International Journal of Inorganic and Bioinorganic Chemistry 2012;2 (2): 15-19..

P.G.P. COLLEGE OF ARTS & SCIENCE NAMAKKAL 637 206

Copyright © 2020Authors

ISSN:0971-2143

Vol-31-Issue-41-May -2020

[6] Tarafder M. T. H, Ali M. A, et al. "Coordination chemistry and biological activity of nickel(II) and copper(II) ion complexes with nitrogen–sulphur donor ligands derived from S-benzyldithiocarbazate (SBDTC)" Transition Met Chem 2016; 26: 613

[7] Colman J, Hegedu L. S, "Principles and Applications of Organotransition Metal Chemistry" University Science Book, California, 1980.

[8] Mahajan K, Swami M, et al. "Microwave synthesis, spectral studies, antimicrobial approach and coordination behavior of antimony(III) and bismuth(III) compoundswith benzothiazoline" Russ. J. Coord. Chem 2009; 35: 179-185

[9] Liu J, Zhang T.X, Ji L.N, "DNA-binding and cleavage studies of macrocyclic copper(II) complexes" J. Inorg. Biochem 2012; 91:269–276.

[10] Mehmet Tumer, Duygu Ekinci, et al. "Synthesis, characterization and properties of some divalent metal(II) complexes: Their electrochemical, catalytic, thermal and antimicrobial activity studies" Spectrochim. Acta Part A 2007; 67: 916–929.

[11] Costamagna J, Vargas J," Coordination compounds of copper, nickel and iron with Schiff bases derived from hydroxynaphthaldehydes and salicylaldehydes" Coord. Chem. Res 1992;119: 67–88.

[12] Debojyoti Lahiri, Ritankar Majumdar, et al. "Anaerobic DNA cleavage in red light by dicopper(II) complexes on disulphide bond activation" J. Chem. Sci 2015;122 (3) 321–333.

[13] Sartaj Tabassum, Mehvash Zaki, et al. "Synthesis of heterobimetallic complexes: In vitro DNA binding, cleavage and antimicrobial studies" Journal of Photochemistry and Photobiology B: Biology 2012; 114: 108–118.

[14] Hassan A. M, Nassar A. M, et al. "Synthesis, Characterization and Biological Evaluation of Fe (III), Co (II), Ni(II), Cu(II), and Zn(Ii) Complexes with Tetradentate Schiff Base Ligand Derived from Protocatechualdehyde with 2-Aminophenol" Appl Biochem Biotechnol 2018; 167:581–594.

[15] Peng B, Chao H, et al. "Synthesis, DNA-binding and photocleavage studies of cobalt(III) mixed-polypyridyl complexes: [Co(phen)2 (dpta)]$^{3+}$ and [Co(phen)2(amtp)]$^{3+}$" J. Inorg. Biochem 2017; 101: 404–411.



PRINCIPAL
PGP College of Arts and Science
Namakkal.

Copyright © 2020Authors

Purakala
(UGC Care Journal)

ISSN:0971-2143
Vol 31 Issue 41:May :2020

Synthesis and Structural Elucidation of Indole bearing Schiff base Mixed ligand metal (II) Complexes: Antimicrobial, Cytotoxicity and DNA Cleavage Interaction

DHIVYA PRIYA. D[1], E. AKILA[2] & and MAHESWARAN .P [1]

Department of Chemistry, PGP College of Arts and Science, Namakkal

Department of Chemistry, Sri Sarada College for women (Autonomous), Salem-16.

Principal and Head, PGP College of Arts and Science, Namakkal

Abstract

A new Schiff base mixed ligand metal complexes were synthesized with the Schiff base derived from 1H-indole-2,3-dione, 2-(2-aminophenyl)benzimidazole and 5-amino-3-methyl-1-phenyl-1H-pyrazole. The isolated Schiff base complexes were formulated as mononuclear species on the basis of analytical data, molar conductance, IR, Far-IR, ^{1}H-NMR, cyclic voltammetry, UV spectra and ESR studies. The empirical formula calculation of the complex compounds indicated the formula $[ML^1L^2X_2]$ for Cu(II), Ni(II) & Co(II) Schiff base mixed ligand complexes. The conductivity data for all the complexes are reliable with those expected for non-electrolyte. The infrared spectral data shows the coordination site that is via C=N and C=O groups of the mentioned ligands. The electronic and ESR spectral data proposed the octahedral geometry for the prepared chelates. The redox potential of ligands and its complexes were analysed by electrochemical method using cyclic voltammetry. The DNA cleavage interactions for prepared chelates were additionally examined and results demonstrate that cleavage viability increased in the chelates comparative with the parental ligand. Apart from these studies, the mixed ligand and its complexes were additionally tried for their antimicrobial action and cytotoxic impact against human breast cancer (MCF7) cell line.

Keywords: Schiff base, Isatin, 2-(2-aminophenyl)benzimidazole, 5-amino-3-methyl-1-phenyl-1H-pyrazole, Antimicrobial, Cytotoxicity and DNA cleavage

Introduction

Schiff bases are significant classes of ligands that coordinate with metal ion through azomethine nitrogen atom [1] and have attracted many researchers to synthesize metal based drugs due to their facile synthesis and wide range of applications including antifungal, antibacterial, anticancer, anti-HIV, antitumor, anticonvulsant, antiviral and catalytic fields [2-5]. The field of mixed ligand complexes was fast emerging account of the wide assortment of

P.G.P. COLLEGE OF ARTS & SCIENCE NAMAKKAL 637 209

Copyright © 2020Author

ISSN:0971-2143
Vol-31-Issue-41-May -2020

potential structures for the ligands reliant upon the aldehydes and amines [6]. The study of mixed ligand complexes formation is pertinent in the field of analytical chemistry, where the utilization of mixed ligand chelates permits the advancement of techniques with improved selectivity, sensitivity and has incredible significance in the field of biological and environmental chemistry [7].

Isatin possess an indole ring structure, it is a flexible lead molecule common to many pharmaceuticals and heterocyclic natural products of biological interest [8]. The chemical versatility of Isatin motivated the prevalent use of this compound in biological synthesis [9]. A lot of work has been done on the synthesis of compounds using substituted isatin and pyrazole moieties. Literature survey exposed that isatin possesses diverse chemotherapeutic activities, such as anticancer, antifungal, antiviral, anti-HIV, anti-mycobacterial, antibacterial, anti-inflammatory and anticonvulsant [10-14].

In view of the above findings, our present work was to synthesis and characterizes a Schiff base ligand derived from condensation of Isatin, 2-(2-aminophenyl)benzimidazole, 5-amino-3-methyl-1phenyl-1Hpyrazole and its metal(II) complexes. The main target of the present article is to examine their antimicrobial activity, cytotoxicity and DNA cleavage of Schiff base mixed ligand complexes.

Experimental protocols

All the reagents were Aldrich products and were used as supplied. IR spectra were recorded on Thermo Nicolet (Avatar 370 model) instrument in the range of 4000–200 cm^{-1} using KBr discs. Electronic spectra were obtained with a Perkin-Elmer Lambda 40(UV-Vis) spectrophotometer using DMF in the range of 200-800 nm. The molar conductance measurements were carried out at room temperature using Elico model conductivity meter. The ESR spectra of powder samples were recorded by means of E-112 ESR Spectrometer, X-band spectrometer (9.1 GHz) with 100 KHZ modulation frequency. ^1H NMR signals were obtained from Bruker Avance III, 400MHz model spectrometer. The Redox nature of the complex in DMF was measured using CHI -760 Electrochemical Analyzer.

Synthesis of (E)-3-((2-(1H-benzo[d]imidazol-2-yl)phenyl)imino)indolin-2-one (L^1)

To a solution of 1H-indole-2,3-dione (1mmol) in methanol, 2-(2-aminophenyl) benzimidazole (1 mmol) in methanol was added dropwise. The above mixture was refluxed for about 3hrs. Then the reaction mixture solvent was kept for slow evaporation and cooled at room temperature. The yellow precipitate was filtered and then washed with ethanol. Schematic route for synthesis of (L^1) is given in scheme 1.

G.T.N. COLLEGE OF ARTS & SCIENCE NAMAKKAL 637 206

Copyright © 2020Author

ISSN:0971-2143
Vol-31-Issue-41-May -2020

Scheme 1: Structure of Schiff base Ligand (L^1)

Synthesis of (E)-3-((3-methyl-1-phenyl-1H-pyrazol-5-yl)imino)indolin-2-one (L^2)

The mixture of 1:1 1H-indole-2,3-dione (1mmol) with -amino-3-methyl-1-phenyl-1H-pyrazole (1mmol) dissolved in methanol. The resultant mixture stirred for 3 hrs, the yellow colored precipitate was obtained and kept for slow evaporation. The colored precipitate was filtered, washed with ethanol and dried. Schematic route for synthesis of (L^2) is given in scheme 2.

Scheme 2: Structure of Schiff base Ligand (L^2)

Synthesis of Schiff base mixed ligand Metal (II) Complexes

The complex was prepared in 1:1:1 molar ratio (Metal: L^1: L^2). Methanolic solution (20 mL) of metal salts (1mmol) was taken in a round bottom flask and methanolic solution (20 mL) of prepared Schiff base ligand (L^1) (mmol) was added drop wise and stirred well, then followed by addition of ligand (L^2). Resulting reaction mixture was refluxed for 3 hours on water bath. On cooling, dark coloured precipitate was formed which was filtered, washed with ethanol and dried in vacuum. The proposed structure of mixed ligand complexes were shown in scheme 3.

P.G.P. COLLEGE OF ARTS & SCIENCE NAMAKKAL 637 206

Copyright © 2020Author

ISSN:0971-2143
Vol-31-Issue-41-May -2020

Scheme 3: Synthesis of Schiff base mixed ligand complexes

RESULTS AND DISCUSSION

The Schiff base ligands (L^1, L^2) were yellow in colour, but the prepared metal chelates of these ligands differ in colour depending on the metal ions. The synthesized metal complexes were coloured, air stable and insoluble in water, but soluble in DMF, DMSO and Chloroform. The elemental analysis of the Schiff base mixed ligand and its complexes is listed in **Table 1**. The data obtained was in a good agreement with the theoretical values and show the formation of 1:1:1 [M: L^1: L^2] ratio where M = Co (II), Ni (II) and Cu (II). The observed values of molar conductance for the mixed ligand complexes (measured in 10^{-3}M DMF) are lower and thus non-electrolytic nature of the mixed ligand complexes was confirmed [15].

Table 1: Analytical data of the Schiff base mixed ligand and its metal complexes

Compounds	Molecular Formula	M.Wt	Yield	Calculated/found%					
				C	H	N	O	Cl	M
L_1	$C_{21}H_{14}N_4O$	338.36	85	(74.54) 74.55	(4.17) 4.14	(16.56) 16.56	(4.73) 4.73	-	-
L_2	$C_{18}H_{14}N_4O$	302.33	80	(71.51) 71.52	(4.67) 4.63	(18.53) 18.54	(5.29) 5.29	-	-
CuL_1L_2	$C_{39}H_{28}CuN_8O_2cl_2$	773.10	75	(60.43) 60.43	(3.64) 3.61	(14.46) 14.46	(4.13) 4.13	(9.15) 9.15	(8.20) 8.20

P.G.P. COLLEGE OF ARTS & SCIENCE NAMAKKAL 637 206

Copyright © 2020Author

ISSN 0971-2143
Vol 31 Issue 41 May 2020

CoL_1L_2	$C_{30}H_{28}CoN_6O_4Cl_2$	769.10	70	(60.79) 60.79	(3.66) 3.63	(14.54) 14.54	(4.15) 4.15	(9.20) 9.20	(7.65) 7.65
NiL_1L_2	$C_{30}H_{28}NiN_6O_4Cl_2$	768.11	65	(60.81) 60.81	(3.66) 3.63	(14.55) 14.55	(4.15) 4.15	(9.21) 9.21	(7.62) 7.62

IR SPECTRA

The IR spectra of the prepared Schiff base ligands and metal complexes were taken in the range of 4000–400 cm^{-1} to interpret the nature of functional groups attached to metal atom. Due to chelation, the intensities of the peaks are expected to differ as related to that of the ligands. The IR spectra of the Schiff base ligands (L^1 & L^2) and metal complexes are shown in **Figure.1 & 2**. The IR spectrum of the ligands displayed a strong band at 1616 cm^{-1} (L^1) and 1611 cm^{-1} (L^2) corresponding to υ (C=N) of imine group [16]. In metal complexes, the imine υ(C=N) of the ligand shifted to lower and higher wavenumbers 1610-1618 cm^{-1} upon coordination to metal. A broad band of medium intensity at 3127-3361cm^{-1} assigned to υ(N–H) was also observed for isatin and benzimidazole moiety. The strong band observed in the ligands at 1725 cm^{-1} (L^1) and 1707 cm^{-1} is characteristic of υ(C=O) amide [17]. In complexes this band was shifted to higher frequencies by 3-16 cm^{-1}, indicating the coordination of carbonyl oxygen of the ligand to metal ions. Further, the appearance of some new bands in the region 519–538 cm^{-1}, 482–489 cm^{-1} and 350–372cm^{-1} region, which may

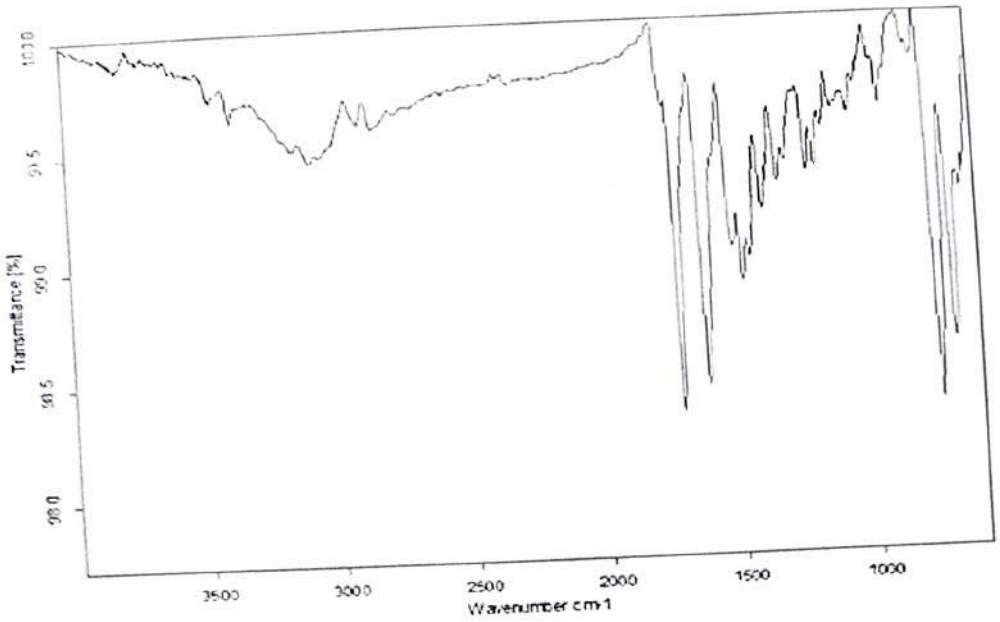


Figure 2: IR Spectra for of Schiff base L^2

^{1}H NMR spectra

The ^{1}H NMR of the ligands L^1 and L^2 was recorded in DMSO-d6 respectively using tetramethylsilane (TMS) as internal standard are given in **Figure.3 &4**. The ^{1}HNMR of the ligand (L^1) gave characteristic signal at 10.8 ppm (s, 1H) and 11.05 ppm (s, 1H) which was assigned to the NH proton of isatin and benzimidazole moiety [20]. Similarly, ligand (L^2) shows a signal at 9.4 ppm, 2.3 ppm which was assigned to the NH [21] and methyl proton. In addition, the aromatic protons of the ligands appeared as multiplets in the range of 6.05–7.85 ppm (L^1) and 6.5-7.4 ppm (L^2).

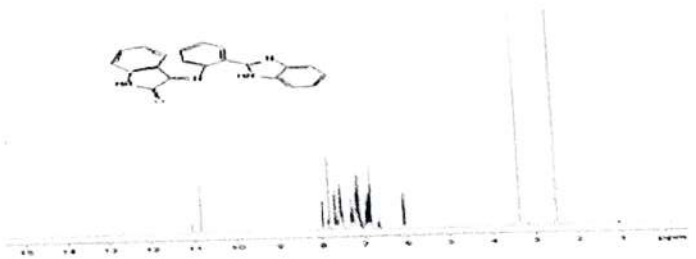


Figure 3: ^{1}H NMR Spectra for of Schiff base L^1

P.G.P. COLLEGE OF ARTS & SCIENCE NAMAKKAL 637 206

Copyright © 2020Author

ISSN 0971-2143
Vol 31 Issue 41 May 2020

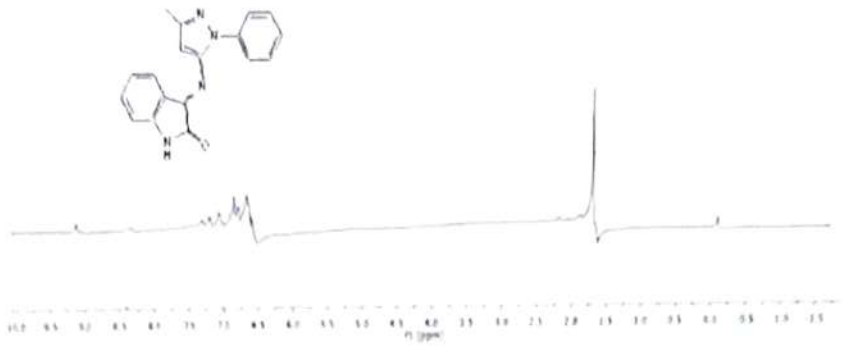


Figure 4: ^{1}H NMR Spectra for of Schiff base L^2

Electronic and Magnetic studies

The electronic spectra of L^1, L^2 and their complexes were recorded in 10^{-3}M DMSO solution in the range of 200–800 nm at room temperature as shown in **Figure.5 & 6**. In both ligands, the bands observed at 270, 271 nm [22] which are attributed to $\pi \rightarrow \pi^*$ transition of the aromatic rings and the band at 335, 379 nm [23] might be attributed to the n-π* transitions of the azomethine group. In metal complexes, these two bands ($\pi \rightarrow \pi^*$ and $n \rightarrow \pi^*$) undergoes shift to lower and higher wavelengths as a consequences of coordination to metal centre. The complex (CoL^1L^2) displayed the broad band in the range of 425 nm may be assigned as the L→M charge transfer transition. In this complex the low intense bands appeared in the range of 550-605 nm corresponds to $4T_1g(F) \rightarrow 4T_2g(P)$ and $4T_1g(F) \rightarrow 4A_2g(F)$ excitations respectively. The magnetic moment of (CoL^1L^2) was found to be 4.46 B.M and spectral data suggest an octahedral geometry around the Co(II) ion. Similar structural features were assigned for other mixed ligand CuL^1L^2 and NiL^1L^2complexes.

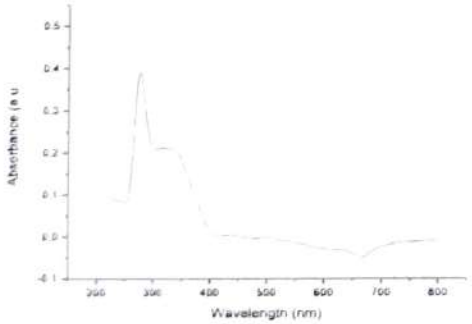


Fig 5: UV Spectra for of Schiff base L^1

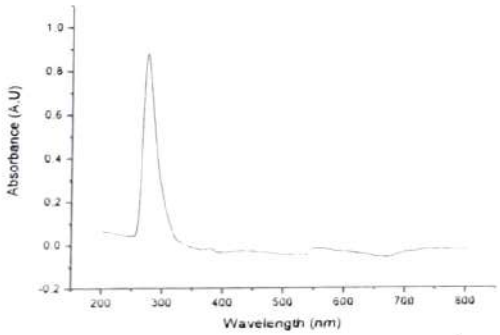


Fig 6: UV Spectra for of Schiff base L^2

PGP COLLEGE OF ARTS & SCIENCE
NAMAKKAL
637 206

Copyright © 2020Author

ISSN:0971-2143
Vol-31-Issue-41-May -2020

Cyclic voltammetry

The electrochemical study is the most effective and versatile methods accessible for study of redox systems. The redox behavior of metal complexes (Cu(II), Co(II) and Ni(II)) has been studied by cyclic voltammogram in DMF using 0.1 M Tetrabutyl ammonium perchlorate (TBAP) as supporting electrolyte. The voltammograms of the mixed ligand Schiff base metal complexes contains two peaks due to oxidative nature of organic molecule and reductive nature of azomethine group. The Cu(II) complex shows an cathodic peak at 0.64 V which is attributed to one electron reduction of Cu(II)/Cu(I) couple and anodic peak of 0.76 V indicates the oxidation process of Cu(I)→Cu(II). The Co(II) complexes exhibit well defined redox process corresponding to quasi reversible Co(II)/Co(I) couple with a peaks at Epa=0.92 V, Epc=0.74 V. The anodic peak at Epa= 0.85 V versus Ag/AgCl and the associated cathodic peak at Epc = 0.94 V correspond to the Ni(II)/Ni(I) couple which provides evidence for quasi reversible in nature. It has been shown that the formal redox potential dependent on factors such as coordination number, hard/soft nature of the ligands and bulkiness of the ligands [24].

ESR studies

The EPR spectra of metal complexes provide information about the geometry, nature of coordinating sites of the Schiff base and the metal. The EPR spectra of the $[Cu(L^1L^2)]$ Schiff base mixed ligand complexes recorded on powder samples with room temperature, on X-band at frequency 9.1 GHz under the magnetic field strength 4000 G. The Schiff base mixed ligand Cu(II) complex display a small broad signal with g_{II} at 2.24 and $g^{\perp}$ at 2.10. Hence the unpaired electron lies in the $dx^2\text{-}y^2$ orbital with $g_{II}>g^{\perp}>g_e$ (2.0027 free spin value). This confirms Cu(II) complex possess a octahedral geometry.

Antibacterial activity

In the present study, various metal complexes of mixed ligand were assessed for their in-vitro antibacterial activity against two pathogens (B.Subtilis and S.typhi) and their potential activity were evaluated by the zone of inhibition and MIC values. Four different concentrations (25µg/ml, 50µg/ml, 75µg/ml and 100µg/ml) of the synthesized compounds have been tested for antibacterial assay. The **Figure.7** shows the antibacterial activity of mixed ligand complexes. The antibacterial activity results showed that all mixed ligand

P.G.P. COLLEGE OF ARTS & SCIENCE NAMAKKAL 637 206

Copyright © 2020Author

ISSN:0971-2143
Vol-31-Issue-41-May -2020

complexes possess good activity against B. subtilis and S.Typhi. The Co(II) and Cu(II) complexes shown better activity against both bacteria examined than the standard drug chloramphenicol. The enrichment observed in activity of the mixed ligand complexes may be attributed to chelation of Schiff bases with metal ion [25]. The polarity of the metal ion gets reduced to a larger extent due to the overlap of the ligand orbital when chelated. Further, the complexes become very stable due to the delocalization of p-electrons and enhance the penetration of the complexes into lipid membranes and blocking of the metal binding sites in the enzymes of pathogens. These complexes also interrupt the respiration process of the cell and thus block the synthesis of proteins, which controls further growth of the microorganism.

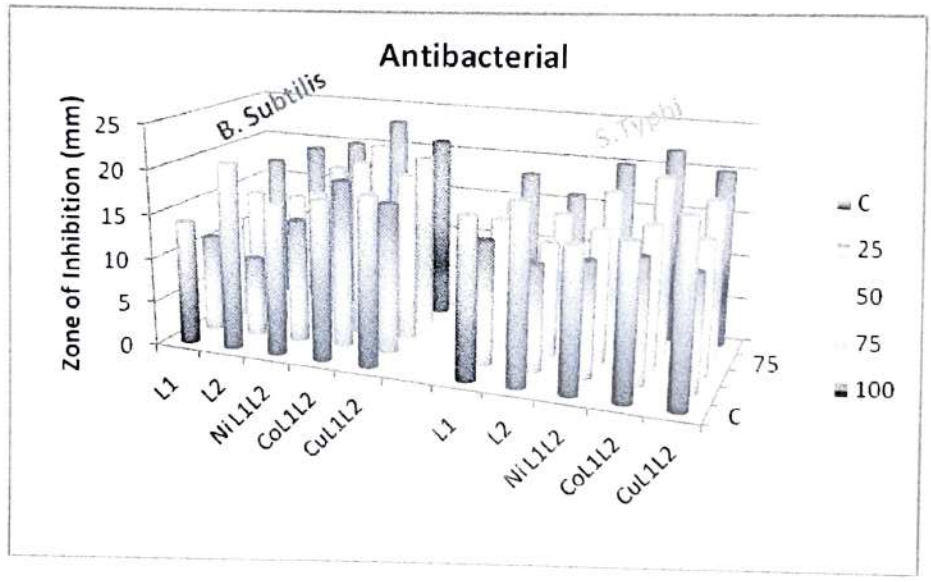


Figure 7: Antibacterial activity for of mixed ligand Schiff base complexes

Antifungal activity

The antifungal activity for the ligands (L^1, L^2) and its NiL^1L^2, CoL^1L^2 and CuL^1L^2 complexes have been tested against two pathogens (A. niger and C. albicans) at four different concentrations. The results are shown in **Figure.8**. The results showed that cobalt complex exhibits enhanced activity against A. niger and C.albicans than the standard drug fluconazole and Ni complex showed moderate effects on both fungal strains.

P.G. COLLEGE OF ARTS & SCIENCE
NAMAKKAL
637 206

Copyright © 2020Author

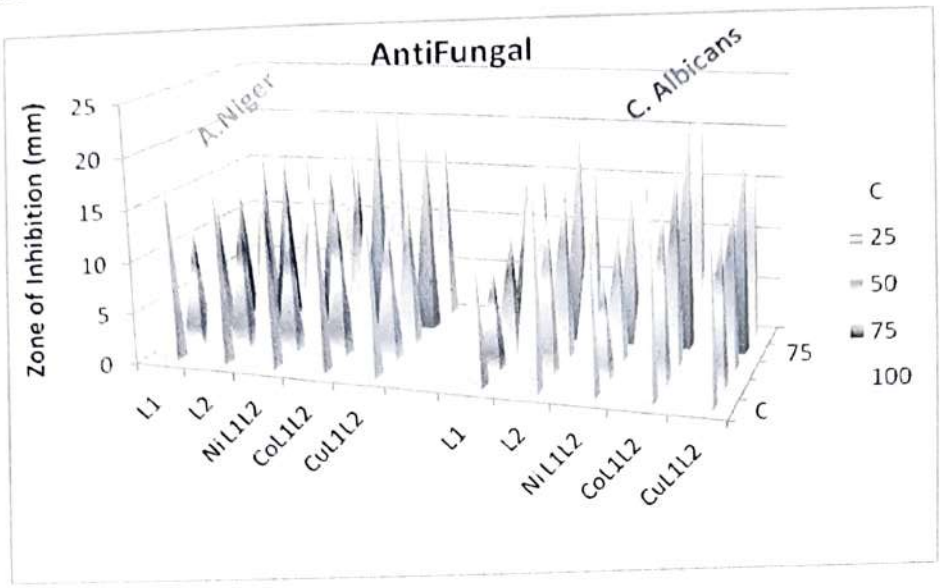


Figure 8: Antifungal activity for of mixed ligand Schiff base complexes

Cytotoxicity

All the synthesized compounds were screened for their cytotoxicity at four different concentrations (5, 10, 50 and 100µg/ml) against breast cancer cell line (MCF7) using standard MTT assay method. From the data (**Figure.9**), it is obvious that all the newly synthesized mixed ligand metal complexes exposed effective activity when compared to the free ligands. The Co(II) complexes displayed significant potent cytotoxic activity than other complexes and IC50 values showed that moderate anticancer activity against MCF7 cell lines without causing significant damage to the normal cells [26].

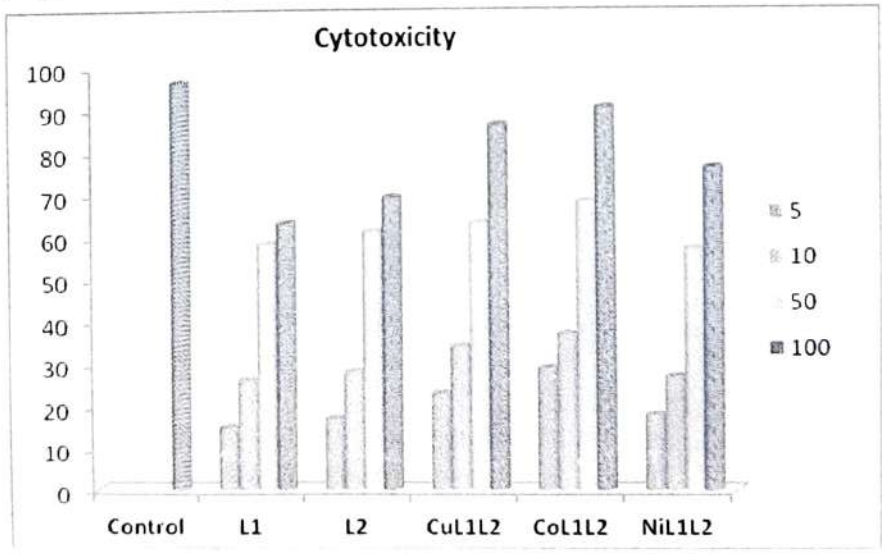


Figure 9: Cytotoxicity activity against MCF-7 Cell line

P.G.P. COLLEGE OF ARTS & SCIENCE NAMAKKAL 637 206

Copyright © 2020Author

ISSN:0971-2143
Vol-31-Issue-41-May -2020

DNA Cleavage Studies

The interaction of pUC18DNA with newly prepared mixed ligand (L^1, L^2) and its Cu(II), Co(II) and Ni(II) complexes was studied using agarose gel electrophoresis method. The gel picture showing the cleavage of pUC18DNA is depicted in **Figure 10.** Mixed ligand and its metal complexes have acted on DNA; chelates are able to convert super coiled DNA into open circular DNA and cleavage activities of chelates depends on concentrations. The mixed ligand complexes showed a difference in lanes compared with the control pUC18DNA due to conversion. Even after a longer exposure time, control DNA alone does not show any apparent cleavage, whereas the ligand and its metal complexes showed cleavage due to presence of oxidant ($OH^{\cdot}$). The $OH^{\cdot}$ free radicals participate in general oxidative mechanisms of deoxyribose moiety, followed by hydrolytic cleavage via abstraction of a hydrogen atom from sugar units. In the present case, mixed ligand complexes showed complete cleavage of DNA in presence of oxidant and clearly reveal the significant role of coordination of O and N groups to the metal ion in these DNA cleavage activities. As the compounds were perceived to cleave the DNA, it can be concluded that all mixed ligand complexes under present study are good pathogenic microorganism inhibitor, as evident on cleavage of pUC18DNA.

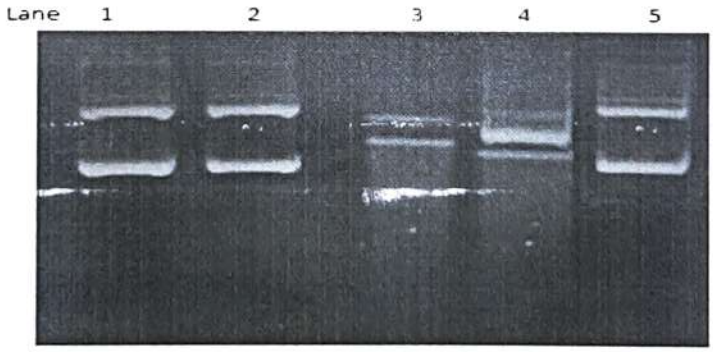


Figure10: The gel picture of DNA cleavage activity on pUC18DNA, Lane 1: DNA alone; Lane 2: DNA+ H_2O_2; Lane 3: DNA+ H_2O_2+CuL^1L^2; Lane 4: DNA+ H_2O_2+CoL^1L^2; Lane 5: DNA+ H_2O_2+ NiL^1L^2

Conclusions

Isatin based mixed ligand complexes were synthesized, characterized and evaluated for their Antimicrobial, Ctotoxicity and DNA cleavagel properties. The octahedral geometry was assigned to mixed ligand complexes, based on various physical and spectroscopic

P.G.P. COLLEGE OF ARTS & SCIENCE NAMAKKAL 637 206

Copyright © 2020Author

techniques. The biological results revealed that these compounds have a potential to be used as antimicrobial drugs and significant potentiators with known antibacterial and antifungal drug (chloramphenicol and Fluconazole). The DNA cleavage activity of newly prepared mixed ligand compounds showed the cleavage of plasmid pUC18 DNA and the cytotoxicities of Co(II) complexes indicate potent cytotoxic agents that might become effective anticancer agent in clinical trials.

Reference

1. P. A. Vigato and S. Tamburini, "The challenge of cyclic and acyclic Schiff bases and related derivatives," Coordination Chemistry Reviews, vol. 248, no. 17–20, pp. 1717–2128, 2004.
2. C. Jayabalakrishnan, R. Karvembu, K. Natarajan, Catalytic and antimicrobial activities of new ruthenium (II) unsymmetrical Schiff base complexes. Trans. Met. Chem.2002, 27: 790 794.
3. R. Prabhakaran, A. Geetha, M. Thilagavathi, R. Karvembu, V. Krishnan, H. Bertagnolli, K. Natarajan, Synthesis, characterization, EXAFS investigation and antibacterial activities of new Ru (III) complexes containing tetradentate Schiff base complexes. J. Inorg. Biochem. 2004, 98: 2131– 2140.
4. K. P. Balasubramanian, R. Karvembu, R. Prabhakaran, V. Chinnusamy, K. Natarajan. Synthesis, spectral, catalytic and antimicrobial studies of PPh3/AsPh3 complexes of Ru (III) with dibasic tridentate O, N, S donor ligands. Spectrochim. Acta Part A. 2007, 68: 50–54.
5. S. A. Sadeek, M. S. Refat, Preparation and Characterization of Tin (II) Complexes with Isomeric Series of Schiff Bases as Ligands. J. Korean Chem. Soc., 2006, 50 (2): 107–115.
6. S. G. Shriodkar, P.S. Mane and T. K. Chondhekar, (2001) synthesis and fungitoxic studies of Mn(II),Co(II),Ni(II) and Cu(II) with some heterocyclic Schiff base ligands, Indian J. Chem., 40 A,1114-1117.
7. Raziyeh Arab Ahmadi and Saeid Amani, Molecules 2012, 17, 6434-6448; doi:10.3390/molecules17066434.
8. G.S. Singh, Z.Y. Desta, Isatins as privileged molecules in design and synthesis of spiro-fused cyclic frameworks, Chem. Rev. 112 (2012) 6104–6155.
9. Joaquim, F. M.; da Silva, Simon J. G.; 1999, J. Braz. Chem. Soc., 2001, 12, 273-324.
10. Debra, C.Q., Kathy, A.K., Kern, E.R., 2006. In vitro and in vivo evaluation of isatin-beta-thiosemicarbazone and marboran against vaccinia and cowpox virus infections. Antiviral Res. 71, 24–30.
11. Gursoy, A., Karal, N., 2003. Synthesis and primary cytotoxicity evaluation of 3-[[(3-phenyl-4(3H)-quinazolinone-2-yl)mercaptoacetyl] hydrazono]-1H-2-indolinones. Eur. J. Med. Chem. 38, 633–643.
12. Karal, N., Gursoy, A., Kandemirli, F., Shvets, N., Kaynak, F.B., Ozbey, S., Kovalishyne, V., Dimoglo, A., 2007. Synthesis and structure–antituberculosis activity relationship of 1H-indole-2, 3-dione derivatives. Bioorg. Med. Chem. 15, 5888–5904.
13. Pandeya, S.N., Sriram, D., Nath, G., Clercq, E.D., 1999a. Synthesis, antibacterial, antifungal and anti-HIV evaluation of Schiff and Mannich bases of isatin derivatives with 3-amino-2-methylmercapto quinazolin-4(3H)-one. Pharm. Acta Helv. 74, 11–17.
14. Verma, M., Pandeya, S.N., Singh, K., Stable, J.P., 2004. Anticonvulsant activity of Schiff bases of isatin derivatives. Acta Pharm. 54, 49–56.

P.G.P. COLLEGE OF ARTS & SCIENCE NAMAKKAL 637 206

Copyright © 2020Author

ISSN:0971-2143
Vol-31-Issue-41-May -2020

15. WJ Gear, Coord Chem Rev, (1971) 7:81.
16. Seema Varghese, RJPBCS.2010,2,347
17. H. Pervez, M. Ahmad, S. Zaib, M. Yaqub, M.M. Naseer, J. Iqbal, Synthesis, cytotoxic and urease inhibitory activities of some novel isatin-derived bis-Schiff bases and their copper(II) complexes, Med.chem.comm 7 (2016) 914–923.
18. G. Cerchiaro, P.L. Saboya, A.M.C. Ferreira, D.M. Tomazela, M.N. Eberlin, " Keto-enol equilibria of an isatin-schiff base Cu(II) complexes & its reactivity toward carbohydrate oxidation"Tran. Met. Chem., vol. 29, 2004, pp. 495-504.
19. M. Muthukkumar, M. Malathy and R. Rajavel, Synthesis and spectral characterization of new mononuclear Schiff base complexes derived from 4-aminoantipyrine, 2, 3-butadione and o-phenylenediamine. Der Chemica Sinica, 2015, 6(11):12-20.
20. Matangi sunitha, Pragathi jogi, Bathini ushaiah, and c. Gyana kumari, Synthesis, Characterization and Antimicrobial Activity of Transition Metal Complexes of Schiff Base Ligand Derived from 3-Ethoxy Salicylaldehyde and 2-(2-Aminophenyl) 1-H-benzimidazole, E-Journal of Chemistry 2012, 9(4), 2516-2523.
21. Ovas Ahmad Dar, Shabir Ahmad Lone, Manzoor Ahmad Malik, Faisal Mohammed Aqlan, Mohmmad Younus Wani, Athar Adil Hashmi, Aijaz Ahmad, Synthesis and synergistic studies of isatin based mixed ligand complexes as potential antifungal therapeutic agents, Heliyon 5 (2019) e02055.
22. Mohammad Shakir, Nausheen Bano, Mohammad Ahmar Rauf and Mohammad Owais, Pharmacologically significant tetraaza macrocyclic metal complexes derived from Isatin and 3,4-diaminobenzophenone: Synthesis, spectral studies and comparative in vitro biological assessment, J. Chem. Sci. Vol. 129, No. 12, December 2017, pp. 1905–1920.
23. Kismat Ara Elachi, Saddam Hossain, M. M. Haque, Ranjan K. Mohapatra, Kudrat-E-Zahan, Synthesis, Spectral and Thermal Characterization of Cu(II) Complexes Containing Schiff Base Ligands and Their Antibacterial Activity Study, American Journal of Materials Synthesis and Processing, 2019; 4(1): 43-53.
24. A.J.Bard and L.R.Izatt, Electrochemical method: Fundamendals and Applications: 2nd Ed., Wiley: New York, 2001.
25. Vairalakshmi M, Princess R, Johnson raja S, Metal complexes of novel schiff base containing isatin: characterization, Antimicrobial, antioxidant and catalytic activity study, Asian J Pharm Clin Res, Vol 12, Issue 8, 2019, 206-210.
26. Emil Bulatov , Regina Sayarova et al, Isatin-Schiff base-copper (II) complex induces cell death in p53-positive tumors, Bulatov et al. Cell Death Discovery (2018) 4:103.

P.G.P. COLLEGE OF ARTS & SCIENCE NAMAKKAL 637 203

PRINCIPAL
PGP College of Arts and Science
Namakkal.

Copyright © 2020Author

Check for updates
Chemistry Europe
European Chemical Societies Publishing

Sustainable Chemistry

Preparation of Reduced ZnO/Ag Nanocomposites by a Green Microwave-Assisted Method and Their Applications in Photodegradation of Methylene Blue Dye, and as Antimicrobial and Anticancer Agents

Arumugam Saranya,[a] Alsawalha Murad,[b] Alomayri Thamer,[c] Arumugam Priyadharsan,[d] and Palanimalai Maheshwaran*[a]

In this present study, we report a facile microwave assisted green synthesis of ZnO/Ag nanocomposites (denoted as G-ZnO/Ag NCs) by employing *Tridax procumbens* leaf extract as a green solvent for photocatalytic, antimicrobial and cytotoxicity activities. The prepared nanocomposites was characterized by various techniques to study its crystallinity, morphology, structure, chemical composition, optical properties, and so on. The nanocomposites exhibited excellent photocatalytic performance (90.2%) toward methylene blue degradation when irradiated under visible light (120 min). Furthermore, the G-ZnO/Ag NCs showed good reusable properties up to four consecutive cycles. In addition, the resultant nanocomposites showed significant antimicrobial activity with the zones of inhibition of 9.85 ± 0.12 and 10.51 ± 0.63 mm against gram positive (*Staphylococcus aureus*) and 11.98 ± 0.22 and 13.76 ± 0.12 mm against gram-negative (*Escherichia coli*), bacteria respectively, as measured using the well diffusion method. Although, the in-vitro cytotoxicity test showed 39.58% viability of MCF-7 cells. In summary, this study suggest that G-ZnO/Ag NCs as a promising tool for wastewater treatment and nano biomedical applications using low cost and eco-friendly approach.

1. Introduction

Currently, the development of nanomaterials is an high demand for various industrial, scientific and medical applications. Particularly, metal/metal oxide nanoparticles are studied as the most promising as they include superior catalytic and biological applications because of their unique properties including small size, large surface area, and uniform size distribution.[1] In the recent decades, various metal/metal oxide nanoparticles including Au, CuO, Co, TiO_2, Fe_2O_3, SnO_2, modified carbon dots, metal-organic framework based materials have gained the researcher interest and they are frequently applied for environmental remediation and pharmaceutical applications. Among different materials, zinc oxide is a well-established semiconductor material because of its excellent adsorptive, transparency, high melting point, optical, conductivity, low cost, stability and controllability properties which drives applications in catalysis, supercapacitors gas storage and separation, biomedical, adsorption, magnetism and sensors.[2–7] On the other hand, silver nanoparticles are also currently one of the most widely commercialized nanomaterials and they are extensively used in various areas such as electrochemical, biosensors, antibacterial coatings, and extremely effective catalysts of organic reactions.[8–11] However, these pristine nanomaterials suffer from numerous shortcomings such as lower sensitivity and reproducibility, slower kinetics of electron transfer, lower conductivity, poor mechanical strength, and lower stability. To overcome these shortcomings, Ag NPs have been incorporated into the surface of ZnO NPs is advisable to prepare ZnO/Ag nanocomposites with desirable properties.

Therefore, various preparation methods including hydrothermal, precipitation, solvothermal, thermal decomposition, electrochemical, sol-gel, and physical vapor deposition techniques have been reported for the preparation of metal or metal oxide nanomaterials.[12–19] Among all preparation techniques, Microwave (MW) synthesis is an modest and effective strategy for the preparation of metal/metal oxides nanomaterials.[20] MW heating provides several advantages over conventional methods, including energy efficiency, high reaction rate, lower energy consumption, short reaction time, small particle size and narrow size distribution.[21,22] However, many of these

[a] A. Saranya, Dr. P. Maheshwaran
Department of Chemistry,
PGP College of Arts and science,
Namakkal-637 207, Tamil Nadu, India
Tel: 04286–267404
E-mail: pm_omk@yahoo.co.in
[b] Dr. A. Murad
Department of Chemical and Process Engineering Technology,
Jubail Industrial College, P.O. Box 10099, Jubail-31961, Saudi Arabia
[c] Dr. A. Thamer
Department of Physics,
Faculty of Applied Science,
Umm Al-Qura University,
PO.Box 21955, Makkah, Saudi Arabia
[d] Dr. A. Priyadharsan
Department of Physics,
E.R.K Arts and Science College,
Erumiyampatti, Tamil Nadu-636 905, India

Supporting information for this article is available on the WWW under https://doi.org/10.1002/slct.202100413

© 2021 Wiley-VCH GmbH

P.G.P. COLLEGE OF ARTS & SCIENCE NAMAKKAL 637 206

procedures required strong acids, toxic capping agents and reducing/stabilizing agents. Hence, there has been a need for an eco-friendly reducing and a nontoxic capping agent for stabilizing the nanoparticles.[23] Incidentally, The green chemistry principles in the preparation of nanomaterials has provided innovative tools to reduces or eliminates the application of hazardous reagents in both research and industry because of their easy availability, non-toxic, better adsorption efficiency and cost effectivity.[24,25] Recently, many attention has been paid to develop eco-friendly green reagents such as bio degradable polymers, cellulose, enzymes, haemoglobin, glucose, plant extracts and tragacanth gel for the synthesis of nanomaterials.[26]

The possibility of nanoparticle formation with bio reagent has been studied in the recent decades. Nadagouda et al. have studied the use of Blackberry, Blueberry, Pomegranate and Turmeric Extracts for the preparation of metal nanoparticles. It was determined that the technique did not require the use of any surfactants or capping agents for the production of stable nanoparticles.[27] Similarly, Green synthesis of silver and palladium nanoparticles were produced by coffee and tea extract at room temperature. The Caffeine/polyphenols of coffee and tea extracts plays an important role to reduce the corresponding metals solution and this approach addresses key requirements from a green chemistry perspective.[28] Kou, J.et al. developed simple route for the preparation of noble metal nanoparticles by using beet juice under MW irradiation method. The prepared nanoparticles with capping prepared using beet juice exhibit higher catalytic activity and durability than those prepared using chemical methods.[29,30] Yeganeh and co-workers have reported a magnetic nanoparticles, which was synthesized using Minidium leavigatum leaves extract. The resulting magnetic nanoparticles showed excellent adsorption capacity for removal RB 222 aqueous solution.[31] Baruwati et al. have demonstrated an extremely easy and completely green preparation process for generation highly crystalline Au, Ag, Pd, and Pt nanoparticles using grape pomace extracts. The polyphenolic compounds of grape pomace could serve as capping and reducing agents during the synthesis process.[32] Recently, the application of green synthesis of Tragacanth gum treated nanocomposite has been extensively investigated for photocatalytic degradation and reusability towards direct black 122 dye, Acid orange 7 and Eriochrome Black T dyes at room conditions, due to their non-toxicity, high surface area, cheap, ease of preparation. Thus, they have shown to have good photocatalytic activity and reusability to treat various pollutants from wastewater.[33–36] In view of these successes, Some of the recent works have explored on preparation of ZnO/Ag nanocomposites include *Thymus vulgaris*,[37] *Prosophis fracta* and *coffee* grounds,[38] Ocimum tenuiflorum seed[39] *oak fruit hull* (Jaft),[40] *Pomegranate* peel extract, Urtica dioica leaf extract[41,42] and Trigonella foenum graecum[43] were investigated for their biomediacal and catalytic activity for environmental remediation.

Tridax procumbens (*T. procumbens*) is a common weed plant belongs to the Asteraceae family, commonly found in tropical Americas and naturalized in tropical Asia, Africa, Australia, and India. The leaves extract contains rich phytochemical constituent and they were used to treat wound healing, antibacterial, antioxidant, anti-inflammatory and anticancer treatments.[44–48] To the best of our knowledge, *T. procumbens* aqueous leaf extract have not been reported as a reducing and gapping agent for the preparation of G-ZnO/Ag NCs. In the present study, a green, ecofriendly exfoliation approach was applied for the preparation of G-ZnO/Ag nanocomposites using *T. procumbens* leaves extract through a microwave assisted hydrothermal method. Moreover, the prepared G-ZnO/Ag NCs were used for their methylene blue dye degradation ability, antimicrobial and anticancer activity.

2. Results and Discussion

2.1. X-ray Diffraction and FT-IR Studies

The phase structure of the G-ZnO and G-Ag/G-ZnO NCs were investigated by

Xray diffraction (XRD) analysis. As shown in Figure 1a, G-ZnO NPs shows typical diffraction peaks observed at 31.8°, 34.5°, 36.4°, 47.7°, 57.3°, 63.2°, 67.2°, 68.3°, 69.6°, 73.1°, and 78.3° corresponding to the (100), (002), (101), (102), (110), (103), (200), (112), (201), (004), and (202) planes of hexagonal wurtzite, which is consistent with JCPDS file no 36–1451. It is noteworthy that three new diffraction peaks appeared for G-ZnO/Ag NCs at 38.4°, 44.5°, and 67.5° can be indexed respectively to the (111), (200) and (220) planes of cubic segment of Ag crystal phase, which confirms the formation of G-ZnO/Ag NCs. Furthermore, no additional peaks were found in the XRD patterns indicating high purity of G-ZnO/Ag NCs. This result indicated that as-prepared G-ZnO/Ag nanocomposites possessed mixed hexagonal structure of ZnO phase and the cubic structure of Ag phase.

To acquire about the functional groups, the G-ZnO NPs, and G-ZnO/Ag NCs were analyzed by FT-IR (Figure 1b). The signature peak of Zn–O stretching vibrations were observed between 400 to 600 cm^{-1}. The characteristic bands displayed in the range of 1448 to 1332 cm^{-1} related to C=C stretching vibration and the bands between 1236 and 720 cm^{-1} resulted from C–H bending. The absorption bands between 2930 to 2830 cm^{-1} was related to C–H stretching vibrations and the wide band ranging from 3600 cm^{-1} to 3250 cm^{-1} attributed to O–H stretching vibration of the absorbed water molecules on surface of the materials. In addition, the bands between the wavenumber of 1780 to 1490 cm^{-1} were allocated to the C=O stretching vibrations of the prepared samples.[49,50] It is worth noting that, after introduction of G–Ag NPs on G-ZnO surface, all the organic functional groups and other some peaks are become weaker, which indicates that the successful formation of G-ZnO/Ag NCs by the microwave assisted synthesis.

2.2. Morphological, Size and Elemental Distribution Analysis

The detailed morphologies and size of the as-obtained pristine G-ZnO NPs, and G-ZnO/Ag NCs photocatalysts were observed by applying the SEM and HR-TEM. The higher magnification

© 2021 Wiley-VCH GmbH

COLLEGE OF ARTS & SCIENCE NAMAKKAL 637 206

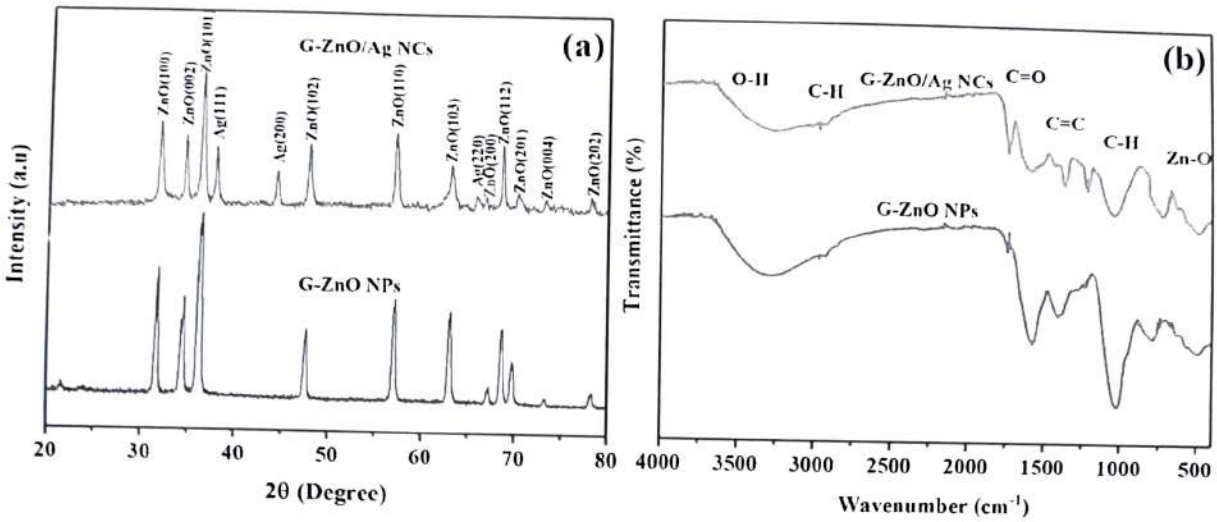


Figure 1. (a) XRD patterns and (b) FT-IR spectra of pristine G-ZnO and G-ZnO/Ag NCs.

SEM (Figure 2a) and HR-TEM images (Figure 2b–c) of as-obtained G-ZnO NPs showed spherical morphology with sizes ranging from 15 to 20 nm (Figure 2d). After incorporation of the two components, The SEM (Figure 2e) images of G-ZnO/Ag NCs clearly reveals that the Ag nanoparticles are well anchored on the surface of G-ZnO indicating that Ag NPs are successfully loaded onto the G-ZnO surface via the microwave-assisted process. HR-TEM images (Figure 2f–g) of G-ZnO/Ag NCs at 50 and 20 nm scale clearly revealing nanospherical morphology and the histograms show that the average size of G-ZnO/Ag NCs are ranging from 25 to 30 nm (Figure 2h) which are much larger than those of pristine G-ZnO NPs. Furthermore, the interplanar distances of 0.28 nm and 0.24 nm (Figure 2i) could be ascribed to the (100) crystal plane of ZnO and Ag respectively, which indicates that Ag nanostructures are present on the surface of G-ZnO and which are good agrees with the XRD results. The EDX spectra of G-ZnO/Ag NCs confirm the existence of zinc, carbon, oxygen and silver elements (Figure 3a) and in can be seen that all constituent elements including carbon (red), oxygen (green), zinc (aqua), and silver elements (purple) are distributed homogeneously in the G-ZnO/Ag NCs (Figure 3b–e), which proved the Ag deposited on the ZnO surface to form G-ZnO/Ag NCs.

2.3. UV-Vis, Electronic Band and PL Spectra Analysis

The optical absorption properties reflects the ability of harvesting photos, thereby playing a important role in determining the photocatalytic efficiency. UV-vis diffuse reflectance spectroscopy (DRS) spectra of G-ZnO and G-ZnO/Ag NCs photocatalysts were shown in Figure 4a. As can be seen that as prepared G-ZnO/Ag NCs exhibit significantly enhanced after introduction of Ag NPs, which was expected to be enhance for photocatalytic activity under solar light irradiation. In addition to that, the Tauc plots was used to determine the band gap of the prepared materials, which was calculated by the following equation.

$$\alpha h\nu = A(h\nu - E_g)^{n/2}$$

where, h is Plank's constant, α denotes the absorption coefficient, A means a proportional constant, v is the light frequency, and Eg is the band gap respectively.[51] The results of Tauc plots (Figure 4b) showed that the optical band gap of G-ZnO/Ag NCs was about 3.12 eV, which is significantly lower compared to that of pristine G-ZnO (3.18 eV). Therefore, the lower band gap energy of G-ZnO/Ag NCs play vital roles in facilitating for the enhanced photocatalytic efficiency for degradation of organic dye pollutants.

Photoluminescence (PL) spectroscopy was employed to study the photoproduced charge carriers of prepared samples. Figure 4c. illustrates the emission spectra of pristine G-ZnO NPs and G-ZnO/Ag NCs. Generally, the electron-hole separation efficiency can be associated with the photoluminescence (PL) emission intensity; the lower PL intensity could reflect less electron-hole pair recombination in the photocatalyst, which leads to the improved photocatalytic performance.[52] Noticeably, the peak intensity of G-ZnO/Ag NCs was less than that of the pristine G-ZnO NPs, which reveals that the G-ZnO/Ag NCs can trap the photoexcited electrons during the solar light irradiation.

2.4. Photocatalytic Performance

The photocatalytic performance of the as-prepared materials were evaluated by the degradation of methylene blue (MB) and the results under various conditions are shown in Figure 5a,the adsorption and desorption equilibrium will be reached after 20 min in darkness reaction. The blank test (absence of the catalysts) shows that there is no observable degradation of MB

© 2021 Wiley-VCH GmbH

P.G.P. COLLEGE OF ARTS & SCIENCE NAMAKKAL 637 206

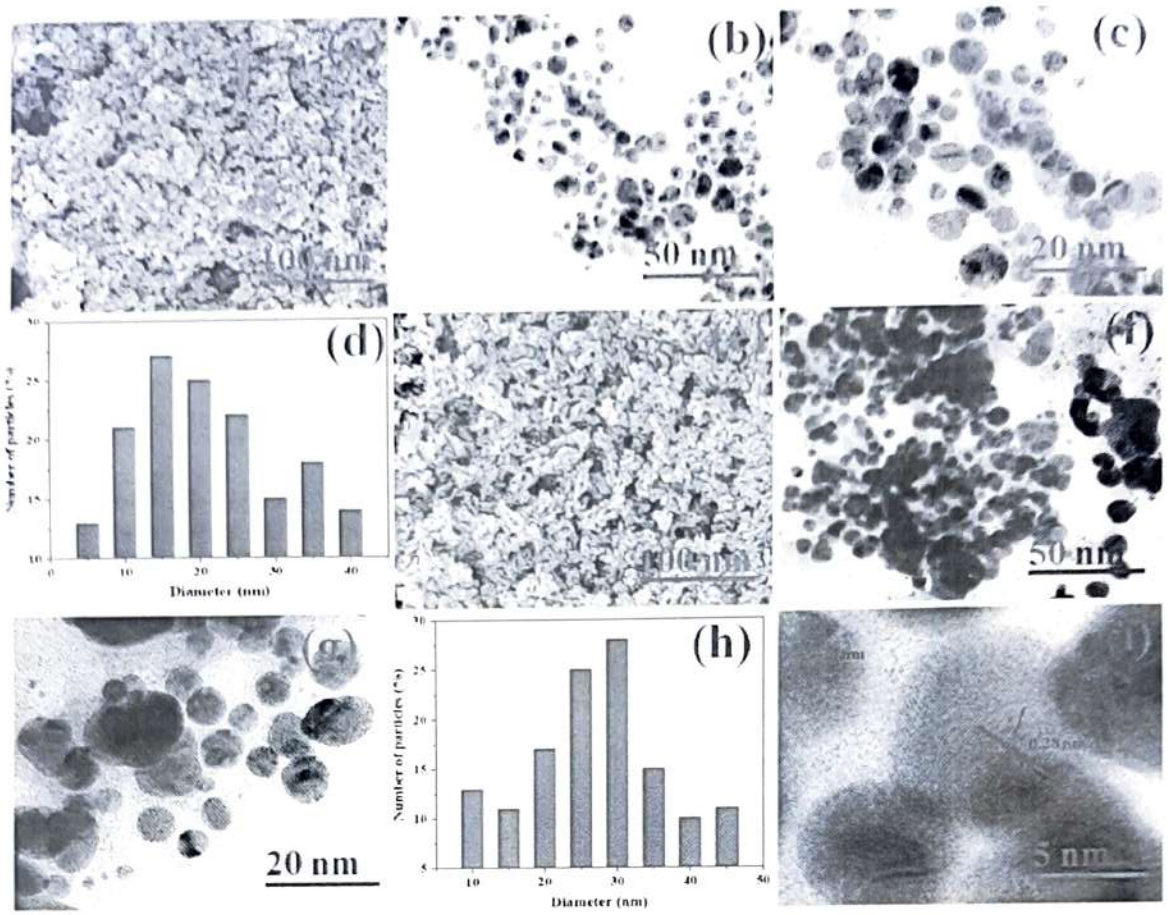


Figure 2. Typical SEM and HR-TEM images of the photocatalysts: (a) SEM and (b–c) HR-TEM and (d) histogram analysis of pristine G-ZnO NPs. (e) SEM, (f–g) HR-TEM, (h) Histogram and (i) Space lattice analysis of G-ZnO/Ag NCs.

Table 1. Measurement of diameters of inhibition zone over G-ZnO NPs and G-ZnO/Ag NCs.

Samples	Zone of inhibition (in mm)			
	S. aureus		*E. coli*	
	50(μg ml^{-1})	100(μg ml^{-1})	50(μg ml^{-1})	100(μg ml^{-1})
G-ZnO NPs	6.51 ± 0.25	7.93 ± 0.34	9.4 ± 0.54	10.94 ± 0.41
G-ZnO/Ag NCs	9.85 ± 0.12	10.51 ± 0.63	11.98 ± 0.22	13.76 ± 0.12
Positive control	16.81 ± 0.23 (10 μg ml^{-1})		18.36 ± 0.49 (10 μg ml^{-1})	

after irradiation for 120 min, the sole effect of light irradiation was almost negligible, with only 4.8% of MB degradation indicating that MB is quite stable under solar irradiation. The pristine G-ZnO NPs exhibited lower photocatalytic efficiency and reaches a maximum degradation activity with 65.5%, However, after assembling the Ag NPs on the surface of the G-ZnO, the photocatalytic degradation efficiency is greatly improved and exhibited 90.2% degradation efficiency after irradiation for 120 min, indicating that Ag NPs content has a significant influence on the photocatalytic efficiency of G-ZnO/Ag NCs. Figure 5b shows time dependent absorption peaks of MB (at 666 nm) over G-ZnO/Ag NCs during the photocatalytic the reaction process. With increasing the irradiation time, the absorption peak of MB gradually decreased, demonstrating the breaking of chemical bonds in MB upon irradiation of solar light.

For better understanding of the photocatalytic performance of the G-ZnO/Ag NCs, the kinetic behavior of the photodegradation of the MB dye was also studied as follows. Generally, the kinetic process of photocatalysis can be described by pseudo-first-order reaction equation: $\ln (C_0/C_t) = kt$. Where, K is the rate constants, C_0 and C_t represent the concentrations at the initial time (t = 0) and time t (min), respectively.[53] Figure 5c describes the plots of $\ln(C_0/C_t)$ versus irradiation time, It can be seen from the results that the G-ZnO/Ag NCs has the fastest rate of rate constants ($K = 0.3715$ min^{-1}) and better fitting correlation index ($R^2 = 0.9554$), which indicates that the G-ZnO/Ag NCs has the best photocatalytic property.

The effect of dosage plays an vital role in the photocatalytic degradation of the organic pollutants. In this regard, Figure 5d

© 2021 Wiley-VCH GmbH

COLLEGE OF ARTS & SCIENCE NAMAKKAL 637 206

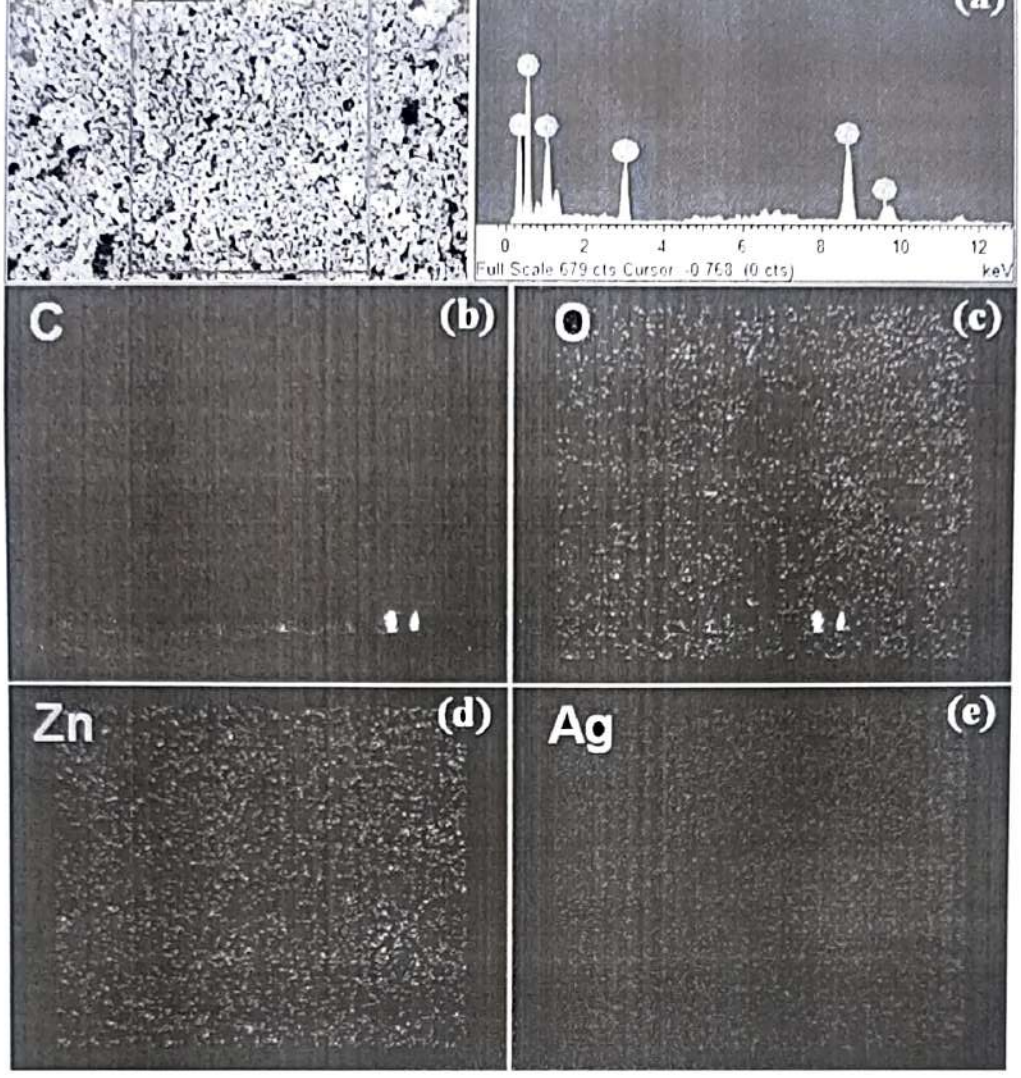


Figure 3. (a) EDX spectrum and elemental distribution mapping analysis of G-ZnO/Ag NCs (b) Carbon, (c) Oxygen, (d) Zinc and (e) Silver respectively.

demonstrates the effect of various catalytic amount of G-ZnO/Ag NCs on the photocatalytic degradation of the MB dye solution. Moreover, it has been observed that after the irradiation of 30 min from the beginning of the reaction, with the increase in the dosage of G-ZnO/Ag NCs from 30 to 70 mg, the degradation efficiency of the MB increased from 65.5% to 90.2%. When further increase in photocatalyst loading, the rate of photodegradation was decreased possibly due to the decrease in light penetration of the G-ZnO/Ag NCs as a result of reduced the photodegradation efficiency. Thus, the G-ZnO/Ag NCs achieved a significant degradation of 90.4% toward the MB solution at a optimum photocatalyst amount of 70 mg under 120 min of irradiation time and the whole study was carried out with the same catalyst dose.

In order to check the reusability of the as prepared photocatalyst G-ZnO/Ag was investigated by performing four successive cycles using MB dye solution under the same experimental conditions. After each cycle, the sample were collected by filtration, washed three times with distilled water, dried at 65 °C, and reused again. As depicted in Figure 6a, the photodegradation efficiency of G-ZnO/Ag NCs for MB dye after second cycle was found to be almost similar with first and a slight decrease in efficiency was observed during third and fourth cycles, which can be attributed to the loss in the amount of photocatalyst during the process of recollection and the results of this study indicated that G-ZnO/Ag NCs processes remarkable recyclability up to four consecutive cycles

Moreover, to address the possible photodegradation mechanism over G-ZnO/Ag NCs illustrated in the schematic diagram in Figure 6b. When switched on the visible light source, catalyst absorbed light energy, and the electrons in the valence band (VB) were transited to the conduction band (CB) to form electronic-hole pairs. The photogenerated electrons from the CB of G-ZnO were transferred to Ag and react with the adsorbed O_2 molecules leading to the formation of superoxide radical anions ($O_2^{\cdot-}$) radicals. Meanwhile, the active positive

© 2021 Wiley-VCH GmbH

GF COLLEGE OF ARTS & SCIENCE NAMAKKAL 637 206

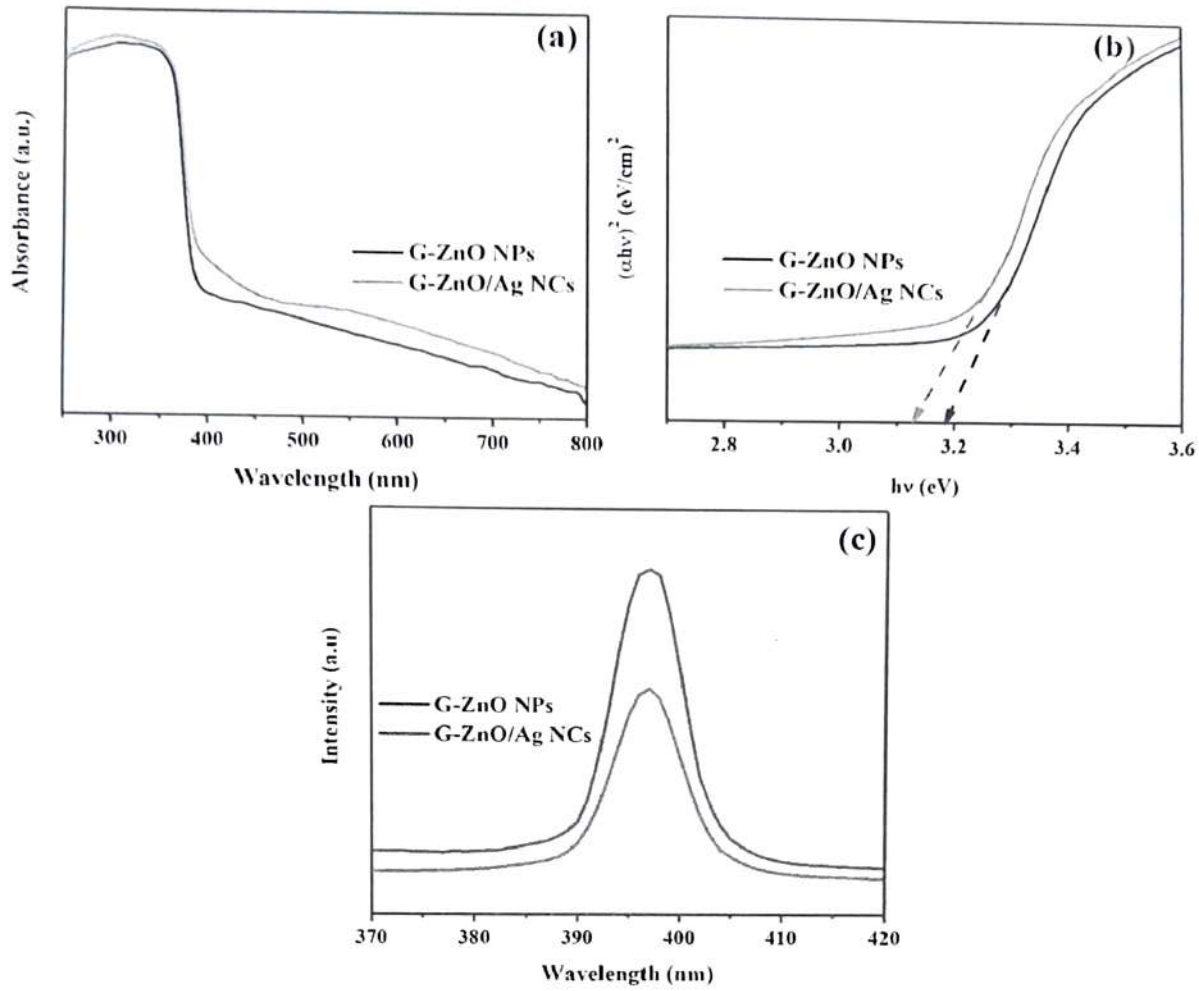


Figure 4. (a) UV-visible diffused reflectance spectra (b) Optical band gap determined by Tauc plot (c) Photoluminescence spectra of pristine G-ZnO NPs and G-ZnO/Ag NCs.

hole (h^+) in the valence-band (VB) react with H_2O to produce hydroxyl radicals ($^{\cdot}OH$). The reactive species of $^{\cdot}O^{2-}$ and $HO^{\cdot}$ produced under visible light irradiation are mainly involved in the degradation of MB dye molecules.[54]

2.5. *In-vitro* Biological Properties

2.5.1. Antimicrobial Properties

The antimicrobial activity of pristine G-ZnO NPs and G-ZnO/Ag NCs were evaluated against gram-positive (*S. aureus*) and gram-negative (*E. coli*) bacterium by well diffusion method. The inhibition zone results were given in Table 1 and Figure 7. It was found that, the pristine G-ZnO NPs showed diameter of inhibition zone against *S. aureus* were 6.51 ± 0.25, and 7.93 ± 0.34 mm, whereas the inhibition zones for *E. coli* were 9.4 ± 0.54 and 10.94 ± 0.41 mm at the concentration of 50 and 100 µg/mL respectively. Interestingly, the same concentration of prepared G-ZnO/Ag NCs exhibited greater antimicrobial effect than pristine G-ZnO NPs and the zones of inhibition against *S. aureus* were 9.85 ± 0.12 and 10.51 ± 0.63 mm, whereas the inhibition zones for *E. coli* were 11.98 ± 0.22 and 13.76 ± 0.12 mm. Meanwhile inhibition zones for control (10 µg/mL Gentamycin) were found to be 16.81 ± 0.23 mm for *S. aureus* and 18.36 ± 0.49 mm for *E. coli* respectively. This enhanced antimicrobial properties of G-ZnO/Ag NCs was due to following phenomena; the direct interaction of G-ZnO/Ag NCs to the bacterial surface, deactivates cellular enzymes, destroying the integrality of the cell membrane, and ultimately causing bacterial cell death.[55] Another major mechanism of G-ZnO/Ag NCs is production of ROS (Reactive oxygen species) which do penetration of membrane lipids, proteins, DNA, and lead to higher antimicrobial activity.[56,57]

© 2021 Wiley-VCH GmbH

PG & RESEARCH DEPARTMENT OF CHEMISTRY KANDASWAMY KANDAR'S COLLEGE OF ARTS & SCIENCE NAMAKKAL 637 206

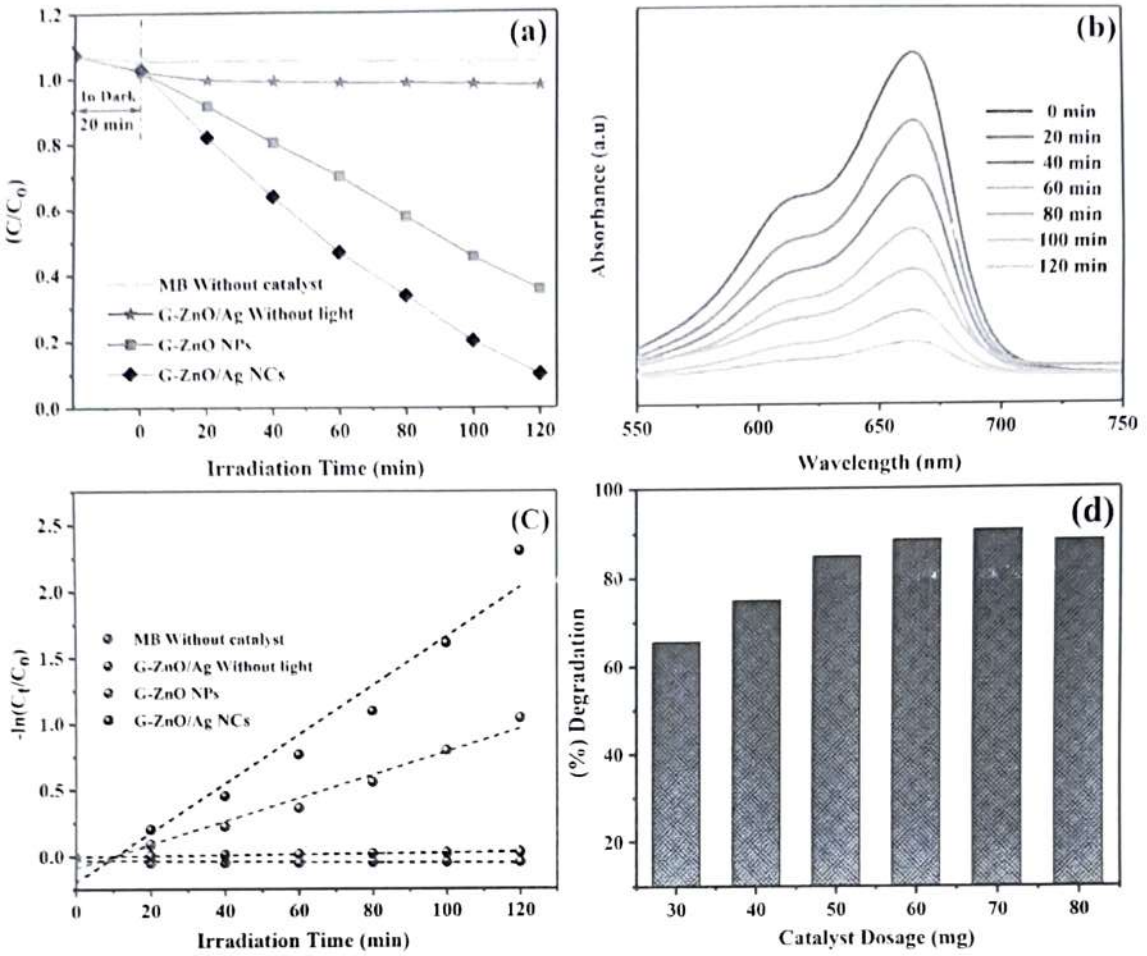


Figure 5. (a) Photocatalytic MB dye degradation of as prepared G-ZnO NPs and G-ZnO/Ag NCs under various conditions. (b) UV-vis spectral changes of MB using G-ZnO/Ag NCs under the optimized conditions. (c) Linear relationship between $\ln(C_t/C_0)$ and irradiation time (min) and (d) dose dependent photodegradation of MB over G-ZnO/Ag NCs.

2.5.2. In-Vitro *Assay for Cytotoxic Properties*

The cytotoxicity effect of pristine G-ZnO NPs and G-ZnO/Ag NCs were screened against A549 cancer cell line by means of MTT assay. Figure 8 shows the obtained results of cell viability of A549 cells after 24 h exposure. Concentration dependent cytotoxicity activity was observed after exposing the cell lines to 50, 100, 200 and 300 µg/mL of green synthesized G-ZnO NPs and G-ZnO/Ag NCs. Compared to the untreated control test, the pristine G-ZnO NPs showed respectively 71.34% and 55.51% of cell viability at the highest concentration of 200 and 300 µg/ml after 24 h exposure. In the meantime, the same concentrations of G-ZnO/Ag NCs (200 and 300 µg/Ml) showed higher cytotoxicity effects toward A549 cells and the percentage of cell viability were respectively 52.24% and 39.58% after 24 h exposure. The IC_{50} value of G-ZnO/Ag NCs was determined as 214.8 µg/mL confers better cytotoxic effects in the proliferation of A549 cell line. This effective cytotoxicity property should be due to different electrostatic interaction between G-ZnO/Ag NCs and A549 cell wall, which leads to cellular toxicity.[58] These results suggest that G-ZnO/Ag NCs possess potential application in cancer chemoprevention and chemotherapy.

3. Conclusions

In this study the G-ZnO/Ag NCs was prepared in an ecofriendly manner and characterized using XRD, FTIR, SEM, EDX, HR-TEM, UV-DRS, and PL analyses. An excellent photodegradation activity was achieved for the optimized dosage of G-ZnO/Ag NCs (70 mg) and exhibited maximum MB dye degradation rate of 90.2% which is much higher compared to that of pristine G-ZnO (65.5%), respectively. Also, the G-ZnO/Ag NCs exhibited good recyclability up to four consecutive cycles, which are

© 2021 Wiley-VCH GmbH



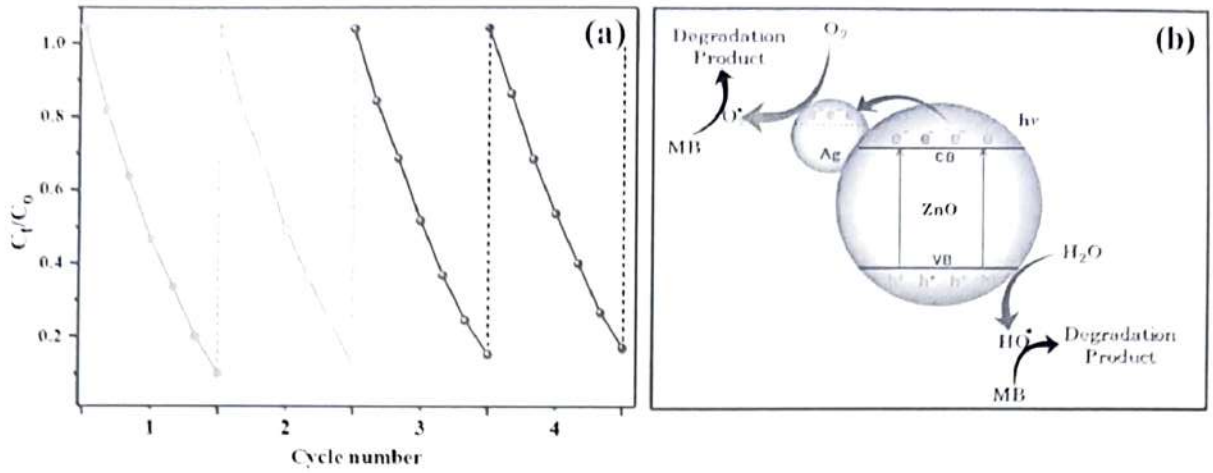


Figure 6. (a) Reusability of the G-ZnO/Ag NCs photocatalyst for four consecutive cycles and (b) Possible mechanism of photoexcitation and MB dye degradation using G-ZnO/Ag NCs.

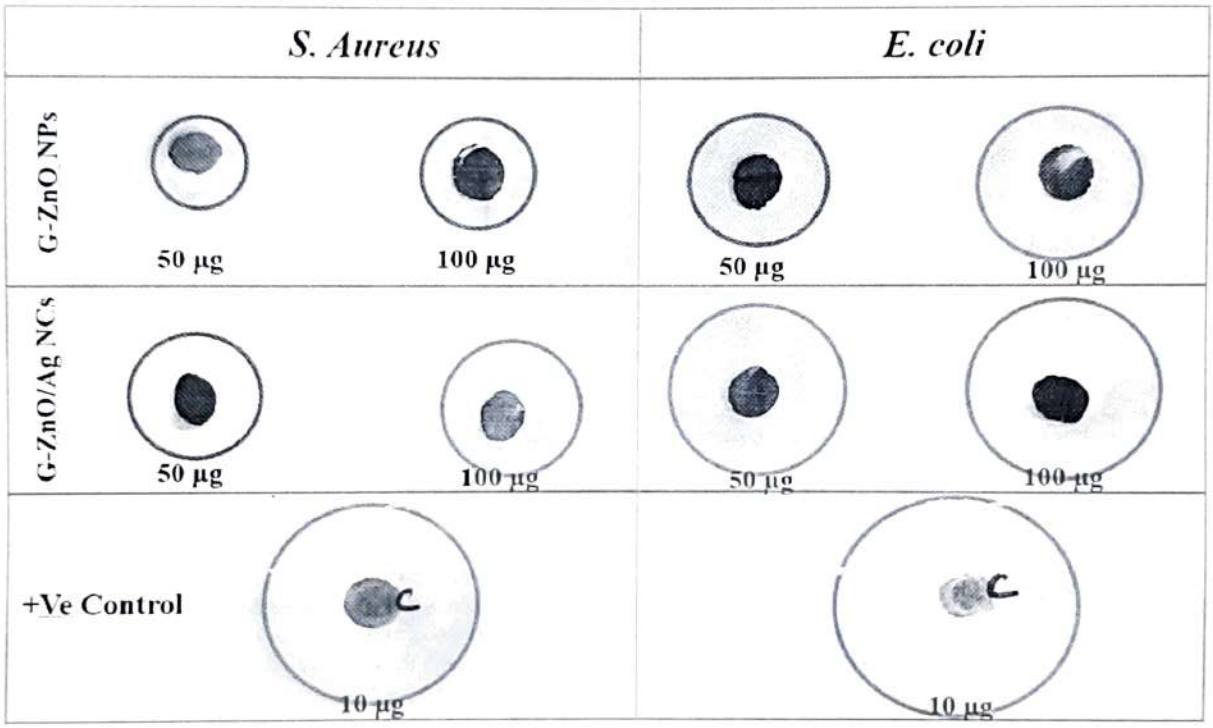


Figure 7. Zone of inhibition observed of *S. aureus* and *E. coli* bacterial strains caused by G-ZnO NPs and G-ZnO/Ag NCs.

important features for practical applications. In addition, the resulting ZnO/Ag nanocomposite demonstrated significant antimicrobial and cytotoxic effects against both gram-positive (*S. aureus*), gram-negative (*E. coli*) bacterial strains and A549 cancer cell line. This remarkable photocatalytic and biological activities was related to the homogenous distribution and synergistic interaction between G–Ag and G-ZnO NPs. Therefore, this work provides a new greener way for in situ synthesizing the photocatalyst and their applications in environmental purification and nano biomedical applications.

© 2021 Wiley-VCH GmbH

P.G.P. COLLEGE OF ARTS & SCIENCE
NAMAKKAL
637 206

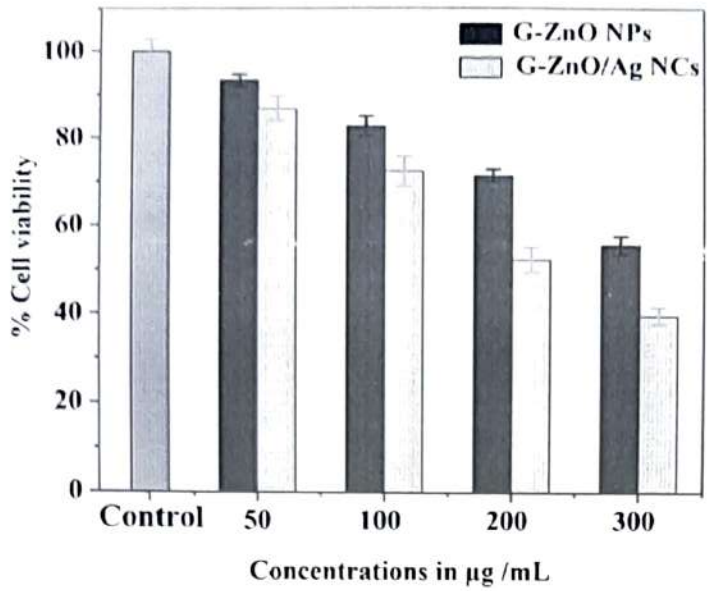


Figure 8. Cell viability analysis of G-ZnO NPs and G-ZnO/Ag NCs against A549 cell lines.

Supporting Information Summary

Experimental and characterization details are given in the Supporting Information.

Conflict of Interest

The authors declare no conflict of interest.

Keywords: Green reduction · G-ZnO/Ag NCs · Photocatalysis · Biological activity

[1] M. M. Khin, A. S. Nair, V. J. Babu, R. Murugan, S. Ramakrishna, *Energy Environ. Sci.* **2012**, *5*, 8075–8109.
[2] N. Talebian, S. M. Amininezhad, M. Doudi, *J. Photochem. Photobiol. B* **2013**, *120*, 66–73.
[3] H. Lu, J. Wang, M. Stoller, T. Wang, Y. Bao, H. Hao, *Adv. Mater. Sci. Eng.* **2016**, 1–10.
[4] J. Jiang, J. Pi, J. Cai, *Bioinorg. Chem. Appl.* **2018**, 1–18.
[5] H. Mirzaei, M. Darroudi, *Ceram. Int.* **2017**, *43*, 907–914.
[6] V. Safarifard, A. Morsali, *Ultrason. Sonochem.* **2018**, *40*, 921–928.
[7] X.-W. Yan, M. Johanian, M. Naghiloo, R. Rasuli, M.-L. Hu, A. Morsali, *Mater. Lett.* **2019**, *252*, 325–328.
[8] X. Zhang, E. M. Hicks, J. Zhao, G. C. Schatz, R. P. Van Duyne, *Nano Lett.* **2005**, *5*, 1503–1507.
[9] G. A. Sotiriou, S. E. Pratsinis, *Curr. Opin. Chem. Eng.* **2011**, *1*, 3–10.
[10] C. H. Xue, J. Chen, W. Yin, S. T. Jia, J. Z. Ma, *Appl. Surf. Sci.* **2012**, *258*, 2408–2414.
[11] X. Y. Dong, Z. W. Gao, K. F. Yang, W. Q. Zhang, L. W. Xu, *Catal. Sci. Technol.* **2015**, *5*, 2554–2560.
[12] P. Lu, W. Zhou, Y. Li, J. Wang, P. Wu, *Appl. Surf. Sci.* **2017**, *399*, 396–402.
[13] J. Gajendiran, V. Rajendran, *Mater. Lett.* **2014**, *116*, 311–313.
[14] J. Zhang, R. Tu, T. Goto, *J. Eur. Ceram. Soc.* **2014**, *34*, 435–441.
[15] R. Saravanan, S. Karthikeyan, V. K. Gupta, G. Sekaran, V. Narayanan, A. Stephen, *Mater. Sci. Eng. C* **2013**, *33*, 91–98.
[16] S. Das, V. C. Srivastava, *Mater. Sci. Semicond. Process.* **2017**, *57*, 173–177.
[17] A. Hasanpour, M. Niyaifar, M. Asan, J. Amighian, *J. Magn. Magn. Mater.* **2013**, *334*, 41–44.
[18] K. Kaviyarasu, C. Maria Magdalane, K. Anand, E. Manikandan, M. Maaza, *Spectrochim. Acta Part A* **2015**, *142*, 405–409.
[19] P. Sathishkumar, R. Sweena, J. J. Wu, S. Anandan, *Chem. Eng. J.* **2011**, *171*, 136–140.
[20] B. Baruwati, V. Polshettiwar, R. S. Varma, *Green Chem.* **2009**, *11*, 926–930.
[21] Y. Y. Dong, S. Liu, Y. J. Liu, L. Y. Meng, M. G. Ma, *J. Mater. Sci.* **2017**, *52*, 8219–8230.
[22] P. D. Ramesh, K. J. Rao, B. Vaidhyanathan, M. Ganguli, *J. Mater. Res.* **1994**, *9*, 3025–3027.
[23] R. S. Varma, *Curr. Opin. Chem. Eng.* **2012**, *1*, 123–128.
[24] H. Duan, D. Wang, Y. Li, *Chem. Soc. Rev.* **2015**, *44*, 5778–5792.
[25] S. Iravani, *Green Chem.* **2011**, *13*, 2638–2650.
[26] D. Hebbalalu, J. Lalley, M. N. Nadagouda, R. S. Varma, *ACS Sustainable Chem. Eng.* **2013**, *1*, 703–712.
[27] M. N. Nadagouda, N. Iyanna, J. Lalley, C. Han, D. D. Dionysiou, R. S. Varma, *in ACS Sustainable Chem. Eng.* **2014**, *2*, 1717–1723.
[28] M. N. Nadagouda, R. S. Varma, *Green Chem.* **2008**, *10*, 859–862.
[29] J. Kou, R. S. Varma, *RSC Adv.* **2012**, *2*, 10283–10290.
[30] J. Kou, R. S. Varma, *ChemSusChem* **2012**, *5*, 2435–2441.
[31] M. Shojaei Yeganeh, A. R. Kazemizadeh, A. Ramazani, P. Eskandari, H. Rabbi Angourani, *Mater. Res. Express* **2020**, *6*, 1250f4.
[32] B. Baruwati, R. S. Varma, *ChemSusChem.* **2009**, *2*, 1041–1044.
[33] B. Eskandari Azar, A. Ramazani, S. Taghavi Fardood, A. Morsali, *Optik (Stuttg)* **2020**, *208*, 164129.
[34] F. Moradnia, S. Taghavi Fardood, A. Ramazani, V. K. Gupta, *J. Photochem. Photobiol. A* **2020**, *392*, 112433.
[35] S. Taghavi Fardood, R. Forootan, F. Moradnia, Z. Afshari, A. Ramazani, *Mater. Res. Express* **2020**, *7*, 015086.
[36] K. Atrak, A. Ramazani, S. Taghavi Fardood, *J. Photochem. Photobiol. A* **2019**, *382*, 111942.
[37] M. Zare, K. Namratha, S. Alghamdi, Y. H. E. Mohammad, A. Hezam, M. Zare, Q. A. Drmosh, K. Byrappa, B. N. Chandrashekar, S. Ramakrishna, X. Zhang, *Sci. Rep.* **2019**, *9*, 8303.
[38] M. Khatami, R. S. Varma, N. Zafarnia, H. Yaghoobi, M. Sarani, V. G. Kumar, *Sustain. Chem. Pharm.* **2018**, *10*, 9–15.
[39] P. Panchal, D. R. Paul, A. Sharma, P. Choudhary, P. Meena, S. P. Nehra, *J. Colloid Interface Sci.* **2020**, *563*, 370–380.
[40] M. Sorbiun, E. Shayegan Mehr, A. Ramazani, S. Taghavi Fardood, *J. Mater. Sci. Mater. Electron.* **2018**, *29*, 2806–2814.

P.G.P. COLLEGE OF ARTS & SCIENCE NAMAKKAL 637 206

© 2021 Wiley-VCH GmbH

[41] S. Kaviya, E. Prasad, *RSC Adv.* **2015**, *5*, 25532–25532.
[42] S. Sohrabnezhad, A. Seifi, *Appl. Surf. Sci.* **2016**, *386*, 33–40.
[43] Z. Noohpisheh, H. Amiri, S. Farhadi, A. Mohammadi-gholami, *Spectrochim. Acta Part A* **2020**, *240*, 118595.
[44] R. Vijay, D. Lenin Singaravelu, A. Vinod, M. R. Sanjay, S. Siengchin, M. Jawaid, A. Khan, J. Parameswaranpillai, *Int. J. Biol. Macromol.* **2019**, *125*, 99–108.
[45] S. Christudas, T. M. Kulathivel, P. Agastian, *Asian Pac. J. Trop. Med.* **2012**, *2*, S159-S161.
[46] J. D. Habila, I. A. Bello, A. A. Dzikwi, H. Musa, N. Abubakar, *African J. Pharm. Pharmacol.* **2010**, *4*, 123–126.
[47] V. Vinoth Prabhu, G. Nalini, N. Chidambaranathan, S. Sudarshan Kisan, *Int. J. Pharm. Pharm. Sci.* **2011**, *3*, 126–30.
[48] A. Jindal, P. Kumar, *Nat. Prod. Res.* **2012**, *26*, 2072–2077.
[49] S. Azizi, R. Mohamad, R. A. Rahim, A. B. Moghaddam, M. Moniri, A. Ariff, W. Z. Saad, F. Namvab, *Appl. Surf. Sci.* **2016**, *384*, 517–524.
[50] Y. Cheng, L. An, J. Lan, F. Gao, R. Tan, X. M. Li, G. H. Wang, *Mater. Res. Bull.* **2013**, *18*, 4287–4293.
[51] S. Shanavas, A. Priyadharsan, V. Vasanthakumar, A. Arunkumar, P. M. Anbarasan, S. Bharathkumar, *J. Photochem. Photobiol. A* **2017**, *340*, 96–108.
[52] A. Malathi, V. Vasanthakumar, P. Arunachalam, J. Madhavan, M. A. Ghanem, *J. Colloid Interface Sci.* **2017**, *506*, 553–563.
[53] V. Vasanthakumar, A. Priyadharsan, P. M. Anbarasan, S. Muthumari, S. Subramanian, V. Raj, *ChemistrySelect* **2017**, *2*, 9501–9510.
[54] P. V. Pimpliskar, S. C. Motekar, G. G. Umarji, W. Lee, S. S. Arbuj, *Photochem. Photobiol. Sci.* **2019**, *18*, 1503–1511.
[55] G. E. Brown, V. E. Henrich, W. H. Casey, D. L. Clark, C. Eggleston, A. Felmy, D. W. Goodman, M. Grätzel, G. Maciel, M. I. McCarthy, K. H. Nealson, D. A. Sverjensky, M. F. Toney, J. M. Zachara, *Chem. Rev.* **1999**, *99*, 77–174.
[56] V. Lakshmi Prasanna, R. Vijayaraghavan, *Langmuir* **2015**, *31*, 9155–9162.
[57] Y. Li, W. Zhang, J. Niu, Y. Chen, *ACS Nano* **2012**, *6*, 5164–5173.
[58] V. Vasanthakumar, A. Saranya, A. Raja, S. Prakash, V. Anbarasu, P. Priya, V. Raj, *RSC Adv.* **2016**, *6*, 54904–54917.

Submitted: February 2, 2021
Accepted: April 19, 2021

© 2021 Wiley-VCH GmbH

PRINCIPAL
PGP College of Arts and Science
Namakkal.
COLLEGE OF ARTS & SCIENCE NAMAKKAL 637 206

Synthesis, Cytotoxicity, and DNA cleavage interaction of (2E, NZ)-N, 2-bis ((E)-3-((1, 5-dimethyl-3-oxo-2-phenyl-2, 3-dihydro-1H-pyrazol-4-yl) imino) indolin-2-ylidene) hydrazinecarbothioamide ligand

D. Dhivya priya[1*] and Dr P. Maheswaran[2]

[1]Department of chemistry, PGP College of Arts and Science, Namakkal-637207

[2]Principal & Head, PGP College of Arts and Science, Namakkal-637207, India

[1]E-mail: dhivyapriyachem@gmail.com, [2]E-mail: pm_omk@ yahoo.co.in

Abstract

A series of mononuclear Schiff base metal complexes of Cu(II), Co(II) and Mn(II) have been synthesized with Schiff base derived from Isatin, Thiosemicarbazide and 4-aminoantipyrine. The binding manner of the ligand to the metal, composition and geometry of the metal complexes were examined by various physicochemical methods like elemental analysis, conductivity measurements, magnetic moments, IR, 1H-NMR, CV, P-XRD, ESR and electronic spectral studies. The molar conductance value of metal complexes in DMF indicates the electrolytic in nature. In IR spectra, the comparison of shift in frequency of the complexes with the ligand reveals the coordination of donor atoms to the metal atom. The formation of ligand was also ascertained by 1H NMR spectra. The electronic spectra and ESR measurements show that Cu(II), Co(II) and Mn(II) complexes has octahedral geometry. The grain size of the complexes is calculated by Scherrer's formula using powder XRD. The Schiff bases and their complexes have been screened for their in vitro antibacterial (staphylococcus aureus, bacillus subtilis, Eschericia coli and Klebsilla pneumonia) activity by paper disc method, it result confirms the mononuclear complexes are more potent than free ligands. The complexes exhibit a remarkable DNA cleavage activity with CT-DNA in the presence of hydroxyl radical. Further, an in vitro cytotoxicity study of the complexes exhibited anticancer activity against the human breast cancer (MCF7) cell lines.

Keywords: Isatin, ThioSemicarbazide, 4-aminoantipyrine, Antibacterial, DNA cleavage and Cytotoxicity

1. Introduction

Coordination of organic compound with metal, i.e., chelation causes drastic change in the biological property of the ligand and also the metal moiety [1-3]. Metal chelate complexes have continued to play the role of one of the most important stereochemical models in main group and transition metal coordination chemistry due to their preparative accessibility, diversity and structural variability [4]. Recently much interest has been shown in isatin and its derivatives. Isatin is a synthetically flexible substrate and an important pharmacophore responsible for the synthesis of efficient chemotherapeutic agents and biological activity [5-6].Thiosemicarbazones drags the attention of researchers because of their unusual coordination modes, good chelating property and pharmacological properties such as antibacterial, antifungal, antihypertensive, antineoplastic, hypnotic and anticonvulsant [7-10]. The biological experiments demonstrated that DNA is the primary intracellular target of anticancer drugs due to the interaction among small molecules and DNA, which can cause damage to DNA in cancer cells, blocking the division of cancer cells and resulting in cell death (Xu et al. 2008). The outstanding criteria for the development of metallo-drugs as chemotherapeutic agents are the ability of the metallo-drug to provoke DNA cleavage.

In view of these finding, this piece of work has devoted with the aim to synthesize some transition metals complexes with Schiff base ligand using Isatin,

P.G.P. COLLEGE OF ARTS & SCIENCE NAMAKKAL 637 206

thiosemicarbazone and 4-Amino antipyrine and to examine their physical properties involving spectral behaviors, the electrical conductance values and to determine the efficiency of the synthesized complexes against pathogenic bacteria, cytotoxic and DNA cleavage.

2. Experimental Methods

All the reagents and solvents were purchased from commercial sources (Aldrich) and used as received. C, H and N contents were determined by Perkin Elmer CHN2400 elemental analyzer. Infrared spectra were recorded on the Perkin Elmer FT-IR 8300 model spectrometer using KBr disc in the range of 4000-400cm-1. Electronic spectra were recorded at 300K on a Perkin-Elmer Lambda 40(UV-Vis) spectrometer using DMF in the range 200-800nm. The molar conductance of the complexes in DMF (10-3) solution was measured at 27±3°C with an Elico model conductivity meter. EPR spectra of compounds were recorded on a Brucker model EMX plus, X-band spectrometer (9.86 GHz) with 100 KHZ modulation frequency. Magnetic susceptibility measurements were carried out by employing the Gouy method at room temperature. NMR signals were obtained from Bruker Advance III, 400MHz model spectrometer. The Redox nature of the complex in DMF was measured using CHI -760 Electrochemical Analyzer by employing a platinum electrode as working electrode, Ag/AgCl as a reference electrode and platinum wire as auxiliary electrode.

2.1. Synthesis of Schiff base ligand

The Schiff base ligand was synthesized by adding thiosemicarbazide (1 mmole) in 20 ml of ethanol and isatin (2 mmole) in 20 ml ethanol slowly with constant stirring followed by the addition of 4- aminoantipyrine (2 mmole). The mixture was then refluxed for 2 hrs. The solution was kept for slow evaporation and colored precipitate was collected. The precipitate was washed with ethanol and then dried in air. Figure 1 shows the preparation of Schiff base ligand.

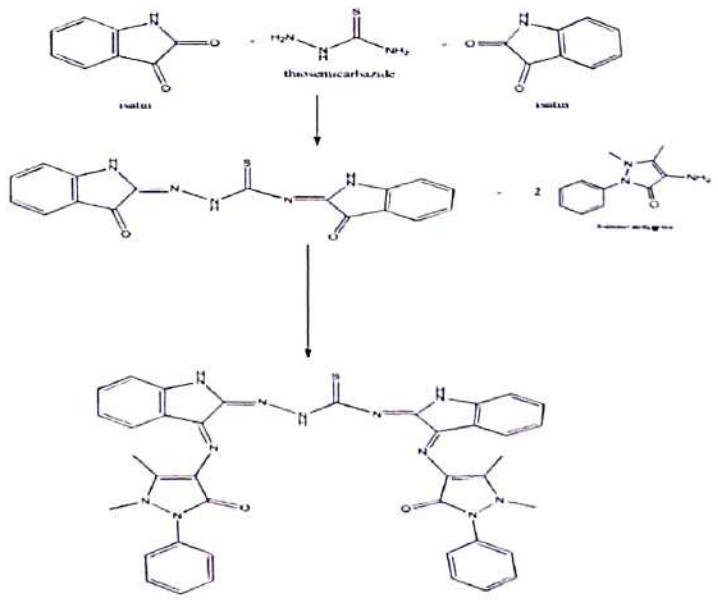


Fig. 1: Synthesis of Schiff base ligand

P.G.P. COLLEGE OF ARTS & SCIENCE NAMAKKAL 637 206

3.1. Molar Conductivity

The nature and stability of the complexes are determined by using molar conductivity studies. The molar Conductance of the synthesized complexes was measured in DMF solution with 10^{-3}M concentration. All the complexes show molar conductance value in the range 65-70 mho cm^2 mol^{-1} which suggest that the complexes are electrolytic in nature.

3.2. IR Spectra

The important IR spectral data of the ligand were compared with those of the metal complexes in order to confirm the binding mode of the Schiff base ligand to metal atom in the complexes. The IR spectra for ligand and complexes are shown in Figure 3 & 4. A sharp band at 1621 cm^{-1} corresponds to the azomethine υ(C=N) frequency of the free ligand which has been shifted towards lower region at around 10-20 cm^{-1} in the complexes indicating the participation of the azomethine group in the complexes formation [11]. The strong band appears at 1132 cm^{-1} for ν(C=S) indicated C=S bond was present in the Schiff base ligand [12]. The observed IR-absorption bands at 3424 and 3264 cm^{-1} due to ^{a}N-H and ^{b}N-H respectively in the free Schiff base ligand [13]. It showed broad band around 1700 cm^{-1} which are attributed to the υ(C=O) of antipyrine system in case of ligand. Upon complexation, υ(C=O) of the antipyrine molecule has shifted to higher frequency region suggesting that carbonyl group is coordinated to the metal ion [14]. The complex formation was further evidenced by the appearance of non-ligand band in the complexes around 543–602 cm^{-1} assigned as υ(M–O) [15] bands and region around 464–494 cm^{-1} are due to υ(M-N) [16] respectively.

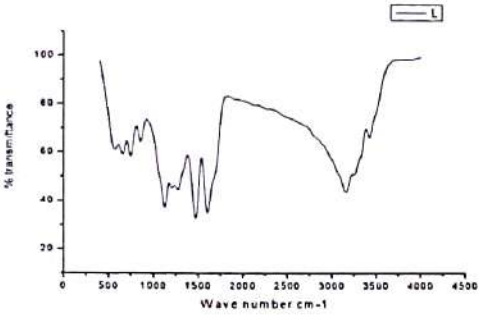


Fig. 3: IR Spectra for Ligand

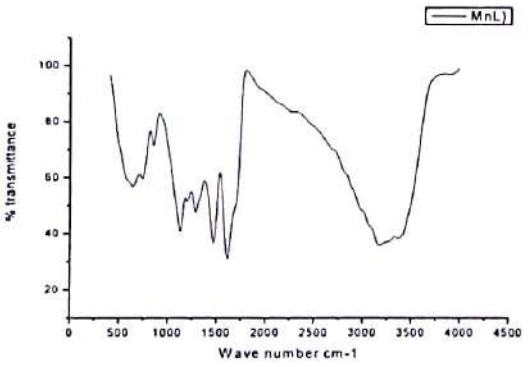


Fig. 4: IR Spectra for Mn (II) complexes

P.G. COLLEGE OF ARTS & SCIENCE NAMAKKAL 637 206

2.2. Synthesis of mononuclear Schiff base metal complexes

An ethanolic solution of the metal salts [Cu(II),Co(II) and Mn(II)] was added gradually to the ethanolic solution of the deprotonated ligand in the molar ratio 1:1. The reaction mixture was stirred for 30 min and then heated to reflux for 2 hr. The settled precipitate was filtered off, washed with ethanol then ether. The preparation of metal complexes is shown in Figure 2.

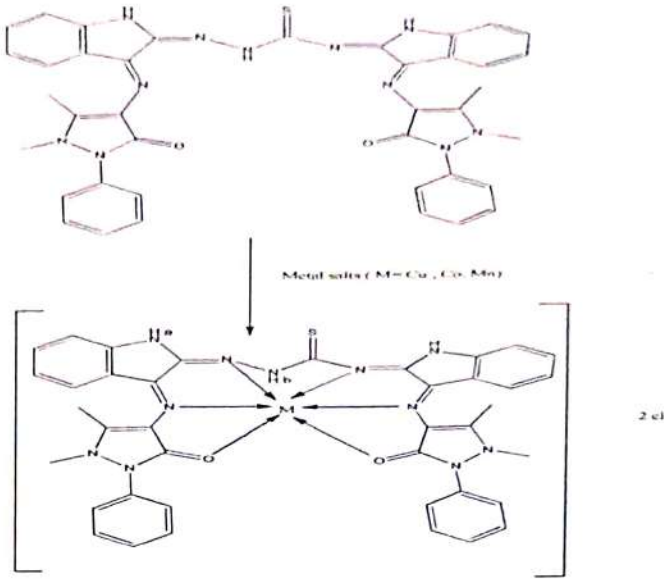


Fig. 2: Synthesis of Schiff base complexes

3. Result and Discussion

Analytical data of the Schiff base ligand and their metal complexes are given in Table.1 and are in well agreement with the expected values. All the Cu(II), Co(II) and Mn(II) complexes are colored non hygroscopic solids, stable in air. They are sparingly soluble in common organic solvents, but soluble in DMF and DMSO.

Table 1. Analytical data of the Schiff base ligand and complexes

Compounds	Molecular Formula	Yield	color	Calculated (found)%					
				C	H	N	O	S	M
Ligand	$C_{39}H_{33}N_{11}O_2S$	80	Light brown	(65.07) 65.09	(4.62) 4.58	(21.40) 21.41	(4.45) 4.45	(4.45) 4.45	-
Cu complex	$C_{39}H_{33}CuN_{11}O_2S$	75	Light brown	(59.80) 59.77	(4.25) 4.21	(19.67) 19.66	(4.08) 4.08	(4.09) 4.08	(8.11) 8.11
Co complex	$C_{39}H_{33}CoN_{11}O_2S$	70	black	(60.15) 60.15	(4.27) 4.24	(19.78) 19.79	(4.11) 4.11	(4.12) 4.11	7.57 (7.57)
Mn complex	$C_{39}H_{33}MnN_{11}O_2S$	72	Dark brown	(60.46) 60.40	(4.29) 4.25	(19.89) 19.87	(4.13) 4.12	(4.14) 4.13	(7.09) 7.08

P.G.P. COLLEGE OF ARTS & SCIENCE NAMAKKAL 637 206

3.3. Electronic and Magnetic moment

The electronic absorption spectra of the metal complexes were recorded in freshly prepared solution in DMF at room temperature and spectrum for metal complexes shown in Figure 5. In the spectra of the Schiff base ligand, the absorption band observed at 260 nm were assigned to $\pi \rightarrow \pi^*$ transition and the band at 370 nm were assigned due to $n \rightarrow \pi^*$ transition associated with the azomethine chromophore (-C=N) [17]. The electronic spectra of copper complex display the d–d transition bands in the region 630 nm, which are due to $^2E_g \rightarrow {}^2T_2g$ transition. This d–d transition band strongly favors an octahedral geometry around the metal ion [18]. The Cu (II) complex showed magnetic moment 1.76 BM is slightly higher than the spin-only value 1.73 BM expected for one unpaired electron, which offers possibility of an octahedral geometry [19]. The electronic spectra of the Co(II) complex showed two bands observed at 570 nm and 652 nm which may be assigned to ^4T_1g (F) $\rightarrow$ ^4A_2g (F) and ^4T_1g (F) $\rightarrow$ ^4T_2g (F) transitions of an octahedral geometry [20] which further supported by effective magnetic values 4.77 B.M. The Mn(II) complexes shows magnetic moment value 5.7 B.M supports octahedral geometry and further confirmed by electronic spectra which shows three transitions corresponding to $^6A_1g \rightarrow {}^4T_1g$ (680 nm), $^6A_1g \rightarrow {}^4T_2g$ (570 nm), and $^6A_1g \rightarrow {}^4A_1g$ (520 nm) in increasing order of energy [21].

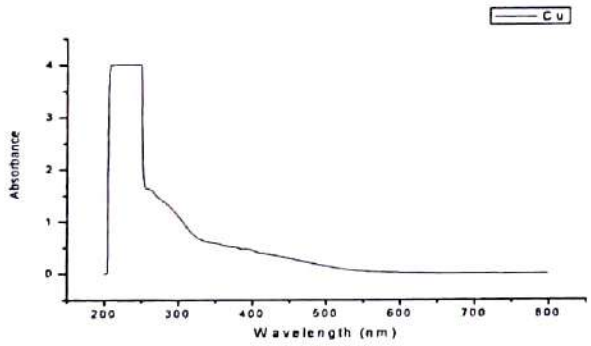


Fig. 5: UV Spectra of Cu (II) complexes

3.4. ^{1}H NMR Spectra

The ^{1}H NMR spectra was recorded in DMSO at room temperature. The peak appearing around 10.2-11.4 ppm is due to the presence of the ring (–NH) of isatin [14] and thiosemicarbazide moiety [22]. The ligand also shows the following signals around 2.7–2.9 ppm ($-CH_3$) and 3.6–4.1 ppm ($N-CH_3$) for methyl proton [23]. The peak resonating around 6–8 ppm in ligand are attributed to the aromatic proton respectively.

3.5. ESR Studies

The ESR spectrum of Cu(II) complex provides information about the geometry and nature of the ligating sites of the Schiff base and the metal. The spectrum of copper (II) complex is shown in Figure 6. The Cu(II) complex shows the $g\|$ 2.15, $g^{\perp}$ 2.02 and gave 2.080. The tendency $g\| > g^{\perp} > 2.002$ observed in Cu(II) complex under study shows that the unpaired electron is localized in the $dx^2–y^2$ orbital of the Cu(II) ion. Consequently, the EPR value supports octahedral geometry for the Cu(II) complex [24].

T.G.P. COLLEGE OF ARTS & SCIENCE NAMAKKAL 637 209

Fig. 6: Spectra of Cu (II) complexes

3.6. Electrochemical Studies

The redox behaviour of metal complexes is studied by cyclic voltammogram in DMF using 0.1 M Tetrabutylammonium perchlorate (TBAP) as supporting electrolyte. The electrochemical data obtained at a glassy carbon electrode in DMF solution are recorded and voltammogram are shown in Figure 7. The cyclic voltammogram of the metal complexes contains two peaks mainly due to oxidative nature of organic molecule and reductive nature of azomethine group.

The Copper complex shows cathodic peak of 1.7 V indicates the one electron reduction of Cu(II)→Cu(I) process and the anodic peak of 0.6 V indicates the oxidation process of Cu(I)→Cu(II) [25,26]. The non-equivalent current intensity of cathodic and anodic peaks (ic/ia = 0.6 V) indicates a quasi-reversible behavior [27, 28]. The cobalt complex exhibit one electron quasi reversible transfer process with a peaks at Epa =0.6 V, Epc =1.4 V which gives evidence for quasi reversible Co(II)/ Co(I) couple. The one electron cyclic response for Manganese complex were observed at Epc =1.4 V and Epa = 0.5 V. This corresponds to Mn(II)/ Mn(I) [29].

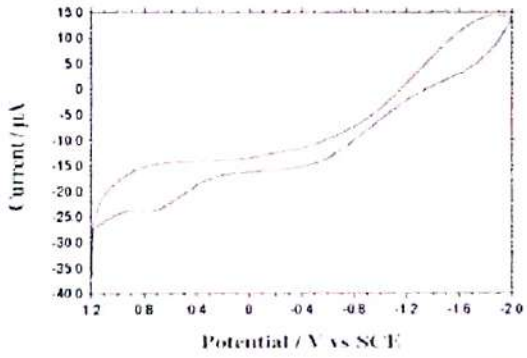


Fig. 7: Cyclic voltammogram of Co(II) complex

3.7. Powder XRD

In the absence of single crystal, X-ray powder data are especially useful to deduce accurate cell parameters. In X-ray diffractogram of the complexes, major refluxes were recorded in the range 10° to 80° 2θ value. The diffraction pattern reveals about the crystalline nature of the complex. The crystallite size (d_{XRD}) of the complexes was calculated using Scherer's formula [30]. The average grain size values for complexes nearly 2.3-2.9 nm which support that the nanocrystalline nature of metal complexes.

P.G.P. COLLEGE OF ARTS & SCIENCE NAMAKKAL 637 206

3.8. Antimicrobial activity

The screening effect of the free Schiff base ligand and their metal complexes was studied by agar well-diffusion method against four bacteria (S. aureus, B.Subtilis, K.Pneumonia and E.Coli) with standard drug. The Figure 8 shows the activity of Schiff base ligand and metal chelates. It has been found out that the activity of metal complexes against bacteria were more potent than their respective ligands. The activity of complexes against pathogens indicated that the complexation to metal enhance the activity of the ligand. The reason of the enhancement of activity of metal complexes is chelation and partial sharing of its positive charge with the donor groups [31]. From the results, it shows that Cu (II) complexes show higher activity and other complexes shows moderate activity as compared to standard bactericide.

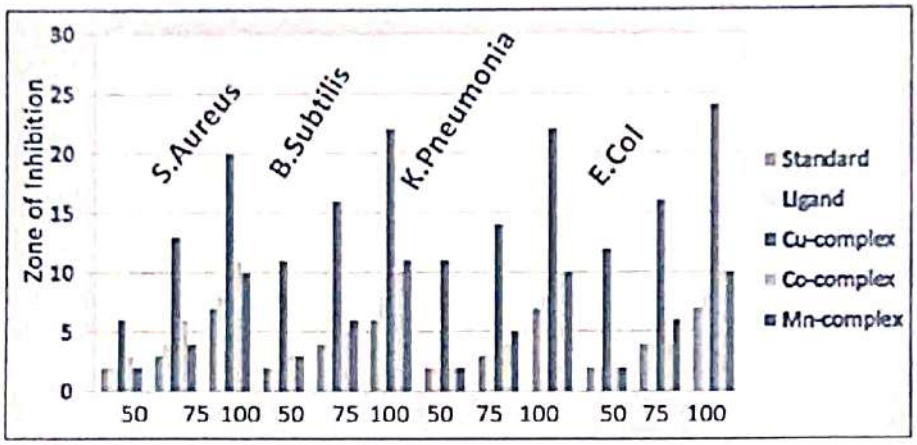
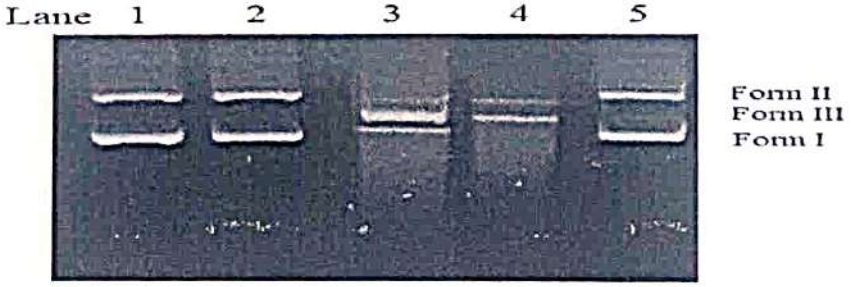


Fig. 8: Antibacterial activity of Schiff base and its metal complexes

3.9. DNA Cleavage

The cleavage activity of complexes has been assessed by their ability to convert super coiled pUC18 DNA from Form I to Form II and Form III by gel electrophoresis. **Figure 9** shows the cleavage pattern of pUC18 DNA. From figure it is evident that the DNA was cleaved by copper complexes more effectively in the presence of oxidant which may be due to hydroxyl radical (OH•) reaction with DNA. This is consistent with the increased production of hydroxyl radicals by cuprous ions similar to the well-known Fenton reaction. The DNA cleavage efficiency of the complexes was due to the different binding affinity of the complex to DNA [32]. From this study, we can come to the conclusion that all the newly synthesize compound are good inhibitors of pathogenic microorganisms, which is evident from the observation on the DNA cleavage.



P.G.P. COLLEGE OF ARTS & SCIENCE
NAMAKKAL
637 206

Fig. 9: Changes in the agarose gel electrophoretic pattern of pUC18DNA induced by H_2O_2 and metal complexes

4. Cytotoxic activity

The anticancer activity of the synthesized compounds was inspected by treating it with MCF-7cell line (human breast cancer cell) and read at 570 nm using a photometer by applying MTT assay. The results were expressed with IC_{50} values in the concentration range of 2.5 - 100 µg/mL and compared with standard anticancer drug. The **Figure 10** shows the inhibiting activity of Schiff complexes. On comparing with standard drug it shows that the highest level of cytotoxic activity was observed in Cu(II) complex. The IC_{50} values of remaining compounds shows moderate activity against MCF7 cell lines without causing significant damage to the normal cells [33, 34]. From the results, it confirms that these complexes have beneficial features for potential anticancer agents.

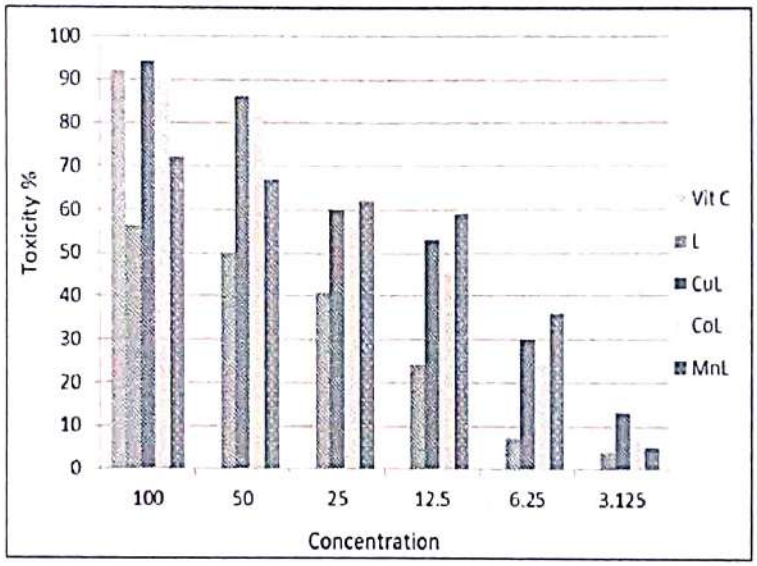


Fig. 10: Cytotoxic activity of metal complexes

5. Conclusion

The design and synthesis of mononuclear Cu(II), Co(II) and Mn(II) Schiff base complexes have been demonstrated in this report. The present study revealed octahedral geometry around Cu(II), Co(II) and Mn(II) complexes, in which the coordinating through nitrogen and oxygen atoms. The results of antimicrobial activity shows that the metal chelates exhibit more inhibitory effects than the parent ligand. DNA cleavage studies show that all the complexes significantly cleaves DNA molecule. Furthermore, the cytotoxicity results concerned that Cu(II) complexes has been more effective against MCF7 cell line without affecting momentous destruction to the normal cells than Schiff base ligand and Co (II), Mn(II) complexes.

References

[1] S. Chandra, L K. Gupta, EPR, mass, IR, electronic, and magnetic studies on copper(II) complexes of semicarbazones and thiosemicarbazones. *Spectrochim. Acta Part A*, 61 (1–2) (2005), pp. 269-275

[2] B. Macías, I. García, M V. Villa, J. Borrás, M. Gonzalez-Álvarez, A. Castiñeiras. Oxidative DNA damage of mixed copper(II) complexes with sulfonamides and 1,10-phenanthroline. Crystal structure of [Cu(N-quinolin-8-yl-p-toluenesulfonamidate)2(1,10-phenanthroline)] *J. Inorg. Biochem.*, 96(2-3) (2003), p. 367-374

[3] R J R. Sorenson (Ed.), Biology of Copper Complexes, Human Press, Clifton, NJ (1987)

[4] Garnovskii, A A., Nivorozhkin, A L., Minkin, V I. Ligand environment and the structure of Schiff base adducts and tetra coordinated metal-chelates. *Coordination Chemistry Reviews* 126 (1993) 1

P.G.P. COLLEGE OF ARTS & SCIENCE NAMAKKAL 637 206

[5] Abdel-Rahman LH, Abu-Dief AM, Mostafa H, Hamdan SK. Ni (II) and Cu (II) complexes with ONNO asymmetric tetradentate Schiff base ligand: Synthesis, spectroscopic characterization, theoretical calculations, DNA interaction and antimicrobial studies. *Appl Organomet Chem* (2017). 31 e3555
[6] Abdel-Rahman LH, Abu-Dief AM, Adam MSS, Hamdan SK. Some new nano-sized mononuclear Cu (II) Schiff base complexes: Design, characterization, molecular modeling and catalytic potentials in benzyl alcohol oxidation. *Catalysis Letters* (2016). 146(8) 1373-96
[7] West DX, Liberta AE, Padhye SB, Chikate RC, Sonawane PB, et al. Thiosemicarbazone complexes of copper(II): structural and biological studies. *Coordination Chemistry Reviews* (1993) Feb, 123(1-2) 49–71
[8] H Beraldo BSP, D Gambinob BSP. The Wide Pharmacological Versatility of Semicarbazones, Thiosemicarbazones and Their Metal Complexes. *Mini-Reviews in Medicinal Chemistry* 2004) Jan 1, 4(1) 31–9
[9] Sridhar SK, Pandeya SN, Stables JP, Ramesh A. Anticonvulsant activity of hydrazones, Schiff and Mannich bases of isatin derivatives. *European Journal of Pharmaceutical Sciences* (2002) Aug, 16(3) 129–32
[10] Yogeeswari P, Ragavendran JV, Sriram D, Nageswari Y, Kavya R, Sreevatsan N, et al. Discovery of 4-Aminobutyric Acid Derivatives Possessing Anticonvulsant and Antinociceptive Activities: A Hybrid Pharmacophore Approach. *Journal of Medicinal Chemistry* (2007) May, 50(10) 2459–67
[11] Hassan Keypour, Parisa Arzhangi, Nasibeh Rahpeyma, Majid Rezaeivala, etal., Synthesis and characterization of Ni(II), Cu(II) and Zn(II) complexes with new macrocyclic Schiff base ligands containing piperazine moiety, *J. Mol. Str.*, (2010), 977,6–11
[12] Moamen S. Refat, H. K. Ibrahim, S. Z. A. Sowellim, M. H. Soliman, E. M. Saeed. Spectroscopic and Thermal Studies of Mn(II), Fe(III), Cr(III) and Zn(II) Complexes Derived from the Ligand Resulted by the Reaction Between 4-Acetyl Pyridine and Thiosemicarbazide. Springer, *J Inorg Organomet Polym*, (2009), 19: 521–531
[13] Md. Saddam Hossain, Shudeepta Sarker, A. S. M. Elias Shaheed, etal., Thermal and Spectral Characterization of Cr(III), Co(II) and Cd(II) Metal Complexes Containing Bis-Imine Novel Schiff Base Ligand Towards Potential Biological Application. *Chemical and Biomolecular Engineering. (2017).* 2(1): 41-50
[14] Gurunath S. Kurdekar, M. P. Sathisha, Srinivasa Budagumpi, etal., 4-Aminoantipyrine-based Schiff-base transition metal complexes as potent anticonvulsant agents, *Med Chem Res* (2012) 21:2273–2279
[15] Ahmed Jasim M. Al-Karawi, Synthesis and characterization of a new N2S2 Schiff base ligand and its complexes with nickel(II), copper(II) and cadmium(II) including the kinetics of complex formation. *Springer. Transition Met Chem.* (2009), 34: 891–897
[16] K. Natamato, (1970) IR spectra of Inorganic and coordination compounds, John wiley, New York
[17] R Dubey, U Dubey, C Mishra, Synthesis and physicochemical characterization of some Schiff base complexes of *Trans. Met. Chem* chromium (III). *Indian J. Chem*, A, (2008), 478, 1208-1212
[18] JA Obaleye, OG Adeyemi, EA Balogun, Some metal tetracycline complexes: Synthesis, characterization and their effects against malarial parasites. *Int. J. Chem*, (2001), 11: 101-106
[19] D P. Singh, R. Kumar, V. Malik, P. Tyagi, "Synthesis and characterization of complexes of Co(II), Ni(II), Cu(II), Zn(II), and Cd(II) with macrocycle 3,4,11,12-tetraoxo-1,2,5,6,9,10,13,14-octaaza-cyclohexadeca-6,8,14,16-tetraene and their biological screening", *Transition Met Chem*, vol. 32, (2007), pp. 1051-1055.
[20] Ali Hossein Kianfara, Masomeh Bahramianb, Hamid Reza Khavasi, Synthesis, spectroscopy and thermal study of some nickel(II) complexes containing tridentate Schiff bases and substituted amine ligands, X-ray crystal structure of nickel(II) complex, *Spectrochim. Acta (A)*, (2012), 94, 302– 307.
[21] M. Nath, A. Kumar and S. Vashistha, Synthesis, Spectral and Thermal Studies of Co(II), Ni(II),Cu(II) and Zn(II) Complexes of Schiff Bases Derived from 2-Amxno-5-Aryl-1,3,4-Thiadizole, *Synth. React. Inorg Met.-Org. Chem*, (1998), 28, 893-906
[22] Mundwiler S, Candreia L, Hafliger P, etal., Preparation of NO-Carrier Added Technetium-99m Complexes via Metal-Assisted Cleavage from a Solid Phase. *Bioconjugate Chemistry* (2004) 15: 195–202
[23] J Anandakumaran, M L Sundararajan, T Jeyakumar and Mohammad Nasir Uddin, Transition Metal Complexes of 4-aminobenzenesulfonamide 1,3-benzodioxole-5-carbaldehyde: Synthesis, Characterization and Biological Activities. *ACSJ*, (2016), 22807, 11(3), 1.
[24] D. R. Lorenz, J. R. Wasson, etal., *Journal of Inorganic Chemistry*: 37 (1975) 2297
[25] A P Mishra, Neha Sharma, Rajendra K Jain, Microwave synthesis, spectral, thermal and antimicrobial studies of some Ni(II) and Cu(II) Schiff base complexes, *Advances in Quimica*, (2012) ,7,1, 77-85
[26] Esref Tas, Ahmet Kilic, Nazli Konak, Ismail Yilmaz, The sterically hindered salicylaldimine ligands with their copper(II) metal complexes: Synthesis, spectroscopy, electrochemical and thin-layer spectro electrochemical features, *Polyhedron*, (2008), 27, 1024–1032.
[27] J K Nag, D Das, S Pal and C Sinha, Synthesis and spectral characterization of homo- and hetero-dinuclear complexes with a new septadentate Schiff base ligand, *J.Chem. Sci*, (2001), 113, 1,11–20.
[28] Ahmet Kilic, Esref Tas and Ismail Yilmaz, Synthesis, spectroscopic and redox properties of the mononuclear NiII, NiII(BPh2)2 containing (B–C) bond and trinuclear CuII–NiII–CuII type-metal complexes of N,N'-(4-amino-1-benzyl piperidine)-glyoxime, *J. Chem. Sci*, (2009), 121, 1, 43–56



PRINCIPAL
PGP College of Arts and Science
Namakkal.

ScienSage

Journal of Advanced Scientific Research

Available online through http://www.sciensage.info

ISSN 0976-9595

Research Article

EVALUATION OF THE PHARMACOLOGICAL PROPERTIES OF SCHIFF BASE MIXED LIGAND Cu(II), Co(II) AND Ni(II) COMPLEXES DERIVED FROM (E)-3-((2-(1H-PYRROL-1-YL)PHENYL)IMINO)INDOLIN-2-ONE

Dhivyapriya D[1], Maheswaran P*[2]

[1]*Department of Chemistry, PGP college of Arts and Science, Namakkal, India*

[2]*PGP college of Arts and Science, Namakkal, India*

**Corresponding author: pm_omk@yahoo.co.in*

ABSTRACT

The coordination chemistry of (E)-3-((2-(1H-pyrrol-1-yl)phenyl)imino)indolin-2-one(L^1) and (E)-3-((2-(1H-benzo[d]imidazol-2-yl)phenyl)imino)indolin-2-one(L^2) has been investigated with the Cu(II), Co(II)and Ni(II)ions. The donor atoms and the plausible geometry of the complexes were examined by means of elemental analyses, molar conductance, magnetic moment, UV- Vis, IR, Far-IR and ESR spectra. The IR spectra results display the binding mode of the ligand involving azomethine nitrogen and carbonyl oxygen atoms. The electronic spectral and magnetic moment results indicate that Co(II) and Ni(II) complexes have octahedral geometry, while Cu(II) complex is distorted octahedral. The *in-vitro* biological screening effects of the investigated compounds were tested against bacterial species (*Bacillus subtilis, Salmonella typhi*) and fungal strains (*Aspergillus niger, Candida albicans*) by disc diffusion method. A comparative study of inhibition values result show that the metal complexes were found to be more active than the ligand. In addition, DNA cleavage studies for the newly prepared compounds were also studied. These studies indicate that the DNA cleavage efficacy increased in the complexes relative to the parental ligand.

Keywords: Schiff base, Isatin, 1-(2-aminophenyl)pyrrole, 2-(2-aminophenyl)benzimidazole, Antimicrobial and DNA cleavage

1. INTRODUCTION

Schiff bases provide possible sites for bio-chemically active compounds and have been studied widely over the past decade. The field of mixed ligand complexes was fast emerging account of the wide variety of potential structures for the ligands reliant upon the aldehydes and amines [1]. The Schiff base mixed-ligand complexes having N and O donor atoms are important due to their extensive antifungal, antibacterial, and anticancer activity [2]. Furthermore, mixed-ligand complexes are mostly found to be more biologically active than the ligand itself and its binary complexes [3, 4].

Isatin possess an indole ring structure, it is a flexible lead molecule common to many pharmaceuticals and heterocyclic natural products of biological interest [5]. The chemical versatility of Isatin motivated the prevalent use of this compound in biological synthesis [6]. Isatin Schiff bases were reported to exhibit a wide range of biological and pharmacological activities such as antibacterial, antifungal, antiviral, anti-HIV, anticancer, anti-tubercular, anticonvulsant, and antihelminthic activities [7-9].The interactions between Isatin Schiff base metal complexes and DNA have gained much attention due to their possible applications in cancer therapy [10-12]. From the literature survey, we find that a vast number of metal complexes because of their redox properties have been used as cleavage agents for DNA.

In view of the above facts, we report the evaluation of pharmacological properties of novel Schiff base ligand derived from the condensation of Isatin, 1-(2-aminophenyl) pyrrole, 2-(2-aminophenyl)benzimidazole and its Co(II), Ni(II) and Cu(II) complexes. The main target of the present article is to examine their antimicrobial activity and DNA cleavage of Schiff base mixed ligand complexes.

2. EXPERIMENTAL

All the reagents were Aldrich products and were used as supplied. IR spectra were recorded on Thermo Nicolet (Avatar 370 model) instrument in the range of 4000-200 cm^{-1} using KBr discs. Electronic spectra were obtained with a Perkin-Elmer Lambda 40(UV-Vis) spectrophoto-

P.G.P. COLLEGE OF ARTS & SCIENCE NAMAKKAL 637 204

-meter using DMF in the range of 200-800 nm. The molar conductance measurements were carried out at room temperature using Elico model conductivity meter. The ESR spectra of powder samples were recorded by means of E-112 ESR Spectrometer, X-band spectrometer (9.1 GHz) with 100 KHZ modulation frequency. ^{1}H NMR signals were obtained from Bruker Avance III, 400MHz model spectrometer. The Redox nature of the complex in DMF was measured using CHI-760 Electrochemical Analyzer.

2.1.Synthesis of (E)-3-((2-(1H-pyrrol-1-yl) phenyl) imino)indolin-2-one (L^1)

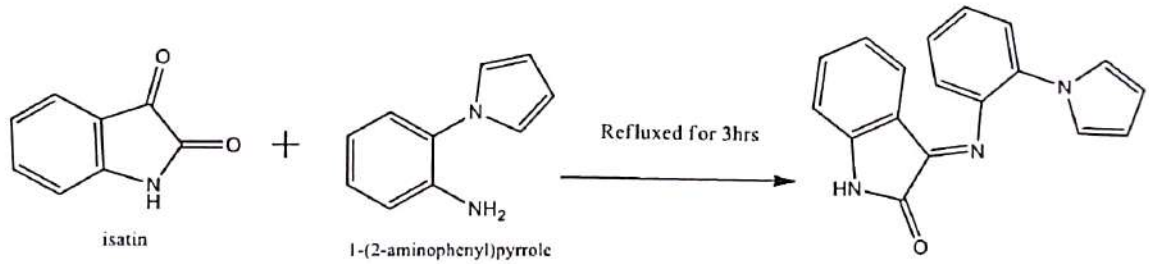
The solution of Isatin (1 mol in 20 mL methanol) was mixed in 1-(2-aminophenyl)pyrrole (1 mol in 20 mL methanol). Then this mixture was refluxed at 70°C for about 3hrs. A yellow precipitate solution was obtained which was allowed to cool at room temperature. The volume of the solvent was reduced by slow evaporation which led to the formation of a yellow solid product and product was washed with ethanol then dried in air. Schematic route for synthesis of (L^1) is given in scheme 1.

2.2.Synthesis of (E)-3-((2-(1H-benzo[d]imidazol-2-yl)phenyl)imino)indolin-2-one(L^2)

To a solution of 1H-indole-2,3-dione (1mmol) in methanol, 2-(2-aminophenyl)benzimidazole (1 mmol) in methanol, was added dropwise. The above mixture was refluxed for about 3hrs. Then the reaction mixture solvent was kept for slow evaporation and cooled at room temperature. The yellow precipitate was filtered and then washed with ethanol. Schematic route for synthesis of (L^2) is given in scheme 2.

2.3.Synthesis of Schiff base mixed ligand Metal (II) Complexes

1 mmole of metal salt in methanol (20 ml) were mixed and stirred with 1 mmole Schiff base ligand (L^1) in warm methanolic solution (20 ml) in round bottom flask followed by the addition of ligand (L^2). Resulting reaction mixture was refluxed for 3 hours on water bath. Dark coloured complex was obtained and allowed for slow evaporation. Then washed with sufficient quantity of ethanol to dryness and dried in vacuum desiccators. Schematic route for synthesis of mixed ligand complexes are shown in scheme 3.

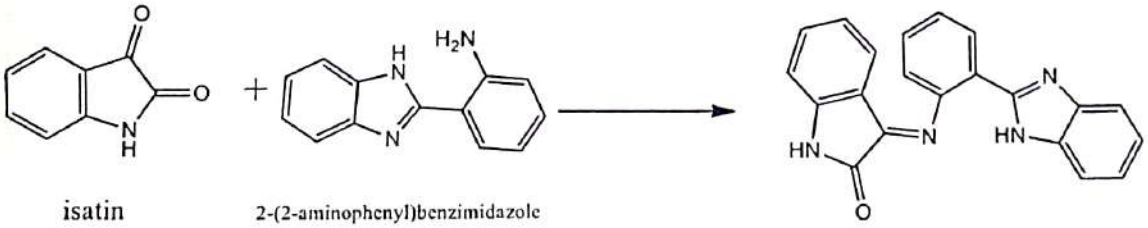


isatin

1-(2-aminophenyl)pyrrole

(*E*)-3-((2-(1*H*-pyrrol-1-yl)phenyl)imino)indolin-2-one

Scheme 1: Structure of Schiff base Ligand (L^1)



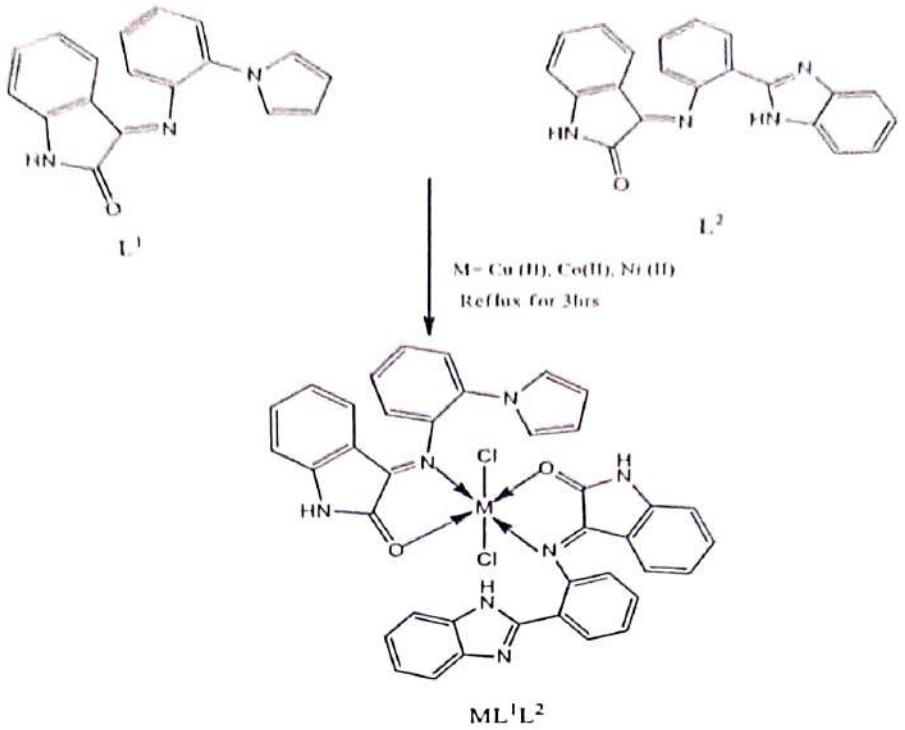
isatin

2-(2-aminophenyl)benzimidazole

(*E*)-3-((2-(1*H*-benzo[*d*]imidazol-2-yl)phenyl)imino)indolin-2-one

Scheme 2: Structure of Schiff base Ligand (L^2)

P.G.P. COLLEGE OF ARTS & SCIENCE NAMAKKAL 637 206



Scheme 3: Synthesis of Schiff base mixed ligand complexes [ML^1L^2]

2.4. Anti-microbial Activity

The ligands namely L^1, L^2 and their complexes were screened for their antibacterial activity against *Bacillus Subtilis, Salmonella typhi* and antifungal activity against *Aspergillus niger, Candida albicans*. The standard drugs Chloramphenicol and Fluconazole were also tested for their antimicrobial activities at the same concentration (1 mg/ml) and compared with tested compounds.

2.5. DNA Cleavage Studies

The DNA cleavage ability of Co(II), Ni(II) and Cu(II)complexes against pUC18DNA was monitored with the aid of agarose gel electrophoresis method. Mixed ligand complexes are able to convert super coiled DNA into open circular DNA and cleavage activities of complexes are obviously depends on concentrations. The cleavage efficacy of the metal complexes compared to that of the control experiments is due to their capable DNA-binding ability.

3. RESULTS AND DISCUSSION

The Schiff base ligands (L^1, L^2) were yellow in colour, but the prepared metal complexes of these ligands vary in colour depending on the metal ions. The elemental analysis of the Schiff base mixed ligand and its complexes is listed in Table 1. The data obtained was in a good agreement with the theoretical values and show the formation of 1:1:1 [M: L^1: L^2] ratio where M = Co (II), Ni (II) andCu (II) The metal complexes were found to be stable in air and insoluble in water, but soluble in DMF, DMSO and Chloroform. The observed values of molar conductance for the mixed ligand complexes (measured in 10^{-3}M DMF) are lower and thus non-electrolytic nature of the mixed ligand complexes was confirmed [13].

3.1. IR Spectra

In coordination chemistry, IR spectra provide a lot of valuable information about the nature of functional group attached to the metal atom [14]. The structure verification of metal complexes can be easily attained by comparing the IR spectra of the free ligands with their metal complexes. The IR spectrum of the ligands (L^1) and (L^2) are shown in Fig.1 and 2. Such comparison exposed that the characteristic absorption band appearing in free ligands spectra at 1616-1631 cm^{-1} due to the azomethine group (C=N) is shifted to lower or higher wave numbers by 2-15 cm^{-1} in the complexes spectra,

P.G.P. COLLEGE OF ARTS & SCIENCE NAMAKKAL 637 209

indicating coordination through the azomethine nitrogen [15]. The Schiff bases and complexes also display bands at 1725-1733 cm^{-1} due to the Carbonyl (C=O) group of isatin moiety, indicating the participation of the oxygen atom of carbonyl group in coordination to the metal ion. Moreover, free ligands and metal complexes show a broadband around 3125-3350 cm^{-1} which can be attributed to N-H stretching vibration of isatin and benzimidazole moiety [16]. The IR spectra of the metal complexes also show some new bands in the 518-532, 435-480 and 330-361cm^{-1} region, which may probably due to the formation of (M-O) [17], (M-N) [18] and (M-Cl) [19] bands respectively.

Table 1: Analytical data of the Schiff base mixed ligand and its metal complexes

Compounds	Molecular Formula	M.Wt	Yield	Calculated/found%					
				C	H	N	O	Cl	M
L_1	$C_{18}H_{13}N_3O$	287.32	85	(75.25) 75.26	(4.56) 4.52	(14.63) 14.63	(5.57) 5.57	-	-
L_2	$C_{21}H_{14}N_4O$	338.36	80	(74.54) 74.55	(4.17) 4.14	(16.56) 16.56	(4.73) 4.73	-	
CuL_1L_2	$C_{39}H_{27}CuN_7O_2cl_2$	758.09	82	(61.62) 61.73	(3.58) 3.56	(12.90) 12.92	(4.21) 4.22	(9.33) 9.24	(8.36) 8.38
CoL_1L_2	$C_{39}H_{27}CoN_7O_2cl_2$	754.09	75	(62.00) 62.06	(3.60) 3.58	(12.98) 12.99	(4.24) 4.24	(9.39) 9.29	(7.80) 7.81
NiL_1L_2	$C_{39}H_{27}NiN_7O_2cl_2$	753.10	70	(62.02) 62.14	(3.60) 3.58	(12.98) 13.01	(4.24) 4.24	(9.39) 9.30	(7.77) 7.79



Fig. 1: IR Spectra for of Schiff base L^1

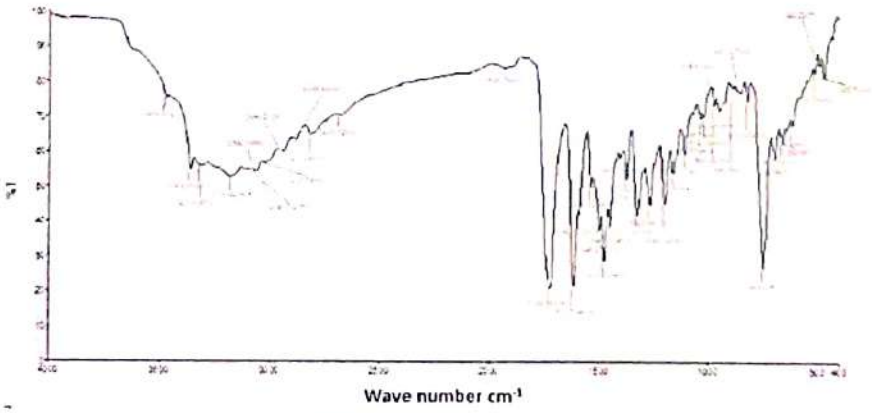


Fig. 2: IR Spectra for of Schiff base L^2

P.G. COLLEGE OF ARTS & SCIENCE NAMAKKAL 637 206

3.2. Electronic spectra and magnetic studies

The UV spectra of the Schiff base ligands and their complexes were recorded in freshly prepared DMF as a solvent (Fig.3 & 4). In electronic spectrum, the absorption band observed around270-290 nm which is assigned to benzene π-π^* transitions and 335-361nm which is attributed to n-π^* transitions of C=N chromophore within the Schiff base molecule (L^1& L^2). On complexation this band was shifted to lower or higher wavelength region showing the coordination of azomethine nitrogen to the central metal ion. The electronic spectrum of the $[CuL^1L^2]Cl_2$ complex shows a broad band at 609 nm which can be assigned to attributed to the $^2Eg \rightarrow {}^2T_2g$ transition, which is compatible with these complexes having an octahedral structure. Similar structural features were assigned for other mixed ligand Co(II) and Ni(II) complexes.

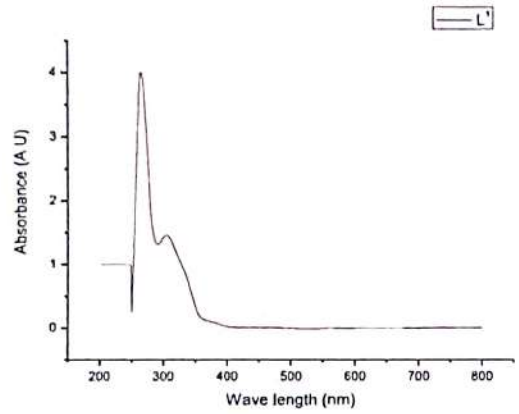


Fig 3: UV Spectra of Schiff base L^1

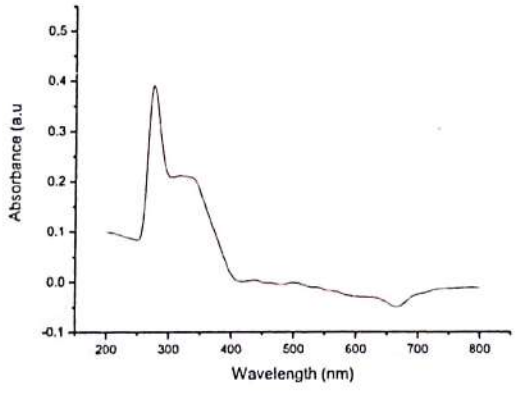


Fig 4: UV Spectra of Schiff base L^2

Magnetic susceptibility study of the present $Cu[C_{39}H_{27}N_7O_2]Cl_2$gives a magnetic moment value of 1.75 BM at room temperature, which are consistent with an octahedral structure. The $Co[C_{39}H_{27}N_7O_2]Cl_2$complex has a magnetic moment value of 4.45 BM, which is in agreement with the reported value for octahedral. The $Ni[C_{39}H_{27}N_7O_2]Cl_2$ complex reported herein has a room temperature magnetic moment value of 3.21 BM which is within the normal range observed for octahedral Ni(II) complex [20-22].

3.3. ^{1}H NMR Spectra

The ^{1}H NMR spectra of ligands (L^1&L^2) were recorded in DMSO-d6. The proton NMR spectrum of both ligands is shown in Fig.5 & 6. The signals due to N-H proton appeared as singlet in the range 10.2-11.05 ppm for Schiff base (L^1& L^2) corresponding to isatin and benzimidazole ring. The spectrum of free ligands, exhibited a signals in 6.2-7.8 ppm region which may be assigned to aromatic protons [15, 23]. The inferences drawn from these studies provide further support to the mode of bonding discussed in their IR spectra.

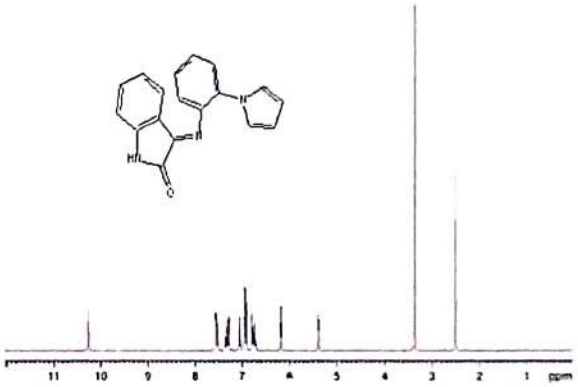


Fig. 5: ^{1}H NMR Spectra of Schiff base L^1

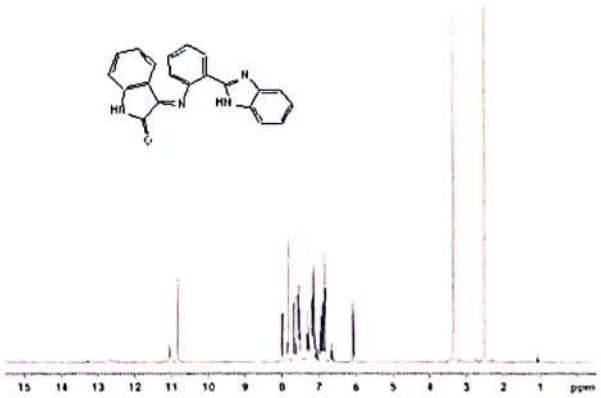


Fig. 6: ^{1}H NMR Spectra of Schiff base L^2

3.4. Cyclic Voltammetry

The electrochemical study is the most effective and versatile methods accessible for study of redox systems.

P.G.P. COLLEGE OF ARTS & SCIENCE NAMAKKAL 637 204

The redox behaviour of Cu(II), Co(II) and Ni(II) complexes has been studied by cyclic voltammogram in DMF using0.1 M Tetrabutyl ammonium perchlorate (TBAP) as supporting electrolyte. The voltammograms of the mixed ligand Schiff base complexes contains two peaks due to oxidative nature of organic molecule and reductive nature of azomethine group. The Cu(II) complex shows an cathodic peak at 0.54 V which is attributed to one electron reduction of Cu(II)/Cu(I) couple and anodic peak of 0.71 V indicates the oxidation process of Cu(I)→Cu(II). The Co(II) complexes exhibit well defined redox process corresponding to quasi reversible Co(II)/Co(I) couple with a peaks at Epa=0.96 V, Epc=0.64 V. The anodic peak at Epa= 0.75 V versus Ag/AgCl and the associated cathodic peak at Epc= 0.840 V correspond to the Ni(II)/Ni(I) couple which provides evidence for quasi reversible in nature. It has been shown that the formal redox potential dependent on factors such as coordination number, hard/soft nature of the ligands and bulkiness of the ligands [24].

3.5. ESR studies

Based on hyperfine structures, the ESR spectrum for metal complexes provides information about the geometry, nature of coordinating sites of the Schiff base and the metal. The Schiff base mixed ligand Cu(II) complex display a small broad signal with $g_{\parallel}$ at 2.08 and $g^{\perp}$ at 2.03.Hence the unpaired electron lies in the dx^2-y^2 orbital with $g_{\parallel} > g^{\perp} > ge$ (2.0027 free spin value) [25]. This confirms Cu(II) complex possess a distorted octahedral geometry.

3.6. Antimicrobial activity

In-vitro antifungal and antibacterial screening results are shown in Fig.7 and 8. Due to chelation, the metal complexes show prominent activity than free ligand [26]. Such higher activity of the metal chelates can be explained on the basis of overtone's concept and chelation theory. Based on overtone's concept, the cell is surrounded by lipid membrane which allows the passage of lipid soluble material thus controls antibacterial activity. On the basis of chelation, the polarity of the metal ion will be reduced to a larger extent due to the overlap of the ligand orbital and partial sharing of the positive charge of the metal ion with donor groups. Further, the complexes become very stable due to the delocalization of p-electrons and enhance the penetration of the complexes into lipid membranes and blocking of the metal binding sites in the enzymes of pathogens. These complexes also interrupt the respiration process of the cell and thus block the synthesis of proteins, which controls further growth of the microorganism [27].

In antifungal activity, the results showed that the mononuclear mixed ligand schiff bases metal complexes are more active against both fungi then the Schiff base. Co(II) complexes exhibited higher activity in both fungal strains than other complexes. This may result in to inhibitory in toxicology of metal ions towards some pathogens.

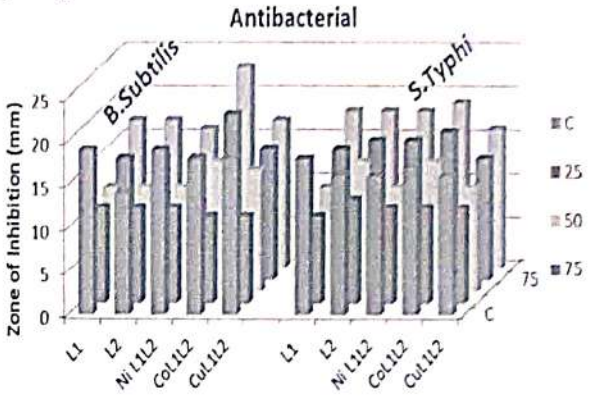


Fig. 7: Antibacterial activity for of mixed ligand Schiff base complexes

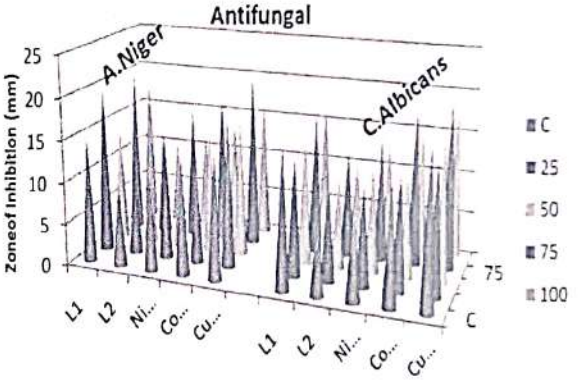


Fig. 8: Antifungal activity for of mixed ligand Schiff base complexes

3.7. DNA cleavage studies

Even after a longer exposure time, Control using DNA alone do not show any significant cleavage of pUC18DNA.The damage of DNA in Co(II), Ni(II) and Cu(II) complexes could be attributed to the DNA cleavage in the presence of oxidant which may be due to hydroxyl radical (OH˙). The OH˙ free radicals participate in general oxidative mechanisms of deoxyribose moiety, followed by hydrolytic cleavage via abstraction of a hydrogen atom from sugar units. The results show that

P.G.P. COLLEGE OF ARTS & SCIENCE NAMAKKAL 637 206

the important role of mixed ligand complexes in DNA cleavage reaction is shown in Fig.9. As the compound was perceived to cleave the DNA, it can be concluded that, all complexes effectively cleave the DNA as compared to control DNA and thus compound prevents the growth of pathogenic organism.



Fig. 9: The gel picture of DNA cleavage activity on pUC18DNA, Lane 1: DNA alone; Lane 2: DNA+ H_2O_2; Lane 3: DNA+ H_2O_2+CuL^1L^2; Lane 4: DNA+ H_2O_2+CoL^1L^2; Lane 5: DNA+ H_2O_2+NiL^1L^2

4. CONCLUSION

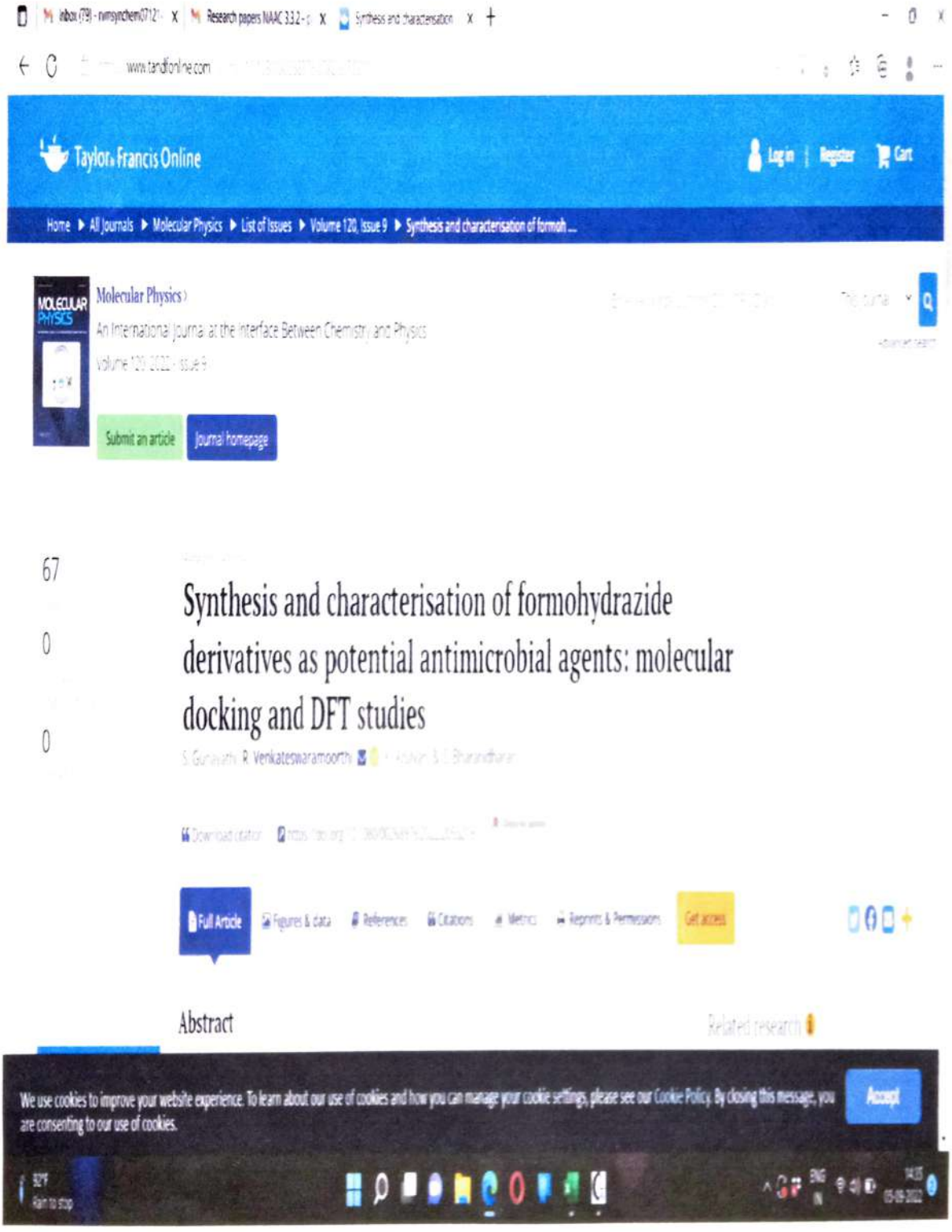
In the present work, Cu(II), Co(II) and Ni (II) complexes have been synthesized from Schiff bases (L^1,L^2) in 1:1:1 ratio and its non-electrolytic nature has been deduced from conductance data. The stoichiometry of complexes has been confirmed by elemental analyses, IR, Far-IR, ^{1}H NMR, UV, Cyclic voltammetry, ESR spectral data and molar conductance studies. Anoctahedral geometry for all complexes has been assigned on the basis of electronic and magnetic moment. The antimicrobial activity results reveal that the cobalt complexes act as more bactericidal and fungicidal agents as compared to the un-complexed Schiff base ligands. The DNA cleavage properties of the mixed ligand complexes have been examined by gel electrophoresis method and results exhibited that all complexes efficiently undergoes DNA cleavage activity via hydroxyl radical pathway.

5. REFERENCES

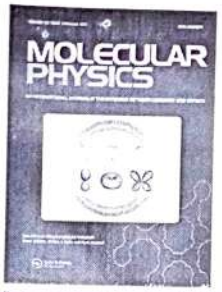
1. Shriodkar SG, Mane PS, Chondhekar TK. *Indian J. Chem.*, 2001; **40A:**1114-1117.
2. Thakor YJ, Patel SG, Patel KN. *J. Chem. Pharm. Res.*, 2010; **5(2):**518-525.
3. Tarafder MTH, Kasbollah A, Saravanan N, Crouse KA, Ali AM, Oo KT. *J. Biochem. Mol. Biol. Biophys*, 2002; **6:**85.
4. Spinu C, Pleniceanu M, Tigae C. *Turk. J. Chem.*, 2008; **32:**487.
5. Singh GS, Desta ZY, *Chem. Rev.*, 2012; **112:**6104-6155.
6. Joaquim FM da Silva, Simon J. Garden, Angelo C Pinto. *J. Braz. Chem. Soc.*, 2001; **12(3):**273-324.
7. Daisley RW, Shah VK. *J. Pharm. Sci.*, 1984; **73:**407-408.
8. Piscopo B, Diumo MV, Godliardi R, Cucciniello M, Veneruso G. *Boll. Soc. Ital. Biol. Sper.*, 1987; **30:63 (9):**827-832.
9. Tarafder MTH, Kasbollah A, Saravanan N, Crouse KA, Ali AM, Tin OK. *J. Biochem. Mol. Biol Biophys*, 2002; **6:**85.
10. Rosenberg B, Van Camp L, Krigas T. *Nature*, 1965; **205:**698-699.
11. Barton JK, Lolis E. *J. Am. Chem. Soc.*, 1985; **107:**708.
12. Guo Z, Sadler P. *J. Adv. Inorg. Chem.*, 2000; **49:**183-306.
13. Gear WJ. *Coord Chem Rev*, 1971; **7:**81.
14. Suresh MS, Prakash V. *Int J Current Res.*, 2011; **3(2):**68-75.
15. Matangi S, Pragathi J, Bathini U, Gyana KC. *E-Journal of Chemistry*, 2012; **9(4):**2516-2523.
16. Suraj B Ade, Deshpande MN, Deshmukh JH. *Rasayan Journal of Chemistry*, 2012; **5(1):**10-15.
17. Thaker BT, Surati KR, Patel P, Parmar SD. *J. Iran. Chem. Soc.*, 2006; **3(4):**371-377.
18. Natamato K. John wiley, NewYork, 1970.
19. Muthukkumar M, Malathy M, Rajavel R. *Der Chemica Sinica*, 2015; **6(11):**12-20.
20. Mohammad S, Nausheen B, Mohammad AR, Mohammad O. *J. Chem. Sci.*, 2017; **129(12):**1905-1920.
21. Figgis B. *Ligand field theory and its applications*, 1st edn.(New York: John-Wiley) 2000.
22. Siddiqi ZA, Siddique A, Shahid M, Sharma PK, Khalid M, Yogi A. *J. Mol. Struct.*, 2013; **1036:**209.
23. Gurunath KS, Sathisha MP, Srinivasa B, Naveen VK, Vidyanand KR, Suresh DK. *Med Chem Res.*, 2012; **21:**2273-2279.
24. Bard AJ, Izatt LR. *Electrochemical method: Fundamendals and Applications*: 2nd Ed., Wiley: New York, 2001.
25. Kivelson D, Neiman R. *J. Chem. Phys.*, 1961; **35:**149-155.
26. Raman N, Dhaveethu RJ, Sakthivel A. *J. Chem.Sci.* 2007a; **119:**303-310.
27. Dharmaraj N, Viswanathamurthi P, Natarajan K. *Trans. Met. Chem.*, 2001; **26:**105-109.

P.G.P. COLLEGE OF ARTS & SCIENCE NAMAKKAL 637 208

PRINCIPAL
PGP College of Arts and Science
Namakkal.



P.G.P. COLLEGE OF ARTS & SCIENCE
NAMAKKAL
637 206



Molecular Physics

An International Journal at the Interface Between Chemistry and Physics

ISSN: (Print) (Online) Journal homepage: https://www.tandfonline.com/loi/tmph20

Synthesis and characterisation of formohydrazide derivatives as potential antimicrobial agents: molecular docking and DFT studies

S. Gunavathi, R. Venkateswaramoorthi, K. Arulvani & S. Bharanidharan

To cite this article: S. Gunavathi, R. Venkateswaramoorthi, K. Arulvani & S. Bharanidharan (2022): Synthesis and characterisation of formohydrazide derivatives as potential antimicrobial agents: molecular docking and DFT studies, Molecular Physics, DOI: 10.1080/00268976.2022.2053219

To link to this article: https://doi.org/10.1080/00268976.2022.2053219

Published online: 22 Mar 2022.

Submit your article to this journal

View related articles

View Crossmark data

P.G.P. COLLEGE OF ARTS & SCIENCE NAMAKKAL 637 206

Full Terms & Conditions of access and use can be found at https://www.tandfonline.com/action/journalInformation?journalCode=tmph20

MOLECULAR PHYSICS e2053219
https://doi.org/10.1080/00268976.2022.2053219

Taylor & Francis
Taylor & Francis Group

RESEARCH ARTICLE

Synthesis and characterisation of formohydrazide derivatives as potential antimicrobial agents: molecular docking and DFT studies

S. Gunavathi[a], R. Venkateswaramoorthi [a], K. Arulvani[a] and S. Bharanidharan[b]

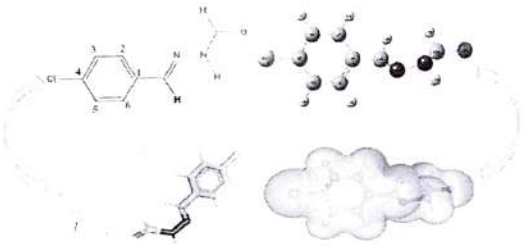
[a]Department of Chemistry, PGP College of Arts and Science, Namakkal, India; [b]Department of Physics, Agni College of Technology, Chennai, India

ABSTRACT

A novel series of formohydrazide derivatives **(3a-3j)** were synthesised and characterised by FT-IR, ^{1}H and ^{13}C NMR spectral techniques. The geometrical parameters of compound **3d** were calculated by using the DFT method B3LYP/6-311++G(d,p) basis set. The title molecule's dipole moment, polarizability, and first-order hyperpolarizability were calculated and interpreted. The HOMO–LUMO transition occurs when a molecule undergoes intra-molecular charge transfer. The reactive sites of the molecule are studied using the Molecular Electrostatic Potential (MEP) surface. In addition, using the DFT/B3LYP/6-311++G(d,p) level of theory, the Mulliken atomic charges of carbon, nitrogen, oxygen, chlorine, and hydrogen atoms were determined. The compounds **3a-j** were tested for their in vitro antibacterial activity against five bacterial strains viz., Gram-Positive bacteria species *Enterococcus faecalis*, *Staphylococcus aurous* and Gram-Negative bacteria species *Escherichia coli*, *Klebsiella pneumonia* and *Pseudomonas aeruginosa*. The tested antimicrobial activities of the compounds were compared with the standard drug of *Ciprofloxacin* for bacteria and *Ketocanazone* for fungal. The compounds **3c**, **3d** and **3e** showed excellent antifungal activities than the standard fungal strains. Molecular docking analysis was used to investigate the interaction of the title compound with a target protein.

ARTICLE HISTORY
Received 30 January 2022
Accepted 8 March 2022

KEYWORDS
Formohydrazide derivatives; spectral studies; DFT; biological activity; molecular docking



1. Introduction

The synthetic Organic Chemistry field is leading to new drug design, synthesis, and development of bioactive molecules. Heterocyclic compounds have been the focus of particular attention from chemists because they are in the structural core of many synthetic and natural drug molecules [1]. Among them, nitrogen-containing organic acyclic compounds are of great importance in life science. Because they have the diversity of electronic structure, abundant in nature, geometry, subunits in natural product, intermolecular interaction, easily bind with enzymes and also finding increasing use as intermediate in medicinal chemistry.

For the synthesis of new drugs, small molecules have played an important role because they have low molecular weight, are easily ingestible, are immediately absorbed, easily penetrate cell membranes, and are capable of modulating biochemical processes [2]. Small molecule drugs include Isoniazid, Chloroprocazine, Chloroquine, Chlorpromazine, Barbituric acid, Captopril, Diazepam and Azidothymidine have been continued to dominate in the pharmaceutical field [3] due

CONTACT R. Venkateswaramoorthi eswarchemistry2011@gmail.com Department of Chemistry, PGP College of Arts and Science, Namakkal 637 207, Tamil Nadu, India

© 2022 Informa UK Limited, trading as Taylor & Francis Group

PGP COLLEGE OF ARTS & SCIENCE NAMAKKAL 637 206

to their structure, function, potency, medicinal usages, ease to make, and highly profitable. Nitrogen-containing small molecules, particularly hydrazones in DFT [4–8], Docking [9,10], Inhibition [11] and spectroscopic [12] studies were investigated and significant extensively used building blocks in pharmaceutical drug discovery systems such as Anticancer [13–15], Antihypertensive [16], Antileishmanial [17], Anti-inflammatory [18], Antituberculosis [19], Antimicrobial [20,21], Antioxidant [22,23], Anti proliferative [24,25], Antitumour [26] and Antiviral [27] activities. Hydrazones have functional diversity of C = N-N moiety and the structure shows nucleophilic imine, electrophilic and nucleophilic character carbon, the intrinsic nature of C = N bond and acetic NH proton and which are determined the physical and chemical properties of the corresponding biomolecules [28].

Acyl hydrazones have been investigated and used in the medicinal field as commonly prescribed marketed drugs bearing –CO–N–N = functional group [29] and which behave as chelating ligands to the formation of various hydrazone complexes [30] and much attention to the investigation against various diseases. According to the above statistics and applications of hydrazones, we have planned and synthesised a series of small molecules of acyl hydrazones and analysed their spectral, theoretical and biological properties.

2. Experimental

2.1. Materials and methods

The reagent and solvents were purchased from Merck commercial suppliers without further purification. ^{1}H NMR was recorded at 400 MHz and ^{13}C NMR spectra at100MH$_Z$ on a BRUKER model using $CDCl_3$ and DMSO as solvent for all the compounds. Tetra methylsilane was used as an internal standard for all NMR spectra. The melting points of the synthesised compounds were measured in open capillaries and are uncorrected. Thin-layer chromatography was performed with Aluminium sheet-silica gel-coated 60F254 purchased from Merck. The column chromatography with silica gel 100–200 mesh using Benzene: Ethyl acetate (9:1) as eluent and spots were visualised under the iodine chamber. The crystallisation of all the target compounds in double-distilled ethanol. IR data was collected from the JASCO FT-IR spectrometer using KBr pellets

2.2. Synthesis of compounds (3a-3j)

The condensation of formic hydrazide (0.02mol) with various aromatic aldehydes (0.02 mol) in the presence of a catalytic amount of acetic acid in Ethanol and Chloroform (1:1) under reflux. The progress of the reaction was monitored by thin-layer chromatography and after completion of the reaction; the reaction mixture was poured into ice. The crude target compounds were filtered, washed with distilled water and dried. The precipitate was recrystallised by Ethanol.

2.2.1. (E)-N′-benzylideneformohydrazide (3a)

White colour, Solid, **Yield**: 78%; **m.p.**: 148–150°C; **MF**: $C_8H_8N_2O$ (148.06); **Elemental analysis Calcd.** (%): C, 64.85; H, 5.44; N, 18.91; O, 10.80; **IR**(cm^{-1}):1684(C = O), 3186(NH), 1622(C = N), 3059-2836(CH); **^{1}H NMR** ($CDCl_3$,400MH$_Z$): δ 9.8(s, 1H, NH), 8.81(s, 1H, CHO); 7.66(s, 1H, CH), 7.25-7.87(Aromatic protons); **^{13}C NMR**($CDCl_3$, 400MH$_Z$): 166.2(CHO), 146.7(CH = N), 127.3-162.1(Aromatic Carbons).

2.2.2. (E)-N′-(4-methoxybenzylidene)formohydrazide (3b)

Brown colour, Solid, **Yield**: 76%; **m.p.**:261-263°C; MF: $C_9H_{10}N_2O_2$ (178.07); **Elemental analysis Calcd.** (%):C, 60.66; H, 5.66; N, 15.72; O, 17.96; **IR**(cm^{-1}):1658(C = O), 3147(NH), 1598(C = N), 2995-2755(CH); **^{1}H NMR** ($CDCl_3$, 400MH$_Z$): δ 10.15(s, 1H, NH),8.78(s, 1H, CHO); 7.80(s, 1H, CH),3.85(s, 3H,OCH_3),6.91-7.61 (Aromatic protons); **^{13}C NMR**($CDCl_3$, 400MH$_Z$): 165.8 (CHO), 146.4(CH = N), 55.3(OCH_3)114.2-162.0 (Aromatic Carbons).

2.2.3. (E)-N′-(4-fluorobenzylidene)formohydrazide (3c)

White colour, Solid, **Yield**: 74%; **m.p.**: 170-172°C; **MF**: $C_8H_7FN_2O$ (166.05); **Elemental analysis Calcd.** (%):C, 57.82; H, 4.25; F, 11.43; N, 16.86; O, 9.63; **IR**(cm^{-1}):1699(C = O), 3184(NH), 1599(C = N), 3058-2828(CH); **^{1}H NMR** ($CDCl_3$, 400MH$_Z$): δ 9.85 (s, 1H, NH), 8.79 (s, 1H, CHO); 7.82(s, 1H, CH), 7.08-8.62 (Aromatic protons); **^{13}C NMR** ($CDCl_3$, 400MH$_Z$): 165.7(CHO), 144.6(CH = N), 115.6-164.8 (Aromatic Carbons).

2.2.4. (E)-N′-(4-chlorobenzylidene)formohydrazide (3d)

Yellow colour, Solid, **Yield**: 80%; **m.p.**: 184-186°C; MF: $C_8H_7ClN_2O$ (182.02); **Elemental analysis Calcd.** (%):C, 52.62; H, 3.86; Cl, 19.41; N, 15.34; O, 8.76; **IR**(cm^{-1}):1676 (C = O), 3193(NH), 1608(C = N), 3063-2717(CH); **^{1}H NMR**($CDCl_3$, 400MH$_Z$): δ 9.5(s, 1H, NH), 8.81(s, 1H, CHO); 8.11(s, 1H, CH), 7.26-7.78(Aromatic protons);

P.G. COLLEGE OF ARTS & SCIENCE NAMAKKAL 637 206

^{13}C NMR($CDCl_3$, 400MH_Z):165.5(CHO), 144.9(CH = N), 128.4-161.1(Aromatic Carbons).

2.2.5. (E)-N'-(3-fluorobenzylidene)formohydrazide (3e)

Yellow colour, Solid, **Yield**: 72%; **m.p.**:143-145°C; **MF**: $C_8H_7FN_2O$ (166.05); **Elemental analysis Calcd.** (%):C, 57.83; H, 4.25; F, 11.43; N, 16.86; O, 9.63; **IR**(cm^{-1}):1688 (C = O), 3162(NH), 1614(C = N), 3061-2845(CH); ^{1}**H NMR**($CDCl_3$, 400MH_Z): δ 8.61(s, 1H, CHO); 7.61(s, 1H, CH), 7.14-7.59(Aromatic protons); ^{13}**C NMR**($CDCl_3$, 400MH_Z):164.2(CHO), 144.1(CH = N), 114.4-161.7 (Aromatic Carbons).

2.2.6. (E)-N'-(3-chlorobenzylidene)formohydrazide (3f)

Yellow colour, Solid, **Yield**: 68%; **m.p.**: 145-147°C; **MF**: $C_8H_7ClN_2O$ (182.02); **Elemental analysis Calcd.** (%):C, 52.62; H, 3.86; Cl, 19.41; N, 15.34; O, 8.76; **IR**(cm^{-1}):1716(C = O), 3172(NH), 1628(C = N),3074-2853(CH); ^{1}**H NMR**($CDCl_3$, 400MH_Z): δ 8.60(s, 1H, CHO); 7.87(s, 1H, CH), 6.94-7.79(Aromatic protons);

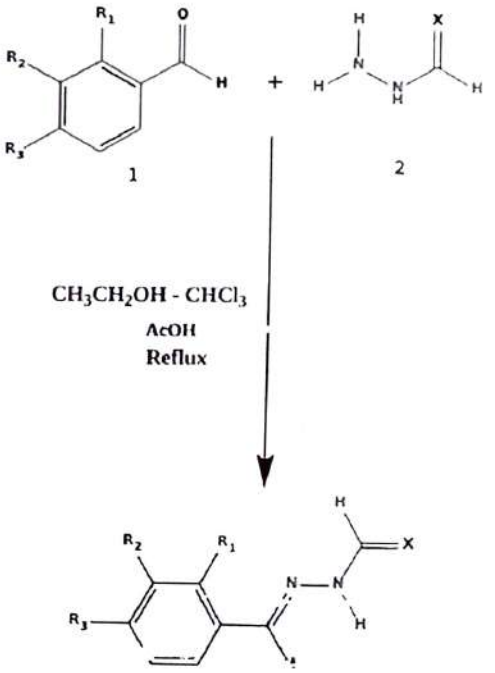
^{13}C NMR($CDCl_3$, 400MH_Z):165.3(CHO), 144.4(CH = N), 114.2-162.0(Aromatic Carbons).

2.2.7. (E)-N'-(3-methylbenzylidene)formohydrazide (3g)

White colour, Solid, **Yield**: 70%; **m.p.**:142-144°C; **MF**: $C_9H_{10}N_2O$ (162.08); **Elemental analysis Calcd.** (%):C, 66.65; H, 6.21; N, 17.27; O, 9.86; **IR**(cm^{-1}):1693(C = O), 3187(NH), 1613(C = N), 3070-2841(CH); ^{1}**H NMR** ($CDCl_3$, 400MH_Z): δ 10.09(s, 1H, NH),8.81(s, 1H, CHO); 7.86(s, 1H, CH), 2.37(s, 3H, CH_3), 7.21-8.82 (Aromatic protons); ^{13}**C NMR**($CDCl_3$, 400MH_Z): 166.2 (CHO), 147.1(CH = N), 21.2(CH_3), 124.7-162.3 (Aromatic Carbons).

2.2.8. (E)-N'-(3-methoxybenzylidene)formohydrazide (3h)

Yellow colour, Solid, **Yield**: 68%; **m.p.**:156-158°C; **MF**: $C_9H_{10}N_2O_2$ (178.07); **Elemental analysis Calcd.** (%):C, 60.66; H, 5.66; N, 15.72; O, 17.96; **IR**(cm^{-1}):1682(C = O), 3195(NH), 1602(C = N), 3057-2706(CH); ^{1}**H NMR** ($CDCl_3$, 400MH_Z): δ 10.48(s, 1H, NH),8.81(s, 1H,



3 a - j

Scheme 1. Synthetic route for compounds **3a-3j**

Entry	R_1	R_2	R_3	X
3a	H	H	H	O
3b	H	H	OCH_3	O
3c	H	H	F	O
3d	H	H	Cl	O
3e	H	F	H	O
3f	H	Cl	H	O
3g	H	CH_3	H	O
3h	H	OCH_3	H	O
3i	Cl	H	H	O
3j	CH_3	H	H	O

P.G.P. COLLEGE OF ARTS & SCIENCE NAMAKKAL 637 206

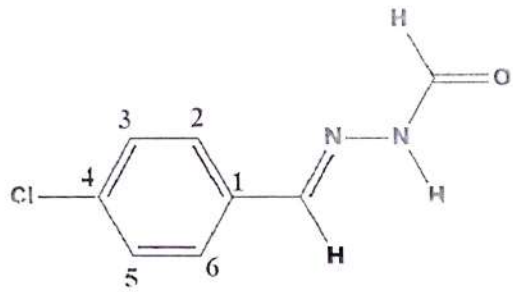


Figure 1. Numbering of the compound **3d**.

CHO); 7.89(s, 1H, CH), 3.85(s, 3H, OCH_3), 6.95-7.37(Aromatic protons); **^{13}C NMR**($CDCl_3$, 400MH_Z): 166.2(CHO), 146.7(CH = N), 55.3(OCH_3),111.0-161.9 (Aromatic Carbons).

2.2.9. (E)-N'-(2-chlorobenzylidene)formohydrazide (3i)

Yellow colour, Solid, **Yield**: 70%; **m.p.**:140-142°C; **MF**: $C_8H_7ClN_2O$ (182.02); **Elemental analysis Calcd.** (%):C, 52.62; H, 3.86; Cl, 19.41; N, 15.34; O, 8.76; **IR**(cm^{-1}):1707 (C = O), 3151(NH), 1650(C = N), 3072-2846(CH); **^{1}H NMR**($CDCl_3$, 400MH_Z): δ 9.08(s, 1H, CHO); 8.21(s, 1H, CH), 7.25-7.44(Aromatic protons); **^{13}C NMR**($CDCl_3$, 400MH_Z): 164.1(CHO), 144.1(CH = N), 127.0-159.1 (Aromatic Carbons).

2.2.10. (E)-N'-(2-methylbenzylidene)formohydrazide (3j)

Yellow colour, Solid, **Yield**: 60%; **m.p.**:82-84°C; **MF**: $C_9H_{10}N_2O$ (162.08); **Elemental analysis Calcd.** (%):C, 66.65; H, 6.21; N, 17.27; O, 9.86; **IR**(cm^{-1}):1706(C = O), 3202(NH), 1607(C = N),3059-2853(CH); **^{1}H NMR** ($CDCl_3$, 400MH_Z): δ 8.99 (s, 1H, CHO); 8.05(s, 1H, CH), 2.54(s, 3H, CH_3), 7.21-7.35(Aromatic protons); **^{13}C NMR** ($CDCl_3$, 400MH_Z): 160.7(CHO), 138.8(CH = N), 19.6(CH_3),126.3-132.2(Aromatic Carbons).

2.3. Computational details

The quantum chemical calculations for **3d** were done by using Gaussian 09W programme package [31] with the help of DFT/B3LYP/6-311++G(d,p) basis set. The bond parameters, NLO, FMO, MEP, and Mulliken

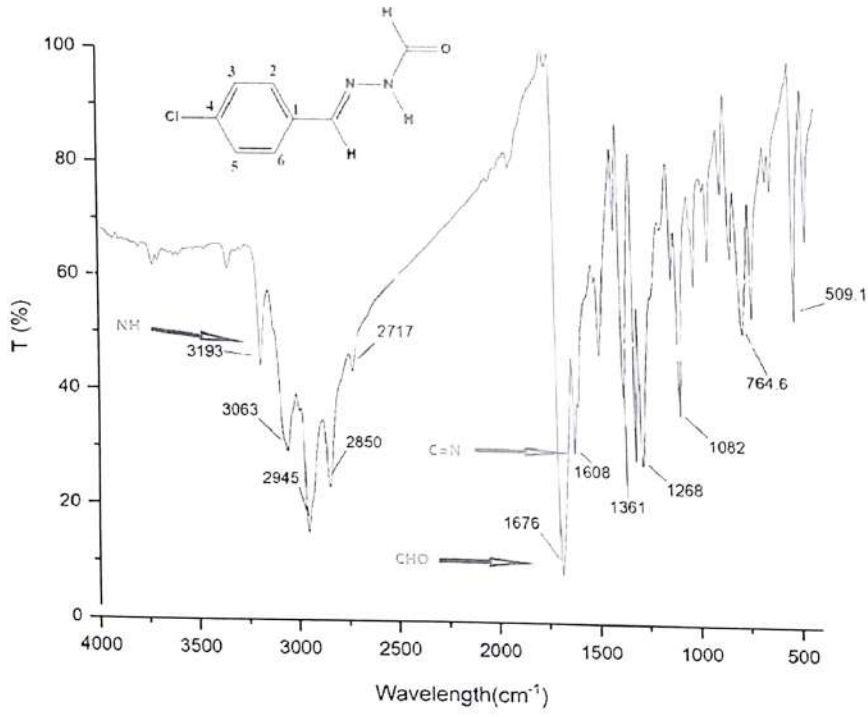


Figure 2. IR spectrum of compound **3d**.

P.G. COLLEGE OF ARTS & SCIENCE
NAMAKKAL
637 206

Table 1. Physical data and IR Spectral analysis of **3a-3j**.

						IR (cm^{-1})			
Entry	Entry	Colour	Yield	Nature	m.p (°C)	C = O	N-H	C = N	C-H
3a	Ph	White	78	Solid	148–150	1684	3186	1622	3059–2836
3b	4-OCH_3	Brown	76	Solid	261–263	1658	3147	1598	2995–2755
3c	4-F	White	74	Solid	170–172	1699	3184	1599	3058–2828
3d	4-Cl	Lite Yellow	80	Solid	184–186	1676	3193	1608	3063–2717
3e	3-F	Yellow	72	Solid	143–145	1688	3162	1614	3061–2845
3f	3-Cl	Yellow	68	Solid	145–147	1716	3172	1625	3074–2853
3g	3-CH_3	White	70	Solid	142–144	1693	3187	1613	3070–2841
3h	3-OCH_3	Lite Yellow	68	Solid	156–158	1682	3195	1602	3057–2706
3i	2-Cl	Yellow	70	Solid	140–142	1707	3151	1609	3072–2846
3j	2-CH_3	Yellow	60	Solid	82–84	1706	3202	1607	3059–2853

atomic charges were calculated and analysed using the DFT/B3LYP/6-311++G(d,p) method. Docking computations were carried out on Mycobacterium Tuberculosis Inhibitors enzyme protein model [32]. Essential hydrogen titles, Kollman united snippet type charges, and solvation parameters were added with the aid of AutoDock tools [33].

3. Results and discussion

Formic hydrazide-hydrazone derivatives were synthesised as described in Scheme 1. The condensation reaction of formic hydrazide with various aromatic aldehydes in the presence of a catalytic amount of acetic acid in ethanol and Chloroform (1:1) under reflux for 3–4 hrs led to target compounds in good yield.

3.1. IR spectral studies of (E)-N'-(4-chlorobenzylidene) formohydrazide (3d)

The numbering scheme of the compound is shown in Figure 1. The FT-IR spectrum of compound **3d** was recorded in the region of 4000–400 cm^{-1} as shown in Figure 2. The formation of target compounds **3a-3j** were confirmed by disappearance of bands at 3400–3300 cm^{-1} (corresponding to $-NH_2$ group of formic hydrazide moiety) and 1690–1740 cm^{-1} (-CHO group of Aromatic

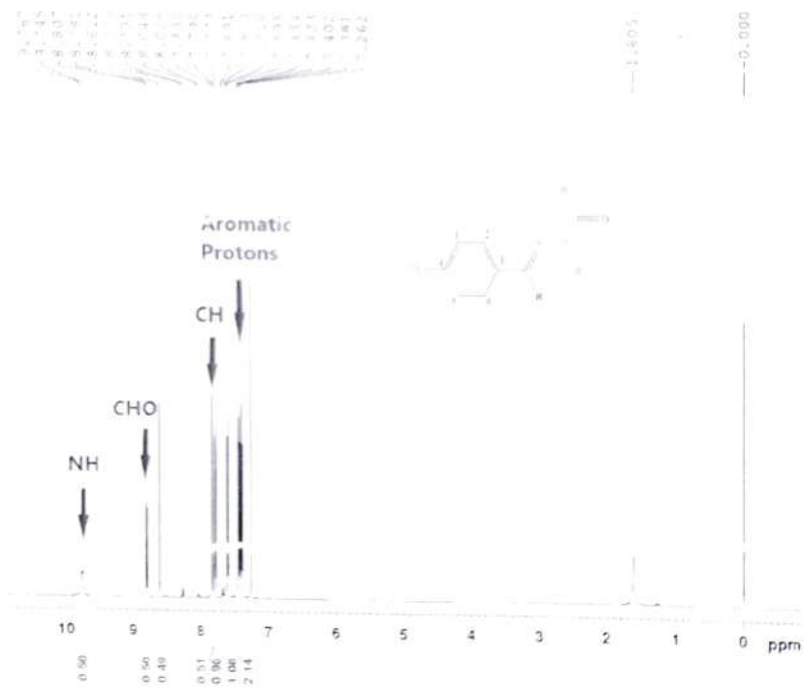


Figure 3. ^1H NMR spectrum of compound **3d**

P.K.P. COLLEGE OF ARTS & SCIENCE
NAMAKKAL
637 206

Table 2. ^{1}H Chemical shift values of **3a-3j**.

		^{1}H NMR (δ, ppm)						
Entry	SUBS	NH	CHO	CH	OCH_3	CH_2	CH_3	Aromatic Protons
3a	PH	9.8	8.81	7.66				7.25-7.87
3b	4-OCH_3	10.15	8.78	7.8	3.85			6.91-7.61
3c	4-F	9.85	8.79	7.82				7.08-8.62
3d	4-Cl	9.5	8.81	8.11				7.26-7.78
3e	3-F		8.41	7.61				7.14-7.59
3f	3-Cl		8.6	7.87				6.94-7.79
3g	3-CH_3	10.09	8.81	7.86			2.37	7.21-8.82
3h	3-OCH_3	10.48	8.81	7.89	3.85			6.95-7.37
3i	2-Cl		9.08	8.21				7.25-7.44
3j	2-CH_3		8.99	8.05			2.54	7.21-7.35

aldehyde). This indicated that both amine and aldehyde reacted to yield imine (-CH = N-). The formation of imine was confirmed by the appearance of band around at 1600 cm^{-1}. The amide carbonyl stretching frequency appeared in the range of 1716–1658 cm^{-1} and CH stretching vibration frequency appeared in the range of 3074–2706 cm^{-1} were further confirmed the formation of the target compounds.

The IR spectrum of the compound **3d** showed an amide carbonyl stretching frequency at 1676 cm^{-1}, imine stretching frequency at 1608 cm^{-1} and secondary amine at 3193 cm^{-1} were confirmed the formation of the compound **3d**. The IR spectrum of compound **3d** is shown in Figure 2. Physical and IR spectral data were shown in Table 1.

3.2. NMR spectral analysis of (E)-N'-(4-chlorobenzylidene) formohydrazide (3d)

For the formic hydrazide-hydrazone derivatives, the only E geometric isomer is the most stable isomer and it has been proved by the previous literature [34–36]. From Figure 3, the ^{1}H NMR spectrum of hydrazones, the -NH proton appeared at 9.5 ppm, the =CH proton appeared as a singlet at 8.11 ppm and aldehyde proton appeared as a singlet at 8.81 ppm. The aromatic protons appeared in the range between 7.26 and 7.78 ppm. The ^{1}H Chemical shift values of **3a-j** are summarised in Table 2.

Similarly, the ^{13}C NMR signals of the compound **3d** were assigned by using the position and intensity of the signals. From Figure 4, the ^{13}C NMR spectrum of **3d**, there is a signal at 165.5 ppm is due to carbonyl carbon of aldehyde group of formic hydrazide.

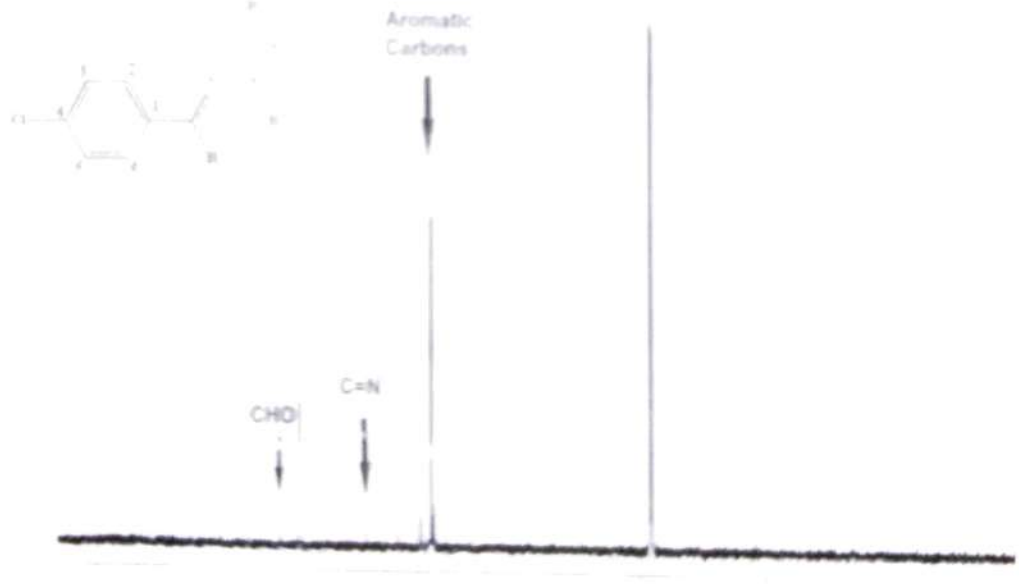


Figure 4. ^{13}C NMR spectrum of compound **3d**.



Table 3. ^{13}C Chemical shift values of **3a-3j**.

		^{13}C NMR (δ, ppm)					
Entry	SUBS	CH = O	CH = N	OCH_3	CH_2	CH_3	Aromatic carbons
3a	Ph	166.2	146.7				127.3-162.1
3b	4-OCH_3	165.8	146.4	55.3			114.2-162.0
3c	4-F	165.7	144.6				115.6-164.8
3d	4-Cl	165.5	144.9				128.4-161.1
3e	3-F	164.2	144.1				114.4-161.7
3f	3-Cl	165.3	144.4				114.2-162.0
3g	3-CH_3	166.2	147.1			21.2	124.7-162.3
3h	3-OCH_3	166.2	146.7	55.3			111.0-161.9
3i	2-Cl	164.1	144.1				127.0-159.1
3j	2-CH_3	160.7	138.8			19.6	126.3-132.2

Low intensity peaks appeared at the downfield region at 144.9 ppm is due to azonitrile (C = N). The signals obtained in the range of 128.4-161.1 ppm are due to the aromatic carbons of the target compounds (Table 3). Figure 5 showed the possible E and Z form of target compounds **3a-j**.

3.3. DFT study

3.3.1. Molecular geometry

The title molecule belongs to C_1 point group harmony. The optimised molecular structure of **3d** is shown in Figure 6, with the numbering scheme adopted in this study. The calculated geometrical parameters of **3d** were calculated by B3LYP with 6-311++G(d,p) basis set are listed in Table 4. The C–C bond lengths of six-membered rings are relatively equal to 1.39Å/B3LYP with some exceptions. Because in benzene, all the C–C bond lengths are equal (equal distribution of π-electrons around the benzene ring). In this study, the benzene ring bond angle values were nearly around 120°. The dihedral angle values reveal the planar of the present molecule.

3.3.2. NLO property

Vibrational spectroscopy was used to investigate many organic compounds possessing conjugated π electrons that have large molecular first hyperpolarizability. Intramolecular charge transfer from the donor to acceptor

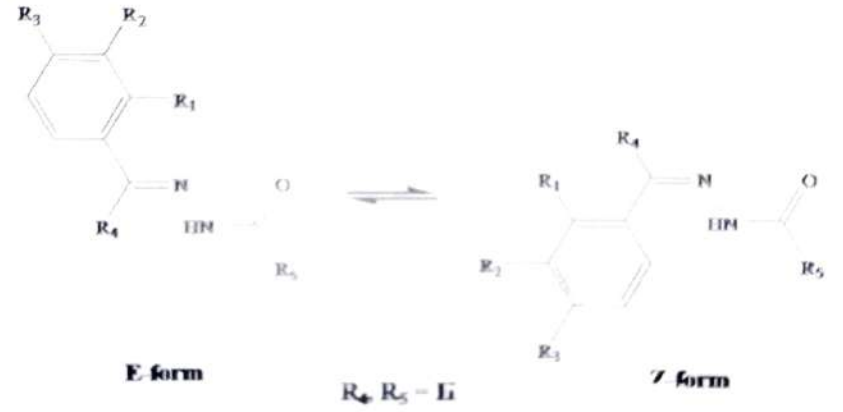


Figure 5. E, Z form of synthesised compounds 3a-j.

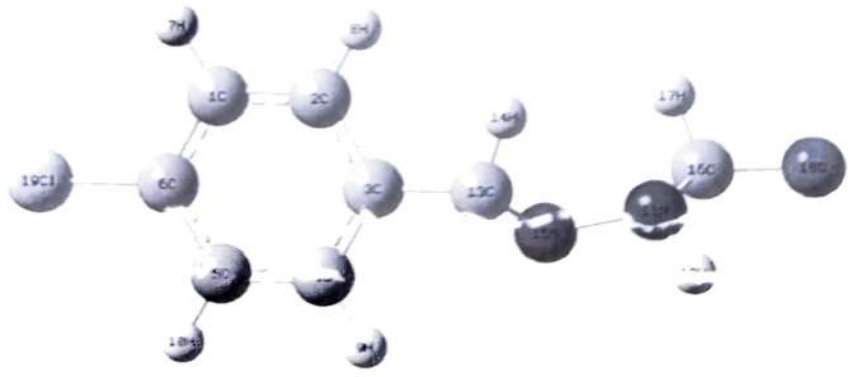


Figure 6. The optimised molecular structure of **3d**.

PSG COLLEGE OF ARTS & SCIENCE COIMBATORE 641 004

Table 4. The optimised bond parameters of **3d**.

Bond Lengths (Å)	DFT	Bond Lengths (Å)	DFT
R(1,2)	1.3952	R(5,6)	1.3951
R(1,6)	1.3948	R(5,10)	1.0998
R(1,7)	1.0996	R(6,19)	1.76
R(2,3)	1.3947	R(11,15)	1.47
R(2,8)	1.0997	R(11,16)	1.47
R(3,4)	1.3954	R(13,14)	1.07
R(3,13)	1.47	R(13,15)	1.47
R(4,5)	1.3948	R(16,17)	1.07
R(4,9)	1.0997	R(16,18)	1.43
Bond Angles (°)	**DFT**	**Bond Angles (°)**	**DFT**
A(2,1,6)	119.999	A(6,5,10)	119.984
A(2,1,7)	119.997	A(1,6,5)	120
A(6,1,7)	120.004	A(1,6,19)	120.008
A(1,2,3)	120.009	A(5,6,19)	119.992
A(1,2,8)	119.981	A(12,11,15)	109.471
A(3,2,8)	120.011	A(12,11,16)	109.471
A(2,3,4)	119.994	A(15,11,16)	109.471
A(3,4,5)	119.994	A(14,13,15)	110.782
A(3,4,9)	119.981	A(11,15,13)	109.471
A(5,4,9)	120.025	A(11,16,17)	109.471
A(4,5,6)	120.005	A(11,16,18)	109.471
A(4,5,10)	120.011	A(17,16,18)	109.471
Dihedral Angles (°)	**DFT**	**Dihedral Angles (°)**	**DFT**
D(6,1,2,3)	0.0323	D(4,3,13,14)	−179.2
D(6,1,2,8)	179.953	D(4,3,13,15)	59.9924
D(7,1,2,3)	−179.97	D(3,4,5,6)	0.0131
D(7,1,2,8)	−0.052	D(3,4,5,10)	−180
D(2,1,6,5)	0.0149	D(9,4,5,6)	−179.96
D(2,1,6,19)	179.989	D(9,4,5,10)	0.031
D(7,1,6,5)	−179.98	D(4,5,6,1)	−0.0376
D(7,1,6,19)	−0.0055	D(4,5,6,19)	179.988
D(1,2,3,4)	−0.0568	D(10,5,6,1)	179.975
D(1,2,3,13)	179.962	D(10,5,6,19)	0.0007
D(8,2,3,4)	−179.98	D(12,11,15,13)	109.176
D(2,3,4,9)	−180	D(12,11,16,18)	−48.057
D(13,3,4,5)	−179.98	D(15,11,16,17)	71.9434
D(2,3,13,15)	−120.03	D(14,13,15,11)	44.5363

Table 5. The NLO measurements of **3d**.

Parameters	B3LYP/6-311++G(d,p)
Dipole moment (μ)	**Debye**
μ_x	−0.9209865
μ_y	−0.5789669
μ_z	−0.4280609
μ	1.16904 **Debye**
Polarizability (α_0)	**x10^{-30}esu**
α_{xx}	257.5269920
α_{xy}	4.5705721
α_{yy}	98.2888119
α_{xz}	−0.5936327
α_{yz}	25.1196493
α_{zz}	85.0622461
α_0	0.38416 × 10^{-30}esu
Hyperpolarizability (β_0)	**x10^{-30}esu**
β_{xxx}	342.5658189
β_{xxy}	−61.6945000
β_{xyy}	1.2139216
β_{yyy}	−47.3843282
β_{xxz}	−52.8885826
β_{xyz}	45.4622600
β_{yyz}	−21.9854326
β_{xzz}	−19.9707224
β_{yzz}	−22.7644038
β_{zzz}	−29.3502052
β_0	3.15183 × 10^{-30}esu

Standard value for urea (μ = 1.3732 Debye, β_0 = 0.3728 × 10^{-30}esu): **esu**-electrostatic unit.

group through a single–double bond conjugated channel can cause substantial fluctuations in both the molecular dipole moment and polarizability, resulting in high IR and Raman activity.

In this study, the dipole moment and first hyperpolarizability (μ and β_0) of **3d** are calculated using the B3LYP/6-311++G(d,p) basis set. Table 5 shows the computed dipole moment and first hyperpolarizability values, which are 1.16904 Debye and 3.15183 × 10^{-30}esu, respectively. In which the β_0 value is eight times greater than that of urea. This result shows that the title molecule has good NLO activity in the present system.

3.3.3. NBO analysis

NBO analysis of **3d** has been performed, in order to explain the intermolecular charge transfer and delocalisation of π-electrons. The intra-molecular hyper conjugative interaction is due to the overlap between π(C–C) and $\pi*$(C–C) the orbitals, which results in intramolecular charge transfer, appearing in the molecular system.

In the present study, the NBO analysis mainly focused on the π-electron transfer because it leads to several intra-molecular charge delocalisations within the molecule. The $E^{(2)}$ values and types of the transition are shown in Table 6. In the same way, π (C2-C3) bond transfers 90.54 KJ/mol of energy to $\pi*$(C1-C6) and π (C1-C6) bond transfers 77.36 KJ/mol of energy to $\pi*$(C2-C3), respectively. This bond also affects the vibrational frequencies of the C–C bond in the benzene ring. The lone pair atoms such as O and Cl have delocalised more hyper conjugative energies with one and each other. It is evident from Table 6, the lone pair atom O18 and Cl19 transfers about 42.47 and 53.26 KJ/mol to N11-C16 and C1-C6, respectively. In addition $\pi*$-$\pi*$ transfer more energies from C1-C6 to anti-bonding orbitals C2-C3/837.18 KJ/Mol and C4-C5/640.53 KJ/Mol, respectively. Hence, these result shows that the title molecule is more applicable to the biological and medicinal field.

3.3.4. HOMO–LUMO analysis

The frontier molecular orbitals play an important part in the electric and optic parcels and chemical responses. The HOMO and LUMO are the main orbitals that take part

P.G. COLLEGE OF ARTS & SCIENCE NAMAKKAL 637 206

Table 6. The NBO analysis of **3d**.

Type	Donor NBO (i)	ED/e	Acceptor NBO (j)	ED/e	$E^{(2)}$ KJ/mol	E(j)-E(i) a.u.	F(i,j) a.u.
σ -σ*	BD(1) C1-C2	1.96946	BD*(1) C1-C6	0.02807	14.43	1.26	0.059
			BD*(1) C6-Cl19	0.032	20.25	0.85	0.057
σ -σ*	BD(1) C1-C6	1.9797	BD*(1) C1-C2	0.01495	12.22	1.3	0.055
			BD*(1) C5-C6	0.0281	14.31	1.29	0.059
π -π*	BD(2) C1-C6	1.65918	BD*(2) C2-C3	0.37843	77.36	0.3	0.067
			BD*(2) C4-C5	0.29557	76.41	0.3	0.067
σ -σ*	BD(1) C2-C3	1.96904	BD*(1) C1-C2	0.01495	11.63	1.28	0.053
			BD*(1) C3-C4	0.02657	17.7	1.28	0.066
π -π*	BD(2) C2-C3	1.6255	BD*(2) C1-C6	0.38925	90.54	0.27	0.069
			BD*(2) C4-C5	0.29557	78.66	0.29	0.067
			BD*(2) C13-N15	0.13765	57.99	0.23	0.054
σ -σ*	BD(1) C3-C4	1.97238	BD*(1) C2-C3	0.02439	17.03	1.27	0.064
π -π*	BD(2) C4-C5	1.6566	BD*(2) C1-C6	0.38925	89.12	0.27	0.068
			BD*(2) C2-C3	0.37843	85.31	0.28	0.068
π -π*	BD(2) C13-N15	1.93513	BD*(2) C2-C3	0.37843	38.37	0.37	0.057
			BD*(1) C13-N15	0.01983	5.56	0.62	0.026
n -σ*	LP(2) O18	1.93168	BD*(1) N11-C16	0.05307	42.47	0.54	0.067
n -π*	LP(3) Cl19	1.92127	BD*(2) C1-C6	0.38925	53.26	0.32	0.062
π*-π*	BD*(2) C1-C6	0.38925	BD*(2) C2-C3	0.37843	837.18	0.02	0.084
			BD*(2) C4-C5	0.29557	640.53	0.02	0.08

in chemical stability. The HOMO represents the capability to contribute an electron, LUMO as an electron acceptor represents the capability to gain an electron. The energy gap for **3d** was calculated using the B3LYP/6-311++G(d,p) level of theory. The bioactivity and chemical activity of the molecule depends on the eigenvalue of HOMO, LUMO, and energy gap. In the title compound **3d**, the HOMO is located over entire molecule except few hydrogen atoms and the energy is calculated at about -8.17959 eV. The LUMO energy occupied in the whole molecule except a few C and H atoms and measured the LUMO value is -3.00398 eV. The energy gap of HOMO and LUMO could be determined at about 5.17561 eV, which leads the molecule to become less stable and more reactive. The frontier molecular orbital of **3d** (HOMO–LUMO) is shown in Figure 7. The physico-chemical properties of **3d** are listed in Table 7. Gauss-Sum 2.2 Program [37] was used to calculate group contributions to the molecular orbitals (HOMO and LUMO) and prepare the density of the state (DOS) as shown in Figure 8.

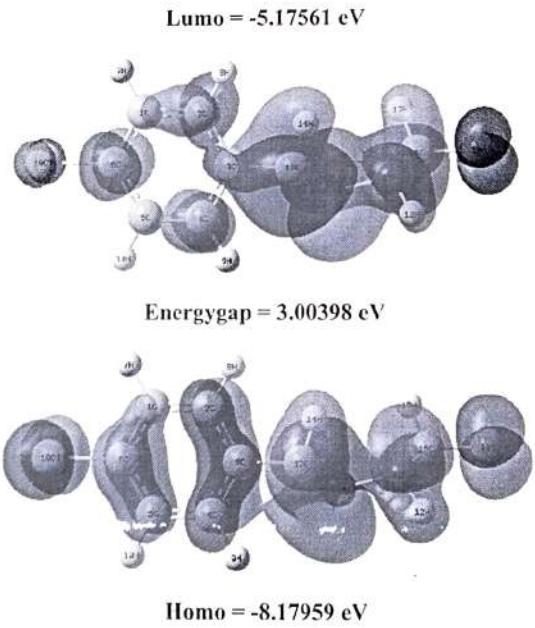


Figure 7. The Frontier molecular orbital of **3d**.

3.3.5. MEP analysis

Molecular electrostatic potential (MEP) provided the electrophiles tend to negative region and nucleophiles tend to the region of positive. The implicit increases is in the order of red < orange < yellow < green < blue. The different values of the electrostatic potential at the surface are represented by different colours; red represents region of most negative electrostatic potential (preferred site for electrophilic), blue represents regions of most positive electrostatic potential (preferred site for nucleophilic) and green represents regions of zero potential. The MEP diagram was calculated with the B3LYP/6-311++G(d,p) level of basis set and is shown in Figure 9. The MEP surface indicates the negative region is observed over the C–O group of the molecule; hence this site is possible for the electrophilic attack. The

Table 7. The Physico-chemical properties of **3d**.

Parameters	Values
HOMO	−8.17959 eV
LUMO	−5.17561 eV
Energy gap	3.00398 eV
Ionisation potential (IP)	8.17959 eV
Electron affinity (EA)	5.17561 eV
Hardness (η)	−3.00398 eV

COLLEGE OF ARTS & SCIENCE
NAMAKKAL
637 206

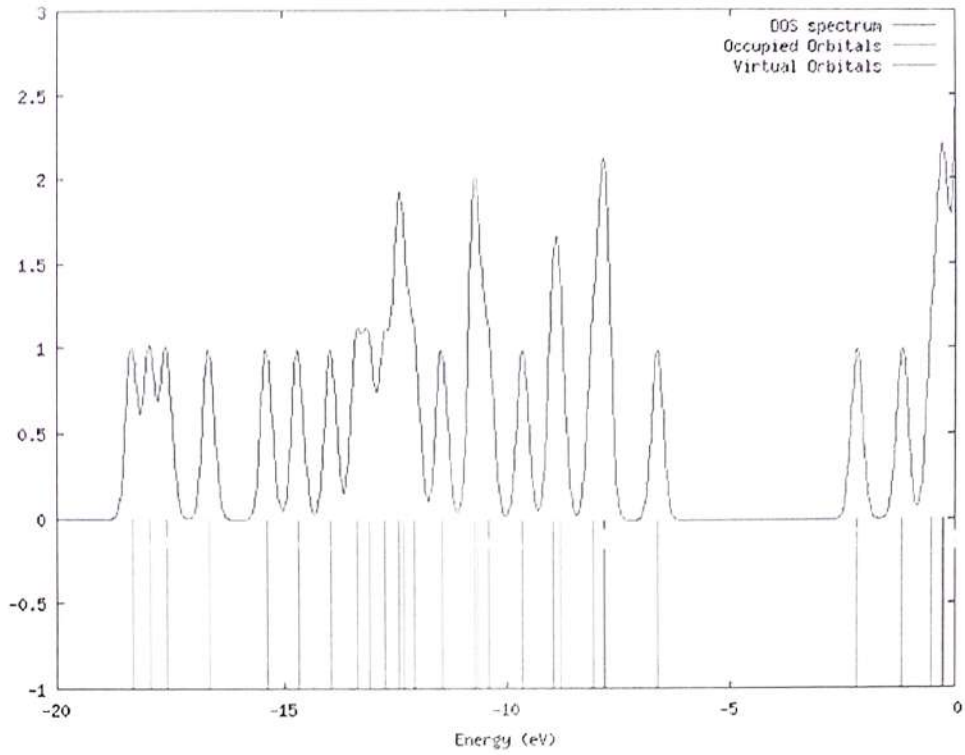


Figure 8. The DOS spectrum of **3d**.

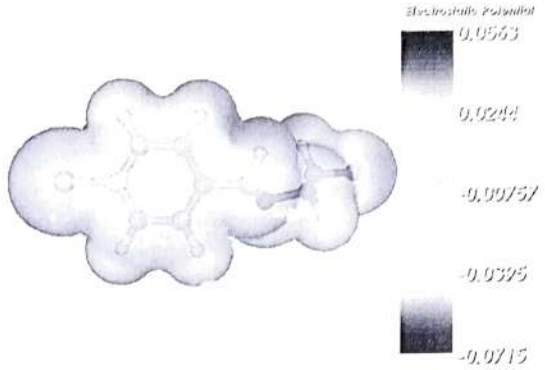


Figure 9. The MEP surface of **3d**.

positive region is observed at all hydrogen atoms in this molecule.

Table 8. The Mulliken and APT charges of **3d**.

Atoms	Mulliken Charges	APT Charges
1C	−0.803785	−0.147522
2C	−0.639857	0.000294
3C	0.150295	−0.040611
4C	−0.011994	−0.021188
5C	−0.438301	−0.158912
6C	0.496054	0.495209
7H	0.188425	0.061314
8H	0.165941	0.039555
9H	0.207872	0.066432
10[illegible]	0.196293	0.060435
11N	−0.061188	−0.871335
12H	0.276259	0.121263
13C	−0.27861	0.271731
14H	0.104924	−0.017922
15N	0.055104	0.18099
16C	0.10092	1.384413
17H	0.131406	0.015514
18O	−0.302831	−1.033373
19Cl	0.463073	−0.406337

3.3.6. Mulliken charges

The Mulliken charges provide net atomic populations in the molecule while electrostatic potentials yield the electric field out of the molecule produced by the internal charge distribution. The charge distributions are calculated by the Mulliken method using the B3LYP/6-311++G(d,p) basis set and atomic charges were listed in Table 8 and the corresponding Mulliken plot is shown in Figure 10. The C16 carbon atom has a more positive charge than the other atoms, which is attached to the chlorine atom. The negative charge is observed at electronegativity atoms (O18/-0.302831 and N11/-0.061188). Hence, the entire hydrogen atom possesses net positive charges.

P.K.R. COLLEGE OF ARTS & SCIENCE
NAMAKKAL
637 206

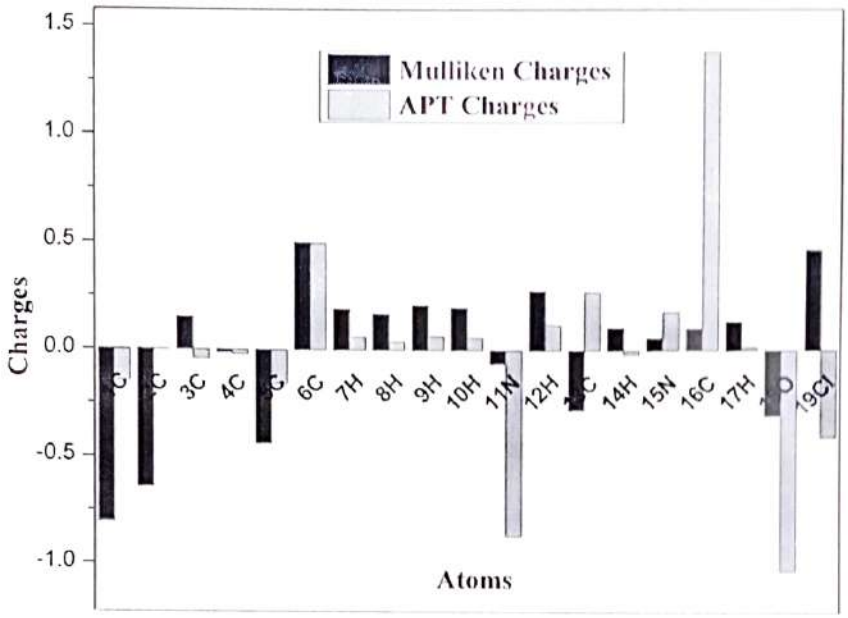


Figure 10. The Mulliken and APT charges of **3d**.

3.4. Pharmacological screening of 3a-j

3.4.1. Antibacterial activity

Target compounds **3a-j** were tested for their in vitro antibacterial activity against five bacterial strains viz., Gram-Positive bacteria species *Enterococcus faecalis*, *Staphylococcus aureus* and Gram-Negative bacteria species *Escherichia coli*, *Klebsiella pneumonia* and *Pseudomonas aeruginosa*. The tested antibacterial activity of the compound was compared with the standard drug of *ciprofloxacin*. The results of zone of inhibition of **3a-j** tested against bacterial strains are summarised in Table 9.

Figure 11 shows the Zone of inhibition in Antibacterial studies of compounds **3a-3j**. Antibacterial activity results showed that compounds **3a**, **3b**, **3c**, **3e**, **3f**, **3g**, **3i** and **3j** failed to inhibit the growth of *K. Pneumonia*, **3a**, **3c**, **3g** and **3h** failed against *E. coli* and **3h** failed against *P. aeuruginaosa*. Likewise compounds **3f**, **3i** and **3j** against Gram-Positive bacteria of *S. aureus* and **3b**, **3c**, **3f**, **3g**, **3h**, **3i** and **3j** against *E. faecalis* bacterial strains. *p*-chloro substituted compound **3d** shows excellent inhibition against *E. Coli*, *S. Aureus* and *E. faecalies*. The *m*-fluoro substituted compound **3e** shown excellent inhibition against *P. Aeruginosa* and good inhibition against *E. facalis* and compounds **3e** and **3g** showed good inhibition against *P. Aeruginosa* and *S. aureus*, respectively while the rest of the compounds shows moderate inhibition against Gram-Negative and Gram-Positive bacterial species.

Table 9. Antibacterial activities of compounds **3a-3j**.

	Zone of inhibition(mm)				
	Gram-Negative			Gram-Positive	
Entry	*K. pneumonia*	*E. coli*	*P. aeruginosa*	*S. aureus*	*E. faecalis*
3a	0	0	11	10	12
3b	0	12	16	11	0
3c	0	0	20	15	0
3d	13	15	15	12	16
3e	0	12	22	15	16
3f	0	10	13	0	0
3g	0	0	13	14	0
3h	0	0	0	18	0
3i	0	8	13	0	0
3j	0	10	13	0	0
Solvent	0	0	0	0	0
Control	15	0	15	10	15

Control – Ciprofloxacin; Solvent – acetone.

3.4.2. Antifungal activity

Figure 12 shows the Zone of inhibition in Antifungal studies of compounds **3a-3j**. The synthesised compounds **3a-j** were investigated for their antifungal activities against five fungal strains viz., *Aspergillus niger*, *Aspergillus flavus*, *Candida albicans*, *Candida glabrata* and *Rhizopus sp.* *Ketoconazole* was used as a control for these antifungal activities.

The antifungal activity of synthesis compounds **3a-j** revealed that all the synthesised compounds showed moderate to good inhibition against the tested fungal strains. But the *p*-fluoro substituted compound **3c** shows excellent inhibition against *A. niger* and *Rhizopus sp.*

P.G. COLLEGE OF ARTS & SCIENCE NAMAKKAL 637 206

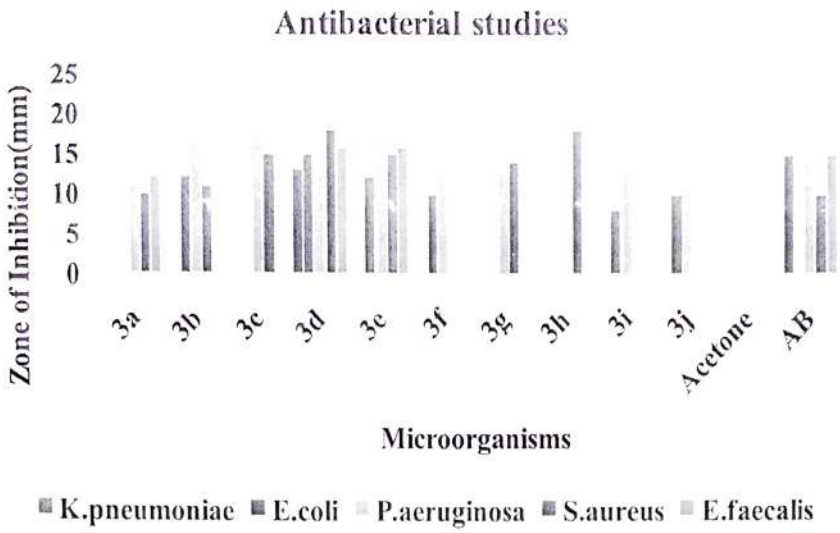


Figure 11. Zone of inhibition in Antibacterial studies of **3a-3j**.

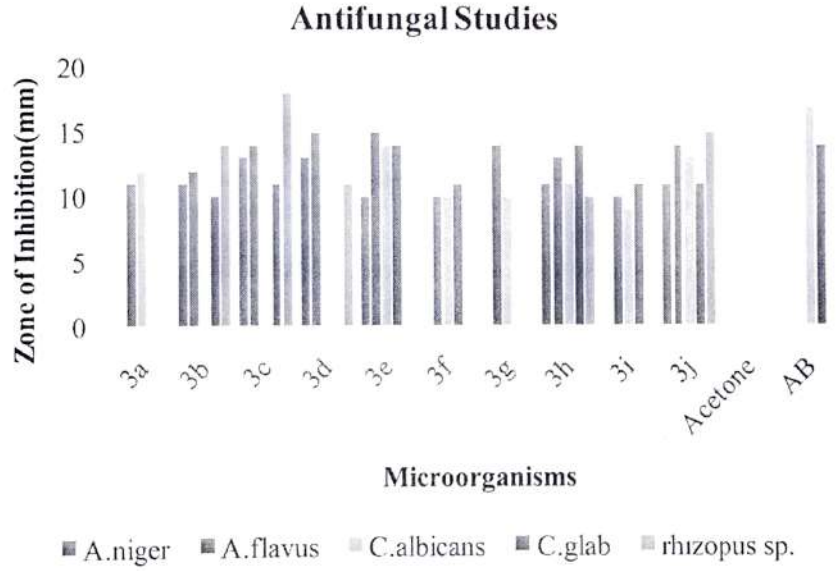


Figure 12. Zone of inhibition in Antifungal studies of **3a-3j**.

While the standard drug has no inhibition. Likewise, *p*-chloro compounds **3d** against *A. niger*, and *A. flavus*. 3-chloro compound **3e** and 2-chloro substituted compound **3i** show excellent activity against *A. flavus* and *Rhizopus sp.* respectively (Table 10)

3.5. Molecular docking

Mycobacterium tuberculosis is a seductive target for the development of new medicine against tuberculosis, a complaint that kills further than two million people each time. Three-dimensional crystal structures of InhA complexed were retrieved from the RCSB (Research Collaboratory for Structural Bioinformatics) protein data bank under PDB ID: 2X22 [38]. The active site of InhA was defined as the collection of residues within 15.0 Å of the bound inhibitor present in the reference structure 2X22. The set impediments were included in the docking runs.

The entire docking calculations were performed using the Auto dock docking module programme. It performs flexible protein–ligand docking and searches for



Table 10. Antifungal activities of compounds **3a**–**3j**.

	Zone of Inhibition(mm)				
Entry	*A. niger*	*A. flavus*	*C. albicans*	*C. glabrata*	*Rhizopus sp.*
3a	0	11	12	0	0
3b	11	12	0	10	14
3c	13	14	0	11	18
3d	13	15	0	0	11
3e	10	15	14	14	0
3f	0	10	10	11	0
3g	0	14	10	0	0
3h	11	11	11	14	10
3i	0	10	9	11	0
3j	11	14	13	11	15
Solvent	0	0	0	0	0
Control	0	0	17	14	0

Control – Ketoconazole; Solvent – Acetone.

Table 11. Hydrogen bond interactions of **Chlorobenzylidene** with amino acids at the active site of **Mycobacterium Tuberculosis Inhibitors.**

		Hydrogen Bonding Interactions		
Compounds	Docking Score	Donor	Acceptor	Distance (Å)
3d	−5.6	TYR158 (O... H-N)	H-N+	**3.5**
Co-Crystal **(5-HEXYL-2-(2-METHYLPHENOXY) PHENOL)**	−4.6	**TYR158(O ... H-O)**	O+	2.8

+Ligand.

favourable interactions between one typically small ligands molecule and a typically larger protein molecule. Docking process, wherein protein preparation inhibited refinement is carried out with a maximum of 20 poses, wherein the side chains are optimised and refinement of residues takes place if the ligands poses are within 5.0Å. The best docked structure was chosen by docking score and the number of amino acids matches (hydrogen bonds) with the original drug complex.

The dock, glide energy and hydrogen bonding interactions of the title compound and co-crystallised ligands are given in Table 11. A view of the X-ray crystal structure of the title compound in the Mycobacterium Tuberculosis Inhibitors Receptor active site showing the key hydrogen contacts between inhibitor and enzyme is depicted in Figures 13 and 14. The cartoon diagram showing the title compound docked at the active site of Mycobacterium Tuberculosis Inhibitors Receptor is depicted in Figure 15. The 2D image of the docking compound is shown in Figure 16.

Molecular analysis of compound (E)-*N*′-(4-chlorobenzylidene) formohydrazide indicated that TYR158 hydrogen bond interaction incorporating the attachment of this ligand to Mycobacterium Tuberculosis Inhibitors acceptor. The co-crystallised ligand also docked well and it shows better relations with active remainders. The results show that **3d** compound has better binding energy and the co-crystallised ligands have comparable interactions. X-ray crystal structures confirmed the expected binding mode, and consideration of binding orientation and electronic properties enabled optimisation to Chlorobenzylidene as a more potent second-generation lead.

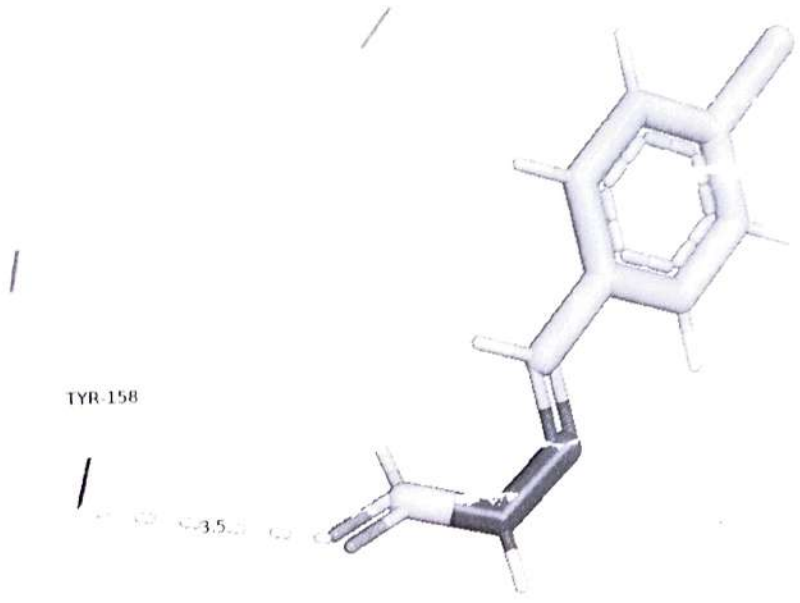


Figure 13. The title compound (**BNC**) in the **Mycobacterium Tuberculosis Inhibitors Receptor** active site showing key hydrogen contacts between **Chlorobenzylidene** inhibitor and enzyme.

P.G.P. COLLEGE OF ARTS & SCIENCE NAMAKKAL 637 206

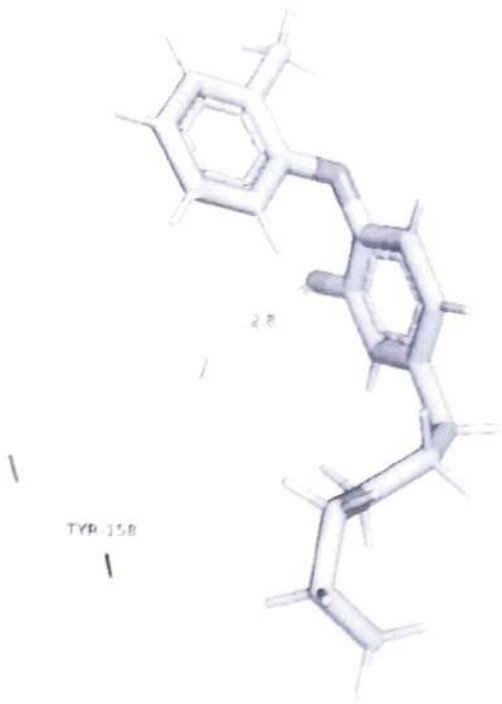


Figure 14. The CO-CRYSTAL compound in the **Mycobacterium Tuberculosis Inhibitors Receptor** active site showing key hydrogen contacts

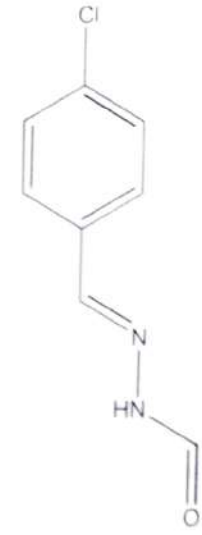


Figure 16. The 2D image of the docking compound

4. Conclusion

The theoretical calculations of compound **3d** were done by using the DFT method for the first time. The optimised geometrical parameters such as bond length, bond angles and dihedral angles were theoretically calculated at the DFT method with B3LYP/6-311++G(d,p) basis

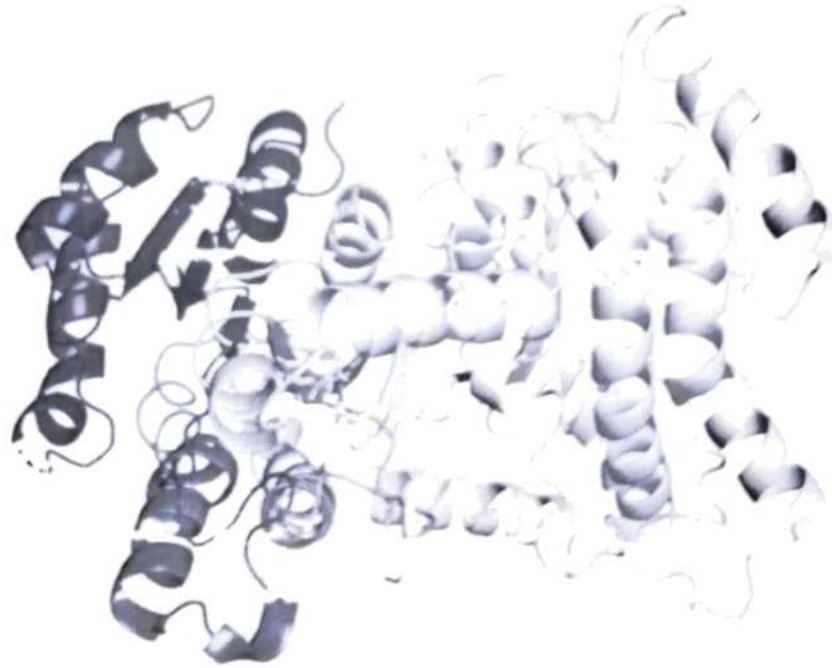


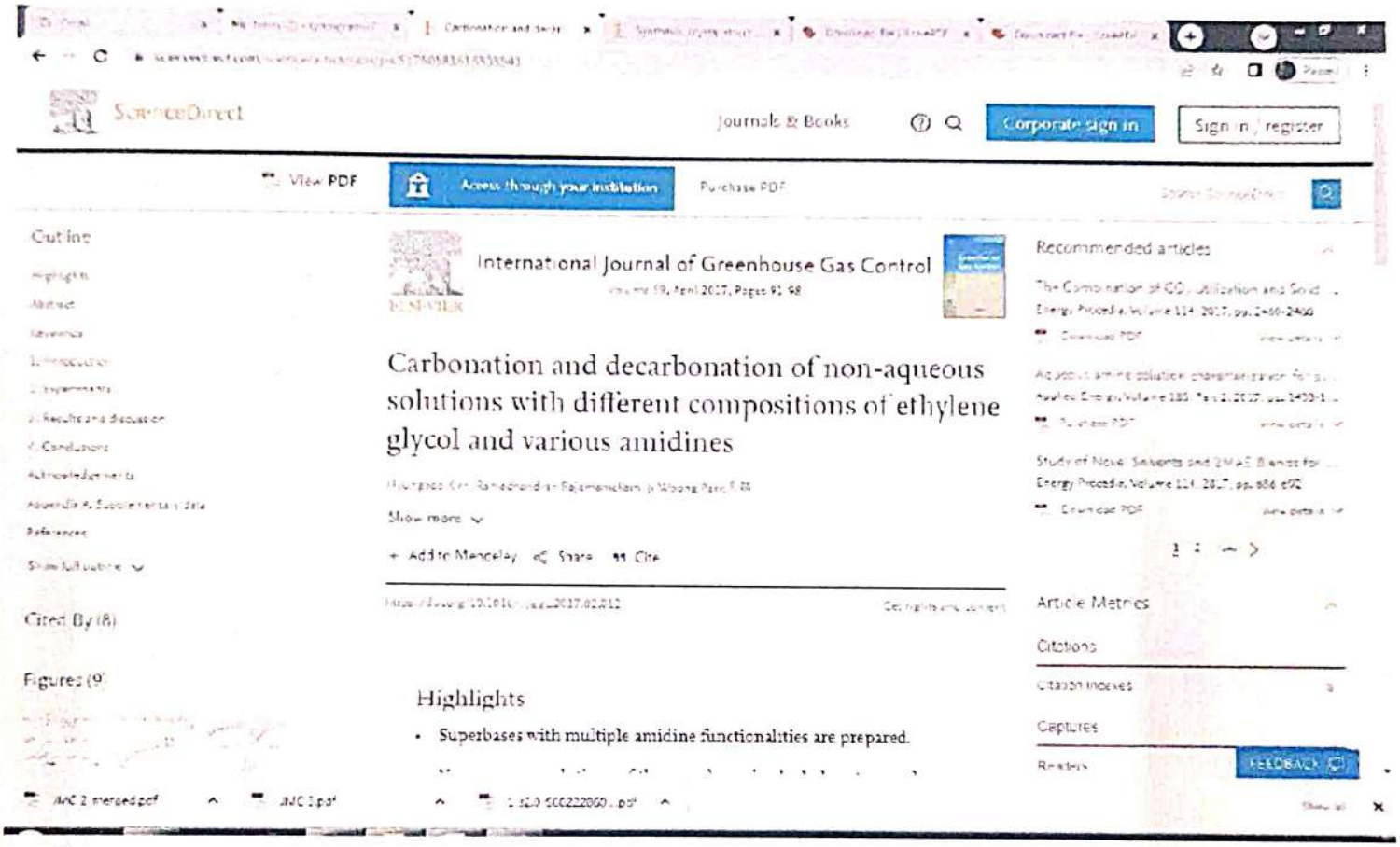
Figure 15. Surface and Cartoon diagram showing the **Chlorobenzylidene** docked at the active site of **Mycobacterium Tuberculosis Inhibitors**



[50] [illegible]
[51] [illegible]
[52] [illegible]
[53] [illegible]
[54] [illegible]
[55] [illegible]
[56] [illegible]
[57] [illegible]
[58] [illegible]



PRINCIPAL
PGP College of Arts and Science
Namakkal.



P.G.P. COLLEGE OF ARTS & SCIENCE
NAMAKKAL
637 001

International Journal of Greenhouse Gas Control 59 (2017) 91–98

Contents lists available at ScienceDirect

International Journal of Greenhouse Gas Control

Journal homepage: www.elsevier.com/locate/ijggc

Carbonation and decarbonation of non-aqueous solutions with different compositions of ethylene glycol and various amidines

Hyungsoo Kim, Ramachandran Rajamanickam, Ji-Woong Park *

School of Materials Science and Engineering and Research Institute for Solar and Sustainable Energies, Gwangju Institute of Science and Technology, 123 Cheomdan-gwagiro, Buk-gu, Gwangju 61005, Republic of Korea

ARTICLE INFO

Article history:
Received 6 July 2016
Received in revised form
29 December 2016
Accepted 17 February 2017

Keywords:
Non-aqueous absorbent
Amidine
Solvent effect
Carbon dioxide capture
Protic solvent
Superbase

ABSTRACT

A mixture of equivalent amounts of amidine, alcohol, and carbon dioxide forms alkylcarbonate amidinium salts. Here we studied the effect of the composition of solutions consisting of ethylene glycol (EG) as the alcohol and one of various amidines on their ability to absorb and desorb carbon dioxide. Compounds containing single or multiple formamidine groups were synthesized and dissolved in EG. The ability of these solutions to absorb carbon dioxide was studied for various ratios of EG to amidine and at various temperatures. An excess of at least ten equivalents of EG relative to the amidine was required for rapid and complete reaction of the base with carbon dioxide. Excess EG also reduced the viscosity of the solution, and in this way increased the absorption rate. However, the excess EG appeared to have stabilized the formed alkyl carbonate salts via hydrogen bonding, resulting in a relatively low degree of decarbonation of the solution at elevated temperatures. This effect would cause the working capacity to be decreased were this type of material be used for carbon dioxide capture applications. Our results suggest that, in general, the compositions of the alcoholic solutions of superbases need to be optimized to achieve high-efficiency absorption and desorption of carbon dioxide.

© 2017 Elsevier Ltd. All rights reserved.

1. Introduction

Carbon dioxide emitted from the combustion of fossil fuels has been considered to cause global warming and ocean acidification (Taub, 2010). To counter these threats, a material that has a large capacity to capture CO_2 and that can be regenerated using little energy has been sought. The most established CO_2-capture technology is based on aqueous amine solutions (Rochelle, 2009); however, the water-based systems have several drawbacks including poor energy efficiency (Yu et al., 2009). Numerous absorbents have been introduced in recent years. Non-aqueous CO_2-capture liquids have recently been suggested as a potential alternative to aqueous amine solutions due to their low heat capacities. Examples of these liquids are anhydrous amines (Im et al., 2011), ionic liquids (Bates et al., 2002; Cadena et al., 2004; Jessop et al., 2005), task-specific ionic liquids (Wang et al., 2010) and superbases (Kim and Park, 2010). A variety of solid-state absorbents or adsorbents have also been introduced in recent decades (Kim and Park, 2010; Gray et al., 2008; Hicks et al., 2008; Yang et al., 2012; Lee et al., 2014).

Among these new materials, the mixtures consisting of superbases (amidines or guanidines) and aliphatic alcohols that can bind CO_2 reversibly to form alkylcarbonate salts have been studied as potential CO_2 absorbents due to their efficient CO_2 absorption at low temperatures as well as the low heat capacity of the non-aqueous solutions. In the mixtures of a superbase and an alcohol, the carbonation transforms the initially non-ionic solutions into polar ionic liquids, which upon heating are transformed back into the non-ionic form (Jessop et al., 2005; Liu et al., 2006). The ion pairs made up of protonated superbase cations and alkylcarbonate anions are stabilized by the strong hydrogen bonding between the cations and anions. Such carbonate salts are stable even at elevated temperatures. Our recent study has shown the stability of the carbonated ionic species in the organic solution to be highly dependent on the composition of hydrogen-bonding components in the solution (Rajamanickam et al., 2015). Such dependence on composition may apply to other organic CO_2 absorbents containing little or no water.

The product of the reaction of the superbase/alcohol mixture with CO_2 is an adduct of the superbase, alcohol, and CO_2 in a 1:1:1 molar ratio (Jessop et al., 2005; Heldebrant et al., 2005). The composition of the absorbent solution, for example, the amidine-to-alcohol molar ratio, may greatly affect the capture performance. While use of alcohols in amounts as small as possible would

* Corresponding author.
E-mail address: jiwoong@gist.ac.kr (J.-W. Park).

http://dx.doi.org/10.1016/j.ijggc.2017.02.012
1750-5836/© 2017 Elsevier Ltd. All rights reserved.

P.G.P. COLLEGE OF ARTS & SCIENCE
NAMAKKAL
637 206

help to increase the gravimetric capture capacity of absorbents (Heldebrant et al., 2008), a sufficient amount of the alcohol component is needed to optimize the absorption rate, equilibrium CO_2 loading and viscosity.

Here we present a systematic study of the carbonation and decarbonation chemistries of mixtures of an alcohol, specifically ethylene glycol (EG), and compounds containing formamidine groups. We synthesized several amidine derivatives containing one to three amidine groups per molecule and mixed them with the EG to produce various solutions. We studied the effect of the EG-to-amidine ratio on the degree of carbonation and decarbonation of the solutions at different temperatures. The best carbonation and decarbonation conditions were sought to achieve the maximum absorption performance and reaction rate while minimizing the difference between the optimal temperatures for absorption and regeneration. We also studied the effect of the chemical structure of the amidines and the composition of their solutions in EG on the viscosity of the resultant solutions to achieve lower solution viscosities that are essential for higher absorption efficiency and reaction rate as well as for their applicability for CO_2 capture process.

2. Experimental

2.1. Materials and characterization

All reagents, unless otherwise noted, were obtained from a commercial supplier (Sigma Aldrich, TCI) and were used without further purification. THF was distilled over sodium benzophenone ketyl in a nitrogen atmosphere. Liquid amines were dried over CaH_2 overnight and distilled under reduced pressure. CO_2 was dried by passing it through a $CaSO_4$ column for capture experiments. ^1H and ^{13}C NMR spectra were recorded on a JEOL-DELTA2 (400 MHz) spectrometer in $CDCl_3$ (reference 7.26 ppm for ^1H and 77.16 ppm for ^{13}C NMR) or DMSO-d_6 (reference 2.50 ppm for ^1H and 39.52 ppm for ^{13}C NMR). Viscosity was measured using a Brookfield DV-II+ Pro viscometer at the desired temperature with a cone and plate geometry (cone radius 24 mm, 0.8° cone angle). The formulation was taken into the cup of the viscometer and measured using spindle CP-40. The stabilization energy of amidinium alkylcarbonate salts (BBF/EG) resulting from the addition of excess EG was measured using a Thermal Hazard Technology (THT) micro reaction calorimeter (μRC) with μW sensitivity at 40 °C. The BBF/EG carbonate salts with 1 eq. EG was prepared from BBF/EG 2 eq. mixture after full CO_2 absorption for 24 h at 60 °C. Heat energy was produced upon addition of excess EG.

2.2. General procedure for the preparation of amidine derivatives

An amine (1 eq.) and *N,N*-dimethylformamide dimethyl acetal (3 eq.) were refluxed with stirring in THF (30 mL/g amine) under nitrogen for 3 h. The reaction was monitored by ^1H NMR analysis. After completion of the reaction, the solution was cooled to room temperature and the excess solvent was evaporated by using a rotary evaporator. Then, the amidine was subjected to reduced pressure overnight at room temperature. The obtained amidine was used to capture CO_2 without further purification.

2.2.1. N'-(4-Methylphenyl)-N,N-dimethyl formamidine (mPF)

^1H NMR (400 MHz, DMSO): 7.65 (s, 1H), 6.98 (m, 2H), 6.79 (m, 2H), 2.88–2.96 (d, 6H), 2.22 (s, 3H). ^{13}C NMR (DMSO): 153.2, 149.5, 130.2, 129.3, 120.5, 39.1, 20.4. FT-IR (KBr): 3024, 2916, 2806, 1635, 1605, 1510, 1102. Yield: >98%.

2.2.2. N'-Benzyl-N,N-dimethylforamidine (BF)

Transparent yellow liquid; ^1H NMR (400 MHz, DMSO): 7.49 (s, 1H), 7.15–7.29 (m, 5H), 4.33 (s, 2H), 2.79 (s, 6H). ^{13}C NMR (DMSO): 155.7, 142.7, 128.1, 127.4, 126.1, 62.9, 58.6. FT-IR (KBr): 3029, 2921, 1652, 1605, 1510, 1104. Yield (%): >99%.

2.2.3. N',N''-(1,4-Phenylenebis(methylene))bis(N,N-dimethylformimidamide) (PBMBF)

^1H NMR (400 MHz, DMSO): 7.47 (s, 2H), 7.12 (s, 4H), 4.29 (s, 4H), 2.77 (s, 12H). ^{13}C NMR ($CDCl_3$): 155.9, 140.4, 127.5, 59.4, 37.3. FT-IR (KBr): 3048, 2916, 2816, 1642, 1488, 1092. Yield: >99%.

2.2.4. N',N''-(Ethane-1,2-diyl)bis(N,N-dimethylformimidamide) (EBF)

^1H NMR (400 MHz, $CDCl_3$): 7.24 (s, 2H), 3.34 (s, 4H), 2.80 (s, 12H). ^{13}C NMR ($CDCl_3$): 156.1, 58.3, 37.3. FT-IR (KBr):2914, 2845, 1646, 1110. Yield: >92%.

2.2.5. N',N''-(Butane-1,4-diyl)bis(N,N-dimethylformimidamide) (BBF)

Transparent yellow liquid; ^1H NMR (400 MHz, $CDCl_3$): 7.25 (s, 2H), 3.22 (m, 4H), 2.81 (s, 12H), 1.49 (m, 4H). ^{13}C NMR ($CDCl_3$): 154.6, 55.2, 36.9, 30.1. FT-IR (KBr): 2922, 1651, 1106. Yield: >99%.

2.2.6. N',N'',N'''-(Nitrilotris(ethane-2,1-diyl))tris(N,N-dimethylformamidine) (NETF)

^1H NMR (400 MHz, $CDCl_3$): 7.33 (s, 3H), 3.30 (t, 6H), 2.81 (s, 18H), 2.62 (t, 6H). ^{13}C NMR ($CDCl_3$): 155.8, 58.0, 54.6, 37.2. FT-IR (KBr): 2916, 2845, 1648, 1109. Yield: >99%.

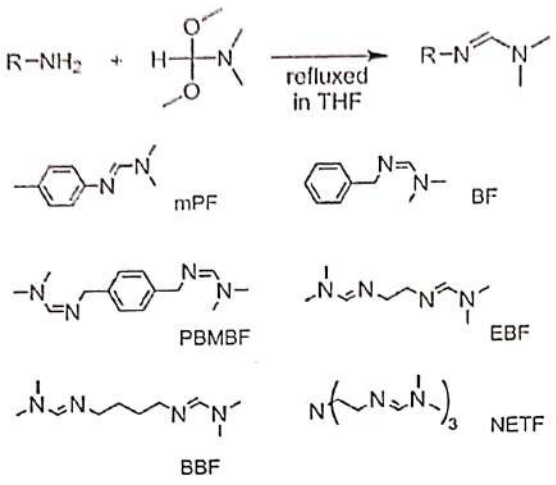
2.3. General procedure for CO_2 absorption/regeneration

The amidine derivative and EG were degassed overnight prior to use. The CO_2 at atmospheric pressure was bubbled through about 15.0 g of an amidine/EG solution in a customized glass flask under a CO_2 flow of 100 and 10 mL/min for absorption and regeneration, respectively. The flask was immersed in an oil bath pre-heated at the desired temperature. The solution was stirred to produce a homogeneous solution prior to starting the absorption process. The amount of CO_2 absorbed was determined by measuring the difference between the mass of the total glassware without the water condenser before and after CO_2 absorption after cooling the reaction solution to room temperature. The molar CO_2 loading and capacity of the mixtures were also determined by measuring the weight at regular time interval. The mass of CO_2 absorbed was determined to within ±0.1 mg by using an analytical balance.

3. Results and discussion

3.1. Synthesis of amidines

A series of organic compounds containing one to three amidine groups per molecule (Scheme 1). Amidines have been synthesized by several methods using organometallic catalysts (Benati et al., 2006; Garigipati, 1990), acidic catalysts (Weintraub et al., 1968; Schnur, 1979), and other methods (Dräger et al., 2002; Spychała, 1999; Zhu and Lu, 2010; Kumagai et al., 2004). In the present study, condensation of aromatic or aliphatic primary amines with *N,N*-dimethylformamide dimethyl acetal (1:3 eq.) in dry THF gave the amidine derivatives in high yield. The synthetic conditions were modified slightly from the known method according to the chemical structures of the reactant amines (Porcheddu et al., 2009). The transformations of the aromatic amines to the corresponding



Scheme 1. Synthesis of various formamidines.

amidines required longer reaction times than did the transformations of the aliphatic amines. Scheme 1 also shows the names (abbreviations) and chemical structures of the various amidine derivatives we synthesized. PBMBF and EBF were obtained as crystalline solids, whereas mPF, BF, BBF and NETF were obtained as liquids.

3.2. Absorption of carbon dioxide by amidine/EG mixtures

We first investigated the CO_2 absorption behavior of mixtures of the alcohol EG with the aromatic amidine mPF or with the aliphatic amidine BF; specifically, the relative reactivities of these mixtures toward carbonation were compared (Fig. 1). Molar CO_2 loading, which is the number of moles of CO_2 absorbed by one equivalent of amidine functionality, was plotted against the duration of time that CO_2 was made to flow into each of the solutions, specifically 30% mPF or BF in EG (Fig. 1b). The rate of flow of the CO_2 gas into the solution in the container shown in Fig. S1 (ESI) was 100 mL/min and the change in the weight of the container was monitored with time. As shown in Fig. 1b, the number of moles of CO_2 loaded per equivalent of amidine differed considerably for the two amidines: the EG solution of BF showed a molar CO_2 loading of 0.9 within 2 h; in contrast, relatively little CO_2 loaded into the EG solution of mPF. Considering that a gram of EG itself is able to simply physically absorb about 20 mg of CO_2 between RT and 40 °C (Yang et al., 2011), the chemical absorption by mPF must have been negligible. The poor CO_2 absorption by mPF was attributed to the lower basicity of aromatic amidines; the pK_a value of aromatic amidine is 7.75 in ethanol whereas that of aliphatic formamidine is about 10.04 at 20 °C (Raczynska et al., 1988).

We next investigated the effect of the ratio of EG to amidine on the rate and efficiency of the carbonation. Fig. 2 shows the CO_2 absorption behaviors of the BF/EG and BBF/EG mixtures as a function of the EG-to-amidine ratio, where BF and BBF are amidines containing one and two functional groups, respectively. The most prominent effect caused by the addition of more EG to either amidine/EG mixture was the increase in the rate of carbonation. The carbonation rates of both BF and BBF increased with an increasing amount of EG. The absorption graphs showed that plateaus corresponding to saturation were reached more quickly for the smaller amounts of amidines in EG (hence the high EG-to-amidine ratio). The plateau was reached in 40 min by the BF solution at molar CO_2 loading of 1.0 in the presence of 20 equivalents of EG, whereas it was in 80 min at molar CO_2 loading of 0.9 in the presence of 12 equivalents of EG. The higher carbonation rate was obviously the result of higher reactant (EG) concentration. However, although the reaction rate and molar CO_2 loading increased with the amount of EG of the solutions, the addition of more EG caused the gravimetric capacity of the solutions to decrease. In other words, as the concentration of amidine is lowered by addition of more EG to the solution, the weight of CO_2 absorbed per unit weight of the total solution decreases. High gravimetric capacity is important for lowering the energy cost for heating the solution in the regeneration process.

Fig. 2a and b also shows that BBF reacts with CO_2 at higher rates than BF at the same ratios of the number of hydroxy to amidine functional groups that are present in their solutions. In addition to the reaction rate, the number of amidine groups per molecule affected how the molar CO_2 loading and the corresponding gravimetric absorption capacity changed with solution composition. The amount of CO_2 absorbed by the EG solution of BF (Fig. 2c) or by that of BBF (Fig. 2d) was plotted as a function of the number of equivalents of EG per equivalent of the amidine (also denoted as the "EG-to-amidine equivalent ratio". Note that one mole of EG was considered to be two equivalents because of its two hydroxyl groups and that the number of amidine groups in each superbase is equal to the equivalent number for one mole.) At each of these EG-to-amidine ratios, the gravimetric CO_2 absorption capacity of BBF was higher than that of BF. Achieving a CO_2 molar absorption efficiency of 1.0 required about 20 equivalents of EG per equivalent of BF, but only 10 equivalents of EG per equivalent of BBF, indicating that the BBF solution absorbed CO_2 more efficiently than did the BF solution at higher amidine concentrations. Fig. 2c and d indicates that both the molar CO2 loading and the gravimetric capacity of BBF also better than BF.

Fig. 3 shows the CO_2 absorption performance of the solutions of five amidines (BF, PBMBF, EBF, BBF, and NETF) in EG when purged with CO_2 at 40 °C for 2 h. In each case, the solution containing fewer than five equivalents of EG per equivalent of amidine absorbed less than 0.5 mol CO_2 per mol amidine, indicating that none of the compounds reacted completely with CO_2 when the amidine concentration was relatively high. For more than 80% of the amidine molecules to be utilized for carbonation, at least about five equivalents of EG must be included per equivalent of amidine.

When comparing identical EG-to-amidine ratios, the different amidines absorbed CO_2 with different levels of efficiency. The amidines containing multiple functional groups separated by an alkyl spacer, i.e., BBF and NETF, absorbed more moles of CO_2 per amidine group than did the other amidines for each EG-to-amidine ratio tested. PBMBF, which has a para-xylene unit in the core, showed a relatively good absorption capacity (see Fig. S20). However, the viscosity (Table S1) of the carbonated PBMBF solution increased the highest as compared with other amidines. EBF, having a short CH_2CH_2 spacer connecting the two amidine groups, absorbed the fewest moles of CO_2 per amidine group. This low absorption level may have been due to the resulting short distance between the two amidinium cations formed upon carbonation. Solvation of two nearby ionic charges in organic solutions is generally unfavorable. The gravimetric CO_2 absorption capacities of BBF and NETF were observed to be about 50% greater than that of the single-functional-group-containing amidine BF (Fig. 3b), due to their lower equivalent molecular weights per amidine group.

After a certain point, diluting the mixtures (i.e., increasing the EG-to-amidine ratio) any further did not improve molar CO_2 absorption performance. The capacity improvement resulting from the reduction in viscosity was counteracted by the consequences of simply having too little amidine in the mixture. Thus, diluting the mixtures too much neither improved molar CO_2 loading nor absorption capacity significantly.

P.G.P. COLLEGE OF ARTS & SCIENCE NAMAKKAL 637 206

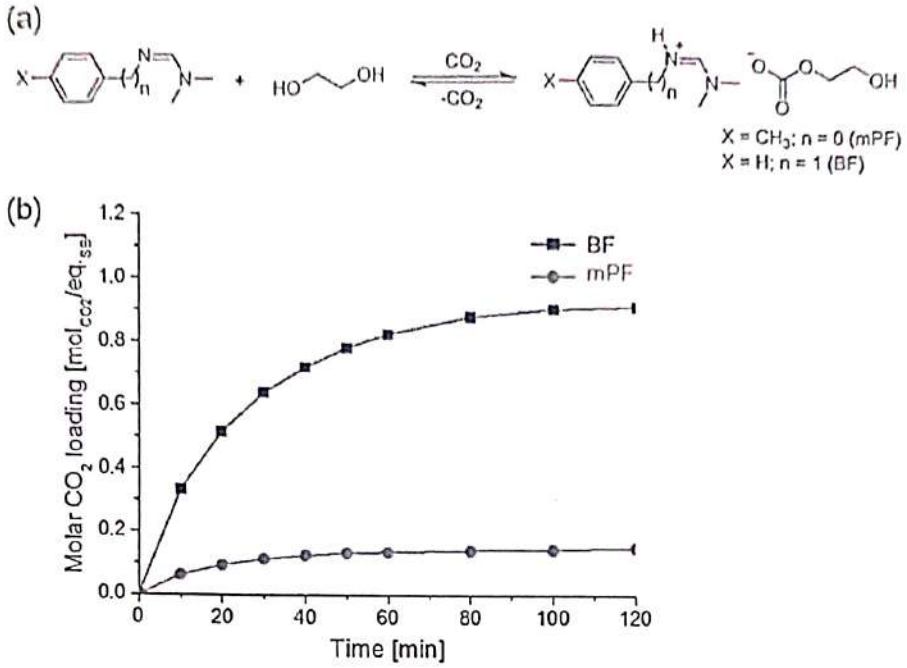


Fig. 1. (a) Carbonation reaction of BF and mPF in EG. (b) Molar CO_2 loadings at various reaction times for 30 wt% BF and mPF solutions in EG. CO_2 gas was made to flow into the solution at a rate of 100 mL/min at 40 °C.

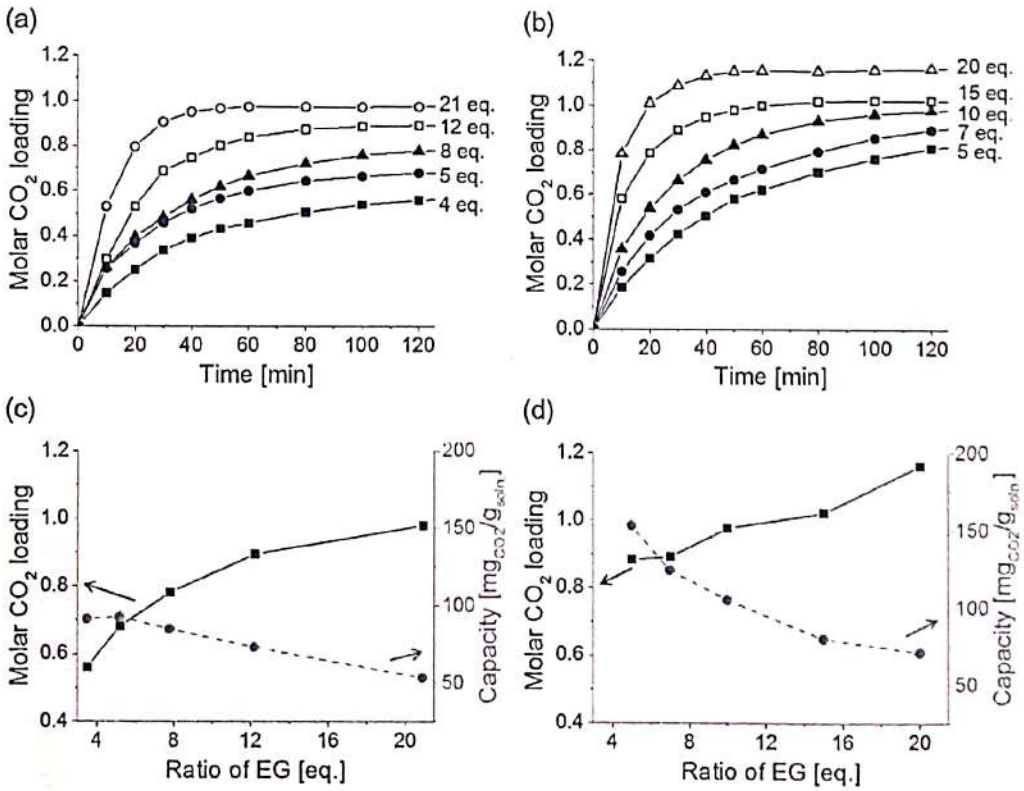


Fig. 2. Absorption of CO_2 by amidine/EG solutions with different numbers of equivalents of EG per equivalent of amidine (i.e., "Ratio of EG [eq.]" in the figure). (a, b) CO_2 loading per equivalent of (a) BF and (b) BBF, for 30 wt% amidine in EG as a function of time under a CO_2 flow at a rate of 100 mL/min at 40 °C. (c, d) Plot of the equilibrium CO_2 loading per base and the gravimetric capacity of the (c) BF and (d) BBF solutions, versus the EG/amidine equivalent ratio.

3.3. Viscosity of the solutions of amidines in EG

Carbonation of amidine/alcohol mixtures generates ion pairs. In organic solvents, the positive and negative ions are not completely separated and tend to exist in the paired form resulting from intermolecular electrostatic interactions (Rohan et al., 2012; Lam et al., 2005). This means that EG, which contains two hydroxyl groups,

P.T.M. COLLEGE OF ARTS & SCIENCE NAMAKKAL 637 206

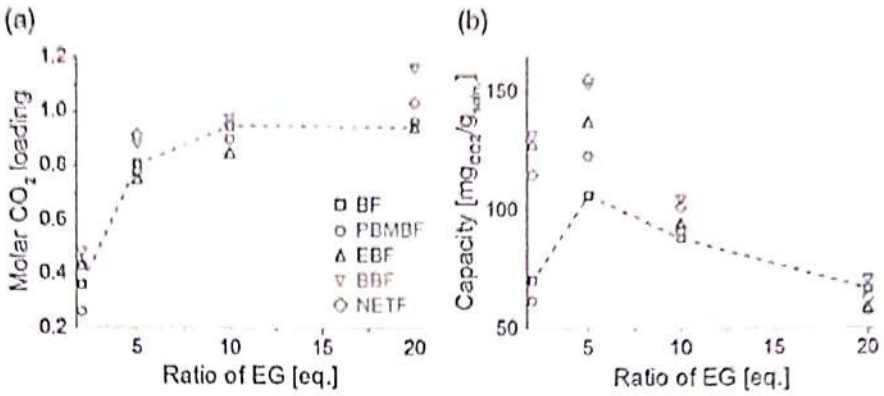


Fig. 3. Absorption of CO_2 by the amidine/EG solutions with different numbers of equivalents of EG per equivalent of amidine at 40 °C for 2 h. (a) Molar CO_2 loading and (b) gravimetric capacity under CO_2 flowing at a rate of 100 mL/min.

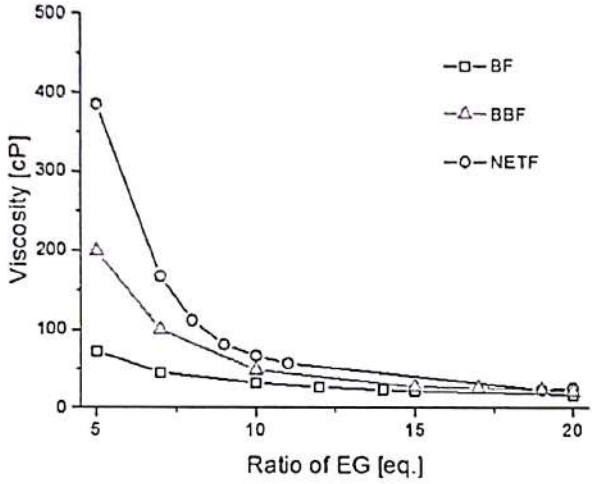


Fig. 4. Viscosity values of carbonated amidine/EG solutions as a function of the EG-to-amidine equivalent ratio at 40 °C.

and the amidines containing multiple functional groups form an electrostatically chained polymer upon being carbonated. The carbonated ionic species are then stabilized by hydrogen bonding of excess EG molecules as has been shown by our previous study (Rajamanickam et al., 2015).

Strong intermolecular electrostatic interactions in the carbonated organic absorbent should result in a steep increase in the viscosity of the solution, which causes problems when such absorbents are applied to the carbon capture process (Zhou et al., 2004). The high viscosity restricts the diffusion of CO_2 in the solution and decreases the rate of absorption of CO_2 significantly. Previous studies on using superbases for CO_2 capture showed that the superbases yielding highly viscous solutions or solid salts exhibited low CO_2 absorption capacity (Kim and Park, 2010; Heldebrant et al., 2011; Koech et al., 2013). The viscosity of solutions is of course reduced by addition of small molecule components; however, the amount of dilution needs to be kept to a minimum for the solution to display a high gravimetric CO_2 absorption of the entire solution. Fig. 4 shows the viscosity values of fully carbonated amidine-EG mixtures as a function of the EG-to-amidine equivalent ratio for each of three amidine compounds, BF, BBF, and NETF, having different number of aliphatic amidine groups. The viscosity of the solutions of the five amidines including BF, BBF, and NETF before and after carbonation are listed in Table S1. The solutions of the amidines that exhibited too high viscosity at low EG-to-amidine ratios were excluded from further study. As expected, the viscosity of the carbonate solutions increased rapidly with decreasing amounts of EG. The rate of viscosity increase with reducing the amount of EG was observed to be different according to the number of functionality. The viscosity of the compound with larger number of amidine functionalities showed steeper dependence on the equivalent number of EG. Large viscosity increase is most likely caused by the intermolecular hydrogen bonding network between EG and carbonate anions. High viscosity affects negatively the rate of carbonation reaction (Fig. 2). In addition, the low absorption efficiency of the mixture at low EG-to-amidine ratios (Figs. 2 and 3) may be partly accounted for by the utilization of hydroxyl groups of EG for hydrogen bonding with the carbonate anions.

3.4. Absorption of CO_2 by BBF/EG solutions at various temperatures

The composition of the amidine/EG solution also affects the degree of carbonation of the absorbent at elevated temperatures. We set out to determine the optimal CO_2-absorption temperature for the best-performing amidine/EG solution, i.e., BBF/EG, at various EG-to-BBF ratios, and did so for each of these BBF/EG solutions by measuring their equilibrium CO_2 absorption levels at various temperatures. Each solution was continuously purged under constant CO_2 flow; thus, the CO_2 partial pressure of each solution was kept constant at 1 atm.

Fig. 5a shows the molar CO_2 loading of the BBF/EG mixture with various amounts of EG (two equivalents to ten equivalents) as a function of temperature. The equilibrium molar CO_2 loading of BBF increased as the relative number of equivalents of EG included was increased throughout the range tested. Moreover, about ten equivalents of EG were required for the complete consumption of the available amidines by the carbonation reaction. The CO_2 absorption generally increased with temperature in the range below 60 °C, and then decreased with temperature above 60 °C. The temperature increase above 60 °C might have shifted the equilibrium toward the decarbonated state by reducing the stability of the amidinium alkylcarbonate salts. Fig. 5b shows the rate of CO_2 absorption of BBF/EG mixture with five equivalents of EG for various temperatures. The initial absorption rate (the initial slope of curve) increased with temperature. The molar CO_2 loading started to decrease when the temperature was raised over 60 °C. From these data we set the maximum carbonation temperature of the amidine/EG solutions to be 60 °C.

M.G.P. COLLEGE OF ARTS & SCIENCE NAMAKKAL 637 206

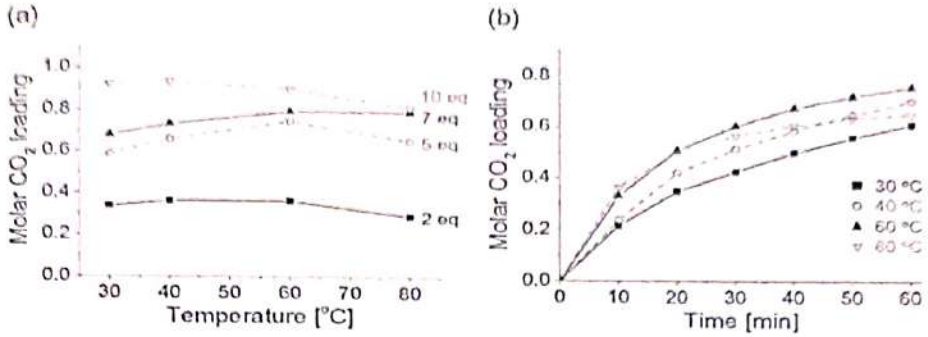


Fig. 5. (a) Molar CO_2 loading of BBF/EG mixtures as a function of temperature. (b) Molar CO_2 loading of the mixture of BBF with 5 eq. of EG as a function of time. Pure CO_2 was bubbled through the mixture at 100 mL/min for 1 h.

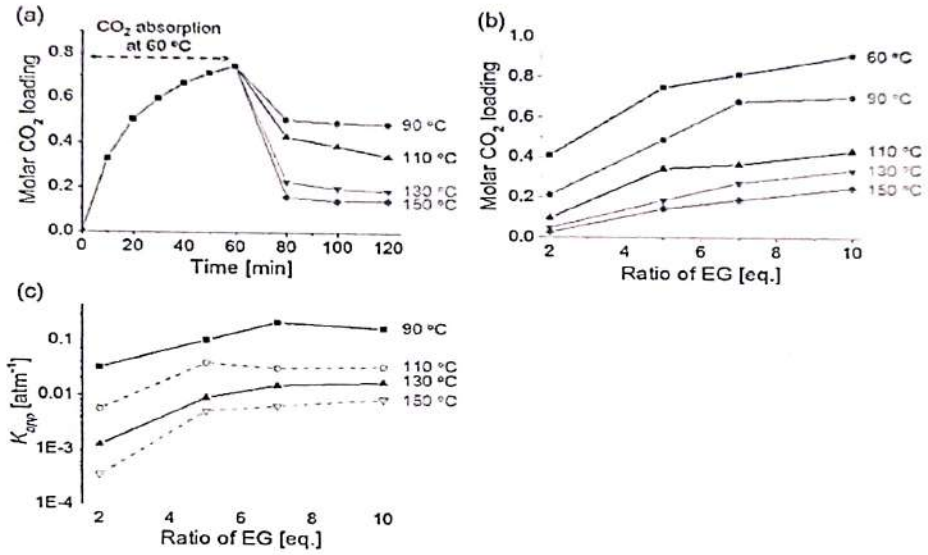


Fig. 6. (a) Change of molar CO_2 loading of a 5 eq. BBF/EG mixture when bubbled with CO_2 for 1 h at 60 °C and subsequently for 1 h at higher temperatures. (b) Molar CO_2 loading of BBF/EG at various temperatures as a function of EG-to-BBF equivalent ratios. (c) The apparent equilibrium constant (K_{app}) of carbonation for various molar ratios of EG to BBF and at various temperatures. Pure CO_2 was bubbled through the mixture for absorption and regeneration at 100 and 10 mL/min, respectively.

3.5. Thermal decarbonation of the carbonated BBF/EG solutions

Once the solutions were fully carbonated, their temperatures were raised to a higher value and measured the weight loss upon decarbonation. Fig. 6a shows the extent of decarbonation of the fully carbonated BBF/EG mixture (with 5 eq. EG) at four different temperatures: 90, 110, 130, and 150 °C. The decarbonation efficacy was found to increase as the temperature was increased; nevertheless, about 20% of the amidine remained carbonated even at 150 °C. This result is consistent with our previous findings on the stability of alkylcarbonate salts of superbases in a protic solvent (Rajamanickam et al., 2015). Moreover, as shown in Fig. 6b, it became more difficult to regenerate the absorbent at higher EG-to-amidine ratios. Therefore, to facilitate decarbonation of the solutions at a relatively low temperature, the amount of EG used should be as low as possible. The stabilization of the carbonated species by hydrogen bonding of solvent has been shown to change the equilibrium constant (K_{app}) of carbonation (Rajamanickam et al., 2015). We defined the apparent equilibrium constant (K_{app}) as shown in Eq. (1), where $[SBH^+]$, $[RCO_3^-]$, $[SB]$, and $[ROH]$ are equivalent concentrations of the amidinium cation, the alkylcarbonate anion, amidine, and the alcohol, respectively, and P_{CO2} is the partial pressure of CO_2. P_{CO2} was 1 atm in all experiments. The equivalent numbers of the species were estimated by using the initial concentration of amidine and EG, and the equilibrium molar CO_2 loadings (obtained by assuming it to be the same as the plateau value of absorption curves). Because one amidine group, one hydroxyl group, and one CO_2 molecule react to form the alkylcarbonate salt as shown in Fig. 1a, the concentrations (in equivalent numbers) of all species can be simply estimated by subtraction.

As shown in Fig. 6c, the K_{app} generally decreased with temperature but increased as the EG-to-amidine equivalent ratio was increased.

$$K_{app} = \frac{[SBH^+]\left[RCO_3^-\right]}{[SB][ROH]P_{CO2}} \quad (1)$$

We carried out CO_2 absorption/regeneration cycling tests between 60 and 140 °C to investigate the stability and reversibility

P.G.P. COLLEGE OF ARTS & SCIENCE NAMAKKAL 637 206

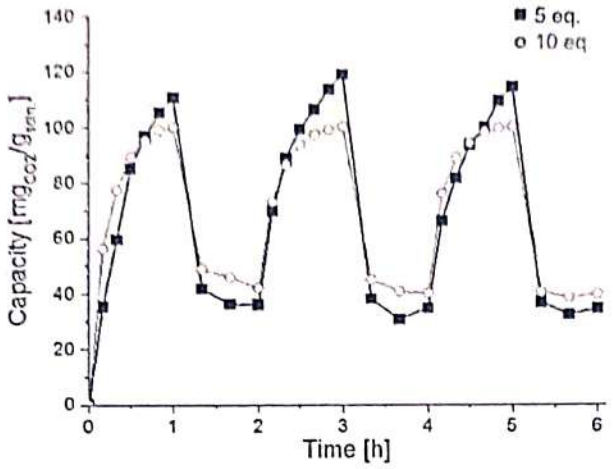


Fig. 7. Cyclic CO_2-absorption (carried out at 60 °C) and regeneration (at 140 °C) of BBF mixed with either 5 or 10 eq. of EG.

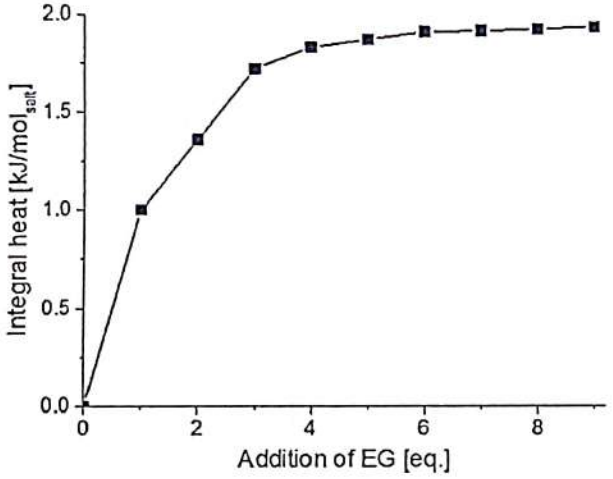


Fig. 8. Effect of the EG solvent on stabilization of amidinium alkylcarbonate salts. Heat evolved upon titration of excess EG to a solution of a carbonated BBF/EG salt with initially 1 eq. EG.

of the BBF absorbent mixed with either five or ten equivalents of EG, as shown in Fig. 7. In both solutions, the absorption/regeneration molar CO_2 loadings did not change from one cycle to the next for the three cycles, demonstrating that the CO_2 absorption by BBF/EG was reversible and stable. The gravimetric working capacities were 9 and 6 wt% for BBF with 5 and 10 eq. EG, respectively.

To estimate the stabilization energy of the carbonated salts resulting from solvation of EG, we carried out microcalorimetric titrations. We first formed a 1:1:1 adduct of BBF/EG/CO_2 in anhydrous solvent and then titrated the salt with EG. Fig. 8 reflects the energy levels of the BBF/EG carbonated salt upon addition of various excess levels of EG. The amount of heat per mole of BBF/EG salt that evolved increased with the addition of more EG for low levels of added EG, and began to plateau at approximately 1.9 kJ when 4 eq. of excess EG was added to the salt solution. The exothermic nature of the addition of excess EG is consistent with the formation of hydrogen bonds between the carbonate salts and the surrounding EG solvent molecules.

4. Conclusions

We have synthesized several compounds containing multiple amidine functionalities by direct amidination of the corresponding amines with *N,N*-dimethylformamide dimethyl acetal. A mixture composed of ethylene glycol and an amidine containing multiple functional groups was observed to capture CO_2 at various temperatures. The CO_2-absorption performances could be controlled by adjusting the relative amount of the alcohol (i.e., the ethylene glycol) in the mixture. Also, the amidine containing multiple functional groups was found to absorb more CO_2 than did the tested amidines containing only one functional group. Although the gravimetric absorption capacity increased by using the solution with multi-functional amidines in a smaller amount of alcohol, a critical amount of alcohols was needed to prevent the formation of hydrogen bonded network which would result in an extremely high viscosity. The excess alcohols appeared to have stabilized the formed alkyl carbonate salts via hydrogen bonding, resulting in a relatively low degree of decarbonation of the solution at elevated temperatures. Our results suggest that, in general, the compositions of the alcoholic solutions of superbases need to be optimized to achieve high-efficiency absorption and desorption of carbon dioxide.

Acknowledgements

This work was supported by the Korea CCS R&D Center (KCRC) grant funded by the Korean government (Ministry of Science, ICT & Future Planning) (NRF-2014M1A8A1049265).

Appendix A. Supplementary data

Supplementary data associated with this article can be found, in the online version, at http://dx.doi.org/10.1016/j.ijggc.2017.02.012.

References

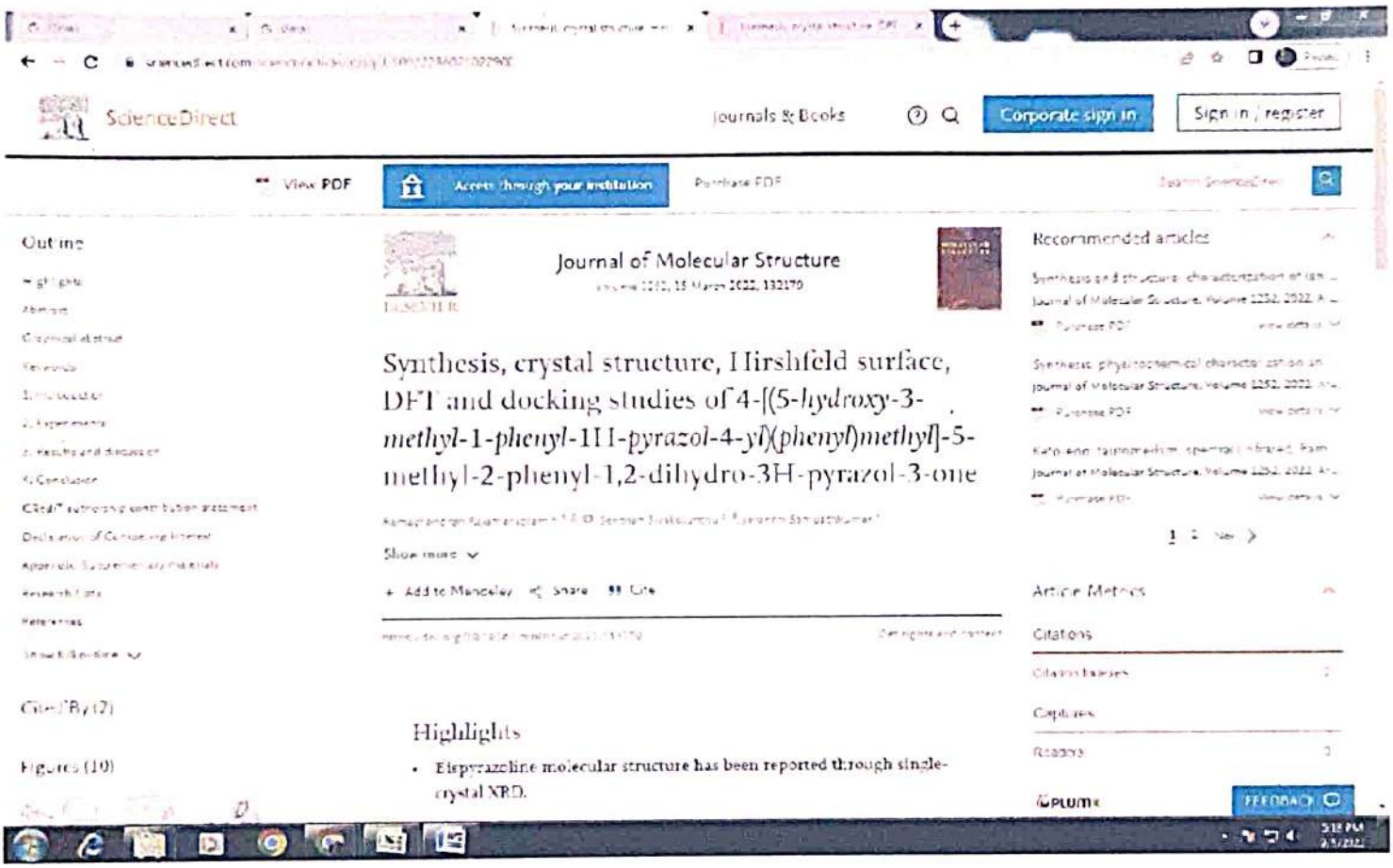
Bates, E.D., Mayton, R.D., Ntai, I., Davis, J.H., 2002. J. Am. Chem. Soc. 124, 926–927.
Benati, L., Bencivenni, G., Leardini, R., Nanni, D., Minozzi, M., Spagnolo, P., Scialpi, R., Zanardi, G., 2006. Org. Lett. 8, 2499–2502.
Cadena, C., Anthony, J.L., Shah, J.K., Morrow, T.I., Brennecke, J.F., Maginn, E.J., 2004. J. Am. Chem. Soc. 126, 5300–5308.
Dräger, G., Solodenko, W., Messinger, J., Schön, U., Kirschning, A., 2002. Tetrahedron Lett. 43, 1401–1403.
Garigipati, R.S., 1990. Tetrahedron Lett. 31, 1969–1972.
Gray, M.L., Champagn·, K.J., Fauth, D., Baltrus, J.P., Pennline, H., 2008. J. Int. Greenh. Gas Control 2, 3–8.
Heldebrant, D.J., Jessop, P.G., Thomas, C.A., Eckert, C.A., Liotta, C.L., 2005. J. Org. Chem. 70, 5335–5338.
Heldebrant, D.J., Yonker, C.R., Jessop, P.G., Phan, L., 2008. Energy Environ. Sci. 1, 487–493.
Heldebrant, D.J., Koech, P.K., Rainbolt, J.E., Zheng, F., Smurthwaite, T., Freeman, C.J., Oss, M., Leito, I., 2011. Chem. Eng. J. 171, 794–800.
Hicks, J.C., Drese, J.H., Fauth, D.J., Gray, M.L., Qi, G., Jones, C.W., 2008. J. Am. Chem. Soc. 130, 2902–2903.
Im, J., Hong, S.Y., Cheon, Y., Lee, J., Lee, J.S., Kim, H.S., Cheong, M., Park, H., 2011. Energy Environ. Sci. 4, 4284–4289.
Jessop, P.G., Heldebrant, D.J., Li, X., Eckert, C.A., Liotta, C.L., 2005. Nature 436, 1102.
Kim, M., Park, J.-W., 2010. Chem. Commun. 46, 2507–2509.
Koech, P.K., Zhang, J., Kutnyakov, I.V., Cosimbescu, L., Lee, S.J., Bowden, M.E., Smurthwaite, T.D., Heldebrant, D.J., 2013. RSC Adv. 3, 566–572.
Kumagai, N., Matsunaga, S., Shibasaki, M., 2004. Angew. Chem. Int. Ed. 43, 478–482.
Lam, C.-K., Xue, F., Zhang, J.-P., Chen, X.-M., Mak, T.C.W., 2005. J. Am. Chem. Soc. 127, 11536–11537.
Lee, S., Moon, S.-Y., Kim, H., Bae, J.-S., Jeon, E., Ahn, H.-Y., Park, J.-W., 2014. RSC Adv. 4, 1543–1550.
Liu, Y., Jessop, P.G., Cunningham, M., Eckert, C.A., Liotta, C.L., 2006. Science 313, 958–960.
Porcheddu, A., Giacomelli, G., Piredda, I., 2009. J. Comb. Chem. 11, 126–130.
Raczynska, E.D., Laurence, C., Nicolet, P., 1988. J. Chem. Soc. Perkin Trans. 2, 1491–1494. http://dx.doi.org/10.1039/P29880001491.
Rajamanickam, R., Kim, H., Park, J.-W., 2015. Sci. Rep. 5, 10688.
Rochelle, G.T., 2009. Science 325, 1652–1654.

P.G.P. COLLEGE OF ARTS & SCIENCE NAMAKKAL 637 206

Rohan, A.L., Switzer, J.R., Hack, K.M., Hart, R.J., Sivaswamy, S., Biddinger, E.J., Talreja, M., Verma, M., Faltermeier, S., Nielsen, P.T., Pollet, P., Schuette, G.F., Eckert, C.A., Liotta, C.L., 2012. ChemSusChem 5, 2181–2187.
Schnur, R.C., 1979. J. Org. Chem. 44, 3726–3727.
Spychała, J., 1999. Tetrahedron Lett. 40, 2841–2844.
Taub, D.R., 2010. Nat. Educ. Knowl. 3, 21.
Wang, C., Mahurin, S.M., Luo, H., Baker, G.A., Li, H., Dai, S., 2010. Green Chem. 12, 870–874.
Weintraub, L., Oles, S.R., Kalish, N., 1968. J. Org. Chem. 33, 1679–1681.
Yang, Z.-Z., He, L.-N., Zhao, Y.-N., Li, B., Yu, B., 2011. Energy Environ. Sci. 4, 3971–3975.
Yang, S., Lin, X., Lewis, W., Suyetin, M., Bichoutskaia, E., Parker, J.E., Tang, C.C., Allan, D.R., Rizkallah, P.J., Hubberstey, P., Champness, N.R., Mark Thomas, K., Blake, A.J., Schröder, M., 2012. Nat. Mater. 11, 710–716.
Yu, Y.-H., Soriano, A.N., Li, M.-H., 2009. J. Chem. Thermodyn. 41, 103–108.
Zhou, Z.-B., Matsumoto, H., Tatsumi, K., 2004. Chem. – Eur. J. 10, 6581–6591.
Zhu, Q., Lu, Y., 2010. Org. Lett. 12, 4156–4159.

P.G.P. COLLEGE OF ARTS & SCIENCE
NAMAKKAL
637 206

PRINCIPAL
PGP College of Arts and Science
Namakkal.


ScienceDirect
Journals & Books
Corporate sign in
Sign in / register
View PDF
Access through your institution
Purchase PDF
Outline
Journal of Molecular Structure
Synthesis, crystal structure, Hirshfeld surface, DFT and docking studies of 4-[(5-hydroxy-3-methyl-1-phenyl-1H-pyrazol-4-yl)(phenyl)methyl]-5-methyl-2-phenyl-1,2-dihydro-3H-pyrazol-3-one
Show more
+ Add to Mendeley
Share
Cite
Highlights
• Etspyrazoline molecular structure has been reported through single-crystal XRD.
Recommended articles
Article Metrics
Citations
Captures
Readers
PLUM
FEEDBACK


P.G.P. COLLEGE OF ARTS & SCIENCE
NAMAKKAL
637 204

Journal of Molecular Structure 1252 (2022) 132170

Contents lists available at ScienceDirect

Journal of Molecular Structure

journal homepage: www.elsevier.com/locate/molstr

Synthesis, crystal structure, Hirshfeld surface, DFT and docking studies of 4-[(5-*hydroxy*-3-*methyl*-1-*phenyl*-1H-*pyrazol*-4-*yl*)(*phenyl*)*methyl*]-5-methyl-2-phenyl-1,2-dihydro-3H-pyrazol-3-one

Ramachandran Rajamanickam[a,b,*], Senthan Sivakolunthu[c,d], Jayanthi Sampathkumar[e]

[a] Department of Image Science and Engineering, Pukyong National University, Busan 608-737, Republic of Korea
[b] Department of Chemistry, PGP College of Arts and Science, (Affiliated to Periyar University-Salem), Namakkal, Tamil Nadu 637 207, India
[c] Department of Chemistry, Annamalai University, Annamalainagar 608 002, India
[d] Department of Chemistry, Kamarajar Government Arts College, Surandai, Tamilnadu 627 859, India
[e] Department of Chemistry, N.K.R Government Arts College for Women, (Affiliated to Periyar University-Salem), Namakkal, Tamil Nadu 637 001, India

ARTICLE INFO

Article history:
Received 10 November 2021
Revised 9 December 2021
Accepted 9 December 2021
Available online 12 December 2021

Keywords:
Pyrazoline
Crystal structure
Hirshfeld surface
NCI-RDG
Docking

ABSTRACT

In the present work, 4-[(5-*hydroxy*-3-*methyl*-1-*phenyl*-1H-*pyrazol*-4-*yl*)(*phenyl*)*methyl*]-5-methyl-2-phenyl-1,2-dihydro-3H-pyrazol-3-one (BPZ) was synthesized by one pot multicomponent reaction of ethylacetoacetate, phenylhydrazine and benzaldehyde in the presence of Ce-MCM-48 catalyst. The title compound was characterized by FT-IR, ^{1}H NMR, and ^{13}C NMR spectral studies and single crystal XRD technique. The intermolecular contacts of the title compound were studied by Hirshfeld surface (d_{norm} surfaces and 2D fingerprint plots) analysis whereas an intra-molecular hydrogen bonding interaction was examined through NCI-RDG plot. The geometry of the molecular structure was optimized by using the density functional theory (DFT) at B3LYP/6–311 g(d,p) level. Molecular electrostatic potential (MEP), natural bond orbital (NBO) analysis, nonlinear optical properties (NLO) and global chemical reactivity parameters (GCRP) were described through computational method. Further, the molecular docking study was done for title compound with COVID-19 caused protein structure (6LU7, nCoV-SARS-2 M^{pro}). The study revealed that the significant conventional hydrogen bonding and other interactions were observed between the active amino acid residue of SARS-nCoV-2 M^{pro} and BPZ ligand.

© 2021 Elsevier B.V. All rights reserved.

1. Introduction

Pyrazoline derivative is an elegant member of the heterocyclic family because of their greater synthetic versatility in organic synthesis. A wide range of synthetic structures based on the pyrazoline analogues have been successfully developed, and they have found in numerous applications such as fluorescent probes, chemosensors, hole-transport material, electroluminescence, organic electronics and brightening agents in synthetic fibers, papers and textiles [1–3]. On the other hand, pyrazoline derivatives remain privileged heterocycles in modern drug discovery. Therefore, this skeleton has been recognized as an omnipresent motif present in a wide range of biologically important drug candidates including ramifenazone, and axitinib [4]. They have been extensively researched by the scientific community and exhibit a wide range of biological and pharmacological activities such as antibacterial [5,6], antifungal [7], anti-inflammatory [8,9], antimalarial [10,11], anticancer [12], antitubercular [13,14], anticonvulsant [15], anti-depressant [16,17], antinociceptive [18], anti-amoebic [19] and antitrypanosomal [20]. To encounter the unprecedented disease and increasing drug resistance around the world, the pyrazoline derivatives have been tackled as an engrossing pharmacophore to design new drug candidate with increased activity and lower the toxicity along with the desired pharmacokinetic profile.

COVID-19, a novel coronavirus causing severe acute respiratory syndrome (SARS-nCoV-2), has been escalating in recent days and destabilizing the global health. SARS-nCoV-2 is not yet associated with any specific treatment option method. COVID-19 is therefore a very rare disease with limited therapeutic options. However, some medications, such as i remdesivir, favipiravir, hydroxychloroquine, lopinavir–ritonavir, tocilizumab and others, have been identified as possible medicines for COVID-19 treatments [21,22]. To control the horrible impact of the disease, several on-going efforts have been made to find potential drugs and vaccines. Molecular docking play a crucial role to identify the potential binding affinity sites between protein structure and lead molecule. Recently, sev-

* Corresponding author at: Department of Chemistry, PGP College of Arts and Science, (Affiliated to Periyar University-Salem), Namakkal, Tamil Nadu 637 207, India.
E-mail address: synorgramu@gmail.com (R. Rajamanickam).

https://doi.org/10.1016/j.molstruc.2021.132170
0022-2860/© 2021 Elsevier B.V. All rights reserved.

P.G.P. COLLEGE OF ARTS & SCIENCE NAMAKKAL 637 206

eral heterocyclic compounds have been identified as a potential lead molecule for SARS nCoV 2 through docking study [23–25].

Organic NLO materials have attracted a great deal of attention owing to their potential applications in transmission and optical processing of information [26–28]. Further, organic materials show higher non-linear optical behavior compared to other traditional NLO materials such as those made on inorganic and semiconductor components, due to low cost and easy to prepare [29,30]. These factors are encouraged the interest to identify new organic materials with superior NLO properties. In this scenario, numerous organic molecules have been undertaken to study the non-linear optical properties through quantum chemical calculations [31–33].

In view of searching new bioactive and optoelectronic organic molecules, we describe a simple and elegant one pot synthesis of bispyrazoline derivative (BPZ) by three component condensation of ethylacetoacetate, phenylhydrazine and benzaldehyde using reusable heterogeneous catalyst. The title compound is fully characterized by physical and spectroscopic techniques (FT-IR, ^{1}H NMR and ^{13}C NMR) and the proposed molecular structure has been confirmed by single crystal x-ray diffraction analysis. Density functional theory (DFT) such as FMO, NBO, NLO and MEP studies have been carried out to explore their electronic properties. In addition, in silico molecular docking has been described for the title compound with COVID-19 caused biomolecule (SARS-nCoV-2 M^{pro}).

2. Experimental

2.1. Synthesis of BPZ and its characterization

A mixture of phenylhydrazine (0.83 g, 7.69 mmol), ethylacetoacetate (0.5 g, 3.8 mmol) and 20 mol% cerium doped SiO_2 (Ce-MCM-48) and water (3 ml) were added and stirred at 60–80 °C for 5 min, then benzaldehyde (0.81 g, 0.76 mmol) was added and continued the stirring for further 15 mins., the white solids were separated out during the course of reaction, which confirms the completion of reaction. This was then filtered and recrystallized with distilled ethanol gave crystals of BPZ.

The experimental FT-IR spectrum for BPZ was recorded in AVATAR-NICOLET 330 FT-IR spectrophotometer using KBr pellet method whereas the ^{1}H and ^{13}C NMR spectra were recorded at 400 and 100 MHz, respectively using BRUKER AMX 400 MHz spectrometer at 296 K. For that $CDCl_3$ and Tetramethylsilane (TMS) were used as NMR solvent and internal standard, respectively. The chemical shift (δ) values are expressed in parts per million (ppm). The coupling constants values are calculated in Hertz (Hz).

2.2. Single crystal X-ray diffraction analysis

Suitable single crystals of BPZ were grown by the slow evaporation method using distilled ethanol. The single crystal X-ray data were collected by Bruker Kappa CCD diffractometer with Mo Ka (k = 0.71073 Å) at room temperature (297 K). The data reduction and cell refinement were performed with SAINT/XPREP (Bruker), and APEX2/SAINT, respectively. The crystal structure was solved by direct method and the refinement was done by least-squares method with full matrix on F_2 with SHELXL-97 [34]. Hydrogen atoms bonded to the carbon in a molecule were placed in chemically suitable position with C–H = 0.93 Å for aromatic, 0.94 Å for methylene and 0.96 Å for methyl, and refined in riding mode with Uiso(H) = 1.2 Ueq(C) for aromatic and Uiso(H) = 1.5 Ueq(C) for methyl. ORTEP-3 program for windows was used to generate molecular graphics [35] whereas PLATON program was used to generate hydrogen bonding parameters [36].

2.3. Computational details

Hirshfeld surface analysis and 2D fingerprint plots were explored with Crystal Explorer 17 program [37]. In order to describe the molecular structure and electronic properties of BPZ, frontier molecular orbitals (FMO), natural bonding orbitals (NBO), non-linear optical property (NLO) and the molecular electrostatic potentials (MEP) were estimated by density functional theory (DFT) method based on B3LYP/6–311 g(d, p) basis set using Gaussian 09 software package [38]. To organize the Gaussian input file and visualize HOMO-LUMO orbitals, MEP surface, and FT-IR spectrum images, Gauss View 5.0 software was used. Non-covalent interaction and radiant density gradient (NCI-RDG) graph was obtained from comprehensive wave function analysis using Multiwfn 3.4.1 program [39]. NCIs map was created by using VMD 1.9.1 [40]. Molecular modeling was studied with Auto dock 4.2.6 program using SARS-nCoV-2 M^{pro} (PDB ID: 6LU7) protein structure which was obtained from protein data bank. The input files were organized by Discovery studio visualizer software. The protein structure was cleaned prior to docking. The grid parameter was generated from the active sites of protein structure.

3. Results and discussion

3.1. Chemistry

4-[(5-*hydroxy*-3-*methyl*-1-*phenyl*-1H-*pyrazol*-4-*yl*)(*phenyl*)*methyl*]–5-methyl-2-phenyl-1,2-dihydro-3H-pyrazol-3-one (BPZ) was synthesized, as outlined in Scheme 1. A mixture of ethyl acetoacetate, phenylhydrazine and benzaldehyde (2: 2: 1 equivalent ratio, respectively) were stirred with 3 mL of water for 15 mins. in the presence of catalytic amount of Ce-MCM-48 (20 mol%) at 60-80 °C. The desired product was obtained as white solid during the reaction. This was then recrystallized from distilled ethanol gave high purity single crystals. The synthesized BPZ was fully characterized by FT-IR, ^{1}H NMR and ^{13}C NMR spectroscopic analysis.

The ^{1}H and ^{13}C NMR of spectra of BPZ are displayed in Fig. S1 and S2, respectively. As shown in Fig. S1, two singlets were observed at 1.16 and 1.21 ppm with three proton integral each, corresponds to two methyl protons at pyrazole ring whereas a singlet showed at 5.0 ppm with one proton integral can be assigned to methine proton. The aromatic proton signals were observed from 6.81 to 7.85 ppm. It should be noted that the OH and NH peaks were not observed in the NMR spectra. This should be due to a fast proton exchange between C=O and NH group in NMR time scale. In ^{13}C NMR spectrum, (Fig. S2), a less intense signal at 160.2 ppm is unambiguously assigned to C=O carbon at pyrazole ring. The two methyl carbon signals were appeared at 25 ppm whereas the methine carbon signal was resonated at 34.5 ppm. The aromatic carbon signals were observed from 122.24 to 139.06 ppm.

3.2. FT-IR analysis

The experimental and theoretical FT-IR spectra are shown in Fig. 1 and their wavenumbers are listed in Table S1. The molecular structure of BPZ consists of 66 atoms which undertake 175 normal mode vibrations. The normal mode vibrational frequencies of title compound were calculated at the B3LYP/6–311G(d,p) level. The wavenumbers from 4000 to 1700 cm^{-1} and below 1700 cm^{-1} were scaled with 0.958 and 0.983, respectively, which have been used by many people in order to reasonably concurrence with experimental data. The molecular conformation yielded by geometry optimization exhibits no special symmetries and hence the molecule belongs to the C1 point group. As a result, all the 175 fundamental vibrations were found to be active in IR spectrum.

P.G. COLLEGE OF ARTS & SCIENCE NAMAKKAL 637 206

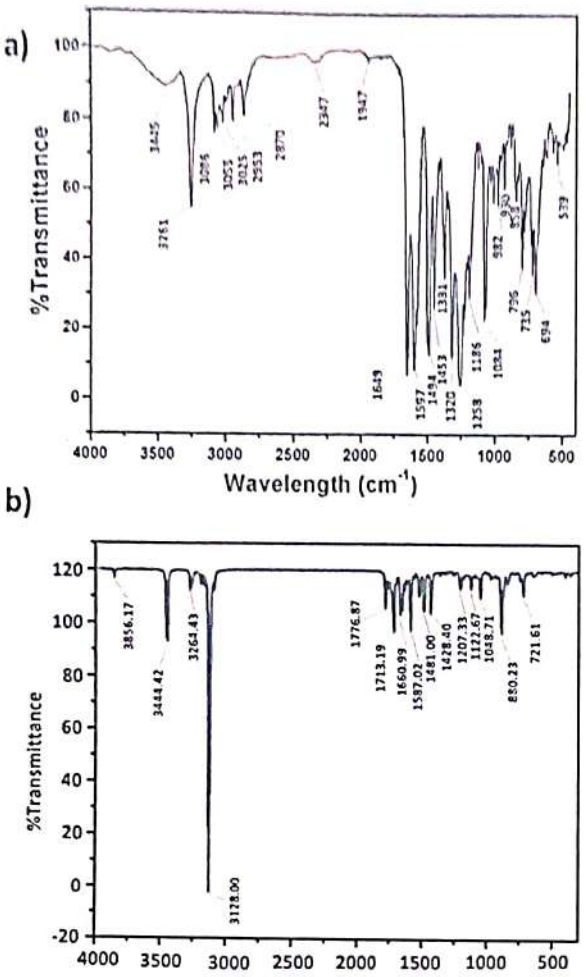


Fig. 1. FT-IR spectrum of BPZ compound a) Experimental; b) simulated by B3LYP/6-31G(d,p).

3.2.1. N–H and C–N vibrations

νN–H stretching vibration band is generally located in the region of 3100–3300 cm^{-1}. In the title molecule, experimental N–H stretching vibration was appeared as sharp and intense peak at 3261 cm^{-1}, whereas the simulated N–H stretching wavenumber was found at 3128 cm^{-1}, as shown in Fig. 1. Further, the N–H out-of-plane deformations were predicted for BPZ and those were observed between 694 and 735 cm^{-1} (experimental wavenumber), whereas the theoretical wavenumber for the same deformations were predicted between 495 and 737 cm^{-1}. However, the N–H in-plane deformations band was found to be at 1523 cm^{-1}.

The νC–N stretching vibrations mode was found as a collection of band in the range of 1382–1266 cm^{-1}, which is typically the result for the assortment of vibrational bands of other functional groups. In BPZ, the C–N stretching vibration was seen at 1186 cm^{-1} in the experimental FT-IR spectrum whereas the same band was predicted theoretically at 1224 and 1221 cm^{-1}.

3.2.2. O–H, C–O and C=O vibrations

The O–H stretching mode of title compound was predicted theoretically at 3444 cm^{-1} which nicely correlated with experimental value that observed at 3445 cm^{-1}. It is worth to mention that the experimental O–H band was observed as broad peak due to strong intramolecular hydrogen bonding between carbonyl and O–H group.

On the other hand, the simulated IR spectrum shows a pair of peak at 1713 and 1669 cm^{-1}, whereas the experimental FT-IR shows a single peak at 1649 cm^{-1}. Out of which, the higher region can be assigned to C=O stretching mode and less intense band with lower intensity can be assigned to C=N group. The C–O stretching vibration values predicted theoretically and those were observed between 1207 and 1048 cm^{-1}, whereas the same vibration was experimentally found at 1186, 1258 and 1320 cm^{-1}.

3.2.3. C–C and C=C vibrations

The six ring carbon atoms occurs over coupled vibrations, predictable as semicircular stretching usually taking place in the region 1400 to 1625 cm^{-1} [41,42]. The certain positions of these modes were determined not so much by the location of the substituents but by the system of replacement after one place to another ring. The C–C stretching vibrations rise to characteristic bands in the experimental IR spectra. The FT-IR bands are noticed with rigid intensities at ~1599, ~1578, ~1500, ~1489, ~1451, ~1375 and ~1317 cm^{-1}. The theoretically computed wavenumbers were predicted at ~1587, ~1481 and ~1428 cm^{-1}. Mostly, these modes of vibrations were found close to the experimental frequencies.

3.2.4. C–H vibrations

A literature reports showed that C–H stretching vibration of phenyl rings were appeared in the region of 3000–3100 cm^{-1} [43]. From the Fig. 1, it is seen that experimental FT-IR vibration for phenyl ring C–H was observed at 3086, 3055, and 3025 cm^{-1} whereas the computational study predicted that the C–H stretching modes of phenyl rings was noted at 3103 and 3026 cm^{-1}. Aliphatic C–H stretching vibrations were calculated in the region of 2989–2776 cm^{-1}. Interestingly, the scaled νC–H stretching vibrations show excellent concurrence with the experimental vibrations at 2953 and 2870 cm^{-1}. However, the C–H in-plane bending or deformation (β) vibrations are expected in the region of 1400–1100 cm^{-1} with medium to weak intense band. For BPZ, some bands due to C–H in plane were observed in the region of 1122–1471 cm^{-1}. On the other hand, the C–H out-plane deformations were observed between 894 and 801 cm^{-1}, which is good agreement with the calculated value (880–721 cm^{-1}).

3.3. Single crystal X-ray diffraction

The molecular structure of 4-[(5-*hydroxy*-3-*methyl*-1-*phenyl*-1H-*pyrazol*-4-*yl*)(*phenyl*)*methyl*]–5-methyl-2-phenyl-1,2-dihydro-3H-pyrazol-3-one, BPZ, ($C_{27}H_{24}N_4O_2$) with the atom numbering view is shown in Fig. 2. Single crystal XRD indicated that the BPZ compound crystallizes into monoclinic with P 21/c. The crystal system belongs to the following lattice parameters: a) 9.32580 (10), b) 22.1130 (3), c) 12.7955 (2) and $\alpha = \delta = 90$ and $\beta = 100.9480$ (10) its unit cell volume is 2590.68 (6). Crystal data collection and the refinement parameters are presented in Table 1. The dihedral angle between two pyrazoline rings was found to be 32°. The bond distances and bond angles are listed in Table 2. It can be seen from Table 2, the bond distances of C11-O1 and O2-H2 were found to be 1.26 and 0.82 Å respectively. Due to strong intramolecular hydrogen bonding interaction between C11-O1 (C=O) and O2-H2 (O –H), the bond distances are slightly deviated from the standard value. Also, the bond distances of O2-C19, C19-C18, C18-C26, and C26-N3 were found to be 1.32, 1.38, 1.40 and 1.33 Å respectively. Similarly, O1-C11, C11-C8, C8-C9 and C9-N1 were found to be at 1.26, 1.42, 1.37 and 1.34 Å respectively. The above bond distances are slightly deviated from the standard values. It is due to amide-iminol tautomerism between O2-C19 and C26-N3 through C18-C26 bond, and O1-C11 and C9-N1 through C8-C9 bond.

P.G.P. COLLEGE OF ARTS & SCIENCE NAMAKKAL 637 206

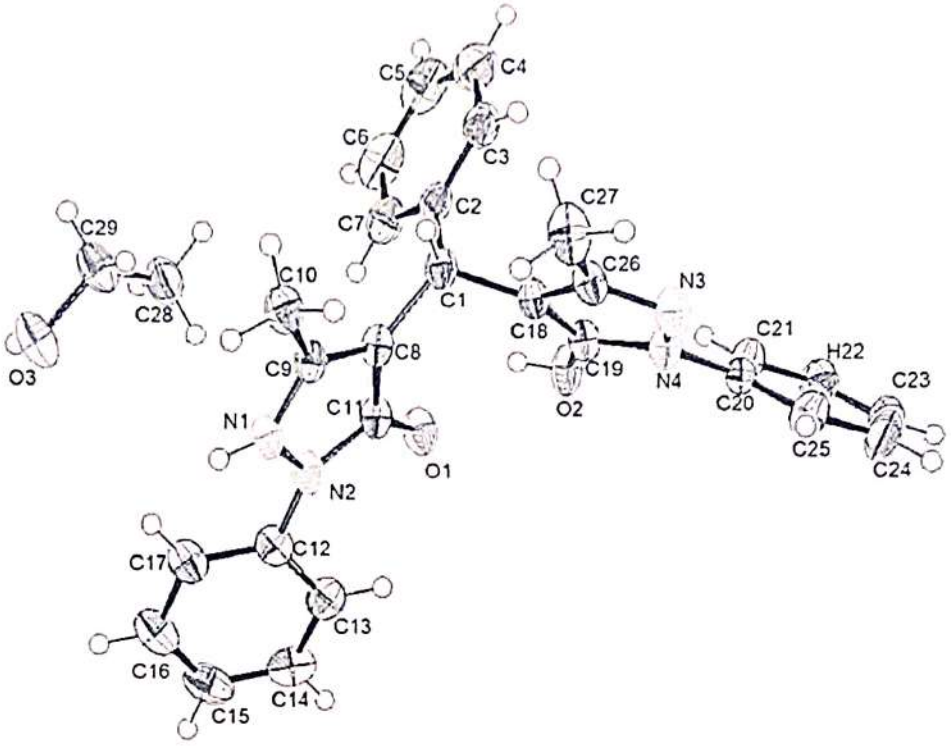


Fig. 2. X-ray structure of compound BPZ with 50% probability.

Table 1
Single crystal XRD data collection and refinement details of BPZ.

Empirical formula	C_{29} H_{30} N_4 O_3
Formula weight	482.57
Temperature	293(2) K
Crystal system, space group	Monoclinic, $P2_1/c$
Unit cell dimensions	a = 9.32580(10) Å alpha = 90° b = 22.1130(3) Åbeta = 100.9480° (10) c = 12.7955(2) Å gamma = 90°
Volume	2590.68(6) A^3
Z, Calculated density	4, 1.191 Mg/m^3
Absorption coefficient	0.076 mm^{-1}
F(000)	984
Crystal size	0.355 × 0.255 × 0.224 mm^3
Theta range for data collection	1.84 to 27.49°
Limiting indices	$-12<=h<=12$, $-28<=k<=26$, $15<=l<=16$
Reflections collected / unique	24,745 / 5937 [R(int) = 0.0361]
Completeness to theta = 27.49	99.90%
Absorption correction	Semi-empirical from equivalents
Refinement method	Full-matrix least-squares on F^2
Data / restraints / parameters	5937 / 0 / 325
Goodness-of-fit on F^2	1.068
Final R indices [I>2sigma(I)]	R1 = 0.0527, wR2 = 0.1358
R indices (all data)	R1 = 0.0775, wR2 = 0.1500
Largest diff. peak and hole	0.330 and −0.336 $e.A^{-3}$
CCDC number	859,834

Inter and intramolecular interactions were studied extensively by means of geometrical analysis, as listed in Table 3. It can be seen from the Table 3 that two conventional intramolecular hydrogen bondings (O2-H2···O1 and C7-H7···O1) with the distances of 1.90 and 2.68 Å respectively. Also, these two hydrogen bondings were generated (S6) and S(8) motifs, as shown in Fig. S3.

Further, the geometry of the structure was predictable to be organized by C-H···π, C-H···O, O-H···C, O-H···N and H···H interactions. In this context, solvent molecule (ethanol) play an important role to interconnect the asymmetric crystal structure in the crystal packing. Fig. 3 provides various types of intermolecular interaction. As shown in Fig. 3, the supramolecular assembly of hydrogen bonding interactions of the benzene ring to ring interactions (C5-H5···Cg(1) was arranged as a layer like structure with regular organization (Fig. 3), constructed with the bond distance of 2.568 and 2.575 Å. Furthermore, the packing projection along the c-axis phase exhibits zig-zag pattern by the intermolecular interactions of O-H···Csp^2 and O-H···N, which were constructed as weak interactions between O-H to pyrazole ring of carbon and nitrogen, assembled with the distance of 1.789 and 2.654 Å, as shown in Fig.

P.G. COLLEGE OF ARTS & SCIENCE NAMAKKAL 637 206

Table 2
Experimental and theoretical geometrical parameters of BPZ.

Atoms	XRD	DFT	Atoms	XRD	DFT
O(1)-C(11)	1.2620(19)	1.248	N(3)-N(4)-C(20)	119.42(13)	118.75
O(2)-C(19)	1.3275(19)	1.337	C(21)-C(20)-N(4)	120.71(15)	119.39
N(1)-C(9)	1.349(2)	1.375	C(25)-C(20)-N(4)	118.94(16)	118.47
N(1)-N(2)	1.361(19)	1.394	C(8)-C(1)-C(18)	113.40(14)	114.33
O(3)-C(29)	1.425(2)	1.436	C(8)-C(1)-C(2)	115.88(14)	116.68
O(3)-H(3)	0.82	0.936	C(18)-C(1)-C(2)	110.46(13)	110.21
N(2)-C(11)	1.383(2)	1.376	C(19)-C(18)-C(1)	127.41(14)	130.33
N(2)-C(12)	1.415(2)	1.41	C(26)-C(18)-C(1)	127.40(15)	125.19
N(3)-C(26)	1.331(2)	1.304	C(9)-C(8)-C(11)	107.20(15)	106.73
N(3)-N(4)	1.3758(19)	1.4	C(9)-C(8)-C(1)	125.94(15)	126.98
N(4)-C(19)	1.357(2)	1.36	C(11)-C(8)-C(1)	126.80(14)	126.28
N(4)-C(20)	1.420(2)	1.417	N(1)-C(9)-C(8)	109.60(14)	111.25
C(1)-C(8)	1.501(2)	1.512	N(1)-C(9)-C(10)	119.85(14)	120.55
C(1)-C(18)	1.508(2)	1.512	C(8)-C(9)-C(10)	130.52(16)	129.16
C(1)-C(2)	1.533(2)	1.535	O(2)-C(19)-N(4)	120.65(14)	119.37
C(8)-C(9)	1.370(2)	1.359	O(2)-C(19)-C(18)	131.98(14)	130.48
C(8)-C(11)	1.421(2)	1.419	N(4)-C(19)-C(18)	107.36(14)	108.12
C(9)-C(10)	1.486(2)	1.473	C(17)-C(12)-N(2)	119.50(16)	119.54
C(26)-C(27)	1.491(2)	1.488	C(13)-C(12)-N(2)	119.95(16)	119.72
C(9)-N(1)-N(2)	108.19(13)	107.98	C(3)-C(2)-C(1)	117.96(16)	118.51
N(1)-N(2)-C(11)	108.67(13)	108.24	C(7)-C(2)-C(1)	123.45(17)	123.03
N(1)-N(2)-C(12)	120.26(13)	120.08	N(3)-C(26)-C(18)	111.69(15)	110.94
C(11)-N(2)-C(12)	130.44(14)	129.73	N(3)-C(26)-C(27)	120.44(16)	119.58
C(26)-N(3)-N(4)	105.02(13)	105.19	O(1)-C(11)-N(2)	122.51(16)	122.98
C(19)-N(4)-N(3)	110.94(13)	109.97	O(1)-C(11)-C(8)	131.32(16)	130.36
C(19)-N(4)-C(20)	129.34(14)	130.26	N(2)-C(11)-C(8)	106.16(14)	106.62

Table 3
Hydrogen-bond geometry (Å, °).

D-H···A	D···A	H-A	D-H	D-H...A
C14-H14···O1^{i}	3.50	2.676	0.93	148.1
O3-H3···N3^{ii}	2.73	1.94	0.81	162.9
N1-H1···O3^{iii}	2.69	1.92	0.86	147.5
C10-H10A···O3^{iii}	3.40	2.66	0.96	135.5
C24-H24···Cg2^{iv}	3.80	2.87	0.93	175.5
O2-H2···O^{v}	2.54	1.90	0.82	133.4
C5-H5···Cg1^{vi}	3.65	2.70	0.93	157.7
C23–H23···Cg2^{vii}	3.57	2.85	0.93	121.6

Symmetry codes: (i) 2-x,1-y,1-z; (ii) 1-x,−1/2 + y,1/2-z; (iii) 1-x,1-y,-z; (iv) 1 + x,1/2-y,1/2 + z; (v) x,y,z; (vi) 1-x,1-y,1-z; (vii) −1 + x,1/2-y,−1/2 + z; Cg1 and Cg2 is the centroid of the C12–C17 and C2-C7 rings, respectively.

S4. Additionally, the crystal packing along the b-axis, the molecular structure was well designed by weak intermolecular interactions of Csp^2-H ...O and Csp^2-H...H-$Csp^3$with the bond distance of 2.55/2.74 and 2.75 Å, respectively (Fig. S5).

3.4. Hirshfeld surface analysis (HSA)

The non-bonded interaction between the molecules of BPZ can be quantitatively explored further more by Hirshfeld surface (HS) and 2D fingerprint plot analysis, which were carried out using Crystal Explorer 17 package [37]. The HS was visualized by normalized function d_{norm} (normalized contact distance) obtained with static color scale between −0.654 au (blue) to 1.590 au (red) and computed with the following equation.

$$d_{norm} = \frac{d_i - r_i^{vdw}}{r_i^{vdw}} + \frac{d_e - r_e^{vdw}}{r_e^{vdw}}$$

where d_e and d_i are denote the distance from the Hirshfeld surface (HS) to nearest outside and inside the nucleus surfaces, respectively, and r_e^{vdw}/ r_i^{vdw} are designates the van der Waals radius of outside and inside the atoms, respectively. The d_{norm} function on the Hirshfeld surface highlights with a tricolor (red-white-blue) Scheme, which represent the various interactions. The bright red spots on HS indicate the intermolecular contacts less than their van der Waals radii, whereas the blue region on the HS demonstrates intermolecular contacts longer than their van der Waals radii. However, the white spots on the HS show the sum of their van der Waals radii. Further, the π-π interaction between two molecules can be easily detected through the shape index mapped surface as exhibits adjacent red-blue triangle conclave.

The close contacts of molecular surface of BPZ were highlighted with conventional mapping of d_{norm}, as shown in Fig. 4. It is seen that there are four significant interactions per molecule were identified from d_{norm} mapped surface (Fig. 4a–e). Among these, two interactions were found between ethanol and pyrazoline fragments (N–H···O and O–H···N), while the third and fourth interactions were found to be as C–H····π and C–H····H, occurred between BPZ molecules. Further, the π-π stacking interaction was detected from shape index mapped surface, as shown the adjacent red and blue triangle concave regions (Fig. 4f). Therefore, it is believed to be that the major stabilization of BPZ crystal structure through the ethanol solvate molecule.

2D-fingerprint plot analysis was employed to calculate the percentage contribution of each contact to the total molecular surface which highlights the most critical intermolecular interactions in the desired molecule. The calculated percentage contributions of each contact are given in Fig. 5. The expanded 2D fingerprint plots are shown with the d_i and d_e distances scales on the graph axis for the total contacts in the range of 0.6–2.8 Å, as shown in Fig 5a and 4e. It can be seen from Fig. 5 that a pair of intense spikes observed at around d_i=d_e=1.1 Å indicates short H···O and H····N interactions. Similarly, a medium intense spike was observed around di=de=1.0 Å corresponds to the H···H interactions, whereas C···H interaction was found at 1.6 Å as less intense spike. From the 2D fingerprint analysis, it is clearly revealed that the H···H (57.9%) non-bonding interaction was found to be a major contributor in the crystal packing, whereas the percentage of C···H, O···H and N···H contacts contributions were calculated as 24.0, 9.4 and 5% respectively to the total surface, as shown in Fig. 5. Finally, it is summarized that the existence of intermolecular contacts on the HS interaction are excellent accordance with single crystal XRD packing results.

PERIYAR COLLEGE OF ARTS & SCIENCE
NAMAKKAL
637 206

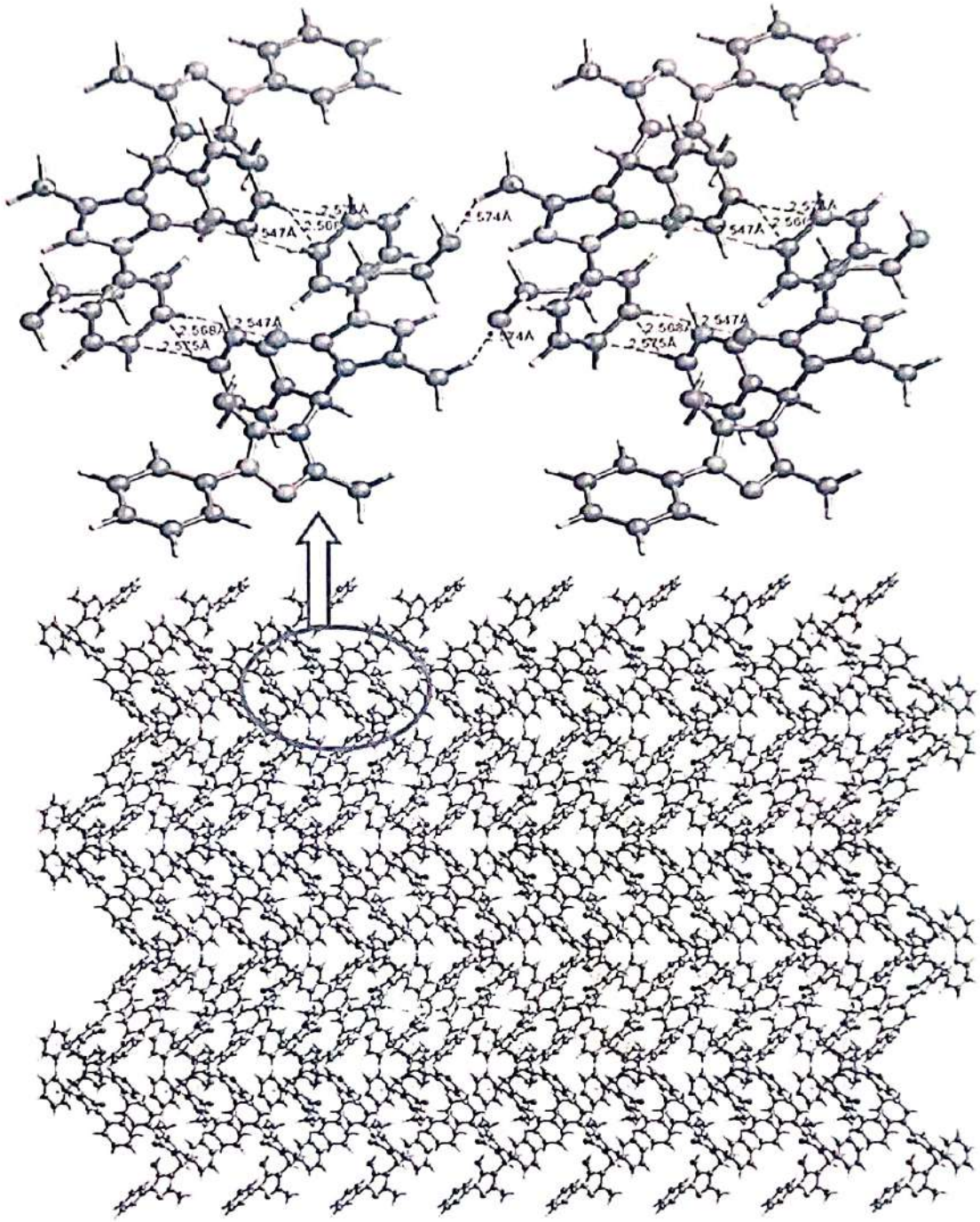


Fig. 3. The packing viewed along the b-axis direction with intermolecular interactions.

3.5. QTAIM analysis

Quantum theory of atoms in a molecule (QTAIM) model was examined to deepen the nature of H-bonding interaction and the molecular self-assembly by non-covalent interactions (NCIs) in a molecule, which can be represented by bond critical points (BCPs) in the graphical description of QTAIM analysis [44,45]. According to QTAIM model, both inter and intramolecular H-bonds could be easily characterized by the BCPs between donor (hydrogen atom) and acceptor atoms. Therefore, the presence of BCPs and the electron density topological properties of BCPs are used to predict the nature of hydrogen bond from the calculated values. Additionally, the ring critical points (RCPs) can also be determined when a ring structure is formed by multiple hydrogen bonding interactions.

For BPZ molecule, atoms in molecule (AIM) analysis was done with AIMAll software package [46] using the wave function input

P.G.P. COLLEGE OF ARTS & SCIENCE NAMAKKAL 637 206

Table 4
QTAIM topological analysis of BPZ.

BCP #	Atoms	ρ (e/Bohr^3)	$\nabla^2\rho$ (e/Bohr^5)	V (a.u)	G (a.u)
1	O1 - H3	0.030341	0.113388	−0.027061	0.027704
2	O2 - H3	0.537942	−5.253383	−1.58145	0.134052
3	N6 - C21	0.301572	−0.720207	−0.766708	0.293078
4	N6 - C16	0.278959	−0.719437	−0.641016	0.230578
5	N4 - C14	0.320991	−0.565887	−0.906028	0.382278
6	N4 - H5	0.491647	−2.997182	−0.932782	0.091743
7	O1 - C21	0.375872	−0.417525	−1.176174	0.535897
8	N4 - N6	0.342328	−0.650471	−0.491755	0.164568
9	N8 - C15	0.32675	−0.88531	−0.836802	0.307737
10	O2 - C15	0.314055	−0.324723	−0.914567	0.416693
11	N7 - N8	0.346163	−0.61366	−0.528624	0.187604
12	N8 - C9	0.281604	−0.811515	−0.603118	0.20012
13	N7 - C20	0.350638	−0.887075	−0.953739	0.365985
14	O1 - H19	0.011653	0.046752	−0.008284	0.009986
15	O2 - H25	0.011397	0.048595	−0.00838	0.010264
16	N4 - H63	0.006201	0.022924	−0.003994	0.004862
17	O58 - H59	0.543975	−4.439245	−1.411992	0.15109
18	O58 - C64	0.251179	−0.413653	−0.605783	0.251185

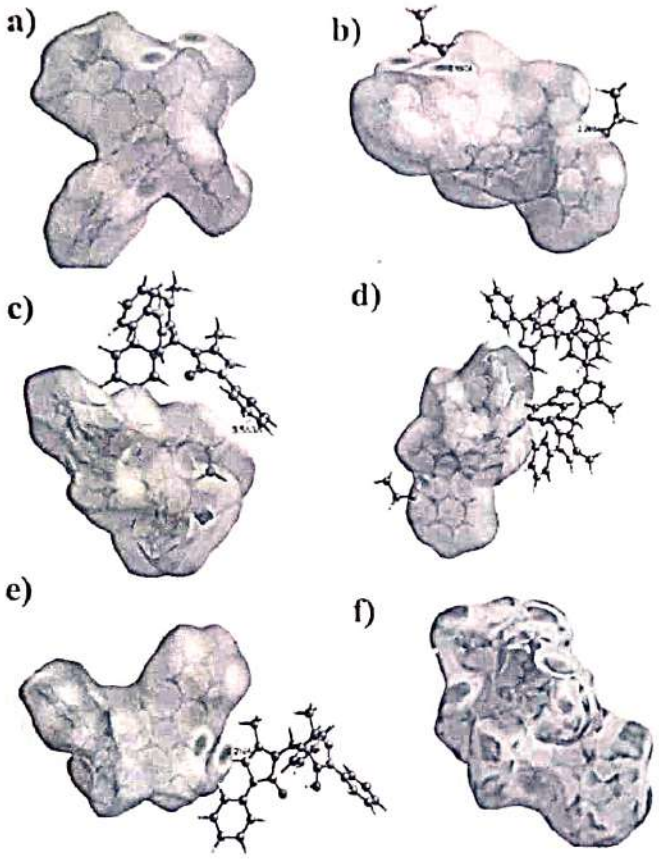


Fig. 4. The Hirshfeld surface mapped over (a) d_{norm} full, (b-e) d_{norm} mapped on the Hirshfeld surface for visualizing the intermolecular (non-covalent) interactions of compound BPZ (f) shape-index of BPZ.

data which were obtained from the optimized molecular geometry at B3LYP/6–311g(d,p) level. The BCPs of BPZ are shown in green sphere (Fig. 6) and their topological parameters such as electron density (ρ_{BCP}), potential energy density (V(r)), Laplacian of electron density ($\nabla^2\rho_{BCP}$), and kinetic energy density (G(r)), are presented in Table 4 It can be seen from the molecular topology graph (Fig. 6), there are three major non-covalent interactions (one H···H, two C–H···O and one O–H···O) were detected.

The ρ_{BCP} for the intramolecular O–H···O hydrogen bonding contacts in the optimized BPZ compound was found to be close to the value of 0.035 a.u. as reported by Koch and Popelier (0.0303 a.u). Similarly, the predicted Laplacian of electron density values for the C–H···O bonds are fall in the range 0.0467–0.0485 a.u, which coincides average range for a large number of the hydrogen bond values reported by Koch-Popelier (0.024–0.139).

On the other hand, the intermolecular C–H···O interaction was also observed between aromatic C–H and ethanol solvent molecule (O–H), which play a significant role in the crystal packing. It can be seen from Table 4 that the ρ and $\nabla^2\rho$ for C–H23···O58 were calculated as insignificant values (0.001 and 0.007 a.u, respectively), suggest that a weak C–H···O interaction. From the crystal structure analysis, we observed that the H-bond distances for O–H···O, C–H···O=Csp^2 and C–H···O–H are 1.907, 2.473, and 2.433 Å, respectively. Additionally, several H···H interaction were also found in the molecular structure including solvent-BPZ intermolecular interactions, out of which, Csp^3-H29···H40-Csp^3 distance was found to be 2.777 Å, and their electron density was calculated to be 0.001 a.u. which is smaller than the value of Koch and Popelier. Therefore, this interaction should be characterized as weak contacts due to less electron density. However, the other H···H contacts were fall in the range of 2.9–3.21 Å. The observed intermolecular contacts are good accordance with single crystal XRD and Hirshfeld surface analysis. In order to classify the nature of H bond, electronic energy density was calculated using the following relation.

$$g(r) = \frac{3}{10}(3\pi^2)^{\frac{2}{3}}\ \rho(r)^{\frac{5}{3}} + \frac{1}{6}\nabla^2\rho(r) \quad (1)$$

$$v(r) = -\frac{3}{5}(3\pi^2)^{\frac{2}{3}}\ \rho(r)^{\frac{5}{3}} - \frac{1}{12}\nabla^2\rho(r) \quad (2)$$

$$h_e(r) = -\frac{3}{10}(3\pi^2)^{\frac{2}{3}}\ \rho(r)^{\frac{5}{3}} + \frac{1}{12}\nabla^2\rho(r) \quad (3)$$

Where $h_e(r)$ is named as Cremer-Kraka electronic energy density which is equal to a sum of the g(r) and $v(r)$ values: i.e., $h_e(r) = v(r) + g(r)$ [47]. Therefore, the Bader theory basic terms and concepts are finding a quantitative confirmation from the X-ray diffraction analysis. From the Eq. (3), the Cremer-Kraka electronic energy density $h_e(r)$ was calculated to be negative sign (−0.000018 a.u) for C–H···O intramolecular contacts. Therefore, it is revealed that this interaction is classified as strong H-bond as they obey $\nabla^2\rho > 0$; $h_e(r) < 0$ rule.

In a nutshell from the above results, the QTAIM analysis is revealed that the intramolecular C–H···O and O–H···O contacts play

P.G. & R. COLLEGE OF ARTS & SCIENCE NAMAKKAL 637 206

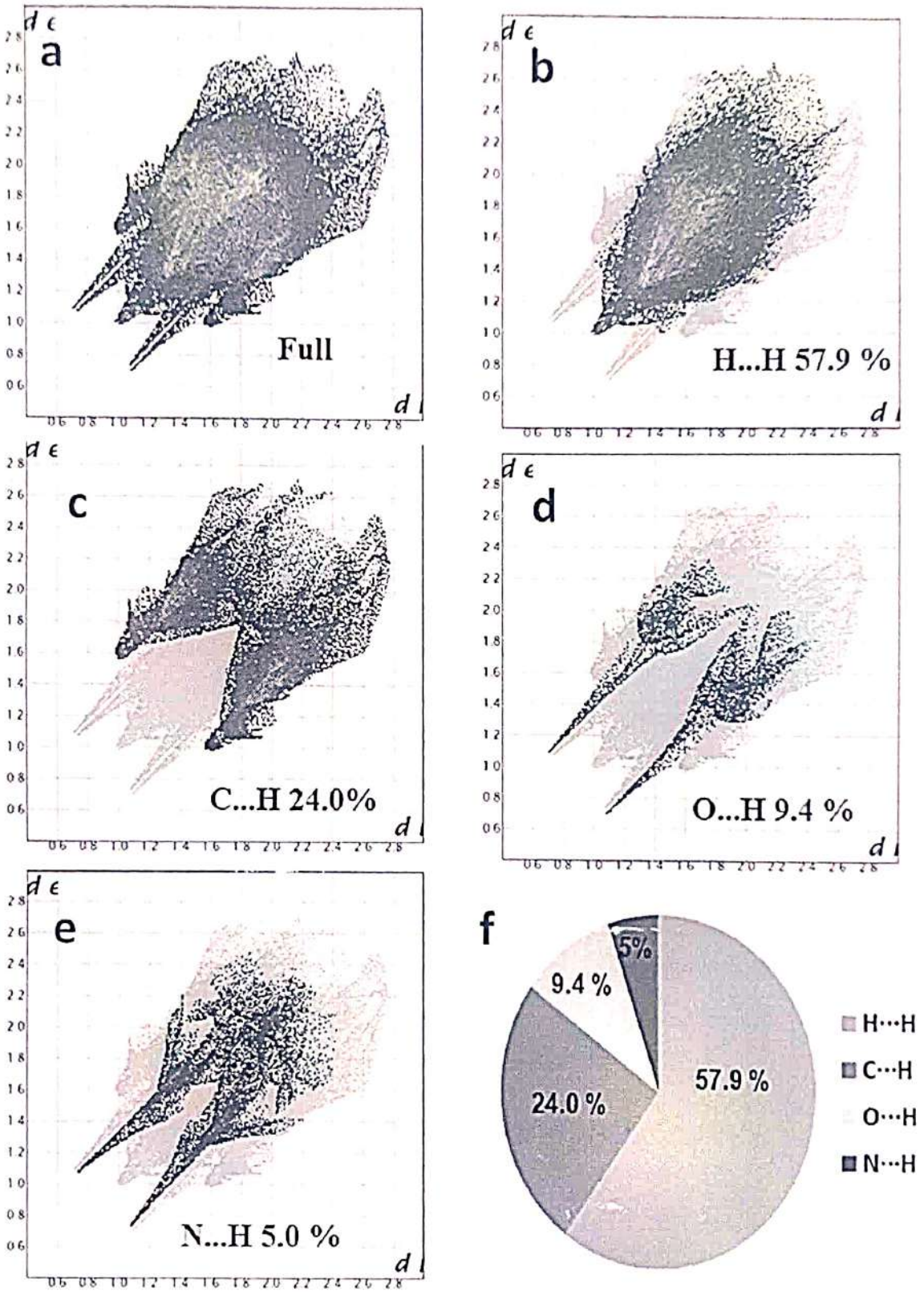


Fig. 5. 2D fingerprint plots resolved into a) full b) H...H/H...H (57.9%); (c) C...H/H...C (24.0%); (d) N...H/H...N (5.0%) and (e) O...H/H...O (9.4%) (f) percentage contribution of various intermolecular contacts.

V.H.N.S.N.P. COLLEGE OF ARTS & SCIENCE

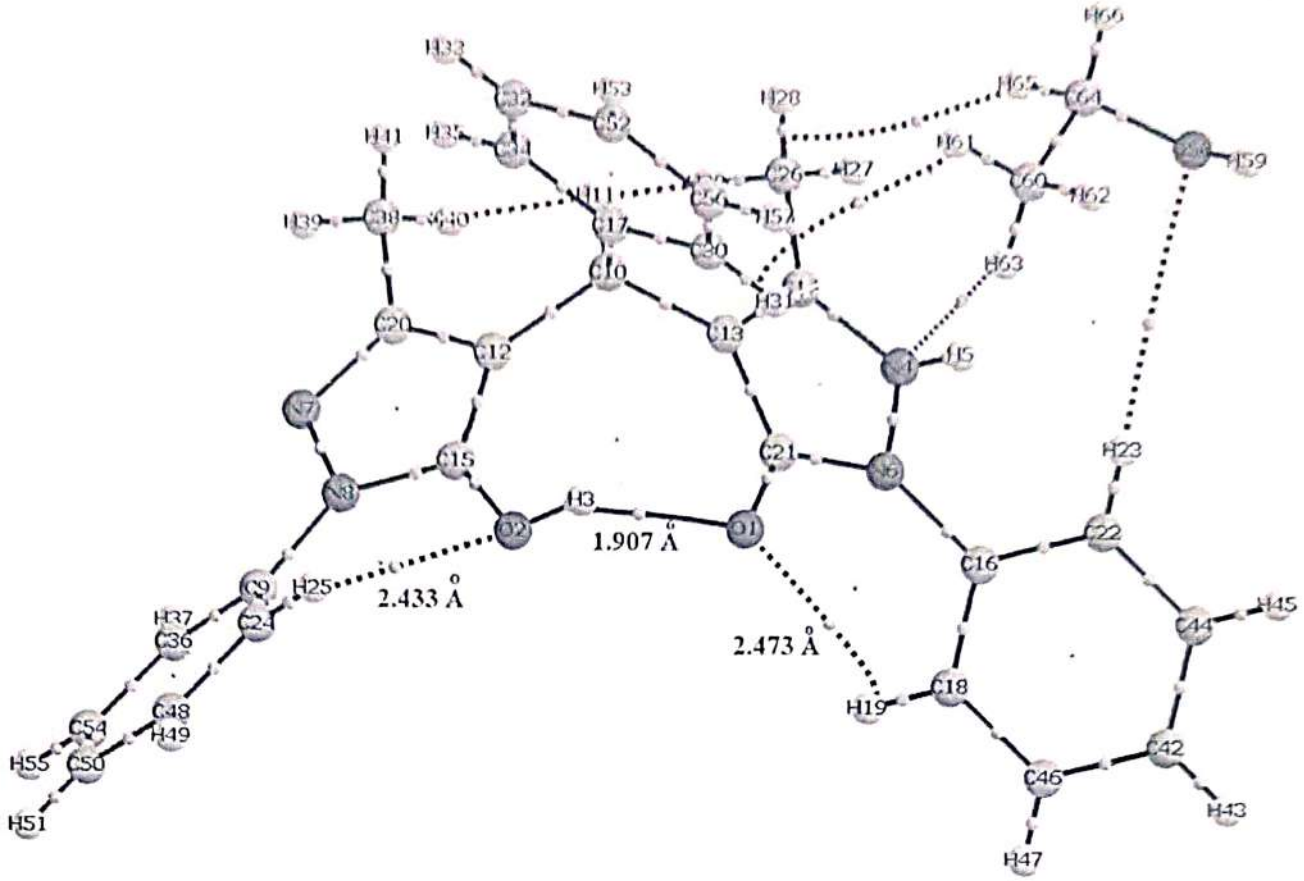


Fig. 6. Molecular graph of the BPZ molecule obtained from QTAIM analysis.

a significant role towards the stabilization of asymmetric unit of molecular structure of the title compound.

3.6. NCI-RDG analysis

The strength of weaker hydrogen bonding interactions cannot generally be determined by the QTAIM study. To describe these interactions, reduced density gradient (RDG) method based on the analysis of non-covalent interactions (NCI), introduced by Jonson and co-workers [48], is a robust topological tool for visualizing of NCIs in a molecule . There could be a several types of non-covalent interactions in the molecular structure under study, all of which can be found by plotting NCI and RDG plots versus electron density ($\sin(\lambda^2)\rho$). The scatter graph of RDG against $\sin(\lambda^2)\rho$ exploring the type of attractive or repulsive forces that exist in the molecular structure. This approach has been enabled the identification of NCI as isosurfaces of RDG in the following the relation.

$$RDG(r) = \frac{1}{2(3\pi^2)^{1/3}} + \frac{|\nabla\rho(r)|}{\rho(r)^{4/3}}$$

The NCI-RDG analyses were carried out for title molecule by VMD program with an iso-surface value of 0.5. The interaction regions are displayed in Fig. 7. It is seen that the low density and low reduced gradient enclosing their real spaces such as blue, green and red circles are indicating that attractive, van der Waals and repulsive forces, respectively. Similarly, the types of interaction can be identified through the RDG scatter graph, as showing tri-color (blue green, and red) scattering zone explore the H-bonding (attractive), Van der Waals (vdW) and steric (repulsive) forces, respectively.

The NCI and RDG plots of BPZ are displayed in Fig. 7a and 7b respectively. It can be clearly noted from Fig. 7, that the existence of O–H···O intra-molecular hydrogen bonding interactions, as shows blue intense circle between O–H and C=O group and blue scattering spots in the negative sign of the RDG graph with the value of −0.03 a.u. (Fig. 7a). The van der Waals interaction was found in the molecule as shown in the green scatter spikes between 0 and −0.01 a.u, (Fig. 7a), whereas two spikes at 0.02 and 0.05 a.u correspond to strong steric clashes which were observed within the aromatic and pyrazoline rings (Fig. 7b). The obtained result of NCI-RDG are matched well with single crystal XRD packing results.

3.7. Structure optimization

The molecular structural parameters for BPZ were simulated at the B3LYP/6-311 g(d,p) level, and their optimized molecular structure is shown in Fig. S6. The simulated geometrical parameters were counterchecked with experimental XRD data, and are furnished in Table 2, It can be seen from Table 2, that the calculated and experimental geometrical outcomes are found to be much closer to each other, as evident by the graphical correlation value (Fig. S7) for bond length and bond angles were determined as R^2 = 0.974 and 0.985 respectively. From XRD analysis, C8-C9, O1-C11, N3-C26 and C18-C19 bond lengths were observed as 1.370, 1.262, 1.331 and 1.380 Å respectively, whereas the calculated values through DFT were 1.392, 1279, 1.346 and 1.393 Å

PG & R. COLLEGE OF ARTS & SCIENCE NAMAKKAL 637 206

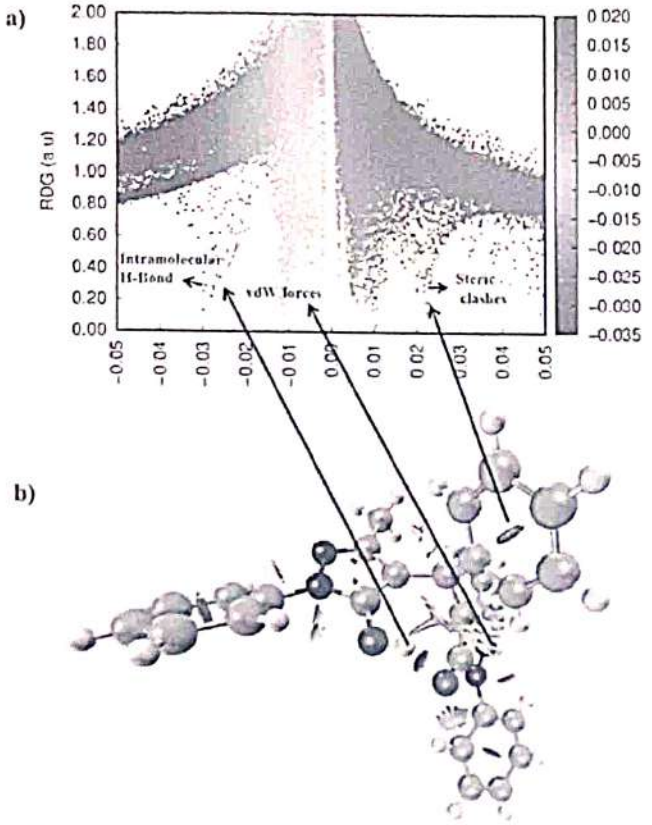


Fig. 7. Non-covalent interactions (NCIs) plot of BPZ molecule: (a) isosurface of reduced density gradient (RDG, represented by s) using s = 0.5 a.u. (b) RDG vs sign(λ2)*ρ.

respectively. Similarly, the single bond of N1-C9, O2-C19, C18-C26, and C8-C11 were found to be 1.349, 1.328, 1.401 and 1.421 Å respectively. The calculated values for these bonds are 1.340, 1.318, 1.389 and 1.416 Å respectively. Both experimental and theoretical values of O-H bond distance is slightly shortened whereas the C=O is becomes lengthen due to intra-molecular hydrogen (O-H···O) bonding between them. In a nutshell from the above findings, good accordance were observed between XRD and DFT structural parameters.

3.8. Frontier molecular orbital (FMO) analysis

The frontier molecular orbitals (FMO) such as HOMO (highest occupied molecular orbital and LUMO (lowest unoccupied molecular orbital) orbitals are an essential tool for determining the molecular interaction with other species, substance reactivity and stability. Among the two orbitals, HOMO orbital provides information about the ability to donate an electron whereas the LUMO orbital has the ability to accept an electron. Additionally, the energy separation between these orbitals can be used to study the reactivity of molecules and their kinetic stability. Also, they play a crucial role in the electrical, chemical and optical properties. The HOMO-LUMO orbitals energy gap was calculated for BPZ molecule using Gaussian 09 with B3LYP/6-311 g(d,p) level. The orbital structure visualization is displayed in Fig. 8. It is seen that the HOMO orbital is mostly localized into the pyrazole ring and some extent to phenyl rings, whereas the LUMO orbital is localized in other pyrazole and phenyl rings. The HOMO and LUMO energies of BPZ was determined as −7.536 eV and −3.0091 eV, respectively. The energy

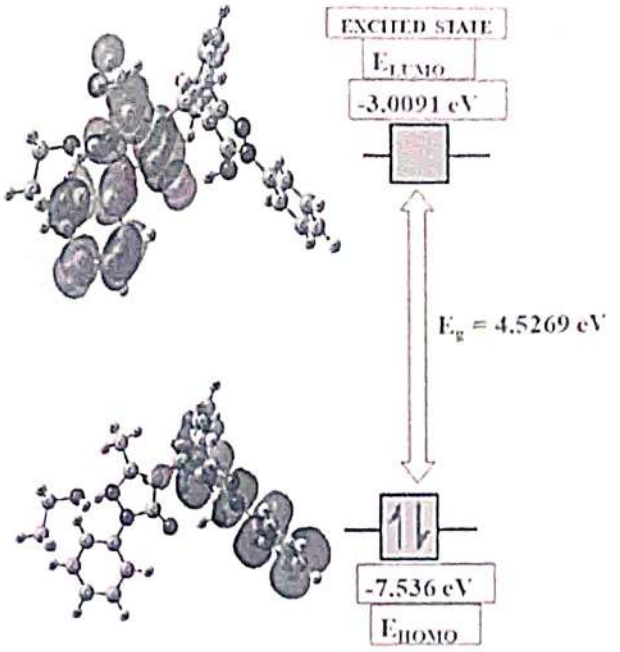


Fig. 8. Frontier molecular orbitals (HOMO and LUMO) of BPZ compound.

Table 5
Calculated energy values of BPZ at B3LYP/6-311 G (d, p) method.

Quantum Descriptors	B3LYP/6-311+G(d, p)
EHOMO (eV)	−7.576
ELUMO (eV)	−3.009
Ionization potential IP (eV)	7.536
Electron affinity EA (eV)	3.009
Energy gap Eg (eV)	4.527
Electronegativity χ (eV)	5.272
Chemical potential V (eV)	−5.272
Chemical hardness η (eV)	2.263
Softness σ (eV)	0.441
Electrophilicity ω (eV)	6.140

difference between these two orbitals was found to be 4.5269 eV. From the Fig. 8, it was observed that both HOMO and LUMO orbitals are typically π-anti-bonding type orbitals.

Further, the energy values of BPZ were predicted to describe the structural stability and global chemical reactivity parameters (GCRD). The chemical reactivity and the hardness of title molecule were obtained from the HOMO and LUMO orbitals energy gap (ΔE) values. The molecular orbital chemical reactivity descriptors such as Ionization potential (I), chemical potential (μ) electron affinity (A), chemical hardness (η), global softness (σ), electronegativity (χ), and electrophilicity (ω), are defined based on the Koopman's relation [49].

Koopman's relation states that, a larger HOMO-LUMO energy gap demonstrates the hardness of the molecule whereas a lower energy gap indicates the softness of the molecule. The calculated electronic properties of BPZ compound is shown in Table 5. It can be seen that the hardness of BPZ compound was calculated to be 2.26 eV which made it soft with rapid electron transfer. The stability of the BPZ molecule is in the direction of hardness, which resources that the molecule with the smallest HOMO-LUMO gap describes it is more reactive and low kinetic stability. The greater value (6.140 eV) shown by electrophilicity index (ω) validate the electrophilic behavior of the molecule.

P.G.P. COLLEGE OF ARTS & SCIENCE NAMAKKAL 637 206

The GCRDs of the present investigation confirms the better chemical strength and stability of BPZ and therefore favours the appropriateness of the material for future optoelectronic applications.

3.9. Natural bond orbital (NBO) analysis

The NBO analysis, [50] offers an important and elegant method for revealing the inter- and intramolecular forces between the bonds in a molecules. This splits the electron density of an entire molecule into atom-like orbitals. An analysis can be performed by exploring the conceivable interactions between a filled NBO's (donor) and empty NBO's (acceptor) of Lewis and non-Lewis types, respectively. An electron cloud delocalization between bonding and anti-bonding orbitals is a major contributor to stabilize the donor-acceptor interactions and its strength can be measurable using second order perturbation theory.

The stabilization energy E(2) between donor and acceptor of delocalized molecule can be described through $E^2 = q_i F_i^2{}_j / (\varepsilon_j - \varepsilon_i)$ where q_i is the donor orbital occupancy, ε_i and ε_j are the energies of the donor and acceptor orbitals, respectively. $F_{i,j}$ is the off-diagonal element of the Fock matrix in the NBO basis [51]. Electron donors and acceptors interact more intensively when the E(2) value is higher. A greater degree of electron donation will result in a greater degree of conjugation of entire molecule. To describe the electron cloud delocalization and intra-molecular rehybridization, NBO analysis was carried out for BPZ with B3LYP/6-311g(d,p) level. The calculated perturbation energies of donor acceptor interaction parameters are listed in Table 6. It is seen that the following transitions were obtained from DFT study. Among the possible electronic transition with greatest magnitude, π (C9-C24) $\rightarrow \pi^*$(C36-C54), π (C9-C24) $\rightarrow \pi^*$(C48-C50), π (C42-C44) $\rightarrow \pi^*$(C16-C22), π (C42-C44) $\rightarrow \pi^*$(C18-C46), π (C48-C50) $\rightarrow \pi^*$(C9-C24) and π (C48-C50) $\rightarrow \pi^*$(C36-C54) and σ (C38-C39) $\rightarrow \pi^*$(C12-C20) exposed stabilization energies are 38.59, 45.05, 41.08, 45.64, 39.60, 45.34 and 19.9 KJ mol^{-1}, respectively. In addition, π (N7-C20) $\rightarrow \pi^*$(C12-C15) electronic transition shows less stabilization energy, which was found to be 15.09 kcal/mol. Moreover, LP $\rightarrow \pi^*$ interactions was seen as LP(O1) $\rightarrow \sigma^*$(N6-C21), LP(O1) $\rightarrow$ RY*(C21) and LP(O2) $\rightarrow$ RY*(C15) afforded stabilization energies of 1.71, 16.06 and 4.76 kJ mol^{-1}, respectively. The Table 6 clearly revealed that the phenyl and pyrazole ring in BPZ molecule is stabilized by strong intra-molecular hyper conjugation of σ and π electrons of C–C to the anti C–C bond.

3.10. Population analysis

Population analysis is utilized to define the charge distribution and derive the atomic charges. In quantum chemical calculation, mulliken atomic charges play a crucial role in determining the properties of molecular system including electronic structure, dipole moment and molecular polarizability [52]. It has been used to describe the method of charge transfer and obtaining equal electronegativity in chemical reactions. Therefore, the concept of atomic charges are very useful for understanding the properties of molecules and important for the design of the drugs.

The mulliken atomic charge plot is depicted in Fig.S8, Table 7. It can be seen that the carbon atom C15 and C21 are more positive charge (0.92373 and 0.997937 a.u), which have been fused together with highly electronegative oxygen atoms (hydroxyl and carbonyl groups, respectively). Similarly, the carbons C9, C14, C16, and C20 exhibits with medium positive charge due to attached with less electronegative nitrogen atoms attached to it. However, two carbon atoms, namely, C26 and C38 (methyl) were appeared with maximum negative charge (−0.9825 a.u), as they were attached with pyrazoline ring. Furthermore, negative charges of oxygen and nitrogen atoms, O1 and O2, shows greater negative charge due to the participation of O–H···O intra-molecular hydrogen bonding. Also, the N6 and N8 atoms exhibit higher negative charge due to π-electron delocalization in phenyl ring. However, all hydrogen atoms were splits with the positive charges, as shown in Fig. S8.

3.11. Molecular electrostatic potential (MEP)

Molecular electrostatic potential (MEP) is an elegant tool used to describe the electron density in the molecular structure that has been examined in a variety of organic molecules. As a result, the charge dispersions of organic molecules can be predicted in three dimensions. The MEP surface analysis enables us to envision variably the charged area of the molecular structures. Furthermore, these studies support the interpretation of molecular surface abundances and lack of electrons. The electrostatic potential can be computed using the ramifications of standard electronic structure theory and experimental X-ray diffraction data. The MEP surface of BPZ was predicted by DFT method with B3LYP/6-311 g(d, p) level and the surface map is depicted in Fig. S9. The MEP surface of title compound lies between 9.057e-2 (dark blue) to −9.057e-2 (dark red) eV. The region around the oxygen atoms of the carbonyl group and one of the pyrazoline ring were seems to be darkest red that is one with the maximum electron density and more negative potential (electron rich), which provide more reactive site in the molecular surface. The region surrounding the hydrogen atoms of the nitrogen atom (another pyrazoline group) was found to be the highest electron deficient site as evident from the deep blue region in the MEP surface. –

3.12. Determination of dipole moment, polarizability and first order hyperpolarizability

Nowadays, organic compounds have been identified as potential candidates for NLO application because of their low cost and high hyperpolarizability. It has been reported that electronic properties of organic molecules are responsible for frequency shifting in telecommunications, optical modulation of signal processing, optical circuitry, optical logic and optical storage devices. The calculations of quantum chemical approach can be used to get better understanding from the electronic structure of the material.

The non-linear optical (NLO) properties are greatly influenced by the values of dipole moment (μ), electron mobility, polarizability (α) and hyperpolarizability (β). The NLO behavior of molecules can be increased by increasing the values of the polarizabilities and first order hyperpolarizabilities. In this context, the molecular NLO properties such as static dipole moment (μ), average polarizability (α), anisotropy of the polarizability ($\Delta\alpha$) and first order molecular hyperpolarizability (β) were predicted theoretically for a title compound by DFT method with B3LYP/6-311 g(d,p) level using the Eqs. (1)-(4). The calculated μ, α, $\Delta\alpha$ and β values along with their contributing tensor components are given in Table 8. The dipole moment and average polarizability α_{tot} were calculated from Eqs. (1) and (2), while anisotropy polarizability and second order hyperpolarizability (β_{tot}) were derived from Eqs. (3) and (4), respectively.

$$\mu_{tot} = (\mu_x^2 + \mu_y^2 + \mu_z^2)^{\frac{1}{2}} \quad \ldots\ldots(1)$$

$$\alpha_{tot} = \frac{1}{3}(\alpha_{xx} + \alpha_{yy} + \alpha_{zz}) \quad \ldots\ldots(2)$$

P.G.P. COLLEGE OF ARTS & SCIENCE NAMAKKAL 637 206

Table 6
Second order Perturbation theory analysis of Fock matrix in NBO basis for BPZ.

Donor (i)	[a]ED(i)(e)	Acceptor (j)	[a]ED(j)(e)	[b]E(2)kJ mol^{-1}	[c]E(j)-E(i) a.u	[d]F(i,j)a.u
σ (O1-C21)	1.99516	σ*(N4-N6)	0.02042	1.33	1.87	0.045
		σ*(C13-C14)	0.02409	0.54	2.28	0.031
σ (O2-C15)	1.99485	σ*(N7-N8)	0.01819	1.32	1.78	0.043
		σ*(C12-C15)	0.02908	1.96	2.1	0.058
σ (N4-H5)	1.97292	π*(C13-C14)	0.22586	4.18	1.07	0.063
		σ*(N6-C16)	0.02944	0.88	1.65	0.034
		σ*(C13-C14)	0.02409	0.51	1.93	0.028
σ (N4-C14)	1.98756	RY*(N6)	0.00175	0.56	2.89	0.036
σ (N6-C16)	1.9869	σ*(C18-C46)	0.01741	1.21	1.93	0.043
σ (N6-C21)	1.98691	RY*(N4)	0.0021	0.75	2.78	0.041
		σ*(C13-C21)	0.04551	0.62	1.85	0.03
		σ*(C16-C22)	0.02176	1.19	1.96	0.043
σ (N7-N8)	1.9803	σ*(C20-C38)	0.01753	5.37	1.67	0.084
σ (N7-C20)	1.98927	σ*(C20-C38)	0.01753	1.65	1.83	0.049
π (N7-C20)	1.93427	π*(C12-C15)	0.34967	15.09	0.59	0.091
σ (N8-C15)	1.9849	σ*(N8-C9)	0.02928	4.98	1.74	0.083
		σ*(C9-C36)	0.02117	1.16	1.95	0.043
		σ*(C10-C12)	0.03021	4.32	1.75	0.078
		σ*(C12-C15)	0.02908	2.19	1.97	0.059
σ (C9-C24)	1.97374	σ*(C48-H49)	0.01004	2.03	1.71	0.053
π (C9-C24)	1.65826	π*(C36-C54)	0.32888	38.59	0.49	0.123
		π*(C48-C50)	0.33752	45.05	0.49	0.133
σ (C10-H11)	1.97389	RY*(C12)	0.00363	1.19	2.11	0.045
		π*(C17-C34)	0.34171	0.56	0.86	0.021
σ (C10-C12)	1.96661	π*(C13-C14)	0.22586	1.47	1	0.036
		π*(C17-C34)	0.34171	2.34	1	0.047
σ (C10-C13)	1.96904	σ*(C17-C34)	0.02159	1.63	1.69	0.047
		π*(C17-C34)	0.34171	0.89	1	0.029
σ (C10-C17)	1.96987	σ*(C32-C34)	0.01699	2.38	1.67	0.056
σ (C12-C20)	1.96842	σ*(C20-C38)	0.01753	3.24	1.57	0.064
		σ*(C38-H39)	0.00394	0.64	1.62	0.029
σ (C13-C14)	1.97059	σ*(C10-C13)	0.03045	6.69	1.65	0.094
π (C30-C56)	1.66689	π*(C17-C34)	0.34171	44.46	0.49	0.131
		π*(C32-C52)	0.338	41.77	0.48	0.127
σ (C32-H33)	1.98424	RY*(C34)	0.00592	1.46	2.25	0.051
		RY*(C52)	0.00547	1.59	2.24	0.054
σ C(38- H39)	1.98628	π*(C12-C20)	0.02045	4.78	1.13	0.066
π (C42-C44)	1.66392	π*(C16-C22)	0.38363	41.08	0.46	0.125
		π*(C18-C46)	0.32819	45.64	0.48	0.133
π (C48-C50)	1.67374	π*(C9-C24)	0.37155	39.6	0.47	0.124
		π*(C36-C54)	0.32888	45.34	0.48	0.132
σ (C50-H51)	1.98437	σ*(C24-C48)	0.01758	3.72	1.58	0.068
		σ*(C36-C54)	0.01692	3.64	1.58	0.068
		σ*(C48-C50)	0.0175	2.57	1.57	0.057
		σ*(C50-C54)	0.01756	2.49	1.57	0.056
σ (C50-C54)	1.97927	σ*(C36-H37)	0.01247	2.46	1.71	0.058
σ (C52-H53	1.98446	σ*(C52-C56)	0.01746	2.48	1.57	0.056
LP(O1)	1.94567	RY*(C21)	0.01626	16.06	1.97	0.16
		σ*(N6-C21)	0.06375	1.71	1.52	0.046
LP(O2)	1.95808	RY*(C15)	0.01011	4.76	1.93	0.086
π*(N7-C20)	0.00006	σ*(C38-H40)	0.00687	1.42	0.54	0.061
		σ*(C38-H41)	0.00705	1.53	0.54	0.063
π*(C9-C24)	0.37155	π*(C36-C54)	0.32888	665.6	0.01	0.124
π*(C16-C22)	0.38363	π*(C18-C46)	0.32819	385.3	0.02	0.125
		π*(C42-C44)	0.33382	417.24	0.02	0.127
π*(C17-C34)	0.34171	σ*(C10-C12)	0.03021	1.92	0.47	0.062
		σ*(C10-C13)	0.03045	0.6	0.47	0.035
σ(N6-C21)	1.98691	LP*(H3)	0.45819	0.26	1.37	0.019
LP (N4)	1.78821	σ*(O58-C64)	0.01578	0.06	0.93	0.007

[a] ED is the occupation number.
[b] $E^{(2)}$is the energy of hyperconjugative interactions.
[c] Energy difference between donor and acceptoriandj NBO orbitals.
[d] F(i, j) is the Fock matrix element betweeniandj NBO orbitals.

$$\Delta\alpha = \frac{1}{\sqrt{2}}[(\alpha_{xx}-\alpha_{yy})^2 + (\alpha_{yy}-\alpha_{zz})^2 + (\alpha_{zz}-\alpha_{xx})^2 + 6\alpha_{xz}^2 + 6_{xy}^2 + 6\alpha_{yz}^2\ ]^{\frac{1}{2}} \quad (3)$$

$$\beta_{tot} = [(\beta_{XXX}+\beta_{XYZ}+\beta_{XZZ})^2 + (\beta_{YYY}+\beta_{YZZ}+\beta_{YXX})^2 + (\beta_{ZZZ}+\beta_{ZXX}+\beta_{ZYY})^2]^{1/2} \ldots\ldots(4)$$

The estimated values of μ, α, and β for BPZ were found to be 7.58 D, 25.4 × 10^{-24}, and 2.04 × 10^{-30} esu, respectively (Table 8). It can be seen that the BPZ was found to be greater NLO value when compared with urea molecule which has been frequently applied as a reference NLO molecule for comparative analysis (0.78 × 10^{-30}). The effective optimization of the molecular polarizability through the larger dipole moment of the molecule leads to an improvement in the molecular hyperpolarizability.

P.G.P. COLLEGE OF ARTS & SCIENCE NAMAKKAL 637 206

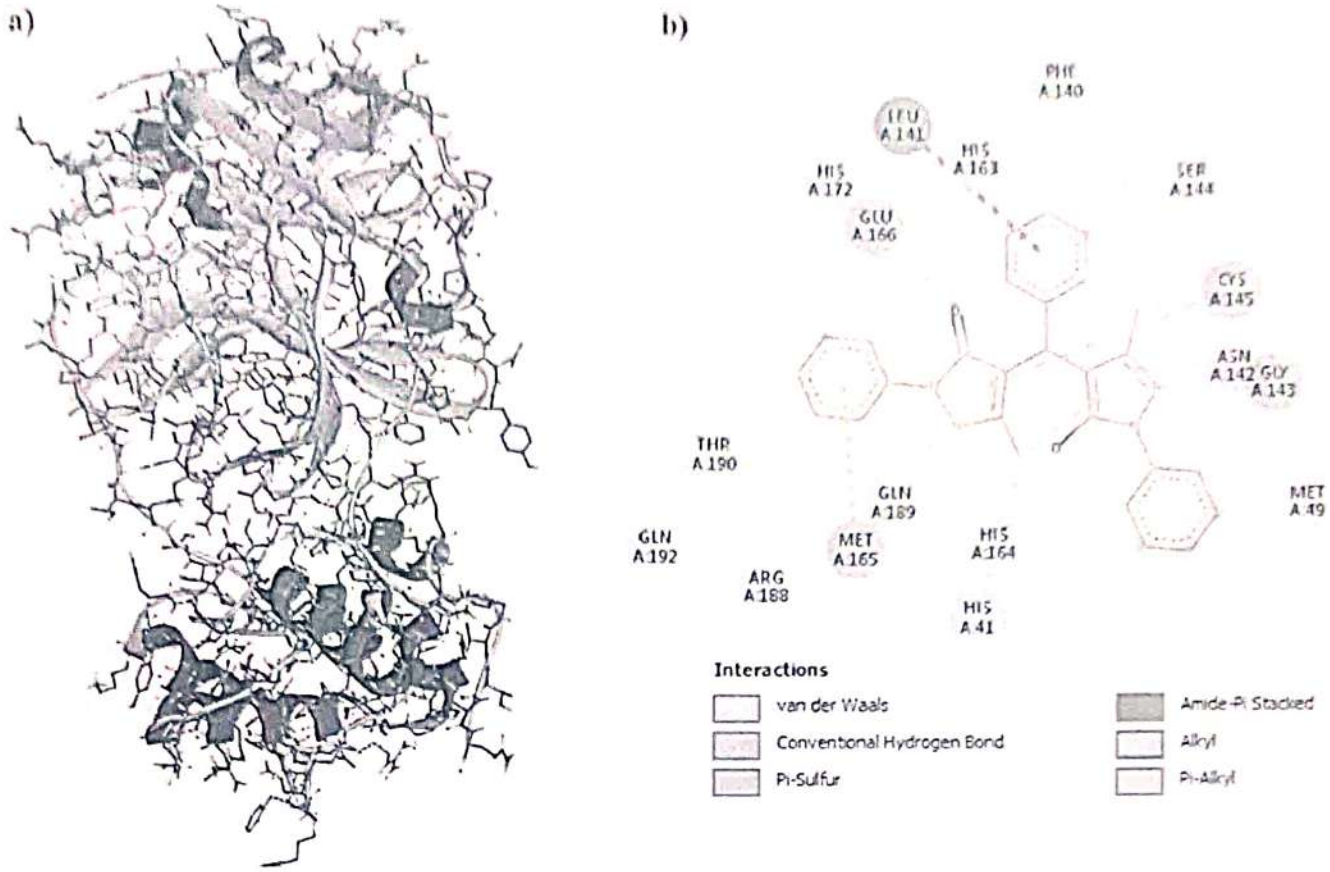


Fig. 9. a) The docked conformation of the BPZ-6LU7 complex b) The possible interactions between BPZ and various amino acids of nCoV-SARS-2 M^{pro} are shown.

Table 7
Natural population analysis and Mulliken population analysis of BPZ molecule.

Atom	Charge/e	Atom	Charge/e	Atom	Charge/e
1 O	−0.74527	23 H	0.259978	45 H	0.240298
2 O	−0.79232	24 C	−0.252804	46 C	−0.22899
3 H	0.466614	25 H	0.297554	47 H	0.249959
4 N	−0.62739	26 C	−0.629914	48 C	−0.23375
5 H	0.418444	27 H	0.250923	49 H	0.235267
6 N	−0.81404	28 H	0.254647	50 C	−0.24963
7 N	−0.39[illegible]35	29 H	0.239237	51 H	0.23[illegible]15
8 N	−0.88004	30 C	−0.254726	52 C	−0.24343
9 C	0.407289	31 H	0.264644	53 H	0.234213
10 C	−0.44141	32 C	−0.233625	54 C	−0.23231
11 H	0.259817	33 H	0.233878	55 H	0.233161
12 C	−0.23212	34 C	−0.217199	56 C	−0.23035
13 C	−0.22069	35 H	0.224597	57 H	0.238436
14 C	0.473325	36 C	−0.24306	58 O	−0.68308
15 C	0.92373	37 H	0.279572	59 H	0.39781
16 C	0.381255	38 C	−0.614743	60 C	−0.63582
17 C	0.022898	39 H	0.245732	61 H	0.216202
18 C	−0.23969	40 H	0.204223	62 H	0.206413
19 H	0.297885	41 H	0.205846	63 H	0.22979
20 C	0.399745	42 C	−0.248086	64 C	−0.09721
21 C	0.997937	43 H	0.242378	65 H	0.232085
22 C	−0.26178	44 C	−0.227892	66 H	0.205911

Molecules have large inter and intramolecular interactions, whereas their dipole moment is larger. These things, in turn, play a key role in the rapid response of the molecules to an electric field by changing their polarizability. Due to this, greater numbers of molecules are oriented in the direction of the applied electric field

Table 8
The dipole moment (μ) (Debye), polarizability (α) and first hyperpolarizability (β) of BPZ.

Parameter	a.u	Parameter	a.u
α_{xx}	−165.2582	β_{xxx}	−181.2861
α_{xy}	−1.2793	β_{xxy}	−50.9531
α_{yy}	−178.3084	β_{xyy}	4.2083
α_{xz}	−15.1607	β_{yyy}	−20.4357
α_{yz}	6.9180	β_{xxz}	6.7510
α_{zz}	−178.4662	β_{xyz}	−27.4107
α_{total}	25.5×10^{-24} esu	β_{yyz}	−9.5002
μ_x	−6.6487	β_{xzz}	−17.0213
μ_y	2.2827	β_{yzz}	29.9614
μ_z	2.8584	β_{zzz}	11.0420
μ_{total}	7.5886	β_{total}	2.041×10^{-30} esu

and, larger nonlinearities could be achieved. Finally, the estimated μ, α, and β values of title compound suggests that the appropriateness of the grown crystal could be the potential candidate for future NLO applications.

3.13. Molecular docking study

The binding affinity is the key function to understand the interaction between inhibitor (ligand) and receptor (biomolecule). The binding affinity is greatly affected by the non-covalent interaction such as H-bond, electrostatic interaction, hydrophobic and van der Waals forces. The molecular docking study was examined for BPZ how the heterocyclic pyrazoline ligand might bind to the COVID-19 caused protein. The viral replication relies mainly on the main

PG COLLEGE OF ARTS & SCIENCE NAMAKKAL 637 206

protease (nCov-SARS-2 M^{pro}) [53]. The protein structure of COVID-19 main protease was obtained from protein data bank (PDB ID: 6LU7). The lead molecule (BPZ) was fitted to interact with the active site of 6LU7 main protease. The binding modes and their nature of interaction of BPZ-6LU7 were investigated, shown in Fig. 9. The docking outcomes revealed that BPZ ligand exhibited good binding affinity towards 6LU7 protein with a (−9.27 kcal/mol binding score (Table S2). It has been noted that the amino acid reside such as HIS41A, LEU141A, GLY143A, CYS145A, MET165A, GLU166A and GLN189A. Out of which, residues GLY143A and GLU166A were formed conventional H-bonding with BPZ ligand [54]. In addition, other interaction such as π-S, amide-π stacking, and π-alkyl interactions were observed with CYS145A/MET165A, LEU141A, and HIS41A, respectively. In conclusion, the molecular docking study discloses that the major contribution of N and O atoms of ligand were found to be effective binding affinity with the chosen biomolecule. This could be attributed to the presence of lone-pair electrons on these atoms. Besides, stacked-π, σ-π, and anion-π contacts were the major contributors in hydrophobic interactions.

4. Conclusion

BPZ was successfully synthesized by one pot three component reactions using reusable heterogeneous cerium doped SiO_2 catalyst. The molecular structure was characterized by single crystal X-ray diffraction technique. The crystal structure is well-designed by inter and intramolecular hydrogen bonding interactions and appears to be a well-constructed supramolecularity. Further, the intermolecular hydrogen bonding was explored through the Hirshfeld surface and 2D finger print analysis, which revealed that C–H···π, C–H···O, O–H···C, O–H···N and H···H were the major contribution to stabilize the crystal packing, whereas the intra molecular hydrogen bonding study was demonstrated through NCI-RDG analysis. The molecular geometry was optimized using DFT method with B3LYP/6–311 g(d,p) level to describe the electronic properties such as FMO, MEP, NPA and NLO. The BPZ molecule is found to be stable due to intramolecular charge transfers and hyperconjugative interactions, as revealed by the NBO analysis. Further, the intermolecular charge transfer was confirmed by Mulliken population analysis. The NLO study showed that the significant responses as compared to the prototype molecule. Hence, it is expected that this experimental and theoretical work of BPZ type molecule may offer a new horizons in the field of optoelectronics. Finally, the molecular docking was discussed and the study revealed that the existence of conventional hydrogen bonding interaction between BPZ and active site of 6LU7 protein structure. The binding affinity energy (−9.27 kcal/mol) is comparable to those of the approved medicines such as remdesivir (−6.96 kcal/mol) and favipiravir (−4.06 kcal/mol).

Declaration of Competing Interest

The authors declare that they have no known competing financial interests or personal relationships that could have appeared to influence the work reported in this paper.

Supplementary materials

CCDC 859,834 contains the supplementary crystallographic data for this paper. These data can be obtained free of charge via http://www.ccdc.cam.ac.uk/conts/retrieving.html (or from the Cambridge Crystallographic Data center, 12, Union Road, Cambridge CB2 1EZ, UK; fax: +44 1223 336,033).Supplementary material associated with this article can be found, in the online version, at doi:10.1016/j.molstruc.2021.132170.

CRediT authorship contribution statement

Ramachandran Rajamanickam: Methodology, Formal analysis, Supervision, Writing – original draft, Writing – review & editing. **Senthan Sivakolunthu:** Conceptualization, Methodology, Formal analysis. **Jayanthi Sampathkumar:** Software, Methodology, Data curation, Investigation.

References

[1] A. Hasan, A. Abbas, M.N. Akhtar, Synthesis, characterization and fluorescent property evaluation of 1,3,5-triaryl-2-pyrazolines, Molecules 16 (2011) 7789–7802. doi:10.3390/molecules16097789.

[2] A. Szukalski, L. Sznitko, K. Cyprych, A. Miniewicz, J. Mysliwiec, Light amplification in derivatives of pyrazoline-based systems, J. Phys. Chem. C. 118 (2014) 8102–8110. doi:10.1021/jp411031b.

[3] I. Papagiannouli, A. Szukalski, K. Haupoulos, J. Mysliwiec, S. Couris, B. Sahraoui, Pyrazoline derivatives with a tailored third order nonlinear optical response, RSC Adv. 5 (2015) 48363–48367. doi:10.1039/C5RA05912G.

[4] B. Nehra, S. Rulhania, S. Jaswal, B. Kumar, G. Singh, V. Monga, Recent advancements in the development of bioactive pyrazoline derivatives, Eur. J. Med. Chem. 205 (2020) 112666. doi:10.1016/j.ejmech.2020.112666.

[5] A. Özdemir, G. Turan-Zitouni, Z. Asim Kaplancikli, G. Revial, K. Güven, Synthesis and antimicrobial activity of 1-(4-aryl-2-thiazolyl)-3-(2-thienyl)-5-aryl-2-pyrazoline derivatives, Eur. J. Med. Chem. 42 (2007) 403–409. doi:10.1016/j.ejmech.2006.10.001.

[6] V. Monga, K. Goyal, M. Steindel, M. Malhotra, D.P. Rajani, S.D. Rajani, Synthesis and evaluation of new chalcones, derived pyrazoline and cyclohexenone derivatives as potent antimicrobial, antitubercular and antileishmanial agents, Med. Chem. Res. 23 (2014) 2019–2032. doi:10.1007/s00044-013-0803-1.

[7] S.Y. Hassan, Synthesis, antibacterial and antifungal activity of some new pyrazoline and pyrazole derivatives, Molecules 18 (2013). doi:10.3390/molecules18032683.

[8] R. Aggarwal, A. Bansal, I. Rozas, B. Kelly, P. Kaushik, D. Kaushik, Synthesis, biological evaluation and molecular modeling study of 5-trifluoromethyl-Δ2-pyrazoline and isomeric 5/3-trifluoromethylpyrazole derivatives as anti-inflammatory agents, Eur. J. Med. Chem. 70 (2013) 350–357. doi:10.1016/j.ejmech.2013.09.052.

[9] C. Kharbanda, M.S. Alam, H. Hamid, K. Javed, S. Bano, A. Dhulap, Y. Ali, S. Nazreen, S. Haider, Synthesis and evaluation of pyrazolines bearing benzothiazole as anti-inflammatory agents, Bioorg. Med. Chem. 22 (2014) 5804–5812. doi:10.1016/j.bmc.2014.09.028.

[10] B.N. Acharya, D. Saraswat, M. Tiwari, A.K. Shrivastava, R. Ghorpade, S. Bapna, M.P. Kaushik, Synthesis and antimalarial evaluation of 1, 3, 5-trisubstituted pyrazolines, Eur. J. Med. Chem. 45 (2010) 430–438. doi:10.1016/j.ejmech.2009.10.023.

[11] G. Wanare, R. Aher, N. Kawathekar, R. Ranjan, N.K. Kaushik, D. Sahal, Synthesis of novel α-pyranochalcones and pyrazoline derivatives as Plasmodium falciparum growth inhibitors, Bioorg. Med. Chem. Lett. 20 (2010) 4675–4678. doi:10.1016/j.bmcl.2010.05.069.

[12] H.H. Wang, K.M. Qiu, H.E. Cui, Y.S. Yang, M.X. Yin-Luo, X.Y. Qiu, L.F. Bai, H.L. Zhu, Synthesis, molecular docking and evaluation of thiazolyl-pyrazoline derivatives containing benzodioxole as potential anticancer agents, Bioorg. Med. Chem. 21 (2013) 448–455. doi:10.1016/j.bmc.2012.11.020.

[13] M.A. Ali, M. Shaharyar, A.A. Siddiqui, Synthesis, structural activity relationship and anti-tubercular activity of novel pyrazoline derivatives, Eur. J. Med. Chem. 42 (2007) 268–275. doi:10.1016/j.ejmech.2006.08.004.

[14] S.D. Joshi, S.R. Dixit, M.N. Kirankumar, T.M. Aminabhavi, K.V.S.N. Raju, R. Narayan, C. Lherbet, K.S. Yang, Synthesis, antimycobacterial screening and ligand-based molecular docking studies on novel pyrrole derivatives bearing pyrazoline, isoxazole and phenyl thiourea moieties, Eur. J. Med. Chem. 107 (2016) 133–152. doi:10.1016/j.ejmech.2015.10.047.

[15] S. Bhandari, A.C. Tripathi, S.K. Saraf, Novel 2-pyrazoline derivatives as potential anticonvulsant agents, Med. Chem. Res. 22 (2013) 5290–5296. doi:10.1007/s00044-013-0530-7.

[16] Y. Rajendra Prasad, A. Lakshmana Rao, L. Prasoona, K. Murali, P.R. Kumar, Synthesis and antidepressant activity of some 1,3,5-triphenyl-2-pyrazolines and 3-(2″-hydroxy naphthalen-1″-yl)-1,5-diphenyl-2-pyrazolines, Bioorg. Med. Chem. Lett. 15 (2005) 5030–5034. doi:10.1016/j.bmcl.2005.08.040.

[17] Z.A. Kaplancıklı, A. Özdemir, G. Turan-Zitouni, M.D. Altıntop, Ö.D. Can, New pyrazoline derivatives and their antidepressant activity, Eur. J. Med. Chem. 45 (2010) 4383–4387. doi:10.1016/j.ejmech.2010.06.011.

[18] Z.A. Kaplancikli, G. Turan-Zitouni, A. Özdemir, O. Devrim Can, P. Chevallet, Synthesis and antinociceptive activities of some pyrazoline derivatives, Eur. J. Med. Chem. 44 (2009) 2606–2610. doi:10.1016/j.ejmech.2008.09.002.

[19] U.P. Singh, H.R. Bhat, A. Verma, M.K. Kumawat, R. Kaur, S.K. Gupta, R.K. Singh, Phenyl hydrazone bearing pyrazole and pyrimidine scaffolds: design and discovery of a novel class of non-nucleoside reverse transcriptase inhibitors (NNRTIs) against HIV-1 and their antibacterial properties, RSC Adv. 3 (2013) 17335. doi:10.1039/c3ra41604f.

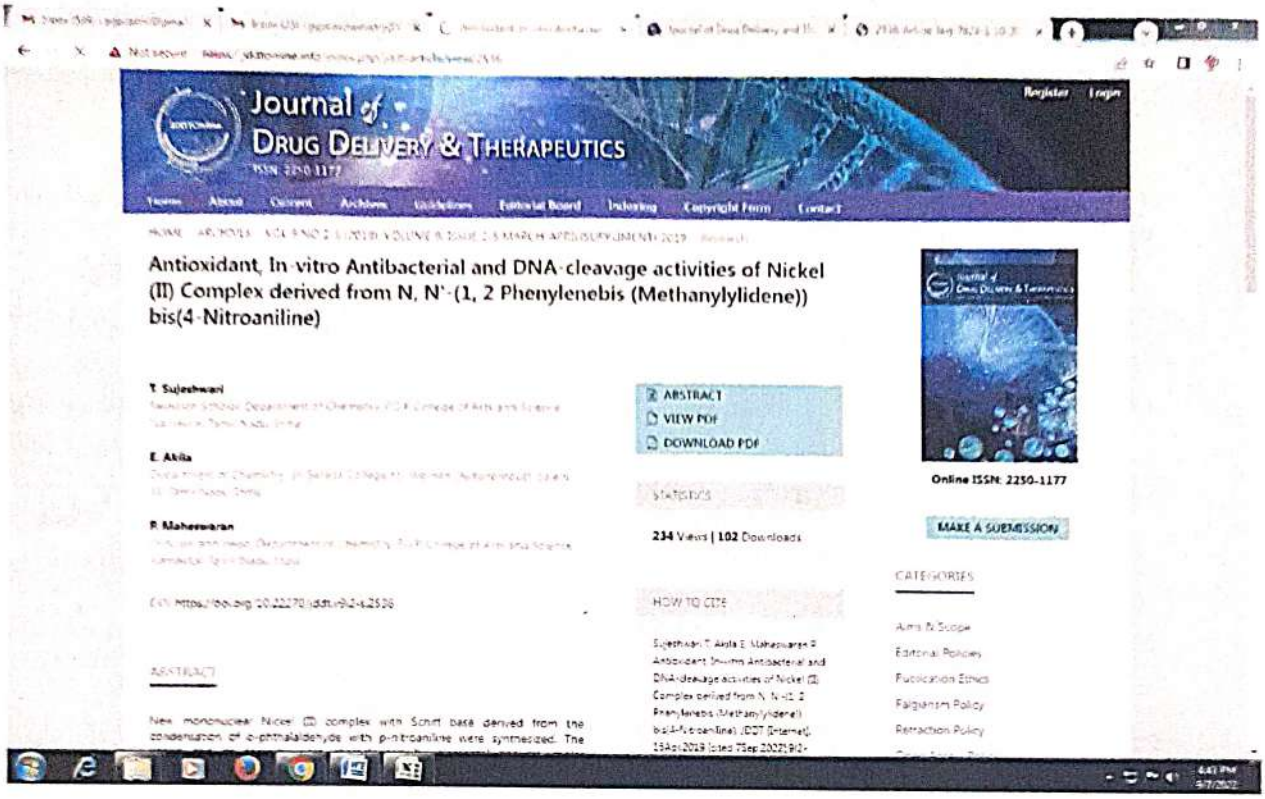
[20] D. Havrylyuk, B. Zimenkovsky, O. Karpenko, P. Grellier, R. Lesyk, Synthesis of pyrazoline-thiazolidinone hybrids with trypanocidal activity, Eur. J. Med. Chem. 85 (2014) 245–254. doi:10.1016/j.ejmech.2014.07.103.

P.G.P. COLLEGE OF ARTS & SCIENCE NAMAKKAL 637 206

[21] A.A. Elfiky, R. Ribavirin, G. Sofosbuvir, Tenofovir against SARS CoV-2 RNA dependent RNA polymerase (RdRp): a molecular docking study, Life Sci. 253 (2020) 117592, doi:10.1016/j.lfs.2020.117592.
[22] B. Nutho, P. Mahalapbutr, K. Hengphasatporn, N.C. Pattaranggoon, N. Simanon, Y. Shigeta, S. Hannongbua, T. Rungrotmongkol, Why are lopinavir and ritonavir effective against the newly emerged coronavirus 2019? Atomistic insights into the inhibitory mechanisms, Biochemistry 59 (2020) 1769–1779, doi:10.1021/acs.biochem.0c00160.
[23] M. Missioui, M.A. Said, G. Demirtaş, J.T. Mague, Y. Ramli, Docking of disordered independent molecules of novel crystal structure of (N-(4-methoxyphenyl)-2-(3-methyl-2-oxo-3,4-dihydroquinoxalin-1(2H)-yl)acetamide as anti-COVID-19 and anti-Alzheimer's disease. Crystal structure, HSA/DFT/XRD, J. Mol. Struct. 1247 (2022) 131420, doi:10.1016/j.molstruc.2021.131420.
[24] V.A. Verma, A.R. Saundane, R.S. Meti, D.R. Vennapu, Synthesis of novel indolo[3,2-c]isoquinoline derivatives bearing pyrimidine, piperazine rings and their biological evaluation and docking studies against COVID-19 virus main protease, J. Mol. Struct. 1229 (2021) 129829, doi:10.1016/j.molstruc.2020.129829.
[25] C.T. Zeyrek, Ö.T. Arpacı, M. Arısoy, F.K. Onurdağ, Synthesis, antimicrobial activity, density functional modelling and molecular docking with COVID-19 main protease studies of benzoxazole derivative: 2-(p-chloro-benzyl)-5-[3-(4-*ethly*-1-*piperazynl*) *propionamido*]-benzoxazole, J. Mol. Struct. 1237 (2021) 130413, doi:10.1016/j.molstruc.2021.130413.
[26] J. Wu, Z. Li, J. Luo, A.K.Y. Jen, High-performance organic second- and third-order nonlinear optical materials for ultrafast information processing, J. Mater. Chem. C 8 (2020) 15009–15026, doi:10.1039/D0TC03224G.
[27] H. Xu, L.E. Johnson, Y. de Coene, D.L. Elder, S.R. Hammond, K. Clays, L.R. Dalton, B.H. Robinson, Bis(4-dialkylaminophenyl)heteroarylamino donor chromophores exhibiting exceptional hyperpolarizabilities, J. Mater. Chem. C 9 (2021) 2721–2728, doi:10.1039/D0TC05700B.
[28] J. Huang, Y. Yang, J. He, Z. He, H. Wu, The important role of tetraphenylethene on designing bichromophores for organic nonlinear optical materials, Mater. Lett. 291 (2021) 129521, doi:10.1016/j.matlet.2021.129521.
[29] G.F. Jasmine, M. Amalanathan, S.D.D. Roy, Molecular structure and charge transfer contributions to nonlinear optical property of 2-Methyl-4-nitroaniline: a DFT study, J. Mol. Struct. 1112 (2016) 63–70, doi:10.1016/j.molstruc.2016.02.013.
[30] M. Hochberg, T. Baehr-Jones, G. Wang, M. Shearn, K. Harvard, J. Luo, B. Chen, Z. Shi, R. Lawson, P. Sullivan, A.K.Y. Jen, L. Dalton, A. Scherer, Terahertz all-optical modulation in a silicon–polymer hybrid system, Nat. Mater. 5 (2006) 703–709, doi:10.1038/nmat1719.
[31] M. Khalid, H.M. Lodhi, M.U. Khan, M. Imran, Structural parameter-modulated nonlinear optical amplitude of acceptor–π–D–π–donor-configured pyrene derivatives: a DFT approach, RSC Adv. 11 (2021) 14237–14250, doi:10.1039/D1RA00876E.
[32] P. Jayaprakash, P. Sangeetha, M. Peer Mohamed, G. Vinitha, S. Muthu, M. Prakash, M. Lydia Caroline, Growth and characterization of dl-mandelic acid ($C_6H_5CH(OH)CO_2H$) single crystal for third-order nonlinear optical applications, J. Mol. Struct. 1148 (2017) 314–321, doi:10.1016/j.molstruc.2017.07.049.
[33] P. Jayaprakash, M.L. Caroline, S. Sudha, R. Ravisankar, G. Vinitha, P. Ramesh, E. Raju, Synthesis, growth, optical and third order nonlinear optical properties of L-Phenylalanine D-mandelic acid single crystal for photonic device applications, J. Mater. Sci. Mater. Electron. 31 (2020) 20460–20471, doi:10.1007/s10854-020-04565-3.
[34] G.M. Sheldrick, No Title, SHELXL-97, University of Göttingen, 1997.
[35] L.J. Farrugia, Ortep-3 for windows, J. Appl. Cryst. 30 (1997) 565.
[36] A.L. Spek, Single-crystal structure validation with the program PLATON, J. Appl. Crystallogr. 36 (2003) 7–13, doi:10.1107/s0021889802022112.
[37] P.R. Spackman, M.J. Turner, J.J. McKinnon, S.K. Wolff, D.J. Grimwood, D. Jayatilaka, M.A. Spackman, Crystal explorer: a program for Hirshfeld surface analysis, visualization and quantitative analysis of molecular crystals, J. Appl. Crystallogr. 54 (2021) 1006–1011, doi:10.1107/s1600576721002910.
[38] Gaussian 09, Revision A.02: M.J. Frisch, G.W. Trucks, H.B. Schlegel, G.E. Scuseria, M.A. Robb, J.R. Cheeseman, V.G. Zakrzewski, J.A. Montgomery, null Jr, J.C. Burant, S. Dapprich, J.M. Millam, A.D. Daniels, K.N. Kudin, M.C. Strain, O. Farkas, J. Tomasi, V. Barone, M. Cossi, R. Cammi, B. Mennucci, C. Pomelli, C. Adamo, S. Clifford, J. Ochterski, G.A. Petersson, P.Y. Ayala, Q. Cui, K. Morokuma, D.K. Malick, A.D. Rabuck, K. Raghavachari, J.B. Foresman, J. Cioslowski, J. V Ortiz, B.B. Stefanov, G. Liu, A. Liashenko, P. Piskorz, I. Komaromi, R. Gomperts, R.L. Martin, D.J. Fox, T. Keith, M.A. Al-Laham, C.Y. Peng, A. Nanayakkara, C. Gonzalez, M. Challacombe, P.M.W. Gill, B.G. Johnson, W. Chen, M.W. Wong, J.L. Andres, M. Head-Gordon, E.S. Replogle, J.A. Pople, Gaussian 98, revision A.7, 1998.
[39] T. Lu, F. Chen, Multiwfn: a multifunctional wavefunction analyzer, J. Comput. Chem. 33 (2012) 580–592, doi:10.1002/jcc.22885.
[40] J.C. Phillips, D.J. Hardy, J.D.C. Maia, J.E. Stone, J.V. Ribeiro, R.C. Bernardi, R. Buch, G. Fiorin, J. Hénin, W. Jiang, R. McGreevy, M.C.R. Melo, B.K. Radak, R.D. Skeel, A. Singharoy, Y. Wang, B. Roux, A. Aksimentiev, Z. Luthey-Schulten, L.V. Kalé, K. Schulten, C. Chipot, E. Tajkhorshid, Scalable molecular dynamics on CPU and GPU architectures with NAMD, J. Chem. Phys. 153 (2020) 44130, doi:10.1063/5.0014475.
[41] K. Karrouchi, S.A. Brandán, M. Hassan, K. Bougrin, S. Radi, M. Ferbinteanu, Y. Garcia, M. Ansar, Synthesis, X-ray, spectroscopy, molecular docking and DFT calculations of (E)-N'-(2,4-dichlorobenzylidene)-5-phenyl-1H-pyrazole-3-carbohydrazide, J. Mol. Struct. 1228 (2021) 129714, doi:10.1016/j.molstruc.2020.129714.
[42] F.C. Chahar, P.E. Alvarez, C. Zampini, M.I. Isla, S.A. Brandán, Experimental and DFT studies on 2',4'-dihydroxychalcone, a product isolated from Zuccagnia punctata Cav. (Fabaceae) medicinal plant, J. Mol. Struct. 1201 (2020) 127221, doi:10.1016/j.molstruc.2019.127221.
[43] K. Karrouchi, S.A. Brandán, Y. Sert, H. El-marzouqi, S. Radi, M. Ferbinteanu, M.E.A. Faouzi, Y. Garcia, M. Ansar, Synthesis, X-ray structure, vibrational spectroscopy, DFT, biological evaluation and molecular docking studies of (E)-N'-(4-(dimethylamino)benzylidene)-5-methyl-1H-pyrazole-3-carbohydrazide, J. Mol. Struct. 1219 (2020) 128541, doi:10.1016/j.molstruc.2020.128541.
[44] R.F.W. Bader, Atoms in molecules, Acc. Chem. Res. 18 (1985) 9–15.
[45] R.F.W. Bader, Bond paths are not chemical bonds, J. Phys. Chem. A 113 (2009) 10391–10396.
[46] Todd, A. Keith, TK Gristmill Software, AIMAll (Version 19.10.12), Overland Park KS, USA, 2019.
[47] B. Lučić, N. Trinajstić, Mathematical Properties of Molecular Descriptors Based on Distances, Croat. Chem. Acta. 83 (2) (2010) 227–242 A1–A1.
[48] E.R. Johnson, S. Keinan, P. Mori-Sánchez, J. Contreras-García, A.J. Cohen, W. Yang, Revealing noncovalent interactions, J. Am. Chem. Soc. 132 (2010) 6498–6506, doi:10.1021/ja100936w.
[49] T. Koopmans, Über die zuordnung von wellenfunktionen und eigenwerten zu den einzelnen elektronen eines atoms, Physica 1 (1934) 104–113, doi:10.1016/S0031-8914(34)90011-2.
[50] E. D. Glendening, J. K. Badenhoop, A. E. Reed, J. E. Carpenter, J. A. Bohmann, C. M. Morales, P. Karafiloglou, C. R. Landis, F. Weinhold, NBO, 7, Theoretical Chemistry Institute, University of WisconsinWI, Madison, 2018.
[51] J.J. Dannenberg, Using perturbation and frontier molecular orbital theory to predict diastereofacial selectivity, Chem. Rev. 99 (1999) 1225–1242, doi:10.1021/cr980382f.
[52] R.S. Mulliken, Electronic population analysis on LCAO–MO molecular wave functions. I, J. Chem. Phys. 23 (1955) 1833–1840, doi:10.1063/1.1740588.
[53] Z. Jin, X. Du, Y. Xu, Y. Deng, M. Liu, Y. Zhao, B. Zhang, X. Li, L. Zhang, C. Peng, Y. Duan, J. Yu, L. Wang, K. Yang, F. Liu, R. Jiang, X. Yang, T. You, X. Liu, X. Yang, F. Bai, H. Liu, X. Liu, L.W. Guddat, W. Xu, G. Xiao, C. Qin, Z. Shi, H. Jiang, Z. Rao, H. Yang, Structure of Mpro from SARS-CoV-2 and discovery of its inhibitors, Nature 582 (2020) 289–293, doi:10.1038/s41586-020-2223-y.
[54] J.M. Gutierrez-Villarreal, T. Campos-Garcia, J. Molina-Torres, M.G. López, J. Vázquez-Martínez, Alkamides and piperamides as potential antivirals against the severe acute respiratory syndrome coronavirus 2 (SARS-CoV-2), J. Phys. Chem. Lett. 11 (2020) 8008–8016, doi:10.1021/acs.jpclett.0c01685.

PRINCIPAL
PGP College of Arts and Science
Namakkal.

P.G.P. COLLEGE OF ARTS & SCIENCE NAMAKKAL 637 206



Journal of Drug Delivery & Therapeutics

ISSN: 2250-1177

Antioxidant, In-vitro Antibacterial and DNA-cleavage activities of Nickel (II) Complex derived from N, N`-(1, 2 Phenylenebis (Methanylylidene)) bis(4-Nitroaniline)

T. Sujeshwari

E. Akila

P. Maheswaran

DOI: https://doi.org/10.22270/jddt.v9i2-s.2536

ABSTRACT

New mononuclear Nickel (II) complex with Schiff base derived from the condensation of o-phthalaldehyde with p-nitroaniline were synthesized. The

ABSTRACT

VIEW PDF

DOWNLOAD PDF

STATISTICS

234 Views | 102 Downloads

HOW TO CITE

Sujeshwari T, Akila E, Maheswaran P. Antioxidant, In-vitro Antibacterial and DNA-cleavage activities of Nickel (II) Complex derived from N, N`-(1, 2 Phenylenebis (Methanylylidene)) bis(4-Nitroaniline). IDDT [Internet]. 15Apr.2019 [cited 7Sep.2022];9(2-

Online ISSN: 2250-1177

MAKE A SUBMISSION

CATEGORIES

Aims & Scope

Editorial Policies

Publication Ethics

Plagiarism Policy

Retraction Policy



Available online on 15.04.2019 at http://jddtonline.info

Journal of Drug Delivery and Therapeutics

Open Access to Pharmaceutical and Medical Research

© 2011-18, publisher and licensee JDDT, This is an Open Access article which permits unrestricted non-commercial use, provided the original work is properly cited

Open Access

Research Article

Antioxidant, *In-vitro* Antibacterial and DNA-cleavage activities of Nickel (II) Complex derived from N, N'-(1, 2 Phenylenebis (Methanylylidene)) bis(4-Nitroaniline)

T. Sujeshwari [1], E. Akila [2] & *P. Maheswaran [3]*

[1] Research Scholar, Department of Chemistry, P.G.P College of Arts and Science, Namakkal, Tamil Nadu, India

[2] Department of Chemistry, Sri Sarada College for Women (Autonomous), Salem-16, Tamil Nadu, India

[3] Principal and Head, Department of Chemistry, P.G.P College of Arts and Science, Namakkal, Tamil Nadu, India

ABSTRACT

New mononuclear Nickel (II) complex with Schiff base derived from the condensation of o-phthalaldehyde with p-nitroaniline were synthesized. The ligand and its complex were characterized by elemental analysis, molar conductivity, magnetic moment, IR, ^{1}H NMR, and electronic spectra. The conductivity data confirmed the non-electrolytic nature of the complex. The spectral and analytical data suggested a distorted octahedral geometry for Ni(II) complex. The synthesized complex with ligand have been screened for antimicrobial activity against two gram-positive bacteria (Staphylococcus aureus and Bacillus subtilis) and two gram-negative bacteria (Escherichia coli and klebsiella pneumoniae). The obtained results showed that Ni(II) complex is more potent than free ligand. DNA cleavage studies of Ni(II) complex have been investigated by gel electrophoresis using super coiled pUC18DNA. The experimental results revealed that the Ni(II) complex cleaved pUC18DNA. in an efficient manner than the parent ligand. In addition, the antioxidant activity of the ligand and its metal complex were investigated through scavenging effects for DPPH radical indicating that the compound show stronger antioxidant activity than free ligand but lower when compared to standard oxidants such as vitamin C.

Keywords: Mononuclear, Antimicrobial studies and DNA cleavage.

Article Info: Received 28 Feb 2019; Review Completed 05 April 2019; Accepted 09 April 2019; Available online 15 April 2019

Cite this article as:

Sujeshwari T, Akila E, Maheswaran P, Antioxidant, *In-vitro* Antibacterial and DNA-cleavage activities of Nickel (II) Complex derived from N, N'-(1, 2 Phenylenebis (Methanylylidene)) bis(4-Nitroaniline), Journal of Drug Delivery and Therapeutics. 2019; 9(2-s):396-401 **http://dx.doi.org/10.22270/jddt.v9i2-s.2536**

***Address for Correspondence:**

T. Sujeshwari, Research Scholar, Department of Chemistry, P.G.P College of Arts and Science, Namakkal, Tamil Nadu, India

INTRODUCTION

The Schiff bases ligand has been found extensive use in the field of research and field of interest now a day. The Schiff bases compounds are recognized due to the presence of azomethine group (-CH=N) which is formed by reacting either by aldehyde or ketone with compounds containing amine group [1]. As the Schiff bases can be synthesized by easy and simple condensation reaction and has been found its extensive use in the field of coordination chemistry due to its property of donating electrons as a ligand. Schiff base mononuclear transition metal complexes due to its synthetic accessibility and its impact in coordination chemistry, as well as the relevance to structural characterization has received a great deal of interest in the field of research [2]. Besides, the DNA interaction of Schiff base metal complexes has also gained much interest towards their applications in biotechnology and medicine. The scientific community has showed that metal coordination compounds have shown some outstanding DNA cleavage properties, as well as antibacterial and antioxidant activities [3-4]. It is seen that transition metals are particularly suitable for this purpose, because they can adopt a wide variety of oxidation states, coordination numbers and geometries, in comparison to other main group elements.

Over the past decades, considerable interest in the synthesis and characterization of transition metal complexes with Schiff Base ligands had been developed to check the role of metal active sites in several catalytic biological processes. In the present study, the synthesis and characterization of mononuclear Ni(II) complex of a Schiff base ligand derived from o-phthalaldehyde and p-nitroaniline has been reported. Schiff base ligand and its metal complex were characterize by the elemental analysis, magnetic susceptibility, molar conductivity measurements, electronic spectra, IR, ^{1}H NMR spectrum to determine the mode of co-ordination and geometry. In order to establish the biological role of metals,

P.G.P. COLLEGE OF ARTS & SCIENCE NAMAKKAL 637 206

the Schiff base and its Ni(II) complex have been screened for their antimicrobial activity against two gram-positive bacteria such as S. aureus and B. subtilis and two gram-negative bacteria such as E. coli and K. pneumonia. The oxidative damage caused by ROS on lipids, proteins, and nucleic acids plays a significant role in the development of life limiting chronic diseases such as cancer, hypertension, cardiac infarction, arteriosclerosis, rheumatism, and cataracts [5]. Thus, the percentage of antioxidant activities of Schiff base and its Ni(II) complex were also determined.

MATERIALS AND INSTRUMENTS

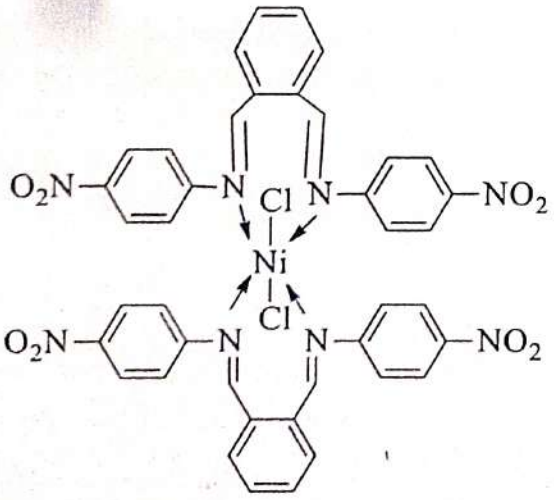
All chemicals and reagents used were of analytical grade and were used as received without any further purification. All the solvents were purified according to standard procedures. The elemental analysis (Carbon, Hydrogen and nitrogen) were performed using a Carlo Eraba 1106 instrument. The molar conductance of the freshly prepared Schiff base transition metal complex (10^{-3} M) was recorded in DMF at room temperature using ELICO CM 185 Conductivity Bridge. The Infrared spectra were recorded on the Perkin Elmer FT-IR-8300 Model spectrometer using KBr disc in the region 4000-200 cm^{-1}. Electronic absorption spectra in the UV-Visible range were recorded on Double beam spectrometer Cyber lab between 200-800 nm by using DMF as the solvent. ^{1}H-NMR spectra of the ligand were recorded on Bruker Spectrometer at 400 MHZ in DMSO-d_6.

Synthesis of Schiff base ligand

The Schiff base ligand was synthesized by adding 1, 2-benzene dicarboxaldehyde (1 mM) in 20 ml of ethanol, and p-nitroaniline (2 mM) in 20 ml of ethanol. The mixture was refluxed for 2½ hrs. Then the solution of the ligand was kept for slow evaporation and collected and dried in air [6].

Synthesis of mononuclear Ni(II) complex

The ethanolic solution of synthesized ligand N, N'-(1, 2 phenylenebis(methanylylidene) bis(4-nitroaniline) (2 mM) was added drop wise and stirring to an ethanolic solution of the metal salt $NiCl_2.6H_2O$ (1 mM) with constant stirring, and the mixture was boiled under reflux for 4½ hrs. Then the volume of the reaction mixture was reduced by evaporation. The resultant product was filtered, washed with ethanol and dried [7].



Scheme 1: Mononuclear Schiff base Ni(II) complex

Antibacterial studies

The synthesized complex and the Schiff base ligand were tested for their antimicrobial studies using bacterial strains such as *Escherichia coli*, *Klebsiella pneumoniae*, *Staphylococcus aureus* and *Bacillus subtilis*. Antibacterial test was performed by using the disc diffusion method. The bacterial strains were subcultured individually in nutrient agar medium. The compounds were dissolved in DMF. The plates were incubated aerobically at 37º C for 24 hours and the antimicrobial activity was assessed by measuring the inhibition of microbial growth around the well. This method involves the exposure of the zone inhibition toward the diffusion of micro-organism on agar plate [8].

Total antioxidant capacity assay

- Different concentrations (10 µl, 20 µl, 30 µl, 40 µl and 50 µl) of synthesized compounds were taken and 1ml of reagent solution was added. [Reagent solution: 0.6 M sulphuric acid, 28 mM sodium phosphate and 4 mM Ammonium molybdate.
- The tubes were capped and incubated in thermal block at 95º C for 90 minutes.
- After the time interval the tubes were cool down at room temperature.
- The absorbance was recorded at 695 nm using shimadzu UV 1800 spectrophotometer [9].

Calculation of 50% Inhibitory Concentration (IC_{50})

The concentration (mg/ ml) of the fractions that was required to scavenge 50% of the radicals was calculated by using the percentage scavenging activities at five different concentrations of the fractions.

Percentage inhibition (I %) was calculated using the formula,

I % = (Ac-As) / Ac x 100

Where, Ac = absorbance of the control and

As = absorbance of the sample.

TAC = Total Antioxidant Capacity assay

DNA cleavage studies

The DNA cleavage studies were done by gel electrophoresis experiment for which pUC18 was used as the plasmid DNA. The DNA cleavage activity was evaluated by monitoring the conversion of supercoiled plasmid DNA to nicked circular DNA and linear DNA. The reaction mixture was prepared by adding 40µl Puc18 DNA, 50 mM Tris-HCl, pH 7.4, 50 mM NaCl, 10 mM H_2O_2 in a different volume, followed by adding Millipore water for final volume. Samples were typically incubated for 1 hr at 37 ºC [10].

RESULTS AND DISCUSSION

The synthesized transition Ni(II) complex are found to be freely soluble in DMSO, DMF and ethanol. The analytical data of the synthesized ligand and its mononuclear metal complex are shown in Table 1. The lower molar conductivity value (7.60 Ω^{-1} cm^2 mol^{-1}) for Ni(II) complex (10^{-3} M) in DMSO at room temperature indicates their non-electrolytic nature [11-12].

COLLEGE OF ARTS & SCIENCE NAMAKKAL 637 206

Table 1: Analytical data of the Schiff base ligand and its mononuclear metal complex

Compound	Molecular formula	Colour	Yield %	Melting point (C)	% of Nitrogen		% of Metal	
					Cal	Exp	Cal	Exp
L	$C_{20}H_{14}N_4O_4$	Yellowish orange	70	145	15.0	14.8	-	-
ML_2X_2	$Ni(C_{40}H_{28}N_8O_8Cl_2)$	Dark Green	60	>200	12.7	12.5	6.7	6.4

IR Spectral analysis

The FT-IR spectral analysis of Schiff base and its metal complex indicated the presence of all expected functionalities are listed in Table 2. The metal complex exhibited the absorptions of azomethine region at lower frequencies than free ligand. The infrared spectrum of the Schiff base ligand showed a medium absorption at 1655.34 cm^{-1} assigned to the C=N stretching vibrations, indicating the formation of the Schiff base linkage. In the complex, this band is shifted to lower frequencies in the 1649.42 cm^{-1} upon complexation with the metal [13], which can be attributed to the coordination of the imine nitrogen to the metal centre. The characteristic bands for the entire complex in the region 691.10 cm^{-1} may assigned for the vibration of aromatic rings and C-H stretching respectively. The other absorption characteristic appeared in the region 484.34 and 315.10 cm^{-1} may be assigned for M-N and M-Cl vibrations [14].

Table 2: IR spectral data (4000-200 cm^{-1}) of Schiff base and its metal complex

Compounds	υ(C=N) (cm^{-1})	υ(M-Cl) (cm^{-1})	υ(M-N) (cm^{-1})
$C_{20}H_{14}N_4O_4$	1655.34	--	--
$Ni(C_{40}H_{28}N_8O_8Cl_2)$	1649.42	315.10	484.34

Electronic spectra and magnetic moment studies

The electronic absorption spectra of the Ni(II) complex were recorded in freshly prepared solution in DMF at room temperature. The electronic spectra of the Schiff base ligand and its complex have been measured in DMF solution 200-800 nm at room temperature [15]. The data are represented in Table 3. In the electronic spectra of the Schiff base ligand, an intense absorption at 365 nm were assigned to a benzene $\pi\rightarrow\pi^*$ transition and the band at 382 nm were assigned due to $n\rightarrow\pi^*$ transition associated with the azomethine chromophore (-C=N). The dark green Ni(II) complex showed three bands at at 562, 585, and 613 nm which are assigned to ^3A_2g (F) $\rightarrow{}^3T_2g$ (F) (ν_1), ^3A_2g (F) $\rightarrow{}^3T_1g$ (F) (ν_2) and ^3A_2g (F) $\rightarrow{}^3T_1g$ (P) (ν_3) transitions respectively, indicating an distorted octahedral geometry. The magnetic moment of 3.41 B.M. falls within the range normally observed for octahedral Ni(II) complex.

Table 3: Electronic Spectral data of Schiff base ligand and its Ni(II) complex.

Compound	Electronic spectra (nm)				Geometry of the complex
	$\pi\rightarrow\pi^*$	$n\rightarrow\pi^*$	L→M	d-d	
$C_{20}H_{14}N_4O_4$	365	382	-	-	-
$Ni(C_{40}H_{28}N_8O_8Cl_2)$	298	365	420	562, 585, 613	Distorted Octahedral

^1H – NMR Spectral studies

The ^1H-NMR spectra of the Schiff base ligand was measured at room temperature in DMSO- d_6. The ^1H NMR spectra of the ligand exhibits well resolved signals and significant differences in their chemical shifts. The spectrum of the Schiff base ligand exhibits a singlet signal in the 8.48 ppm, which is attributed to the azomethine group (-CH=N-) proton and the multiplets around 6.6-7.9 ppm are assigned due to aromatic protons [16]. The spectra of the ligand is shown in Fig 1.



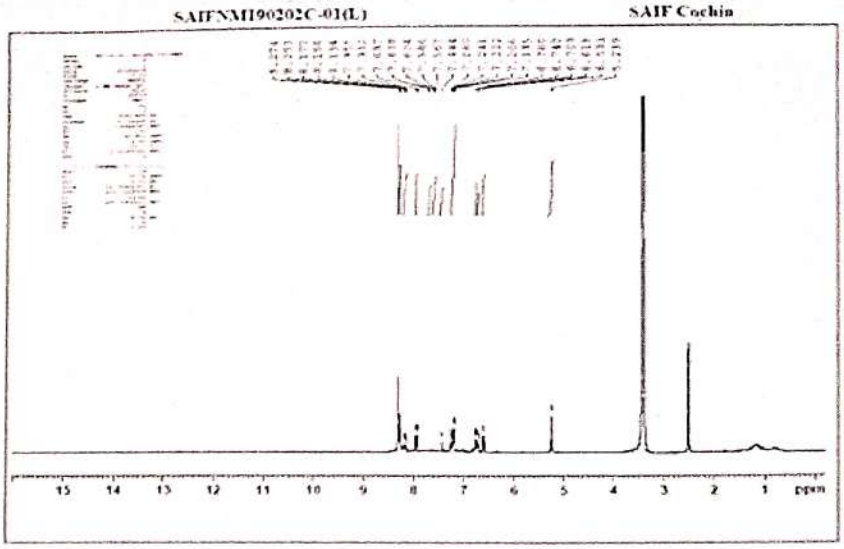


Figure 1: ^{1}H NMR spectrum of $C_{20}H_{14}N_4O_4$

Antibacterial activity

The synthesized ligand and its complex were screened for their antibacterial activity against *Staphylococcus aureus, Bacillus subtilis* while *Escherichia coli* and *Klebsilla pneumonia*. The standard drug streptomycin was also tested for their antibacterial activities at the same concentration and conditions similar to tested compound concentration. From the antibacterial studies, it is inferred that the Schiff bases and its Ni(II) complex were found to be potentially active against *Staphylococcus aureus, Bacillus subtilis, Escherichia coli* and *Klebsilla pneumonia* [17]. The antibacterial activity of Schiff base and its metal complex against different bacteria are shown in Fig 2, 3, 4, and 5.

From the obtained results, it can be observed that the Ni(II) complex showed greater activity as compared to the Schiff base. The improved activities of the metal complex as compared to the ligand can be explained on the basis of chelation theory.

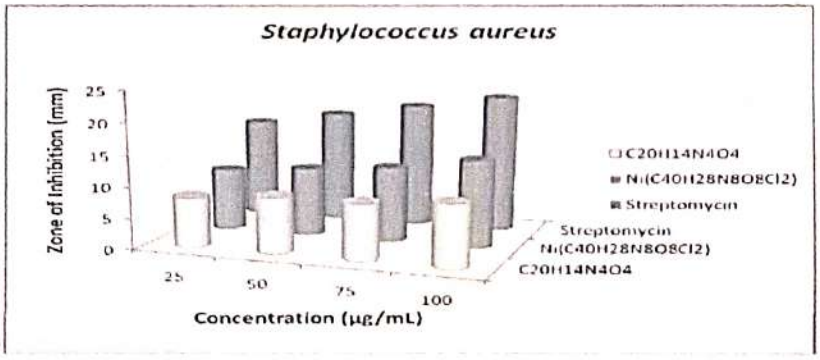


Figure 2: Antibacterial activity of Schiff base ligand and its mononuclear Schiff base metal complex against *Staphylococcus aureus*

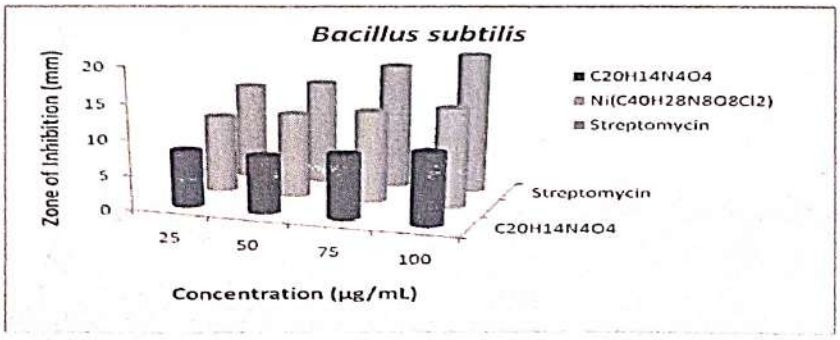


Figure 3: Antibacterial activity of Schiff base ligand and its mononuclear Schiff base metal complex against *Bacillus subtilis*

P.G.P. COLLEGE OF ARTS & SCIENCE NAMAKKAL 637 206

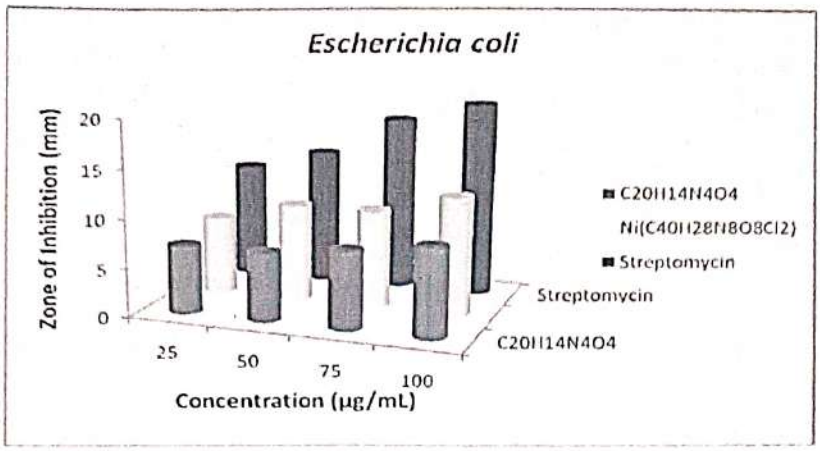


Figure 4: Antibacterial activity of Schiff base ligand and its mononuclear Schiff base metal complexes against *Escherichia coli*

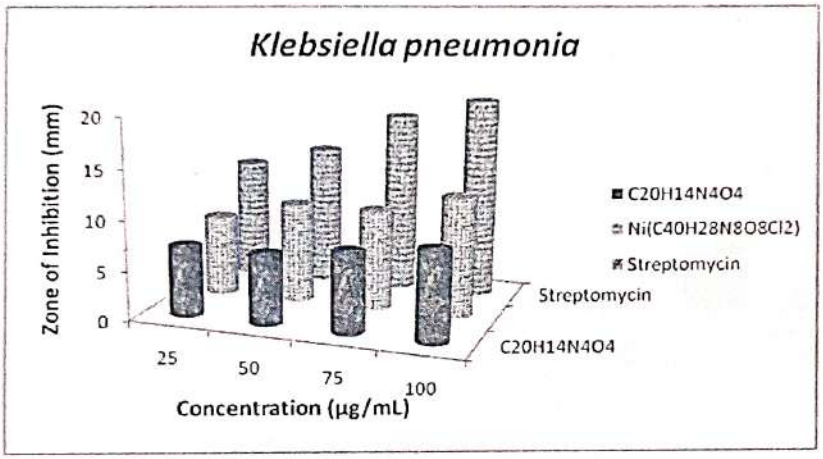


Figure 5: Antibacterial activity of Schiff base ligand and its mononuclear Schiff base metal complex against *Klebsiella pneumonia*

Antioxidant activity

The antioxidant assay was carried out using different concentrations of the Schiff base and its Ni(II) metal complex with radical, while ascorbic acid (vitamin C) was used as standard.

Total Antioxidant Capacity assay

The total antioxidant capacity of $Ni(C_{40}H_{28}N_8O_8Cl_2)$ is significantly higher than that of free ligand, indicating that this complex is a much better antioxidant than ligand but lower when compared to ascorbic acid (vitamin C) as standard [18]. Total antioxidant capacity of $C_{20}H_{14}N_4O_4$ and $Ni(C_{40}H_{28}N_8O_8Cl_2)$ as well as the standard was increased in a dose-dependent manner, antioxidant ability of Schiff base, increased significantly after chelation of transition metal ion (Fig 6 and 7). The $Ni(C_{40}H_{28}N_8O_8Cl_2)$ complex possess higher antioxidant potential (IC_{50}) than vitamin C (standard drugs) and lower than $C_{20}H_{14}N_4O_4$ ligand.

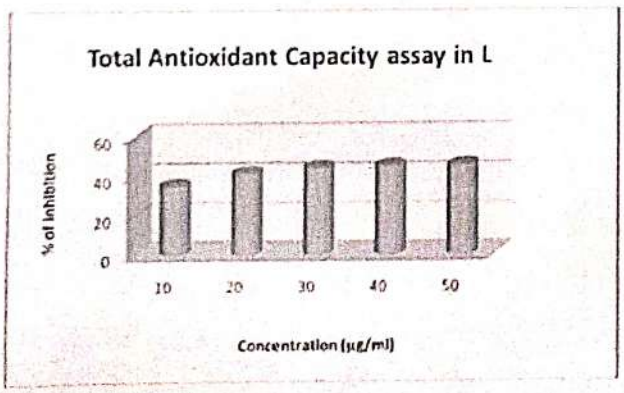


Figure 6: Total Antioxidant Capacity of $C_{20}H_{14}N_4O_4$

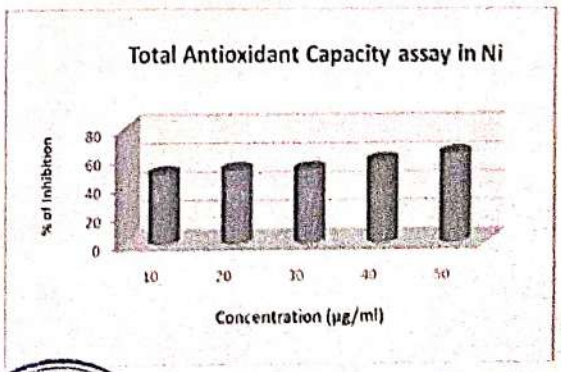


Fig 7:. Total Antioxidant Capacity of $Ni(C_{40}H_{28}N_8O_8Cl_2)$

P.G.P. COLLEGE OF ARTS & SCIENCE NAMAKKAL 637 206

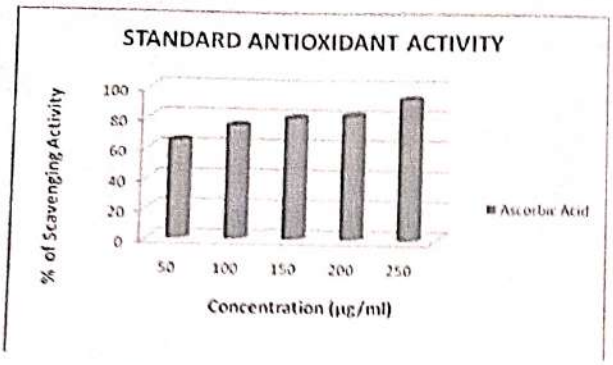


Figure 8: Total Antioxidant Capacity of Ascorbic acid

DNA cleavage activity

The Schiff base and its $Ni(C_{40}H_{28}N_8O_8Cl_2)$ complex were studied for their DNA cleavage activity by agarose gel electrophoresis. Gel electrophoresis is used in DNA typing, where DNA is fragmented at particular sequence points on the genome and compared to a control sample. Hence, it can be used in the detection of DNA damage also. DNA cleavage is controlled by relaxation of supercoiled circular conformation of pUC18DNA to nicked circular conformation and linear conformation. This type of damage will only give an indication to the extent of strand breakage in a sample of damaged DNA.

The results (Fig 9.) of gel electrophoretic separations of pUC18DNA induced by metal complex (lane 3) and ligand (lane 4) in the presence of H_2O_2. Under the same conditions, lane 1 and 2 did not show any apparent cleavage. $Ni(C_{40}H_{28}N_8O_8Cl_2)$ complex (lane 3) shows more cleavage activity in the presence of H_2O_2 at higher concentration (40 µM). $C_{20}H_{14}N_4O_4$ (lane 4) at higher concentration (40 µM) also shows the conversion of supercoiled form (Form-I) into linear form (Form-III).

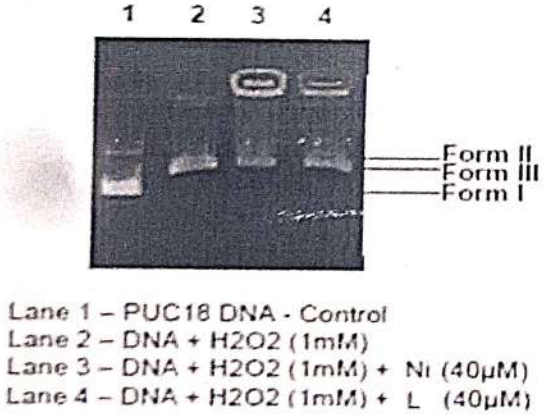


Figure 9: Agarose gel electrophoresis pattern showing effect of pUC18 DNA induced by H_2O_2 and metal complex. Lane 1-DNA alone; Lane 2- DNA alone + H_2O_2; Lane 3-DNA + $Ni(C_{40}H_{28}N_8O_8Cl_2)$ + H_2O_2; Lane 4-DNA + $C_{20}H_{14}N_4O_4$ + H_2O_2.

From the observed results we concluded that ligand and its metal complex behave as efficient chemical nuclease for double strand cleavage of DNA [19]. This may be attributed to the formation of hydroxyl free radicals. Control experiments using DNA alone do not show any significant cleavage of pUC18 DNA even on longer exposure time. From the observed results, it is concluded that Schiff base and $Ni(C_{40}H_{28}N_8O_8Cl_2)$ complex have better cleavage activity.

CONCLUSION

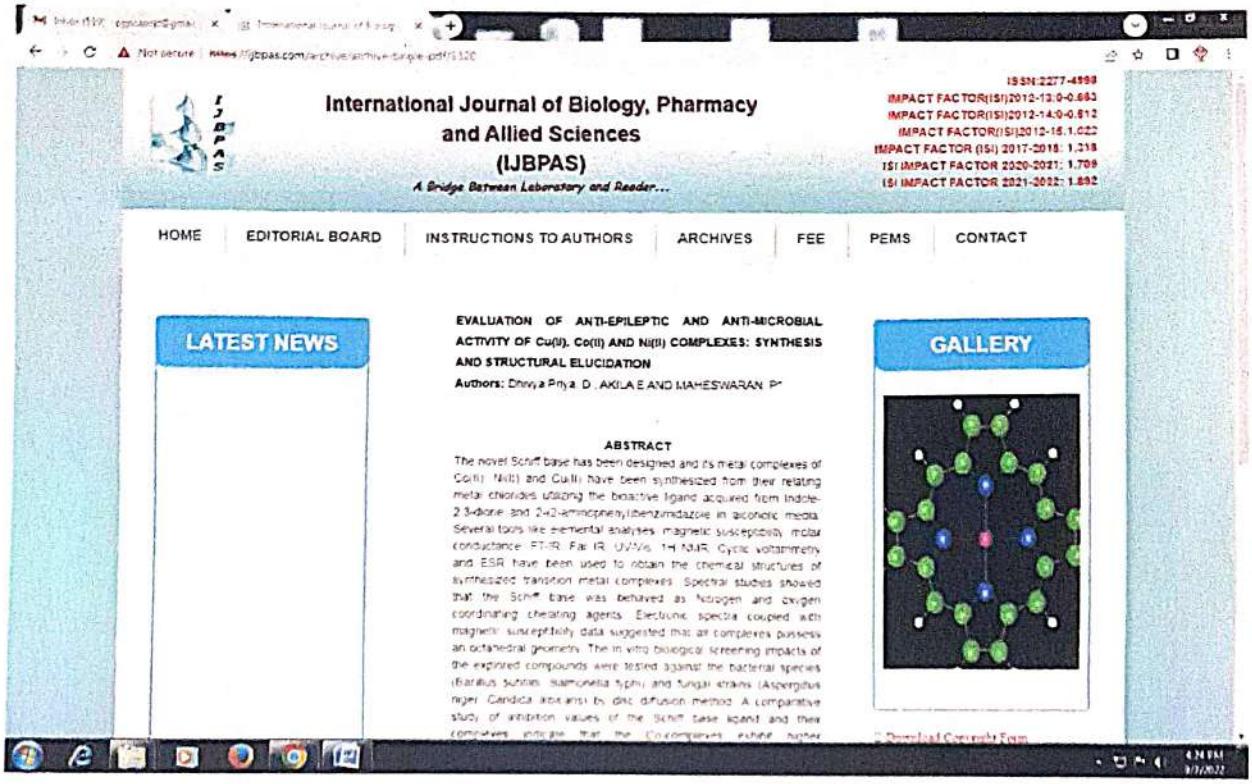
In this report, the mononuclear Schiff base $Ni(C_{40}H_{28}N_8O_8Cl_2)$ complex derived from N, N' – (1, 2-phenylenebis (methanylylidene)bis(4-nitroaniline), have been synthesized and characterized by using various physico-chemical and spectral analyses techniques. The molar conductance value indicates that the complex is non-electrolyte in nature. The IR spectra of synthesized compounds confirmed the coordination of ligand to the metal ion. The UV-Vis and magnetic moment data of the complex suggest a distorted octahedral geometry. The synthesized compounds have antibacterial activity against the two Gram-positive bacteria: *Staphylococcus aureus* and *Bacillus subtilis* and also against the two Gram-negative bacteria: *Escherichia coli* and *Klebsilla pneumonia*. Unlike the parent Schiff base ligand, the complex showed significant antibacterial activity. DNA cleavage studies show that $Ni(C_{40}H_{28}N_8O_8Cl_2)$ complex cleave the DNA molecule completely. Further, the results obtained in antioxidant activity confirmed that the complex is more effective to arrest the formation of radicals and the lower IC_{50} value observed in antioxidant assay did demonstrate that the complex exhibited differential and selective effects to scavenge radicals and hence the potential as drugs to eliminate the radicals.

REFERENCES

1. Alabdali A.J., *J. Appl. Chem.*, **2012;** 3:5.
2. Nabil Ramanadan Bardar, *Res. J. Chem.*, **2010;** 3:660.
3. Erkkila K.E., Odom D.T., Barto J.K., *Chem. Rev.*, **1999;** 99:2777.
4. Ji L.-N., Zou X.-H., Liu J.-G., *Coord. Chem. Rev.*, **2001;** 216:513.
5. Arulpriya P, Lalitha P, and S.Hemalatha, *Der Chemica Sinica.*, **2010; 2:73.**
6. Mohammed Fakruddin Ali Ahmed and V. Mahammad Yunus. *J. Chem.*, **2014;** 30:111.
7. Fugu M. B., Ndahi N. P., Paul B. B. and Mustapha A. N., *J. Chem. Pharm. Res.*, **2013;** 5:2228.
8. Metcalfe C and. Thomas J. A, *Chem. Soc. Rev.*, **2003;** 32:215.
9. Senthil Kumar R, Arunachalam S, Euro. *J. Med. Chem.*, **2009;** 44:1878.
10. Maribel N., *Biol. Inorg. Chem.*, **2003;** 4:401.
11. Robert Boggess K.; A. David Zatko, *J. Chem. Edn.*, **1975;** 52:649.
12. Geary W. J., *Coord. Chem. Rev.*, **1971;** 7:81.
13. Olar R., Badea M., Marinescu D. J., *Therm. Anal. Calorim.*, **2012;** 99:893.
14. Venkateswara Rao B., *J. Therm. Anal. Calorim*, **2010;** 100:577.
15. Emara A., *Spectrochim. Acta A.*, **2016;** 77:117.
16. Amali I. B., Kesavan M. P., Vijayakumar V., Gandhi N. I., J. Rajesh, and G. Rajagopal, *J. Mol. Str.*, **2019.**
17. Zare N, Zabardasti A. *Appl. Organometal. Chemistry.*, **2019.**
18. Aidi M., Keypour H., A. Shooshtari, M. Mahmoudabadi, M. Bayat, Z. Ahmadvand, R. Karamian, M. Asadbegy, S. Tavatli, R.W. Gable, *Polyhedron.*, **2019.**
19. Dong,s D.. Tian and S. Ping Yan, *J. Inorg. Bio. Chem.*, **2014;** 104:171.



PRINCIPAL
PGP College of Arts and Science
Namakkal.



International Journal of Biology, Pharmacy and Allied Sciences
(IJBPAS)
A Bridge Between Laboratory and Reader...

ISSN:2277-4998
IMPACT FACTOR(ISI)2012-13:0-0.663
IMPACT FACTOR(ISI)2012-14:0-0.812
IMPACT FACTOR(ISI)2012-15:1.022
IMPACT FACTOR (ISI) 2017-2018: 1.218
ISI IMPACT FACTOR 2020-2021: 1.709
ISI IMPACT FACTOR 2021-2022: 1.892

LATEST NEWS

EVALUATION OF ANTI-EPILEPTIC AND ANTI-MICROBIAL ACTIVITY OF Cu(II), Co(II) AND Ni(II) COMPLEXES: SYNTHESIS AND STRUCTURAL ELUCIDATION

Authors: Dhivya Priya D, AKILA E AND MAHESWARAN P*

ABSTRACT

The novel Schiff base has been designed and its metal complexes of Co(II), Ni(II) and Cu(II) have been synthesized from their relating metal chlorides utilizing the bioactive ligand acquired from Indole-2,3-dione and 2-(2-aminophenyl)benzimidazole in alcoholic media. Several tools like elemental analyses, magnetic susceptibility, molar conductance, FT-IR, Far IR, UV-Vis, 1H NMR, Cyclic voltammetry and ESR have been used to obtain the chemical structures of synthesized transition metal complexes. Spectral studies showed that the Schiff base was behaved as Nitrogen and oxygen coordinating chelating agents. Electronic spectra coupled with magnetic susceptibility data suggested that all complexes possess an octahedral geometry. The in vitro biological screening impacts of the explored compounds were tested against the bacterial species (Bacillus subtilis, Salmonella typhi) and fungal strains (Aspergillus niger, Candida albicans) by disc diffusion method. A comparative study of inhibition values of the Schiff base ligand and their complexes indicate that the Co-complexes exhibit better

GALLERY

Download Copyright Form

P.G.P. COLLEGE OF ARTS & SCIENCE
NAMAKKAL
637 001

IJBPAS, May, 2020, 9(5): 1090-1107

ISSN: 2277–4998

International Journal of Biology, Pharmacy and Allied Sciences (IJBPAS)

'A Bridge Between Laboratory and Reader'

www.ijbpas.com

EVALUATION OF ANTI-EPILEPTIC AND ANTI-MICROBIAL ACTIVITY OF Cu(II), Co(II) AND Ni(II) COMPLEXES: SYNTHESIS AND STRUCTURAL ELUCIDATION

DHIVYA PRIYA. D[1], AKILA E[2] AND MAHESWARAN. P [1*]

1: Department of Chemistry, PGP College of Arts and Science, Namakkal

2: Department of Chemistry, Sri Sarada College for women (Autonomous), Salem-16

3: Principal and Head, PGP College of Arts and Science, Namakkal

***Corresponding Author: E Mail: pm_omk@yahoo.co.in**

Received 5th Nov. 2019; Revised 3rd Dec. 2019; Accepted 3rd Jan. 2020; Available online 1st May 2020

https://doi.org/10.31032/IJBPAS/2020/9.5.5066

ABSTRACT

The novel Schiff base has been designed and its metal complexes of Co(II), Ni(II) and Cu(II) have been synthesized from their relating metal chlorides utilizing the bioactive ligand acquired from Indole-2,3-dione and 2-(2-aminophenyl)benzimidazole in alcoholic media. Several tools like elemental analyses, magnetic susceptibility, molar conductance, FT-IR, Far IR, UV-Vis, ^{1}H NMR, Cyclic voltammetry and ESR have been used to obtain the chemical structures of synthesized transition metal complexes. Spectral studies showed that the Schiff base was behaved as Nitrogen and oxygen coordinating chelating agents. Electronic spectra coupled with magnetic susceptibility data suggested that all complexes possess an octahedral geometry. The in vitro biological screening impacts of the explored compounds were tested against the bacterial species (*Bacillus subtilis, Salmonella typhi*) and fungal strains (*Aspergillus niger, Candida albicans)* by disc diffusion method. A comparative study of inhibition values of the Schiff base ligand and their complexes indicate that the Co-complexes exhibit higher antimicrobial activity than other complexes. The compounds synthesized were screened for anticonvulsant potentialities in *Albino Wistar Rats* by maximal electroshock seizure (MES) and pentylenetetrazole (PTZ) test respectively. The toxicity and hematological properties were inspected for prepared compounds by sub-acute toxicity study. The results revealed that compounds were found to exhibit significant

P.G.P. COLLEGE OF ARTS & SCIENCE 1090 NAMAKKAL 637 206

anticonvulsant property at 10 mg/kg dose level when compared with the reference drug phenytoin in both seizure tests.

Keywords: Schiff base, Isatin, 2-(2-aminophenyl)benzimidazole, Antimicrobial, acute toxicity and Anticonvulsant activity

INTRODUCTION

The discovery of new effective antiepileptic drugs for the treatment of epilepsy still remains a top priority as it affects approximately 1–2 % of the world population [1]. Convulsions or epilepsy is most devastating chronic neurological disorder characterized by recurrent spontaneous seizures, in addition to unpredictable and periodic occurrence of a transient alteration of behavior due to the disordered, synchronous and rhythmic firing of populations of brain neurons. At present, available antiepileptic drugs (AEDs) have proven to be effective in reducing convulsions at the same time their therapeutic efficacy is conquered by some undesirable side effects such as drowsiness, mental dullness, ataxia, hepatotoxicity, megaloblastic anemia [2-4]. Therefore, the development of newer antiepileptic drugs with novel therapeutic targets, enhanced efficacy (increase seizure control, increased tolerability and pharmacokinetic properties) and minimal side-effects become a major goal in epilepsy research [5]. The synthetic chemistry is a major target in the search of new lead drugs to be used for protection against this debilitating neurological disorder. Heterocyclic nucleus namely indole has gained importance in medicinal chemistry due to its diverse biological activities [6, 7] and numerous indole derivatives are reported to exhibit effective anticonvulsant activity [8, 9].

Schiff base ligands are widely significant and considered generally on the grounds that they can promptly frame stable complexes with most of the metal ions [10, 11]. Metal complexes of these ligands are pervasive due to their facile synthesis, wide applications and also the accessibility of different structural modifications [12]. Their chelating structures, moderate donating of electron and easy tunable electronic and steric impacts additionally make Schiff bases as flexible ligands equipped for setting various metals in different oxidation states with unusual structural features and controlling the performance of metals in an assortment of suitable catalytic transformations [13-16]. Schiff base complexes involving oxygen and nitrogen donor ligands are notable [17] and have empowered unprecedented eagerness among chemists due to their applications in catalysis and their pertinence to bioinorganic system [18].

COLLEGE OF ARTS & SCIENCE NAMAKKAL 637 206

Benzimidazoles considered being significant class of heterocyclic organic compounds and containing a phenyl ring intertwined to an imidazole ring **[19, 20]**. In recent years, this class of organic compounds has gathered a great deal of consideration, particularly because of their applications in diverse biological and chemical studies **[21]**. Schiff bases of benzimidazole have been reported with remarkable antimicrobial **[22]**, antiviral **[23]** and analgesic **[24]**, anti-inflammatory **[25]**, anti-tumor agents **[26]**, anti-parasitic agents **[27]**, and anti-proliferative **[28]** activities. To best of our insight, the physiological action and commercial applications of Schiff base metal complexes derived from 2-(2-aminophenyl)-1-H-benzimidazole has scarcely been explored. In this correspondence, we depict the chelation behavior of Schiff base got from the condensation of indole-2, 3-dione and 2-(2-aminophenyl)benzimidazole. Further the metal complexes were acquired utilizing distinctive metal particles like Co(II), Ni(II), and Cu(II) so as to acquire increasingly intense Biological active compounds. To know the geometry of the Schiff base complexes, all the compounds were examined by Physico-chemical and spectral methods. Biocidal and Pharmacological action was carried for every one of the compounds.

EXPERIMENTAL PROTOCOLS

Materials and Physical measurements

The entire chemicals were supplied by sigma Aldrich and used without purification. Melting points were examined by open tube capillary method and are uncorrected. Elemental analyses (C, H and N) were performed by the aid of Perkin-Elmer Elemental analyzer. The molar conductance measurements were carried out at room temperature using Elico model conductivity meter. IR spectra were obtained on a Thermo Nicolet, FT-IR spectrometer (Avatar 370 model) by using KBr pellets. ^{1}H NMR spectra were recorded on a Bruker Avance III, 400 MHz spectrometer using DMSO with TMS as an internal standard. Electronic spectra were obtained with a Perkin-Elmer Lambda 40(UV-Vis) using DMF in the range 200-800nm. The ESR spectra of powder samples were recorded by E-112 ESR Spectrometer with X-band microwave frequency (9.1 GHz).

Synthesis of Schiff base [(E)-3-((2-(1H-benzo[d]imidazol-2-yl)phenyl)imino)indolin-2-one]

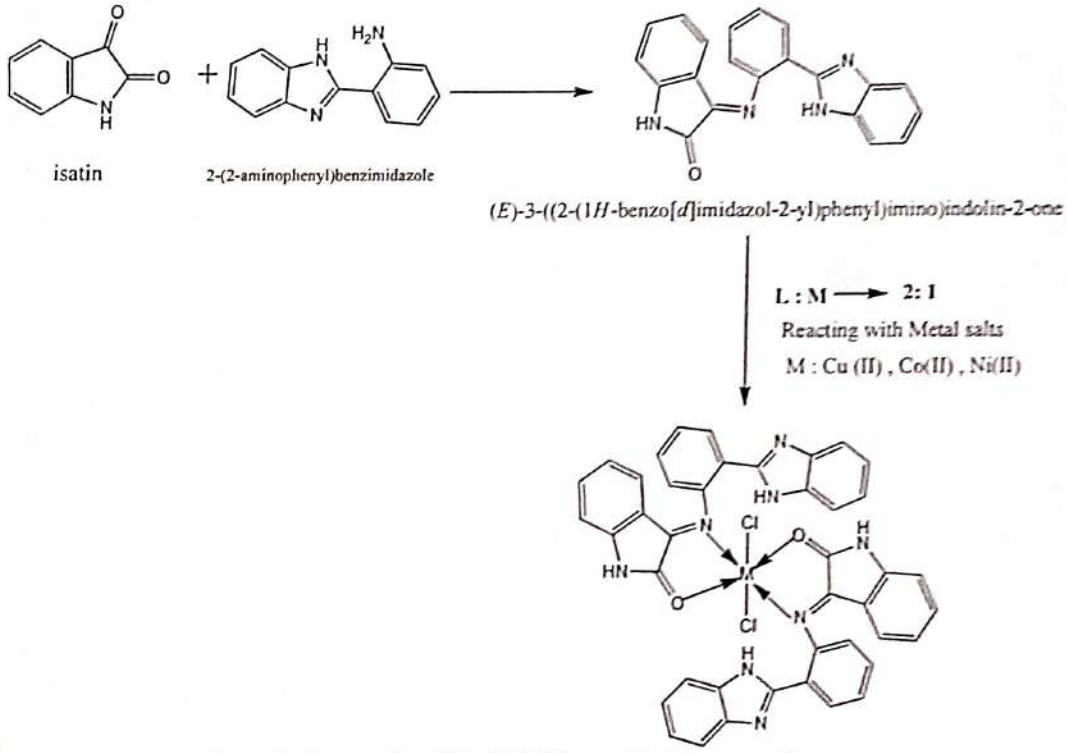
1H-indole-2, 3-dione (1mmol) was dissolved in absolute methanol (20ml) added dropwise to a solution of 2-(2-aminophenyl) benzimidazole (1mmol) in absolute methanol (20 ml) with constant stirring. On stirring the solution turns orange color and the mixture was then

P.G.P. COLLEGE OF ARTS & SCIENCE NAMAKKAL 637 206

refluxed at 70oC for 3 hrs. The solution was kept for slow evaporation to obtain yellow colored precipitate. The precipitate was washed with ethanol and then dried in air.

Synthesis of metal complexes

The methanolic solution of corresponding salts [$CoCl_2.6H_2O$, $CuCl_2.2H_2O$ and $NiCl_2.6H_2O$] was slowly mixed to hot stirring methanolic solution of ligand L in 2:1 (L: M) molar ratio. The reaction mixture was kept under reflux at 70°C for 3 hrs. Then, the reaction mixture was allowed to cool by slow evaporation and colored precipitates were collected (**Scheme 1**). The collected precipitates were filtered, washed with cold ethanol and dried in air.



Scheme 1: Preparation of the Schiff base and its Metal complexes

Biological activity

The biological activities of the newly prepared Schiff base and its metal complexes have been screened for their antibacterial and antifungal activities by disc diffusion method **[29]**. In-vitro antimicrobial activity was screened by using Muller Hinton Agar (MHA) obtained from Hi-media (Mumbai). The antibacterial and antifungal activities were done by using the following organisms (*Bacillus subtilis, salmonella typhi* and *Aspergillus niger, Candida albicans*). These bacterial and fungal strains were chosen as they are the known pathogens of human body and used at 25, 50, 75 and 100 μmL^{-1} concentrations in DMSO. The Petri plates were kept for incubation at 37°C for 24 hrs (bacterial) and at 37°C for 72 hrs (fungal). At the end of incubation, inhibition zones

P.G.P. COLLEGE OF ARTS & SCIENCE NAMAKKAL 637 206

formed around the disc were measured with transparent ruler in milli-meter. Standard antimicrobial drug (chloramphenicol and Fluconazole) was also screened under similar conditions for comparison.

Pharmacology

The entire compounds incorporated in the present study were screened for their anticonvulsant and acute toxicity activities.

Maximal electroshock seizure (MES) test

Maximal electroshock seizure model was used to evaluate the anticonvulsant activity of various synthetic compounds. Seizures were induced in rats by delivering electroshock of 150 mA for 0.2 sec. by means of an electro-convulsometer through a pair of ear clip electrodes **[30]**. The test animal (n=6) received 10 mg/kg between various synthetic compounds through intraperitoneally and standard group received phenytoin (25 mg/kg) injected i.p and tested after 30 minutes for MES induced seizure response. All the experimental groups were compared with the control treated with vehicle.

Pentylenetetrazole (PTZ) induced seizures

PTZ at the dose of 80 mg/kg was injected i.p. to induce tonic-clonic convulsions in rats. The animal (n=6) received 10 mg/kg various synthetic compounds intra-peritoneally and standard group received Phenytoin (25 mg/kg) injected i.p. PTZ was injected i.p. 60 min. after the administration of drug. Occurrence of HLTE (Hind Limb Tonic Expens) and duration seizure were noted.

Acute toxicity

Male and female Wistar rats weighing 180 ± 10 g are used for the present study. The animals are divided into 6 groups of four animals each. The dose of the preparation is calculated based on the body weight of the animal. The animals in Group I are administered with a single daily dose of 0.5 ml of Tween 80 orally for 20 days. The animals in Group II to VI are administered with 10 $mgkg^{-1}$ between various synthetic drugs once daily for 20 days. The animals are then weighed every five days, from the start of the treatment, to record the weight variation. At the end of the treatment, blood samples are collected by puncturing retro orbital plexus after mild anesthesia for biochemical analysis. The collected blood sample is centrifuged within 5 min of collection at 4000 g for 10 min, which is analyzed for total cholesterol, total triglyceride, HDL-cholesterol levels, LDL-cholesterol, plasma glucose, alanine aminotransferase (ALT), aspartate aminotransferase (AST), creatinine and urea.

Statistical analysis

Data were expressed as percentage (%) protection and mean ± SEM and were analyzed by one-way ANOVA followed by Dunnett's test for multiple comparisons.

P.G.P. COLLEGE OF ARTS & SCIENCE NAMAKKAL 637 206

using the SPSS version 10. Results were considered significant at $p < 0.05$.

RESULTS AND DISCUSSION

The Schiff base ligand (L) was acquired as a yellow solid precipitate and dissolvable in common organic solvents. The resultant Schiff base complexes are soluble in DMF and DMSO but sparingly soluble in common organic solvents. The analytical data and physical properties of the ligand and its mononuclear complexes are listed in **Table 1**. The analytical data indicate that the metal to ligand proportion is 1:2 for all the complexes. The electrolytic nature of complexes was measured in DMSO using 10^{-3} M solutions at room temperature. From the result, the molar conductance values lies in the range of 17-26 $ohm^{-1}cm^2mol^{-1}$ for the derived mononuclear Schiff base metal complexes. The molar conductance data suggested that no anions are present outside the coordination sphere which indicates that complexes were non-electrolytic in nature **[31]**.

Infrared Spectra

The structure confirmation of metal complexes can be effectively accomplished by contrasting the IR spectra of the free ligands with their metal complexes (**Table 2**). Such comparison exposed that the absorption band showing up in the ligand spectra at 1619 –1616 cm^{-1} due to the azomethine group is shifted to higher wavenumbers by 1–3 cm^{-1} in the complexes spectra, proposing coordination through the azomethine nitrogen **[32, 33]**. The band appeared at 1725cm^{-1} is characteristic of C= O group ligand **[34]** and upon complexation, this band is shifted to higher frequency 1726–1733 cm^{-1}, showing the coordination of carbonyl oxygen to the metal ion which is further bolstered by the appearance of a non-ligand bands in the regions 486–489 cm^{-1}, 521-531 cm^{-1} and 338-355 cm^{-1} which are expected to (M–N), (M–O) and (M-Cl) bands **[35-38]**, respectively. Further, the ligand and complexes also display bands at 3174-3361cm^{-1} due to ν (N-H) stretching vibration of isatin and benzimidazole moiety **[39]**.

^{1}H NMR spectra of the ligand

^{1}H NMR spectra of the Schiff base were recorded in DMSO and represented in **Figure 1**. The ^{1}H-NMR spectra of the ligand exhibited a multiple within the range 6.05–7.85 ppm which assigned to aromatic protons. The signals observed as a singlet is due to N-H Protons of Isatin and benzimidazole moieties and appeared at 10.8–11.05 ppm **[39, 40]**. These signals provide structural arrangement for the synthesized ligand.

Electronic spectra and magnetic moments

The electronic spectra were utilized for assigning the stereochemistry of the metal ions in the complexes reliant on the number

P.G.P. COLLEGE OF ARTS & SCIENCE NAMAKKAL 637 206

of d–d and charge transfer transitions (**Table 3**). The electronic spectrum of free Schiff base ligand shows mainly two bands at 270 and 335 nm which is assigned to π–π* transition of phenyl ring and n–π* transitions related with in C=N chromophore. On complexation this band was shifted to lower and higher wavelength region proposing the coordination of azomethine nitrogen to the central metal ion. The copper (II) complex shows a broad absorption peak at 560 nm which corresponds to $^2Eg \rightarrow {}^2T_2g$ transition. The intensity of the bands and the magnetic moment value (1.70 BM) obtained for this complex confirms the octahedral geometry around Cu(II) ion. The spectrum of Co(II) complex are consistent with the formation of an octahedral geometry with the appearance of two absorption bands at 555 nm and 608 nm which may correspond to $4T_1g$ (F) → $4T_2g$ (F) and $4T_1g$(F) → $4A_2g$(F) transitions, respectively, further supported by the value obtained for magnetic moment 4.29 B.M. The magnetic moment of the Ni(II) complex lies at 3.12 B.M corresponds to two unpaired electrons, the spectrum of reported Ni (II) complexes shows band at 362 nm, 718 nm are ascribed to ^3A_2g(F) → ^3T_1g(F) and ^3A_2g(F) → ^3T_1g(P) transitions respectively, which is consistent with a formation of octahedral geometry as expected.

ESR spectra of Cu(II) complex

The ESR spectra of $C_{42}H_{28}CuN_8O_2cl_2$ complex were recorded at 9.1 GHz frequency at room temperature and the figure were shown in **Figure 2**. The ESR spectral study of Cu(II) complex provides information around the metal ion environment. The ESR spectrum of the mononuclear schiff base Cu(II) complexes exhibits two signals gl at 2.234 and $g^{\perp}$ at 2.012 respectively. The gav (gav = $1/3(g\| +2g^{\perp})$ value was calculated to be 2.08. The value of gl< 2.3 in the present Cu-complex gives a clear indication of covalent character of the metal–ligand bond and delocalisation of the unpaired electron into the ligand. These values follows the same trend $g\| > g^{\perp} >$ ge (2.00276) which suggest that the presence of unpaired electron dx_2-y_2 orbital giving octahedral geometry **[39]**.

Electrochemical studies

Electroanalytical methods are the most effectual and flexible techniques accessible for the mechanistic study of redox systems. The cyclic voltammogram of Co(II), Ni(II) and Cu(II) complex in DMF solution containing TBAP as supporting electrolyte were recorded in the potential range from 0.5 to 2.0 V. A cyclic voltammogram for metal complexes are conferred in **Figure 3**.

The cyclic voltammogram of Schiff base complexes contains two peaks and are due to oxidative nature of organic molecule and reductive nature of azomethine group

P.G.P. COLLEGE OF ARTS & SCIENCE NAMAKKAL 637 206

which is present in Schiff base. The copper $[C_{42}H_{28}CuN_8O_2cl_2]$ complex shows well-defined redox process and ΔEp values falls in the range of 160 mV, 230 mV which demonstrates quasi-reversible reduction-oxidation waves. The $E_{1/2}$ values falls in the range of -1.32 V indicates one electron reduction of Cu(II)→Cu(I)process whereas 0.96 V indicates the oxidation process of Cu(I)→Cu(II). The cobalt $[C_{42}H_{28}CoN_8O_2cl_2]$ complex exhibit ΔEp values in the range of 180 mV and 110 mV which corresponds to quasi-reversible reduction-oxidation waves. The $E_{1/2}$ values lies in the range of -0.73 V indicates one electron reduction of Co(II)/Co(I) process whereas 0.89 V indicates the oxidation process. The Nickel $[C_{42}H_{28}NiN_8O_2cl_2]$ complex shows well-characterized redox process relating to the formation of the quasi-reversible reduction Ni(II)/Ni(I) and oxidation Ni(I)/ Ni(II) couple. The both ΔEp (100/160 mV) and $E_{1/2}$ (-1.03 / 0.46 V) values indicate that each couple corresponds to quasi-reversible one electron transfer process.

Antimicrobial Studies

The bacterial and fungicidal effect of the Schiff base and its metal complexes (Cu, Co, Ni) were determined against microorganisms such as *Bacillus Subtilis*, *Salmonella typhi*, *Aspergillus niger* and *Candida albicans* using the agar diffusion technique under four different concentration. The microbial activity of the synthesized compounds was also compared with standard antibacterial agent (Chloramphenicol) and antifungal agent (Fluconazole). The results of MIC values and zone of inhibition (in mm) for microbial activity are presented in **Figure 4 & 5**. The MIC values of the ligand (100µg/ml) against bacteria (*S.typhi and B.subtilis*) are higher to standard drug chloramphenicol though for fungal strains (100µg/ml) shows lower action for *Aspergillus niger* and higher activity for *Candida albicans*. A similar investigation of minimum inhibitory concentration (MIC) values indicated that the metal complexes have moderate action when contrasted with the standard but all the complexes are more active than their respective ligand. From the consequence of the antimicrobial, it has been uncovered that cobalt complex shows better activity than other complexes for both bacterial and fungal strains. A possible reason behind the enhanced activity of the metal complexes has been postulated in the light of chelation theory. It was suggested that chelation significantly lessens the charge of the metal ion mainly due to partial sharing of its positive charge with the donor groups and viable p-electron delocalization over the entire chelate ring **[41]**. Such a chelation could improve the lipophilic character of the central metal atom, which in this way supports its penetration through the lipid

P.G.P. COLLEGE OF ARTS & SCIENCE NAMAKKAL 637 206

layers of the cell membrane and hindering the metal binding sites on enzymes of microorganism [42, 43]. Besides, the method of activity of the compound may include the formation of a hydrogen bond through the azomethine group with the active centre of the cell, ensuing in interference with the normal cell processes.

Anticonvulsant activity

Antiepileptic activity data of the Schiff base and its metal complexes are presented in **Table 4**. In the present investigation, the synthetic compounds were exposed to a screening anticonvulsant assays including MES and PTZ induced seizure tests in Wister albino rats. The standard medication phenytoin (25 mg/kg) and the various synthetic compounds (10 mg/ kg) exhibited significant anticonvulsant action against electroshock induced HLTE. In the MES, protection against HLTE predicts the anticonvulsant activity of the tested agents and furthermore demonstrates the ability of various synthetic drugs to either stop or to slow down the discharge of the seizure within the brain stem substrate [44]. Seizure of MES can be blocked either by hindering the voltage-dependent Na^+channels or by blocking glutamatergic excitation intervened by the N-methyl-D-aspartate (NMDA) receptors [45].

Since various synthetic drugs showed anti-epileptic activity in the MES, they may act by inhibiting the voltage-dependent Na^+channels or by obstructing the glutamatergic neurotransmission intervened by NMDA receptors.

In PTZ test, the outcomes showed that all synthetic compounds possess anticonvulsant activity compared to standard drug. The ability of all synthetic compounds to delay the onset of convulsions and/or shorten the duration of convulsions was considered an indication of anticonvulsant activity. Therefore, the anticonvulsant activities of various synthetic compounds against PTZ seizures might be due to an enhancement on the release of the inhibitory neurotransmitter GABA in the central nervous system, inhibiting T-type Ca^{2+} currents or blocking the glutamatergic neurotransmission mediated by NMDA receptors.

Sub-Acute toxicity

The assessment of sub-chronic and chronic dosing in experimental animals may be more relevant in determining the overall toxicity of the synthetic drug preparation. In the present study, where the acute toxicity study of various synthetic drugs was carried out as per OECD-423 guidelines, no mortality was observed in animals of control group as well as animals treated with synthetic drugs at dose 10 $mgkg^{-1}$. From the results, we found that there was no significant change in animal behavior due to the absence of toxicity. The animals treated with various synthetic

P.G.P. COLLEGE OF ARTS & SCIENCE NAMAKKAL 637 209

drugs showed normal growth pattern and body weight compared with control rats treated with normal saline are shown in **Table 5**. So the adjustments in body weight can be utilized as a pointer of antagonistic impacts of medications and synthetic substances **[46-48]**.

The changes in enzymes like ALP, AST and ALT levels show liver impairment, due to toxicity **[49]**. After 14 days of administration of various synthetic drugs, it was found that at all concentrations drugs do not produce liver damage. The biochemical parameters are shown in **Table 6-8**.

The consequences of hematological parameters are tabulated in **Table 9**. After 14 days of treatment, there were no critical changes in the hematological parameter levels of WBC, RBC among control and test groups following repeated administration of various synthetic drugs. Interestingly, significant increase in the levels of hemoglobin was found in treatment and the possible reason could be that one of the constituents of various synthetic drugs may increase absorption of iron. From the overall toxicity results, it concludes that various synthetic drugs are non-toxic to the hematopoietic and leucopoietic system.

Table 1: Physical properties of ligand and its mononuclear metal complexes

Compounds	Molecular Formula	color	Yield	Melting point (°c)	Calculated (found)%						Molar conductance Am (ohm^{-1} cm^2mol^{-1})
					C	H	N	O	cl	M	
Ligand	$C_{21}H_{14}N_4O$	Yellow	85	178	(74.54) 74.55	(4.17) 4.14	(16.56) 16.56	(4.73) 4.73	-	-	-
CuL	$C_{42}H_{28}CuN_8O_2Cl_2$	Dark green	80	200	(62.18) 62.2	(3.45) 3.45	(13.81) 13.82	(3.94) 3.95	(8.74) 8.64	(7.84) 7.84	26
CoL	$C_{42}H_{28}CoN_8O_2Cl_2$	Light brown	75	195	(62.54) 62.6	(3.47) 3.47	(13.89) 13.91	(3.97) 3.97	(8.79) 8.69	(7.31) 7.32	23
NiL	$C_{42}H_{28}NiN_8OCl_2$	Dark brown	70	242	(62.56) 62.6	(3.47) 3.47	(13.90) 13.91	(3.97) 3.97	(8.80) 8.80	(7.28) 7.29	17

Table 2: IR Spectroscopic studies of Schiff base ligand and its metal complexes

COMPOUNDS	C=N (v, cm^{-1})	C=O (v, cm^{-1})	N-H (v,cm^{-1})	M-O (v, cm^{-1})	M-N (v, cm^{-1})	M-Cl (v, cm^{-1})
Ligand	1616	1725	3174	-	-	-
CuL	1617	1733	3158	528	487	338
CoL	1619	1726	3168	531	486	355
NiL	1618	1731	3361	521	489	347

P.G.P. COLLEGE OF ARTS & SCIENCE NAMAKKAL 637 206

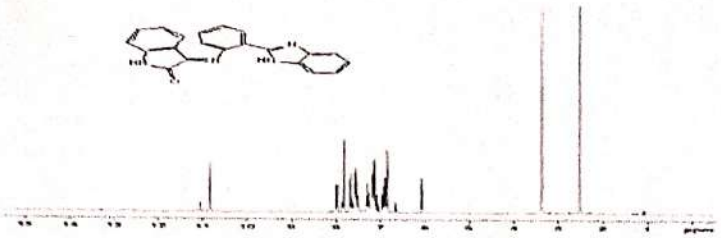


Figure 1: ^{1}H NMR Spectra for of Schiff base ligand

Table 3: Electronic spectral data of the ligand and their complexes

COMPOUNDS	$\pi-\pi^*$ (nm)	$n-\pi^*$ (nm)	L → M (nm)	d-d (nm)	Magnetic moment value (μ_{eff}) BM
Ligand	270	335	-	-	-
CuL	261	339	361	560	1.70
CoL	284	361	377	555,608	4.29
NiL	259	329	362	718	3.12

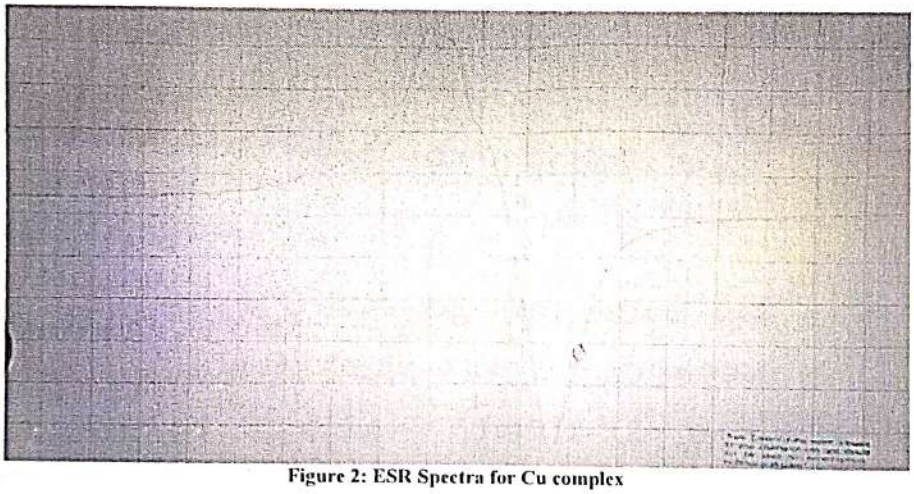


Figure 2: ESR Spectra for Cu complex

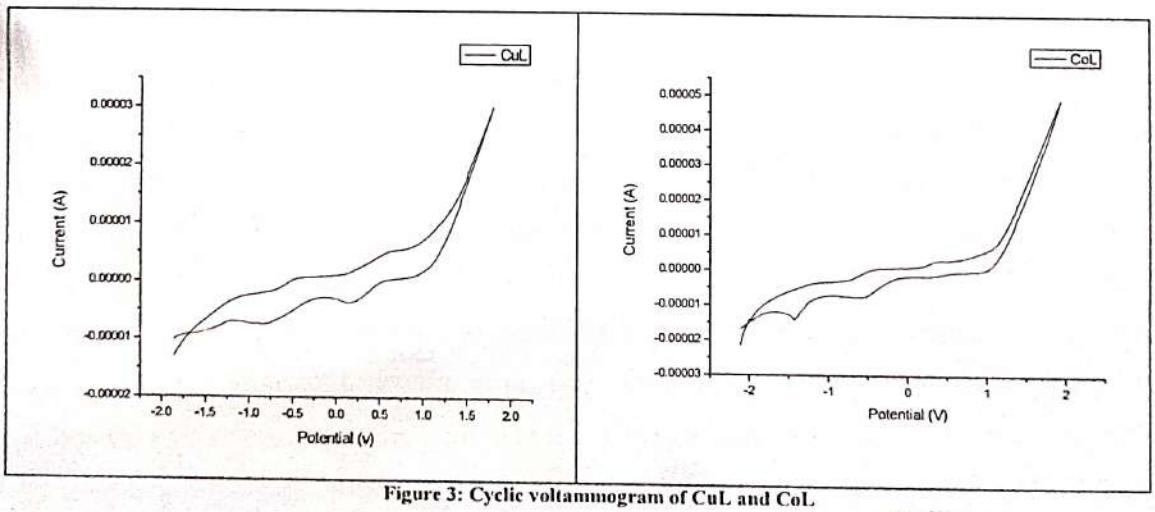


Figure 3: Cyclic voltammogram of CuL and CoL

P.G.P. COLLEGE OF ARTS & SCIENCE NAMAKKAL 637 206

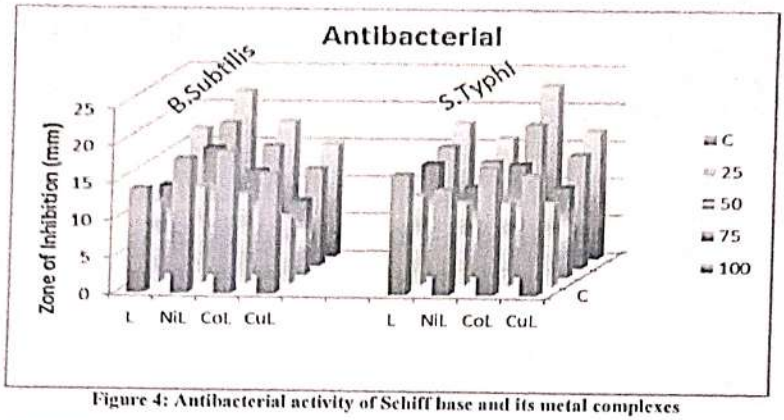


Figure 4: Antibacterial activity of Schiff base and its metal complexes

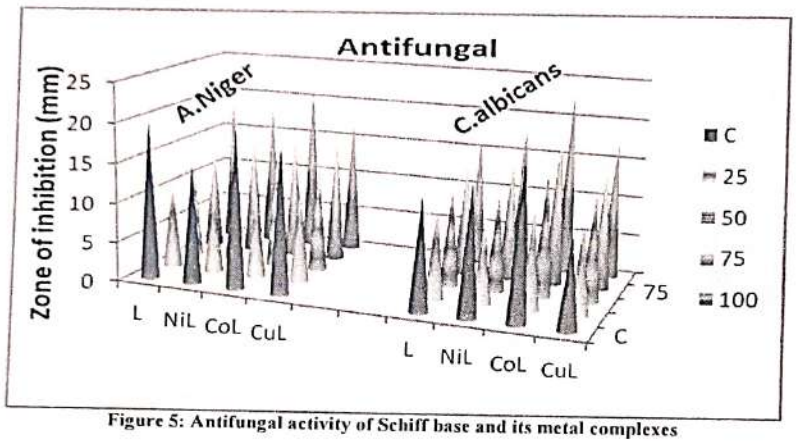


Figure 5: Antifungal activity of Schiff base and its metal complexes

Table 4: Anticonvulsant activity data of Schiff base and metal (II) complexes

Compound	Anticonvulsant activity			
	MES Screen		PTZ Screen	
	Dose ml/mg /kg	HLTE (Sec)	Onset time (sec.)	Duration of HLTE (sec.)
saline	10	13.45± 0.80	53.20± 1.05	34.20± 1.75
phenytoin sodium	25	1.0± 0.25a	0± 00	0± 00
L	10	2.70± 0.65a	54.90± 1.16	22.8± 0.68 a
CuL	10	2.66± 0.58a	56.15± 1.26	24.9± 0.77 a
CoL	10	2.38± 0.42a	55.35± 1.15	25.0± 0.78 a
NiL	10	2.56± 0.52a	55.22± 1.08	23.0± 0.75a

Table 5: Effect of Various synthetic drugs on body weight changes in rats

Compound	Dose (mg/kg)	Day 1	Day 5	Day 10	Day 20
Control	10	189.20±5.6	190.20 ±6.10	198.10 ±6.25	199.6±6.35
L	10	193.65 ±6.4	199.45 ±6.65	197.35 ±6.25	206.28±6.40
CuL	10	192.15 ±5.8	196.50 ±6.20	198.30 ±6.60	203.90±6.50
CoL	10	196.25 ±6.3	200.80±6.45	202.60 ±6.55	207.35±6.80
NiL	10	198.10 ±6.2	199.85 ±6.55	202.60 ±6.75	206.40±6.85

Table 6: Effect of Various synthetic drugs on kidney, heart, liver and brain in rats

Compound	Dose (mg/kg)	Heart (gms)	Kidney (gms)	Liver (gms)	Brain (gms)
Control	10	0.35 ± 0.04	0.72± 0.03	3.32± 0.14	0.72± 0.05
L	10	0.36± 0.05	0.77± 0.02	3.40± 0.18	0.76± 0.20
CuL	10	0.37± 0.06	0.84± 0.04	3.47±0.21	0.70± 0.06
CoL	10	0.35± 0.03	0.76± 0.02	3.38± 0.20	0.78± 0.10
NiL	10	0.38± 0.05	0.83± 0.05	3.45± 0.19	0.72± 0.05

P.G.P. COLLEGE OF ARTS & SCIENCE NAMAKKAL 637 206

Table 7: Effect of Various synthetic drugs on biochemical profiles of rats

Compound	Dose (mg/kg)	Glucose ($mg.dl^{-1}$)	Cholesterol ($mg.dl^{-1}$)	Triglyceride ($mg.dl^{-1}$)	HDL ($mg.dl^{-1}$)	LDL ($mg.dl^{-1}$)
Control	10	94.42± 1.74	39.05± 0.62	33.25± 1.43	143.45± 3.15	90.30±1.85
L	10	97.32±1.45**	41.55± 0.47	22.15± 1.18*	188.25± 3.62*	50.22±1.15
CuL	10	94.18± 1.54	27.90± 0.48*	18.58± 0.92*	172.22±3.35*	73.50±1.25
CoL	10	95.25±1.40**	40.45± 0.42	20.05± 0.96*	190.35± 3.40*	50.45±1.20
NiL	10	93.45± 1.60	26.22± 0.40*	18.40± 0.88*	182.35± 3.70*	75.80±1.40

Table 8: Effect of Various synthetic drugs on biochemical parameters such as AST, ALT, ALP, TP and Albumin in rats

Compound	Dose (mg/kg)	AST ($IU.l^{-1}$)	ALT ($IU.l^{-1}$)	ALP ($IU.l^{-1}$)	TP ($g.l^{-1}$)	ALBUMIN ($g.l^{-1}$)
Control	10	320.3±11.60	65.4± 3.42	245.35± 8.60	63.36± 3.28	33.30±2.45
L	10	308.8±9.62	57.4±2.48	257.35±8.45	74.84± 3.85	32.88±2.34
CuL	10	308.6±9.45**	61.4± 2.78**	257.40± 8.25**	72.20± 3.86	32.20±2.48
CoL	10	311.7±9.98	56.2± 2.35	256.30± 8.40	73.40± 3.72	33.30±2.42
NiL	10	312.3±10.60**	62.8± 2.85**	256.20± 8.80**	64.22± 3.45	31.85±2.22

Table 9: Effect of Various synthetic drugs on hematological parameters in rats

Compound	Dose (mg/kg)	Hemoglobin ($mg.dl^{-1}$)	RBC ($10^6/mm^3$)	WBC ($10^6/mm^3$)	Calcium ($mg.dl^{-1}$)
Control	10	13.56± 1.28	9.24± 0.93	11.55± 0.90	9.44 ±0.60
L	10	12.80±1.15*	8.55± 0.95*	10.15± 1.05*	9.78 ±0.68
CuL	10	13.30± 1.85*	8.60± 1.02*	8.40± 0.85*	9.32 ±0.48
CoL	10	13.05±1.28*	8.30± 0.80*	9.50± 0.90*	9.58 ±0.60
NiL	10	12.40±1.45*	9.25± 1.08*	8.05± 0.80*	9.05 ±0.42

CONCLUSION

In the present work, a series of novel indole ring containing Schiff base has been structured and their relating metal complexes are synthesized by condensation method. The bonding of ligand to Metal ions and the overall geometry of metal complexes have been deduced on the basis of analytical data and various spectroscopic techniques. From the results, the chelation of metal ions to the ligand occurs through the oxygen atom of carbonyl group and the nitrogen atoms of the azomethine group. Electrochemical study indicates that metal complexes exhibit a single electron transfer quasi-reversible nature. The antimicrobial studies proposed that the Schiff bases were found to be biologically active and their metal complexes exhibited significantly enhanced antibacterial and antifungal activities against microbial strains in comparison to the free ligands. The in-vitro cytotoxicity results showed that the complexes exhibited a significant inhibitory potency towards proliferation of the MCF-7 cell line. The anticonvulsant screening indicated that among the tested compounds, metal complexes exhibited noteworthy activity in both MES and PTZ Seizure test. The results of sub-acute toxicity study show that there was no significant change in animal behavior, hematological parameters due to the absence of toxicity.

Acknowledgement

The authors thank Dr. N. Chidambaranathan, Department of Pharmacology, K.M. College of Pharmacy, Madurai, India for extending facilities to

carry out the anticonvulsant activity.

Conflict of interests

The authors declare that they have no conflict of interest

REFERENCES

[1] Visweswari G, Prasad K, Chetan P, Lokanatha V, Rajendra W, (2010), Evaluation of the anticonvulsant effect of Centella asiatica (gotu kola) in pentylenetetrazol induced seizures with respect to cholinergic neurotransmission. Epilepsy & Behavior, 17: 332-335.

[2] Bialer, M., Johannessen, S.I., Kupferberg, H.J., Levy, R.H., Perucca, E., Tomson, T., 2004. Progress report on new antiepileptic drugs: a summary of the Seventh Eilat Conference (EILAT VII).Epilepsy Res. Sep-Oct; 61(1-3): 1-48.

[3] Lerer, B and Macciardi, F., 2002. Pharmacogenetics of antidepressant and mood-stabilizing drugs: a review of candidate-gene studies and future diections. Int. J. Neuropsychopharmacol. 15, 255.

[4] Luszczki JJ, Antkiewicz-Michaluk L, Czuczwar SJ, (2006), 1-Methyl-1, 2, 3, 4 tetrahydroisoquinoline enhances the anticonvulsant action of carbamazepine and valproate in the mouse maximal electroshock seizure model. Neuropharmacology, 50: 133–42.

[5] Miziak B, Chroscin' ska-Krawczyk M, Blaszczyk B, Radzik I, Czuczwar SJ. 2013; Novel approaches to anticonvulsant drug discovery. Expert Opin Drug Discov 8:1415–27.

[6] Panda, S.S., Chaudhari, P.V.R., 2008. Ind. J. Pharm. Sci. 208.

[7] Biradar, J.S., Sasidhar, S.B., Parveen, R.E., 2010. Synthesis, antioxidant and DNA cleavage activities of novel indole derivatives. Eur. J. Med. Chem. 45, 4074.

[8] Singh, G.S., Siddiqui, N., Pandeya, S.N., 1992. Synthesis and anticonvulsant and anti-inflammatory activities of new 3-aryl/alkylimino-1-methylindol-2-ones, Arch. Pharm. Res. 15, 272-274.

[9] Sharma, V., Kumar, P., Pathak, D., 2010. Biological Importance of the Indole Nucleus in Recent Years: A Comprehensive Review. J. Heterocycl. Chem. 47, 491.

[10] Lin, H., Feng, Y.L., 2005. Chin. J. Struct. Chem. 24, 346–348.

[11] Yu Q., Zhu L.G., Bian H.D., Deng J.H., Yang X.E., Guo G.Q., Liang H., 2005. Synthesis anderystal structure of a Zinc(II) complex salt with the Schiff base of

P.G.P. COLLEGE OF ARTS & SCIENCE NAMAKKAL 637 206

picolinaldehyde N-oxide and semicarbazone. Chin. J. Struct. Chem. 24, 1271–1275.

[12] Coles S., Hursthouse, M., Kelly, D., Toner, A., Walker, N.M., 1998. Halide titanium(IV) Schiff base complexes; fluoride and bromide derivatives and evidence for a new seven-coordinate chloride intermediate J. Chem. Soc. Dalton Trans., 3489–3494.

[13] Cozzi, P.G., 2004. Metal-Salen Schiff base complexes in catalysis: Practical aspects. Chem. Soc. Rev. 33, 410.

[14] Garnoviskii, A.D., Nirorozhkin, A.L., Minkin, V.I., 1993. Coord. Chem. Rev. 126, 1.

[15] Makio, H., Kashiwa, N., Fujita, T., 2002. FI Catalysts: A New Family of High Performance Catalysts for Olefin Polymerization. Adv. Synth. Catal. Vol.344, 477-493.

[16] Atwood, D.A., Harrey, M.J., 2001. Group 13 compounds incorporating Salen ligands. Chem. Rev. vol. 101, 37-52.

[17] Abdallah, Sayed, M., Zayed, M.A., Mohamed, Gehad, G., 2010. Synthesis and spectroscopic characterization of new tetradentate Schiff base and its coordination compounds of NOON donor atoms and their antibacterial and antifungal activity. Arabian J. Chem. Vol.3, 103-113

[18] Raman, N., Sobha, S., 2010. Spectrochim. Acta A 278, 888–898.

[19] Dey M., Deb K., Dhar S.S, 2011, VO(acac)2 catalyzed condensation of ophenylenediamine with aromatic carboxylic acids/aldehydes under microwave radiation affording benzimidazoles, Chinese Chem. Lett., 22, 296–299.

[20] Maiti D.K., Halder S., Pandit P., Chatterjee N., 2009, Joarder D., Pramanik N., Saima Y., Patra A., Maiti P.K., Synthesis of glycal-based chiral benzimidazoles by $VO(acac)_2$-$CeCl_3$ combo catalyst and their self-aggregated nanostructure, Materials J. Org. Chem., 74, 8086–8097.

[21] Keri R.S., Hosamani K.M., Reddy H.R.S., Shingalapur R.V., 2009, Wells dawson heteropolyacid: an efficient recyclable catalyst for the synthesis of benzimidazoles under microwave condition, Catal. Lett., 131, 552-559.

[22] Chhonker Y.S., Veenu B., Hasim S.R., Kaushik N., Kumar D., Kumar P., 2009, Synthesis and pharmacological evaluation of

P.G.P. COLLEGE OF ARTS & SCIENCE NAMAKKAL 637 206

some new 2- phenyl benzimidazoles derivatives and their Schiff's bases, E. J. Chem,6, S342-S346.

[23] Koc Z.E., Aladag M.O., Uysal A., 2013, Synthesis of novel dopamine derived multidirectional ligands from cyanuric chloride: structural and antimicrobial studies, EXCLI Journal, 12, 396 403.

[24] Jesudason E.P., Sridhar S.K., Malar E.J.P., Shanmugapandiyan P.Inayathullah M., Arul V., Selvaraj D., Jayakumar R., 2009, Synthesis, pharmacological screening, quantum chemical and in vitro permeability studies of N-Mannich bases of benzimidazoles through bovine cornea, Eur. J. Med. Chem., 44, 2307-2312.

[25] Reddy B.A., 2010, Synthesis, Characterization and biological evaluation of 1,2-disubstituted benzimidazole derivatives using Mannich bases, Eur.J. Chem., 7, 222-226.

[26] Denny W.A., Rewcastle G.W., Baguley B.C, 1990, Potential antitumor agents. 59. Structure activity relationships for 2-phenylbenzimidazole-4-carboxamides, a new class of minimal DNA-intercalating agents which may not act via topoisomerase II, J. Med. Chem. 33, 814 819.

[27] Villanueva J.P., Santos R., Campos A.H., Giulianotti M.A., Castillo R., Franco J.L.M., 2011, Structure–activity relationships of benzimidazole derivatives as antiparasitic agents, Med. Chem. Commun., 2, 44-49.

[28] Hranjec M., Starčević K., Pavelić S.K., Lučin P., Pavelić K., Zamola G.K., Marijana H., Kristina S., Sandra K., 2011, Synthesis, spectroscopic characterization and antiproliferative evaluation in vitro of novel Schiff bases related to benzimidazoles, Eur. J. Med. Chem., 46, 2274-2279.

[29] A.M.Hassan, A.M.Nassar, Y.Z.Hussien & A.N.Elkmash, (2012) Synthesis, Characterization and Biological Evaluation of Fe (III), Co (II), Ni(II), Cu(II), and Zn(II) Complexes with Tetradentate Schiff Base Ligand Derived from Protocatechualdehyde with 2-Aminophenol, Appl Biochem Biotechnol, 167: 581–594.

[30] K.Thirupathi, D.R. Krishna, B. Ravi Kumar, P.Tirumala Rao and G.Krishna Mohan, (2009) Anticonvulsant Activity of

P.R.G. COLLEGE OF ARTS & SCIENCE NAMAKKAL 637 206

Pericarpium Extract of Balanites Roxburghii Planch in Mice, Pharmacologyonline., 1: 1150-1157.

[31] Mozaffar Asadia, Mohammad Hadi Ghateea, Susan Torabia, Khosro Mohammadib and Fatemeh Moosavia, 2010, J Chem Sci., 122, 539.

[32] Seema Varghese, RJPBCS.2010, 2, 347.

[33] Subudhi B.B, Panda P.K, Bhatta D, Jena, A, (2009) Anticonvulsant and Antimicrobial Activity of Cu (II), Zn (II) and Co (II) Complex of Isatin 3-Glycine. Iranian Journal of Pharmaceutical Sciences, 5(2), 83.

[34] Anand Mishra P, Rudra Mishra, Rajendra Jain and Santosh Gupta, (2012) Synthesis of New VO(II), Co(II), Ni(II) and Cu(II) Complexes with Isatin-3-Chloro-4-Floroaniline and 2-Pyridinecarboxylidene-4-Aminoantipyrine and their Antimicrobial Studies. Mycobiology, 40(1): 20-26.

[35] Muna Abass Hadi, 2013, Coordination behavior of n/o donor ligand with some transition metals, Acta Chim. Pharm. Indica: 3(2), 127-134.

[36] Neeraj Sharma, 2013, Synthesis, Characterization and Antimicrobial studies of Co(II), Ni(II), Cu(II), Zn(II) and Fe(III) Complexes with Isatin Derivative, International Journal of Emerging Technologies in Computational and Applied Sciences, 4(4), pp. 354-361.

[37] Swathy S.S, Selwin Joseyphus R, Nisha V.P, Subhadrambika N, Mohanan K, (2016), Synthesis, spectroscopic investigation and antimicrobial activities of some transition metal complexes of a [(2-hydroxyacetophenone)-3-isatin]-bishydrazone. Arab. J. Chem, 9, S1847 S1857.

[38] MuthukkumarM, Malathy M and Rajavel R, (2015) Synthesis and spectral characterization of new mononuclear schiff base complexes derived from 4-aminoantipyrine, 2, 3-butadione and o-phenylenediamine. Der Chemica Sinica, 6(11): 12-20.

[39] Matangi sunitha, Pragathi jogi, Bathini ushaiah, and Gyana kumara C, 2012, Synthesis, Characterization and Antimicrobial Activity of Transition Metal Complexes of Schiff Base Ligand Derived from 3-Ethoxy Salicylaldehyde and 2-(2-Aminophenyl) 1-H-

P.G.P. COLLEGE OF ARTS & SCIENCE NAMAKKAL 637 206

benzimidazole, E-Journal of Chemistry, 9(4), 2516-2523.

[40] Abdulghani A. J and Ahmed Z. Z., (2011), Synthesis, Structure and Characterization of New Metal Complexes of Schiff Bases Derived from Isatin N-Benzylisatin and 4Aminoantipyrine, Pak. J. Chem. 1(3): 100-113.

[41] Singh Jadon S.C, Gupta N, Singh R.V, (1995) synthetic and biochemical studies of some hydrazine carbodithioic acid derivatives of dioxomolybdenum (VI) Ind. J. Chem. 34A, 733.

[42] Pelczar M.J, E.C.S. Chan, N.R. Krieg, Microbiology, fifth ed., McGraw-Hill, New York, 1998.

[43] Abou Hussein A.A, El-Kholy S.S, El-Sabee M.Z, (2004) Metal uptake by a novel bidentate thiosemicarbazide chelating polymer, J. Coord. Chem. 57, 1027.

[44] Nagaraja T, Mohamood R., Krishna V., Thippeswamy B., Veerapur V., (2012), Anticonvulsant activity of Erythrin amysorensis bark extract in an animal model of epilepsy. J Pharmacol Pharmacother, 3: 62–64.

[45] Luszczki JJ, Lucyna A, Czuczwar SJ, (2006) 1-methyl-1, 2, 3, 4-tetrahydroisoquinoline enhances the anticonvulsant action of carbamazepine and valproate in the mouse maximal electroshock seizure model. Neuropharmacol; 50: 133–142.

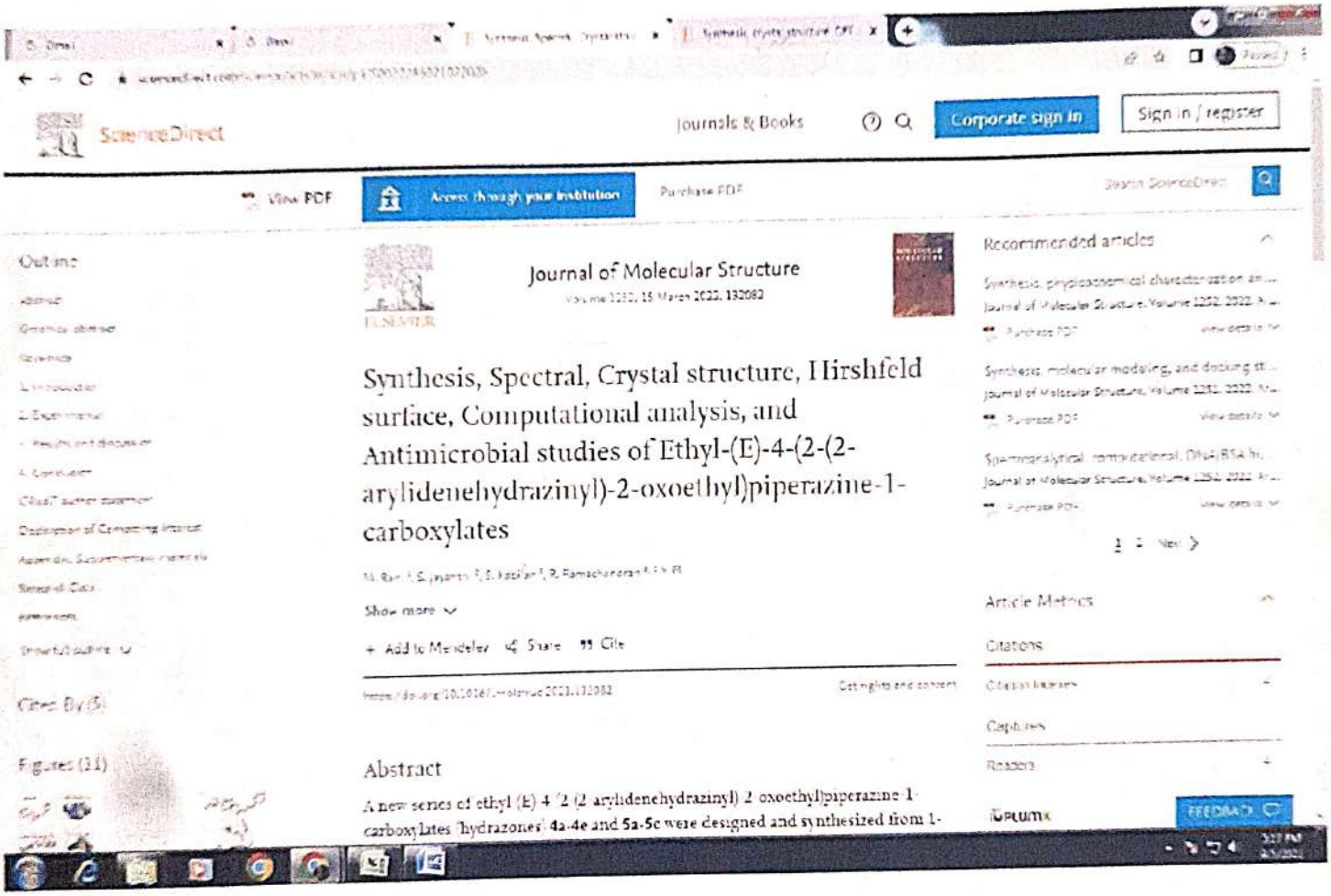
[46] Tofovic S.P., Jackson E.K, (1999), Effect of long-term caffeine consumption on renal function in spontaneously hypertensive heart failure prone rats. Journal of Cardiovascular Pharmacology, 33, 360-366.

[47] Raza M, Al-Shabanah O.A, M.El-Hadiyah T, Al-Majed A.A., (2002) Effect of prolonged vigabatrin treatment on haematological and biochemical parameters in plasma, liver and kidney of Swiss albino mice. Scientia Pharmaceutica, 70, 135-145.

[48] Teo S., Stirling D., Thomas S., Hobermann A., Kiorpes A., Khetani V., A 90- days oral gavage toxicity study of D-methyl penidate and DL methyl penidate in Sprague- Dawley rats. Toxicology, (2002) 179, 183.

[49] Hayes A.W., (1989) Guidelines for acute oral toxicity testing, In: Principles and methods of toxicity. New York: Raven Press Ltd, 184.

PRINCIPAL
PGP College of Arts and Science
Namakkal.



ScienceDirect

Journals & Books

Corporate sign in

Sign in / register

View PDF

Access through your institution

Purchase PDF

Search ScienceDirect

Outline

Abstract

Graphical abstract

Keywords

1. Introduction

2. Experimental

3. Results and discussion

4. Conclusion

CRediT author statement

Declaration of Competing Interest

Appendix. Supplementary material

Data availability

Acknowledgments

Show full outline

Cited By (5)

Figures (11)

Journal of Molecular Structure

Volume 1252, 15 March 2022, 132082

Synthesis, Spectral, Crystal structure, Hirshfeld surface, Computational analysis, and Antimicrobial studies of Ethyl-(E)-4-(2-(2-arylidenehydrazinyl)-2-oxoethyl)piperazine-1-carboxylates

M. Ravi, S. Jayarama, P.S. Nayaka, P. Ramacharyulu, K.S.R.

Show more

+ Add to Mendeley Share Cite

https://doi.org/10.1016/j.molstruc.2021.132082

Get rights and content

Abstract

A new series of ethyl (E) 4 (2 (2 arylidenehydrazinyl) 2 oxoethyl)piperazine 1 carboxylates hydrazones 4a-4e and 5a-5e were designed and synthesized from 1-

Recommended articles

Synthesis, physicochemical characterization an...
Journal of Molecular Structure, Volume 1252, 2022, A...
Purchase PDF View details

Synthesis, molecular modeling, and docking st...
Journal of Molecular Structure, Volume 1252, 2022, N...
Purchase PDF View details

Spectroanalytical, computational, DNA/BSA bi...
Journal of Molecular Structure, Volume 1252, 2022, A...
Purchase PDF View details

1 2 Next >

Article Metrics

Citations

Citation Indexes

Captures

Readers

PlumX

FEEDBACK

P.G.D. COLLEGE OF ARTS & SCIENCE
NAMAKKAL
637 205

Journal of Molecular Structure 1252 (2022) 132082

Contents lists available at ScienceDirect

Journal of Molecular Structure

journal homepage: www.elsevier.com/locate/molstr

Synthesis, Spectral, Crystal structure, Hirshfeld surface, Computational analysis, and Antimicrobial studies of Ethyl-(E)-4-(2-(2-arylidenehydrazinyl)-2-oxoethyl)piperazine-1-carboxylates

M. Rani[a], S. Jayanthi[b], S. Kabilan[a], R. Ramachandran[a,c,*]

[a] Department of Chemistry, Annamalai University, Annamalainagar 608 002, Tamil Nadu, India
[b] Department of Chemistry, NKR Government Arts college for Women (Affiliated to Periyar University-Salem), Namakkal 637 001, Tamil Nadu, India
[c] Department of Chemistry, PGP College of Arts and Science (Affiliated to Periyar University-Salem), Namakkal 637 207, Tamil Nadu, India

ARTICLE INFO

Article history:
Received 25 August 2021
Revised 1 December 2021
Accepted 1 December 2021
Available online 4 December 2021

Keywords:
Hydrazones
Crystal structure
Hirshfeld surface
Docking
nCoV-SARS-2

ABSTRACT

A new series of ethyl-(E)-4-(2-(2-arylidenehydrazinyl)-2-oxoethyl)piperazine-1-carboxylates (hydrazones) **4a-4e** and **5a-5c** were designed and synthesized from 1-ethoxycarbonylpiperazine. The hydrazones structure interpretations were achieved by spectroscopic analysis using FT-IR, 1D and 2D NMR and mass. Among the aforementioned hydrazones **4a-4e** and **5a-5c**, single crystal XRD structure was reported for hydrazone **4a**. Both NMR and single crystal XRD analysis are clearly indicated the existence of E configuration of the azomethine group (-C=N-) and *cis* conformation of the amide group. Hirshfeld surface analysis and 2D fingerprint plot were employed to get a better understanding of non-covalent interactions (NCIs), which showed that the N–H···O and C–H···O intermolecular hydrogen bonding interactions are the key contributor to stabilize the molecular solids. Density functional theory (DFT) study was carried out to explore the geometrical parameters and electronic properties of frontiers molecular orbitals (FMO), global chemical reactivity descriptor parameter (GCRD), natural bond orbital (NBO), and non-linear optical (NLO) properties for **4a** at B3LYP/6–311G(d,p) level. The molecular docking study was performed for hydrazone **4a** with nCoV-SARS-2 main protease for COVID-19. Finally, the hydrazones in this synthetic series were screened for their antibacterial and antifungal activities using selected strains. Antimicrobial studies revealed that **4a** and **5b** against *A. niger*, **4c** and **5c** against *K. pneumonia*, **4e** against *B. subtilis*, **5a**, **5b**, and **5c** against *A. flavus*, *A.niger* and *C. neoformans*, respectively exhibits remarkable antibacterial and antifungal activity at a minimum concentration of 6.25 μg/mL.

© 2021 Elsevier B.V. All rights reserved.

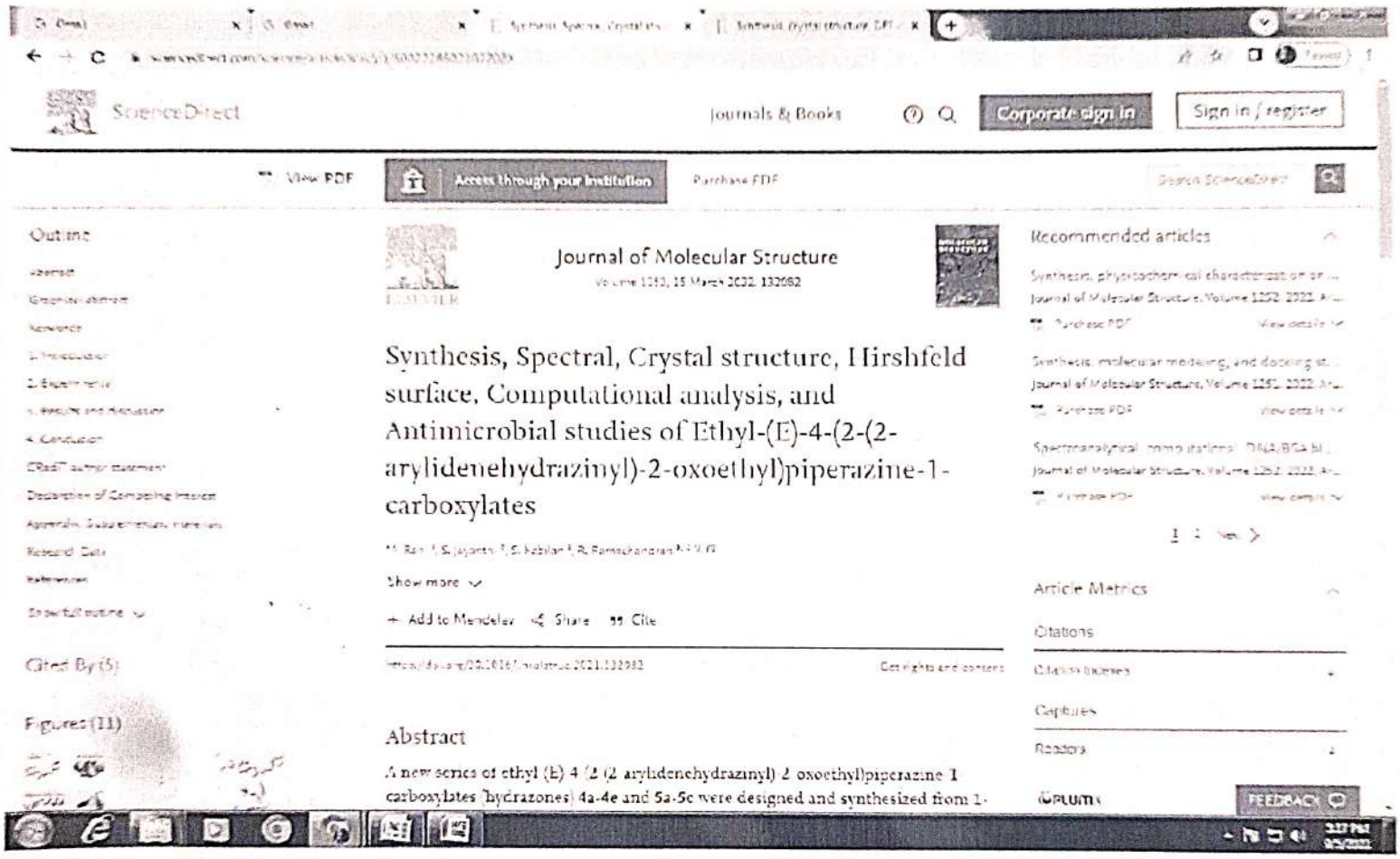
1. Introduction

The development of novel hydrazone derivatives continuously attracts both organic and medicinal chemists due to their unique structural features (R_1R_2C=N–NH–CO–NR_2), as they have a nucleophilic site on the imine nitrogen (*sp*-nitrogen), the electrophilic and nucleophilic character of an imine carbon (*sp*-carbon), configurational isomerism from C=N double bond, and an acidic N–H hydrogen [1], enable them as versatile building blocks in organic synthesis such as N-heterocycles, C–H activation, and organometallic compounds. On the other hand, hydrazone derivatives have been reported as potential antimicrobial [2], antibacterial [3] anti-inflammatory [4,5]anticancer [6–8], analgesic [9], anti-tuberculosis [10,11], anti-HIV [12–14], antidepressant, [15] and anticonvulsant [16] agents. Moreover, hydrazone derivatives are the most widely used organic ligands in coordination chemistry, because they can easily form stable metal organic complexes with several transition elements [17–19]. Therefore, they have been successfully used as chelating agents to deflate metal toxicity [20]. Additionally, these ligands display good hydrogen bond donor and acceptor as they have amide and imine subunits in the molecular structure [21] provide three-dimensional supramolecular networks by self-assembly [22].

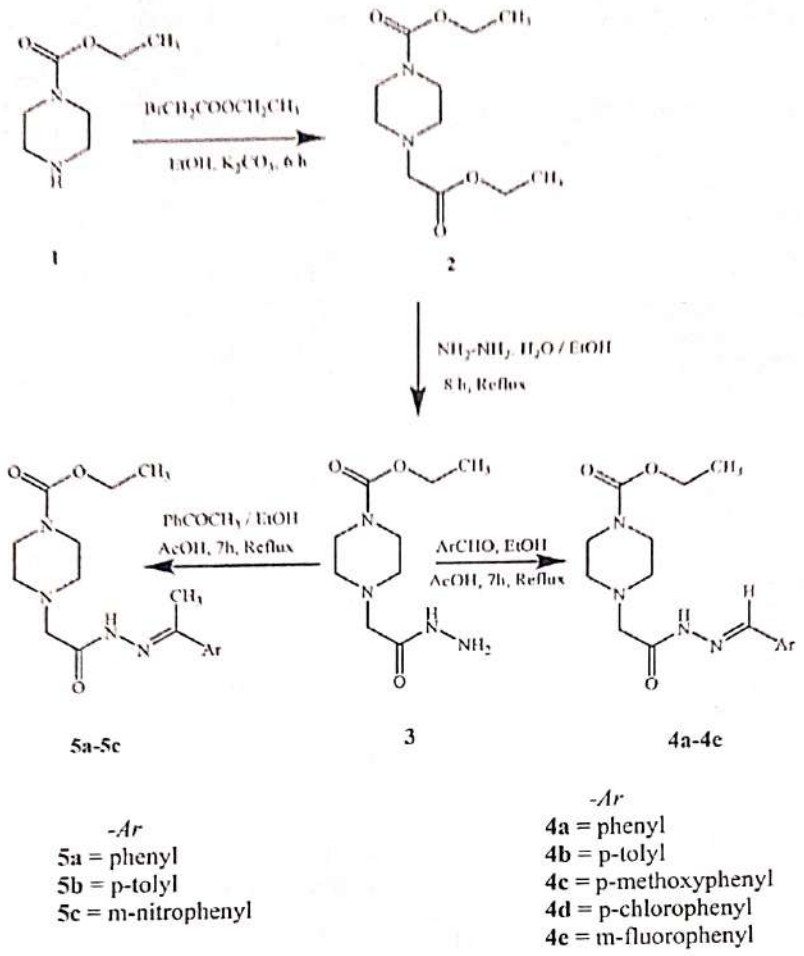
Piperazine derivatives have been widely studied in the field of medicinal chemistry owing to their versatile and eminent biological and pharmacological profile. A large number of biological activities such as analgesic, antipyretic [23] antimicrobial [24], anti-tuberculosis [25], cytotoxic [26], anti-mycobacterial [27] and anti-HIV [28] activities have been reported by compounds adjoining piperazine analogue. Further, the piperazine analogue shows distinct conformations such as chair, boat, twist-boat, and half-boat [29].

* Corresponding author.
E-mail address: synorgramu@gmail.com (R. Ramachandran).

https://doi.org/10.1016/j.molstruc.2021.132082
0022-2860/© 2021 Elsevier B.V. All rights reserved.



P.G.& R. COLLEGE OF ARTS & SCIENCE
NAMAKKAL
637 206



-*Ar*
5a = phenyl
5b = p-tolyl
5c = m-nitrophenyl

-*Ar*
4a = phenyl
4b = p-tolyl
4c = p-methoxyphenyl
4d = p-chlorophenyl
4e = m-fluorophenyl

Scheme 1. Synthesis of compounds **4a-4e** and **5a-5c**.

In recent years, interdisciplinary research has received enormous attention and has provided a new tool for studying the electronic and magnetic properties of newly synthesized organic compounds through computer studies, particularly density functional theory (DFT) technique, which is widely used to determine the kinetic stability and electronic properties such as frontier molecular orbital (FMO), natural bond orbital (NBO), hyperpolarizability, global chemical reactivity descriptor (GCRD) parameters, noncovalent interactions (NCIs), and molecular electrostatic potential (MEP) surfaces [30–36]. Thus, the above findings are spurred us to explore the experimental and computational studies to get a clear understanding of structural and electronic properties of hydrazone derivatives.

In this paper, we are presenting our research outcomes concerning the synthesis and molecular structural studies of crystalline piperazine based hydrazones, i.e., ethyl-(E)–4-(2-(2-arylidenehydrazinyl)–2-oxoethyl)piperazine-1-carboxylates, as shown in Scheme 1. Spectroscopic techniques such as FT-IR, ^{1}H & ^{13}C NMR, and in addition, single crystal XRD has been used for structural characterization of title compounds. The prime objective of this study is to explore the non-covalent interactions (NCIs) through single crystal XRD, Hirshfeld surface, and QT-AIM analysis and electronic properties of title compound using density functional theory. Further, molecular docking study is explored for model compound with nCoV-SARS-2 main protease. In addition, antibacterial and antifungal studies have also been explored for the synthesized hydrazones against selected bacterial and fungal strains.

2. Experimental

2.1. General

All chemicals were purchased from Sigma Aldrich and TCI Chemicals-India. Analytical grade solvents and other reagents were used, for this study, without further purifications. Aldehydes and amines were purified by recrystallization or distillation prior to use.

2.2. Physical measurements

The melting points of all the newly reported hydrazones **4a-4e** and **5a-5c** were recorded using an open capillary tube and are uncorrected. The experimental FT-IR spectra for all hydrazones including intermediate compounds were recorded in AVATAR-NICOLET 330 FT-IR spectrophotometer using KBr pellet method. Similarly, ^{1}H and ^{13}C NMR spectra were recorded for compounds **4a-4e** and **5a-5c** at 500 and 100 MHz, respectively, using BRUKER AMX 500 MHz spectrometer at 298 K. For that, $CDCl_3$ and tetramethylsilane (TMS) were chosen as NMR solvent and internal standard, respectively. Chemical shift values are expressed in δ = ppm).

COLLEGE OF ARTS & SCIENCE MAMAKKAL

Mass spectra of compounds **2–5** were recorded using VARIAN 4000 Mass spectrophotometer.

2.3. Synthesis of ethyl 4(2-ethoxy-2-oxoethyl)piperazine-1-carboxylate (2)

To a solution of 1-ethoxycarbonylpiperazine (3 g, 18.98 mmol) in distilled ethanol (50 mL) were added 4.12 g (24.68 mmol) of ethylbromoacetate and 2.5 g of anhydrous K_2CO_3 and the reaction mixture was refluxed for about 6–8 h. After completion of the reaction, as shown by TLC using hexane-ethylacetate mixture (10:1 ratio), the excess solvent was removed under reduced pressure and poured into ice-cold water, and extracted with ethylacetate. This was then dried over anhydrous sodium sulfate followed by column chromatographic purification using (2:1) benzene:ethyl acetate as eluent afforded white solids.

2.4. Synthesis of ethyl 4(2-hydrazinyl-2-oxoethyl)piperazine-1-carboxylate (3)

An ethanolic solution containing 2 g (8.19 mmol) of compound **2** was refluxed with hydrazine hydrate (0.6 g, 12.15 mmol) for 8 h. The progress of the reaction was monitored by TLC. At the end of the reaction, the solution was concentrated under reduced pressure and poured into ice-cold water and extracted with ethyl acetate, and dried over anhydrous sodium sulfate. White solid hydrazide was obtained after column chromatographic purification using (2:1) benzene:ethyl acetate as the eluent.

2.5. Synthesis of (E)-ethyl-4-(2-oxo-2-(2-(1-arylethylidene)hydrazinyl)ethyl)piperazine-1-carboxylates (4a-4e and 5a-5c)

A mixture of hydrazide **3** (1 g, 4.3 mmol) and acetophenone (0.62 g, 5.2 mmol) or aromatic aldehydes (1.2 eq.) and 30 mL of ethanol were refluxed in the presence of a few drops of glacial acetic acid for 4 h. After completion of the reaction, as indicated by TLC, the reaction mixture was cooled and poured into ice-cold water. Ethyl acetate was added to the aqueous solution and extracted, followed by column chromatography purification using (2:1) benzene:ethyl acetate as eluent, gave white solids.

2.6. Single crystal X-ray diffraction analysis

A suitable single crystal **4a** was grown by the slow evaporation technique using absolute ethanol as a solvent. The single crystal X-ray data for **4a** were collected with Bruker Kappa CCD diffractometer with Mo Ka (k = 0.71073 Å) at room temperature (296 K). The data reduction and cell refinement were performed using SAINT/XPREP (Bruker, and APEX2/SAINT, respectively. The crystal structure was solved using the direct method and the refinement was made by full-matrix least-squares method on F_2 with SHELXL-97 [37]. All hydrogen atoms bonded to the carbon atoms in a molecule were placed in a chemically acceptable position with C–H = 0.93 Å for aromatic, 0.94 Å for methylene, and 0.96 Å for methyl, and refined in riding mode with U_{iso}(H) = 1.2 U_{eq} (C) for aromatic and U_{iso}(H) = 1.5 U_{eq} (C) for methyl. The ORTEP-3 program for Windows was used to generate molecular graphics and geometric calculations [38]. Hydrogen bonding interaction was explained using PLATON [39] whereas Mercury 2020.3.0 program was used to analyse the geometrical parameters [40]. The crystallographic data (CIF) of hydrazone **4a** is deposited at the Cambridge crystallographic data center (CCDC No. 793256).

2.7. Computational studies

Computational investigations were explored for hydrazone **4a** with Gaussian 09 W using the basis set of density functional theory using B3LYP/6-311G(d, p) level on a personal computer [41]. Gaussview 5.08 program was used to organize the input file and analyze the electronic properties of frontier molecular orbitals. The 3D Hirshfeld surface analysis, 2D fingerprint plots, and shorts contacts were explored with CrystalExplorer 17 program [42]. Further, the strength of non-covalent interactions (NCIs), isodensity surface plot, and reduced density gradient (RDG) surface were obtained through multiwfn and AIMAll package [43,44].

Auto dock 4.2.6 Tools was used to construct the initial structures to run the docking simulations. nCoV-SARS-2 M^{pro} (PDB ID: 6LU7) was obtained from the Protein Data bank. The input files were organized and constructed by using BIOVIA discovery studio 2021.

2.8. Antimicrobial studies

In vitro antibacterial and antifungal activities of the hydrazones **4a-4e** and **5a-5c** were tested in Nutrient broth (NB) and Sabourauds Dextrose Broth (SDB), respectively, by two-fold serial dilution method [45]. The seeded broth for bacteria (NB) was obtained from 24 h old bacterial cultures on nutrient agar at 38 °C whereas fungal spores were prepared from 24 h to 7 days old Sabourauds agar slant cultures suspended in SDB. The hydrazone compounds under investigation and reference drugs were prepared by two-fold serial dilution to get the required concentrations of 200, 100, 50 25, 12.5 and 6.25 μg/mL. Incubation was carried out at 38 °C for bacteria and 27 °C for fungi. In order to compare the bacterial and fungal study results, streptomycin and amphotericin B were used as reference drugs, respectively.

3. Results and discussion

3.1. Chemistry

A multistep synthetic route was employed to synthesize new hydrazone-molecular hybrids of piperazine precursors, as shown in Scheme 1. Compounds **2** and **3** were synthesized by modification of the earlier reported procedure. Initially, N-ethoxycarbonyl piperazine undergone condensation with bromoethylacetate in the presence of K_2CO_3, afforded ethyl 4-(2-ethoxy-2-oxoethyl)piperazine-1-carboxylate (Compound **2**). This on further reaction with hydrazine hydrate in ethanol medium, under reflux condition, gave an excellent synthetic intermediate, ethyl 4-(2-hydrazinyl-2-oxoethyl)piperazine-1-carboxylate (Compound **3**). This was then refluxed with aromatic aldehydes or aromatic ketones under acidic condition to afford piperazine precursor hydrazones **4a–4e** and **5a-5c** in good to excellent yield. The structures of all hydrazone were elucidated using FT-IR, ^{1}H & ^{13}C NMR, and HSQC and mass spectral analysis. In addition, single crystal XRD was recorded for hydrazone **4a** to describe the molecular structure. The analytical and mass spectra data of compounds **4a-4e** and **5a-5c** are given in Table S1.

3.2. FT-IR analysis

FT-IR spectra of hydrazones**4a-4e** and **5a-5c** were interpreted by comparing the literature reports of similar hydrazone derivatives [46]. For hydrazones **4a-4e** and **5a-5c**, collections of functional and non-functional group stretching frequencies were observed in the region of 900–4000 cm^{-1}. The selected stretching frequencies of the functional groups are listed in Table 1. In general, the carbonyl stretching frequencies for aliphatic ketones and

P.G.R. COLLEGE OF ARTS & SCIENCE NAMAKKAL 637 206

most downfield region at 165.87 and 155.39 ppm which are assigned to two amide carbonyl carbon signals (C=O). Among these two signals, shielded signal is due to carbonyl group of hydrazone moiety whereas deshielded signal can be assigned to carbonyl group of ethoxycarbonyl moiety. Additionally, one more carbon signal was observed at 148.85 ppm and this should be assigned to imine carbon (C = N) of azomethane group. A collection of signals were resonated in the shielded region at 61.60, 61.25, 53.33/53.21 and 43.66 ppm. Among these, deshielded signals at 61.60 and 61.25 ppm are assigned to OCH_2, and NCH_2 carbons, respectively, whereas other signals (53.33/53.21 and 43.66 ppm) are assigned to A and B types methylene carbons of piperazine analogue. Out of which, shielded signal (43.66 ppm) should be due to B type methylene carbon whereas deshielded signals at 53.33/53.21 ppm are ascribed to A type methylene carbon. The large chemical shift variation for A type proton (about 10 ppm) is due to anisotropic effect or cone effect between carbonyl or imine group and methylene protons in piperazine analogue [48], as shown in Fig. S10. Owing to this effect, piperazine ring carbon (A type) acquires negative charge where attached proton gets positive charge.

The above proton and carbon NMR assignments are further unambiguously confirmed by HSQC analysis. The observed cross peak between proton and carbon NMR are listed in Table S2 and their spectrum is depicted in Fig.S11. As shown in Table S2 and Fig.S11, a quartet at 4.16 ppm exhibits a strong cross peak with the carbon signal at 61.60 ppm which suggests that the signal at 61.60 ppm is due to OCH_2 carbon of N-ethoxycarbonyl piperazine analogue. Similarly, a broad singlet at 3.56 ppm and a doublet at 3.23 ppm having cross peak with the carbon signals at 43.66 and 61.25 ppm revealed that the carbon signals are due to B type methylenic carbons of piperazine ring and methylenic carbon adjacent to Nitrogen atom (N-acetyl side chain), respectively. Further, two singlets at 2.65 and 2.57 ppm showed the cross peak with carbon signals at 53.33 and 53.21 ppm. It is inferred that the abovementioned carbon signals are due to A type methylenic carbons of piperazine moiety. Besides, a triplet at 1.27 ppm showed cross peak with the carbon signal at 14.68 ppm reveals that the signal is due to CH_3 carbon of compound **4a**. The azomethane (CH=N) signal at 8.25 ppm has exhibited HSQC correlation with signal at 148. 85 ppm. Therefore, this should be due to azomethane (C=N) carbon. The signals at 165.87 and 155.39 ppm were found to be no HSQC correlation with any protons, which confirms that the signal represents carbonyl and amide carbonyl carbons, respectively. The NMR signals for the rest of the hydrazones **4b-4e** were observed the same pattern as that of compound **4a**. Therefore, the signal assignments for **4b-4e** were done based on the assignment of compound **4a**.

Another type of hydrazones (**5a-5c**) were obtained by the condensation of hydrazide **3** with substituted acetophenone, and their NMR signal assignments were made as for hydrazones **4a**. NMR chemical shift values of **5a-5c** are listed in Table 1 and 2. It can be seen from the Table 1 that the proton NMR signal for methyl group in azomethane appeared as a singlet at 2.14 ppm with two proton integration (for compound **5a**). Similarly, the carbon NMR signal for same methyl group was observed at 14.59 ppm. The other signals were observed similar to hydrazone **4a** (Table 2).

3.5. Stereochemistry of hydrazones

Generally, hydrazone derivatives may exist as pair of isomers: namely, geometric isomers ($Z_{C=N}/E_{C=N}$) and *cis*/*trans* amide conformers. Several hydrazone derivatives have been reported that existence of two isomers in solution state [49] while other studies shown that some hydrazones were afforded single isomer, particularly, the $Z_{C=N}$ conformer is not realized due to severe steric hindrances. The $E_{C=N}$ configuration would be preferred for present hydrazone molecular structure, as evident from the absence of non-planar conformation of C=N–NH fragment and violate the n-π conjugation. Also, it is pertinent to mention that the substituted carbonyl group at hydrazone nitrogen can adopt either a perpendicular or coplanar orientation with respect to reference plane.

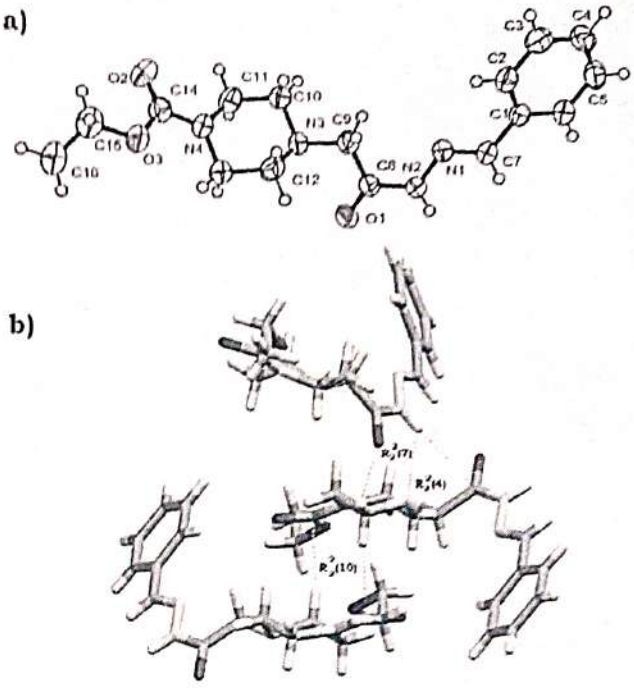


Fig. 1. a) ORTEP diagram of hydrazone **4a**; b) Close contacts between two Independent molecules.

Further, the NMR spectrum of hydrazone **4a** revealed that only one configurational isomer is present, as observing one type of NMR signals. Nevertheless, the N–H signal observed at 10.01 ppm revealed the presence of *E*-isomer, while the same signal was reported for the *Z* isomer at 15 ppm.

3.6. Single crystal XRD analysis

A suitable single crystal of hydrazone **4a** was grown by slow evaporation technique using absolute ethanol as solvent. The hydrazone **4a** crystallizes in monoclinic form with P21/c symmetry and the unit cell dimensions are a=10.6694(4) Å, b=12.1390(4) Å, c=12.9815(5) Å, α=79.311(10)°, β=81.561(10)° and γ=71.702(10)°. The details on data collection and structure refinement are furnished in Table 3. Selected geometrical parameters are given in Table 4. Fig. 1a shows the ORTEP diagram of hydrazone **4a** with atom numbering scheme. The sum of the bond angles around N1 atom [360 (3)°] indicates the sp^2 hybridization. The torsion angles of C15-O3-C14-O2 and C15-O3-C14-N4 were found to be −2.9 (6)°) and [175.3 (3)°, respectively, suggesting that atoms C15 and C14 lie in the plane of the six membered ring (N4/C11/C10/N3/C12/C13). Similarly, the torsion angles of N3-C9-C8-O1 and N3-C9-C8-N2 were found to be 1.1 (5)°] and 178.2 (3)°, respectively, suggesting that the substituted moiety at N3 lie in the plane of the ring.

The C–O and C–N bond length for C8-O1 (C = O) and C8-N2 (C–N) were measured by XRD as 1.222 and 1.357 Å, respectively. Both the bond lengths of the functional groups are not consistent with the standard value of respective groups [50]. It is attributed to the electron delocalization between nitrogen atom and carbonyl group, which enables the partial double bond character between N2-C8 and C8-O1. Owing to the electron delocalization, the free rotation of N–C=O bond leads to *cis* or *trans* isomerism. But, **4a** pre-

P.G. & R. COLLEGE OF ARTS & SCIENCE NAMAKKAL

Table 1
IR and ^{1}H NMR signals of hydrazones **4a-4e** and **5a-5c**.

Hydrazones	O-CH_2	N-CH_2	CH_2-CH_3	CH_2 (A)	CH_2 (B)	NH	CH(CH$_3$)$_2$	Aryl protons	IR Frequencies
4a	4.16 (q,)	3.22 (s)	1.28 (t)	2.65 (s) /2.67 (s)	3.56	10.01 (s)	8.25 (d, 1H)	7.65 (d, 2H), 7.41 (d, 2H)	1216, 1073, 2922, 1686
4b	4.12 (q)	3.18 (s)	1.25 (t)	2.61 (s) /2.53 (s)	3.52	10.11 (s)	8.14 (s, 1H)	2.55 (dd, 1H), 7.17 (t, 2H), 2.35 (d, 3H, CH_3)	1325, 1051, 2971, 1671
4c	4.15 (q)	3.20 (s)	1.27 (t)	2.64 (s) /2.56 (s)	3.54	9.93 (s)	8.15 (s, 1H)	7.60 (m, 2H), 6.91 (d, 1H 1.83 (s, 3H)	1196, 2928, 2839, 1633
4d	4.16 (q)	3.22 (s)	1.27 (t)	2.64 (s) /2.57 (s)	3.55	10.05 (s)	8.24 (s, 1H)	7.68 (d, 1H, 7.17 (d, 2H)	1414, 1056, 2927, 1623
4e	4.13 (q)	3.21 (s)	1.25 (t)	2.63 (s) / 2.56 (s)	3.34	10.14 (s)	8.22 (s,1H)	2.39 (m, 3H, 7.03 (t, 1H)	1405, 2993, 1652
5a	4.02 (q)	3.11 (s)	1.14 (t)	2.52 (t) / 2.45 (t)	3.41 (t)	10.04 (s)	2.14 (d, 3H)	7.68, 7.60, 7.25 (3 m, 1H, 1H, 3H	1270, 1069, 1645
5b	4.13 (q)	3.23 (s)	1.25 (t)	2.63 (t) / 2.58 (t)	3.54 (t)	10.08 (s)	2.21 (d, 3H)	7.71 (d, 2H,), 7.59 (s, 1H), 7.17 (d, 1H)	1414, 1056, 2927, 1623
5c	4.16 (q)	3.30 (s)	1.27 (t)	2.63 (t) / 2.53 (t)	3.57 (t)	10.28 (s)	2.29 (d, 3H)	8.24 (d, 2H, 8.01 (d, 1H,7.87(d, 1H)	1220 2946, 1648

Table 2
^{13}C NMR signals of hydrazones **4a-4e** and **5a-5c**.

Hydrazones	O-CH_2	N-CH_2	CH_2-CH_3	CH_2 (A)	CH_2 (B)	CH_3C=O	NC=O	C = N	Aryl carbons
4a	61.60	61.25	14.66	53.33/53.21	43.66	165.87	155.39	148.85	127.14, 128.71, 130.26, 133.44,
4b	61.56	61.33	14.62/21.48[a]	53.24/53.16	43.60	165.91	155.40	148.98	127.68, 129.44, 130.67, 140.50, 141.03, 144.65
4c	61.58	61.20	14.63/55.35[b]	53.30/53.18	43.65	165.63	155.39	148.68	114.20, 126.68, 128.68, 129.35, 161.68
4d	61.63	61.22	14.63	53.32/53.18	43.63	165.99	155.39	147.55	128.28, 129.04, 132.03, 136.57
4e	61.40	61.17	14.61	53.28/53.17	43.59	166.20	155.40	147.55	113.71, 117.45, 123.72, 130.25, 161.00
5a	61.46	61.01	13.27/14.59	53.06/52.97	43.85	172.02	155.29	137.93	126.03, 126.57, 128.28, 128.35, 129.61
5b	61.60	61.20	13.26/14.65 21.27[a]	53.24/53.12	43.96	171.70	155.41	147.84	126.02, 129.09, 129.18, 134.69, 135.01, 139.94
5c	61.71	61.21	13.21/14.63	53.31/53.31	43.97	171.68	155.44	149.36	123.66, 126.84, 127.49, 143.41

[a] methyl carbon signal at azomethane (C = N) group.
[a] methyl
[b] methoxy carbons at phenyl group.

amides were observed in the region of 1650-1710 cm^{-1}. As expected, the amide carbonyl stretching frequencies for all hydrazone derivatives were observed around 1690 cm^{-1}and the C=N stretching frequency of the azomethane analogue was observed around 1650 cm^{-1}with the exception of hydrazones **4a** and **4b**, which did not show the stretching frequency for C = N in the above range, because, it should be merged with amide C = O peaks.

Since the C=O and N-H groups are adjacent to each other in the molecular structure of hydrazone, it is subject to an amido-imidol tautomerism and can be easily distinguished from IR spectrum as two different vibrational frequencies were observed. The higher vibrational frequency is assignable to C=O (amido) group and the lower vibrational frequency is ascribed to C=N (imidol) group. A strong absorption band observed around 3300 cm^{-1} in the infra-red spectrum is normally assigned to N-H stretching mode of amines. From Table 1, it is inferred that the existence of a sharp intense band around 3200-3300 cm^{-1} is due to presence of N-H group which indicates the absence of imidol form in the molecular structure. Aliphatic and aromatic C-H frequencies for these hydrazones were observed in the region of 2800-3084 cm^{-1} (Table 1 and Fig. S1).

3.3. ^{1}H NMR analysis

NMR spectra of hydrazones **4a-4e & 5a-5c** were recorded at an operating frequency of 500 MHz (for ^{1}H NMR) and 100 MHz (for ^{13}C NMR) and their chemical shifts (δ=ppm) values are summarized in Table 1 and Table 2, respectively. The NMR spectra of all hydrazones were displayed in Fig. S2-S9.The NMR signals of hydrazones are assigned based on their positions, spin multiplicities, coupling constant and integral values [47]. Moreover, the observed chemical shift values are compared with the chemical shift values of intermediate compounds **2** and **3**. To analyze the observed proton and carbon NMR signals, we have chosen hydrazone **4a** as the representative compound (Fig. S2a). As seen in Table 1 and Fig. S2a, a pair of singlet was observed in the most downfield region at 8.25 and 10.01 ppm with one proton integral each is attributed to azomethine (CH=N) and hydrazide N-H protons, respectively. The methyl and methylene protons of N-ethoxycarbonyl group were observed as a quartet and triplet at 4.16 and 1.28 ppm which corresponds to two and three protons integration, respectively.

A collection of ^{1}H NMR signals with different multiplicity were located between 2.5-3.7 ppm (2.57, 2.65, 3.23 and 3.56 ppm). Among these signals, the signal at 3.23 ppm with two proton integral value is due to methylene proton of the side chain (N-CH_2-CO) of the piperazine ring, and the rest of the signals (2.57, 2.65 and 3.56 ppm) are due to piperazine ring methylene protons. To assign these protons unambiguously, they were named as A and B, as shown in Fig. S10. As seen in Table 1, the signal resonated at 3.56 ppm as triplet with four protons integral value should be due to B type methylene proton of piperazine ring, whereas, the other two signals resonated at 2.57 and 2.65 ppm each of which integrates two protons are assigned to A type methylene protons. Further, the A type methylene protons can be named as axial and equatorial as they are in the cyclic ring. Thus, the NMR signal was observed as two distinct signals for these protons. Unlike B type protons, A type protons can be explained by considering the anisotropic effect or cone effect [48], as shown in Fig. S10. It is seen that there should be a non-covalent interaction between A type equatorial protons and π bond of C=O and C=N (C-H···π). Owing to this non-covalent interaction, the equatorial protons acquired partial positive charge and the attached carbon developed partial negative charge. Therefore, based on the cone effect, the higher chemical shift value at 2.65 ppm can be assigned to axial protons whereas the shielded signal at 2.57 ppm is due to equatorial protons. Finally, an aromatic signals for hydrazone **4a** were appeared as a multiplet in the region from 7.2 −7.87 ppm with an integral value of five protons.

3.4. ^{13}C NMR analysis

^{13}C NMR spectrum of hydrazone **4a** is displayed in Fig. S2a and their chemicals shift values are represented in Table 2. In general, the aromatic carbons present in a molecule could be easily diagnosed from rest of the carbon NMR signals due to their characteristic absorption in the region of around 120 ppm. It can be seen from Table 2, the hydrazone **4a** shows a bunch of signals in the region of 127.14-130.66 ppm are assigned to aromatic carbons whereas two less intense signals were appeared in the

P.G.P. COLLEGE OF ARTS & SCIENCE NAMAKKAL 637 001

Table 5
Hydrogen bonding parameters of hydrazone **4a**.

D-H...A	D - H	H...A	D...A	D - H..A
N2-H2···O1[a]	0.86	2.37	3.190(3)	160
N2-H2···N3[a]	0.86	2.53	3.161(3)	132
C10-H10A···O1[b]	0.97	2.54	3.319(3)	137
C11-H11A···O2	0.97	2.37	2.762(2)	103
C12-H12B···O3	0.97	2.27	2.689(2	104
C15-H15B···O2	0.97	2.27	2.709(2)	106
C10-H10B···C14(π)	0.97	2.69	3.599 (3)	156
N2-H2···C8(π)	0.867	2.78	3.616 (3)	164

Symmetry code:[a] 1-x,1/2 + y,1/2-z.
[b] 1-x,-1/2 + y,1/2-.

From Fig. 1b, a major intermolecular hydrogen bonding interaction was observed between *N–H*····N and C–H····O contacts resulted in an$R_2^2(7)$loop, where N-H (donor) is from the hydrazone part, N (acceptor) is from piperazine analogue of another asymmetric unit, O (acceptor) atom is from hydrazone amide carbonyl, and C-H is from piperazine analogue. The hydrogen bonding parameters were found to be 2.53 and 2.54 Å, for *N–H*····N and C – H····O interactions, respectively (Table 5). Further, the dimers are connected by non-covalent *N* – *H*···O and *N–H*···N interactions to complete the $R_2^2(5)$loop, where N and O (acceptor) are from piperazine and hydrazone part, respectively, the donor N-H group comes from another asymmetric unit, the bond distances were found to be 2.37 and 2.53 Å, respectively. On the other hand, a pair of $C_{sp}{}^2(\pi)$.....H interactions were observed between two symmetric units (C10-H10···C14) with 2.841 and 2.69 Å distances resulted in an$R_2^2(10)$loop, where donor C-H comes from piperazine analogue and C_{sp2} (π) from the carbonyl group of N-ethoxy carbonyl, as shown in Fig. 1b. The observed hydrogen bond and other short contacts are further analyzed with Hirshfeld surface analysis.

3.7. Hirshfeld surface analysis

Hirshfeld surface analysis was carried out to determine the closed contacts between two neighboring molecules (intermolecular atomic contacts) in the crystal packing structure of hydrazone **4a** [42]. Crystal Explorer program was used to generate and quantify the Hirshfeld surface with 2D-fingerprint plots from crystallographic information file. The normalized contact distance (d_{norm}) in the hirshfeld surface analysis is based on the contact distance between d_i and d_e, where d_i and d_e are the nearest inner (internal) and outer (external) surface atoms, respectively. This can be expressed as d_i-$r_i{}^{vdw}$/ri ^{vdw}) / (d_e-$r_e{}^{vdw}$/$r_e{}^{vdw}$); where$r_i{}^{vdw}$ and $r_e{}^{vdw}$ are the forces of the van der Waals radii of internal and external atoms to the surfaces, respectively [52]

The molecular Hirshfeld surfaces are mapped with d_{norm} which provide three different colours (red-white-blue) on the surface of the molecule, which indicates a certain type of non-bonded interactions. Red color highlights the short contact between two adjacent molecules while white and blue colours represent van der Waals radii and longer contacts, respectively [53]. Fig. 2a-2d shows the Hirshfeld surface analysis of the crystal structure **4a**. As shown in Fig. 2a, the strongly intense red spot on the molecular surface corresponding to the hydrogen bond interaction between N-H···O, and the less intense red spot corresponding to the N-H···N interaction suggest that N-H····O interaction is stronger than N-H····N interaction. Nevertheless, the other short contact such as C-H····O, C-H····$C_{sp}{}^2(\pi)$, and N-H····$C_{sp}{}^2(\pi)$ were observed as mild red spots, as shown in Fig. 2b and 2c. The shape-index map of Hirshfeld Surface is used to visualize the $\pi\cdots\pi$ interaction by the presence of adjacent red-blue triangles in the mapped surface; if there are no adjacent red-blue triangles in the mapped surface (shape index), then there are no $\pi\cdots\pi$ stacking. It can be seen from Fig. 2d there are no $\pi\cdots\pi$ interactions in the hydrazone molecular structure **4a**.

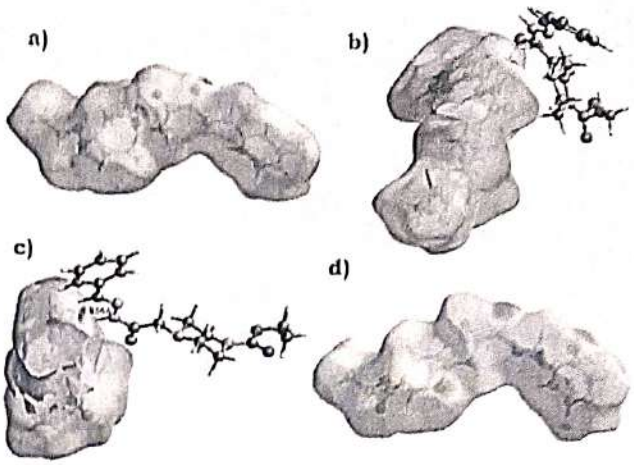


Fig. 2. a-c) Hirshfeld Surface of hydrazone **4a** compound with N-H...O and N-H...N contacts, d) shape index.

The 2D Fingerprint plot of the asymmetric unit of hydrazone **4a** shows a significant contribution to the important contacts [54] and their percentage on the Hirshfeld surface is shown in Fig. 3a-3e. It can be seen that the hydrazone crystal structure under the study had a significant amount of H···H, O···H, C···H and N···H contacts. The percentages of these contacts were found to be 56.3, 19.2, 17.6, and 6.4%, respectively (Fig. 3f). These interactions made a significant percentage contribution to the O···H plot (19.2%) suggesting that O···H interactions play a vital role in crystal packing through hydrogen bonding. Similarly, $C_{sp}{}^3(\sigma)$....H contact including $C_{sp}{}^2(\pi)$ ···H was observed as 17.6% indicating the second major contribution in the molecular networks. In addition, a small contribution of 6.4% was observed for the N···H plot, which signifies a weak contact, as can be seen from thes mall red region in the Hirshfeld surface analysis (Fig. 2a and Fig. 3f).

Finally, the 2D fingerprint analysis summarized that the shortest contact is the N···H interaction, O···H and C···H interaction exhibited as moderate to maximum red region in the d_{norm} and significant sharp spikes in the fingerprint plots were found to be the driving force in the molecular arrangement.

3.8. QT-AIM analysis

The QT-AIM analysis was carried out to understand both inter and intra-molecular hydrogen bonding interactions, Van der Waals forces, hydrophobic bonds and short contacts for monomer and dimer of hydrazine **4a** (Fig. 4). Non-covalent intermolecular interactions play a key role in the stabilization of molecular arrangement through crystal packing. Non-covalent interactions (NCIs) can be accomplished by determining real-space regions using Quantum Theory of Atoms in Molecules (QTAIM) calculations performed using the AIMAll software package. Table 6 shows the selected topological parameters of hydrogen bond critical point (BCP). The AIM analysis showed that the hydrazone **4a** is stabilized via intermolecular interactions rather than intra-molecular interaction, as seeming the dashed bond paths (BPs) between the attractors (atoms) (Fig. 4). It is further proven that the existence of positive V^2r values shows non-covalent interactions. The topology of the electron density of bond critical point (ρBCP) is an indicator of the strength of intermolecular interactions.

COLLEGE OF ARTS & SCIENCE
NAMAKKAL
637 206

Table 3
Single crystal XRD data collection and refinement details of hydrazone **4a**.

Empirical formula	$C_{16}H_{22}N_4O_3$
Formula weight	318.38
Temperature	293(2) K
Wavelength	0.71073 Å
Crystal system, space group	Monoclinic, P21/c
Cell dimensions	a = 11.6633(8) Å b = 7.3426(5) Å β = 90.383(3)° c = 19.2952(16) Å
Volume	1652.4(2) Å^3
Z, Calculated density	4, 1.280 Mg/m^3
Absorption coefficient	0.090 mm^-1
F(000)	680
Crystal size	0.30 × 0.25 × 0.20 mm
Theta range for data collection	1.75 to 21.70 deg.
Limiting indices	-10<=h<=12, -7<=k<=7, -20<=l<=20
Reflections collected/unique	11,107 / 1956 [R(int) = 0.0326]
Completeness to theta	21.70 99.9%
Absorption correction	Semi-empirical from equivalents
Max. and min. transmission	0.9821 and 0.9734
Refinement method	Full-matrix least-squares on F^2
Data / restraints / parameters	1956 / 0 / 208
Goodness-of-fit on F^2	1.179
Final R indices [I>2sigma(I)]	R1 = 0.0460, wR2 = 0.1446
R indices (all data)	R1 = 0.0572, wR2 = 0.1630
Largest diff. peak and hole	0.281 and -0.183 e.A^-3
CCDC No.	793,256

Table 4
Experimental and theoretical geometrical parameters of hydrazone **4a**.

Bond No.	Bond type	Bond length (Å)		Angle No	Angle Type	Angle value (°)	
		XRD	DFT			XRD	DFT
1	O1 - C8	1.222	1.215	1	C9-N3-C10	111.9	111.81
2	N3 - C9	1.457	1.448	2	C9-N3-C13	111.8	112.26
3	N3 - C10	1.457	1.463	3	C10-N3-C13	108.4	108.53
4	N3 - C13	1.462	1.465	4	N2-N1-C7	116.5	117.6
5	N1 - N2	1.375	1.366	5	N1-N2-C8	120.1	121.33
6	N1 - C7	1.272	1.281	6	C14-O3-C15	118	117.61
7	N2 - C8	1.357	1.384	7	C14-N4-C12	125.2	125.86
8	O2 - C14	1.207	1.217	8	C14-N4-C11	119.8	119.2
9	O3 - C14	1.338	1.36	9	C12-N4-C11	114.4	114.72
10	O3 - C15	1.458	1.445	10	N3-C9-C8	111.4	111.27
11	N4 - C14	1.338	1.364	11	C2-C1-C6	118.7	118.87
12	N4 - C12	1.461	1.463	12	C2-C1-C7	122	122.24
13	N4 - C11	1.451	1.46	13	C6-C1-C7	119.3	118.87
14	C9 - C8	1.498	1.516	14	N3-C10-C11	110.2	110.59
15	C1 - C2	1.385	1.393	15	C1-C2-C3	120.1	120.27
16	C1 - C6	1.385	1.396	16	C1-C6-C5	121	120.7
17	C1 - C7	1.459	1.459	17	O1-C8-N2	119.8	119.28
18	C10 - C11	1.5	1.526	18	O1-C8-C9	123.9	125.41
19	C2 - C3	1.38	1.388	19	N2-C8-C9	116.2	115.29
20	C6 - C5	1.37	1.392	20	N1-C7-C1	120.8	121.61
21	C13 - C12	1.499	1.516	21	O2-C14-O3	123.4	123.15
22	C3 - C4	1.376	1.367	22	O2-C14-N4	124.8	124.95
23	C5 - C4	1.369	1.372	23	O3-C14-N4	111.7	111.88
24	C16 - C15	1.453	1.466	24	N3-C13-C12	111	110.75
				25	C2-C3-C4	120.2	120.43
				26	C6-C5-C4	119.9	119.98
				27	C3-C4-C5	120	119.73
				28	N4-C12-C13	110.5	110.2
				29	N4-C11-C10	110.2	110.19
				30	O3-C15-C16	108.6	107.46

dominantly exists in *cis* conformation as evident by the torsional angle of 0.47° for N1-N2-C8-C9. However, the torsional angle of C7-N1-N2-C8 was found to be −172.65° which is evident that the crystal structure **4a** exhibits in E configuration. The observed torsion angles are in good accordance with the earlier reports on the *cis* conformation.

The conformation of the six-membered heterocyclic piperazine ring can be described by Cremer and Pole puckering parameters [51], which are q_2 and q_3 = 0.082 (3) Å and 0.556 (4) Å, respectively. The total puckering amplitude was calculated as Q_T = 0.562 (3) Å; θ = 8.5 (3)°, suggest that the piperazine ring adopts the normal chair conformation with the out of plane of N atoms .

The hydrazone molecules are inter linked with each other in the form of dimers through various contacts including hydrogen bonding, short contact, etc., The observed interactions and their geometrical parameters are given in Fig. 1b and Table 4.

G.R. COLLEGE OF ARTS & SCIENCE NAMAKKAL

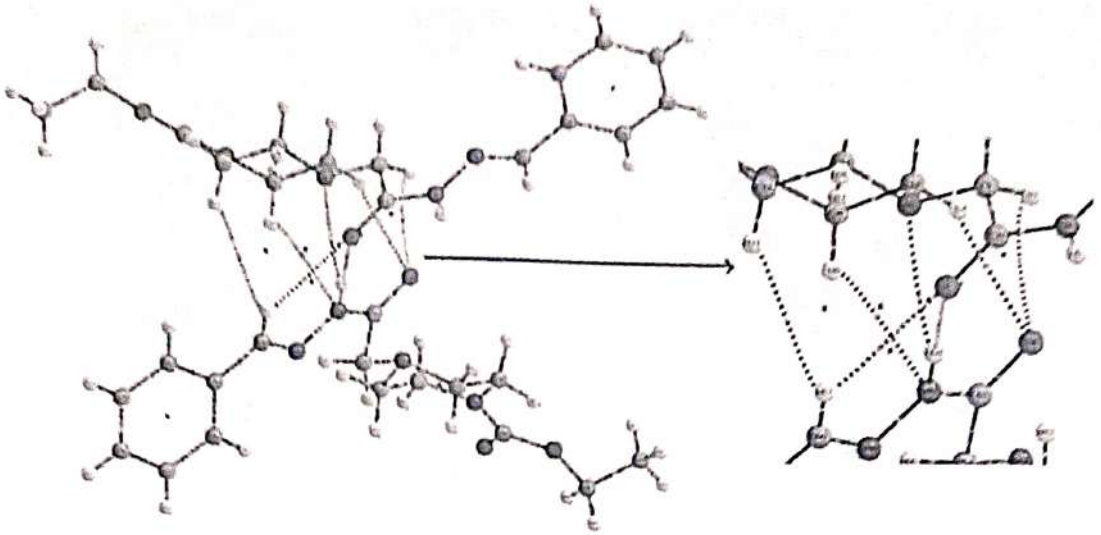


Fig. 4. Molecular graphs as the title compound (**4a**) obtained from QT-AIM analysis.

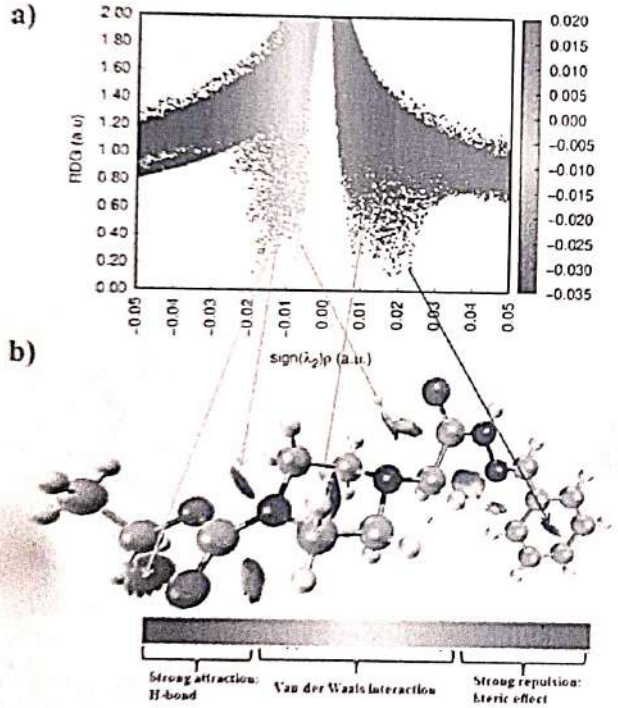


Fig. 5. Non-covalent interactions (NCIs) and reduced density gradient (RDG) interactions of hydrazone **4a** compound.

3.9. NCI-RDG analysis

Non-covalent interactions such as weak inter and intra molecular hydrogen bonding play a major contribution to the stability of molecular structure, which can be estimated by the analysis of reduced density gradient (RDG) calculations using multiwfn program. The NCI-RDG analysis of **4a** was employed with an isosurfaces value of 0.5 and is displayed in Fig. 5a and Fig. 5b. RDG interaction isosurfaces can be plotted in various colors including blue, green and red which represent the long-range forces such as hydrogen bonding, van der Waals forces and steric effects, respectively. As can be seen in Fig. 5a, the asymmetric molecular unit structure is stabilized only by van der Waals forces, observed as a green spot, and not by hydrogen bonding interaction, which was not observed as a blue spot in the RDG plot. Also, it is seen that the van der Waals interactions are favored to orient the position of the functional groups such as carbonyl, ethoxy and azine. In addition, a strong steric repulsion, which was observed in red color in the Fig. 5b (between two nitrogen atoms in piperazine ring), indicates that the piperazine ring adopts normal chair conformation.

In general, the electron withdrawing group (C=O) on the six-membered heterocyclic ring adopts boat conformation. In the case of **4a**, however, the piperazine ring linked to C=O group adopts normal chair conformations, which is due to Vander Waals forces between the methylene proton in piperazine analogue and the carbonyl group, as shown in Fig. 5b (green color).

3.10. DFT structure analysis

The molecular structural parameters of **4a** were simulated at the higher base set level of B3LYP/6–311G(d,p), and the optimized structure is shown in Fig. 6. The simulated geometrical parameters are counterchecked with experimental crystallographic data of hydrazone **4a**, both simulated and experimental geometric parameters are furnished in Table 5. It is seen that the calculated and experimental geometrical outcomes are much closer to each other (Fig. S22a and S22c). Moreover, the graphical correlation value for bond length and bond angles is determined to be $R^2 = 0.978$ (Fig. S22b) and 0.0.974 (Fig. S22 d), respectively. As observed from the crystallographic data, the C(8)-N(2) and C(6)-O(1) bond lengths are found to be 1.384and 1.215 Å, respectively, which deviate slightly from the standard values of these bonds, however, good agreements were found between experimental and calculated values. The optimized molecular structure of N4-C14-O2 bond shows partial double bond character, as shown in Fig. 6. It is evident that N4-C14 and C14-O2 bond lengths obtained through DFT are found to be 1.364 and 1.217 Å, respectively and XRD values measured are 1.338 and 1.207 Å, respectively. Therefore, both in solid and gas phases, π electron delocalized via the C–N and C–O bond. DFT studies on geometric parameters revealed that the piperazine ring exists in normal chair conformation, as indicated by the torsional angle values of N3-C10-C11-N4, C10-C11-N2-C12, C11-N4-C12-C13, N4-C12-C13-N3 and C12-C13-N3-C10 which are 54.9, −52.58, 52.26, 54.29 and 59.12 respectively, these values are in

P.G. COLLEGE OF ARTS & SCIENCE NAMAKKAL 637 206

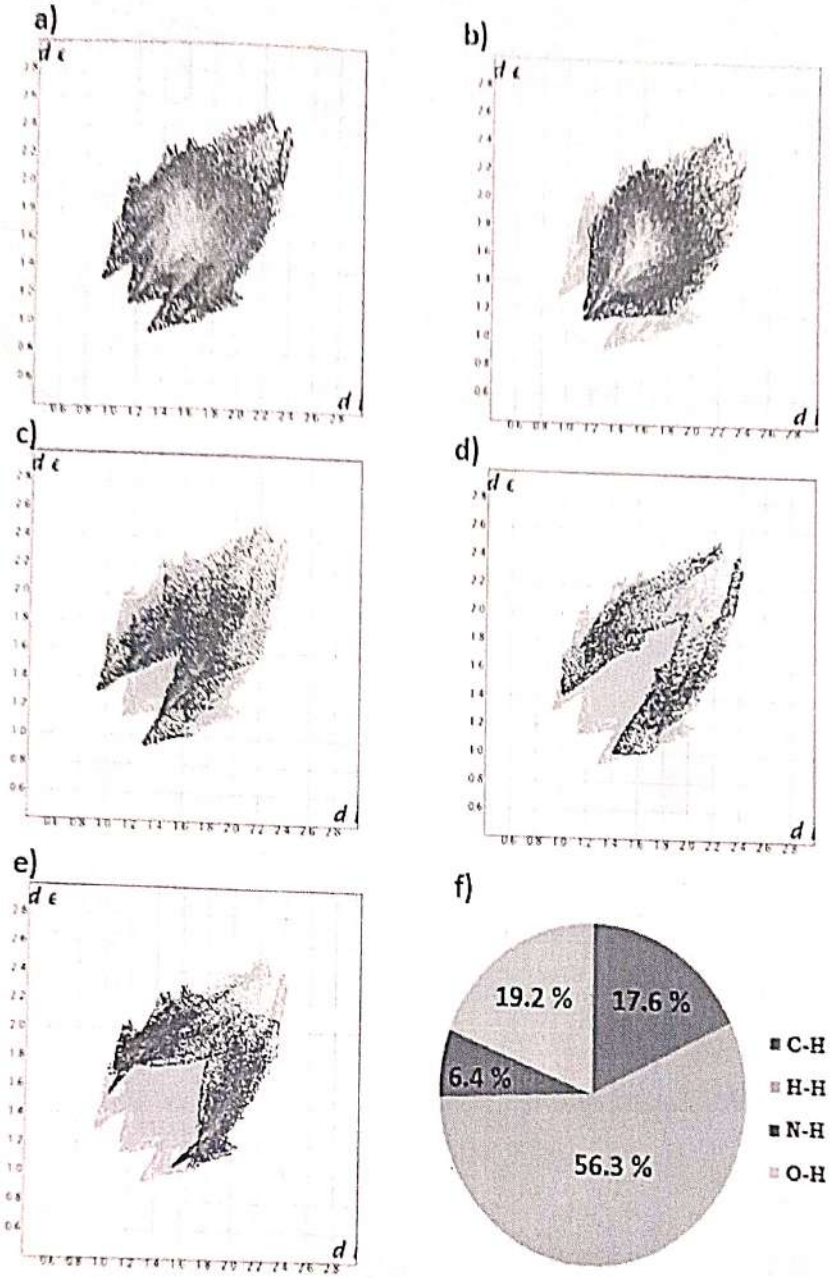


Fig. 3. 2D fingerprint plots resolved into a) full b) H...H/H...H, (c) O...H/H...O (d) N...H/H...N, (e) C...H/H...C, (f) percentage contribution of various intermolecularcontacts.

Table 6
QT-AIM Topological analysis of hydrazone **4a**.

BCP	Atoms	P (e/Bohr^3)	$\nabla^2\rho$ (e/Bohr^5)	E (a.u)	V (a.u)
28	H38 - N49	0.003573	0.011726	1.109285	−0.001977
77	O1 - H67	0.00426	0.015223	0.384681	−0.002492
7	H11 - O46	0.004062	0.015262	0.29617	−0.002366
11	N2 - H50	0.010884	0.034153	0.28853	−0.006099
54	H34 - H67	0.00172	0.00577	0.164367	−0.000748
14	H14 - O46	0.008253	0.027175	0.04179	−0.004961
53	O1 - H50	0.009698	0.035553	0.132589	−0.00148

For hydrazone **4a** dimer, the AIM protocol confirms the presence of N49-H50···O1 and N49-H50···N2 intermolecular hydrogen bonding contacts, as the ρ values at BCPs H50-O1 and H50-N2 were found to be +0.003573 and 0.010884 e/a^3, respectively. Moreover, the QTAIM approach also suggested the possible C–H···O hydrogen bonding contacts from hydrazone **4a** dimeric structure, as the ρ values at BCPs H11-O46, H14-O46 and H50-O1 were determined as 0.004062, 0.008253 and 0.009698 e/a^3,respectively. As seen above, the electron density (ρBCP) was obtained in a wide range from 0.0017 to 0.0108 e/a^3. However, the relatively large electron densities (ρBCP) were found for N49-H50···N2 and N49- H50···O1, indicating that stronger hydrogen bonding interaction than other NCIs. Finally, it is concluded that the AIM analysis of hydrazone **4a** dimers showed the formation of several new intermolecular contacts (Fig. 4), such as hydrogen bonding and non-classical contacts that stabilize the molecules and direct the molecular arrangement through crystal packing.

P.G.P. COLLEGE OF ARTS & SCIENCE NAMAKKAL 637 206

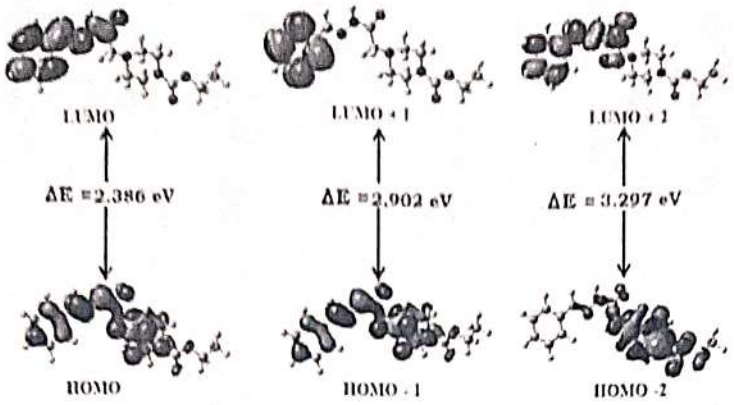


Fig. 7. (a) HOMO/LUMO shape and energy of hydrazone **4a** compound.

Table 8
Dipole moment (μ) Polarizabilities (α) and First order hyperpolarizabilities (β) of hydrazone **4a**.

Dipole moment			Polarizabilities			First order hyperpolarizabilities		
Components	Urea	**4a**	Components	Urea	**4a**	Components	Urea	**4a**
μ_x	1.28	5.5082	α_{xx}	39.260	−112.9406	β_{xxx}	24.729	197.4060
μ_y	0.00004	0.8894	α_{xy}	0.2947	−11.2036	β_{xxy}	−0.499	162.2318
μ_z	−0.830	1.6309	α_{yy}	24.690	−141.7378	β_{xyy}	31.817	−9.2147
μ	1.527	5.8130	α_{xz}	−1.159	−0.4446	β_{yyy}	0.006	−5.1722
			α_{yz}	0.454	1.3851	β_{xxz}	−61.443	35.8219
			α_{zz}	38.219	−135.0867	β_{xyz}	−0.225	−15.3604
			α_{total}	5.664×10^{-24} esu	1.917×10^{-23} esu	β_{yyz}	−20.593	−0.2557
						β_{xzz}	19.374	2.8435
						β_{yzz}	0.5057	−2.8823
						β_{zzz}	32.896	−0.5604
						β_o	0.13×10^{-30} esu	2.14×10^{-30} esu

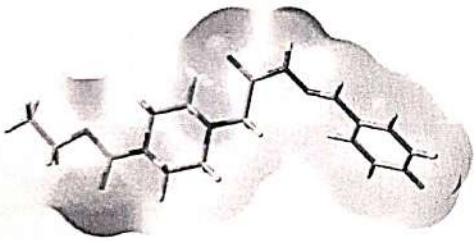


Fig. 8. MEP surface map of the hydrazone **4a** compound.

It can be described the above result that if the molecule is hard, the HOMO–LUMO energy gap (ΔE) will be large and is usually associated with a lower chemical reactivity and high kinetic stability. On the other hand, the energy gap (ΔE) is small, the molecule becomes soft nature, and it is usually associated with a high chemical reactivity and poor kinetic stability. The electron density of soft molecules can change easily compared to hard molecules. As indicated by the outcomes for the chemical reactivity descriptors (Table 8), the high hardness (2.139 eV) and low softness (0.233 eV) values exhibit lower intra-molecular charge transfer.

3.14. Net charges (NPA and MPA)

The charge distribution of molecule is crucial for understanding chemical reactivity, molecular electrostatic potential and electrostatic interactions. The natural atomic charge and Mulliken charges can be used to determine the distribution of electrons among atoms in a molecule [57,58]. By studying them, we can determine which atom accepts an electron and which loses an electron. In order to explore the electrostatic potential (electrophilic/nucleophilic properties) of the title molecule, natural population analysis (NPA) and Mulliken population analysis (MPA) were also performed using the DFT method. The two methods (NPA & MPA) produced similar results. The values of the net atomic charges are shown in Table S3.

As expected, the most negative charges were found predominantly on N, O, and some of the carbon atoms C12, C16, C18, C27, and C29. Therefore, these regions act as electrophilic regions in the hydrazone molecular structure. According to Mulliken and NPA methods, the calculated atomic charge shows that the H5 and C20 atoms has bigger positive atomic charges 0.38499 (NPA), 0.137221(MPA) and 0.6887 (NPA) 0.414682 (MPA), than the other hydrogen and carbon atoms, respectively. This is due to the presence of intermolecular hydrogen bonding of N2-H2···O1. However, C9, C13, C20, C24, C36, and C43 atoms in a molecule possess significant positive charges due to the electronegative atoms that are directly bonded to it.

Therefore, the electrophilic/nucleophilic regions of the MEP surface and the MPA/NPA charges show similar results. It can be said that hydrazone **4a** is highly electrophilic because of the small differences in atomic charge estimates between the two models.

3.15. Natural bond orbital (NBO) analysis

Natural bond orbital (NBO) analysis can provide the most accurate Lewis structure of a molecule because it provides information about interactions between filled and virtual orbitals of a molecule [59]. It is generally considered a sensitive tool for understanding interactions in molecules since it allows for the analysis of interactions between molecules. Furthermore, it provides information about the changes in charge density of the proton donor and acceptor of bonding and anti-bonding orbitals, respectively.

P.G.P. COLLEGE OF ARTS & SCIENCE NAMAKKAL 637 206

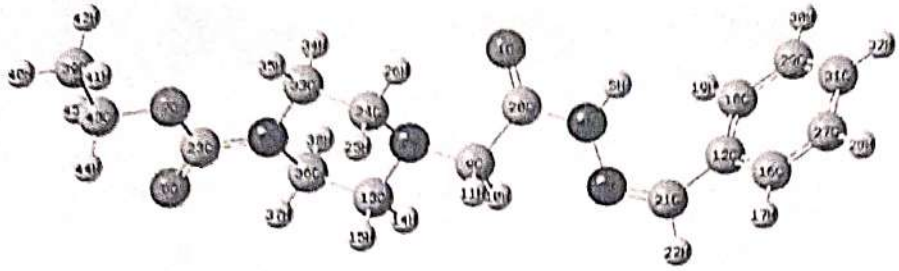


Fig. 6. Optimized geometry of hydrazone **4a** compound.

Table 7
Calculated energy values of **4a** at B3LYP/6–311 G (d, p) method.

Quantum Descriptors (eV)	B3LYP/6–311G(d, p)
E_{HOMO}	−6.174 eV
E_{LUMO}	−1.896 eV
Ionization potential (IP)	6.174 eV
Electron affinity (EA)	1.896 eV
Energy gap (ΔE)	4.278 eV
Electronegativity (χ)	4.035 eV
Chemical potential (μ)	−4.035 eV
Chemical hardness (η)	2.139 eV
Softness (σ)	0.233 eV
Electrophilicity (ω)	3.805 eV

good agreement with measured XRD values, that is, 57.5, 51.85, 50.33, 54.37, and 61.03, respectively. The torsional angle between N1-N2-C8-C9 is −2.15, indicating that the N-C(O) bond has free rotation, which is preferred for the *cis* conformation. The measured values of DFT and XRD for bond lengths C1-C7, N1-C7, N1-N2, N3-C9 and 01-C9 are 1.463, 1.281, 1.356, 1.448 and 1.526 Å (through DFT), and 1.45, 1.272, 1.375, 1.457 and 1.498 Å (through XRD), respectively, these values were found to be in good agreement. In a nutshell from the above discussion, good accordance between structural parameters estimated through XRD and DFT studies are observed.

3.11. Frontier molecular orbital analysis

The interaction between the highest occupied molecular orbital (HOMO) and the lowest unoccupied molecular orbital (LUMO) and the reacting chemical species are very crucial in accelerating the chemical reaction to afford the desired product by the stabilization of the transition state structure [55]. The HOMO-LUMO energy separation is generally employed to get better understanding of kinetic stability and reactivity of the molecular structure including electrophilic and nucleophilic attack. Since the hydrazones **4a-4e** and **5a-5c** are very good synthetic intermediates for the construction of a wide range of heterocycles, it is necessary to analyze the reactivity and stability of the molecular structure. The electronic properties of hydrazone **4a** were determined by Frontier Molecular orbital analysis (FMO) at the B3LYP/6-311G(d,p) level using Gaussian 09 package. The FMOs consist of HOMO, HOMO−1, HOMO − 2, LUMO, LUMO+1, LUMO+2, and their observed energy gaps ($\Delta E = E_{LUMO}-E_{HOMO}$) are furnished in Table 7.The energy gaps from the HOMO to LUMO in **4a** was observed as 2.386 eV. Further, the energy gaps of HOMO−1 → LUMO+1 and HOMO−2 → LUMO+2 were determined as 2.902 and 3.297 eV, respectively.

The HOMO-LUMO energy gap separation was carried out for hydrazone **4a** and depicted in Fig. 7. It is seen that, the electronic density in HOMO for hydrazone **4a** was dispersed on the heterocyclic piperazine ring with small contribution from C=N group, while in LUMO the electron density was dispersed on the phenyl ring and hydrazone fragment as well.

3.12. Molecular electrostatic potential (MEP)

The molecular electrostatic potential (MEP) study is a reliable method to examine chemical reactivity of molecular structure, electrophilic and nucleophilic regions and viscosity of hydrogen bond interactions [56]. The surface of MEP exhibits different electrostatic potentials which are represented by different color scheme. Red color indicates a negative electrostatic potential, blue color represents high positive electrostatic potential, and green color shows a relatively low positive electrostatic potential. The MEP analysis for hydrazone **4a** was carried out using B3LYP/6–311G(d,p) level. The obtained MEP surface of the hydrazine **4a** is shown in Fig. 8. It can be seen that the most negative potential area in the molecular structure was found to be on the oxygen atoms of hydrazone group, and ester carbonyl group, which could be the most appropriate region for electrophilic attack. On the other hand, blue and green region with positive potentials were mostly localized around the hydrogen atoms of entire molecule which are the most susceptible regions to nucleophilic reaction.

3.13. Global chemical reactivity descriptors (GCRD)

The energy values of hydrazone **4a** were computed with the DFT method to further investigates the structural stability and global chemical reactivity. As indicated by FMO theory, the HOMO and LUMO energy values are very similar to the Ionization potential (I) and electron affinity (A), respectively. These ionization potentials and electron affinity are derived from energy values which give rise to different global chemical reactivity descriptors such as chemical hardness (η), global softness (σ), electrophilicity (ω), Electronegativity (χ), and chemical potential (μ) are defined according to the Koopman's equation. The theoretically calculated values of all GCRD parameters are given in Table 7. It can be seen that the ionization energy of molecule **4a** was calculated as 6.174 eV. It is a measure of an element's ability to participate in chemical reactions that require the formation of ions or the donation of electrons.

Similarly, the electron affinity (A) of a molecule represents the change of a neutral molecule to a molecule with a negative ion when both of them are in their most stable states. The molecular negative ion becomes the HOMO when the added electron enters the LUMO orbitals. However, the electron affinity will be greater and vice as lowering the energy of LUMO. For the hydrazone **4a**, the value of electron affinity was calculated as 1.896 eV. The other parameters such as chemical potential (μ), chemical hardness (η), global softness (σ), and electrophilicity (ω) were calculated using Eq. (3), 4, 5, and 6, and their values were found to be −4.035, 2.139, 0.233 and 3.805 eV respectively.



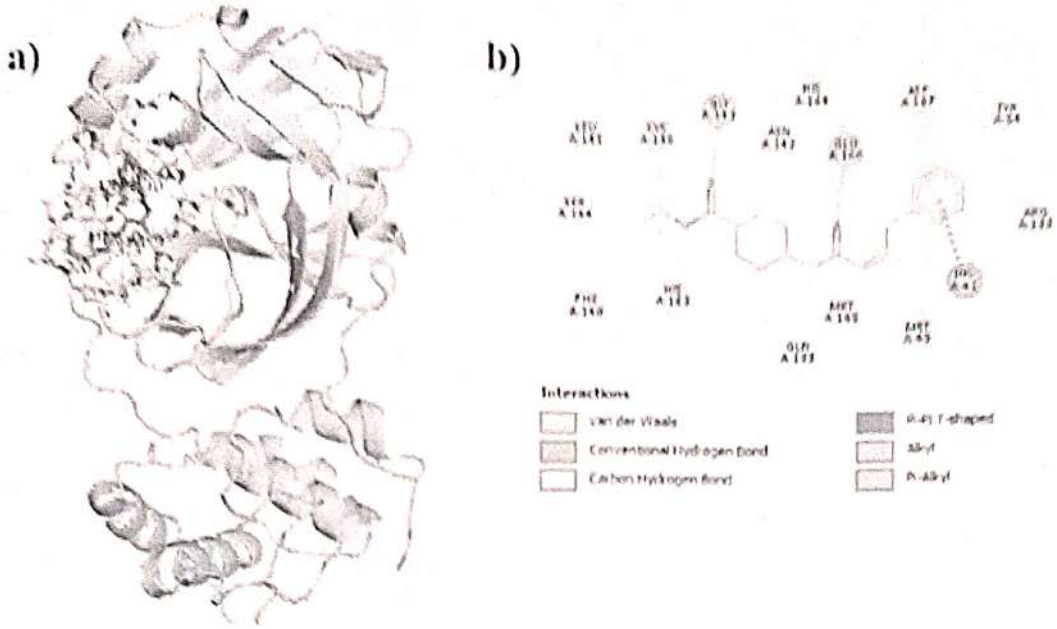


Fig. 8. Molecular docking for nCoV-SARS-2 against Compound **4a**: Interaction between 6LU7 (3D Protein structure) and ligand **4a**: b) 2D structure of **4a** with possible amino acid interactions.

Table 9
Antibacterial and antifungal activities of hydrazone **4a-4e** and **5a-5c**.

S. No.	Organism	Minimum inhibitory concentration (MIC) in µg/mL							
		4a	4b	4c	4d	4e	5a	5b	5c
1	***S. aureus***	–	12.5	50	25	50	–	100	12.5
2	*B. Subtilis*	100	100	12.5	50	6.25	100	25	200
3	*S. typhi*	100	–	50	12.5	100	25	12.5	25
4	*E. coli*	50	12.5	25	25	12.5	200	50	200
5	*K. pneumonia*	50	6.25	6.25	200	50	200	12.5	6.25
6	*C. neoformans*	12.5	50	25	50	12.5	–	50	6.25
7	*C. albicans*	50	12.5	50	25	12.5	50	50	25
8	*Rhizopus* sp.	50	200	–	–	100	100	12.5	25
9	*A. niger*	6.25	50	12.5	12.5	25	100	6.25	25
10	*A. flavus*	25	50	50	25	25	6.25	–	12.5

Streptomycin– 50 µg/ml for *S. aureus*, 12.5 µg/ml for *B.Subtilis*, 50 µg/ml for *S. typhi*, 12.5 µg/ml for *E. coli*, 25 µg/ml for *K. pneumonia*.
Amphotericin B – 25 µg/ml for *C.neoformans*, 25 µg/ml for *C. albicans*, 25 µg/ml for *Rhizopus sp*., 50 µg/ml for *A. niger*, 50 µg/ml for *A. flavus*.

Similarly, an in vitro antifungal activity for hydrazone derivatives was performed against five pathogenic fungal strains viz. *C. neoformans*, *C. albicans*, *Rhizopus sp*., *A. niger* and *A. flavus*, their results along with the standard drug are depicted in Table 9. Compounds (**4a** and **5a**) without substitution on the phenyl group show an inhibitory activity in the range of 12.5– 100 µg/mL with the exception of **4a** against *A.niger* and **5a** against *A. flavus*, which were exhibited good impact on fungal activity at minimum concentration of 6.25 µg/mL. But the introduction of methyl group in **4a** (compound **4b**) showed a one-fold decrease in inhibitory activity against *C. albicans* and a two-fold decrease against other strains. No fungal growth inhibition was found for compounds **4c** and **4d** against *Rhizopus sp* and **5b** against *A. flavus* even at the maximum concentration of 200 µg/mL.The rest of the hydrazones in this series showed low to moderate fungal activity against the strains tested.

4. Conclusion

A series of new ethyl-(E)-4-{2-(2-arylidenehydrazinyl)–2-oxoethyl}piperazine-1-[illegible]dates based hydrazones **4a-4e** and **5a-5c** were synthesized and characterized by FT-IR, ^{1}H NMR, ^{13}C NMR, HSQC, and mass spectroscopic techniques. Further, single crystal XRD analysis was studied for hydrazone **4a**. Hirshfeld surface analysis was performed for hydrazone **4a** and their intermolecular interactions were quantified. Strong N–H···O and C–H···O intermolecular hydrogen bonding were detected which results in close contact between two independent molecules. The 2D fingerprint calculation revealed that H....H interaction (56.3%) signifying that van der Waals forces are contributing more to the crystal packing. The electronic properties of hydrazone **4a** were quantified by DFT method. The theoretical analysis of the HOMO-LUMO orbitals band gap suggest that the softness of the hydrazone molecule with large polarizability which results in accomplishing greater nonlinear susceptibility. The NLO property of **4a** was found as a significant NLO response as compared to the prototype compound. In-silico molecular docking results showed significant binding affinity towards nCov-SARS-2 M^{pro} with –6.92 kcal/mol. Finally, we concluded that compounds **4a-4e** and **5a-5c** containing hydrazone and amide functional group in molecules seemed to be appropriate candidates for further chemical modifications and may be biologically active molecules.

P.G.P. COLLEGE OF ARTS & SCIENCE NAMAKKAL 637 256

Electron density delocalization between occupied bonding or loan pair (Lewis type) NBO orbitals and unoccupied anti-bonding or Rydgberg (non-Lewis type) NBO orbitals correspond to a stabilizing donor-acceptor interaction. However, this interaction can be quantized based on the stabilization energy E(2) calculated from Fock-matrix analysis using second-order perturbation theory. By considering donor NBO (i) and acceptor NBO (j), we estimate the stabilization energy E(2) associated with electron delocalization between donor and acceptor as $E(2) = \Delta E_{ij} = q_i(F_{i,j}^2/\varepsilon_j - \varepsilon_i)$, where $F_{(i,j)}$ is the Fock matrix element between the NBOs, q_i is the orbital occupancy, ε_j and ε_i are representing the diagonal elements and F(i,j) is the Fock matrix element between the natural bonding orbitals. A larger E(2) value indicates a more intensive interaction between the electron donor and acceptor, the more donating tendency from electron donor to acceptor and the larger the extent of conjugation of the whole system. The most significant interactions between Lewis type NBOs (filled or donor) and non-Lewis type NBOs (empty or acceptor) are reported. It can be seen from the Table S4 the resonance interaction energies for donor-acceptor excitations of the bonding to anti-bonding orbitals (π to π^*) are π(O1-C20) → π^*(N3 - N4), π (N3 - C21) → π^*(C12 - C16), π (N3 - C21) → π^*(C12 - C18), π(C12 - C16) → π^*(N3 - C21), π(C12 - C16) → π^*(C12 - C18),π(C12 - C16) → π^*(C16 - C27), π (C12 - C18) → π^*(C12 - C16), π (C12 - C18) → π^*(C18 - C29), π (C12 - C18) → π^* (N3 - C21), π (C12 - C18) → π^*(N3 - C21), π (C12 - C18) → π^*(C16 - C27), π (C12 - C18) → π^*(C29 - C31), π (C12 - C21) → π^*(N3 - C21), π (C12 - C21) → π^*(C12 - C16), π (C12 - C21) → π^*(C12 - C18), π (C12 - C21) → π^*(C16 - C27), π (C12 - C21) → π^*(C18 - C29), π (C29 - C31) → π^*(C27 - C31), π (C29 - C31) →π^*(C12 - C18), π (C29 - C31) → π^*(C16 - C27), π (N3 - C21) → π^*(N3 - C21), π (C12 - C18) → π^*(N3 - C21) are 2.1, 0.8, 5.26, 2.03, 3.79, 2.76, 3.8, 2.93, 0.97, 11.59, 19.13, 19.78, 2.04, 2.2, 2.18, 2.32, 2.29, 2.78, 2.59, 21.1, 19.89, 0.8, and 0.57 kcal/mol respectively. Among these, greatest stabilization energies were found to be for π (C12 - C18) → π^* (N3 - C21), π (C12 - C18) → π^* (C16 - C27), π (C12 - C18) → π^*(C29 - C31) and π (C29 - C31) → π^*(C16 - C27) transition. Therefore, the intermolecular interactions are greatly affecting the crystal packing in this system as shown the strong donor-acceptor interactions in NBO analysis.

3.16. Non-linear optical (NLO) analysis

The non-linear optical (NLO) behavior of hydrazone **4a** was calculated with the B3LYP method using the 6–311G(d,p) level. The calculated parameters from the quantum chemical approach can be used to get more insight into the electronic structure of the organic compounds. The NLO properties of molecules are greatly influenced by the following values (i) dipole moment (μ), (ii) electron mobility, (iii) polarizability (α), and (iv) hyperpolarizability (β). The NLO property of molecules can be enhanced by increasing the values of the polarizabilities and first-order hyperpolarizabilities. Additionally, the second-order NLO properties can serve as a standard for further theoretical and experimental studies. The following Eq. (3) and (4) were used in the NLO analysis.

$$\mu_{tot} = (\mu_x^2 + \mu_y^2 + \mu_z^2)^{\frac{1}{2}} \quad (1)$$

$$\alpha_{tot} = \frac{1}{3}(\alpha_{xx} + \alpha_{yy} + \alpha_{zz}) \quad (2)$$

$$\Delta\alpha = \frac{1}{\sqrt{2}}\left[(\alpha_{xx} - \alpha_{yy})^2 + (\alpha_{yy} - \alpha_{zz})^2 + (\alpha_{zz} - \alpha_{xx})^2 + 6\alpha_{xz}^2 + 6\alpha_{xy}^2 + 6\alpha_{yz}^2\right]^{1/2} \quad (3)$$

$$\beta_{tot} = \left[(\beta_{XXX} + \beta_{XYZ} + \beta_{XZZ})^2 + (\beta_{YYY} + \beta_{YZZ} + \beta_{YXX})^2 + (\beta_{ZZZ} + \beta_{ZXX} + \beta_{ZYY})^2\right]^{1/2} \quad (4)$$

For **4a**, the anisotropy of polarizability: $\Delta\alpha = 9.8716 \times 10^{-24}$ esu, the mean polarizability: $\alpha_{total} = 1.917 \times 10^{-23}$ esu and the first-order hyperpolarizability value: $\beta_o = 2.14 \times 10^{-30}$ esu were calculated. The theoretically calculated dipole moment and polarizability values are given in Table 8. The results indicated that the hydrazone **4a** was found to be a potential candidate for nonlinear optical materials when the experimentally high order polarizability is compared to that of standard urea [60].

3.17. Molecular docking study

The molecular docking studies exposed how heterocyclic hydrazone ligand might bind to the nCov-SARS-2 (COVID-19) main protease (6LU7). The docked molecule was fitted to interact with the active site of 6LU7 main protease. The binding interaction is key function to understand the interaction between inhibitor (ligand) and receptor (biomolecule). The binding affinity is greatly affected by the non-covalent interaction such as H-bond, electrostatic interaction, hydrophobic and van der Waals forces.

The hydrazone **4a** ligand exhibits the strongest interaction with nCov-SARS-2 (COVID-19) main protease as shown in Fig. 9. As shown in Fig. 9, the hydrazone **4a** ligand observed good binding affinity as lead compound for developing SARS-CoV-2 M^{pro} inhibitors with −6.92 kcal/mol binding score (Table S5). The interacting residues of SARS-CoV-2 M^{pro} with hydrazone **4a** were HIS41A, MET49A, ASN142A, GLY143A, CYS145A, GLU166A and GLN189A. Among these, residues GLY143A, and GLU166A were formed conventional H-bonding with ligand **4a** whereas residue HIA41A formed π - π stacked interaction. However, MET49A and CYS145A were formed alkyl group interaction with protein molecule [61,62].

3.18. Antibacterial and antifungal activity

The synthesized hydrazones were preliminarily screened for antibacterial and antifungal activity by two- fold serial dilution method using the selected bacterial strains viz.,*Staphylococcus aureus*, *Bacillus subtilis*, *Salmonella typhi*, *Escherichia coli* and *Klebsiella pneumoniae* and fungal strains viz.,*Cryptococcus neoformans*, *Candida albicans*, *Rhizopus sp.*, *Aspergillus niger*, and *Aspergillus flavus*. Dimethyl sulphoxide (DMSO) was used as a control, while streptomycin and amphotericin B were used as bacterial and fungal strains, respectively, as standards.

The minimum inhibitory concentration (MIC in μg/mL) of hydrazones **4a-4e** and **5a-5c** against the tested microbial agents are summarized in Table 9. It can be seen from the Table 9 that the MIC values for the compounds **4a–4e** and **5a-5c** against all bacterial strains tested show a moderate to excellent growth inhibition activity, with the exception of the compounds**4a** and **5a** against *S. aureus* and **4b** against *S. typhi* which seldom show inhibitory activity even at a maximum concentration 200 μg/mL, indicating that the absence of any substituent attached to the phenyl group shows no growth inhibition. In order to gain better insight into the structure activity relationship (SAR), various substituents such as methyl, mehoxy, chloro and fluoro functions were introduced to the phenyl group and tested for their inhibitory activity. Electron donating groups such as *p*-tolyl (**4b**) and *p*-methoxyphenyl group substituted hydrazone (**4c**) display significant bacterial inhibition activity against *K. pneumoniae* at 6.25 µg/mL. On the other hand, electron withdrawing group substituted phenyl compounds (fluoro function) showed remarkable anti-bacterial activity at a minimum concentration of 6.25 µg/mL, **4e** against *B.subtilis* and **5c** against *K. pneumonia*, whereas **4d** and **4e** showed minimum to moderate bacterial activity (25–200 µg/mL). **4d** against *S. typhi*, 4e against *E.coli* whose inhibition concentration was found to be 12.5 µg/mL.

P.A.C. COLLEGE OF ARTS & SCIENCE NAMAKKAL 637 236

CRediT author statement

I declare that the following information is about the role of authors in the submitted manuscript.

M. Rani: Synthesis, Methodology, Investigation, Formal Analysis
S. Jayanthi: Software, Methodology, Data Curation, Investigation
S. Kabilan: Formal Analysis, Investigation
R. Ramachandran: Software, Methodology, Formal Analysis; Data Curation, Writing - Review & Editing

Authors **M. Rani** and **S. Jayanthi** are contributed equally to this paper

Declaration of Competing Interest

The authors declare that they have no known competing financial interests or personal relationships that could have appeared to influence the work reported in this paper.

Supplementary materials

Supplementary material associated with this article can be found, in the online version, at doi:10.1016/j.molstruc.2021.132082.

References

[1] X. Su, I. Aprahamian, Hydrazone-based switches, metallo-assemblies and sensors, Chem. Soc. Rev. 43 (2014) 1963–1981, doi:10.1039/c3cs60385g.

[2] M.A. Abdelrahman, I. Salama, M.S. Gomaa, M.M. Elaasser, M.M. Abdel-Aziz, D.H. Soliman, Design, synthesis and 2D QSAR study of novel pyridine and quinolone hydrazone derivatives as potential antimicrobial and antitubercular agents, Eur. J. Med. Chem. 138 (2017) 698–714, doi:10.1016/j.ejmech.2017.07.004.

[3] A.-A.S. El-Etrawy, F.F. Sherbiny, Design, synthesis, biological evaluation and molecular modeling investigation of new N'-(2-Thiouracil-5-oyl) hydrazone derivatives as potential anti-breast cancer and anti-bacterial agents, J. Mol. Struct. 1232 (2021) 129993, doi:10.1016/j.molstruc.2021.129993.

[4] V. Kamat, R. Santosh, B. Poojary, S.P. Nayak, B.K. Kumar, M. Sankaranarayanan, S.Khanapure Faheem, D.A. Barretto, S.K. Vootla, Pyridine- and thiazole-based hydrazides with promising anti-inflammatory and antimicrobial activities along with their in silico studies, ACS Omega 5 (2020) 25228–25239, doi:10.1021/acsomega.0c03386.

[5] A. Kajal, S. Bala, N. Sharma, S. Kamboj, V. Saini, Therapeutic potential of hydrazones as anti-inflammatory agents, Int. J. Med. Chem 2014 (2014) 761030, doi:10.1155/2014/761030.

[6] T. Nasr, S. Bondock, M. Youns, Anticancer activity of new coumarin substituted hydrazide-hydrazone derivatives, Eur. J. Med. Chem. 76 (2014) 539–548, doi:10.1016/j.ejmech.2014.02.026.

[7] R. Kaplanek, M. Jakubek, J. Rak, Z. Kejik, M. Havlik, B. Dolensky, I. Frydrych, M. Hajduch, M. Kolar, K. Bogdanova, J. Kralova, P. Dzubak, V. Kral, Caffeine-hydrazones as anticancer agents with pronounced selectivity toward T-lymphoblastic leukaemia cells, Bioorg. Chem. 60 (2015) 19–29, doi:10.1016/j.bioorg.2015.03.003.

[8] C. Xu, W. Zhou, G. Dong, H. Qiao, J. Peng, P. Jia, Y. Li, H. Liu, K. Sun, W. Zhao, Novel [1,2,3]triazolo[4,5-d]pyrimidine derivatives containing hydrazone fragment as potent and selective anticancer agents, Bioorg. Chem. 105 (2020) 104424, doi:10.1016/j.bioorg.2020.104424.

[9] N. Kumar, L.S. Chauhan, C.S. Sharma, N. Dashora, R. Bera, Synthesis, analgesic and anti-inflammatory activities of chalconyl-incorporated hydrazone derivatives of mefenamic acid, Med. Chem. Res. 24 (2015) 2580–2590, doi:10.1007/s00044-015-1318-8.

[10] S.A. Bonnett, D. Dennison, M. Files, A. Bajpai, T. Parish, A class of hydrazones are active against non-replicating Mycobacterium tuberculosis, PLoS ONE 13 (2018) e0198059, doi:10.1371/journal.pone.0198059.

[11] M.C. Mandewale, B. Thorat, Y. Nivid, R. Jadhav, A. Nagarsekar, R. Yamgar, Synthesis, structural studies and antituberculosis evaluation of new hydrazone derivatives of quinoline and their Zn(II) complexes, J. Saudi Chem. Soc. 22 (2018) 218–228, doi:10.1016/j.jscs.2016.04.003.

[12] U.P. Singh, H.R. Bhat, A. Verma, M.K. Kumawat, R. Kaur, S.K. Gupta, R.K. Singh, Phenyl hydrazone bearing pyrazole and pyrimidine scaffolds: design and discovery of a novel class of non-nucleoside reverse transcriptase inhibitors (NNRTIs) against HIV-1 and their antibacterial properties, RSC Adv. 3 (2013) 17335, doi:10.1039/c3ra41604f.

[13] P. Vicini, M. Incerti, P.La Colla, R. Loddo, Anti-HIV evaluation of benzo[d]isothiazole hydrazones, Eur. J. Med. Chem. 44 (2009) 1801–1807, doi:10.1016/j.ejmech.2008.05.030.

[14] P. Shah, L.F. Abadi, S. Gaikwad, D. Chaudhari, V. Kushwah, S. Jain, K.K. Bhutani, S. Kulkarni, I.P. Singh, Synthesis and Biological Evaluation of 8-Hydroxyquinoline-hydrazones for Anti-HIV-1 and Anticancer Potential, ChemistrySelect 3 (2018) 10727–10731, doi:10.1002/slct.201802283.

[15] U. Salgin-Goksen, G. Telli, A. Erikci, E. Dedecengiz, B.C. Tel, F.B. Kaynak, K. Yelekci, G. Ucar, N. Gokhan-Kelekci, New 2-Pyrazoline and hydrazone derivatives as potent and selective monoamine oxidase A inhibitors, J. Med. Chem. 64 (2021) 1989–2009, doi:10.1021/acs.jmedchem.0c01504.

[16] S. Emami, M. Valipour, F. Kazemi Komishani, F. Sadati-Ashrafi, M. Rasoulian, M. Ghasemian, M. Tajbakhsh, P. Honarchian Masihi, A. Shafiha, H. Irannejad, N. Ahangar, Synthesis, in silico, in vitro and in vivo evaluations of isatin aroylhydrazones as highly potent anticonvulsant agents, Bioorg. Chem. 112 (2021) 104941, doi:10.1016/j.bioorg.2021.104943.

[17] B. Barta Holló, J. Magyari, S. Armaković, G.A. Bogdanović, M.V. Rodić, S.J. Armaković, J. Molnár, G. Spengler, V.M. Leovac, K. Mészáros Szécsényi, Coordination compounds of a hydrazone derivative with Co(III), Ni(II), Cu(II) and Zn(II): synthesis, characterization, reactivity assessment and biological evaluation, New J. Chem. 40 (2016) 5885–5895, doi:10.1039/c6nj00560h.

[18] J.D. Curry, M.A. Robinson, D.H. Busch, Metal complexes derived from substituted hydrazones of 2,6-diacetylpyridine, Inorg. Chem. 6 (2002) 1570–1574, doi:10.1021/ic50054a032.

[19] G. Ayyannan, M. Mohanraj, M. Gopiraman, R. Uthayamalar, G. Raja, N. Bhuvanesh, R. Nandhakumar, C. Jayabalakrishnan, New Palladium(II) complexes with ONO chelated hydrazone ligand: synthesis, characterization, DNA/BSA interaction, antioxidant and cytotoxicity, Inorganica Chim. Acta. 512 (2020) 119868, doi:10.1016/j.ica.2020.119868.

[20] H. Jansova, J. Kubes, P. Reimerova, P. Sterbova-Kovarikova, J. Roh, T. Simunek, 2,6-Dihydroxybenzaldehyde analogues of the iron chelator salicylaldehyde isonicotinoyl Hydrazone: increased hydrolytic stability and cytoprotective activity against oxidative stress, Chem Res Toxicol. 31 (2018) 1151–1163, doi:10.1021/acs.chemrestox.8b00165.

[21] V. Meenatchi, S. Siva, L. Cheng, Synthesis, crystal growth, spectroscopic characterization, Hirshfeld surface analysis and DFT investigations of novel nonlinear optically active 4-benzoylpyridine-derived hydrazone, J. Mol. Struct. 1243 (2021) 130858, doi:10.1016/j.molstruc.2021.130858.

[22] D. Sadhukhan, M. Maiti, G. Pilet, A. Bauzá, A. Frontera, S. Mitra, Hydrogen Bond, $\pi-\pi$, and CH–π interactions governing the supramolecular assembly of some hydrazone ligands and their MnII Complexes – Structural and Theoretical Interpretation, Eur. J. Inorg. Chem. 2015 (2015) 1958–1972, doi:10.1002/ejic.201500030.

[23] G. Aridoss, S. Balasubramanian, P. Parthiban, S. Kabilan, Synthesis and NMR spectral studies of N-chloroacetyl-2,6-diarylpiperidin-4-ones, Spectrochim. Acta Part A Mol. Biomol. Spectrosc. 68 (2007) 1153–1163, doi:10.1016/j.saa.2007.01.013.

[24] M. Rani, P. Parthiban, R. Ramachandran, S. Kabilan, Design and synthesis of novel piperazine unit condensed 2,6-diarylpiperidin-4-one derivatives as antituberculosis and antimicrobial agents, Med. Chem. Res. 21 (2012) 653–662, doi:10.1007/s00044-011-9573-9.

[25] T. Goněc, I. Malík, J. Csöllei, J. Jampílek, J. Stolaříková, I. Solovič, P. Mikuš, S. Keltošová, P. Kollár, J. O'Mahony, A. Coffey, Synthesis and In Vitro Antimycobacterial Activity of Novel N-Arylpiperazines Containing an Ethane-1,2-diyl Connecting Chain, Mol. (2017) 22, doi:10.3390/molecules22122100.

[26] M.-X. Wei, J.-Y. Yu, X.-X. Liu, X.-Q. Li, M.-W. Zhang, P.-W. Yang, J.-H. Yang, Synthesis of artemisinin-piperazine-furan ether hybrids and evaluation of in vitro cytotoxic activity, Eur. J. Med. Chem. 215 (2021) 113295, doi:10.1016/j.ejmech.2021.113295.

[27] P.S. Girase, S. Dhawan, V. Kumar, S.R. Shinde, M.B. Palkar, R. Karpoormath, An appraisal of anti-mycobacterial activity with structure-activity relationship of piperazine and its analogues: a review, Eur. J. Med. Chem. 210 (2021) 112967, doi:10.1016/j.ejmech.2020.112967.

[28] V. Bala, D. Mandalapu, S. Gupta, S. Jangir, B. Kushwaha, Y.S. Chhonker, H. Chandasana, S. Krishna, K. Rawat, A. Krishna, M. Singh, S.N. Sankhwar, P.K. Shukla, J.P. Maikhuri, R.S. Bhatta, M.I. Siddiqi, R. Tripathi, G. Gupta, V.L. Sharma, N-Alkyl/aryl-4-(3-substituted-3-phenylpropyl)piperazine-1-carbothioamide as dual-action vaginal microbicides with reverse transcriptase inhibition, Eur. J. Med. Chem. 101 (2015) 640–650, doi:10.1016/j.ejmech.2015.07.021.

[29] C.-C. Lee, S.-C. Hsu, L.-L. Lai, K.-L. Lu, Chair–Boat form transformation of piperazine-containing ligand toward the preparation of Dirhenium Metallacycles, Inorg. Chem. 48 (2009) 6329–6331, doi:10.1021/ic900040a.

[30] K. Singh, I. bala, R. Katana, Crystal structure, Hirshfeld surface and DFT based NBO, NLO, ECT and MEP of benzothiazole based hydrazone, Chem. Phys. 538 (2020) 110873, doi:10.1016/j.chemphys.2020.110873.

[31] A. Suvitha, S. Periandy, P. Gayathri, NBO, HOMO–LUMO, UV, NLO, NMR and vibrational analysis of veratrole using FT-IR, FT-Raman, FT-NMR spectra and HF-DFT computational methods, Spectrochim. Acta Part A Mol. Biomol. Spectrosc. 138 (2015) 357–369, doi:10.1016/j.saa.2014.11.011.

[32] S. Guidara, H. Feki, Y. Abid, Molecular structure, NLO, MEP, NBO analysis and spectroscopic characterization of 2,5-dimethylanilinium dihydrogen phosphate with experimental (FT-IR and FT-Raman) techniques and DFT calculations, Spectrochim. Acta Part A Mol. Biomol. Spectrosc. 133 (2014) 856–866, doi:10.1016/j.saa.2014.06.021.

[33] I. Aprahamian, Hydrazone switches and things in between, Chem. Commun. 53 (2017) 6674–6684, doi:10.1039/c7cc02879b.

[34] L. Koivusalo, J. Karvinen, E. Sorsa, I. Jonkkari, J. Valliaho, P. Kallio, T. Ilmarinen, S. Miettinen, H. Skottman, M. Kellomaki, Hydrazone crosslinked hyaluronan-based hydrogels for therapeutic delivery of adipose stem cells to treat corneal defects, Mater Sci Eng C Mater Biol Appl 85 (2018) 68–78, doi:10.1016/j.msec.2017.12.013.

[35] Q. Wu, Z. Zheng, W. Ye, Q. Guo, T. Liao, D. Yang, C. Zhao, W. Liao, H. Chai, Z. Zhou, Synthesis, crystal and molecular structure, vibrational spec-

P.G.P. COLLEGE OF ARTS & SCIENCE NAMAKKAL 637 206

troscopic, DFT and molecular docking of 4-(2-chlorobenzyl)-1-(4-hydroxy-3- ((4-hydroxypiperidin-1-yl) methyl-5-methoxyphenyl)-[1,2,4] triazolo [4,3-a] quinazolin-5(4H)-one, J. Mol. Struct. 1247 (2022) 131367, doi:10.1016/j.molstruc.2021.131367.
[36] D. Li, Q. Wang, N. Rao, Y. Zhang, Y. Le, L. Liu, L. Li, L. Huang, L. Yan, Development of Imidazo[1,2-a]pyridine-based probe for detection of hydrazine and its applications in imaging of HepG2 cell, J. Mol. Struct. 1239 (2021) 130521, doi:10.1016/j.molstruc.2021.130521.
[37] G.M. Sheldrick, No Title, SHELXL-97, Univ. Gottingen, Gottingen, Ger, 1997.
[38] L.J. Farrugia, Ortep-3 for windows, J. Appl. Cryst. 30 (1997) 565.
[39] A.L. Spek, Single-crystal structure validation with the programPLATON, J. Appl. Crystallogr. 36 (2003) 7–13, doi:10.1107/s0021889802022112.
[40] C.F. Macrae, I. Sovago, S.J. Cottrell, P.T.A. Galek, P. McCabe, E. Pidcock, M. Platings, G.P. Shields, J.S. Stevens, M. Towler, P.A. Wood, Mercury 4.0: from visualization to analysis, design and prediction, J. Appl. Crystallogr. 53 (2020) 226–235, doi:10.1107/S1600576719014092.
[41] G.W.T.M.J. Frisch, H.B. Schlegel, G.E. Scuseria, M.A. Robb, J.R. Cheeseman, G. Scalmani, V. Barone, G.A. Petersson, H. Nakatsuji, X. Li, M. Caricato, A. Marenich, J. Bloino, B.G. Janesko, R. Gomperts, B. Mennucci, H.P. Hratchian, J.V. Ortiz, A.F. Izma, Gaussian 09,Revision A.02 No Title, Gaussian, Inc, Wallingford, CT, USA, 2013.
[42] P.R. Spackman, M.J. Turner, J.J. McKinnon, S.K. Wolff, D.J. Grimwood, D. Jayatilaka, M.A. Spackman, CrystalExplorer: a program for Hirshfeld surface analysis, visualization and quantitative analysis of molecular crystals, J. Appl. Crystallogr. 54 (2021) 1006–1011, doi:10.1107/s1600576721002910.
[43] T. Lu, F. Chen, Multiwfn: a multifunctional wavefunction analyzer, J. Comput. Chem. 33 (2012) 580–592, doi:10.1002/jcc.22885.
[44] T.G.S. Todd, A. Keith, AIMAll (Version 19.10.12) No Title, Overland P, 2019.
[45] I. Wiegand, K. Hilpert, R.E.W. Hancock, Agar and broth dilution methods to determine the minimal inhibitory concentration (MIC) of antimicrobial substances, Nat. Protoc. 3 (2008) 163–175, doi:10.1038/nprot.2007.521.
[46] R.R. Meethale Pallolathil, R. Rathikha, R. Nithyabalaji, R. Sribalan, Synthesis, characterization, in vitro and in silico studies of bis-hydrazone complexes derived from terephthalic dihydrazide, J. Mol. Struct. 1242 (2021) 130683, doi:10.1016/j.molstruc.2021.130683.
[47] R.M. Silverstein, G.C. Bassler, Spectrometric identification of organic compounds, J. Chem. Educ. 39 (1962) 546, doi:10.1021/ed039p546.
[48] R.J. Abraham, M. Mobli, R.J. Smith, 1H chemical shifts in NMR: part 19. Carbonyl anisotropies and steric effects in aromatic aldehydes and ketones, Magn. Reson. Chem. 41 (2003) 26–36, doi:10.1002/mrc.1125.
[49] G. Palla, G. Predieri, P. Domiano, C. Vignali, W. Turner, Conformational behaviour and E/Z isomerization of N-acyl and N-aroylhydrazones, Tetrahedron 42 (1986) 3649–3654, doi:10.1016/S0040-4020(01)87332-4.
[50] R. Ramachandran, M. Rani, S. Kabilan, Synthesis, structure and conformational analysis of 2,4-diaryl-3-azabicyclo[3.3.1]nonan-9-one thiosemicarbazones and semicarbazones, J. Mol. Struct. 970 (2010) 42–50, doi:10.1016/j.molstruc.2010.02.005.
[51] D. Cremer, J.A. Pople, General definition of ring puckering coordinates, J. Am. Chem. Soc. 97 (1975) 1354–1358, doi:10.1021/ja00839a011.
[52] M.A. Spackman, D. Jayatilaka, Hirshfeld surface analysis, CrystEngComm 11 (2009) 19–32, doi:10.1039/b818330a.
[53] Y.-H. Luo, G.-G. Wu, S.-L. Mao, B.-W. Sun, Complexation of different metals with a novel N-donor bridging receptor and Hirshfeld surfaces analysis, Inorganica Chim. Acta. 397 (2013) 1–9, doi:10.1016/j.ica.2012.11.010.
[54] M.A. Spackman, P.G. Byrom, A novel definition of a molecule in a crystal, Chem. Phys. Lett. 267 (1997) 215–220, doi:10.1016/S0009-2614(97)00100-0.
[55] Y. Ruiz-Morales, HOMO–LUMO Gap as an index of molecular size and structure for polycyclic aromatic hydrocarbons (PAHs) and Asphaltenes: A theoretical study. I, J. Phys. Chem. A. 106 (2002) 11283–11308, doi:10.1021/jp021152e.
[56] L. Liu, L. Miao, L. Li, F. Li, Y. Lu, Z. Shang, J. Chen, Molecular Electrostatic Potential: a New Tool to Predict the Lithiation Process of Organic Battery Materials, J. Phys. Chem. Lett. 9 (2018) 3573–3579, doi:10.1021/acs.jpclett.8b01123.
[57] R.S. Mulliken, Electronic Population Analysis on LCAO–MO Molecular Wave Functions. I, J. Chem. Phys. 23 (1955) 1833–1840, doi:10.1063/1.1740588.
[58] A.E. Reed, R.B. Weinstock, F. Weinhold, Natural population analysis, J. Chem. Phys. 83 (1985) 735–746, doi:10.1063/1.449486.
[59] J. Liu, Z. Chen, S. Yuan, Study on the prediction of visible absorption maxima of azobenzene compounds, J. Zhejiang Univ. Sci. B. 6 (2005) 584–589, doi:10.1631/jzus.2005.B0584.
[60] H. Alyar, Z. Kantarci, M. Bahat, E. Kasap, Investigation of torsional barriers and nonlinear optical (NLO) properties of phenyltriazines, J. Mol. Struct. 834–836 (2007) 516–520, doi:10.1016/j.molstruc.2006.11.066.
[61] Z. Jin, X. Du, Y. Xu, Y. Deng, M. Liu, Y. Zhao, B. Zhang, X. Li, L. Zhang, C. Peng, Y. Duan, J. Yu, L. Wang, K. Yang, F. Liu, R. Jiang, X. Yang, T. You, X. Liu, X. Yang, F. Bai, H. Liu, X. Liu, L.W. Guddat, W. Xu, G. Xiao, C. Qin, Z. Shi, H. Jiang, Z. Rao, H. Yang, Structure of Mpro from SARS-CoV-2 and discovery of its inhibitors, Nature 582 (2020) 289–293, doi:10.1038/s41586-020-2223-y.
[62] J. Wang, Fast Identification of Possible Drug Treatment of Coronavirus Disease-19 (COVID-19) through Computational Drug Repurposing Study, J. Chem. Inf. Model. 60 (2020) 3277–3286, doi:10.1021/acs.jcim.0c00179.

P.G.P. COLLEGE OF ARTS & SCIENCE NAMAKKAL 637 206

PRINCIPAL.
PGP College of Arts and Science
Namakkal

International Journal of Advanced and Innovative Research (2278-7844)/

Volume 8 Issue 4

SPECTRAL INVESTIGATION AND BIOLOGICAL EVALUATION OF MONONUCLEAR MANGANESE(II) COMPLEX OF A NEWLY SYNTHESIZEDSCHIFF BASE LIGAND DERIVED FROM 4-NITROANILINE AND O-PHTHALADEHYDE

T. Sujeshwari [1], E. Akila [2] & *P. Maheswaran [3*]

[1] Research Scholar, Department of Chemistry, P.G.P college of Arts and science, Namakkal.
[2] Department of Chemistry, Sri Sarada College for women (Autonomous), salem-16.
[3] Principal and Head, Department of Chemistry, P.G.P college of Arts and science, Namakkal.*

ABSTRACT

The aim of the present work was to synthesis Schiff base ligand and its Mn(II) metal complex from the condensation of o- phthalaldehyde and p-nitroaniline. The synthesized Schiff base ligand and metal complex were characterized by elemental analysis, FT-IR, ^{1}H NMR, UV spectral studies. From the observed data, the complex is octahedral geometry for the Mn(II) complex. The biological activity involves antibacterial, antioxidant screening and DNA cleavage showed better activity.

Keywords - Schiff base metal complex, p-nitroaniline, o- phthalaldehyde.

INTRODUCTION

Schiff base is one of the most widely used ligand due to the ease of formation and remarkable versatility. They have played an important role in the development of coordination chemistry as they readily form stable complex with most of the transition metals [1-3]. Mn(II) complex thus play an important role in developing the coordination chemistry, catalyst, enzymatic reaction and bioinorganic modeling studies. Schiff base have wide application in food industry, dye industry, analytical chemistry, fungicidal, agrochemical and biological activities. The research field dealing with Schiff base metal complex is very broad due to their potential interest for a number of interdisciplinary areas that include bioinorganic chemistry and catalyst [4]. Schiff base have been widely used ligand because of high stability of the coordination compounds, and their good solubility in common solvent. In general mechanism of synthesis of Schiff base,an aromatic amine reacts with a carbonyl compound by nueclophilic addition. This form a hemiaminal, followed by dehydration to produce imines carbon-

©2019 IJAIR. All Rights Reserved

PRINCIPAL
PGP College of Arts and Science
Namakkal.

P.G.P. COLLEGE OF ARTS & SCIENCE NAMAKKAL 637 206

nitrogen double bond provides a significant contribution in various progresses of chemical sciences [5].

Physical measurements

Elemental analysis (C, H and N) was performed using a Carlo Eraba 1106 instrument. Molar conductance of the complex in DMF solution was measured using ELICO CM 185 Conductivity Bridge. IR spectra of ligand and its metal complexes were recorded as KBr disk pellets on a perkin Elmer-Spectrum RX-I FTIR spectrophotometer covering the range 4000-200 cm^{-1}. ^{1}H NMR spectra of ligand were recorded on the FT-NMR spectrometer model Bruker Avance II, 400 MHz using d_6-DMSO as solvent.

Synthesis of Schiff base ligand

An equimolar mixture of p- nitroaniline (0.5533) and o- phthalaldehyde (0.2689) in ethanol (30 mL) was refluxed with 21/2 h at 75 ^{0}C. The reaction mixture was cooled to room temperature as a result deep yellow orange compound was obtained. It is separated, filtered and dried.

Synthesis of Mononuclear Schiff base metal complex

The ethanolic solution of synthesized ligand (2mM) was added drop wise to an ethanolic solution of the metal salt(1mM) (0.3963) with costant stirring, and the mixture was boiled under reflux for 4 ½ hrs. Then the volume of the reaction mixture was reduced by evaporation. The precipitated complex were filtered off, washed with ethanol and then dried in air.

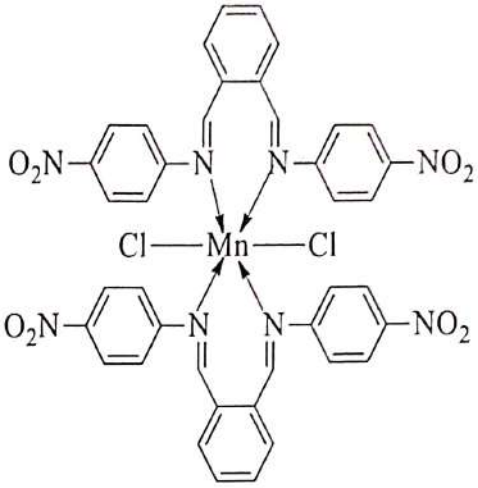


Fig 1. Synthesis of Mn(II) Schiff base metal complex

Antibacterial Studies

The synthesized Schiff base and corresponding Mn (II) complex were screened for their biological activities against four bacterial strains namely Klebsiella pneumonia, Escherichia coli, Staphylococcus aurous and Bacillus subtilis. The bacterial strains were sub cultured individually in nutrient agr medium [6].The plates were incubated for 24h at 37 ^{0}C. During the incubation period the test solution diffused and the growth of the inoculated microorganism was affected. This inhibition zone was noted. The standard antibacterial drug was compared with our synthesized compounds.

©2019 IJAIR. All Rights Reserved

http://ijairjournal.com



Total antioxidant capacity assay

Different concentrations (10 µl, 20 µl, 30 µl, 40 µl and 50 µl) of synthesized compounds were taken and 1ml of reagent solution was added. [Reagent solution: 0.6 M sulphuric acid, 28 mM sodium phosphate and 4 mM Ammonium molybdate]. The tubes were capped and incubated in thermal block at 95°C for 90 minutes. After the time interval the tubes were cool down at room temperature.The absorbance was recorded at 695 nm using shimadzu UV 1800 spectrophotometer [7].

Calculation of 50% Inhibitory Concentration (IC_{50})

The concentration (mg/ ml) of the fractions that was required to scavenge 50% of the radicals was calculated by using the percentage scavenging activities at five different concentrations of the fractions.

Percentage inhibition (I %) was calculated using the formula,

I % = (Ac-As) / Ac x 100

Where, Ac = absorbance of the control and

As = absorbance of the sample.

TAC = Total Antioxidant Capacity assay

DNA Cleavage experiment

The DNA cleavage of supercoiled pUC18DNA promoted by metal complex was proceeded by addition of reaction mixture (40µl). The reaction mixture (40µl) containing pUC18 DNA, 50mM Tris-HCl, pH 7.4, 50mm NaCl, 10mM H_2O_2 added in a different volume, followed by adding Millipore water for final volume. Then the mixed solutions were incubated at 37 °C for 1 hr. They checked by agarose electrophoresis methods.

RESULTS AND DISCUSSION

All the synthesized Schiff base ligands metal complex were highly coloured, they are insoluble in water, absolutly soluble in alcoholic solution and sparingly soluble in organic solvents. The synthesized metal complex are soluble in absolute alcohol and found to be a stable upto certain temperature. The elemental analysis analytical data of the newly synthesized Schiff bases and their metal complexes were recorded in Table 1.

©2019 IJAIR. All Rights Reserved

PRINCIPAL
PGP College of Arts and Science
Namakkal.

P.G.P. COLLEGE OF ARTS & SCIENCE NAMAKKAL

Table 1. Analytical data of the Schiff base ligand and its mononuclear metal complex

Compounds	Molecular Formula	Color	Yield (%)	Melting Point (°c)	% of Nitrogen		% of Metal	
					Cal	Exp	Cal	Exp
L	$C_{20}H_{14}N_4O_4$	Yellowish orange	75	145	15	14.7	-	-
ML_2X_2	$Mn(C_{40}H_{28}N_8O_8Cl_2)$	Dark Green	65	>200	12.7	12.8	6.3	6.1

Molar conductivity

The molar conductance values at 10^{-3} M concentration were too low to account for any dissociation of the complexes in DMF. Hence, Mn(II) complex may be regarded as non electrolytes. Molar conductance values have been complied. The lower conductance value in the range of 9.20 Ω^{-1} cm^2 mol^{-1} of the chelates supports their non-electrolytic nature of the metal complex [8].

IR spectral analysis

The IR spectra of the reported ligand and its complex were measured as KBr disk and the important spectral features along with their tentative assignments are given in Table 2.

The comparison of the IR spectra of Schiff base (and its metal complexes indicated that the ligands are principally coordinated to the metal ions. The band appearing at ~ 1655.34 cm^{-1}due to azomethine linkage [9] in the ligands is shifted by indicating the participation of the azomethine nitrogen in interaction with the metal ion. Lowering of (C=N) in the complex as compared to the ligand (1653.02 cm^{-1}) indicates the coordination of metal ion to ligand [10]. Metal- ligand bond is further confirmed by the appearance of a medium intensity band in the range 483.56 and 320.10 cm^{-1} in the spectra of the complex assigned to stretching frequencies of (M-N) bond and (M-Cl) bond formation respectively [11].

Table 2. IR spectra data (4000–200 cm^{-1}) of Schiff base and its metal complex

Compounds	υ(C=N) (cm^{-1})	υ(M-Cl) (cm^{-1})	υ(M-N) (cm^{-1})
$C_{20}H_{14}N_4O_4$	1655.34	--	--

©2019 IJAIR. All Rights Reserved

http://ijairjournal.com

P.G.P. COLLEGE OF ARTS & SCIENCE NAMAKKAL 637 206

$Mn(C_{40}H_{28}N_8O_8Cl_2)$	1653 02	320 10	483 56

Electronic Spectral data

A moderately intensive band was observed in the range of 345- 382 nm which might be due to n-π* transition and strong band was observed in the range of 294- 365 nm due to π- π* interactions [10]. The electronic spectra of Mn(II) complexes show the absorption bands in the range 565, 595, 630 nm. These absorption bands may be assigned to the $^6A_1g \rightarrow {}^4A_1g$, $^6A_1g \rightarrow {}^4A_2g$, and $^6A_1g \rightarrow {}^4Eg$, ^4A_1g transitions, respectively [12]. These bands suggest that the complexes possess a distorted octahedral geometry.

Table 3. Electronic Spectral data of Schiff base ligand and its Mn(II) complex.

Compound	Electronic spectra (nm)				Geometry of the complex
	π→π*	n→π*	L→M	d-d	
$C_{20}H_{14}N_4O_4$	365	382	-	-	-
$Mn(C_{40}H_{28}N_8O_8Cl_2)$	294	345	405	565, 595, 630	Distorted Octahedral

^{1}H – NMR Spectral studies

The ^{1}H-NMR spectra of the Schiff base ligand was measured at room temperature in DMSO- d_6. The spectrum of the Schiff base ligand exhibits a singlet signal in the 8.48 ppm, which is attributed to the azomethine group (–CH=N–) proton and the multiplets around 6.6-7.9 ppm are assigned due to aromatic protons [13].

***In Vitro* Antibacterial Activity**

The in vitro antibacterial activity of all the synthesized compounds was screened against gram positive and gram negative bacteria. The complex exhibited promising results compared to the ligand against mentioned microorganisms, and this activity is found to been enhanced on coordination with the metal ions. This enhancement in the activity may be to the structures of Schiff base ligand by possessing an azomethine (C=N) linkage [14]. The toxic activity of the complexes with the ligand can be ascribed to the increase in the lipophilic nature of the complexes arising from chelation. The higher activity of $Mn(C_{40}H_{28}N_8O_8Cl_2)$ complex can be explained as, on chelation the polarity of metal ion is found to be reduced to a greater extent due to the overlap of the ligand orbital and partial sharing of the positive charge of the copper ion with donor groups. Therefore, metal ion is adsorbed on the surface of the cell wall of microorganisms. The adsorbed metal ion disturb the respiratory process of the cells, thus blocking the synthesis of proteins and this, in turn, restricts further growth of the organisms [15]. The result shows that the $Mn(C_{40}H_{28}N_8O_8Cl_2)$ complex

©2019 IJAIR. All Rights Reserved

http://ijairjournal.com

P.G.P. COLLEGE OF ARTS & SCIENCE NAMAKKAL 637 206

exhibit antibacterial activity and enhanced it comparing with the parent Schiff base.

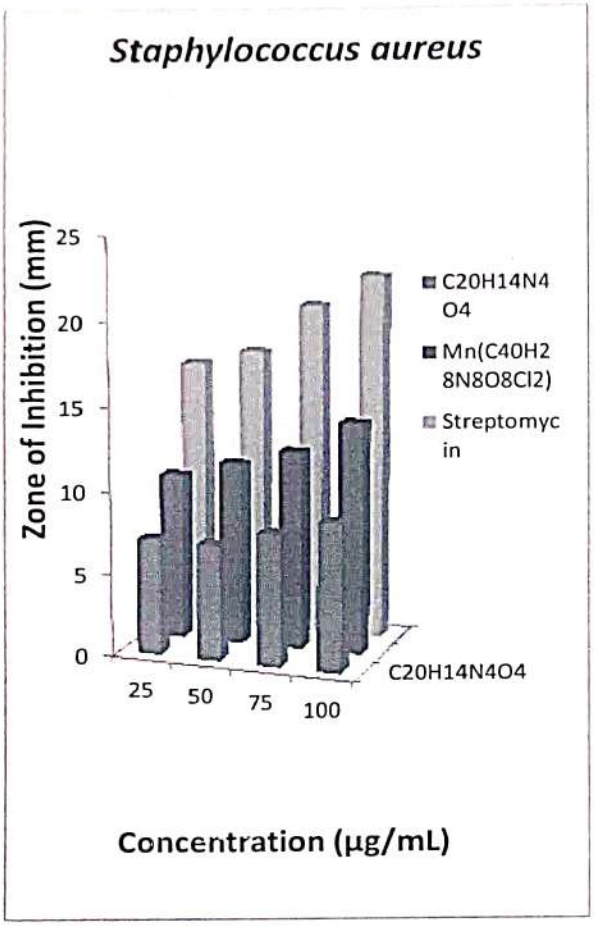


Fig 2. Antibacterial activity of Schiff base ligand and its mononuclear Schiff base metal complex against *Staphylococcus aureus*

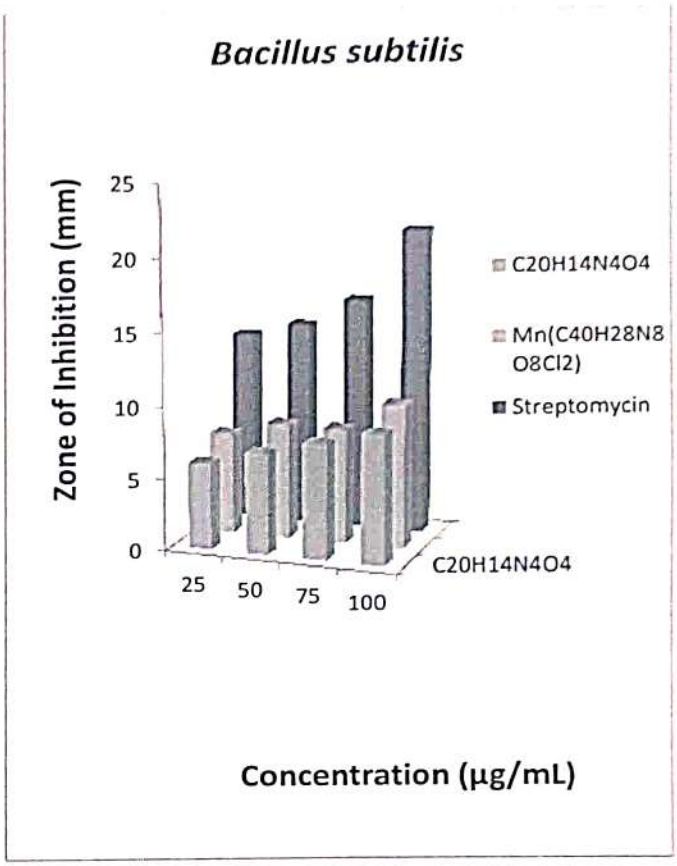


Fig 3. Antibacterial activity of Schiff base ligand and its mononuclear Schiff base metal complex against *Bacillus subtilis*

©2019 IJAIR. All Rights Reserved

P.G.P. COLLEGE OF ARTS & SCIENCE NAMAKKAL 637 206

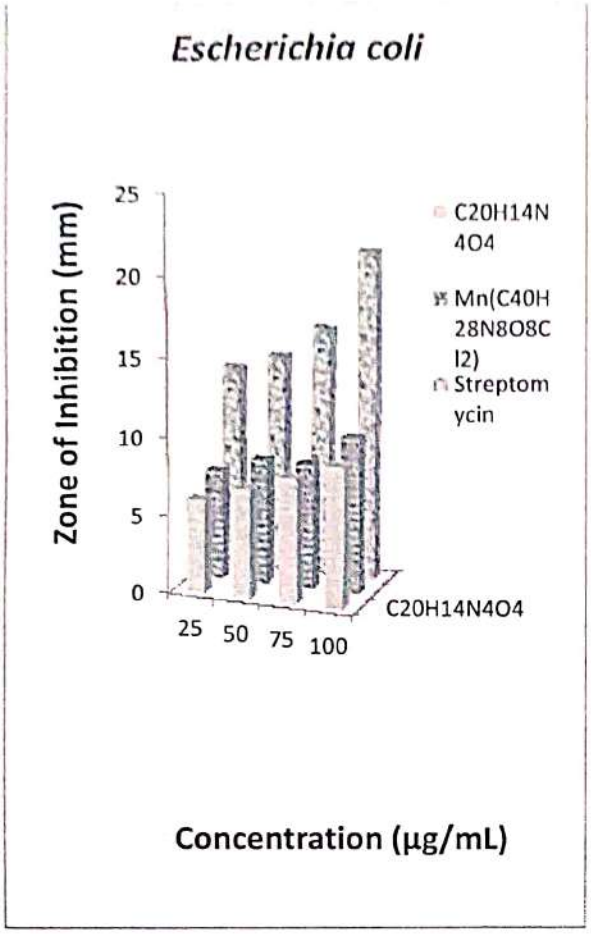


Fig 4. Antibacterial activity of Schiff base ligand and its mononuclear Schiff base metal complexes against *Escherichia coli*

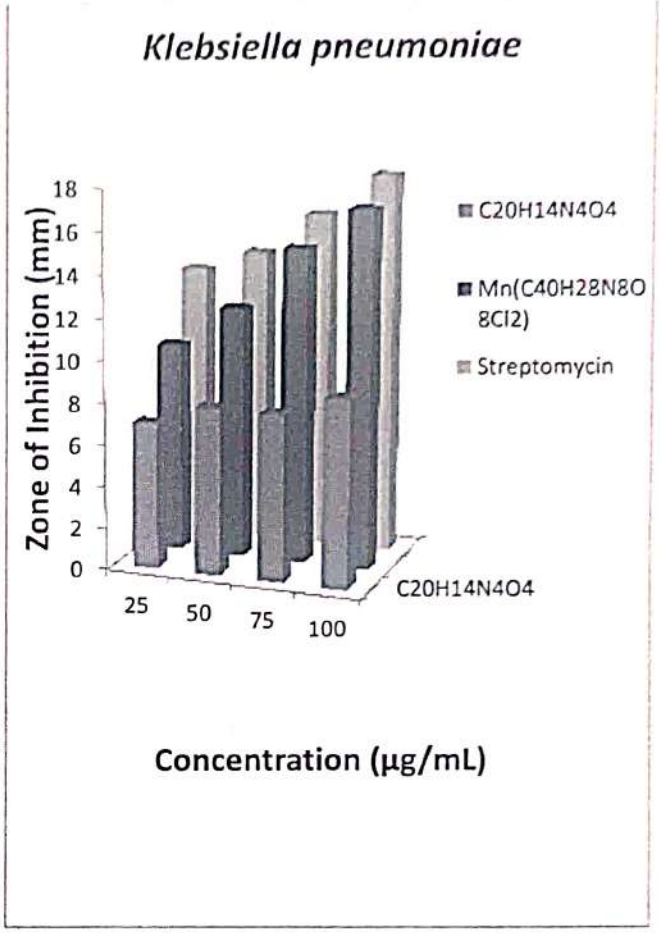


Fig 5. Antibacterial activity of Schiff base ligand and its mononuclear Schiff base metal complex against *Klebsiella pneumonia*

Antioxidant Activity

The antioxidant activity of the ligand and its $Mn(C_{40}H_{28}N_8O_8Cl_2)$ complex have attracted increasing interests and been substantially investigated [16]. Figure 7 & 8 shows the free radical scavenging activity for the ligand and its Mn(II) complex. It is obvious that the scavenging activity

©2019 IJAIR. All Rights Reserved

P.G.P. COLLEGE OF ARTS & SCIENCE NAMAKKAL 637 206

increases with increasing sample concentration in the range tested. Ascorbic acid (vitamin C) is used as standard. As shown in Figure 7 & 8 Mn(II) complex possess more efficient activity in quenching free radical than the free ligand L. When the ligand L interacts with the positively charged metal ions, electron density is drawn from the oxygen. This flow of electron density causes the O–H bond to become more polarized; as a result, the H atom have a greater tendency to ionize than those in the free ligand L not bound to the metal ions in DMF and thus increases the possibility of scavenging ability. The result shows that, the free ligand **L** has less scavenging activity than the $Mn(C_{40}H_{28}N_8O_8Cl_2)$ complex. IC_{50} value of the tested samples is presented in (Table 4, 5 and 6). The $Mn(C_{40}H_{28}N_8O_8Cl_2)$ complex possess higher antioxidant potential (IC_{50}) than vitamin C (standard drugs) and lower than $C_{20}H_{14}N_4O_4$ ligand. The higher IC_{50} value lowers the antioxidant potential.

Table 4. Free radical scavenging activities of (L) in Total Antioxidant Capacity assay (%).

S.No.	Extract Concentration (µg/ml)	TAC Assaay		
		Absorbance	% of SCV	IC_{50}
1.	10	0.507	34.79	63.34
2.	20	0.480	35.02	
3.	30	0.478	37.97	
4.	40	0.420	40.79	
5.	50	0.373	41.10	

Table 5. Free radical scavenging activities of (Mn) in Total Antioxidant Capacity assay (%).

S.No.	Extract Concentration (µg/ml)	TAC Assaay		
		Absorbance	% of SCV	IC_{50}
1.	10	0.630	35.71	55.35
2.	20	0.610	37.75	
3.	30	0.562	42.65	
4.	40	0.557	43.16	
5.	50	0.496	49.38	

P.G.P. COLLEGE OF ARTS & SCIENCE NAMAKKAL 637 206

©2019 IJAIR. All Rights Reserved

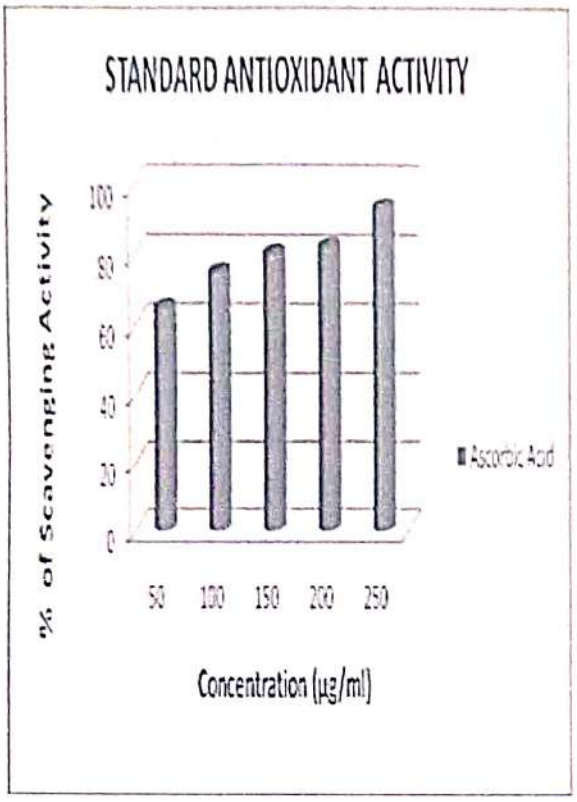
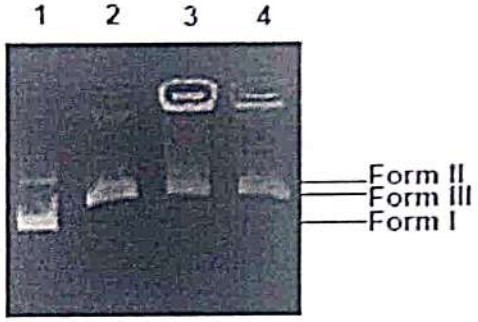


Fig 8. Total Antioxidant Capacity of Ascorbic acid

DNA Cleavage Studies

The representative Mn(II) complexes were studied for their DNA cleavage activity by the agarose gel electrophoresis method, as shown in Fig 4. Control experiments clearly revealed that the untreated DNA and DNA with H_2O_2 do not show any cleavage, indicating non-involvement of the hydroxyl radical in the cleavage reaction, whereas the complexes exhibit cleavage activity on DNA [17]. Metal complex exhibited a degradation effect on the pUC18DNA. The results indicate the important role of metal ions in isolated DNA cleavage reactions. The metal complexes were able to convert supercoiled DNA into open circular DNA. The proposed general oxidative mechanisms and account of DNA cleavage by hydroxyl radicals via abstraction of a hydrogen atom from sugar units, which predict the release of specific residues arising from the transformed sugars, depend on the position from which the hydrogen atom is removed. According to these results, we infer that $Mn(C_{40}H_{28}N_8O_8Cl_2)$ complex and its ligand act as a potent nuclease agents to cleave DNA.



Lane 1 – PUC18 DNA - Control
Lane 2 – DNA + H2O2 (1mM)
Lane 3 – DNA + H2O2 (1mM) + Mn (40µM)
Lane 4 – DNA + H2O2 (1mM) + L (40µM)

Fig 9.Agarose gel electrophoresis pattern showing effect of pUC18DNA induced by H_2O_2 and metal complex. Lane 1-DNA alone; Lane 2- DNA alone + H_2O_2; Lane 3-DNA + $Mn(C_{40}H_{28}N_8O_8Cl_2)$ + H_2O_2; Lane 4-DNA + $C_{20}H_{14}N_4O_4$ + H_2O_2.

©2019 IJAIR. All Rights Reserved

P.G.P. COLLEGE OF ARTS & SCIENCE
NAMAKKAL
637 206

Table 5. Standard Antioxidant Activity

S.No	Standard	Concentration (µg/ml)	Antioxidant Activity % of inhibition
			TAC (695nm)
1	Ascorbic Acid used as a Standard (OD Value)	50	64.71
2		100	74.88
3		150	80.43
4		200	82.28
5		250	93.52

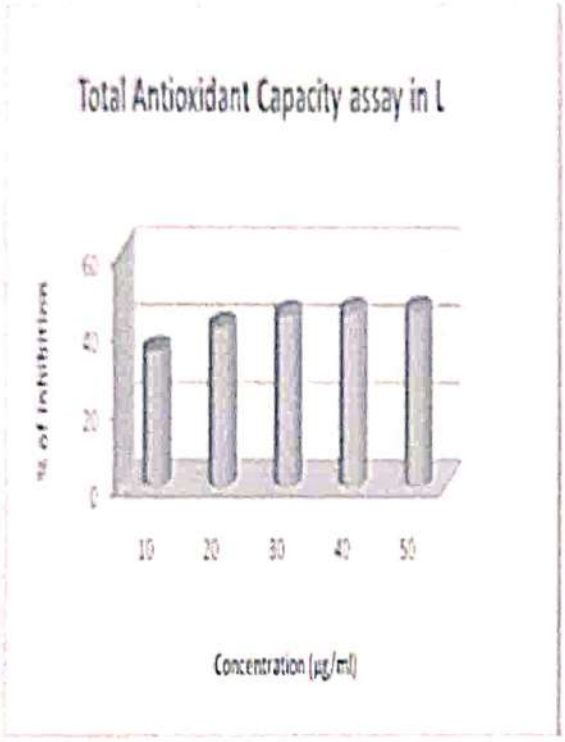


Fig 6. Total Antioxidant Capacity of $C_{20}H_{14}N_4O_4$

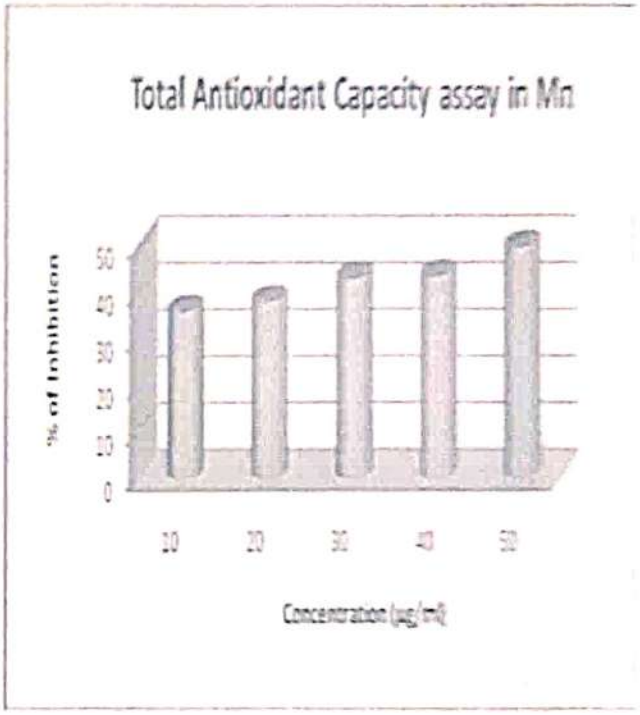


Fig 7. Total Antioxidant Capacity of $Mn(C_{40}H_{28}N_8O_8Cl_2)$

©2019 IJAIR. All Rights Reserved

Conclusion

The design and synthesis of Schiff base and its mononuclear $Mn(C_{40}H_{28}N_8O_8Cl_2)$ complex have been demonstrated in this report. The synthesized compounds were characterized by spectral and analytical data. The molar conductance values indicate that the complex are non-electrolytic in nature. FT-IR spectra reveal that the azomethine stretching frequency observed for $Mn(C_{40}H_{28}N_8O_8Cl_2)$ complex and its ligand suggesting the complex formation and far IR spectra indicate that the chloride ion bonded to the metal ion. The UV-Vis and magnetic moment studies of the complex suggest a distorted octahedral geometry. The DNA cleavage studies reveals that the $Mn(C_{40}H_{28}N_8O_8Cl_2)$ complex cleaved DNA more effectively as compared with the ligand. The antibacterial activity of the $Mn(C_{40}H_{28}N_8O_8Cl_2)$ complex are higher than the ligand. Furthermore, the synthesized ligand and its complex show potent scavenging activity.

REFERENCES

1. F. D. Koria and P. H. Parsania, Asian J. Chem., 11, **1999,** 199.
2. J. Mendham, R. C. Denny, J. D. Barnes, M. J. K. Thomas, Quant. Chem. Anal., 6, **2000.**
3. G.G. Mohamed and Z.H. Abd El-Wahwb, *J. Thermal Anal.*, 73, **2003**, 347.
4. M. A. Ashraf, K. Mahmood and A. Wajid, *Int. Conf. Chem. Chem. Sci., 10*, **2011**, 1.
5. I Kostova and L. Sasa, *Curr. Med. Chem. 20*, **2013,** 4609
6. V. L. Borde, S. S. Shankarwar, C. D. Thanur and A. G. Shankarwar, *Ind. J. Pharm Env Res.*, 5, **2014**, 87
7. G.G. Mohamed and Z.H. Abd El-Wahwb, *J. Thermal Anal.*, 73, **2003**, 347.
8. C. Anitha, C.D. Sheela, P. Tharmaraj and S. Johnson Raja. *Spectrochimica Acta*, 98, **2012,** 35.
9. M. Kurtomglu, M.M. Dagdelen and S. Toroglu, Trans. Met. Chem. 31, **2006,** 382.
10. Q.L. Zhang, J.G. Liu, J.Z. Liu, H. Li, Y. Yang, H. Chao and L.N. Ji, Inorg. Chim. Acta. 34, **2012,** 339.
11. Behrouz Shaabani, Ali Akbar Khandar, Haedeh Mobaiyen, Nahid Ramazani, S. Salete Balula and Luis Cunha-Silva, *Polyhedron,* 31, **2014.**
12. S.I. Kirin, C.M. Happle, S. Hrubanova, T. Weyhermuller, C. Klein and N. Metzler-Nolte, Dalton Trans. 120, **2014.**
13. Priya, Devi and R. H. Hemakumar Singh, *Rasayan. J. Chem.*, 2, **2010**, 266.
14. Sunil Kumar and Tobriya, *Int. J. Sci. Res.*, 5, **2012**, 65.
15. Rishu Katwal, Harpreet Kaur and Brij Kishore Kapur, *Sci. Revs. Chem. Commun.*, 3, **2013**, 69.
16. M. Aidi, H. Keypour, A. Shooshtari, M. Mahmoudabadi, M. Bayat, Z. Ahmadvand, R. Karamian, M. Asadbegy, S. Tavatli, R.W. Gable, *Polyhedron.*, **2019**.
17. D. Dong,s J. Tian and S. Ping Yan, *J. Inorg. Bio. Chem.*, 104, **2014**, 171.

PRINCIPAL
PGP College of Arts and Science
Namakkal.

P.G.P. COLLEGE OF ARTS & SCIENCE NAMAKKAL 637 204

©2019 IJAIR. All Rights Reserved

International Journal of Advanced and Innovative Research (2278-7844)/

Volume 8 Issue 4

SPECTRAL INVESTIGATION AND BIOLOGICAL EVALUATION OF MONONUCLEAR MANGANESE(II) COMPLEX OF A NEWLY SYNTHESIZEDSCHIFF BASE LIGAND DERIVED FROM 4-NITROANILINE AND O-PHTHALADEHYDE

T. Sujeshwari [1], E. Akila [2] & *P. Maheswaran [3*]

[1] Research Scholar, Department of Chemistry, P.G.P college of Arts and science, Namakkal.
[2] Department of Chemistry, Sri Sarada College for women (Autonomous), salem-16.
[3] Principal and Head, Department of Chemistry, P.G.P college of Arts and science, Namakkal.*

ABSTRACT

The aim of the present work was to synthesis Schiff base ligand and its Mn(II) metal complex from the condensation of o- phthalaldehyde and p-nitroaniline. The synthesized Schiff base ligand and metal complex were characterized by elemental analysis, FT-IR, ^{1}H NMR, UV spectral studies. From the observed data, the complex is octahedral geometry for the Mn(II) complex. The biological activity involves antibacterial, antioxidant screening and DNA cleavage showed better activity.

Keywords - Schiff base metal complex, p-nitroaniline, o- phthalaldehyde.

INTRODUCTION

Schiff base is one of the most widely used ligand due to the ease of formation and remarkable versatility. They have played an important role in the development of coordination chemistry as they readily form stable complex with most of the transition metals [1-3]. Mn(II) complex thus play an important role in developing the coordination chemistry, catalyst, enzymatic reaction and bioinorganic modeling studies. Schiff base have wide application in food industry, dye industry, analytical chemistry, fungicidal, agrochemical and biological activities. The research field dealing with Schiff base metal complex is very broad due to their potential interest for a number of interdisciplinary areas that include bioinorganic chemistry and catalyst [4]. Schiff base have been widely used ligand because of high stability of the coordination compounds, and their good solubility in common solvent. In general mechanism of synthesis of Schiff base,an aromatic amine reacts with a carbonyl compound by nueclophilic addition. This form a hemiaminal, followed by dehydration to produce imines carbon-

©2019 IJAIR. All Rights Reserved

PRINCIPAL
PGP College of Arts and Science
Namakkal.

P.G.P. COLLEGE OF ARTS & SCIENCE NAMAKKAL 637 206

nitrogen double bond provides a significant contribution in various progresses of chemical sciences [5].

Physical measurements

Elemental analysis (C, H and N) was performed using a Carlo Eraba 1106 instrument. Molar conductance of the complex in DMF solution was measured using ELICO CM 185 Conductivity Bridge. IR spectra of ligand and its metal complexes were recorded as KBr disk pellets on a perkin Elmer-Spectrum RX-I FTIR spectrophotometer covering the range 4000-200 cm^{-1}. ^{1}H NMR spectra of ligand were recorded on the FT-NMR spectrometer model Bruker Avance II, 400 MHz using d_6-DMSO as solvent.

Synthesis of Schiff base ligand

An equimolar mixture of p- nitroaniline (0.5533) and o- phthalaldehyde (0.2689) in ethanol (30 mL) was refluxed with 21/2 h at 75 ^{0}C. The reaction mixture was cooled to room temperature as a result deep yellow orange compound was obtained. It is separated, filtered and dried.

Synthesis of Mononuclear Schiff base metal complex

The ethanolic solution of synthesized ligand (2mM) was added drop wise to an ethanolic solution of the metal salt(1mM) (0.3963) with costant stirring, and the mixture was boiled under reflux for 4 ½ hrs. Then the volume of the reaction mixture was reduced by evaporation. The precipitated complex were filtered off, washed with ethanol and then dried in air.

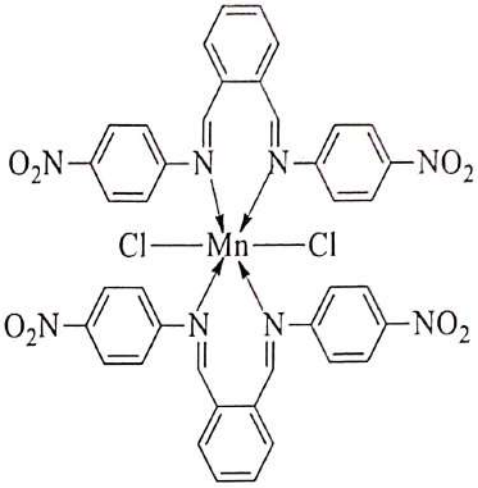


Fig 1. Synthesis of Mn(II) Schiff base metal complex

Antibacterial Studies

The synthesized Schiff base and corresponding Mn (II) complex were screened for their biological activities against four bacterial strains namely Klebsiella pneumonia, Escherichia coli, Staphylococcus aurous and Bacillus subtilis. The bacterial strains were sub cultured individually in nutrient agr medium [6].The plates were incubated for 24h at 37 ^{0}C. During the incubation period the test solution diffused and the growth of the inoculated microorganism was affected. This inhibition zone was noted. The standard antibacterial drug was compared with our synthesized compounds.

©2019 IJAIR. All Rights Reserved

http://ijairjournal.com



Total antioxidant capacity assay

Different concentrations (10 µl, 20 µl, 30 µl, 40 µl and 50 µl) of synthesized compounds were taken and 1ml of reagent solution was added. [Reagent solution: 0.6 M sulphuric acid, 28 mM sodium phosphate and 4 mM Ammonium molybdate]. The tubes were capped and incubated in thermal block at 95°C for 90 minutes. After the time interval the tubes were cool down at room temperature.The absorbance was recorded at 695 nm using shimadzu UV 1800 spectrophotometer [7].

Calculation of 50% Inhibitory Concentration (IC_{50})

The concentration (mg/ ml) of the fractions that was required to scavenge 50% of the radicals was calculated by using the percentage scavenging activities at five different concentrations of the fractions.

Percentage inhibition (I %) was calculated using the formula,

I % = (Ac-As) / Ac x 100

Where, Ac = absorbance of the control and

As = absorbance of the sample.

TAC = Total Antioxidant Capacity assay

DNA Cleavage experiment

The DNA cleavage of supercoiled pUC18DNA promoted by metal complex was proceeded by addition of reaction mixture (40µl). The reaction mixture (40µl) containing pUC18 DNA, 50mM Tris-HCl, pH 7.4, 50mm NaCl, 10mM H_2O_2 added in a different volume, followed by adding Millipore water for final volume. Then the mixed solutions were incubated at 37 °C for 1 hr. They checked by agarose electrophoresis methods.

RESULTS AND DISCUSSION

All the synthesized Schiff base ligands metal complex were highly coloured, they are insoluble in water, absolutly soluble in alcoholic solution and sparingly soluble in organic solvents. The synthesized metal complex are soluble in absolute alcohol and found to be a stable upto certain temperature. The elemental analysis analytical data of the newly synthesized Schiff bases and their metal complexes were recorded in Table 1.

©2019 IJAIR. All Rights Reserved

PRINCIPAL
PGP College of Arts and Science
Namakkal.

P.G.P. COLLEGE OF ARTS & SCIENCE NAMAKKAL

Table 1. Analytical data of the Schiff base ligand and its mononuclear metal complex

Compounds	Molecular Formula	Color	Yield (%)	Melting Point (°c)	% of Nitrogen		% of Metal	
					Cal	Exp	Cal	Exp
L	$C_{20}H_{14}N_4O_4$	Yellowish orange	75	145	15	14.7	-	-
ML_2X_2	$Mn(C_{40}H_{28}N_8O_8Cl_2)$	Dark Green	65	>200	12.7	12.8	6.3	6.1

Molar conductivity

The molar conductance values at 10^{-3} M concentration were too low to account for any dissociation of the complexes in DMF. Hence, Mn(II) complex may be regarded as non electrolytes. Molar conductance values have been complied. The lower conductance value in the range of 9.20 Ω^{-1} cm^2 mol^{-1} of the chelates supports their non-electrolytic nature of the metal complex [8].

IR spectral analysis

The IR spectra of the reported ligand and its complex were measured as KBr disk and the important spectral features along with their tentative assignments are given in Table 2.

The comparison of the IR spectra of Schiff base (and its metal complexes indicated that the ligands are principally coordinated to the metal ions. The band appearing at ~ 1655.34 cm^{-1}due to azomethine linkage [9] in the ligands is shifted by indicating the participation of the azomethine nitrogen in interaction with the metal ion. Lowering of (C=N) in the complex as compared to the ligand (1653.02 cm^{-1}) indicates the coordination of metal ion to ligand [10]. Metal- ligand bond is further confirmed by the appearance of a medium intensity band in the range 483.56 and 320.10 cm^{-1} in the spectra of the complex assigned to stretching frequencies of (M-N) bond and (M-Cl) bond formation respectively [11].

Table 2. IR spectra data (4000–200 cm^{-1}) of Schiff base and its metal complex

Compounds	υ(C=N) (cm^{-1})	υ(M-Cl) (cm^{-1})	υ(M-N) (cm^{-1})
$C_{20}H_{14}N_4O_4$	1655.34	--	--

©2019 IJAIR. All Rights Reserved

http://ijairjournal.com

P.G.P. COLLEGE OF ARTS & SCIENCE NAMAKKAL 637 206

$Mn(C_{40}H_{28}N_8O_8Cl_2)$	1653 02	320 10	483 56

Electronic Spectral data

A moderately intensive band was observed in the range of 345- 382 nm which might be due to n-π* transition and strong band was observed in the range of 294- 365 nm due to π- π* interactions [10]. The electronic spectra of Mn(II) complexes show the absorption bands in the range 565, 595, 630 nm. These absorption bands may be assigned to the $^6A_1g \rightarrow {}^4A_1g$, $^6A_1g \rightarrow {}^4A_2g$, and $^6A_1g \rightarrow {}^4Eg$, ^4A_1g transitions, respectively [12]. These bands suggest that the complexes possess a distorted octahedral geometry.

Table 3. Electronic Spectral data of Schiff base ligand and its Mn(II) complex.

Compound	Electronic spectra (nm)				Geometry of the complex
	π→π*	n→π*	L→M	d-d	
$C_{20}H_{14}N_4O_4$	365	382	-	-	-
$Mn(C_{40}H_{28}N_8O_8Cl_2)$	294	345	405	565, 595, 630	Distorted Octahedral

^{1}H – NMR Spectral studies

The ^{1}H-NMR spectra of the Schiff base ligand was measured at room temperature in DMSO- d_6. The spectrum of the Schiff base ligand exhibits a singlet signal in the 8.48 ppm, which is attributed to the azomethine group (–CH=N–) proton and the multiplets around 6.6-7.9 ppm are assigned due to aromatic protons [13].

***In Vitro* Antibacterial Activity**

The in vitro antibacterial activity of all the synthesized compounds was screened against gram positive and gram negative bacteria. The complex exhibited promising results compared to the ligand against mentioned microorganisms, and this activity is found to been enhanced on coordination with the metal ions. This enhancement in the activity may be to the structures of Schiff base ligand by possessing an azomethine (C=N) linkage [14]. The toxic activity of the complexes with the ligand can be ascribed to the increase in the lipophilic nature of the complexes arising from chelation. The higher activity of $Mn(C_{40}H_{28}N_8O_8Cl_2)$ complex can be explained as, on chelation the polarity of metal ion is found to be reduced to a greater extent due to the overlap of the ligand orbital and partial sharing of the positive charge of the copper ion with donor groups. Therefore, metal ion is adsorbed on the surface of the cell wall of microorganisms. The adsorbed metal ion disturb the respiratory process of the cells, thus blocking the synthesis of proteins and this, in turn, restricts further growth of the organisms [15]. The result shows that the $Mn(C_{40}H_{28}N_8O_8Cl_2)$ complex

©2019 IJAIR. All Rights Reserved

http://ijairjournal.com

P.G.P. COLLEGE OF ARTS & SCIENCE NAMAKKAL 637 206

exhibit antibacterial activity and enhanced it comparing with the parent Schiff base.

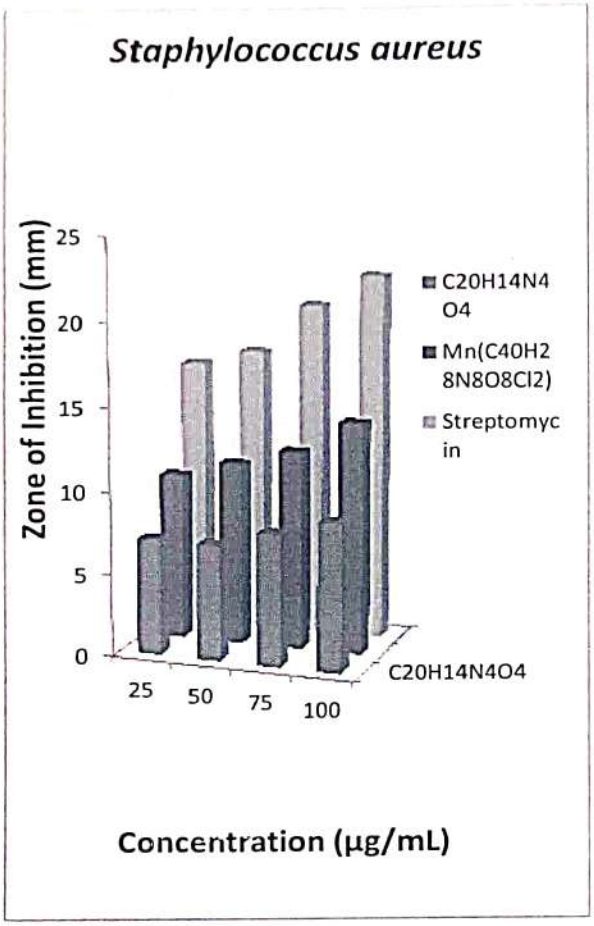


Fig 2. Antibacterial activity of Schiff base ligand and its mononuclear Schiff base metal complex against *Staphylococcus aureus*

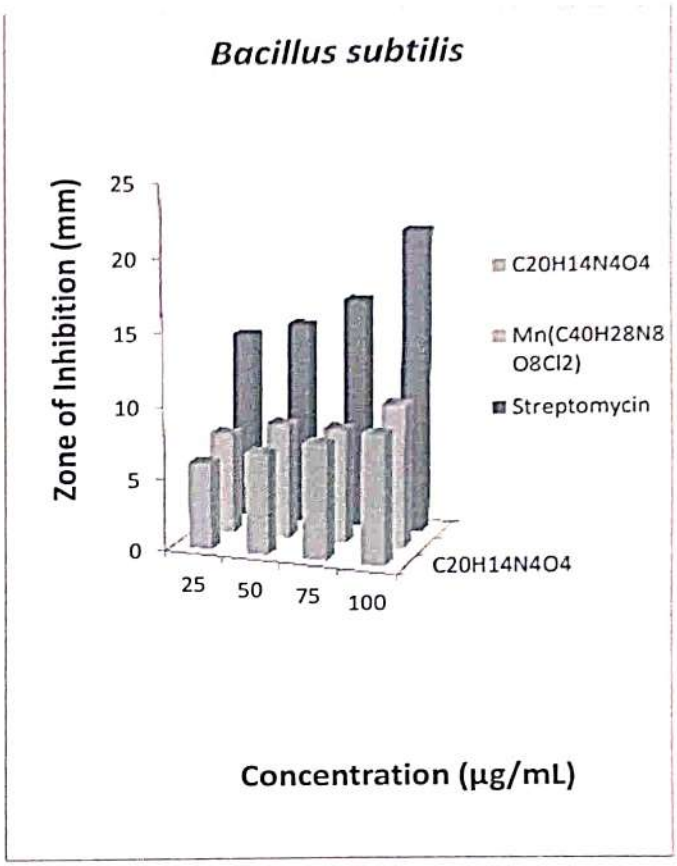


Fig 3. Antibacterial activity of Schiff base ligand and its mononuclear Schiff base metal complex against *Bacillus subtilis*

©2019 IJAIR. All Rights Reserved

P.G.P. COLLEGE OF ARTS & SCIENCE NAMAKKAL 637 206

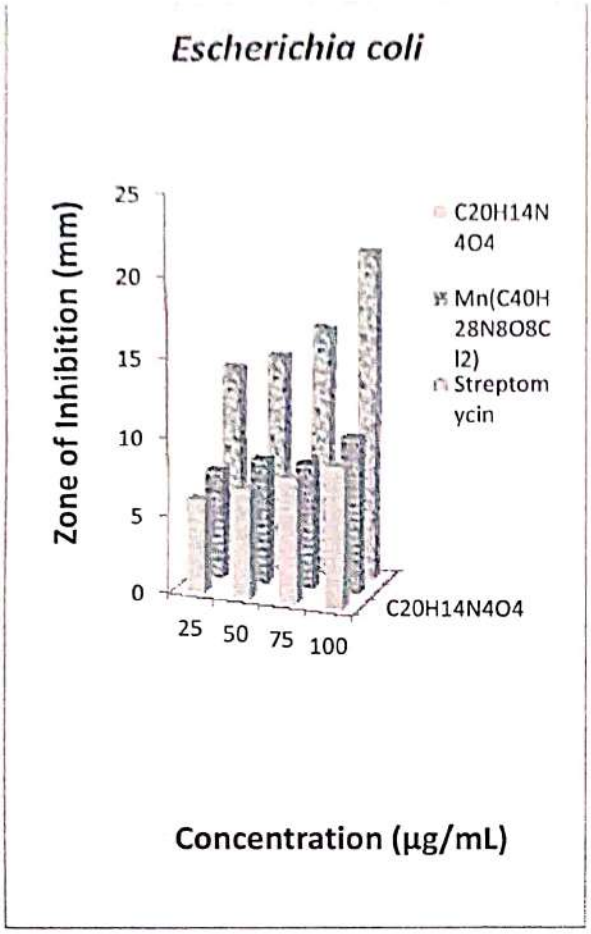


Fig 4. Antibacterial activity of Schiff base ligand and its mononuclear Schiff base metal complexes against *Escherichia coli*

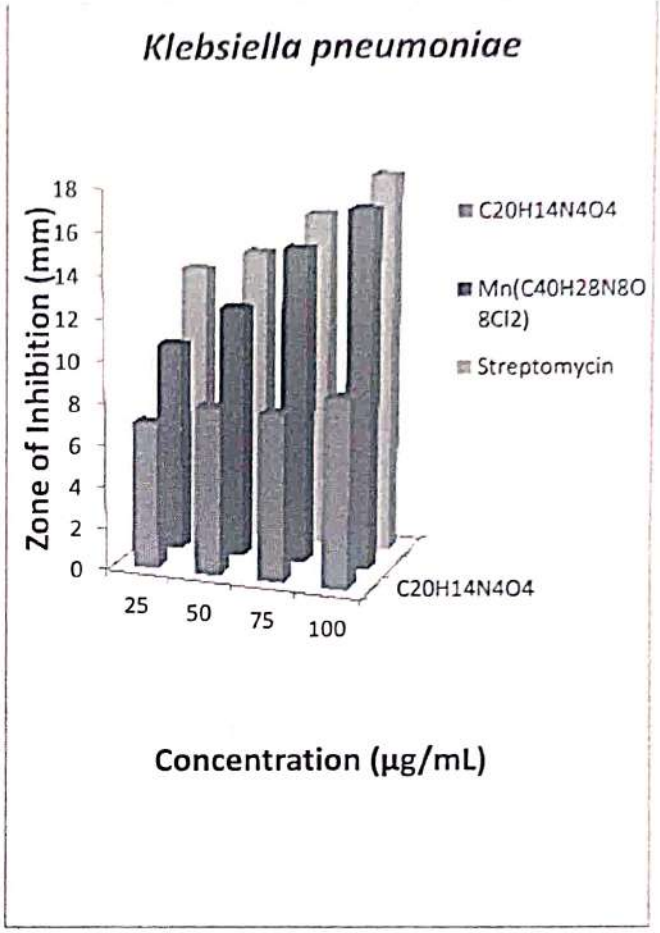


Fig 5. Antibacterial activity of Schiff base ligand and its mononuclear Schiff base metal complex against *Klebsiella pneumonia*

Antioxidant Activity

The antioxidant activity of the ligand and its $Mn(C_{40}H_{28}N_8O_8Cl_2)$ complex have attracted increasing interests and been substantially investigated [16]. Figure 7 & 8 shows the free radical scavenging activity for the ligand and its Mn(II) complex. It is obvious that the scavenging activity

©2019 IJAIR. All Rights Reserved

P.G.P. COLLEGE OF ARTS & SCIENCE NAMAKKAL 637 206

increases with increasing sample concentration in the range tested. Ascorbic acid (vitamin C) is used as standard. As shown in Figure 7 & 8 Mn(II) complex possess more efficient activity in quenching free radical than the free ligand L. When the ligand L interacts with the positively charged metal ions, electron density is drawn from the oxygen. This flow of electron density causes the O–H bond to become more polarized; as a result, the H atom have a greater tendency to ionize than those in the free ligand L not bound to the metal ions in DMF and thus increases the possibility of scavenging ability. The result shows that, the free ligand **L** has less scavenging activity than the $Mn(C_{40}H_{28}N_8O_8Cl_2)$ complex. IC_{50} value of the tested samples is presented in (Table 4, 5 and 6). The $Mn(C_{40}H_{28}N_8O_8Cl_2)$ complex possess higher antioxidant potential (IC_{50}) than vitamin C (standard drugs) and lower than $C_{20}H_{14}N_4O_4$ ligand. The higher IC_{50} value lowers the antioxidant potential.

Table 4. Free radical scavenging activities of (L) in Total Antioxidant Capacity assay (%).

S.No.	Extract Concentration (µg/ml)	TAC Assaay		
		Absorbance	% of SCV	IC_{50}
1.	10	0.507	34.79	63.34
2.	20	0.480	35.02	
3.	30	0.478	37.97	
4.	40	0.420	40.79	
5.	50	0.373	41.10	

Table 5. Free radical scavenging activities of (Mn) in Total Antioxidant Capacity assay (%).

S.No.	Extract Concentration (µg/ml)	TAC Assaay		
		Absorbance	% of SCV	IC_{50}
1.	10	0.630	35.71	55.35
2.	20	0.610	37.75	
3.	30	0.562	42.65	
4.	40	0.557	43.16	
5.	50	0.496	49.38	

P.G.P. COLLEGE OF ARTS & SCIENCE NAMAKKAL 637 206

©2019 IJAIR. All Rights Reserved

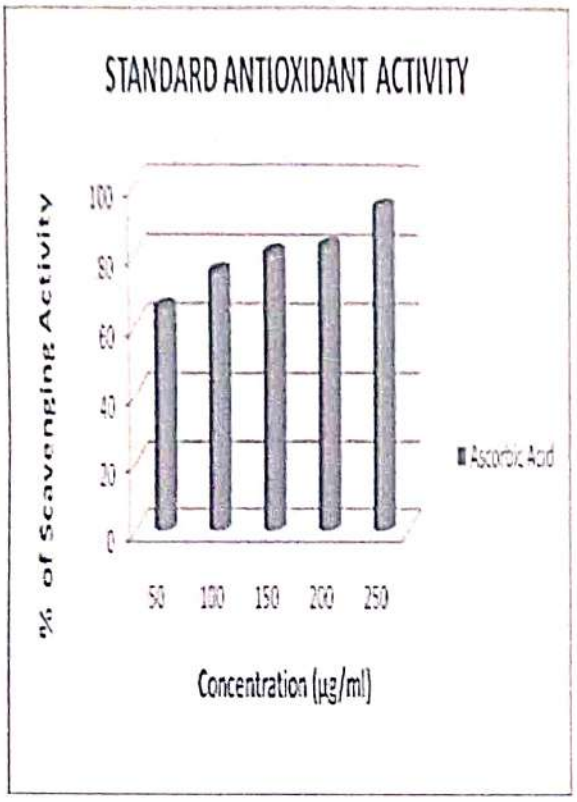
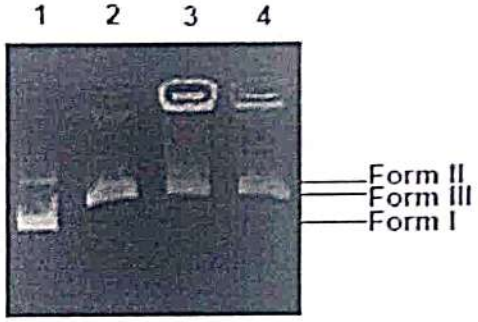


Fig 8. Total Antioxidant Capacity of Ascorbic acid

DNA Cleavage Studies

The representative Mn(II) complexes were studied for their DNA cleavage activity by the agarose gel electrophoresis method, as shown in Fig 4. Control experiments clearly revealed that the untreated DNA and DNA with H_2O_2 do not show any cleavage, indicating non-involvement of the hydroxyl radical in the cleavage reaction, whereas the complexes exhibit cleavage activity on DNA [17]. Metal complex exhibited a degradation effect on the pUC18DNA. The results indicate the important role of metal ions in isolated DNA cleavage reactions. The metal complexes were able to convert supercoiled DNA into open circular DNA. The proposed general oxidative mechanisms and account of DNA cleavage by hydroxyl radicals via abstraction of a hydrogen atom from sugar units, which predict the release of specific residues arising from the transformed sugars, depend on the position from which the hydrogen atom is removed. According to these results, we infer that $Mn(C_{40}H_{28}N_8O_8Cl_2)$ complex and its ligand act as a potent nuclease agents to cleave DNA.



Lane 1 – PUC18 DNA - Control
Lane 2 – DNA + H2O2 (1mM)
Lane 3 – DNA + H2O2 (1mM) + Mn (40µM)
Lane 4 – DNA + H2O2 (1mM) + L (40µM)

Fig 9.Agarose gel electrophoresis pattern showing effect of pUC18DNA induced by H_2O_2 and metal complex. Lane 1-DNA alone; Lane 2- DNA alone + H_2O_2; Lane 3-DNA + $Mn(C_{40}H_{28}N_8O_8Cl_2)$ + H_2O_2; Lane 4-DNA + $C_{20}H_{14}N_4O_4$ + H_2O_2.

©2019 IJAIR. All Rights Reserved

P.G.P. COLLEGE OF ARTS & SCIENCE
NAMAKKAL
637 206

Table 5. Standard Antioxidant Activity

S.No	Standard	Concentration (µg/ml)	Antioxidant Activity % of inhibition
			TAC (695nm)
1	Ascorbic Acid used as a Standard (OD Value)	50	64.71
2		100	74.88
3		150	80.43
4		200	82.28
5		250	93.52

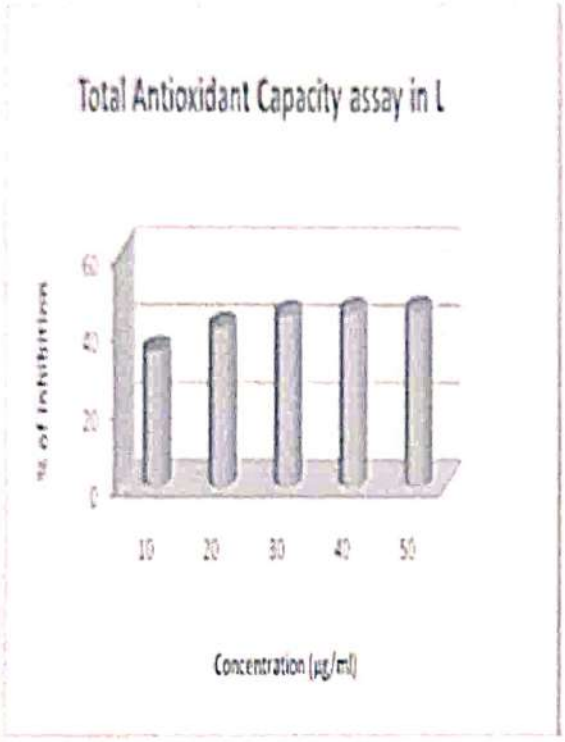


Fig 6. Total Antioxidant Capacity of $C_{20}H_{14}N_4O_4$

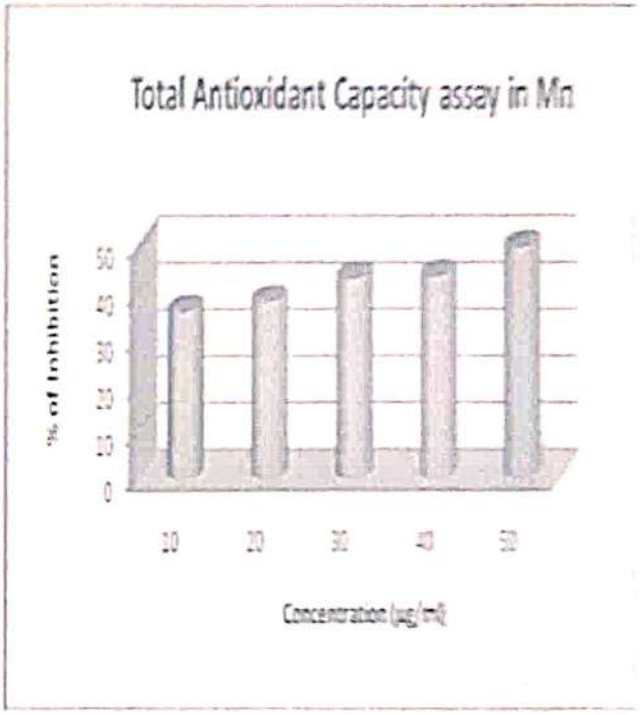


Fig 7. Total Antioxidant Capacity of $Mn(C_{40}H_{28}N_8O_8Cl_2)$

©2019 IJAIR. All Rights Reserved

Conclusion

The design and synthesis of Schiff base and its mononuclear $Mn(C_{40}H_{28}N_8O_8Cl_2)$ complex have been demonstrated in this report. The synthesized compounds were characterized by spectral and analytical data. The molar conductance values indicate that the complex are non-electrolytic in nature. FT-IR spectra reveal that the azomethine stretching frequency observed for $Mn(C_{40}H_{28}N_8O_8Cl_2)$ complex and its ligand suggesting the complex formation and far IR spectra indicate that the chloride ion bonded to the metal ion. The UV-Vis and magnetic moment studies of the complex suggest a distorted octahedral geometry. The DNA cleavage studies reveals that the $Mn(C_{40}H_{28}N_8O_8Cl_2)$ complex cleaved DNA more effectively as compared with the ligand. The antibacterial activity of the $Mn(C_{40}H_{28}N_8O_8Cl_2)$ complex are higher than the ligand. Furthermore, the synthesized ligand and its complex show potent scavenging activity.

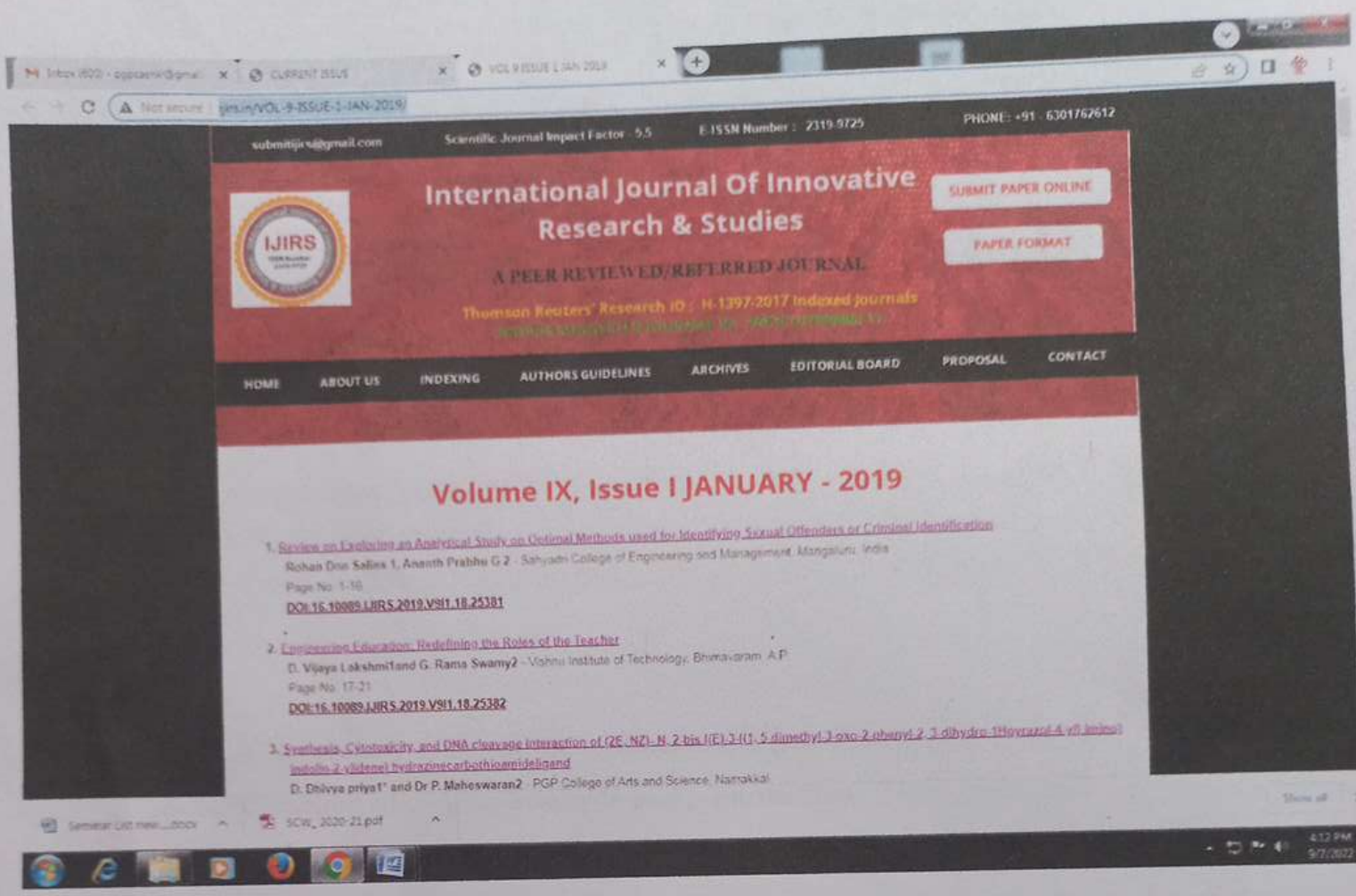
REFERENCES

1. F. D. Koria and P. H. Parsania, Asian J. Chem., 11, **1999,** 199.
2. J. Mendham, R. C. Denny, J. D. Barnes, M. J. K. Thomas, Quant. Chem. Anal., 6, **2000.**
3. G.G. Mohamed and Z.H. Abd El-Wahwb, *J. Thermal Anal.*, 73, **2003**, 347.
4. M. A. Ashraf, K. Mahmood and A. Wajid, *Int. Conf. Chem. Chem. Sci., 10*, **2011**, 1.
5. I Kostova and L. Sasa, *Curr. Med. Chem. 20*, **2013,** 4609
6. V. L. Borde, S. S. Shankarwar, C. D. Thanur and A. G. Shankarwar, *Ind. J. Pharm Env Res.*, 5, **2014**, 87
7. G.G. Mohamed and Z.H. Abd El-Wahwb, *J. Thermal Anal.*, 73, **2003**, 347.
8. C. Anitha, C.D. Sheela, P. Tharmaraj and S. Johnson Raja. *Spectrochimica Acta*, 98, **2012,** 35.
9. M. Kurtomglu, M.M. Dagdelen and S. Toroglu, Trans. Met. Chem. 31, **2006,** 382.
10. Q.L. Zhang, J.G. Liu, J.Z. Liu, H. Li, Y. Yang, H. Chao and L.N. Ji, Inorg. Chim. Acta. 34, **2012,** 339.
11. Behrouz Shaabani, Ali Akbar Khandar, Haedeh Mobaiyen, Nahid Ramazani, S. Salete Balula and Luis Cunha-Silva, *Polyhedron,* 31, **2014.**
12. S.I. Kirin, C.M. Happle, S. Hrubanova, T. Weyhermuller, C. Klein and N. Metzler-Nolte, Dalton Trans. 120, **2014.**
13. Priya, Devi and R. H. Hemakumar Singh, *Rasayan. J. Chem.*, 2, **2010**, 266.
14. Sunil Kumar and Tobriya, *Int. J. Sci. Res.*, 5, **2012**, 65.
15. Rishu Katwal, Harpreet Kaur and Brij Kishore Kapur, *Sci. Revs. Chem. Commun.*, 3, **2013**, 69.
16. M. Aidi, H. Keypour, A. Shooshtari, M. Mahmoudabadi, M. Bayat, Z. Ahmadvand, R. Karamian, M. Asadbegy, S. Tavatli, R.W. Gable, *Polyhedron.*, **2019**.
17. D. Dong,s J. Tian and S. Ping Yan, *J. Inorg. Bio. Chem.*, 104, **2014**, 171.

PRINCIPAL
PGP College of Arts and Science
Namakkal.

P.G.P. COLLEGE OF ARTS & SCIENCE NAMAKKAL 637 204

©2019 IJAIR. All Rights Reserved



COLLEGE OF ARTS & SCIENCE
NAMAKKAL

DNA CLEAVAGE, ANTIOXIDANT AND ANTIBACTERIAL STUDIES OF COPPER(II) COMPLEX DERIVED FROM N, N'-(1, 2 PHENYLENEBIS(METHANYLYLIDENE)) BIS(4-NITROANILINE)

T. Sujeshwari [1], E. Akila [2] & *P. Maheswaran [3*]

[1] Research Scholar, Department of Chemistry, P.G.P college of Arts and science, Namakkal.
[2] Department of Chemistry, Sri Sarada College for women (Autonomous), salem-16.
[3*] Principal and Head, Department of Chemistry, P.G.P college of Arts and science, Namakkal.

ABSTRACT

Objective: The aim of the present work was to synthesize the Schiff base ligand and its Copper(II) metal complex from the condensation of o-phthalaldehyde and p-nitroaniline. The synthesized Schiff base and its metal complex were characterized by elemental analysis, FTIR, ^{1}HNMR and UV spectral studies. **Results:** The study reveals that the Schiff base ligand implicated the N_4 donor atom. On the basis of spectral data, distorted octahedral geometry is proposed for the Cu(II) complex. The Schiff base and its metal complex were screened for their antibacterial, antioxidant and DNA cleavage activities. **Conclusion:** The Cu(II) complex exhibited good antimicrobial activity when compared to the free ligand.

KEYWORDS: Schiff base, antibacterial, antioxidant activities and DNA cleavage

INTRODUCTION:

Schiff base acts as active ligands due to the presence of low electronegativity of nitrogen, of the azomethine group (>C=N), lone pair of electrons on the nitrogen atom, electron donating character of the double bond [1-2]. An interesting application of Schiff bases is their use as an effective corrosion inhibitor, which is based on their ability to spontaneously form a monolayer on the surface to be protected. Schiff base and its metal complex had a variety of applications including biological, clinical, analytical and industrial in addition to their important roles in catalysis and organic synthesis. The present developments of Schiff bases and metal complexes are more fascinating. Metal complexes of Schiff bases have been extensively studied due to synthetic flexibility, selectivity and sensitivity towards a variety of metal atoms. The strong attraction for the bonding of Schiff bases to inner and non-inner transition metal ions is essential in the synthesis of metal complex. The aim of this work deals with the synthesis, spectral

© 2019 DNA

characterization like elemental analysis, FTIR, UV and ^{1}HNMR, antibacterial, antioxidant, DNA cleavage activities of mononuclear Schiff base Cu(II) metal complex [3-4].

Analysis and physical measurement

The elemental analysis (Carbon, Hydrogen and Nitrogen) was performed on a Carlo Eraba 1106 instrument. Molar conductivity of the complex in DMF solution was measured using ELICO CM 185 conductivity Bridge. The Infrared spectra were recorded on the Perkin Elmer FT-IR-8300 model spectrometer using KBr disc in the region 4000 - 200 cm^{-1}. Electronic absorption spectra in the UV-Vis range were recorded on Double beam spectrometer Cyber lab between 200 – 800 nm by using DMF as the solvent. ^{1}H-NMR spectra of the ligand were recorded on Bruker Spectrometer at 400 MHZ in DMSO. The chemical shifts are given in PPM, using Tetramethylsilane (TMS) as the internal reference.

Synthesis of N, N'-(1, 2-phenylenebis(methanylylidene))bis(4-nitroaniline)

The Schiff base ligand was synthesized by adding o-phthalaldehyde (1 mM) in 20 ml of ethanol, and p-nitroaniline (2 mM) in 20 ml of ethanol. This condensation reaction was carried out by using acid catalyst (few drops of HCl). The mixture was refluxed for 2 ½ hrs. After completion of the reaction, the mixture was reduced to half of its original volume using water bath and kept aside at room temperatureand coloured precipitate was collected and dried in air [5].

Synthesis of mononuclear Schiff base metal complex

The ethanolic solution of synthesized ligand (2 mM) was added drop wise to an ethanolic solution of the metal salt (1 mM) with constant stirring, and the mixture was boiled under reflux for 4 ½ hrs. Then, the volume of the reaction mixture was reduced by evaporation. The precipitated complex were filtered off, washed with ethanol and then dried in vacuuo [6].

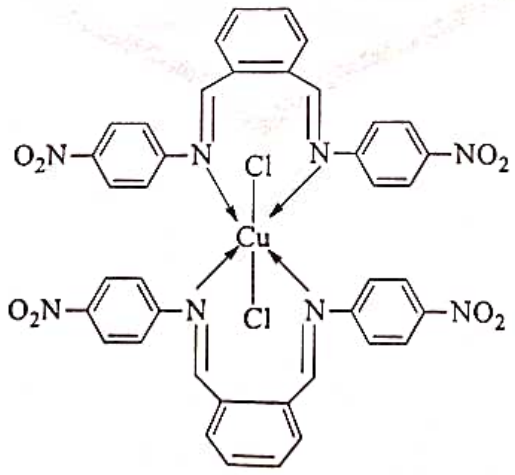


Fig 1. Synthesis of Cu(II) Schiff base metal complex

P.G.P. COLLEGE OF ARTS & SCIENCE NAMAKKAL 637 206

DNA cleavage activity

Gel electrophoresis

The DNA cleavage of supercoiled pUC18DNA promoted by metal complex was proceeded by addition of reaction mixture (40µl). The reaction mixture (40µl) containing pUC18DNA, 50mM Tris-HCl, pH 7.4, 50 mm NaCl, 10 mM H_2O_2 added in a different volume, followed by adding Millipore water for final volume. Then the mixed solutions were incubated at 37° C for 1 hr. They checked by agarose electrophoresis methods [7].

Antibacterial activity

The antibacterial screening effects of the Schiff base ligand and their corresponding Cu(II) complex were tested against four bacterial strains namely *Bacillus subtilis, Staphylococcus aureus, Klebsilla pneumonia and Escherichia coli* by disc diffusion method, using nutrient agar medium. The compounds were dissolved in DMF. The plates were incubated aerobically at 37° C for 24 hours and the antimicrobial activity was assessed by measuring the inhibition of microbial growth around the well. This method involves the exposure of the zone inhibition toward the diffusion of micro-organism on agar plate [8].

Total antioxidant capacity assay

- Different concentrations (10 µl, 20 µl, 30 µl, 40 µl and 50 µl) of synthesized compounds were taken and 1ml of reagent solution was added. [Reagent solution: 0.6 M sulphuric acid, 28 mM sodium phosphate and 4 mM Ammonium molybdate.
- The tubes were capped and incubated in thermal block at 95°C for 90 minutes.
- After the time interval the tubes were cool down at room temperature.
- The absorbance was recorded at 695 nm using shimadzu UV 1800 spectrophotometer [9].

RESULTS AND DISCUSSION:

The synthesized compounds i.e. Schiff base and its Cu(II) complex were coloured, stable in air and non-hygroscopic. They were sparingly soluble in common organic solvents; however, these synthesized compounds were completely soluble in DMF and DMSO. Schiff base and its metal complex were obtained in good yield. The molar conductance value at 10^{-3} M concentration were too low to account for any dissociation of the complex in DMF. Hence, the Cu(II) complex may be regarded as nonelectrolyte. The spectral and analytical data showed the formula of the complex is ML_2X_2 type, where L = Schiff base ligand X = chloride ions and M = Cu(II). The elemental analysis data shows the formation of Cu(II) complex is in 2:1 [L:M] stoichoimetry ratio.

P.G.P. COLLEGE OF ARTS & SCIENCE NAMAKKAL 637 206

Table 1. Analytical and physical data of synthesized N, N'-(1, 2-phenylenebis(methanylylidene))bis(4-nitroaniline) and its corresponding metal complex

Compound	Molecular formula	Colour	Yield %	Melting point (°C)	% of Nitrogen		% of Metal	
					Cal	Exp	Cal	Exp
L	$C_{20}H_{14}N_4O_4$	Yellowish orange	75	145	15.0	14.8	-	-
CuL_2X_2	$Cu(C_{40}H_{28}N_8O_8Cl_2)$	Black	70	>200	12.6	12.4	7.2	6.8

IR spectral studies

The important IR frequencies of the Schiff base and its Cu (II) complex are presented in Table 2. In order to study the binding mode of the Schiff base to metal ions, the IR spectrum of the free Schiff base was compared with the IR spectrum of the metal complex. The comparative analysis of the IR spectra of the complex and of the free ligand revealed that the absorption band characteristic of the stretching vibrations of υ(C=N) (azomethine group) is shifted towards lower wave number from 1655.34 cm^{-1} in the spectrum of the ligand to 1649.42 cm^{-1} in the complex. This indicates the coordination of the nitrogen of this group with the metal ion. In addition, the appearance of new band at 335.10 cm^{-1} showing the involvement of M–Cl bond in complex formation, supporting the IR spectral study. Further coordination of metal to azomethine nitrogen is confirmed by a new band at 530.88 cm^{-1} with the involvement of nitrogen in the coordination with metal ion [10] due to (M–N).

Table 2. IR spectral data (4000–200 cm^{-1}) of Schiff base and its metal complex

Compounds	υ(C=N) (cm^{-1})	υ(M-Cl) (cm^{-1})	υ(M-N) (cm^{-1})
$C_{20}H_{14}N_4O_4$	1655.34	--	--
$Cu(C_{40}H_{28}N_8O_8Cl_2)$	1649.42	335.10	530.88

Electronic spectra and magnetic moment studies

The electronic spectral data of the synthesized compounds in DMF solution are displayed in Table 3. Electronic spectra of the ligand and $Cu(C_{40}H_{28}N_8O_8Cl_2)$ complex were obtained in DMF medium .The nature of the ligand field around the metal ion was deduced from the electronic spectra. The ^2Eg and ^2T_2g states of the octahedral Cu(II) (d^9) split under the influence of the distortion and the distortion can be such as to cause the $^2B_1g \rightarrow {}^2Eg$ transition to remain unresolved in the spectra. Further the d-d transition showed

NAMAKKAL 637 206

a strong band at 655 nm for Cu(II) complex. This is due to $^2B_1g \rightarrow ^2Eg$ transition suggesting that Cu(II) is in distorted octahedral geometry [11]. In the spectrum of the Schiff base ligand, the absorption band observed at 365 and 312 nm were assigned to intra-ligand $\pi \rightarrow \pi^*$ transition and the band at 382 and 378 nm were assigned due to $n \rightarrow \pi^*$ transition associated with the azomethine chromophore (-C=N). The magnetic moment of 1.97 B.M. falls within the range normally observed for octahedral Cu(II) complex.

Table 3. Electronic Spectral data of Schiff base ligand and its Cu(II) complex

Compound	Electronic spectra (nm)				Geometry of the complex
	$\pi \rightarrow \pi^*$	$n \rightarrow \pi^*$	L→M	d-d	
$C_{20}H_{14}N_4O_4$	365	382	-	-	-
$Cu(C_{40}H_{28}N_8O_8Cl_2)$	312	378	410	655	Distorted Octahedral

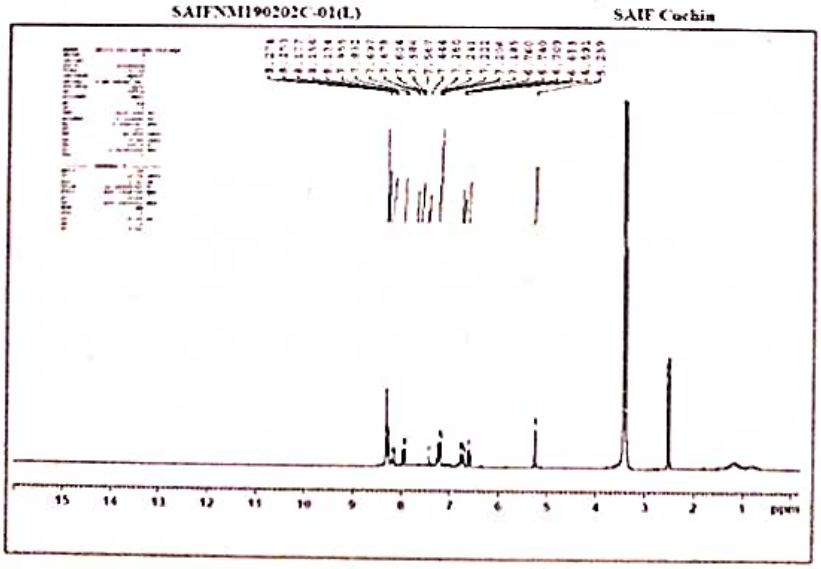
^{1}H – NMR Spectra

The ^{1}H NMR spectrum of the Schiff base was recorded in DMSO- d_6 at room temperature. The ^{1}H NMR spectrum of the Schiff base ligand exhibits well resolved signals and significant differences in their chemical shifts.

Two different type of protons were identified

i) The multiplets at around 6.6-7.9 ppm are assigned to aromatic protons,

ii) The azomethine group in the Schiff base appears 8.48 ppm was observed [12].



P.G.P. COLLEGE OF ARTS & SCIENCE NAMAKKAL 637 206

Fig 2. ^{1}H NMR spectrum of $C_{20}H_{14}N_4O_4$

Antibacterial screening

The antibacterial activity of the ligand and its $Cu(C_{40}H_{28}N_8O_8Cl_2)$ complex was studied by using Steptomycin as positive standard. The Cu(II) complex was found to show bactericidal activity against selected types of bacteria such as *Staphylococcus aureus, Bacillus subtilis, Escherichia coli* and *Klebsilla pneumonia* respectively. In general, complexes have been shown to be more effective than the free ligand and the same was observed in this study, i.e., the Cu(II) complex is more active than the parent ligand. The variation in the activity of complex against different organisms depends either on the impermeability of cells of the microbes or differences in the ribosomes of microbial cells [13]. The higher antibacterial activity of M-complex than the free Schiff base ligand can be explained by chelation theory. From the results it is observed that $Cu(C_{40}H_{28}N_8O_8Cl_2)$ complex is more active than the free ligand .

Anti-oxidant assay

The newly synthesized ligand and its $Cu(C_{40}H_{28}N_8O_8Cl_2)$ complex were investigated for their antioxidant properties by total antioxidant capacity assay [14]. Fig 4 & 5 and Table 5 & 6 demonstrate the free radical scavenging activity of $Cu(C_{40}H_{28}N_8O_8Cl_2)$ complex and its ligand. The decreasing absorbance as well as the lower IC_{50} value indicated the higher antioxidant activity of test compounds. From the result it is observed that the free radical scavenging activity of complex is better than $C_{20}H_{14}N_4O_4$ free ligand but lower than that of standard ascorbic acid (vitamin C).

Table 4. Standard Antioxidant Activity

S.No.	Standard	Concentration (µg/ml)	Antioxidant Activity% of inhibition
			TAC (695nm)
1.	Ascorbic Acid used as a Standard (OD Value)	50	64.71
2.		100	74.88
3.		150	80.43
4.		200	82.28
5.		250	93.52

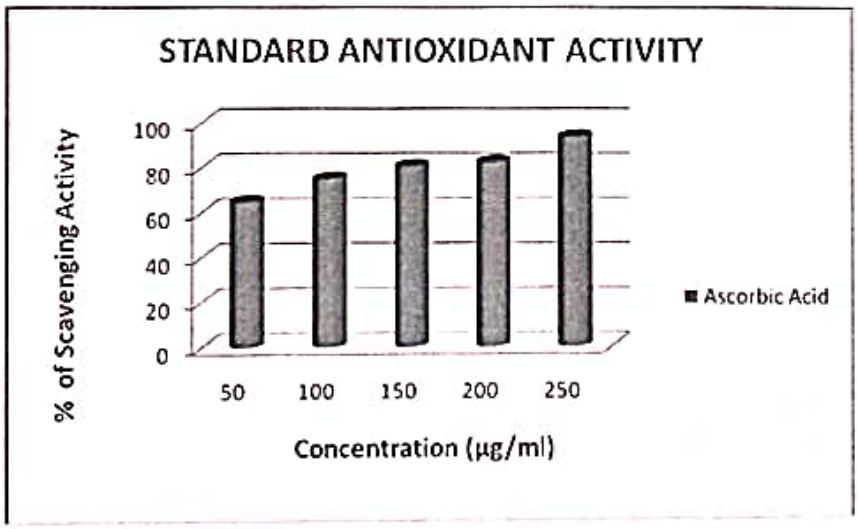


Table 5. Free radical scavenging activities of (L) in Total Antioxidant Capacity assay (%).

S.No.	Compound Concentration (µg/ml)	TAC Assaay		
		Absorbance	% of SCV	IC_{50}
1.	10	0.507	34.79	63.34
2.	20	0.480	35.02	
3.	30	0.478	37.97	
4.	40	0.420	40.79	
5.	50	0.373	41.10	

Table 6. Free radical scavenging activities of (Cu) in Total Antioxidant Capacity assay (%).

S.No.	Compound Concentration (µg/ml)	TAC Assaay		
		Absorbance	% of SCV	IC_{50}
1.	10	0.521	46.83	23.26
2.	20	0.502	48.77	
3.	30	0.474	51.63	
4.	40	0.469	52.14	
5.	50	0.369	62.34	



P.G.P. COLLEGE OF ARTS & SCIENCE NAMAKKAL 637 206

Fig 3. Total Antioxidant Capacity of Ascorbic acid

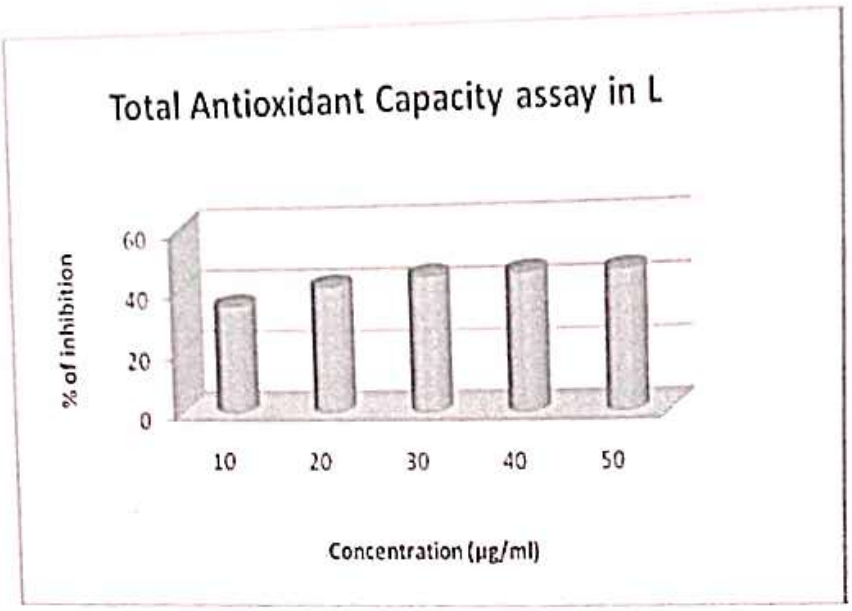


Fig 4. Total Antioxidant Capacity of $C_{20}H_{14}N_4O_4$

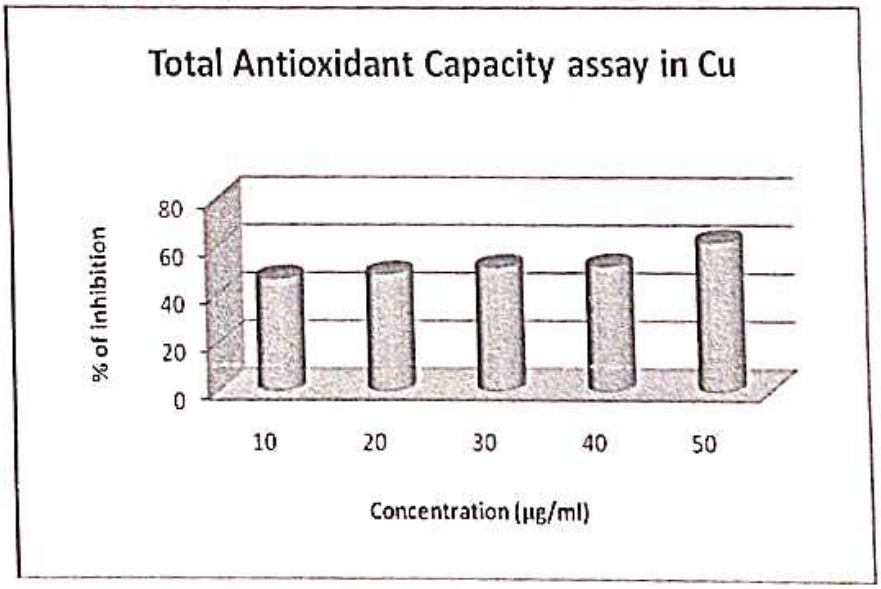
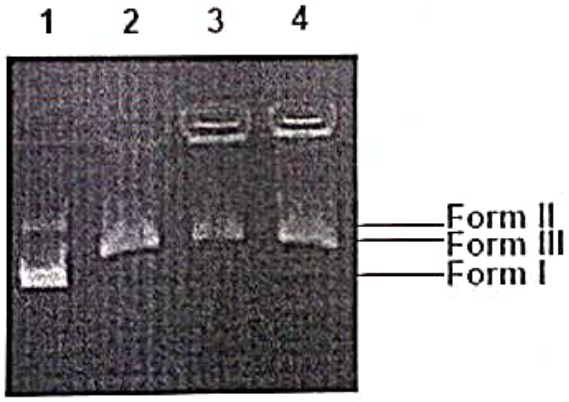


Fig 5. Total Antioxidant Capacity of $Cu(C_{40}H_{28}N_8O_8Cl_2)$

P.G.P. COLLEGE OF ARTS & SCIENCE NAMAKKAL 637 206

DNA cleavage study

Gel electrophoresis experiments were performed using pUC18DNA with ligand and $Cu(C_{40}H_{28}N_8O_8Cl_2)$ complex in presence of H_2O_2. The results of DNA cleavage studies have been shown in Fig 6. $Cu(C_{40}H_{28}N_8O_8Cl_2)$ complex exhibit cleavage ability at low concentration (40 µM). The ligand exhibits significant activity in the presence of oxidant. Also the activity was much higher for the $Cu(C_{40}H_{28}N_8O_8Cl_2)$ complex in presence of H_2O_2 When pUC18DNA is subjected to electrophoresis, relatively fast migration will be observed for the intact super coil form (Form I). If scission occurs on one strand (nicking), the super coil will relax to generate a slower moving open circular form (Form II). If both strands are cleaved, a linear form (Form III) that migrates between Forms I and II will be generated. From Fig 6, the $Cu(C_{40}H_{28}N_8O_8Cl_2)$ complex show more activity in the presence of oxidant which may be due to the reaction of hydroxyl radical with DNA. $Cu(C_{40}H_{28}N_8O_8Cl_2)$ complex were able to convert DNA (Form I) into linear form (Form III). The mononuclear $Cu(C_{40}H_{28}N_8O_8Cl_2)$ complex was found to be highly active in cleaving DNA than the free ligand [15].



Lane 1 – PUC18 DNA - Control
Lane 2 – DNA + H2O2 (1mM)
Lane 3 – DNA + H2O2 (1mM) + Cu (40µM)
Lane 4 – DNA + H2O2 (1mM) + L (40µM)

Fig 6. Agarose gel electrophoresis pattern showing effect of pUC18DNA induced by H_2O_2 and metal complex. Lane 1-DNA alone; Lane 2- DNA alone + H_2O_2; Lane 3-DNA + $Cu(C_{40}H_{28}N_8O_8Cl_2)$ + H_2O_2; Lane 4-DNA + $C_{20}H_{14}N_4O_4$ + H_2O_2.

CONCLUSION

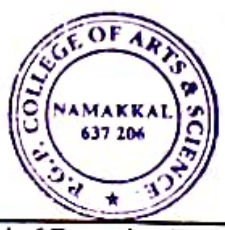
On the basis of various physico-chemical and spectral data presented and discussed in this paper, the $Cu(C_{40}H_{28}N_8O_8Cl_2)$ complex may tentatively be suggested to have distorted octahedral geometry. The coordination and the type of geometry of mononuclear copper(II) complex were determined by IR, electronic, magnetic and molar conductivity studies. Lower molar conductivity value obtained for the complex indicates that it is a non-electrolyte. The electronic and magnetic susceptibility studies reveal that the geometry of the newly synthesized $Cu(C_{40}H_{28}N_8O_8Cl_2)$ complex is distorted octahedral. The

P.G.P. COLLEGE OF ARTS & SCIENCE NAMAKKAL

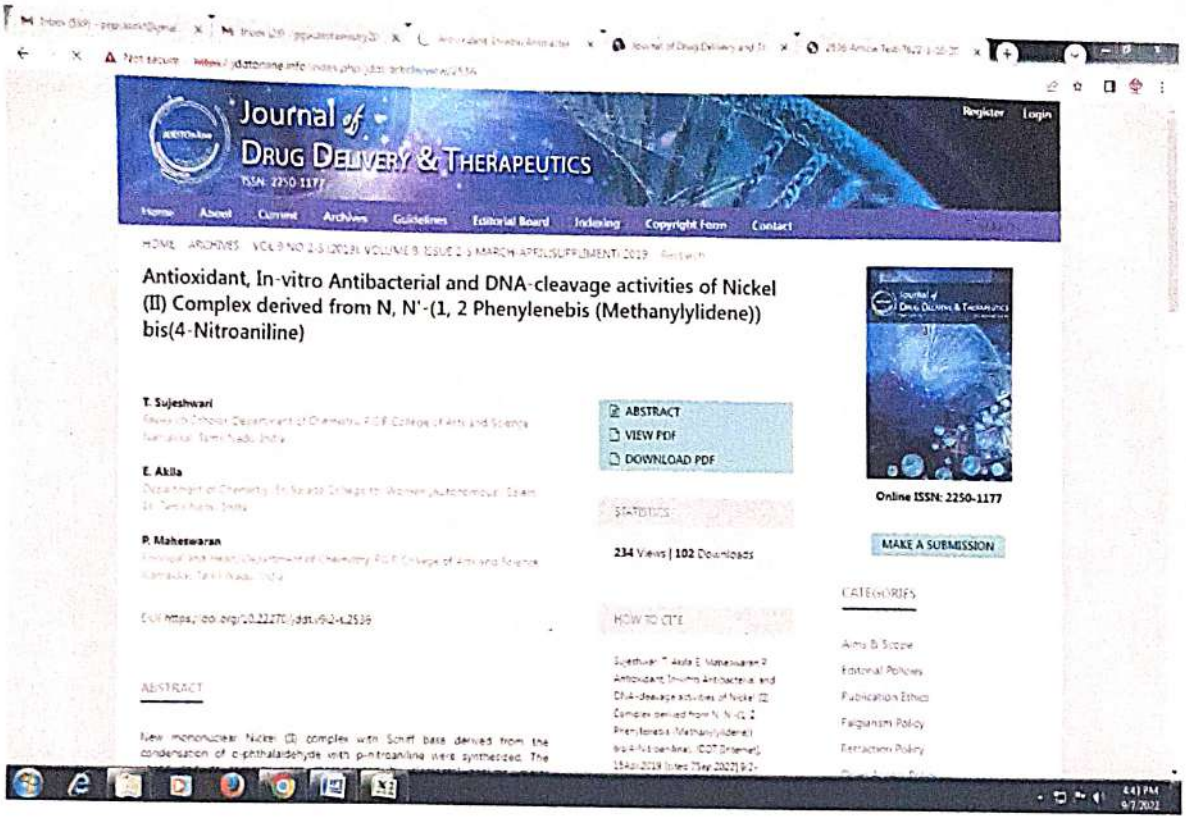
therapeutic promise of the investigated Cu(II) complex were found to exhibit higher antibacterial activity than the ligand. The interaction of Schiff base and Cu(II) complex with pUC18DNA were investigated by gel electrophoresis and concluded that Cu(II) complex cleave DNA effectively in the presence of H_2O_2. Moreover, the ligand and its complex were screened for antioxidant activity and the $Cu(C_{40}H_{28}N_8O_8Cl_2)$ complex showed better activity when compared to ligand.

REFERENCES

1. M. A. Ashraf, K. Mahmood and A. Wajid, *Int. Conf. Chem. Chem. Sci., 10*, **2011**, 1.
2. I. Kostova and L. Sasa, *Curr. Med. Chem. 20*, **2013**, 4609.
3. F. D. Koria and P. H. Parsania, Asian J. Chem., 11, **1999**, 199.
4. J. Mendham, R. C. Denny, J. D. Barnes, M. J. K. Thomas, Quant. Chem. Anal., 6, **2000**.
5. G.G. Mohamed and Z.H. Abd El-Wahwb, *J. Thermal Anal.*, 73, **2003**, 347.
6. V. L. Borde, S. S. Shankarwar, C. D. Thanur and A. G. Shankarwar, *Ind. J. Pharm. Env. Res.*, 5, **2014**, 87
7. Priya, Devi and R. H. Hemakumar Singh, *Rasayan. J. Chem.*, 2, **2010**, 266.
8. Sunil Kumar and Tobriya, *Int. J. Sci. Res.*, 5, **2012**, 65.
9. Rishu Katwal, Harpreet Kaur and Brij Kishore Kapur, *Sci. Revs. Chem. Commun.*, 3, **2013**, 69.
10. G.G. Mohamed and Z.H. Abd El-Wahwb, *J. Thermal Anal.*, 73, **2003**, 347.
11. C. Anitha, C.D. Sheela, P. Tharmaraj and S. Johnson Raja, *Spectrochimica Acta*, 98, **2012**, 35.
12. M. Kurtomglu, M.M. Dagdelen and S. Toroglu, Trans. Met. Chem. 31, **2006**, 382.
13. Q.L. Zhang, J.G. Liu, J.Z. Liu, H. Li, Y. Yang, H. Chao and L.N. Ji, Inorg. Chim. Acta. 34, **2012**, 339.
14. Behrouz Shaabani, Ali Akbar Khandar, Haedeh Mobaiyen, Nahid Ramazani, S. Salete Balula and Luís Cunha-Silva, *Polyhedron*, 31, **2014**.
15. S.I. Kirin, C.M. Happle, S. Hrubanova, T. Weyhermuller, C. Klein and N. Metzler-Nolte, Dalton Trans. 120, **2014**.



PRINCIPAL
PGP College of Arts and Science
Namakkal.



Journal of Drug Delivery & Therapeutics
ISSN: 2250-1177
Register Login
Home About Current Archives Guidelines Editorial Board Indexing Copyright Form Contact

HOME ARCHIVES VOL 8 NO 2-S (2018): VOLUME 8 ISSUE 2-S MARCH-APRIL(SUPPLEMENT) 2018 Research

Antioxidant, In-vitro Antibacterial and DNA-cleavage activities of Nickel (II) Complex derived from N, N'-(1, 2 Phenylenebis (Methanylylidene)) bis(4-Nitroaniline)

T. Sujeshwari
Research Scholar, Department of Chemistry, PG & Research, Arignar Anna College of Arts and Science, Namakkal, Tamil Nadu, India

E. Akila
Department of Chemistry, Sri Navalar Nedunchezhiyan College for Women (Autonomous), Salem-16, Tamil Nadu, India

P. Maheswaran
Principal and Head, Department of Chemistry, PG & Research, Arignar Anna College of Arts and Science, Namakkal, Tamil Nadu, India

DOI: https://doi.org/10.22270/jddt.v8i2-s.2536

ABSTRACT

New mononuclear Nickel (II) complex with Schiff base derived from the condensation of o-phthalaldehyde with p-nitroaniline were synthesized. The

ABSTRACT
VIEW PDF
DOWNLOAD PDF

STATISTICS

234 Views | 102 Downloads

HOW TO CITE

Sujeshwari T, Akila E, Maheswaran P. Antioxidant, In-vitro Antibacterial and DNA-cleavage activities of Nickel (II) Complex derived from N, N'-(1, 2 Phenylenebis (Methanylylidene)) bis(4-Nitroaniline). IDOT [Internet]. 15Apr.2018 [cited 7Sep.2022];8(2-

Online ISSN: 2250-1177

MAKE A SUBMISSION

CATEGORIES

Aims & Scope
Editorial Policies
Publication Ethics
Plagiarism Policy
Retraction Policy

P.G.P. COLLEGE OF ARTS & SCIENCE
NAMAKKAL
637 206

Available online on 15.04.2019 at http://jddtonline.info

Journal of Drug Delivery and Therapeutics

Open Access to Pharmaceutical and Medical Research

© 2011-18, publisher and licensee JDDT, This is an Open Access article which permits unrestricted non-commercial use, provided the original work is properly cited

Open Access Research Article

Antioxidant, *In-vitro* Antibacterial and DNA-cleavage activities of Nickel (II) Complex derived from N, N'-(1, 2 Phenylenebis (Methanylylidene)) bis(4-Nitroaniline)

T. Sujeshwari [1], E. Akila [2] & *P. Maheswaran [3]*

[1] Research Scholar, Department of Chemistry, P.G.P College of Arts and Science, Namakkal, Tamil Nadu, India

[2] Department of Chemistry, Sri Sarada College for Women (Autonomous), Salem-16, Tamil Nadu, India

[3] Principal and Head, Department of Chemistry, P.G.P College of Arts and Science, Namakkal, Tamil Nadu, India

ABSTRACT

New mononuclear Nickel (II) complex with Schiff base derived from the condensation of o-phthalaldehyde with p-nitroaniline were synthesized. The ligand and its complex were characterized by elemental analysis, molar conductivity, magnetic moment, IR, ^{1}H NMR, and electronic spectra. The conductivity data confirmed the non-electrolytic nature of the complex. The spectral and analytical data suggested a distorted octahedral geometry for Ni(II) complex. The synthesized complex with ligand have been screened for antimicrobial activity against two gram-positive bacteria (Staphylococcus aureus and Bacillus subtilis) and two gram-negative bacteria (Escherichia coli and klebsiella pneumoniae). The obtained results showed that Ni(II) complex is more potent than free ligand. DNA cleavage studies of Ni(II) complex have been investigated by gel electrophoresis using super coiled pUC18DNA. The experimental results revealed that the Ni(II) complex cleaved pUC18DNA. in an efficient manner than the parent ligand. In addition, the antioxidant activity of the ligand and its metal complex were investigated through scavenging effects for DPPH radical indicating that the compound show stronger antioxidant activity than free ligand but lower when compared to standard oxidants such as vitamin C.

Keywords: Mononuclear, Antimicrobial studies and DNA cleavage.

Article Info: Received 28 Feb 2019; Review Completed 05 April 2019; Accepted 09 April 2019; Available online 15 April 2019

Cite this article as:

Sujeshwari T, Akila E, Maheswaran P, Antioxidant, *In-vitro* Antibacterial and DNA-cleavage activities of Nickel (II) Complex derived from N, N'-(1, 2 Phenylenebis (Methanylylidene)) bis(4-Nitroaniline), Journal of Drug Delivery and Therapeutics. 2019; 9(2-s):396-401 **http://dx.doi.org/10.22270/jddt.v9i2-s.2536**

***Address for Correspondence:**

T. Sujeshwari, Research Scholar, Department of Chemistry, P.G.P College of Arts and Science, Namakkal, Tamil Nadu, India

INTRODUCTION

The Schiff bases ligand has been found extensive use in the field of research and field of interest now a day. The Schiff bases compounds are recognized due to the presence of azomethine group (-CH=N) which is formed by reacting either by aldehyde or ketone with compounds containing amine group [1]. As the Schiff bases can be synthesized by easy and simple condensation reaction and has been found its extensive use in the field of coordination chemistry due to its property of donating electrons as a ligand. Schiff base mononuclear transition metal complexes due to its synthetic accessibility and its impact in coordination chemistry, as well as the relevance to structural characterization has received a great deal of interest in the field of research [2]. Besides, the DNA interaction of Schiff base metal complexes has also gained much interest towards their applications in biotechnology and medicine. The scientific community has showed that metal coordination compounds have shown some outstanding DNA cleavage properties, as well as antibacterial and antioxidant activities [3-4]. It is seen that transition metals are particularly suitable for this purpose, because they can adopt a wide variety of oxidation states, coordination numbers and geometries, in comparison to other main group elements.

Over the past decades, considerable interest in the synthesis and characterization of transition metal complexes with Schiff Base ligands had been developed to check the role of metal active sites in several catalytic biological processes. In the present study, the synthesis and characterization of mononuclear Ni(II) complex of a Schiff base ligand derived from o-phthalaldehyde and p-nitroaniline has been reported. Schiff base ligand and its metal complex were characterize by the elemental analysis, magnetic susceptibility, molar conductivity measurements, electronic spectra, IR, ^{1}H NMR spectrum to determine the mode of co-ordination and geometry. In order to establish the biological role of metals,

P.G.P. COLLEGE OF ARTS & SCIENCE NAMAKKAL 637 206

the Schiff base and its Ni(II) complex have been screened for their antimicrobial activity against two gram-positive bacteria such as S. aureus and B. subtilis and two gram-negative bacteria such as E. coli and K. pneumonia. The oxidative damage caused by ROS on lipids, proteins, and nucleic acids plays a significant role in the development of life limiting chronic diseases such as cancer, hypertension, cardiac infarction, arteriosclerosis, rheumatism, and cataracts [5]. Thus, the percentage of antioxidant activities of Schiff base and its Ni(II) complex were also determined.

MATERIALS AND INSTRUMENTS

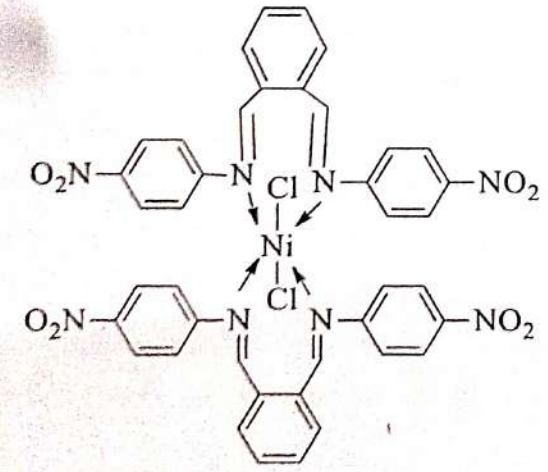
All chemicals and reagents used were of analytical grade and were used as received without any further purification. All the solvents were purified according to standard procedures. The elemental analysis (Carbon, Hydrogen and nitrogen) were performed using a Carlo Eraba 1106 instrument. The molar conductance of the freshly prepared Schiff base transition metal complex (10^{-3} M) was recorded in DMF at room temperature using ELICO CM 185 Conductivity Bridge. The Infrared spectra were recorded on the Perkin Elmer FT-IR-8300 Model spectrometer using KBr disc in the region 4000-200 cm^{-1}. Electronic absorption spectra in the UV-Visible range were recorded on Double beam spectrometer Cyber lab between 200-800 nm by using DMF as the solvent. ^{1}H-NMR spectra of the ligand were recorded on Bruker Spectrometer at 400 MHZ in DMSO-d_6.

Synthesis of Schiff base ligand

The Schiff base ligand was synthesized by adding 1, 2-benzene dicarboxaldehyde (1 mM) in 20 ml of ethanol, and p-nitroaniline (2 mM) in 20 ml of ethanol. The mixture was refluxed for 2½ hrs. Then the solution of the ligand was kept for slow evaporation and collected and dried in air [6].

Synthesis of mononuclear Ni(II) complex

The ethanolic solution of synthesized ligand N, N'–(1, 2 phenylenebis(methanylylidene) bis(4-nitroaniline) (2 mM) was added drop wise and strirring to an ethanolic solution of the metal salt $NiCl_2.6H_2O$ (1 mM) with constant stirring, and the mixture was boiled under reflux for 4½ hrs. Then the volume of the reaction mixture was reduced by evaporation. The resultant product was filtered, washed with ethanol and dried [7].



Scheme 1: Mononuclear Schiff base Ni(II) complex

Antibacterial studies

The synthesized complex and the Schiff base ligand were tested for their antimicrobial studies using bacterial strains such as *Escherichia coli*, *Klebsiella pneumoniae*, *Staphylococcus aureus* and *Bacillus subtilis*. Antibacterial test was performed by using the disc diffusion method. The bacterial strains were subcultured individually in nutrient agar medium. The compounds were dissolved in DMF. The plates were incubated aerobically at 37º C for 24 hours and the antimicrobial activity was assessed by measuring the inhibition of microbial growth around the well. This method involves the exposure of the zone inhibition toward the diffusion of micro-organism on agar plate [8].

Total antioxidant capacity assay

- Different concentrations (10 µl, 20 µl, 30 µl, 40 µl and 50 µl) of synthesized compounds were taken and 1ml of reagent solution was added. [Reagent solution: 0.6 M sulphuric acid, 28 mM sodium phosphate and 4 mM Ammonium molybdate.
- The tubes were capped and incubated in thermal block at 95º C for 90 minutes.
- After the time interval the tubes were cool down at room temperature.
- The absorbance was recorded at 695 nm using shimadzu UV 1800 spectrophotometer [9].

Calculation of 50% Inhibitory Concentration (IC_{50})

The concentration (mg/ ml) of the fractions that was required to scavenge 50% of the radicals was calculated by using the percentage scavenging activities at five different concentrations of the fractions.

Percentage inhibition (I %) was calculated using the formula,

I % = (Ac-As) / Ac x 100

Where, Ac = absorbance of the control and

As = absorbance of the sample.

TAC = Total Antioxidant Capacity assay

DNA cleavage studies

The DNA cleavage studies were done by gel electrophoresis experiment for which pUC18 was used as the plasmid DNA. The DNA cleavage activity was evaluated by monitoring the conversion of supercoiled plasmid DNA to nicked circular DNA and linear DNA. The reaction mixture was prepared by adding 40µl Puc18 DNA, 50 mM Tris-HCl, pH 7.4, 50 mM NaCl, 10 mM H_2O_2 in a different volume, followed by adding Millipore water for final volume. Samples were typically incubated for 1 hr at 37 ºC [10].

RESULTS AND DISCUSSION

The synthesized transition Ni(II) complex are found to be freely soluble in DMSO, DMF and ethanol. The analytical data of the synthesized ligand and its mononuclear metal complex are shown in Table 1. The lower molar conductivity value (7.60 Ω^{-1} cm^2 mol^{-1}) for Ni(II) complex (10^{-3} M) in DMSO at room temperature indicates their non-electrolytic nature [11-12].

P.G.P. COLLEGE OF ARTS & SCIENCE NAMAKKAL 637 206

Table 1: Analytical data of the Schiff base ligand and its mononuclear metal complex

Compound	Molecular formula	Colour	Yield %	Melting point (C)	% of Nitrogen		% of Metal	
					Cal	Exp	Cal	Exp
L	$C_{20}H_{14}N_4O_4$	Yellowish orange	70	145	15.0	14.8	-	-
ML_2X_2	$Ni(C_{40}H_{28}N_8O_8Cl_2)$	Dark Green	60	>200	12.7	12.5	6.7	6.4

IR Spectral analysis

The FT-IR spectral analysis of Schiff base and its metal complex indicated the presence of all expected functionalities are listed in Table 2. The metal complex exhibited the absorptions of azomethine region at lower frequencies than free ligand. The infrared spectrum of the Schiff base ligand showed a medium absorption at 1655.34 cm^{-1} assigned to the C=N stretching vibrations, indicating the formation of the Schiff base linkage. In the complex, this band is shifted to lower frequencies in the 1649.42 cm^{-1} upon complexation with the metal [13], which can be attributed to the coordination of the imine nitrogen to the metal centre. The characteristic bands for the entire complex in the region 691.10 cm^{-1} may assigned for the vibration of aromatic rings and C-H stretching respectively. The other absorption characteristic appeared in the region 484.34 and 315.10 cm^{-1} may be assigned for M-N and M-Cl vibrations [14].

Table 2: IR spectral data (4000-200 cm^{-1}) of Schiff base and its metal complex

Compounds	υ(C=N) (cm^{-1})	υ(M-Cl) (cm^{-1})	υ(M-N) (cm^{-1})
$C_{20}H_{14}N_4O_4$	1655.34	--	--
$Ni(C_{40}H_{28}N_8O_8Cl_2)$	1649.42	315.10	484.34

Electronic spectra and magnetic moment studies

The electronic absorption spectra of the Ni(II) complex were recorded in freshly prepared solution in DMF at room temperature. The electronic spectra of the Schiff base ligand and its complex have been measured in DMF solution 200-800 nm at room temperature [15]. The data are represented in Table 3. In the electronic spectra of the Schiff base ligand, an intense absorption at 365 nm were assigned to a benzene $\pi \rightarrow \pi^*$ transition and the band at 382 nm were assigned due to $n \rightarrow \pi^*$ transition associated with the azomethine chromophore (-C=N). The dark green Ni(II) complex showed three bands at at 562, 585, and 613 nm which are assigned to ^3A_2g (F) $\rightarrow ^3T_2g$ (F) (ν_1), ^3A_2g (F) $\rightarrow ^3T_1g$ (F) (ν_2) and ^3A_2g (F) $\rightarrow ^3T_1g$ (P) (ν_3) transitions respectively, indicating an distorted octahedral geometry. The magnetic moment of 3.41 B.M. falls within the range normally observed for octahedral Ni(II) complex.

Table 3: Electronic Spectral data of Schiff base ligand and its Ni(II) complex.

Compound	Electronic spectra (nm)				Geometry of the complex
	$\pi \rightarrow \pi^*$	$n \rightarrow \pi^*$	L→M	d-d	
$C_{20}H_{14}N_4O_4$	365	382	-	-	-
$Ni(C_{40}H_{28}N_8O_8Cl_2)$	298	365	420	562, 585, 613	Distorted Octahedral

^1H – NMR Spectral studies

The ^1H-NMR spectra of the Schiff base ligand was measured at room temperature in DMSO- d_6. The ^1H NMR spectra of the ligand exhibits well resolved signals and significant differences in their chemical shifts. The spectrum of the Schiff base ligand exhibits a singlet signal in the 8.48 ppm, which is attributed to the azomethine group (-CH=N-) proton and the multiplets around 6.6-7.9 ppm are assigned due to aromatic protons [16]. The spectra of the ligand is shown in Fig 1.



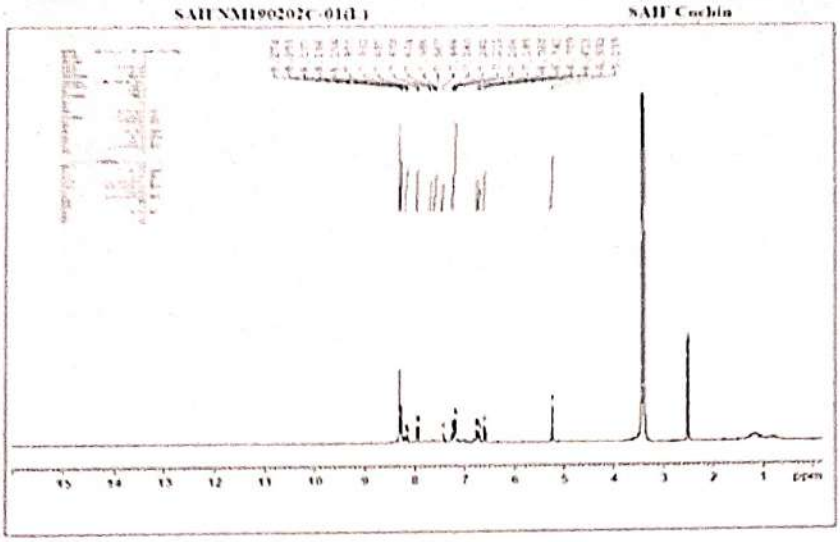


Figure 1: ^1H NMR spectrum of $C_{20}H_{14}N_4O_4$

Antibacterial activity

The synthesized ligand and its complex were screened for their antibacterial activity against *Staphylococcus aureus, Bacillus subtilis* while *Escherichia coli* and *Klebsilla pneumonia*. The standard drug streptomycin was also tested for their antibacterial activities at the same concentration and conditions similar to tested compound concentration. From the antibacterial studies, it is inferred that the Schiff bases and its Ni(II) complex were found to be potentially active against *Staphylococcus aureus, Bacillus subtilis, Escherichia coli* and *Klebsilla pneumonia* [17]. The antibacterial activity of Schiff base and its metal complex against different bacteria are shown in Fig 2, 3, 4, and 5.

From the obtained results, it can be observed that the Ni(II) complex showed greater activity as compared to the Schiff base. The improved activities of the metal complex as compared to the ligand can be explained on the basis of chelation theory.

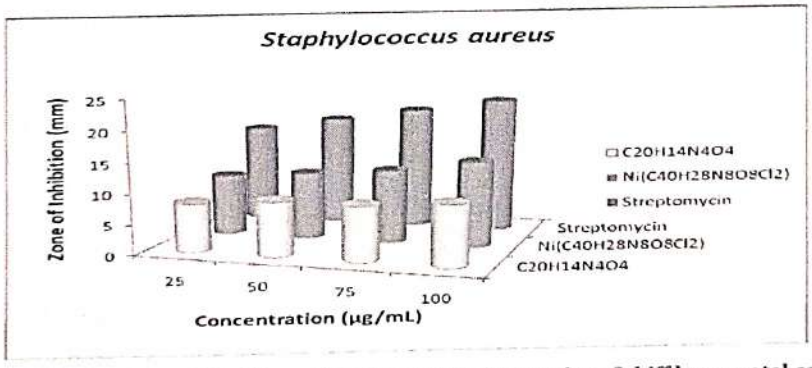


Figure 2: Antibacterial activity of Schiff base ligand and its mononuclear Schiff base metal complex against *Staphylococcus aureus*

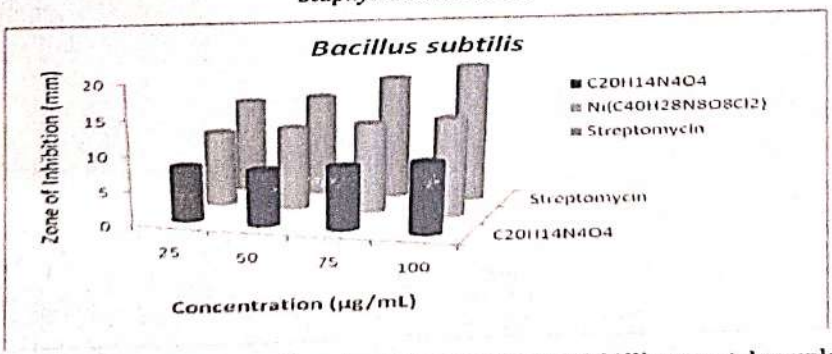


Figure 3: Antibacterial activity of Schiff base ligand and its mononuclear Schiff base metal complex against *Bacillus subtilis*

P.G.P. COLLEGE OF ARTS & SCIENCE NAMAKKAL 637 206

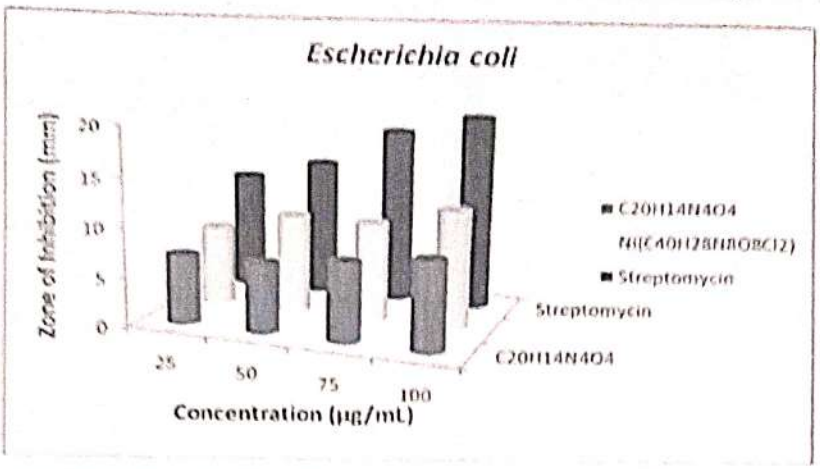


Figure 4: Antibacterial activity of Schiff base ligand and its mononuclear Schiff base metal complexes against *Escherichia coli*

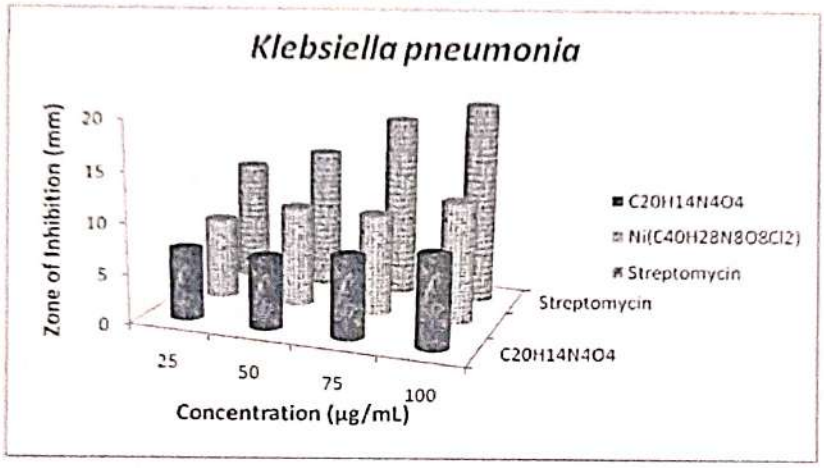


Figure 5: Antibacterial activity of Schiff base ligand and its mononuclear Schiff base metal complex against *Klebsiella pneumonia*

Antioxidant activity

The antioxidant assay was carried out using different concentrations of the Schiff base and its Ni(II) metal complex with radical, while ascorbic acid (vitamin C) was used as standard.

Total Antioxidant Capacity assay

The total antioxidant capacity of $Ni(C_{40}H_{28}N_8O_8Cl_2)$ is significantly higher than that of free ligand, indicating that this complex is a much better antioxidant than ligand but lower when compared to ascorbic acid (vitamin C) as standard [18]. Total antioxidant capacity of $C_{20}H_{14}N_4O_4$ and $Ni(C_{40}H_{28}N_8O_8Cl_2)$ as well as the standard was increased in a dose-dependent manner, antioxidant ability of Schiff base, increased significantly after chelation of transition metal ion (Fig 6 and 7). The $Ni(C_{40}H_{28}N_8O_8Cl_2)$ complex possess higher antioxidant potential (IC_{50}) than vitamin C (standard drugs) and lower than $C_{20}H_{14}N_4O_4$ ligand.

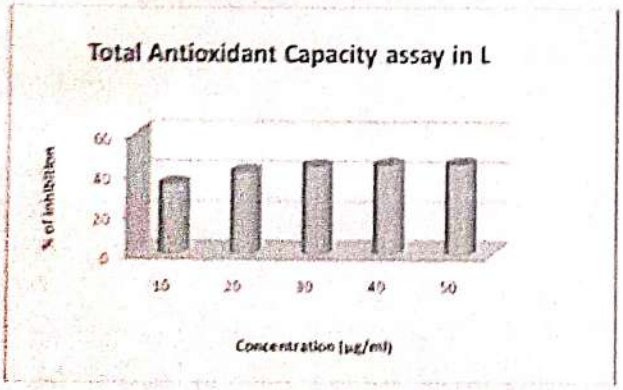


Figure 6: Total Antioxidant Capacity of $C_{20}H_{14}N_4O_4$

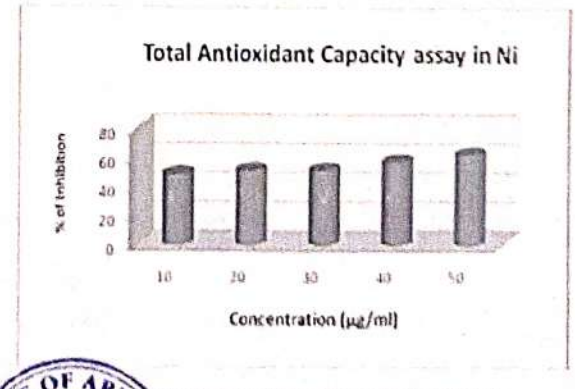


Figure 7:. Total Antioxidant Capacity of $Ni(C_{40}H_{28}N_8O_8Cl_2)$

P.G.P. COLLEGE OF ARTS & SCIENCE
NAMAKKAL
637 206

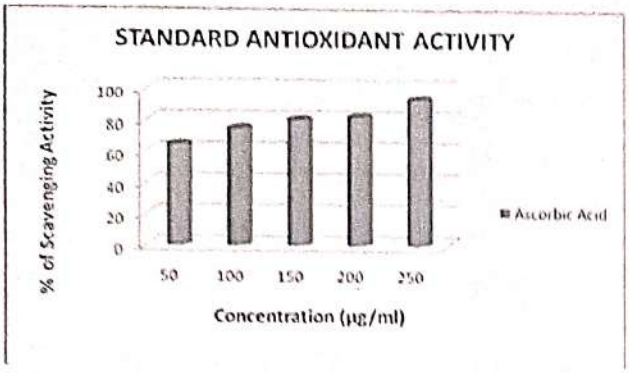
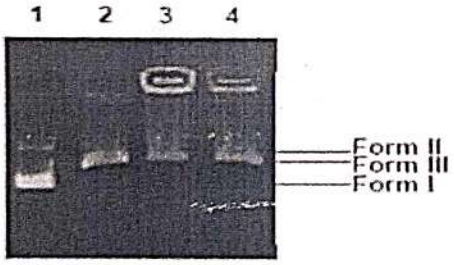


Figure 8: Total Antioxidant Capacity of Ascorbic acid

DNA cleavage activity

The Schiff base and its $Ni(C_{40}H_{28}N_8O_8Cl_2)$ complex were studied for their DNA cleavage activity by agarose gel electrophoresis. Gel electrophoresis is used in DNA typing, where DNA is fragmented at particular sequence points on the genome and compared to a control sample. Hence, it can be used in the detection of DNA damage also. DNA cleavage is controlled by relaxation of supercoiled circular conformation of pUC18DNA to nicked circular conformation and linear conformation. This type of damage will only give an indication to the extent of strand breakage in a sample of damaged DNA.

The results (Fig 9.) of gel electrophoretic separations of pUC18DNA induced by metal complex (lane 3) and ligand (lane 4) in the presence of H_2O_2. Under the same conditions, lane 1 and 2 did not show any apparent cleavage. $Ni(C_{40}H_{28}N_8O_8Cl_2)$ complex (lane 3) shows more cleavage activity in the presence of H_2O_2 at higher concentration (40 µM). $C_{20}H_{14}N_4O_4$ (lane 4) at higher concentration (40 µM) also shows the conversion of supercoiled form (Form-I) into linear form (Form-III).



Lane 1 – PUC18 DNA - Control
Lane 2 – DNA + H2O2 (1mM)
Lane 3 – DNA + H2O2 (1mM) + Ni (40µM)
Lane 4 – DNA + H2O2 (1mM) + L (40µM)

Figure 9: Agarose gel electrophoresis pattern showing effect of pUC18 DNA induced by H_2O_2 and metal complex. Lane 1-DNA alone; Lane 2- DNA alone + H_2O_2; Lane 3-DNA + $Ni(C_{40}H_{28}N_8O_8Cl_2)$ + H_2O_2; Lane 4-DNA + $C_{20}H_{14}N_4O_4$ + H_2O_2.

From the observed results we concluded that ligand and its metal complex behave as efficient chemical nuclease for double strand cleavage of DNA [19]. This may be attributed to the formation of hydroxyl free radicals. Control experiments using DNA alone do not show any significant cleavage of pUC18 DNA even on longer exposure time. From the observed results, it is concluded that Schiff base and $Ni(C_{40}H_{28}N_8O_8Cl_2)$ complex have better cleavage activity.

CONCLUSION

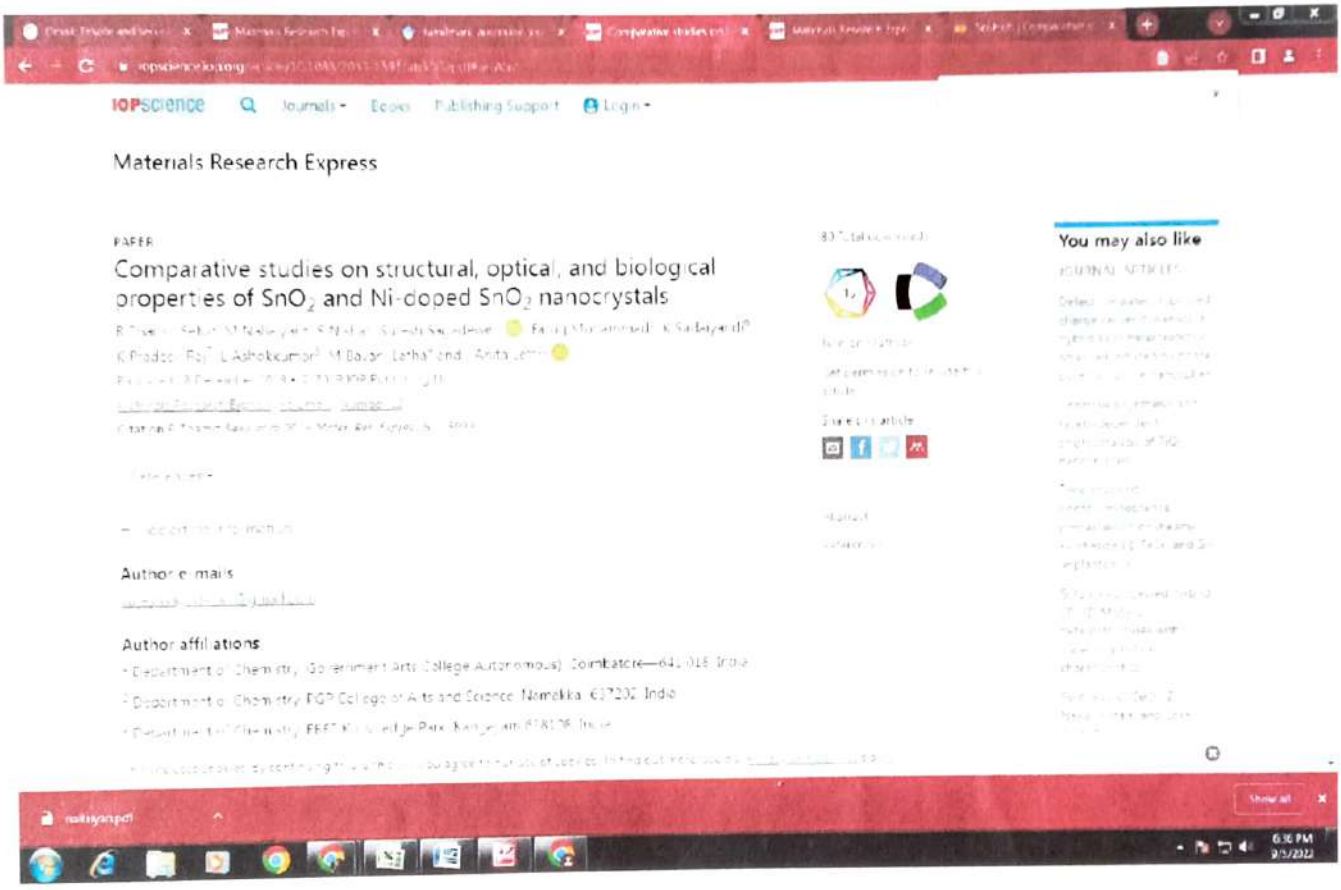
In this report, the mononuclear Schiff base $Ni(C_{40}H_{28}N_8O_8Cl_2)$ complex derived from *N, N'* – (1, 2-phenylenebis (methanylylidene)bis(4-nitroaniline), have been synthesized and characterized by using various physico-chemical and spectral analyses techniques. The molar conductance value indicates that the complex is non-electrolyte in nature. The IR spectra of synthesized compounds confirmed the coordination of ligand to the metal ion. The UV-Vis and magnetic moment data of the complex suggest a distorted octahedral geometry. The synthesized compounds have antibacterial activity against the two Gram-positive bacteria: *Staphylococcus aureus* and *Bacillus subtilis* and also against the two Gram-negative bacteria: *Escherichia coli* and *Klebsilla pneumonia*. Unlike the parent Schiff base ligand, the complex showed significant antibacterial activity. DNA cleavage studies show that $Ni(C_{40}H_{28}N_8O_8Cl_2)$ complex cleave the DNA molecule completely. Further, the results obtained in antioxidant activity confirmed that the complex is more effective to arrest the formation of radicals and the lower IC_{50} value observed in antioxidant assay did demonstrate that the complex exhibited differential and selective effects to scavenge radicals and hence the potential as drugs to eliminate the radicals.

REFERENCES

1. Alabdali A.J., *J. Appl. Chem.*, **2012;** 3:5.
2. Nabil Ramanadan Bardar, *Res. J. Chem.*, **2010;** 3:660.
3. Erkkila K.E., Odom D.T., Barto J.K., *Chem. Rev.*, **1999;** 99:2777.
4. Ji L.-N., Zou X.-H., Liu J.-G., *Coord. Chem. Rev.*, **2001;** 216:513.
5. Arulpriya P, Lalitha P, and S.Hemalatha, *Der Chemica Sinica.*, **2010; 2:73.**
6. Mohammed Fakruddin Ali Ahmed and V. Mahammad Yunus. *J. Chem.*, **2014; 30:111.**
7. Fugu M. B., Ndahi N. P., Paul B. B. and Mustapha A. N., *J. Chem. Pharm. Res.*, **2013;** 5:2228.
8. Metcalfe C and. Thomas J. A, *Chem. Soc. Rev.*, **2003;** 32:215.
9. Senthil Kumar R, Arunachalam S, Euro. *J. Med. Chem.*, **2009;** 44:1878.
10. Maribel N., *Biol. Inorg. Chem.*, **2003;** 4:401.
11. Robert Boggess K.; A. David Zatko, *J. Chem. Edn.*, **1975;** 52:649.
12. Geary W. J., *Coord. Chem. Rev.*, **1971;** 7:81.
13. Olar R., Badea M., Marinescu D. J., *Therm. Anal. Calorim.*, **2012;** 99:893.
14. Venkateswara Rao B., *J. Therm. Anal. Calorim*, **2010;** 100:577.
15. Emara A., *Spectrochim. Acta A.*, **2016;** 77:117.
16. Amali I. B., Kesavan M. P., Vijayakumar V., Gandhi N. I., J. Rajesh, and G. Rajagopal, *J. Mol. Str.*, **2019.**
17. Zare N, Zabardasti A. *Appl. Organometal. Chemistry.*, **2019.**
18. Aidi M., Keypour H., A. Shooshtari, M. Mahmoudabadi, M. Bayat, Z. Ahmadvand, R. Karamian, M. Asadbegy, S. Tavath, R.W. Gable, *Polyhedron.*, **2019.**
19. Dong,s D., Tian and S. Ping Yan, *J. Inorg. Bio. Chem.*, **2014;** 104:171.



PRINCIPAL
PGP College of Arts and Science
Namakkal.



IOPscience Journals Books Publishing Support Login

Materials Research Express

PAPER

Comparative studies on structural, optical, and biological properties of SnO_2 and Ni-doped SnO_2 nanocrystals

Author e-mails

Author affiliations

You may also like

GOVERNMENT ARTS COLLEGE (AUTONOMOUS) SCIENCE P.G.P. COLLEGE OF ARTS & SCIENCE NAMAKKAL 637 206

Materials Research Express

PAPER

Comparative studies on structural, optical, and biological properties of SnO_2 and Ni-doped SnO_2 nanocrystals

To cite this article: R Thamiz Selvi *et al* 2019 *Mater. Res. Express* **6** 125099

View the article online for updates and enhancements.





IOP ebooks™

Bringing you innovative digital publishing with leading voices to create your essential collection of books in STEM research.

Start exploring the collection - download the first chapter of every title for free.

This content was downloaded from IP address 129.16.69.49 on 20/12/2019 at 16:53

Materials Research Express

PAPER

Comparative studies on structural, optical, and biological properties of SnO_2 and Ni-doped SnO_2 nanocrystals

R Thamiz Selvi [1], M Nallaiyan [2], S Nisha [3], Suresh Sagadevan [4], Faruq Mohammad [5], K Sadaiyandi [6], K Pradeev Raj [7], L Ashokkumar [8], M Bavani Latha [9] and J Anita Lett [10]

[1] Department of Chemistry, Government Arts College(Autonomous), Coimbatore—641 018, India
[2] Department of Chemistry, PGP College of Arts and Science, Namakkal-637202, India
[3] Department of Chemistry, EBET Knowledge Park, Kangayam 638108, India
[4] Nanotechnology & Catalysis Research Centre, University of Malaya, Kuala Lumpur 50603, Malaysia
[5] Surfactants Research Chair, Department of Chemistry, College of Science, King Saud University, Riyadh 11451, Saudi Arabia
[6] Department of Physics, Govt Arts College for Women, Nilakkottai, Dindukkal, 624202, India
[7] Department of Physics, CSI College of Engineering, Ooty 643 215, Tamil Nadu, India
[8] Department of Microbiology, PGP College of Arts and Science, Namakkal-637 202, India
[9] Department of Biotechnology, Sathyabama Institute of Science and technology, Chennai-600 119, Tamil Nadu, India
[10] Department of Physics, Satyabhama Institute of Science and Technology, Chennai-600 119, Tamil Nadu, India

E-mail: sureshsagadevan@gmail.com

RECEIVED
19 September 2019

REVISED
27 November 2019

ACCEPTED FOR PUBLICATION
6 December 2019

PUBLISHED
18 December 2019

Keywords: SnO_2-Ni-doped nanocrystals, vero cell lines, HEp–2 cell lines, antibacterial studies, cytotoxicity studies

Abstract

The present study highlights a simple and eco-friendly route for the synthesis of pure and nickel doped (1%–3%) tin oxide (SnO_2) nanocrystals (NCs) with the use of *Azadirachta indica* (Neem) leaf extract. The synthesized pure and Ni-doped (1%–3%) SnO_2 NCs were characterized thoroughly for their optical, structural, functional, and morphological characteristics. The results of the study revealed that the Ni^{2+}-doped SnO_2 NCs are maintaining the tetragonal crystalline phase and the Ni doping (1%–3%) caused a shift in the bandgap energy to 3.87 eV as against the pure SnO_2 of 3.61 eV. Also, the photoluminescence (PL) spectrum revealed for the intrinsic defects encountered in the visible emission peaks in the range of 400–560 nm. Further, the biological activity with the help of antibacterial efficacy and *in vitro* toxicity was tested and the results of antibacterial studies revealed that higher concentrations of Ni doping have enhanced efficacy towards both Gram-positive *Staphylococcus aureus* and Gram-negative *Escherichia coli bacterias*. The *in vitro* cytotoxicity studies on Vero (non-cancer) and HEp–2 cells (cancer) exhibited greater cytotoxicity toward Vero than HEp-2 cells at its half-maximal inhibitory concentration (IC_{50}) associated with the cell rounding and detachment. Thus, the doping of Ni^{2+} metal ions in SnO_2 tends to improve the photocatalytic activity, in addition to finding the extended applications in the biomedical field for the delivery of antimicrobial agents or drug molecules.

1. Introduction

In recent years, the field of nanoscience and nanotechnology has become the most fascinating scientific areas of interest because of the ever increasing applications in many different sectors like biomedicine, optics, and integrated circuit technology, to mention few [1–3]. Taking into consideration of the fundamental principles of nanoscience and nanotechnology, further exploration into other research areas is of boundless scientific concern as it effectively bridges the gap between bulk materials and atomic or molecular assemblies [4, 5]. As an example, the metal oxide nanostructures predominantly, transition-metal doped ones have established a miscellaneous and enthralling class of materials whose properties have been anticipated to modify the inbuilt fundamental properties of conventional semiconductor materials. Since the doped transition metal oxides as compared to the pure ones exhibit some upgraded properties due to the changes occurring in their size, shape, optical nature, solvent distribution and surface morphology [6]. So, in view of the doping principles, there has

P.G. COLLEGE OF ARTS & SCIENCE NAMAKKAL 637 206

© 2019 IOP Publishing Ltd

been a remarkable growth with diverse methodologies industrialized to synthesize various nanocrystals of definite morphology and size based on the explicit necessities. In addition, the preparation of these materials at the nanoscale with an improved band gap is of more significance due to the increased surface-to-volume ratio and outstanding catalytic properties [7].

Tin dioxide (SnO_2) being a crystal-clear conductor exhibits the contradictory properties of high metallic conductivity due to its massive structural non-stoichiometry, it behaves as a transparent insulator in the visible range. Also, due to its wider band gap (3.6 eV), the SnO_2 material generates reasonable research focus in various fields because of its high electrical conductivity united with a fairly high optical broadcast in the visible region. The size of nanoparticles makes the necessary changes in the band energy gap which brings the transformations in the optical properties of doped nanostructured metal oxides [8]. The doping of some commonly used metal ions like Zn, Cu, Ni, Mn, Co, Fe, etc to the semiconductor platforms usually modifies the physiological characteristics of the semiconductor. At present, the SnO_2 materials are being doped deliberately by integrating atoms or ions of appropriate elements so as to improve their cycling stability [9]. For instance, Wang *et al* reported the outstanding cycling concert maintained by the antimony-doped SnO_2 [10]. A 637 mAh g^{-1} specific discharge measurement was initiated subsequently after 100 cycles inconsistent with 49.5% of the preliminary specific capacity. Efforts have been made by researchers including Gopinadhan *et al* who made an experimental attempt on the transition metal-doped SnO_2 (Co-doped SnO_2) to discover its high-temperature ferromagnetic behavior [11].

By keeping in view of doping applications, many different techniques are available in the literature for the fabrication of Ni-doped SnO_2 nanocrystals (NCs) which includes sol-gel, pulsed laser deposition method, spin coating technique, vapour transport process, spray pyrolysis, thermal decomposition, flash evaporation procedure etc. Predominantly, the Ni-doped SnO_2 revealed ferromagnetism at normal temperature conditions and displayed a reduced band gap with respect to an increase in the Ni content. Also the added features like structural, optical, and magnetic characteristics depending on the growth situations making this material to be used for the sensory or electrode material applications [12, 13]. For example, Yogamalar *et al* produced thin rod fashioned Ni-doped SnO_2 NCs by the sol-gel method that can exhibit the gas sensing characteristics. These hallow nano-fibers fabricated by the electro-spinning technique proved to be the probable candidates for the highly sensitive gas sensing application [14]. Recently, Xiaomin Ye *et al* synthesized Ni-doped SnO_2 nanospheres using the hydrothermal technique for Li-ion batteries as an anode substantial. Correspondingly, the material exhibited electro-catalytic action for the ozone progress. It was also found investigated that the band gap properties of the doped semiconductor NCs can be modified by fine tuning the particles size and magnitude with the help of various chemical synthesis approaches [15]. Nevertheless, studies on Ni-doped SnO_2 with enhanced photocatalytic activity and simultaneously boosted cytotoxicity and antimicrobial efficiency have been rarely testified. Herein, the present study deals with the green synthesis of Ni-doped SnO_2 NCs using *Azadirachta indica* (Neem) leaf extract and tested the biological efficacy so as to have any significance in the biomedical sector. From the cumulative analysis of results, it was investigated that the prepared Ni-doped SnO_2 NCs can serve as the promising probe for the extended applications in the biomedical sector in order to deliver the antimicrobial agents or drug molecules.

2. Material and methods

2.1. Materials

Tin chloride ($SnCl_2$) and Nickel chloride ($NiCl_2$; analytical grade) were purchased from Merck. *Azadirachta indica* (Neem) leaves were collected from the nearby farm, Tirupur, Tamil Nadu, India. All the collected Neem leaves were shade dried at room temperature and used for the further process.

2.2. Preparation of Azadirachta indica (Neem) leaf extract

The *Azadirachta indica* (Neem) leaves collected were washed numerous times with double distilled (DD) water to remove the dirt/impurities and then shade dried. The dried leaves (6.5 g) were taken, crushed into a fine powder and heated in a 250 ml Erlenmeyer flask along with 100 ml of DD water for 10 min at 60 °C–70 °C. During the heating process, the color of the aqueous solution changed from watery to brownish yellow. The aqueous extract was filtered using Whatman filter paper and the prepared Neem leaf extract was used for the biosynthesis of SnO_2 NCs.

2.3. Synthesis of Ni-doped SnO_2 NCs

For the synthesis, about 25 ml of a 1 mM solution of $SnCl_2$ was taken in a round bottom flask followed by the magnetic stirring for 20 min to form the homogeneous solution. Now, 25 ml of *Azadirachta indica* (Neem) leaf extract was added to the precursor in a dropwise manner and with constant stirring. After the complete addition

P.G. & RESEARCH DEPARTMENT OF SCIENCE NAMAKKAL 637 206

of leaf extract, the mixture was allowed to stir constantly for another 2 h and after the period, the change in color of leaf extract indicated the formation of SnO_2 NCs. In a similar way, the Ni-doped samples were also prepared by adding $NiCl_2$ with different molar concentrations (1, 2, and 3 mol %) to the mixture (precursor + Neem leaf extract) after 30 min of the reaction process.

2.4. Instrumental analysis

To study the crystalline nature and particle sizes of pure SnO_2 and Ni-doped SnO_2 NCs in powdered form at room temperature, the powdered x-ray diffraction (XRD) measurements were carried and for that, the Panalytical X'PERT–PRO instrument having the ceramic Cu radiation was used. The functional groups were interpreted by using SHIMADZU–8400 Fourier transform infrared spectrometer (FTIR) in the wavelength range of 3750–500 cm^{-1}. For the optical absorption studies at room temperature, the UV–vis spectrophotometer from Perkin Elmer and for the photoluminescence (PL) emission studies, JobHR800 in Yoon Horbe spectrometer using a He–Cd laser source having a wavelength of 325 nm was used. The surface morphology was analyzed by Scanning electron microscopy (SEM) ZEISS (EVO-50) and the particle sizes were measured by using transmission electron microscopy (TEM) Philips CM12. The energy dispersive x-ray spectrum (EDX) was recorded using the RONTEC instrument.

2.5. Testing of antibacterial activity

The antibacterial susceptibility for the synthesized pure and doped SnO_2 NCs was evaluated using the agar diffusion method. To examine the bacterial inhibition rate, Gram-positive *Staphylococcus aureus (S. aureus)* Gram-negative *Escherichia coli (E. coli)* and were grown in the nutrient broth medium (NB) and the turbidity adjusted to 0.5 McFarland standard. Fresh nutrient agar plates were inoculated with the above-mentioned bacteria using a sterile swab and wells of 6 mm diameter were made using a sterile gel puncture. Pure SnO_2 NCs + 1% Ni–SnO_2 NCs—A, and Pure SnO_2 NCs + 2% Ni–SnO_2 NCs—B and Pure SnO_2 NCs + 3% Ni- SnO_2 NCs—C at concentrations 25 μl were added to the wells using a sterile pipette. Now the prepared plates were incubated for another 24 h period at 37 °C and further observed for any zone of inhibition (ZOI).

2.6. Testing of *in vitro* cytotoxicity

For testing the cytotoxicity due to pure and Ni-doped SnO_2 NCs, two different cell lines, Vero (isolated from the kidney of African green monkey; non-cancer and healthy) and HEp-2 (Human epithelial type-2; human laryngeal carcinoma; cancer) were selected and are obtained from NCCS (Pune, India). The confluent cells were observed under the phase contrast optical microscope and contamination possibilities ruled out. The tissue culture flasks were maintained in an incubator at 37 °C with 5% CO_2 supply.

During the assay, the Vero and HEp-2 cells were seeded in 96-well microplates at a density of 1×10^5 cells /well in a DMEM (Dulbecco's Modified Eagle Medium) medium that contains 10% FBS (fetal bovine serum) and incubated for 18 h at 37 °C. When we see the cell growth to be 80% confluence, different concentrations (500, 250, 125, 62.5, 31.25, 15.625 μg/ml) of the testing samples were prepared in a 2% FBS containing DMEM media, added to the cells, and incubated for another 24 h. For the reference, the control measurements were selected the well that has only 100 µl of the medium. After the required period, 10 μl of MTT solution (3-(4, 5-Dimethylthiazol-2-yl)-2,5-diphenyltetrazolium bromide; 5 mg ml^{-1}) was added to each well and further incubated to another 4 h. Now the formazan crystals formed were solubilized in 100 µl of DMSO (dimethyl sulfoxide) where the optical dispersion (OD) was measured at an absorption wavelength of 540 nm using the ELISA plate reader. With the OD values, the percentage (%) cell viability was calculated using the following formula.

$$\%\text{Cell viability} = \frac{\text{Mean OD of test sample}}{\text{Mean OD of experimental control}} \text{X100}$$

2.7. Statistical analysis

Each experiment was repeated thrice for the accuracy and the values shown are the Mean ± standard error of three different values. Also, the results were subjected to the Student's *t*-test and the *p*-value ≤ 0.05 considered as the statistically significant value.

3. Results and discussion

3.1. Physicochemical analysis

The prepared SnO_2 and Ni-doped SnO_2 NCs were subjected to powder XRD analysis in the 2θ range of 10°–80° and the obtained results are compared and shown in figure 1 where the peaks were indexed to the tetragonal

P.G. & R. COLLEGE OF ARTS & SCIENCE NAMAKKAL 637 206

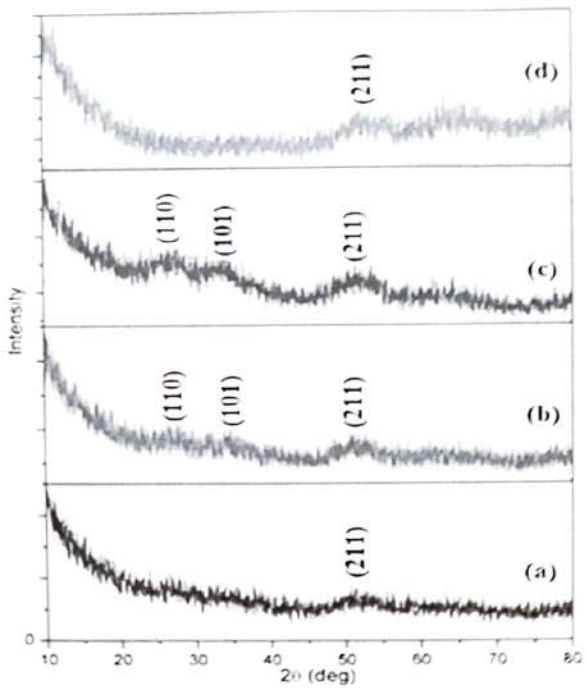


Figure 1. Powdered XRD patterns, (a) undoped SnO_2, (b) 1% Ni-doped, (c) 2% Ni-doped, and (d) 3% Ni-doped SnO_2 NCs.

Table 1. Powdered XRD derived parameters of pure and Ni-doped SnO_2 NCs.

Sample	Particle size (nm)	Lattice parameters (Å)			Volume (Å)^3
		a = b	c	c/a	
SnO_2	68	4.756	3.126	0.6572	70.70
SnO_2:Ni(1%)	43	4.754	3.125	0.6573	70.62
SnO_2:Ni(2%)	31	4.753	3.123	0.6570	70.55
SnO_2:Ni(3%)	22	4.752	3.123	0.6571	70.52

phase of SnO_2 NCs which is in a good agreement with the cassiterite, JCPDS No. 41–1445 [15]. This indicates that all the peaks resembled a pure phase related to SnO_2 or Ni–SnO_2 and no diffracted peaks linked to the unwanted byproducts like NiO or NiO2 were seem to be noted. It was also observed that the diffraction peaks are getting broadened which clearly represents for the crystal form of SnO_2 NCs. The broadening and weakening of some peaks may be due to the relatively lower crystallinity and size-quantization effect of the nanomaterials [16].

For calculating the crystalline size (D), the following Debye-Scherrer's equation was used [17],

$$D = \frac{0.9\lambda}{\beta \cos\theta}$$

where λ corresponds to the wavelength (1.54 Å), β the full-width half maximum, θ is the Bragg's diffraction angle.

The comparison of average crystalline sizes of the pure and Ni-doped SnO_2 NCs is tabulated in table 1. From the table, it can be observed that the increased Ni content is decreasing the crystalline size of the particles and this can be due to the reduction in diffusion rate which makes the NCs intact and also the distortions occurring in the host SnO_2 lattice by the foreign impurities [18].

Figure 2 shows the comparison of the FTIR spectrums of pure and different concentrations of Ni-doped SnO_2 NCs in the wavelength range of 3750–500 cm^{-1}. From the figure, the broad absorption band at 3444 cm^{-1} can be attributed to the fundamental stretching vibrations of the O–H bond from the free or bonded hydroxyl groups, while the other bands around 3100 and 3400 cm^{-1} and the peaks at 1620 and 1230 cm^{-1} are due to the stretching and bending vibrations of the hydroxyl groups [19]. Also, the other bands at 1058 and 1020 cm^{-1} are from the stretching vibration of Sn, O and Sn–O surface cation-oxygen bonds [20]. However, the bands in the range of 530–700 cm^{-1} are from the Sn–O–Sn vibrations (typical M–O–M) and the same was observed to be

NAMAKKAL 637 206

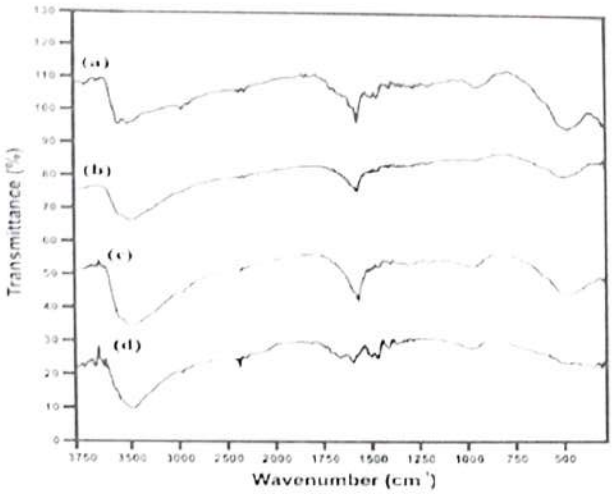


Figure 2. FTIR spectrums for (a) undoped SnO_2, (b) 1% Ni-doped, (c) 2% Ni-doped, and (d) 3% Ni-doped SnO_2 NCs.

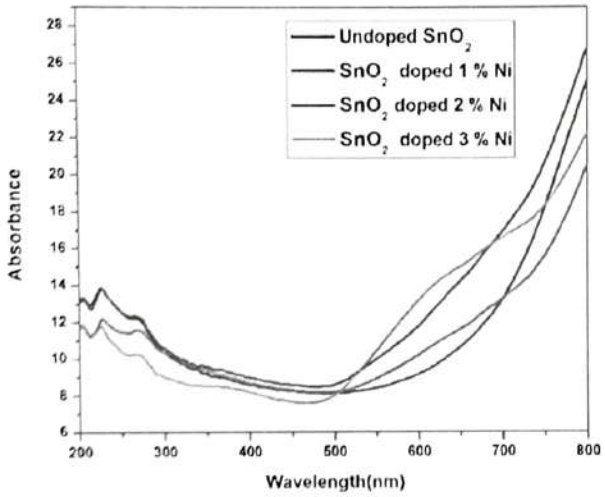


Figure 3. Optical absorption spectrum pure SnO_2 and Ni-doped SnO_2 NCs.

missing for the samples with an increase of Ni doping towards SnO_2. This may be due to the fact that the doping species affects the spectra and broaden the metal oxide bands. One such band can be assigned to Ni–O stretching (around 520 cm^{-1}) due to the Ni ion present in the doped samples [15].

The optical absorption studies for the samples (pure and Ni-doped SnO_2 NCs) were measured by using the UV-Visible spectroscopy and the results are compared in figure 3. As observed, the optical absorption edge for pure and Ni-doped SnO_2 was found to be around 220–250 nm, qualified due to the excitation of electrons from the valence band by the photons. There was some higher absorbance observed in the case of pure SnO_2 but with an increase in the concentration of Ni dopant (1%–3%), the absorbance tends to be decreased. This possibly can be due to the photon interaction with sufficient energy and thereby causing higher absorption and associated lowered transmission in the UV-region. Further, the absorption edge increased with varying concentrations of Ni in the doping protocol as the absorbance value hinges on quite a few factors, such as band gap, deficiency in oxygen, impurity centers [21].

The following Tauc-plot equation was used for calculating the optical band gap (E_g) [22].

$$\alpha = \frac{A(h\nu - E_g)^{1/2}}{h\nu}$$

where α corresponds to the absorption coefficient, h for the Plank's constant, ν the frequency of the light radiation used, E_g is the band gap.

P.K.R. COLLEGE OF ARTS & SCIENCE NAMAKKAL 637 206

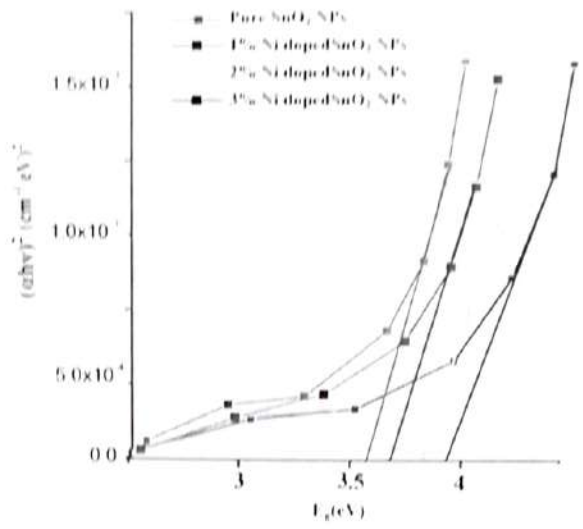


Figure 4. Band energy gaps (Eg) for the pure SnO_2 and Ni-doped SnO_2 NCs.

Table 2. Optical band gap energy values for pure and Ni-doped SnO_2 NCs.

Sample	Optical band gap energy (E_g) eV
Pure SnO_2 NCs	3.61
1% Ni-doped SnO_2 NCs	3.72
2% Ni-doped SnO_2 NCs	3.79
3% Ni-doped SnO_2 NCs	3.87

Figure 4 shows the comparison of the band energy gaps among the pure SnO_2 and Ni-doped SnO_2 NCs, while the calculated values are tabulated in table 2. From the figure 4, it is interesting to note that the E_g value is getting raised with an increase in the intensification of Ni doping into the SnO_2 matrix (3.61 eV to 3.87 eV). This rise in E_g might be due to the decrease in the size of the particle with a larger surface area and strong quantum confinement effects [23].

With the use of PL technique, it is possible to identify the defective states and their associated effects in optical studies and so the figure 5 shows the comparison of the PL spectrums among pure SnO_2 and Ni-doped SnO_2 NCs at 500–900 nm range. As detected from the figure that a strong peak at 550 nm is protruding with an increase of Ni doping into the SnO_2 NC. The intensity of the peak for 1%, 2%, and 3% doping of Ni tend to move towards a shorter wavelength region. These results validate well with the absorbance spectra and are consistent with our observations. In general for the semiconductor NCs, the oxygen deviancies the most common defects which act as a radiative center for the radiative recombination in the visible region. In the circumstance of doped samples, it is easier for Ni^{2+} ions to replace Sn^{4+} ions due to the fact that the ionic radius of both Ni^{2+} and Sn^{4+} are virtually equal [24]. Additionally, the charge (−2) of the replaced Sn position has to be compensated in the form of oxygen vacancy in the positions. Thus, the vacancy creates defects giving rise to absorption and emission of the visible spectrum.

The comparison of SEM micrographs of undoped and Ni-doped SnO_2 NCs is shown in figures 6(a)–(d). It was clear from the SEM images that the synthesized nanostructures are homogeneous, uniformly distributed with spherical to oval-shaped structures. Alongside, the plate-like structures were also observed in the case of pure SnO_2 nanostructures which further rupture into loosely aggregated crystal pattern on doping with the Ni into the SnO_2 matrix. Further, the elemental composition of pure and Ni-doped SnO_2 NCs (2%) was evaluated using EDX analysis and the results are shown in figures 6(e), (f). From the comparison of peaks in the respective spectrums, it confirms that Sn and O are present in the pure SnO_2 sample (figure 6(e)), while Sn, O, and Ni elements are in the 2% Ni-doped SnO_2 (figure 6(f)). The persistence of these elements in the samples confirms for the successful formation of the respective composites and in addition, provides a proof for the induction of dominant effect by the Ni doping into the SnO_2 compound's structural and optical properties. Moreover, the EDX spectrum confirmed the presence of no other foreign elements as byproducts in the synthesized samples.

P.G.P. COLLEGE OF ARTS & SCIENCE NAMAKKAL 637 20

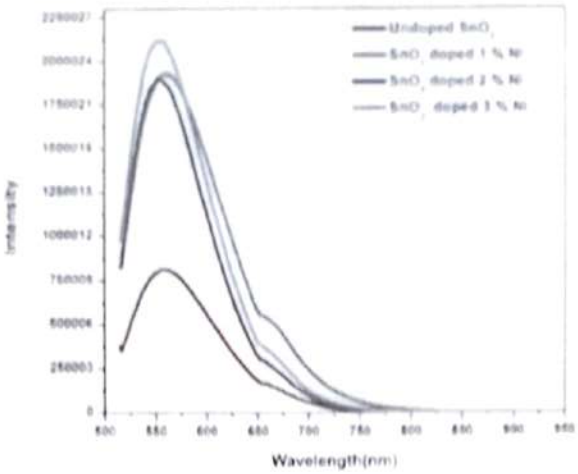


Figure 5. PL spectrums for the pure SnO_2 and Ni doped SnO_2 NCs

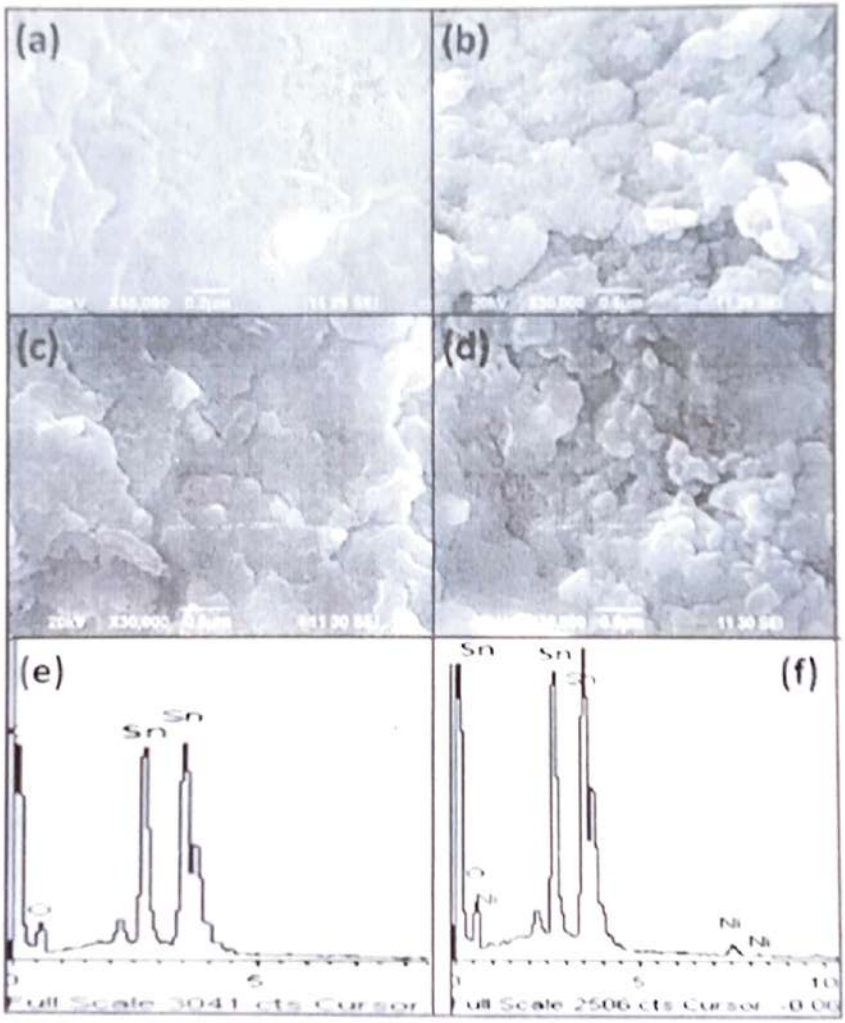


Figure 6. SEM photographs of (a) pure SnO_2, (b) 1% Ni doped, (c) 2% Ni doped, and (d) 3% Ni doped SnO_2 NCs. (e) and (f) corresponds to the respective EDX spectrums of pure SnO_2 and 2% Ni doped SnO_2 NCs

COLLEGE OF ARTS & SCIENCE NAMAKKAL 637 206

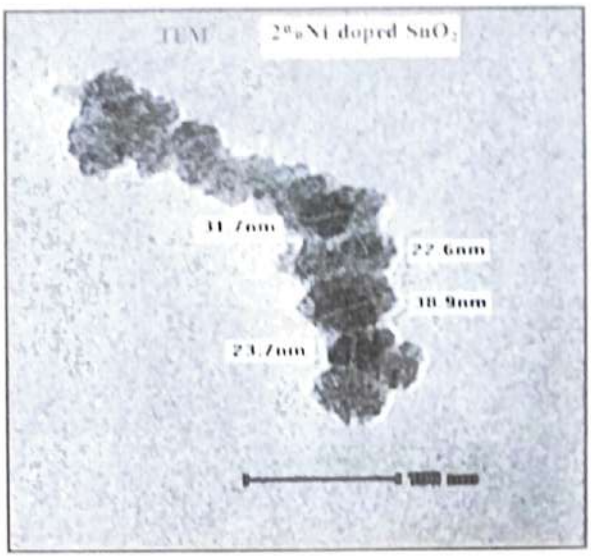


Figure 7. TEM photograph of Ni-doped SnO_2 NCs.

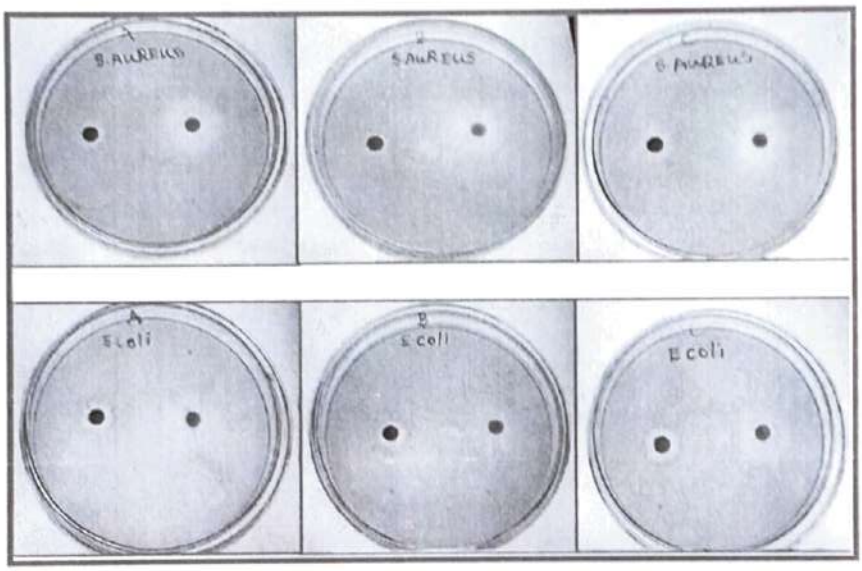


Figure 8. Comparison of the ZoI of pure SnO_2 and Ni-doped SnO_2 NCs against Gram-negative *E. coli* and Gram-positive *Staphylococcus aureus*. Each plate compares the activity of pure SnO_2 and Ni-doped SnO_2, where A, B, and C correspond to 1%, 2%, and 3% Ni-doped SnO_2 NCs respectively.

Also, the TEM micrograph for the 2% of Ni-doped SnO_2 NCs shown in figure 7 indicates that the particles are fully agglomerated and maintaining the particle size in the range 22–38 nm.

3.2. Testing of biological efficacy

In order to test the biological efficacy of the synthesized pure and Ni-doped SnO_2 NCs, the tests of antibacterial activity and *in vitro* cytotoxicity were studied. The antibacterial susceptibility testing SnO_2 NCs at 25 μl concentrations against the Gram-negative *E. coli* and Gram-positive *S. aureus* was evaluated using the agar diffusion method as evident from the diameter of the ZoI after the 24 h of the incubation period. The ZoI of pure and varying concentrations of Ni-doped SnO_2 NCs against the Gram-negative *E. coli* and Gram-positive *Staphylococcus aureus* are shown in figure 8 and the corresponding graphical representations are in figure 9. There was a typical synergistic antibacterial effect when Pure SnO_2 was combined with the different percentages

P.G. COLLEGE OF ARTS & SCIENCE NAMAKKAL 637 206

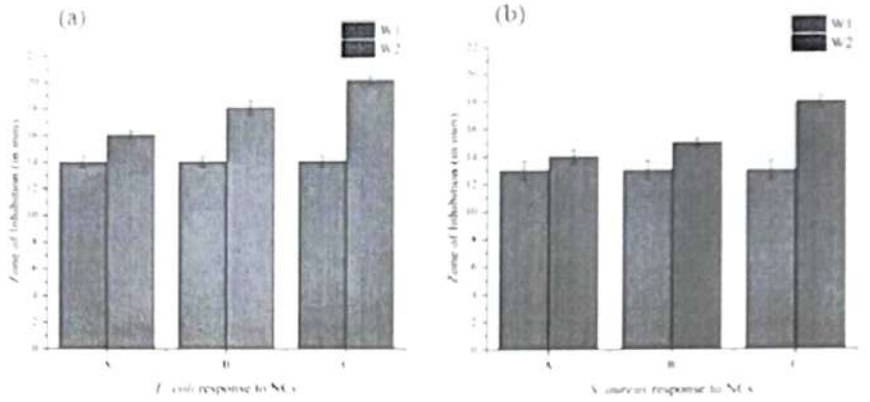


Figure 9. Comparison of the antibacterial susceptibility pure and Ni-doped SnO_2 NCs for (a) Gram-negative *E. coli*, (W1 – well 1), and (b) Gram-positive *S. aureus* (W2 – well). A, B, and C corresponds to the 1%, 2%, and 3% Ni-doped SnO_2 NCs respectively.

of Ni-doped SnO_2 NCs. The fold increase of 14.2%, 28.5%, and 42.8% was observed in *E. coli* on a pure SnO_2 (control). Similarly, a fold increase of 7.6%, 15.3%, and 38.4% was also exhibited by *S. aureus* exposed plate.

The difference in activity of pure SnO_2 and in combination with doped NCs against these two types of bacteria was shown in figure 9. The Ni-doped SnO_2 exhibited a higher ZOI as compared with pure SnO_2 NCs in the event of microbial cell death. In fact, the Ni-doped SnO_2 NCs at different concentrations showed an enhanced antibacterial effect as compared with the previously reported antibacterial studies data [25].

From the antibacterial studies, it was observed that the tested compounds have offered significant levels of activity against both the Gram-positive and Gram-negative bacteria. The observation of such activity can be due to the electrostatic interaction between the positively charged NCs and negatively charged bacteria where these small-sized NCs can penetrate easily inside the cell wall and paralyses the cell [26]. Once inside the cell, the prepared Ni-doped SnO_2 NPs from respective ions *viz.* Ni^{2+} and Sn^{4+} oxidize the cell walls by getting themselves reduced into more stable ones. In the process of oxidation, Ni^{2+} and Sn^{4+} ions induces oxidative stress in extensive amounts to the cells where they generate reactive oxygen species (ROS) in the form of superoxide anion (O^{2-}), hydroxyl radicals (OH^-), peroxides ($(O–O)^{2-}$), organic hydroperoxides (OHPs) etc and all these pathways finally leads the cells to lose viability. As similar to our results, Adegoke *et al* also observed the antibacterial activity and phytochemical analysis of leaf extracts of *Lasienthera africanum* [27]. Further, it was confirmed from the study that the gram-negative *E. coli* suffered severe damage than the respective Gram-positive *S. aureus*. Although the exact cause of differences in such activity cannot be known at this stage but can be mostly due to the immune responses maintained by the *S. aureus* cells as compared against the *E. coli* following exposure to the samples.

The antiproliferative activity of phytochemical mediated synthesis of pure SnO_2 and Ni-doped SnO_2 NCs against the Vero and HEp-2 cells were tested based on the MTT reduction route where the results are shown in figures 10 and 11 respectively. From the comparison of MTT data when tested over a 24 h period, both the cell types are experiencing significant levels of toxicity under the testing concentrations and the cell viability losses are getting increased with respect to an increase in the Ni ion concentration. Also, the IC_{50} concentration (maximum concentration required for 50% cell death) for the pure SnO_2 and 1%, 2% and 3% Ni-doped SnO_2 NCs exposed Vero cells were determined to be 93.75 $\mu g\ ml^{-1}$, 52.08 $\mu g\ ml^{-1}$, 41.6 $\mu g\ ml^{-1}$ and 31.25 $\mu g\ ml^{-1}$ respectively. Similarly, the IC_{50} for pure SnO_2 and 2%, 4% and 6% Ni-doped SnO_2 nanocrystals exposed to HEp-2 cells worked out to be 173.06 $\mu g\ ml^{-1}$, 138.8 $\mu g\ ml^{-1}$, 93.75 $\mu g\ ml^{-1}$ and 48.29 $\mu g\ ml^{-1}$ respectively. From the comparison of IC_{50} values among the Vero and HEp-2 cells, the tested compounds are more effective against the Vero cells as compared to the HEp-2 cells and this difference of activity can be attributed to the intracellular mechanistic response of each cell type against the tested compounds.

The visual observation of cells in the form of rounding, clumping, or non-adherence to the cell walls at increased concentrations of Ni also confirms for the cytotoxicity effects as shown in figures 8(D)–(F). There was a significantly increased trend in the cytotoxicity induced by Ni-doped SnO_2 NCs than pure SnO_2 attributing to its synergistic effect. Both the cells were adversely affected by the NCs, wherein the normal cells (Vero) showed increased susceptibility than the cancer cells (HEp-2). Anita let *et al* also used the Vero cells to showcase the excellent cytocompatibility and cell viability of the synthesized mesoporous hydroxyapatite [28]. It was believed that the nanomaterials trigger the generation of ROS leading to oxidative stress. Furthermore, these

P.K.R. COLLEGE OF ARTS & SCIENCE NAMAKKAL 637 206

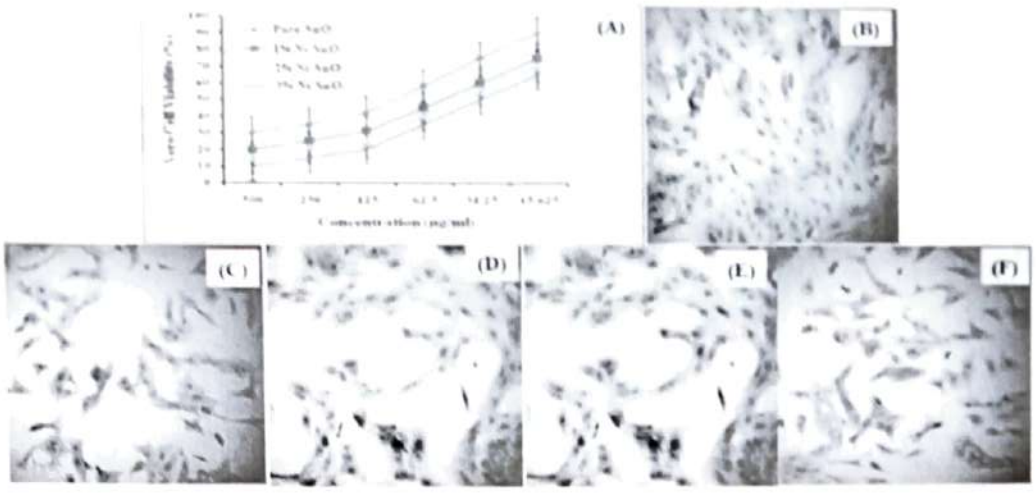


Figure 10. Comparison of MTT assay data (A), and phase contrast optical microscopic images of control (B), Pure SnO_2 (C), 1% Ni-doped (D), 2% Ni-doped (E), and 3% Ni-doped SnO_2 (F) NCs exposed to Vero cells with crystal violet stain.

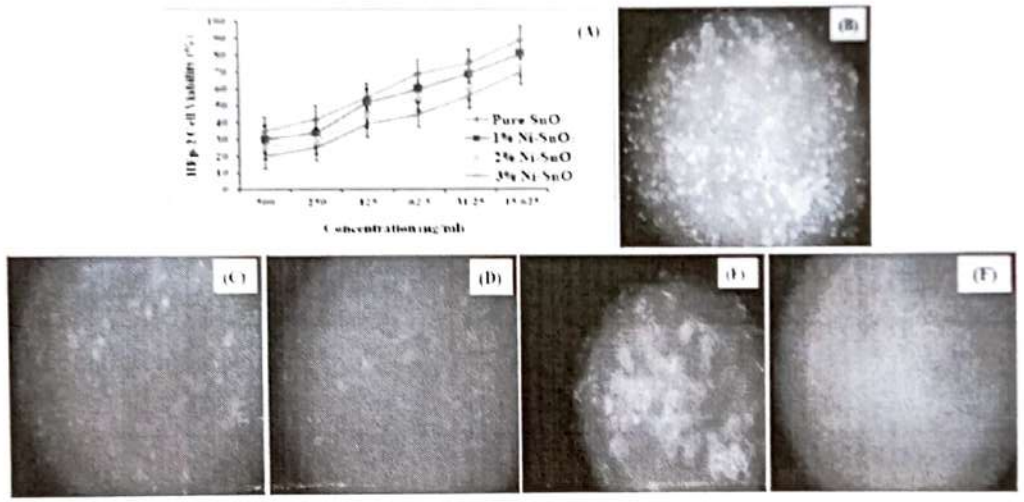


Figure 11. Comparison of MTT assay data (A), and the microscopic images of control (B), Pure SnO_2 (C), 1% Ni-doped (D), 2% Ni-doped (E), and 3% Ni-doped SnO_2 (F) NCs exposed to HEp-2 cells with crystal violet stain.

nanomaterials possess a high surface to volume ratio that corroborates with its high interfacial physical and chemical reactivity that in turn gets transformed into biological activity [29]. The experimental results showed that the incorporation of Ni into SnO_2 at different concentrations had a significantly beneficial influence on the bioactivity than that devoid of Ni. The increased concentration of Ni as a dopant in the NCs enhanced the cytotoxicity of SnO_2 hypothesizing the direct interaction of NCs with the cell membrane and the generation of oxidative stress for the enhanced antimicrobial and cytotoxic effects of Ni-doped SnO_2 NCs [30].

4. Conclusion

In conclusion, we have compared and studied the biological activity of pure and Ni-doped SnO_2 NCs formed by the simple co-precipitation method. From the physical characterization, the powdered XRD data confirmed the tetragonal crystalline phase structure of SnO_2 and the existence of Ni ions along with SnO_2 does not show any variations in its lattice parameters. Also, the average crystal sizes for the pure and Ni-doped SnO_2 were investigated to be in the 68–22 nm range and the SEM images showed the distribution of SnO_2 NCs with

P.G.P. COLLEGE OF ARTS & SCIENCE NAMAKKAL 637 206

homogeneity. There was a great reduction in the crystal size with higher Ni content on SnO_2 matrix. The absorption edge slightly shifted towards the shorter wavelength region with an increased energy band gap and increased Ni concentration from 1–3 molar % (3.61 to 3.87 eV). The PL spectrum showed the defective states encountered an enhanced visible emission for the Ni doped SnO_2 NCs and so the doped NCs maintains improved photoactive behavior than the corresponding un-doped ones due to the availability of more surface area and newly trapped centers related to doping. Taking into consideration of the enhanced photoactivity, the prepared Ni doped SnO_2 NCs can show incredibly intense green emission. Further, the prepared NCs exhibited effective antibacterial activity against *E. coli* (Gram -ve) than *S. aureus* (Gram +ve). Alongside the pure and doped SnO_2 NCs exhibited cytotoxicity effect toward Vero and HEp-2 cells as evident from the IC_{50} concentration. The cytotoxicity toward HEp-2 cells was found to be double the IC_{50} value of Vero cells with typical cell rounding, morphological disturbances, and detachment. It is noteworthy to say that higher Ni doping towards SnO_2 NCs exhibited good antibacterial activity and cytotoxicity. Further, the results generated in this study supports for their use in the biomedical sector with a view to serve as bacteriostatic agents directly or indirectly with other molecules to control the bacterial infections. Alongside, they also can be used to inhibit the cancerous cell proliferations once their toxicity effects at *in vivo* levels are validated.

Acknowledgments

The King Saud University author is grateful to the Deanship of Scientific Research, King Saud University for funding through Vice Deanship of Scientific Research Chairs.

ORCID iDs

Suresh Sagadevan https://orcid.org/0000-0003-0393-7344
J Anita Lett https://orcid.org/0000-0003-2917-4277

References

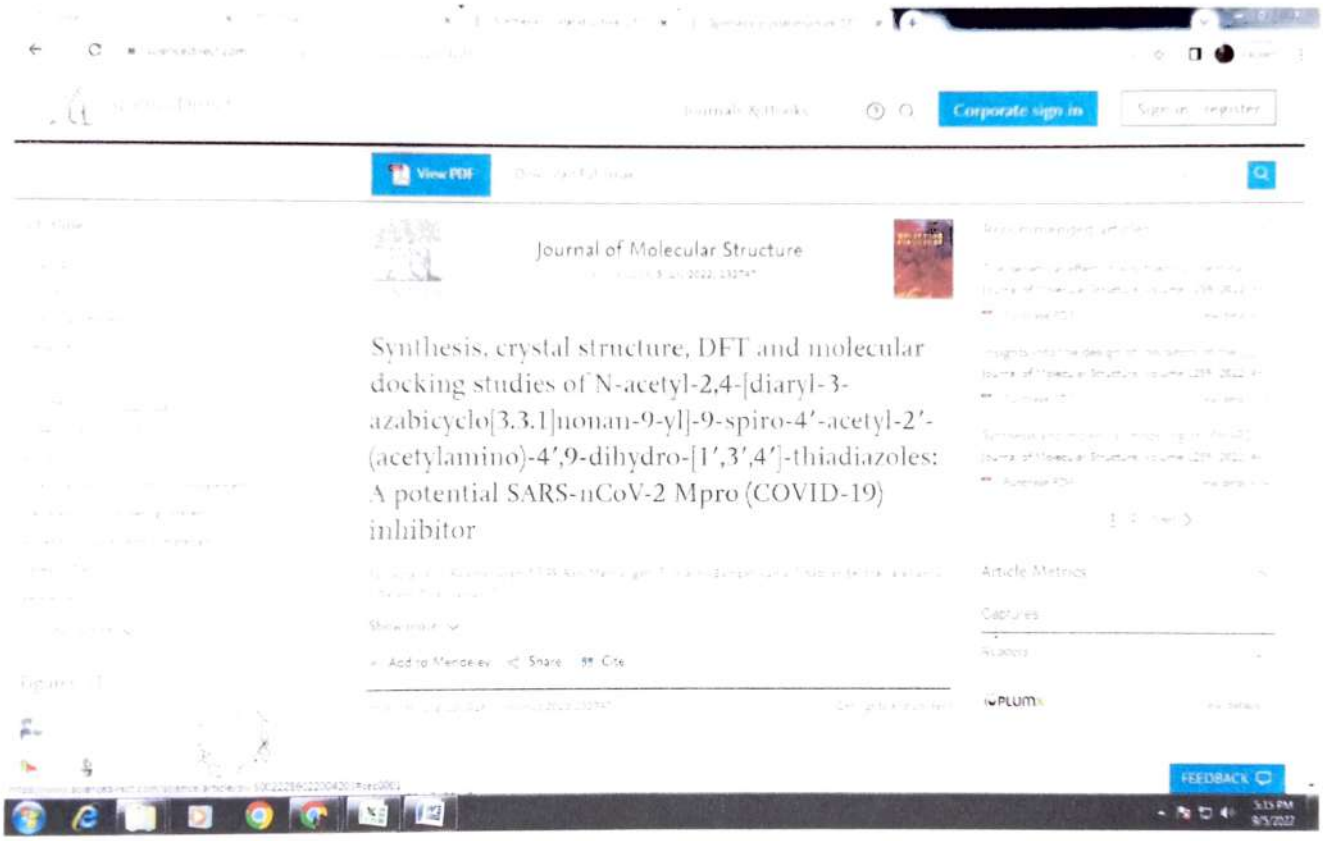
[1] Muhammad N *et al* 2017 Investigation of ionic liquids as a pretreatment solvent for extraction of collagen biopolymer from waste fish scales using COSMO-RS and experiment *J. Mol. Liq.* **232** 258–64
[2] Gu J, Yin B, Fu S, Feng M, Zhang Z, Dong H, Gao F and Zhao Y S 2018 Surface tension driven aggregation of organic nanowires via lab in a droplet *Nanoscale* **10** 11006–12
[3] Yin B, Gu J, Feng M, Zhang G C, Zhang Z, Zhong J, Zhang C, Wen B and Zhao Y S 2019 Epitaxial growth of dual-color-emitting organic heterostructures via binary solvent synergism driven sequential crystallization *Nanoscale* **11** 7111–6
[4] Zhang G C, Zhong J, Xu M, Yang Y, Li Y, Fang Z, Tang S, Yuan D, Wen B and Gu J 2019 Ternary $BiVO_4$/NiS/Au nanocomposites with efficient charge separations for enhanced visible light photocatalytic performance *Chem. Eng. J.* **375** 122093 (9 pp)
[5] Chu Y, Zhong J, Fang Z, Yang Y, Qi J, Yu S and Gu J 2020 $Ni(HCO_3)_2$ nanosheet/nickel tetraphosphate ($Ni(P_4O_{11})$) nanowire composite as a high-performance electrode material for asymmetric supercapacitors *Nanotechnology* **31** 015401
[6] Dixit R, Singh S and Yadav B C 2014 A review on synthesis, fabrication, and properties of nanostructured pure and doped tin oxide films *International Journal of Scientific and Innovative Research* **2** 41–57
[7] Sirelkhatim A, Mahmud S, Seeni A, Kaus N H M, Ann L C, Bakhori S K M, Hasan H and Mohamad D 2015 Review on zinc oxide nanoparticles: antibacterial activity and toxicity mechanism *Nano-Micro Letters* **7** 219–42
[8] Suresh S 2013 Semiconductor nanomaterials, methods, and applications: a review *Nanoscience and Nanotechnology* **3** 62–74
[9] El-Shinawi H, Böhm M, Leichtweiß T, Peppler K and Janek J 2013 A simple synthesis of nanostructured Cu-incorporated SnO_2 phases with improved cycle performance for lithium ion batteries *Electrochemical Communication* **36** 33–7
[10] Wang Y, Djerdj I, Smarsly B and Antonietti M 2009 Antimony-doped SnO_2 nanopowders with high crystallinity for lithium-ion battery electrode *Chem. Mater.* **21** 3202–9
[11] Gopinadhan K, Kashyap S, Pandya D and Chaudhary S 2007 High-temperature ferromagnetism in Mn-doped SnO_2 nanocrystalline thin films *Journal of Applied Physics*, **102** 113513–113513-8
[12] Thabethe B S, Malgas G F, Motaung D E, Malwela T and Arendse C J 2013 Self-catalytic growth of tin oxide nanowires by chemical vapor deposition process *J. Nanomater.* **712361** 1–7
[13] Salavati-Niasari M, Mir N and Davar F 2010 Synthesis, characterization and optical properties of tin oxide nanoclusters prepared from a novel precursor via thermal decomposition route *Inorg. Chim. Acta* **363** 1719–26
[14] Yogamalar R, Mahendran V, Srinivasan R, Beitollahi A, Kumar R P, Bose A C and Vinu A 2010 Gas-sensing properties of needle-shaped Ni-doped SnO_2 nanocrystals prepared by a simple sol–gel chemical precipitation method *Chem. Asian J.* **5** 2379–85
[15] Ye X, Liu W Z Q, Wang S, Yang Y and We H 2015 One-step synthesis of Ni-doped SnO_2 nanospheres with enhanced lithium ion storage performance *New J. Chem.* **39** 130–5
[16] Zhu Z F, Zhou J, Liu H, He Z and Wang X 2012 Enhanced photocatalytic activity of polyvinyl pyrrolidone assisted microwave hydrothermal grown tin oxide photocatalysts *Journal of Nanomaterials & Molecular Nanotechnology* **2** 1–5
[17] Talam S, Karumuri S R and Gunnam N 2012 Synthesis, characterization and spectroscopic properties of ZnO nanoparticles *ISRN Nanotechnology* **2012** 1–6
[18] Geetha Devi P and Velu A S 2016 Synthesis, structural and optical properties of pure ZnO and Co-doped ZnO nanoparticles prepared by the co-precipitation method *Journal of Theoriotical and Applied Physics* **10** 233–40
[19] Yang H G and Zeng H C 2004 Preparation of hollow anatase TiO nanospheres via ostwald ripening *J. Phys. Chem.* B **108** 3492–5

P.G.P. COLLEGE OF ARTS & SCIENCE NAMAKKAL 637 206

[20] Pillai K, Sreejaram L M S and Hillie T K 2010 Synthesis, characterization, and photoluminescence properties of Dy^{3+} doped nanocrystalline SnO_2 *Mater. Chem. Phys.* **120** 619–24
[21] Nilavazhagan S, Muthukumaran and Ashokkumar M 2015 Microstructural and band gap exploration on Ni doped SnO_2 nanoparticles co-doped with Cu *J. Mater. Sci.: Mater. Electron.* **26** 9889–96
[22] Nair A S and Isac J 2013 Effect of temperature on optical properties of nanocrystalline ceramics $Fe_3Mn_2Ni_2Zn_3O_{12}$ *International Journal of Science and Research (IJSR)* **6** 1862–7
[23] Lin H, Huang C P, Li W, Ni C, Shah I and Tseng Y H 2006 Size dependency of nanocrystalline TiO_2 on its optical property and photocatalytic reactivity exemplified by 2-chlorophenol *Appl. Catalysis B* **68** 1–11
[24] Brajesh Nandan B, Vengopal S, Amirthapandian B K and Panigrahi P L 2014 Effect of Pd ion doping in the band gap of SnO_2 nanoparticles: structural and optical studies *J. Nanopart. Res.* **15** 48–57
[25] Sonia S, Jayram N D, Suresh Kumar P, Mangalaraj D, Poupandian N and Viswanathan C 2014 Effect of NaOH concentration on structural, surface and antibacterial activity of CuO nanorods synthesized by direct sonochemical method *Superlattices Microstruct.* **66** 1–9
[26] Kaliaraj G S *et al* YSZ coated titanium by EBPVD for biomedical applications *Surf. Coat. Technol.* **307** 2016 227–33
[27] Indhumathy M, Bavanilathanuthiah and Malar C G 2014 Anticancer activity of Zingiber officinale bound dendrimera *in vitro* analysis *International Journal of Drug Discovery* **5** 77–81
[28] Anita Lett J, Sundareswari M, Ravichandran K, Latha M B, Sagadevan S and Bin Johan M R 2019 Tailoring the morphological features of sol–gel synthesized mesoporous hydroxyapatite using fatty acids as an organic modifier *RSC Adv.* **9** 6228
[29] Jones C F and Grainger D W 2009 *In vitro* assessments of nanomaterial toxicity *Adv. Drug Delivery Rev.* **61** 438–56
[30] Alkahtane A 2015 Indium tin oxide nanoparticles-mediated DNA fragmentation and cell death by apoptosis in human lung epithelial cells *Toxicological & Environmental Chemistry* **97** 1–29







P.G.P. COLLEGE OF ARTS & SCIENCE
NAMAKKAL
637 206

Journal of Molecular Structure 1259 (2022) 132747

Contents lists available at ScienceDirect

Journal of Molecular Structure

journal homepage: www.elsevier.com/locate/molstr

Synthesis, crystal structure, DFT and molecular docking studies of N-acetyl-2,4-[diaryl-3-azabicyclo[3.3.1]nonan-9-yl]-9-spiro-4′-acetyl-2′-(acetylamino)-4′,9-dihydro-[1′,3′,4′]-thiadiazoles: A potential SARS-nCoV-2 Mpro (COVID-19) inhibitor

Ramachandran Rajamanickam[a,*], Rani Mannangatty[b], Jayanthi Sampathkumar[c], Kabilan Senthamaraikannan[b], Barathi Diravidamani[d]

[a] Department of Chemistry, PGP College of Arts and Science (Affiliated to Periyar University, Salem), Namakkal, 637 207, Tamil Nadu, India
[b] Department of Chemistry, Annamalai University, Annamalainagar, 608 002, Tamil Nadu, India
[c] Department of Chemistry, N.K.R. Government Arts college for Women (Affiliated to Periyar University, Salem), Namakkal, 637 001, Tamil Nadu, India
[d] Department of Physics, N.K.R. Government Arts college for Women (Affiliated to Periyar University, Salem), Namakkal, 637 001, Tamil Nadu, India

ARTICLE INFO

Article history:
Received 7 January 2022
Revised 15 February 2022
Accepted 1 March 2022
Available online 2 March 2022

Keywords:
Azabicyclo[3.3.1]nonan-9-ones
Spiro thiadiazoles
Chalcogen bond
SARS-nCoV-2 M^{pro}
Molecular docking

ABSTRACT

In this paper, we describe the synthesis and crystal structure analysis of N-acetyl-2,4-[diphenyl-3-azabicyclo[3.3.1]nonan-9-yl]-9-spiro-4′-acetyl-2′-(acetylamino)-4′,9-dihydro-[1′,3′,4′]-thiadiazole (**3a**) and N-acetyl-2,4-[bis(*p*-methoxyphenyl)-3-azabicyclo[3.3.1]nonan-9-yl]-9-spiro-4′-acetyl-2′-(acetylamino)-4′,9-dihydro-[1′,3′,4′]-thiadiazole (**3b**). The title compounds **3a** and **3b** are characterized by 1D NMR and single crystal x-ray diffraction analysis. Non-covalent interactions in a molecule were identified by Hirshfeld surface (d_{norm} contacts and 2D fingerprint plot) analysis. In addition, the existence of chalcogen bond (S•••O bond) in the molecular structures (**3a** and **3b**) are described by NCI-RDG and QTAIM analysis. NBO analysis is employed to describe the orbital interactions and electron transfer between sulfur and oxygen atoms. Molecular docking is carried out for compounds **3a** and **3b** with COVID-19 viral protein SARS-nCoV-2 M^{pro} (PDB ID: 6LU7).

© 2022 Elsevier B.V. All rights reserved.

1. Introduction

Spiro heterocyclic structure is a unique feature of a several natural and synthetic products that possess remarkable biological activities [1,2]. The potential use of spiro heterocycles in medicinal chemistry has been well documented owing to their prominent pharmacological properties [3]. The thiadiazole moiety is associated with a broad spectrum of biological activities such as antifungal [4], antioxidant [5], anticonvulsant, antiviral [4], plant growth regulatory [6], CNS depressant [7], and anticancer [8] activitiy. Methazolamide is a thiadiazole based drug being used to treat reduction of high pressure inside the eyes, prevents blindness, nerve damage, and vision loss and glaucoma [9]. Similarly, acetazolamide is an another thiadiazole drug candidate being used as drug for the treatment of epileptic seizure, and periodic paralysis [10].

1,3,4-thiadiazole core has been reported as an electron-deficient nature, electron-accepting ability and good thermal as well as chemical stability [11]. Thus, thiadiazole derivatives are often used to create liquid crystals due to charge-transporting ability, photoconductivity, photoluminescence and mesomorphism [12]. Therefore, development of new spiro-heterocycles having thiadiazole ring is worthwhile from the perspective of medicinal and material chemistry [13,14].

Piperidine is an another heterocyclic compound that found naturally in alkaloids, and its derivatives have good biological and pharmacological properties [15]. On the other hand, the six membered piperidine ring undergoes several conformational changes when introducing electron donating or withdrawing substituents at the nitrogen site. For example, the piperidine ring adopts chair conformation with electron donating substituent (H, CH_3, CH_2Ph) whereas the electron withdrawing group (heteroatom group, COR, NO) on the same site adopts boat conformation [16]. Recently, several piperidine derivatives along with the incorporation of hetero conjugate groups at the nitrogen atom of piperidine ring have been well explored by spectroscopic and X-ray analysis [17–19]. Earlier reports disclosed that the blocking of secondary nitrogen atom in the piperidine ring by electron donating or withdrawing groups, abrupt changes were observed in the ring conformations.

* Corresponding author.
E-mail address: synorgramu@gmail.com (R. Rajamanickam).

https://doi.org/10.1016/j.molstruc.2022.132747
0022-2860/© 2022 Elsevier B.V. All rights reserved.

P.G.P. COLLEGE OF ARTS & SCIENCE NAMAKKAL 637 206

As a result, the molecule displays different conformation such as chair, boat or twist-boat forms.

The novel coronavirus 2019 (nCoV, also called as COVID-19) is a new strain and highly contagious viral disease. The coronavirus causes a severe acute respiratory syndrome (SARS nCoV-2) has showed to be the most deadly global health crisis since the 1918 influenza pandemic [20]. The novel virus (SARS nCoV-2) has proven to be a worldwide unprecedented disaster that affects billions of lives across the world in many ways. Currently, there are no specific treatment options for SARS CoV-2. Thus, it has been classified that COVID-19 is a very rare disease with a limited number of treatment options [21]. Molecular docking is the preliminary study in the drug designing, which help us to find the possible binding site between lead molecule and protein structure. For Covid-19, several docking studies have been reported to find potential antiviral drugs and vaccines [22–26].

In this paper, we have selected bicyclic ring system that contains both heterocyclic (piperidine) and non-heterocyclic (cyclohexane) rings based on spiro derivatives viz. N-acetyl-2,4-[diaryl-3-azabicyclo[3.3.1]nonan-9-yl]-9-spiro-4′-acetyl-2′-(acetylamino)-4′,9-dihydro-[1′,3′,4′] thiadiazoles (**3a** and **3b**) to describe the spectral characterization and single crystal structure analysis. Also, the DFT studies have been employed to explore the electronic properties of molecules **3a** and **3b**. In addition, the molecular docking is carried out to extend the scope of molecular structure with novel coronavirus causing protein.

2. Experimental

^{1}H and ^{13}C NMR spectra of **3a** and **3b** were obtained from BRUKER AMX 500 MHz FT-NMR spectrometer using $CDCl_3$ as the NMR solvent, whereas TMS was used as an internal reference. The NMR chemical shift (δ) and coupling constants values were measured in ppm and coupling constants in Hz, respectively.

2.1. Synthesis of compounds 3a and 3b

The title compounds **3a** and **3b** were synthesized according to the Scheme 1. Initially, 2,4-diaryl-3-azabicyclo[3.3.1]nonan-9-one thiosemicarbazones (**2a** and **2b**) were synthesized according to the literature precedent [27]. The title compounds **3a** and **3b** were synthesized by modification of our earlier reports [28]. A mixture of 2,4-diaryl-3-azabicyclo[3.3.1]nonan-9-one thiosemicarbazone (**2a** or **2b**, 0.5 g) and 20 mL of distilled acetic anhydride were heated at 60°C on water bath for 6 h. After completion of the reaction, as confirmed by TLC, the reaction mixture was kept in the freezer at overnight and the separated solid was filtered off, dried and purified by column chromatography. The pure crystals of **3a** and **3b** for X-ray diffraction analysis were grown by slow evaporation technique using distilled ethanol.

2.1.1. N-Acetyl-2,4-[diphenyl-3-azabicyclo[3.3.1]nonan-9-yl]-5-spiro-4-acetyl-2-(acetylamino)-Δ^2-1,3,4-thiadiazoline (3a)

^{1}H NMR, (δ=ppm): 6.13 (d, 2H, H-2a & H-4a); 3.30 (d, 2H, H-1e & H-5e); 1.70 (s, 4H, amide CH_3 & H-7a); 1.66 (s, 3H, H-6e, H-8e); 1.30 (d, 2H, H-6a & H-8a); 1.24 (m, 1H, H-7e); 9.67 (bs, 1H, spiro NH); 2.20, 1.90 (s, 3H, amide CH_3); 7.40 & 7.51 (t & bs, 10H, aryl protons); ^{13}C NMR (δ=ppm) $CDCl_3$: 61.58 (C-2 & C-4); 41.38 (C-1 & C-5); 25.61 (C-6 & C-8); 18.30 (C-7); 87.28 (C-9); 27.23, 24.63 & 22.36 (amide CH_3); 176.20, 174.22 & 169.55 (amide C=O); 155.60 (C=N); 142.95, 142.18 (C-2′ & C-4′); 128.53, 126.59, 125.58 (other aryl carbons).

2.1.2. N-Acetyl-2,4-[bis(p-methoxyphenyl)-3-azabicyclo[3.3.1]nonan-9-yl]-5-spiro-4-acetyl-2-(acetylamino)-Δ^2-1,3,4-thiadiazoline (3b)

^{1}H NMR, (δ=ppm): 6.11 (d, 2H, H-2a & H-4a); 3.22 (d, 2H, H-1e & H-5e); 1.75 (bs, 4H, amide CH_3 & H-7a); 1.68 (m, 2H, H-6e & H-8e); 1.34 (d, 2H, H-6a & H-8a); 1.23 (m, 1H, H-7e); 9.73 (bs, 1H, spiro NH); 2.19, 1.90 (s, 6H, amide CH_3); 6.91 (d, 5H, aryl protons *ortho* to OCH_3 group, 7.41 (bs, 3H, aryl protons *meta* to OCH_3 group); 3.82 (s, 6H, OCH_3 group at phenyl group ^{13}C NMR (δ ppm) $CDCl_3$: 61.09 (C-2 & C-4), 41.43 (C-1 & C-5), 25.60 (C-6 & C-8), 16.78 (C-7), 87.45 (C-9), 27.37, 24.65 & 22.57 (amide CH_3), 176.90, 174.01 & 169.37 (amide C=O), 155.32 (C=N), 158.21,158.14 (C-2′′′ & C-4′′′), 134.94, 134.24 (C-2′ & C-4′), 126.70, 113.93 (other aryl carbons), 55.30 (OCH_3 group at the phenyl group).

2.2. Single crystal X-ray analysis

Colorless rectangular crystals (0.25, 0.20, 0.20 mm for **3a** and 0.20, 0.20, 0.25 mm for **3b**) were used for the data collections. The single crystal X-ray diffraction data were recorded using a CCD area detector at room temperature (273 K). The data reduction and cell refinement were carried out using SAINT/XPREP (Bruker), and APEX2/SAINT, respectively. The crystal structures (**3a** and **3b**) were solved by direct methods using SHELX-97 [29]. All the non-hydrogen atoms were treated anisotropically by the full-matrix least squares method, whereas hydrogen atom bound to the carbon atoms were constrained isotropically. However, the hydrogen atoms bound to the nitrogen atoms refined freely. Graphical molecular illustrations were done with ORTEP 3 for Windows [30]. The Crystallographic information files (CIFs) were deposited in the Cambridge Crystallographic Data Centre. The CCDC number for **3a** and **3b** are 796611 and 793237, respectively. CIF data of **3a** and **3b** can be obtained free of charge from www.ccdc.cam.ac.uk/data_request/cif.

2.3. Hirshfeld surface analysis

The Crystal Explorer 21.5 program was used to generate Hirshfeld surfaces (HS) mapped over d_{norm}, shape-index and curvedness plots [31], as previously studied in reference [32]. The structural input files of **3a** and **3b** were obtained from CIF data. The normalized intermolecular contact distance was denoted as d_{norm} using the following relation.

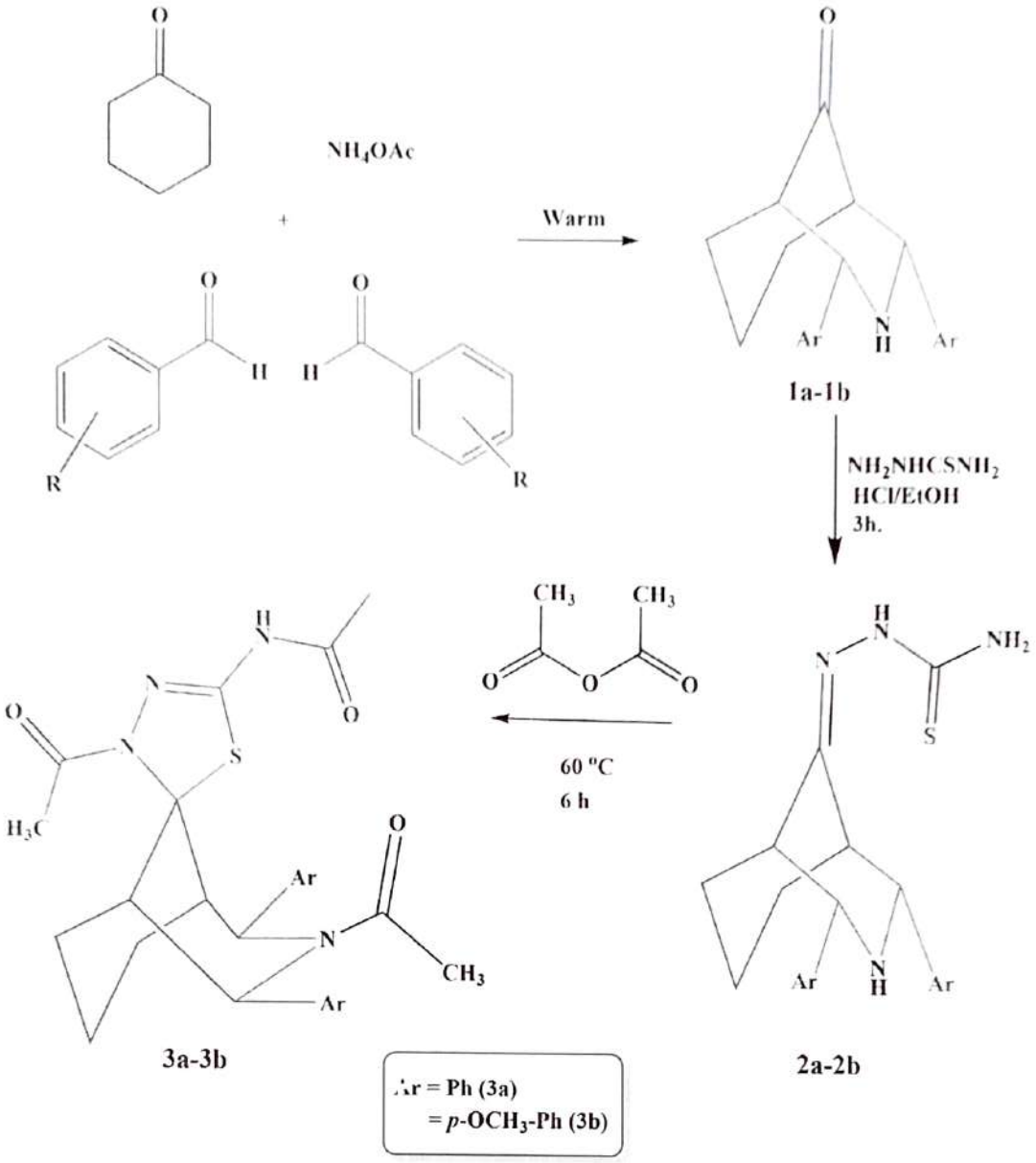
$$d_{norm} = \frac{d_i - r_i^{vdw}}{r_i^{vdw}} + \frac{d_e - r_e^{vdw}}{r_e^{vdw}}$$

where d_e and d_i define the distance from the Hirshfeld surface to nearest outside and inside the nucleus surfaces, respectively, r_e^{vdw} / r_i^{vdw} define the van der Waals radii of outside and inside the atoms, respectively. The value of intermolecular contacts (d_{norm}) such as hydrogen bonding, van der Waals radii and steric interaction are distinguished by tricolor code; red-white-blue-colors, respectively. The bright red spots on the Hirshfeld surface show the intermolecular contacts less than their van der Waals radii, whereas the blue region on the HS demonstrates intermolecular contacts longer than their van der Waals radii. However, the white spot on the HS indicates the sum of their van der Waals radii. Further, the π–π interaction between asymmetric units can be detected through the shape index mapped surface as they exhibit adjacent red-blue triangle concave.

2.4. Computational study

All quantum chemical calculations were carried out by using Gaussian 09 software with DFT method at B3LYP/6-311G (d,p) level [33]. Gauss view 5.0.9 was used to prepare and inspect the input

P.G.P. COLLEGE OF ARTS & SCIENCE NAMAKKAL 637 206



Scheme 1. Synthetic route for the synthesis of compounds **3a** and **3b**

and output files. Quantum theory of atoms in a molecule (QTAIM) was done with AIMALL software [34] whereas non-covalent interaction and radiant density gradient (NCI-RDG) were executed with Multiwin and VMD molecular visualization programmes [35]. The docking study was carried out using AutoDockTools 1.5.7 [36]. The selected protein structure for this study was obtained from Protein Data Bank (PDB ID: 6LU7). Both ligands (**3a** and **3b**) and protein structure (6LU7) were cleaned prior to the docking using Discovery Studio 2021 Client [37]. The grid box was centered using −19.173, 10.969, and 68.039 Å along *x, y, and z* axes was prepared with 70 × 65 × 70 A with spacing of 0.375 Å. The genetic algorithm was employed for ligand **3a** and **3b** as the search parameter with 100 runs.

3. Results and Discussion

3.1. NMR analysis of 3a and 3b

NMR signals were assigned based on the signal position, multiplicity and integral values [38]. The proton and carbon NMR chemical shift values of **3a** and **3b** are presented in section 2.4. It is seen that, two doublets were observed at 6.13 and 3.30 ppm (for **3a**) ppm and 6.11 and 3.22 ppm (for **3b**) with two protons integral each should be assigned to benzylic (H-2/H-4) and bridgehead (H-1/H-5) protons, respectively. The observed chemical shift value of H-2/H-4 is deshielded about 2 ppm as compared to 2,4-diaryl-3-azabicyclo[3.3.1nonane-9-one thiosemicarbazones [27], which

P.G.P. COLLEGE OF ARTS & SCIENCE NAMAKKAL 637 206

were reported at 4.26/4.36 ppm [27]. The large chemical shift variation should be due to incorporation of acetyl group at the nitrogen site of piperidine ring, where the acetyl group undergoes NCO bond free rotation in NMR time scale. Owing to this, the benzylic protons are deshielded significantly. Further, it was expected that broad signal for benzylic protons, as that of our earlier study on N-chloroacetyl-2,6-diarylpiperidin-4-ones [17]. Contrary to this, sharp signal appeared due to perpendicular orientation of acetyl group [39].

Further, a collection of signals for H-2/H-4were observed in the upfield region from 1.24-2.73 ppm are due to signals of methylene protons of cyclohexane ring, as shown in Fig S1-S2. It is seen that, three multiplets appeared at 1.70, 1.66 and 1.30 ppm (for **3a**) and 1.72, 1.60 and 1.28 ppm (for **3b**). It is worth to mention that due to the anisotropy effect of C-C bond, the equatorial proton in methylene carbon of cyclohexane ring is more deshielded than its axial proton. Based on this, the deshielded multiplets at 1.70 ppm (**3a**), and 1.72 ppm (**3b**) is attributed to H-6e/H-8e protons whereas the signal at 1.66 (**3a**), and 1.60 ppm (**3b**) should be due to H-6a/H-8a protons. However, the signal 1.30 ppm (**3a**), 1.28 ppm (**3b**) with one proton integral value is due to H-7e proton. Similarly, a multiplet at 2.61 with one proton value is due to another H-7 proton (H-7a). The chemical shift value of cyclohexane methylene proton of **3a** and **3b** are in good agreement with the earlier report on parent compounds reported by us [27,40]. Additionally, two singlets were resonated at 2.20, 1.90 (**3a**) and 2.19 and 2.20 (**3b**) ppm with six proton integral value should be due to acetyl methyl protons. The signal at the deshielded region 9.67 ppm (**3a**) and 9.73 ppm (**3b**) with one proton integral value is ascribed to N-H proton in the side chain acetylamino group.

^{13}C NMR spectra of compounds **3a** and **3b** are depicted in Fig. S3 and S4 respectively. It is seen that, two signals with equal intensity were observed at 61.58 and 41.38 ppm (for **3a**) and 61.09 and 41.43 ppm (for **3b**) are attributed to benzylic carbons (C2/C4) and bridgehead carbons (C1/C5), respectively. The methylene carbons of cyclohexane ring signals were observed at 25.61 and 18.30 (for **3a**) and 25.60 and 16.78 ppm (for **3b**). Out of which, the deshielded signal at 25.61 and 25.60 ppm in each compound can be assigned to C6/C8 carbons, whereas the shielded signals at 18.30 and 16.78 ppm in **3a** and **3b**, respectively, are due to C7 carbon. Further, the signals at 87.28 ppm (**3a**) and 87.25 ppm (**3b**) respectively for **3a** and **3b** can be assigned to C9 spiro carbon in the molecular structure.

In both compounds (**3a** and **3b**), collection of signals appeared at 176.20, 174.22, 169.55 and 155.60 ppm (for **3a**) and 176.90, 174.01, 169.37 and 155.32 ppm (for **3b**). Among these, signals in the region of 176.20-169.55 ppm (for **3a**) and 176.90-169.33 (for **3b**) are due to amide carbonyl carbons, whereas the signal at 155.60 (for **3a**) and 155.32 (for **3b**) should be due to imine carbon signals. Signals at 27.23, 24.63 and 22.36 ppm (for **3a**) and 27.37, 24.65 and 22.57 ppm (for **3b**), are due to methyl carbon signal in acetyl group. The aryl carbon signals in both compounds were observed in the region of 158-113 ppm. The methoxy carbon signal in **3b** was observed at 55.30 ppm.

3.2. Single crystal X-ray diffraction analysis

The molecular structures with atom-numbering schemes of **3a** and **3b** are shown in Fig. 1a and Fig. 1b, respectively. The structure refinements and selected geometrical parameters are enumerated in Table **1** and Table **2**, respectively. The compounds **3a** and **3b** were crystallized into a monoclinic lattice with P21/c symmetry. Further, all the C-C and C -H bond lengths in the benzene rings were found to be in the normal range and bond angles were found to be approximately 120°. The C-C-C bond angles and C-C-C-C torsion angles of piperidine and cyclohexane rings are greatly deviated from the parent crystal structures [27]. As a result, significant changes are observed in the conformation of saturated cyclic rings.

To describe the conformation of piperidine and cyclohexane rings, the puckering parameters were derived for compound **3b** using X-ray data. Based on the data, one of the six membered (piperidine) ring adopts boat conformation with the puckering parameters being q_2 and q_3 are 0.045 Å and 0.5773 Å, respectively. The total puckering amplitude Q_T and θ were calculated as 0.5791 Å and 4.46° respectively. However, the cyclohexane ring is preferably adopts normal chair conformation with the puckering parameters of q_2 and q_3 were predicted to be 0.136 Å and 0.559 Å, respectively and Q_T and θ were calculated to be 0.575 (2) Å, and 13.73° respectively [41]. Further, the saturated piperidine ring adopts boat conformation as suggested by the torsion angles around the bonds involving the ring atoms N1-C1-C2-C3 and N1-C5-C4-C3 were found as 22.05 and -39.9° (for **3a**) and 41.6 and -24.6° (for **3b**), respectively. These torsion angles suggest that the piperidine ring N1-C1-C2-C3-C4-C5 deviated significantly from the ideal value of 56° reported for the chair conformation of cyclohexane [16]. Therefore, the piperidine preferred to adopt boat conformation. On the other hand, the cyclohexane ring adopts chair conformation as they shows torsion angle of C3-C4-C20-C19 and C3-C2-C18-C19, were found to be -61.71 and 52.4° (for **3a**) and 62.17 and -53.7° (for **3b**), respectively. In both the crystal structures, the phenyl rings C2 and C4 occupy equatorial orientations as they confirmed by bond angles of C12-C1-C2, C12-C1-N1, C6-C5-C4 and C6-C5-N1 are, 112.5, 114.6, 112.1 and 112.2° (for **3a**) and 111.7, 77.9, 113.7 and 112.4° (for **3b**), respectively. The observed bond lengths and bond angles are in good agreement with those observed for similar bicyclic compounds [27,42].

In **3a** and **3b**, the five membered 1,3,4-thiadiazole ring was found to be in flattened boat conformation, as they undergo N-C=O bond free rotation by N-acetyl group. Further, the observed torsion angles of S1-C3-N2-N3/S-C21-N3-N2 are 36.9 /4.03 and -31.62/-4.01 for **3a** and **3b**, respectively, proved that the existence of boat form.

The crystal structures of **3a** and **3b** are packed by several non-bonded contacts such as C-H$^{\delta+}$•••$^{\delta+}$H-C, S•••O, N-H•••O, C-H•••O and C-H•••C_π interactions. Out of which, the most important contacts were found as N-H•••O and C-H•••O hydrogen bonds. The hydrogen bonding and other contacts parameters are listed in Table 3. The solid state structure of **3a** are packed in three dimension by N(4)-H(4)•••O(1) and C(16)-H(16)•••O(1), and C(17-C(21)•••C(21), hydrogen bonds with donor-acceptor distances of 2.816 and 3.513, and 3.559 Å respectively. Unlike the crystal structure **3a, 3b** is packed through the water molecule. It can be seen from Table 3, C(27)-H(27) •••O(3), O(6)-H(6)•••O1, N(4)-H(3)•••O(6) are the major hydrogen bonds with donor-acceptor distances of 3.547 and 2.850, and 2.828 Å respectively.

The nature and strength of intramolecular S···O chalcogen bonds play a key role in biological activity and in supramolecular recognition due to presence of sigma hole in the sulfur atom [43,44]. In both crystal structures **3a** and **3b**, the chalcogen interaction geometry is created R_5^2 motifs, which shows the S-O interaction distances of 2.710 Å with ∠C3-S1-O3 angle of 160.46° for **3a**, whereas for **3b**, the S-O distance and ∠C3-S1-O3 were found to be 2.798 Å and 156.84° respectively. Further, it was noted that the, the S-O interaction distance was found to be within the vander Waals radii of sum of the S and O atoms [45]. Therefore, we suggest that there is a charge transfer component to this chalcogen interaction. The bond lengths and bond angles of thiadiazole ring is similar to other previously reported crystal structures [46].

P.G. & R. COLLEGE OF ARTS & SCIENCE NAMAKKAL 637 206

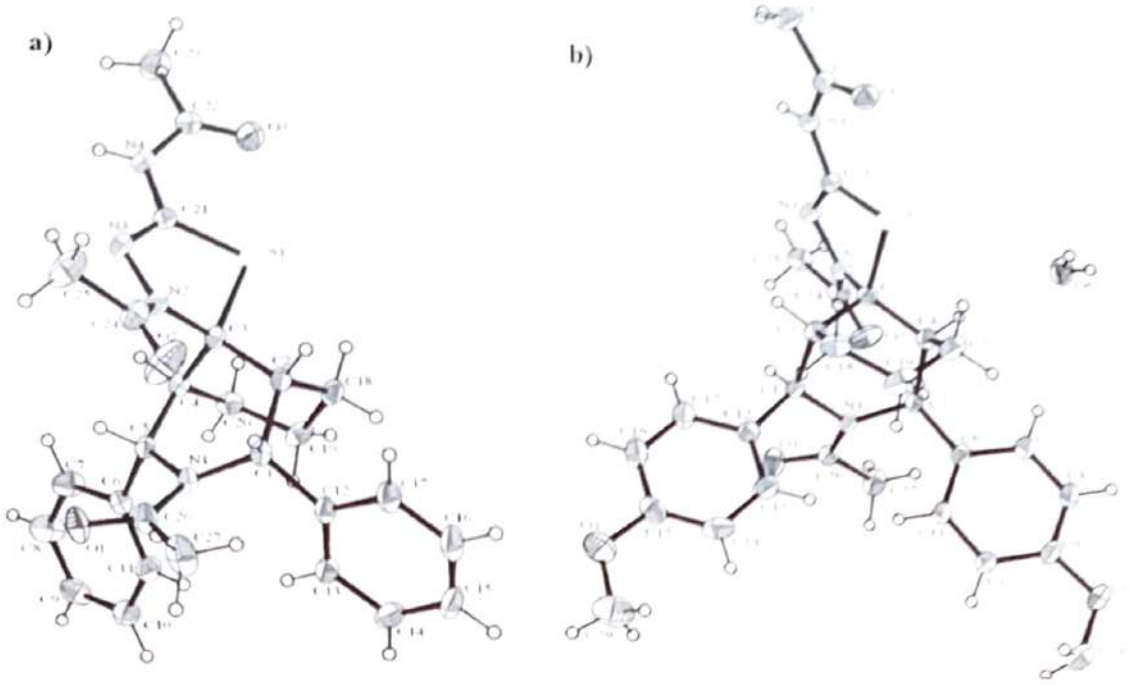


Fig. 1. a) ORTEP diagram of compound **3a**. b) ORTEP diagram of compound **3b**.

Table 1
Single crystal XRD data collection and refinement details of **3a** and **3b**

	Compound **3a**	Compound **3b**
Empirical formula	C_{27} H_{30} N_4 O_3 S	C29 H36 N4 O6 S
Formula weight	490.61	568.68
Temperature	293(2) K	293(2) K
Wavelength	0.71073 A	0.71073 A
Crystal system, space group	Monoclinic, P 21/c	Monoclinic, P 21/c
Unit cell dimensions	a = 9.8486(3) Å; b = 13.8532(3) Å; c = 19.0571(4) Å α = 90 ° deg. β= 101.7150(10) deg. gamma = 90 deg.	a=17.2963(9) b=9.2931(5); c=17.6126(8) α =90.00; β= 97.5020(10) gamma = 90 deg.
Volume	2545.89(11) A^3	2806.8(2)
Z, Calculated density	4, 1.280 Mg/m^3	4, 1.346 Mg/m^3
Absorption coefficient	0.163 mm^{-1}	0.166
F(000)	1040	1208
Crystal size	0.25 × 0.20 × 0.20 mm	0.20 × 0.20 × 0.25 mm
Theta range for data collection	1.83 to 26.18°	1.19 to 26.93
Limiting indices	-12<=h<=12, -17<=k<=14, -23<=l<=17	-22 =< h =< 21, -11 =< k =< 11, -22 =< l =< 22
Reflections collected / unique	25678 / 5073 [R(int) = 0.0338]	29917 / 6081 [R(int) = 0.037]
Completeness to theta	26.18 99.5 %	26.93° 100 %
Absorption correction	Semi-empirical from equivalents	Semi-empirical from equivalents
Max. and min. transmission	0.9681 and 0.9604	
Refinement method	Full-matrix least-squares on F^2	Full-matrix least-squares on F^2
Data / restraints / parameters	5073 / 0 / 316	6081 / 0 / 369
Goodness-of-fit on F^2	1.040	1.046
Final R indices [I>2sigma(I)]	R1 = 0.0798, wR2 = 0.2466	R1 = 0.0487, wR2 = 0.1402
R indices (all data)	R1 = 0.1008, wR2 = 0.2717	R1 = 0.0707, wR2 = 0.1619
Largest diff. peak and hole	2.841 and -0.333 e.A^{-3}	0.686 and -0.456 e.Å-3
CCDC	796611	793237

3.3. *Hirshfeld surface analysis*

3D Hirshfeld surface and 2D fingerprint plots of compounds **3a** and **3b** were obtained from Crystal Explorer 21.5 to describe the contacts of molecular surface, which have been highlighted with conventional mapping of d_{norm}, as shown in Fig. 2 and Fig. 3, respectively. Due to the presence of multiple electronegative atoms and hydrogen donor group in the title compounds, the crystal structures stabilized through multiple hydrogen bonds. The d_{norm} plots of **3a** and **3b** were mapped with a colour scale range of 0.0432 au (blue) and 1.084 au (red). It can be seen from d_{norm} mapped surface (Fig. 2 and Fig. 3) that there are two major interactions per molecule were detected. As shown in Fig. 2, (for compound **3a**) there are two intense red regions on the oxygen

P.G.P. COLLEGE OF ARTS & SCIENCE NAMAKKAL 637 206

Table 2
Selected geometrical parameters of **3a** and **3b** obtained from XRD

Compound **3a**					
Atoms	**3a**	**3b**	**Atoms**	**3a**	**3b**
S(1)-C(21)	1.741(4)	1.734(2)	N(3)-C(21)	1.275(5)	1.275(3)
S(1)-C(3)	1.860(3)	1.865(2)	C(5)-C(6)	1.530(5)	1.531(3)
O(1)-C(26)	1.233(4)	1.229(3)	C(1)-C(12)	1.528(4)	1.513(3)
N(1)-C(26)	1.369(4)	1.369(3)	C(1)-C(2)	1.556(5)	1.548(3)
N(1)-C(1)	1.487(4)	1.490(2)	C(4)-C(20)	1.532(4)	1.540(3)
N(1)-C(5)	1.488(4)	1.489(2)	O(2)-C(24)	1.205(5)	1.209(3)
O(3)-C(22)	1.209(5)	1.223(3)	C(2)-C(18)	1.532(5)	1.528(3)
N(2)-C(24)	1.359(5)	1.369(3)	C(19)-C(20)	1.513(5)	1.517(4)
N(2)-N(3)	1.418(4)	1.405(2)	C(26)-C(27)	1.508(6)	1.509(3)
N(2)-C(3)	1.494(4)	1.495(3)	C(22)-C(23)	1.495(6)	1.501(3)
N(4)-C(22)	1.373(5)	1.357(3)	N(4)-C(21)	1.377(5)	1.386(3)
C(21)-S(1)-C(3)	87.60(16)	88.29(9)	N(1)-C(1)-C(2)	113.7(3)	114.70(16)
C(26)-N(1)-C(1)	117.6(3)	112.7(2)	N(3)-C(21)-S(1)	118.0(3)	118.31(16)
C(26)-N(1)-C(5)	113.0(3)	117.2(2)	N(4)-C(21)-S(1)	122.5(3)	123.7(2)
C(1)-N(1)-C(5)	124.2(3)	124.4(2)	N(1)-C(5)-C(6)	112.2(3)	112.40(17)
C(24)-N(2)-N(3)	115.9(3)	114.01(17)	N(1)-C(5)-C(4)	115.6(3)	114.31(16)
C(24)-N(2)-C(3)	132.3(3)	132.60(17)	N(2)-C(3)-C(4)	109.0(3)	120.4(2)
N(3)-N(2)-C(3)	111.6(3)	113.3(2)	N(2)-C(3)-C(2)	121.1(3)	110.5(2)
C(22)-N(4)-C(21)	123.5(3)	125.8(2)	N(2)-C(3)-S(1)	100.2(2)	100.6(1)
C(21)-N(3)-N(2)	109.9(3)	110.35(17)	C(4)-C(3)-S(1)	111.0(2)	108.6(1)
N(1)-C(1)-C(12)	114.7(3)	113.53(16)	C(2)-C(3)-S(1)	108.2(2)	109.5(1)
C3-C2-C1-N1	-22.05	41.6(2)	C3-C2-C18-C19	52.4	-53.7
N1-C5-C4-C3	-39.9	-24.6	S1-C3-N2-N3	36.9	-31.62
C3-C4-C20-C19	61.71	62.17	S-C21-N3-N2	4.03	-4.01

Table 3
Hydrogen bonding parameters of compound **3a** and **3b**

Compound **3a**					
Entry	**Atoms**	**D....A**	**D-H**	**D-H....A**	**D-H....A**
1	S1•••O3^{i}	2.71			
2	N1•••O2^{i}	2.973			
3	N4-H4•••O1^{ii}	2.816	0.86	2.02	153.37
4	C23-H23A•••O1^{ii}	3.506	0.961	2.711	140.5
5	C8-H8•••C14^{iii}	3.634	0.93	2.862	
6	C8-H8•••C15^{iii}	3.534	0.93	2.765	
7	C17-H17•••N4^{iv}	3.453	0.93	2.74	134.17
8	C17-H17•••C21^{iv}	3.559	0.93	2.68	157.91
9	C19-H19A•••C16^{v}	3.612	0.97	2.759	146.98
10	C16-H16•••O1^{vi}	3.513	0.93	2.593	169.97
Symmetry code: (i) x,y,z; (ii) -x,-1/2+y,1.5-z; (iii) 1-x,-1/2+y,1.5-z; (iv) -x,1-y,1-z; (v) 1-x,1-y,1-z; (vi) x,1.5-y,-1/2+z					
Compound **3b**					
Entry	**Atoms**	**D....A**	**D-H**	**D-H....A**	**D-H....A**
1	S1•••O3^{i}	2.798			
2	N1•••O2^{i}	2.884			
3	O6-H6•••O1^{ii}	2.85	0.827	2.85	166.8
4	N4-H3•••O6^{iii}	2.828	0.86	2.828	177.36
5	O6-H6•••O3^{iv}	2.877	0.825	2.877	165.21
6	C28-H28B•••C13^{v}	3.551	0.961	2.764	139.77
7	C25-H25B•••O3^{vi}	3.327	0.961	2.449	151.67
8	C29-H29A•••C10^{vii}	3.471	0.961	2.874	121.32
9	C27-H27B•••O3^{viii}	3.437	0.961	2.559	152.22
Symmetry code: (i) x,y,z; (ii) x,1+y,z; (iii) -x,-y,1-z; (iv) x,-1/2-y,-1/2+z; (v) 1-x,-1/2+y,1.5-z; (vi) -x,-y,1-z; (vii) 1-x,1-y,1-z; (viii) x,1/2-y,-1/2+z					

and nitrogen atoms in the d_{norm} maps, which corresponds to two O...H/H...O contacts belonging to N-H...O (where O from acetyl group and NH from acetylamino group). The donor-acceptor bond distance was found to be 2.344 Å. Further, there are three less intense red spot on the phenyl ring and acetylamino carbon atoms in the d_{norm} maps, corresponds to C...H/H...C contacts belonging to C-G...C. The shape index surface map shows red-blue concave; indicate the presence of π-π stacking interactions in **3a**. Similarly, for compound **3b**, there is a pair of reddish spot on the oxygen atom of d_{norm} map (Fig. 3) corresponds to H...O/O...H contacts belonging to H-O...H (where O from water and H from N-H of acetylamino group, similarly, O-H from water and O from the acetyl group). However, a weak contact was also observed by C-H...O, as shown in weak red spot on the Hirshfeld surface (Fig. 3). In addition, a weak π-π stacking interactions was detected as shown the red-blue triangle concave in shape index (Fig. S5).

2D-fingerprint plot analysis was executed to determine the percentage contribution of intermolecular contacts of **3a** and **3b** with the d_i and d_e distances scales on the graph axes for the total contacts in the range of 0.6-2.6 Å, as shown in Fig. 4 and Fig. 5, respectively. For compound **3a** (Fig. 4), the H••H/H••H and O••H/H••O close contact contribution rate were predicted as 61.6 and 16.5 % at de+di ~ 1.1 and 0.8-1.2 Å respectively, whereas C••H/H••C and N•••H/H•••N contribution were determined as 15

COLLEGE OF ARTS & SCIENCE NAMAKKAL 637 206

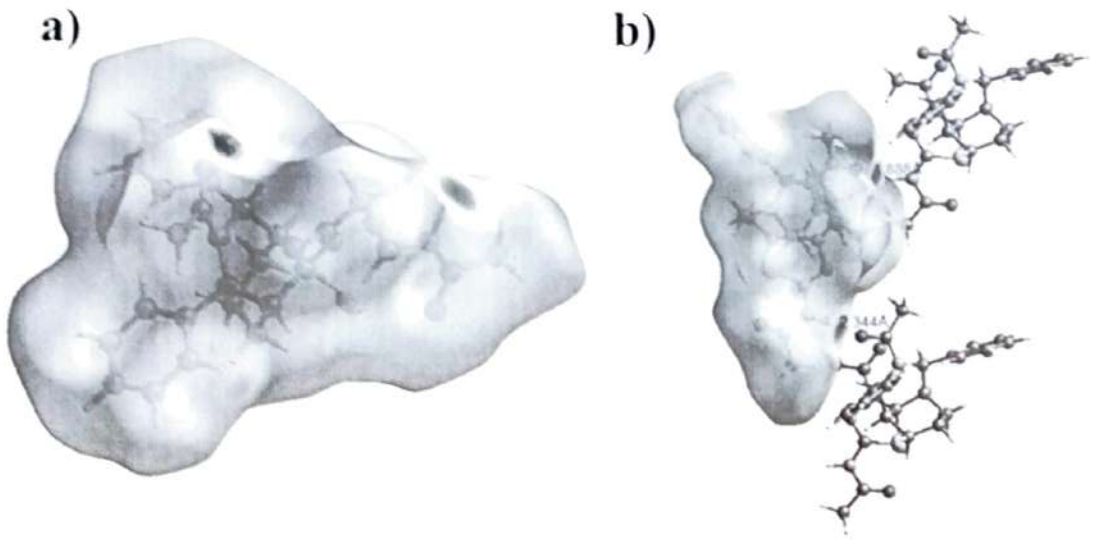


Fig. 2. Hirshfeld surface mapped over (a) d_{norm} (b) d_{norm} mapped on the Hirshfeld surface along with intermolecular interactions of compound **3a**.

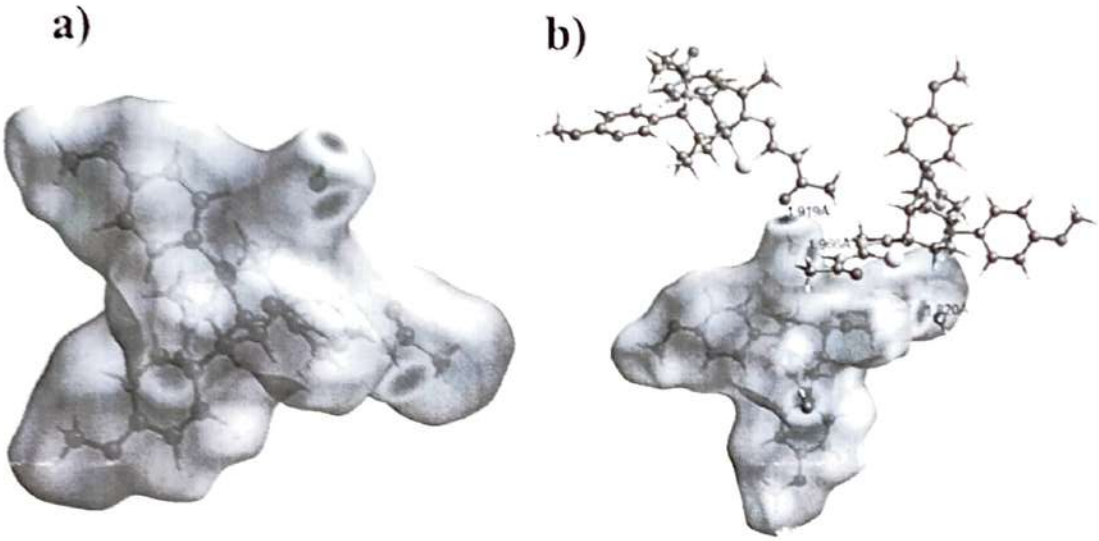


Fig. 3. Hirshfeld surface mapped over (a) d_{norm} (b) d_{norm} mapped on the Hirshfeld surface along with intermolecular interactions of compound **3b**.

and 3.8 % at de+di ~ 1.1 and 1.0-1.6 Å, respectively. Similarly, for compound **3b** (Fig.5), the H••H/H••H and O••H/H••O percentage contributions were found to be 58.6 and 23.7 % at de+di ~ 1.0 and 0.7-1.1 Å respectively. A pair of broad spike peaks were observed for C••H/H••C and N•••H/H•••N contacts at de+di ~ 1.1-1.6 and 1.2-1.7 Å which calculated to be 11.4 and 2.0 % respectively. In both crystals (**3a** and **3b**), the existence of highest percentage contribution of H•••H interaction by 2D-fingerprint plots analysis is in good agreement with the single crystal X-ray analysis.

3.4. QTAIM analysis

Quantum theory of atoms in a molecule (QTAIM) analysis was performed for molecular structures (**3a** and **3b**) to understand the type of non-bonded interactions, particularly classical hydrogen and chalcogen bonds. This can be demonstrated by the bond critical point and electron density topological parameters such as electron density (ρ), positive Laplacian ($\nabla^2\rho$), potential energy density (V) and local kinetic energy density (G), are summarized in Table 4. The bond critical points (BCPs) of molecular structure **3a** and **3b** are shown in Fig. S6. As shown in Fig. S6, bond critical point (ρBCP) was observed between chalcogen atoms (sulfur and oxygen). The electron density ρ and positive Laplacian $\nabla^2\rho$ value were calculated to be 0.017 and 0.053 (for **3a** and **3b** respectively, Table 4). The accumulation of electron density ρ in the interaction region and the $\nabla^2\rho$ values at the S•••O chalcogen bond for compound **3a** and **3b** were found to be quite similar to the results from experimental charge density and quantum chemical studies on sulfa-drugs [45]. Further, the crystal structure analysis of compounds **3a** and **3b** show a short S•••O interaction of 2.710 and 2.798 Å with a linear C21-S1-O3 angle of 73.44 and 72.77°, respectively. However, the sum of the Van der Waals radii of sulfur and oxygen atoms are significantly shorter than S•••O interaction. Further, the linearity of the chalcogen bond angle is linked to the nature of $n \rightarrow \sigma^*$ interactions.

P.G. & R. COLLEGE OF ARTS & SCIENCE NAMAKKAL 637 209

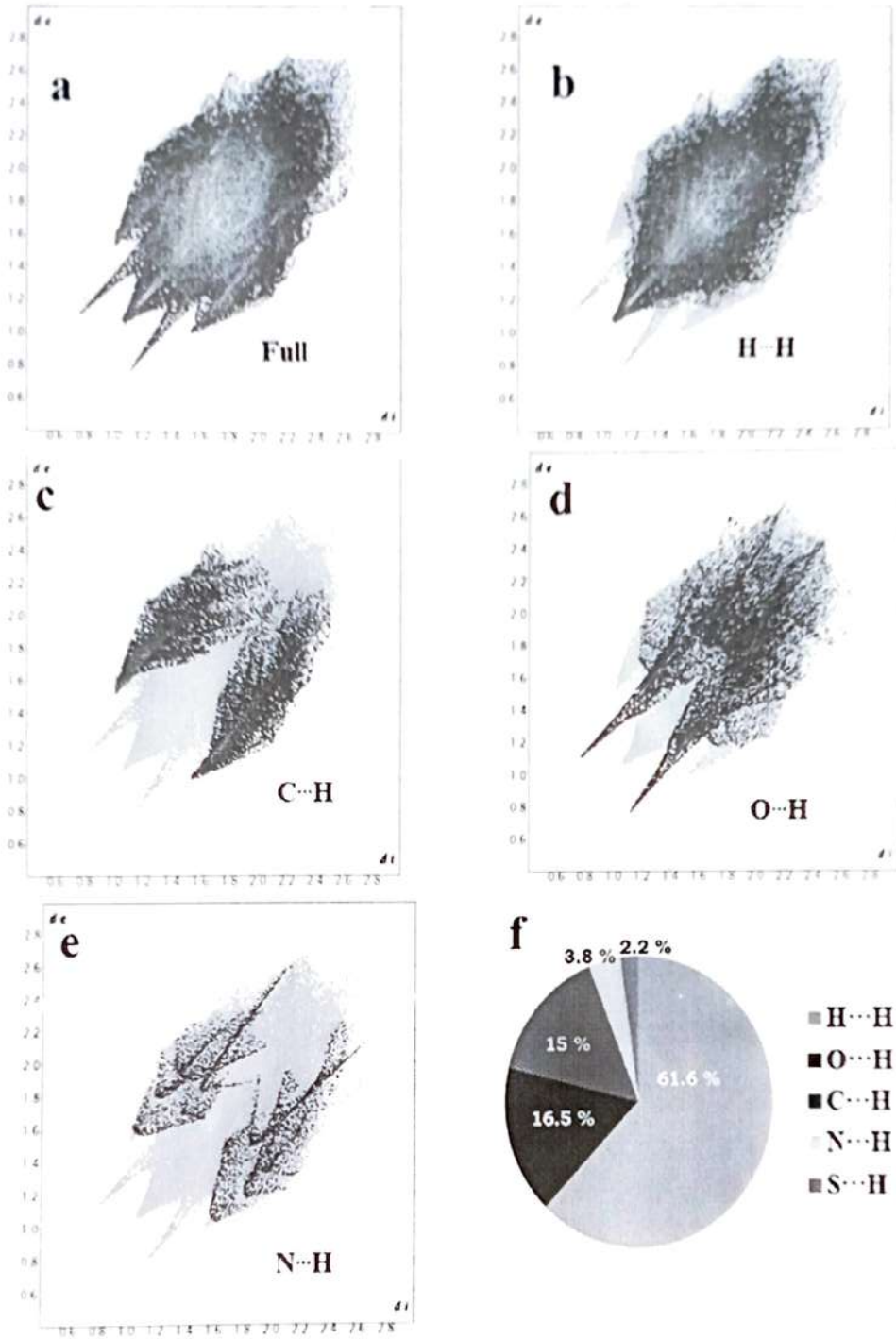


Fig. 4. The 2D fingerprint plots for the **3a** showing the most intercontacts. a) full, b) H···H/H···H (61.6%), (c) C···H/H···C (15.0%), (d) O···H/H···O (16.5%), (e) N···H/H···N (3.8%), (f) percentage contribution of various intermolecular contacts.

P.G.P. COLLEGE OF ARTS & SCIENCE
NAMAKKAL
637 206

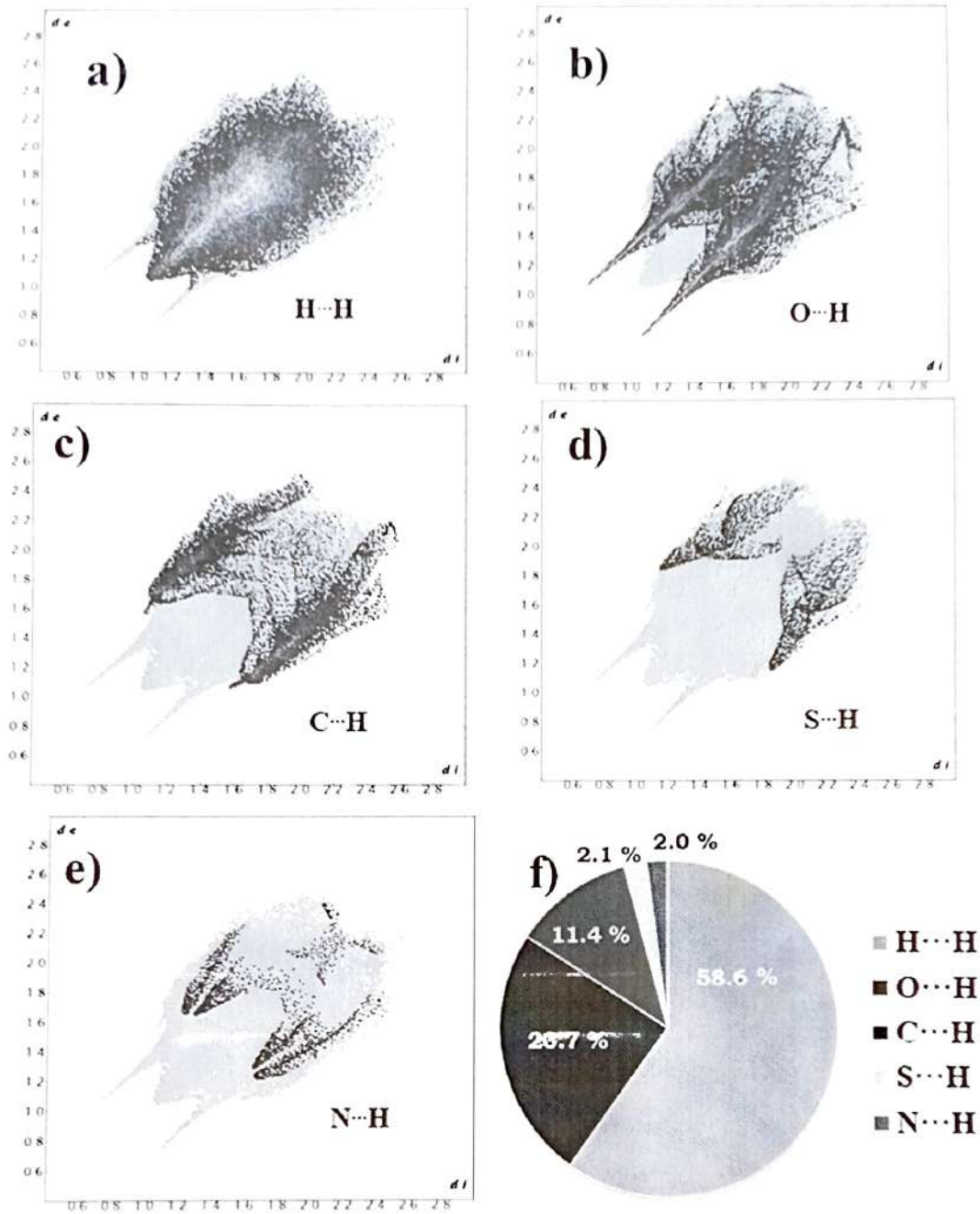


Fig. 5. The 2D fingerprint plots for the **3b** showing the most intercontacts. a) H...H/H...H (58.6%); (b) O...H/H...O (23.7%); (c) C...H/H...C (11.4%); (d) S...H/H...S (1.4%) e) N...H/H...N (2.0%); (f) percentage contribution of various intermolecular contacts.

In addition, other contacts such as C18-H...O17 and C13-H...O17 was observed with 0.0122 and 0.04 (for **3a**) and 0.024 and 0.093 (for **3b**) electron density ρ, and positive Laplacian $\nabla^2\rho$ respectively (Table 4).

3.5. NCI-RDG analysis

Non-covalent interactions-reduced density gradient (NCI-RDG) method was used to explore the various attractive and repulsive forces in a molecule such as H-bond, van der Waals and steric forces. Recently, the classical chalcogen bonding interaction in a molecule has been explored widely using NCI-RDG method [47]. The scatter graph of RDG against $\text{sin}(\lambda^2)\rho$ exploring the type of attractive or repulsive forces that exist in the molecular structure by tri-color scheme (blue-green-red). Blue and green scattering graph at the negative sign indicates attractive forces (hydrogen and chalcogen bonding and van der Waals forces) whereas red spot on the positive sign express the repulsive forces, which mostly

P.G. COLLEGE OF ARTS & SCIENCE NAMAKKAL 637 206

Table 4
QTAIM topological analysis of compounds **3a** and **3b**

Compound **3a**							
BCP #	**Atoms**	**Rho**	**DelSqRho**	**K**	**V**	**G**	**DelSqV**
1	S1 - O4	0.017166	0.053585	-0.000736	-0.01192	0.01266	-0.04129
2	H14 - O17	0.024281	0.093234	-0.002862	-0.01759	0.020447	-0.13332
3	C20 - H52	0.010473	0.033852	-0.00142	-0.00562	0.007043	-0.02415
4	C24 - H29	0.008146	0.024771	-0.001078	-0.00404	0.005114	-0.0148
5	H29 - H44	0.006226	0.018595	-0.000715	-0.00322	0.003934	-0.00769
6	H25 - H44	0.009692	0.027709	-0.001139	-0.00465	0.005788	-0.01914
Compound **3a**							
3	S1 - O4	0.017056	0.053269	-0.000734	-0.011848	0.012583	-0.040829
18	O6 - H16	0.023652	0.091046	-0.002845	-0.017071	0.019916	-0.125536
26	C9 - H40	0.010041	0.032541	-0.001367	-0.005401	0.006768	-0.022363
51	H23 - H38	0.009399	0.02765	-0.00114	-0.004632	0.005772	-0.016634
63	C9 - H48	0.008472	0.025686	-0.001134	-0.004153	0.005287	-0.014533
64	H38 - H48	0.007647	0.022341	-0.000819	-0.003947	0.004766	-0.009975

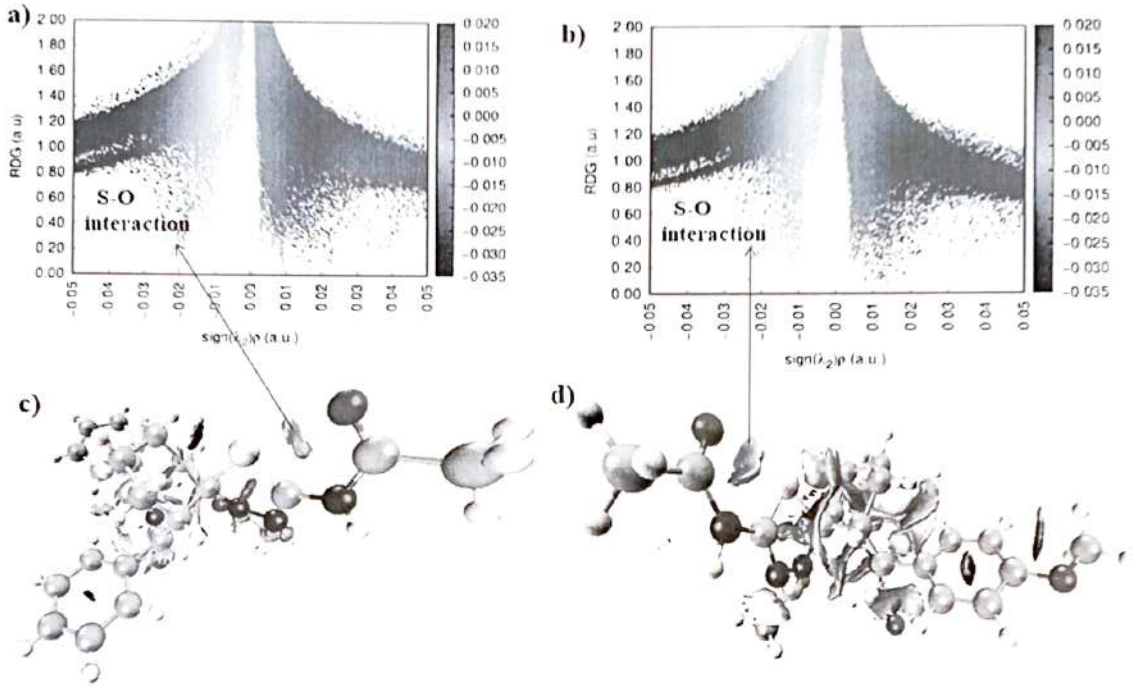


Fig. 6. Non-covalent interactions (NCIs) and reduced density gradient (RDG) Interactions: (a) Compound **3a**; b) Compound **3b**

occurred in the rings. The following relation can be used for the detection of NCI isosurfaces in RDG using this technique.

$$s = \frac{1}{2\left(3\pi^2\right)^{1/3}} + \frac{|\nabla\rho(r)|}{\rho(r))^{4/3}}$$

To get deep understanding the characteristics of intramolecular chalcogen bonds and other forces in a molecules (**3a** and **3b**), the plot of s versus electron density ($\sin(\lambda^2)\rho$) multiplied by the sign of second Eigen value λ_2 was also investigated for compound **3a** and **3b**, as shown in Fig. 6. It can be seen from Fig. 6a and 6b, the blue scattering spike at the negative sign of $\lambda_2\rho$ (-0.02 a.u) indicate the presence of S•••O intramolecular chalcogen bond. Further, some green peaks were lying at the negative sign of $\lambda_2\rho$ (-0.01 a.u) values illustrate the van der Waals and repulsive forces whereas, the red spots scattering at the positive $\lambda_2\rho$ demonstrates the steric interaction in the molecule **3a** and **3b**. Jindani et al. [48] examined the NCI-RDG analysis for thiazole molecular structure, which showed the electron density (λ_2) value which is similar to the electron density of title compounds **3a** and **3b**.

3.6. DFT study

Density functional theory (DFT) method was employed to inspect the structural geometry (bond lengths and bond angles) and electronic parameters (E_{HOMO} and E_{LUMO}). To describe these, molecular structures **3a** and **3b** were optimized at B3LYP/6-311g(d,p) level, which are depicted in Fig. S7 and S8, respectively. The selected geometrical parameters are presented in Table S1. It can be seen from the Table S1 that the optimized bond lengths and bond angles by theoretical analysis were found to be well replicated with the experimental XRD results, as indicated by the correlation coefficient analysis, Fig. S9 [49]. However, the minor deviations were observed between theoretical and experimental results due to the differences in the molecular environment.

P.G.P. COLLEGE OF ARTS & SCIENCE NAMAKKAL 637 206

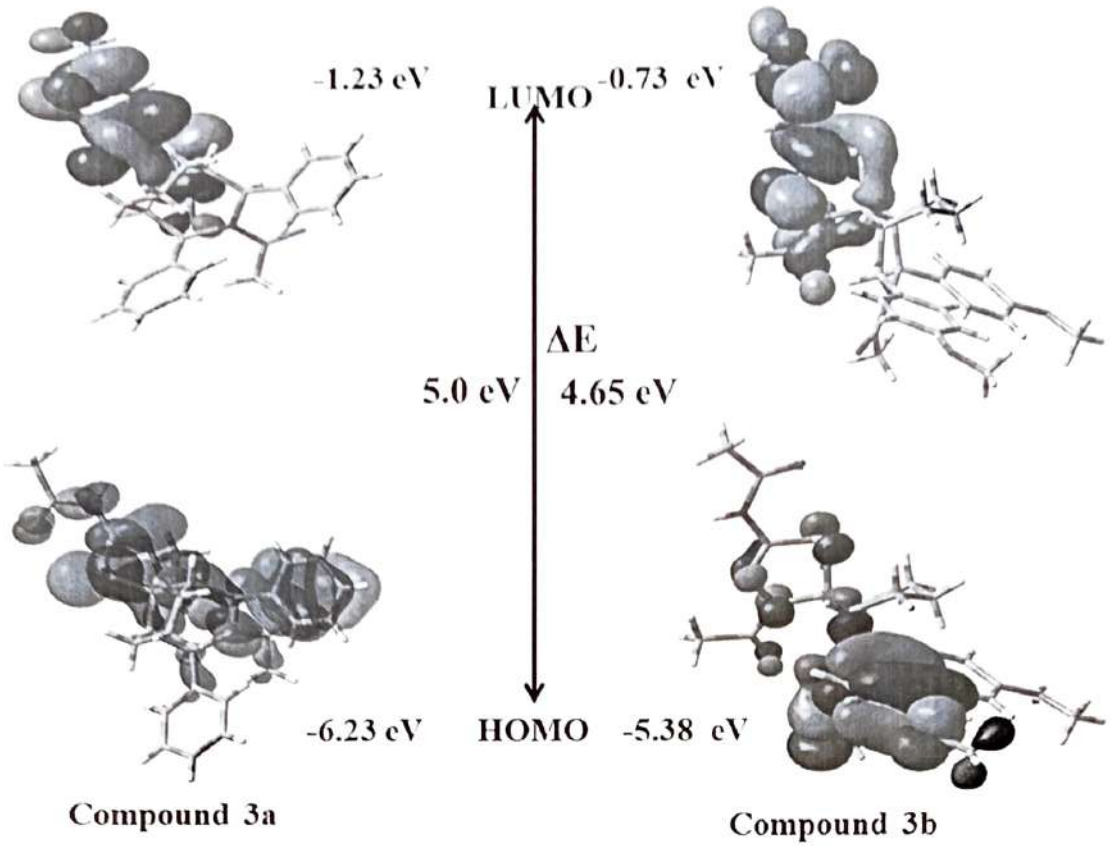


Fig. 7. HOMO/LUMO energy diagram of compounds **3a** and **3b**

In the DFT method of **3a** and **3b**, the C11-S1 bond distance was calculated as 1.90 Å whereas the XRD value found to be 1.86 Å. This should be due to stronger interaction between sulfur and oxygen atoms in the gas phase. However, the non-bonded distance between the sulfur and oxygen in the optimized structures (**3a** and **3b**) were estimated as 2.84 Å (**3a**) and 2.79 Å (**3b**), well less than the combined van der Waals radii of the sulfur-oxygen atoms (3.25 Å) and consistent with the previously reported S–O chalcogen bond distances [50]. The conformational analysis of two six membered rings (cyclohexane and piperidine) were described with torsion angle of the corresponding ring atoms. For **3a**, the observed torsion angle for C3-C4-C20-C19 and C3-C2-C18-C19 were calculated as 52.56 and -61.06° respectively, indicates the cyclohexane ring adopts chair conformation whereas the piperidine undergoes boat conformation with an angle of 26.22 and -41.74° for N1-C1-C2-C3 and N1-C5-C4-C3 respectively. Further, the torsion angle of piperidine and cyclohexane rings are in excellent agreement with the X-ray results. Similarly, for **3b**, the torsion angles of piperidine and cyclohexane rings, C3-C4-C2-C20-C19/C3-C2-C18-C19 and C3-C2-C1-N1/N1-C5-C4-C3, were predicted to be 61.53/-61.90 and 26.20/39.50 respectively.

The frontier molecular orbital (FMO) analysis is widely used to predict the molecular interactions, reactivity, charge transfer, optical and electronic properties of molecules through highest occupied molecular orbital (HOMO) and lowest unoccupied molecular orbital (LUMO). HOMO is the electron rich molecular orbital with high energy (nucleophile) and electron donating capability whereas LUMO is the electron deficient molecular orbital with smaller energy (electrophile) and own electron accepting ability. The energy difference between HOMO-LUMO orbital is called energy gap (ΔE), which is used to describe the stability of molecules. For compounds **3a** and **3b**, E_{HOMO} and E_{LUMO} values were obtained by the DFT method using B3LYP/6-311 g(d,p) level and the 3D molecular orbital energies of the compounds **3a** and **3b** are depicted in Fig. 7. From the Fig. 7, the band gap energy (ΔE) between HOMO and LUMO orbitals were found to be 5.0 and 4.65 eV, respectively for **3a** and **3b**. It can be further discussed that **3b** shows about 0.5 eV less compared to **3a** due to the presence of electron donating methoxy substituent in the phenyl group, which further increase the electron delocalization.

Further using the energy of HOMO-LUMO orbitals, global chemical reactivity descriptor (GCRD) such as electron affinity (EA), ionization potential (IP), Electronegativity (χ), hardness (η), softness (S) potential (μ), and electrophilicity index (ω) were calculated. The calculated GCRD parameters are presented in Table 5. It is seen that the chemical hardness and softness were calculated to be 0.20 and 0.21 eV for **3a** and **3b**, respectively. Therefore, the molecule **3a** and **3b** have good chemical stability and strength. However, the electronegativity (χ), and chemical potential (μ), were estimated as -3.73 / -3.05 eV; and 3.73 / 3.05 eV, respectively for **3a** / **3b**. From the Table 5, it can be concluded that the GCRD parameters of molecule **3b** is significantly lower due presence of methoxy group at the phenyl substituent.

The molecular electrostatic potential (MEP) of an organic molecule can be defined in terms of total charge distribution of the molecule. 3D MEP surface encompassing different color scheme between blue to red, are depicted in Fig. 8a (for **3a**) and Fig. 8b (for **3b**), generated from the optimized structure at B3LYP/6-311 g(d,p)

P.G.P. COLLEGE OF ARTS & SCIENCE NAMAKKAL 637 206

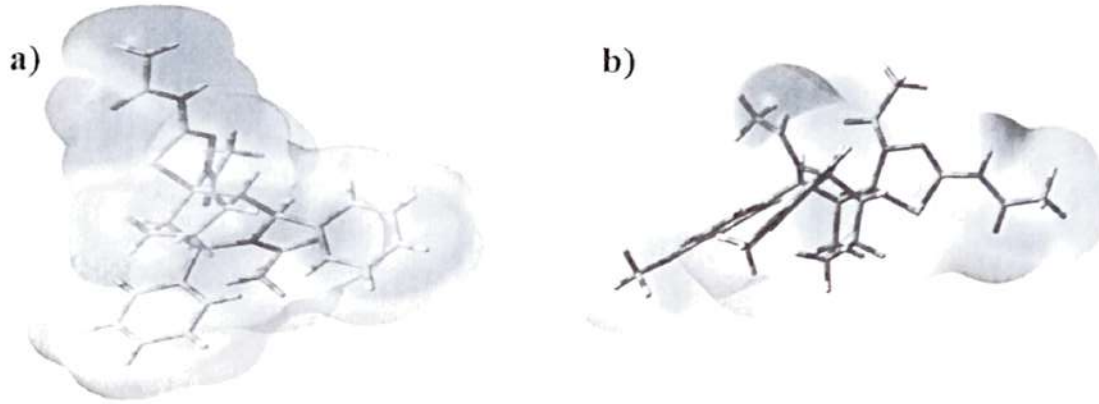


Fig. 8. MEP Map of the compounds **3a** and **3b**

Table 5
Calculated energy values of **3a** and **3b** at B3LYP/6-311 G (d, p) method

Quantum Descriptors (eV)	Compound 3a	Compound 3b
E_{HOMO}	-6.23 eV	-5.38 eV
E_{LUMO}	-1.23 eV	-0.73 eV
Ionization potential (IP)	6.23 eV	5.38 eV
Electron affinity (EA)	1.23 eV	0.73 eV
Energy gap (ΔE)	5.0 eV	4.65 eV
Electronegativity (χ)	-3.73 eV	-3.05 eV
Chemical potential (μ)	3.73 eV	3.05 eV
Chemical hardness (η)	2.50 eV	2.32 eV
Softness (σ)	0.20 eV	0.21 eV
Electrophilicity (ω)	2.78 eV	2.00 eV

level. It is seen that red, blue and green are the three major color scheme, which define the electrostatic potential value. Further, the color scheme expands in the order of blue > green > yellow > orange > red. Out of which, the blue regions on the surface signify the positive potential corresponds to the electron deficient site and favor for nucleophilic attack, whereas the red surface region with negative potential, corresponds to electron rich regions and favor for electrophilic reactivity. The green color on the MEP surface indicates zero potential. In addition, the pale blue and yellow colors on the surface map denote the slightly electron deficient and electron rich areas, respectively. For **3a**, (Fig. 8a) the red and yellow region are corresponds to the negative electrostatic potential which associated with electron rich regions (high electron density) such as electronegative groups, and targeted by electrophiles whereas the blue region indicates the positive electrostatic potential (low electron density) which found mostly on the alkyl groups and associated with nucleophilic attack. For compounds **3b**, (Fig. 8b), the negative potential is dominated over the carbonyl group whereas the positive potential exists only on the N-H group.

3.7. NBO analysis

As the presence of sulfur and oxygen atoms close in the molecular structure (**3a** and **3b**), we sought to evaluate the strength of S•••O (chalcogen bonding) interaction. To do this, NBO analysis was performed to get better understanding of inter and intra molecular charge transfer and electron delocalization between filled Lewis type orbital (bonding) and empty non-Lewis type orbital (anti-bonding) of **3a** and **3b** using DFT method at B3LYP/6-311g(d,p) level. The 2nd order perturbation energies of **3a** and **3b** were used to predict the strength and type of interaction between donor and acceptor orbitals, and the interacting stabilization energy. Further, the stabilization energy E(2) is used to define the hyper conjugative interactions and charge transfers in a molecule. Larger stabilization energy provides a stronger interaction between donor and acceptor atoms. Therefore, it is concluded that the stabilization energy E(2) is closely associated with each donor and acceptor NBO orbitals which are denoted as (i) and (j), respectively. The energy delocalization between each donor NBO (i) and acceptor NBO (j) can be predicted using the given equation:

$$E^{(2)} = \Delta E_{ij} = q_i \frac{F_{i,j}^2}{\varepsilon_j - \varepsilon_i}$$

The electron delocalization and its stabilization energies E(2) of **3a** and **3b** are presented in Table S2-S3. Based on the results presented in Table S2 - S3, a number of σ-σ^*, $\pi \rightarrow \pi^*$, $n \rightarrow \pi^*$, and $n \rightarrow \sigma^*$, intramolecular charge transfer processes observed for compounds **3a** and **3b**. Also, the results revealed that the significant

Table 6
The dipole moment (μ) (Debye), polarizability (α) and first hyperpolarizability (β) of **3a** and **3b**

Parameter	3a	3b	Parameter	3a	3b
α_{xx}	-177.40	-175.31	β_{xxx}	234.1427	-122.88
α_{xy}	16.37	-4.72	β_{xxy}	34.1925	100.94
α_{yy}	-213.46	-243.03	β_{xyy}	-1.6442	32.70
α_{xz}	21.40	-19.97	β_{yyy}	12.4273	42.42
α_{yz}	6.44	-11.87	β_{xxz}	21.6636	-13.68
α_{zz}	224.12	-251.81	β_{xyz}	-1.9129	-4.78
α_{total}	8.18×10^{-24}	33.05×10^{-24}	β_{yyz}	-19.7101	-38.09
μ_x	4.18	-1.6750	β_{xzz}	11.6066	14.11
μ_y	0.32	1.5398	β_{yzz}	-14.7295	1.02
μ_z	1.1273	-2.6231	β_{zzz}	24.7215	0.79
μ_{total}	4.34	3.47233	β_{total}	2.136×10^{-30}	9.145×10^{-29}

P.G.P. COLLEGE OF ARTS & SCIENCE NAMAKKAL 637 206

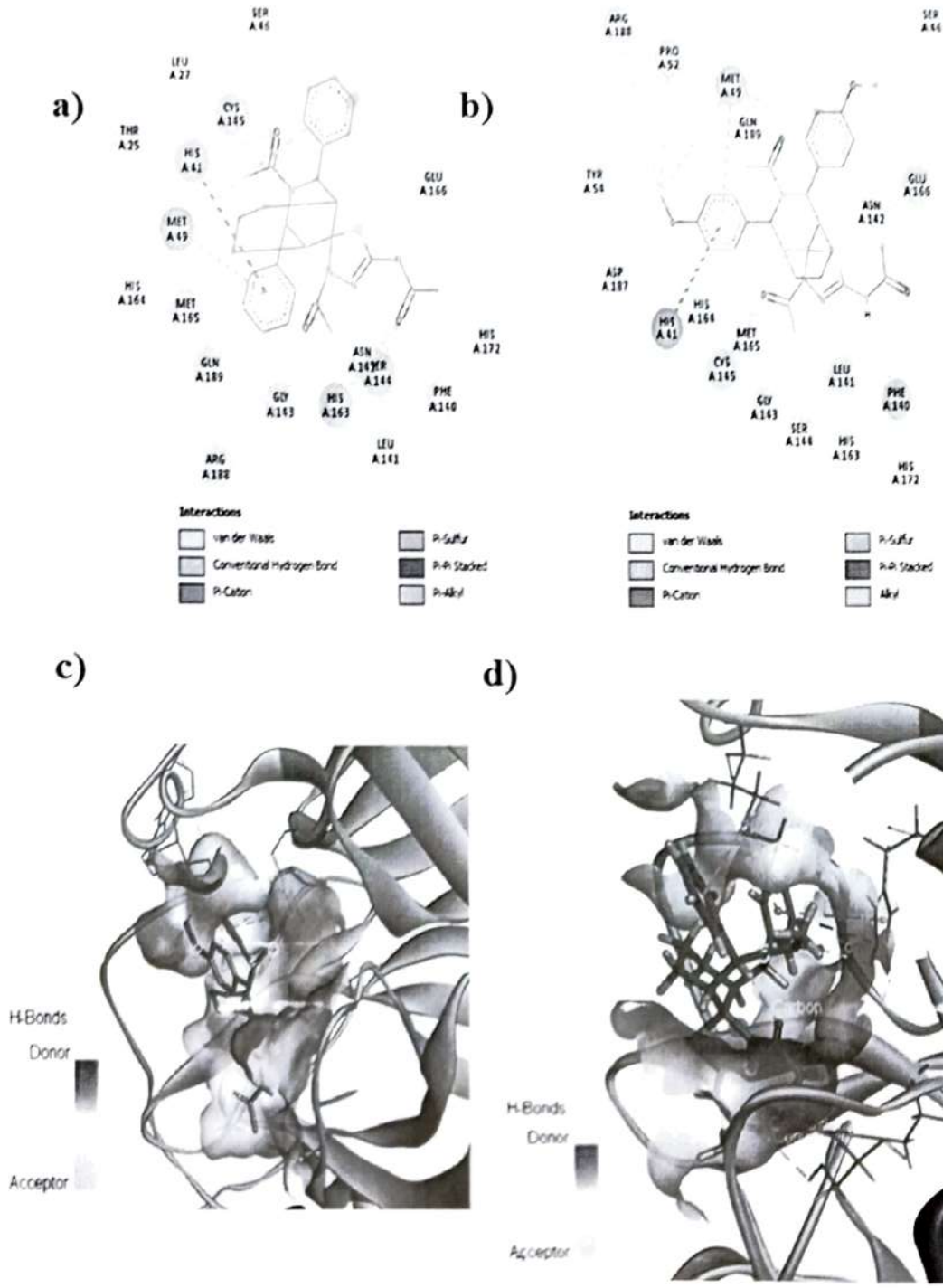


Fig. 9. a) and b) show two dimensional binding interaction between ligands **3a** and **3b** with active site of 6LU7 amino acid resdues; c) and d) Compounds **3a** and **3b** show hydrogen bonds interactions with SARS-nCoV-2 Main protease (PDB: 6LU7) active site

orbital interaction between the oxygen lone pair (donor-bonding) and sulfur-carbon antibonding (acceptor) orbital (S–C σ^* orbital), in **3a** and **3b** were calculated as 2.01 kcal/mol (O4 LP → S1-C11 σ^* orbital) and 1.99 kcal/mol (O4 LP → S1-C17 σ^* orbital, respectively.

3.8. NLO Study

Theoretical NLO study was explored for spiro thiadiazole compounds **3a** and **3b** by quantum chemical calculation to estimate the NLO efficiency. The relationship between NLO property and

P.K.R. COLLEGE OF ARTS & SCIENCE
NAMAKKAL
637 206

molecular structure was studied theoretically with the aid of dipole moment, polarizability and hyperpolarizability, which have been calculated using B3LYP/6-311g(d,p) level and the results are summarized in Table 6. Based on the data presented in Table 6, the dipole moment (μ), polarizability and hyperpolarizability values were predicted to be 4.34 Debye, 8.18 × 10^{-24} e.s.u and 2.136 × 10^{-30} e.s.u. (for **3a**); 3.47 Debye, 33.05 × 10^{-24} e.s.u and 9.145 × 10^{-29} e.s.u. (for **3b**), respectively. The calculated first order hyperpolarizability value is significantly higher than that of urea, which has been used as the reference value for many organic compounds [26]. Therefore, the high values of first order hyperpolarizability reveal that the synthesized spiro compounds **3a** and **3b** have efficient NLO behavior.

It should be mentioned that the NLO of organic material originates from delocalized electron density of the substituents. In this case, both **3a** and **3b** were found to be polar in nature and have non zero dipole moment components. However, out of **3a** and **3b**, compound **3b** contains electron donating *p*-methoxy phenyl group which further increase the electron delocalization. Therefore, **3b** exhibits greater (βo) values than their unsubstituted phenyl group based spiro thiadiazole **3a**.

3.9. Docking study

Molecular docking has proven to be highly efficient method for screening potential drug candidates against specific disease by using computer aided design [51]. Studies of ligand binding to receptor proteins using molecular docking provide insights into the effectiveness of the interactions. Recent studies have identified that the main protease (M^{pro}) of SARS-CoV-2 have consist of three domain such as, domain I (residues 8–101), domain II (residues 102–184) and domain III (residues 201–303), which were similar to other coronaviruses, COVID-19 viral protein (SARS-CoV-2 M^{pro}) also reside a similar catalytic dyad (Cys145-His41), located in a cleft between domain I and II [52,53]. Further, these catalytic dyads of M^{pro} are the major protease activity [54]. It was disclosed that inhibition of M^{pro} catalytic dyad was found to be potential and attractive target for designing and screening of anti-coronavirus drug [55]. Also, it was reported that no specific therapeutic agents or vaccines yet to be identified to treat the infection caused by COVID-19. However, only few clinically trial antiviral drugs such as antimalarial, and anti HIV have been used as the supportive measures to treat COVID-19 infections [55,56]. Virtual screening of molecular docking provides an alternative approach to screen the potential drug candidates for the specific illness at relatively short time.

Studies have been reported various therapeutic options against the COVID-19 causing protein (SARS-CoV-2) through molecular docking studies [57,58]. The docking studies have been applied on compounds **3a** and **3b** with "6LU7" protein which was taken from protein data bank (PDB ID: 6LU7). To examine the protein-ligand binding affinity, 6LU7 and lead compounds (**3a** and **3b**) were fitted to interact with the active site of amino acid residues by using autodock tools. The obtained binding interactions are shown in Fig. 9a and Fig. 9b of **3a** and **3b** respectively. The docking results showed that the lead compounds **3a** and **3b** are formed various binding interactions including H-bond, π-cation, and π-sulfur interactions. Also, this Fig. 9 presents the best docked poses of our ligand in 6LU7. It can be seen from Fig. 9a, Compound **3a** showed significant binding affinity with His41, Met49, Ser144, Cys145, and His163 residues, whereas lead compound **3b** (Fig. 9b) showed interactions with His41, Met49, Pro52, Phe140, Asn142, Cys145, Glu166, and Arg188 residues of $3CL^{pro}$. Among these, His41, Ser144, Cys145, and His163 (for **3a**) and Phe140, Cys145, and Glu166 (for **3b**) displays conventional hydrogen bonding, whereas Met49 forms π-cation, and π-sulfur interactions with compounds **3a** and **3b**. "Further, it can be seen in Fig. 9, the carbonyl group of acetyl function in **3a** exhibits conventional hydrogen bonding with His41, Ser144, Cys145, and His163 residues (Compound **3a**). Unlike **3a**, in compound **3b**, sulphur atom in thiadiazole ring and amino group of acetylamino function show hydrogen bond with Phe140, and Glu166 residues. The interacting amino acid residues were compared with earlier reports [25,26,59], which showed that the residues His41 and Cys145 are the major catalytic active residues in 6LU7. Interestingly, lead compounds **3a** and **3b** exhibit similar binding affinity with His41 and Cys145 amino acid residues. The binding energies of **3a** and **3b** were calculated to be -7.90 and -7.85 kcal/mol, (Table S4) [60]. As clearly seen from Table S4, the existence of methoxy function in the phenyl group was found to be insignificant contribution towards the binding affinity". In conclusion, the above docking results proved that the ligands **3a** and **3b** could be the potential lead molecule for antiviral drug against SARS-nCoV-2 M^{pro}.

4. Conclusion

Thiazole based spiro derivatives **3a** and 3**b** were synthesized and characterized by spectroscopic and single crystal X-ray diffraction techniques. Both the NMR and XRD results proved that the bicyclic rings adopt chair and boat conformation of cyclohexane and piperdine rings, respectively. The asymmetric unit of crystal structures **3a** and **3b** are stabilized mainly due to chalcogen bond, whereas as the crystal packing is stabilized due to divalent hydrogen bond, C-H•••π, C-H•••O, O-H•••C, O-H•••N and H•••H interactions. 3D Hirshfeld surfaces and 2D fingerprint plots analysis were considered to visually spot the different interactions within the molecular structures. Based on the results, the structures **3a** and **3b** were stabilized through H...H, O...H/H...O, C...H/H...C, and N...H/H...N contacts. Further, the 2D fingerprint plot analysis revealed that conventional hydrogen bonding contribution O...H/H...O was calculated to be 16.7 and 23.5 % (respectively for **3a** and **3b**), which could be the strong interaction to stabilize the crystal packing. The presences of chalcogen bond in the studied compounds were identified from the NCI-RDG and QTAIM analyses. NBO analysis suggests that the intramolecular charge transfer between oxygen and sulfur and hyperconjugative interactions are dominated in the molecular structure. NLO study showed that the significant response as compared to the prototype molecule (urea). Finally, the molecular docking study was explored for the compounds **3a** and **3b** with COVID-19 viral protein (SARS-nCoV-2 M^{pro}, 6LU7). The results revealed that the various interactions strongly anchored the lead compounds to the active sites with minimum binding energy, which was calculated to be -7.90 and -7.85 kcal/mol for **3a** and **3b**, respectively.

Declaration of Competing Interest

The authors declare that they have no known competing financial interests or personal relationships that could have appeared to influence the work reported in this paper.

Supplementary materials

Supplementary material associated with this article can be found, in the online version, at doi:10.1016/j.molstruc.2022.132747.

CRediT authorship contribution statement

Ramachandran Rajamanickam: Methodology, Formal analysis, Data curation, Writing – review & editing. **Rani Mannangatty:**



Methodology, Investigation, Formal analysis. **Jayanthi Sampathkumar**: Software, Data curation, Investigation. **Kabilan Senthamaraikannan**: Formal analysis, Investigation. **Barathi Diravidamani**: Software, Data curation, Investigation.

References

[1] I. Natsutani, R. Iwata, Y. Yamai, K. Ishida, Y. Nagaoka, T. Sumiyoshi, Design, synthesis and evaluations of spiro fused benzoxaborin derivatives as novel boron-containing compounds, Chem. Biol. Drug Des. 93 (2019) 657–665 https://doi.org/. doi:10.1111/cbdd.13496.

[2] M. Moghaddam-Manesh, D. Ghazanfari, E. Sheikhhosseini, M. Akhgar, MgO Nanoparticle-Catalyzed Synthesis and Evaluation of Antimicrobial and Antioxidant Activity of New Multi-Ring Compounds Containing Spiro[indoline-3,4′-[1,3]dithiine], ChemistrySelect 4 (2019) 9247–9251 https://doi.org/, doi:10.1002/slct.201900935.

[3] S. Balasubramanian, C. Ramalingan, G. Aridoss, S. Kabilan, Synthesis and study of antibacterial and antifungal activities of novel 8-methyl-7,9-diaryl-1,2,4,8-tetraazaspiro[4.5]decan-3-thiones, Eur. J. Med. Chem. 40 (2005) 694–700 https://doi.org/, doi:10.1016/j.ejmech.2005.02.001.

[4] B. Chudzik, K. Bonio, W. Dabrowski, D. Pietrzak, A. Niewiadomy, A. Olender, K. Malodobry, M. Gagoś, Synergistic antifungal interactions of amphotericin B with 4-(5-methyl-1,3,4-thiadiazole-2-yl) benzene-1,3-diol, Sci. Rep. 9 (2019) 12945, doi:10.1038/s41598-019-49425-1.

[5] H. Muğlu, M. Akın, M.S. Çavuş, H. Yakan, N. Şaki, E. Güzel, Exploring of antioxidant and antibacterial properties of novel 1,3,4-thiadiazole derivatives: Facile synthesis, structural elucidation and DFT approach to antioxidant characteristics, Comput. Biol. Chem. 96 (2022) 107618 https://doi.org/, doi:10.1016/j.compbiolchem.2021.107618.

[6] N.A. Al-Quraan, M.L. Al-Smadi, A.F. Swaleh, GABA metabolism and ROS induction in lentil (Lens culinaris Medik) plants by synthetic 1,2,3-Thiadiazole compounds, J. Plant Interact. 10 (2015) 185–194, doi:10.1080/17429145.2015.1056262.

[7] V. Jatav, P. Mishra, S. Kashaw, J.P. Stables, CNS depressant and anticonvulsant activities of some novel 3-[5-substituted 1,3,4-thiadiazole-2-yl]-2-styryl quinazoline-4(3H)-ones, Eur. J. Med. Chem. 43 (2008) 1945–1954 https://doi.org/, doi:10.1016/j.ejmech.2007.12.003.

[8] A. Bahadur, S. Iqbal, S. Muneer, H.O. Alsaab, N.S. Awwad, H.A. Ibrahium, Synthesis, carbonic anhydrase enzyme inhibition evaluations, and anticancer studies of sulfonamide based thiadiazole derivatives, Bioorg. Med. Chem. Lett. 57 (2022) 128520 https://doi.org/, doi:10.1016/j.bmcl.2021.128520.

[9] M. Madhu Sekhar, U. Nagarjuna, V. Padmavathi, A. Padmaja, N.V. Reddy, T. Vijaya, Synthesis and antimicrobial activity of pyrimidinyl 1,3,4-oxadiazoles, 1,3,4-thiadiazoles and 1,2,4-triazoles, Eur. J. Med. Chem. 145 (2018) 1–10 https://doi.org/, doi:10.1016/j.ejmech.2017.12.067.

[10] E. Matthews, S. Portaro, Q. Ke, R. Sud, A. Haworth, M.B. Davis, R.C. Griggs, M.G. Hanna, Acetazolamide efficacy in hypokalemic periodic paralysis and the predictive role of genotype, Neurology 77 (2011) 1964 1960 LP–, doi:10.1212/WNL.0b013e31823a0cb6.

[11] J. Jiang, X. Li, M. Hanif, J. Zhou, D. Hu, S. Su, Z. Xie, Y. Gao, B. Yang, Y. Ma, Pyridal[2,1,3]thiadiazole as strong electron-withdrawing and less sterically-hindered acceptor for highly efficient donor–acceptor type NIR materials, J. Mater. Chem. C. 5 (2017) 11053–11058, doi:10.1039/C7TC03978F.

[12] T. Ghosh, M. Lehmann, Recent advances in heterocycle-based metal-free calamitics, J. Mater. Chem. C. 5 (2017) 12308–12337, doi:10.1039/C7TC03502K.

[13] D. Bora, A. Kaushal, N. Sankaranarayanan, Anticancer potential of spirocompounds in medicinal chemistry: A pentennial expedition, Eur. J. Med. Chem. 215 (2021) 113263 https://doi.org/, doi:10.1016/j.ejmech.2021.113263.

[14] L.M.T. Frija, A.J.L. Pombeiro, M.N. Kopylovich, Building 1,2,4-Thiadiazole: Ten Years of Progress, European J. Org. Chem. 2017 (2017) 2670–2682 https://doi.org/, doi:10.1002/ejoc.201601642.

[15] R. Ramachandran, M. Rani, S. Senthan, Y.T. Jeong, S. Kabilan, Synthesis, spectral, crystal structure and in vitro antimicrobial evaluation of imidazole/benzotriazole substituted piperidin-4-one derivatives, Eur. J. Med. Chem. 46 (2011) 1926–1934 https://doi.org/, doi:10.1016/j.ejmech.2011.02.036.

[16] A. Sethukumar, P.S. Anand, C.U. Kumar, B.A. Prakasam, Synthesis, stereochemical and biological studies of some N-cyclohexylcarbamoyl -2,6-diarylpiperidin-4-ones, J. Mol. Struct. 1130 (2017) 352–362 https://doi.org/, doi:10.1016/j.molstruc.2016.10.035.

[17] G. Aridoss, S. Balasubramanian, P. Parthiban, S. Kabilan, Synthesis and NMR spectral studies of N-chloroacetyl-2,6-diarylpiperidin-4-ones, Spectrochim. Acta Part A Mol. Biomol. Spectrosc. 68 (2007) 1153–1163 https://doi.org/, doi:10.1016/j.saa.2007.01.013.

[18] S. Ponnuswamy, S. Sethuvasan, K. Thirunavukarasu, Synthesis, characterisation, stereochemistry and dynamic NMR studies of N-nitroso and N-formyl-t-3-isopropyl-r-2,c-6-bis(4-methoxyphenyl)piperidin-4-ones, J. Mol. Struct. 1089 (2015) 86–94 https://doi.org/, doi:10.1016/j.molstruc.2015.02.045.

[19] J. Chakkaravarthy, G. Muthukumaran, K. Pandiarajan, Conformational study of some N-acyl-2r,6c-diphenylpiperidin-4-one oximes using NMR spectra, J. Mol. Struct. 889 (2008) 297–307 https://doi.org/, doi:10.1016/j.molstruc.2008.02.008.

[20] B. Gates, Responding to Covid-19 — A Once-in-a-Century Pandemic? N. Engl. J. Med. 382 (2020) 1677–1679, doi:10.1056/NEJMp2003762.

[21] M.J. Ali, M. Hanif, M.A. Haider, M.U. Ahmed, F.N.U. Sundas, A. Hirani, I.A. Khan, K. Anis, A.H. Karim, Treatment Options for COVID-19: A Review, Front. Med. 7 (2020) 480 https://www.frontiersin.org/article/10.3389/fmed.2020.00480.

[22] R. Batra, H. Chan, G. Kamath, R. Ramprasad, M.J. Cherukara, S.K.R.S. Sankaranarayanan, Screening of Therapeutic Agents for COVID-19 Using Machine Learning and Ensemble Docking Studies, J. Phys. Chem. Lett. 11 (2020) 7058–7065, doi:10.1021/acs.jpclett.0c02278.

[23] I. Khater, A. Nassar, In silico molecular docking analysis for repurposing approved antiviral drugs against SARS-CoV-2 main protease, Biochem. Biophys. Reports. 27 (2021) 101032 https://doi.org/, doi:10.1016/j.bbrep.2021.101032.

[24] S. Kumar, P.P. Sharma, U. Shankar, D. Kumar, S.K. Joshi, L. Pena, R. Durvasula, A. Kumar, P. Kempaiah, B.Rathi, Poonam, Discovery of New Hydroxyethylamine Analogs against 3CLpro Protein Target of SARS-CoV-2: Molecular Docking, Molecular Dynamics Simulation, and Structure Activity Relationship Studies, J. Chem. Inf. Model. 60 (2020) 5754–5770, doi:10.1021/acs.jcim.0c00326.

[25] M. Rani, S. Jayanthi, S. Kabilan, R. Ramachandran, Spectral, Synthesis, Crystal structure, Hirshfeld surface, Computational analysis, and Antimicrobial studies of Ethyl-(E)-4-(2-(2-arylidenehydrazinyl)-2-oxoethyl)piperazine-1-carboxylates, J. Mol. Struct. 1252 (2022) 132082 https://doi.org/, doi:10.1016/j.molstruc.2021.132082.

[26] R. Rajamanickam, S. Sivakolunthu, J. Sampathkumar, Synthesis, crystal structure, Hirshfeld surface, DFT and docking studies of 4-[(5-hydroxy-3-methyl-1-phenyl-1H-pyrazol-4-yl)(phenyl)methyl] 5-methyl-2-phenyl-1,2-dihydro-3H-pyrazol-3-one, J. Mol. Struct. 1252 (2022) 132170 https://doi.org/, doi:10.1016/j.molstruc.2021.132170.

[27] R. Ramachandran, M. Rani, S. Kabilan, Synthesis, structure and conformational analysis of 2,4-diaryl 3-azabicyclo[3.3.1]nonan-9-one thiosemicarbazones and semicarbazones, J. Mol. Struct. 970 (2010) 42–50 https://doi.org/, doi:10.1016/j.molstruc.2010.02.005.

[28] M. Rani, R. Ramachandran, S. Kabilan, Efficient synthesis, spectral analysis and antimicrobial studies of nitrogen and sulfur containing spiro heterocycles from 2,4-diaryl-3-azabicyclo[3.3.1]nonan-9-ones, Bioorg. Med. Chem. Lett. 20 (2010) 6637–6643 https://doi.org/, doi:10.1016/j.bmcl.2010.09.021.

[29] G.M. Sheldrick, SHELXL-97 No Title, Univ. Gottingen, Gottingen, Ger. 1997.

[30] L.J. Farrugia, Ortep-3 for Windows, J. Appl. Cryst. 30 (1997) 565.

[31] P.R. Spackman, M.J. Turner, J.J. McKinnon, S.K. Wolff, D.J. Grimwood, D. Jayatilaka, M.A. Spackman, CrystalExplorer: a program for Hirshfeld surface analysis, visualization and quantitative analysis of molecular crystals, J. Appl. Crystallogr. 54 (2021) 1006–1011, doi:10.1107/s1600576721002910.

[32] D. Shobana, S. Sudha, D. Ramarajan, D. Dimić, Synthesis, crystal structure, spectral characterization and Hirshfeld surface analysis of (E)-N′-(3-ethoxy-4-hydroxybenzylidene)-4-fluorobenzohydrazide single-crystal - a novel NLO active material, J. Mol. Struct. 1250 (2022) 131856 https://doi.org/, doi:10.1016/j.molstruc.2021.131856.

[33] G.W.T.M.J. Frisch, H.B. Schlegel, G.E. Scuseria, M.A. Robb, J.R. Cheeseman, G. Scalmani, V. Barone, G.A. Petersson, H. Nakatsuji, X. Li, M. Caricato, A. Marenich, J. Bloino, B.G. Janesko, R. Gomperts, B. Mennucci, H.P. Hratchian, J.V. Ortiz, A.F. Izma, Gaussian 09,Revision A.02 No Title, Gaussian, Inc, Wallingford, CT, USA, 2013.

[34] AIMAll (Version 19.10.12), Todd A. Keith, TK Gristmill Software, Overland Park KS, USA, 2019.

[35] T. Lu, F. Chen, Multiwfn: a multifunctional wavefunction analyzer, J. Comput. Chem. 33 (2012) 580–592, doi:10.1002/jcc.22885.

[36] S. Forli, R. Huey, M.E. Pique, M.F. Sanner, D.S. Goodsell, A.J. Olson, Computational protein–ligand docking and virtual drug screening with the AutoDock suite, Nat. Protoc. 11 (2016) 905–919, doi:10.1038/nprot.2016.051.

[37] BIOVIA, Discovery studio visualizer 4.5, Dassault Systèmes (2016).

[38] R.M. Silverstein Webster, X. Francis, David J. Kiemle, David L. Bryce, Spectrometric identification of organic compounds, 8th ed. (2015).

[39] L. Lunazzi, D. Macciantelli, D. Tassi, A. Dondoni, Conformational studies by dynamic nuclear magnetic resonance. Part 17. Stereodynamic processes in hindered piperidyl-amides and -amidines, J. Chem. Soc. Perkin Trans. 2 (1980) 717–723, doi:10.1039/P29800000717.

[40] P. Parthiban, G. Aridoss, P. Rathika, V. Ramkumar, S. Kabilan, Synthesis, stereochemistry and antimicrobial studies of novel oxime ethers of aza/diazabicycles, Bioorg. Med. Chem. Lett. 19 (2009) 6981–6985 https://doi.org/, doi:10.1016/j.bmcl.2009.10.042.

[41] D. Cremer, J.A. Pople, General definition of ring puckering coordinates, J. Am. Chem. Soc. 97 (1975) 1354–1358, doi:10.1021/ja00839a011.

[42] A. Akila, S. Ponnuswamy, V. Shreevidhyaa Suressh, G. Usha, Synthesis, characterization and stereochemistry of N-acyl-r-2,c-4-bis(4-methoxyphenyl)-3-azabicyclo[3.3.1]nonanes, J. Mol. Struct. 1093 (2015) 113–118 https://doi.org/, doi:10.1016/j.molstruc.2015.03.052.

[43] O. Carugo, G. Resnati, P. Metrangolo, Chalcogen Bonds Involving Selenium in Protein Structures, ACS Chem. Biol. 16 (2021) 1622–1627, doi:10.1021/acschembio.1c00441.

[44] R. Zeng, Z. Gong, Q. Yan, Chalcogen-Bonding Supramolecular Polymers, J. Org. Chem. 85 (2020) 8397–8404, doi:10.1021/acs.joc.0c00723.

[45] S.P. Thomas, D. Jayatilaka, T.N. Guru Row, S···O chalcogen bonding in sulfa drugs: insights from multipole charge density and X-ray wavefunction of acetazolamide, Phys. Chem. Chem. Phys. 17 (2015) 25411–25420, doi:10.1039/C5CP04412J.

[46] S. Umamatheswari, S. Kabilan, Spectral characterization and crystal structure of 5-spiro-(3-methyl-2,6-diphenyltetrahydropyran-4-yl)-4,5-dihydro-[1,3,4]thiadiazole, J. Mol. Struct. 938 (2009) 142–149 https://doi.org/, doi:10.1016/j.molstruc.2009.09.016.

COLLEGE OF ARTS & SCIENCE NAMAKKAL 637 206

[47] M.A.A. Ibrahim, E.M.Z. Telb, σ-Hole and Lone-Pair Hole Interactions in Chalcogen-Containing Complexes: A Comparative Study, ACS Omega 5 (2020) 21631–21640, doi:10.1021/acsomega.0c02362.
[48] S. Jindani, B. Ganguly, Exploiting the role of stereoelectronic effects to design the antagonists of the human complement C3a receptor, New J. Chem. 45 (2021) 9443–9455, doi:10.1039/D1NJ00730K.
[49] E. Kavitha, D. Ramarajan, A. Rakić, D. Dimić, S. Sudha, P.N. Nirmala, Structural, spectroscopic, quantum chemical, and molecular docking investigation of (E)-N'-(2,5-dimethoxybenzylidene)picolinohydrazide, J. Mol. Struct. 1253 (2022) 132259 https://doi.org/, doi:10.1016/j.molstruc.2021.132259.
[50] S.V Meille, A. Farina, F. Bezziccheri, M.C. Gallazzi, The influence of alkoxy side chains on the conformational flexibility of oligo- and polythiophenes, Adv. Mater. 6 (1994) 848–851 https://doi.org/, doi:10.1002/adma.19940061109.
[51] R. Al-Salahi, H.A. Abuelizz, H.A. Ghabbour, R. El-Dib, M. Marzouk, Molecular docking study and antiviral evaluation of 2-thioxo-benzo[g]quinazolin-4(3H)-one derivatives, Chem. Cent. J. 10 (2016) 21, doi:10.1186/s13065-016-0168-x.
[52] Z. Jin, X. Du, Y. Xu, Y. Deng, M. Liu, Y. Zhao, B. Zhang, X. Li, L. Zhang, C. Peng, Y. Duan, J. Yu, L. Wang, K. Yang, F. Liu, R. Jiang, X. Yang, T. You, X. Liu, X. Yang, F. Bai, H. Liu, X. Liu, L.W. Guddat, W. Xu, G. Xiao, C. Qin, Z. Shi, H. Jiang, Z. Rao, H. Yang, Structure of Mpro from SARS-CoV-2 and discovery of its inhibitors, Nature 582 (2020) 289–293, doi:10.1038/s41586-020-2223-y.
[53] X. Xiaoyu, Y. Hongwei, Y. Haitao, X. Fei, W. Zhixin, S. Wei, L. Jun, Z. Zhe, D. Yi, Z. Qi, Z.X. C, L. Ming, B. Mark, R. Zihe, Structures of Two Coronavirus Main Proteases: Implications for Substrate Binding and Antiviral Drug Design, J. Virol. 82 (2008) 2515–2527, doi:10.1128/JVI.02114-07.
[54] H. Yang, W. Xie, X. Xue, K. Yang, J. Ma, W. Liang, Q. Zhao, Z. Zhou, D. Pei, J. Ziebuhr, R. Hilgenfeld, K.Y. Yuen, L. Wong, G. Gao, S. Chen, Z. Chen, D. Ma, M. Bartlam, Z. Rao, Design of Wide-Spectrum Inhibitors Targeting Coronavirus Main Proteases, PLOS Biol 3 (2005) e324, doi:10.1371/journal.pbio.0030324.
[55] Y. Shimamoto, Y. Hattori, K. Kobayashi, K. Teruya, A. Sanjoh, A. Nakagawa, E. Yamashita, K. Akaji, Fused-ring structure of decahydroisoquinolin as a novel scaffold for SARS 3CL protease inhibitors, Bioorg. Med. Chem. 23 (2015) 876–890 https://doi.org/, doi:10.1016/j.bmc.2014.12.028.
[56] M. Wang, R. Cao, L. Zhang, X. Yang, J. Liu, M. Xu, Z. Shi, Z. Hu, W. Zhong, G. Xiao, Remdesivir and chloroquine effectively inhibit the recently emerged novel coronavirus (2019-nCoV) in vitro, Cell Res. 30 (2020) 269–271, doi:10.1038/s41422-020-0282-0.
[57] B. Nutho, P. Mahalapbutr, K. Hengphasatporn, N.C. Pattaranggoon, N. Simanon, Y. Shigeta, S. Hannongbua, T. Rungrotmongkol, Why Are Lopinavir and Ritonavir Effective against the Newly Emerged Coronavirus 2019? Atomistic Insights into the Inhibitory Mechanisms, Biochemistry 59 (2020) 1769–1779, doi:10.1021/acs.biochem.0c00160.
[58] M.M. Ghahremanpour, J. Tirado-Rives, M. Deshmukh, J.A. Ippolito, C.-H. Zhang, I. Cabeza de Vaca, M.-E. Liosi, K.S. Anderson, W.L. Jorgensen, Identification of 14 Known Drugs as Inhibitors of the Main Protease of SARS-CoV-2, ACS Med. Chem. Lett. 11 (2020) 2526–2533, doi:10.1021/acsmedchemlett.0c00521.
[59] R. Hatada, K. Okuwaki, Y. Mochizuki, Y. Handa, K. Fukuzawa, Y. Komeiji, Y. Okiyama, S. Tanaka, Fragment Molecular Orbital Based Interaction Analyses on COVID-19 Main Protease – Inhibitor N3 Complex (PDB ID: 6LU7), J. Chem. Inf. Model. 60 (2020) 3593–3602, doi:10.1021/acs.jcim.0c00283.
[60] Ž.B. Milanović, M.R. Antonijević, A.D. Amić, E.H. Avdović, D.S. Dimić, D.A. Milenković, Z.S. Marković, Inhibitory activity of quercetin, its metabolite, and standard antiviral drugs towards enzymes essential for SARS-CoV-2: the role of acid–base equilibria, RSC Adv. 11 (2021) 2838–2847, doi:10.1039/D0RA09632F.



PRINCIPAL
PGP College of Arts and Science
Namakkal.

IJBPAS, March, 2020, 9(3): 458-467

ISSN: 2277–4998

International Journal of Biology, Pharmacy and Allied Sciences (IJBPAS)

'A Bridge Between Laboratory and Reader'

www.ijbpas.com

DESIGN, SYNTHESIS, CHEMICAL NUCLEASE ACTIVITY AND ANTIBACTERIAL EVALUATION OF Cu(II), Co(II), Ni(II) and Mn(II) SCHIFF BASE METAL COMPLEXES

T. SUJESHWARI [1], E. AKILA [2] AND P. MAHESWARAN[3*]

1: Research Scholar, Department of Chemistry, P.G.P College of Arts and Science, Namakkal, Tamil Nadu, 637207

2: Department of Chemistry, Sri Sarada College for Women (Autonomous), Salem, Tamil Nadu, 636016

3: Principal and Head, Department of Chemistry, P.G.P college of Arts and Science, Namakkal, Tamil Nadu, 637207

Received 8th Oct. 2019; Revised 6th Nov. 2019; Accepted 7th Dec. 2019; Available online 1st March 2020

https://doi.org/10.31032/IJBPAS/2020/9.3.4989

ABSTRACT

Four new Cu(II), Ni(II), Co(II) and Mn(II) metalloinsertors have been synthesized by using a Schiff base, formed by the condensation reaction of isatin, p-chloroaniline with 1, 10-phenanthroline. They have been structurally characterized by IR, UV–vis, NMR, EPR, elemental analyses, molar conductivity and magnetic susceptibility studies. The molar conductance data of the complexes indicate that they are non-electrolytes in nature. The spectral and analytical data reveal that the complexes take up distorted octahedral geometry. They have been examined for their antibacterial activities against few pathogens. The data reveal that the complexes exhibit better biocidal activities against bacteria than the free Schiff base ligand. The gel electrophoresis experiment reveals that the complexes are good chemical nucleases.

Keywords: Metal complexes, Antibacterial activity and DNA cleavage

INTRODUCTION

DNA binding of metal complexes has been widely investigated because they can be used as potential anticancer drugs, DNA structural probes, DNA foot printing

ARTS & SCIENCE P.G.P. COLLEGE OF NAMAKKAL 637 208

agents, DNA dependent electron transfer probes, sequence-specific cleaving agents and so on **[1]**. DNA is the primary target molecule for mainly anticancer and antiviral therapies according to cell biologists. Investigations on the interaction of DNA with small molecules are significant in the aim of new types of pharmaceutical molecules. While the chemical nuclease activity of transition metal complexes was discovered in the year 1980, studying the interaction model and the mechanism of transition metal complexes with DNA moecule, and exploring the application of metal complexes in antineoplastic medication, molecular biology and bioengineering have turn out to be hotspots in recent years. Some kind of metal complexes when interacted with DNA might induce the breakage of DNA strands by appropriate methods **[2]**. Schiff bases form a vital separation of organic compounds in chemistry due to their useful physical and chemical properties and great number of reactions that they undergo. Schiff bases, derived from substituted aliphatic amines and aromatic aldehydes, have an extensive variety of applications in many fields, e.g. inorganic, biological, and analytical chemistry **[3-4]**.

In literature, several reports associate the consequence of the biological activity of metal complexes with the metal ions rather than the ligands. To our knowledge, no work has been reported on the condensed reaction of the isatin, p-chloroaniline with 1, 10-phenanthroline and its transition metal complexes as chemical nucleases. In continuation of our journey toward the exploration of novel potentially active drugs, we herein report the synthesis, characterization and DNA interaction of Schiff base transition metal(II) complexes.

EXPERIMENTAL

All reagents and chemicals used, isatin, p-chloroaniline with 1, 10-phenanthroline and various metal(II) chlorides, were Merck products and used as supplied. Commercial solvents were distilled and then used for the preparation of ligand and its complexes.

Microanalyses (C, H and N) were performed in Carlo Erba1108 analyzer at Sophisticated Analytical Instrument Facility (SAIF). The electronic absorbance spectra in the 200–800 nm were recorded on Double beam spectrometer Cyber lab between 200 – 800 nm. Magnetic susceptibility measurements of the complexes were carried out by Gouy balance using copper sulfate pentahydrate as the calibrant. IR spectra were recorded with Perkin–Elmer FT-IR-8300 spectrophotometer in the 4000–400 cm^{-1}

P.G.P. COLLEGE OF ARTS & SCIENCE NAMAKKAL 637 206

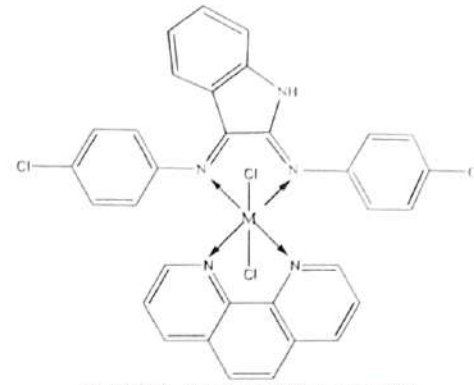
range using KBr pellets. NMR spectra were recorded on a Bruker Spectrometer at 400 MHZ in DMSO. Electron paramagnetic resonance spectra of the mixed ligand complexes of copper(II) were recorded on a Varian E 112 EPR spectrometer in DMSO solution both at room temperature and liquid nitrogen temperature (77 K) using TCNE (tetracyanoethylene) as the g-marker.

Synthesis of Schiff base ligand (4-Chloro-phenyl)-(2-imino-1,2-dihydro-indol-3-ylidene)-amine)-1-chloro-4-methyl-benzene

The Schiff base ligand was synthesized by adding Isatin (1 mM) in 20 ml of ethanol, p-chloroaniline (2 mM) in 20 ml of ethanol. The mixture was refluxed for 2-3 hrs. Then solution of the ligand was kept for slow evaporation and yellow colored precipitate was collected and dried in air **[5]**.

Synthesis of Schiff base metal complexes

The ethanolic solution of synthesized ligand (1 mM) was added dropwise stirring to an ethanolic solution of the metal chloride (1 mM) (Metal = Cu(II), Co(II), Ni(II) and Mn(II)) with constant stirring and followed by an ethanolic solution of 1, 10-phenanthroline is added and the mixture was boiled under reflux for 3-5 hrs. Then, the volume of the reaction mixture was reduced by evaporation. The precipitated complexes were filtered off, washed with ethanol and then dried in vacuuo **[6-7]**.



M=Cu(II), Ni(II), Co(II) and Mn(II)

Figure 1: Structure of Mononuclear Schiff base Metal(II) complexes

RESULTS AND DISCUSSION

The Schiff base ligand and its Cu(II), Ni(II), Co(II) and Mn(II) complexes have been synthesized and characterized by spectral and elemental analytical data. They are found to be air stable. The ligand is soluble in common organic solvents and all the complexes are freely soluble in $CHCl_3$, DMF and DMSO but partially soluble in methanol and ethanol and insoluble in water.

Elemental analysis and molar conductivity measurements

The elemental analysis results for the metal complexes are in good agreement with that of the calculated values **(Table 1)** showing that the complexes have 1:1:1 metal–ligand stoichiometry of the type ML_1L_2, wherein L_1 is (4-Chloro-phenyl)-(2-imino-1,2-dihydro-indol-3-ylidene)-amine)-1-chloro-4-methyl-benzene and L_2

P.G.P. COLLEGE OF ARTS & SCIENCE NAMAKKAL 637 206

= 1, 10-phenanthroline. The metal(II) complexes were dissolved in DMF and the molar conductivities of 10^{-3} M of their solution at room temperaturewere measured. The lower conductance values 5.4–10.2 ohm^{-1} cm^2 mol^{-1} of the complexes support their non-electrolytic nature of the compounds.

IR spectra

IR spectra of the complexes clearly point out the bonding association of the ligand with the metal ion. The spectrum of free ligand showed a band in the region 1616 cm^{-1} characteristics of the ν(C=N) (azomethine) stretching mode indicating the formation of the Schiff base product. This band was shifted toward lower frequencies in the spectrum of its metal complexes (1602–1610 cm^{-1}) compared with the above Schiff base indicating the involvement of the azomethine nitrogen in coordination with metal ion **[8]**. The coordination of nitrogen to the metal ion could be expected to reduce the electron density of the azomethine link and thus caused a shift in the ν(C=N) group. Conclusive evidence of the bonding was also shown by the observation that new bands in the spectra of all metal complexes appearing in the low frequency regions at 483–465 cm^{-1} characteristic to ν(M–N) stretching vibrations, respectively, that were not observed in the spectrum of free ligand. In addition, the appearance of new bands at 335.10-348.22 cm^{-1} showing the involvement of ν(M–Cl) bond in the complexes formation, supporting the IR spectral study **(Table 2)**.

^{1}H-NMR spectra

^{1}H NMR spectra of the ligand were recorded in DMSO- d_6 at room temperature. The azomethine proton (–CH=N) signal in the spectrum of the ligand was shifted down field (8.7 d) compared to the free ligand, suggesting deshielding of azomethine group due to the coordination with metal ion. And the other signals in the region 6.24–7.72 ppm exhibits due to aromatic protons. The peak observed at the range of 3.6 ppm due to -NH proton in ligand **[9]**.

Electronic spectra and magnetic moment

The electronic spectral data of the metal(II) complexes in DMF solution are displayed in **Table 3**. The nature of the ligand field around the metal ion was deduced from the electronic spectra. The electronic spectrum of Co(II) complex exhibited three bands in the region of 650, 585 and 550 nm which were tentatively assigned to $^4T1g\rightarrow 4T_2g(F)$ (v_1), $^4T_1g\rightarrow{}^4A_2g(F)$ (v_2) and $^4T_1g\rightarrow{}^4T_1g(P)$ (v_3) transitions, respectively. The value of magnetic moment was 5.10 B.M. which indicates the presence of Co(II) complex in octahedral geometry. The electronic

P.G.P. COLLEGE OF ARTS & SCIENCE NAMAKKAL 637 206

spectrum of the Ni(II) complex showed three bands at 690, 545 and 570 nm assignable to $^3A_2g \rightarrow {}^3T_2g$ (F) (v_1), $^3A_2g \rightarrow {}^3T_1g$ (F) (v_2) and $^3A_2g \rightarrow {}^3T_1g$ (P) (v_3) transitions, respectively. The value of magnetic moment was 3.40 B.M; therefore octahedral geometry is suggested for this complex [10]. The ^2Eg and ^2T_2g states of the octahedral Cu(II) (d^9) split under the influence of the tetragonal distortion and the distortion can be such as to cause the three transitions $^2B_1g \rightarrow {}^2B_2g$; $^2B_1g \rightarrow {}^2Eg$ and $^2B_1g \rightarrow {}^2A_1g$ to remain unresolved in the spectra. It is concluded that, all three transitions 640, 555 and 520 nm lie within the single broad envelope centered at the same range previously mentioned. This assignment is in agreement with the general observation that Cu(II) d–d transitions are normally close in energy. The magnetic moment of 1.97 B.M. falls within the range normally observed for octahedral Cu(II) complexes. The electronic spectra of Mn(II) complexes show the absorption bands in the range 684, 545 and 520 nm. These absorption bands may be assigned to the $^6A_1g \rightarrow {}^4A_1g$, $^6A_1g \rightarrow {}^4A_2g$, and $^6A_1g \rightarrow {}^4Eg$, ^4A_1g transitions, respectively. These bands suggest that the complexes possess an octahedral geometry. The Mn(II) complex show magnetic moments is 5.92 B.M. at room temperature corresponding to five unpaired electrons which suggest octahedral geometry. In the spectra of the Schiff base ligand, the absorption band observed at 281-294 nm were assigned to intra-ligand $\pi \rightarrow \pi^*$ transition and the band at 342-390 nm were assigned due to $n \rightarrow \pi^*$ transition associated with the azomethine chromophore (-C=N).

EPR Studies

The EPR spectra of complexes provide information of importance in studying the metal ion environment. The ESR spectrum of Cu(II) complex were recorded on X-band at frequency 9.1 GHz at room temperature. The spectra exhibited a single anisotropic intense sharp signal at room temperature with no hyperfine splitting as shown in **Figure 2**. This suggests that copper ions are in mononuclear environment.

The EPR spectrum of the $[Cu(C_{20}H_{13}N_5Cl_4)]$ complexes show a broad signal with g_{iso} at 2.0001 which is consistent with an distorted octahedral geometry **[10]**.

Antibacterial activity

The synthesized ligand and the complexes were tested for their *in vitro* antibacterial activity. They were tested against the bacteria *S. aureus*, *B. subtilis*, *E. coli* and *K. pneumonia* and the values of the investigated compounds are summarized in **Tables 4**. A comparative study of values of ligand and the complexes indicates that the

P.G. & R. COLLEGE OF ARTS & SCIENCE NAMAKKAL 637 206

metal complexes exhibit higher antibacterial activity than the free ligand. Such increased activity of the complexes is able to be explained on the basis of the Tweedy's chelation theory **[11]**. Chelation reduces the polarity of the metal ion significantly because of the biased sharing of its positive charge with the donor group and also due to p-electron delocalization on the whole chelate ring. The lipids and polysaccharides are some significant constituents of the cell wall and membranes which are favoured for metal ion interaction. Apart from this, the cell walls also hold many phosphates, carbonyl and cystenyl ligands which keep up the integrity of the membrane by acting as a diffusion barrier and also give appropriate sites for binding. Furthermore, the reduction in polarity increases the lipophilic character of the chelates and an interaction among the metal ion and the lipid is favored. This may lead to the breakdown of the permeability barrier of the cell resulting in interfering with the normal cell processes. Besides this, the complexes might also indulge in the formation of hydrogen bonded interaction throughout the coordinated anions and azomethine group with the active centers of the cell constituents. Factors able of increasing lipophilic nature are expected to improve the antibacterial property. The synthesized Schiff base ligand has reasonable inhibitory effects on the growth of tested microorganism. This is owing to the presence of azomethine groups which contain chelating properties. These properties may be used in metal transport across the bacterial membranes or to connect to the bacterial cells at a specific site from which it can get in the way with their growth. The present investigations of antimicrobial activity data indicated that all of the newly synthesized complexes exhibited slightly different antibacterial activity as compared to that of the control drugs.

Chemical nuclease activity

The DNA cleavage efficacy of the complexes compared to that of the control is due to their efficient DNA-binding ability **[12]**. When super coiled pUC18DNA is subjected to electrophoresis, relatively fast migration will be observed for the intact super coiled form (Form I). If scission occurs on one strand (nicking), the super coiled form will relax to make a slower moving nicked form (Form II). If both strands are cleaved, a linear form (Form III) that migrates between Forms I and II will be generated. In the current study, DNA cleavage was analyzed by monitor the conversion of super coiled DNA (Form I) to nicked DNA (Form II) in the presence of oxidant H_2O_2. From **Figure**

P.G.P. COLLEGE OF ARTS & SCIENCE NAMAKKAL 637 206

3 (lanes 3–6), it is evident that the complexes cleave DNA more efficiently in the presence of an oxidant (H_2O_2). This may be attributed to the formation of hydroxyl free radicals. The OH^o free radicals participate in the oxidation of the deoxyribose moiety, followed by hydrolytic cleavage of a sugar phosphate back bone. All the complexes showed prominent nuclease activity in the presence of oxidant H_2O_2 which may be due to the increased production of hydroxyl radicals. Control experiments by means of DNA alone (lane 1) did not show any significant cleavage of pUC18DNA even on longer exposure time. From the observed results, it is concluded that all the complexes efficiently cleave the DNA as compared to control DNA.

Table 1: Analytical data of the Schiff base ligand and its mononuclear metal complexes

Compound	Molecular Formula	color	Yield %	Melting Point (°)	% of Nitrogen		% of Metal		Molar conductance A_m (ohm^{-1} cm^2 mol^{-1})
					Cal	Exp	Cal	Exp	
L	$C_{20}H_{13}N_3Cl_2$	Yellowish orange	80	140	9.88	9.86	-	-	-
$[CuL_1L_2]$	$[Cu(C_{20}H_{13}N_5Cl_4)]$	Green	70	>200	11.15	11.14	12.64	12.63	5.4
$[NiL_1L_2]$	$[Ni(C_{20}H_{13}N_5Cl_4)]$	Brown	75	>200	11.26	11.23	11.80	11.79	8.2
$[CoL_1L_2]$	$[Co(C_{20}H_{13}N_5Cl_4)]$	Brown	70	>200	11.25	11.23	11.83	11.82	7.9
$[MnL_1L_2]$	$[Mn(C_{20}H_{13}N_5Cl_4)]$	Black	75	>200	11.34	11.33	11.12	11.10	10.2

Table 2: Infrared Spectroscopic Data of the Schiff Base Ligand and its mononuclear metal complex

Compounds	(C=N) (cm^{-1})	(C-O) (cm^{-1})	(M−N) (cm^{-1})	(M−Cl) (cm^{-1})
$C_{20}H_{13}N_3Cl_2$	1616	1255	--	--
$[Cu(C_{20}H_{13}N_5Cl_4)]$	1608	1270	465	338.12
$[Ni(C_{20}H_{13}N_5Cl_4)]$	1610	1310	470	335.10
$[Co(C_{20}H_{13}N_5Cl_4)]$	1615	1330	483	348.22
$[Mn(C_{20}H_{13}N_5Cl_4)]$	1602	1325	480	345.36

Table 3: Electronic Spectral data of Schiff base ligand and its complexes

Compound	Electronic spectra (nm)				Geometry of the complex
	$\pi\rightarrow\pi^*$	$n\rightarrow\pi^*$	L→M	d-d	
$C_{20}H_{13}N_3Cl_2$	295	374	-	-	-
$[Cu(C_{20}H_{13}N_5Cl_4)]$	280	375	450	640, 555, 520	Distorted Octahedral
$[Ni(C_{20}H_{13}N_5Cl_4)]$	290	395	445	690, 545, 570	
$[Co(C_{20}H_{13}N_5Cl_4)]$	285	340	455	650, 585, 550	
$[Mn(C_{20}H_{13}N_5Cl_4)]$	290	344	435	684, 545, 520	

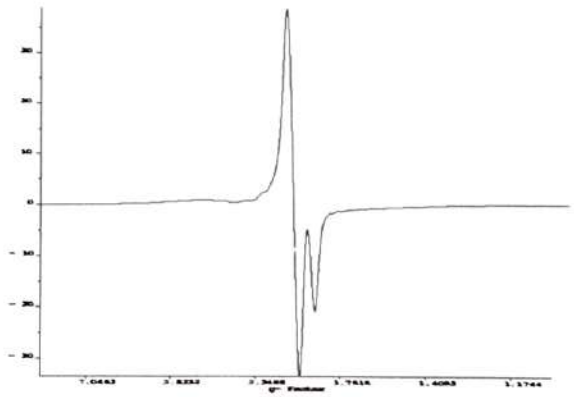


Figure 3: EPR spectra of $[Cu(C_{20}H_{13}N_5Cl_4)]$ complex

P.G.P. COLLEGE OF ARTS & SCIENCE NAMAKKAL 637 206

Table 4: Antibacterial activity for heterocyclic Schiff base ligands and its mononuclear metal complexes

Compounds	Zone of inhibition (mm)															
	Gram positive bacteria								Gram negative bacteria							
	Staphylococcus aureus				*Bacillus subtilis*				*Escherichia coli*				*Klebsiella pneumoniae*			
	Concentration (µg/ml.)															
	25	50	75	100	25	50	75	100	25	50	75	100	25	50	75	100
$C_{20}H_{13}N_3Cl_2$	7	7	8	9	7	7	9	9	6	6	7	8	7	8	8	9
$[Cu(C_{20}H_{13}N_5Cl_4)]$	12	13	14	15	12	10	13	14	10	10	12	13	11	12	15	17
$[Ni(C_{20}H_{13}N_5Cl_4)]$	9	8	10	12	9	8	11	12	6	7	7	9	9	8	9	10
$[Co(C_{20}H_{13}N_5Cl_4)]$	10	9	12	13	10	11	12	14	8	9	9	11	9	10	11	12
$[Mn(C_{20}H_{13}N_5Cl_4)]$	8	9	9	10	8	9	9	10	7	8	9	9	7	8	9	10
Streptomycin	16	17	20	22	14	15	17	20	12	13	16	20	13	14	16	18

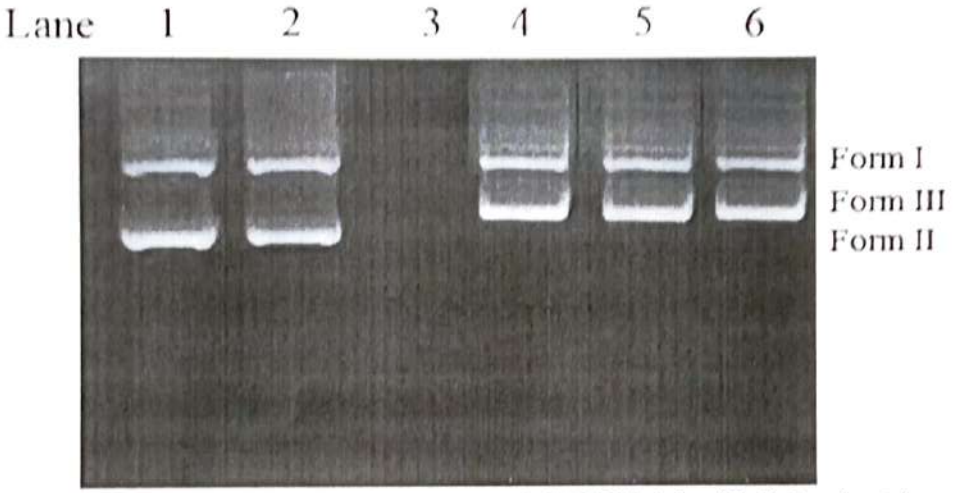


Figure 3: Changes in the agarose gel electrophoretic pattern of pUC18DNA induced by H_2O_2 and metal complexes. Lane 1-DNA alone; Lane 2- DNA alone + H_2O_2; Lane 3-DNA + $[Cu(C_{20}H_{13}N_5Cl_4)]$ + H_2O_2; Lane 4-DNA + $[Ni(C_{20}H_{13}N_5Cl_4)]$ + H_2O_2; Lane5-DNA + $[Co(C_{20}H_{13}N_5Cl_4)]$; Lane 6-DNA + $[Mn(C_{20}H_{13}N_5Cl_4)]$ + H_2O_2

CONCLUSIONS

From the elemental analysis, molar conductivity, UV–Vis, magnetic, IR and ^1H NMR spectral data, it is possible to decide the type of coordination of the ligand in their metal complexes. Based on these data, a distorted octahedral geometry is assigned to these complexes. Chemical nuclease activity of these metal complexes with super coiled pUC18DNA was investigated by gel electrophoresis. From the results, it is found that the metal complexes cleaved DNA effectively in the presence of H_2O_2 as compared to the control DNA. Further, the promising results have been observed for the antimicrobial screening particularly for the metal complexes against bacteria and what may be attributed to the fact that the metal complexes are potentially active against bacterial cells.

DECLARATIONS

Acknowledgments

The author is indebted to Supervisor for his constant encouragement and support. STIC Cochin, St. Joseph College, Trichy and Progen lab, Salem are gratefully acknowledged for providing instrumental facilities.

P.G.P. COLLEGE OF ARTS & SCIENCE NAMAKKAL 637 206

Conflict of interests

The authors declare that they have no conflict of interest

REFERENCES

[1] Akila, E., Usharani, M., Ramachandran, S., Jayaseelan, P., Velraj, G., Rajavel, R., Tetradentate-Arm Schiff base Derived from the Condensation Reaction of 3, 3′-dihydroxy-benzidine, glyoxal/ diacetyl and 2-aminophenol: Designing, Structural Elucidation and Properties of their Binuclear Metal(II) Complexes Arabian. J. Chem, http://dx.doi.org/10.1016/j.arabjc.2013.11.031.

[2] Akila. E, Usharani. M., Maheswaran. P. & Rajavel. R, Spectral, Magnetic, Biocidal Screening and DNA Cleavage Studies Of Binuclear Metal(II) Complexes of Tetracoordinate Schiff Base Ligand Of 3, 3′-Dihydroxybenzidine, International Journal of Recent Scientific Research 2013; 4(10): 1497-1503.

[3] Sima J, Mechanism of Photoredox Reactions of Iron(III)Complexes Containing Salen-type Ligands Crao. Chem. Acta 2001; 74: 593.

[4] E. Akila, M. Usharani and R. Rajavel, Design, synthesis and interpretation of binuclear schiff base metal complexes and their application; antibacterial activity, International Journal of Inorganic and Bioinorganic Chemistry 2012;2 (2): 15-19..

[5] Tarafder M. T. H, Ali M. A, Saravana N, Weng W. Y, Kumar S, Tsafe N. U, Crouse K. A, Coordination chemistry and biological activity of nickel(II) and copper(II) ion complexes with nitrogen–sulphur donor ligands derived from S-benzyldithio-carbazate (SBDTC), Transition Met Chem 2016; 26: 613

[6] Colman J, Hegedu L. S, Principles and Applications of Organo-transition Metal Chemistry, University Science Book, California, 1980.

[7] Mahajan K, Swami M, and Singh R.V, Microwave synthesis, spectral studies, antimicrobial approach and coordination behavior of antimony(III) and bismuth(III) compounds with benzothiazoline, Russ. J. Coord. Chem 2009; 35: 179-185

[8] Liu J, Zhang T.X, Ji L.N, DNA-binding and cleavage studies of macrocyclic copper(II) complexes,

T.K. COLLEGE OF ARTS & SCIENCE NAMAKKAL 637 206

J. Inorg. Biochem 2012, 91: 269–276.

[9] Mehmet Tumer, Duygu Ekinci, Ferhan Tumer, Akif Bulut, Synthesis, characterization and properties of some divalent metal(II) complexes. Their electrochemical, catalytic, thermal and antimicrobial activity studies, Spectrochim. Acta Part A 2007; 67: 916–929.

[10] Costamagna J, Vargas J, Latorre R, Alvarado A, Mena G, Coordination compounds of copper, nickel and iron with Schiff bases derived from hydroxynaphthaldehydes and salicylaldehydes, Coord. Chem. Res 1992; 119: 67–88.

[11] Debojyoti Lahiri, Ritankar Majumdar, Ashis K Patra And Akhil R Chakravarty, Anaerobic DNA cleavage in red light by dicopper(II) complexes on disulphide bond activation, J. Chem. Sci 2015; 122 (3): 321–333.

[12] Ren S, Wang R, Komastu K, Krause P.B, Zyrianov Y, Mckenna C. E, Csipke C, Tokes Z. A, Lien E. J, Synthesis, biological evaluation, and quantitative structure-activity relationship analysis of new Schiff bases of hydroxylsemicarbazide as potential antitumor agents J. Med Chem 2002, 45: 410.

PRINCIPAL
PGP College of Arts and Science
Namakkal.

P.G.P. COLLEGE OF ARTS & SCIENCE
NAMAKKAL
637 206

ISSN NO: 1301-2746

A STUDY ON FINANCIAL BOTTOMLINE (EAT) OF IRON AND STEEL INDUSTRY WITH RESPECT TO SELECT FIRMS IN INDIA

Dr. K. VENKATACHALAM,
Assistant Professor, Department of Commerce,
PGP College of Arts and Science, Namakkal, Tamil Nadu, India.
venkatukv@gmail.com.

Mr. D. SARAVANAKUMAR
Ph.D, Research Scholar,Department of Commerce,
PGP College of Arts and Science, Namakkal, Tamil Nadu, India.
saravana.utc@gmail.com

ABSTRACT

Every firm uses its limited resources of production in its business endeavor to supply goods and services to the society. In this process, it always experts a fair return on its invested resources in production – supply chain. This fair return, often termed as earning after tax or financial bottom-line, can be reaped by the firm, only if its scarce resources are used to the full potential. Thus, the very objective of a firm is to make earning after tax (EAT) by using its resources efficiently. In this connection, the researcher made an attempt to study the position of earning after tax of the select firms in Iron and Steel industry over the years to know how these firms commands or otherwise of their EAT. The researcher has chosen the iron and steel industry because the industry is responsible for building state-of- the- art infrastructure and drives the Indian economy towards growth-making. The researcher has selected firms, such as, TSL, SAIL, JSWSL, JSPL and SEIL for this study of the basis of assets size and turnover. The financial statement of these firms from the year 2008 – 2009 to 2017 – 2018 has been considered for the study. The researcher used ratio analysis and vital statistical techniques to analysis the financial bottom-line, i.e. EAT of these firms during the considered time period. The researcher has concluded this study with the following inferences:

- TSL earns more operating profits
- JSPL earns more EAT and gives good return on equity
- SEIL earns goods return on capital employed
- SAIL reported red financial bottom line (EAT) over the years.

Key Words: Bottom-line, Growth-making, Infrastructure, Potential, Resources

P.G.P. COLLEGE OF ARTS & SCIENCE NAMAKKAL 637 206

Scanned with OKEN Scanner

ISSN NO: 1301-27
ADALYA JOURNAL

1.1 INTRODUCTION

Indian economy drives its wheels through the tracks of its major passage, such agriculture, industry and service. Of these passages, industry is considered to be the major passage. The reason being that the industry propels India's economic growth to a large extend. Though the industry is a large propeller of growth for decades, its recent performance on its economic and social fronts keep the country worrying. Among the core industries, the performance of iron and steel industry poses a dismal outlook over the last 10 years or so.

The success or performance of any industry can be gauged by the state of its financial bottom line (EAT) from time to time. A thermo-reading of all the industries, particularly iron and steel industry, suggest that all is not well in the industry and industry have been in the red over the years.

The growth of any economy in the world is much assured, if the economy is taken care of its infrastructural needs. In this respect, the iron and steel industry has been making its huge contribution particularly in India. Having characters, such as, capital-intensive, productivity-oriented, highly-turnover and mass employment provider, the iron and steel industry is still grappling with poor financial bottom-line (EAT) in some of its units. This ultimately results in poor rate of return on equity, poor rate of return on invested capital etc., which led to opposite to the objective of shareholders' wealth maximization. This general state of the industry poses some negativity in the minds of all the shareholders and the new players in the economy.

1.2 STATEMENT OF THE PROBLEM

The iron and steel industry significantly contributes to the economic growth of India over the years. Because of this support of this industry, India is equipped with good infrastructure and logistics in recent years. But, there is a vacuum created in some of the firms in the industry because of structural deficiency in finance front. As a result, the goodness of the industry is over-shadowed by this financial structural deficiency. It can be vouched by the fact that most of the firm in the industry has been continuously reported red financial bottom line (EAT) over the years. These scenarios prompt the researcher to undertake a study on the financial bottom-line of some of the industry's firms. Hence, the present study.

1.3 OBJECTIVES OF THE STUDY

- To study the financial bottom line (EAT) of selected firms in Indian iron and steel industry

P.G.P. COLLEGE OF ARTS & SCIENCE NAMAKKAL 637 206

Scanned with OKEN Scanner

- To infer the study in the form of findings, make suggestions and draw conclusion about Indian iron and steel industry on the financial bottom-line (EAT)

1.4 REVIEW OF LITERATURE

Literature review navigates the researcher towards the explored and unexplored areas in the research under his hand. Not only that, this review of earlier researches on the current domain gives the researcher a sense of research knowledge and direction in which the present research is being carried on. The following are some of the reviews of the previous works the researcher put his sight.

Waqas Bin Khidmat et. al. (2014), have studied the impact of liquidity and solvency on the profitability of chemical firms. They inferred that poor solvency position has greatly affected the return on assets and equity. They also came out with the inference that highly-levered firm reports low profit.

Mohan Kumar M.S. et. al. (2015), have employed production-marketing-supply chain approach to study the profitability of cement industry in India. The concluded that cements industry must concentrate on modernizing its cement plants and adopt efficient and workable marketing strategies in order to stay relevant in the market.

Veerakumar V.K. (2016), have analyzed the financial performance of Indian steel industry in the scales of operating efficiency, production performance and profit performance. They found that the financial strength of TISCO and SAIL were good. They concluded that the operating profit was affected by unexpected fluctuations in production and profit performance.

Manoj Singh Negi et. al. (2017), have studied the growth of Uttarakhand paper industry on the parameter of profitability and found that all the firms in the industry has reported good profits and has handed over fair and equal return to their shareholders.

Brindha K. et. al. (2018), have analyzed the financial performance of iron and steel industry in India on the yardsticks of sales and profitability. They found that the return on capital employed, sales and profitability have been considerably increased in some of the firms in the industry. They suggested that others can also follow the footsteps of these firms in order to taste the successful financial performance.

1.5. METHODOLOGY OF THE STUDY

Research Design

The present study adopts an analytical and descriptive research design. The data of the sample firms for a period of ten years from 2008 – 09 to 2017-18 has been collected from

P.G.P. COLLEGE OF ARTS & SCIENCE NAMAKKAL 637 206

Scanned with OKEN Scanner

ISSN NO: 1301-274X
ADALYA JOURNAL

by using a software prowess software. The sample size of selected iron and steel firms has been selected for the purpose of the study on the basis of assets size and turnover. They are:

1. Tata Steel Limited (TSL)
2. Steel Authority of India Limited (SAIL)
3. JSW Steel Limited (JSWSL)
4. Jindal Steel and Power Limited (JSPL)
5. Steel Exchange of India Limited (SEIL)

Tools used for Analysis

Ratio Analysis: Profitability ratios have been applied for the past ten years for the purpose of analysis. Ratio analysis helps the firms in analyzing the financial bottom-line (EAT) in the following parameters in the study.

Operating profit ratio implies the percentage of operating profit, the difference between the gross profit and the operating expenses, in relation to sales.

- Net profit ratio implies the percentage of net profit to sales.
- Return on equity signifies how a firm generates its return, i.e. available for distribution among shareholders. This will help the firm to know whether the shareholder's wealth is maximized.
- Return on capital employed signifies how a firm has deployed its capital in the business operations and what return the firm got out of it. This will help the firm to assess the performance of capital employed, in relation to the end result i.e. return.
- Operating expenses, expenses in operating the business, such as, office, administrative, selling and distribution expenses.

  Non operating expenses, expenses in connection with servicing the debt, such as, finance cost, depreciation and taxes.

Accordingly, the following ratios have been used:

- Operating Profit Ratio
- Net profit ratio
- Return on equity
- Return on capital employed
- Operating expenses ratio
- Non operating expenses ratio

P.G.P. COLLEGE OF ARTS & SCIENCE NAMAKKAL 637 206

Scanned with OKEN Scanner

ISSN NO: 1301-2746

Statistical Tools: Mean, Standard Deviation, Co-efficient of Variation and Compound Annual Growth Rate were used for to identify by the relationship between the long term and short term profitability position for the selected firms for the period of ten years from 2008-09 to 2017-18.

1.6 ANALYSIS AND INTERPRETATION

Table 1. Analysis of Profitability Ratios of Selected Iron and Steel Firms in India

Operating Profit Ratio					
Companies	TSL	SAIL	JSWSL	JSPL	SEIL
Mean	27.94	9.03	11.93	18.54	5.47
SD	8.55	11.61	7.01	10.57	5.78
CV (%)	30.59	128.59	58.78	57.01	105.63
CAGR (%)	-8.58	-18.14	6.50	-10.95	-209.09
Net Profit Ratio					
Companies	TSL	SAIL	JSWSL	JSPL	SEIL
Mean	15.70	4.78	4.55	12.08	-1.41
SD	5.68	8.65	5.60	7.19	7.17
CV (%)	36.18	181.09	123.25	59.48	-509.82
CAGR (%)	-11.49	-173.10	9.25	-21.99	-242.26
Return on Equity					
Companies	TSL	SAIL	JSWSL	JSPL	SEIL
Mean	10.84	6.16	8.47	13.11	-11.54
SD	3.67	10.74	10.13	9.67	47.03
CV (%)	33.82	174.36	119.64	73.82	-407.75
CAGR (%)	-10.01	-173.31	12.46	-27.40	-245.62
Return on Capital Employed					
Companies	TSL	SAIL	JSWSL	JSPL	SEIL
Mean	0.12	0.08	0.11	0.11	0.15
SD	0.03	0.18	0.06	0.08	0.17
CV (%)	24.56	129.02	57.11	71.87	111.84
CAGR (%)	-5.52	-21.33	11.06	-17.26	-206.17
Operating Expenses Ratio					
Companies	TSL	SAIL	JSWSL	JSPL	SEIL
Mean	41.18	42.82	19.27	35.06	7.78
SD	14.47	14.01	6.75	13.02	4.70
CV (%)	35.13	32.71	35.01	37.13	60.40
CAGR (%)	13.25	8.52	10.08	15.21	6.15
Non Operating Expenses Ratio					
Companies	TSL	SAIL	JSWSL	JSPL	SEIL

P.G.P. COLLEGE OF ARTS & SCIENCE NAMAKKAL 637 206

Scanned with OKEN Scanner

ISSN NO: 1301-2746

ADALYA JOURNAL

Mean	10.22	6.94	11.61	19.44	8.43
SD	1.39	3.28	2.20	10.90	4.40
CV (%)	13.55	47.34	18.96	56.08	52.19
CAGR (%)	1.10	12.69	-0.80	12.74	21.49

Source: Computed

Operating Profit Ratio

TSL earn more operating profits among the selected firms on an average and also this firm found less deviation in operating profit ratio over the years. TSL was also relatively more consistent in earning the operating profits over the years. But, none of the selected firms shows a growth in operating profits over the years except JSWSL. In later part of the years, SAIL, JSWSL and SEIL reported operating losses on few occasions.

Net Profit Ratio

An average net profit of TSL (15.70 percent) was more and in JSPL, it was (12.08 percent) and SEIL, the average shows a negative trend. The deviation of net profit was also less in the case of JSWSL and the firms maintain consistency in earning net profits. But, no selected firm registers a positive growth in net profit generation over the years except JSWSL. In SAIL, JSWSL and SEIL, there was net loss in some of the years after 2014-15.

Return on Equity

As far as the average return on equity is concerned, JSPL stood first (13.11 percent), followed by TSL (10.84 percent), JSWSL (8.47 percent) and SAIL (6.16 percent) respectively. There was a more deviation of this return reported in SEIL. TSL registered consistent growth in generating return for its shareholder over the years. But, no company ever has seen its return growing positively over the years except JSWSL. In SAIL and SEIL, consequently, there was a negative return in the later part of the years under study.

Return on Capital Employed

SEIL stood first in generating return on capital employed on an average (0.15 times), as compared to others and much deviation in return on capital employed was reported in SAIL. There exists high inconsistency in return on capital employed in SAIL. JSWSL reported a positive growth on return on capital employed over the years.

Operating Expenses Ratio

As far as average ratio is concerned, it was more in SAIL (42.82 percent) and less in SEIL (7.78 percent). It implies that SEIL was comparatively in control of operating expenses.

P.G. COLLEGE OF ARTS & SCIENCE NAMAKKAL 637 206

Scanned with OKEN Scanner

Much deviation of this ratio was reported in TSL and more inconsistency was reported in SAIL. JSPL seen more expenses growing in the years of the study, as compared to the other selected firms.

Non Operating Expenses Ratio

The average ratio was more in JSPL (19.44 percent) and less in SAIL (6.44 percent). JSPL seen more deviation of this ratio and reported more inconsistency in the ratio, as compared to others. In SEIL, the non operating expenses over the years increased in relation to other selected firms.

Chart 1 Operating Profit Ratio of Selected Iron and Steel Firms in India

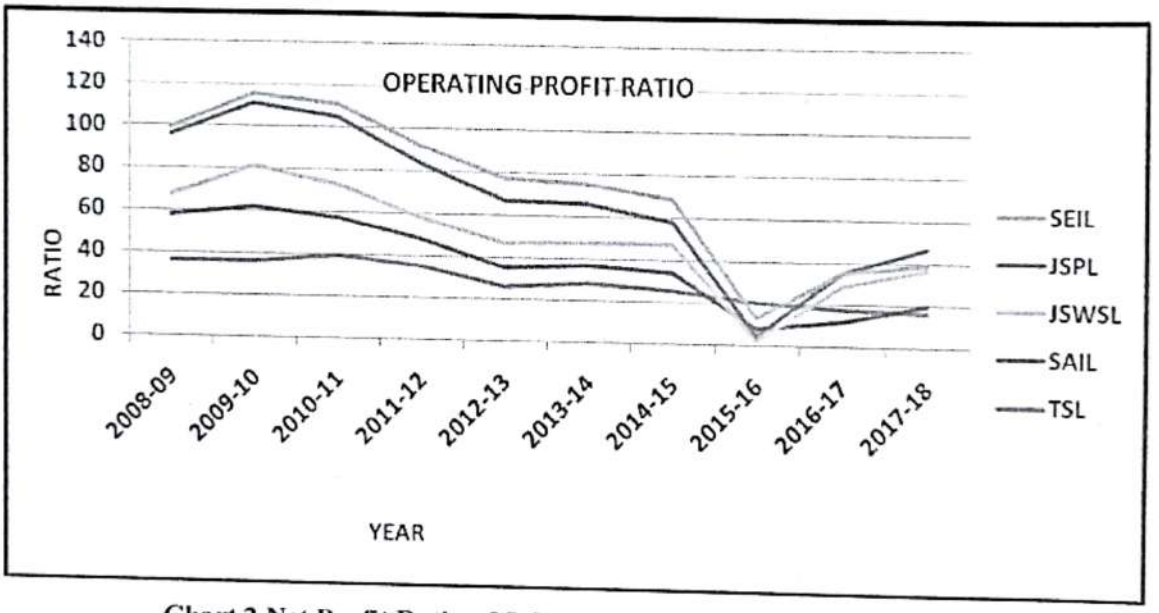
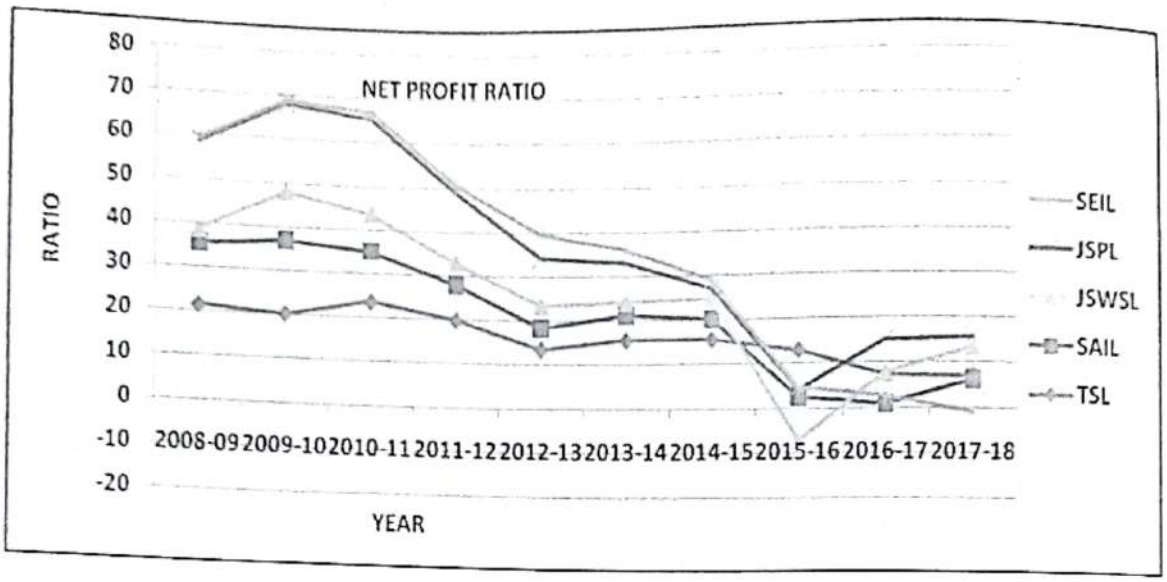


Chart 2 Net Profit Ratio of Selected Iron and Steel Firms in India

P.G.P. COLLEGE OF ARTS & SCIENCE NAMAKKAL 637 206

Scanned with OKEN Scanner

ISSN NO: 1301-2746
ADALYA JOURNAL



1.7 FINDINGS

Based on the analysis of the present study, the researcher has comment with the following inferences. These inferences are presented by the researcher in the form of the following findings:-

- The operating profits of TSL are more and SEIL is less. JSWSL witnessed growth in its operating profits over the years.
- The net profits of TSL are more and SEIL is less. JSWSL witnessed growth in net profits over the years.
- JSWSL returned higher amount on its equity and SAIL returned lower or negative amounts on equity.
- The return on capital employed is good in SEIL. There is a positive growth in return on capital employed in JSWSL.
- Operating expenses of SAIL is more and of SEIL is less.
- Non-operating expenses of JSPL are more.

1.8 SUGGESTIONS

- Based on the above findings, the researcher was suggest the following points to improve the financial bottom-line (EAT) of selected firms in iron and steel industry.

P.G.P. COLLEGE OF ARTS & SCIENCE
NAMAKKAL
637 206

Scanned with OKEN Scanner

- TSL must maintained a same tempo of operating profits, net profits, return on equity and return on capital employed. The firm must take steps to control its non – operating expenses.
- SEIL must re-structure its financial setup so as to have more operating profits and net profits.
- SAIL must re-invent the good financial structure so as to turn around its losses into profits.

1.9 CONCLUSION

Financial bottom-line (EAT) plays a significant role in firm's life cycle. To have a good financial bottom-line (EAT), the firm must use its scarce resources diligently. Of all the scarce resources, finance plays a vital part in the sense that it integrates all other resources. Hence, a vibrant plant, involving acquisition of financial resources and its effect utilization, is the need of the hour for all the firms, especially, the capital intensive firm such as firm in iron and steel-making industry. This, in-turn, helps the firms increasing the financial bottom-line (EAT). Based on this study, it is found that these are a structural financial deficiency faced by the selected firms. The route-cause of this deficiency may be contributed to firms' poor planning of financial resources and its effective implementation. Hence, it is concluded that all the firms in the iron and steel industry must take steps to chalk out and put action the strategic financial plan to improve their financial bottom-line (EAT) to stay aloft in the market.

References

1. Pandey, I.M (2010), "Financial Management;" Vikash Publication, New Delhi, 10th Edition.
2. Gupta, S. K., and Sharma, R. K. (2011), "Financial Management-Theory and Practice", Kaliyani Publisher, Ludhiana, Punjab, 7th Edition.
3. Waqas Bin Khidmat and Mobeen Ur Rehman (2014) "Impact of Liquidity & Solvency on Profitability Chemical Sector of Pakistan", Economics Management Innovation, Volume 6(3), pp. 1-13.
4. Mohan Kumar M S, Safeer Pasha M and Bhanu Prakash T N (2015), "Profitability Analysis of Selected Cement Firms in India", International Journal of Multidisciplinary Research and Modern Education, Volume I, Issue II, pp. 95-99.
5. Veerakumar V.K. (2016), "Financial Performance of Steel Industry in India With Special Reference to TISCO and SSIL", Intercontinental Journal of Finance Research Review, Volume 4, Issue 8, August, pp. 98-102.

P.G.P. COLLEGE OF ARTS & SCIENCE NAMAKKAL 637 206

Scanned with OKEN Scanner

ISSN NO: 1301-2746

6. Manoj Singh Negi and Hem Chandra Kothari (2017), "Analysis of Profitability of Paper Industry in Uttarakhand", International Journal of Engineering and Management Research, Volume-7, Issue-2, March-April, pp. 264-272.

7. Sweta Singh (2017), "Ratio Analysis in Manufacturing Sector-A Study", International Journal of Innovative Research in Engineering & Management, Volume-4, Issue-4, July, pp. 690-693.

8. Deepak Cherian and George V Kallarackal (2017), "Analysis of Liquidity and Profitability Position of a Cattle Feed Manufacturing Firm", International Journal of Advance Engineering and Research Development Volume 4, Issue 5, May, pp.332-336.

9. Brindha K. and Suseelamani K. (2018), "Financial Performance of Selected Firms of Iron and Steel Industry in India", International Journal of Management, Technology and Engineering, Volume 8, Issue XI, November, pp. 376-388.

10. Malgorzata Kowalik (2018), "Profitability and Financial Liquidity of Chemical Industry Firms", Finanse, Rynki Finansowe, Ubezpieczenia nr 1/2018 (91), pp. 47-58.

11. Kavitha Muthukumaran and Vani Haridasan (2018), "Performance Analysis of Select Firms in Cement Industry Using Various Models", International Journal of Civil Engineering and Technology, Volume 9, Issue 3, March, pp. 839–852.

P.G.P. COLLEGE OF ARTS & SCIENCE NAMAKKAL 637 206

PRINCIPAL
PGP College of Arts and Science
Namakkal

Scanned with OKEN Scanner

ISSN NO: 1021-9056

FINANCIAL LIQUIDITY AND HEALTH ANALYSIS OF SELECTED IRON AND STEEL FIRMS IN INDIA

Dr. K. VENKATACHALAM,
Assistant Professor, Department of Commerce,
PGP College of Arts and Science, Namakkal, Tamil Nadu, India.
venkatukv@gmail.com.

Mr. D. SARAVANAKUMAR
Ph.D, Research Scholar,Department of Commerce,
PGP College of Arts and Science, Namakkal, Tamil Nadu, India.
saravana.utc@gmail.com

Abstract

The success of the business depends on how efficiently the resources of the business are being managed of all the resources of the business, finance plays a major role. So, it is paramount importance to manage the funds of the business in an effective manner. Here, financial management, both short term as well as long term, comes into play. Among the core industries which determines the economic development of a nation, the iron and steel industry's contribution is so significant. The industry wheels the Indian economy towards growth trajectory by way of providing mass employment to the people, building sound infrastructure and contributing substantially to the reveals of the government. Hence, it is obvious to track the growth of the industry through the lens of financial management. The financial management can be tracked through the sound analysis of the liquidity, solvency and financial health. Towards this purpose, the researcher has undertaken this study to analyze the liquidity, solvency and financial health of selected Iron and Steel firms in India. Ratio's, significant statistical tools and Z score model have been employed by the researcher to analyze the ten years financial data of the chosen five NSE and BSE listed steel producing firms. Core findings of the study include poor liquidity management of all the firms, better solvency management in TSL and sad financial health of all the firms.

Key Words: Financial Health, Infrastructure, Ratio's, Solvency, Trajectory.

P.G.P. COLLEGE OF ARTS & SCIENCE
NAMAKKAL
637 206

Scanned with OKEN Scanner

1.1. Introduction

The Iron and Steel industry in India enjoys the competitive edge over its peers in the world. The primary reasons for this advantage is being seen, as the industry sources all its required resources domestically act cheap cost. The industry elevates the country to the 3rd place in the production and consumption of steel, after China and Japan. The share of the industry to the growth of the economy is so significant, as it contributes 7 to 7.5% annually.

Liquidity refers to the firm's ability to meet its short term financial commitments to keep its operation cycle going all the times uninterrupted. Through liquidity analysis, a firm self analyze itself to know whether it's short term financial creditors are satisfied and their financial interest are being protected.

Long term solvency refers to the decision of the firm relating to judicial mixture of capital structure. The capital structure decision must be taken by a firm in the context of maximizing share holders' wealth. Through the analysis of long term solvency, a firm can insure weather its capital structure decisions contribute to the shareholders' wealth maximization.

The financial health of a firm can be taken as another parameter to know the survival of the business, both in long term and short term. To put it differently, the financial health analysis reveals how a firm manages its short term and long term financial commitments to satisfy the financial and commercial interest of all the stake holders.

1.2. Statement of the Problem

Though the Iron and Steel industry contribute significantly to the nation's economy over the years, its financial picture is not that much rosy in some of the firms in the industry. Particularly so, even some of the major firms are bleeding in their financial bottom-line. Hence, the researcher is quit interested to know the reasons for such dismal financial performance of the firms in the industry. So, this study is born out.

1.3. Review of Literature

Review helps the researcher to frame a few concepts used in the study and to formulate an analytical frame work. It has been carried out with the help of articles, reports published in different, journals and magazines by different financial institutions and from books also.

Chandra. H. et. al. (2013), have studied financial health of steel firms in India by applying Altman's Z score and found out that the financial health is satisfactory but not good enough in major steel firms in India. They suggest that proper maintenance among liquidity, solvency and profitability is the only way to have good financial health for these firms.

P.G. COLLEGE OF ARTS & SCIENCE NAMAKKAL 637 206

Scanned with OKEN Scanner

Sanjeeb Kumar Dey (2014), has compared various firms in paper industry on the criteria of liquidity, solvency and efficiency management. He is of the view that liquidity, solvency and efficiency management are closely related and mutually inclusive. So, he suggests that, a special care should be taken to include liquidity, solvency and efficiency concern, while framing the financial policies of the company.

Ata Takeh et. al. (2015), have analyzed the impact of capital structure of financial performance of steel industry. They have related the capital structure of the industry with return on capital employed, return on equity and return on assets and studied how these variables affect the financial performance of Indian steel industry. They have found out that capital structure and ROCE, ROE and ROA are inter - related. They have advocated that any small change in capital structure affects these variables in a big way and significantly, affects the financial performance of the company.

Chetana R Marvadi (2016), has evaluated the financial health of steel firms in India and came out with the conclusion that financial health of Jindal steel limited is satisfactory, whereas the financial health of SAIL is too healthy over a period of time. Further, he suggested that financial health of Jindal steel limited can be improved by paying attention to working capital management.

Shrabanti Pal (2018), has analyzed the behaviour of financial ratios of India steel industry post –recession era and reveals that there was a positive relationship between liquidity and profitability among most of the firms in steel industry in India. Further, any behavioural change in market conditions also significantly affects the liquidity and profitability of these firms.

1.4. Objectives of the Study

The study has been conducted with the following objectives:

- To evaluate the short term and long term solvency position of selected iron and steel firms in India
- To assess the financial health of the selected iron and steel firms in India.

1.5. Hypothesis of the Study:

To fulfill the above objectives, the researcher has formulated the following Hypotheses:

- There is no significant difference exist in short term solvency ratios between the firms in the selected iron and steel firms in India.

P.G.P. COLLEGE OF ARTS & SCIENCE NAMAKKAL 637 206

Scanned with OKEN Scanner

- There is no significant difference exist in long term solvency ratios between the firms in the selected iron and steel firms in India.

1.6. Research Methodology

Source of Data: This study is based on secondary data collected from the published Annual Reports of respective iron and steel firms in India.

Sample Size: The study has been based on NSE and BSE listed steel companies. It is related with major five steel producing firms in India. Which are as follows: Tata Steel Limited (TSL), Steel Authority of India Limited (SAIL), JSW Steel Limited (JSWSL), Jindal Steel and Power Limited (JSWL) and Steel Exchange of India Limited SEIL).

Period of Study: The period of study covers ten years (20108-09 to 2017-18).

Statistical Tools for Analysis: Data analysis is based on some selected short term and long term financial ratios. It is fundamentally analytical in nature. Various tools like mean, standard deviation, Co-efficient of Variations and ANOVA single factor test has been applied to analyze the trends, consistency and stability along with different ratios used in Altman's Z- Score model.

1.7. Analysis and Interpretation

Table 1 Short Term Solvency Analysis of Selected Iron and Steel Firms in India

CURRENT RATIO					
FIRMS	**TSL**	**SAIL**	**JSWSL**	**JSPL**	**SEIL**
MEAN	0.93	1.16	0.74	0.77	1.02
SD	0.29	0.51	0.12	0.19	0.16
C.V. (%)	31.59	43.46	16.73	24.05	16.06
CAGR (%)	3.86	-10.47	4.09	-7.25	-4.35
QUICK RATIO					
FIRMS	**TSL**	**SAIL**	**JSWSL**	**JSPL**	**SEIL**
MEAN	0.57	0.66	0.41	0.55	0.51
SD	0.30	0.46	0.10	0.15	0.21
C.V. (%)	52.85	70.25	24.93	26.39	40.36
CAGR (%)	4.30	-15.35	2.43	-8.45	-12.77
ABSOLUTE LIQUID RATIO					
FIRMS	**TSL**	**SAIL**	**JSWSL**	**JSPL**	**SEIL**
MEAN	0.15	0.35	0.07	0.02	0.05
SD	0.11	0.42	0.05	0.02	0.02
C.V. (%)	74.37	120.40	76.78	122.28	47.11
CAGR (%)	2.05	-39.85	-9.68	-19.44	-18.05
ANALYSIS OF VARIANCE (ONE WAY ANOVA)					
RATIOS	F	P-value	F crit	S/NS	

P.G.P. COLLEGE OF ARTS & SCIENCE NAMAKKAL 637 206

Scanned with OKEN Scanner

CURRENT RATIO	3.35	0.01*	2.58	S
QUICK RATIO	1.06	0.39	2.58	NS
ABSOLUTE LIQUID RATIO	4.56	0.00*	2.58	S

Source: Computed, S- significant, NS- not significant, *S- significant at 5 percent Level

The current assets management of all the selected firms was not satisfactory because all the firms maintained their current ratio below the standard norm 2:1. Comparatively, SAIL fared better and JSWSL fared poor in maintaining current assets to current liabilities.

The quick ratio of all selected firms under study was not commendable. Comparatively, the quick ratio position of SAIL was good, followed by TSL, JSPL, SEIL and JSWSL respectively. The compound annual growth rate of quick ratio reveals a negative trend in all the firms except TSL and JSWSL. The absolute liquid ratios of all the selected firms were not found to be satisfactory. But, comparatively SAIL stood first, followed by TSL, JSWSL, SEIL and JSPL on the yard stick of average ratio. All firms reported a negative growth rate in respect absolute liquid assets over the years except TSL. From the above reveals that a difference in the current ratio is significant between the firms as the calculated value of F (24.37) is greater than the table value of F (2.50) at five percent level of significance.

The result of one way ANOVA test shows that, in quick ratio there is no significant difference exist in quick ratio between the firms calculated F (1.06) Value is less than the table value of F (2.58) at five percent level. In respect of current ratio and absolute liquid ratio, the result of one way ANOVA shows that there is a significant difference exist in current ratio and absolute liquid ratio between the firms of selected firms in iron and steel industry in India calculated F (3.35) & (4.56) value is greater than the table value of F (2.58) at five percent level.

Table 2 Long Term Solvency Analysis of Selected Iron and Steel Firms in India

DEBT-EQUITY RATIO					
FIRMS	TSL	SAIL	JSWSL	JSPL	SEIL
MEAN	0.92	1.32	2.03	2.03	4.51
SD	0.21	0.44	0.37	0.37	2.33
C.V. (%)	22.61	33.37	18.41	18.27	51.66
CAGR	-2.96	9.53	-2.38	-0.27	13.75
PROPRIETORY RATIO					
FIRMS	TSL	SAIL	JSWSL	JSPL	SEIL
MEAN	0.52	0.44	0.34	0.33	0.20
SD	0.05	0.07	0.04	0.04	0.05
C.V. (%)	9.67	16.42	12.29	11.85	23.83
CAGR	1.46	-5.38	1.84	0.30	-10.63
INTEREST COVERAGE RATIO					

P.G.R. COLLEGE OF ARTS & SCIENCE NAMAKKAL 637 206

Scanned with OKEN Scanner

FIRMS	TSL	SAIL	JSWSL	JSPL	SEIL
MEAN	5.19	10.01	2.41	4.23	1.09
SD	1.20	13.39	1.39	4.03	0.76
C.V. (%)	23.20	133.70	57.67	95.17	69.63
CAGR	-6.08	-35.70	5.79	-24.97	-190.11
ANALYSIS OF VARIANCE (ONE WAY ANOVA)					
RATIOS	F	P-value	F crit	S/NS	
DEBT-EAUITY RATIO	16.42	0.00*	2.58	S	
PROPRIETORY RATIO	56.67	0.00*	2.58	S	
INTEREST COVERAGE RATIO	2.94	0.03*	2.58	S	

Source: Computed, S- significant, NS- not significant, *S- significant at 5 percent Level

The average debt equity ratio over the years was more in SEIL (4.51 times) and less in TSL (0.92 times), indicating that SEIL was heavily debt – loaded and TSL was lightly debt-loaded.

The average proprietary ratio was more in TSL (0.52 times), followed by SAIL (0.44 times) and JSWSL, JSPL (0.33 times) and SEIL (0.20 times). Less deviation of this ratio was reported in JSPL. JSPL was consistent in maintain this ratio over the years. In TSL, the growth of this ratio was more, as compared to others. SEIL and SAIL is registered a negative growth in proprietary ratio.

The interest cover for SAIL was more, on an average, and the firm reported more deviation in the interest cover. Consistency in interest cover was more in JSWSL and the firm has recorded a positive growth (5.79 percent) in interest cover over the years, due to growth in net profits.

The result of one way ANOVA test shows that, in debt – equity ratio, proprietary ratio and interest coverage ratio there is significant difference exist in all the long term solvency ratios between the firms calculated F value more than the table value of F (2.58) at five percent level.

Financial Health (Altman's Z Score Model) Analysis

$$Z=1.2X_1+1.4X_2+3.3X_3+0.6X_4+0.99X_5,$$

Where,

X_1 =Working Capital/Total Assets,
X_2 =Retained Earnings/Total Assets,
X_3 =EBIT/Total Assets,
X_4 =Market Value of Equity/Total Debts
X_5 =Sales/Total Assets
Z = Index

Table 3 Altman Guidelines for Healthy and Bankruptcy Zone

	Situation	'Z' scores	Zones

P.K.R. COLLEGE OF ARTS & SCIENCE NAMAKKAL 637 206

Scanned with OKEN Scanner

I	3 and above	Too Healthy zone	Not to all
II	1.8 - 3.0	Healthy zone	Uncertain to predict
III	Below 1.8	Bankruptcy zone	Certain to all

Source: Altman (1968)

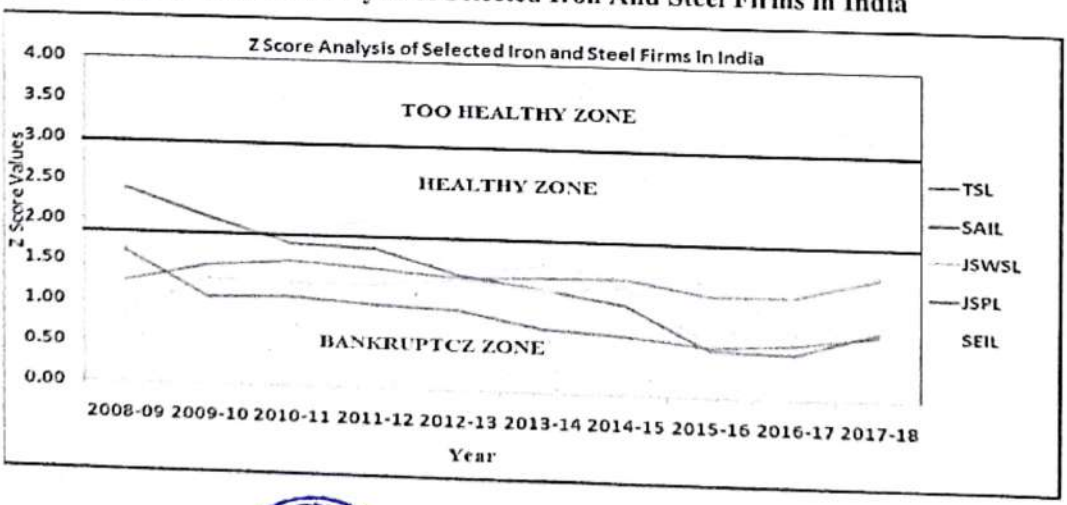
Table 4 Financial Health (Altman's Z Score Model) Analysis of Selected Iron and Steel Firms in India

Year	TSL	SAIL	JSWSL	JSPL	SEIL
2008-09	1.26	2.40	0.84	1.63	1.83
2009-10	1.47	2.05	1.30	1.08	1.84
2010-11	1.54	1.75	1.28	1.10	1.91
2011-12	1.47	1.72	1.27	1.03	2.07
2012-13	1.38	1.42	1.37	0.99	1.41
2013-14	1.40	1.26	1.25	0.79	1.57
2014-15	1.41	1.11	1.31	0.72	1.41
2015-16	1.24	0.58	0.65	0.62	1.41
2016-17	1.25	0.56	1.28	0.66	0.81
2017-18	1.49	0.83	1.52	0.79	0.19

Source: Computed

The Z score of the all selected firms were less than 1.80 benchmark in all the years, except SAIL in the year 2008-09 and 2009-10 and SEIL the year 2011-12. This implies that all the firms were on the track of financial bankruptcy. The reason attributed to this state of financial health may be due to negative working capital, less EBIT and less sales.

Chart 1 Z Score Analysis of Selected Iron And Steel Firms in India



COLLEGE OF ARTS & SCIENCE MAMAKKAL P.G.P.

Scanned with OKEN Scanner

1.8. Findings

Bases on the above analysis, the researcher has summarized the results of the study in the form of the following findings:

Financial Liquidity:

i) Quick ratio of all the selected firms were more or less similar

ii) Current ratio and absolute liquid ratio of all the selected firms differ

iii) Liquidity of all the selected firms was not under the mark during the period of study.

Financial Solvency:

i) SEIL was more leveraged and TSL was less leveraged financially

ii) The proprietary ratio of TSL was good and in SAIL, not good

iii) Solvency position of all the selected firm's differ

iv) Long term solvency position of all the selected firms were not satisfactory.

Financial Health:

i) SAIL shows a good financial health in the year 2008-09 and SEIL in the year 2011-12.

ii) All the selected firms registered a poor financial health in most of the years due to working capital mismanagement.

1.9. Suggestions

Based on the above key findings, the following actions may be suggested by the researcher:

i) The selected firms must focus their liquidity management in such a manner so that short term solvency position is ensured in the coming years.

ii) The selected firms must pay attention particularly to the interest covered in such a way that profits are increased and future financial payments in the form of interest cover is sufficiently met.

1.10. Conclusion

From the above study, it can be concluded that, almost all the selected firms have been suffering from financial mismanagement over the years. The firms in the industry, being capital intensive in nature, must pay proper attention to their financials, from the stage of procurement of funds to the stage of its effective utilization. Hence, all the firms in the industry must see that

P.G.P. COLLEGE OF ARTS & SCIENCE NAMAKKAL 637 206

Scanned with OKEN Scanner

no stone left unturned, as far us, good financial management. This will result in increasing shareholders wealth and ultimately leads to nation – building.

References

1. Altman,(1968)."Financial ratios discriminate analysis and prediction of corporate bankruptcy", Journal of finance, sep. 598.
2. Khan, M.Y. & Jain, P.K. (2007) "Financial Management", Text, Problems and Cases, Tata McGraw Hill Publishing Company Ltd., New Delhi, 4th ed.
3. Bhunia, A., & Khan, I. (2011) "Liquidity management efficiency of Indian Steel Companies (A Case Study)". Far East Journal of Psychology and Business, 3(3), 3-13.
4. Chandra H. and Selvaraj A (2013), "A Study on Financial Health of Selected Indian Steel Companies", SMART Journal of Business Management and Studies, Volume 9, No.1. January- June, pp. 36-42.
5. Sumita Sinku, Prashant Kumar (2014). "Analysis of Financial Health of Steel Authority of India Limited", Industrial Engineering Letters. 4(4). ISSN: 2224-6096P, ISSN: 2225-05810.
6. Sanjeeb Kumar Dey (2014), "Paper Industry in India: A Comparative Study", European Journal of Business and Management, Volume.6, No.31, pp. 251-260.
7. Ata Takeh and Jubiliy Navaprabha (2015), "Capital Structure and Its Impact on Financial Performance of Indian Steel Industry", International Journal of Management, Volume. 6, Issue 6, June, pp. 29-38.
8. Chetana R Marvadi (2016), "Evaluating Financial Health of Selected Steel Companies In India through 'Z' Score Model", International Journal of Multidisciplinary Research and Development, Volume 3, Issue 12, December, pp. 01-05.
9. Shrabanti Pal (2018), "Behavior of Financial Ratios of Indian Steel Industry during Post Recession Period", IOSR Journal of Business and Management, Volume 20, Issue 1. Vol. I ,January, pp. 39-43
10. Małgorzata Kowalik (2018), "Profitability and Financial Liquidity of Chemical Industry Companies", Finanse, Rynki Finansowe, Ubezpieczenia nr 1/2018 (91), pp. 47-58.
11. Brindha K. and Suseelamani K. (2018), "Financial Performance of Selected Companies of Iron and Steel Industry in India", International Journal of Management, Technology and Engineering, Volume 8, Issue XI, November, pp. 376-388.

P.G. COLLEGE OF ARTS & SCIENCE NAMAKKAL 637 206

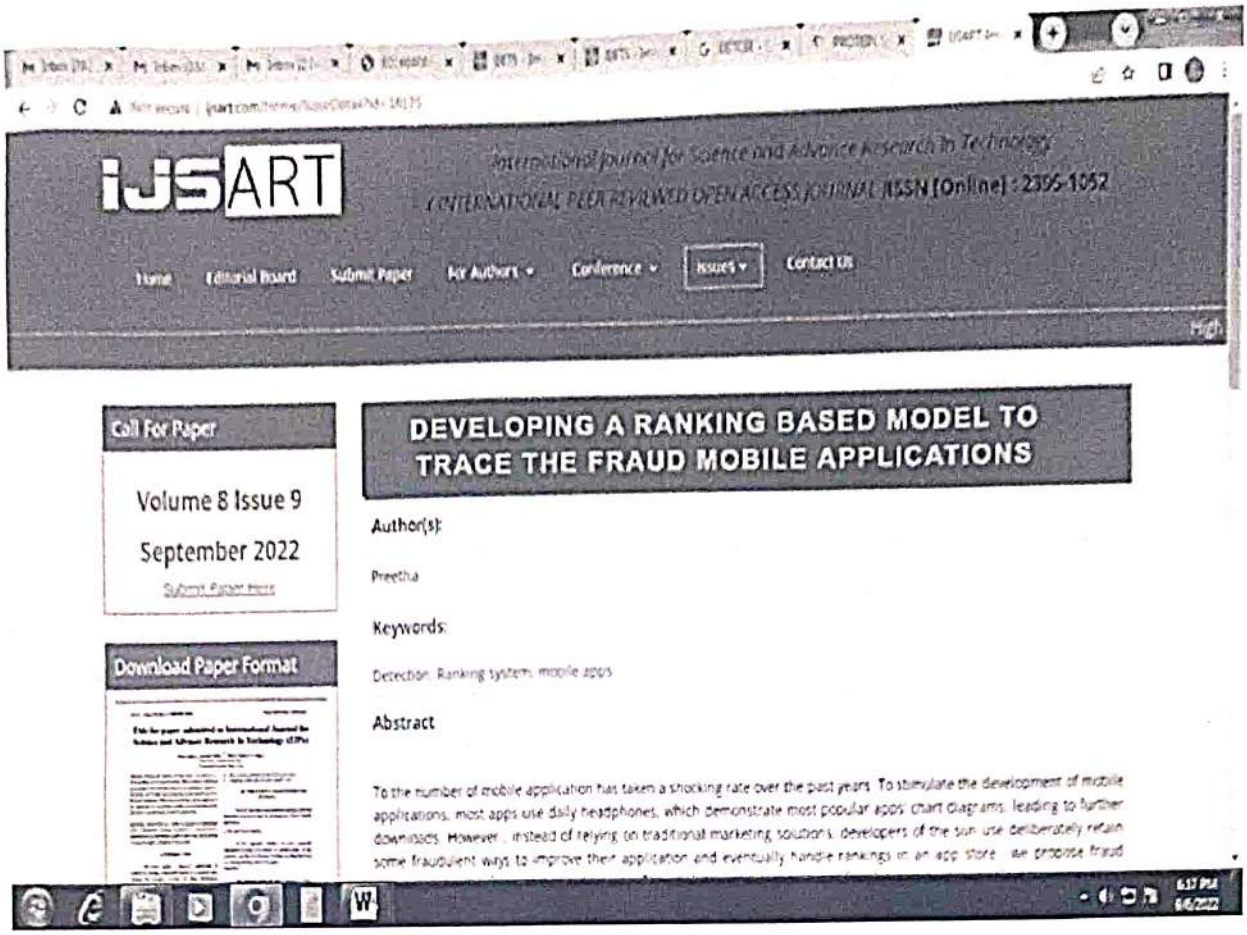
Scanned with OKEN Scanner

12. www.ibef.org/industry/steel.aspx.
13. Report of Department of Industrial Policy and Promotion, 2018.

P.G.P. COLLEGE OF ARTS & SCIENCE NAMAKKAL 637 206

PRINCIPAL
PGP College of Arts and Science
Namakkal

Scanned with OKEN Scanner



iJSART

International Journal for Science and Advance Research in Technology

[INTERNATIONAL PEER REVIEWED OPEN ACCESS JOURNAL] ISSN [Online] : 2395-1052

Home | Editorial Board | Submit Paper | for Authors | Conference | Issues | Contact Us

Call For Paper

Volume 8 Issue 9

September 2022

Submit Paper Here

Download Paper Format

DEVELOPING A RANKING BASED MODEL TO TRACE THE FRAUD MOBILE APPLICATIONS

Author(s):

Preetha

Keywords:

Detection, Ranking system, mobile apps

Abstract

To the number of mobile application has taken a shocking rate over the past years. To stimulate the development of mobile applications, most apps use daily headphones, which demonstrate most popular apps chart diagrams, leading to further downloads. However, instead of relying on traditional marketing solutions, developers of the sun use deliberately retain some fraudulent ways to improve their application and eventually handle rankings in an app store. we propose fraud

P.G.P. COLLEGE OF ARTS & SCIENCE NAMAKKAL 637 206

DEVELOPING A RANKING BASED MODEL TO TRACE THE FRAUD MOBILE APPLICATIONS

Mrs. Preetha.M
PGP COLLEGE OF ARTS &SCIENCE,NAMAKKAL,M C A,M Phil ,
Asst Professor,Department of Computer Science and Applications

Abstract-*Now Days, Ranking fraud plays major role in mobile applications store like play store and IOS store. Applications Developer gives fake ranking to their applications to rank up their apps in top most list of application market. Surely it turns out to increase number downloads to their applications. In this paper I am going to analysis the ranking fraud and what are the proposes of ranking fraud detection system for mobile applications store. First of all we find positioning misrepresentation by some mining techniques on static period namely leading season of mobile applications. That time frame can be utilized for detecting the irregularity of applications ranking. In this research I am going to investigate three type of data i.e., information based on ranking, information based on rating and information based on reviews, Likewise I will propose an improvement based on aggregation algorithm by using all the data or information that are misinterpreting users. Finally I examine the proposed system with real-world applications data collected from different-different applications store. I am validating the adequacy of proposed algorithm, and show how it will detects some regularity of fraud activities.*

Keywords-Ranking Fraud, Mobile Applications, Aggregation.

I. INTRODUCTION

In Today's world the demand of the mobile applications market is continually increasing at a very fast rate from last few year. For an example, as of the end of April 2012, there're over sixteen Million applications at mobile application stores like Google play, windows, and apple app store. Many applications store developed/build their own daily applications leader board to track them the most popularity which help to show the chart rankings. This leader board helps applications of their development. Applications leader board is the best way for promoting mobile applications the more you get ranked in leader board, the more you get a number of downloads which leads to earning of million dollars revenue. Such that Developers do some various tricks like advertising to promote their applications in order to keep application ranking higher as much as possible in various leader boards, but this is a traditional method, now days they are doing some kind of frauds that they are forcefully boost their applications and easily manipulate of ranking of their charts on an applications store. This is implemented using virtual human armies to increase the number of downloads like giving fraud ratings and fake reviews is limited time. As an e.g., some articles was published in that article applications was promoted for helping the ranking fraud in the ranking charts because of that article it could crawled from 2000 to the top of twenty-five in Application's Store top baton board that are free and added than 100000 new users can be acquired within the same day. Indeed, such positioning misrepresentation raises awesome worries to some versatile Applications industry. Such instance, Application's Store like Apple cautioned about getting serious about application developers who submit positioning extortion in their Application's store. In this thesis report we are going to study how fraud is to be done in the mobile application market. How developers giving a fake ranking of their applications, giving fake comments and so on. We are implementing applications to track how much time users or developers has given ratings, ranking and comments.

Table 1.1 Mobile Applications Fraud (Examples)

	Technical Fraud	**Compliance Fraud**
Impression Fraud	**Stacking Advertisements** It is a process which developers place various types of banners on top of the other developer's applications.	**View ability** Advertising their applications where it can see sometimes a day.
Click Fraud	**Fraud Clicks** Generating false transactions id through some websites that having no relationship with advertised applications, but when user download that applications revenue is automatically credited into developer's account.	**Miss usage Of Creative Design** Example: Displaying fake promise or displaying different applications than one of the advertisement actually they leads to.

P.G.P. COLLEGE OF ARTS & SCIENCE NAMAKKAL 637 206

Post install Fraud	**Faked Post Backs** Post Back events to fake either an install or post install event.	**Un Disclosed Rebrokering** Rebroking promoting offers starting with one distributer then onto the next makes for an extremely cloudy publicizing biological community, as promotes wind up without knowing where the introduce originates from

II. LITERATURE REVIEW

The Existing system works on past data of historical data it takes reviews, rating and results given by market user. The major disadvantages of the current system can be used for detection of fraud applications based on historical rating and historical reviews and past records. They cannot extract fraud evidences for a particular period of time. We are not able to find fraud applications on based on historical data. There is no existing bookmark which helps to decide which applications is fraud and which one are genuine.

On The main drawback of an existing system is that it works only on historical data. It cannot work on leading sessions (Particular time frame). No bookmark is available in existing systems so we are not able to decide which applications are fake and which one is genuine.

Identify Leading Sessions

Mobile applications ranking fraud happens only in some limited time period (leading sessions). When developers upload applications in the cloud/server after uploading at that time leading session starts, Firstly, we are proposing an algorithm to identify where leading sessions start. Each application based on its previous data. Now we are doing analysis of ranking behaviors of applications, by doing this we can find that fraud applications have different-different raking patterns as compared with other normal applications.

Analyzing some major sessions

There are two major steps to mine the time frames (leading sessions) i.e. to discover the events from the applications generated from the usage of applications over the years and to merge the events that are adjacent of building the sessions together.

Evidences Based on Rankings

In Evidences based on rankings time frame is compared with several time frames. So first of all we have to analyze the same characteristics of time frame (that is called leading sessions) for identifying fraud users who are doing fake rankings. By studying the Apps historic ranking facts, we take a look at that Apps rating behaviors in a leading session is continually fulfill a particular rating sample, which comprises of three diverse positioning stages, to be specific, rising stage, keeping up stage and subsidence stage. In particular, in each driving occasion, an App's positioning first increment to a pinnacle position on the Leaderboard (i.e., rising stage), then keeps such pinnacle position for a period (i.e., looking after stage), lastly diminishes till the end of the occasion (i.e., retreat stage).

Aggregation Evidence

After mining on previous evidences (Rating based, Ranking Based, Review based), next move is to how to join them for identifying ranking fraud detection. Surely, there are many positioning and confirmation accumulation strategies in the writing, However, a number of those techniques, awareness about getting to know an international ranking of all candidates. for example, change based models, models based on score and DSR(Dempster-!Shafer rules). This is not appropriate for recognizing positioning misrepresentation for fresh out of the box new Apps. Some different strategies are constructing absolutely with respect to administered becoming acquainted with methods, which depend upon the sorted tutoring records and are difficult to be misused. We recommend a freely techniques depends on the parallel of fraud to use all these evidences at the same time.

Evidences Based on Ratings

The positioning based confirmations are valuable for positioning extortion identification. But on a daily basis, it isn't sufficient to simplest use evidences based on the ranking given by the developer or user. . Specifically, after an application has been posted, it is able to be routed via any person who use it or download it. Indeed, person or use's review/ratings are one of the most important functions on a play store in the mobile application market. An Application which has better score or ranking in the play store may

COLLEGE OF ARTS & SCIENCE NAMAKKAL 637 206

additionally appeal or attract more customers to download and can also be ranked better inside the Leaderboard. Thus, rating control is likewise a very crucial aspect in ranking fraud which is done by the developers. Naturally, if an Application has positioned misrepresentation in a main session (leading sessions s), the evaluations for the length of the day and age of us can likewise have peculiarity styles contrasted and its memorable scores.

Evidences Based on Reviews

Rather than Ranting and ranking many applications store play store, IOS store and other permit applications, users or application downloads to give their view in textual format (comments). Such assessments can mirror the non-open recognitions and use investigations of present clients for specific mobile applications. Certainly evaluate manipulation is one of the very critical aspect of mobile Applications ranking fraud. But when new applications, user download application from play store by IOS store, they often go through historic reviews, this will help downloaders that applications is useful or not this review also helps applications owners to attract more number of users. Subsequently, con artists consistently submit fake audits inside the leading themes of a particular Application keeping in mind the end goal to rank up the Applications downloads, and as needs to drive the Applications positioning position on the top of the chart. The bother of distinguishing the neighborhood inconsistency of audits inside the main classes and catching them as confirmations for positioning extortion identification are still under-investigated. In this quiet end, right here we endorse or proposed some fraud evidences based on Applications reviews behaviors in main periods for detecting ranking fraud. In this quiet end, right here we endorse or proposed some fraud evidences based on Applications comments or reviews behaviors in main periods(leading time ofs applications) for detecting ranking fraud..

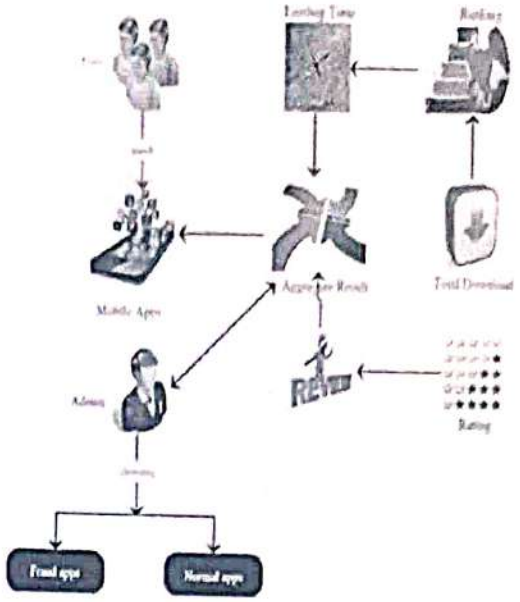


Figure.1 Proposed System Architecture

Figure.1 shows that admin can do data analysis on mobile applications and find whether application is fraud apps or the normal one. When user downloads mobile applications the number of download will increase if number of download is higher the aggregate results appear on mobile application's store. Admin find aggregate results appear based on based on number of reviews; number of ratings, total number of downloads.

III. PROPOSED SYSTEMS

As a proposal we are proposing a system which detects fraud applications for mobile stores. Usually ranking does not appear in the accomplished in time application so we charge to ascertain that time usually when fraud happens. This time frame is also called as leading sessions or high time. Firstly, we propose an algorithm to analyze arch seasons of every application. Then it analysis the behavior of applications based on ranking, rating, and reviews. The proposal is that the user should need permission from admin to access applications. What admin do is that admin gives an access key to a particular device to particular user so it helps from fraud applications.

Advantages of Proposed Systems

- The main advantage of proposed algorithm is that it will show only those applications that are genuine.
- The admin of mobile application market can easily track which applications are getting fake review, ranking, and ratings,

P.G.P. COLLEGE OF ARTS & SCIENCE NAMAKKAL 637 206

- It helps to save lots of money on mobile applications markets like play store and IOS store.
- Giving all rights to admin only. Admin will decide which applications should be on the leader board.

IV. CONCLUSIONS

In this research, we have designed a ranking fraud applications system for mobile applications. Categorically, are detection systems shows that when ranking and rating fraud is happening in a particular time frame so we are providing a methods to mine all the time frame for each and every applications from its previous ranking and rating records. Then, we found evidences based on ranking, evidences based on rating and evidences based on reviews for searching fraud in ranking of mobile applications. Now I am proposing an optimization techniques depends on aggregation algorithm for using all the records for measuring the reliability of a particular time frame (leading sessions), for mobile applications. An different angle of this access is that all the evidences should be designed by statistical antecedent tests, appropriately it is simple to be continued with added evidences from area ability to ascertain baronial fraud applications. In last, we are validating the system which we are proposing with some effective experiments on the real-time applications which we are collecting from the play store. The results which we got in experiments are very effective by using proposed approach.

FUTURE RESEARCH RECOMMENDATIONS

For future work we are planning to study more evidences based on fraud and we will do analysis on the relationship between all the major aspects for promoting mobile applications like ranking, rating, reviews. Additionally we are planning to enhance our fraud detection systems for with added accompanying applications services for eg. We will recommend mobile applications for user's better experience.

REFERENCES

[1] Ge, Yong, Hui Xiong, Chuanren Liu, and Zhi-Hua Zhou. "A taxi driving fraud detection system." In Data Mining (ICDM), 2011 IEEE 11th International Conference on, pp. 181-190. IEEE, 2011.

[2] Gleich, David F., and Lek-heng Lim. "Rank aggregation via nuclear norm minimization." In Proceedings of the 17th ACM SIGKDD international conference on Knowledge discovery and data mining, pp. 60-68. ACM, 2011.

[3] Griffiths, T.L. and Steyvers, M., 2004. Finding scientific topics. Proceedings of the National academy of Sciences, 101(suppl 1), pp.5228-5235.

[4] Mukherjee, Arjun, Abhinav Kumar, Bing Liu, Junhui Wang, Meichun Hsu, Malu Castellanos, and Riddhiman Ghosh. "Spotting opinion spammers using behavioral footprints." In Proceedings of the 19th ACM SIGKDD international conference on Knowledge discovery and data mining, pp. 632-640. ACM, 2013.

[5] Ntoulas, Alexandros, Marc Najork, Mark Manasse, and Dennis Fetterly. "Detecting spam web pages through content analysis." In Proceedings of the 15th international conference on World Wide Web, pp. 83-92. ACM, 2006.

[6] Spirin, Nikita, and Jiawei Han. "Survey on web spam detection: principles and algorithms." ACM SIGKDD Explorations Newsletter 13, no. 2 (2012): 50-64.

[7] Volkovs, Maksims N., and Richard S. Zemel. "A flexible generative model for preference aggregation." In Proceedings of the 21st international conference on World Wide Web, pp. 479-488. ACM, 2012.

[8] Mukherjee, Arjun, Abhinav Kumar, Bing Liu, Junhui Wang, Meichun Hsu, Malu Castellanos, and Riddhiman Ghosh. "Spotting opinion spammers using behavioral footprints." In Proceedings of the 19th ACM SIGKDD international conference on Knowledge discovery and data mining, pp. 632-640. ACM, 2013.

[9] (2012), (Online).Available: https://developer.apple.com/news/index.php?=02062012abc.

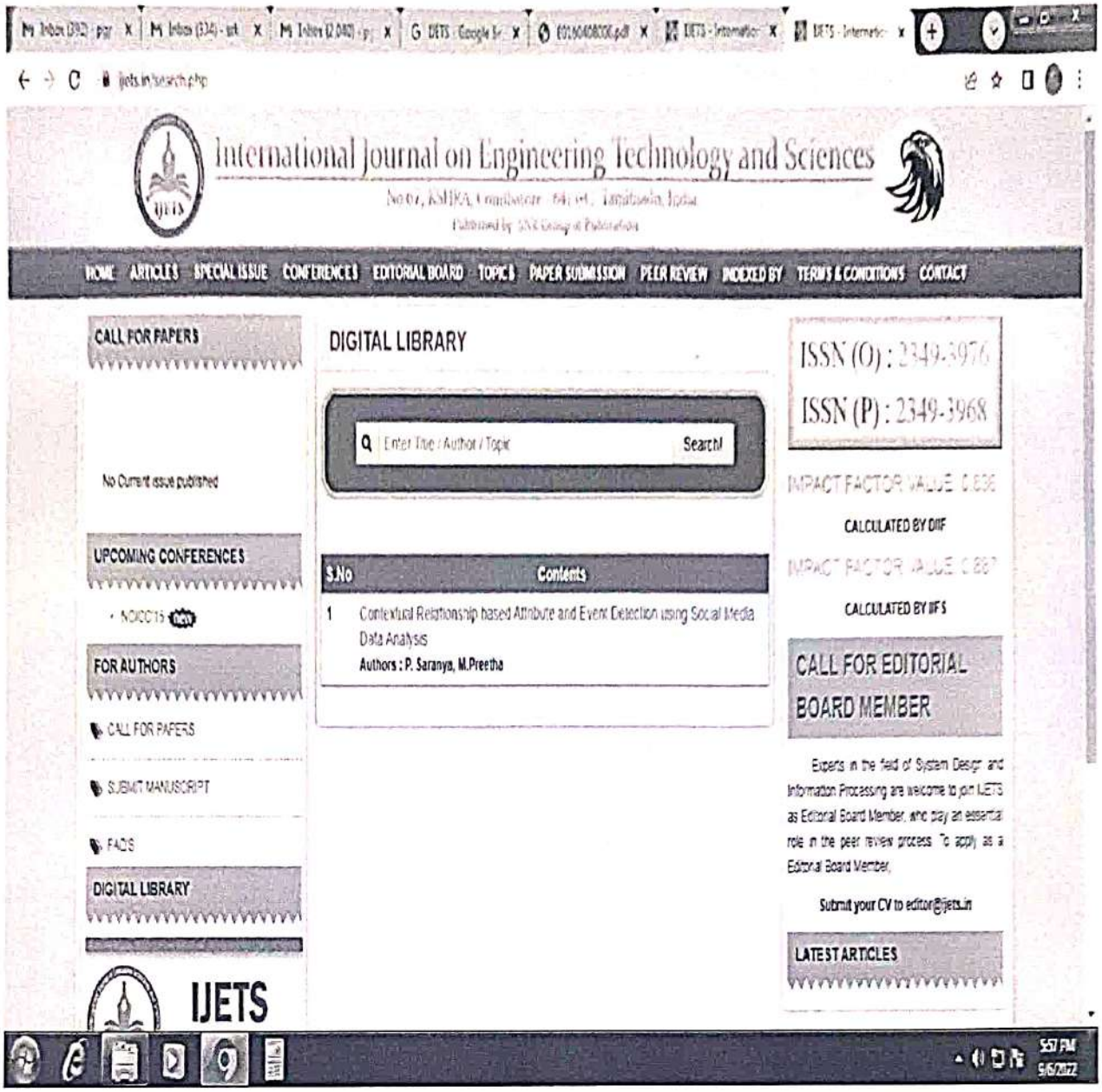
[10] 2012[Online]., Available: http://venturebeat.com/2012/07/03/ apples- crackdown-on-app ranking-manipulation/

[11] 2012 [Online]. index.html Available at: http://www.lextek.com/manuals/ /onix

[12] (2012). [Online]. Available at: http://www.ling.gu.se/lager/ porter-stemmer/mogul

P.G.P. COLLEGE OF ARTS & SCIENCE NAMAKKAL 637 206

PRINCIPAL
PGP College of Arts and Science
Namakkal



P.G.P. COLLEGE OF ARTS & SCIENCE
NAMAKKAL
637 206

International Journal On Engineering Technology and Sciences – IJETS™
ISSN(P): 2349-3968, ISSN (O): 2349-3976
Volume IV, Issue VIII, August - 2017

Contextual Relationship based Attribute and Event Detection using Social Media Data Analysis

Ms. P. Saranya, MPhil Research Scholar,
Mrs. M. Preetha, MCA, MPhil., Assistant Professor,
PGP College of Arts and Science., Namakkal, Tamilnadu, India,

Abstract

The social networks are the medium used to share the views and opinions of the people. The social media interactions are carried out from anywhere and anytime. The location and time information are collected and maintained under the Location Based Social Networks (LBSN). The social media data analytics models are used to discover the user behaviors, product reviews and events. The health, pollution and social unrest events are discovered using the social media data analysis. The spatial and temporal parameters can also used in the social media data analysis.

The social network produces huge volume of data values. The feature learning and event discovery models are processed sequentially. The concurrent learning models are applied in the Multi Task Learning (MTL) framework. The Constrained Multi Task Feature Learning (CMTFL) scheme performs the feature learning and event detection simultaneously on each spatial points. The static features and dynamic features are used in the feature learning and event discovery process. The iterative group hard thresholding model is adapted for the event discovery process.

The feature learning and event discovery process is enhanced with user domain knowledge based data analysis models. The contextual information is employed to indicate the location and time details for the social network users. The Hybrid Multi Task Feature Learning (HMTFL) scheme is build with spatio temporal relationship based feature learning and event discovery process. The spatial relationships are analyzed to group the spatial points with proximity information. The temporal correlations are adapted to discover the events based on the time relationships. The user -venue relationship and venue user relationship based index model is used to improve the accuracy level of the event discovery process.

Index Terms: Social media data analysis, Multi Task Learning, Feature learning and event detection and Spatio temporal mining

1. Introduction

Social networks are phenomena of these days. Increasing number of users and personal character of data leads to the problem with security and unwilling loss of privacy. The advantages of using social networks are in free and fast communication with friends usually in a form of objects such as tweets, pictures, videos and texts Another feature is creation of networks – friends, colleagues, family members. The problem comes with the possibility to trace activities, relations and communication together with limited possibility to manage critical activities such as delete of data. The information managed by different kinds of social networks is very interesting mostly for its potential to form overall personal profile.

Social network analysis (SNA) is the process of investigating social structures through the use of networks and graph theory. It characterizes networked structures in terms of nodes and the ties, edges, or links connect them. Examples of social structures commonly visualized through social network analysis include social media networks, memes spread, friendship and acquaintance networks, collaboration graphs, kinship, disease transmission and sexual relationships. These networks are often visualized through sociograms in which nodes are represented as points and ties are represented as lines. Social network analysis has emerged as a key technique in modern sociology. It has also gained a significant following in anthropology, biology, demography, communication studies, economics, geography, history, information science, organizational studies, political science, social psychology, development studies and sociolinguistics and computer science and is now commonly available as a consumer tool.

Social network analysis is used extensively in a wide range of applications and disciplines. Some common network analysis applications include data aggregation and mining, network propagation modeling, network modeling and sampling, user attribute and behavior analysis, community maintained resource support, location-based interaction analysis, social sharing and filtering, recommender systems development and link prediction and entity resolution. In the private sector, businesses use social network analysis to support activities such as customer interaction and analysis, information system development analysis, marketing and business intelligence needs. Some public sector uses include development of leader engagement strategies, analysis of individual and group engagement and media use and community – based problem solving.

Social network analysis is also used in intelligence, counter-intelligence and law enforcement activities. This technique allows the analysts to map a clandestine or covert organization such as a espionage ring, an organized crime family or a street gang. The National Security Agency (NSA) uses its clandestine mass electronic surveillance programs to generate the data needed to perform this type of analysis on terrorist cells and other networks deemed relevant to national security. The NSA looks up to three nodes deep during this network analysis. After the initial mapping of the social network is complete, analysis is performed to determine the structure of the network and determine. The NSA has been performing social network analysis on call detail records (CDRs), also known as metadata.

Large textual corpora can be turned into networks and then analyzed with the method of social network analysis. In these networks, the nodes are Social Actors and the links are Actions. The ex traction of these networks can be automated, by using parsers. The resulting networks, which can contain thousands of nodes, are then analyzed by using tools from network theory to identify the key actors, the key communities or parties and general properties such as robustness or structural stability of the overall network, or centrality of certain nodes. This automates the approach introduced by Quantitative Narrative Analysis, whereby subject-verb-object triplets are identified with pairs of actors linked by an action, or pairs formed by actor-object.

In computer-supported collaborative learning One of the most current methods of the application of SNA is to the study of computer-supported collaborative learning (CSCL). When applied to CSCL, SNA is used to help understand how learners collaborate in terms of amount, frequency and length, as well as the quality, topic and strategies of communication. Additionally, SNA can focus on specific aspects of the network connection, or the entire network as a whole. It uses graphical representations, written representations and data representations to help ex amine the connections within a CSCL network. When applying SNA to a CSCL environment the interactions of the participants are treated as a social network. The focus of the analysis is on the "connections" made among the participants – how they interact and communicate – as opposed to how each participant behaved on his or her own.

2. Related Work

There are several threads of related work of this paper. Query expansion in microblogs retrieval. Query expansion is a process that reformulates the seed query in order to improve the coverage and accuracy of information retrieval. To improve the performance of retrieval in Twitter, a new thread of work utilizes query expansion to dynamically expand keywords retrieve tweets [11] and discover events [2]. The expanded keywords are typically extracted by exploring their co-occurrence with the user-specified initial query in textual content, but information diffusion through social network has not been comprehensively explored. Event detection in Twitter. There exists a large amount of work on event detection in Twitter. Event detection methods utilize supervised or unsupervised framework to extract tweets subset related to potential events that can be formalized as spatial burstiness [13], [2], temporal burstiness [4], [12], or spatiotemporal burstiness [7], [3]. This thread of work has a different goal from our paper: it detects the emergence instead of the evolution of events, whereas our paper focuses on continuously tracking the evolutionary dynamics of a theme.

P.G.P. COLLEGE OF ARTS & SCIENCE NAMAKKAL 637 206

General theme tracking. A considerable body of work focuses on characterizing the general pattern of Twitter streams. The pattern is typically conceptualized as a mixture of "latent topics". For example, Blei *et al.* aligned the proportion priors and distributions of latent topics over time [10]. Yang *et al.* proposed an efficient Twitter stream summarization approach that can fit in a limited memory [1]. Hong *et al.* analyzed the inter-relationships of multiple social media streams by considering both local topics and shared topics [14]. Mei and Zhai modeled latent topics through a mixture language model, and discovered the transitions among them [5]. Because "latent topics" are typically extracted purely statistically based on data without human prior knowledge, they do not necessarily have real563 world meaning. Hence this thread of work is generally not appropriate to track targeted themes.

Targeted theme tracking. A thread of work focuses on tracking targeted themes, such as earthquakes [15]. The majority of research adopts classification framework to extract themerelated tweets based on contextual features only [6]. Hence, it is challenging to select an appropriate set of features. Li *et al.* proposed a generic framework for themerelated feature selection, whereas this approach is specially designed for scrawling two specific types of Twitter APIs and is not appropriate for the task of this paper [9]. A handful of methods have been proposed to take into account social relationships. Lin *et al.* implemented a probabilistic mixture model to characterize the temporal textual pattern and diffusion via friendship [10]. Ratkiewicz *et al.* applied a framework specifically designed to track the so-called "political astroturf" based on mentioning networks [8].

3. Multitask Learning on Social Networks

Microblogs such as Twitter and Weibo are experiencing an explosive level of growth. Millions of microblog users across the world broadcast their daily observations on an enormous variety of topics, such as crime, sports and politics. The spatial event forecasting from microblogs are focused for events such as civil unrest, disease outbreaks and crime hotspots. The approach searches for subtle patterns in specific cities that serve as indicators of ongoing or future events, where each pattern is a burst of context features relevant to a specific event. For instance, expressions of discontent about gas price increases could be a potential precursor to a protest about government policies.

Three technical challenges must be overcome when addressing this problem: 1) Dynamic features. The language used in microblogs is highly informal, ungrammatical and dynamic. Most existing methods treat fixed keywords as features, but expressions in tweets may dynamically evolve, rendering the use of fixed features and historical training data insufficient. For example, the most significant Twitter keyword for the Mexican protests in Aug 2012 was "#YoSoy132", alluding to the protests against the Mexican presidential election, but "#CNTE" had become the most popular term by the beginning of 2013 due to the growing resistance to Mexican education reform. Ideally, an event forecasting system must combine the judicious use of static features with an awareness of subtle changes involving dynamic features. 2) Geographic heterogeneity. Existing models usually build a single predictive model for all the different locations. Different cities have different characteristics, such as population, weather and administrative structures. As a result, it is difficult to impute basal levels of occurrence uniformly. Considering civil unrest as an example, finding 1000 tweets mentioning the keyword "protest" is not likely to be a strong indicator of an upcoming civil unrest event in a city with a population of a few million users but could be a strong signal in a much smaller city with a population of only 10,000. To consider the geographical heterogeneity, some works adapted to establish the corresponding model for each different location separately. But because each model only utilizes the data of its corresponding location, the data scarcity problem is a serious challenge that degrades the model performance and generalization. 3) Scalability. Spatiotemporal event forecasting in social media streams prefers real-time framework and has emphasis on computation efficiency. The efficiency is challenged by the huge scale of the data, including (1) High dimension features to characterize the rich text and network information; (2) large number of time points; and (3) heterogeneity in enormous geo-locations. This means that even a

P.G.P. ARTS & SCIENCE NAMAKKAL 637 206

medium-scale problem that contains 1000 keywords, 1000 dates and 1000 locations will involve at least 1 billion data points in the optimization computation. Some scalable forecasting methods are desired for this problem.

In order to concurrently address all these technical challenges, this work presents a novel computational approach in the form of a framework of multi task learning (MTL) that combines the strengths of methods that use static features and those that use dynamic features. In individually, for event forecasting, but the system tackles the challenges involved in unifying these contrasting approaches in a single framework. Learning multiple related tasks simultaneously effectively increases the sample size for each location, thus potentially also improving the forecasting performance, especially when the sample size for each task is small. One critical issue in multi-task learning is how to define and exploit the commonality among different tasks. Intuitively, events that occur around the same time may involve similar topics and therefore tweets from different cities may share many common keywords that are related to the event(s). The issues are focused on four multi-task feature learning (MTFL) formulations for event forecasting that differ in the specifics of how common features are extracted. Formulation of a multi-task learning framework for event forecasting. Here, event forecasting for multiple cities/states in the same country are treated as a multitask learning problem. Event forecasting models are build for different cities/states simultaneously by restricting all cities/states to select a common set of features with different weights exclusive to corresponding tasks. The system explores both penalized and constrained MTL formulations, applying 4 different strategies to control the common set of features selected. Concurrent modeling of static and dynamic terms. The existing models (LASSO and DQE) use different but complementary information: LASSO uses static terms, while DQE identifies dynamic terms. The MTL formulations make use of both types of information by integrating the strengths of LASSO into DQE.

Development of efficient algorithms is to both convex and non-convex optimization formulations are explored. For convex problems, the system employs proximal methods, such as FISTA have been shown to be efficient for solving sparse and multi-task learning problems. The iterative Group Hard Thresholding (IGHT) framework is guaranteed to converge to a local solution.

Two different Twitter datasets are used to the evaluation method: the Latin America civil unrest dataset and the United States influenza outbreaks dataset. The methods consistently outperformed the competing methods, namely LASSO, DQE, traditional multitask learning models and their variants. The sensitivity analyses is also performed to reveal the impact of the parameters on the performance methods. Multiple case studies are provided to demonstrate the utility of the method in practical applications.

4. Issues on Multi Task Learning Schemes

The social media data analysis operations are carried out to discover the events. The spatial event forecasting is a complex task in social media data analysis process. The dynamic features and geographic heterogeneity factors suffers the event forecasting operations. The spatial correlations, imbalanced samples and different population in different locations parameters are the spatial heterogeneity measures. The LASSO regression, dynamic query expansion and burst detection methods are applied for the spatial event detection process. The Multi Task Learning Framework (MTLF) is build to solve the dynamic patterns of features and geographic heterogeneity problems. Simultaneous event forecasting for all the locations is carried out under the multi task learning model. The data values for each location are passed and analyzed in the simultaneous learning process. The static features and dynamic features are used in the event forecasting model. The static features are derived from the predefined vocabulary prepared by domain experts. The dynamic features are fetched from the dynamic query expansion process. The iterative group hard thresholding based algorithms are used in the training and prediction operations. The Constrained Multi Task Feature Learning (CMTFL) algorithm is applied for the feature learning operations. The following issuses are identified from the existing system.

P.G.P. COLLEGE OF ARTS & SCIENCE NAMAKKAL 637 001

- Location relationships are not focused
- Human domain knowledge utilization is low
- Stand alone event discovery model
- Temporal relationships are not analyzed in the training process

5. Contextual Relationship based Attribute and Event Detection

The social network data analysis system integrates the location, time and textual data values for the event detection process. The event classification is performed with sub class details. The Multi Task Learning (MTL) scheme is used for the concurrent analysis process. The system is divided into four major modules. They are Social Network Data Analysis, Newsfeeds Analysis, multi task learning process and event discovery process.

Social network data analysis module is used to manage user profile and location details. Newsfeeds analysis is used to extract features from the textual data values. The multi task learning model identifies the features that are used for the event forecasting process. The event discovery module is build to identifies the events in the social media data values.

Social Network Data Analysis

The social network account profiles are extracted for the spatio temporal behavior analysis process. The user account creation and check in points are fetched for the analysis. User profile, check in details and newsfeeds are collected from social networks. Foursquare and Twitter social network data values are used in the system. User check-in venue and time details are maintained in location data values. The latitude and longitude values are used to indicate the geographical location information for the user checkin operations. User submitted messages are maintained under newsfeeds data collection.

Newsfeeds Analysis

User messages are analyzed in newsfeeds analysis. The news feeds are maintained as textual data elements. Feature selection is performed on textual data values. Noisy data are eliminated from the messages. The Term Frequency (TF) and Inverse Document Frequency (IDF) are used in the term level analysis process. The term frequency and inverse document frequency values are used in the term weight estimation process. The term weights are used in the document weight estimation process. The entire tweet weight is utilized in the similarity relationship estimation process. Term level relationships are analyzed in the similarity estimation process.

Multi Task Learning Process

The multi task learning models are used to extract the features that are used for the event forecasting process. The indexing process is called to arrange the user and location relationships. The indexing process is carried out with two levels. They are user-venue relationship based model and Venue – user relationship models. The indexing process arranges all the data items that are submitted by the users. The Constrained Multi Task Feature Learning (CMTFL) model uses the location and news fed relationships for the feature extraction process. The Hybrid Multi Task Feature Learning (HMTFL) scheme combines the spatio temporal correlations with news feed features. The feature learning operations are simultaneously carried out with each location levels. The location and time proximity is used in the HMTFL scheme. All the feature learning results are represented in tree structured data models.

Event Discovery Process

The event discovery process is build to discover the social activities that are reflected in the social media data values. The event discovery operations are carried out for each location context. The event discovery process is carried out with two models. They are constrained event discovery model and hybrid event discovery model. The constrained event discovery model uses the features that are extracted using the Constrained Multi Task Feature Learning (CMTFL) scheme. The CMTFL scheme mainly focuses on the newsfeed relationships. The hybrid event discovery process uses the features that are extracted from the Hybrid Multi Task Feature Learning (HMTFL) scheme. The location and time relationships are combined with the news feeds features. The combination of events is

P.G.P. COLLEGE OF ARTS & SCIENCE NAMAKKAL 637 206

also discovered from the hybrid event discovery process.

6. Conclusion and Future Work

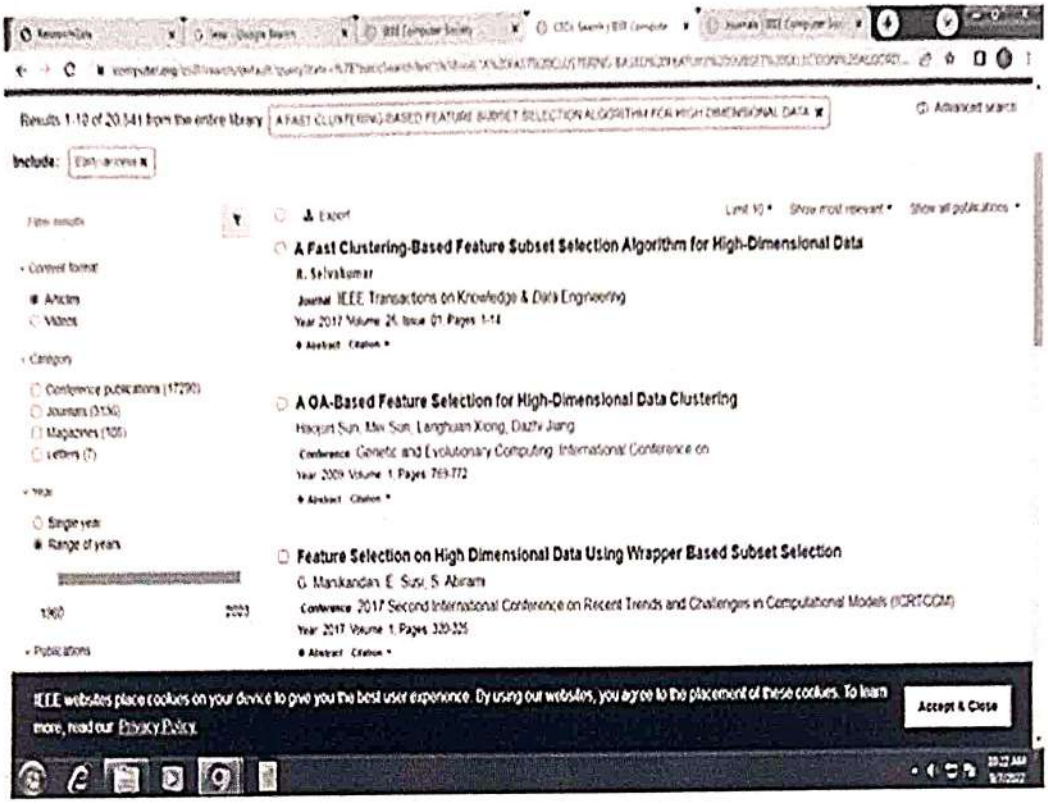
The social networks are the key medium to people to express their views and ideas. The social network data analysis methods are employed to discover the events. The feature learning methods are used for the data analysis and learning operations. The Multi Task Learning (MTL) schemes support simultaneous learning operations. The concurrent learning operations are carried out for each location environment. The Constrained Multi Task Feature Learning (CMTFL) scheme is used to fetch the features that are required for the training process. The Hybrid Multi Task Feature Learning (HMTFL) scheme utilizes the spatio temporal parameters and the social media data values. The location and time relationships are utilized in the hybrid feature learning and event discovery process. The hybrid feature learning and event discovery scheme can be enhanced with privacy preserved learning and event discovery models. The stream based data analysis mechanism can be integrated with the social media data analysis process.

References

1. X. Yang, A. Ghoting, Y. Ruan, and S. Parthasarathy. A framework for summarizing and analyzing Twitter feeds. In KDD, pages 370–378. ACM, 2012.
2. L. Zhao, F. Chen, J. Dai, T. Hua, C.-T. Lu, and N. Ramakrishnan. Unsupervised spatial event detection in targeted domains with applications to civil unrest modeling. PloS one, 9(10):e110206, 2014.
3. L. Zhao, F. Chen, C.-T. Lu, and N. Ramakrishnan. Spatiotemporal event forecasting in social media. In SDM, pages 963– 971. SIAM, 2015.
4. C. C. Aggarwal and K. Subbian. Event detection in social streams. In SDM, volume 12, pages 624–635. SIAM, 2012.
5. Liang Zhao, "Dynamic Theme Tracking in Twitter", IEEE International Conference on Big Data (Big Data) 2015
6. J. Lin, R. Snow, and W. Morgan. Smoothing techniques for adaptive online language models: topic tracking in tweet streams. In KDD, pages 422–429. ACM, 2011.
7. T. Lappas, M. R. Vieira, D. Gunopulos, and V. J. Tsotras. On the spatiotemporal burstiness of terms. VLDB, 5(9):836–847, 2012.
8. J. Ratkiewicz, M. Conover, M. Meiss, B. Gonc¸alves, A. Flammini, and F. Menczer. Detecting and tracking political abuse in social media. In ICWSM, pages 297–304, 2011.
9. R. Li, S. Wang, and K. C.-C. Chang. Towards social data platform: automatic topic-focused monitor for Twitter stream. VLDB, 6(14):1966–1977, 2013.
10. C. X. Lin, Q. Mei, J. Han, Y. Jiang, and M. Danilevsky. The joint inference of topic diffusion and evolution in social communities. In ICDM, pages 378–387. IEEE, 2011.
11. K. Massoudi, M. Tsagkias, M. de Rijke, and W. Weerkamp. Incorporating query expansion and quality indicators in searching microblog posts. In Advances in Information Retrieval, pages 362–367. Springer, 2011.
12. N. Ramakrishnan, P. Butler, S. Muthiah, N. Self, R. Khandpur, P. Saraf, W. Wang, J. Cadena, A. Vullikanti, G. Korkmaz, et al. 'beating the news' with embers: forecasting civil unrest using open source indicators. In Proceedings of the 20th ACM SIGKDD international conference on Knowledge discovery and data mining, pages 1799–1808. ACM, 2014.
13. L. Zhao, Q. Sun, J. Ye, F. Chen, C.-T. Lu, and N. Ramakrishnan. Multi-task learning for spatio-temporal even In KDD, pages 1503–1512. ACM, 2015.
14. L. Hong, B. Dom, S. Gurumurthy, and K. Tsioutsiouliklis. A time-dependent topic model for multiple text streams. In KDD, pages 832–840. ACM, 2011.
15. Ben Verhoeven, Walter Daelemans and Barbara Plank. Twisty: A multilingual twitter stylometry corpus for gender and personality profiling. In Proceedings of the Tenth International Conference on Language Resources and Evaluation LREC, pages 1632–1637, 2016.

P.G.P. COLLEGE OF ARTS & SCIENCE NAMAKKAL 637 206

PRINCIPAL
PGP College of Arts and Science
Namakkal



P.G.P. COLLEGE OF ARTS & SCIENCE
NAMAKKAL
637 206

IEEE TRANSACTIONS ON KNOWLEDGE AND DATA ENGINEERING VOL:25 NO:1 YEAR 2017

A Fast Clustering-Based Feature Subset Selection Algorithm for High Dimensional Data

Mr.R.Selvakumar,Assistant Professor,Department of Computer Science & Applications,

PGP College of Arts & Science,Namakkal,Tamilnadu,India

Qinbao Song, Jingjie Ni and Guangtao Wang

Abstract–Feature selection involves identifying a subset of the most useful features that produces compatible results as the original entire set of features. A feature selection algorithm may be evaluated from both the efficiency and effectiveness points of view. While the efficiency concerns the time required to find a subset of features, the effectiveness is related to the quality of the subset of features. Based on these criteria, a fast clustering-based feature selection algorithm, FAST, is proposed and experimentally evaluated in this paper. The FAST algorithm works in two steps. In the first step, features are divided into clusters by using graph-theoretic clustering methods. In the second step, the most representative feature that is strongly related to target classes is selected from each cluster to form a subset of features. Features in different clusters are relatively independent, the clustering-based strategy of FAST has a high probability of producing a subset of useful and independent features. To ensure the efficiency of FAST, we adopt the efficient minimum-spanning tree clustering method. The efficiency and effectiveness of the FAST algorithm are evaluated through an empirical study. Extensive experiments are carried out to compare FAST and several representative feature selection algorithms, namely, FCBF, ReliefF, CFS, Consist, and FOCUS-SF, with respect to four types of well-known classifiers, namely, the probability-based Naive Bayes, the tree-based C4.5, the instance-based IB1, and the rule-based RIPPER before and after feature selection. The results, on 35 publicly available real-world high dimensional image, microarray, and text data, demonstrate that FAST not only produces smaller subsets of features but also improves the performances of the four types of classifiers.

Index Terms–Feature subset selection, filter method, feature clustering, graph-based clustering

P.G.P. COLLEGE OF ARTS & SCIENCE
NAMAKKAL
637 206

1 Introduction

With the aim of choosing a subset of good features with respect to the target concepts, feature subset selection is an effective way for reducing dimensionality, removing irrelevant data, increasing learning accuracy, and improving result comprehensibility [43], [46]. Many feature subset selection methods have been proposed and studied for machine learning applications. They can be divided into four broad categories: the Embedded, Wrapper, Filter, and Hybrid approaches.

The embedded methods incorporate feature selection as a part of the training process and are usually specific to given learning algorithms, and therefore may be more efficient than the other three categories[28]. Traditional machine learning algorithms like decision trees or artificial neural networks are examples of embedded approaches[44]. The wrapper methods use the predictive accuracy of a predetermined learning algorithm to determine the goodness of the selected subsets, the accuracy of the learning algorithms is usually high. However, the generality of the selected features is limited and the computational complexity is large. The filter methods are independent of learning algorithms, with good generality. Their computational complexity is low, but the accuracy of the learning algorithms is not guaranteed [13], [63], [39]. The hybrid methods are a combination of filter and wrapper methods [49], [15], [66], [63], [67] by using a filter method to reduce search space that will be considered by the subsequent wrapper. They mainly focus on combining filter and wrapper methods to achieve the best possible performance with a particular learning algorithm with similar time com- plexity of the filter methods. The wrapper methods are computationally expensive and tend to overfit on small training sets [13], [15]. The filter methods, in addition to their generality, are usually a good choice when the number of features is very large. Thus, we will focus on the filter method in this paper.

With respect to the filter feature selection methods, the application of cluster analysis has been demonstrated to be more effective than traditional feature selection algo- rithms. Pereira et al. [52], Baker et al. [4], and Dhillon et al. [18] employed the distributional clustering of words to reduce the dimensionality of text data.

In cluster analysis, graph-theoretic methods have been well studied and used in many applications. Their results have, sometimes, the best agreement with human performance [32]. The general graph-theoretic clustering is simple: Compute a neighborhood graph of instances, then delete any edge in the graph that is much longer/shorter (according to some criterion) than its neighbors. The result is a forest and each tree in the forest represents a cluster. In our study, we apply graph-theoretic clustering methods to features. In particular, we adopt the minimum spanning tree (MST) based clustering algorithms, because they do not assume that data points are grouped around centers or separated by a regular geometric curve and have been widely used in practice.

Based on the MST method, we propose a Fast clustering-bAsed feature Selection algoriThm (FAST).The FAST algorithm works in two steps. In the first step, fea- tures are divided into clusters by using graph-theoretic clustering methods. In the second step, the most repre- sentative feature that is strongly related to target classesis selected from each cluster to form the final subset of features. Features in different clusters are relatively independent, the clustering-based strategy of FAST has a high probability of producing a subset of useful and independent features. The proposed feature subset se- lection algorithm FAST was tested upon 35 publicly available image, microarray, and text data sets. The experimental results show that, compared with other five different types of feature subset selection algorithms, the proposed algorithm not only reduces the number of features, but also improves the performances of the four well-known different types of classifiers.

The rest of the article is organized as follows: In Section 2, we describe the related works. In Section 3, we present the new feature subset selection algorithm FAST. In Section 4, we report extensive experimental results to support the proposed FAST algorithm. Finally, in Section 5, we summarize the present study and draw some conclusions.

2 Related work

Feature subset selection can be viewed as the process of identifying and removing as many irrelevant and redundant features as possible. This is because: (i) irrelevant features do not contribute to the predictive accuracy [33], and (ii) redundant features do not redound to getting a better predictor for that they provide mostly information which is already present in other feature(s).

Of the many feature subset selection algorithms, some can effectively eliminate irrelevant features but fail to handle redundant features [23], [31], [37], [34], [45], [59], yet some of others can eliminate the irrelevant while taking care of the redundant features [5], [29], [42],[68]. Our proposed FAST algorithm falls into the secondgroup.

Traditionally, feature subset selection research has focused on searching for relevant features. A well known example is Relief [34], which weighs each feature according to its ability to discriminate instances under different targets based on distance-based criteria function. However, Relief is ineffective at removing redundant features as two predictive but highly correlated features are likely both to be highly weighted [36]. Relief-F [37] extends Relief, enabling this method to work with noisy and incomplete data sets and to deal with multi-class problems,

- Q. Song, J. Ni and G. Wang are with the Dept. of Computer Science and Technology, Xi'an Jiaotong University, Xi'an, 710049 China. E-mail: qbsong@mail.xjtu.edu.cn, ni.jingjie@stu.xjtu.edu.cn, gt.wang@stu.xjtu.edu.cn.

Manuscript received XX XXX. XXXX; revised XX XXX. XXXX; accepted XX XXX. XXXX; published online XX XXX. XXXX. Recommended for acceptance by X. XXXX. For information on obtaining reprints of this article, please send e-mail to: tkde@computer.org, and reference IEEECS Log Number TKDESI-XXXX-XX-XXXX. Digital Object Identifier no. XX.XXXX/TKDE.XXXX.XX.

NAMAKKAL 637 206

but still cannot identify redundant features.

However, along with irrelevant features, redundant features also affect the speed and accuracy of learning algorithms, and thus should be eliminated as well [36], [35], [31]. CFS [29], FCBF [68] and CMIM [22] are examples that take into consideration the redundant features. CFS [29] is achieved by the hypothesis that a good feature subset is one that contains features highly correlated with the target, yet uncorrelated with each other. FCBF ([68], [71]) is a fast filter method which can identify relevant features as well as redundancy among relevant features without pairwise correlation analysis. CMIM [22] iteratively picks features which maximize their mutual information with the class to predict, con- ditionally to the response of any feature already picked. Different from these algorithms, our proposed FAST algorithm employs clustering based method to choose features.

Recently, hierarchical clustering has been adopted in word selection in the context of text classification (e.g., [52], [4], and [18]). Distributional clustering has been used to cluster words into groups based either on their participation in particular grammatical relations with other words by Pereira et al. [52] or on the distribution of class labels associated with each word by Baker and McCallum [4]. As distributional clustering of words are agglomerative in nature, and result in sub-optimal word clusters and high computational cost, Dhillon et al. [18] proposed a new information-theoretic divisive algorithm for word clustering and applied it to text classification. Butterworth et al. [8] proposed to cluster features using a special metric of Barthelemy-Montjardet distance, and then makes use of the dendrogram of the resultingcluster hierarchy to choose the most relevant attributes. Unfortunately, the cluster evaluation measure based on Barthelemy-Montjardet distance does not identify a fea- ture subset that allows the classifiers to improve their original performance accuracy. Further more, even com- pared with other feature selection methods, the obtained accuracy is lower.

Hierarchical clustering also has been used to select features on spectral data. Van Dijk and Van Hullefor [64] proposed a hybrid filter/wrapper feature subset selec- tion algorithm for regression. Krier et al. [38] presented a methodology combining hierarchical constrained clus- tering of spectral variables and selection of clusters by mutual information. Their feature clustering method is similar to that of Van Dijk and Van Hullefor [64] except that the former forces every cluster to contain consecutive features only. Both methods employed ag- glomerative hierarchical clustering to remove redundantfeatures.

Quite different from these hierarchical clustering based algorithms, our proposed FAST algorithm uses minimum spanning tree based method to cluster fea- tures. Meanwhile, it does not assume that data points are grouped around centers or separated by a regular geometric curve. Moreover, our proposed FAST does not limit to some specific types of data.

3 Feature Subset Selection Algorithm

Framework and definitions

Irrelevant features, along with redundant features, severely affect the accuracy of the learning machines [31], [35]. Thus, feature subset selection should be able to identify and remove as much of the irrelevant and redundant information as possible. Moreover, *"good feature subsets contain features highly correlated with (predictive of) the class, yet uncorrelated with (not predictive of) each other."* [30]

relevant to the target concept; (ii) when $\square' \subsetneq \square_{\square}$, from the definition we may obtain that $\square(\square\ \square_{\square}, \square_{\square}) = \square(\square\ \square_{\square})$. It seems that $\square_{\square}$ is irrelevant to the target concept. However, the definition shows that feature $\square_{\square}$ is relevant when using $\square'$ $\square_{\square}$ to describe the target concept. The

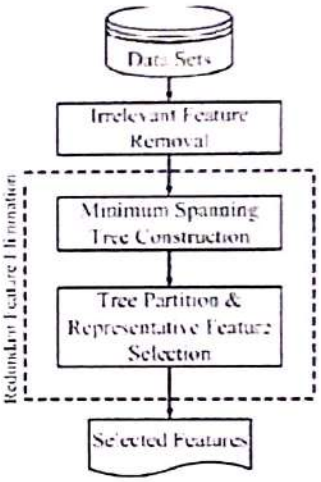


Fig. 1: Framework of the proposed feature subset selection algorithm

P.G.P. COLLEGE OF ARTS & SCIENCE NAMAKKAL 637 206

Keeping these in mind, we develop a novel algorithm which can efficiently and effectively deal with both irrelevant and redundant features, and obtain a good feature subset. We achieve this through a new feature selection framework (shown in Fig.1) which composed of the two connected components of *irrelevant feature removal* and *redundant feature elimination*. The former obtains features relevant to the target concept by eliminating irrelevant ones, and the latter removes redundant features from relevant ones via choosing representatives from different feature clusters, and thus produces the final subset.

The *irrelevant feature removal* is straightforward once the right relevance measure is defined or selected, while the *redundant feature elimination* is a bit of sophisticated. In our proposed FAST algorithm, it involves (i) the construction of the minimum spanning tree (MST) from a weighted complete graph; (ii) the partitioning of the MST into a forest with each tree representing a cluster; and (iii) the selection of representative features from the clusters.

In order to more precisely introduce the algorithm, and because our proposed feature subset selection framework involves irrelevant feature removal and redundant feature elimination, we firstly present the traditional definitions of relevant and redundant features, then provide our definitions based on variable correlation as follows.

John et al. [33] presented a definition of relevant $\square_{\square}$ is redundant with $\square_{\square}$ $\square$. In this case, we say $\square_{\square}$ is indirectly relevant to the target concept.

Most of the information contained in redundant features is already present in other features. As a result, redundant features do not contribute to getting better interpreting ability to the target concept. It is formally features. Suppose $\square$ to be the full set of features, $\square_{\square} \in \square$ be a feature, $\square_{\square} = \square - \{\square_{\square}\}$ and $\square_{\square} \subseteq \square_{\square}$. Let $\square_{\square}$ be a value-assignment of all features in $\square_{\square}$, $\square_{\square}$ a value-assignment of feature $\square_{\square}$, and $\square$ a value-assignment of the target concept $\square$. The definition can be formalized as follows.

Definition 1: (Relevant feature) $\square_{\square}$ is relevant to the target concept $\square$ if and only if there exists some $\square_{\square}$, $\square_{\square}$ and $\square$, such that, for probability $\square(\square_{\square} = \square_{\square}, \square_{\square} = \square_{\square}) > 0$,

$$\square(\square = \square \mid \square_{\square} = \square_{\square}, \square_{\square} = \square_{\square}) \neq \square(\square = \square \mid \square_{\square} = \square_{\square}).$$

Otherwise, feature $\square_{\square}$ is an *irrelevant feature.*

Definition 1 indicates that there are two kinds of relevant features due to different $\square_{\square}$: (i) when $\square_{\square} = \square_{\square}$, from the definition we can know that $\square_{\square}$ is directly reason behind is that either $\square_{\square}$ is interactive with $\square'$ or $\square \cup \{\square\}$

defined by Yu and Liu [70] based on Markov blanket [36]. The definitions of Markov blanket and redundant feature are introduced as follows, respectively.

Definition 2: (Markov blanket) Given a feature $\square \in \square$ let $\square_{\square} \subseteq (\square - \{\square_{\square}, \square_{\square}\})$, $\square_{\square}$ is said to be a Markov blanket for $\square_{\square}$ if and only if

$$\square(\square - \square_{\square} - \{\square_{\square}\}, \square \mid \square_{\square}, \square_{\square}) = \square(\square - \square_{\square} - \{\square_{\square}\}, \square \mid \square_{\square}).$$

Definition 3: (Redundant feature) Let $\square$ be a set of features, a feature in $\square$ is redundant if and only if it has a Markov Blanket within $\square$.

Relevant features have strong correlation with target concept so are always necessary for a best subset, while redundant features are not because their values are completely correlated with each other. Thus, notions of feature redundancy and feature relevance are normally in terms of feature correlation and feature-target concept correlation.

Mutual information measures how much the distribution of the feature values and target classes differ from statistical independence. This is a nonlinear estimation of correlation between feature values or feature values and target classes. The *symmetric uncertainty* ($\square\square$) [53] is derived from the mutual information by normalizing it to the entropies of feature values or feature values and target classes, and has been used to evaluate the goodness of features for classification by a number of researchers (e.g., Hall [29], Hall and Smith [30], Yu and Liu [68], [71], Zhao and Liu [72], [73]). Therefore, we choose symmetric uncertainty as the measure of correlation between either two features or a feature and the target concept.

The *symmetric uncertainty* is defined as follows

$$\square(\square, \square) = \frac{2 \times \square\square\square\square(\square \mid \square)}{\square(\square) + \square(\square)}. \quad (1)$$

Where, $\square(\square)$ is the entropy of a discrete random variable $\square$. Suppose $(\square)$ is the prior probabilities for all values of $\square$, $\square(\square)$ is defined by

1) $$\square(\square) = -\sum \square(\square) \log_2 \square(\square). \quad (2)$$

2) *Gain*$(\square \mid \square)$ is the amount by which the entropy of $\square$ decreases. It reflects the additional information about $\square$ provided by $\square$ and is called the information gain [55] which is given by

$$\begin{aligned} \square\square\square\square(\square \mid \square) &= \square(\square) - \square(\square \mid \square) \\ &= \square(\square) - \square(\square \mid \square). \end{aligned} \quad (3)$$

P.G. COLLEGE OF ARTS & SCIENCE
NAMAKKAL
637 206

Where (□ 卬) is the conditional entropy which quantifies the remaining entropy (i.e. uncertainty) of a random variable □ given that the value of another random variable □ is known. Suppose (□) is the prior probabilities for all values of □ and □(□|□) is the posterior probabilities of □ given the values of □, □(□|□) is defined by

$$(\square|\square) = -\sum_{\square\in\square} \square(\square) \sum_{\square\in\square} \square(\square|\square)\log_2 \square(\square|\square). \quad (4)$$

Information gain is a symmetrical measure. That is the amount of information gained about □ after observing □ is equal to the amount of information gained about □ after observing □. This ensures that the order of two variables (e.g.,(□, □) or (□, □)) will not affect the value of the measure.

Symmetric uncertainty treats a pair of variables symmetrically, it compensates for information gain's bias toward variables with more values and normalizes its value to the range [0,1]. A value 1 of □(□, □) indicates that knowledge of the value of either one completely predicts the value of the other and the value 0 reveals that □ and □ are independent. Although the entropy-based measure handles nominal or discrete variables, they can deal with continuous features as well, if the values are discretized properly in advance [20].

Given □□(□, □) the symmetric uncertainty of variables □ and □, the relevance *T-Relevance* between a feature and the target concept □, the correlation *F-Correlation* between a pair of features, the feature redundance *F-Redundancy* and the representative feature*R-Feature* of a feature cluster can be defined as follows.

Deflnition 4: (T-Relevance) The relevance between the feature □□∈ □ and the target concept □ is referred to as the *T-Relevance* of □□ and □, and denoted by □□(□□, □).

If □(□□, □) is greater than a predetermined threshold □, we say that □□ is a strong *T-Relevance* feature.

Deflnition 5: (F-Correlation) The correlation between any pair of features □□ and □□ (□□, □□ ∈ □ ∧ □ □) is called the *F-Correlation* of □□ and □□, and denoted by □□(□□, □□).

Deflnition 6: (F-Redundancy) Let = {□1, □2, ..., □□, ..., □□<|□|} be a cluster of features. if ∃□□ ∈ □, □□(□□, □) ≥ □□(□□, □) ∧ □□(□□, □□) > □□(□□, □) is always corrected for each □□ ∈ □ (□ □), then □□ are redundant features with respect to the given □□ (i.e. each □□ is a *F-Redundancy*).

Deflnition 7: (R-Feature) A feature □□ ∈ □ = {□1, □2, ..., □□} (□ < |□|) is a representative feature of the cluster □ (i.e. □□ is a *R-Feature*) if and only if,

$$\square_\square = \text{argmax}_{\square_\square\in\square}\, \square(\square_\square, \square).$$

This means the feature, which has the strongest *T-Relevance*, can act as a *R-Feature* for all the features in the cluster.

According to the above definitions, feature subset selection can be the process that identifies and retains the strong *T-Relevance* features and selects *R-Features* from feature clusters. The behind heuristics are that

1) irrelevant features have no/weak correlation with target concept;
2) redundant features are assembled in a cluster and a representative feature can be taken out of the cluster.

Algorithm and analysis

The proposed FAST algorithm logically consists of tree steps: (i) removing irrelevant features, (ii) constructing a MST from relative ones, and (iii) partitioning the MST and selecting representative features.

For a data set □ with □ features □ = {□1, □2, ..., □□ } and class □, we compute the *T-Relevance* □□(□□, □) value for each feature □□ (1 ≤ □ ≤ □) in the first step. The features whose □□(□□, □) values are greater than a predefined threshold □ comprise the target-relevant feature subset □′ = {□1′, □2′, ..., □□′ } (□ ≤ □).

In the second step, we first calculate the *F-Correlation* □□(□□′, □□′) value for each pair of features □□′ and □□′ (□□′, □□′ ∈ □′ ∧ □ □). Then, viewing features □□′ and □□′ as vertices and □□(□□′, □□′) (□ □) as the weight of the edge between vertices □□′ and □□′, a weighted complete graph □ = (□, □) is constructed where □ = {□□′ | □□′ ∈ □′ ∧ □ ∈ [1, □]} and □ = {(□□′, □□′) | (□□′, □□′ ∈ □′ ∧ □, □ ∈ [1, □]∧ □ □} . As symmetric uncertainty is symmetric further the *F-Correlation* □(□□′, □□′) is symmetric as well, thus □ is an undirected graph.

The complete graph □ reflects the correlations among all the target-relevant features. Unfortunately, graph has □ vertices and □(□_ 1)/2 edges. For high dimensional data, it is heavily dense and the edges with different weights are strongly interweaved. Moreover, the decomposition of complete graph is NP-hard [26]. Thus for graph □, we build a MST, which connects all vertices such that the sum of the weights of the edges is the minimum, using the well-known Prim algorithm [54]. The weight of edge (□□′, □□′) is *F-Correlation* □□(□□′, □□′).

After building the MST, in the third step, we first remove the edges □ = {(□□′, □□′) | (□□′, □□′ ∈ □′ ∧ □, □ ∈ [1, □]^ /□ =} , whose weights are smaller than both of the *T-Relevance* □□(□□′, □) and □□(□□′, □), from the MST. Each deletion results in two disconnected trees □1 and □2.

Assuming the set of vertices in any one of the final trees to be □ ( ), we have the property that for each pair of vertices (□□′, □□′ ∈ □ (□)), □□(□□′, □□′) ≥ □□(□□′, □) ∨ □(□□′, □□′) ≥ □□(□□′, □) always holds. From Definition 6 we know that this property guarantees the features in □ ( ) are redundant.

This can be illustrated by an example. Suppose the MST shown in Fig.2 is generated from a complete graph □. In order to cluster the features, we first traverse all the six edges, and then decide to remove the edge (□0, □4) because its weight □(□0, □4) = 0.3 is smaller than both □(□0, □) = 0.5 and □□(□4, □) = 0.7. This makes the MST is clustered into two clusters denoted as □ (□1) and □ (□2). Each cluster is a MST as well. Take (□1) as an example. From Fig.2 we know that □□(□0, □1) >

P.G. COLLEGE OF ARTS & SCIENCE NAMAKKAL 637 105

□(□1, □), □□(□1, □2) > □□(□1, □) ∧ □□(□1, □2) > □(□2, □), □□(□1, □3) > □□(□1, □) ∧ □□(□1, □3) > □(□3, □). We also observed that there is no edge exists between □0 and □2, □0 and □3, and □2 and □3. Considering that □1 is a MST, so the □□(□0, □2) is greater than □(□0, □1) and □□(□1, □2), □□(□0, □3) is greater than □□(□0, □1) and □□(□1, □3), and □□(□2, □3) is greater than □□(□1, □2) and □□(□2, □3). Thus, □(□0, □2) > □(□0, □) ∧ □□(□0, □2) > □□(□2, □), □□(□0, □3) > □(□0, □) ∧ □□(□0, □3) > □□(□3, □), and □□(□2, □3) > □(□2, □) ∧□□(□2, □3) > □□(□3, □) also hold. As the mutual information between any pair (□□, □□)(□, □ = 0, 1, 2, 3 ∧ □ □) of □0, □1, □2, and □3 is greater than the mutual information between class □ and □□ or □□, features □0, □1, □2, and □3 are redundant.

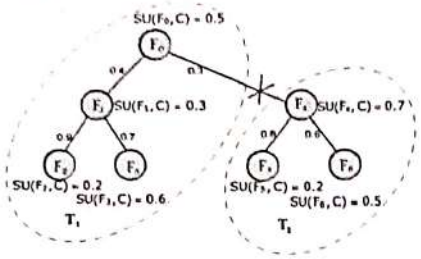


Fig. 2: Example of the clustering step

After removing all the unnecessary edges, a forest *Forest* is obtained. Each tree □□∈*Forest* represents a cluster that is denoted as □(□□), which is the vertex set of □□ as well. As illustrated above, the features in each cluster are redundant, so for each cluster □(□□) we choose a representative feature □□□ whose *T-Relevance* □□(□□□, □) is the greatest. All □□□ (□ = 1...|*Forest*|) comprise the final feature subset ∪□□□.

The details of the FAST algorithm is shown in Algorithm 1.

Algorithm 1: FAST

```
inputs: D(□1, □2, ..., □□, □) - the given data set
        □ - the T-Relevance threshold.
output: S - selected feature subset .
//==== Part 1 : Irrelevant Feature Removal ====
for i = 1 to m do
    T-Relevance = SU (□□□, □)
    if T-Relevance > □ then
        S = S ∪ {□□};
//==== Part 2 : Minimum Spanning Tree Construction ====
G = NULL; //G is a complete graph
for each pair of features {□□′, □□′} ⊂ S do
    F-Correlation = SU (□□′, □□′)
    □□□ □□′ □□□/□□ □□′ □□ □ □□□□ F-Correlation □□ □□□ □□□□□□ □□
    □□□ □□□□□□□□□□□□ □□□□;
minSpanTree = Prim (G); //Using Prim Algorithm to generate the
    minimum spanning tree
//==== Part 3 : Tree Partition and Representative Feature Selection ====
Forest = minSpanTree
for each edge □□□ ∈ Forest do
    if SU(□□′, □□′) < SU(□□′, □) ∧ SU(□□′, □□′) < SU(□□′, □) then
        Forest = Forest − □□□
S = □
for each tree □□ ∈ Forest do
    □□□ = argmax□□′∈□□ SU(□□′, □)
    S = S ∪ {□□};
return S
```

Time complexity analysis. The major amount of work for Algorithm 1 involves the computation of □□ values for *T-Relevance* and *F-Correlation*, which has linear complexity in terms of the number of instances in a given data set. The first part of the algorithm has a linear time complexity (□) in terms of the number of features □. Assuming (1 ≤ □ ≤ □) features are selected as relevant ones in the first part, when □ = 1, only one feature is selected. Thus, there is no need to continue the rest parts of the algorithm, and the complexity is (□). When 1 < □≤□, the second part of the algorithm firstly constructs a complete graph from relevant features and the complexity is □(□²), and then generates a MST from the graph using Prim algorithm whose time complexity is □(□²). The third part partitions the MST and chooses the representative features with the complexity of □(□). Thus when 1 < □ ≤ □, the complexity of the algorithm is (□+□²). This means when □ ≤ √□, FAST has linear complexity □(□), while obtains the worst complexity (□²) when □ = □. However, □ is heuristically set to be ⌊√□ ∗ lg □⌋ in the implementation of FAST. So the complexity is □(□ ∗ lg² □), which is typically less than □(□²) since □□²□ < □. This can be explained as follows. Let □(□) = □ − lg² □, so the derivative □′(□) = 1 − 2 lg □/□, which is greater than zero when □ > 1. So □ (□) is a increasing function and it is greater than □(1) which is equal to 1, i.e., □ > lg² □, when □ > 1. This means the bigger the □ is, the farther the time complexity of FAST deviates from (□²). Thus, on high dimensional data, the time complexity of FAST is far more less than (□²). This makes FAST has a better runtime performance with high dimensional data as shown in Subsection 4.4.2.

4 Empirical Study

Data source

For the purposes of evaluating the performance and effectiveness of our proposed FAST algorithm, verifying whether or not the method is potentially useful in practice, and allowing other researchers to confirm our results, 35 publicly available data sets[1] were used.

The numbers of features of the 35 data sets vary from 37 to 49152 with a mean of 7874. The dimensionality of the 54.3% data sets exceed 5000, of which 28.6% data sets have more than 10000 features.

The 35 data sets cover a range of application domains such as text, image and bio microarray data classification. Table 1[2] shows the corresponding statistical information.

Note that for the data sets with continuous-valued features, the well-known off-the-shelf MDL method [74] was used to discretize the continuous values.

Experiment setup

To evaluate the performance of our proposed FAST algorithm and compare it with other feature selection

1. The data sets can be downloaded at: http://archive.ics.uci.edu/ml/, http://tunedit.org/repo/Data/Text-wc, http://featureselection.asu.edu/datasets.php, http://www.lsi.us.es/aguilar/datasets.html

2. F, I, and T denote the number of features, the number of instances, and the number of classes, respectively

P.G.P. COLLEGE OF ARTS & SCIENCE NAMAKKAL 637 206

algorithms in a fair and reasonable way, we set up our experimental study as follows.

1) The proposed algorithm is compared with five different types of representative feature selection algorithms. They are (i) FCBF [68], [71], (ii) ReliefF [57], (iii) CFS [29], (iv) Consist [14], and (v) FOCUS-SF [2], respectively.
   FCBF and ReliefF evaluate features individually. For FCBF, in the experiments, we set the relevance threshold to be the □□ value of the □/log□ ranked feature for each data set (□ is the number of features in a given data set) as suggested by Yu and Liu [68], [71]. ReliefF searches for nearest neighbors of instances of different classes and weights features according to how well they differentiate instances of different classes.
   The other three feature selection algorithms are based on subset evaluation. CFS exploits best-first search based on the evaluation of a subset that contains features highly correlated with the target concept, yet uncorrelated with each other. The Consist method searches for the minimal subset that separates classes as consistently as the full set can under best-first search strategy. FOCUS-SF is a variation of FOCUS [2]. FOCUS has the same evaluation strategy as Consist, but it examines all subsets of features. Considering the time efficiency, FOUCS-SF replaces exhaustive search in FOCUS with sequential forward selection.
   For our proposed FAST algorithm, we heuristically set □ to be the □□ value of the □ ranked feature for each data set.

TABLE 1: Summary of the 35 benchmark data sets

Data ID	Data Name	F	I	T	Domain
1	chess	37	3196	2	Text
2	mfeat-fourier	77	2000	10	Image,Face
3	coil2000	86	9822	2	Text
4	elephant	232	1391	2	Microarray,Bio
5	arrhythmia	280	452	16	Microarray,Bio
6	fqs-nowe	320	265	2	Image,Face
7	colon	2001	62	2	Microarray,Bio
8	fbis.wc	2001	2463	17	Text
9	AR10P	2401	130	10	Image,Face
10	PIE10P	2421	210	10	Image,Face
11	oh0.wc	3183	1003	10	Text
12	oh10.wc	3239	1050	10	Text
13	B-cell1	4027	45	2	Microarray,Bio
14	B-cell2	4027	96	11	Microarray,Bio
15	B-cell3	4027	96	9	Microarray,Bio
16	base-hock	4863	1993	2	Text
17	TOX-171	5749	171	4	Microarray,Bio
18	tr12.wc	5805	313	8	Text
19	tr23.wc	5833	204	6	Text
20	tr11.wc	6430	414	9	Text
21	embryonal-tumours	7130	60	2	Microarray,Bio
22	leukemia1	7130	34	2	Microarray,Bio
23	leukemia2	7130	38	2	Microarray,Bio
24	tr21.wc	7903	336	6	Text
25	wap.wc	8461	1560	20	Text
26	PIX10P	10001	100	10	Image,Face
27	ORL10P	10305	100	10	Image,Face
28	CLL-SUB-111	11341	111	3	Microarray,Bio
29	ohscal.wc	11466	11162	10	Text
30	la2s.wc	12433	3075	6	Text
31	la1s.wc	13196	3204	6	Text
32	GCM	16064	144	14	Microarray,Bio
33	SMK-CAN-187	19994	187	2	Microarray,Bio
34	new3s.wc	26833	9558	44	Text
35	GLA-BRA-180	49152	180	4	Microarray,Bio



2) Four different types of classification algorithms are employed to classify data sets before and after feature selection. They are (i) the probability-based Naive Bayes (NB), (ii) the tree-based C4.5, (iii) the instance-based lazy learning algorithm IB1, and (iv) the rule-based RIPPER, respectively.
   Naive Bayes utilizes a probabilistic method for classification by multiplying the individual probabilities of every feature-value pair. This algorithm assumes independence among the features and even then provides excellent classification results.
   Decision tree learning algorithm C4.5 is an extension of ID3 that accounts for unavailable values, continuous attribute value ranges, pruning of decision trees, rule derivation, and so on. The tree comprises of nodes (features) that are selected by information entropy.
   Instance-based learner IB1 is a single-nearest-neighbor algorithm, and it classifies entities taking the class of the closest associated vectors in the training set via distance metrics. It is the simplest among the algorithms used in our study.
   Inductive rule learner RIPPER (Repeated Incremental Pruning to Produce Error Reduction) [12] is a propositional rule learner that defines a rule based detection model and seeks to improve it iteratively by using different heuristic techniques. The constructed rule set is then used to classify new instances.
3) When evaluating the performance of the feature subset selection algorithms, four metrics, (i) the proportion of selected features (ii) the time to obtain the feature subset, (iii) the classification accuracy, and (iv) the Win/Draw/Loss record [65], are used.
   The proportion of selected features is the ratio of the number of features selected by a feature selection algorithm to the original number of features of a data set.
   The Win/Draw/Loss record presents three values on a given measure, i.e. the numbers of data sets for which our proposed algorithm FAST obtains better, equal, and worse performance than other five feature selection algorithms, respectively. The measure can be the proportion of selected features, the runtime to obtain a feature subset, and the classification accuracy, respectively.

Experimental procedure

In order to make the best use of the data and obtain stable results, a (M = 5)×(N = 10)-cross-validation strategy is used. That is, for each data set, each feature subset selection algorithm and each classification algorithm, the 10-fold cross-validation is repeated M = 5 times, with each time the order of the instances of the data set being randomized. This is because many of the algorithms exhibit order effects, in that certain orderings dramatically improve or degrade performance [21]. Randomizing the order of the inputs can help diminish the order effects.

In the experiment, for each feature subset selection algorithm, we obtain M ×N feature subsets *Subset* and the corresponding runtime *Time* with each data set. Average $|Subset|$ and *Time*, we obtain the number of selected features further the proportion of selected features and the corresponding runtime for each feature selection algorithm on each data set. For each classification algorithm, we obtain M ×N classification *Accuracy* for each feature selection algorithm and each data set. Average these *Accuracy*, we obtain mean accuracy of each classification algorithm under each feature selection algorithm and each data set. The procedure *Experimental Process* shows the details.

Procedure *Experimental Process*

```
1  M = 5, N = 10
2  DATA = { D1, D2, ..., D85 }
3  Learners = {NB, C4.5, IB1, RIPPER }
4  FeatureSelectors ={FAST, FCBF, ReliefF, CFS, Consist, FOCUS-SF }
5  for each data ∈ DATA do
6      for each times ∈ [1, M] do
7          randomize instance-order for data
8          generate N bins from the randomized data
9          for each fold ∈ [1, N] do
10             TestData = bin[fold]
11             TrainingData = data - TestData
12             for each selector ∈ FeatureSelectors do
13                 (Subset, Time) = selector(TrainingData)
14                 TrainingData' = select Subset from TrainingData
15                 TestData' = select Subset from TestData
16                 for each learner ∈ Learners do
17                     classifier = learner(TrainingData')
18                     Accuracy = apply classifier to TestData'
```

Results and analysis

In this section we present the experimental results in terms of the proportion of selected features, the time to obtain the feature subset, the classification accuracy, and the Win/Draw/Loss record.

For the purpose of exploring the statistical significance of the results, we performed a nonparametric Friedman test [24] followed by Nemenyi post-hoc test [47], as advised by Demsar[17] and Garcia and Herrerato [25] to statistically compare algorithms on multiple data sets. Thus the Friedman and the Nemenyi test results are reported as well.

Proportion of selected features

Table 2 records the proportion of selected features of the six feature selection algorithms for each data set. From it we observe that

1) Generally all the six algorithms achieve significant reduction of dimensionality by selecting only a small portion of the original features. FAST on average obtains the best proportion of selected features of 1.82%. The Win/Draw/Loss records show FAST wins other algorithms as well.
2) For image data, the proportion of selected features of each algorithm has an increment compared with the corresponding average proportion of selected features on the given data sets except Consist has an improvement. This reveals that the five algorithms are not very suitable to choose features for image data compared with for microarray and text data. FAST ranks 3 with the proportion of selected features of 3.59% that has a tiny margin of 0.11% to the first and second best proportion of selected features 3.48% of Consist and FOCUS-SF, and a margin of 76.59% to the worst proportion of selected features 79.85% of ReliefF.
3) For microarray data, the proportion of selected features has been improved by each of the six algorithms compared with that on the given data sets. This indicates that the six algorithms work well with microarray data. FAST ranks 1 again with the proportion of selected features of 0.71%. Of the six algorithms, only CFS cannot choose features for two data sets whose dimensionalities are 19994 and 49152, respectively.
4) For text data, FAST ranks 1 again with a margin of 0.48% to the second best algorithm FOCUS-SF.

TABLE 2: Proportion of selected features of the six feature selection algorithms

	Proportion of selected features (%) of					
Data set	FAST	FCBF	CFS	ReliefF	Consist	FOCUS-SF
chess	16.22	21.62	10.81	62.16	81.08	18.92
mfeat-fourier	19.48	49.35	24.68	98.70	15.58	15.58
coil2000	3.49	8.14	11.63	50.00	37.21	1.16
elephant	0.86	3.88	5.60	6.03	0.86	0.86
arrhythmia	2.50	4.64	9.29	50.00	8.93	8.93
fqs-nowe	0.31	2.19	5.63	26.56	4.69	4.69
colon	0.30	0.75	1.35	39.13	0.30	0.30
fbis.wc	0.80	1.45	2.30	0.95	1.75	1.75
AR10P	0.21	1.04	2.12	62.89	0.29	0.29
PIE10P	1.07	1.98	2.52	91.00	0.25	0.25
oh0.wc	0.38	0.88	1.10	0.38	1.82	1.82
oh10.wc	0.34	0.80	0.56	0.40	1.61	1.61
B-cell1	0.52	1.61	1.07	30.49	0.10	0.10
B-cell2	1.66	6.13	3.85	96.87	0.15	0.15
B-cell3	2.06	7.95	4.20	98.24	0.12	0.12
base-hock	0.58	1.27	0.82	0.12	1.19	1.19
TOX-171	0.28	1.41	2.09	64.60	0.19	0.19
tr12.wc	0.16	0.28	0.26	0.59	0.28	0.28
tr23.wc	0.15	0.27	0.19	1.46	0.21	0.21
tr11.wc	0.16	0.25	0.40	0.37	0.31	0.31
embryonal-tumours	0.14	0.03	0.03	13.96	0.03	0.03
leukemia1	0.07	0.03	0.03	41.35	0.03	0.03
leukemia2	0.01	0.41	0.52	60.63	0.08	0.08
tr21.wc	0.10	0.22	0.37	2.04	0.20	0.20
wap.wc	0.20	0.53	0.65	1.10	0.41	0.41
PIX10P	0.15	3.04	2.35	100.00	0.03	0.03
ORL10P	0.30	2.61	2.76	99.97	0.04	0.04
CLL-SUB-111	0.04	0.78	1.23	54.35	0.08	0.08
ohscal.wc	0.34	0.44	0.18	0.03	NA	NA
la2s.wc	0.15	0.33	0.54	0.09	0.37	NA
la1s.wc	0.17	0.35	0.51	0.06	0.34	NA
GCM	0.13	0.42	0.68	79.41	0.06	0.06
SMK-CAN-187	0.13	0.25	NA	14.23	0.06	0.06
new3s.wc	0.10	0.15	NA	0.03	NA	NA
GLA-BRA-180	0.03	0.35	NA	53.06	0.02	0.02
Average(Image)	3.59	10.04	6.68	79.85	3.48	3.48
Average(Microarry)	0.71	2.34	2.50	52.92	0.91	0.91
Average(Text)	2.05	3.25	2.64	10.87	11.46	2.53
Average	1.82	4.27	3.42	42.54	5.44	2.06
Win/Draw/Loss	-	33/0/2	31/0/4	29/1/5	20/2/13	19/2/14

The Friedman test [24] can be used to compare k algorithms over N data sets by ranking each algorithm on each data set separately. The algorithm obtained the best performance gets the rank of 1, the second best ranks 2, and so on. In case of ties, average ranks are assigned. Then the average ranks of all algorithms on all data sets are calculated and compared. If the null hypothesis, which is all algorithms are performing equivalently, is rejected under the Friedman test statistic, post-hoc tests such as the Nemenyi test [47] can be used to determine which algorithms perform statistically different.

The Nemenyi test compares classifiers in a pairwise manner. According to this test, the performances of two classifiers are significantly different if the distance of

P.G. COLLEGE OF ARTS & SCIENCE NAMAKKAL 637 206

the average ranks exceeds the critical distance $CD = q_\alpha \sqrt{\frac{k(k+1)}{6N}}$, where the q_α is based on the Studentized range statistic [48] divided by $\sqrt{2}$.

In order to further explore whether the reduction rates are significantly different we performed a Friedman test followed by a Nemenyi post-hoc test.

The null hypothesis of the Friedman test is that all the feature selection algorithms are equivalent in terms of proportion of selected features. The test result is $p = 0$. This means that at $\alpha = 0.1$, there is evidence to reject the null hypothesis and all the six feature selection algorithms are different in terms of proportion of selected features.

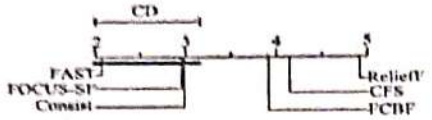


Fig. 3: Proportion of selected features comparison of all feature selection algorithms against each other with the Nemenyi test.

In order to further explore feature selection algorithms whose reduction rates have statistically significant differences, we performed a Nemenyi test. Fig. 3 shows the results with $\alpha = 0.1$ on the 35 data sets. The results indicate that the proportion of selected features of FAST is statistically smaller than those of ReliefF, CFS and FCBF, and there is no consistent evidence to indicate statistical differences between FAST , Consist, and FOCUS-SF, respectively.

Runtime

TABLE 3: Runtime (in ms) of the six feature selection algorithms

Data set	FAST	FCBF	CFS	ReliefF	Consist	FOCUS-SF
chess	105	60	352	12660	1999	653
mfeat-fourier	1472	716	938	13918	3227	660
coil2000	866	875	1483	304162	53850	1281
elephant	783	312	905	20991	2439	1098
arrhythmia	110	115	821	3684	3492	2940
fqs-nowe	977	97	736	1072	1360	1032
colon	166	148	12249	744	1624	960
fbis.wc	14761	16207	66058	79527	579376	479651
AR10P	706	458	57319	3874	3568	2083
PIE10P	678	1223	77579	7636	4149	2910
oh0.wc	5283	5990	59624	4898	488261	420116
oh10.wc	5549	6033	28438	5652	428459	402853
B-cell1	160	248	103871	1162	2476	1310
B-cell2	626	1618	930465	4334	5102	2556
B-cell3	635	2168	1097122	7001	4666	2348
base-hock	8059	21793	146454	728900	999232	1017412
TOX-171	1750	1558	1341345	9757	17185	8446
tr12.wc	3089	3585	51360	2558	53304	34270
tr23.wc	4266	2506	32647	1585	29165	16649
tr11.wc	5086	5575	136063	4418	111073	79000
embryonal-tumours	754	314	10154	1681	5045	1273
leukemia1	449	270	10900	790	5708	1263
leukemia2	1141	456	216888	894	10407	3471
tr21.wc	4662	5543	218436	4572	89761	55644
wap.wc	25146	28724	768642	33073	1362376	1093222
PIX10P	2957	9056	25372209	11231	9875	4292
ORL10P	2330	12991	30383928	11547	13905	5780
CLL-SUB-111	1687	1870	6327479	12720	17554	12307
ohscal.wc	353283	391761	981868	655400	NA	NA
la2s.wc	70776	99019	2299244	118624	7400287	NA
la1s.wc	79623	107110	2660871	120452	7030978	NA
GCM	9351	4939	3780146	32950	39303	26644
SMK-CAN-187	4307	5114	NA	34881	67364	38606
new3s.wc	790690	960738	NA	2228746	NA	NA
GLA-BRA-180	29854	17348	NA	97641	220734	152536
Average(Image)	1520	4090	9315452	8213	6014	2793
Average(Microarry)	1468	1169	1152695	8059	9590	5385
Average(Text)	6989	8808	137232	107528	381532	327341
Average	3573	4671	2456366	45820	149932	126970
Win/Draw/Loss	-	22/0/13	33/0/2	29/0/6	35/0/0	34/0/1

Table 3 records the runtime of the six feature selection algorithms. From it we observe that

1) Generally the individual evaluation based feature selection algorithms of FAST, FCBF and ReliefF are much faster than the subset evaluation based algorithms of CFS, Consist and FOCUS-SF. FAST is consistently faster than all other algorithms. The runtime of FAST is only 0.1% of that of CFS, 2.4% of that of Consist, 2.8% of that of FOCUS-SF, 7.8% of that of ReliefF, and 76.5% of that of FCBF, respectively. The Win/Draw/Loss records show that FAST outperforms other algorithms as well.
2) For image data, FAST obtains the rank of 1. Its runtime is only 0.02% of that of CFS, 18.50% of that of ReliefF, 25.27% of that of Consist, 37.16% of that of FCBF, and 54.42% of that of FOCUS-SF, respectively. This reveals that FAST is more efficient than others when choosing features for image data.
3) For microarray data, FAST ranks 2. Its runtime is only 0.12% of that of CFS, 15.30% of that of Consist, 18.21% of that of ReliefF, 27.25% of that of FOCUS-SF, and 125.59% of that of FCBF, respectively.
4) For text data, FAST ranks 1. Its runtime is 1.83% of that of Consist, 2.13% of that of FOCUS-SF, 5.09% of that of CFS, 6.50% of that of ReliefF, and 79.34% of that of FCBF, respectively. This indicates that FAST is more efficient than others when choosing features for text data as well.

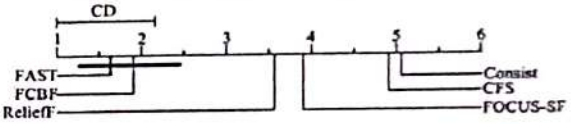


Fig. 4: Runtime comparison of all feature selection algorithms against each other with the Nemenyi test.

In order to further explore whether the runtime of the six feature selection algorithms are significantly different we performed a Friedman test. The null hypothesis of the Friedman test is that all the feature selection algorithms are equivalent in terms of runtime. The test result is $p = 0$. This means that at $\alpha = 0.1$, there is evidence to reject the null hypothesis and all the six feature selection algorithms are different in terms of runtime. Thus a post-hoc Nemenyi test was conducted. Fig. 4 shows the results with $\alpha = 0.1$ on the 35 data sets. The results indicate that the runtime of FAST is statistically better than those of ReliefF, FOCUS-SF, CFS, and Consist, and there is no consistent evidence to indicate statistical runtime differences between FAST and FCBF.

Classification accuracy

Tables 4, 5, 6 and 7 show the 10-fold cross-validation accuracies of the four different types of classifiers on the 35 data sets before and after each feature selection algorithm is performed, respectively.

Table 4 shows the classification accuracy of Naive Bayes. From it we observe that

1) Compared with original data, the classification accuracy of Naive Bayes has been improved by FAST, CFS, and FCBF by 12.86%, 6.62%, and 4.32%,

P.G.P. COLLEGE OF ARTS & SCIENCE
NAMAKKAL
637 206

respectively. Unfortunately, ReliefF, Consist, and FOCUS-SF have decreased the classification accuracy by 0.32%, 1.35%, and 0.86%, respectively. FAST ranks 1 with a margin of 6.24% to the second best accuracy 80.60% of CFS. At the same time, the Win/Draw/Loss records show that FAST outperforms all other five algorithms.

2) For image data, the classification accuracy of Naive Bayes has been improved by FCBF, CFS, FAST, and ReliefF by 6.13%, 5.39%, 4.29%, and 3.78%, respectively. However, Consist and FOCUS-SF have decreased the classification accuracy by 4.69% and 4.69%, respectively. This time FAST ranks 3 with a margin of 1.83% to the best accuracy 87.32% of FCBF.
3) For microarray data, the classification accuracy of Naive Bayes has been improved by all the six algorithms FAST, CFS, FCBF, ReliefF, Consist, and FOCUS-SF by 16.24%, 12.09%, 9.16%, 4.08%, 4.45%, and 4.45%, respectively. FAST ranks 1 with a margin of 4.16% to the second best accuracy 87.22% of CFS. This indicates that FAST is more effective than others when using Naive Bayes to classify microarray data.
4) For text data, FAST and CFS have improved the classification accuracy of Naive Bayes by 13.83% and 1.33%, respectively. Other four algorithms ReliefF, Consist, FOCUS-SF, and FCBF have decreased the accuracy by 7.36%, 5.87%, 4.57%, and 1.96%, respectively. FAST ranks 1 with a margin of 12.50% to the second best accuracy 70.12% of CFS.

TABLE 4: Accuracy of Naive Bayes with the six feature selection algorithms

Data set	Classification accuracy of Naive Bayes with						
	FAST	FCBF	CFS	ReliefF	Consist	FOCUS-SF	Full set
chess	92.92	92.12	90.43	88.56	89.50	94.34	87.68
mfeat-fourier	80.05	78.57	79.31	76.32	76.72	76.72	76.07
coil2000	94.04	93.53	92.59	76.96	84.64	94.03	78.04
elephant	99.47	67.96	85.98	87.54	99.94	99.94	82.34
arrhythmia	73.01	65.98	69.64	64.53	69.24	69.24	63.06
fqs-nowe	69.81	71.57	70.45	66.44	71.35	71.35	65.61
colon	95.08	84.81	84.81	68.33	85.48	85.48	56.33
fbis.wc	70.04	49.79	61.26	38.75	39.20	39.20	61.89
AR10P	69.23	81.08	82.77	80.77	62.46	62.46	72.62
PIE10P	96.83	95.71	94.57	93.97	73.90	73.90	90.67
oh0.wc	72.31	67.75	75.97	49.38	73.44	73.44	80.10
oh10.wc	69.65	70.02	69.54	50.79	69.73	69.73	72.40
B-cell1	100.00	100.00	100.00	100.00	91.50	91.50	91.30
B-cell2	96.63	83.53	83.47	77.63	62.71	62.71	74.58
B-cell3	98.22	82.47	85.47	79.26	82.24	82.24	75.40
base-hock	93.18	90.09	90.98	51.05	81.92	81.92	90.12
TOX-171	85.56	90.53	93.09	79.93	74.27	74.27	76.27
tr12.wc	84.88	57.77	60.01	66.33	49.50	49.50	56.00
tr23.wc	93.77	53.06	55.25	51.11	54.80	54.80	55.96
tr11.wc	82.47	50.72	53.49	63.92	46.58	46.58	54.39
embryonal-tumours	92.22	97.00	97.00	96.39	97.00	97.00	94.33
leukemia1	100.00	100.00	100.00	75.00	100.00	100.00	92.17
leukemia2	100.00	77.33	78.00	95.00	55.33	55.33	62.00
tr21.wc	89.97	48.26	53.61	70.43	44.04	44.04	47.01
wap.wc	65.64	61.23	60.19	60.43	58.02	58.02	73.05
PIX10P	98.00	98.20	96.80	98.00	90.00	90.00	96.00
ORL10P	99.00	98.00	95.60	94.33	84.60	84.60	96.20
CLL-SUB-111	85.45	84.97	87.86	69.32	74.71	74.71	67.00
ohscal.wc	68.06	58.48	59.24	23.81	NA	NA	NA
la2s.wc	69.68	60.48	71.89	40.99	61.94	NA	75.27
la1s.wc	71.96	60.46	70.42	33.51	58.74	NA	75.16
GCM	70.90	77.00	81.33	57.65	62.62	62.62	66.83
SMK-CAN-187	85.96	75.63	NA	68.14	73.78	73.78	60.36
new3s.wc	56.69	33.73	NA	16.13	NA	NA	NA
GLA-BRA-180	76.48	77.89	NA	69.07	63.44	63.44	67.00
Average(Image)	85.49	87.32	86.56	84.97	76.51	76.51	81.20
Average(Microarry)	91.38	84.30	87.22	79.22	79.59	79.59	75.13
Average(Text)	82.62	66.83	70.12	61.43	62.92	64.22	68.79
Average	86.84	78.30	80.60	73.66	72.63	73.12	73.98
Win/Draw/Loss	-	25/2/8	24/2/9	31/2/2	29/1/5	20/1/6	20/0/7

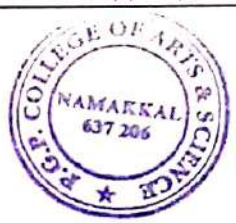


TABLE 5: Accuracy of C4.5 with the six feature selection algorithms

Data set	Classification accuracy of C4.5 with						
	FAST	FCBF	CFS	ReliefF	Consist	FOCUS-SF	Full set
chess	94.02	94.02	90.43	97.81	99.44	94.34	99.44
mfeat-fourier	71.25	75.74	77.80	76.40	71.06	71.06	75.93
coil2000	94.03	94.03	94.03	94.03	93.97	94.01	93.91
elephant	99.90	99.94	99.94	99.90	99.94	99.94	95.27
arrhythmia	71.53	78.05	69.21	66.15	66.59	66.59	65.23
fqs-nowe	69.81	73.35	69.13	66.46	68.42	68.42	66.96
colon	90.40	90.76	89.14	82.38	86.90	86.90	82.33
fbis.wc	69.41	69.35	77.52	57.03	68.70	68.70	NA
AR10P	77.69	75.54	79.54	71.54	64.92	64.92	70.92
PIE10P	84.13	82.95	84.10	80.32	81.33	81.33	79.14
oh0.wc	71.80	75.45	84.20	57.43	83.47	83.47	81.37
oh10.wc	69.33	73.75	74.65	67.65	75.60	75.60	72.38
B-cell1	87.33	81.60	82.90	78.17	88.60	88.60	74.90
B-cell2	71.00	63.24	64.07	65.05	60.00	60.00	64.31
B-cell3	78.07	81.07	77.02	83.04	72.84	72.84	77.96
base-hock	92.02	89.81	89.57	49.92	90.57	90.57	91.54
TOX-171	76.85	64.92	69.69	60.24	68.66	68.66	58.44
tr12.wc	81.68	85.43	31.96	74.02	43.76	84.47	81.19
tr23.wc	89.87	94.80	46.38	86.78	67.07	96.57	92.93
tr11.wc	80.22	82.04	36.95	69.25	46.81	84.11	79.09
embryonal-tumours	87.78	97.00	97.00	88.89	97.00	97.00	87.50
leukemia1	100.00	97.00	97.00	61.11	97.00	97.00	89.17
leukemia2	100.00	75.00	78.00	88.89	81.33	81.33	60.33
tr21.wc	90.47	88.32	69.23	80.26	68.76	89.21	80.72
wap.wc	62.26	67.60	32.87	64.32	21.86	63.27	NA
PIX10P	97.00	93.40	98.80	93.33	92.20	92.20	93.00
ORL10P	90.33	82.60	90.20	74.67	84.00	84.00	72.40
CLL-SUB-111	83.64	73.85	74.36	64.80	78.76	78.76	60.89
ohscal.wc	67.73	66.69	68.42	27.30	NA	NA	NA
la2s.wc	72.40	72.53	79.08	51.52	75.53	NA	NA
la1s.wc	72.45	72.57	77.63	47.05	75.33	NA	NA
GCM	58.73	59.16	60.92	52.73	45.79	45.79	51.81
SMK-CAN-187	85.19	71.42	NA	66.14	77.83	77.83	62.17
new3s.wc	55.64	60.51	NA	17.83	NA	NA	NA
GLA-BRA-180	71.30	68.22	NA	65.00	64.56	64.56	63.22
Average(Image)	81.70	80.93	81.60	77.12	76.99	76.99	76.39
Average(Microarry)	83.77	79.48	79.85	74.35	78.68	78.68	72.35
Average(Text)	81.38	83.15	66.16	72.59	69.09	83.94	85.84
Average	82.44	81.17	75.43	74.25	74.69	80.33	77.74
Win/Draw/Loss	-	17/2/16	21/1/13	28/2/5	27/0/8	19/1/10	30/0/5

Table 5 shows the classification accuracy of C4.5. From it we observe that

1) Compared with original data, the classification accuracy of C4.5 has been improved by FAST, FCBF, and FOCUS-SF by 4.69%, 3.43%, and 2.58%, respectively. Unfortunately, ReliefF, Consist, and CFS have decreased the classification accuracy by 3.49%, 3.05%, and 2.31%, respectively. FAST obtains the rank of 1 with a margin of 1.26% to the second best accuracy 81.17% of FCBF.
2) For image data, the classification accuracy of C4.5 has been improved by all the six feature selection algorithms FAST, FCBF, CFS, ReliefF, Consist, and FOCUS-SF by 5.31%, 4.54%, 7.20%, 0.73%, 0.60%, and 0.60%, respectively. This time FAST ranks 2 with a margin of 1.89% to the best accuracy 83.6% of CFS and a margin of 4.71% to the worst accuracy 76.99% of Consist and FOCUS-SF.
3) For microarray data, the classification accuracy of C4.5 has been improved by all the six algorithms FAST, FCBF, CFS, ReliefF, Consist, and FOCUS-SF by 11.42%, 7.14%, 7.51%, 2.00%, 6.34%, and 6.34%, respectively. FAST ranks 1 with a margin of 3.92% to the second best accuracy 79.85% of CFS.
4) For text data, the classification accuracy of C4.5 has been decreased by algorithms FAST, FCBF, CFS, ReliefF, Consist and FOCUS-SF by 4.46%, 2.70%, 19.68%, 13.25%, 16.75%, and 1.90% respectively. FAST ranks 3 with a margin of 2.56% to the best accuracy 83.94% of FOCUS-SF and a margin of 15.22% to the worst accuracy 66.16% of CFS.

TABLE 6: Accuracy of IB1 with the six feature selection algorithms

Data set	Classificati n accuracy of IB1 w th						
	FAST	FCBF	CFS	ReliefF	Consist	FOCUS-SF	Full set
chess	90.18	91.47	84.78	96.86	95.09	90.79	90.60
mfeat-fourier	77.07	81.69	83.72	80.00	77.71	77.71	80.13
coil2000	88.42	89.27	89.42	89.16	89.96	67.62	89.07
elephant	98.07	99.99	99.99	100.00	99.92	99.97	99.31
arrhythmia	64.48	60.10	63.67	54.35	59.22	55.22	53.27
fqs-nowe	56.59	66.20	70.48	70.74	63.02	63.02	65.32
colon	91.90	78.76	84.30	82.54	85.95	85.95	76.14
fbis.wc	60.09	61.91	72.94	43.69	60.03	60.03	NA
AR10P	73.33	79.00	86.77	71.79	80.46	80.46	49.54
PIE10P	99.21	99.90	99.05	99.37	92.19	92.19	99.62
oh0.wc	67.33	63.19	75.53	48.12	68.34	68.34	20.64
oh10.wc	64.06	63.56	66.46	56.67	63.41	63.41	8.40
B-cell1	100.00	94.90	95.40	92.17	93.30	93.30	73.00
B-cell2	97.00	87.02	86.42	71.78	58.00	58.00	70.20
B-cell3	98.96	95.02	95.02	83.40	80.20	80.20	83.98
base-hock	89.06	92.24	92.60	50.86	92.95	92.95	78.81
TOX-171	75.60	95.92	97.90	96.32	65.14	65.14	86.44
tr12.wc	82.11	83.43	84.92	61.02	84.91	84.91	40.13
tr23.wc	90.18	86.55	88.90	67.62	86.00	86.00	56.11
tr11.wc	78.43	79.65	81.89	59.81	81.26	81.26	49.58
embryonal-tumours	90.56	97.00	97.00	90.56	97.00	97.00	89.50
leukemia1	100.00	97.00	97.00	67.22	97.00	97.00	76.50
leukemia2	100.00	84.33	75.00	79.72	71.00	71.00	59.67
tr21.wc	87.98	85.34	91.23	76.41	87.23	87.23	67.85
wap.wc	56.47	57.31	68.49	61.03	58.74	58.74	NA
PIX10P	99.00	99.00	99.00	99.00	95.00	95.00	99.00
ORL10P	100.00	97.60	95.20	94.67	95.00	95.00	94.40
CLL-SUB-111	79.09	74.94	81.62	68.66	65.83	65.83	NA
ohscal.wc	52.94	49.52	57.98	19.67	NA	NA	NA
la2s.wc	68.33	60.16	79.88	39.95	73.43	NA	NA
la1s.wc	67.44	67.01	76.41	33.98	71.42	NA	NA
GCM	68.49	66.71	69.50	58.59	52.54	52.54	58.87
SMK-CAN-187	76.28	66.08	NA	70.40	70.58	70.58	63.57
new3s.wc	49.46	52.38	NA	8.82	NA	NA	NA
GLA-BRA-180	72.96	73.89	NA	68.33	73.00	73.00	61.78
Average(Image)	84.33	87.25	89.04	85.93	83.90	83.90	81.34
Average(Microarry)	88.75	85.97	86.91	78.78	76.76	76.76	75.17
Average(Text)	77.66	77.63	81.56	64.66	79.05	76.63	55.78
Average	83.63	83.07	85.32	74.90	79.11	78.19	69.88
Win/Draw/Loss	-	18/1/16	14/1/20	25/2/8	20/0/15	23/0/12	27/1/7

Table 6 shows the classification accuracy of IB1. From it we observe that

1) Compared with original data, the classification accuracy of IB1 has been improved by all the six feature selection algorithms FAST, FCBF, CFS, ReliefF, Consist, and FOCUS-SF by 13.75%, 13.19%, 15.44%, 5.02%, 9.23%, and 8.31%, respectively. FAST ranks 2 with a margin of 1.69% to the best accuracy 85.32% of CFS. The Win/Draw/Loss records show that FAST outperforms all other algorithms except for CFS, winning and losing on 14 and 20 out of the 35 data sets, respectively.
   Although FAST does not perform better than CFS, we observe that CFS is not available on the three biggest data sets of the 35 data sets. Moreover, CFS is very slow compared with other algorithms as reported in Section 4.4.2.
2) For image data, the classification accuracy of IB1 has been improved by all the six feature selection algorithms FAST, FCBF, CFS, ReliefF, Consist, and FOCUS-SF by 3.00%, 5.91%, 7.70%, 4.59%, 2.56%, and 2.56%, respectively. FAST ranks 4 with a margin of 4.70% to the best accuracy 89.04% of CFS.
3) For microarray data, the classification accuracy of IB1 has been improved by all the six algorithms FAST, FCBF, CFS, ReliefF, Consist, and FOCUS-SF by 13.58%, 10.80%, 11.74%, 3.61%, 1.59%, and 1.59%, respectively. FAST ranks 1 with a margin of 1.85% to the second best accuracy 86.91% of CFS and a margin of 11.99% to the worst accuracy 76.76% of Consist and FOCUS-SF.
4) For text data, the classification accuracy of IB1 has been improved by the five feature selection algorithms FAST, FCBF, CFS, ReliefF, Consist, and FOCUS-SF by 21.89%, 21.85%, 25.78%, 8.88%, 23.27%, and 20.85%, respectively. FAST ranks 3 with a margin of 3.90% to the best accuracy 81.56% of CFS.

TABLE 7: Accuracy of RIPPER with the six feature selection algorithms

Data set	Classification accuracy of RIPPER with						
	FAST	FCBF	CFS	ReliefF	Consist	FOCUS-SF	Full set
chess	94.09	94.09	90.43	97.81	99.17	94.34	99.16
mfeat-fourier	70.40	73.46	75.35	72.58	69.13	69.13	73.36
coil2000	94.02	94.03	94.03	94.03	93.93	94.03	93.89
elephant	72.57	66.84	70.85	77.31	98.62	98.62	79.38
arrhythmia	68.36	72.21	70.97	71.01	71.27	71.27	71.36
fqs-nowe	69.81	73.66	69.15	69.05	68.52	68.52	63.62
colon	93.41	80.14	79.76	77.14	84.05	84.05	74.19
fbis.wc	65.58	68.18	75.49	53.29	65.10	65.10	NA
AR10P	73.08	64.62	65.08	59.23	57.23	57.23	54.62
PIE10P	88.57	80.57	80.00	79.37	76.67	76.67	79.33
oh0.wc	65.90	69.93	78.98	41.27	79.12	79.12	NA
oh10.wc	67.90	69.41	70.08	62.22	71.47	71.47	NA
B-cell1	86.50	79.50	85.50	80.67	89.60	89.60	74.10
B-cell2	80.67	61.31	55.13	58.56	53.53	53.53	53.42
B-cell3	82.52	76.24	59.42	72.07	72.31	72.31	60.67
base-hock	91.04	89.29	90.72	51.13	92.34	92.34	88.26
TOX-171	78.22	67.61	70.59	63.39	60.12	60.12	62.58
tr12.wc	82.53	81.13	79.67	71.56	83.07	83.07	77.94
tr23.wc	91.15	95.96	93.22	84.80	95.11	95.11	89.91
tr11.wc	80.13	79.52	80.72	66.67	81.46	81.46	NA
embryonal-tumours	80.56	97.00	97.00	85.28	97.00	97.00	82.83
leukemia1	100.00	97.00	97.00	64.44	97.00	97.00	86.67
leukemia2	100.00	70.67	71.00	92.50	76.33	76.33	63.67
tr21.wc	91.07	89.75	90.53	84.63	87.59	87.59	NA
wap.wc	50.90	63.54	67.06	58.48	60.00	60.00	NA
PIX10P	96.67	93.00	85.80	86.67	92.00	92.00	82.60
ORL10P	85.33	73.80	62.40	66.00	75.60	75.60	54.20
CLL-SUB-111	83.99	74.91	70.61	68.76	81.83	81.83	66.77
ohscal.wc	62.34	62.98	62.06	24.98	NA	NA	NA
la2s.wc	69.37	70.06	79.73	40.93	76.52	NA	NA
la1s.wc	67.56	68.03	78.50	41.11	74.26	NA	NA
GCM	53.13	49.86	50.32	47.41	46.26	46.26	44.09
SMK-CAN-187	77.53	68.88	NA	61.81	72.47	72.47	59.55
new3s.wc	44.46	52.69	NA	9.69	NA	NA	NA
GLA-BRA-180	70.19	68.11	NA	59.44	65.22	65.22	60.56
Average(Image)	80.64	76.52	72.96	72.15	73.19	73.19	68.29
Average(Microarry)	81.66	74.44	73.85	71.55	77.33	77.33	68.31
Average(Text)	79.48	81.35	82.81	69.63	82.58	82.15	89.83
Average	80.62	77.49	77.06	70.94	78.46	78.30	72.98
Win/Draw/Loss	-	20/1/14	22/0/13	28/0/7	21/0/14	22/0/13	30/0/5

Table 7 shows the classification accuracy of RIPPER. From it we observe that

1) Compared with original data, the classification accuracy of RIPPER has been improved by the five feature selection algorithms FAST, FCBF, CFS, Consist, and FOCUS-SF by 7.64%, 4.51%, 4.08%, 5.48%, and 5.32%, respectively; and has been decreased by ReliefF by 2.04%. FAST ranks 1 with a margin of 2.16% to the second best accuracy 78.46% of Consist. The Win/Draw/Loss records show that FAST outperforms all other algorithms.
2) For image data, the classification accuracy of RIPPER has been improved by all the six feature selection algorithms FAST, FCBF, CFS, ReliefF, Consist, and FOCUS-SF by 12.35%, 8.23 %, 4.67%, 3.86%, 4.90%, and 4.90%, respectively. FAST ranks 1 with a margin of 4.13% to the second best accuracy 76.52% of FCBF.
3) For microarray data, the classification accuracy of RIPPER has been improved by all the six algorithms FAST, FCBF, CFS, ReliefF, Consist, and FOCUS-SF by 13.35%, 6.13%, 5.54%, 3.23%, 9.02%, and 9.02%, respectively. FAST ranks 1 with a mar-

P.G.P. COLLEGE OF ARTS & SCIENCE
NAMAKKAL
637 206

TABLE 8: Rank of the six feature selection algorithms under different types of data

	Image Data						Microarray Data						Text Data						All Data					
	FAST	FCBF	CFS	ReliefF	Consist	FOCUS -SF	FAST	FCBF	CFS	ReliefF	Consist	FOCUS -SF	FAST	FCBF	CFS	ReliefF	Consist	FOCUS -SF	FAST	FCBF	CFS	ReliefF	Consist	FOCUS -SF
NB	3	1	2	4	5	5	1	3	2	6	4	4	1	3	2	6	5	4	1	3	2	4	6	5
C4.5	2	3	1	4	5	5	1	3	2	6	4	4	3	4	1	6	2	4	2	3	1	6	4	5
IB1	4	2	1	3	5	5	1	3	2	4	5	5	3	4	1	6	2	4	2	3	1	6	4	5
RIPPER	1	2	1	6	3	3	1	4	5	6	2	2	5	3	1	6	2	4	1	4	5	6	2	3
Sum	10	8	5	17	18	18	4	13	11	22	15	15	12	12	10	22	14	13	5	13	10	22	17	18
Rank	3	2	1	4	5	5	1	3	2	6	4	4	2	2	1	6	5	4	1	2	2	6	5	4

gin of 4.33% to the second best accuracy 77.33% of Consist and FOCUS-SF.

4) For text data, the classification accuracy of RIPPER has been decreased by FAST, FCBF, CFS, ReliefF, Consist, and FOCUS-SF by 10.35%, 8.48%, 7.02%, 20.21%, 7.25%, and 7.68%, respectively. FAST ranks 5 with a margin of 3.33% to the best accuracy 82.81% of CFS.

In order to further explore whether the classification accuracies of each classifier with the six feature selection algorithms are significantly different, we performed four Friedman tests individually. The null hypotheses are that the accuracies are equivalent for each of the four classifiers with the six feature selection algorithms. The test results are $p = 0$. This means that at $\square = 0.1$, there are evidences to reject the null hypotheses and the accuracies are different further differences exist in the six feature selection algorithms. Thus four post-hoc Nemenyi tests were conducted. Figs. 5, 6, 7, and 8 show the results with $\square = 0.1$ on the 35 data sets.

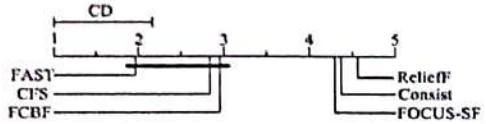


Fig. 5: Accuracy comparison of Naive Bayes with the six feature selection algorithms against each other with the Nemenyi test.

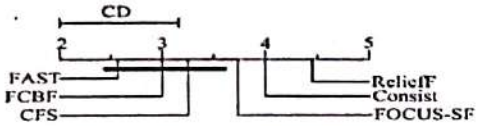


Fig. 6: Accuracy comparison of C4.5 with the six feature selection algorithms against each other with the Nemenyi test.

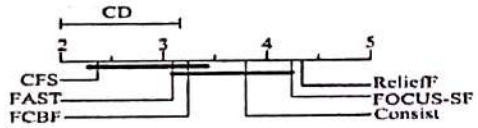


Fig. 7: Accuracy comparison of IB1 with the six feature selection algorithms against each other with the Nemenyi test.

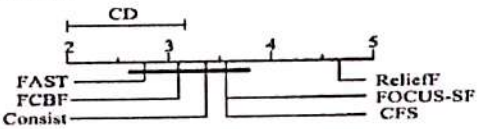


Fig. 8: Accuracy comparison of RIPPER with the six feature selection algorithms against each other with the Nemenyi test.

P.G.P. COLLEGE OF ARTS & SCIENCE
NAMAKKAL
637 205

From Fig. 5 we observe that the accuracy of Naive Bayes with FAST is statistically better than those with ReliefF, Consist, and FOCUS-SF. But there is no consistent evidence to indicate statistical accuracy differences between Naive Bayes with FAST and with CFS, which also holds for Naive Bayes with FAST and with FCBF.

From Fig. 6 we observe that the accuracy of C4.5 with FAST is statistically better than those with ReliefF, Consist, and FOCUS-SF. But there is no consistent evidence to indicate statistical accuracy differences between C4.5 with FAST and with FCBF, which also holds for C4.5 with FAST and with CFS.

From Fig. 7 we observe that the accuracy of IB1 with FAST is statistically better than those with ReliefF. But there is no consistent evidence to indicate statistical accuracy differences between IB1 with FAST and with FCBF, Consist, and FOCUS-SF, respectively, which also holds for IB1 with FAST and with CFS.

From Fig. 8 we observe that the accuracy of RIPPER with FAST is statistically better than those with ReliefF. But there is no consistent evidence to indicate statistical accuracy differences between RIPPER with FAST and with FCBF, CFS, Consist, and FOCUS-SF, respectively.

For the purpose of exploring the relationship between feature selection algorithms and data types, i.e. which algorithms are more suitable for which types of data, we rank the six feature selection algorithms according to the classification accuracy of a given classifier on a specific type of data after the feature selection algorithms are performed. Then we summarize the ranks of the feature selection algorithms under the four different classifiers, and give the final ranks of the feature selection algorithms on different types of data. Table 8 shows the results.

From Table 8 we observe that (i) for image data, CFS obtains the rank of 1, and FAST ranks 3; (ii) for microarray data, FAST ranks 1 and should be the undisputed first choice, and CFS is a good alternative; (iii) for text data, CFS obtains the rank of 1, and FAST and FCBF are alternatives; and (iv) for all data, FAST ranks 1 and should be the undisputed first choice, and FCBF, CFS are good alternatives.

From the analysis above we can know that FAST performs very well on the microarray data. The reason lies in both the characteristics of the data set itself and the property of the proposed algorithm.

Microarray data has the nature of the large number of features (genes) but small sample size, which can cause "curse of dimensionality" and over-fitting of the training data [19]. In the presence of hundreds or thousands of

features, researchers notice that it is common that a large number of features are not informative because they are either irrelevant or redundant with respect to the class concept [66]. Therefore, selecting a small number of discriminative genes from thousands of genes is essential for successful sample classification [27], [66].

Our proposed FAST effectively filters out a mass of irrelevant features in the first step. This reduces the possibility of improperly bringing the irrelevant features into the subsequent analysis. Then, in the second step, FAST removes a large number of redundant features by choosing a single representative feature from each cluster of redundant features. As a result, only a very small number of discriminative features are selected. This coincides with the desire happens of the microarray data analysis.

Sensitivity analysis

Like many other feature selection algorithms, our proposed FAST also requires a parameter □ that is the threshold of feature relevance. Different □ values might end with different classification results.

In order to explore which parameter value results in the best classification accuracy for a specific classification problem with a given classifier, a 10 fold cross-validation strategy was employed to reveal how the classification accuracy is changing with value of the parameter □.

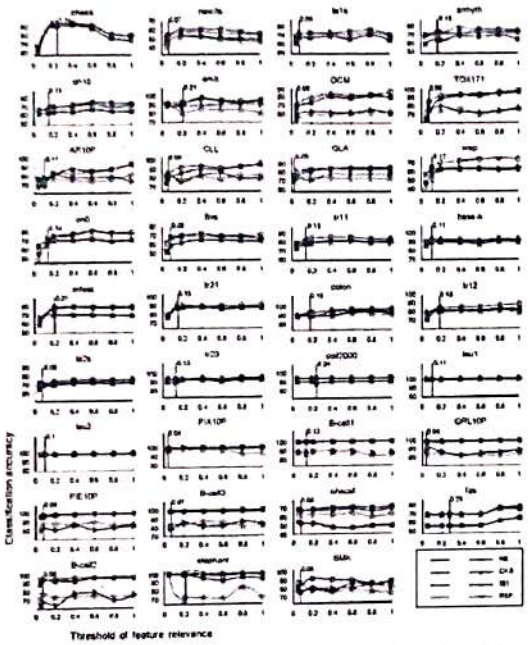


Fig. 9: Accuracies of the four classification algorithms with different □ values.

Fig. 9 shows the results where the 35 subfigures represent the 35 data sets, respectively. In each subfigure, the four curves denotes the classification accuracies of the four classifiers with the different □ values. The cross points of the vertical line with the horizontal axis represent the default values of the parameter □ recommended by FAST, and the cross points of the vertical line with the four curves are the classification accuracies of the corresponding classifiers with the □ values. From it we observe that:

1) Generally, for each of the four classification algorithms, (i) different □ values result in different classification accuracies; (ii) there is a □ value where the corresponding classification accuracy is the best; and (iii) the □ values, in which the best classification accuracies are obtained, are different for both the different data sets and the different classification algorithms. Therefore, an appropriate □ value is desired for a specific classification problem and a given classification algorithm.
2) In most cases, the default □ values recommended by FAST are not the optimal. Especially, in a few cases (e. g., data sets GCM, CLL-SUB-11, and TOX-171), the corresponding classification accuracies are very small. This means the results presented in Section 4.4.3 are not the best, and the performance could be better.
3) For each of the four classification algorithms, although the □ values where the best classification accuracies are obtained are different for different data sets, The value of 0.2 is commonly accepted because the corresponding classification accuracies are among the best or nearly the best ones.

When determining the value of □, besides classification accuracy, the proportion of the selected features should be taken into account as well. This is because improper proportion of the selected features results in a large number of features are retained, and further affects the classification efficiency.

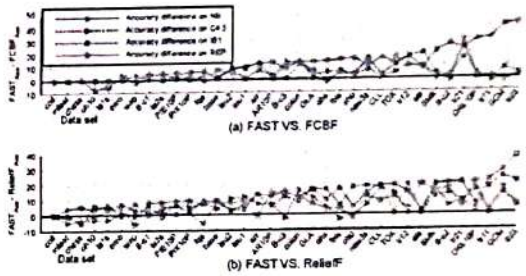


Fig. 10: Accuracy differences between FAST and the comparing algorithms

Just like the default □ values used for FAST in the experiments are often not the optimal in terms of classification accuracy, the default threshold values used for FCBF and ReliefF (CFS, Consist, and FOCUS-SF do not require any input parameter) could be so. In order to explore whether or not FAST still outperforms when optimal threshold values are used for the comparing algorithms, 10-fold cross-validation methods were firstly used to determine the optimal threshold values and then were employed to conduct classification for each of the four classification methods with the different feature subset selection algorithms upon the 35 data sets. The results reveal that FAST still outperforms both FCBF and ReliefF for all the four classification methods, Fig. 10 shows the full details. At the same time, Wilcoxon

P.G.P. COLLEGE OF ARTS & SCIENCE NAMAKKAL 637 204

signed ranks tests [75] with □ = 0.05 were performed to confirm the results as advised by Demsar [76]. All the □ values are smaller than 0.05, this indicates that the FAST is significantly better than both FCBF and ReliefF (please refer to Table 9 for details).

TABLE 9: p values of the Wilcoxon tests

Alternative hypothesis	NB	C4.5	IB1	RIPPER
FAST > FCBF	8.94E-07	0.0013	5.08E-05	8.78E-05
FAST > ReliefF	4.37E-07	3.41E-04	4.88E-06	7.20E-06

Note that the optimal θ value can be obtained via the cross-validation method. Unfortunately, it is very time consuming.

5 Conclusion

In this paper, we have presented a novel clustering-based feature subset selection algorithm for high dimensional data. The algorithm involves (i) removing irrelevant features, (ii) constructing a minimum spanning tree from relative ones, and (iii) partitioning the MST and selecting representative features. In the proposed algorithm, a cluster consists of features. Each cluster is treated as a single feature and thus dimensionality is drastically reduced.

We have compared the performance of the proposed algorithm with those of the five well-known feature selection algorithms FCBF, ReliefF, CFS, Consist, and FOCUS-SF on the 35 publicly available image, microarray, and text data from the four different aspects of the proportion of selected features, runtime, classification accuracy of a given classifier, and the Win/Draw/Loss record. Generally, the proposed algorithm obtained the best proportion of selected features, the best runtime, and the best classification accuracy for Naive Bayes, C4.5, and RIPPER, and the second best classification accuracy for IB1. The Win/Draw/Loss records confirmed the conclusions.

We also found that FAST obtains the rank of 1 for microarray data, the rank of 2 for text data, and the rank of 3 for image data in terms of classification accuracy of the four different types of classifiers, and CFS is a good alternative. At the same time, FCBF is a good alternative for image and text data. Moreover, Consist and FOCUS-SF are alternatives for text data.

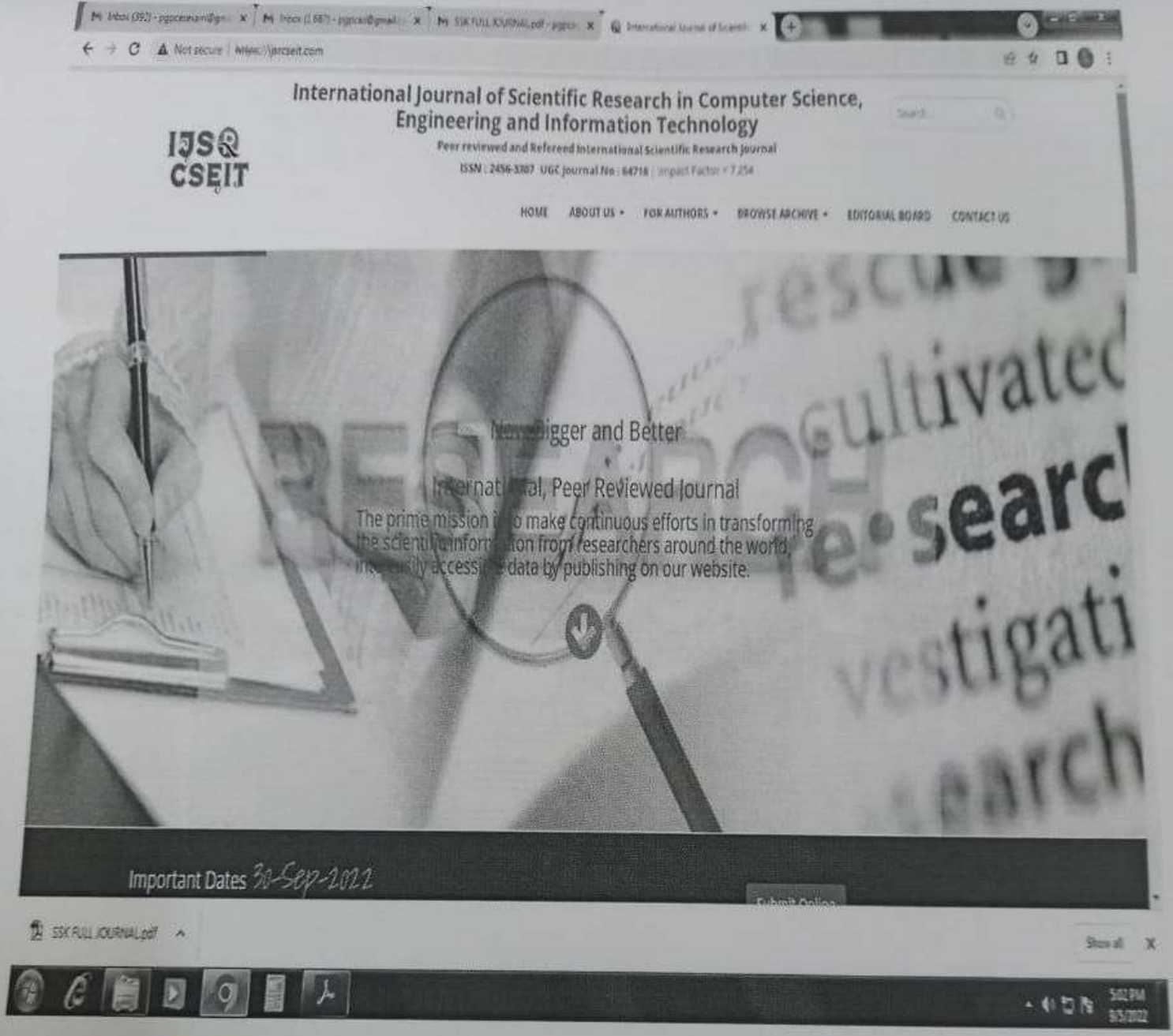
For the future work, we plan to explore different types of correlation measures, and study some formal properties of feature space.

Acknowledgements

The authors would like to the editors and the anonymous reviewers for their insightful and helpful comments and suggestions, which resulted in substantial improvements to this work. This work is supported by the National Natural Science Foundation of China under grant 61070006.

P.G.P. College of Arts & Science Namakkal 637 206

PRINCIPAL
PGP College of Arts and Science
Namakkal



ARTS & SCIENCE COLLEGE OF
NAMAKKAL
637 206

IJSRCSEIT
International Journal of Scientific Research in Computer Science, Engineering and Information Technology
© 2017 IJSRCSEIT | Volume 2 | Issue 4 | ISSN : 2456-3307

Comparative Analysis of Various Advance Resource Reservation Algorithms In Grid Computing Environments

[1]S. Sivakumar, [2]Dr. D. Maruthanayagam
[1]Research Scholar, Sri Vijay Vidyalaya College of Arts & Science, Dharmapuri, Tamilnadu. India
[2] Head/Professor, PG and Research Department of Computer Science, Sri Vijay Vidyalaya College of Arts & Science, Dharmapuri, Tamilnadu, India

ABSTRACT

Grid computing is an emerging paradigm for next generation distributed computing. The Grid is a highly dynamic environment with servers coming on-line, going off-line, and with continuously varying demand from the clients. Advance Reservation is a process of requesting resources for use at a specific time in the future. Common resources whose usage can be reserved or requested are CPUs, memory, disk space and network bandwidth. Reservation for a grid resource solves the above problem by allowing users to gain concurrent access to adequate resources for applications to be executed. Reservation also guarantees the availability of resources to users and applications at the required times. In this paper experiments analyzed and compared Average Waiting Time and Resource Idle Time of four different Reservation techniques such as RSPB, ORR, TARR and DRR.

Keywords: Grid Computing, Resource, Reservation, RSPB, ORR, TARR and DRR

I. INTRODUCTION

Grid computing uses middleware to coordinate dissimilar IT resources across a network, allowing them to function as a virtual whole. The goal of a computing grid, like that of the electrical grid, is to provide users with access to the resources they need, when they need them. Grids address two distinct but related goals: providing remote access to IT assets, and aggregating processing power. The most obvious resource included in a grid is a processor, but grids also include sensors, data-storage systems, applications, and other resources [1].

Grid resource management (administration) plays a substantial role while enabling the sharing and coordinating of resources in grid computing environments. Resource reservation is an important element of the grid resource management. An advance resource reservation is a scheduling object which reserves a group of resources for a particular timeframe for access only by a specified entity or group of entities. Requests of advance reservation with fixed parameters (Start time, End time and resource capability) may be rejected due to instantaneous peaks of resource utilization. Gaps between these peaks are too narrow for additional requests to fit in. As a result, the call acceptance rate of reservation would decrease dramatically, and the performance of resource may be reduced. In fact, many resource reservations for grid applications do not need fixed parameters. In flexible advance reservation, parameters can be modified according to resource status in order to fill the gaps of resources. Particular admission control algorithm for this new type of reservation is also provided. Simulation shows that it can improve performance of resource reservation in terms of both call acceptance rate and resource utilization [2].

The advance resource reservation technique makes it possible to obtain a guaranteed start time for a job, giving several advantages. It makes it possible to meet deadlines for time-critical jobs and to coordinate the job with other activities. The reservation protocol supports two operations: requesting a reservation and releasing a reservation. The reservation request contains the start time and requested duration of the reservation and the required number of CPUs. Upon receiving a reservation request from the broker, the server on the resource

P.G. COLLEGE OF ARTS & SCIENCE NAMAKKAL 637 206

authorizes the requestor. After authorizing the user, the job management plug-in of the server invokes a script to request a reservation from the local scheduler. If the scheduler accepts the request and creates the reservation, the server returns a unique identifier and the start time of the reservation to the broker. If no reservation can be created, a message indicating failure is returned [3]. The server saves the reservation identifier and a copy of the user's proxy for every successful reservation, enabling subsequent authorization of the user who made the reservation. To release a reservation, the broker uploads a release message containing the reservation identifier and the server confirms that the reservation is released. Within larger combined distributed systems, the efficient description of resources plays a significant role in the performance of the computing system. However, distributed resource allocations can also result in lower resource utilization owing to the delay involved in arbitration, the delay in taking up the agreed resources, and the tentative allocation of resources during the arbitration process. Resource oversubscription allows for better utilization of resources in distributed systems, however, this must be done in a controlled way to ensure that the resulting allocations can be fulfilled.

II. ADVANCE RESERVATION ALGORITHMS

A. Reservation Scheduler With Priorities And Benefit Functions (RSPB)

The [4] proposes and evaluates several algorithms for supporting advance reservations in supercomputer scheduling systems. These algorithms improve traditional scheduling algorithms by unifying scheduling traditional tasks from job queues with the reservation requests. These advance reservations allow users to request multiple resources simultaneously from scheduling systems at specific times. However, [4] allocates the "time slots" exclusively, i.e., the resources are not reserved in a shared fashion by multiple clients for the same duration. The applications are assumed to operate on a "best effort" basis and the reservation requests are assumed to have different priority than the applications. These differences in priorities are considered while the reservations and applications are scheduled by the system. A Reservation Scheduler with Priorities and Benefit Functions (RSPB) algorithm schedules reservations while considering the relative priorities of the various reservation requests. In RSPB, each reservation request has an associated benefit function that quantifies the "profit" for the client accrued by the client by securing the resource at the requested level. When the client is willing to negotiate for lower service levels, it could indicate this by providing a benefit function that shows a reduced but positive benefit for lower resource levels. This facility provided by the benefit functions removes the need for negotiations when there is a resource scarcity. The RSPB can be implemented on top of a CPU scheduler such as the DSRT [5] or a QoS enhanced operating system kernel such as QLinux [5].

Reservation Scheduling with Priorities and Benefit Functions: The algorithm is based on the following underlying assumptions. Once a request is granted reservation, a contract for the reservation is signed between the application and the system. The reservation scheduler won't examine the same request more than once except when a QoS violation occurred. This situation should be handled by a higher level QoS broker that engages in renegotiation to establish another reservation or a continuation of the current reservation. Based on the operating policies, the reservation scheduler may find another reservation or the application may operate under best-effort conditions. In this algorithm, each reservation request involves a single resource, i.e., no co-reservation of resources is considered here [6]. Figure 1 shows the outline of the dynamic reservation scheduler. In this scheduler, dynamically arriving requests are collected for a predefined time interval to form a meta-request.

```
t=t0 ;; scheduler start time
Δt ;; inter-schedule time
while (true)
t = t + Δt;
while (current time < t)
get current request R;
add R to Rmeta
if (requested start time of R < t)
t = current time;
endif
endwhile
schedule Rmeta(Rmeta)
endwhile
```

Figure 1: Outline of dynamic reservation scheduler.

COLLEGE OF ARTS & SCIENCE NAMAKKAL 637 206

B. Optimal Resource Reservation

In the ORR (Optimal Resource Reservation) approach the best fetch strategy is considered. During reservation, if the slots requested are empty then they are reserved. The conflict occurs only when the slots are not available. Normally, the reservation denial is done in FCFS approach. In TARR, the free slots are considered and the reservation slots are provided rather than as a single slot. For this purpose, in addition to the proposed start time and finish time, the defer time (DT) is also considered. The defer time is time until which the job can be completed or considered for reservation. In TARR approach, whenever a free slot is available it is allotted as such. TARR necessitates more context switching i.e., whenever a small chunk of time slice is available, then that is reserved which requires more process suspension and resumption. The entity resource can be reserved for a period of time. After the elapse of time the current process in execution need to undergo process switching. The current status of the PCB (Process Control Block) is stored. And the detail on process to be resumed is retrieved. The new process possesses the resource. The state transition or process switching causes additional overhead. Hence in this ORR the slicequeue and select slicequeue are maintained [6].

Slice Queue: The reservation list of a resource maintains the details on resource and also the job which has reserved the respective resource. Figure 2 depicts the resource list with reservation and empty slots.

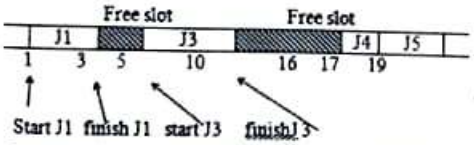


Figure 2: Reservation List maintained by resources.

To find the empty slice initially the reservation list is taken as input. The reservation list consists of the job id which has reserved the resource with its period of reservation i.e., its start time and finish time. The free slots are identified. The difference between the finish time of the previous reservation and the start time of the current reservation is computed. If there exist any time then that free slice is inserted into the slice queue.

Thus the slice queue maintains the free time slices. The Slice queue consists of slice id, the slice start time (SST) and the slice finish time (SFT) of a free slice. The following algorithm inserts the free time slices into the queue.

```
Algorithm
SliceQueue_Insert(reserve_list)
Begin
      front = 0, rear = 0
      for i = 0 to list_size - 1
            timeslice =
      starti+1 - finishi
            if timeslice > 0
      then
            sst =finishi
            sft = starti+1
            slicequeue[rear]=
      {sid,SST,SFT}
            end if
      end for
end
```

While considering the Figure 2, the free slots from 3 to 5 and from 10 to 16 are placed in the slice queue. The Slice queue maintains all the free time slots. The time slots are taken in first free slot available approach as in TARR. The slice queue for Figure 2 is shown in Figure 3. This leads to more context switching which leads to increase in overhead.

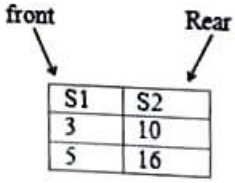


Figure 3: Slice Queue.

Select Slice Queue: After generating the slice queue, the slice is searched for reservation. The slice queue consists of all the free slices. But not all the free slices can be used. Hence, the select slice queue algorithm finds the slice which is more relevant to the required slot. The algorithm considers the free slot and the Defer Time (DT) to fetch the slots [7].

```
Algorithm
selectslicequeue(slicequeue)
begin
      if slicequeue is empty then
            return no_slice
      else
            for i = 0 to
      size(slicequeue)
```




```
        if ( slicequeue.sft <
DT) then
        insert
selectslicequeue(sid,sliceque
ue.sst,
        slicequeue.sft)
        end if
        end for
end if
end
```

The selectslicequeue algorithm selects the slots only when the time slice is within the defer time.

ORR Algorithm: The ORR algorithm finds the optimal time slice from the selectslicequeue. For this the algorithm takes in the job id of the process and the selectslicequeue as input. And it returns the optimal reservation of resource which is explained in following algorithm. The selectslicequeue maintains the time slices that can be reserved. The size function in ORR returns the number of elements in the particular queue. Initially the time required for the job is estimated. It is computed by calculating the difference between the finish time of that job and the start time of the job. Then they found value is set to zero. It is used as a flag variable. If it is left as zero then it means that the reservation is not made possible. Only when it is turned to one the slot is available. The size of the free slice is computed from the selectslicequeue. Since the selectslicequeue maintains the slice start time and slice finish time the difference between the two is computed and maintained in slot variable. In this algorithm if the first slice itself is in required size then it is allocated and it is the optimized allotment as it doesn't require the context switching. Otherwise the slot is allotted and the required time is reduced by the slot value. So that the required time value contains the required time slot after partial reservation. The found value indicates the number of time slices considered for reservation for the particular job id. The found value is compared with the threshold value. If they found is greater than the threshold value then the randomize function is called on the selectslicequeue. This function shuffles the time slices and the time slices are selected. When the numbers of time slices are below the threshold value then the selected slices are assigned for the job [8].

```
Algorithm ORR(JID, SelectSliceQueue)
      begin
            requiredtime = FT - ST
            found = 0
      for i = 1 to size(selectslicequeue)
            slot = selectslicequeue.sft -
      selectslicequeue.sst
      if (slot >= requiredtime && found =
      0) then
            allot(sid,
      selectslicequeue.sst,
      selectslicequeue.sft)
      return
      else
            requiredtime = requiredtime -
      slot
            allot(sid,selectslicequeue.ss
      t,selectslicequeue.sft)
            found = found + 1
      end if
      end for
      if found > T then
            randomize(selectslicequeue)
            ORR(JID, selectslicequeue)
      else
            assignslice(found)
      return
      end if
      end
```

C. Time-Slice based Advance Resource Reservation (TARR)

A new reservation scheme called Time-Slice based Advance Resource Reservation (TARR) is proposed. In this scheme, the reservation is done when the resource is free. If the resource is already reserved during that timeslot then the free the time slices can be used for the reservation. This splits the resource utilization period, i.e., whenever a free time-slice is available the resource is reserved for that duration and the remaining is deferred over a period of time where the free time slice is available. In all the existing approaches only when the resource is available in the specified start time and finish time the reservation is done. Because of this even if the resource is available for short duration than expected then the resource is kept unused. The TARR approach tries to remove this drawback by allowing the usage of time-slices between the existing reservations The Start, finish and defer time for using the resources are given by the user while submitting a job for execution. The start time and finish time are the expected start and finish time for using the resources. Sometimes it is not possible to reserve the resource at the stipulated start and finish time. In such case the reservation can be done until the defer time. Defer time is the time until which the reservation can be postponed [9].



TARR Algorithm

```
Algorithm TARR
      if List is empty then
            no conflict found. Hence
      accept the new reservation.
      else
      for i = 0 to List-Size -1 do
            Put i into templist if one of
      the properties are true
            Startnew ≤ starti&&finishnew≥
      finishi || Startnew ≤ finishi||
      finishnew≤ finishi
      end for

      if templist is empty then
            no conflict found. Hence
      accept this reservation.
      else
            requiredtime = finishnew-
      startnew
            balancereserve = requiredtime
      for i = 1 to n
            timeslice = starti+1 -finishi
      if timeslice> 0 then
            Put into
      slicequeue_insert(id,sst,sft)
      end if
      end for
      while (slicequeue&&balancereserve)
      if sst ≥ Startnew then
            assign new reserve
            currentreserve=sft - sst
            Balancereserve = requiredtime
      -currentreserve
      end if
      end while
      end if
      end if
```

Dynamic Resource Reservation (DRR)

There were various resource reservation schemes available as FCFS (First Come First Served), reservation based on negotiation, TARR (Time Slice based Advanced Resource Reservation), ORR (Optimized Resource Reservation). In all these methods, the reservations done are not checked for utilization at any period of time. But there are chances of unutilized reservation due to network failure, termination of parent process, termination of current process etc., In the DRR (Dynamic Resource Reservation) scheme, the resource is checked for availability. If the resources are available then it is allotted. If the resources are already reserved then it is checked for the reservation requirement at that particular point of time. If the reservation requirement is not required then the current reserved slot is provided to the current process [10].

Slice Queue: The free time slots are maintained in the slicequeue for every resource upto a specified time. Normally, the slicequeue used to have the start time and finish time. Whenever the resource request is made then the availability is checked in this slicequeue. If the time slot is available then it is provided. If the time slot is not available then the DRR algorithm can be used to get the required slice from the slice queue depending upon the possibility. The algorithm DRR shows the proposed reservation scheme. The algorithm takes in the process id, start time (ST), finish time (FT) and defer time (DT) as input.

```
Algorithm DRR (Process_id, ST, FT, DT)
      begin
      If the list is empty then
            No conflict found. Hence
      accept the reservation.
      else
            get_jobid(timeslot)
      if isalive(jobid)
      if isrequire(timeslot)
            return()
      else
            allot(current_jobid,
      timeslot)
      end if
      else
            allot(current_jobid,
      timeslot)
      end if
      end if
      end
```

If the reservation list is empty then it means that the resource is free during the required time slot. Hence the reservation can be done. When reservation is already available during the time slot, then the job can be checked for the availability. The isalive function returns whether the reserved job id is still alive or not. If the reserved job is not alive then the slot is available for the current reservation hence that can be allotted for the current reservation. If the required time slot is reserved then the isrequire function is called which determines whether the reservation made is further required or not. If it is not required then the time slot can be used for the current reservation.

III. PERFORMANCE METRICS

There were various performance metrics that are considered to evaluate the performance of the Reservation algorithms. Here, The average waiting time and Resource Idle Time taken as metrics for evaluation [10][11][12].

A) Average Waiting Time (AWT): The waiting time (WT) of the reservations are computed. Sometimes the resources are not available at the time of reservation requirement. But the resources can be reserved within the deferred time. In that case, the difference between the expected start time and the actual reserved start time is the waiting time.

$$\text{Waiting Time (WT)} = \text{Start}_{reserve} - \text{Start}_{new}$$

The Total Waiting Time (TWT) is computed as the sum of all the waiting time at a specific point of time.

$$\text{Total Waiting Time (TWT)} = \text{WT} \sum_{i=1}^{size}$$

Where size refers to the length of the reservation list at a specific point of time. Then ,

$$\text{AWT} = \text{TWT} / \text{No of Reservations}$$

B) Resource Idle Time (RIT): The resources may be idle even when the reservation request available. This happens when the idle time does not fit into the allocation policy. Thus TARR provides a better allocation policy, as even the time-slices are used for reservation rather than allocating the entire request as a single unit. The RIT is computed by applying the below formula

$$\text{RIT} = \text{Finish}_{previous} - \text{Start}_{current}$$

When there exists a reservation request with a conflict. The total resource idle time is computed by the following equation

$$\text{Total RIT} = \sum_{i=1}^{size} \text{RIT}$$

IV. COMPARATIVE ANALYSIS

To compare the Existing algorithms as RSPB, 0RR, TARR and DRR in Two Grid Environments are considered. The Expected start time (EST),Expected finish time (FT) and Rescheduling time (RT) for 5 jobs fewer than 2 Grid Environment are listed in table 1 and table 2. The table 1 depicts the reservation of Grid Environment 1 based on the four different models with its Average waiting time and Grid Resource idle time. The table 2 depicts the reservation of Grid Environment 2 based on the four different models with its Average waiting time and Grid Resource idle time.

Table 1: Reservation of Grid Environment 1

GRID ENVIRONMENT 1											
Job Allotment	EXPECTED STARTING TIME	EXPECTED FINISHING TIME	Average Waiting Time(AWT)				Grid Resource Idle Time(RIT)				RESCHEDULE TIME
			RSPB	ORR	TARR	DRR	RSPB	ORR	TARR	DRR	
Job1	0.25	7.56	5.41	5.24	4.8	3.69	5.16	4.99	4.55	3.44	7.81
Job2	0.59	8.52	6.71	6.54	6.1	4.99	6.12	5.95	5.51	4.4	9.11
Job3	1.25	9.57	8.42	8.25	7.81	6.7	7.17	7.0	6.56	5.45	10.82
Job4	1.55	10.24	9.39	9.22	8.78	7.67	7.84	7.67	7.23	6.12	11.79
Job5	2.08	10.59	10.27	10.1	9.66	8.55	8.19	8.02	7.58	6.47	12.67

Table 2: Reservation of Grid Environment 2

GRID ENVIRONMENT 2											
Job Allotment	EXPECTED STARTING TIME	EXPECTED FINISHING TIME	Average Waiting Time(AWT)				Grid Resource Idle Time(RIT)				RESCHEDULE TIME
			RSPB	ORR	TARR	DRR	RSPB	ORR	TARR	DRR	
Job1	0.13	6.24	3.97	3.8	3.36	2.25	3.84	3.67	3.23	2.12	6.37
Job2	0.19	7.03	4.82	4.65	4.21	3.1	4.63	4.46	4.02	2.91	7.22

Job3	0.59	7.56	5.75	5.58	5.14	4.03	5.16	4.99	4.55	3.44	8.15
Job4	1.26	8.14	7	6.83	6.39	5.28	5.74	5.57	5.13	4.02	9.4
Job5	1.58	9.07	8.25	8.08	7.64	6.53	6.67	6.5	6.06	4.95	10.65

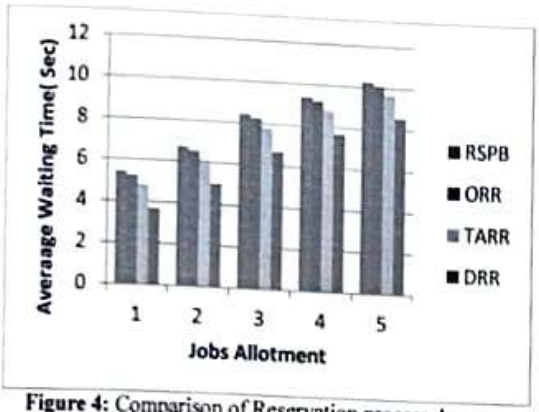


Figure 4: Comparison of Reservation process Average Waiting Time (AWT) in Grid Environment1

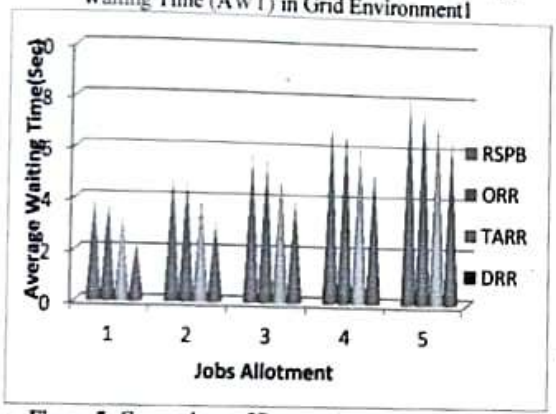


Figure 5: Comparison of Reservation process Average Waiting Time (AWT) in Grid Environment2

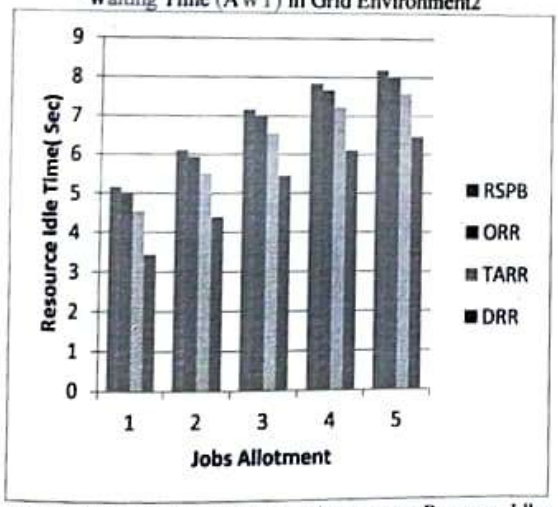


Figure 6: Comparison of Reservation process Resource Idle Time (RIT) in Grid Environment1

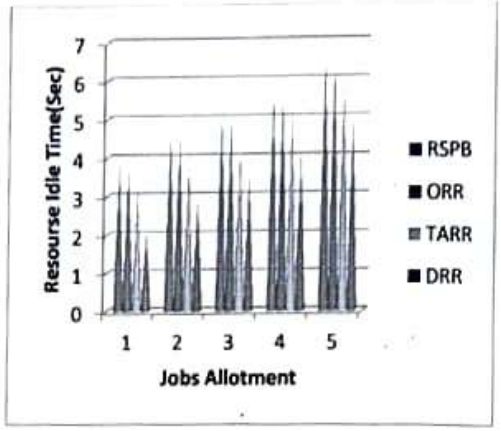


Figure 7: Comparison of Reservation process Resource Idle Time (RIT) in Grid Environment2

V. CONCLUSION

Resource reservation provides a way through which the resources are made readily available for the entire execution of the process. This reduces the waiting time which in turn reduces the execution time also. Two parameters such as average waiting time and resource idle time are considered for evaluation in all the existing reservation techniques. Finally, the existing reservation algorithm DRR provides better result when compared with RSPB, ORR, and TARR reservation algorithms.

VI. REFERENCES

[1]. A. W. Mu'alem and D. G. Feitelson. Utilization, Predictability, Workloads, and User Runtime Estimates in Scheduling the IBM SP2 with Backfilling. IEEE transactions on Parallel and Distributed Systems, 12(6):529{543, 2001}.

[2]. J. MacLaren, editor. Advance Reservations: State of the Art (draft). GWD-I, Global Grid Forum (GGF), June 2003. http://www.ggf.org. 69

[3]. W. Smith, I. Foster, and V. Taylor. Scheduling with advanced reservations. In Proceedings of the International Parallel and Distributed Processing Symposium (IPDPS'00), Cancun, Mexico, May 1{5, 2000}.

COLLEGE OF ARTS & SCIENCE NAMAKKAL

[4]. A. Schill, F. Breiter, and S. Kuhn. Design and evaluation of an advance reservation protocol on top of rsvp. In Proceedings of the IFIP TC6/WG6.2 4th International Conference on roadband Communications (BC'98), Stuttgart, Germany, April 1998.

[5]. J. MacLaren (Ed.), Advance Reservations: State of the Art (draft), GWD-I, Global Grid Forum (GGF), June 2003 http: www.ggf.org

[6]. A. Roy and V. Sander, Advance Reservation API, GFD-E.5, Scheduling Working Group, Global Grid Forum (GGF), May 2002.

[7]. H. Chu and K. Nahrstedt, "A Soft Real Time Scheduling Server in UNIX Operating System," *European Workshop on Interactive Distributed Multimedia Systems and Telecommunication Services (IDMS '97)*, Sep. 1997.

[8]. P. Goyal, X. Guo, and H. M. Vin, "A Hierarchical CPU Scheduler for Multimedia Operating Systems," *2nd Symposium on Operating System Design and Implementation (OSDI '96)*, Oct. 1996, pp. 107-122.

[9]. W. Smith, I. Foster, and V. Taylor, "Scheduling with Advanced Reservations," *International Parallel and Distributed Processing Symposium (IPDPS '00)*, May 2000.

[10]. **S.Nirmala Devi and A.Pethalakshmi** ORR: Optimal Resource Reservation In Grid Computing Environments, Indian Journal of Science and Technology, *Vol 9(48), DOI: 10.17485/ijst/2016/v9i48/102500, December 2016*

[11]. **S.Nirmala Devi and A.Pethalakshmi, "**DRR: Dynamic Resource Reservation in Grid Computing", *International Journal of Computer Applications (0975 – 8887) Volume 159 – No 6, February 2017* 27

[12]. **S.Nirmala Devi and A.Pethalakshmi,** TARR: Time Slice based Advance Resource Reservation in Grid Computing Environments, International Journal of Computational Intelligence and Informatics, Vol. 6: No. 1, June 2016

VII. AUTHORS PROFILE

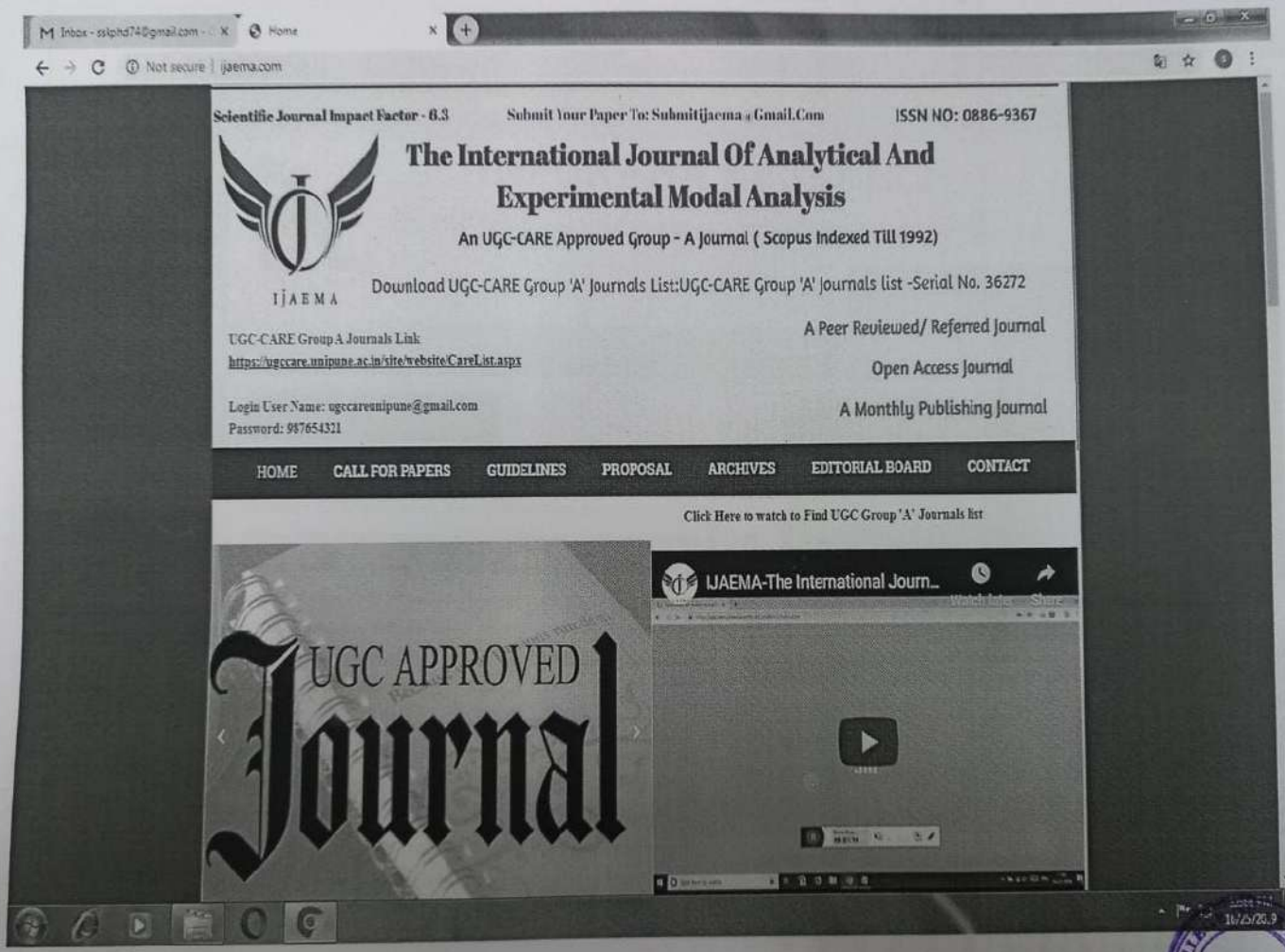


S. Sivakumar received his M.Phil Degree from Alagappa University, Karaikudi in the year 2005. He has received his M.C.A Degree from Periyar University, Salem in the year 2001. He is working as Assistant Professor, Department of Computer Science, PGP College of Arts & Science, Namakkal, Tamilnadu, India. He is pursuing his Ph.D Degree at at Sri Vijay Vidyalaya College of Arts & Science (Affiliated Periyar University),Dharmapuri, Tamilnadu, India. His areas of interest include Grid Computing and Data Mining.



Dr.D.Maruthanayagam received his Ph.D Degree from Manonmanium Sundaranar University, Tirunelveli in the year 2014. He has received his M.Phil, Degree from Bharathidasan University, Trichy in the year 2005. He has received his M.C.A Degree from Madras University, Chennai in the year 2000. He is working as HOD Cum Professor, PG & Research Department of Computer Science, Sri Vijay Vidyalaya College of Arts & Science, Dharmapuri, Tamilnadu, India. He has 15 years of experience in academic field. He has published 4 books, 23 International Journal papers and 28 papers in National and International Conferences so far. His areas of interest include Computer Networks, Grid Computing, Cloud Computing and Mobile Computing.

PRINCIPAL
PGP College of Arts and Science
Namakkal


Inbox - sslphd74@gmail.com
Home
Not secure | ijaema.com
Scientific Journal Impact Factor - 6.3
Submit Your Paper To: Submitijaema@Gmail.Com
ISSN NO: 0886-9367
The International Journal Of Analytical And Experimental Modal Analysis
An UGC-CARE Approved Group - A Journal (Scopus Indexed Till 1992)
IJAEMA
Download UGC-CARE Group 'A' Journals List:UGC-CARE Group 'A' Journals list -Serial No. 36272
UGC-CARE Group A Journals Link
https://ugccare.unipune.ac.in/site/website/CareList.aspx
Login User Name: ugccareunipune@gmail.com
Password: 987654321
A Peer Reviewed/ Referred Journal
Open Access Journal
A Monthly Publishing Journal
HOME
CALL FOR PAPERS
GUIDELINES
PROPOSAL
ARCHIVES
EDITORIAL BOARD
CONTACT
Click Here to watch to Find UGC Group 'A' Journals list
UGC APPROVED
Journal
IJAEMA-The International Journ...

ANALYSIS OF PROPOSED ADVANCED DYNAMIC RESOURCE RESERVATION (ADRR) TECHNIQUES FOR GRID COMPUTING

[1]S.Sivakumar, [2]Dr. D. Maruthanayagam
[1]Research Scholar, Sri Vijay Vidyalaya College of Arts & Science, Dharmapuri, Tamilnadu, India
[2]Head/Professor, PG and Research Department of Computer Science, Sri Vijay Vidyalaya College of Arts & Science, Dharmapuri, Tamilnadu, India

Abstract: Grid is a collection of resources owned by multiple organizations. Grid has the ability to combine multiple, heterogeneous, distributed, and separately managed data resources. Due to complexity in a Grid arising from heterogeneous nature of these resources and the dynamically changing demand and supply of resources there is a strong need to manage Grid users, jobs, resources, Grid information and related updates, implementation of allocation policies, reservations and reservation related policies. In this paper, ***proposed an Advanced Dynamic Resource Reservation (ADRR) framework for grid computing.*** The imitation results establish that the proposed grid resources reservation technology performs better than existing techniques.

Keywords: Grid Computing, Dynamic Resource Reservation, Optimal Resource Reservation, Job handler, Makespan and tasks management

I. INTRODUCTION

Grid computing systems use geographically dispersed and distributive owned resources for producing a broad category of services for different applications [1]. One of the key factors in Grid computing systems is resource management with quality of service limitations. The quality of service limitations talks that submitted tasks should be made by the Grid in a timely fashion while delivering at least a particular level of service for the duration of execution [2]. Because the Grid is a highly "dynamic" system due to the entry and exit of tasks and resources, it is important to perform places of resources to assure their availability to meet the requirements of the different tasks. There are various resource reservation schemes available as FCFS [3], priority based reservation, dynamic resource reservation, time slice based reservation, and optimal resource reservation etc [1, 5]. All these reservations on ensuring the availability of resources when required with its own pros and cons. The work of this paper is to develop an Advanced Dynamic Resource Reservation (ADRR) technique which is empowered with all the desired capabilities which can provide solutions for the identified problem areas in a grid scenario. The proposed framework and its policies are different from other existing techniques in terms following unique features:

- To ***dynamically resolve job priorities*** of users on the basis of their preferences, history of timely payments, amount of business given to the grid, paying capacity etc
- To ***perform advanced reservation of resources*** and at the same time use quota based policy to prevent starvation of jobs due to long jobs with high priority
- Address the limitation of the deadlock avoidance techniques by proposing a dynamic budget which eliminates the need of prior knowledge of the resource requirement of any process, the budget is adjusted dynamically to cater the need of the process
- To ***speed up the allocation process*** by minimizing the searching complexity using energy aware searching engine
- To make the system more reliable to the changing environment by considering the ***dynamicity of the resources***
- To ***assign best resource*** to job by considering the diversity in the resource behavior
- To assure the successful allocation of job by ranking the resources and ***rescheduling the ranked resources***
- This helped in providing quality of service, fulfillment of commitments and ***better revenue generation***
- Allows service providers to get best revenues and vice a versa for best offers for consumers
- Enforces a Service Level Agreement with penalties and rewards where execution of deals and settlements work under a constitutional framework
- Allows reservation of resources and provides compensations in the event of failures

To prove the usability of a simulation test bench was made using the GridSim and successful simulation was completed [4]. The experimental results showed a significant increase in terms of the **average waiting time, resource utilization time, average turnaround time,** percentage of successful jobs and **makespan** as compared to the already existing Grid reservation techniques.

II. METHODOLOGY

A. Dynamic Resource Reservation (DRR)

The computationally hazardous problems require deploying the complexity in the grid environment for the more initial execution. This can only be achieved through resource sharing. To assure the availability of resources at the required time, the resources are reserved in advance. The available advanced resource reservation schemes are priority based reservation, time slice-based advance resource reservation, and optimized resource reservation. In all the reservations, it is expected that the reservations have done are used, but there are some positions where the appropriated resources are put idle due to some network failure, end of the parent process, end of the current process, etc.,. In this dynamic resource

NAMAKKAL

reservation **(DRR)** scheme [6], analyzes the reservations which are unutilized and allocates the unutilized reservations to the current requirements and these unutilized reservations can be used for the current reservation. In the grid environment, there are several computational nodes. These computational nodes used to have resources associated with it. The Local Resource Manager **(LRM)** at the computational node checks the features about the resources and manages the resources. Once the computational node becomes the participating node in the grid, then the resources associated with that computational node move to the available state [7]. The available state means that the resources are available for reservation or use. When the process requires the resources immediately then it can use, hence the resource moves to the in-use state. When the process requires the resources after some time, then the resources can be reserved during that time slot. For that time slot, only the resource would be in reserve state [8]. The resources needed are reserved for prospective use. There are some abnormalities like a) termination of parent process may lead to the termination of child process b) network failure c) suspension of current process d) blocking of current process etc,. After having the resources due to these abnormalities, the place may not be required but these abnormalities.

DRR Algorithm

The algorithm DRR shows the proposed reservation scheme. The algorithm takes in the process id, start time (ST), finish time (FT) and defer time (DT) as input.

```
Algorithm DRR ( process_id, ST, FT, DT)
begin
If the list is empty then
        No conflict found. Hence accept the reservation.
else
        get_jobid(timeslot)
if isalive(jobid)
if isrequire(timeslot)
        return()
else
        allot(current_jobid, timeslot)
end if
else
        allot(current_jobid, timeslot)
end if
end if
end
```

If the reservation list is empty then it means that the resource is free during the required time slot. Hence the reservation can be done. When reservation is already available during the time slot, then the job can be checked for the availability. The islive function returns whether the reserved job id is still ***alive or not***. If the reserved job is not active then the slot is available for the current reservation so that it can be given for the current reservation. If the expected time slot is reserved then the isrequire function is called which decides whether the reservation made is more ***required or not.*** If it is not required then the time slot can be used for the current reservation.

B. Optimal Resource Reservation (ORR)

The **ORR** algorithm finds the optimal time slice from the selectslicequeue. For this, the algorithm takes in the job id of the process and the selectslicequeue as input. And it returns the optimal reservation of resources. The selectslicequeue ***maintains the time slots*** that can be maintained. The size function in ORR returns the number of elements in the particular queue. Initially, the time required for the job is estimated [9]. It is computed by calculating the difference between the finish time of that job and the start time of the job. Then they found value is set to zero. It is used as a flag variable. If it is left as zero then it means that the reservation is not made possible. Only when it is turned to one the slot is available. The scope of the free slice is computed from the selectslicequeue. Since the selectslicequeue maintains the slice start time and slice finish time the difference between the two is computed and maintained in slot variable. In this algorithm if the first slice it is in required size then it is allocated and it is the optimized allotment as it doesn't require the context switching [10]. Otherwise the slot is allotted and the required time is reduced by the slot value. So that the required time value contains the required time slot after partial reservation. The found value indicates the number of time slices considered for reservation for the particular job id. The found value is compared with the threshold value [11]. If they found is greater than the threshold value then the randomize function is called on the selectslicequeue. This function shuffles the time slices and the time slices are selected. When the numbers of ***time slices are below the threshold value then*** the selected slices are ***assigned for the job.***

```
Algorithm ORR(JID, SelectSliceQueue)
begin
        requiredtime = FT – ST
        found = 0
        for i = 1 to size(selectslicequeue)
                slot = selectslicequeue.sft -
        selectslicequeue.sst
        if (slot >= requiredtime && found = 0) then
                allot(sid, selectslicequeue.sst,
        selectslicequeue.sft)
                return
        else
                requiredtime = requiredtime – slot
                allot(sid,selectslicequeue.sst,selectsliceque
        ue.sft)
                found = found + 1
end if
end for
if found > T then
        randomize(selectslicequeue)
        ORR(JID, selectslicequeue)
else
        assignslice(found)
return
end if
end
```

III. PROPOSED METHOD

The **Advanced Dynamic Resource Reservation Model (ADRR)** is shown in Figure 1. When the user submits the job to the job handler, job handler goes through **five** states. In the **first** state, users are sorted according to their priorities. In the **second** state, the job handler identifies the job as new or mature and forwards the job to the Dynamic Priority Resolution **(DPR).** When the job handler recognizes the job as new, it forwards the new job with user requirements to the DPR. When the job handler recognizes the job as mature, it

forwards the mature job and the matched job_id to the DPR. The DPR queues the new job in the new_job queue and the mature job in the mature_job queue. In the **third** state, the jobs of each user are sorted based on the lengths of jobs. In the **fourth** state, the jobs of various users are sorted in accordance with the job's priority based on job length and on priority of the user to which the jobs belong. This is done by Dynamic Priority Resolution (DPR) technique. Gridlet Sorting Policy **(GSP)** is based on a predefined value decides that how many jobs of a given user are to be scheduled and send to reservation. Finally in the **last** state, jobs are placed in a queue called **Gridlet queue** from where they are sent to resource analyst. The resource analyst comprises of two components viz. User Resource Information **(URI)** and Rank List Unit **(RLU)**. The User Resource Information **(URI)** receives the new job with the user requirements from the job handler and the Rank List Unit **(RLU)** receives the mature job with the matched Job_id from the job handler. The User Resource Information (URI) maintains Resource Information Table and the Rank List Unit maintains Rank_List Table. For mature jobs, the Rank List Unit (RLU) gets the rank_list of the united job_id from the rank_List table and forwards the mature job with the rank_list to the resource handler for allocation. For new jobs, the User Resource Information (URI) performs the preliminary selection of resources by considering the static parameter (Resource name, Resource location, Resource CPU type, Resource OS, and Memory capacity) resource type of resources. The resource handler proposes an initial budget of resources to be given to each new process. This budget is initialized with no prior knowledge of the process resource requirement rather on the current request made by it. However, this budget is updated to accommodate the resource requests made by a process. Thus, every time the process makes a new resource request within the budget allotment is done using available resources and reservation pool. However, if the requested resources are beyond the budget granted to a process then the budget is modified to accommodate the new request. The resources capabilities selected in the preliminary selection and the job with user requirements is forwarded to the Resource Search Engine **(RSE).** The Resource Search Engine (RSE) prepares a **new rank_list** for the new job and forwards the job and the new rank_list to the resource handler for allocation.

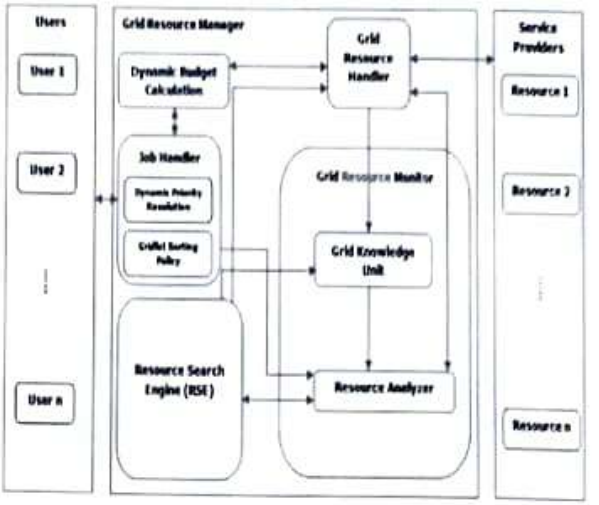


Figure 1: ADRR Framework

A. Grid Resource Manager

The Grid manager is responsible for managing all grid activities. It is an **interface between the user and the service provider.** It has job handler, grid resource handler, resource search engine, dynamic budget calculation and grid resource monitor.

1. Job handler

The functions of the job handler are, when the user wants to register itself, the user sends the user_registration message to the job handler. The information field contains the ***metadata*** given by the user at the time of registration. The job handler receives the user_registration message. It assigns the user a unique user_id and sends the user_ack message to the user as an acknowledgement. The user receives the user_id and utilizes the user_id to submit the job to the job handler. The user submits the job by sending the job_submission message to the job handler. The job_submission message includes the requirements of the user and the executable data. After the user submits the job, the job handler assigns the submitted job a unique job_id. The job handler sends the user the assigned job_id as an acknowledgement for the received job. The job handler maintains the job table. The job handler stores the user requirements of the job along with the user_name, user_id, job_name, job_id, arrival date of the job, and etc., in the job table.

Whenever a user enters grid, it is enlisted by the proposed algorithm in a queue called User List referred by job table. The users from the User List are sorted based on their priority and are located in a queue called User queue. Thereafter jobs that are generated by various users are ordered on the basis of their lengths and are placed in another queue named Gridlet List referred by job table. The jobs are prioritized again. The proposed algorithm prioritizes them by using a Gridlet Sorting policy and Dynamic Priority Resolution (DPR) technique. The sorting policy decides on the number of jobs of each user to be prioritized and finally to be sent for reservation. Thus the Sorting policy ensures that jobs of various users are entertained in a way so as to avoid starvation among the jobs. On the other hand, the DPR

technique is used to resolve the priority of jobs by considering the parameters associated with jobs priority. The DPR therefore is consequential in determining the priority of incoming jobs having higher user priority and higher job priority based on the job length. The proposed algorithm finally stores prioritized jobs in a queue called Gridlet queue. The jobs thus scheduled by proposed algorithm are submitted to resource allocation.

The priority work done by ***proposed algorithm*** can be broadly ***divided into two phases*** namely User Priority Phase and Gridlet Priority Phase. The first phase deals with the user priority whereas the second phase takes care of job priority of the jobs.

(i) **User Priority Phase**

These users can have one or multiple jobs. In this phase, first the users are sorted and then the jobs of each user are sorted. The users are sorted in decreasing order of their priorities using User Sorting Policy. If the users have equal priorities they are arranged on ***first come first*** basis else insertion sort technique is used. Once the users have been sorted, jobs of each user are sorted on the basis of their lengths. The jobs are sorted using insertion sort technique. The jobs thus sorted are placed in the **Gridlet List**. This technique is used as it ***saves time and therefore is more efficient.*** This is due to the fact that insertion sort has complexity of O(n) which is comparatively less than the time complexities O(nlog(n)) and O(n2) of other sorting methods in the best or worst case respectively.

(ii) **Gridlet Priority Phase**

In this phase, jobs already sorted in User priority phase are further prioritized based on two criteria. This criterion can either be UserPriority or job length or both referred to as UserHighPriority **(UHP)** phase and UserJobPriority **(UJP)** phase respectively. DPR technique decides whether jobs will be sorted in UHP or UJP phase depending on the difference in priority of the jobs (that is UserPriority). DPR technique takes two users at a time that are competing for reservation and compares their UserPriority. If the difference between UserPriority is larger than significant difference SD, only the jobs belonging to the **higher priority user are sorted**. The jobs belonging to lower priority user are queued up. These jobs are treated as pending jobs which will further participate in the next sorting process in the User priority phase. Out of these sorted jobs of a higher priority user, only a predefined number of **jobs are considered for reservation** (as ***decided by pre-defined function***) and rest are discarded. This is referred to as **UHP** phase. Whereas if the difference between the UserPriority of the two users competing for reservation is less than a significant difference SD, the priority of jobs is evaluated on the basis of their job length and UserPriority. SD ensures that competing jobs are well differentiated among themselves. As the jobs keep arriving, the sorting process is repeated and the pending jobs of lower priority users are allowed to participate again and hence they are prevented from getting starved. This phase is known UserJobPriority phase.

(iii) **Gridlet Sorting Policy**

The sorting technique used to sort the jobs in the above phases is decided by **GSP**. The GSP uses shortest first job technique for sorting the jobs of various users. This policy also uses a pre-defined function in UHP or UJP phase to decide as to how many jobs of high priority user are to be considered for reservation. The policy prevents all the jobs of high priority user from getting entertained and therefore avoids starvation of jobs of low priority users. The policy takes this decision on the ***basis of a pre-defined value***.

- ✓ Start.
- ✓ **Create a UserList** and add users to this list as users arrive and join the grid.
- ✓ **Sort the users in the UserList** based on assigned UserPriority using insertion sort following UserSortingPolicy.
- ✓ **Create a Gridletlist** and insert Gridlets in this list according to their UserPriority such that all Gridlets of each user are placed in a sequence.
- ✓ Sort the Gridlets of various users joined.
- ✓ Dynamic Priority Resolution **(DPR)** is calculated at runtime by using
  DPR = User[i].priority-User [i+1].priority
- ✓ Compare DPR with SD which is significant difference between UserPriority.
  If (DPR>SD)
  UserHighPriority (UHP) phase: Sort the Gridlets of each user according to shortest order and place into a user's Gridlet queue. Consider only N number of shortest jobs of higher priority user to be ***sent for reservation schedule as decided by GSP.***
  Else
  UserJobPriority (UJP) phase: Sort the Gridlets of users according to GSP, taking into account the UserPriority of both the users which being compared, are placed into a queue. This leads to Gridlets from both the users in the Gridlet list.
- ✓ If (new user)
  Go to step 2
- ✓ If (new Gridlet)
  Go to step 4
- ✓ Stop

After the dynamic priority resolution done the result submits to the job handler, the job handler ***verifies the Gridlet queue*** to know whether the submitted job has been before processed, by calculating the community Index *SI* of the submitted job with all jobs in the job table whose time of arrival is less than Δt (where **Δt is the time interval** at which the resource's dynamic and behavioral parameters are updated in the resource analyst by the grid knowledge unit). The similarity index *SI* for each submitted job is calculated using the Equation 1.

$$SI = \frac{2n_{xy}}{(n_x + n_y)} \quad \text{----- (1)}$$

Where,

n_{xy} is the number of parameters matched with the job in the job table.

n_x is the number of parameters of the job in the job table

n_y is the number of parameters of the submitted job

If the submitted job's similarity index *SI* is equal to 1 concerning a particular job in the job table, the job handler identifies the submitted job as 'mature'. The job handler then sends the job to the resource analyst by sending the job_description message. If the submitted job's similarity index *SI* is not equal to 1 with respect to a particular job in

the job table, the job handler identifies the job as 'new'. The job handler then sends the job to the resource analyst by sending the job_description message for analyze the initial budget values.

When the user wants to know the situation of the submitted job, the user sends a status_request message to the job handler to retrieve the situation of the submitted job. The job handler receives the status_request message from the user. The job handler forwards the status_request message to the resource handler. The resource handler fetches the status of the submitted job from the resource table in the resource handler and sends the status_ response message to the job handler. The job handler forwards the status_response message to the user.

2. Resource handler

The functions of the resource handler are, when the service provider wants to register itself with the grid, the service provider sends a service provider_registration message to the resource handler. The resource handler receives the service provider_registration message. It assigns the service provider a unique service provider_id and sends the service provider_ack message to the service provider as an acknowledgement. The service provider receives the service provider_id and uses the service provider_id to register the resource with the **resource analyst** through the resource handler. The service provider registers the resource capabilities (static and dynamic parameter values) with the resource analyst through resource handler by sending the resource_registration message to the resource handler. The resource handler receives the resource capabilities from the service provider. The resource handler assigns a unique resource_id to the registered resource and sends the resource_registration_ack message to the service provider as an acknowledgement. The resource handler forwards the registered resource's capabilities to the resource analyst by sending the resource_submission message to the resource analyst. The ***resource handler maintains a resource table***. For each newly submitted job, the ***resource search engine*** calculates a rank_list. The resource search engine then sends the rank_list to the resource handler. The resource handler allocates the highly ranked resource in the rank_list to the job. The resource handler stores the rank_list in the resource table for rescheduling of resources using initial budget in case of resource/job failures. The resource handler stores the rank_list, job status and the resource status in the resource table.

3. Dynamic budget calculation using threshold

The assumption that the resource requirement is known in advance is serious limitation of most of the deadlock avoidance techniques as this estimation has considerable overhead. The ***present work used a dynamic budget technique*** using threshold to overcome the limitation of existing technique of assuming that the maximum resources required by each process is recognized in advance.

The **resource handler proposes an initial budget of resources** to be given to each new process. This budget is initialized with no prior knowledge of the process resource requirement rather on the current request made by it. However, this budget is updated to accommodate the resource requests made by a process. The safety sequence test ensures that the system is deadlock free with the proposed budget. Thus, every time the process makes a new resource request within the budget allotment is done using available resources and reservation pool. However, if the requested resources are beyond the budget granted to a process then the budget is modified to accommodate the new request. To ensure the deadlock Free State, the safety sequence is estimated. If the system is safe the requested resources are granted. However, if the safety sequence does not exist the process state is stored (check pointed) and queued in the pending state with its budget updated to the actual resource request. This process may be aborted to prevent the hold and wait condition which may lead to a deadlock. However, this can be postponed till some process requests for the resources held by this pending process. This will reduce the repercussions of over budgeting.

Begin

1. Initialize Threshold_Value[y] =Reserve[y] =[[Request[x][y] ∀x=1,2…n], 0]∀ y=1, 2, …m
2. Initialize Budget_Value[x][y]= Allocation [x][y] = Need[x][y]= {0}∀x=1,2…n and ∀y=1, 2, …m
3. Available[y]= Available[y]-Reserve[y] ∀ y=1, 2 …m
4. For (Request[x][y] by a process Pi)

Do

A. If Request[x][y]>Need[x][y] for any y = 1, 2, … m

I. Budget_Value[x][y] = Allocation[x][y] + Request[x][y]+ Threshold_Value[x][y]

II. If Safety Sequence exists

i. Accept process P_x

ii. If (Request[x][y]<=Available[x][y])

a. Allocate (Allocation, Request, Available, 0)

Else

b. Allocate (Allocation, Need, Available, Reserve)

iii. Request[x][y] ={0}

Else

iv. Save the status and insert the process Pi in pending queue

v. Budget_Value[x][y] =Allocation[x][y] + Request[x][y]

Else

B. If (Request[x][y]<=Need[x][y] && Request[x][y]<=Available[x][y])

I. Allocate (Allocation, Request, Available, 0)

II. Request[x][y] ={0}

Else

I. Allocate (Allocation, Need, Available, Reserve)

II. Request[x][y] ={0}

5. When a Process completes and releases resources.

End

Allocate (Allocation, To_Allocate, Available, Reserve)

I. For (y=1 to m)

a. Available[y] =Available[y] + Reserve[y]

b. Available[y] =Available[y] – To_Allocate[x][y]

c. Allocation[x][y] = Allocation[x][y] + To_Allocate[x][y]

d. Need[x][y] = Budget[x][y] – Allocation[x][y]

e. Reserve[y] = min (Available[y], Threshold[y])

f. Available[y] =Available[y]-Reserve[y]

End

4. Resource Search Engine (RSE)

This is the **core part of the proposed algorithm.** The primary function of the resource search engine is to ***match the user requirements of the submitted job with the resource capabilities.*** The resource analyst performs the preliminary selection of resources using the static parameter viz. resource type and forwards the selected resource's capabilities and the submitted job with user requirements to the resource search engine. The functions of the resource search engine are,

- ✓ Filter resources using Bloom filer method
- ✓ Static parameters matching using assignment method
- ✓ Dynamic resource matching using correlation method
- ✓ Rank_list calculation
- ✓ Behavioral parameters (Hit rate and failure rate) updation.

1. The resources capabilities selected in the preliminary selection and the job with user requirements is forwarded to the Resource Search Engine (RSE) from resource analyzer, local grid information service extracts positions from them. On this basis, positions in counting Bloom filter themselves; perform the trend of resources inquiry as follows: if counter value is 0 at least in one position in Bloom filter, requested resources do not exist in local grid. If counter values of none of these positions in Bloom filter is 0, then string codes pertaining to positions 1st to K-1th are created as stated previously[1] and the list connected to position Kth in Bloom filter is searched according to string codes. If targeted member is found on the list, then the list of identifiers of similar resources registered in this member is sent along with task's identifier to user. If the list is empty and/or is not but does not contain targeted member, then false positive are detected, indicating that no requested resource exists in local grid.

```
Receive (index , id) from user ;
bloom_index= extract(index); j=0; str=null;
(user_id , job_id) = extract(id);
for i=0 to k-1 do
        j=bloom_index[i];
        if bloomfilter[j].counter==0 then
                send (index , id, RegionalGIS_id) to GIS;
                return;
        else if i<k-1 then str=str+'j';
        end if
end for
LocalResourcelist=search( bloomfilter[j].list , str);
If LocalResourcelist ==null then
        Preliminary selection of resources using the static
parameter by assignment method;
return;
else
send (LocalResourcelist, job_id) to user;
```

2. The resource search engine also uses the ***assignment method to match the job's*** static parameter values with the resource's static parameter values. The static parameters are Resource name, Resource location, Resource CPU type, and Resource OS and Memory capacity. Assignment method is used for the optimal assignment of a static parameter to a resource to ensure maximum efficiency. For each submitted job, the resource search engine computes a relative parameter match value (C_{isk}) by comparing the job's static parameters and the preliminarily selected resource's static parameters.

$$C_{isk} = \begin{cases} 1 & \text{if } X_{ik} - R_{sk} \\ X_{ik} - R_{sk} & \text{otherwise} \end{cases}$$

X_{ik} Represents **job parameters**

R_{sk} Represents **resource parameters**

3. The resource search engine uses the correlation method to match the job's dynamic and behavioral parameter values with the resource's dynamic and behavioral parameter values. Correlation method is used to find the correlation between the dynamic and behavioral parameters of the submitted job and the resource. The dynamic parameters are Hard disk availability, Economic state, Dedication rate, Resource budget and Deadline. The behavioral parameters are Hit rate, Success rate, Failure rate and Recovery time.

The correlation of any resource R_s with the job X_i of the ith user is given in below equation

$$R_s = \frac{k\sum_{k=1}^{n} X_{ik}R_{sk} - \sum_{k=1}^{n} X_{ik} \cdot \sum_{k=1}^{n} X_{ik}R_{sk}}{\sqrt{(k\sum_{k=1}^{n}(X_{ik})^2 - (\sum_{k=1}^{n} X_{ik})^2) \cdot (k\sum_{k=1}^{n}(R_{sk})^2 - (\sum_{k=1}^{n} R_{sk})^2)}}$$

Where ***n is number of dynamic and behavioral parameters.***

The resources are ranked according to the correlated value of the resource parameter with the job parameter. The resource whose correlated value is almost equal to one is given the most leading rank.

4. The rank values are obtained for each dimensions viz. static, dynamic and behavioral using assignment method and correlation method. The resource search engine finally calculates the rank_list for the submitted job using measures of dispersion. In case of un normalized ranks, priority is given to the highly ranked resource in the first dimension since the first dimension matching considers the static weighted parameters. The three dimensional Matchmaking engine forwards the rank_list and the submitted job to the resource handler for allocation. The **rank_list is also stored in the resource repository table** of the resource analyst.

5. The resource search engine finds for each resource, the number of occurrences of the resource in the rank_list and the number of occurrences of a resource in the ***three dimensional matchmaking engine and calculates the hit rate for every Δt_i time*** and updates the calculated hit rate at every Δt time with the grid knowledge unit by sending the hit_rate_update message. The failure rate of a resource is updated in the grid knowledge unit by the resource search engine. The failure rate of a resource is updated whenever the resource is rejected in the rank_list the resource occurs in the resource search engine and the resource search engine updates the failure rate of a resource in the grid knowledge unit by sending the failure_rate_update message to the grid knowledge unit.

5. Resource Monitor

The resource director monitors the resources in the network site in the resource handler. It carries two components. They are Resource analyst and Grid knowledge unit.

1. Resource analyst

Resource analyst is the central part of the matchmaking architecture. The functions of the resource analyst are Resource repository table maintenance and Preliminary resource selection.

Resource repository table maintenance: Every service provider registers the static and dynamic parameter values of its resources in the resource repository table through resource

handler. The resource analyst stores the resources' static, dynamic and behavioral parameter values along with the resource_id and the serviceprovider_id in the resource repository table. Initially the resource search engine sets the values of the behavioral parameters like success rate, Hit rate, Failure rate of each resource to 1.0, and the Recovery time to 0 in the resource repository table. The service provider updates the dynamic parameters of the registered resources at every Δt time in the resource repository table. The knowledge unit updates the behavioral parameters of the registered resources at every Δt time in the resource repository table.

Preliminary resource selection: The resource analyst performs the preliminary resource selection by considering the static parameter. When the user submits a new job, the resource interpreter performs the preliminary selection of resources by reflecting the first static parameter. The resource analyst selects all the resources of that particular resource type. The resource analyst then forwards the three-dimensional parameter values of the chosen resources and the submitted job along with the user requirements to the resource search engine for rank_list calculation.

2. Grid Knowledge Unit

The grid knowledge unit receives the information about the history of behavior of resources in the resource pool from the resource search engine and the resource handler. It receives the values of resources for success rate calculation and recovery time profiles of resources for recovery time calculation from the resource handler. ***It takes the hit rate of a resource at every Δt1 time*** and values of resources for failure rate calculation from the resource search engine. The ***network knowledge system predicts (guess) the hit rate, success rate, recovery time and failure rate for each resource*** for the following matchmaking a cycle based upon its previous behavior with the jobs. It also updates the predicted values of success rate, hit rate, failure rate and recovery time for each resource in the resource repository table of resource analyst at every Δt time interval. It maintains the **behavior parameter table** and stores the predicted success rate, Hit rate, Failure rate and Recovery time of the resources in it.

IV. SIMULATION ENVIRONMENT AND RESULTS

4.1 Test Bed

The algorithms for comparison are implemented on a machine based on Intel(R) Core (TM) 2 Duo CPU, GB HDD and RAM of 512 MB on Microsoft Windows XP. The experiments are performed on a **simulated grid environment provided by GridSim 5.2.**

The recreation environment consists of 10 resources. These 10 resources have 47 processing environments in total having different processing capabilities in terms of Millions of Instructions per Second **(MIPS).** However processing environments belonging to a particular resource have same processes capabilities. For case one of the resources may have five processing environments with the processing capability of 417 MIPS. Further, it is assumed that there are 50 users with 100 jobs each. These 5000 jobs may join the grid simultaneously and request for reserving the resource. As the number of resources is far less than the number of jobs submitting them, it is imperative that not all the jobs will get the resource reservation.

There are various performance metrics that are considered to evaluate the performance of the proposed ADRR algorithm. The **average waiting time, resource utilization time, average turnaround time, percentage of successful jobs and makespan** are taken as metrics for evaluation.

Average Turnaround Time: The effect of process load on the average turnaround time can be seen in the figure 2.The increase in process load implies more processes in the system, hence higher contention for the resources. Higher contention may lead to more frequent deadlocks if not managed properly.

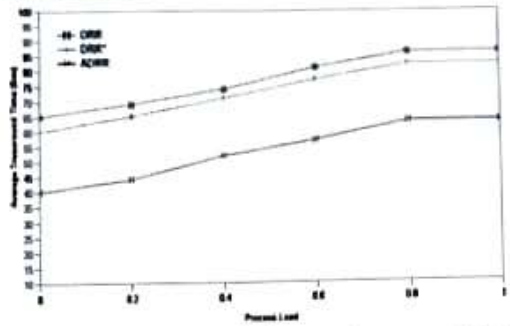


Figure 2: Process load VS. Average turnaround time

It is experiential that the ***average turnaround time increases for the pre-existing techniques (ORR, DRR) than our proposed ADRR*** as the load increases. In our proposed technique **DB-TRA** (a procedure) eliminates the overhead for estimating the resources required by all the processes in the system. Further, DB-TRA also uses a **resource reservation pool** which reduces the overhead of safety sequence test for decision on granting resource allocation. The overhead saved prevents process accumulation. Lower accumulation of process in turn reduces the wait time of a process and also distributes the resource request. Hence, the proposed ADRR technique facilitates faster completion of the processes **reducing the turnaround time** as indicated in the figure 2.

Average Waiting Time: From Figure 3 see that when the number of jobs increases, the average waiting time decreases and by comparing the three curves of Figure 3, notice that proposed algorithm allowed us to **reduce the average waiting time of the jobs compared to the other algorithms.** This is due to the advance reservation that ensures the availability of the resources and minimizes the waiting time in the Gridlet queue, unlike the DRR and ORR algorithms that uses the advance reservation mechanism to ensure the availability of the resources in the future.

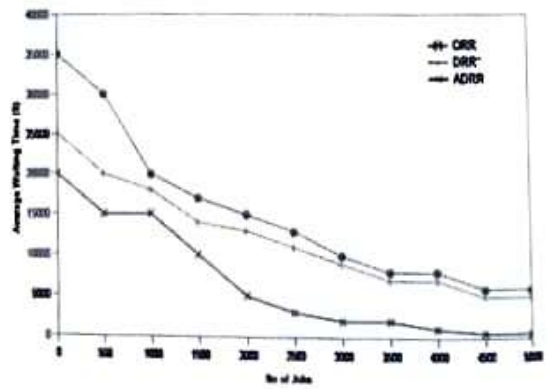


Figure 3: Average waiting time of all the submitted jobs

Resource Utilization: The graph in figure 4 shows variation in percentage of resource utilization with respect to the change in percentage of jobs using advance reservation in ADRR, ORR and DRR.

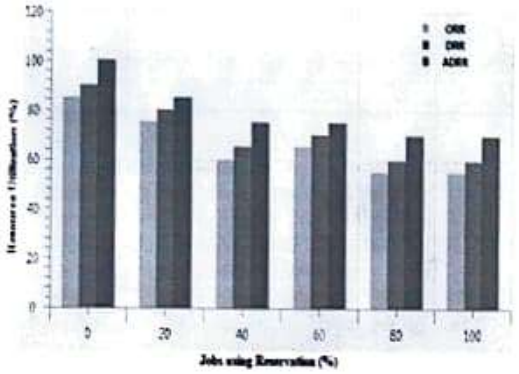


Figure 4: Compare algorithms using resource utilization

The resource utilization in **ADRR (superior Utilization) shows better results when compared to ORR and DRR,** as the ADRR schedules jobs in shortest job first order. ADRR not only provides committed reservations to the jobs but also takes care of job priorities. Therefore, ADRR ascertains (find out) job reservation to **more deserving jobs** thereby ***enhancing the overall utility of resources.***

Makespan: From the Figure 5 view that when the number of jobs increases the Makespan increases and by comparing the three curves of the Figure 5, make out that proposed algorithm have obtained a ***gain in total Makespan in minimize scale by using ADRR algorithm*** compared to the **DRR *and* ORR *algorithms.*** This is due to the budget strategy that allows the distribution of the job's execution time on the most available resources, unlike the ORR and DRR algorithms that try to estimates the best resources that can satisfy the job's requirements.

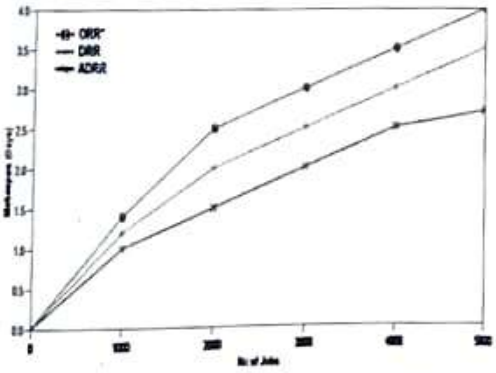


Figure 5: Total makespan to execute all the jobs

Percentage of successful jobs: The experiment is conducted to test the ADRR ability to adapt to the changing grid environment. The experiment is ***started by dynamically*** populating the resource pool with varying number of resources. The resources are steadily registered to the resource pool, depending on their availability, and some resources are removed from the resource pool. This inspects the effect of change in the type of resources in ***successfully completing the jobs.*** For different resource levels, the number of jobs completed by DRR, ORR and ADRR are noted. In this scenario the proposed **ADRR** method ***successful job completion rate (%) is best one compare than others.***

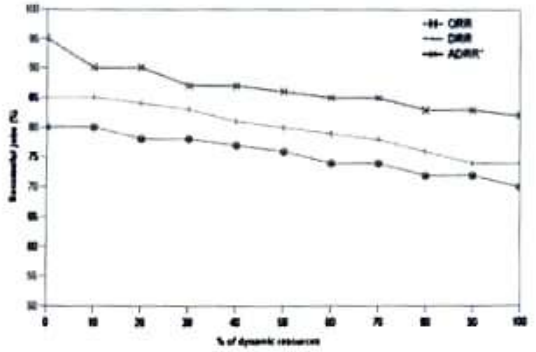


Figure 6: compare using Percentage of successful jobs

V. CONCLUSION

Grid computing has emerged as an important discipline through an increased focus on ***manageability, coordination, resource sharing, and high performance***. The success of grid computing will depend on the effective utilization of the grid's resources for various computationally jobs. Advance resource reservation assures the availability of resources when required, which ***enhances the efficient utilization*** of resources and also ***reduces the execution time*** of a process. There were various approaches available for advance resource reservation but those approaches strive (struggle) hard to provide the resource as a whole slot. This paper, the proposed Advance Dynamic Resource Reservation **(ADRR)** provides a guaranteed availability of resource, when it is required. In this paper, experimental result discussed about the novel ADRR and then various metrics performances are evaluated with graph representation. This novel ADRR matches the user's requirements with the resource capabilities to a great extent by successfully completing more number of jobs and reducing the average response time. ***Thus ADRR guarantees high system performance in the grid environment.***

VI. REFERENCES

[1]. B Madhavi Devi, Smriti Agrawal, Ch. Srinivasulu, "An Efficient Resource Allocation Technique for Uni-Processor System", in Int' Journal of Advances in Engg & Tech (IJAET) Vol. 6 II, March 2013.

[2]. Gomes E, Dantas M AR., "Towards a resource reservation approach for an Opportunistic Computing Environment", Journal of Physics: Conference Series. 2014; 540:1–9.

[3]. L. L. Lan, Y. Tao and S. H. Ya, "Service level agreement in quality of service management system in manufacturing grid", Computer Integrated Manufacturing Systems-CIMS, vol. 8, no. 12, (2006), pp.1322-132.

[4]. Deadlock-Free Scheduler, Hindawi Mathematical Problems in Engineering, Volume 2018, Article ID 1438792, 18 pages.

[5]. SivadonChaisiri, Student Member, IEEE, Bu-Sung Lee, Member, IEEE, and DusitNiyato, Member, IEEE "Optimization of Resource Provisioning Cost in Cloud Computing" IEEE TRANSACTIONS ON SERVICES COMPUTING, VOL. 5, NO. 2, APRIL-JUNE 2012

[6]. S. Nirmala Devi , A. Pethalakshmi, PhD, " DRR: Dynamic Resource Reservation in Grid Computing", International Journal of Computer Applications (0975 – 8887) Volume 159 – No 6, February 2017

[7]. Rui Min, Muthucumaru Maheswaran, "Scheduling Advance Reservations with Priorities in Grid Computing Systems". In proceedings of 2002 2nd IEEE / ACM International Symposium on Cluster Computing and the Grid, 266 – 268.

[8]. Anthony Sulistio and Rajkumar Buyya, "A Grid Simulation Infrastructure supporting Advance Reservation", proceedings of the 16th International Conference on parallel and Distributed Computing and Systems, Nov 9 – 11 2004, MIT, Cambridge, USA, pp. 1-7.

[9]. S.Nirmala Devi1 and A.Pethalakshmi, " ORR: Optimal Resource Reservation In Grid Computing Environments", Indian Journal of Science and Technology, Vol 9(48), DOI: 10.17485/ijst/2016/v9i48/102300, December 2016

[10]. Devi SN, Pethalakshmi., "An Object Oriented Approach to Disseminate Education by Applying Grid Computing Techniques in Universities and Educational Institutions in India", Proceedings of 2012 IEEE International Conference on Technology Enhanced Education (ICTEE).INDIA: 2012.

[11]. Barzegar B, Esmaeelzadeh H, Shirgahi H.A, "New Method on Resource Management in Grid Computing Systems Based on QoS and Semantics", Indian Journal of Science and Technology. 2011 Nov; 4(11):1–4.

Authors Profile

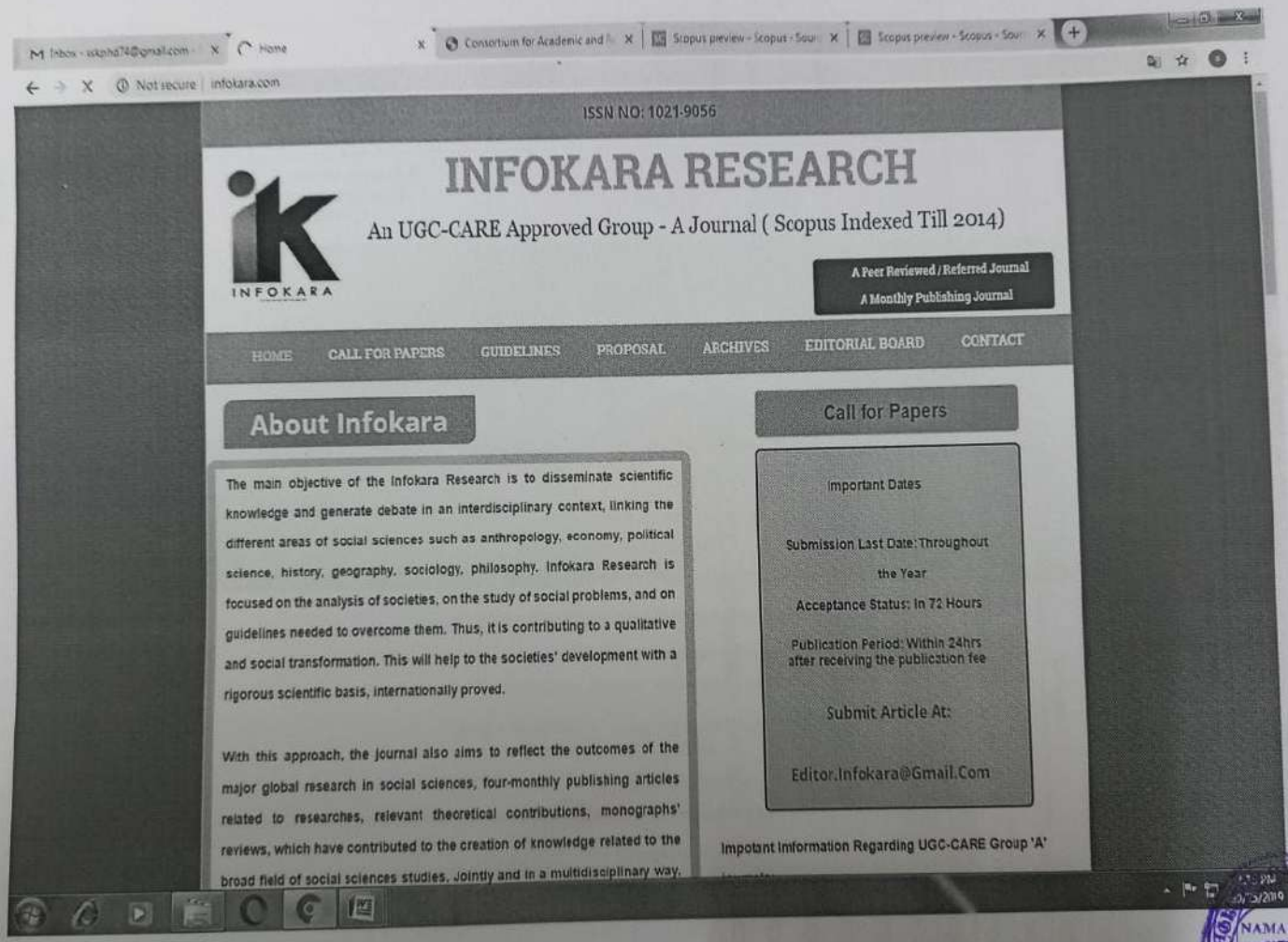


S.Sivakumar received his **M.Phil** Degree from Alagappa University, Karaikudi in the year 2005. He has received his **M.C.A** Degree from Periyar University, Salem in the year 2001. He is working as Assistant Professor, Department of Computer Science, PGP College of Arts & Science, Namakkal, Tamilnadu, India. He has around **16** years of experience in Academic Field. He is **pursuing** his **Ph.D** Degree (Part-Time) at Sri Vijay Vidyalaya College of Arts & Science (Affiliated Periyar University), Dharmapuri, Tamilnadu, India. His areas of interest include Grid Computing, Cloud Computing and Computer Networks.



Dr.D.Maruthanayagam received his **Ph.D** Degree from Manonmaniam Sundaranar University, Tirunelveli in the year 2014. He received his **M.Phil** Degree from Bharathidasan University, Trichy in the year 2005. He received his **M.C.A** Degree from Madras University, Chennai in the year 2000. He is working as **Head & Professor**, PG and Research Department of Computer Science, Sri Vijay Vidyalaya College of Arts & Science, Dharmapuri, Tamilnadu, India. He has **19 years** of experience in academic field. He has published **5 books**, more than **40 papers** in International Journals and **30 papers** in National & International Conferences so far. His areas of interest include Computer Networks, Grid Computing, Cloud Computing and Mobile Computing.

PRINCIPAL
PGP College of Arts and Science
Namakkal


Not secure | infokara.com
ISSN NO: 1021-9056
INFOKARA RESEARCH
An UGC-CARE Approved Group - A Journal (Scopus Indexed Till 2014)
INFOKARA
A Peer Reviewed / Referred Journal
A Monthly Publishing Journal
HOME
CALL FOR PAPERS
GUIDELINES
PROPOSAL
ARCHIVES
EDITORIAL BOARD
CONTACT
About Infokara
The main objective of the Infokara Research is to disseminate scientific knowledge and generate debate in an interdisciplinary context, linking the different areas of social sciences such as anthropology, economy, political science, history, geography, sociology, philosophy. Infokara Research is focused on the analysis of societies, on the study of social problems, and on guidelines needed to overcome them. Thus, it is contributing to a qualitative and social transformation. This will help to the societies' development with a rigorous scientific basis, internationally proved.
With this approach, the journal also aims to reflect the outcomes of the major global research in social sciences, four-monthly publishing articles related to researches, relevant theoretical contributions, monographs' reviews, which have contributed to the creation of knowledge related to the broad field of social sciences studies. Jointly and in a multidisciplinary way,
Call for Papers
Important Dates
Submission Last Date: Throughout the Year
Acceptance Status: In 72 Hours
Publication Period: Within 24hrs after receiving the publication fee
Submit Article At:
Editor.Infokara@Gmail.Com
Impotant Information Regarding UGC-CARE Group 'A'

INVESTIGATION OF RESOURCE RESERVATION IN GRID COMPUTING ENVIRONMENT USING PROPOSED ADRR (ADVANCED DYNAMIC RESOURCE RESERVATION)

[1]S.Sivakumar, [2]Dr. D. Maruthanayagam
[1]Research Scholar, Sri Vijay Vidyalaya College of Arts & Science, Dharmapuri, Tamilnadu, India
[2]Head/Professor, PG and Research Department of Computer Science, Sri Vijay Vidyalaya College of Arts & Science, Dharmapuri, Tamilnadu, India

Abstract: Grid resource management plays an important role while enabling the sharing and coordinating of resources in Grid computing environments. Resource reservation is an important part of the Grid resource management. Currently existing resource management systems provide only means to reserve resources starting with the reservation attempt and lasting for an unspecified duration. However, for several applications such as video conferencing the ability to reserve the required resources in advance is needed. In this paper, propose an Advanced Dynamic Resource Reservation **(ADRR)** framework for grid computing. Thus the simulation result reveals that the ***proposed reservation (ADRR) methods are able to provide high performance by decreasing the completion time and increasing the resource utilization*** in a dynamic fluctuated distributed environment.

Keywords: Grid Computing, Dynamic Resource Reservation, Reservation Scheduler, Resource Manager, Reservation Scheduler with Priorities and Benefit Functions and Time-Slice based Advance Resource Reservatio.

I. INTRODUCTION

In most grid systems with traditional scheduler, submitted jobs are placed in the wait queue if mandated resources are not available for them [1]. Every grid system may use a different scheduling algorithm, for example First Come First Serve (FCFS), Shortest Job First (SJF), Earliest Deadline First (EDF), or EASY Backfilling [2] that executes jobs based on different parameters, such as number of resources, submission time, and duration of execution. With these scheduling algorithms, there is no guarantee about when these jobs will be executed [3]. To address the unwarranted waiting time issue and ensure that the specified resources are available for applications at a particular time in the future, we need an advance planning and reservation system [4]. Advance reservations [5] allow a user to request resources from multiple scheduling systems at a specific time in the future and thus gain simultaneous access to enough resources for their applications.

The work of this paper is to develop an Advanced Dynamic Resource Reservation (ADRR) technique which is empowered with all the desired capabilities which can provide solutions for the identified problem areas in a grid scenario. To demonstrate the usability of proposed techniques, a simulation test bench was implemented using the GridSim and successful simulation was achieved [6]. GridSim toolkit supports simulation of various types of grids and application models scheduling. GridSim is an open-source software platform, written in Java, which provides features for application composition, information services for resource discovery, and interfaces for assigning applications to resources. The GridSim toolkit also provides a comprehensive facility for simulation of different classes of heterogeneous resources, users, applications, resource brokers and schedulers. It can be used to simulate application schedulers for single or multiple administrative domain(s) distributed computing systems such as clusters and grids. The results show that the ADRR performs better than the other algorithms by reducing both the reservation duration time and the total completion time, increase resource utilization and reduce no of rejections, etc.

II. RESERVATION ALGORITHMS

A. Reservation Scheduler With Priorities And Benefit Functions (RSPB)

In RSPB [7], each reservation request has an associated benefit function that quantifies the "profit" for the client accrued by the client by securing the resource at the requested level. When the client is willing to negotiate for lower service levels, it could indicate this by providing a benefit function that shows a reduced but positive benefit for lower resource levels. This facility provided by the benefit functions removes the need for negotiations when there is a resource scarcity. A centralized resource reservation scheduler is assumed, i.e., all the resource reservations are performed by a centralized unit. Requests arrive randomly based on a Poisson arrival process. Because the requests are arriving in a random fashion at real time, the reservation scheduler cannot wait until all the requests have arrived to commence the scheduling. It should make the decisions on the requests as each one arrives or make a decision after the arrival of a batch of requests. Let m be the number of machines in the system. The machines are assumed to be homogeneous. Let CPU_sysj represent the percentage of CPU of the j-th machine Mj that is dedicated to the Grid system. For each request, Rk arriving at the reservation scheduler following parameters are defined. tk-start: start time of the reservation Rk. tk-end: end time of reservation for Rk. CPUmax-k: minimum CPU requirement of Rk for delivering the maximum benefit to the application. pk: priority of Rk, due to limited amount of resources, the scheduler cannot meet the demands of all the requests. When the overall demand exceeds the available resources, the objective of the reservation scheduler is to minimize the sum of priority of the requests that are rejected. This algorithm uses heuristic approaches to achieve this objective [8]. Bk(pcpu): the benefit function associated with Rk. It gives the benefit the client will receive if it is reserved CPU at the requested level. Although, in this paper, benefit functions are used only for quantifying the CPU requirements, it may be used for other resources as well as the time constraints.

In this reservation model, a CPU resource may be temporally shared by multiple reservations, i.e., multiple reservations may overlap in time. Therefore, this algorithm need to determine the current CPU usage for a given time interval before admitting a reservation. In Lines (19) and (38), the current CPU (machine) usage is determined using *time slot* tables that keep track of reservations that have already been accepted. The time slot tables only keep track of the partition of the CPU that is dedicated to the Grid and thus, managed by the reservation scheduler. Line (21)

P.G.P. COLLEGE OF ARTS & SCIENCE NAMAKKAL

determines whether the examined machine can satisfy the hard QoS requirement of request *Rk*. If yes, this machine is put into a machine queue named *machQueuehard* for later selection in line (38). Although it is not shown in pseudo-code in Figure 2, the search for a machine that satisfies the reservation request can be stopped when a machine that satisfies the hard QoS is found. If none of the machines in the system can satisfy the hard QoS requirement of *Rk*, the reservation scheduler will attempt to schedule the reservation with a degradation of the CPU requirement for *Rk* provided the benefit function allows for the degradation. Line (24) to (32) attempt to find a machine that satisfies this situation and this machine is considered to satisfy the soft QoS requirement of *Rk*. Lines (26) to (32) attempts to maximize the benefit delivered to the application by the reservation. Lines (34) and (35) deal with the case where the system cannot provide the requested level of service to *Rk*. The reservation scheduler checks the meta-request *Rnonsatisfy* and sends rejections messages to the clients that submitted the reservation requests in *Rnonsatisfy*. The clients may resubmit their reservation requests with modifications and these submissions will be considered for reservation at the next scheduling event [9]. Line (38) ensures that the load is distributed across the machines.

RSPB Algorithm:

function scheduleRmeta (meta-request Rmeta)
(2) Rk : the kth request in Rmeta;
(3) Mj : the jth machine in the system;
(4) CPUmin-k : minimum CPU requirement when Rk get lowest acceptable benefit from reservation;
(5) load_heaviestj(tm, tn) : the heaviest load of Mj within a reservation duration tm to tn;
(6) CPU_smallestj(tm, tn) : the smallest availability of CPU to reserve for Mj within a duration tm to tn;
(7) machQueuehard : queue for storing machines that satisfy hard QoS request of Rk;
(8) machQueuesoft : queue used to store machine which can satisfy soft QoS request of Rk;
(9) Bjk : benefit value which Rk can get from Mj;
(10) Rnonsatisfy : meta-request to store rejected requests;
(11) for all requests Rk in Rmeta
(12) sort the requests in descending order by pk;
(14) for each sorted request Rk in Rmeta
(15) reset machQueuehard and machQueuesoft
(16) get tk-start and tk-end;
(17) calculate CPUmin-k according to selected benefit function shape;
(18) for each machine Mj in the system
(19) get load_heaviestj(tk-start, tk-end);
(20) CPU_smallestj(tk-start, tk-end) = CPU_sysj - load_heaviestj(tk-start, tk-end);
(21) if (CPU_smallestj(tk-start, tk-end) ≥CPUmax-k);
(22) machQueue$_{hard}$← Mj;
(23) else
(24) if (machQueuehard is empty)
(25) if (CPU_smallestj(tk-start, tk-end) ≥CPU$_{min-k}$)
(26) if (machQueuesoft contain machine Mi)
(27) Bjk = Bk(CPU_ smallestj(tk-start, tk-end));
(28) Bik = Bk(CPU_ smallesti(tk-start, tk-end));
(29) if (Bjk > Bik)
(30) machQueuesoft$_{Bjk}$← Mj;
(31) else
(32) machQueuesoft$_{Bik}$← Mj;
(33) endfor
(34) if (both the machQueuehard and machQueuesoft are empty)
(35) put the request Rk into meta-request Rnonsatisfy;
(36) else
(37) if (machQueuehard is not empty)
(38) select the machine with the lowest average CPU load within duration (tm, tn).
(39) else
(40) the machine in the machQueuesoft is the choice
(41) mark the time slot table for this machine with requested reservation.
(42) end for

B. Time-Slice based Advance Resource Reservation (TARR)

In this resource reservation approach [10], the resources are reserved even in the time slices where the resource is kept idle after the start time of the reservation. This time slice reservation can be done until the Defer Time (DT) accepted by the user for a particular reservation. Moreover an upper limit is imposed on the number of time slice (NTS), to reduce the overhead on the resuming and suspension of the job due to the resource availability. The Start, finish and defer time for using the resources are given by the user while submitting a job for execution. The start time and finish time are the expected start and finish time for using the resources. Sometimes it is not possible to reserve the resource at the stipulated start and finish time. In such case the reservation can be done until the defer time. Defer time is the time until which the reservation can be postponed.

TARR Algorithm:

1. if List is empty then
2. no conflict found. Hence accept the new reservation.
3. else
4. for i = 0 to List-Size -1 do
5. Put i into templist if one of the properties are true
6. Startnew ≤ starti&&finishnew≥ finishi || Startnew ≤ finishi|| finishnew≤ finishi
7. end for
8. if templist is empty then
9. no conflict found. Hence accept this reservation.
10. else
11. requiredtime = finishnew– startnew
12. balancereserve = requiredtime
13. for i = 1 to n
14. timeslice = starti+1 -finishi
15. if timeslice> 0 then
16. Put into slicequeue_insert(id,sst,sft)
17. end if
18. end for
19. while (slicequeue&&balancereserve)
20. if sst ≥ Startnew then
21. assign new reserve
22. currentreserve=sft – sst
23. Balancereserve = requiredtime –currentreserve
24. end if
25. end while
26. end if
27. end if

A reservation list is maintained at each resource. The list consists of the reservation id, ST and FT of the reservation. When there is no reservation for the resource then the list is empty. The new reservations can be added immediately when the list is empty. It is given in line 1 to 2 in the algorithm. If the reservation list is not empty then it is required to find out whether the required slot is free. For this the start$_{new}$ and finish$_{new}$ are compared with the existing list. To finding the availability for new reservation, the start and finish time of the new reservation is checked with the existing one. If start$_{new}$ is less than the start of the any of the reservations and the finish$_{new}$ is greater than the finish of the any of the reservation then it means there is a conflict. Even if start$_{new}$ or finish$_{new}$ is less than finish of any of the available reservations then also there exists the conflict. Only when there is no conflict there is

slot available for reservation. Hence the reservation can be made when there is no conflict. To Forming SliceQueue, when reservations are not made possible within the slots available, then the empty time slices are arrived and placed into the SliceQueue. For this the difference between the current finish time and the next start time is computed as TimeSlice in this equation. TimeSlice = $Finish_{current}$ -$Start_{next}$

These timeslices are placed into the SliceQueue with an id and the $finish_{current}$ and $start_{next}$ values. The $finish_{current}$ and the $start_{next}$ are stored as SST(Slice Start time) and SFT (Slice Finish Time). To get the availing timeslices from SliceQueue, when there is reservation required in time slices for a job, then it can be provided. The balancereserve holds the expected reservation at that particular time. As and when a time slice is reserved then the time slice duration is reduced from the balancereserve which is computed using this equation. balancereserve = requiredtime – currentreserve. Where currentreserve = SFT – SST. The reservation is done until the balancereserve becomes null.

III. PROPOSED METHODOLOGY

The Advanced Dynamic Resource Reservation Model (ADRR) is shown in Figure 1. When the user submits the job to the job handler, job handler goes through five states. In the first state, users are sorted according to their priorities. In the second state, the job handler identifies the job as new or mature and forwards the job to the Dynamic Priority Resolution (DPR). When the job handler identifies the job as new, it forwards the new job with user requirements to the DPR. When the job handler identifies the job as mature, it forwards the mature job and the matched job_id to the DPR. The DPR queues the new job in the new_job queue and the mature job in the mature_job queue. In the third state, the jobs of each user are sorted based on the lengths of jobs. In the fourth state, the jobs of various users are sorted in accordance with the job's priority based on job length and on priority of the user to which the jobs belong. This is done by Dynamic Priority Resolution (DPR) technique. Gridlet Sorting Policy (GSP) is based on a predefined value decides that how many jobs of a given user are to be scheduled and send to reservation. Finally in the last state, jobs are placed in a queue called Gridlet queue from where they are sent to resource analyst. The resource analyst comprises of two components viz. User Resource Information (URI) and Rank List Unit (RLU). The User Resource Information (URI) receives the new job with the user requirements from the job handler and the Rank List Unit (RLU) receives the mature job with the matched Job_id from the job handler.

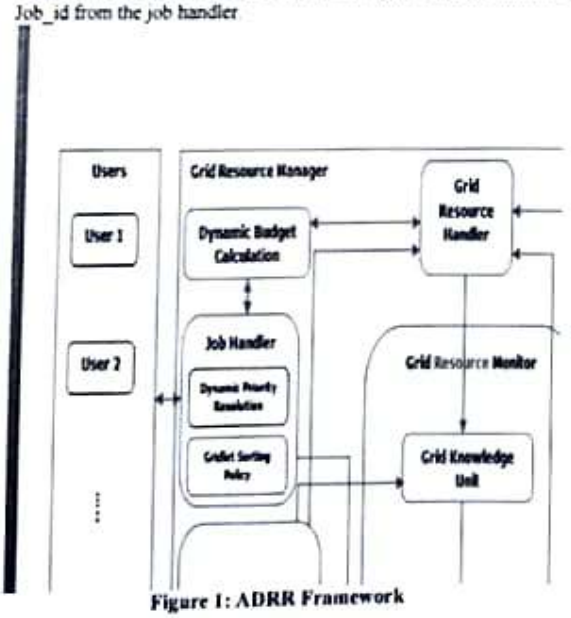


Figure 1: ADRR Framework

The User Resource Information (URI) maintains Resource Information Table and the Rank List Unit maintains Rank_List Table. For mature jobs, the Rank List Unit (RLU) fetches the rank_list of the matched job_id from the rank List table and forwards the mature job with the rank_list to the resource handler for allocation. For new jobs, the User Resource Information (URI) performs the preliminary selection of resources by considering the static parameter (Resource name, Resource location, Resource CPU type, Resource OS, and Memory capacity) resource type of resources. The resource handler proposes an initial budget of resources to be given to each new process. This budget is initialized with no prior knowledge of the process resource requirement rather on the current request made by it. However, this budget is updated to accommodate the resource requests made by a process. Thus, every time the process makes a new resource request within the budget allotment is done using available resources and reservation pool. However, if the requested resources are beyond the budget granted to a process then the budget is modified to accommodate the new request. The resources capabilities selected in the preliminary selection and the job with user requirements is forwarded to the Resource Search Engine (RSE). The Resource Search Engine (RSE) prepares a new rank_list for the new job and forwards the job and the new rank_list to the resource handler for allocation.

A. Grid Resource Manager

The Grid manager is responsible for managing all grid activities. It is an **interface between the user and the service provider**. It has job handler, grid resource handler, resource search engine, dynamic budget calculation and grid resource monitor.

1. Job handler

The functions of the job handler are, when the user wants to register itself, the user sends the user_registration message to the job handler. The information field contains the metadata given by the user at the time of registration. The job handler receives the user_registration message. It assigns the user a unique user_id and sends the user_ack message to the user as an acknowledgement. The user receives the user_id and utilizes the user_id to submit the job to the job handler. The user submits the job by sending the job_submission message to the job handler. The job_submission message includes the requirements of the user and the executable data. After the user submits the job, the job handler assigns the submitted job a unique job_id. The job handler sends the user the assigned job_id as an acknowledgement for the received job. The job handler maintains the job table. The job handler stores the user requirements of the job along with the user_name, user_id, job_name, job_id, arrival date of the job, and etc., in the job table.

Whenever a user enters grid, it is enlisted by the proposed algorithm in a queue called User List referred by job table. The users from the User List are sorted based on their priority and are placed in a queue called User queue. Thereafter jobs that are generated by various users are ordered on the basis of their lengths and are placed in another queue named Gridlet List referred by job table. The jobs are prioritized again. The proposed algorithm prioritizes them by using a Gridlet Sorting policy and Dynamic Priority Resolution (DPR) technique. The sorting policy decides on the number of jobs of each user to be prioritized and finally to be sent for reservation. Thus the Sorting policy ensures that jobs of various users are entertained in a way so as to avoid starvation among the jobs. On the other hand, the DPR technique is used to resolve the priority of jobs by considering the parameters associated with jobs priority. The DPR therefore is consequential in determining the priority of incoming jobs having higher user priority and higher job priority based on the job length. The proposed algorithm finally stores prioritized jobs in a queue called Gridlet queue. The jobs thus scheduled by proposed algorithm are submitted to resource allocation.

The priority work done by proposed algorithm can be broadly divided into two phases namely User Priority Phase and Gridlet

Priority Phase. The first phase deals with the user priority whereas the second phase takes care of job priority of the jobs.

(i) **User Priority Phase**

These users can have one or multiple jobs. In this phase, first the users are sorted and then the jobs of each user are sorted. The users are sorted in decreasing order of their priorities using User Sorting Policy. If the users have equal priorities they are arranged on first come first basis else insertion sort technique is used. Once the users have been sorted, jobs of each user are sorted on the basis of their lengths. The jobs are sorted using insertion sort technique. The jobs thus sorted are placed in the Gridlet List. This technique is used as it saves time and therefore is more efficient. This is due to the fact that insertion sort has complexity of O(n) which is comparatively less than the time complexities O(nlog(n)) and O(n2) of other sorting methods in the best or worst case respectively.

(ii) **Gridlet Priority Phase**

In this phase, jobs already sorted in User priority phase are further prioritized based on two criteria. This criterion can either be UserPriority or job length or both referred to as UserHighPriority (UHP) phase and UserJobPriority (UJP) phase respectively. DPR technique decides whether jobs will be sorted in UHP or UJP phase depending on the difference in priority of the jobs (that is UserPriority). DPR technique takes two users at a time that are competing for reservation and compares their UserPriority. If the difference between UserPriority is larger than significant difference SD, only the jobs belonging to the higher priority user are sorted. The jobs belonging to lower priority user are queued up. These jobs are treated as pending jobs which will further participate in the next sorting process in the User priority phase. Out of these sorted jobs of a higher priority user, only a predefined number of jobs are considered for reservation (as decided by pre-defined function) and rest are discarded. This is referred to as UHP phase. Whereas if the difference between the UserPriority of the two users competing for reservation is less than a significant difference SD, the priority of jobs is evaluated on the basis of their job length and UserPriority. SD ensures that competing jobs are well differentiated among themselves. As the jobs keep arriving, the sorting process is repeated and the pending jobs of lower priority users are allowed to participate again and hence they are prevented from getting starved. This phase is known UserJobPriority phase.

(iii) **Gridlet Sorting Policy**

The sorting technique used to sort the jobs in the above phases is decided by GSP. The GSP uses shortest first job technique for sorting the jobs of various users. This policy also uses a pre-defined function in UHP or UJP phase to decide as to how many jobs of high priority user are to be considered for reservation. The policy prevents all the jobs of high priority user from getting entertained and therefore avoids starvation of jobs of low priority users. The policy takes this decision on the basis of a pre-defined value.

- Start.
- Create a UserList and add users to this list as users arrive and join the grid.
- Sort the users in the UserList based on assigned UserPriority using insertion sort following UserSortingPolicy.
- Create a Gridletlist and insert Gridlets in this list according to their UserPriority such that all Gridlets of each user are placed in a sequence.
- Sort the Gridlets of various users joined.
- Dynamic Priority Resolution (DPR) is calculated at runtime by using
  DPR = User[i].priority-User [i+1].priority
- Compare DPR with SD which is significant difference between UserPriority.
  If (DPR>SD)

  UserHighPriority (UHP) phase: Sort the Gridlets of each user according to shortest order and place into a user's Gridlet queue. Consider only N number of shortest jobs of higher priority user to be sent for reservation schedule as decided by GSP.
  Else
  UserJobPriority (UJP) phase: Sort the Gridlets of users according to GSP, taking into account the UserPriority of both the users which being compared, are placed into a queue. This leads to Gridlets from both the users in the Gridlet list.
- If (new user)
  Go to step 2
- If (new Gridlet)
  Go to step 4
- Stop

After the dynamic priority resolution done the result submits to the job handler, the job handler verifies the Gridlet queue to know whether the submitted job has been previously processed, by calculating the similarity index *SI* of the submitted job with all jobs in the job table whose time of arrival is less than Δt (where Δt is the time interval at which the resource's dynamic and behavioral parameters are updated in the resource analyst by the grid knowledge unit). The similarity index *SI* for each submitted job is calculated using the Equation.

$$SI = \frac{2n_{xy}}{(n_x + n_y)}$$

Where,

n_{xy} is the number of parameters matched with the job in the job table.

n_x is the number of parameters of the job in the job table

n_y is the number of parameters of the submitted job

If the submitted job's similarity index *SI* is equal to 1 with respect to a particular job in the job table, the job handler identifies the submitted job as 'mature'. The job handler then sends the job to the resource analyst by sending the job_description message. If the submitted job's similarity index *SI* is not equal to 1 with respect to a particular job in the job table, the job handler identifies the job as 'new'. The job handler then sends the job to the resource analyst by sending the job_description message for analyze the initial budget values.

When the user wants to know the status of the submitted job, the user sends a status_request message to the job handler to retrieve the status of the submitted job. The job handler receives the status_request message from the user. The job handler forwards the status_request message to the resource handler. The resource handler fetches the status of the submitted job from the resource table in the resource handler and sends the status_ response message to the job handler. The job handler forwards the status_response message to the user.

2. Resource handler

The functions of the resource handler are, when the service provider wants to register itself with the grid, the service provider sends a serviceprovider_registration message to the resource handler. The resource handler receives the serviceprovider_registration message. It assigns the service provider a unique serviceprovider _id and sends the serviceprovider_ack message to the service provider as an acknowledgement. The service provider receives the serviceprovider_id and uses the serviceprovider_id to register the resource with the resource analyst through the resource handler. The service provider registers the resource capabilities (static and dynamic parameter values) with the resource analyst through resource handler by sending the resource_registration message to the resource handler. The resource handler receives the resource capabilities from the service provider. The resource handler assigns a unique resource_id to the registered resource and sends the

ISSN NO: 1021-9056

resource_registration_ack message to the service provider as an acknowledgement. The resource handler forwards the registered resource's capabilities to the resource analyst by sending the resource_submission message to the resource analyst. The resource handler maintains a resource table. For each newly submitted job, the resource search engine calculates a rank_list. The resource search engine then sends the rank_list to the resource handler. The resource handler allocates the highly ranked resource in the rank_list to the job. The resource handler stores the rank_list in the resource table for rescheduling of resources using initial budget in case of resource/job failures. The resource handler stores the rank_list, job status and the resource status in the resource table.

3. Dynamic budget calculation using threshold

The assumption that the resource requirement is known in advance is serious limitation of most of the deadlock avoidance techniques as this estimation has considerable overhead. The present work used a dynamic budget technique using threshold to overcome the limitation of existing technique of assuming that the maximum resources required by each process is known in advance.

The **resource handler proposes an initial budget of resources** to be given to each new process. This budget is initialized with no prior knowledge of the process resource requirement rather on the current request made by it. However, this budget is updated to accommodate the resource requests made by a process. The safety sequence test ensures that the system is deadlock free with the proposed budget. Thus, every time the process makes a new resource request within the budget allotment is done using available resources and reservation pool. However, if the requested resources are beyond the budget granted to a process then the budget is modified to accommodate the new request. To ensure the deadlock Free State, the safety sequence is estimated. If the system is safe the requested resources are granted. However, if the safety sequence does not exist the process state is stored (check pointed) and queued in the pending state with its budget updated to the actual resource request. This process may be aborted to prevent the hold and wait condition which may lead to a deadlock. However, this can be postponed till some process requests for the resources held by this pending process. This will reduce the repercussions of over budgeting.

```
Begin
1. Initialize Threshold_Value[y] =Reserve[y] =[[Request[x][y] ∀x=1,2...n], 0]∀ y=1, 2, ...m
2. Initialize Budget_Value[x][y]= Allocation [x][y] = Need[x][y]= {0}∀x=1,2...n and ∀y=1, 2, ...m
3. Available[y]= Available[y]-Reserve[y] ∀ y=1, 2, ...m
4. For (Request[x][y] by a process Pi)
Do
        A. If Request[x][y]>Need[x][y] for any y = 1, 2, ... m
        I.  Budget_Value[x][y] = Allocation[x][y] + Request[x][y]+ Threshold_Value[x][y]
        II. If Safety Sequence exists
                i. Accept process P,
                ii. If (Request[x][y]<=Available[x][y])
                        a. Allocate (Allocation, Request, Available, 0)
                        Else
                        b. Allocate (Allocation, Need, Available, Reserve)
                iii. Request[x][y] ={0}
                Else
                iv. Save the status and insert the process Pi in pending queue
                v. Budget_Value[x][y] =Allocation[x][y] + Request[x][y]
Else
B.      If (Request[x][y]<=Need[x][y] && Request[x][y]<=Available[x][y])
        I. Allocate (Allocation, Request, Available, 0)
        II. Request[x][y] ={0}
Else
        I. Allocate (Allocation, Need, Available, Reserve)
        II. Request[x][y] ={0}
5. When a Process completes and releases resources.
End
Allocate (Allocation, To_Allocate, Available, Reserve)
I. For (y=1 to m)
        a. Available[y] =Available[y] + Reserve[y]
        b. Available[y] =Available[y] – To_Allocate[x][y]
        c. Allocation[x][y] = Allocation[x][y] + To_Allocate[x][y]
        d. Need[x][y] = Budget[x][y] – Allocation[x][y]
        e. Reserve[y] = min (Available[y], Threshold[y])
        f. Available[y] =Available[y]-Reserve[y]
End
```

4. Resource Search Engine (RSE)

This is the core part of the proposed algorithm. The primary function of the resource search engine is to match the user requirements of the submitted job with the resource capabilities. The resource analyst performs the preliminary selection of resources using the static parameter viz. resource type and forwards the selected resource's capabilities and the submitted job with user requirements to the resource search engine. The functions of the resource search engine are,

- Filter resources using Bloom filer method
- Static parameters matching using assignment method
- Dynamic resource matching using correlation method
- Rank_list calculation
- Behavioral parameters (Hit rate and failure rate) updation.

1. The resources capabilities selected in the preliminary selection and the job with user requirements is forwarded to the Resource Search Engine (RSE) from resource analyzer, local grid information service extracts positions from them. On this basis, positions in counting Bloom filter themselves; perform the trend of resources inquiry as follows: if counter value is 0 at least in one position in Bloom filter, requested resources do not exist in local grid. If counter values of none of these positions in Bloom filter is 0, then string codes pertaining to positions 1st to K-1th are created as stated previously[1] and the list connected to position Kth in Bloom filter is searched according to string codes. If targeted member is found on the list, then the list of identifiers of similar resources registered in this member is sent along with task's identifier to user. If the list is empty and/or is not but does not contain targeted member, then false positive are detected, indicating that no requested resource exists in local grid.

```
Receive (index , id) from user ;
bloom_index= extract(index); j=0; str=null;
(user_id , job_id) = extract(id);
for i=0 to k-1 do
        j=bloom_index[i];
        if bloomfilter[j].counter==0 then
                send (index , id, RegionalGIS_id) to GIS;
                return;
        else if i<k-1 then str=str+'j';
        end if
end for
LocalResourcelist=search( bloomfilter[j].list , str);
If LocalResourcelist ==null then
        Preliminary selection of resources using the static parameter by assignment method;
return;
else
send (LocalResourcelist, job_id) to user;
```

2. The resource search engine uses the assignment method to match the job's static parameter values with the resource's static

ISSN NO: 1021-9056

parameter values. The static parameters are Resource name, Resource location, Resource CPU type, and Resource OS and Memory capacity. Assignment method is used for the optimal assignment of a static parameter to a resource to ensure maximum efficiency. For each submitted job, the resource search engine computes a relative parameter match value (C_{isk}) by comparing the job's static parameters and the preliminarily selected resource's static parameters.

$$C_{isk} = \begin{cases} 1 & \text{if } X_{ik} - R_{sk} \\ X_{ik} - R_{sk} & \text{otherwise} \end{cases}$$

X_{ik} Represents job parameters

R_{sk} Represents resource parameters

3. The resource search engine uses the correlation method to match the job's dynamic and behavioral parameter values with the resource's dynamic and behavioral parameter values. Correlation method is used to find the correlation between the dynamic and behavioral parameters of the submitted job and the resource. The dynamic parameters are Hard disk availability, Economic state, Dedication rate, Resource budget and Deadline. The behavioral parameters are Success rate, Hit rate, Failure rate and Recovery time.

The correlation of any resource R_s with the job X_i of the i-th user is given in below equation

$$R_s = \frac{k\sum_{k=1}^{n} X_{ik}R_{sk} - \sum_{k=1}^{n} X_{ik}\sum_{k=1}^{n} X_{ik}R_{sk}}{\sqrt{(k\sum_{k=1}^{n}(X_{ik})^2 - (\sum_{k=1}^{n} X_{ik})^2)*(k\sum_{k=1}^{n}(R_{sk})^2 - (\sum_{k=1}^{n} R_{sk})^2)}}$$

Where n is number of dynamic and behavioral parameters. The resources are ranked according to the correlated value of the resource parameter with the job parameter. The resource whose correlated value is nearly equal to one is given the highest rank.

4. The rank values are obtained for each dimensions viz. static, dynamic and behavioral using assignment method and correlation method. The resource search engine finally calculates the rank_list for the submitted job using measures of dispersion. In case of unnormalized ranks, priority is given to the highly ranked resource in the first dimension since the first dimension matching considers the static weighted parameters. The three dimensional Matchmaking engine forwards the rank_list and the submitted job to the resource handler for allocation. The rank_list is also stored in the resource repository table of the resource analyst.

5. The resource search engine finds for each resource, the number of occurrences of the resource in the rank_list and the number of occurrences of a resource in the three dimensional matchmaking engine and calculates the hit rate for every Δt_1 time and updates the calculated hit rate at every Δt time with the grid knowledge unit by sending the hit_rate_update message. The failure rate of a resource is updated in the grid knowledge unit by the resource search engine. The failure rate of a resource is updated whenever the resource is rejected in the rank_list the resource occurs in the resource search engine and the resource search engine updates the failure rate of a resource in the grid knowledge unit by sending the failure_rate_update message to the grid knowledge unit.

5. Resource Monitor

The resource monitor monitors the resources in the grid site through the resource handler. It contains two components. They are Resource analyst and Grid knowledge unit.

a). Resource analyst

Resource analyst is the central part of the matchmaking architecture. The functions of the resource analyst are Resource repository table maintenance and Preliminary resource selection.

Resource repository table maintenance: Every service provider registers the static and dynamic parameter values of its resources in the resource repository table through resource handler. The resource analyst stores the resources' static, dynamic and behavioral parameter values along with the resource_id and the serviceprovider_id in the resource repository table. Initially the resource search engine sets the values of the behavioral parameters like success rate, Hit rate, Failure rate of each resource to 1.0 , and the Recovery time to 0 in the resource repository table. The service provider updates the dynamic parameters of the registered resources at every Δt time in the resource repository table. The knowledge unit updates the behavioral parameters of the registered resources at every Δt time in the resource repository table.

Preliminary resource selection: The resource analyst performs the preliminary resource selection by considering the static parameter. When the user submits new job, the resource analyst performs the preliminary selection of resources by considering the first static parameter. The resource analyst selects all the resources of that particular resource type. The resource analyst then forwards the three dimensional parameter values of the selected resources and the submitted job along with the user requirements to the resource search engine for rank_list calculation.

b). Grid Knowledge Unit

The grid knowledge unit receives the information about the history of behavior of resources in the resource pool from the resource search engine and the resource handler. It receives the values of resources for success rate calculation and recovery time profiles of resources for recovery time calculation from the resource handler. It receives the hit rate of a resource at every Δt_1 time and values of resources for failure rate calculation from the resource search engine. The grid knowledge unit predicts the success rate, hit rate, failure rate and recovery time for each resource for the next matchmaking cycle based upon its previous behavior with the jobs. It also updates the predicted values of success rate, hit rate, failure rate and recovery time for each resource in the resource repository table of resource analyst at every Δt time interval. It maintains the behavior parameter table and stores the predicted success rate, Hit rate, Failure rate and Recovery time of the resources in it.

IV. EXPREMENTAL RESULTS AND DISCUSSIONS

The proposed algorithm is simulated in GridSim 5.2 and following simulation parameters (given by Table 1) are used:

Table 1: Simulation Parameters

Simulation runs	50
No. of Resources	10
No. of Users	10 – 50
No. of Jobs	1000– 5000
Processing power of Resources (In MIPS)	200

Execution Time

The effect on execution time of jobs by varying the number of users from 10 to 50 and fixing the number of resources at 10 for the proposed algorithm (ADRR) and other algorithms is represented in Figure 2. The graph shows that ***the resource reservation time and execution time of jobs under ADRR is less*** as the incoming job is assigned to the resource with minimal queue length. ***So, ADRR reveals better performance than RSPB and TARR.***

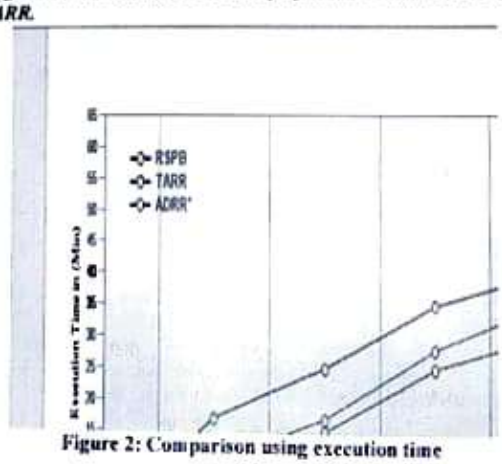


Figure 2: Comparison using execution time

Makespan analysis: The makespan values of the best solutions throughout the optimization run were recorded and the averages were calculated from the different trials. In a grid environment, the main emphasis was to allocate the job and resource as fast as possible by using appropriate resource reservation algorithm. The following Figure 3 shows the makespan time of jobs run in each node of grid environment. These developments indicate the fastest of each node by using proposed resource reservation algorithm ADRR. This shows that the ***proposed algorithm makespan is minimized when compared to other algorithms.***

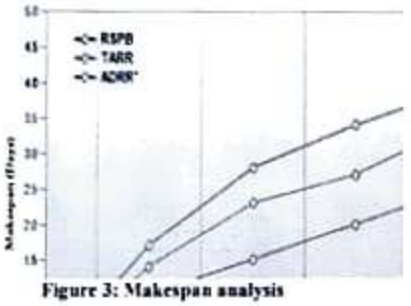


Figure 3: Makespan analysis

Resource utilization : The resource utilization is a Quality of Service (QOS) criterion. Below Equation gives the average utilization of resources for a schedule S. The value of average_utilization has to be maximized.

$$\text{average}_{\text{utilization}} = \frac{\sum_{[\text{nMachines}]} \text{completion}[i]}{\text{makespan} \times \text{nb_machines}}$$

Where nb_machines denotes the number of resources, this Equation gives the completion time of a machine m. It is evident that the average utilization of resources for all algorithms is ranked as: 1) ADRR 2) TARR and 3) RSPB. ***The overall performance of ADRR is good while considering the average resource utilization.***

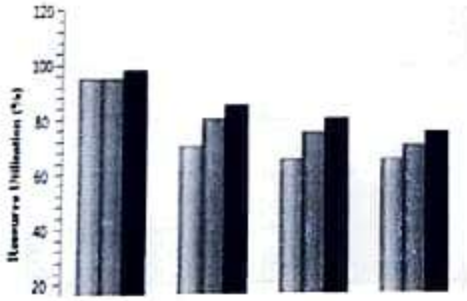


Figure 4: Graph between percentage of utilization and percentage of jobs reserved

No of Rejections: Figure 5 depicts an analysis between number of rejections and the percentage of jobs seeks reservation, the number of rejections goes up. As seen ***from the figure, the ADRR gives improved results over TARR and RSPB.*** This is due to the reason that the shortest jobs of higher priority users are entertained dynamically at the run time.

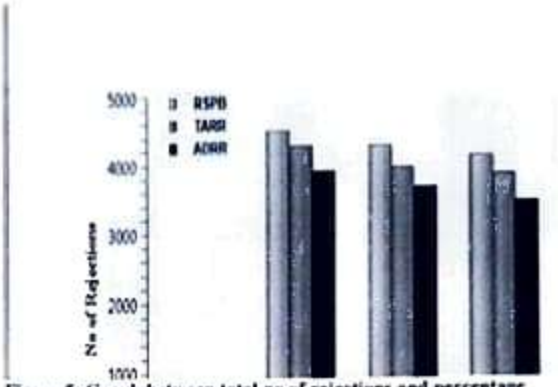


Figure 5: Graph between total no of rejections and percentage of jobs reserved

V. CONCLUSION

Resource reservations mechanisms and scheduling efficiency are keys to the success of computational Grids, and especially to Grid capability to deliver commercial applications a guaranteed and personalized Quality of Service (QoS). This paper introduces a ***novel way of incorporating QoS constraints and priority*** into an advance reservation scheduling algorithm for in Grid computing systems. The paper compares the performance of the proposed algorithm (ADRR) with an existing advanced reservation algorithm, namely the TARR, RSPB and analyzes the simulation results. ***The evaluation results indicated an increase in the efficiency of resource utilization, a decrease in the process execution delays and also a decrease in the request rejection*** rate for the proposed method compared with ***other two methods.***

VI. REFERENCES

[1]. U. Rusydi, A. Arun and C. R. Rao, "Data Structure for Advance Planning and Reservation in a Grid System," International Journal of Computer Applications (IJCA), vol. NCRTC, no. 1, pp. 33-37, 2012.

[2]. A. W. Mu'alem and D. G. Feitelson, "Utilization, Predictability, Workloads, and User Runtime Estimates in Scheduling the IBM SP2 with Backfilling," IEEE 135 Transactions on Parallel and Distributed Systems, vol. 12, pp. 529-543, 2001.

[3]. A. Sulistio and R. Buyya , "A Grid simulation infrastructure supporting advance reservation," in 16th International Conference on Parallel and Distributed Computing and Systems, pp. 1--7. ACTA Press, Calgary, 2004.

[4]. J. MacLaren, "Advance Reservations: State of the Art," Working Draft, Global Grid Forum , 2003.

[5]. W. Smith, I. Foster and V. Taylor, "Scheduling with Advanced Reservations," in 14th IEEE International Symposium on Parallel and Distributed Processing, pp. 127--132. IEEE Press, Cancun, 2000.

[6]. Deadlock-Free Scheduler, Hindawi Mathematical Problems in Engineering, Volume 2018, Article ID 1438792, 18 pages.

[7]. H. Chu and K. Nahrstedt, "A Soft Real Time Scheduling Server in UNIX Operating System,"European Workshop on Interactive Distributed Multimedia Systems and Telecommunication Services (IDMS '97), Sep. 1997.

[8]. P. Goyal, X. Guo, and H. M. Vin, "A Hierarchical CPU Scheduler for Multimedia Operating Systems," 2nd Symposium on Operating System Design and Implementation (OSDI '96), Oct. 1996, pp. 107-122.

[9] W. Smith, I. Foster, and V. Taylor, "Scheduling with Advanced Reservations," International Parallel and Distributed Processing Symposium (IPDPS '00), May 2000.

[10] S. Nirmala Devi, A. Pethalakshmi," TARR: Time Slice based Advance Resource Reservation in Grid Computing Environments", International Journal of Computational Intelligence and Informatics, Vol. 6: No. 1, June 2016

Authors Profile



S. Sivakumar received his **M.Phil** Degree from Alagappa University, Karaikudi in the year 2005. He has received his **M.C.A** Degree from Periyar University, Salem in the year 2001. He is working as Assistant Professor, Department of Computer Science, PGP College of Arts & Science, Namakkal, Tamilnadu, India. He has around **16** years of experience in Academic Field. He is **pursuing** his **Ph.D** Degree (Part-Time) at Sri Vijay Vidyalaya College of Arts & Science (Affiliated Periyar University), Dharmapuri, Tamilnadu, India. His areas of interest include Grid Computing, Cloud Computing and Computer Networks.



Dr.D.Maruthanayagam received his **Ph.D** Degree from Manonmaniam Sundaranar University, Tirunelveli in the year 2014. He received his **M.Phil** Degree from Bharathidasan University, Trichy in the year 2005. He received his **M.C.A** Degree from Madras University, Chennai in the year 2000. He is working as **Head & Professor**, PG and Research Department of Computer Science, Sri Vijay Vidyalaya College of Arts & Science, Dharmapuri, Tamilnadu, India. He has **19 years** of experience in academic field. He has published **5 books**, more than **45 papers** in International Journals and **30 papers** in National & International Conferences so far. His areas of interest include Computer Networks, Grid Computing, Cloud Computing and Mobile Computing.

PRINCIPAL
PGP College of Arts and Science.
Namakkal

Inbox - sslchd74@gmail.com | Home | Consortium for Academic and R | Scopus preview - Scopus - Sour | Scopus preview - Scopus - Sour

Not secure | joics.org

A Peer Reviewed/ Referred Journal

ISSN: 1548 - 7741

Journal of Information and Computational Science

HOME CALL FOR PAPERS GUIDELINES INDEXING AIM & SCOPE

PROPOSAL ARCHIVES EDITORIAL BOARD CONTACT



Information Regarding UGC-CARE Group 'A' Journals

UGC-CARE Group A Journals Link

https://ugccare.unipune.ac.in/site/Website/CareList.aspx

Login User Name : ugccaregroupa@gmail.com
Password : 123456789

Direct UGC-CARE Group 'A' Journal Link

https://www.scopus.com/sources?sortField=citescore&sortDirection=desc&isHiddenField=false&field=issn&issn=15487741

Serial No : 21148

COMPARATIVE ANALYSIS OF RESOURCE RESERVATION ALGORITHMS (DRR, ORR, RSPB AND TARR) WITH NOVEL ADVANCED DYNAMIC RESOURCE RESERVATION (ADRR)

[1]S.Sivakumar, [2]Dr. D. Maruthanayagam

[1]*Research Scholar, Sri Vijay Vidyalaya College of Arts & Science, Dharmapuri, Tamilnadu, India*

[2] *Head/Professor, PG and Research Department of Computer Science, Sri Vijay Vidyalaya College of Arts & Science, Dharmapuri, Tamilnadu, India*

Abstract: Grid computing is a term referring to the combination of computer resources from multiple administrative domains to reach a common goal. A Grid system is comprised of large sets of heterogeneous and geographically distributed resources that are aggregated as a virtual computing platform for executing large-scale scientific applications. As the number of resources in Grid increases rapidly, selecting appropriate resource for a job is a complex undertaking as resources are distributed and heterogeneous in nature. Matching the users' requirements with the resource capabilities plays a vital role in the resource selection process. In this paper, propose an Advanced Dynamic Resource Reservation **(ADRR)** framework for grid computing. ***The proposed ADRR*** approach ensures the availability of resources when it is required in the grid computing environment. The ***end-to-end QoS can be achieved and guaranteed through proper configuration, reservation and allocation of corresponding resources.*** The performance comparison of proposed algorithm is done using the following parameters; average waiting time, resource utilization time, average turnaround time, percentage of successful jobs, request rejection rate and makespan. ***The simulation results show that the proposed grid resources reservation technology performs better than existing techniques.***

Keywords: Grid Computing, Dynamic Resource Reservation, Reservation Scheduler, Resource Manager, Time-Slice based Advance Resource Reservation, Optimal Resource Reservation and Dynamic Resource Reservation

I. INTRODUCTION

One of the primary goals of grid computing [1] [2] is to share access to geographically distributed heterogeneous resources in a transparent manner. There will be many benefits when this goal is realized, including the ability to execute applications whose requirements exceed local resources and the reduction of job turnaround time through workload balancing across multiple computing facilities. The development of data grids and the associated middleware has therefore been actively pursued in recent years. However, many major technical hurdles stand in the way of realizing these benefits. Among the myriad research issues to be addressed is the problem of distributed resource management and job scheduling for data grids. In most grid systems, submitted jobs are initially placed into a queue if there are no available resources in the local resource manager or scheduler. However, each grid system may organize a different scheduling algorithm that executes jobs based on different parameters, such as submission time, number of resources, and duration of execution. Therefore, there is no guarantee as to when these jobs will be executed. Several researchers have proposed the need for advance reservation [3] [4] [5] to address these issues. Common resources that can be reserved or requested are compute nodes, storage elements, network bandwidth or a combination of any of those. Advance resource reservation can be useful for several applications such as parallel applications, where each task requires multiple compute nodes simultaneously for execution, workflow applications, where each job may depend on the execution of other jobs in the application. Hence, it needs to wait for all the dependencies to be satisfied before it can be executed and multimedia or soft real-time applications, such as video conferencing and player, where they need to have a certain amount of bandwidth to ensure a smooth broadcast of video and audio over the network. In this paper suitable approach to this problem begins with defining advance reservation of the resources with scheduling architecture is

proposed. The proposed framework and its policies are different from other existing techniques in terms following unique features:

- To dynamically resolve job priorities of users on the basis of their preferences, history of timely payments, amount of business given to the grid, paying capacity etc
- To perform advanced reservation of resources and at the same time use quota based policy to prevent starvation of jobs due to long jobs with high priority
- Address the limitation of the deadlock avoidance techniques by proposing a dynamic budget which eliminates the need of prior knowledge of the resource requirement of any process, the budget is adjusted dynamically to cater the need of the process
- To speed up the allocation process by minimizing the searching complexity using energy aware searching engine
- To make the system more reliable to the changing environment by considering the dynamicity of the resources
- To assign best resource to job by considering the diversity in the resource behavior
- To assure the successful allocation of job by ranking the resources and rescheduling the ranked resources
- This helped in providing quality of service, fulfillment of commitments and better revenue generation
- Allows service providers to get best revenues and vice a versa for best offers for consumers
- Enforces a Service Level Agreement with penalties and rewards where execution of deals and settlements work under a constitutional framework
- Allows reservation of resources and provides compensations in the event of failures

To demonstrate the usability of proposed techniques, a simulation test bench was implemented using the GridSim and successful simulation was achieved [6]. The experimental results showed a significant improvement in terms of the average waiting time, resource utilization time, average turnaround time, percentage of successful jobs, request rejection rate and makespan as compared to the already existing Grid reservation technique.

II. RESOURCE RESERVATION METHODOLOGIES

A. Dynamic Resource Reservation

The computationally hazardous problems necessitate deploying the complexity in the grid environment for the earlier execution. This can only be achieved by resource sharing. To ensure the availability of resources at the required time, the resources are reserved in advance. The available advance resource reservation schemes are priority based reservation, time slice based advance resource reservation and optimized resource reservation. In all the reservations, it is assumed that the reservations done are utilized, but there are some situations where the reserved resources are kept idle due to some network failure, termination of parent process, termination of current process etc.,. In this dynamic resource reservation (DRR) scheme [7], analyzes the reservations which are unutilized and allocates the unutilized reservations to the current requirements and these unutilized reservations can be used for the current reservation. In the grid environment, there are many computational nodes. These computational nodes used to have resources associated with it. The Local Resource Manager (LRM) at the computational node handles the details about the resources and manages the resources. Once the computational node becomes the participating node in the grid, then the resources associated with that computational node move to the available state [8]. The available state means that the resources are available for reservation or use. When the process requires the resources immediately then it can use, hence the resource moves to the in-use state. When the process requires the resources after a period of time, then the resources can be reserved during that time slot. For that time slot alone the resource would be in reserve state [9]. The resources required are reserved for future use. There are some abnormalities like a) termination of parent process may lead to the termination of child process b) network failure c) suspension of current process d) blocking of current process etc,. After reserving the resources due to these abnormalities, the reservation may not be required. But these abnormalities.

DRR Algorithm

The algorithm DRR shows the proposed reservation scheme. The algorithm takes in the process id, start time (ST), finish time(FT) and defer time (DT) as input.

```
Algorithm DRR ( process_id, ST, FT, DT)
begin
If the list is empty then
        No conflict found. Hence accept the reservation
else
        get_jobId(timeslot)
if isalive(jobId)
if isrequire(timeslot)
        return()
else
```

```
        allot(current_jobid, timeslot)
end if
else
        allot(current_jobid, timeslot)
end if
end if
end
```

If the reservation list is empty then it means that the resource is free during the required time slot. Hence the reservation can be done. When reservation is already available during the time slot, then the job can be checked for the availability. The islive function returns whether the reserved job id is still alive or not. If the reserved job is not alive then the slot is available for the current reservation hence that can be allotted for the current reservation. If the required time slot is reserved then the isrequire function is called which determines whether the reservation made is further required or not. If it is not required then the time slot can be used for the current reservation.

B. Optimal Resource Reservation (ORR)

The ORR algorithm finds the optimal time slice from the selectslicequeue. For this the algorithm takes in the job id of the process and the selectslicequeue as input. And it returns the optimal reservation of resource. The selectslicequeue maintains the time slices that can be reserved. The size function in ORR returns the number of elements in the particular queue. Initially the time required for the job is estimated [10]. It is computed by calculating the difference between the finish time of that job and the start time of the job. Then they found value is set to zero. It is used as a flag variable. If it is left as zero then it means that the reservation is not made possible. Only when it is turned to one the slot is available. The size of the free slice is computed from the selectslicequeue. Since the selectslicequeue maintains the slice start time and slice finish time the difference between the two is computed and maintained in slot variable. In this algorithm if the first slice it is in required size then it is allocated and it is the optimized allotment as it doesn't require the context switching [11]. Otherwise the slot is allotted and the required time is reduced by the slot value. So that the required time value contains the required time slot after partial reservation. The found value indicates the number of time slices considered for reservation for the particular job id. The found value is compared with the threshold value [12]. If they found is greater than the threshold value then the randomize function is called on the selectslicequeue. This function shuffles the time slices and the time slices are selected. When the numbers of time slices are below the threshold value then the selected slices are assigned for the job.

```
Algorithm ORR(JID, SelectSlice(Queue)
begin
        requiredtime = FT – ST
        found = 0
        for i = 1 to size(selectslicequeue)
                slot = selectslicequeue.sft -
        selectslicequeue.sst
        if (slot >= requiredtime && found = 0)
then
                allot(sid, selectslicequeue.sst,
        selectslicequeue.sft)
                return
        else
                requiredtime = requiredtime –
        slot
                allot(sid,selectslicequeue.sst,sele
        ctslicequeue.sft)
                found = found + 1
end if
end for
if found > T then
        randomize(selectslicequeue)
        ORR(JID, selectslicequeue)
else
        assignslice(found)
return
end if
end
```

C. Reservation Scheduler With Priorities And Benefit Functions (RSPB)

In RSPB [13], each reservation request has an associated benefit function that quantifies the "profit" for the client accrued by the client by securing the resource at the requested level. When the client is willing to negotiate for lower service levels, it could indicate this by providing a benefit function that shows a reduced but positive benefit for lower resource levels. This facility provided by the benefit functions removes the need for negotiations when there is a resource scarcity. A centralized resource reservation scheduler is assumed, i.e., all the resource reservations are performed by a centralized unit. Requests arrive randomly based on a Poisson arrival process. Because the requests are arriving in a random fashion at real time, the reservation scheduler cannot wait until all the requests have arrived to commence the scheduling. It should make the decisions on the requests as each one arrives or make a decision after the arrival of a batch of requests. Let m be the number of machines in the system. The machines are assumed to be homogeneous. Let CPU_sysj represent the percentage of CPU of the j-th machine Mj that is dedicated to the Grid system. For each request, Rk arriving at the reservation scheduler following parameters are defined. tk-start: start time of the reservation Rk. tk-end: end time of reservation for

Rk. CPUmax-k: minimum CPU requirement of Rk for delivering the maximum benefit to the application. pk: priority of Rk, due to limited amount of resources, the scheduler cannot meet the demands of all the requests. When the overall demand exceeds the available resources, the objective of the reservation scheduler is to minimize the sum of priority of the requests that are rejected. This algorithms uses heuristic approaches to achieve this objective [14]. Bk(pepu): the benefit function associated with Rk. It gives the benefit the client will receive if it is reserved CPU at the requested level. Although, in this paper, benefit functions are used only for quantifying the CPU requirements, it may be used for other resources as well as the time constraints.

In this reservation model, a CPU resource may be temporally shared by multiple reservations, i.e., multiple reservations may overlap in time. Therefore, this algorithm need to determine the current CPU usage for a given time interval before admitting a reservation. In Lines (19) and (38), the current CPU (machine) usage is determined using *time slot* tables that keep track of reservations that have already been accepted. The time slot tables only keep track of the partition of the CPU that is dedicated to the Grid and thus, managed by the reservation scheduler. Line (21) determines whether the examined machine can satisfy the hard QoS requirement of request *Rk*. If yes, this machine is put into a machine queue named *machQueuehard* for later selection in line (38). Although it is not shown in pseudo-code in Figure 2, the search for a machine that satisfies the reservation request can be stopped when a machine that satisfies the hard QoS is found. If none of the machines in the system can satisfy the hard QoS requirement of *Rk*, the reservation scheduler will attempt to schedule the reservation with a degradation of the CPU requirement for *Rk* provided the benefit function allows for the degradation. Line (24) to (32) attempt to find a machine that satisfies this situation and this machine is considered to satisfy the soft QoS requirement of *Rk*. Lines (26) to (32) attempts to maximize the benefit delivered to the application by the reservation. Lines (34) and (35) deal with the case where the system cannot provide the requested level of service to *Rk*. The reservation scheduler checks the meta-request *Rnonsatisfy* and sends rejections messages to the clients that submitted the reservation requests in *Rnonsatisfy*. The clients may resubmit their reservation requests with modifications and these submissions will be considered for reservation at the next scheduling event [15]. Line (38) ensures that the load is distributed across the machines.

RSPB Algorithm:

function scheduleRmeta (meta-request Rmeta)
(2) Rk : the kth request in Rmeta;
(3) Mj : the jth machine in the system;
(4) CPUmin-k : minimum CPU requirement when Rk
get lowest acceptable
benefit from reservation;
(5) load_heaviestj(tm, tn) : the heaviest load of Mj within
a reservation duration tm to tn;
(6) CPU_smallestj(tm, tn) : the smallest availability of CPU
to reserve for Mj within a duration tm to tn;
(7) machQueuehard : queue for storing machines that satisfy hard QoS request of Rk;
(8) machQueuesoft : queue used to store machine which can satisfy soft QoS request of Rk;
(9) Bjk : benefit value which Rk can get from Mj;
(10) Rnonsatisfy : meta-request to store rejected requests;
(11) for all requests Rk in Rmeta
(12) sort the requests in descending order by pk;
(14) for each sorted request Rk in Rmeta
(15) reset machQueuehard and machQueuesoft
(16) get tk-start and tk-end;
(17) calculate CPUmin-k according to selected benefit function shape;
(18) for each machine Mj in the system
(19) get load_heaviestj(tk-start, tk-end);
(20) CPU_smallestj(tk-start, tk-end) = CPU_sysj - load_heaviestj(tk-start, tk-end);
(21) if (CPU_smallestj(tk-start, tk-end) ≥CPUmax-k);
(22) machQueue$_{hard}$← Mj;
(23) else
(24) if (machQueuehard is empty)
(25) if (CPU_smallestj(tk-start, tk-end) ≥CPU_{min-k})
(26) if (machQueuesoft contain machine Mi)
(27) Bjk = Bk(CPU_ smallestj(tk-start, tk-end));
(28) Bik = Bk(CPU_ smallesti(tk-start, tk-end));
(29) if (Bjk > Bik)
(30) machQueuesoft ← Mj;
(31) else
(32) machQueuesoft ← Mj;
(33) endfor
(34) if (both the machQueuehard and machQueuesoft are empty)
(35) put the request Rk into meta-request Rnonsatisfy;
(36) else
(37) if (machQueuehard is not empty)
(38) select the machine with the lowest average CPU load within duration (tm, tn);
(39) else
(40) the machine in the machQueuesoft is the choice
(41) mark the time slot table for this machine with requested reservation;
(42) endfor

D. Time-Slice based Advance Resource Reservation (TARR)

In this resource reservation approach [16], the resources are reserved even in the time slices where the resource is kept idle after the start time of the reservation. This time slice reservation can be done until the Defer Time (DT) accepted by the user for a particular reservation. Moreover an upper limit is imposed on the number of time slice (NTS), to reduce the overhead on the resuming and suspension of the job due to the resource availability. The Start, finish and defer time for using the resources are given by the user while submitting a job for execution. The start time and finish time are the expected start and finish time for using the resources. Sometimes it is not possible to reserve the resource at the stipulated start and finish time. In such case the reservation can be done until the defer time. Defer time is the time until which the reservation can be postponed.

TARR Algorithm:

1. if List is empty then
2. no conflict found. Hence accept the new reservation.
3. else
4. for i = 0 to List-Size -1 do
5. Put i into templist if one of the properties are true
6. Startnew ≤ starti&&finishnew≥ finishi ‖ Startnew ≤ finishi‖ finishnew≤ finishi
7. end for
8. if templist is empty then
9. no conflict found. Hence accept this reservation.
10. else
11. requiredtime = finishnew– startnew
12. balancereserve = requiredtime
13. for i = 1 to n
14. timeslice = starti+1 -finishi
15. if timeslice> 0 then
16. Put into slicequeue_insert(id,sst,sft)
17. end if
18. end for
19. while (slicequeue&&balancereserve)
20. if sst ≥ Startnew then
21. assign new reserve
22. currentreserve=sft – sst
23. Balancereserve = requiredtime –currentreserve
24. end if
25. end while
26. end if
27. end if

A reservation list is maintained at each resource. The list consists of the reservation id, ST and FT of the reservation. When there is no reservation for the resource then the list is empty. The new reservations can be added immediately when the list is empty. It is given in line 1 to 2 in the algorithm. If the reservation list is not empty then it is required to find out whether the required slot is free. For this the $start_{new}$ and $finish_{new}$ are compared with the existing list. To finding the availability for new reservation, the start and finish time of the new reservation is checked with the existing one. If $start_{new}$ is less than the start of the any of the reservations and the $finish_{new}$ is greater than the finish of the any of the reservation then it means there is a conflict. Even if $start_{new}$ or $finish_{new}$ is less than finish of any of the available reservations then also there exists the conflict. Only when there is no conflict there is slot available for reservation. Hence the reservation can be made when there is no conflict. To Forming SliceQueue, when reservations are not made possible within the slots available, then the empty time slices are arrived and placed into the SliceQueue. For this the difference between the current finish time and the next start time is computed as TimeSlice in this equation. $TimeSlice = Finish_{current} - Start_{next}$.

These timeslices are placed into the SliceQueue with an id and the $finish_{current}$ and $start_{next}$ values. The $finish_{current}$ and the $start_{new}$ are stored as SST(Slice Start time) and SFT (Slice Finish Time). To get the availing timeslices from SliceQueue, when there is reservation required in time slices for a job, then it can be provided. The balancereserve holds the expected reservation at that particular time. As and when a time slice is reserved then the time slice duration is reduced from the balancereserve which is computed using this equation. balancereserve = requiredtime – currentreserve. Where currentreserve = SFT – SST. The reservation is done until the balancereserve becomes null.

III. PROPOSED METHODOLOGY

The Advanced Dynamic Resource Reservation Model (**ADRR**) is shown in Figure 1. When the user submits the job to the job handler, job handler goes through five states. In the first state, users are sorted according to their priorities. In the second state, the job handler identifies the job as new or mature and forwards the job to the ***Dynamic Priority Resolution (DPR)***. When the job handler identifies the job as new, it forwards the new job with user requirements to the DPR. When the job handler identifies the job as mature, it forwards the mature job and the matched job_id to the DPR. The

seen from the figure, ***the ADRR gives improved results over DRR, TARR, ORR and RSPB***. This is due to the reason that the shortest jobs of higher priority users are entertained dynamically at the run time.

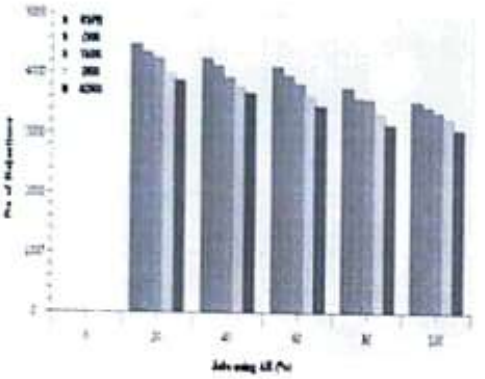


Figure 5: Graph between total no of rejections and percentage of jobs reserved

Resource utilization

The resource utilization is a Quality of Service (QOS) criterion. Below Equation gives the average utilization of resources for a schedule S. The value of average_utilization has to be maximized.

$$\text{average}_{\text{utilization}} = \frac{\sum_{[\text{nbMachines}]} \text{completion}[i]}{\text{makespan} \times \text{nb_machines}}$$

Where nb_machines denotes the number of resources, this Equation gives the completion time of a machine m. It is evident that the average utilization of resources for all algorithms is ranked as: 1) DRR 2) TARR 3) ORR and 4) RSPB. ***The overall performance of ADRR is good while considering the average resource utilization.***

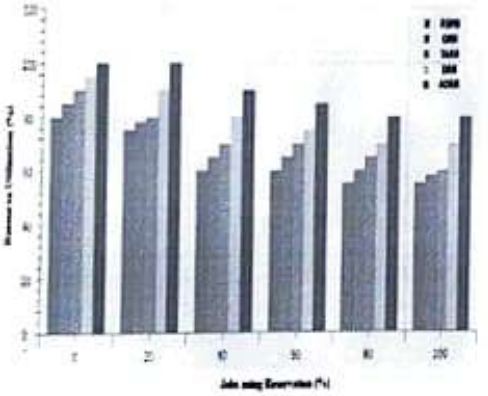


Figure 6: Graph between percentage of utilization and percentage of jobs reserved

Percentage of successful jobs

The experiment is conducted to test the ADRR ability to adapt to the changing grid environment. The experiment is started by dynamically populating the resource pool with varying number of resources. The resources are steadily registered to the resource pool, depending on their availability, and some resources are removed from the resource pool. This examines the effect of change in the type of resources in successfully completing the jobs. For different resource levels, the number of jobs completed by DRR, TARR, ORR, RSPB and ADRR are noted. ***ADRR provides better performance than others.***

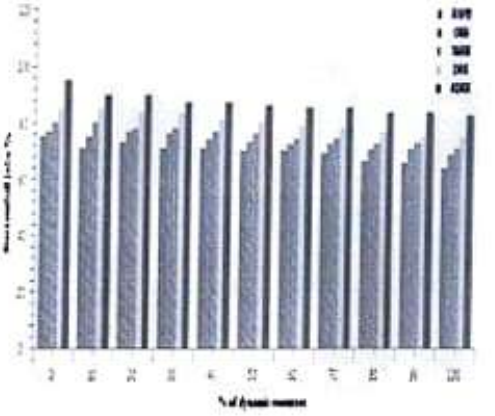


Figure 7: Comparison the Percentage of Successful Jobs

V. CONCLUSION

Grid technologies represent a significant achievement towards the aggregation of networked resources for solving large-scale data-intensive or compute-intensive applications. Grids has evolved as the next generation computing platform for hosting distributed services for computing, content management and data sharing. The present work identifies and proposes the design and development of ADRR architecture with the support of advance reservation and scheduling concept. This paper has compared the various parameters with pre-existing methods along with novel proposed method of ADRR. ***The GridSim toolkit is used to evaluate the performance of ADRR algorithm through a series of simulations.*** The simulation uses various numbers of users and optimization strategies. ***As a result, the ADRR algorithm improves the utility of the system significantly compared to the other algorithms.***

VI. REFERENCES

[1]. I.Foster, K.Kesselman, "The Grid: Blueprint for a New Computing

Infrastructure", 1st ed. Morgan Kaufmann Publisher, ISBN: 1558604758, November 1998.

[2]. F.Donno, H.Stockinger, R.Puccinelli and K.Stockinger, "Data Grid Tutorials with Hands-on Experience", 1st International Workshop on Grid Education (Grid.Edu 2004), Chicago, Illinois, April 19-22, 2004, IEEE Computer Society Press.

[3]. J.MacLaren, "Advance Reservations: State of the Art (draft)", Global Grid Forum (GGF), June 2003. http://www.ggf.org.

[4]. W.Smith, I.Foster and V.Taylor, "Scheduling with advanced reservations", In Proceedings of the International Parallel and Distributed Processing Symposium (IPDPS'00), Cancun, Mexico, May 1-5, 2000.

[5]. A.Schill, F.Breiter and S.Kuhn, "Design and evaluation of an advance reservation protocol on top of rsvp", In Proceedings of the IFIP TC6/WG6.2 4th International Conference on Broadband Communications (BC'98), Stuttgart, Germany, April 1998.

[6]. Deadlock-Free Scheduler, Hindawi Mathematical Problems in Engineering, Volume 2018, Article ID 1438792, 18 pages.

[7]. S. Nirmala Devi , A. Pethalakshmi, PhD, " DRR: Dynamic Resource Reservation in Grid Computing", International Journal of Computer Applications (0975 – 8887) Volume 159 – No 6, February 2017

[8]. Rui Min, Muthucumaru Maheswaran, "Scheduling Advance Reservations with Priorities in Grid Computing Systems". In proceedings of 2002 2nd IEEE / ACM International Symposium on Cluster Computing and the Grid, 266 – 268.

[9]. Anthony Sulistio and Rajkumar Buyya, "A Grid Simulation Infrastructure supporting Advance Reservation", proceedings of the 16th International Conference on parallel and Distributed Computing and Systems, Nov 9 – 11 2004, MIT, Cambridge, USA, pp. 1-7.

[10]. **S.Nirmala Devi and A.Pethalakshmi,** " ORR: Optimal Resource Reservation In Grid Computing Environments", Indian Journal of Science and Technology, Vol 9(48), DOI: 10.17485/ijst/2016/v9i48/102300, December 2016

[11]. Devi SN, Pethalakshmi., "An Object Oriented Approach to Disseminate Education by Applying Grid Computing Techniques in Universities and Educational Institutions in India", Proceedings of 2012 IEEE International Conference on Technology Enhanced Education (ICTEE),INDIA: 2012.

[12]. Barzegar B, Esmaeelzadeh H, Shirgahi H.A, "New Method on Resource Management in Grid Computing Systems Based on QoS and Semantics", Indian Journal of Science and Technology, 2011 Nov; 4(11):1–4.

[13]. H. Chu and K. Nahrstedt, "A Soft Real Time Scheduling Server in UNIX Operating System,"European Workshop on Interactive Distributed Multimedia Systems and Telecommunication Services (IDMS '97), Sep. 1997.

[14]. P. Goyal, X. Guo, and H. M. Vin, "A Hierarchical CPU Scheduler for Multimedia Operating Systems," 2nd Symposium on Operating System Design and Implementation (OSDI '96), Oct. 1996, pp. 107-122.

[15]. W. Smith, I. Foster, and V. Taylor, "Scheduling with Advanced Reservations," International Parallel and Distributed Processing Symposium (IPDPS '00), May 2000.

[16]. S. Nirmala Devi, A. Pethalakshmi," TARR: Time Slice based Advance Resource Reservation in Grid Computing Environments", International Journal of Computational Intelligence and Informatics, Vol. 6: No. 1, June 2016

Authors Profile

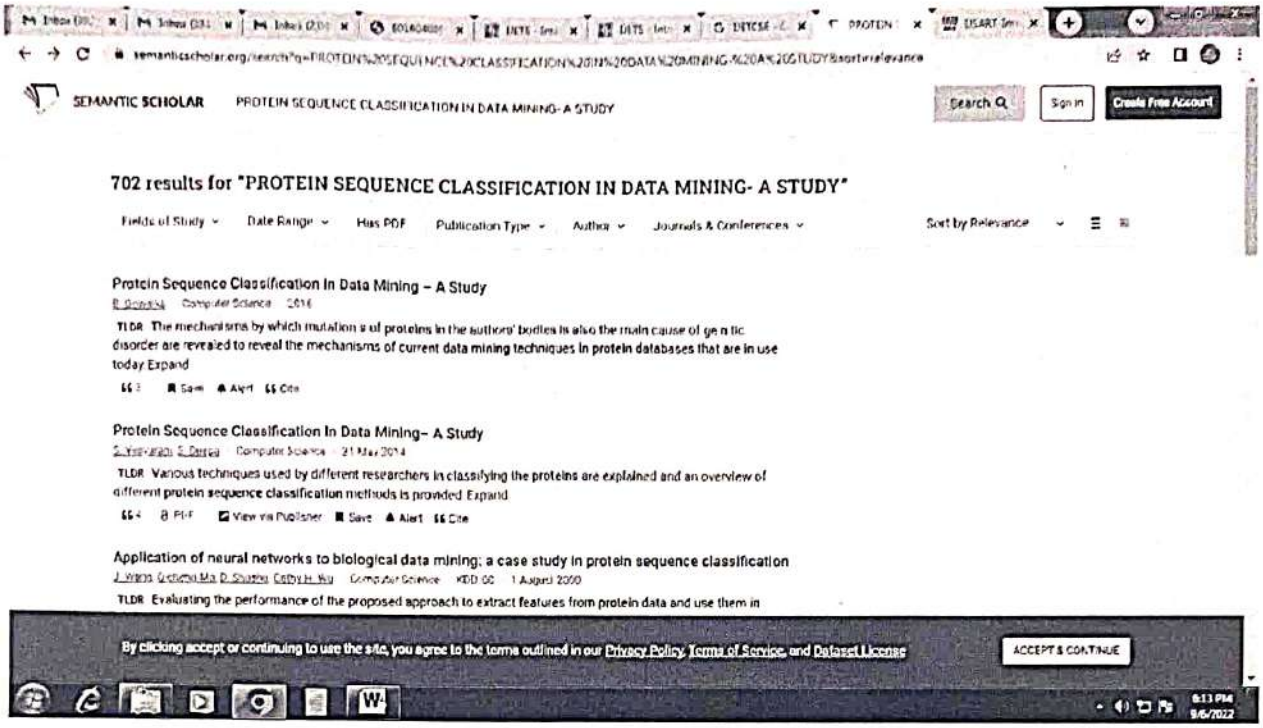


S. Sivakumar received his **M.Phil** Degree from Alagappa University, Karaikudi in the year 2005. He has received his **M.C.A** Degree from Periyar University, Salem in the year 2001. He is working as Assistant Professor, Department of Computer Science, PGP College of Arts & Science, Namakkal, Tamilnadu, India. He has around **16** years of experience in Academic Field. He is **pursuing** his **Ph.D** Degree (Part-Time) at Sri Vijay Vidyalaya College of Arts & Science (Affiliated Periyar University), Dharmapuri, Tamilnadu, India. His areas of interest include Grid Computing, Cloud Computing and Computer Networks.



Dr.D.Maruthanayagam received his **Ph.D** Degree from Manonmaniam Sundaranar University, Tirunelveli in the year 2014. He received his **M.Phil** Degree from Bharathidasan University, Trichy in the year 2005. He received his **M.C.A** Degree from Madras University, Chennai in the year 2000. He is working as **Head & Professor**, PG and Research Department of Computer Science, Sri Vijay Vidyalaya College of Arts & Science, Dharmapuri, Tamilnadu, India. He has **19 years** of experience in academic field. He has published **5 books**, more than **45 papers** in International Journals and **30 papers** in National & International Conferences so far. His areas of interest include Computer Networks, Grid Computing, Cloud Computing and Mobile Computing.

PRINCIPAL
PGP College of Arts and Science
Namakkal


semanticscholar.org/search?q=PROTEIN%20SEQUENCE%20CLASSIFICATION%20IN%20DATA%20MINING-%20A%20STUDY&sort=relevance
SEMANTIC SCHOLAR
PROTEIN SEQUENCE CLASSIFICATION IN DATA MINING- A STUDY
Search
Sign In
Create Free Account
702 results for "PROTEIN SEQUENCE CLASSIFICATION IN DATA MINING- A STUDY"
Fields of Study
Date Range
Has PDF
Publication Type
Author
Journals & Conferences
Sort by Relevance
Protein Sequence Classification In Data Mining – A Study
Protein Sequence Classification In Data Mining– A Study
Application of neural networks to biological data mining: a case study in protein sequence classification
By clicking accept or continuing to use the site, you agree to the terms outlined in our Privacy Policy, Terms of Service, and Dataset License
ACCEPT & CONTINUE


COLLEGE OF ARTS & SCIENCE
PRINCIPAL

ISSN (Print) 0975 – 1353

IJETCSE

International Journal of Emerging Technology in Computer Science and Electronics

Vol 23 Issue 7, October 2016

PROTEIN SEQUENCE CLASSIFICATION IN DATA MINING– A STUDY

Mrs. R.Suguna

P.G.P College of arts and science, Namakkal· M.C.A., M.Phil.,

Asst.Professor, Department of Computer Science and

Applications,

P.G.P College of Arts and Science, Namakkal

ABSTRACT

Since the computerized applications are used all around the world, there occurs the collection of a vast amount of data. The important information hidden in vast data is attracting the researchers of multiple disciplines to make study in developing effective approaches to derive the hidden knowledge within them. Data mining may be considered to be the process of extracting or mining the useful and valuable knowledge from large amounts of data. There are various different domains in data mining such as text mining, image mining, sequential pattern mining, web mining and etc. Among these, sequence mining is one of the most important research area which helps to finding the sequential relationships found in the data. Sequence mining is applied in wide range of application areas such as the analysis of customer purchase patterns, web access patterns, weather observations, protein sequencing, DNA sequencing, etc. In protein and DNA analysis, sequence mining techniques are used for sequence alignment, sequence searching and sequence classification. In the area of protein sequence analysis, the researchers are showing their interest in the field of protein sequence classification. It has the ability to discover the recurring structures that exist in the protein sequences. This paper explains various techniques used by different researchers in classifying the proteins and also provides an overview of different protein sequence classification methods.

KEYWORDS

Sequence, Feature hashing, Neural Network Model, Rough set theory, Fuzzy modeling, Classification

1. INTRODUCTION

In recent years, developments in the field of genomics and proteomics is proceeding at a rapid rate and it have generated a large amount of biological data. Obtaining conclusions from these data requires the application of sophisticated computational analyses methods. Bioinformatics is the interdisciplinary science that interprets the biological data using information technology and



computer science. The significance of this new field of research will grow as large quantities of genomic, proteomic and other data continue to be generated and integrated. Bioinformatics and computational biology are fields that require skills from a variety of fields to enable the gathering and storing, handling and analyzing, interpreting and spreading of biological information. It requires the usage of high performance computers and innovative software tools to manage and organize enormous quantities of genomic and proteomic data. It also comprises the development and application of innovative algorithmic techniques necessary for the analysis and interpretation of sequential data. It is also used for the classification and prediction of sequential data which provides insight into the design and validation of experiments for the life sciences. This is required now with the rapid increase of the amounts of data generated on a daily basis.

Bioinformatics is a field that is committed to the interpretation and analysis of the biological data using computational techniques. Since there had been a fiery growth of biological information which has been generated by the scientific community, the bioinformatics field has developed to a greater extent. [14]. A number of data mining related tasks such as manipulation, searching and data mining of DNA sequence data are performed efficiently. The advancement in techniques for storing and searching DNA sequences have led to the widely applied advances in computer science. Several methods such as string searching algorithms, machine learning and database theory have been introduced and used effectivey. Solving the biological problems is the particular active area of research in bioinformatics where the data mining techniques are applied effectively.

Both the data mining and bioinformatics fields are fast expanding research frontiers. It is important to examine the important research issues in bioinformatics and develop new data mining methods for scalable and effective bio-data analysis [7]. Data mining can assist the researcher in finding out the new knowledge from plenty of biological data at the molecular level [5]. Sequential pattern mining[1] is an important field of data mining, in which a very small alphabet (i.e., 4 for DNA sequences and 20 for protein sequences) and long patterns with a typical length of few hundreds or even thousands frequently appear.

A number of different algorithms have been introduced to carry out the pattern mining task well. The main task involves the finding out of all the sequential patterns with higher or equal support to a predefined minimum support threshold in a sequence database [1]. Sequential data occurs frequently in many scientific, medical, security, business and other applications. Sequence data mining provides the necessary tools and approaches for unlocking useful knowledge hidden in the mountains of sequence data. A sequence is normally an ordered list of objects.

The term sequence in proteins denotes the arrangement of sequence of amino acids that constitutes protein. The sequences of proteins that are identified are being stored in various databases. Each database stores a specific classification of protein sequences. Different classification methods or algorithms have been projected by different scientists to classify the protein sequences. Researchers apply some well-known classification techniques like Naive bayes classification, neural networks, Genetic algorithm, Decision tree Classifier etc for accurate protein classifications.

The rest of the paper is organized as follows: Section 2 describes the basics of protein sequences and the need for classification of protein sequences into families. Section 3 describes the various research challenges related to classification of protein sequences. Section 4 deals with various methods developed by researchers for protein sequence classification and conclusion is given in section 5.

P.G.P. COLLEGE OF ARTS & SCIENCE NAMAKKAL 637 206

2. PROTEIN SEQUENCES:

Proteins are large molecules that are composed of one or more chains of amino acids in a specific order. The normal size of a protein molecule may be hundred amino acids, while the large proteins can have a thousand amino acids. 20 amino acids, i.e., {A, C, D, E, F, G, H, I, K, L, M, N, P, Q, R, S, T, V, W, Y}, make up the diverse array of proteins found in living things. Protein Sequence is considered as a very important part of biological sequence data where the analysis and study have become an important research direction and content in bioinformatics domain. This technique involves the determination of the amino acid sequence that makes up the protein. Some research can be performed on a protein sequence or a protein family sequence making the protein sequence pattern mining a much important task in this field. One of the basic tools for the analysis of proteins is similarity searching [11]. The process can be implemented in the amino acid sequence or in the spatial structure of the protein.

Searching for similarity among the proteins may have different applications. Based upon the area , the proteins can be analyzed at the level of amino acid sequence or with respect to various features of their structures. Comparative analysis of the protein sequences may be helpful for the identification of proteins, identification of their functions and determination of their fundamental physical-chemical properties. The comparative analysis of the protein sequences brings much more information and is extremely important in the processes such as the prediction of the properties of the newly discovered proteins that are difficult to be identified on the basis of amino acid sequence.

PROTEIN SEQUENCE DATABASES:

Researchers have found out that the sequences of various proteins and their details are stored in databases. Some well-known databases include Protein Data Bank (PDB), UniProt, Swiss-Prot, SCOP, etc. The sequence of the proteins can be extracted from these databases.

An example of protein sequence of Haemoglobin beta chain is shown below:

VHLTPEEKSAVTALWGKVNVDEVGGEALGRLLVVYPWTQ
RFFESFGDLSTPDAVMGNPKVKAHGKKVLGAFSDGLAHLD
NLKGTFATLSELHCDKLHVDPENFRLLGNVLVCVLAHHFG
KEFTPPVQAAYQKVVAGVANALAHKYH

CLASSIFICATION IN PROTEIN SEQUENCES:

There is a need for the advancements in the development of an intelligent system in order to classify the incoming protein into a particular super family. Proteins are composed of a sequence of 20 different types of amino acids. The gene sequence is defined by the sequence of aminoacids which is encoded in the genetic code. During the synthesis of proteins, the residues in the proteins are often chemically altered. This is due to the posttranslational modification which may change the physical and chemical properties of the proteins and also alters their folding activity. Finally it changes the function of the proteins resulting in the disease conditions.

Two proteins can be classified into a same super family if they acquire similar sequence of amino acids, which may therefore be functionally and structurally related. If two protein sequences have

P.G.P. COLLEGE OF ARTS & SCIENCE NAMAKKAL 637 206

high similarity i.e. have most of the features in common, then they can be classified in to the same class [11]. This plays important part in classifying new proteins based upon amino acid sequences, identifying diseased protein sequences, aligning multiple sequences, etc. The aim of protein super family classification is to predict the super family to which input protein belongs to. Protein classification aims on predicting the function or the structure of new proteins.

NEED FOR CLASSIFICATION TECHNIQUES IN PROTEIN SEQUENCES:

Different classification techniques have been used to classify the protein sequence into its particular class or sub class or family. Some of the features of the proteins can be extracted, then the value of these features can be matched and finally the protein sequence can be classified. In order to classify a data using classification or clustering techniques, a set of data is analyzed and a set of grouping rules are generated. For instance, one may classify diseases and provide the symptoms which describe each class or subclass.

In the analysis of biological data, an important problem is to classify the bio sequences or structures based on their critical features and functions. For instance, the protein and gene sequences that are isolated from the diseased and healthy tissues can be compared to identify the critical differences between the two classes of genes. Such features can be used for the classification of bio-data and prediction of the behaviors. For bio-data classification, several methods have been developed. For example, one can first retrieve the protein sequences from the two tissue classes and then find and compare the frequently occurring patterns of each class.

Analysis and interpretation of biological sequence data is a fundamental task in bioinformatics. The techniques such as classification and prediction are one way to deal with such task. In fact, the researchers are often involved in identifying the family to which a newly sequenced protein belongs. This helps in knowing the evolution of this protein and to discover its biological functions. In addition, the study of proteins and the prediction of proteins are very useful in biology and medicine for many reasons. Biologists also try to spot out the active sites in proteins and enzymes to classify parts of DNA or protein sequences into coding or non-coding zones or to determine the function of the nucleic sequences such as the identification of the promoter sites and the junction sites and the identification of position of mutation which results in diseased conditions [3].

3. RELATED WORK:

A wide range of classification techniques have been developed to classify the protein sequence into its particular class, sub class or family. All these methods have a tendency to extract some of the features of the proteins and then these feature values are compared and finally the protein sequence are classified.

Jason T. L. Wang, Qic Heng Ma, Dennis Shasha, Cathy H Wu In [6] had used a neural network model in their work for classifying the existing protein sequences. To implement this, some characteristics were extracted from the protein sequences to be used as an input. The high level features are extracted using some encoding techniques from the sequences considering both global and local similarity of the sequences. The methods that were used to find the global similarity are 2-gram encoding method and 6-letter exchange group. Certain user defined variables were used to achieve local similarity. Minimum description length (MDL) principle was

COLLEGE OF ARTS & SCI NAMAKKAL 637 206

also applied to calculate the significance of motif. Some features that were already defined were used as intermediate layers or hidden layers of the neural network. This model produces 90% to 92% accuracy [6].

Ramadevi Yellasiri, C.R.Rao [12] had proposed a new classification model called Rough Set Classifier for classifying the voluminous protein data based on structural and functional properties of protein. This model is fast and accurate and it can be used as an efficient classification tool than the others. This Classifier provides 97.7% accuracy. It is a hybridized tool comprising Sequence Arithmetic, Concept Lattice and Rough Set Theory. It can reduce the domain search space to 9% without losing the potentiality for the classification of proteins. The information about the family is identified using special arithmetic and utilize it for reducing the domain search space is proposed. The rules that are generated are stored in Sequence Arithmetic database.

Suprativ Saha and Rituparna Chaki [13] had proposed a three phase model for classifying the unknown proteins into known families. In first phase, the input dataset is reduced in order to remove the noisy sequences. It in turn will increase the accuracy and minimizes the computational time. In second phase, the necessary features such as molecular weight and isometric point are obtained and then feature ranking algorithm is applied to rank the features. This ranking is used to classify the sequences. In the final phase, the input sequence is classified in to the particular class or family using Neighbourhood Analysis. This rule has a power to extract the particular association relationships between the protein sequence and classes, sub classes and families. This type of classification produces the knowledge based information besides the data analysis technique.

Cornelia Caragea, Adrian Silvescu, Prasenjit Mitra [4] had used the feature hashing technique in their research work for the classification of protein sequences. Three issues are handled in this method. They are i) the influence of hash size on the performance of protein sequence classifiers that use hash features and the hash size at which the performance starts degrading due to hash collisions (ii) the effectiveness of feature hashing on prohibitively high dimensional representations (iii) the performance of feature hashing compared to that of feature selection by average mutual information. The results of the experiments on the protein data sets showed that feature hashing is an effective approach for reducing the dimensionality on protein sequence classification tasks.

Muhammad Mahbubur Rahman, Arif Ul Alam, Abdullah-Al-Mamun, Tamnun E Mursalin [9], had considered certain properties of protein for its classification namely structure comparison, Cluster Index, Connectivity, Interactivity, Taxonomic, etc. The probability of each protein that newly enters in the system is found against the already existing proteins in the system and they are added together. The aggregated probabilistic value is identified and it is compared with the probabilistic value of the protein that resides at the root. Based on guided search algorithm, the node which has the highest probability of level 1 is chosen. Then the probabilistic values of level 2 of selected node from level 1 are compared. Then the node having highest probability is chosen and continued until getting the exact position of newly entered protein reveals some of the functions based on the properties of proteins. These things are yet to be derived in different bioinformatics research lab such as cluster index, connectivity and interactivity. Then this can be efficiently used for protein classifications.

M.P. COLLEGE OF ARTS & SCIENCE NAMAKKAL 637 206

Xing-Ming Zhao1, De-Shuang Huang, Yiu-ming Cheung, Hong-qiang Wang and Xin Huang [15] had proposed a hybrid GA/SVM algorithm for protein sequence classification. The most important steps in the classification of protein sequences are the identification of the most informative features and reducing the dimensionality of the feature vectors. A novel hybrid GA/SVM system has been proposed that selects the features of proteins containing accurate and enough discriminative information for classification and train the SVM classifier simultaneously. Experimental results for protein sequences classification of six protein super families obtained from the Protein Information Resource (PIR) database showed that the hybrid GA/SVM system outperforms BLAST and HMMer techniques.

The above literature study clearly shows that till now, there is no technique that has been developed to classify the proteins based on the amino acid sequence of the proteins. Hence a new approach can be implemented for classifying the proteins based on sequences rather than considering the structural and functional characteristics.

4. RESEARCH CHALLENGES:

Recently, the assortment of biological data like protein sequences, DNA sequences etc. is growing at explosive rate due to the introduction of new ones. The results of recent research prove that it is very difficult to classify large amount of biological data like protein sequences using traditional database system. Data mining technique are suitable to handle the large data sources. A number of different techniques are already identified for classifying protein sequences. One important area of research is to classify protein sequences into different families, classes or sub classes. Some important research challenges include the following:

- The most important challenge in the area of protein sequence classification involves the organization of a huge volume of data such as the ones generated by the human genome project and to improve database design. For database access and manipulation and device data-entry procedures, several softwares need to be developed which in turn compensates for the varied computer procedures and systems used in different laboratories.
- In pattern matching, the entire protein sequence patterns cannot be matched accurately and the similarity among sequences are very difficult to identify. Hence computational work with data mining tasks must be developed which in turn minimizes the work of sequence comparison.
- Various classification methods are yet to be developed which provides easier way to classify the protein sequences based upon the user's needs.
- Fuzzy modeling [13] helps in the sequence data analysis although storage and time requirement are high. But in the construction of fuzzy sets, the computational complexity is added in each iteration as well. Hence the fuzzy modeling can be enhanced to perform better.
- The protein sequence pattern mining process can be extended further which in turn determines the biological significance of the patterns. This will allow discriminating the weight of each pattern in the overall classification results [10].
- The researchers are preparing for a larger study to examine the notion that more extensive data mining studies of the protein database will yield both statistically significant and verifiable improvements within environments as well as meaningful comparisons across them.

P.G.P. COLLEGE OF ARTS & SCIENCE NAMAKKAL 637 206

- One of the most important technique for drug design and the design of novel enzymes is protein structure prediction. A general clarification to such predictions remains an open problem for the researchers [8].
- Another important research area in protein sequence classification is the usage of feature hashing technique to other types of biological sequence data, e.g., DNA data, and other tasks [4].

5. CONCLUSION:

In recent trends, analysis of large amount of biological data like protein sequences is very difficult using traditional database system. Data mining techniques can be used to classify the unknown protein sequence. But the different models, which are used to classify the protein sequence is not perfect regarding the both accuracy level and computational time. Data mining approaches prove to be efficiently well suited for the bioinformatics applications since the bioinformatics is data-rich but there is no comprehensive theory of life's organization at the molecular level. This paper provided an overview of the ongoing research works involving different techniques to classify the protein sequences. It has been observed that knowledge based and analysis of data form an integral part of protein sequence classification. The classification of protein sequence produces knowledge based information besides data analysis techniques. In future, different analysis has to be done for better performance of protein sequence classifications.

REFERENCES:

[1] Anita Zala, Mehul Barot," Mining Sequential Pattern with Time-Constraint", International Journal of Engineering and Innovative Technology (IJEIT) Volume 2, Issue 7, January 2013, ISSN: 2277-3754

[2] Arabinda Panda, "Bio-Data Mining:Concepts & Applications", International Journal of Computer Science and Management Research Conference Issue DPDM 2012, ISSN 2278-733x

[3] Christian Schaefer, Yana Bromberg, Dominik Achten, Burkhard Rost, "Disease-Related Mutations predicted to Impact Protein Function", From SNP-SIG 2011:Identification and Annotation of SNPs in the Context of Structure, Function and Disease Vienna, Austria, 15 July 2011.

[4] Cornelia Caragea, Adrian Silvescu, Prasenjit Mitra, "Protein Sequence Classification using Feature Hashing".

[5] Hui-Huang Hsu, "Introduction to Data Mining in Bioinformatics", Idea Group Publishing, ITB12936.

[6] Jason T. L. Wang, Qic Heng Ma, Dennis Shasha, Cathy H Wu, "Application of Neural Networks to Biological Data Mining: A case study in Protein Sequence Classification", pp: 305-309, KDD, Boston, MA, USA (2000).

[7] Jiawei Han, "How can Data Mining Help Bio-Data Analysis?", BIOKDD02: Workshop on Data Mining in Bioinformatics (with SIGKDD02 Conference)

[8] KJiawei Hanhalid Raza, "Application of data mining in Bioinformatics", Indian Journal of Computer Science and Engineering, Vol 1 No 2, 114-118.

[9] Muhammad Mahbubur Rahman, Arif Ul Alam, Abdullah-Al-Mamun, Tamnun E Mursalin, "A more appropriate protein classification using Data mining", Journal of Theoretical and Applied Information Technology.

[10] Padro Gabriel Ferreira, Paulo J.Azevedo, "Protein sequence classification through Relevant sequence Mining and Bayes Classifiers"

[11] Rabie Said, Mondher Maddouri , Engelbert Mephu Nguifo, "Protein sequences classification by means of feature extraction with substitution matrices"

[12] Ramadevi Yellasiri, C.R.Rao, "Rough Set Protein Classifier", Journal of Theoretical and Applied Information Technology, (2009).

P.G.P. COLLEGE OF ARTS & SCIENCE NAMAKKAL 637 206

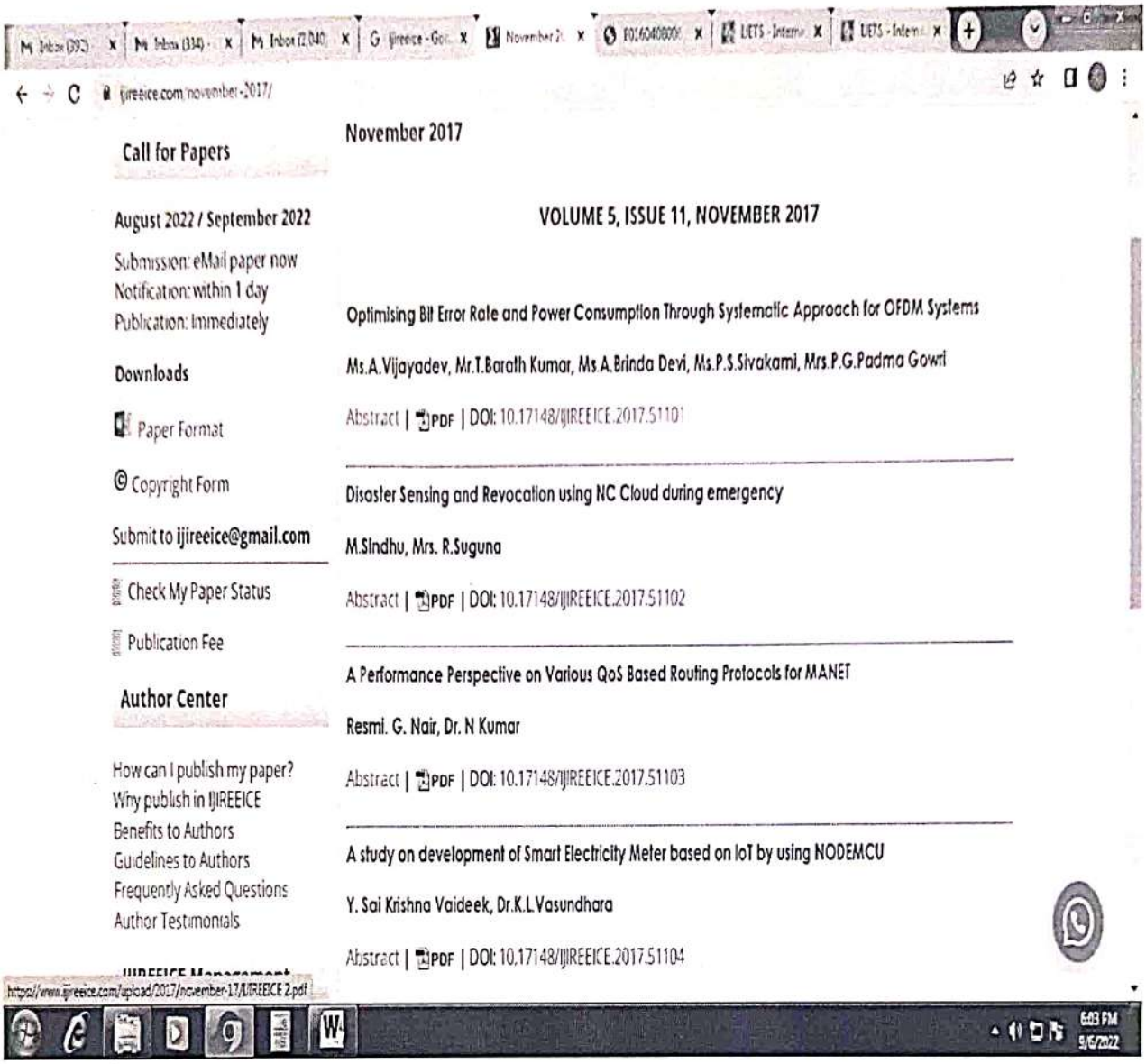
[13] Suprativ Saha and Rituparna Chaki, "A Brief Review of Data Mining Application Involving Protein Sequence Classification"

[14] P.K.Vaishali, Dr.A.Vinayababu," Application of Data mining and Soft Computing in Bioinformatics", International Journal of Engineering Research and Applications (IJERA) ISSN: 2248-9622

[15] Xing-Ming Zhao1, De-Shuang Huang, Yiu-ming Cheung, Hong-qiang Wang and Xin Huang, "A Novel Hybrid GA/SVM System for Protein Sequences Classification"



PRINCIPAL
PGP College of Arts and Science
Namakkal.



ijireeice.com/november-2017/

Call for Papers

August 2022 / September 2022

Submission: eMail paper now
Notification: within 1 day
Publication: Immediately

Downloads

Paper Format

© Copyright Form

Submit to ijireeice@gmail.com

Check My Paper Status

Publication Fee

Author Center

How can I publish my paper?
Why publish in IJIREEICE
Benefits to Authors
Guidelines to Authors
Frequently Asked Questions
Author Testimonials

IJIREEICE Management

November 2017

VOLUME 5, ISSUE 11, NOVEMBER 2017

Optimising Bit Error Rate and Power Consumption Through Systematic Approach for OFDM Systems

Ms.A.Vijayadev, Mr.T.Barath Kumar, Ms.A.Brinda Devi, Ms.P.S.Sivakami, Mrs.P.G.Padma Gowri

Abstract | PDF | DOI: 10.17148/IJIREEICE.2017.51101

Disaster Sensing and Revocation using NC Cloud during emergency

M.Sindhu, Mrs. R.Suguna

Abstract | PDF | DOI: 10.17148/IJIREEICE.2017.51102

A Performance Perspective on Various QoS Based Routing Protocols for MANET

Resmi. G. Nair, Dr. N Kumar

Abstract | PDF | DOI: 10.17148/IJIREEICE.2017.51103

A study on development of Smart Electricity Meter based on IoT by using NODEMCU

Y. Sai Krishna Vaideek, Dr.K.L.Vasundhara

Abstract | PDF | DOI: 10.17148/IJIREEICE.2017.51104

https://www.ijireeice.com/upload/2017/november-17/IJIREEICE 2.pdf

6:03 PM
9/6/2022

P.G.P. COLLEGE OF ARTS & SCIENCE
NAMAKKAL
637 206

IJIREEICE

ISSN (Online) 2321 – 2004
ISSN (Print) 2321 – 5526

International Journal of Innovative Research in
Electrical, Electronics, Instrumentation and Control Engineering

ISO 3297:2007 Certified

Vol. 5, Issue 11, November 2017

Disaster Sensing and Revocation using NC Cloud during emergency

M.Sindhu[1], Mrs. R.Suguna[2]

M.Phil Scholar in Computer Science, P.G.P College of arts and science, Namakkal[1]

M.C.A., M.Phil., Asst.Professor, Department of Computer Science and Applications,

P.G.P College of Arts and Science, Namakkal[2]

Abstract: The main objective of this project is to enhance the data storage security during disaster. So that IaaS (Infrastructure as a Service) methodology will be implemented here. This is to provide more security for the storage devices during malware attacks and also during disaster. The remote monitoring system is growing very rapidly due to the growth of supporting technologies as well. And also problem that may occur in remote monitoring such as the number of objects to be monitored and how fast, how much data to be transmitted to the data centre to be processed properly. This study proposes using a cloud computing infrastructure as processing centre in the remote sensing data. This study focuses on the situation for sensing on the environment condition and disaster early detection. Where those two things, it has become an important issue, especially in big cities big cities that have many residents. This study proposes to build the conceptual and also prototype model in a comprehensive manner from the remote terminal unit until development method for data retrieval. We also propose using DCN method to guarantee the delivery from remote client to server. In added with the remote monitoring system will keep on tracking the database architecture for the data transfer. Whenever destruction occur the data base architecture will transfer the database to the concern location assigned from the admin. So that data base can be saving exactly with the last fine transaction. Here data loss will not occur at any cost. This method is based on IP conflict procedure. So that roll backing process can also be possible. Using the same procedure of IP conflict method and this method will shows the data up to last minute transaction. Enhanced DCN has been used for encrypt the data during the time of data transaction. When a database has been encrypted using a DCN means, the DB could not access by third party.

Keywords: Disaster analysis, local optimization, remote monitoring, software engineering, Data processing

INTRODUCTION

As per survey most of the banking server and data centres are placed in metropolitan cities, most of the metropolitan cities are in sea shore. For example in India: Chennai, Mumbai and etc. Even in USA New York city is in sea shore only. For last 10 years tsunami destroyed the cities 3 times. In some case data centres may get destroyed due to earth quake or in flood. In our project we are finding out a solution to safe hand the data centres and banking servers. Basically massive computation power and storage capacity of cloud computing systems allow scientists to deploy computation and data intensive applications without infrastructure investment, where large application data sets can be stored in the cloud. However, they are either insufficiently cost-effective for the storage or impractical to be used at runtime. In this paper, toward achieving the minimum cost benchmark, we propose a novel highly cost-effective and practical storage strategy that can automatically decide whether a generated data set should be stored or not at runtime in the cloud. The main focus of this strategy is the local-optimization for the trade off between computation and storage, while secondarily also taking users' (optional) preferences on storage into consideration. Both theoretical analysis and simulations conducted on general (random) data sets as well as specific real world applications with Amazon's cost model show that the cost-effectiveness of our strategy is close to or even the same as the minimum cost benchmark, and the efficiency is very high for practical runtime utilization in the cloud.

RELATED WORKS

Our ID management algorithm is the rest to enjoy all of the following properties: (a) both arrivals and departures of hosts are handled, (b) departure of a host causes at most one existing host to change its ID, (c) the ratio of the largest to the smallest partition is at most 4, with high probability, and (d) the expected cost per arrival / departure is (R + log n) messages, where n denotes the current number of participants, and R denotes the cost of routing one message in the DHT. In fact, our algorithm is independent of the topology of the overlay network used for routing[1]. This paper presents the design and evaluation of Pastry, a scalable, distributed object location and routing substrate for wide-area peer-to-peer applications. Pastry performs application-level routing and object location in a potentially very large overlay network of nodes connected via the Internet. It can be used to support a variety of peer-to-peer applications, including global data storage, data sharing, group communication and naming[2]. We consider the problem of

Copyright to IJIREEICE

DOI 10.17148/IJIREEICE.2017.51102

NAMAKKAL 637 206

IJIREEICE
ISSN (Online) 2321 – 2004
ISSN (Print) 2321 – 5526
International Journal of Innovative Research in
Electrical, Electronics, Instrumentation and Control Engineering
ISO 3297:2007 Certified
Vol. 5, Issue 11, November 2017

horizontally partitioning a dynamic relation across a large number of disks/nodes by the use of range partitioning. Such partitioning is often desirable in large-scale parallel databases, as well as in peer-to-peer (P2P) systems. As tuples are inserted and deleted, the partitions may need to be adjusted, and data moved, in order to achieve storage balance across the partici-pant disks/nodes. We propose efficient, asymptotically optimal algorithms that ensure storage balance at all times, even against an adversarial in-section and deletion of tuples[3].

The rapid growth of communication technology has led to many data-intensive applications that produce huge volumes of data. Most of those applications are relying on data centre networks (DCNs) to store and process their huge data. Mean while, DCNs are vulnerable to potential disasters. Some recent natural disasters like 2012 Sandy Hurricane, 2011 Japan Tsunami, 2008 China Wenchuan earthquake, etc., which cause failures of a set of network components and Break downs of some DCNs. For example, China Wenchuan Earthquake in 2008 leads to the damages of over 60 enterprise DCNs and Japan Tsunami and earthquake causes the devastations often of DCNs. Thus, in order to improve the survivability of data in DCNs, the data should be backed up among geo-distributed DCNs . The disasters can be roughly classified into three categories, i.e., predictable disasters, unpredictable disasters, and human Made attacks, in which predictable disasters (e.g. hurricane, flood, and tsunami) can be forecasted before hand by atmospheric and environmental conditions. For a predictable disaster, we can obtain a nearly warning time for DCNs that will be affected by such disaster. Therefore, considering the newly-generated data that fails to be protected by regular backup in those DCN sunder risk during the early warning time, it is highly desirable that such data can be backed up in the other safe DCNs with in the early warning time such that the data loss is minimized under disaster.

Primary Objective

The main objective of this project is to enhance the data storage security and secured data transfer during disaster. Infrastructure as a service method has been implemented, this is because IaaS deal with storage and data in cloud computing Quantum Cryptography has been used for secures the data and database during the time of data transfer. Transferred data can be roll back at any time.

DCN DISASTER ANALYSIS

Due to global warming our earth may face many types of disasters like earthquake, tsunami, storm, flood and etc. This disaster can be analysed through cloud remote monitoring. This research main function to capture data from sensor both in digital or analog input. Package of specific sensors with Remote Terminal Unit will be placed in some places or objects prone to disasters. Cloud computing could be proposed as central of data processing to run service like service listener. It has function to capture and store information sent from the remote client. Otherwise, it could be used for the central data storage and application server to display the processed results to the user.

DATA PRESERVATION USING CLOUD SERVICE PROVIDER

CSP deals with the software architecture of the cloud service provider, which is inter related with the remote disaster tool, so that when ever disaster will occur the cloud service provider will trigger out the malware process. This process may execute through Intranet, Internet and also through GPS. So that global communication will be possible here. This architecture should be assigned during the server configuration. The Cloud service provider will the triggering function with the TPA(Third Party Auditing). This method will take cares the database migration process. So that when ever disaster will occur the CSP will trigger through the IP conflict and the data base will be restored in the concern location assigned by the admin. Admin can customize the database by providing priority to the table sets. The transfer will works according to the assigned priority with the DCN Node. This saves the database from data loss. The nest process will execute after the disaster and CSP trigger out process. The roll back process too needs IP conflict procedure for analysing the failure calculation as the location of the database. According to the admin request original database can be transfer to the default location and also transfer of duplicate database also possible.

ALGORITHM

1: At each beacon interval and data ensure
2: if p>t1ands6¼Uthen calculate tables
3: s U data partition
4: PutþID to a beacon message.
5:end if
6:ifp t1ands¼Uthen
7: s NU lime slot in the schedule
8: PutID to a beacon message.
9:end if not scheduled data
10: Upon receiving a beacon message onVi
11:foreach ID in the received beacon messagedo

Copyright to IJIREEICE
DOI 10.17148/IJIREEICE.2017.51102

IJIREEICE
ISSN (Online) 2321 - 2004
ISSN (Print) 2321 - 5526
International Journal of Innovative Research in
Electrical, Electronics, Instrumentation and Control Engineering
ISO 3297:2007 Certified
Vol. 5, Issue 11, November 2017

12: ifID >0then
13: ID ID S fIDg:
14: else
15: ID IDnfIDg:
16: end if
17:end for
18:if ID fg jj>t2then
19: NotifyVdelandV delinitinte topology discovery
21:end if
22:Add the ID inV 0 i sbeacon message.

The objective function minimizes integer variable Y, which is the largest number of tasks on one node. W i j is a decision variable similar to W i j defined previously. The first constraint ensures that the schedule cannot consume more energy that the E min calculated previously. The second constraint schedules each task exactly once. The third constraint for c es Y to be the largest number of tasks on one node. The last constraint is a binary requirement for decision matrix W. Once tasks are scheduled, we then rearrange tasks—tasks are moved to earlier time slots as long as there is free time slot and no same task is executed on other node simultaneously. Algorithm 1 depicts the procedure. Note that k-out-of-n data processing ensures that k or more functional processing nodes complete all tasks of a job with probability1.Ingeneral, it may be possible that a subset of processing nodes, of size less thank, complete all tasks. The Topology Monitoring component monitors the network topology continuously and runs in distributed manner on all nodes. Whenever a client node needs to create a file, the Topology Monitoring component provides the client with the most recent topology information immediately. When there is a significant topology change, it notifies the frame-work to update the current solution. We first give several notations. A term refers to a state of a node, which can be either U or NU. The state becomes U when a node finds that its neighbour table has drastically changed; otherwise, a node keeps the state as NU. We let p be the number of entries in the neighbour table that has changed. A set I D contains the node IDs with p greater thant1, a threshold parameter for a significant local topology change.

PERFORMANCE METRICS

According to the performance metrics, the data will be transferred to a desired three locations for back up. At the time of back up the database will be partitioned and start to splitting up. At that time the speed is depends on the hardware and the receiving point's configuration. The same process will be reversed for back up process. But according to the result back up takes less time then restore. This is because back up is working under a emergency situation, but restoring works on relaxing situation.

Drive	Back up in seconds	Restore in seconds
Loc1	3.87767	17.5281
Loc 2	3.87878	17.5506
Loc 3	3.98989	15.9381

CONCLUSION

In this paper, we propose an effective and flexible distributed scheme with banking application and explicit dynamic data support to ensure the correctness of user's data in the cloud. This construction drastically reduces the communication and storage overhead as compared to the traditional replication-based file distribution techniques. By utilizing the homomorphism token with distributed verification of erasure-coded data, our scheme achieves the storage correctness insurance as well as data error localization: whenever data corruption has been detected during the storage correctness verification, our scheme can almost guarantee the simultaneous localization of data errors, i.e., the identification of the misbehaving server(s). It is concluded that the application works well and satisfy the owner and customers. The application is tested very well and errors are properly debugged. The site is simultaneously accessed from more than one system. Simultaneous login from more than one place is tested. The project works according to the restrictions provided in their respective browsers. Further enhancements can be made to the application, so that the web site functions very attractive and useful manner than the present one. The speed of the transactions become more enough now.

REFERENCES

[1] Balanced Binary Trees for ID Management and Load Balance in Distributed Hash Tables. G.S. Manku, -Balanced Binary Trees for ID Management and Load Balance in Distributed Hash Tables,IProc. 23rd ACM Symp. Principles Distributed Computing (PODC '04),pp. 197-205, July 2004.

[2] Pastry: Scalable, Distributed Object Location and Routing for Large-Scale Peer-to-Peer Systems A. Rowstron and P. Druschel, -Pastry: Scalable, Distributed Object Location and Routing for Large-Scale Peer-to-Peer Systems,IProc. IFIP/ACM Int'l Conf. Distributed Systems Platforms Heidelberg, pp. 161-172, Nov. 2001

Copyright to IJIREEICE
DOI 10.17148/IJIREEICE.2017.51102

IJIREEICE

ISSN (Online) 2321 – 2004
ISSN (Print) 2321 – 5526

International Journal of Innovative Research in
Electrical, Electronics, Instrumentation and Control Engineering

ISO 3297:2007 Certified

Vol. 5, Issue 11, November 2017

[3].Online Balancing of Range-Partitioned Data with Applications to Peer-to-Peer Systems. P. Ganesan, M. Bawa, and H. Garcia-Molina, -Online Balancing of Range-Partitioned Data with Applications to Peer-to-Peer Systems,I Proc. 13th Int'l Conf. Very Large Data Bases (VLDB '04), pp. 444-455, Sept. 2004.

[4] Smarter Cities Series: Introducing the IBM City Operations and Management Solution, IBM White Paper, 2011

[5] Yongqiang Zhang, Guozhen Zhao, Yongjian Zhang, "Design of a remote image onitorinmg system based on GPRS", International Conference on Machine Learning and Computing, 2009

[6] B. Durai, Timothy A. Gonsalves and Krishna M. Sivalingam, "Adaptive Push Based Data Collection Method for Online Performance Monitoring"

[7] Stuart Clayman et all, "Monitoring Service Clouds in the Future Internet", IOS Press, 2010

[8] Sinung Suakanto, Suhono Harso Supangkat, Suhardi, -Introduction to Finite Time Response-HTTP: a Simplest Way to Guarantee Quality of Service of Web Application under Best Effort Network‖, Proceedings International Conference AOTULE 2010

[9] Donald Kossmann, Tim Kraska, Simon Loesing, "An Evaluation of Alternative Architectures for Transaction Processing in the Cloud", SIGMOD'10, June 2010.

[10] Rajkumar Buyya, Chee Shin Yeo, Srikumar Venugopal, "Market-Oriented Cloud Computing: Vision, Hype, and Reality for Delivering IT Services as Computing", Grid Computing and Distributed Systems (GRIDS) Laboratory - University of Melbourne, Australia, 2008.

[11] B. J. S. Chee and J. Curtis Franklin, Cloud Computing: Technologies and Strategies of the Ubiquitous Data Center. CRC Press, Inc., 2010.

[12] Murray, -Enterprise grade cloud computing,‖in Proceedings ofthe ThirdWorkshop on Dependable Distributed Data Management, Nuremberg, Germany, 2009, pp. 1-1.

[13] Leimeister,C.Riedl,H.Krcmar,andM.Böhm,-CloudComputing- Outsourcing 2.0 or anewBusinessModelforITProvisioning?,‖pp.2-26.

[14] Youseff,M.Butrico,andD.DaSilva,-TowardaUnifiedOntologyof Cloud Computing,‖inGridComputingEnvironmentsWorkshop,2008.GCE'08,2008,pp.1-10.

[15] B. Schweiger, P. Ehnert, and J. Schlichter, -Simulative Evaluation of the Potential of Car2XCommunication in Term sof Efficiency,‖in Communication Technologiesfor Vehicles, vol. 6596, T. Strang, A. Festag, A. Vinel, R. Mehmood, C. Rico Garcia, and M. Röckl, Eds. Berlin, Heidelberg: Springer Berlin Heidelberg, 2011, pp. 155-164.

[16] R.Mehmood and M.Nekovee,-Vehicular Adhocand Grid Networks: Discussion, Design and Evaluation,‖in In Procofthe14th World Congresson Intelligent Transport Systems, 2007, pp. 8.

[17] R.Mehmood, J.Crowcroft, S.Hand, and S.Smith,-Grid-Level Computing Needs Pervasive Debugging,‖ in The 6th IEEE/ACM International Workshop on Grid Computing, 2005., Seattle, WA, USA, pp. 186-193.

18. S.V.R.K.Raoand V.Diwanji, -WiMax'blePervasive Cloud– Empowering Next Generation Intelligent Railway Infrastructure,‖inCommunicationTechnologiesforVehicles, vol. 6596, T. Strang, A. Festag, A. Vinel, R. Mehmood, C. Rico Garcia, and M. Röckl, Eds. Berlin, Heidelberg: Springer Berlin Heidelberg, 2011, pp. 58-68.

P.G. COLLEGE OF ARTS & SCIENCE NAMAKKAL 637 206

PRINCIPAL
PGP College of Arts and Science
Namakkal

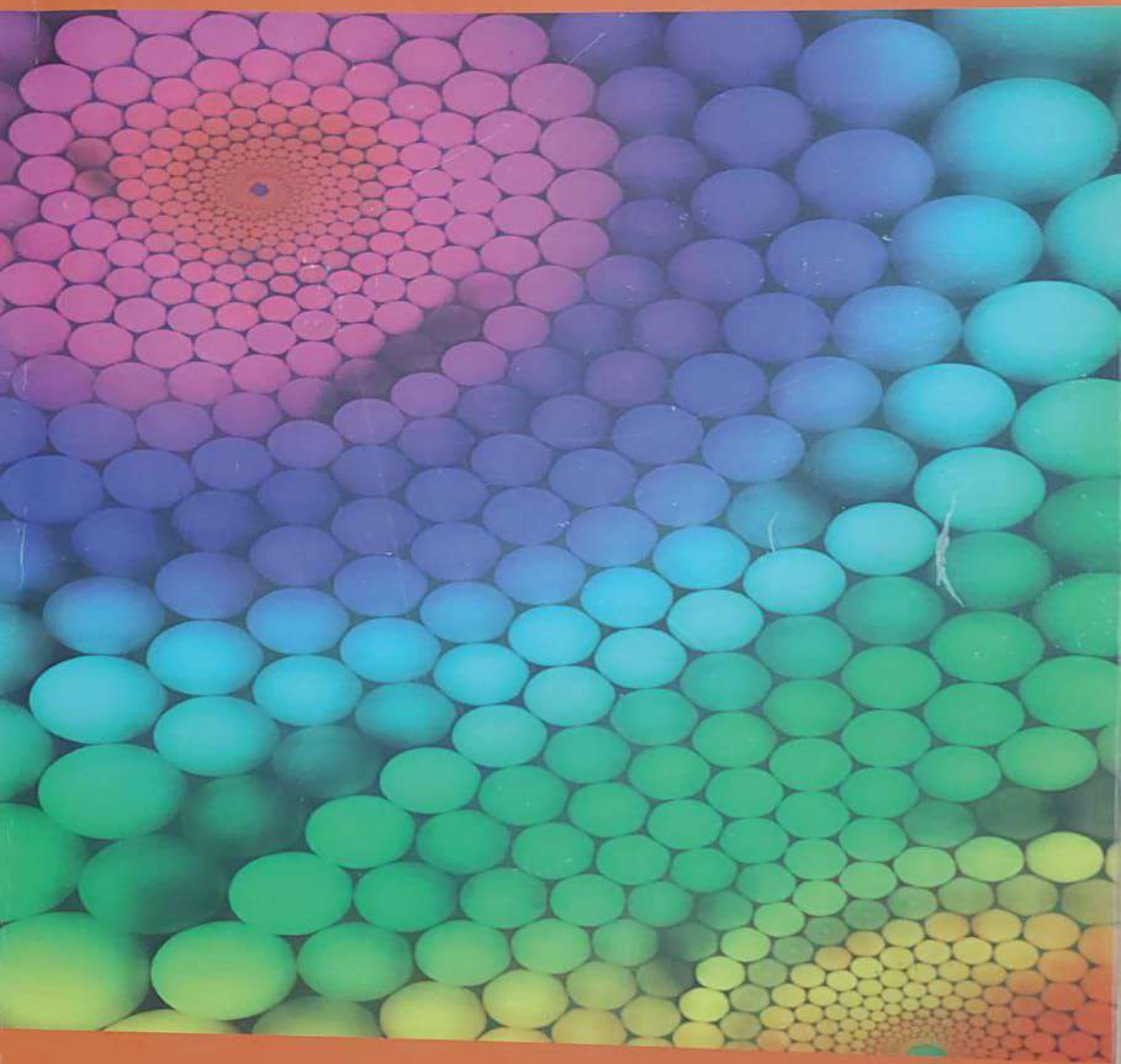
Copyright to IJIREEICE

DOI 10.17148/IJIREEICE.2017.51102

impact Journals

IMPACT: INTERNATIONAL JOURNAL OF RESEARCH IN HUMANITIES, ARTS AND LITERATURE

[IMPACT: IJRHAL]



APRIL - 2019

IMPACT: International Journal of Research in Humanities, Arts and Literature (IMPACT: IJRHAL)
ISSN (P): 2347-4564; ISSN (E): 2321-8878
Vol. 7, Issue 4, April 2019, 293-297
© Impact Journals

PIYALI ROY DARES VENTURE IN THE DANGER OF SUNDARBANS TIDE AND TIGERS-AN EXPLORATIVE STUDY OF AMITAV GHOSH'S THE HUNGRY TIDE

L. SoundarRajan[1] & Dr. S. Subramanian[2]

[1]Ph.D Research scholar (F.T), Department of English
Chikkaiah Naicker College, Erode(Dt), Tamilnadu
[2]Assistant professor of English, Department of English
Chikkaiah Naicker College, Erode(Dt), Tamilnadu

ABSTRACT

The Hungry Tide goes succeeds in highlighting the plight of the subaltern of sundarbans in WestBengal were socio political turmoil extracts as heavy a tall as the revenging tiles Amitav Ghosh has introduced a character of Piyali Roy who is the representative of raising voice against anti-environmental activities. Piyali Roy also narrates the beauty of sunderbans at the same time she was not forget to say the danger of tide and tigers in sundarbans. Amitav Ghosh one side he explained the beauty of nature and on another side he cautioned the danger part of the nature. It simply explains ups and downs of life as a normal phenomenon but take our life in a challenging way. This is the message he gave through the voice of Piyali Roy by Amitav Ghosh

INTRODUCTION

The Hungry Tide is the fiction also serves to reinforce Ghosh's political upheaval. As Lawrence Buell argues, eco-critics explore literary texts as "refractions of physical environments and human interactions with those environments, notwithstanding the artifactual properties of textual representation and their intercession by ideological and other socio-historical factors". In this vein, Ghosh's novel reveals the interactions between the state, the poor, the flora, and the physical environment, and in doing so this work highlights both the misfortune and the insincerity that were inborn in the conservation efforts in the Sundarbans. More precisely, it is the discursive construction of the Sundarbans waterscape in Ghosh's novel that helps achieve this purpose.

In The Hungry Tide Ghosh problematizes the nervousness between and within human communities, their particular relations with the natural world, and the actuality of nature that changes and is simultaneously changed by humanity. Ghosh sets his novel in the Sundarbans, the tide country where the curves of land constantly transform with the ebb and flow of water. But Ghosh presses this point further. He utilizes water as the agent that rewrites the social matrix of the Sundarbans in the novel. Water is both motif and agent, shaping not only the story but also the geography and history of the land. The unusual agency of water is highlighted here and its potential to act, as well as to move from object/other position to that of the subject and, in doing so, reverse the object/subject status of the characters.

In the eastern most of the coast of India, the Bay of Bengal, lies the enormous tangle of tiny islands known as the Sundarbans. Life becomes enormously precarious for the migrated people. Attack by deadly tigers is frequent. Turbulence and eviction are constant dangers. Without indication, at any time, tidal floods rise and rush over the land, leaving devastation in their wake. In this place of pitiless beauty, the lives of three people from different worlds collide. Piyali Roy, a young marine biologist, of Indian descent but intractably American, in search of a rare, endangered river dolphin, *Orcaella brevirostris*. Her journey commences with a

disaster when she is thrown from a boat into crocodile-contaminated waters. Rescue comes in the form of a young, uneducated fisherman, Fokir. Although they have no language between them, Piyali Roy and Fokir are impressively drawn to one another, sharing a mysterious instinct for the ways of the sea. Piyali Roy engages Fokir to help with her research and finds a translator in Kanai Dutt, a businessman from Delhi whose optimistic aunt and uncle are longtime settlers in the Sundarbans.

PIYALI ROY EXPEDITION

Piyali Roy is a cetologist (a biologist specializing in marine mammals) who comes to the Sundarbans to carry out a study of the river dolphins. Though she was born in Calcutta to Bengali parents, Piyali Roy grows up in Seattle and never learned Bengali. However, she knows that in her line of work, she doesn't always need spoken language to converse. This idea comes to the forefront when she meets the fisherman Fokir. Even though the two can't speak to each other, Piyali Roy recognize that Fokir and she can exchange a few words in such a way that seems more honest and more meaningful than she believes they'd be able to could they speak to each other. This stands as a stark difference to her relationship with Kanai even though they can speak to each other. Kanai at first has little interest in getting to know who Piyali Roy is, and keeps Piyali Roy from feeling contented opening up to him. Piyali Roy begins the novel believe wholly in the power and kindness of conservation efforts. As the novel progress, Piyali Royli Roy is forced to be familiar with that conservation isn't always a force for good and it often happens at the expenditure of poor people like Fokir. Though Piyali Roy and Fokir are clearly involved together other and develop a quiet romance throughout the novel, they never act on their feelings for each other. About six weeks after the cyclone, when Piyali Roy returns to Lusibari, she suggest that she'd like to name her continuing project after Fokir. She also wants to work with local fishermen to carry out her project and share financial support with the Babadon Trust, which suggests that she has learnt that management efforts and that are most efficient when implemented in a way that really helps locals.

PIYALI ROY BIOGRAPHY

Piyali Roy had been born in Kolkata, but had shifted to the United States when she was just one year old. She does not be familiar with Bengali, but she recalls that this is the language in which her parents quarrel. A graduate student in cytology from the Scripps Institution of Oceanography in California, she is attracted in observing the 147 marine mammals that she thinks are exclusive to the Sundarbans. Her destination is the settlement of Canning, the train discontinue for that area. Kanai's actual destination, on the other hand, is Lusibari, the outermost of the inhabited islands, where his seventy six years old aunt runs a supportive organization called Badabon Trust. Soon after they turn up in Canning, Piyali Roy hires a dubious guide and an even more dubious security enforced upon her by the government functionaries. The two men soon become quite frightening to Piyali Roy. Then she employs the service of an under privileged fisherman by name, Fokir to direct her to the dolphins she needs to study. In the process she plunges into the river and Fokir saves her from drowning in the salty, vegetation-filled water. She pays her collaborators to leave her with Fokir, who guarantees to take her to the dolphin region. Fokir does not know English, but they administer to do the best with what they can to communicate.

PIYALI ROY VOICE AGAINST CREATION OF ARTIFICIAL AQUARIUMS

Piyali Roy is also unenthusiastic to the opening of new aquariums in Eastern Asia where the Irrawaddy dolphins were stared upon as "valuable commodity" price catching nearly one hundred thousand US dollars. To

Piyali Roy, the sea swarming with her Chcaella i an everlasting one existing entirely independent of any require for human interpretation, but as necessary to human survival as bread and water The novel is a influential plea to the humankind to exchange its profit making mindset Piyali Roy's focus on the spiritual dimension of the dwelling places of living creatures reinforces the notion of the ground as a vital living organism and also attaches the earth to a larger cosmic realm The small apparently trivial dwellings of creatures are as morally significant for their survival and function in the natural process as the whole of the ground itself Ghosh persists that man must nurture a more saintly connection with the planet and its inhabitants

WOMEN MERCIFUL NATURE

Women are commonly associated with the quality of mercy Piyali Roy is one step forward of others in voicing for protecting the tiger, a man-eater that gobbles up people and cattle frequently When the village dwellers gather around the tiger in incarceration and take steps to kill it, Piyali Roy, the naturalist objects intensely Though Kanai explains to her the damages it has created on the islanders by marauding on the people and their herds, she says "This is an animal You can't take vengeance on an animal". However Kanai justifies the vehemence of the villagers who had killed the tiger by stressing that it was a question of life for them But Piyali Roy disputes from the standpoint that it made a lot of differentiation to keep the animals in their habitat which was nature's way She creates the reader wonder what would befall on him if We crossed that imaginary line that prevents us from deciding that no other species matters accept ourselves. And she foresees man's change of attitude - "Once we decide we can slay off other species, it'll be the people next. People who are deprived and unnoticed". Later when she studies that the tiger had gone past her boat, she ironically comments "since we were all asleep, it was in no peril of being spotted"

By placing both Piyali Roy and Fokir in front of this most dreaded Tsunami, Ghosh decreases the gap between the learned westerner and the illiterate native Everyone is one the same footing left in the midst of the jagged environment rich or poor, man or woman, civilized or uncivilized. Water becomes a returning image for physical and psychological healing in a contemporary world of sexism, drought, violence, and hunger

RENDERING SOCIAL SERVICE

Piyali Roy and Fokir are kept separately by language and class and by the social institution of marriage; Nirmal and Nilima live side by side for years but are unknown to each other, divided by different imaginings for their lives, and by a lack of respect for other's way of embracing life. This aged couple is, in fact, evocative of Balaram and his wife in *The Circle of Reason*. Balaram's wife is ambitious to distraction by her husband's obsessions So is Nilima She complains to her husband Before they can get very far, though, Kanai senses that cyclone is approaching They also learn that Piyali Roy and Fokir have gone out in Fokir's hazardously small boat As the storm approaches, Horen chooses that he can no longer wait for the two and so he and Kanai return to Lusibari Meanwhile Fokir steers to Garjontola in what amounts to a tender impulse handed on to him by his mother, and laden with the hope of Bon Bibi's intervention on behalf of the poor and he and Piyali Roy climb the highest mangrove tree and tie themselves to of the trunk. The storm is soon upon them, pausing only momentarily before drumming them frequently with full force, followed by a massive tidal wave Ultimately it subsides Fokir shields Piyali Roy from flying objects, lashing water, at the cost of his life The act of shielding Piyali Roy with his body soon takes on sexual under tones Their bodies were so close, so finely merged that she could feel the impact of everything beating him, she could sense the blows drizzling down on his back She could feel the bones of his chest, as if they had been super imposed upon her own it

was as if the storm had given them what life could not. it had combined them together and made them one. Thus, class, caste, gender, linguistic, and national boundaries collapse in the expression of nature's fury that cleanses all personalities of their developed sensibilities.

FOKIR- SHORT SPAN OF LIFE OF A SPIRITUAL MAN AND LOST PIYALI'S GUIDE

Fokir first appears on the picture as something of a knight in immaculate armour saving Piyali Roy from the two guides. He is an honest, possibly multifarious figure and has the subaltern personality. Fokir is cremated. A few days surpass and Kanai come backs to New Delhi, leaving a letter for Piyali Roy. He makes clear in the letter that he understands himself very inadequately and wishes her happiness. He leaves her a full conversion of the Bon Bibi legend as a way to understand better Fokir's theology, and his great effort in his short life, and an request to her to understand that, in differing ways, she is loved by both of them, as if human relationships reflect the ebb and tide, the mix of clean water and salt water of the Sundarbans. Piyali Roy was able to do her research habitually due to Fokir's generosity. At the beginning, Piyali Roy was an immense skeptic of relationships, reading them through her own knowledge of her parents' relationship. The two of them, Fokir and herself, they could have been boulders or trees for all they knew of each other; and wasn't it enhanced in a way, more honest, that they could not speak? The ways in which dolphins echoes reflected the world, speech was only a bag of swindles that fooled you into believing that you could see through the eyes of another being. Fokir is the trust soul in the Fiction. He is an uneducated man, but possesses more knowledge of the river and its wild life than all the outsiders who do not understand him. Piyali Roy leaves for a month, but then returns to work at the Badabon Trust. She sets her sights on raising money to see to it that Nilima's dreams will live on first by financing a house for Moyna and a college teaching for her son, Tutul. Piyali Roy also decides that she will move the Trust in the direction of conservation of the endangered dolphins, in consultation with local fishermen. It was the early view of life for Piyali Roy which was very sad and seemed to her a ideal way to avoid human connections. As with many of her observes, she had been drawn to field biology as much for the life it offered as for its intellectual content because it permitted her to be on her own, to have no attached address, to be far from the familiar, while still being a part of a trustworthy but loose-knit community. But this same lady is completely dissimilar at the fiction end.

CONCLUSION

Piyali is a novel character of the fiction of *The Hungry Tide*. She explored the species which existed in sundarbans and saw the life of tribes where they survive with at most challenge. In the fiction, mainly through the tones of Nirmal, Fokir, and Piyali Roy, Ghosh communicates the unique natural history of the Sundarbans. Piyali traces the etymology of the "Sundarbans" to its literal translation as the "beautiful forest," to the presence of the Sundari tree and to Mughal records which named the region after a tide the bhati tide, giving the region the name bhatirdesh or tide country except that bhati is not just the 'tide' but one tide in particular, the ebb-tide, the bhata. Apart from this distinctive feature, the very quality of the water in the Sundarbans sustains a vast profusion of aquatic life. Those information's are outspoken through Piyali for the understanding of the sundarbans beauties and at the same time she also understand the danger of Tide and Tiger. She knows very well this natural creation is also part and parcel of life.

P.G. COLLEGE OF ARTS & SCIENCE NAMAKKAL

REFERENCES

1) *The Hungry Tide*, New Delhi, Ravi Dayal, Permanent Black, 2004 print

2) Ross, Mallick Refugee Resettlement in Forest Reserves: Morichjhapi Massacre, Journal of Asian Studies, 1999:58:1

3) Mukherji, Meenakshi. The Twice Born Fiction: Themes and Techniques of the Indian Novel in English. New Delhi: Arnold Heiman, 1974. 32.

4) Ghose, sagarika. Quoted in John C. Hawley, Amitav Ghosh: An Introduction, Contemporary Indian Writers in English Series. New Delhi: Foundation Books Private Limited. 2005

P.G.P. COLLEGE OF ARTS & SCIENCE
NAMAKKAL
637 206

PRINCIPAL
PGP College of Arts and Science
Namakkal

WWW.JETIR.ORG

editor@jetir.org

An International Open Access Journal
UGC and ISSN Approved | ISSN: 2349-5162

INTERNATIONAL JOURNAL OF EMERGING TECHNOLOGIES AND INNOVATIVE RESEARCH

JETIR.ORG

INTERNATIONAL JOURNAL OF EMERGING TECHNOLOGIES AND INNOVATIVE RESEARCH

International Peer Reviewed, Open Access Journal

ISSN: 2349-5162 | Impact Factor: 5.87

UGC and ISSN Approved Journals.

Website: www.jetir.org



Website: www.jetir.org

JETIR

INTERNATIONAL JOURNAL OF EMERGING TECHNOLOGIES AND INNOVATIVE RESEARCH

(ISSN: 2349-5162)

International Peer Reviewed, Open Access Journal

ISSN: 2349-5162 | Impact Factor: 5.87 | UGC and ISSN Approved

ISSN (Online): 2349-5162

This work is subjected to be copyright. All rights are reserved whether the whole or part of the material is concerned, specifically the rights of translation, reprinting, re-use of illusions, recitation, broadcasting, reproduction on microfilms or in any other way, and storage in data banks. Duplication of this publication of parts thereof is permitted only under the provision of the copyright law, in its current version, and permission of use must always be obtained from JETIR www.jetir.org Publishers.

International Journal of Emerging Technologies and Innovative Research is published under the name of JETIR publication and URL: www.jetir.org.

© JETIR Journal

Published in India

Typesetting: Camera-ready by author, data conversation by JETIR Publishing Services – JETIR Journal.

JETIR Journal, WWW. JETIR.ORG

ISSN (Online): 2349-5162

International Journal of Emerging Technologies and Innovative Research (JETIR) is published in online form over Internet. This journal is published at the Website http://www.jetir.org maintained by JETIR Gujarat, India.

ISSN : 2349-5162

9 772349 516207

Disposition of Rajkumar in Amitav Ghosh's The Glass Palace-An Optimistic fiction

L. SoundarRajan[1] & Dr. S. Subramanian[2]
[1]Ph.D Research scholar (F/T), Department of English
Chikkaiah Naicker College,Erode(Dt), Tamilnadu
[2]Assistant professor of English, Department of English
Chikkaiah Naicker College,Erode(Dt), Tamilnadu

Abstract

Amitav Ghosh has introduced a character of Rajkumar, an orphan who is transported to Burma from India by accident. In Burma he joined as a labour in tea shop. He started his life with impoverishment. Slowly he improved his capabilities through exploring spirit, Keen perception, and Optimistic attitude and acquires capabilities to take calculated risks. Further, he got friendship business. Slowly, Rajkumar also learnt some techniques in the teak business and started the same, with the help of his Christian friend Saya Jhon. After involved his business he became a successful business man. In this way, Rajkumar characteristics are sculptured in a optimistic way by the author. The present study is narrating Rajkumar's temperament and his remarkable achievements in his life.

The Glass Palace is a fiction was written by Indian writer Amitav Ghosh and it is about dynastic families in mid 18th and early 19th century Burma and India. Rajkumar Raha is the story's main character and protagonist. He is an orphan who later achieves fortune in the teakwood trade, he is first seen in the story as an impoverished youth at the age of eleven . It is the story of Rajkumar who is transported to Burma by accident. As a child, RajKumar is remarkable for his exploring spirit, keen perception, optimistic attitude and his ability to take calculated risks. In this context, the present study is going to concentrate how the disposition of Rajkumar is narrated in an optimistic manner by the author.

The fiction starts with eleven years old boy called Rajkumar running through the city of Mandalay to find a woman called Ma Cho. He is the last existing member of his family and comes to Burma from India with a brilliant entrepreneurial spirit and a hunger for success. Rajkumar works as an assistant on Ma Cho's food stall which takes place in the shadow of the Glass Palace, in which King Thibaw and his wife reside with their daughters, the princesses. As the British invasion comes to tumble the incumbent regime.

everyday citizens of Mandalay are able to enter the preserved building, and it is then that Rajkumar spots Dolly, one of the princesses' attendants, and instantaneously falls in love with her. However, the complete Royal Family and their encourage are hurriedly extradited by the British and forced into house arrest thousands of miles away on the West coast of India.

RajKumar works in a tea stall of a matronly lady Ma Cho. He loves exaggerating his age just to experience like an adult. A well-travelled orphan, RajKumar is worldly-wise. Right at the beginning of the narrative, the author drops enough hints for the legitimacy of his choice of a protagonist. Even though, he is a child, an orphan, yet this boy is created as bold, and extraordinary. Once Raj Kumar lands in Mandalay, his life-long search for places and people begins. He is taken in by the city. 'Long straight roads radiated outwards from the walls, outlining a neat geometrical grid. So intriguing was the ordered pattern of these streets that Raj Kumar wandered, far a field, exploring. And we must remember that this explorer-boy is a complete destitute in an alien city with absolutely no acquaintances. Lastly he goes to Ma Cho for occupation and he obtains a thorough reproach and admonishment at the very outset. But his keen perception helps him to know that this outburst was not aimed directly at him: that it had more to do with the dust, the splattering oil and the price of vegetables than with his own occurrence or with anything he had said.

Luckily, in Burma, Rajkumar happens to meet Saya John, a Chinese contractor from Malaya, an orphan like him, who, having been brought up by Catholic priests in Malacca, had worked as an doubt in a military hospital in Singapore. As a subaltern beneficiary of the Burmese capture, Saya John is a previously prototype of Rajkumar. As a teak service provider for English Company he produces a huge profit that enables him to fulfill his neo-colonialist ambitions of constructing a large house and of enjoying a European life-style. Rajkumar is provided a job by Saya John in his teak transportation business because of the former's exceptional curiosity, worldliness and hunger for money and material: There was something unusual about the boy a kind of attentive determination. Rajkumar respects him as a guide in all matters and

regards him as his mentor who teaches him how to bend the work of nature to your will; to create the trees of the ground valuable to human beings. It is his love and respect for Saya John that prompts him to secure a European Company official who rebukes Saya John.

Even as Rajkumar's swiftly evolving career begins to take shape with the help of Saya John, a victorious teak merchant (Ma Cho's sometime lover), we are given a glimpse into the embarrassed beginnings of a new life for King Thebaw and his family as they strive to settle into the port town of Ratnagiri, north of Goa. Incidents combine to weave Outram House (the name of the residence the British provide to house the family and what remains of their assistants) more determinedly into the life of Ratnagiri than had been imagined. King Thebaw is admired by the local community, and in time the family comes to feel protected and even happy in their fresh surroundings. The appearance of a new Collector stirs up feelings of antipathy towards the colonial regime, but Uma, the Collector's headstrong wife, is able to help bridge the gap by befriending Dolly.

Meanwhile, Rajkumar has been enduring the hardships of the teak trade, having witnessed man and beast working together on an epic range as elephants transport large amounts of wood down from the forests for sale into the British Empire's immeasurably expanding markets. Being the opportunist that he is, Rajkumar starts to make his own way in world after getting guidance from his new friend and colleague Doh Say. Borrowing cash from Saya John, he makes the journey to India to recruit poverty-stricken village-dwellers into the comparatively beneficial (yet undoubtedly perilous) world of early oil-mining in Burma. Having made adequate money this way, Rajkumar does what has been his hallucination for some time: buy a timber-yard of his own, with Doh Say as a big business partner.

Having built a more than unassuming commercial empire, Rajkumar had one piece of unfinished business: to pathway down the only girl he would ever loved, Dolly. Through an Indian association in Rangoon (Yangon), Rajkumar makes contact with Ratnagiri via Uma, and is consequently granted a spectators with the Collector and his wife over a food that of course awkwardly conforms to colonial best perform. To his surprise, Dolly is present, and after some drama, he finally persuades her to leave the family she has been separated with, and return with him to Burma as his wife.

P.G. COLLEGE OF ARTS & SCIENCE NAMAKKAL

Being a practical businessman, Raj Kumar brings with him a letter for the Collector of Ratangiri from a relative of the Collector's wife Uma Dey. Usually no one from Burma is allowed to meet the over throwned king or staff lest such a meeting may not create problems of revolt at Burma. Uma, who is a good friend of Dolly assembles the meeting between Dolly and Raj Kumar. But before going to that, the letter of endorsement that Raj Kumar brought with him speaks volumes about his character and reputation. He have had several other achievements and had risen to distinction within the business community. And all this at the age of thirty, before he had even had time to marry Raj Kumar babu is not the kind of person to whose humanity you are accustomed. Some of the richest people in the city are Indians and most of them began with nothing more than a bundle of clothes and a tin box. Raj Kumar is an individual as well as a delegate, a symbol of a whole migrated community. His fate and rise have been linked to that of his community and what we get in a wonderful individual picturization as well as functioning of an entire group of people in an alien land.

RajKumar's gathering with Dolly is catastrophic. There is no clue, no meeting point, and no headway. It is all blocked, and clogged. Dolly has her own troubles. She has to clear her psychological picture. But this the researcher shall discuss later while talking about Dolly. For no fault of his, RajKumar receives a cold and aggressive response from Dolly. His dreams are all but broken. As a matter of fate would have it, they are married at Ratangiri. Uma is their benefactor, protector, everything. They would not have been married but for the Collector's companion Uma Dey. RajKumar's life begins as a family man. He gets two sons Neel and Dinu. He celebrates to compensate for all the missed celebrations of his own life. But his life cannot be called perfect as he cascade victim to the turbulent times in his old age and his world is torn apart. Dinu moves away from him, Neel dies and Dolly goes to a monastery. Although the end can be blamed at fate, one fatal flaw is very much of RajKumar's own. One time, Dinu as a child develops minor polio in one leg. Dolly consumes herself day and night in Dinu's care. She becomes more and more recluse. She engraves herself off from the world, including her elder son, Neel and husband. Dinu and his well being remain the central point of her survival for months or even a year or so. It is as though the mother and the son have reentered the prenatal period of oneness. The child is securely in mother's defensive attendance,

her womb and all his needs are accomplished without asking. During this period RajKumar goes into physical relationship with one of the workers forcibly and Ilongo, his illegitimate son is the effect of this extramarital mating. We can only attribute this act on RajKumar's part to his gratis will and the kind of a man that he actually is. Saya Jhon, his adviser, was the same and so is he. Our civilized and often hypocritical rules of morality will not work here simply because this novel, like other good novels, is a true depiction of life. Howsoever absurd such an act may look to the cold, distant gaze, it is perhaps the most natural thing to happen in the mess of life. Devoid of the power of reasoning as to why Dolly has withdrawn, RajKumar succumbs to his physical needs. He remains, despite his achievements, an uneducated orphan.

As far as love stories are concerned, this fiction has many love stories in it. The First one is Dolly and Rajkumar, an astonishing love story, Rajkumar saw Dolly when she was nine years old and longed for her for another 20 years. After becoming a triumphant businessman he came back to India, only to wed Dolly. Another love story is of first princess and of coachman Sawant, even though it is not wrapped in that much detail. Another story is that of Uma and collector, that is more of an arrangement, how collector wants to wed Uma since she is young and can learn contemporary ways of living as a collector's wife. Uma's consent was never taken while taking assessment about her life. The apologize for that came Alison's way, her discovery of true love, only after making love with Arjun, Alison noticed that how much she loved Dinu. Well! Alison and Arjun both died but thank God Alison got likelihood to admit this thing to Dinu. Otherwise, it would have been a difficult life for him.

The fiction, arrangement as a saga of subaltern families, is relatively a thick book which is divided into seven parts: *Mandalay, Ratnagiri, The Money Tree, The Wedding, Morning Side, The Front and The Glass Palace* The earlier part of the fiction is dominated by Rajkumar, Dolly and Saya John, and the latter part by Dinu, Alison, Arjun, Bela and Jaya. The fiction comes full circle with Rajkumar and Dolly living in the end in their countries of birth from where their narrative journeys begin: Rajkumar makes a journey

P.G.P. COLLEGE OF ARTS & SCIENCE NAMAKKAL 637 206

from India to Burma where as a businessman he makes traverses into India and Malaya and towards the end returns to India as the Second World War refugee. Dolly creates a journey from Burma to India as an exile, and then she returns to Burma to lead a married life. But she is again forced to move along with her husband to India as an impoverished, which is finally followed by her return to Burma

It is during the problematic period in Burma that Rajkumar's upward journey begins. After the fall of the Burmese empire he begins developing the local people and resources and becomes a victorious timber merchant and consequently a rubber business. It is in the year 1885 when the stolen goods were going on in the castle of Mandalay; Rajkumar observes the face of a ten year old girl Dolly who go always an ineradicable intuition in his mind. Later when Rajkumar becomes a foremost business tycoon of Burma, he travels to distant Ratnagiri to claim her hand for marriage. Therefore, the orphan in the beginning of the fiction turns himself into a living myth of material success and affluence by taking advantages of the troubled time of war, colonial antagonism and majestic invasion. Rajkumar implements a utilitarian approach to life and turns every opportunity to his favour.

Rajkumar has always been independent in his way as he be a stray he dissatisfies Dolly in several aspects like having an untruthful child names Ilongo, developing misunderstanding with Uma. He has an unlawful affair with a women working in his land when Dolly was busy in taking care of their second son Dinu. All these characters rotate around the life of Rajkumar who knowingly or unknowingly generates a bond among the families of his, Uma's and Saya John's. Hence, a family creates that bonds, Bond fetches them together looking at themselves as individuals rather than representing their nations. The characters in the novel are not representatives of a particular nation, but as individuals. Their identities are seen not with their nationalistic but as individuals who are in search of their own identities, locating themselves in a liberty where they feel contented by displacing themselves away from the nationalistic myths.

References

1. Ghosh, Amitav. (2000) The Glass Palace. India: Harper Collins Publishers. www.amitavghosh.com
2. Kodam manasing G. *Amitav Ghosh's The Glass Palace: A post colonial Novel Litterit. Indian Response to Ilterature* [December 2004].

P.G. & RESEARCH DEPARTMENT OF ENGLISH NAMAKKAL 637 206

3. Choudhury, Bibhash. (2009). *Amitav Ghosh, Modernity and the Theory of the Novel.(*Ed.), Amitav Ghosh:Critical Essays. (pp. 1-13). New Delhi: PHI Learning Private Limited.





A STUDY ON THE IMPACT OF DEMONETIZATION ON CONSUMER BUYING BEHAVIOUR WITH REFERENCE TO CONSUMER GOODS IN NAMAKKAL DISTRICT

Dr.D.Kanchana
Assistant Professor cum HOD
Department of Business Administration
Arignar Anna Govt.Arts College, Namakkal

N.Rajeswari
Research Scholar,
Department of Business Administration
Arignar Anna Govt.Arts College, Namakkal

ABSTRACT

Consumer buying behaviour concept has been argumentative from the past for so many periods. Many researchers have undertaken the research to identify, analyze, observeand find the outcomes of the study to understand the determinant of the product price effect over the product quality of consumer buying behaviour. The necessity of marketer reviews has been for the consumer buying behaviour towards psychological aspect than the societal aspect. Following demonetization, the government has been encouraging the dream of cashless society in India, urging the people to use POS machine, e-wallet, plastic money, online payment, etc., in their day-to-day transactions. Before demonetization, people used to buy impulsively from the retail malls by using hard cash because of more convenience, but with the implementation of demonetization, people have to think twice before making any kind of purchase due to less money on hand as well as less habit of cashless transactions. An impulsive buying is made instinctively and generally without regard to costs or negative consequences. They are usually motivated by the need for instant self-satisfaction. The present paper examines the impact of demonetization on on consumer buying behaviour with reference to consumer goods in Namakkal districtby using the primary data collected from 150 respondents in Namakkal city with the help of a structured questionnaire. Data analysis has been done. The study found that a majority of the customers have moved from buying luxury products to essential products and reduced their consumption due to demonetization.

INTRODUCTION

Demonetisation is the generations 'memorable experience and is going to be one of the economic events of our time. Its impact is felt by every Indian citizen. Demonetisation affects the economy through the liquidity side. The demonetisation of high denomination notes (of Rs1,000 and Rs500) has put over 85% of currency out of circulation. This has resulted in short-term disruptions in transactions in agriculture and related sectors, small establishments,

P.G. COLLEGE OF ARTS & SCIENCE NAMAKKAL

households and among professionals. Since injection of liquidity is slow, incomes in both formal and informal sectors have been affected with the intensity of adverse impact being greater for the informal sector. Since self-employed and casual workers dominate in the overall economy, their incomes may suffer a setback. While some may view it as deferring expenditure and income, a part of it may actually be revenue and income forgone forever.

Product demonstrations generally aim to increase sales for specific merchandise in a target market. Product demonstrations are a form of sales promotion that involves interactive sales presentations such as providing test samples and showing video presentations of a product. This marketing technique is used to introduce new products into retail markets, such as mass-merchandise outlets, by attracting prospective customers to demonstration booths.

IMPACT OF DEMONETIZATION

The demonetization that has been in effect since November 9 is expected to have a negative impact on inflation. Consumer spending activity fell to a near halt. Consumers are refraining from making any purchases except essential items from the consumer staples, healthcare, and energy segments. Activity in the real estate sector, which includes a lot of cash and undocumented transactions, slowed down significantly, Metropolitan and Tier 1 cities reported up to a 30% fall in house prices. Food item inflation, measured by changes in the Consumer Food Price Index, accounts for 47.3% of the overall CPI. Due to 86.4% of the value of the currency notes in circulation going out of the financial system and re-monetization being slow, the supply and demand of food items fell. It will exert more downward pressure on inflation. Investors in India-focused funds should continue to monitor CPI inflation. It will determine future rate cuts by the RBI. A change in the repo rate will impact interest rate–sensitive sectors and industries like financials (HDB) (IBN) and automobiles (TTM), among other sectors like the tech (WIT) (INFY) sector and also due to demonetization the consumer buying behaviour are changed and sales volume are increased.

OBJECTIVE OF STUDY

- To determine the measures taken to tackle the impact of the demonetisation
- To analyse the Impact of demonetization on consumer buying behaviour
- To find out the factors influencing buying behaviour after demonetization



REVIEW OF LITERATURE

Ansari (2015) examined the impact of real per capita GDP, the size of overseas trade and density of population on the tax revenue by making an inter country comparison. The study concluded that real gross domestic product and foreign trade were positively correlated with tax revenue, whereas density of population was negatively correlated with tax revenue and also buying behaviour also changed after demonstration

Kumar (2017) presented an analytic view about the impact of demonetization on the Indian Economy. His analysis showed that demonetization had adverse effects on the Indian economy. The cashless transaction has been promoted but it takes lot of efforts to convince rural people to adopt those skills.

Rani (2018) studied the effects of demonetization on retail outlets. The study revealed that initially the demonetization effects on market were painful but this also instigate the shopkeepers and consumers to adopt cashless means such as paytm, debit card use, internet banking to buy goods. Demonetization effect will be positive in coming time for Indian Economy. Indian consumers will strive to learn new ways of cashless transactionsand consumer buying behaviour affect to consumer goods due to demonstration

RESEARCH METHODOLOGY

The data are collected from the primary and secondary data. The primary data are collected through well designed questionnaire and detailed discussion with the respondents. The secondary data were taken from Newspaper and magazines which were published.

(a) Sampling Design

The researcher is a scientific way toward the achievement of the objectives of the study. The researcher has undertaken this study based on the Descriptive Design. Descriptive design had helped the researcher to describe the existing phenomenon of preferences given to the impact of the demonstration on consumer buying behaviour.

(b)Sample Size

The total sample size decided by researcher was 150 respondents in Namakkal district. All clusters namely housewife, students, service class, self -employed, business class and professional were considered for the same. Researcher had made an attempt that the sample size

P.G.P. COLLEGE OF ARTS & SCIENCE NAMAKKAL 637 206

was adequate representative and estimate with sufficiently high precision.

(c)Sampling Method

The researcher had deployed non- probability sampling method known as convenient sampling. This method will attempt to obtain a sample of convenient elements that were ready to give information. The sampling elements or consumers of online shopping were identified as follows; the convenient sample was divided into the following clusters namely housewife, students, services class, and business class, self- employed and professional.

AREA OF THE STUDY

The researcher took Namakkal district as area of research. The respondents were of different age, sex, occupation, income group, etc.,

TOOLS FOR ANALYSIS

In order to analysis the data, various statistical tools are used in this study the following statistical tools are used in the study. (i) Percentage Analysis and Chi square test.

LIMITATIONS OF THE STUDY

- The study is confined to Namakkal district only.
- The sample size is limited to 150 respondents therefore, the result of the study can not be considered as universal.
- Findings of the research are based on the assumption that the respondents have given correct information. .

ANALYSIS AND INTERPRETATION OF DATA

TABLE NO: 1
GENDER WISE CLASSIFICATION

S. No.	Gender	No. of respondents	Percentage
1	Male	55	37%
2	Female	95	63%
	Total	**150**	**100%**

Source: Primary Data

Inference:

The above table shows that 63% of the respondents are female and 37% of the

P.G.P. COLLEGE OF ARTS & SCIENCE NAMAKKAL

respondents are male.

TABLE NO: 2
AGE WISE CLASSIFICATION

S. No.	Age	No. of respondents	Percentage
1	20-30 yrs	20	13%
2	31-40 yrs	60	40%
3	41-50 yrs	45	30%
4	More than 50 yrs	25	17%
	Total	**150**	**100%**

Source:Primary Data

Inference:

The above table shows that 40% of the respondents belong to the age group of 31-40 years, 30% of the respondents belong to the age group of 41-50 years, 17% of respondents belong to the age group of more than 50 years and 13% of respondents belong to the age group of 20-30 years.

From this it is clear that 70% respondent's age group fall between 31-50 years.

TABLE NO. 4.3
EDUCATIONAL QUALIFICATION WISE CLASSIFICATION

S. No.	Educational Qualification	No. of respondents	Percentage
1	Schooling	15	11%
2	Diploma	20	13%
3	Under Graduation	41	27%
4	Post Graduation	39	26%
5	Professional Degree	35	23%
	Total	**150**	**100%**

Source:Primary Data



Inference:

The above tables shows that 27% of respondents are under graduate degree holders, 26% of the respondents are post graduate degree holders, 23% of respondents are professional degree holders, 13% of respondents are diploma holders and 11% of respondents are in schooling level.From, this it is clear that majority of the respondent 76% are highly educated.

TABLE NO. 4.4
MONTHLY INCOME OF THE FAMILY WISE CLASSIFICATION

S. No.	Monthly Income	No. of respondents	Percentage
1	Below Rs. 20000	18	7%
2	Rs. 20001 – Rs. 40000	15	10%
3	Rs. 40001 – Rs. 60000	33	22%
4	Rs. 60001 to Rs. 80000	65	43%
5	More than Rs. 80000	42	28%
	Total	**150**	**100%**

Source:Primary Data

Inference:

The above table reveals that 43% of the respondents belong to income group of more than Rs.60001 to 80000, 28% of the respondents belong to income group of more than Rs.80000, 22% of respondents belong to income group of Rs.40001-60000, 10% of respondents belong to income group of Rs.20001-40000 and 7% of respondents belong to income group of below Rs.20000.

From the above table it is clear that majority of the respondents 71% fall in the income group of Rs.60001-80000 and above Rs.80000.

P.G. COLLEGE OF ARTS & SCIENCE NAMAKKAL

ANNOVA TEST

	Sum of Squares	Df	Mean Square	F	Sig.
Between Groups	23.529	2	11.765	4.058	.019
Within Groups	484.147	167	2.899		
Total	507.676	169			

As the level of significance computed in anova test is below 0.05 , this signifies that the way in which retailers and wholesalers have responded to demonetization in terms of cash and cashless transactions is different.

CONCLUSION

It was quite evident that there were widespread effects of demonetization which affected the consumers. The businesses which run on cash were badly affected for a couple of months after demonetization. Consumers' buying behaviour was impacted. There was a considerable decrease even in the purchase of daily-use products as there was no cash and limited digital payments platforms. The purchase frequency of maximum number of consumers decreased considerably after demonetization. However respondents have taken demonetization on a positive note and are of the opinion that it is going to improve Indian economy.

REFERENCES

- The Economic Times, Wednesday, Dec 28, 2016.
- The Times of India, Monday, Jan 2, 2017.
- Bhargava S. Impact of demonetization on online shopping in 2017. Available from:http://www.indiaretailing.com/2017/01/04
- /retail/impact-demonetization-online-shopping-2017/.
- Rathore HS. Adoption of Digital Wallet by Consumers. Available from: http://www. bvimsr.com/documents/publication/2016 V8N1/10.pdf.
- Mittal A. E-commerce: It's Impact on Consumer Behavior. Available from: https://www.ripublication.com/gjmbs_spl/ gjmbsv3n2spl_09.pdf.
- Financial JR. Impact of Demonetization on various sectors & the Economy. Available from: http://www.jrfinancial.in/blog/impact-demonetization-rs-500-rs-1000-note-various-sectors-economy/.

P.G.P. COLLEGE OF ARTS & SCIENCE NAMAKKAL

JOURNAL OF XI'AN UNIVERSITY OF ARCHITECTURE & TECHNOLOGY

Impact Factor : 3.7, Issn : 1006-7930

CERTIFICATE OF PUBLICATION

This is to certify that the paper entitled

" A STUDY ON THE IMPACT OF DEMONETIZATION ON CONSUMER BUYING BEHAVIOUR WITH REFERENCE TO CONSUMER GOODS IN NAMAKKAL DISTRICT "

Authored by

N. Rajeswari

From

Arignar Anna Govt.Arts College, Namakkal

Has been published in

JXAT JOURNAL, VOLUME XI, ISSUE XII, DECEMBER - 2019

GU Chaolin
(Tsinghua University)
Editor-In-Chief
JXAT Journal
www.xajzkjdx.cn

International Organization for Standardization
7021-2008

DOI : 20.19001/JXAT

CROSSREF.ORG
THE CITATION LINKING BACKBONE

International Journal of Disaster Recovery and Business Continuity
Vol.11, No. 1, (2020), pp. 2929-2936

A Study On The Impact Of Demonetisation On Consumer Buying Behaviour With Special Reference To Consumer Goods In Namakkal District

Dr.D.Kanchana
Assistant Professor cum HOD
Department of Business Administration
Arignar Anna Govt.Arts College, Namakkal.

N.Rajeswari
Research Scholar,
Department of Business Administration,
Arignar Anna Govt.Arts College, Namakkal.

Abstract

Demonetization performs the stripping a currency unit of its position as legal tender. It happens whenever there is a transform of national currency: The present form or forms of currency is pulled from flow and retired, often to be replaced with fresh notes or coins. Sometimes, a nation completely replaces the old money with new currency. The opposite of demonetization is remonetization, in which a type of payment is restored as legal tender. The consumer goods sector was hit when government announced that a major portion of currency would no longer be legal from 8th November 2016. Leading newspapers quoted a drop in sales from around 20-40 percent and a loss in revenue to the industry in lakhs of crores. Therefore in order to measure the various impacts of demonetization a study like this holds importance in eyes of the business as well as academics. Demonetization impacts on buying behavior in all sectors, especially it impacts on buying behavior of consumer goods, Hence the study is taken to analyse on the topic. The scope of the study is limited to consumer goods. This conceptual study focuses on few aspects such as, im pact on buying behavior and customer perception about the buying behavior during demonization. The present study is analyzed in Namakkal district. The scope of the study is limited to consumer goods. This conceptual study focuses on few aspects such as, impact on buying behavior and customer perception about the buying behavior during demonization. The present study is analyzed in Namakkal district. The truth is that its design was fundamentally flawed. There was no "policy skeleton," no analysis , and no evidence that alternative policy options were considered. Government should ensure the availability and trade of consumer goods for the sake of convenience of the end users before implement the demonitisation.

Keyword: *Demonitisation, buying behavior and consumer goods.*

Introduction

Demonetization performs the stripping a currency unit of its position as legal tender. It happens whenever there is a transform of national currency: The present form or forms of currency is pulled from

ISSN: 2005-4289 IJDRBC
Copyright ©2020 SERSC

P.G.P. COLLEGE OF ARTS & SCIENCE
NAMAKKAL
637 206

flow and retired, often to be replaced with fresh notes or coins. Sometimes, a nation completely replaces the old money with new currency. The opposite of demonetization is remonetization, in which a type of payment is restored as legal tender.

It is a process of removing or abolishing the values attached to the money or monetary system of any institution or the government bodies in a country or the world. It is executed to replace the old currency with a new one, and is necessary whenever there is a need to bring about a change in the national currency of any country. The chief motto of implementing this method is to get rid with the carry out of using money for unjust means in the society. So far, many nations have witnessed demonetization of their currency, with India being able to experience it for the third time.

Statement of the Problem

The consumer goods sector was hit when government announced that a major portion of currency would no longer be legal from 8th November 2016. Leading newspapers quoted a drop in sales from around 20-40 percent and a loss in revenue to the industry in lakhs of crores. Therefore in order to measure the various impacts of demonetization a study like this holds importance in eyes of the business as well as academics. Demonetization impacts on buying behavior in all sectors, especially it impacts on buying behavior of consumer goods, Hence the study is taken to analyse on the topic.

Objectives of the study

- To the socio economic profile of the respondents
- To study the awareness about demonitisation among the consumers
- To analyse the problems facing by consumers during demonitisation
- To study the perception towards buying behavior in demonitisation

Scope of the study

The scope of the study is limited to consumer goods. This conceptual study focuses on few aspects such as, impact on buying behavior and customer perception about the buying behavior during demonization. The present study is analyzed in Namakkal district.

ISSN: 2005-4289 IJDRBC
Copyright ©2020 SERSC



Limitations

- The study is restricted to Namakkal district.
- The study assumes that the information was given by the consumers without any bios.
- The analysis is done based on the opinions of the sample drawn at random, the size of which is 150.
- The analysis is only with the perception of consumer buying behavior during demonitisation.

Review of literature

Geeta Rani (2016) researched on the effect of demonetization on retail outlets. This study states that at initial stage shopkeepers faced huge problems and the markets were very much affected by the cash crunch but this move also compelled the shopkeepers and consumers to adopt cashless means which will create a sound or hassle free transaction process in the future. Indian consumers will strive to learn new ways of cashless transactionsand consumer buying behaviour affect to consumer goods due to demonstration.

Several Theoretical Perspectives" by "Parag Waknis" make clear the impact of demonetization on three markets: Money Market, Goods Market and Labor Market (a) Money Market-Supply Side Demonetization cut currency supply in economy so M move left, it's denotes that consumers have a smaller amount cash now so output's demand go down with the reason to fall in consumption (in Goods Market) and graph of IS move left and it outputs to a fall in real interest rate r, At current we seek at the labor Demand side- concern have a smaller amount cash during demonetization so they cut their labor demand and its output to labor demand shift left and also output supply move left.

This study explores the effect of demonetisation policy (launched on 8th November'2016) on grocery retailing in India. The study is exploratory in nature and secondary data was used to collect the data. It was found that the sudden cash crunch evoked by demonetization proved to be a significant motivator for transacting online. Even the connoisseurs of kirana stores and roadside shops for consumer goods shopping became to e-stores for their every day necessities. Although demonetization successfully created a space for e-stores esp. e-grocers in the retail industry, its position is limited only to being a shifting barrier.



ISSN: 2005-4289 IJDRBC
Copyright ©2020 SERSC

Online business or online shopping has brought big changes in the opportunities and challenges for the business houses during demonitisation. From customers' viewpoint, the line of demarcation between domestic and national business firms and/or products has tapering down where quality, value, time, convenience, style etc. matters a lot (Gajjar, 2016; Bhat and Singh, 2018).

Research Methodology

The primary objective of this study is to research the impact of demonitisation on consumer buying behavior. Hence it is descriptive in nature. For the purpose of the study, the researcher applied convenient sampling in selecting the consumers in Namakkal district and thus primary data is collected through structured questionnaire from the sample of 150 respondents. The primary data thus collected were analyzed using percentage analysis.

Analysis and interpretation of the study

TABLE NO: 4.1 GENDER OF THE RESPONDENT

GENDER	NO.OF RESPONDENTS	PERCENTAGE
Male	72	48
Female	78	52
Total	**150**	**100**

SOURCES: PRIMARY DATA

INTERPERTATION

The above table shows 48% of the respondents are male and 52% of the respondents are female. Thus the majority of the respondents are female.

TABLE NO: 4.2 AGE OF THE RESPONDENTS

AGE	NO.OF RESPONDENTS	PERCENTAGE
Below 20 years	35	23
20years-40years	45	30
41years-60years	40	27
Above 60years	30	20
Total	**150**	**100**

ISSN: 2005-4289 IJDRBC
Copyright ©2020 SERSC

P.G.P. COLLEGE OF ARTS & SCIENCE NAMAKKAL 637 206

SOURCES: PRIMARY DATA

INTERPERTATION

The above table depicts that 23% of the respondents are in the group of below 20, 30% of the respondents are 20-40 , 27% of the respondents are 41- 60 and 20% of the respondents are above 60years. Thus the majority of the respondents are 20-40 years.

TABLE NO: 4.3 ANNUAL INCOME

INCOME	NO.OF RESPONDENT	PERCENTAGE
Below Rs.15000	30	20
Rs.15001-30000	48	32
Rs. 30000-Rs.45000	54	36
Above-Rs.45000	18	12
Total	**150**	**100**

SOURCES: PRIMARY DATA

INTERPERTATION

The above table said that 20% of the respondents have below Rs.15,000, 32% of the respondents have Rs.15,001- 30,000, 36% of the respondents have Rs.30,000 – 45,000 and 12% of the respondents have above Rs, 45,000 as their annual income. Thus the majority of the respondents have Rs.30,000 – Rs,45,000 as their annual income.

TABLE NO: 4.4 AWARENESS ABOUT DEMONITISATION

PARTICULARS	NO. OF RESPONDENTS	PERCENTAGE (%)
Fully aware	80	53
Partly aware	32	21
No Aware	38	26
TOTAL	**150**	100

SOURCES: PRIMARY DATA

INTERPERTATION

The above table shows that 53% of the respondents are fully aware, 21% of the respondents are partly aware and 26% of the respondents are no aware about demonetization. Thus the majority of the respondents are fully aware about demonitisation.

ISSN: 2005-4289 IJDRBC
Copyright ©2020 SERSC



TABLE NO: 4.5 PROBLEMS DURING DEMONITISATION WHEN BUYING CONSUMER GOODS

PARTICULARS	NO.OF RESPONDENTS	PERCENTAGE
Purchasing power	18	12
Availability of consumer goods	16	11
Payment method	62	41
Issue with traders	54	36
TOTAL	**150**	**100**

SOURCES: PRIMARY DATA

INTERPERTATION

The above table shows that 12% of the respondents said that purchasing power, 11% of the respondents said that availability of consumer goods, 41% of the respondents said that payment method and 36% of the respondents said that issue with traders is the problems during demonitisation with buying consumer goods.

TABLE NO: 4.6 DEMONITISATION CHANGE THE BUYING BEHAVIOUR

PARTICULARS	NO. OF RESPONDENTS	PERCENTAGE (%)
Strongly agree	42	28
Agree	40	27
Neither agree nor disagree	36	24
Disagree	12	8
Strongly disagree	20	13
TOTAL	**150**	100

SOURCES: PRIMARY DATA

INTERPERTATION

It is interpreted that 28% of the respondents said that strongly agree, 27% of the respondents said that agree, 24% of the respondents said that neither agree nor disagree, 8% of the respondents said that disagree and 13% of the respondents said that strongly disagree towards demonitisation change the buying behavior. .

TABLE NO: 4.6 DEMONITISATION SHIFT YOU FROM TRADITIONAL BUYING TO ONLINE BUYING

PARTICULARS	NO. OF RESPONDENTS	PERCENTAGE (%)
Strongly agree	72	48
Agree	28	19
Neither agree nor disagree	20	13
Disagree	16	11

ISSN: 2005-4289 IJDRBC
Copyright ©2020 SERSC

P.K.R. COLLEGE OF ARTS & SCIENCE NAMAKKAL 637 206

Strongly disagree	14	9
TOTAL	**150**	100

SOURCES: PRIMARY DATA

INTERPERTATION

It is interpreted that 48% of the respondents said that strongly agree, 19% of the respondents said that agree, 13% of the respondents said that neither agree nor disagree, 11% of the respondents said that disagree and 9% of the respondents said that strongly disagree towards demonitisation shift them from traditional buying to online buying.

Suggestions

- The government should have been create awareness about demonization in prior.
- The government should have been announce a proper e-cash payment method to the public in prior.
- The government should bring common norms among buyers and sellers during demonetizations in order to avoid conflicts between them.
- The government should have been take steps to avail all the consumer goods in market without any delay by keeping this demonitisation.
- The consumers must learn and be updated with online buying methods and to know various platform to buy the consumer goods.

Conclusion

Demonetization is a longtime practice in monetary policy to tackle black money. But as the Government expected the results are far away from the expectations. Initially people praised the government decision but in a bigger picture the effect of demonetization became reverse. Specially for the consumers, consumer goods players, retailers and wholesalers who are dealing with consumer goods have suffered a lot because of lack of proper planning, intelligence, infrastructure and foresight such as recalibration of ATM machines. There was need to pile up enough 100 Rupee notes and other smaller denomination notes in the market before taking this step so as to able to buy consumer goods. People face problems because the limit of withdrawal has not been kept at a better level. The truth is that its design was fundamentally flawed. There was no "policy skeleton," no analysis , and no evidence that alternative policy options were considered. Government should ensure the availability and trade of consumer goods for the sake of convenience of the end users before implement the demonitisation.

ISSN: 2005-4289 IJDRBC
Copyright ©2020 SERSC

P.G.P. COLLEGE OF ARTS & SCIENCE
NAMAKKAL
637 206

References

1. Geeta Rani (2016) Effect of demonetization on retail outlets International Journal of Commerce, International Journal of Applied Research 2016; 2(12): 400-401.
2. Parag Waknis. (2017, February 27). Demonetisation through Segmented Markets: Some Theoretical Perspectives, Economic and Political Weekly, Vol. 52, Issue No. 9.
3. Ishfaq Hussain Bhat, Soumya Singh. Examining the Effect of Demonetisation on Grocery Retailing in India. Asian Journal of Management. 2018; 9(3):1208-1212. doi: 10.5958/2321-5763.2018.00194.4.
4. Gajjar, N. (2016). Black Money in India: Present Status and Future Challenges and Demonetization. International Journal of Advance Research in Computer Science and Management Studies, 4(12).



ISSN: 2005-4289 IJDRBC
Copyright ©2020 SERSC

IOSR Journal of Business and Management (IOSR-JBM)
e-ISSN: 2278-487X, p-ISSN: 2319-7668. Volume 19, Issue 12. Ver. IV (December. 2017), PP 75-80
www.iosrjournals.org

A Study on the Workplace Spirituality of The Staff Members Of Engineering Colleges With Special Reference To Namakkal District

R. Florence Bharathi[1], Dr. M. G. Saravana Raj[2]
[1]Research Scholar Manonmaniam Sundaranar University Tirunelveli
[2]Director Department Of Management Studies Mahendra Engineering College Rasipuram
Corresponding Author : R. Florence Bharathi

Abstract: *The emerging paradigm called 'Workplace Spirituality' is interpreted by many in many ways. The recent researches on 'Workplace Spirituality' reveal that there is a common set of theme that most of the sources agree upon. Most of the researchers in this field use reference from "The Handbook of workplace Spirituality and Organizational Performance" by Giacalone and Jurwierokz (2003). Ashmos and Duchon (2000) describe workplace Spirituality as involving three levels, individual, work-unit and organization-wide. The work-unit dimension entails how much employees have a sense of connection and community with their management, principal, head of the department, colleagues and students, as well as assessing the extent to which they are caring and encouraging. This research is aimed at finding out the workplace spirituality of the staff members by finding out the interpersonal relationship. The staff members who have good interpersonal relationship would be more productive in their jobs and would have good individual and organizational performance. This study is useful for the management, staff members and researchers for their professional working. It is a descriptive type of research. The sample size was 100. The questionnaire was prepared for measuring the workplace spirituality at Engineering Colleges. Data was analyzed by using Weighted Average, Pearson Correlation Analysis, Regression Analysis and Chi-Square Test.*

Keywords: *workplace, spirituality, staff members, interpersonal relationship, engineering college.*

Date of Submission: 05-11-2017 Date of acceptance: 22-12-2017

I. Introduction

Engineering colleges of any country acts as a backbone for that country as it provides skilled human resource. Higher education sector, especially the engineering colleges today are facing global challenges from a dynamic environment characterized by rapid technological change. Engineering colleges are in need of producing skilled and corporate ready graduates. It is the need of the hour for the management of these engineering colleges to focus more on developing the performance of the teaching staff. This is made possible by creating an environment that inculcates good interpersonal relationship. Interpersonal relationship of teaching staff in college includes the relationship with the management, Principal, Head of the department, colleagues and the students. The quality of the relationship is essential for the healthy developments of staff members and students alike. We know for example that teacher learning thrives when principals facilitate accommodating and safe organization culture. Productive environment is characterized by supportive and warm interactions throughout the college. Positive interpersonal relationships have been proposed as a buffer against stress and risk, instrumental help for tasks, emotional support in daily life, companionship in shared activities and a basis for social and emotional development. Therefore, positive interpersonal relationship leads to better workplace spirituality. The researcher believed that the employees who have good interpersonal relationship with the management, the principal, the head of the department, the colleagues and the students would have good organizational behavior which is the indicator of workplace spirituality.

OBJECTIVES

PRIMARY OBJECTIVE

To find out the workplace spirituality of the staff members of Engineering colleges with special reference to Namakkal District.

SECONDARY OBJECTIVES

1. To find out the interpersonal relationship of the staff members with the management.
2. To find out the interpersonal relationship of the staff members with the principal.

P.G.P. COLLEGE OF ARTS & SCIENCE NAMAKKAL 637 204

Scanned by CamScanner

IOSR Journals

IOSR Journals
International Organization
of Scientific Research

International Organization
of Scientific Research
Community of Researchers

Is hereby honoring this certificate to
R. Florence Bharathi et al.
In recognition of the Publication of Manuscript entitled
A Study on the Workplace Spirituality of The Staff Members Of Engineering Colleges With Special Reference To Namakkal District
Published in IOSR Journal of Business and Management
Vol. 19, Issue 12,Ver.4 December. 2017

P.G.P. COLLEGE OF ARTS & SCIENCE NAMAKKAL EST 1996

E-mail id : jbm@iosrmail.org
Web.: www.iosrjournals.org

Editor-in-Chief
IOSR-JBM

Scanned by CamScanner

P.G.R. COLLEGE OF ARTS & SCIENCE
NAMAKKAL
Date Stamp

Kanpur Philosophers, ISSN 2348-8301
International Journal of humanities, Law and Social Sciences
Published biannually by New Archaeological & Genological Society
Kanpur India

Vol. VIII, Issue II December 2021
DOI:
www.kanpurhistorians.org

A STUDY ON IMPACT OF DEMONETIZATION ON CONSUMER BEHAVIOUR WITH SPECIAL REFERENCE TO CONSUMER GOODS IN NAMAKKAL DISTRICT

N. RAJESWARI
Research Scholar
Department of Business Administration
Arignar Anna Government Arts College
Namakkal India
DR. D. KANCHANA
Assistant Professor and Head
Department of Business Administration
Arignar Anna Government Arts College
Namakkal India

Abstract:
For many years, the principle of consumer behaviour has been a source of contention. Many researchers have worked to identify, analyses, observe, and discover the study's findings in order to assess the factor in determining of the product price effect on consumer buying behaviour. The necessity of marketer feedback has been for the customer purchasing behaviour against emotional approach than the societal aspect. Regarding demonetization, the state has pushed for a cashless society in India, encouraging people to use machines, e-wallets, transfer system, online payment, and other similar technologies in their daily transactions. Before demonetization, consumers used to buy impulsively from the retail malls by using hard cash because of more convenience, but with the introduction of demonetization, people have had to think carefully before making any kind of purchase due to less money on hand as well as less habit of cashless transactions. Impulsive purchases are undertaken on the spur of the moment, with no concern for costs or negative effects. They are normally guided by a desire for immediate gratification. Using primary data obtained from 50 respondents in Namakkal city using a structured questionnaire, the current paper investigates the impact of

Scanned by TapScanner

demonetization on consumer behaviour with regard to consumer goods in Namakkal district.

Keywords:*Need for the study, scope, objectives, research design and results and discussion*

Introduction

Individuals' behaviour is affected by demonstration effects, which are caused by observation of others' actions and their consequences. The term is most often used in political science and sociology to explain how events in one location can sometimes serve as a catalyst for events in another. Parents can look after their parents in order to create a demonstration effect in which their children may later look after them. Countries and local governments can adopt laws and economic policies that tend to be effective in other places. The policies' demonstrated success creates a demonstration effect, prompting other governments to try to replicate their success. The Indian government made the two highest denomination currency notes invalid overnight in November 2016. While this change was suggested for possible future gains, it caused significant liquidity constraints for many households since these two notes accounted for 86 percent of all currency in circulation. Using Consumer Pyramids panel info, I investigate the effect of resulting liquidity constraints on household consumption in this paper. In the first months after demonetization, I discovered that household durable and non-durable consumption decreased. The loss was more pronounced for wealthier families. I also discovered that after demonetization, households increased their borrowing, particularly from money lenders. Poorer households saw a greater rise in borrowing. Focusing on farmer heterogeneity, I show that those households that rely on cash have a higher use of credit. The findings suggest that while wealthier households reduced their consumption as a result of lower utility costs, poorer households were forced to rely on informal credit to maintain their consumption. Almost all of the work on consumption smoothing in the development economics literature has focused on consumption shocks that work through income shocks, that is, a decrease in income that can lead to a decrease in consumption. Additionally, demonization works on income, even if it doesn't lead to loss of purchasing power. Employers cannot pay their employees if they are broke. That will decrease the income available to pay taxes and therefore increase the number of people without a job. For similar reasons, the demand and supply of traders' goods would also be impacted if the amount of cash disappeared. When people are not making their day-to-to-day payments, spending has no impact on revenue. However, however, there could be an impact on the overall economy because of that Rather, households could turn to the use of credit. Even at the expense of getting less A fall in income will lead to a fall in consumption, but liquidity constraints can impact the propensity to consume directly.

You need to understand customer behaviour in order to be successful with existing products, as well as in developing new ones. Your customer's purchasing habits and preferences are completely different from one another,

P.G.P. COLLEGE OF ARTS & SCIENCE NAMAKKAL

Scanned by TapScanner

even if the product is exactly the same. If a business does not consider the consumer's reaction to its product, there are high risks of failure. How fashion, technology, patterns, income, and the economy interact to influence purchasing is one of the reasons for change in the behaviour of the market. In order to adjust a marketer's overall strategy, a marketer must keep track of variables that are changing.The aim of this study is to examine consumer behaviour as a result of product demonstrations. The majority of customer styles and shopping habits are altered as a result of this demonstration. Nowadays, the majority of customers buy a variety of products on a regular basis. As a result, the research was beneficial to customers who were influenced by the demonstration in their purchasing behaviour.

The study's findings are focused on the responses of consumers in a particular geographic region. This research would aid in gaining an understanding of consumer behaviour during demonstrations and its implications for improving consumer behaviour on consumer goods..

The research is focused on both primary and secondary data sources. The primary data was collected using a structured questionnaire with a sample size of 50 people for this study. The samples were validated and taken for further analysis after they were collected using a convenient sampling method. Secondary data is gathered from database sites and articles as well. The information gathered was analysed using the appropriate software (Chi-square technique). This study's participants are chosen at random. After explaining the various aspects mentioned in the questionnaire, we asked all respondents to fill it out on their own. It had questions in a well-structured format that was simple to understand at first glance. Only primary data is used for analysis and interpretation. However, both primary and secondary data, as well as verbal knowledge and information obtained from respondents, were included in the conclusion and recommendations, even though they were outside the scope of the questionnaire. Various tools, such as bar charts, chi-square tests, and percentages, were used to analyse the data collected from these sources.

DATA DISCUSSION

In our study, we found that product demonstrations are an effective way to raise consumer awareness. The material and knowledge used in the presentation are the key reasons for building awareness in the minds of the consumers. Similarly, the content of the demonstration shapes the expectations of the consumers watching the demonstrations. The findings of our study show that presentations are the most effective means of raising consumer awareness and influencing their attitudes. The two key factors that influence purchasing decisions are customer understanding and consumer expectations.

Table -1

General profile of the Respondents

Elements	*Gender*	*Age*	*Level Of Education*	*How Much Is Your Purchasing Value During Demonstration*
Valid	48	51	50	50

P.G.P. COLLEGE OF ARTS & SCIENCE NAMAKKAL 637 001

Scanned by TapScanner

Missing	1	1	2	0
Mean	1.4302	2.250	3.458	3.825
Median	3.000	4.000	3.000	3.500
Mode	1.00	3.00	5.00	3.00

Table -2
Level Of Education

Valid	*Level of education*	*Frequency*	*Percentage*	*Valid percentage*	*Cumulative percentage*
	Undergraduate	65	29	26	27
	Graduate to Post graduate	35	71	74	98
	Total	50	100	100	

Table -3
Does impact of demonstration to affect consumer behaviour to buy the product

Age	*Does impact of demonstration to affect consumer behaviour to buy the product*			
	Yes	*No*	*Mean*	*Toatl*
Up to23yrs	7	2	1	10
24-30	16	3	1	19
Above	15	5	1	21
Total	38	10	3	50

From the above table, we can infer that there is significant relationship between demonstration and buying behavior of consumer goods.

Table- 4
Chi- Square test

Tools	*Value*	*d.f*	*Asymp.sig(2-sided)*
Person chi square	6.981	4	.096
Likelihood ratio	6.092	4	.131
Linear by linear association	7.290	1	.593
Total	50		

We conclude that there is a substantial relationship between demonstration and consumer behaviour of consumer products from the above SPSS Chi-square measure, so we reject the null hypothesis that there is no relationship between demonstration and consumer behaviour.

Table -5
Symmetric Measures

Factor	*Tools*	*Value*	*Asymp.std.error*	*Approx.*	*Approx.sig*
Nominal by	Phi	.397	-	-	.096
	Cramer's V	.281	-	-	.096

P.G. COLLEGE OF ARTS & SCIENCE NAMAKKAL 637 206

Scanned by TapScanner

nominal					
Interval by interval	Pearson's R	.076	.177	.530	.598
Ordinal by ordinal	Spearman Correlation	.162	.153	1.137	.261

- The null hypothesis is not assumed.
- Assuming the null hypothesis, use the asymptotic standard error.
- Based on a standard approximation.

FINDINGS

- Customers are more likely to watch demonstrations that influence their opinions.
- Demonstration is an excellent way to persuade consumers to buy your product.
- Demonstrations are an effective way to communicate the desired message to a specific group of customers.
- They can entice consumers to participate in the demonstration by being attractive and engaging.

Conclusion

The findings in this paper show how demonetization affects consumer behaviour on consumer goods. Although I do not rule out the possibility of demonetization having no effect on aggregate income, I believe that the shock had a negative impact on both durable and non-durable consumption. For the impact to persist, consumption has to go back to where it was, which only takes a few months. Before 2016, households with lower expenditure saw a smaller decrease in spending than those with a higher one above the median. Stretton as a result, these households turned to more flexible sources of credit like pawnbrokers and moneylenders. The findings show that because they started out with lower spending, they paid higher interest to stay within their means, leading to lower expenditures. Lower- and middle-income households, however, had a lower opportunity cost of reducing their consumption and thus chose to accept the higher level of debt to maintain the same level of consumption. The paper doesn't address the benefits, but rather focuses on the consequences. Many families had reduced welfare due to borrowing from high-interest lenders, and reduced their consumption to save money. Lastly, my research shows that the informal sector played a critical role in facilitating the movement toward formalization, and that possible drive has subsequently grown informal networks. This research was done to establish how demonstrations impact on the customers' behaviour. It is noted in the study that two critical factors can influence customers' purchasing decisions, but they are not the only factors that will affect purchasing decisions. these two things are special effects and the customers' or clients' purchasing power (pocket money). buying something can be described as an optimization

COLLEGE OF ARTS & SCIENCE
NAMAKKAL
637 206

Scanned by TapScanner

process, wherein customers seek out the best product or brand for them. The selection process is analogous to a search for the perfect mix of brands.This perspective on the role of demonstration in purchasing decision-making has implications for utility maximization.

References

1. Abiodun AO. The impact of Advertising on Sales Volume of a Product a case study of Starcomms Plc, Nigeria. Valkeakoski Degree Programme in International Business Global Marketing, 2011.
2. Desai K. A study on consumer buying behaviour of cosmetic products in Kolhapur. Reviews of Literature, 2014, 1(10)
3. Fazal ur Rehman TN. How Advertising Affects the Buying Behavior of Consumers in Rural Areas: A Case of Pakistan. Academic Research, 2014.
4. Gupta SA. Impact of Promotional Activities on Consumer Buying Behavior: A Study of Cosmetic Industry. International Journal of Commerce, Business and Management 2013, 2
5. Rai N. Impact of Advertising on Consumer Behaviour and Attitude with Reference to Consumer Durables. International journal of management research and business Startegy. 2013, 2(2)

COLLEGE OF ARTS & SCIENCE NAMAKKAL 637 001

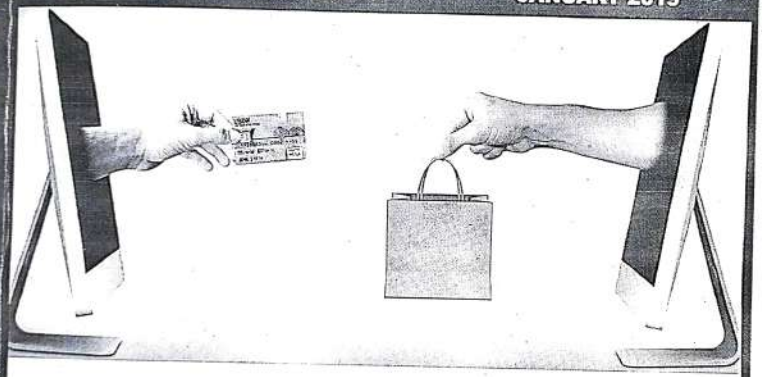
Scanned by TapScanner

ISSN NO: 2394-2886 Impact Factor 6.1

SURAJ PUNJ JOURNAL FOR MULTIDISCIPLINARY RESEARCH

(A PEER REVIEWED/REFERRED JOURNAL)

VOL: 9 ISSUE: 1 JANUARY 2019



International Organization for Standardization 7021-2008

6.1 IMPACT FACTOR

UGC

UGC S.No: 64786

Suraj Punj Journal for Multidisciplinary Research

www.spjmr.com

Scanned by CamScanner

F.G.P. COLLEGE OF ARTS & SCIENCE MANAKAL

Suraj Punj Journal for Multidisciplinary Research ISSN: 2394-2886

A STUDY ON OCCUPATIONAL STRESS AMONG BANK EMPLOYEES

S.Inthu[1] Dr.S.Rajasekar[2] Dr.R.Florence Bharathi[3]

Abstract

In this modern era and highly competitive world, there is no work without stress. Stress is universal. The employees working in various organizations undergo various forms of stress in order to accomplish the work assigned to reach the target. Occupational stress is related to the job of an individual. The root of occupational stress emerges from the unexpected responsibilities expected from an employee to work beyond his knowledge and capacity. Banks play a dominant role in the economic development of a country. Banks maintain the flow of money in a country. It caters the need of credit for all sections of the society. A bank is a financial institution that accepts deposits from the public and creates credit. A reasonable amount of occupational stress can be motivating, whereas long time stress causes drastic changes in the performance level of employees thereby reducing the overall productivity of the organization. This study gives an overview of work related stress in banking sectors.

KEYWORDS : *Occupational stress, unexpected responsibilities, economic development, credit, performance, productivity*

Introduction

Stress at work place is a common feature and majority people experience it. Some

jobs are more associated with stress. The persons holding these jobs come under stress and suffer from its consequences. Stress is a reality of our everyday life. People experience stress at home or with friends or from other non work situations. Stress is highly individualistic in nature. Some people have high tolerance for stress and thrive well in the face of several stressors in the environment. In fact, some individuals will not Perform well unless they experience a level of stress which activates and energizes them to put for their best efforts. On the other hand, some people have very low level of tolerance for stress and they become paralyzed when they have to interface with routine everyday factors that appear undesirable to them.

The stresses in an individual's environment are too many or too intense, so their efforts on performance will be adverse. Errors will increase; bad decisions will be made and the individual will experience insomnia, stomach problems and psychosomatic illness. From the individual's point of view stress is body's physical, mental and chemical reactions to circumstances that frighten, confuse, danger and irritates. If controlled, it becomes an enemy which can cause diseases like high blood pressure, ulcer, asthma and thyroid.

Personality of a person is the most dominating factor which influence the way he or she responds to all events and situations. In personality, we include values, attitudes and behavior patterns that make up the uniqueness of individuals and ultimately make him more or less vulnerable to stress.

The origin of much personal stress lies within our perception on our concepts of itself. Low self esteem can lead to a number of stress inducing problems and inability to adapt willingness to place excessively high demands on yourself and lack of assertiveness. Those with high self esteem handle stress with ease since a high self concept and confidence in their abilities allows them to develop positive attitude towards the management of stress and enables them to deal with stressful situations with calmness and clear thinking.

Review of Literature

The concept of stress means an extreme condition which involves tension. In Physics 'stress' is a force, which acts on a body to produce strain. In Physiology, stress refers to the changes in physiological function in response to the factors causing stress. In Psychology it refers to a state of the organism resulting from serve interaction with the environment. In Psycho - Physiology, the term 'stress' is that stimulates which imposes detectable strain that cannot be easily accommodated by the body and so presents itself as impaired health or behavior.

1. Assistant Professor, PGP College of Arts and Science, Namakkal,Tamil Nadu, India.
2. Advisor, AIMS, Coimbatore, Tamil Nadu, India
3. HOD, Dept of MBA, PGP College of Arts and Science, Namakkal, Tamil Nadu, India.

P.G. COLLEGE OF ARTS & SCIENCE NAMAKKAL 637 206

Scanned by CamScanner

EDUINDEX

PUBLICATION CERTIFICATE

This publication certificate has been issued to

N.Rajeswari

For publication of research paper titled

THE IMPACT OF DEMONETIZATION ON CONSUMER BUYING BEHAVIOUR WITH REFERENCE TO CONSUMER GOODS IN NAMAKKAL DISTRICT

Published in

Studies in Indian Place Names with ISSN no. 2394-3114

Vol:*40* **issue:** *48* **Month:** *March* **Year:** *2020*

Impact factor:*6.3*

The journal is indexed, peer reviewed and listed in UGC Care

Editor

Eduindex Journals

www.eduindex.org
editor@eduindex.org

Note: This eCertificate is valid with published papers and the paper must be available online at the website under the network of EDUindex. For cross check you can contact at editor@eduindex.org

P.G.P. COLLEGE OF ARTS & SCIENCE NAMAKKAL 637 208

ISSN: 2394-3114
Vol-40 Issue-48 March 2020

THE IMPACT OF DEMONETIZATION ON CONSUMER BUYING BEHAVIOUR WITH REFERENCE TO CONSUMER GOODS IN NAMAKKAL DISTRICT

Dr.D.Kanchana
Assistant Professor cum HOD
Department of Business Administration
Arignar Anna Govt.Arts College, Namakkal

N.Rajeswari
Research Scholar,
Department of Business Administration
Arignar Anna Govt.Arts College, Namakkal

Abstract

Consumer buying behaviour is the total sum of consumer's attitudes, preference intentions and decision regarding the consumer's behaviour in the market place while purchasing the product or service. Recently two important remarkable events took place in our country has a severe impact on consumer behaviour. Initially demonetization that was announced on Nov 8, 2016 with the aim of cracking down the shadow economy and later on implementation of GST from July 01, 2017 with the aim of improving tax administration system and business transactions. This study will examine the impact of demonetization and GST on buying behaviour of FMCG consumers, particularly in Namakkal district. Here, for this study we will use descriptive research method and data will be collected through primary source and secondary sources. Sample size for the study will be 150 respondents. The study is mainly focused the impact of demonetization on consumer buying behaviour through consumer goods. Now a days the consumer demand very increasing because their daily purchased necessary goods for surviving their life even though impact of demonetization stages also consumer demand not reduced because they have to fulfill their needs and wants through consumer goods.

INTRODUCTION

The overall performance of the consumer goods sector will be adversely impacted by demonetization as consumers curtailed spending following lesser currency notes in circulation, JM Financial said in its report. "The quarter began on a promising note for most businesses, aided by good festive demand, but as is now well-known, the move to demonetize high denomination currency notes in the country from November 8 would make third quarter (October-December) 2016-17, a likely washout quarter for most businesses," the financial services company said in the report.

In today's competitive market, consumers are the kings. They are the decision makers. The behaviour pattern of the Indian consumer has undergone a major change in the organized retail sector. The consumer landscape is changing very fast. Occupational changes and

P.G.P. COLLEGE OF ARTS & SCIENCE NAMAKKAL 637 206

Copyright © 2020 Authors

ISSN: 2394-3114
Vol-40 Issue-48 March 2020

penetration of media have caused a significant change in the way the consumer spends his money. The consumer now wants to eat shop and get entertained under the same roof. Consumers today see an exciting explosion of choices, new categories and new shopping options and have increasing disposable income to fulfill their aspirations.

Consumer dynamics in India is changing and the retailers need to take note of this and formulate their strategies and tactics to deliver value to the consumer. Therefore each retailer needs to evaluate the enablers and deterrents in the retail market place. This primarily involves identifying the key drivers of growth, the consumer's profile and consumer's expectations. It also means evaluating the nature of competition and challenges in the market place. All these have led the Indian organized retail sector to pay more attention to analyses the consumer behaviour in order to satisfy the target market's needs more effectively than its competitors.

CONSUMER BUYING BEHAVIOUR

It is the process by which individuals search, select, purchase, use and dispose of goods and services in satisfaction of their needs and wants. Management is the youngest of sciences and oldest of arts and consumer behaviour in management is a very young discipline. Various scholars and academicians concentrated on it at a much later stage. It was during the 1950s, that marketing concept developed, and thus the need to study the behaviour of consumers was recognized. Marketing starts with the needs of the customer and ends with his satisfaction. When everything revolves round the customer, then the study of consumer behaviour becomes a necessity. It starts with the buying of goods. Goods can be bought individually, or in groups. Goods can be bought under stress (to satisfy an immediate need), for comfort and luxury in small quantities or in bulk. For all this, exchange is required. This exchange is usually between the seller and the buyer. It can also be between consumers. In simple words, consumer behavior can be defined as the set of activities and actions of consumer in purchasing and using goods and services. However, it involves a study of buying motives in order to examine the selection criteria of the consumers for the products they choose and what motivates them to behave as they do in the market places. It focuses on how individuals make decisions to spend their available resources like time, money and effort on consumption related items.

REVIEW OF LITERATURE

Bhattacharya and Sen (2013) stated that consumer behaviour referred to the mental and emotional process and the observable behaviour of consumers during searching, purchasing and post consumption of a product or service. Consumer behaviour involved study of how people buy, what they buy, when they buy and why they buy. It blended the elements from psychology,

P.G.P. COLLEGE OF ARTS & SCIENCE NAMAKKAL 637 206
Copyright © 2020 Authors

ISSN: 2394-3114
Vol-40 Issue-48 March 2020

sociology, socio-psychology, anthropology and economics, to assess the influence on the consumer from groups such as family, friends, reference groups and society in general.

Yue and George (2016) suggested the retail patronage idea such as the concepts of store choice and frequency of visit. In this study, meta-analysis suggested that various predictors (eg., service, product selection, quality) were strongly related to shoppers' retail choice, whereas others (eg., store attitude, store image) were important antecedents of shopping frequency. However, the relationships between the predictors and retail patronage vary according to the study characteristics (e.g., experimental Vs other designs).

Wanninayake and Pradeep (2017) identified that design layout and product displays were highly considered in selecting a specific supermarket outlet. They also felt that most of the professionally qualified customers selected design layout and product display as important variables in selecting the supermarkets. They also further stated that most of the female customers gave priority to product display in supermarket selection.

Dineshkumar and Vikkraman (2017) noted that customer satisfaction was widely recognized as a key pressure in the formation of consumers' future purchase intentions. Satisfied customers were also likely to tell others of their favorable experiences and thus engage in positive word of mouth advertising. It aimed to investigate the impact of demonetization on consumer buying behaviuor. The objectives were to identify the determinants of consumer buying behaviour in the organized retail outlets in Namakkal district, to identify the attitude and behavior of the customers those who were purchasing in consumer goods with impact of demonstrations.

Gomathi et al. (2018) studied the impact of demonetization on consumer buying behaviour with reference to Namakkal district. The preferences of the consumers clearly indicate the importance of advertisement in influencing their purchase, the additional facilities expected, improvement expected in handling defective goods and many more. They analyzed the attitude of the consumer towards departmental stores they have to buy the goods daily with effect of demonetization.

OBJECTIVES OF THESTUDY

The following are the objectives framed for the study:

- To study the demographic characteristics of impact of demonetization on consumer buying behaviour through consumer goods
- To study the consumers' behaviour after the demonetization process.
- To provide valuable suggestions to impact demonetization on consumer buying behaviour

P.G.P. COLLEGE OF ARTS & SCIENCE NAMAKKAL 637 206

Copyright © 2020 Authors

ISSN: 2394-3114
Vol-40 Issue-48 March 2020

RESEARCH METHODOLOGY

For the present study, the universe comprised of the impact of consumer buying behaviour with special reference to Namakkal district. The sampling units were selected by covering the five taluks of Namakkal district. The size of sample was 150 respondents. These samples were carefully selected by the researcher from the respondents in the five taluks of the study area. Both primary and secondary data were used in the study for the purpose of analysis. For collecting primary data, field survey technique was employed in Namakkal district. A well framed questionnaire was used to collect the primary data. The five selected taluks fromNamakkal district based on the convenience sampling technique for collecting the data. First-hand information pertaining to the impact of consumer buying behaviour changes through demonetization.

LIMITATIONS OF THE STUDY

The research had following limitations:

- The study was conducted only in Namakkal district hence, various other potential samples outside city were not considered
- Since the data was analysed specific conditions therefore it can be generalized.
- The study was not exhaustive.
- Time was another limitation.

STATISTICAL TOOLS USED FOR ANALYSIS

The extent of using of consumer goods between the different types of respondents based on their age, gender, educational qualification, occupation, monthly family income, family size, preferred type of stores, frequency of visit and type of product preferred was studied by means of Percentage analysis and Multiple regression analysis were used appropriately.

RESULTS AND DISCUSSION

Multiple regression analysis is a statistical technique that can be used to analysesthe relationship between a single dependent variable and several independent variables. The main objective of multiple regression analysis is to use the independent variables whose values are known to predict the single dependent value selected by the researcher. Each independent variable is weighted by the regression analysis procedure to ensure maximal prediction from the set of independent variables. The weights denote the relative contribution of the independent variables to the overall prediction and facilitate interpretation as to the influenceof each variable in making the prediction, although correlation among the independent variables complicates the interpretative process. The set of weighted independent variables form the regression equation, a linear combination of the independent variables that best predicts the dependent variable.In this

COLLEGE OF ARTS & SCIENCE NAMAKKAL 637 206
Copyright © 2020 Authors

ISSN: 2394-3114
Vol-40 Issue-48 March 2020

following analysis, the researcher took six independent variables viz., age of the respondents, family monthly income, family size, frequency of visit to the stores to buy consumer goods, attitude score, satisfaction score and a dependent variable level of perception, Attitude and satisfaction. To find out the relationship between the level of perception, Attitude and satisfaction towards organized retail stores among the customers and selected six independent variables, the following regression model has been formulated and discussed in the following tables:

Factors Contributing to the impact of demonetizationon Consumer buying behaviour-consumer goods

Consumer perception (Y) = a + b1 (age) + b2 (family monthly income) + b3 (family size) + b4 (frequency ofvisit to the stores) + b5 (attitude score) + b6 (satisfaction score)

Where, a = Constant; b1, b2, b3, b4, b5, b6 = regressioncoefficients

Mean and standard deviation of the regression predictors is discussed in the following table:

TABLE NO: 01
MEAN AND STANDARD DEVIATION OF THE REGRESSION PREDICTORS

S.No.	Predictors	Mean	SD
1	Perception score	89.296	10.135
2	Age	28.87	9.59
3	Family Monthly Income	28444.275	51351.198
4	Family Size	2.011	0.501
5	Frequency of visit to the stores to buy consumer goods	2.904	1.544
6	Attitude score	123.505	15.686
7	Satisfaction score	72.452	9.257

The above table shows the mean and standard deviation of the regression predictors. The mean values of perception score, age, family monthly income, family size, frequency of visit tothestores,attitudescoreandsatisfactionscoreare89.296,28.87,28444.275,2.011,2.904,123.505, and 72.452 respectively.

In order to measure the interdependence of independent factors and level of perception of the consumer buying behavior after demonetization, the results were subjected to multiple regression analysis. The relationship between the consumer perception and six predictors were studied and discussed.

Consumer Perception = 0.986 + 0.009 (age) + 0.020 (family monthly income) – 0.083 (family size) – 0.005 (frequency of visit to the stores) + 0.430 (Attitude score) + 0.331

G.P. COLLEGE OF ARTS & SCIENCE NAMAKKAL 637 206
Copyright © 2020 Authors

ISSN: 2394-3114
Vol-40 Issue-48 March 2020

(Satisfaction score).

The multiple linear regression co-efficient (dependent variable) is found to be statisticallyfit as R2 is 0.642 for consumer perception. It shows that the independent variables contribute about 64.2 per cent of the variation in the consumer perception and this is statistically significant at1%.

TABLE NO: 02:

FACTORS CONTRIBUTING TO CONSUMER PERCEPTION

S.No.	Variables	Coefficient	SE	't' value	P value
	(Constant)	0.986	0.081		
1	Age	0.009	0.010	0.858	0.391^{NS}
2	Family Monthly Income	0.020	0.010	2.052	0.040*
3	Family Size	-0.083	0.015	-5.536	0.000**
4	Frequency of visit to the stores to buy the consumer goods	-0.005	0.005	-1.013	0.311^{NS}
5	Attitude score	0.430	0.025	17.243	0.000**
6	Satisfaction score	0.331	0.024	13.632	0.000**
	R Value	**0.801**			
	R^2 Value	**0.642**			
	F Value	**296.56****			

Note:**-Significantat1%level,*-Significantat5%levels – NotSignificant

CONCLUSION

Encouraging customers for going digital by providing some discounts or cash back schemes by virtue of clubbing with an M-payment could be beneficial for the trade. Consumer goods van and Bingo should be done on order capture basis so that retailers dependent on cash could be provided with some time in order to arrange cash. In case of convenience credit time should be provided to retailers with good transaction records in order to reduce issues related to cash crunch. Fast moving consumer goods sectorto recoverfully from demonetization effect in this fiscal year. Inspite of all the flaws in the entire process of demonetization and various problems faced by the entire country, recovery is expected at the earliest. Life is getting back to normal with change in withdrawals from ATMs per day, shorter questat the ATMs, less pressure on the bankers, increased amount of cash in hand, people equipping to use digital methods of payments etc. As a positive effect of demonetization, there is a move towards formal economy and organized national players. It might be challenging for the regional players who are largely unorganized in nature. Sooner we adapt to varied means of transactions easier it will be to evadelosses. So the consumer buying behavior changed according to demonetization

P.G.P. COLLEGE OF ARTS & SCIENCE NAMAKKAL 637 206

Copyright © 2020 Authors

ISSN: 2394-3114
Vol-40 Issue-48 March 2020

REFERENCES

- http://www.livemint.com/Industry/icjsM7LulrspWY3WV2dzMI/Demonetisation-took-a-toll-on-rural-sales-of-FMCG-industry.html?li_source=LI&li_medium=news_rec
- http://www.livemint.com/Money/O16Oy4RPynrc5nYeoh45ZI/Demonetization-and-FMCG-industry- no-lasting-impact.html
- https://www.linkedin.com/pulse/impact-demonetization-fmcg-industry-impulse-products-raunak-gokhale
- http://www.dnaindia.com/money/report-demonetization-to-have-positive-impact-on-organised-fmcg- players-dabur-2279996
- http://timesofindia.indiatimes.com/business/india-business/FMCG-cos-stare-at-big-fall-in- sales/articleshow/55609099.cms
- http://www.hindustantimes.com/business-news/demonetisation-impact-data-shows-20-40-drop-in-fmcg-sales/story-wmfAGMM2Xz35HjPBNs17gL.html
- http://info.shine.com/industry/fmcg/6.html
- Investopedia http://www.investopedia.com/terms/d/demonetization.asp#ixzz4UgJr7FMD
- The Tribune, 13th January 2017, page no 13
- India Today, December 2016 edition
- https://rmoneyindia.com/research/equity/demonetizations-hits-fmcg-personal-care-sector



Copyright © 2020 Authors

ScienceDirect

Journals & Books

Corporate sign in

Sign in / register

View PDF

Download full issue

Outline

Abstract

Keywords

1. Introduction

2. Materials and methods

3. Results and discussion

4. Conclusion

Conflict of interest

Acknowledgements

References

Show full outline

Cited By (9)

Figures (3)

Tables (1)

Journal of King Saud University - Science

Volume 32, Issue 1, October 2019, Pages 729-733

Short communication

Anti-oxidant activity, phytochemical screening and HPLC profile of rare endemic *Cordia diffusa*

Show more

Add to Mendeley

Share

Cite

Get rights and content

Open access

Under a Creative Commons license

Abstract

The present study deals with the investigation of phytochemical screening, anti-oxidant activity and HPLC analysis of methanol and petroleum ether extract of *Cordia diffusa* leaves. The invitro anti-oxidant activity of *Cordia diffusa* leaf samples were investigated spectrophotometrically using 2,2-diphenyl-1-picrylhydrazyl

thanolic extract showed significant anti-oxidant activity compared to

Recommended articles

Article Metrics

Citations

Citation Indexes

Captures

Readers

FEEDBACK

COLLEGE OF AGRICULTURE
NAMAKKAL
637 20

Contents lists available at ScienceDirect

Journal of King Saud University – Science

journal homepage: www.sciencedirect.com

Short communication

Anti-oxidant activity, phytochemical screening and HPLC profile of rare endemic *Cordia diffusa*

Kanagaraj Prabu [a], Arunachalam Rajasekaran [b], Devaraj Bharathi [c], Subbiah Ramalakshmi [a,*]

[a] PG & Research Department of Biotechnology, Hindusthan College of Arts & Science, Coimbatore, Tamilnadu 641028, India
[b] Forest Research & Information Management Division, Institute of Forest Genetics and Tree Breeding, Coimbatore, Tamilnadu 641002, India
[c] PG & Research Department of Biotechnology, Kongunadu Arts & Science College, Coimbatore, Tamilnadu 641029, India

ARTICLE INFO

Article history
Received 24 December 2017
Accepted 17 April 2018
Available online 18 April 2018

Keywords
Cordia diffusa
Phytochemical screening
HPLC
Anti-oxidant activity

ABSTRACT

The present study deals with the investigation of phytochemical screening, anti-oxidant activity and HPLC analysis of methanol and petroleum ether extract of *Cordia diffusa* leaves. The invitro anti-oxidant activity of *Cordia diffusa* leaf samples were investigated spectrophotometrically using 2,2-diphenyl-1-picrylhydrazyl (DPPH). Methanolic extract showed significant anti-oxidant activity compared to petroleum ether extract. Determination of phytochemical constituents like phenols, flavonoids, tannins, saponins, alkaloids, steroids, terpenoids, anthocyanin, betacyanin and glycoside tests were carried out. HPLC chromatogram supported the presence of 1–8 phytocompounds. In conclusion, *Cordia diffusa* leaves might be used as a potential antioxidant source in pharmaceutical and food industries.
© 2018 The Authors. Production and hosting by Elsevier B.V. on behalf of King Saud University. This is an open access article under the CC BY-NC-ND license (http://creativecommons.org/licenses/by-nc-nd/4.0/)

1. Introduction

The scientific attention towards nature for the use in food and medicine has increased considerably in recent years due to synthetic ones are restricted in various countries based on food safety regulation (Michelin et al., 2011). Antioxidants are substance which protects the human immune system against free radicals that may cause pathological conditions such as anaemia, asthma, inflammation, ischemia, ageing process (Makari and Patil, 2008). In living cells, free radicals are continuously produced as a result of abnormal metabolisms or external factors. Free radicals cause single and double strand break. This nucleotide break or damage leads to mutagenesis and aging (Bursal and Gulçin, 2011).

Naturally plants have the ability to produce secondary metabolites such as phenols, essential oils, flavonoid, tannins, saponins, which act as a protective agents against free radicals and pathological attack (Bajalan et al., 2017). Secondary metabolites are generally not important for the growth and reproduction of plants but they play significant role in pharmaceutical and food industries (Makari and Patil, 2008; Casuga et al., 2016).

The *Cordia* genus contains more than 300 species distributed worldwide, mostly in the warm region of the world (Al-Musayeib et al., 2011). Biological studies related to the different extract and compounds isolated from *Cordia* genus reported as antiviral, cytotoxic activities in tumour cells, anti-inflammatory and free radical scavenging properties (Ficarra et al., 1995; Rapisarda et al., 1992). Some substance from *C. corymbosa* and *C. goetsei*, are mentioned in the literature for their fungicidal activity against phytopathogens (Ficarra et al., 1995). Phytochemicals isolated from *Cordia dichotoma* leaves showed significant cytotoxic activity against human prostate carcinoma cell line (Rahman et al., 2017).

Cordia diffusa Jacob (Boraginaceae) is an endemic plant mainly distributed in southern parts of the Tamilnadu State, India (Ahmedullah and Nayar, 1987). The population of this species from *Cordia* genus is found rare and becoming endangered. Nair and Henry (1983) have included this species in their list of rare and threatened flowering plants of Asia. Medicinal and pharmacological value of the genus Cordia (Prasad et al., 2013) represents the importance of this plant. However, to date, less attention has been paid to study the biological properties of this genus *Cordia*. To the best of our knowledge, this is the first report on phytochemical screening and antioxidant free radical scavenging activity of the methanol and petroleum ether extract of *Cordia diffusa* leaves.

* Corresponding author.
E-mail addresses: prabubt1@gmail.com (K. Prabu), bharathi.deva@yahoo.in (D. Bharathi), ramalaksh34@gmail.com (S. Ramalakshmi).
Peer review under responsibility of King Saud University.

Production and hosting by Elsevier

https://doi.org/10.1016/j.jksus.2018.04.035
1018-3647/© 2018 The Authors. Production and hosting by Elsevier B.V. on behalf of King Saud University.
This is an open access article under the CC BY-NC-ND license (http://creativecommons.org/licenses/by-nc-nd/4.0/).

COLLEGE OF ARTS NAMAKKAL 637 205

2. Materials and methods

2.1. Chemicals and reagents

2,2-diphenyl-1-picrylhydrazyl (DPPH), ascorbic acid, methanol (HPLC grade), Petroleum ether, quercetin were purchased from sigma Aldrich. All other chemicals and reagents used in this study were of analytical grade.

2.2. Plant collection and authentication

The leaves of *Cordia diffusa* (Fig. 1) were collected from Institute of Forest Genetic and Tree Breading (IFGTB) campus, Coimbatore, Tamilnadu, India. It was identified at Botanical Survey of India (Ref. BSI/SRC/23/01/15/T/0011-02), TNAU, Coimbatore, Tamilnadu, India.

2.3. Preparation of methanol and petroleum ether extract

Plant leaf extract was prepared using methanol and petroleum ether by soxhlet extractor. It was performed as described by Redlem et al. (2014). After completion of extract, the methanol and petroleum ether solvents were evaporated by using rotatory evaporator. Prepared extract were concentrated, dried and kept at 4 °C until further analysis.

2.4. Qualitative phytochemical analysis

Phytochemical screening of methanol and petroleum ether extract of *C. diffusa* leaf samples were performed for the qualitative detection of different phytochemicals such as alkaloids, flavonoids, saponins, glycosidas, phenols, steroids, anthocyanin, betacyanin, tannin and terpenoids. All phytochemical tests were performed according to the stranded methods described by Siddiqui and Ali (1997), Trease (1989), Sithara et al. (2016).

2.5. Quantitative determinations of phytochemicals

2.5.1. Estimation of total phenol and flavonoids content

Total polyphenol content of *Cordia diffusa* leaves were estimated according to the protocol prescribed by Bursal and Gülcin (2011). The amount of phenols in both extracts was expressed as μg of catechol equivalent per mg of extract. Total flavonoid content of methanol and petroleum ether extract was estimated according to Jamien-meda et al. (2008). The result was expressed μg of quercetin equivalent per mg of extract.

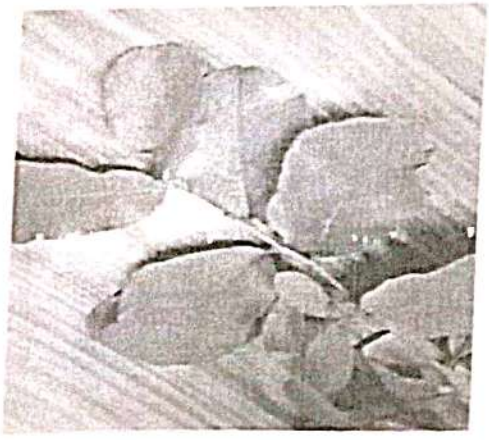


Fig. 1. Leaf sample of *C. diffusa*.

2.6. HPLC analysis

High Performance Liquid Chromatography (HPLC) was used to identify the presence of phytocompounds in leaf extracts of *Cordia diffusa*. HPLC analyzed with Hitachi instrument and L-4000 UV detector was used. HPLC analysis was performed according to Tone et al. (2015).

Methanolic and petroleum ether extract of *Cordia diffusa* and mobile phase solvents (acetonitrile with HCl) were filtered through 0.45 μm membrane filter. Prepared solvents and extracts were degassed by ultrasonic method. 23 Polyphenol standards such as resorcinol, vanillin, vanillic acid, phloroglucinol, gallic acid, pyrocatechol, salicylic acid, benzoic acid, syringic acid, syringaldehyde, pyrogalcol, tannic acid, morphillin, catecol, cinnamic acid, catechin, picric acid, phenyl acetic acid, elagic acid, ferulic acid, chlorogenic acid, hydroxyl benzoic acid and oxalic acid were used for characterization and identification of the phenolic compounds in *Cordia diffusa* leaf samples. Identification of each compound was done by comparison of their retention's time and UV absorption spectrum with those of the standards.

2.7. Invitro anti-oxidant activity

2.7.1. Determination of DPPH anti-oxidant activity

The DPPH free radical scavenging activity of leaf extracts of *Cordia diffusa* were carried out spectrophotometrically according to the method reported by Govindappa et al. (2013). Different concentration (20, 40, 60, 80, 100 μg/mL) of methanol and petroleum ether extract was added to an equal volume, to 0.002% methanolic DPPH solution. Samples were incubated for 20 min at room temperature and spectral absorbance was measure at 517 nm. Ascorbic acid is used as a reference stranded. Percentage of inhibition was calculated using the following equation

$$\% \text{ inhibition} = (|\text{control absorbance} - \text{Blank absorbance}|/\text{Control Absorbance}) \times 100$$

2.8. Statistical analysis

All experiments were carried out in triplicate and results were expressed as mean ± SEM (standard error of mean). All statistical analysis were performed using MS excel 2007.

3. Results and discussion

3.1. Qualitative phytochemical screening

The results of qualitative phytochemical screening were present in Table 1. Phytochemical screening revealed the presence of alka-

Table 1
Phytochemical screening of *C. diffusa*.

S.No.	Test(s)	Extract	
		Methanol	Petroleum ether
1	Phenols	+	+
2	Alkaloid	+	+
3	Glycosides	+	–
4	Saponins	+	–
5	Flavonoids	+	+
6	Steroids	+	–
7	Terpenoids	+	–
8	Anthocyanin	–	–
9	Betacyanin	+	–
10	Tannins	–	+

Notes: + denotes positive and – denotes negative.

R.G.P. COLLEGE OF ARTS & SCIENCE NAMAKKAL 637 206

loid, flavonoids, saponins, glycosidas, betacynin, phenols, steroids in methanolic extract and petroleum ether contain phenolic acids, flavonoids, tannins, alkaloids. Presence of these phytochemicals in plants greatly determined the antimicrobial, anti-oxidant and other biological activities (Zheng and Wang, 2001). Among the phytochemicals, phenols, flavonoids and terpenoids have been proven to be of great importance because they play important role in immune defense activity (Idris et al., 2017). The presence of these phytochemical in the both methanol and petroleum ether leaf extract of *C. diffusa* could possibly play a significant role in the anti-oxidative activity observed in this present study. Similarly, it has been reported that the other species of this genus *C. myxa* leaves contain various phytochemicals such as alkaloids, phenols, tannins, saponins and glycosides (Jasieni et al., 2016). The difference observed in the results of phytochemical constituents between the methanol and petroleum ether extract may be attributed to the solvent of extraction, nature of processing method and micro change in lab environment (Odeyemi et al., 2017).

3.2. Estimation of total phenol and flavonoids content

Total phenolic content of *C. diffusa* leaves were measured by Folin Ciocalteu reagent in terms of catechol equivalent and stranded quercetin equivalent were used for flavonoid estimation. The total phenol content of methanolic extract was 5.03 ± 0.50 µg/mL and petroleum ether contains 4.00 ± 0.21 µg/mL. The total flavonoid content of methanolic and petroleum ether extract was measured as 5.65 ± 0.43 µg/mL and 4.03 ± 0.57 µg/mL. Flavonoids play a major role in anti-oxidant activity but depend on their molecular structure and position of OH groups (Iqbal et al., 2012). Result obtained the present study revealed that the level of phenolic compounds in the both extract of the *C. diffusa* leaves was considerably higher in methanol extract then that in petroleum ether extract. This is due to different degree of solvents used for the extraction of polyphenols in plant (Bouaziz et al., 2015).

3.3. HPLC chromatogram analysis

The HPLC analysis of both extracts of *Cordia diffusa* showed the presence of 1–8 compounds such as morpholin, tannic acid, ellagic acid, ferulic acid, phloroglucinol, catechin, benzoic acid and syringaldehyde. Chromatogram of a methanol and petroleum ether extracts are shown in Fig. 2.

The HPLC chromatogram of the *C. diffusa* leaf methanol extract showed the presence of eight peaks of which they identified as morpholin, phloroglucinol, tannic acid, catechin, ferulic acid, benzoic acid and the identity of 2 peaks are unknown which needs detailed analysis. The HPLC chromatogram of petroleum ether extract showed the presence of morpholin, ellagic acid, syringic acid, syringaldehyde and two unknown compounds. It was noticed that morpholin compound are highly presented in the both solvent extract. Morpholin compound has a potential effect against pathogenic bacteria and fungus (Bektaş et al., 2013). Phloroglucinol, tannic acid, catechin, ferulic acid and syringaldehyde are phenolic compounds which has potential biological and pharmacological activities. Presence of benzoic acid represents the antiseptic value of the plant leaves (Lillard, 1904).

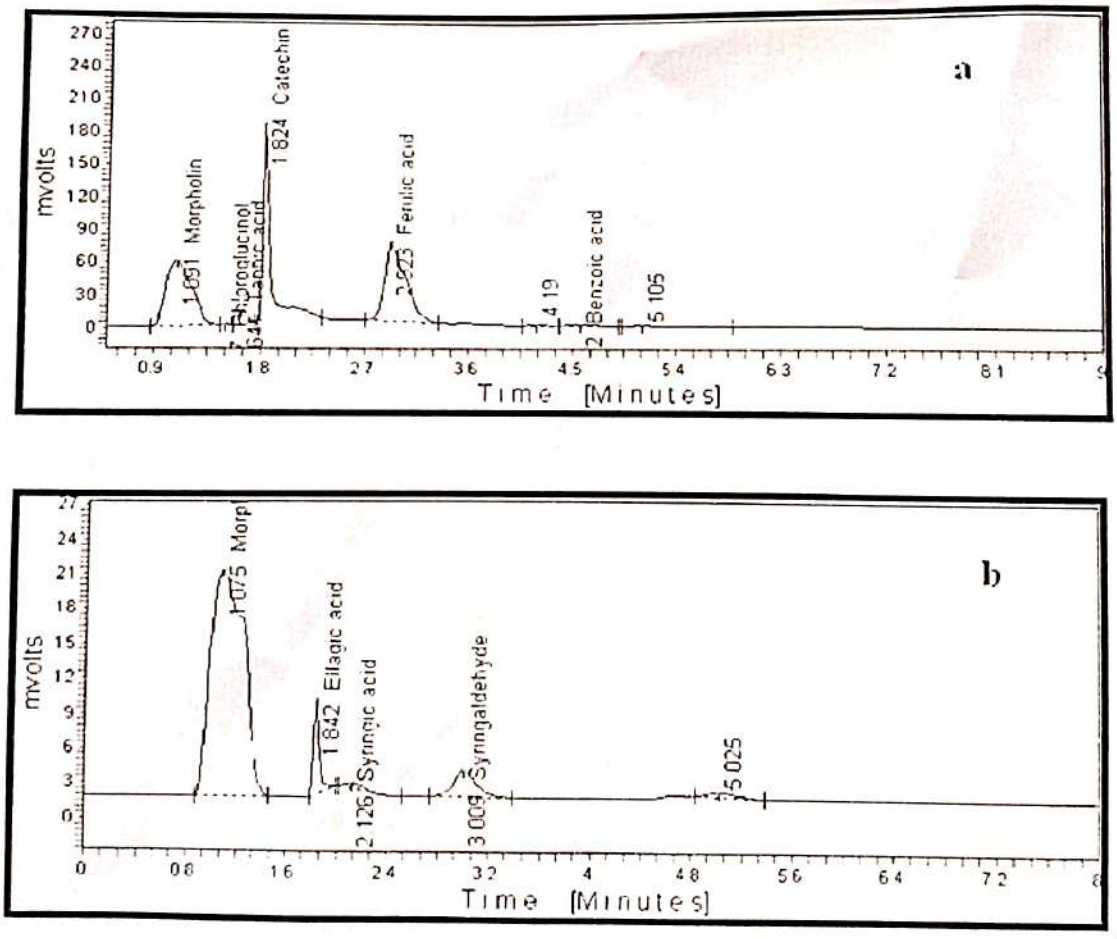


Fig. 2. HPLC chromatogram of *C. diffusa* leaf samples; a) methanol extract, b) petroleum ether extract.

COLLEGE OF ARTS & SCIENCE NAMAKKAL 637 206

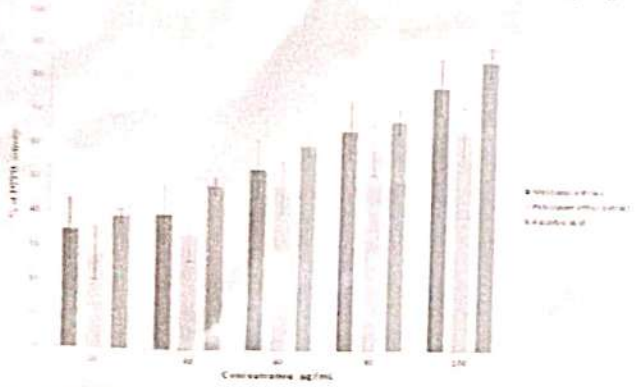


Fig. 3. DPPH anti-oxidant activity of methanol and petroleum ether extract of *C. diffusa*.

3.4. Invitro anti-oxidant activity

In this study, petroleum ether and methanol leaf extract of *C. diffusa* were investigated for the free radical scavenging activity with 2,2-diphenyl-1-picrylhydrazyl (DPPH) assay. Result showed that maximum inhibition of anti-oxidant activity was noticed in methanol extract compared to petroleum ether (Fig. 3). It was observed that free radical scavenging of free radicals occurred in a concentration dependent manner. Methanolic extract of *C. diffusa* leaf extract has potential anti-oxidant activity that close to the ascorbic acid. This anti-oxidant capability might be due to the presence of polyphenolic compounds, especially phenols that have the ability to donate the hydrogen atoms in their hydroxyl groups (Bouzaar et al., 2015; Sagbo et al., 2017). It was reported that *Cordia wallichii* has 25.85% DPPH racial scavenging activity and also reported that methanolic extract of *C. wallichii* plant was found most effective than hexane (Makari and Patil, 2008).

4. Conclusion

The present study supported the anti-oxidant activity of methanol and petroleum ether extract of *Cordia diffusa* leaves. Moreover, presence of phytochemicals was analyzed by stranded method and chemical content of both methanol and petroleum ether extract were identified by HPLC. Further studies would involve separation and identification of individual components, anti-microbial and anti-cancer activity test.

Conflict of interest

The authors have declared no conflict of interest

Acknowledgements

Authors would like to thank Bio prospecting Division, Institute of Forest Genetics and Tree Breeding (IFGTB), Coimbatore for providing the facilities for working and also to the laboratory assistance.

References

Ahmedullah, M., Nayar, M.P., 1987. Endemic Plants of the Indian Region. Botanical Survey of India, Calcutta. 1:190–194.

Al-Musayeib, N., Perveen, S., Fatima, I., Nasir, M., Hussain, A., 2011. Antioxidant, anti-glycation and anti-inflammatory activities of phenolic constituents from *Cordia sebestena*. Molecules. 16 (12), 10224–10229.

Bajpai, J., Jamil, S., Pradhan, M., Bajaj, M., 2011. Antioxidant activity and total phenolic and flavonoid content of the extract and chemical composition of the essential oil of *Hemionitis farinosa* collected from Katni. Asian Pac. J. Trop. Biomed. 1 (2), 144–146.

Bektas, H., Ceylan, S., Demirbas, N., Alpay-Karaoglu, S., Sokmen, B.B., 2014. Antimicrobial and antitumor activities of newly synthesized morpholine derivatives containing an azole nucleus. Med. Chem. Res. 23 (8), 3629–3639.

Bouzaiz, A., Abdulla, S., Bighiero, A., Charef, N., 2015. Phytochemical analysis, hypotensive effect and antioxidant properties of *Myrtus communis* L. growing in Algeria. Asian Pac. J. Trop. Biomed. 5 (1), 19–28.

Bursal, E., Gulcin, I., 2011. Polyphenol contents and in vitro antioxidant activities of lyophilized aqueous extract of Fewitfoil (*Achillea deficiens*). Food Res. Int. 44 (5), 1482–1489.

Cariaga, T.P., Castillo, A.J., Corpuz, M.J.A.T., 2016. GC–MS analysis of bioactive compounds present in different extracts of an endemic plant *Eriosolenia hirsuta* Blanco (Malvaceae) leaves. Asian Pac. J. Trop. Biomed. 6 (11), 957–961.

Ficarra, R., Ficarra, P., Tommasini, S., Calabro, M.L., Ragusa, S., Romeo, R., Ramsarda, A., 1992. Leaf extracts of some Cordia species: analgesic and anti-inflammatory activities as well as their chromatographic analysis. Farmaco; societa chimica italiana) 50 (4), 245–256.

Govindappa, M., Channabasava, R., Kumar, R.S., Pushpalatha, K.C., 2013. Antioxidant activity and phytochemical screening of crude endophytes extracts of *Talaromyces trachyspermus* Rifai & K. Sch. Am. J. Plant Sci. 4 (08), 1651–1658.

Idris, O.A., Wintola, O.A., Afolayan, A.J., 2017. Phytochemical and antioxidant activities of *Rumex crispus* L. in treatment of gastrointestinal helminths in Eastern Cape Province, South Africa. Asian Pac. J. Trop. Biomed. 7 (12), 1071–1078.

Iqbal, J., Salim, S.A., Lim, L.B., 2015. Phytochemical screening, total phenolics and antioxidant activities of bark and leaf extracts of *Goniothalamus velutinus* (Airy Shaw) from Brunei Darussalam. J. King Saud Univ. Sci. 27 (3), 224–232.

Jassim, T.M., Al-mendalawi, S.I.H., Aljuboury, I.S., Jafet, Q.N., 2016. Phytochemical study and antibacterial activity of crude alkaloids and mucilage of *Cordia myxa* in Iraq. Int. J. Pharm. Sci. Rev. Res. 39 (1), 252–256.

Lamien-Meda, A., Lamien, C.E., Compaore, M.M., Meda, R.N., Kiendrebeogo, M., Zeba, B., Nacoulma, O.G., 2008. Polyphenol content and antioxidant activity of fourteen wild edible fruits from Burkina Faso. Molecules 13 (3), 581–594.

Lillard, B., Ed, J. 1904. Practical Druggist And Pharmaceutical Review of Reviews. Lillard & Company.

Lone, S.H., Bhat, K.A., Khuroo, M.A., 2015. Phytochemical Screening and HPLC Analysis of Artemisia amygdalina. In: Chemical and Pharmacological Perspective of *Artemisia amygdalina*. Springer International Publishing, pp. 7–13.

Makari, H.K., Patil, R., 2008. In vitro antioxidant activity of the hexane and methanolic extracts of *Cordia wallichii* and *Celastrus paniculata*. Int. J. Aesthetic Antiag. med. 1, 1–10.

Michelin, E.M., de Lemos Wiese, L.P., Ferreira, E.A., Pedrosa, R.C., Ferreira, S.R., 2011. Radical-scavenging activity of extracts from *Cordia verbenacea* DC obtained by different methods. J. Supercrit. Fluids 56 (1), 89–96.

Nair, N.C., Henry, A.N., 1983. Flora of Tamilnadu, India. Botanical Survey of India, Coimbatore.

Odeyemi, S., Afolayan, A., Bradley, G., 2017. Phytochemical analysis and antioxidant activities of *Albuca bracteata* Jacq. and *Albuca setosa* Jacq. bulb extracts used for the management of diabetes in the Eastern Cape, South Africa. Asian Pac. J. Trop. Biomed. 7 (6), 577–584.

Prasad, G., Bride, S.R., Shailesh, T., Patwekar, Patil, S.T., 2013. Plant profile, phytochemistry and pharmacology of *cordia dichotoma* (Indian cherry): a review. Asian Pac. J. Trop. Biomed. 3 (12), 1009–1012.

Rahman, M.A., Sahabjada, Akhtar, J., 2017. Evaluation of anticancer activity of *Cordia dichotoma* leaves against a human prostate carcinoma cell line, PC3. J. Tradit. Complement. Med. 7 (3), 315–321.

Ramsarda, A., Barbera, R., De Pasquale, A., Ficarra, P., Ficarra, R., Tommasini, S., Ragusa, S., 1992. *Cordia francisci*, *C. monticolensis*, *C. myxa*, *C. serratifolia*, and *C. ulmifolia* leaves as new sources of rutin: analgesic and anti-inflammatory activity. Planta Medica 58 (S1), 643–643.

Redfern, J., Kinninmonth, M., Burdass, D., Verran, J., 2014. Using soxhlet ethanol extraction to produce and test plant material (essential oils) for their antimicrobial properties. J. Microbiol. Biol. Educ. 15 (1), 45.

Sagbo, I.J., Afolayan, A.J., Bradley, G., 2017. Antioxidant, antibacterial and phytochemical properties of two medicinal plants against the wound infecting bacteria. Asian Pac. J. Trop. Biomed. 7 (9), 817–825.

Siddiqui, A., Ali, M., 1997. Practical Pharmaceutical Chemistry. CBS Publishers and distributors, New Delhi, pp. 129–131.

Sultana, N.V., Kamathi, S., Rajalakshmi, S., Queen, J., Bharathi, D., 2016. Phytochemical analysis of *Andrographis paniculata* using different solvents. Eur. J. Biotechnol. Biosci. 4 (8), 28–30.

Trease, G.E., 1989. Trease and Evans pharmacognosy: a physicians guide to herbal medicine. Bailliere Tindall, London edn. 13, 912.

Zheng, W., Wang, S.Y., 2001. Antioxidant activity and phenolic compounds in selected herbs. J. Agric. Food Chem. 49 (11), 5165–5170.

PGP COLLEGE OF ARTS & SCIENCE NAMAKKAL

PRINCIPAL
PGP College of Arts and Science
Namakkal

GALE ACADEMIC ONEFILE

A study of estimation of serum uric acid level in patients with psoriasis

Authors: V Shanmugapriyadarsini, D Nirmala Lourdh Sunitha and P Amalraj*
Date: Feb 11, 2016

From: Journal of Evolution of Medical and Dental Sciences (Vol. 5, Issue 12)
Publisher: Anjanibala Enterprises Private Limited

Document Type: Article
Length: 1,462 words
Lexile Measure: 1570L

EXPLORE

Abstract

Psoriasis is a disease characterized by increased epidermal cell turnover and hence an increase in purine catabolism. The serum uric acid levels in psoriasis are expected to be raised because of the high purine catabolism. AIM To study the levels of serum uric acid in 25 cases of uncomplicated chronic plaque type psoriasis. MATERIALS AND METHODS Twenty five consecutive patients with chronic plaque type psoriasis attending the Dermatology OPD of a Tertiary Care Hospital were selected and their serum uric acid levels were estimated. RESULTS The average uric acid levels in males psoriatic patients was between 3.6-7.7mg/dl and in the female psoriasis patients, the serum uric acid values were between 2.5-6.8mg/dl. DISCUSSION The serum levels of uric acid in uncomplicated chronic plaque type psoriasis were within the normal ranges for both male and female patients. Since only chronic plaque type psoriasis patients were included in the study and the severity of disease is less in such patients when compared to erythrodermic or unstable psoriasis, the serum uric levels were observed to be within the normal ranges. CONCLUSION This study concludes that the serum

Related Subjects

- Alkaloids
- Medical research
- Psoriasis
- Uric acid

COLLEGE OF ARTS & SCIENCE
NAMAKKAL
637 206
P.G. & R.

A STUDY OF ESTIMATION OF SERUM URIC ACID LEVEL IN PATIENTS WITH PSORIASIS

Shanmugasundaram V[1], Nithya D[2], Sunu Joseph[3], Akilandeswari P[4]

[1]Associate Professor, Department of Dermatology, Karpagam Faculty of Medical Sciences & Research, Coimbatore.
[2]Assistant Professor, Department of Dermatology, Karpagam Faculty of Medical Sciences & Research, Coimbatore.
[3]Senior Resident, Department of Dermatology, Karpagam Faculty of Medical Sciences & Research, Coimbatore.
[4]PhD Research Scholar, Department of Microbiology, Karpagam Academy of Higher Education, Coimbatore.

ABSTRACT

Psoriasis is a disease characterized by increased epidermal cell turnover and hence an increase in purine catabolism. The serum uric acid levels in psoriasis are expected to be raised because of the high purine catabolism.

AIM

To study the levels of serum uric acid in 25 cases of uncomplicated chronic plaque type psoriasis.

MATERIALS AND METHODS

Twenty five consecutive patients with chronic plaque type psoriasis attending the Dermatology OPD of a Tertiary Care Hospital were selected and their serum uric acid levels were estimated.

RESULTS

The average uric acid levels in males psoriatic patients was between 3.6-7.7mg/dl and in the female psoriasis patients, the serum uric acid values were between 2.5-6.8mg/dl.

DISCUSSION

The serum levels of uric acid in uncomplicated chronic plaque type psoriasis were within the normal ranges for both male and female patients. Since only chronic plaque type psoriasis patients were included in the study and the severity of disease is less in such patients when compared to erythrodermic or unstable psoriasis, the serum uric levels were observed to be within the normal ranges.

CONCLUSION

This study concludes that the serum uric acid levels are not raised in chronic plaque type psoriasis, patients with less disease severity.

KEYWORDS

Chronic Plaque Type Psoriasis, Serum Uric Acid, Purine Catabolism, Accelerated Epidermal Kinetics.

HOW TO CITE THIS ARTICLE: Shanmugasundaram V, Nithya D, Joseph S, et al. A study of estimation of serum uric acid level in patients with psoriasis. J. Evolution Med. Dent. Sci. 2016;5(12):506-508, DOI: 10.14260/jemds/2016/115

INTRODUCTION

Psoriasis is an immune mediated papulosquamous disorder with accelerated epidermal pkinetics. Psoriasis is a common, chronic disease of the skin and both genetic and environmental factors play a critical role in its inducement.[1] Recently, it was noted that elevated serum levels of uric acid are associated with factors that contribute to metabolic syndrome including hypertriglyceridemia, obesity, hypertension and diabetes.[2,3,4,5] The cell proliferation index is increased; the cell transit time is shortened, leading to a high cell turnover state. It is expected that such high cell turnovers will be associated with an increase in the serum uric acid. In recent times, there is much interest in the raised levels of serum uric acid in psoriasis patients with some studies even linking it to increased incidence of psoriatic arthritis and increased prevalence of metabolic syndrome.

Financial or Other, Competing Interest: None.
Submission 13-01-2016, Peer Review 24-01-2016,
Acceptance 27-01-2016, Published 10-02-2016.
Corresponding Author:
Dr. Shanmugasundaram V,
411, G. V. Residency, Sowripalayam,
Coimbatore 641028.
E-mail: shanmugammd@yahoo.com
DOI: 10.14260/jemds/2016/115

Some studies even go on to state that raised serum uric acid levels contributes to metabolic syndrome, which in turn may be connected to immunological abnormalities and that psoriasis may be considered as an immune-metabolic disease.[6] Since there are not many studies on the relationship between serum uric acid and psoriasis we conducted this study to estimate the levels of serum uric acid in chronic plaque type psoriasis patients.

MATERIALS AND METHODS

Twenty five consecutive psoriatic patients with chronic plaque type psoriasis irrespective of the duration of their disease were selected amongst the patients attending the Dermatology OPD in a Tertiary Care Hospital. The patients with renal diseases, gout and malignancy and on drugs lowering uric acid level like allopurinol, colchicine and febuxostat were excluded from the study. All the patients were thoroughly examined to note the areas of involvement and extent of the disease. Also patients with psoriatic erythroderma, generalized pustular psoriasis, palmoplantar psoriasis and psoriatic arthritis were not included in the study, since this study is aimed at estimating the uric acid levels only in the chronic plaque type of psoriasis. After obtaining informed consent, blood was drawn for serum uric acid estimation.

The estimation was done using fully automated clinical chemistry analyzer.[7] The results were reported in mg/dL.

NAMAKKAL 637 206

RESULTS

The range of serum uric acid levels for 25 patients included in the study was between 3.6–7.9mg/dl, among the 25 patients, there were 16 males and 9 females. The range of serum uric acid in the male patients was between 3.6–7.9mg/dl (Table 1). The range of serum uric acid in the female patients was 3.8–6.4 (Table 2). The age wise distribution, minimum/maximum and average uric acid levels in patients with chronic plaque type psoriasis are presented in Table 4 and 5.

DISCUSSION

In our study, the serum uric acid levels of all patients except one male patient was well within the normal range of 3.6–7.7 (For male) and 2.5–6.8 (For females). Compared to female patients, the serum uric acid levels in male patients was higher. This is expected as it is a normal physiological variation to find higher uric acid levels in males when compared to female.

In majority of the patients (i.e.) in 75% of the patients the serum uric acid was within the lower and middle limits of the normal, (i.e.) it was between 3-6mg/dl. In the rest of the patients (25%), the serum uric acid was between 6-7mg/dl which can be considered to be normal to higher or higher limits.

The average value of serum uric acid levels in male was 5.32mg/dl and in females it was 5.18mg/dl, which is in mid-ranges of serum uric levels. Our study is in concordance with that of little et al. (1975).[8] whose study showed that the serum uric acid levels in patients with severe psoriasis was found to be in the middle of their normal range.

But the result of our study is in contrary to that reported by Lambert et al. and Wright (1977).[9] and Isha et al. (2011).[10] reported larger prevalence of values above the normal range in male with psoriatic arthritis uncontrolled by medications (13-15%). Moreover in the study by Isha et al.[10] the serum uric acid in their patients was found to be more than 10mg/dl.

Herrman et al. (1930).[11] reported levels of uric acid above the upper limit of normal in 44 of 140 patients with psoriasis. Especially in those with arthritis, similar association was seen by Choi et al. (2004).[12]

As stated earlier the serum uric acid levels were found be normal in all but one, most likely because this study was conducted among patients with less severity of diseases in the outpatient set-up, besides only chronic plaque type psoriasis were included, no erythrodermic or generalized pustular psoriasis were included in the study. Psoriasis is a disease with rapid epidermal cell turnover, which in turn results in hyperuricemia.[13] Furthermore, in hyperuricemia patients, there is an increase in purine catabolism. The serum uric acid levels are exacerbated by in the severity and duration of psoriasis.[1]

The severity of the diseases in chronic plaque psoriasis is less when compared to erythrodermic pustular psoriasis due to lower body surface area involvement. Hence, this may explain the normal levels of serum uric acid in the study.

CONCLUSION

This study concludes that the serum uric acid levels are not increased in all psoriatic patients. In patients with less severe disease such as uncomplicated chronic plaque type psoriasis, the serum uric acid level was well within the normal range.

REFERENCES

1. Maryam G, Amir HE, Arash D, et al. Serum uric acid levels in patients with psoriasis. TUMJ 2012;70:58-63.
2. Feig DI, Kang DH, Johnson RJ, et al. Uric acid and cardiovascular risk. N Engl J Med 2008;359:1811-1821.
3. Ishizaka N, Ishizaka Y, Toda E, et al. Association between serum uric acid, metabolic syndrome and carotid atherosclerosis in Japanese individual. Arterioscler Thromb Vasc Biol 2005;25:1038-1044.
4. Gonzalez-Gay MA, Gonzalez-Juanatey C, Vazquez-Rodriguez TR, et al. Asymptomatic hyperuricemia and serum uric acid concentration correlate with subclinical atherosclerosis in psoriatic arthritis patients without clinically evident cardiovascular disease. Semin Arthritis Rheum 2009;39:157-162.
5. Yoo TW, Sung KC, Shin HS, et al. Relationship between serum uric acid concentration and insulin resistance and metabolic syndrome. Circ J 2005;69:928-933.
6. Agnieszka G, Aldona P, Jacek CS, et al. Biochemical markers of psoriasis as a metabolic disease. Folia Histochemica Et Cytobiologica 2012;50:155-170.
7. Trivedi RC, Rebar L, Berka ES, et al. Uric acid enzymatic method. ClinChem 1978;14:1908–1912.
8. Little H, Harvie JN, Lester RS, et al. Psoriatic arthritis in severe psoriasis. Canadian Medical Association Journal 1975;112:317-319.
9. Lambert JR, Wright V. Serum uric acid levels in psoriatic arthritis. Ann Rheum Dis 1977;36(3):264–267.
10. Isha, Jain VK, Harbans Lal, et al. C-reactive protein and uric acid levels in patients with psoriasis. Indian J Clin Biochem. 2011;26(3):309–311. doi: 10.1007/s12291-011-0132-4.
11. Herrmann F. Harnsaureuntersuchungenbei Psoriasis. Archiv fur Dermatologie and syphilis 1930;161:114-126.
12. Choi HK, Atkinson K, Karlson EW, et al. Purine rich foods and the risk of gout in men. N Eng J Med 2004;350:1093-1103. doi: 10.1056/NEJMoa035700.
13. Steinberg AG, Becker SW, Fitzpatrick TB, et al. A genetic and statistical study of psoriasis. American Journal of Human Genetics 1951;3:267-281.

Sl. No.	Uric acid level in serum (Male)	
	Age	mg/dL
1	45	3.9
2	60	4.7
3	50	3.6
4	45	7.0
5	63	6.2
6	62	3.8
7	60	7.6
8	69	4.1
9	41	3.6
10	38	7.1
11	49	4.1
12	49	7.9
13	60	6.8
14	26	5.8
15	30	4.8
16	46	3.7

Table 1: Serum uric acid level in psoriatic male patients

COLLEGE OF ARTS & SCIENCE NAMAKKAL 637 206

Sl. No.	Uric acid level in serum (Female)	
	Age	mg/dl.
1	60	3.8
2	62	4.1
3	30	4.8
4	18	6.2
5	50	5.8
6	49	4.9
7	68	5.1
8	54	6.4
9	41	5.7

Table 2: Serum uric acid level in psoriatic female patients

Sex	No. of Patients	Percentage (%)
Male	16	64
Female	9	36
Total	25	100

Table 3: Gender wise distribution of psoriasis patients enrolled in this study (n=25)

Study Group	> 18	19-30	31-50	> 50
Male	0	2	8	6
Female	1	1	4	3
Total	1 (4%)	3 (12%)	12 (48%)	9 (36%)

Table 4: Age wise distribution of psoriasis patients enrolled in this study (n=25)

Study Group	Minimum value of serum uric acid (mg/L)	Maximum value of serum uric acid (mg/L)	Average value of serum uric acid (mg/L)
Male	3.6	7.9	5.322
Female	3.8	6.4	5.181

Table 5: Uric acid value in psoriasis patients in this study (n=25)

P.G.P. COLLEGE OF ARTS & SCIENCE NAMAKKAL 637 206

PRINCIPAL
PGP College of Arts and Science
Namakkal

ChemTech
International Journal of ChemTech Research
CODEN (USA) : IJCRGG ISSN : 0974-4290, ISSN(Online):2455-9555
Vol. 10, No. 05, 2017
This website is best viewed in 1024 x 768

INDEX Page 2.

S.N.(Page Numbers)	Title of Paper and Names of Authors
(402-408)	Emissions Inventory and Emission factors for Cement Industry S. Anand Kumar Varma, R. Madan kumar and A. Bharani kumar Abstract Full Text PDF Full Text XML
(799-801)	Isolation and Screening of Multi Drug Resistant Bacteria from Exposed Tablet Dumped Garbage S. Anbazhagi, K. Priyanga and Albeana Raj Abstract Full Text PDF Full Text XML
(802-810)	Process design of production of essential oil from Pimenta racemosa Israel Bonifaz Cortes, Karel Diegnez-Santana, Yunia Lopez Pérez, Borys Magaly Guzmán, Alicia Rodríguez Gregorich, Estela Guardado Yordi & Amaury Pérez Martínez Abstract Full Text PDF Full Text XML
(811-816)	Pharmaceutical and Bulk Drug Industry Wastewater – Solutions for Water Treatment Ashok Kumar Poputi Abstract Full Text PDF Full Text XML
(817-823)	Application of Six Sigma Presence for Quality Improvement in Textile Industry M.S. Kumaravel, G.Boopathy, S. Mohamed iqbal Abstract Full Text PDF Full Text XML
(824-833)	Standardisation, synthesis and characterisation of nanodrug from Tabebuia rosea leaves for breast cancer Ramalakshmi Subbiah, Muthuchelian Krishnaswamy Abstract Full Text PDF Full Text XML

P.G.P. COLLEGE OF ARTS & SCIENCE
NAMAKKAL
637 208

See discussions, stats, and author profiles for this publication at: https://www.researchgate.net/publication/317763164

Standardisation, synthesis and characterisation of nanodrug from Tabebuia rosea leaves for breast cancer

Article · June 2017

CITATIONS
0

READS
441

Some of the authors of this publication are also working on these related projects:

Project INDUSTRIAL MICROBIOLOGY View project

Project phytochemical isolation View project



www.sphinxsai.com

ChemTech

International Journal of ChemTech Research
CODEN (USA): IJCRGG, ISSN: 0974-4290, ISSN(Online):2455-9555
Vol.10 No.5, pp 824-833, 2017

Standardisation, synthesis and characterisation of nanodrug from *Tabebuia rosea* leaves for breast cancer

Ramalakshmi Subbiah[1]*, Muthuchelian Krishnaswamy[2]

[1]Department of Microbiology, Karpagam University, Coimbatore-641021, India.
[2]Department of Bioenergy, School of Energy, Environment and Natural Resources, Madurai Kamaraj University, Madurai – 625 021, India.

Abstract : In this paper silver nanoparticles (AgNP) were developed using *Tabebuia rosea* (TR) leaves as reducing agent and its anticancer potential against cancer cells was studied. The standardisation for synthesis of nanoparticle formation was carried out at different pH, temperature and reaction time. The AgNPs was studied using UV-Vis spectrum showed the high absorption band at 420 nm, size range of 49 to 98 nm, with an average size of 70 nm as determined by SEM, AFM. The energy dispersive x-ray spectroscopy (EDX) profile for AgNPs showed typical optical absorption peak approximately at 3 keV and it was found that O-H stretching of phenolic compounds and O-H, C=O stretchings in carboxylic acids are involved in formation of AgNPs studied by FTIR. NP showed specific toxicity on breast carcinoma T47D cells at 20 µg/mL concentration, showing almost 95 % cancer cell growth inhibition at 48hrs. Thus silver nanoparticles using *Tabebuia rosea* (TR) leaves have future application as nanodrug.

Keywords: Cytotoxicity, *Tabebuia rosea*, green synthesis, silver nanoparticles, Nanodrug.

Introduction

There is an increasing interest among researchers to explore the secondary metabolites of medicinal plants for use in medicine to treat diseases. But due to the advances in nanotechnology, the long process of isolating the drug compound and studying for its biological property is reduced. The green synthesis method of producing metal nanoparticles is said to be easy, eco friendly and cheap when compared to costly medicines. Thus the medicinal property of medicinal plants is explored for synthesis of silver nanoparticles. *Tabebuia* sp have a long history of use as traditional medicine for treating cancer due to its compound lapachol and its derivatives from bark of the tree[1] .

The essential oil of *Tabebuia rosea* leaf and bark is reported to be cytotoxic which may be due to the presence of o-xylene (2.13%), 2,4-dimethylhexane (1.03%), methyl cyclohexane (53.13%), methyl benzene (12.75%), 3-Pentene-2-one (9.11%)[2]. The earlier investigations on the phytochemical constituents of *Tabebuia rosea* leaves revealed the presence of saponins, tannins, phenolic acids, flavonoids and alkaloids[3]. The active compounds present in the *Tabebuia rosea* ethanolic leaf extract showed the presence of 2-furancarboxaldehyde, 5-hydroxy methyl (19.39%), 2-deoxy, D-erythropentose (11.01%), Santolina triene (8.28%), 4H-Pyran-4-one, 2,3-dihydro-3,5-dihydroxy-6-methyl (6.07%), 7-Quinolinol (6.01%), phenol, 2-(2-methyl propyl) (5.41%) and Cinnamadehyde (2.42%)[4].The leaf extract has been reported for various activities such as antimicrobial[5], cytotoxicity on MOLT-4 cells[6], cytotoxicity on brine shrimps[7] and phytotoxicity on radish seeds[8]. Also the flowers of TR have been reported for antioxidant, cytotoxicity and phytotoxicity due to presence of volatile

P.G.P. COLLEGE OF ARTS & SCIENCE NAMAKKAL 637 206

constituents 4H- pyran-4--one, 2, 3- dihydro-3, 5- dihydroxy-6- methyl, 3, 4, 5-trimethyl phenol, thiocyanic acid, 2-propynyl ester and 2-propenoic acid, 3-(2-hydroxy phenol) compounds analysed by GC-MS[9].

Thus due to various medicinal reports on TR leaves have been explored for synthesis of silver nanoparticles. Silver have been used traditionally for curing various diseases due to its antibacterial properties. Recently silver is gaining a role in cancer therapy, biosensors, dressings, devices, formulations[10]. The objective was to characterize and study the anticancer drug synthesized from TR leaf extract.

Materials and methods

Plant material and preparation of the extract

Healthy leaves of TR were collected from Madurai Kamaraj University (MKU) campus, authenticated by Prof. K. Muthuchelian, Director, and Centre for Biodiversity and Forest Studies (CBFS), Madurai Kamaraj University and voucher specimens were deposited in the herbarium of CBFS of university (No.CBFS-01). The dry TR leaves was cut into small pieces and powdered finely. About 5g of the leaf powder was boiled for 10 min in 100 ml sterile double distilled water and further filtered through Whatman No. 1 filter paper and used for the present study.

Synthesis of silver nanoparticles

Silver nitrate ($AgNO_3$) was procured from Sigma-Aldrich (Bangalore, India) was used. For the synthesis of silver nanoparticles, $AgNO_3$ (2 mM) and aqueous plant extract (10 mg/ml) were mixed in different ratios. Briefly, 1 ml of plant extract was mixed with 9 ml of $AgNO_3$ (1:9 ratio). The subsequent mixtures were prepared by increasing plant extract and decreasing $AgNO_3$ volumes by 1 ml, until the final ratio of 9:1was attained. Furthermore, appropriate concentrations of $AgNO_3$ and plant extracts vice versa from 1 to 9 ratio mixed in a series of reactions for optimization of synthesis of silver nanoparticles, incubated overnight at room temperature in dark. The resultant yellowish brown solution indicated formation of silver nanoparticles. The silver nanoparticle synthesis was optimized at different temperature and pH. The reaction temperature was studied at 30 °C to 70 °C. The pH was studied in the range of 5, 6, 7, 8 and 9 by using 0.1 N HCl and 0.1 N NaOH respectively.

Purification of Silver Nanoparticles

The broth containing nanoparticles was centrifuged, redispersed in sterile deionized water to get rid of any biological molecule. This process was repeated thrice to obtain better separation of entities from the metal nanoparticles. The purified pellet was then freeze dried using Lyophillizer (Micro Modulyo 230 freeze dryer, Thermo Electron Corporation, India).

UV–visible spectral analysis

The color change from green to brown was observed in the silver nitrate solution incubated with aqueous plant extract. The bioreduction of Ag nanoparticles was monitored by periodic sampling of aliquots (0.2 mL) of aqueous component and measuring the absorbance and spectrum of the solution in UV spectrophotometer (Shimadzu ,UV 2500,Japan), at a resolution of 1 nm between 300 and 600 nm.

Atomic Force Microscopy

A thin film of the sample was prepared on a cover slip by droping 0.1 ml of the sample on the slide, and allowed to dry for 30 minutes. The slide was then scanned with AFM (APE Research- model no: A100SGS). The AFM characterization was carried out in ambient temperature in non contact mode using silicon nitrate tips with varying resonance frequencies. These tips have spring constants of approximately 0.15 Nm^{-1} and are conical in shape with a cone angle of 20° and an effective radius of curvature at the tip of 10 nm.

Fourier transform infra-red (FTIR) spectroscopy

Silver NP dried powder (50mg) was analyzed using FTIR by drying and ground with KBr pellets and analyzed in a SHIZAMAZU model no 8400S spectrum instrument where spectrum was recorded in the region of 500 to 4500 cm^{-1}.

Scanning electron microscopy (SEM) & Energy dispersive X-ray analysis (EDX)

The lyophilized silver NPs were mounted on the copper stubs and the images were studied using scanning electron microscope (SEM). EDX analysis was done with (JEOL model-L6390) secondary electron detectors at an operating voltage of 30 kV.

Cytotoxic activity

Cell culture

Human ductal breast carcinoma cells (T47D) was obtained from the National Centre for Cell Science (NCCS), Pune, and maintained in Roswell Park Memorial Institute (RPMI) medium containing 10% fetal bovine serum (FBS). For evaluation of the cytotoxicity, cell was seeded on a 96 well plate with a density of 1×10^4 cells/cm^2. Normal cells of L929 (human fibroblast cell line) was maintained in MEM (Minimum essential Medium) containing 10% fetal bovine serum (FBS) provided by Promo Cell Germany.

Assessment of cytotoxicity

Cytotoxicity of NTR was evaluated by using MTT [3-(4,5-dimethylthiazole-2-yl)-2,5-diphenyltetrazolium] assay. In MTT test viable cells reduce the tetrazolium component of MTT into purple colored formazan crystals. Stock solution of the samples were freshly prepared (1mg/1mL) and diluted with cell culture medium to the desired concentrations (20, 50 and 100 µg/mL). The compound with different concentration was added and incubated with phosphate buffer saline (PBS) resuspended cells, after attaining 90% confluency. Cells in media devoid of compound acted as the negative control and wells treated with Triton X-100 as the positive control for a period of 48 h. 5 mg of MTT (Sigma) was dissolved in 1 ml of PBS and filter sterilized. 10 µl of the MTT solution was further diluted to 100 µl with 90 µl of serum and phenol red free medium. 100 µl of the solubilisation solution (10% Triton X-100, 0.1 N HCl and isopropanol) was added to each well and incubated at room temperature for 1 h to dissolve the formazan crystals. The absorbance of the solution was measured at a wavelength = 570 nm using a Beckmann Coulter Elisa plate reader (BioTek Power Wave XS). Triplicate samples were analyzed for each experiment.

Statistical analysis

The values are presented as mean ± SD (standard deviation) of triplicate measurements.

Results and discussion

Biosynthesis of silver nanoparticles

The silver nanoparticles are formed by reduction of silver nitrate to silver ions because of the reducing agents present in the plant extract, indicated by light yellowish color which turned to dark brown color after 24 hrs (Fig. 1). The size and shape of nanoparticles was examined by UV-Vis spectroscopy at range of 300–600 nm. Mixture of 6:4 (S6) of silver nitrate and plant extract gave optimized synthesis of silver nanoparticles of uniform size among the various combinations (Fig. 2A, 2B) studied at absorption spectrum of 420 nm characteristic for surface plasmon resonance for silver nanoparticles (Fig. 2C). The bioactive molecules present in the leaf extract of TR have played a role in the reduction of silver nitrate to silver, which can be reasoned due to the presence of saponins, tannins, phenolic acids, flavonoids and alkaloids[3], also because of the functional groups present in the tannins and phenolic compounds of the extract.

COLLEGE OF ARTS & SC NAMAKKAL 637 206

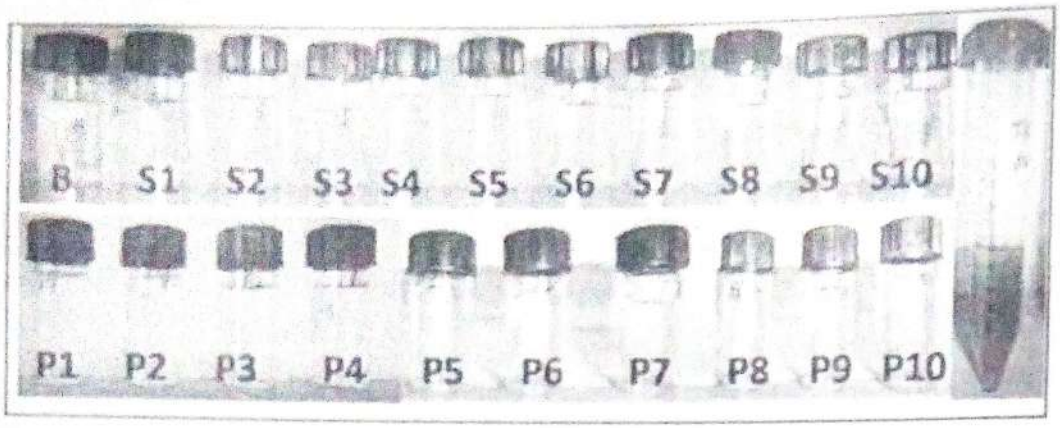


Figure1. The bottles containing silver nitrate solutions, TR plant extracts at different concentrations (A, B) denoted as S1-S10; P1-P10 respectively and bottle containing purified, concentrated silver nanoparticles (C).

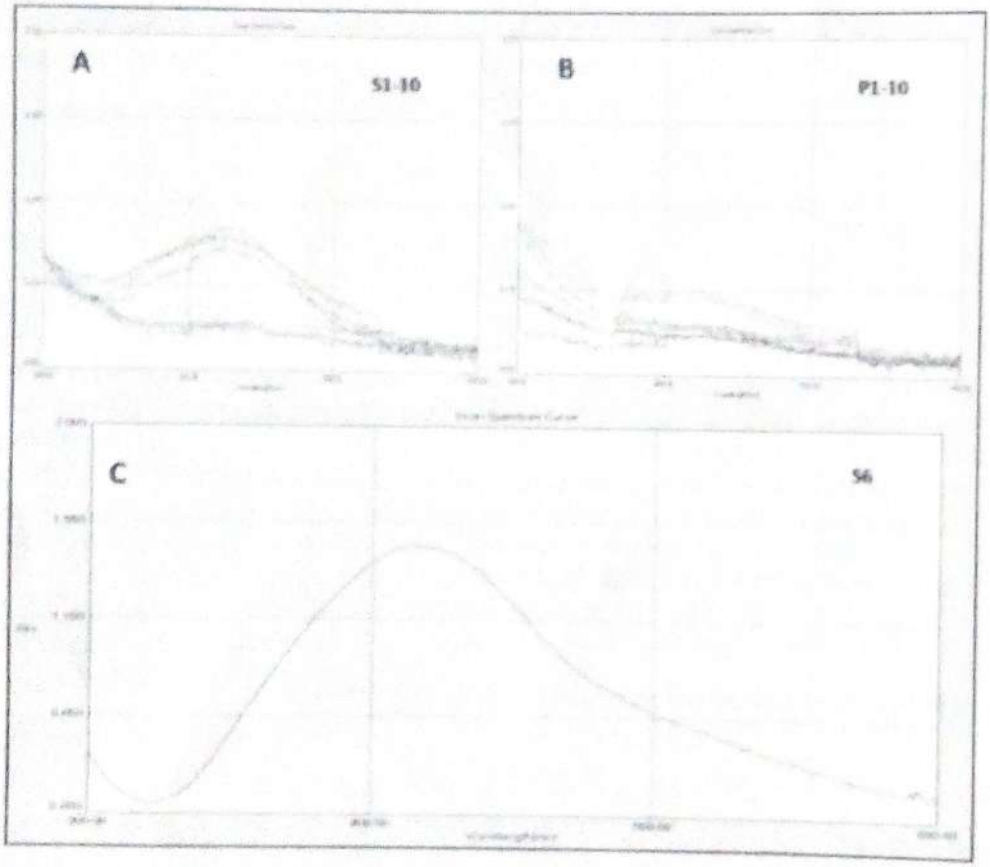


Figure2. UV-Visible spectrum of a mixture of solutions of silver nitrate S1-S10 (A), plant extracts P1-P10 (B) and standardised silver nanoparticles synthesized using *Tabebuia rosea* leaves.

Optimization of physicochemical parameters for synthesis of silver nanoparticles

The silver nanoparticles synthesis were standardized, optimized using parameters of pH and temperature, which plays very significant role in controlling shape and size of AgNPs. The pH 7 was found to synthesize non-agglomerated, monodispersed distribution of silver nanoparticles as indicated by their absorbance peaks at 420 nm confirmed by UV-Vis spectrum readings (Figure 3). For different temperature checked, optimal production was observed at 60°C, where high temperature favours the synthesis (Figure 3). Same temperature of 60°C has been reported during green synthesis of silver nanoparticles from *Tecomella undulata*[11].



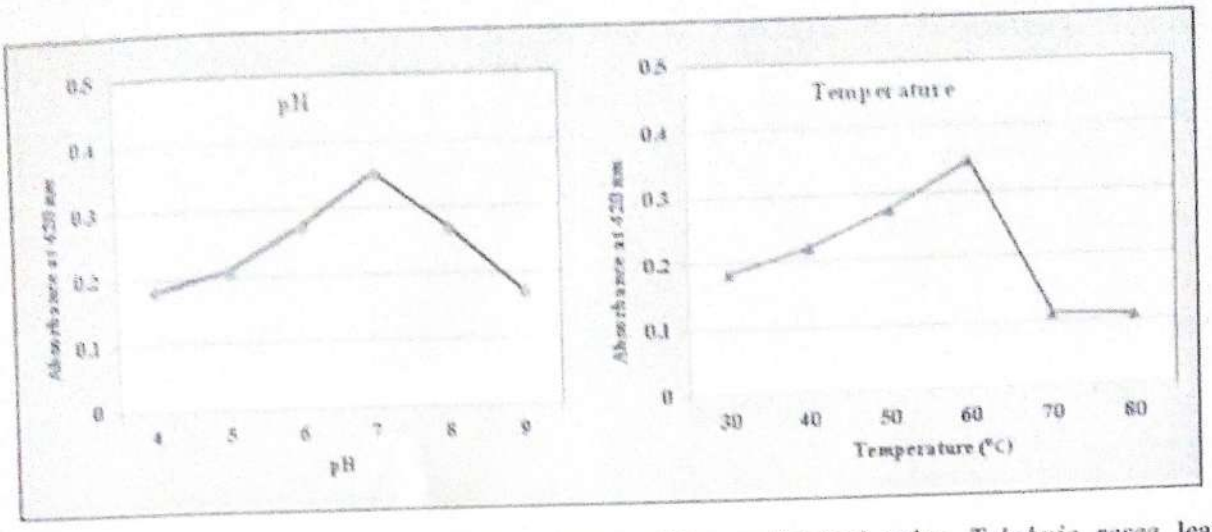


Figure3. Absorption spectrum for silver nanoparticles synthesized using *Tabebuia rosea* leaves at different pH and Temperature.

Analysis of Silver nanoparticle in AFM

The surface morphology of optimized Ag NPs was studied using atomic force spectroscopy, were almost spherical in shape confirmed by absorbance spectrum (Figure 4). The size of the silver nanoparticles studied from AFM showed size in the range of 49 to 98 nm, with an average size of 70 nm. The particles were found to be monodispersed and non-agglomerated due to the binding of some stabilising agents present in the TR extract. Figure 4 shows two and three dimensional view of sample surface over a 2 x 2 µm and at 5 µm scan that shows non-agglomerated, monodispersed biosynthesized silver nanoparticles.

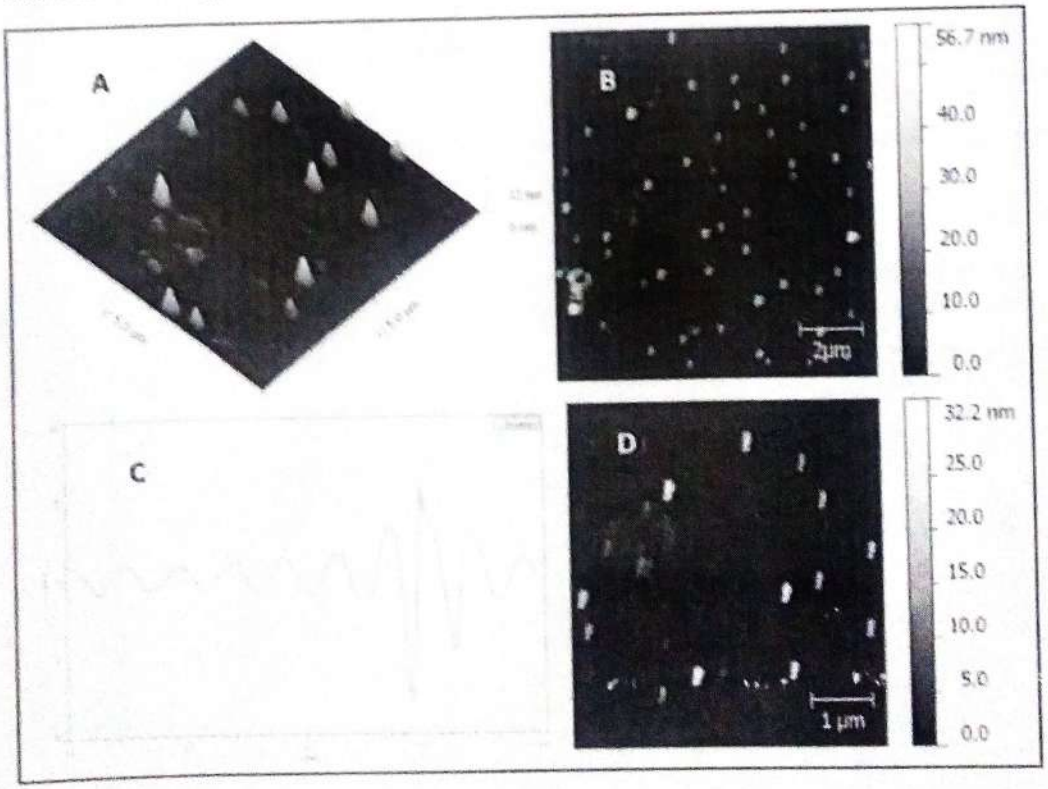


Figure 4. AFM images obtained from lyophilized sample of silver nanoparticles obtained from *Tabebuia rosea*, indicating the two dimensional images at magnification of 2µm (B), 1 µm (D), roughness data of nanoparticles at 2 µm (C) and three dimensional image of nanoparticles size in the range of 46 to 100 nm (A).

COLLEGE OF ARTS & SC NAMAKKAL 637 206

Fourier transforms infrared spectroscopy (FTIR)

FTIR analysis reveals the functional groups involved in reduction of silver nitrate to nanosilver for nanoparticle formation. The FTIR spectrum of the silver nanoparticle showed bands at 3423, 2918, 2848, 2368, 1593, 1375, 1020, 678 cm^{-1} but highly intense broad absorbance peak was observed at 3423 cm^{-1} characteristic of the O-H stretching of phenolic compounds (Figure 5). Also at 1020 and 2918 cm^{-1} corresponds to the stretch vibration of amine and C-H stretch (alkane H). Thus the silver nanoparticles are formed by interacting with the functional groups of secondary metabolites of *TR* extract such as alkaloids, alkanes, amines, alcohols, phenols and carboxylic acids.

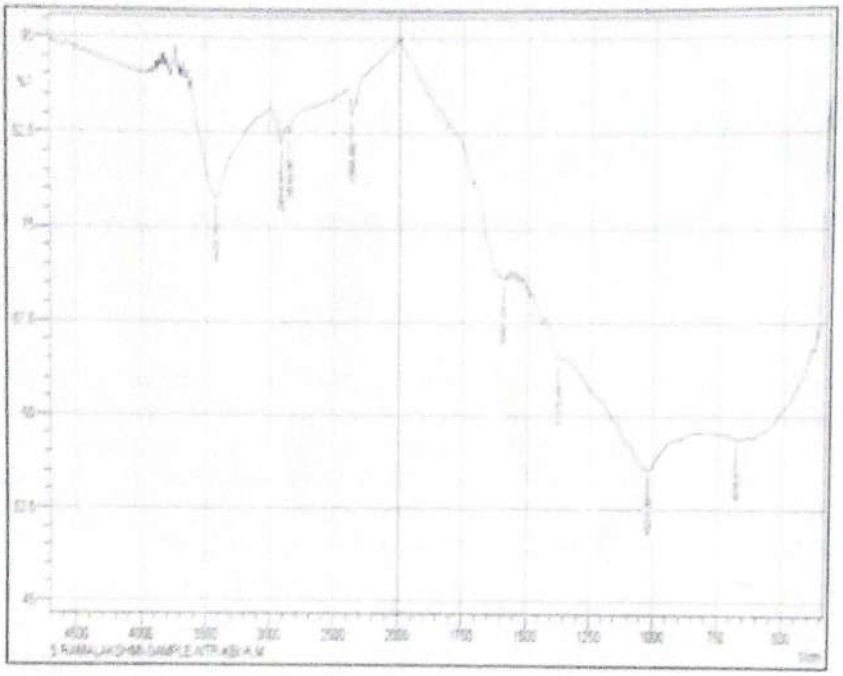
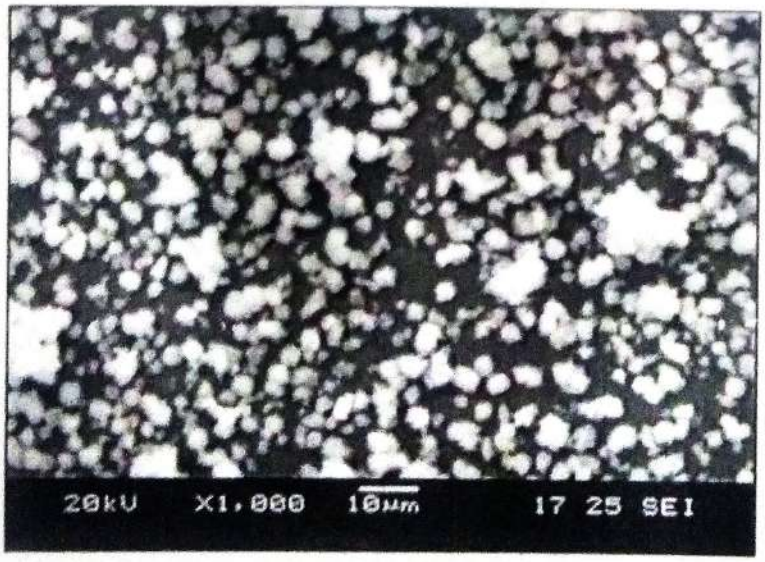


Figure 5. FTIR spectrum for silver nanoparticles synthesized using *Tabebuia rosea* leaf extract.

SEM and EDX profile

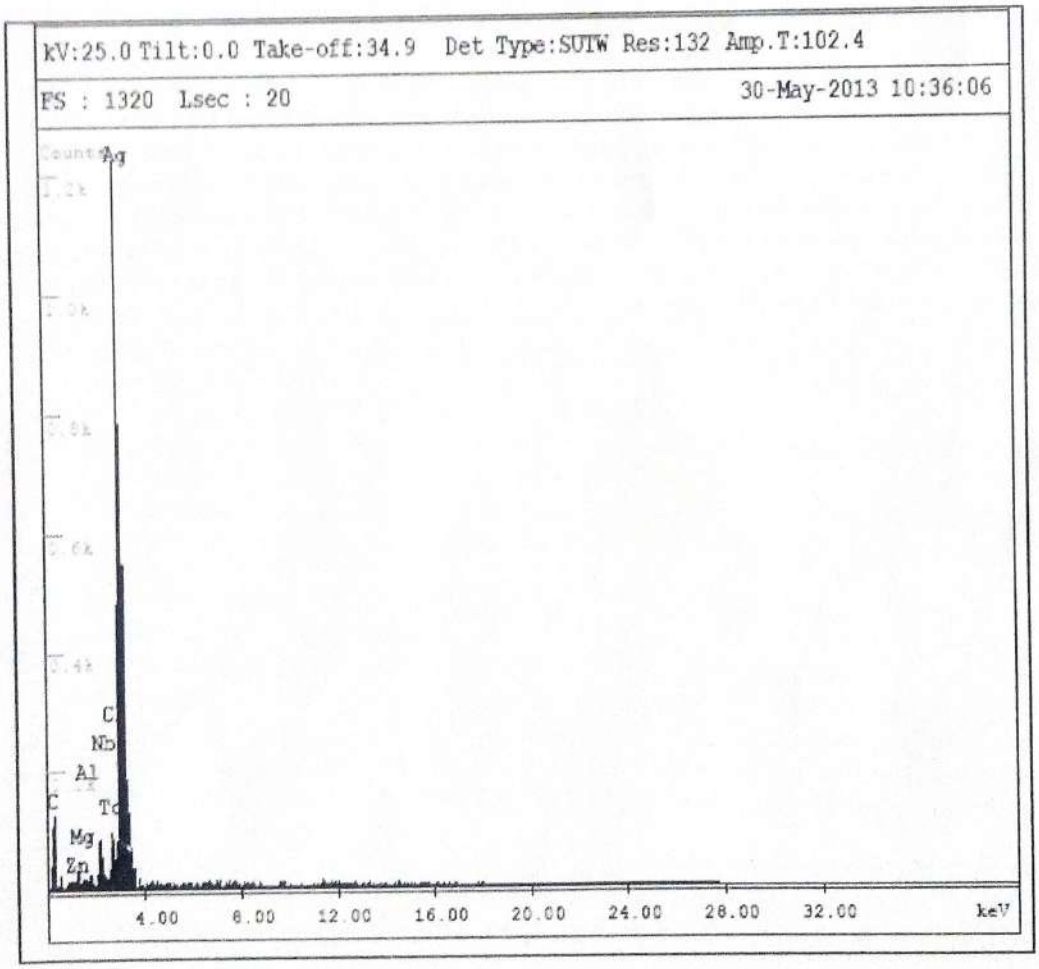
Scanning electron microscope images of the silver nano powder showed spherical morphology without agglomeration (Figure 6), with size distribution of 70 nm similar to that found in AFM.

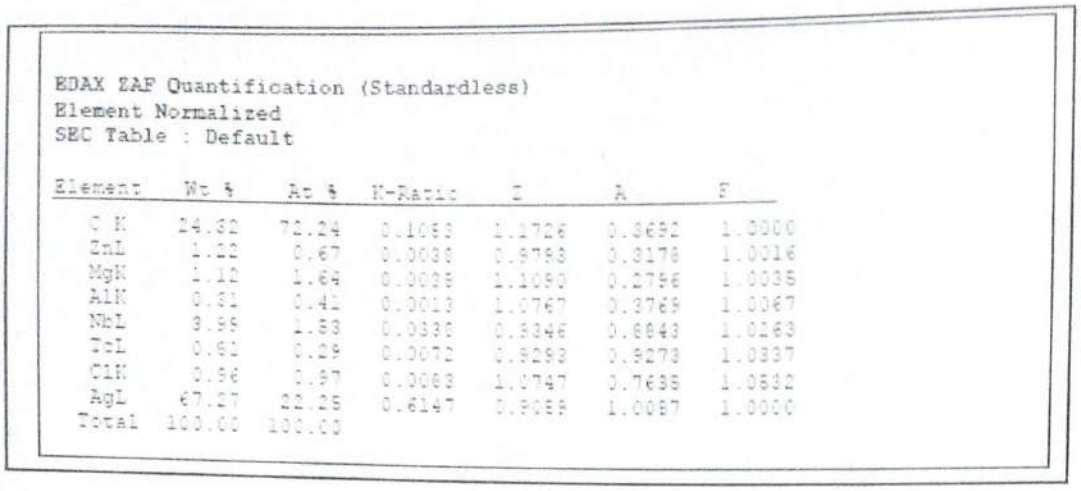


COLLEGE OF ARTS & SCIENCE NAMAKKAL



Figure 6. SEM images of silver nanoparticles synthesized using *Tabebuia rosea* leaf extract at 10 μm and 1 μm magnification.





EDAX ZAF Quantification (Standardless)
Element Normalized
SEC Table : Default

Element	Wt %	At %	K-Ratio	Z	A	F
C K	24.32	72.24	0.1063	1.1726	0.8692	1.0000
ZnL	1.22	0.67	0.0038	0.9798	0.8178	1.0016
MgK	1.12	1.64	0.0028	1.1080	0.2796	1.0035
AlK	0.31	0.41	0.0013	1.0767	0.3769	1.0067
NbL	3.99	1.53	0.0330	0.8346	0.6843	1.0263
TcL	0.81	0.29	0.0072	0.8293	0.9273	1.0337
ClK	0.96	0.97	0.0063	1.0747	0.7685	1.0532
AgL	67.27	22.25	0.6147	0.9089	1.0087	1.0000
Total	100.00	100.00				

Figure 7. EDX images of silver nanoparticles synthesized using *Tabebuia rosea* leaf extract.

The energy dispersive x-ray spectroscopy profile for silver nanoparticles showed strong silver signal (67.27 %) at 3 keV due to surface plasmon resonance[12] along with signals for C, Al, Zn, Mg, Al and Cl (Figure 7) confirming the formation of silver nanoparticles. In this study the AgNP synthesized from plant extracts are stabilized because of the active phytochemicals which act as stabilizing and capping agents which make the particles stable for long time proved by other researchers also[13, 14].

In vitro assessment of biosynthesized AgNPs cytotoxicity

Thus the cytotoxicity study results on normal human fibroblast cells (L929) and human ductal breast carcinoma cells (T47D) are given as percentage of cytotoxicity (Figure 8). The anticancer activity of crude ethanolic extract on normal and cancer studies was compared with nanoparticles prepared from plants. The results proved that when compared to NTR, TR leaf extract displayed cytotoxicity activities lesser. The cytotoxicity values of TR on normal cells were found to be from 12.67 to 30.69 % respectively. Also the cytotoxicity on tumour cells were found to be from 20.98 to 58.34 % respectively (Figure 8). NTR exhibited the highest activity on cancer cells (88.32 to 96.57 %) but it also displayed high toxicity on normal cells (20.43 to 50.68 %) at concentrations of 20 to 100 µg/ml (Figure 8).

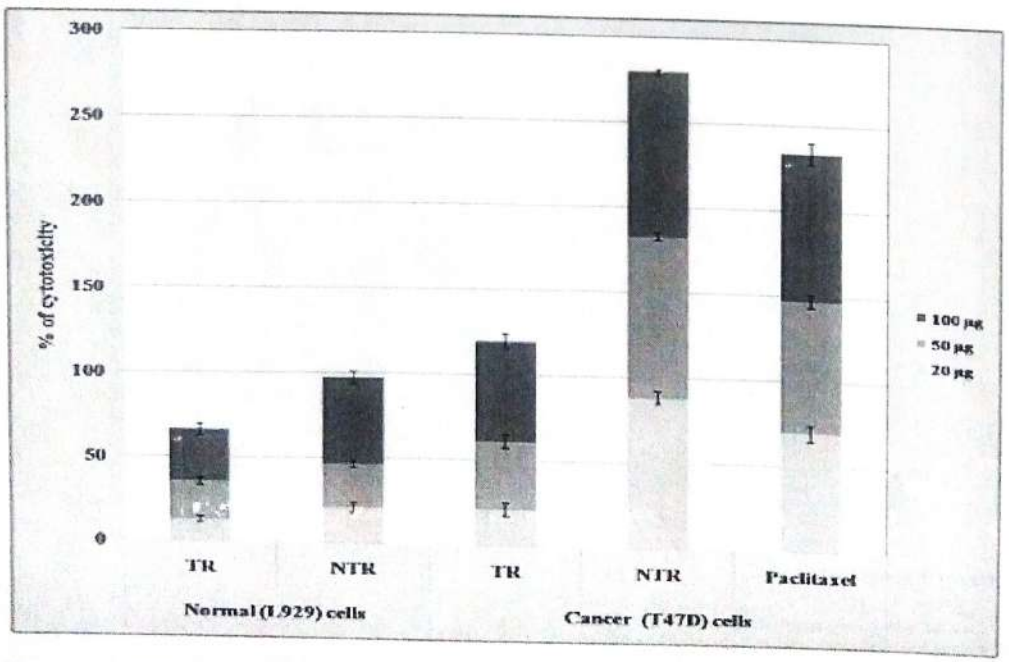


Figure 8. MTT assay results confirming the *in vitro* cytotoxicity effects of TR leaf extracts and AgNPs from TR against the normal L929 cells and cancer T47D cells at 48 h.

Studies on nanodrug from *Mallotus tetracoccus* showed anticancer activity on breast cancer cells, and silver nanoparticles were agglomerated with size of 73 nm[15]. Similar study reports show that these AgNPs are effective at lower concentrations[16]. The reported anti cancer properties of AgNPs whose possible mode of activity has been reported due to oxidative stress, lipid peroxidation, generation of free radicals[17, 18], interrupting ATP synthesis, mitochondrial damage resulting in genotoxicity[19]. The AgNP with DNA finally leads to cell cycle arrest in the G2/M phase[20] also it involves mitochondria-dependent jun-N terminal kinase (JNK) pathway involved in AgNP toxicity leading to cell death[21].

Conclusion

The green synthesis of silver nanoparticles using *Tabebuia rosea* leaf extract was found to be very effective against breast cancer. The optimized synthesis of silver nanoparticles were standardised at pH 7 and temperature 60°C. FTIR analysis of nanoparticle sample indicates the involvement of hydroxyl and carboxyl functional groups of phenols taking part in reduction of silver nitrate to silver nanoparticles. The nanoparticles showed spherical morphology with size range of 49 to 98 nm, also giving strong silver signal for EDX analysis. The AgNPs synthesized from TR leaf showed upto 90 % cytotoxicity at concentrations of less than 20 µg/mL. Thus further investigations (*in vivo* studies) are needed for proving this nanodrug efficiency for applying in cancer therapy.

Acknowledgement

The author Ramalakshmi Subbiah is thankful to University Grants Commission for providing meritorious fellowship (UGC-BSR) (Grant No. F.4-1/2006(BSR)/7-121/2007 (BSR)). The author is also thankful to USIC (University Science Instrumentation Centre), Dr. Suguna Shanmugasundram and Mr. K. Balachander, MKU for FTIR and AFM analysis. The author Ramalakshmi Subbiah acknowledges the Management and Dean of Faculty of Arts, Science and Humanities, Karpagam University for constant support and encouragement.

References

1. Gentry AH. A Synopsis of Bignoniaceae Ethnobotany and Economic Botany, Annuals of Missouri Botanical Garden, 1992, 79: 53-64.
2. Oloyede GK, Oladosu IA, Shodia AF, Oloyade OO. Cytotoxic Effects of *Tabebuia Rosea* Oils (Leaf and Stem Bark). *Archives. App. Sci. Res*., 2010, 2: 127-130.
3. Sathiya M, Muthuchelian K. Studies on Phytochemical Profile and Antibacterial Activity of Ethanolic Leaf Extract of *Tabebuia rosea* (Bertol.) DC. Ethnobotanical Leaflets., 2008,12 :1153-57.
4. Ramalakshmi S, Muthuchelian K. Analysis of bio-active constituents of the ethanolic leaf extract of *Tabebuia rosea* (Bertol.) DC by Gas Chromatography-Mass Spectrometry. *I. J. ChemTech. Res*., 2011, 3: 1054-59.
5. Binutu OA, Lajubutu BA. Antimicrobial potentials of some plant species of the Bignoniaceae family. *Afr. J. Med. Sci.*, 1994, 23: 269-73.
6. Sathiya M, Muthuchelian K. Antitumor Potential of Total Alkaloid Extract from *Tabebuia rosea* (Bertol.) DC. Leaves on MOLT-4 Cells, *In Vitro. Nature and Science.*, 2010, 8: 77-85.
7. Ramalakshmi S, Saravanan S and Muthuchelian K. Radical scavenging activities and cytotoxic studies on different extracts of Tabebuia rosea leaves. A Treatise on Medicinal Plants and Herbal Products published by Virudhunagar Hindu Nadar's Senthilkumara Nadar College. Pg No.143-150, 2013 (ISBN NO. 978-93-81723-18-0).
8. Ramalakshmi S, Muthuchelian K. Phytotoxicity studies on leaf fractions of leaf fractions of *Tabebuia rosea* (Bertol.) DC. Indian journal of science., 2015, 15(48): 189-201.
9. Ramalakshmi S, Muthuchelian K. Studies on cytotoxicity, phytotoxicity and volatile profile of flower extract of *Tabebuia rosea* (Bertol.) DC. *Medicinal plants-I. J. Phytomed. Related Ind*., 2012,4: 154-161.
10. Prabhu S, Poulose EK. Silver nanoparticles: mechanism of antimicrobial action, synthesis, medical applications, and toxicity effects, I. Nano. Letters., 2012, 2:125-132.
11. Chaudhuri SK, Chandela S, Malodia L. Plant Mediated Green Synthesis of Silver Nanoparticles Using *Tecomella undulata* Leaf Extract and Their Characterization. Nano Biomed. Eng., 2016, 8(1): 1-8.

12. Magudapathi P, Gangopadhyay P, Panigrahi EK, Nair KGM, Dhara S. Electrical transport studies of silver nanoparticles embedded in glass matrix, Physica B., 2001, 299: 142–146.
13. Song JY, Kim BS. Rapid biological synthesis of silver nanoparticles using plant leaf extracts, Bioprocess. Biosyst. Eng., 2009, 32: 79–84.
14. Singh M, Kalaivani RC, Anand M, Ramakritinan CM, Kumaraguru AK. Rapid Biomimetic Synthesis Of Silver Nanoparticles From Asiatic Mangrove (*Rhizopora Mucronata*) And Its Antimicrobial Activity Against Clinically Isolated Pathogens. Proceedings of the "International Conference on Nanoscience, Engineering and Technology" (ICONSET 2011), Kalpakkam, 28-30 November, 2011.
15. Ramalakshmi S, Muthuchelian K. Development of nanodrug for treatment of breast cancer using *Mallotus tetracoccus* leaves - standardisation, synthesis and characterization. *Nano Biomedicine engineering.*, 2016, 8(2): 82-90.
16. Das S, Das J, Samadder A, Bhattacharyya SS, Das D, Khuda-Bukhsh AR. Biosynthesized silver nanoparticles by ethanolic extracts of *Phytolacca decandra, Gelsemium sempervirens, Hydrastis canadensis* and *Thuja occidentalis* induce differential cytotoxicity through G2/M arrest in A375 cells. Colloids and Surfaces B: Biointerfaces., 2013, 101: 325– 336.
17. Jeyaraj M, Rajesh M, Arun R, MubarakAli D, Sathishkumar G, Sivanandhan G, Kapil Dev G, Manickavasagam M, Premkumar K, Thajuddin N, Ganapathi A. An investigation on the cytotoxicity and caspase-mediated apoptotic effect of biologically synthesized silver nanoparticles using *Podophyllum hexandrum* on human cervical carcinoma cells. Colloids Surf. B., 2013,102: 708–717.
18. Suliman AO, Ali D, Alarifi S, Harrath AH, Mansour L, Alwasel SH. Evaluation of cytotoxic, oxidative stress, proinflammatory and genotoxic effect of silver nanoparticles in human lung epithelial cells. Environ. Toxicol., 2013, 21:315-335.
19. Foldbjerg R, Dang DA, Autrup H. Cytotoxicity and genotoxicity of silver nanoparticles in the human lung cancer cell line, A549. Arch. Toxicol.,2011, 85: 743–750
20. Asharani PV, Mun GLK, Hande MP, Valiyaveettil S. Cytotoxicity and genotoxicity of silver nanoparticles in human cells. ACS nano., 2009, 3: 279–290.
21. Hsin YH, Chen CF, Huang S, Shih TS, Lai PS, Chueh PJ. The apoptotic effect of nanosilver is mediated by a ROS- and JNK- dependent mechanism involving the mitochondrial pathway in nih3t3 cells. Toxicol. Lett., 2008, 179: 130–139.

*****

PRINCIPAL
PGP College of Arts and Science
Namakkal

P.G.P. COLLEGE OF ARTS & SCIENCE NAMAKKAL 637 203

View publication stats

submitjasc@gmail.com ISSN NO: 1076-5131 IMPACT FACTOR - 5.8 +91 - 7881064362

JASC

JOURNAL OF APPLIED SCIENCE AND COMPUTATIONS

A Peer Reviewed/ Referred Journal

An ISO 7021 : 2008 Certified Journal

SCOPUS SUGGESTED JOURNAL ID: 50E0TF02C8886FF83

SUBMIT ONLINE

NEW ITEM | ABOUT US | FOR AUTHORS | ARCHIVES | EDITORIAL BOARD | PROPOSAL | CONFERENCES | CONTACTS

VOLUME VI - ISSUE IV - APRIL - 2019

Download front cover page

Download Back cover page

1. STUDY ON EFFECT OF MAGNETIC FIELD TREATED WATER ON FRESH AND HARDENED CONCRETE PROPERTIES
Dr.R.Malathy, N.Karuppusamy, U.Vinitha, Sona College of Technology
Page No.1-7
DOI: 10.10039/JASC/2019/V6I4/453459/150010639

2. Factors Influencing Online Shopping Intention: The Role of Perceived Risk
Dr.E.RAMATRABA, Dr.Nanikuppusamy,Arts college Manakkarambal,Thanjavur
Page No.8-14
DOI:10.10039/JASC/2019/V6I4/453460/150010630

3. AN EXPERIMENTAL AND THEORITICAL STUDY OF THE VIBRATIONAL SPECTRA AND STRUCTURE OF ACETOPHENONE
S. Saravanan, G. Kanagaraj, S. Pari, National College (Autonomous), Tiruchirappalli
R. Sambasivam, Ummu Dhanalakshmi College, Trichy
Page No.757-764
DOI: 10.10039/JASC/2019/V6I4/453458/150010720

4. Experimental and Theoretical Investigation of FTIR and FT-RAMAN HOMO-LUMO and Mulliken atomic charge of 2, 5- Dimethoxy acetophenone
R. Sambasivam, Ummu Dhanalakshmi College, Trichy
S. Saravanan, G. Satheesh Kumar, S. Pari, National College (Autonomous), Tiruchirappalli
Page No.765-773
DOI:10.10039/JASC/2019/V6I4/453457/150010721

5. NEED AND NECESSITY FOR WIND ENERGY LEGISLATION — AN INDIAN VIEW POINT
Prof. (Dr.) Dipesh M. Patel, Parmar Mehul, Parmar Harshad, Parmar Shakti, Gohil Brijraj, Ipcowala Institute of Engineering and Technology, Dharmaj, Anand, Gujarat
Page No.774-779
DOI:10.10039/JASC/2019/V6I4/453455/150010722

6. **Antimicrobial and Anticancer studies of pure and Cassia auriculata doped Brushite and Struvite crystals**
S. Ramalakshmi, Sri Meenambigai Arts and Science for Women, Palacode, Dharmapuri, Tamilnadu
G. Arulsilva, R. Mahesh and T.H. Freeda, S.T. Hindu College, Nagercoil, Tamilnadu
Page No.795-788
DOI:10.10039/JASC/2019/V6I4/453456/150010723

7. A review of Advance Metering Infrastructer (AMI) for Smart Grid In India
Atmiya Patel, Dr. Jinraj Mehta Institute of Technology, Mogar, Anand, Gujarat
Page No.780-794
DOI:10.10039/JASC/2019/V6I4/453458/150010724

8. A Maintenance Model for a Deteriorating System with Imperfect Delayed Repair under Partial Product Process
Babu. D, Thantha Periyar Government Institute of Technology, Vellore
Govindaraju. P and Rizwan. U, Islamiah College, Vaniyambadi
Page No.789-801
DOI:10.10039/JASC/2019/V6I4/453452/150010725

9. The Behaviour of longitudinal roughness in hydrostatic circular footstep bearing
P. I. Anchana, Hardik Pandya, Maharaja Krishnakumarsinhji Bhavnagar University, Bhavnagar
Page No.802-811
DOI:10.10039/JASC/2019/V6I4/453454/150010726

P.G.P. COLLEGE OF ARTS & SCIENCE NAMAKKAL 637 206

Antimicrobial and Anticancer studies of pure and *Cassia auriculata* doped Brushite and Struvite crystals

S. Ramalakshmi[a], G. Anushya[b], R. Mahesh[c] and T.H. Freeda[b]

Department of Microbiology, Sri Moogambigai Arts and Science College for Women, Palacode, Dharmapuri-636805, Tamilnadu, India
[b]Physics Research Centre, S.T. Hindu College, Nagercoil – 629002, Tamilnadu, India
[c]PG & Research Department of Botany, S.T. Hindu College, Nagercoil – 629002, Tamilnadu, India
(Affiliated to Manonmaniam Sundaranar University, Abishekapatti, Tirunelveli- 627012, Tamilnadu, India)

Email: arulaksh24@gmail.com

Abstract

Brushite and struvite crystals at pure and doped forms were studied for antibacterial activity against pathogens and anticancer activities on normal human and kidney cancer cell lines. The study results reveals that the sample Glucored forte added brushite and struvite have better antimicrobial activities against *E.coli* and *P. aeruginosa*. The anti-cancer effects of undoped and 50 mg *Cassia auriculata* doped brushite and struvite are analyzed and the results showed that *Cassia auriculata* doped samples have effect on cancer cells than normal cells at high concentrations.

Keywords: **Brushite, Struvite, *Cassia auriculata*, Antibacterial, Anticancer.**

INTRODUCTION

Calcium hydrogen phosphate dihydrate (CHPD, $CaHPO_4.2H_2O$) also known as brushite mineral. It also is the precursor to form apatite, a bone forming mineral. Calculi or kidney stone formation, occurs dominantly in men due to deposits of calcium oxalate or phosphate (apatite or brushite) [1]. Calcium phosphate has been reported to be causative in 15% of the stone forming population. Brushite formation occurs due to various medical disease conditions in body and is reported to cause mortality during earlier times. Kidney stones are formed due to deposits of calcium phosphate minerals within the kidneys, renal tubules and/or interstitium. Initially crystal nucleation, growth and aggregation occurs and secondarily nidus forms by precipitation and develops as stones.

The next important mineral constituent involved in kidney stone is ammonium magnesium phosphate hexahydrate known as struvite. Other medical names for struvite are 'urine sand', 'triple phosphate stone', 'phosphatic stone', 'infection stone', or 'urease stone', occurs when infected by urease-producing microorganisms. Struvite forms calculi only in 30 % humans and upto 75 % in dogs and cats [2].

It predominantly affects women and children. Struvite stones grows as 'staghorn-calculi' leading to more painful urological disorder causes serious disease and when untreated lead to kidney removal [3]. The formation of the struvite calculi requires microbial infection and NH_4^+, $PO4^{3-}$and Mg^{2+}ions in the urine and alkaline pH.

Cassia auriculata Linn, of family Caesalpiniaceae also commonly called as avaram. The flowers are bright yellow, and used in the treatment of diabetes to control the blood sugar level. The phytochemical constituents of avaram flowers showed occurrence of terpenoids, tannin, flavonoids, saponin, cardiac glycosides and steroids. The plant has been reported for several activities such as antipyretic, hepatoprotective, anti-peroxidative, anti-hyperglycemic and antimicrobial [4-5]. The flowers are widely used for urinary discharges, nocturnal emissions, diabetes and throat irritation [6]. This study was aimed at understanding the potential of antibacterial effects of pure and anti-diabetic drug doped brushite and struvite crystals. Also pure and ***Cassia auriculata*** doped brushite and struvite crystals has been analyzed for anti-cancer effects.

MATERIALS AND METHODS

A. Antimicrobial studies

The microorganisms ***Staphylococcus aureus*** (ATCC 25923), ***Pseudomonas aeruginosa*** (MTCC 2453) and ***Escherichia coli*** (MTCC 443) was studied against samples B (Undoped CHPD), B_1 (50 mg Cetapin XR added CHPD), B_2 (50 mg Glucored forte added CHPD), B_3 (50 mg Glycomet added CHPD) and S (Undoped MAPH), S_1 (50 mg Cetapin XR added MAPH), S_2 (50 mg Glucored forte added CHPD), S_3 (50 mg Glycomet added CHPD) to monitor the effect of grown crystals in inhibiting the growth of microorganisms.

The test organisms was sub cultured in Luria-Bertani medium grown aerobically overnight at 37 °C. *In vitro* antibacterial activity of study samples was studied by disc diffusion method in Mueller-Hinton agar media. Samples at concentrations of 5, 10, 15, 20 *µg/ml* was taken and $1X10^8$ CFU/ml of microorganisms was used for study. 20µl of DMSO was used as control for all the experiments.

B. Anti-cancer studies

Study samples

The pure brushite and struvite samples are denoted as B; S and 50 mg of ***Cassia auriculata*** flower extracts doped brushite and struvite samples are denoted as B_1 and S_1 respectively. The concentrations taken for all samples was 10-50 mg/ml.

P.G.P. COLLEGE OF ARTS & SCIENCE NAMAKKAL 637 206

Cell cultures

The Human Embryonic Kidney cells (HEK) cells and Human lung carcinoma cells (A-549) are procured from the National Center for Cell Sciences (NCCS), Pune, India and maintained in Minimals Essential medium (MEM) supplemented with 2mM l-glutamine and balanced salt solution (BSS) adjusted to contain 1.5 g/L Na_2CO_3, 0.1 mM nonessential amino acids, 1 mM sodium pyruvate, 2 mM l-glutamine, 1.5 g/L glucose, 10 mM (4-(2-hydroxyethyl)-1-piperazineethane sulfonic acid) (HEPES) and 10% fetal bovine serum (GIBCO, USA). Penicillin and streptomycin (100 IU/100µg) are used at 1mL/L. The cell lines are maintained at 37°C with 5% CO_2 in a humidified CO_2 incubator.

MTT assay

The inhibitory concentration (IC_{50}) value was evaluated using an MTT [3-(4,5- dimethylthiazol-2-yl)-2,5-diphenyltetrazolium bromide] assay. Cells are grown (1×10^4 cells/well) in a 96-well plate for 48 h in to 75% confluence. The medium is replaced with fresh medium containing serially diluted (10-100µg/ml) compounds, and the cells further incubated for 48 h. The culture medium is removed, and 100µL of the MTT [3-(4,5-dimethylthiozol-2-yl)-3,5-diphenyl tetrazolium bromide] (Hi-Media) solution was added to each well and incubated at 37 °C for 4 h. After removal of the supernatant, 50 µL of DMSO is added to each of the wells and incubated for 10 min to solubilize the formazan crystals. The optical density is measured at 620 nm in an ELISA multiwell plate reader (Thermo Multiskan EX, USA). The OD value is used to calculate the percentage of viability using the following formula.

OD value of experimental sample

$$\% \text{ of viability} = \frac{\text{OD value of experimental sample}}{\text{OD value of experimental control}} \times 100$$

Statistics:

All the *in vitro* experiments were done in triplicate, and the experiments were repeated at least thrice. The statistical software SPSS version 17.0 was used for the analysis. *P* value <0.01 was considered significant.



RESULTS AND DISCUSSION

A. Antimicrobial Studies

The inhibitory zone formation is shown in Figures 1 & 2

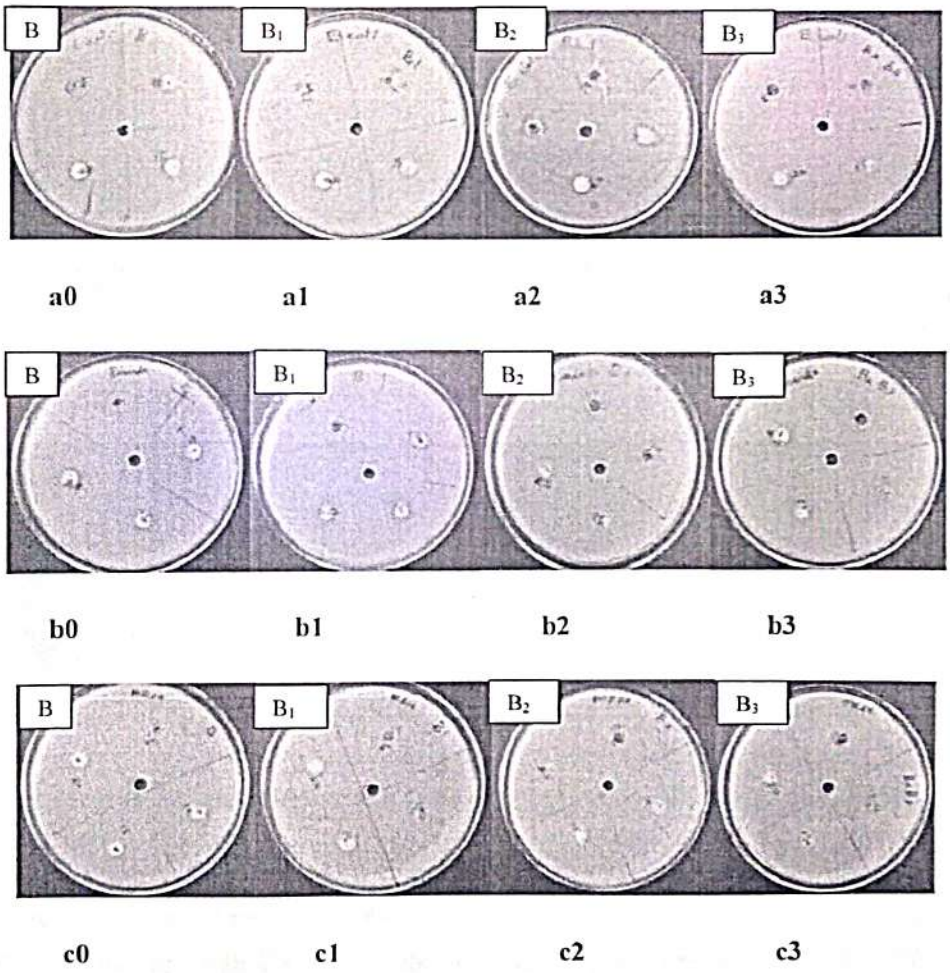


Fig 1: **Zone inhibition of samples B, B_1, B_2, B_3 against microorganisms, *Escherichia coli* (a0-a3), *Pseudomonas aeruginosa* (b0-b3) *and Staphylococcus aureus* (c0-c3).**

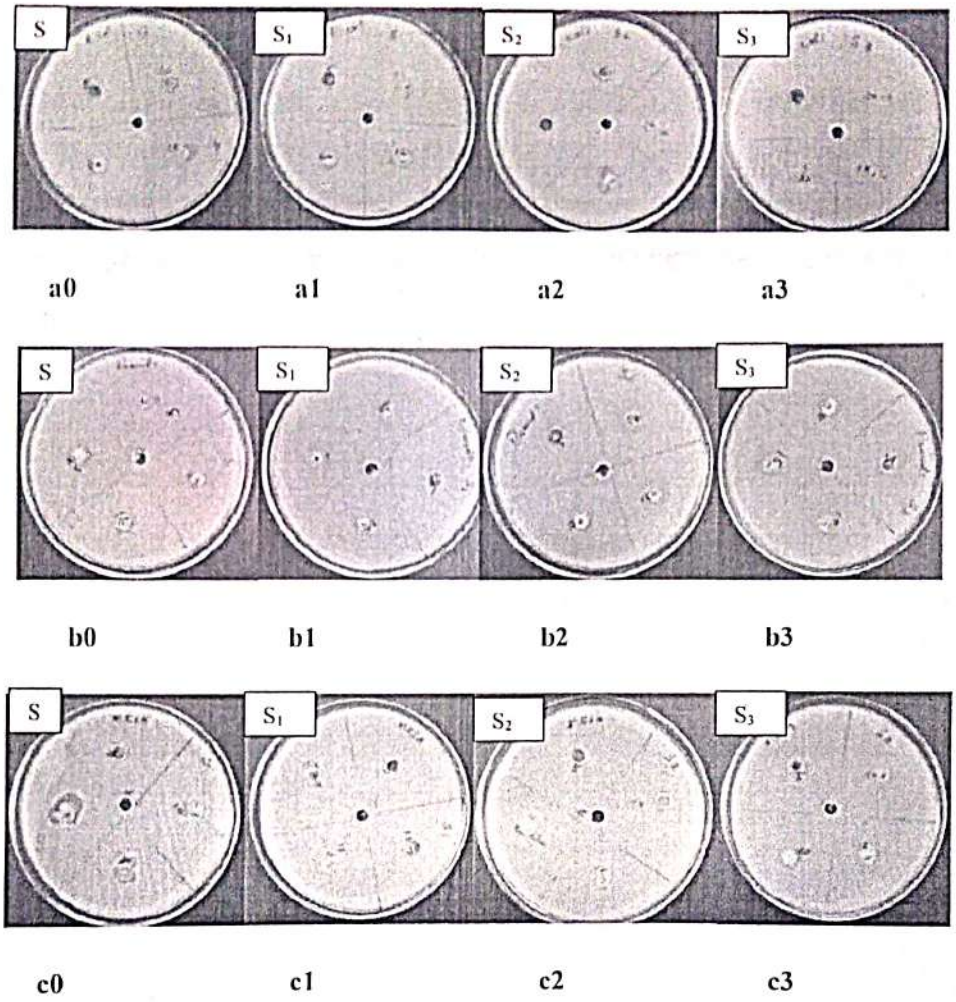


Fig 2: **Zone inhibition of samples S, S_1, S_2, S_3 against microorganisms, *Escherichia coli* (a0-a3), *Pseudomonas aeruginosa* (b0-b3) and *Staphylococcus aureus* (c0-c3).**

The samples B, B_1 and B_3 have no activity against ***E.coli*** at different test concentrations. Whereas the sample B_2 shows moderate activities at all concentrations studied. Similarly the samples S, S_1 and S_3 have no activity against ***E.coli*** but S_2 at 5-20 µg/ml show better results.

The samples B, B_1, B_2, B_3, S and S_1 show no activity against ***P. aeruginosa*** at test concentrations. The samples S_2 and S_3 reveal significant activities on ***P. aeruginosa*** at test concentrations of 5-20 µg/ml. Thus with increasing concentrations, increasing antimicrobial activity is observed.

COLLEGE OF ARTS & SCIENCE NAMAKKAL 637 208

All the samples show no antimicrobial response against test pathogen ***S.aureus*** studied at different concentrations. Calcium Hydrogen Phosphate Dihydrate (brushite) has been the precursor of apatite, a bone forming mineral. Thus the Calcium phosphate bone cements (CPCs) possessing antibacterial properties are of high requirement for clinical applications.

Similarly Biphasic calcium phosphate powders with partial substitutions of Ca^{2+} by silver, copper, zinc and strontium ions were synthesized and silver-doped powders exhibited significant activity against ***S. aureus*** [7]. The paraben nanoparticles at 1 % concentration embedded in brushite as bone cement showed better antimicrobial activity against postorthopedic surgery infections than other materials [8]. Silver-doped CPCs (CPCs-Ag) with high silver had inhibitory action on ***E.coli*** [9]. In contrast, the Studies on Fe-doped brushite bone cements have better antimicrobial activities on ***S. aureus*** and ***P. aeruginosa*** and had no activity on ***E.coli*** [11]. Nisin F-loaded self-setting brushite cement has been reported to control the growth of ***Staphylococcus aureus*** *in vivo* [10]

B. Anti-cancer studies

We studied the anticancer activity of undoped CHPD (Brushite), Undoped MAPH (Struvite) and 50 mg of ***Cassia auriculata*** doped CHPD and MAPH samples separately. The cytotoxicity study results on normal embryonic kidney cells (HEK) cells and human lung carcinoma cells (A-549) are presented in figures 3 & 4. Thus the results show that undoped form of both CHPD and MAPH possessed lethal effect on normal embryonic kidney cell lines and on cancer cells. The cytotoxicity IC_{50} values recorded are of 22 and 33 (µg/ml) respectively. At concentrations of 10-50 mg/ml of CHPD, the cell viability reduced gradually and 20 % recorded at 50 µg/ml. The undoped MAPH have high lethality on normal cells than cancer cells. The cytotoxicity IC_{50} values of ***Cassia auriculata*** doped CHPD and MAPH on normal cells are found to be 17 and 23 µg/ml respectively. Also IC_{50} values of ***Cassia auriculata*** doped CHPD and MAPH on lung cancer cells are found to be 24 and 13 µg/ml respectively. At increasing concentrations of ***Cassia auriculata*** doped CHPD, 80 % cell viability is found showing no lethal effects, whereas on kidney cancer cells, there is only 20 % cell viability. Similar results have been recorded for ***Cassia auriculata*** doped MAPH samples also, where increasing concentrations have effect on cancer cells rather than normal cells.

P.G.P. COLLEGE OF ARTS & SCIENCE NAMAKKAL 637 206

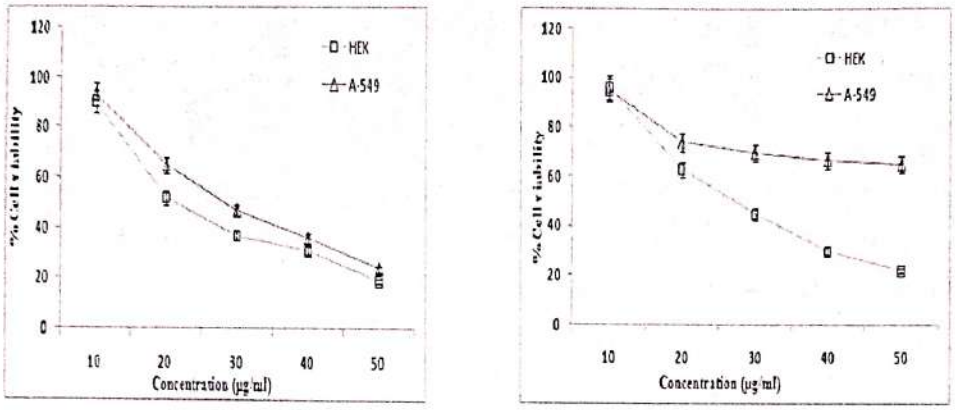


Fig 3: Cytotoxicity of (a) undoped CHPD (b) undoped MAPH crystals

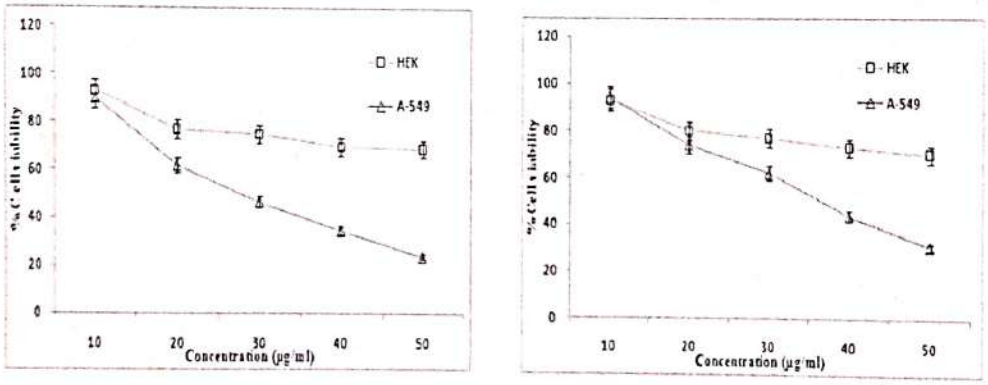


Fig 4: Cytotoxicity of (a) 50 mg *Cassia auriculata* doped CHPD (b) 50 mg *Cassia auriculata* doped MAPH crystals

There are reports on ***Cassia auriculata*** plant extracts studied for various biological activities. Prasanna et al. [12] has reported the anticancer activity of ***Cassia auriculata*** leaf extract on breast and larynx cancer cells by decreasing expression of anti-apoptotic Bcl-2 protein, increased expression of pro-apoptotic Bax protein thereby inducing apoptosis. Ahmed et al. [14] has reported the antiurolithiatic activity of ***Cassia auriculata*** among various other plants used. But to our knowledge there are no reports on the anticancer activity of brushite and struvite doped with ***Cassia auriculata*** plant extracts.

There are recent reports on the usage of brushite and struvite for various biomedical applications. Uskokovic et al. [13] has reported the combined antibacterial, osteoinductive and anticancer properties on K7M2 osteosarcoma cells of selenite-incorporated hydroxyapatite. Brushite containing 0.67 wt% of selenium (Se-Bru) has been reported for potential use in bone tissue impairments treatment [15].

CONCLUSION

Thus the innovative antimicrobial Glucored forte added CHPD crystals and Glucored forte added MAPH crystals have the ability to prevent calculi formation in urinary bladder, tubules and kidneys, as it possesses activity against ***E.coli*** and no activity on ***S.aureus***. Further *in-vivo* and *in-vitro* anti-urolithic studies are required to develop formulations in near future to cure against kidney stones.

The cytotoxicity of brushite and struvite doped with 50 mg ***Cassia auriculata*** studies on kidney cancer cells show that they have high toxicity at lower concentrations, which are attributed to the presence of bioactive compounds present in the extract. Also the purest compounds of brushite and struvite have lethal effects on normal cells. Thus this study gives an insight into the biomaterial which can be used for biomedical applications.

REFERENCES

[1] Reilly, RF 2005, Chapter 13: Nephrolithiasis. In: Reilly Jr. and Perazella, pp. 192-207.

[2] Meng, M, Stoller, ML & Minor, T 2011, Struvite and staghorn calculi, Website of e-medicine by WebMD /http://emedicine.medscape.com/article/439127S- overview [1 June 2011].

[3] Rao ,KN and Vedavathy, S 1996, 'Antipyretic activity of six indigenous medicinal plants of Tirumala Hills, Andhra Pradesh, India', Journal of Ethnopharmacology, vol. 33, no. 1-2, pp. 193-196.

[4] Pari, L & Latha, M 2003, 'Preventive effects of *Cassia auriculata L.* flowers on brain lipid peroxidation in rats treated with streptozotocin', Molecular and Cellular Biochemistry, vol. 243, no. 1-2, pp. 23-28.

[5] Sharada, N 2012, 'Salubrious effect of ethanolic extract of *cassia auriculata* leaves *Linn* in streptozotocin - nicotanimide induced diabetes in rat model', Asian Journal of Pharmacy and Technology, vol. 2, no. 3, pp. 104-106.

[6] Wojewski, A & Zajaczkowski, T 1974, 'The treatment of bilateral staghorn calculi of the kidneys', International Urology and Nephrology, vol. 5, no. 3, pp. 249-260.

P.G.P. COLLEGE OF ARTS & SCIENCE NAMAKKAL 637 206

[7] Marques CF, Olhero, S, Abrantes, JCC, Marote, A, Ferreira, S, Vieira, SI, Ferreira, JMF 2017, 'Biocompatibility and antimicrobial activity of biphasic calcium phosphate powders doped with metal ions for regenerative medicine', Ceramics International, vol. 43, no. 17, pp. 15719-15728.

[8] Perni, S, Thenault, V, Abdo, P, Margulis K, Magdassi, S & Prokopovich P 2015, 'Antimicrobial activity of bone cements embedded with organic nanoparticles', International Journal of Nanomedicine, vol. 10, pp. 6317–6329.

[9] Rau , JV, Fosca, M, Graziani, V, Egorov, AA, Zobkov, Yu,V, Fedotov, Yu, A, Ortenzi, M, Caminiti, R, Baranchikov , AE & Komlev, VS 2016, 'Silver-Doped Calcium Phosphate Bone Cements with Antibacterial Properties', Journal of Functional Biomaterials, vol. 7, no. 2, pp. 10.

[10] Staden, ADV, Brand, AM & Dicks, LMT 2012, 'Nisin F-loaded brushite bone cement prevented the growth of Staphylococcus aureus in vivo', Journal of Applied Microbiology, vol. 112, no. 4, pp. 831–840

[11] Li G, Zhang, N, Zhao, S, Zhang, K, Li, X, Jing, A, Liu, X & Zhang, T 2018, 'Fe-doped brushite bone cements with antibacterial property', Materials Letters, vol. 215, pp. 27-30.

[12] Prasanna, R, Harish, CC, Pichai, R, Sakthisekaran, D & Gunasekaran, P 2009, 'Anti-cancer effect of Cassia auriculata leaf extract in vitro through cell cycle arrest and induction of apoptosis in human breast and larynx cancer cell lines', Cell Biology International, vol. 33, no. 2, pp. 127-134.

[13] Uskoković, V, Iyer, MA & Wu VM 2017, 'One ion to rule them all: the combined antibacterial, osteoinductive and anticancer properties of selenite-incorporated hydroxyapatite', Journal of Materials Chemistry B, vol.5, no. 7, pp. 1430-1445.

[14] Ahmed, S, Hasan, M & Mahmood, Z 2016, 'Antiurolithiatic plants in different countries and cultures', Journal of Pharmacognosy and Phytochemistry, vol. 5, no. 1, pp.102-115.

[15] Laskus, A, Zgadzaj, A & Kolmas, J 2018, 'Selenium-Enriched Brushite: A Novel Biomaterial for Potential Use in Bone Tissue Engineering', International Journal of Molecular Sciences, vol. 19, no. 12, pp. pp. 4042.

P.G.P. COLLEGE OF ARTS & SCIENCE NAMAKKAL 637 001

PRINCIPAL
PGP College of Arts and Science
Namakkal

Not secure | https://link.springer.com/article/10.1007/s00253-015-7233-3

Advertisement

Springer Link

Search Log in

Mini-Review | Published: 23 December 2015

Exploration of industrially important pigments from soil fungi

P. Abilangeswari & E. V. Pradeep

Applied Microbiology and Biotechnology 100, 1631–1643 (2016) | Cite this article

2029 Accesses | 47 Citations | Metrics

Abstract

The worldwide interest of the current era is to increase tendency towards the use of natural substances instead of synthetic ones. So, alternative and effective environment friendly sustainable technologies are highly needed. Due to a broad range of biological activities, fungi are considered as a significant source of pigments. Among the fungal species in the soil, the genera of *Aspergillus*, *Fusarium*, *Penicillium*, *Paecilomyces*, and *Trichoderma* are dominant. [illegible] ng to aromatic polyketide groups such as

establishing secure connection...

Access via your institution →

Access options

Buy article PDF

39,95 €

Price includes VAT (India)

Instant access to the full article PDF.

Learn more about institutional subscriptions

Sections Figures References

P.G.P. COLLEGE OF ARTS & SCIENCE NAMAKKAL 637 206

Exploration of industrially important pigments from soil fungi

P. Akilandeswari & B. V. Pradeep

Applied Microbiology and Biotechnology

ISSN 0175-7598
Volume 100
Number 4

Appl Microbiol Biotechnol (2016)
100:1631-1643
DOI 10.1007/s00253-015-7231-8



COLLEGE OF ARTS & SCIENCE
NAMAKKAL
P.G.P.

Springer

Your article is protected by copyright and all rights are held exclusively by Springer-Verlag Berlin Heidelberg. This e-offprint is for personal use only and shall not be self-archived in electronic repositories. If you wish to self-archive your article, please use the accepted manuscript version for posting on your own website. You may further deposit the accepted manuscript version in any repository, provided it is only made publicly available 12 months after official publication or later and provided acknowledgement is given to the original source of publication and a link is inserted to the published article on Springer's website. The link must be accompanied by the following text: "The final publication is available at link.springer.com".



Springer

Appl Microbiol Biotechnol (2016) 100:1531–1542
DOI 10.1007/s00253-015-7231-9

MINI-REVIEW

Exploration of industrially important pigments from soil fungi

P. Akilandeswari[1] · B. V. Pradeep[1]

Received: 18 September 2015 / Revised: 30 November 2015 / Accepted: 2 December 2015 / Published online: 23 December 2015
© Springer-Verlag Berlin Heidelberg 2015

Abstract The worldwide interest of the current era is to increase tendency towards the use of natural substances instead of synthetic ones. So, alternative and effective environment friendly sustainable technologies are highly needed. Due to a broad range of biological activities, fungi are considered as a significant source of pigments. Among the fungal species in the soil, the genera of *Aspergillus*, *Fusarium*, *Penicillium*, *Paecilomyces*, and *Trichoderma* are dominant. The pigments commonly produced by fungi belong to aromatic polyketide groups such as melanins, quinones, flavins, ankaflavin, anthraquinone, and naphthoquinone. The use of fungal pigments has benefits which comprise easy and fast growth in the cheap culture medium and different color shades being independent of weather conditions and would be useful in various industrial applications. In relation to the toxic effects of the synthetic dyes, the natural dyes are easily degradable since they cause no detrimental effects. Thus, the study of pigments produced by soil fungi has tremendous use in medical, textile coloring, food coloring, and cosmetics.

Keywords Fungi · Pigments · Fermentation · Industrial application · Eco-friendly

Introduction

Due to negative assessment with several artificial synthetic colorants, developmental process for the production of pigments from natural sources has become significant worldwide. These products have been extensively used in foodstuff, cosmetics, pharmaceutical, and textile manufacturing processes. The natural dyes have been used for various purposes as coloring agents. Over the centuries, many active metabolites were discovered from diverse natural sources such as higher plants, animals, insects, and microorganisms. Among these sources, the microorganisms are most likely the group that generates metabolites possessing the most ready industrial applications as they are chemo-organotrophic, presenting a high growing rate on a short cycle of life and producing large amounts of biomass in a short time (Dufosse 2006). As a lot of synthetic dyestuffs have been found to be hazardous to human health, only limited kinds of such dyestuffs are acceptable to be used in food in many countries, and hence, there is a need to develop alternative sources (Lee et al. 2001). Thus, there is a strong interest in natural pigments produced from microbial source and that would be a good alternative one compared to other available synthetic dyes (Sasidharan et al. 2013).

Soil fungi are a wide range of organisms that may be actively freely growing, closely associated with other organisms. The quality as well as quantity of organic matter in the soil has a direct correlation to the growth of fungi, because most fungi consume organic matter for nutrition. Fungi thrive in acidic environments. Soil fungi are metabolically very active and are able to produce many substances of economic value such as secondary metabolites and pigments. Among the fungal species in the soil, the genera of *Aspergillus*, *Fusarium*, *Penicillium*, *Paecilomyces*, and *Trichoderma* are dominant (Celestino et al. 2014). Organisms capable of synthesizing pigments are plants, animals, bacteria, fungi, and algae. Among these, fungi are reported to produce large amounts of pigments (Mortensen 2006; Kirti et al. 2014). Fungi produce numerous extracellular enzymes and secondary

✉ B. V. Pradeep
bvpradeepku@gmail.com

Department of Microbiology, Karpagam Academy of Higher Education, Coimbatore 641 021, Tamil Nadu, India

PG & RESEARCH DEPT. OF BOTANY GOVT. ARTS COLLEGE NAMAKKAL 637 001

metabolites, including organic acids, pigments, and other food additives. Nevertheless, they are more associated with their pharmacological properties, such as antibiotics and immunosuppressant, than to their nutritional value (Takahashi and Carvalho 2010). Fungi are significant source of pigments, since some fungal species are rich in stable colorants (Nagia and EL-Mohamedy 2007). The use of filamentous fungi cultured on different agro-industrial by-products have been proved to be an alternative to obtain pigments (Lopes et al. 2013). The pigments commonly produced by fungi belong to aromatic polyketide groups such as melanins, quinones (Dufosse et al. 2005; Caro et al. 2012), flavins, ankaflavin, anthraquinone, and naphthoquinone (Dufosse 2006). Due to a broad range of biological activities of pharmaceutical properties, fungi are considered to have intense benefit to humankind (Zhang et al. 2004). The use of microbial pigments have benefits which comprise easy and fast growth in the cheap culture medium, different color shades being independent of weather conditions, and useful in various industrial applications (Venil and Lakshmanaperumalsamy 2009). Owing to the increase in price of the raw material, pollution, complexity of the synthetic material, and its products, natural substances are becoming important. The natural colorant has antimicrobial activity and is less allergenic and more stable in use instead of the synthetic ones (Mehrabian et al. 2000). Consequently, the synthetic dyes are hazardous to the environment and they must be replaced by eco-friendly natural dyes (Sewekow 1988; Velmurugan et al. 2010a).

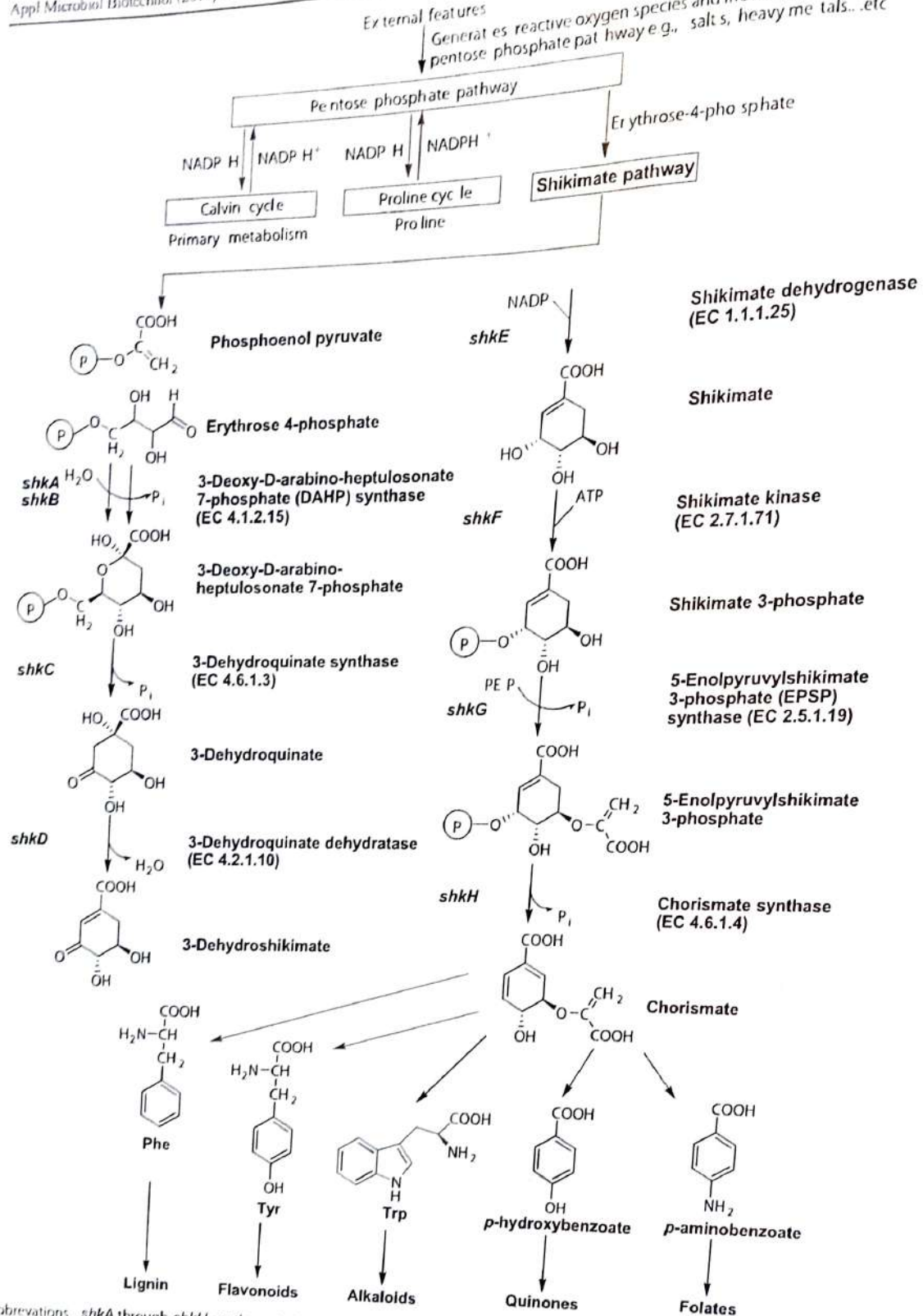
Pigments

The microorganisms producing pigments must satisfy several criteria such as capability to use a wide range of carbon and nitrogen sources, tolerance to pH, temperature, mineral concentration, possession of being moderate growth conditions, reasonable color yield, non-toxic, non-pathogenic, and easily separable from the cell mass (Babitha et al. 2009). In addition, these organisms can grow in different culture systems (submerged and solid) and can be genetically modified to increase productivity and quality of the produced pigments (Espinoza-Hernandez et al. 2013). Microbial pigment is the term used to refer to the microbial cells that produce color (Joshi et al. 2003). Pigments come in a wide range of colors, and certain bio-pigments like anthocyanin are water soluble (Chattopadhyay et al. 2008). As natural dyes derived from dried raw material have disadvantages towards extraction yield factors, the use of biological sources such as fungi, bacteria, algae, and plant cell cultures are used as natural pigment (Santis et al. 2005). Due to ever rising demand by the consumers, the use of natural colorants obtained from fungal pigment has replaced the use of synthetic dyes in food applications (Dufosse 2014). Moreover, toxicological test confirms that the pigment extracted from fungi could be an alternative source of natural dye (Velmurugan et al. 2010b). The utilization of natural pigments in foodstuff, cosmetic, and pharmaceutical manufacturing processes has been increasing in recent years. This is due to the concern about the toxicity problems caused by synthetic compounds and their industrial by-products on human beings and the environment (Boonyapranai et al. 2008). The effect of light in extracellular and intracellular pigment and biomass production was effective when incubated in total darkness (Velmurugan et al. 2010c).

Metabolic pathway of pigment biosynthesis by shikimate pathway

Fungal metabolites have been divided into primary, which are metabolites essential for growth and reproduction and secondary, which comprise of important metabolites not essential to cellular life. But, this difference is arbitrary when applied to metabolic pathways rather than their products (Keller et al. 2005). Many of the pigments of fungi are quinones or similar conjugated structures that are mostly classified according to the perceived biosynthetic pathway which reflect their structure to pigments derived from the shikimate (chorismate) pathway (Fig. 1). The shikimate pathway is a seven-step metabolic route used by fungi for the biosynthesis of amino acids such as phenylalanine, tyrosine, and tryptophan. Seven enzymes are involved in this pathway, and the gene *shk* has been selected to avoid potential conflicts with genes encoding enzymes of nonchorismate-derived aromatic biosynthesis. In the first step, the glycolytic intermediate phosphoenol pyruvate and pentose phosphate pathway intermediate erythrose-4-phosphate are condensed to a seven-carbon-six membered heterocyclic compound, 3-deoxy-D-arabinose-heptulosonate-7-phosphate derivative (DAHP). In the second step, the ring oxygen is exchanged for the exocyclic C7 of DAHP to form a highly substituted cyclohexane derivative, 3-dehydroquinate. The remaining five steps serve to introduce a side chain and two of the three double bonds that convert this cyclohexane into the benzene ring, the property of aromatic amino acids. Chorismate which is the final product of shikimate pathway is a substrate for a number of secondary compounds. Thus, the amino acids are precursors for a wide range of compounds that represent the building blocks for many pigments of fungi (Herrmann 1995; Velisek and Cejpek 2011). The metabolic routes differ for different classes of pigments. Example, in *Monascus* pigment, octanoic acid and hexanoic acid are the precursors of the azaphilone compound. These fatty acids are formed by a separate polyketide synthase. The orange pigments, monascorubrin, and rubropuntatin are synthesized on the cytosol from acetyl coenzyme A. These pigments have a structure responsible by their high affinity to compounds containing primary amino groups. Reaction with amino acids lead to formations of

P.G.P. COLLEGE OF ARTS & SCIENCE NAMAKKAL 637 206



The abbrevations *shkA* through *shkH* are the notations proposed for the wild-type genes encoding shikimate pathway enzymes.

Fig. 1 Metabolic pathway of pigment biosynthesis by shikimate pathway (Herrmann 1995; Scholes and Paige 2015)

P.G.P. COLLEGE OF ARTS & SCIENCE NAMAKKAL 637 206

hydro soluble red pigments, monascorubramine, and rubropunctamine. The mechanism of yellow pigment formations is not clear; some authors consider that these are products of the alteration of orange pigments, while others believe it to be pigments with their own metabolic pathway (Lin and Demain 1991; Juzlova and Martinkova 1996).

Fungal pigments

Fungal pigments are secondary metabolites since these pigments are commercially used and made possible in the same way as antibiotics are mass produced from fungi by deep-tank fermentation. The color productions by this fungal source under controlled experimentation on a mass scale basis using a wide variety of substrates are eco-friendly (Sudha et al. 2014). Likewise, the ascomycetes fungi showed potential in the extraordinary color range of pigments in the red and yellow spectra using quantitative colorimetry and these fungal pigments are comparable to the existing natural food colorants which serve as a new source in food coloring (Mapari et al. 2006). A number of different species of fungi from soil niche producing natural colorants, molecular formula, and their suggested application in various industrial areas are summarized and presented in Table 1. *Paecilomyces sinclairii* has shown a quantitative yield of 4.40 g/L of pigments which was high compared to others (Cho et al. 2002b), and quantitative yield of pigments isolated from few other soil fungi under submerged fermentation are presented in Table 2.

Fungi produce an inspiring group of secondary metabolites (Khaldi et al. 2010). Fungi such as *Aspergillus*, *Fusarium*, *Penicillium*, and *Trichoderma* produce pigments during their growth as intermediate metabolites (Atalla et al. 2011). Fungal pigments which are produced as secondary metabolite can be classified chemically as carotenoids and polyketides. Fungal polyketide pigments are made of tetraketides and octoketides which have eight C_2 units that contribute to the polyketide chain. Anthraquinone, hydroxyanthraquinones, naphthoquinone, and azaphilone are represented classes which exhibit an array in any color, and this rational approach is potentially safe for fungal cell factories of polyketide pigments used for other industrially important polyketides (Mapari et al. 2009, 2010). Anthraquinone belongs to the class of quinone family which consists of several hundreds of compounds that vary in the nature and position of substituent groups (Liu et al. 2008). Anthraquinones are the most important pigments for a long time in the dyestuff industries. A number of fungi such as *Trichoderma*, *Aspergillus*, and *Fusarium* produce anthraquinone compounds through biotechnological techniques, and most of these fungi produce mixture of anthraquinone (Hobson and Wales 1998; Durán et al. 2002). Hydroxyanthraquinone (Fig. 2a) is the derivative of an anthraquinone through replacement of one hydrogen atom by a hydroxyl group. Filamentous fungi produce hydroxyanthraquinone compounds particularly by the polyketide pathway that can be used for the production of dyestuff as natural food grade colorant (Caro et al. 2012). Napthoquinones play an important role as dyes in pigmentation, and the colors range between yellow, orange, and brown. The fungal naphthoquinones include a wide range of biological activities and found to be extensive in *Fusarium* sp. (Mendentsev and Akimenko 1998; Babula et al. 2009). Azaphilones, the group of fungal metabolites, have similar molecular structures as well as similar chemical properties produced by the genus *Monascus* (Dufosse 2009). *Monascus* are known to produce six major pigments of polyketide origin that have been categorized into three groups based on color (Fig. 2g). They are yellow: monascin and ankaflavin, orange: monascorubrin and rubropunctatin, and red: monascorubramine and rubropuntamine (Sweeny et al. 1981). *Monascus* pigments are sensitive to heat, fade with light, unstable in the pH range of 2–10, and have low water solubility, and their stability is affected by acidity, temperature, light, oxygen, water activity, and time. When these pigments react with amino group-containing compounds in the medium such as protein, amino acids, and nucleic acids, they form water soluble pigments (Dufosse 2009).

Fermentation development of fungal pigment

In fungal fermentation, either the vegetative cells or spore suspension has been used for inoculum. But the inoculum of spores in the fermentation process has many advantages compared to the vegetative cells such as the ease in handling, high viability, and stability for a long period of storage, maintenance, and preservation (Ajdari et al. 2011). Consequently, submerged fermentation and solid state fermentation are followed based on their own merits and demerits for the production of fungal pigments (Vendruscolo et al. 2010). In view of this fact, exploitation of submerged fermentation has been studied for the production of *Monascus* pigments to overcome the problems of space, scale-up, and development control of solid culture. Similarly, the utilization of submerged culture can benefit the production of many secondary metabolites and decrease the production costs in reducing the labor involved in solid state fermentation (Vendruscolo et al. 2013). A new red pigment from *Monascus purpureus* can be isolated and purified in submerged fermentation through large scale fermentation which could be economical for industrial application (Mukherjee and Singh 2011). During submerged fermentation, *Penicillium sclerotiorum* 2AV2 produced yellow-orange pigment in Czapeck broth (Celestino et al. 2014). Moreover, solid state fermentation was one of the traditional processes involved in pigment production (Vendruscolo et al. 2010). Since, in solid state fermentation, *Monascus* LPB97 produced pigments using jack fruit seed powder which opens

Table 1 Natural occurrence of fungal pigments from soil and their suggested application

Fungi	Color	Pigment	Molecular formula	Applications	References
Aspergillus niger	Black	Aspergillin	$C_{23}H_{35}NO_4$	Antimicrobial activity	Ray and Eakin (1975)
Aspergillus niger	Brown	–	–	Textile dyeing Antibacterial activity	Atalla et al. (2011); Aishwarya and Aishwarya (2014)
Aspergillus sclerotiorum	Yellow	Neoaspergillic acid	–	Antibacterial activity	Micetich and Macdonald (1965); Teixeria et al. (2012)
Aspergillus versicolor	Yellow	Asperversin	$C_{47}H_{58}O_{10}$	Antifungal activity	Miao et al. (2012)
Fusarium oxysporum	Pink/violet	Anthraquinone	$C_{14}H_8O_2$	Textile dyeing Antibacterial activity	Gessler et al. (2013)
Fusarium verticillioides	Yellow	Naphthoquinone	$C_{10}H_6O_2$	Antibacterial activity	Boonyapranai et al. (2008); Kurobane et al. (1986)
Monascus sp.	Yellow	Monascin	$C_{21}H_{26}O_5$	Food colorant	Juzlova and Martinkova (1996); Mostafa and Abbady (2014); Babitha et al. (2008); Moharram et al. (2012); Babula et al. (2009); Yang et al. (2014)
		Ankaflavin	$C_{23}H_{30}O_5$	Pharmaceuticals	
	Orange	Monascorubrin	$C_{23}H_{26}O_5$	Antibacterial activity	
		Rubropuntatin	$C_{21}H_{22}O_5$	Anticancer activity	
	Red	Monascorubramine	$C_{23}H_{27}O_4$	Antioxidant	
		Rubropuntamine	$C_{21}H_{23}O_4$		
Penicillium herquei	Yellow	Atronenetin	–	Food additive Antioxidant	Takahashi and Carvalho (2010)
Penicillium oxalicum	Red	Anthraquinone	$C_{14}H_8O_2$	Anticancer effect in food and pharmaceuticals Textile dyeing	Dufosse (2006); Atalla et al. (2011)
Penicillium purpurogenum	Orange to Yellow	Purpurogenone	$C_{14}H_{12}O_5$	Dyeing of cotton fabrics	Buchi et al. (1965); King et al. (1970); Martinkova et al. (1995); Mapari et al.(2005); Takahashi and Carvalho (2010); Teixeria et al. (2012); Santos-ebinuma et al. (2013b);
	Yellow to Orange	Mitorubrin	$C_{21}H_{18}O_7$	Food, pharmaceuticals, and cosmetics	
	Red	Mitorubrinol	$C_{21}H_{18}O_8$		
Penicillium sclerotiorum	Yellow to Orange	Pencolide	$C_9H_9NO_4$	Antibacterial activity	Brikinshaw et al. (1963)); Chidananda and Sattur (2007); Lucas et al. (2007); Lucas et al. (2010)
		Sclerotiorin	$C_{21}H_{23}ClO_5$	Antibacterial activity Antifungal activity	
		Isochromophilone VI	–	Antibacterial Activity	
Trichoderma viride	Yellow Green	Viridin	$C_{20}H_{16}O_6$	Textile dyeing Antifungal activity	Chitale et al. (2012); Neethu et al. (2012); Gupta et al. (2013)
	Brown	–	–	Food industry	
Trichoderma virens	Yellow	Viridol	$C_{20}H_{18}O_6$	Textile dyeing	Mukherjee and Kenerley (2010); Sharma et al. (2012); Kamala et al. (2015)
		Virone	$C_{22}H_{24}O_4$	Antifungal Activity	

a way for industrial application as a potent food colorant (Babitha et al. 2007). Under solid state fermentation, *M. purpureus* KACC 42430 produced highest yield of pigments when corn cob powder was used as a substrate.

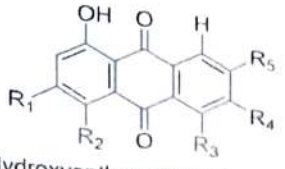
Table 2 Quantitative yield of pigments isolated from soil fungi (submerged fermentation)

Fungi	pH	Color	Yield (g/L)	Reference
Monascus purpureus	5	Red	0.07	Mukherjee and Singh (2011)
Paecilomyces sinclairii	6	Red	4.40	Cho et al. (2002b)
Penicillium funiculosum IBT3954	8	Red	0.13	Jens et al. (2012)
Penicillium sp.	5	Violet	0.20	Ogihara et al. (2000)
Penicillium sclerotiorum	5	Orange	0.31	Lucas et al. (2010)

P.G.P. COLLEGE OF ARTS & SCIENCE NAMAKKAL 637 206

Appl Microbiol Biotechnol (2016) 100:1631–1643

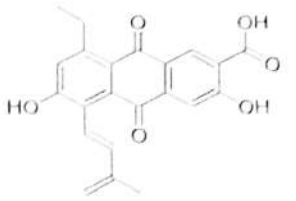
a



Hydroxyanthraquinones

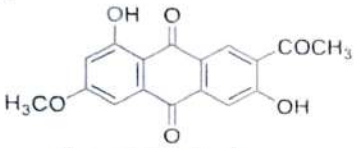
Name	R_1	R_2	R_3	R_4	R_5	Colour
Catenarin	OH	H	OH	CH_3	H	Red
Chrysophanol	H	H	H	CH_3	H	Red
Cynodontin	H	OH	OH	H	CH_3	Bronze
Helminthosporin	H	OH	H	CH_3	H	Maroon
Tritisporin	OH	H	OH	CH_2OH	H	Red-Brown
Erythroglaucin	OCH_3	H	OH	CH_3	H	Red

b

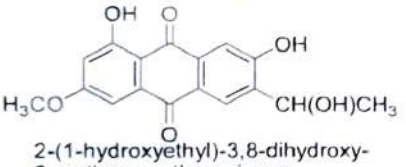


Ar pink Red

c



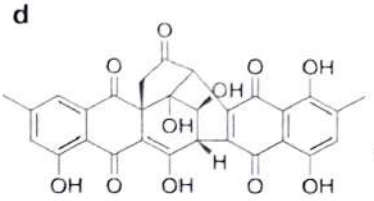
2-acetyl-3,8-dihydroxy-6-methoxy anthraquinone



2-(1-hydroxyethyl)-3,8-dihydroxy-6-methoxy anthraquinone

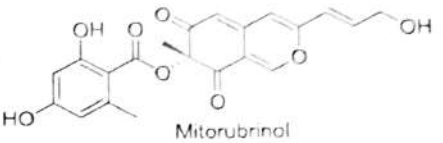
Fusarium oxysporum anthraquinone

d



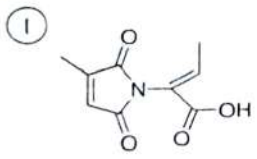
Purpurogenone

e

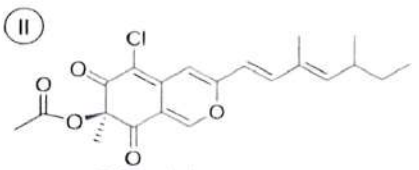


Mitorubrinol

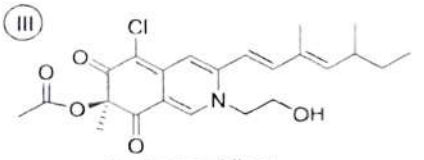
f



Pencolide

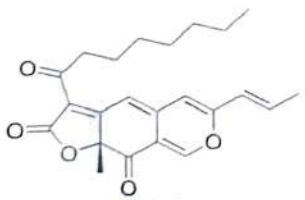


Sclerotiorin

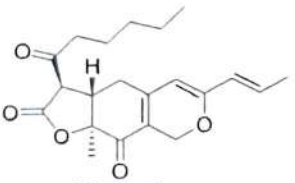


Isochromophilone

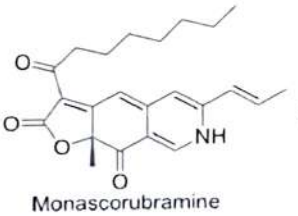
g



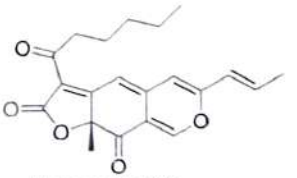
Monascorubrin



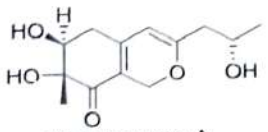
Monascin



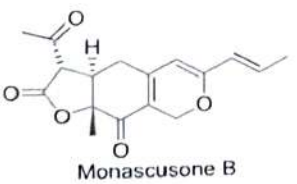
Monascorubramine



Rubropunctatin



Monascusone A

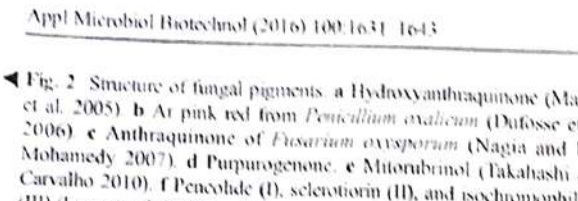


Monascusone B



Ankaflavin

P.G. & R. COLLEGE OF ARTS & SCIENCE NAMAKKAL 637 208



◀ Fig. 2 Structure of fungal pigments. **a** Hydroxyanthraquinone (Mapari et al. 2005). **b** Ar pink red from *Penicillium ovalicum* (Dufosse et al. 2006). **c** Anthraquinone of *Fusarium oxysporum* (Nagia and EL-Mohamedy 2007). **d** Purpurogenone. **e** Mitorubrinol (Takahashi and Carvalho 2010). **f** Penicolide (I), sclerotiorin (II), and isochromophilone (III) (Lucas et al. 2007). **g** *Monascus* pigments (Mapari et al. 2005)

Eventually, corn cob supplies nutrients to the organism as it contains considerable amount of cellulose and hemicellulose (polysaccharides) which promote the growth and pigment production. As corn cobs are a significant source of furfural (aromatic aldehyde), it has been used in a wide variety of industrial processes. Compared to other substrates (rice bran, wheat bran, coconut oil cake, sesame oil cake, jack fruit seed powder), corn cob was found to be an economical and useful alternative liquid culture-based technology (Babitha et al. 2007; Velmurugan et al. 2010d). The red pigment production by *M. ruber* in solid state fermentation using corn steep liquor is a suitable source of nitrogen and salts thus substituting various salts and yeast extract (Hamano and Kilikian 2006). Rice is the best substrate for pigment production in *Monascus* under solid state fermentation at optimum fermentation time (7 days), and the production of yellow is better than red pigment. The extraction of pigments in solid state fermentation is ethanol as it is cheap, non-toxic, and volatile (Carvalho et al. 2007). *Penicillium purpurogenum* was reported to produce color both in solid and liquid media which is water soluble and have possible benefits (Mendez et al. 2011). At the same time, *P. purpurogenum* DUPA 1275 in submerged cultures produces natural colorant with an intension of safe alternative for the use of synthetic colorants (Santos-ebinuma et al. 2013a).

Intrinsic and extrinsic factors for the development and production of fungal pigments

Fungal pigments are generally biosynthesized as secondary products during metabolism—such secondary metabolites are known as polyketides. The production of secondary metabolites is influenced by the development stage of the fungus and also by the intrinsic and extrinsic factors of the environment such as substrate, composition, oxygen, pH, water activity, temperature, and light availability (Sagaram et al. 2006). The production varies as much as their chemistry. The medium composition, aeration, agitation, and nutrient limitation in the excess of carbon source stimulate the production of secondary metabolites. For example, *Monascus* pigments vary from orange-yellow to scarlet to purple-red. The color can be influenced by the culture conditions, in particular by the pH and by the phosphorous and nitrogen source in the substrate. But, little has been known about the influence of light in the medium for pigment production (Mapari et al. 2010). The biosynthesis of natural colorants from fungi could ensure "colorant production is accomplished under controlled conditions in bioreactors that offer the colorant manufacturer independence from the external, seasonal supply of raw materials and potentially minimize batch-to-batch variations". For commercial development, the major factors influencing the biomass and pigment production are light, temperature, etc. (Velmurugan et al. 2010d). The oxygen and carbon dioxide level in the gas environment result in higher growth and pigmentation. As oxygen level increases and carbon dioxide level decreased, the ratio of biomass decreased significantly to pigment production (Han and Mudgett 1992). The fungus *M. purpureus* is considered to be the source of various secondary metabolites of polyketide groups (Musaalbakri et al. 2006). Previous studies have reported that through strain improvement, carbon sources change and perfection of culture conditions have enhanced the production of *Monascus* pigments (Lim et al. 2000). Likewise, growth conditions such as pH, aeration, and nitrogen source for *Monascus* sp. can result in the formation of extracellular and water soluble pigments, but intracellular pigments are insoluble in water (Hajjaj et al. 1998). Moreover, the pigment production by *M. purpureus* changes depending on the light condition. The different light sources used were direct light, total darkness, partially exposed to light, red light, blue light, and green light. The incubation in total darkness was found to be effective in inducing red pigment production, whereas direct illumination resulted in absence of pigment production, thus postulating the existence of photoreceptors responsive to dark and light by this fungus. It was also found that both red and blue light influenced pigment yield as well as culture morphology (Babitha et al. 2008). *Monascus* red or yellow pigments that were efficiently produced by several strains were commercially important. *M. purpureus* produced red pigment that was highly dependent on nutritional and environmental conditions (Musaalbakri et al. 2006). The optimum temperature for *M. purpureus* was found to be within 28–30 °C, as they can survive on a wide range of pH 4.5–8.5. Maximum reported biomass was observed at pH 4.5 (acidic pH), and around this range, yellow-orange pigments were dominant (Dikshit and Tallapragada 2011). In solid substrate fermentation, *Monascus* LPB 31 cultivated over potato dextrose agar showed higher pigment concentration with lower citrinin concentration and these strains were found to be unstable at low pH and high temperature and, therefore, applied in processes with pH near neutrality and temperature inferior to 60 °C (Carvalho et al. 2005). Under submerged fermentation, *Penicillium* sp. produced extracellular pigment at optimum culture conditions of pH 9.0 and temperature 30 °C with relatively high production yield and light stability (Gunasekaran and Poorniammal

2008). Similarly, in solid state fermentation, *P. purpurogenum* GH2 produced highest amount of pigment at temperature 24 °C and pH 10 (Espinoza-Hernandez et al. 2013). Usually, higher fungi require long periods for mycelial growth and pigment production in submerged culture, exposing them to contamination risk and, to avoid this, optimal temperature (25 °C) is regarded as a favorable physiological property of *P. sinclairii*. The pigment color secreted by this fungus was red and water soluble (Cho et al. 2002b).

Through monospore isolation technique, *M. purpureus* FTC 5391 produced red pigment in different carbon sources such as glucose, potato starch, and rice starch (Musaalbakri et al. 2006). Indeed, the effect of nitrogen source such as tryptophan or 6-furfuryl aminopurine in the fermentation broth produced extracellular pigment (Zhang et al. 2013). Hence, the maximum production of pigment and biomass concentration was favored by the effect of the nitrogen source (Meinicke et al. 2012; Buhler et al. 2013). *M. purpureus* ATCC 1603 produced red pigment in the presence of vitamin B_2, gibberellic acid, and amino acids (glycine and L-leucine) in the liquid culture (Baneshi et al. 2014). The fungi *Fusarium verticillioides* isolated from soil was evaluated as a potential naphthoquinone pigment. The pigment formation was dependent on the composition of the medium and the mycelial growth. Furthermore, pigment production was increased proportionally to the concentration of carbon source, glucose, and yeast extract as nitrogen source (Boonyapranai et al. 2008). *Fusarium moniliforme* KUMBF1201 could utilize different carbon and nitrogen sources, but peptone as carbon source and yeast extract as nitrogen source were found to be suitable for growth and pigment production (Pradeep et al. 2013). *P. purpurogenum* GH2 produced red pigment under submerged culture in Czapek-Dox media with D-Xylose as a carbon source was optimal for pigment production and the pigment produced in new medium was extracellular while pigment produced in the original medium was cell-bound (Lin and Demain 1991). The characteristic growth rate of *P. sinclairii* on sucrose as carbon source was higher than that in starch medium, but the production rate of red pigments was favorable in the starch medium (Cho et al. 2002a).

Biological activities of fungal pigment and their application in food colorant

The present trend in the society for natural ingredients has spurred resurgence in exploring novel means and sources for the biotechnological production of food colorants (Mapari et al. 2005). In addition, the food industry is facing great challenges to produce naturally occurring antimicrobial and antioxidant products that are regarded as healthy reducing the use of synthetic chemical preservatives (Vendruscolo et al. 2013). The pigments used in food industry, for example, carotenoids and betanins, contain labile hydrogen which easily decolorized by oxidation making them sensitive to light, heat, and oxygen. These features limit the robustness of these color additives during the processing, storage, and display of the foods to which they have been added (Mapari et al. 2005). *Monascus* was first discovered and used in Asia as a natural food colorant or as the Chinese medicine, although the first classification of *Monascus* strains was performed in other countries (Hamano and Kilikian 2006; Srianta et al. 2014). The red pigment produced from *M. purpureus* showed antibacterial activity, and the extract of *M. purpureus* was found to be 81 % effective as compared with antibiotic ciprofloxacin (Kumar et al. 2012). *Monascus* strain AUMC 5705 showed good production of butyric acid, pyran, and fatty acids which have anticancer activity and AUMC 4066 secondary metabolites which have many significant applications in food, pharmaceutical, and other industries (Moharram et al. 2012). The toxin issue, especially citrinin, has certainly limited the food use of *Monascus* because of safety concerns over its use directly in food or as an added pigment. Meanwhile, much research in the past 20 years on *Monascus* pigments has focused on ways to minimizing citrinin production or developing strains that are incapable of co-producing citrinin (Wang et al. 2004; Pisareva et al. 2005; Xu et al. 2009). The genetic basis for polyketide pigment biosynthesis in fungi has not yet been examined in detail. However, the genes responsible for pigment production in *Monascus* pigment biosynthesis are still a controversy and only few related genes have been reported. *MpigE*, a gene involved in *Monascus* pigment biosynthesis in *Monascus ruber*, was analyzed. The disruption, complementation, and overexpression of *MpigE* gene had more effects on pigment production, whereas overexpression of *MpigE* gene made citrinin decrease drastically in the fermentation medium (Liu et al. 2014). The bioactive metabolite sclerotiorin by *P. sclerotiorum* produced in the presence of dextrose, peptone, and mineral salts with sodium chloride supplementation was used in pharmaceutical industry (Lucas et al. 2010). *P. sclerotiorum* isolated from Serrado Cipo National Park soil in large scale liquid culture led to the isolation of pencolide, sclerotiorin, and isochromophilone (Fig. 2f). The compound pencolide and sclerotiorin showed antibacterial activity against gram positive bacteria such as *Streptococcus pyogenes*, *Staphylococcus aureus*, *Salmonella typhimurium*, and gram negative bacteria such as *Escherichia coli* and against yeast *Candida albicans*. Isochromophilone showed antibacterial activity against *S. aureus* (Lucas et al. 2007).

Based on the clinical and preclinical investigations, *Monascus* metabolites are found to have a new therapeutic approach for cancer prevention and therapy. Due to these reasons, the development of novel anticancer *Monascus* food products and pharmaceuticals has been found to decrease the incidence and mortality of human malignances (Yang et al. 2014). *Penicillium* sp. produces many

COLLEGE OF ARTS NAMAKKAL

secondary metabolites with high bioactive compounds in pharmacy to produce drugs used to treat many diseases, and these compounds are also used in agriculture (Tajick et al. 2014). *Penicillium* sp. HSDO7B co-cultured with *Candida tropicalis* produced red pigment was stable and apparently non-toxic which are potentially applicable for coloring (Hailei et al. 2011). The red colorant of the anthraquinone class is produced by a variety of *Penicillium oxalicum* with favorable characteristics such as water solubility, wide array of colors, and do not require a stabilizing agent to be added to foodstuffs (Takahashi and Carvalho 2010). *P. oxalicum* var. Armeniaca CCM 8242 produced a chromophore of the anthraquinone type. Ar pink red (Fig. 2b) of anthraquinone derivative has anticancer effect application in food and pharmaceuticals (Dufosse 2006). The natural food colorant hydroxyanthraquinoid manufactured by the Czech company has been produced using the soil fungal strain *P. oxalicum* var. Armeniaca CCM 8242 by fermentation and bioprocess engineering (Dufosse et al. 2014). In the case of *P. oxalicum*, a yellow toxic pigment, secalonic acid D produced by this species cannot be used directly in foods. Some important secondary metabolites are regulated by blue light which inhibits mycotoxins produced by *Aspergillus flavus* and *Aspergillus parasiticus* (Haggblom and Unestam 1979). *Aspergillus* sp., screened from soil, has bioactive compounds especially the secondary metabolites that are produced biotechnologically in agrochemical industry. The most active extract obtained from this organism was phytotoxic and has herbicidal activities. *Aspergillus sclertiorum* DPUA 585 produced yellow pigment, neoaspergillic acid that showed antibacterial activity against *E. coli*, *Mycobacterium smegmatis*, and *S. aureus* and antifungal activity against *C. albicans* (Micetich and Macdonald 1965; Teixeria et al. 2012). *Aspergillus versicolor* pt 20 isolated from endophytic fungus showed antibacterial activity (Miao et al. 2012). The pigment isolated from *P. purpurogenum* produced orange-yellow compound, purpurogenone (Fig. 2d), and orange-red compound, mitorubrinol (Fig. 2e) (Takahashi and Carvalho 2010). Furthermore, *Penicillium* species isolated from Brazilian cerrado soil showed antimicrobial activity possessing significant activity against *C. albicans* (MIC 32 μg/ml), *Listeria monocytogenes*, and *Bacillus cereus* (MIC 64 μg/ml) respectively (Petit et al. 2009). The production of pigment by *Penicillium* sp. NIMO-02 indicated its importance in food and pharmaceutical industries (Dhale and Vijay Raj 2009). *P. purpurogenum* produced higher extracellular pigments with antimicrobial activity in darkness that have the possibility of pharmaceutical production of drugs useful to biotechnological approach in pharmaceutical and health care industries (Geweely 2011), and *Trichoderma virens* have antifungal properties that are eco-friendly (Sharma et al. 2012).

Pigmented compound of fungi in textile dyeing

For successful commercial use of natural dyes, the suitable and standardized dyeing technique has to be adopted for dyeing textile materials (Samanta and Agarwal 2009). Besides, natural pigments exhibit better biodegradability and higher compatibility with the environment as well. The production being independent of season, the large scale industries produced pigments under controlled fermentation technologies (Nerurka et al. 2013). The black pigment of *Aspergillus niger*, aspergillin, involves high molecular weight melanins which comprise sites existing for saturation by pentacyclic quinoid derivative (Ray and Eakin 1975). *A. niger* isolated from soil sample produced pigment in potato dextrose broth, and the purified pigments were dyed on the fabrics such as cotton, silk, and silk cotton. The purified dyes were dyed on the fabrics, and the percentage absorption of dye onto the fabrics was measured using UV spectrophotometer and the comparative study was done. The premordanted fabrics showed higher percentage of dye absorbance than unmordanted fabrics. Cotton fabric was found to be more effective and had higher absorption than silk and silk cotton (Aishwarya 2014). *A. niger* NRC 95 produced brown pigment that was found at the end of the incubation period as it decreased during the third week of incubation. The dye produced showed good reflectance at 482 nm, as the pigments were used in dyeing wool (Atalla et al. 2011). Anthraquinone compounds (Fig. 2c) from *Fusarium oxysporum* are used as natural dyes and can be used to dyeing wool (Nagia and EL-Mohamedy 2007). Moreover, the purified pigments from *P. purpurogenum* is an alternative source for natural dyeing for cotton fabrics and has good scope to produce antibacterial activity (Velmurugan et al. 2009) and antibacterial finishes are used in textile for medical applications (Poorniammal et al. 2013). *P. oxalicum* NRC M25 produced faint reddish brown pigment which is applied in textile dyeing (Atalla et al. 2011). The color pigment of *Trichoderma* sp. grown in aerobic fermentation broth was separated and identified by reversed phase thin layer chromatography (RP-TLC), fourier transform infra red spectroscopy (FT-IR), and high performance liquid chromatography (HPLC)-diode array detection. It was established that the pigments were successfully separated by RP-TLC and RP-HPLC whereas FT-IR and MS measurements were unable to identify the exact chemical structures of the main pigment fractions, the presence of OH, = CH, and C=O (RP-TLC, FT-IR) and OH and NH_2 substructures (RP-HPLC-MS) was confirmed (Kiss et al. 2000). *Trichoderma* can also benefit from studies of molecular physiology and regulatory processes to expose novel and valuable metabolites and enzyme. These fungi are versatile model organism for research on both industrial fermentation as well as natural phenomena (Schuster and Schmoll 2012). The pigment of *T. virens* applied on textile was found to be

non-toxic to human skin, and this species are eco-friendly (Sharma et al. 2012).

Conclusion

Owing to the contradictory reports on the safety of synthetic dyes and due to the indiscriminate use of non-permitted colors, there is an important need to identify natural pigment sources as safe colorant. It is known that fungi isolated from soil produced pigments are used for various industrial applications. The use of fungal pigments is gaining accessibility in textile dyeing, food colorant, antimicrobial, and anticancer activities. Incidentally, the fungal pigments are natural without creating undesirable effects when they enter the environment. Considering the toxic effects of the synthetic dyes, the natural dyes are eco-friendly and easily degradable since they cause no detrimental effects. Based on the review, previous studies have proved that pigments produced by soil fungi are a safer alternative use to synthetic colorants and offer good scope for feasible industrial applications.

Acknowledgments The authors are sincerely grateful to the Management, Karpagam Academy of Higher Education, Coimbatore—641 021, Tamil Nadu, India, for the constant encouragement and support.

Compliance with ethical standards

Conflict of interest The authors declare that they have no competing interests.

Ethical statement This article does not contain any studies with human participants or animals performed by any of the authors.

References

Aishwarya A d (2014) Extraction of natural dyes from fungus—an alternative for textile dyeing. J Nat Sci Res 4:1–6

Ajdari Z, Ebrahimpour A, Manan MA, Hamid M, Mohamad R, Ariff AB (2011) Nutritional requirements for the improvement of growth and sporulation of several strains of *Monascus purpureus* on solid state cultivation. J Biomed Biotechnol. 1–9. doi:10.1155/2011/487329

Atalla MM, Elkhrisy EAM, Asem MA (2011) Production of textile reddish brown dyes by fungi. Malaysian J Microbiol 7:33–40

Babitha S (2009) Microbial pigments. Biotechnol Agro-Ind Residues Utilisation 153–168. doi: 10.1007/978-1-4020-9942-7_8

Babitha S, Soccol CR, Pandey A (2007) Solid-state fermentation for the production of *Monascus* pigments from jack fruit seed. Biores Technol 98:1554–1560. doi:10.1016/j.biortech.2006.06.005

Babitha S, Carvahlo JC, Soccol CR, Pandey A (2008) Effect of light on growth, pigment production and culture morphology of *Monascus purpureus* in solid state fermentation. World J Microbiol Biotechnol 24:2671–2675. doi:10.1007/s11274-008-9794-3

Babula P, Adam V, Havel L, Kizek R (2009) Noteworthy secondary metabolites naphthoquinones—occurrence, pharmacological properties and analysis. Curr Pharma Analysis 5:47–68. doi:10.2174/157341209787314936

Baneshi F, Azizi M, Saberi M, Farsi M (2014) Gibberellic acid, amino acids (glycine and L-leucine), vitamin B2 and zinc as factors affecting the production pigments by Monascus purpureus in a liquid culture using response surface methodology. Afric J Biotechnol 13:1484–1490

Boonyapranai K, Tungpradit R, Hicochaiphant S (2008) Optimization of submerged culture for the production of naphthoquinones pigment by *Fusarium verticillioides*. Chiag Mai J Sci 35:457–466

Brikinshaw JH, Kalyanpur MG, Stickings CE (1963) Studies in the biochemistry of microorganisms 113. Pencolide a nitrogen containing metabolite of *Penicillium* multicolor grigorieva-manilova and poradielova. Biochem J 86:237–243

Buchi G, White JD, Wogan GN (1965) The structures of mitorubrin and mitorubrinol. J American Chem Society 87:3484–3489. doi:10.1021/ja01093a036

Buhler RMM, Dutra AC, Vendruscolo F, Moritz DE, Ninow JL (2013) *Monascus* pigment production in bioreactor using a co-product of biodiesel as substrate. Cienc Technol Aliment Campinas 33:9–13. doi:10.1590/S0101-20612013000500002

Caro Y, Anamale L, Fouillaud M, Laurent P, Petit T, Dufosse L (2012) Natural hydroxyanthraquinoid pigments as potent food grade colorants: an overview. Nat Prod Bioprospect 2:174–193. doi:10.1007/s13659-012-0086-0

Carvalho JCD, Oishi BO, Pandey A, Soccol CR (2005) Biopigments from *Monascus*: strains selection, citrinin production and color stability. Braz Arch Biol Technol 48:885–894. doi:10.1590/S1516-89132005000800004

Carvalho JC, Oishi BO, Woiciechowski AL, Pandey A, Babitha S, Soccol CR (2007) Effect of substrates on the production of *Monascus* biopigments by solid-state fermentation and pigment extraction using different solvents. Indian J Biotechnol 6:194–199

Celestino JR, Carvalho LE, Lima MP, Lima AM, Ogusku MM, Souza JVB (2014) Bioprospecting of Amazon soil fungi with the potential for pigment production. Proc Biochem 49:569–575. doi:10.1016/j.procbio.2014.01.018

Chattopadhyay P, Chatterjee S, Sen SK (2008) Biotechnological potential of natural food grade biocolorants. Afr J Biotechnol 7:2972–2985

Chidananda C, Sattur AP (2007) Sclerotiorin, a novel inhibitor of lipoxygenase from *Penicillium frequentans*. J Agric Food Chem 55:2879–2883. doi:10.1021/jf062032x

Chitale A, Jadhav DV, Waghmare SR, Sahoo AK, Ranveer RC (2012) Production and characterization of brown colored pigment from *Trichoderma viride*. Electronic J Environ Agric Food Chem 11:529–537

Cho YJ, Hwang HJ, Kim SW, Song CH, Yun JW (2002a) Effect of carbon source and aeration rate on broth rheology and fungal morphology during red pigment production by *Paecilomyces sinclairii* in a batch bioreactor. J Biotechnol 95:13–23. doi:10.1016/S0168-1656(01)00445-X

Cho YJ, Park JP, Hwang HJ, Kim SW, Choi JW, Yun JW (2002b) Production of red pigment by submerged culture of *Paecilomyces sinclairii*. Lett Appl Microbiol 35:195–202. doi:10.1046/j.1472-765X.2002.01168.x

Dhale MA, Vijay Raj AS (2009) Pigment and amylase production in *Penicillium* sp NIOM-02 and its scavenging activity. Int J Food Sci Technol 44:224–2430

Dikshit R, Tallapragada P (2011) *Monascus purpureus*: a potential source for natural pigment production. J Microbiol Biotechnol Res 1:164–174

Dufosse L (2006) Microbial production of food grade pigments. Food Technol Biotechnol 44:313–321

Dufosse L (2009) Pigment, Microbial. Appl Microbiol: Industrial 457–471

Dufosse L (2014) Anthraquinones, the Dr Jekyll and Mr. Hyde of the food pigment family. Food Res Int 65:132–136. doi:10.1016/j.foodres.2014.09.012

P.G. & R. COLLEGE OF ARTS & SCIENCE NAMAKKAL 637 206

Dufosse L, Galaup P, Yaron A, Arad SM, Blanc P, Murthy KNC, Ravishankar GA (2005) Microorganism and microalgae as source of pigments for food use: a scientific oddity or an industrial reality. Trends Food Sci Technol 16:389–406. doi:10.1016/j.tifs.2005.02.006

Dufosse F, Fouillaud M, Caro Y, Mapari SAS, Sutthiwong N (2014) Filamentous fungi are large-scale producers of pigments and colorants for the food industry. Curr Opin Biotechnol 26:56–61. doi:10.1016/j.copbio.2013.09.007

Durán N, Teixeira MFS, Conti RD, Esposito E (2002) Ecological-friendly pigments from fungi. Critical Rev Food Sci Nutrition 42:53–66. doi:10.1080/10408690290825457

Espinoza-Hernandez TC, Rodriguez-Herrera R, Aguilar-Gonzalez CO, Lara-Victoriano F, Reyes-Valdes MH, Castillo-Reyes F (2013) Characterization of three novel pigment-producing *Penicillium* strains isolated from the Mexican semi-desert. Afric J Biotechnol 12:3405–3413. doi:10.5897/AJB2013.12338

Gessler NN, Egorova AS, Belozerskaya TA (2013) Fungal anthraquinones. Appl Biochem Microbiol 49:85–99. doi:10.1134/S000368381302004X

Geweely NS (2011) Investigation of the optimum condition and antimicrobial activities of pigments from four potent-producing fungal species. J Life Sci 5:697–711. doi:10.4172/2153-2435.10000S2

Gunasekaran S, Poorniammal R (2008) Optimization of fermentation conditions for red pigment production from *Penicillium* sp under submerged fermentation. Afric J Biotechnol 7:1894–1898

Gupta C, Sharma D, Aggarwal S, Nagpal N (2013) Pigment production from *Trichoderma* sp. for dyeing of silk and wool. Int J Sci Nature 4:351–355

Haggblom P, Unestam T (1979) Blue light inhibits mycotoxin production and increases total lipids and pigmentation in *Alternaria alternate*. Appl Environ Microbiol 38:1074–1077

Hailei W, Zhifang R, Ping L, Yanchang G, Guoshang L, Jianming Y (2011) Improvement of the production of a red pigment in *Penicillium* sp HSDO7B synthesized during co-culture with *Candida tropicalis*. Biores Technol 102:6082–6087. doi:10.1016/j.biortech.2011.01.040

Hajjaj H, Blanc PJ, Goma G, Francois J (1998) Sampling techniques and comparative extaction procedures for quantitative determination of intra – and extracellular metabolites in filamentous fungi. FEMS Microbiol Letters 164:195–200

Hamano PS, Kilikian BV (2006) Production of red pigments by *Monascus ruber* in culture media containing corn steep liquor. Braz J Chem Eng 23:443–449. doi:10.1590/S0104-66322006000400002

Han O, Mudgett RE (1992) Effects of oxygen and carbon dioxide partial pressure on Monascus growth and pigment production in solid-state fermentations. Biotechnol Prog 8:5–10

Herrmann KM (1995) The shikimate pathway: early steps in the biosynthesis of aromatic compounds. Plant Cell 7:907–919. doi:10.1105/tpc.7.7.907

Hobson DK, Wales DS (1998) Green dyes. J Studies Dynamics Change 114:42–44

Jens F, Mapari SAS, Meyer AS, Ulf T (2012) Production of *Monascus* like pigment. Technical University Denmark

Joshi VK, Attri D, Bala A, Bhushan S (2003) Microbial pigments. Int J Biotechnol 2:362–369

Juzlova P, Martinkova KV (1996) Secondary metabolites of the fungus *Monascus*: a review. J Ind Microbiol 16:163–170. doi:10.1007/BF01569999

Kamala T, Indiradevi S, Chandradev Sharma K, Kennedy K (2015) Phylogeny and taxonomical investigation of *Trichoderma* spp. From Indian region of Indo-Burma biodiversity hot spot region with special reference to Manipur. BioMed Res International 1–21. doi:10.1155/2015/285261

Keller N, Turner G, Bennett J (2005) Fungal secondary metabolism from biochemistry to genomics. Nat Rev Microbiol 3:937–947. doi:10.1038/nrmicro1286

Khaldi N, Seifuddin FT, Turner G, Haft D, Nierman WC, Wolfe KH, Fedorova ND (2010) SMURF: genomic mapping of fungal secondary metabolite clusters. Fungal Gen Biol 47:736–741. doi:10.1016/j.fgb.2010.06.003

King TJ, Roberts JC, Thompson DJ (1970) The structure of purpurogenone, a metabolite of *Penicillium purpurogenum* stoll: an X-Ray study. J Chem Soc D. doi:10.1039/C2970001499A

Kirti K, Amita S, Priti S, Kumar AM, Jyoti S (2014) Colorful world of microbes: Carotenoids and their applications. Adv Biol 1–13. doi.org/10.1155/2014/837891

Kiss GC, Forgacsa E, Cserhatia T, Vizcainob JA (2000) Colour pigments of *Trichoderma harzianum*: preliminary investigations with thin-layer chromatography–Fourier transform infrared spectroscopy and high-performance liquid chromatography with diode array and mass spectrometric detection. J Chromatography A 896:61–68. doi:10.1016/S0021-9673(00)00413-1

Kumar A, Verma U, Sharma U (2012) Antibacterial activity *Monascus purpureus* (red pigment) isolated from rice malt. Asian J Biol life Sci 1:252–255

Kurobane I, Zaita N, Fukuda A (1986) New metabolites of *Fusarium martii* related to dihydrofusarubin. J Antibiot 39:205–214. doi:10.7164/antibiotics.39.205

Lee BK, Park NH, Piao HY, Chung WJ (2001) Production of red pigments by *Monascus purpureus* in submerged culture. Biotechnol Bioprocess Eng 6:341–346

Lim HS, Yoo SK, Shin CS, Hyun YM (2000) *Monascus* red pigment overproduction by coculture with recombinant *Saccharomyces cervisiae* secreting glucoamylase. J Microbiol 38:48–51

Lin TF, Demain AL (1991) Effect of nutrition of *Monascus* sp. on formation of red pigments. Appl Microbiol Biotechnol 36:70–75. doi:10.1007/BF00164701

Liu R, Lu Y, Wu T, Pan Y (2008) Simultaneous isolation and purification of mollugin and two anthraquinones from *Rubia cordifolia* by HSCCC. Chromatographia 68:95–99. doi:10.1365/s10337-008-0629-z

Liu Q, Xie N, He Y, Wang L, Shao Y, Chen F (2014) MpigE, a gene involved in pigment biosynthesis in *Monascus ruber* M7. Appl Microbiol Biotechnol 98:285–296. doi:10.1007/s00253-013-5289-8

Lopes FC, Tichota DM, Pereira JQ, Segalin J, Rios AO, Brandelli A (2013) Pigment production by filamentous fungi on agro-industrial byproducts: an ecofriendly alternative. Appl Biochem Biotechnol 171:616–625. doi:10.1007/s12010-013-0392-y

Lucas EMF, MonteirodeCastro MC, Takashi JA (2007) Antimicrobial properties of sclerotiorin, isochromophilone VI and pencolide, metabolites from a Brazalian Cerrado isolate of *Penicillium sclerotiorum* van beyma. Braz J Microbiol 38:785–789. doi:10.1590/1517-83822007000400036

Lucas EMF, Machado Y, Ferreira AA, Dolabella LMP, Takahashi JA (2010) Improved production of pharmacologically-active sclerotiorin by *Penicillium sclerotiorum*. Tropical J Pharma Res 9:365–371

Mapari SAS, Nielsen KF, Larsen TO, Frisvad JC, Meyer AS, Thrane U (2005) Exploring fungal biodiversity for the production of water-soluble pigments as potential natural food colorants. Curr Opin Biotechnol 16:231–238. doi:10.1016/j.copbio.2005.03.004

Mapari SAS, Meyer AS, Thrane U (2006) Colorimetric characterization for comparative analysis of fungal pigments and natural food colorants. J Agric Food Chem 54:7027–7035. doi:10.1021/jf062094n

Mapari SAS, Meyer AS, Thrane U, Risvad JCF (2009) Identification of potentially safe promising fungal cell factories for the production of polyketide natural food colorants using chemotaxonomic rationale microbial cell factories. Microb Cell Factories 8:1–15. doi:10.1186/1475-2859-8-24

COLLEGE OF ARTS

Mapari SAS, Thrane U, Meyer AS (2010) Fungal polyketide azaphilone pigments as future natural food colorants. Trends Biotechnol 28: 300–307. doi:10.1016/j.tibtech.2010.03.004

Martinkova L, Juzlova P, Vesely D (1995) Biological activity of polyketide pigments produced by the fungus *Monascus*. J Appl Bacteriol 79:609–616. doi:10.1111/j.1365-2672.1995.tb00944.x

Meinicke RM, Vendruscolo F, Moritz DE, Dd O, Schmidell W, Samohyl RW, Ninow JL (2012) Potential use of glycerol as substrate for the production of red pigments by *Monascus ruber* in submerged fermentation. Biocatal Agric Biotechnol 1:258–242. doi:10.1016/j.beab.2012.03.001

Mendentsev AG, Akimenko VK (1998) Naphthoquinone metabolites of the fungi. Phytochem 47:935–959

Mendez A, Perez C, Montanez JC, Martinez G, Aguilar CN (2011) Red pigment production by *Penicillium purpurogenum* GH2 is influenced by pH and temperature. J Zhejiang Univ-Sci B (Biomed & Biotechnol) 12:961–968. doi:10.1631/jzus.B1100039

Mehrabian S, Majd A, Majd I (2000) Antimicrobial effects of three plants (Rubia tinctorum, Carthamus tinctorius and Juglans regia) on some airborne microorganisms. Aerobiologia 16:455–458

Miao F-P, Li X-D, Liu X-H, Cichewicz RH, Ji N-Y (2012) Secondary metabolites from an algicolous *Aspergillus versicolor* strain. Marine drugs 10:131–139. doi:10.3390/md10010131

Micetich RG, Macdonald JC (1965) Biosynthesis of neoaspergillic and neohydroxyaspergillic acids. J Biol Chem 240:1692–1695

Moharram AM, Eman MM, Ismail MA (2012) Chemical profile of *Monascus ruber* strains. Food Technol Biotechnol 50:490–499

Mortensen A (2006) Carotenoids and other pigments as natural colorants. Pure Appl Chem 78:1477–1491

Mostafa ME, Abbady MS (2014) Secondary metabolites and bioactivity of the *Monascus* pigments review article. Global J Biotechnol Biochem 9:1–13. doi:10.5829/idosi.gjbb.2014.9.1.8268

Mukherjee PK, Kenerley CM (2010) Regulation of morphogenesis and biocontrol properties in *Trichoderma virens* by a velvet protein, vel1. Appl Environ Microbiol 76:2345–2352. doi:10.1128/AEM.02391-09

Mukherjee G, Singh SK (2011) Purification and characterization of a red pigment from *Monascus purpureus* in submerged fermentation. Process Biochem 46:188–192. doi:10.1016/j.procbio.2010.08.006

Musaalbakri AM, Ariff A, Rosfarizan M, Ismail AKM (2006) Improvement of red pigment producing fungal strain (*Monascus purpureus* FTC 5391) using monospore isolation technique. J Trop Agric Fd Sci 34:77–87

Nagia FA, EL-Mohamedy RSR (2007) Dyeing of wool with natural anthraquinone dyes from *Fusarium oxysporum*. Dyes and pigm 75: 550–555. doi:10.1016/j.dyepig.2006.07.002

Neethu K, Rubeena M, Sajith S, Sreedevi S, Priji P, Unni KN, Sarathlosh MK, Jisha VN, Pradeep S, Benjamin S (2012) A novel strain of *Trichoderma viride* shows complete lignocellulolytic activities. Advances in Biosci Biotechnol 3:1160–1166. doi:10.4236/abb.2012.38142

Nerurka M, Vaidyanathan J, Adivarekar R, Langdana ZB (2013) Use of natural dye from *Serratia marcescens* subspecies *marcescens* in dyeing of textile fabrics. Octa J Environ Res 1:129–135

Ogihara J, Kato J, Oishi K, Fujimoto Y, Eguchi T (2000) Production and structural analysis of PP-V, a homologue of monascorubramine, produced by a new isolate of *Penicillium* sp. J Biosci Bioeng 90:549–554

Petit P, Lucas EMF, Abreu LM, Pfenning LH, Takahashi JA (2009) Novel antimicrobial secondary metabolites from a *Penicillium* sp. isolated from Brazilian cerrado soil. Electro J Biotechnol 12:1–9. doi:10.2225/vol12-issue4-fulltext-9

Pisareva E, Savov V, Kujumdzieva V (2005) Pigments and citrinin biosynthesis by fungi belonging to genus *Monascus*. Z Naturforsch C 60:116–120

Poorniammal R, Parthiban M, Gunasekaran S, Murugesan R, Thilagavathy R (2013) Natural dye production from *Thermomyces* sp. fungi for textile application. Indian J Fiber Textile Res 38:276–279

Pradeep FS, Shakilabegum M, Palanisswamy M, Pradeep BV (2013) Influence of culture media on growth and pigment production by *Fusarium moniliforme* KUMBF1201 isolated from paddy field soil. World Appl Sci J 22:70–77. doi:10.5829/idosi.wasj.2013.22.01.7265

Ray AC, Eakin RE (1975) Studies on the biosynthesis of Aspergillin by *Aspergillus niger*. Appl Microbiol 30:909–915

Sagaram US, Kolomiets M, Shim W (2006) Regulation of fumonisin biosynthesis in *Fusarium verticilloides*—maize system. Plant Pathol J 22:203–210

Samanta AK, Agarwal P (2009) Applications of natural dyes on textile dyes. Indian J Fiber Textile Res 34:384–399

Santis DD, Moresi M, Gallo AM, Petruccioli M (2005) Assessment of the dyeing properties of pigments from Monascus purpureus. J Chem Technol Biotechnol 80:1072–1079

Santos-ebinuma VC, Roberto IC, Teixeira MFS, Passoajr A (2013a) Improving of red colorants production by a new *Penicillium purpurogenum* strain in submerged culture and the effect of different parameters in their stability. Biotechnol Prog 29:778–785. doi:10.1002/btpr.1720

Santos-ebinuma VC, Teixeira MFS, Pessoajr A (2013b) Submerged culture conditions for the production of alternative natural colorants by a new isolated *Penicillium purpurogenum* DPUA 1275. J Microbiol Biotechnol 23:802–810. doi:10.4014/jmb.1211.11057

Sasidharan P, Raja R, Karthik C, Sharma R, Indra Arulselvi P (2013) Isolation and characterization of yellow pigment producing *Exiguobacterium* sp. J Biochem Tech 4:632–635

Scholes DR, Paige KN (2015) Plasticity in ploidy: a generalized response to stress. Trends Plant Sci 20:165–175

Schuster A, Schmoll M (2012) Biology and biotechnology of *Trichoderma*. Appl Microbiol Biotechnol 87:787–799. doi:10.1007/s00253-010-2632-1

Sewekow U (1988) Natural dyes—an alternative to synthetic dyes. Melliand Textilber 69:145–148

Sharma D, Gupta C, Aggarwal S, Nagpal N (2012) Pigment extraction from fungus for textile dyeing. Indian J Fiber Textile Res 37:68–75

Srianta I, Ristiarini S, Nugerahani I, Sen SK, Zhang BB, Xu GR, Blanc PJ (2014) Recent research and development of *Monascus* fermentation products. Int Food Res J 21:1–12

Sudha, Gupta C, Aggarwal S (2014) Novel Bio-colorants for textile application from fungi. J Textile Ass 282–287

Sweeny JG, Estrda-Valdes MC, Iacobucci GA, Sato H, Sakamura S (1981) Photoprotection of the red pigments of *Monascus anka* in aqueous media by 1, 4, 6-Trihydroxynaphthalene. J Agric Food Chem 29:1189–1193. doi:10.1021/jf00108a023

Tajick MA, Khani HSM, Babaeizad V (2014) Identification of biological secondary metabolites in three *Penicillium* species, *P. goditanum*, *P. moldavicum* and *P. corylophilum*. Prog biol sci 4:53–61

Takahashi JA, Carvalho SA (2010) Nutritional potential of biomass metabolites from filamentous fungi. Curr Res Edu Topics Appl Microbiol Microbial Biotechnol 1126–1135

Teixeria MFS, Martins MS, Silva JCD, Kirsch LS, Fernandes OC, Carneirol ALB, Conti RD, Duran N (2012) Amazonian biodiversity: pigments from *Aspergillus* and *Penicillium*—characterizations, antibacterial activities and their toxicities. Current Trends Biotechnol Pharmacy 6:300–311

Velisek J, Cejpek K (2011) Pigments of higher fungi: a review. Czech J Food Sci 29:87–102

Velmurugan P, Chae JC, Lakshmanaperumalsamy P, Yun BS, Lee KJ, Oh BT (2009) Assessment of the dyeing properties of pigments from five fungi and anti-bacterial activity of dyed cotton fabric and leather. Coloration Technol 125:334–341. doi:10.1111/j.1478-4408.2009.00215.x

Velmurugan P, Kamala Kannan S, Balachandar V, Lakshmanaperumalsamy P, Chae JC, Oh BT (2010a) Natural pigment extraction from five filamentous fungi for industrial application and dyeing of leather. Carbohydrate polymer 79:262–268. doi:10.1016/j.carbpol.2009.07.058

COLLEGE OF ARTS & SCIENCE NAMAKKAL 637 206

Velmurugan P, Kim MJ, Park JS, Karthikeyan K, Lakshmanaperumalsamy P, Lee KJ, Park YJ, Oh BT (2010b) Dyeing of cotton yarn with five water soluble fungal pigments obtained from five fungi. Fibers and Polymers 11:598–605. doi:10.1007/s12221-010-0598-5

Velmurugan P, Lee YH, Nanthakumar K, Kamalakannan S, Dufosse L, Mapari SAS, Oh BT (2010c) Water soluble red pigments from *Isaria farinosa* and structural characterization of the main colored component. J Basic Microbiol 50:581–590. doi:10.1002/jobm.201000097

Velmurugan P, Lee YH, Venil CK, Lakshmanaperumalsamy P, Chae JC, TaekOh B (2010d) Effect of light on growth, intracellular and extracellular pigment production by five pigment-producing filamentous fungi in synthetic medium. J Biosci Bioeng 109:346–350. doi:10.1016/j.jbiosc.2009.10.003

Vendruscolo F, Pitol LO, Carciofi BAM, Moritz DE, Laurindo JB, Schmidell W, Ninow JL (2010) Construction and application a vane system in a rotational rheometer for determination of the rheological properties of *Monascus ruber* CCT 3802. J Biorheol 24:29–35. doi:10.1007/s12573-010-0019-7

Vendruscolo F, Tosin I, Giachini AJ, Schmidelli W, Ninowi J (2013) Antimicrobial activity of *Monascus* pigments produced in submerged fermentation. J Food Processing Preservation 38:1860–1865. doi:10.1111/jfpp.12157

Venil CK, Lakshmanaperumalsamy P (2009) An insightful overview on microbial pigment, prodiogiosin. Electro J Biol 5:49–61

Wang JJ, Lee CL, Pan TM (2004) Modified mutation method for screening low citrinin-producing strains of *Monascus purpureus* on rice culture. J Agric Food Chem 52:6977–6982. doi:10.1021/jf049783o

Xu MJ, Yang ZL, Liang ZZ, Zhou SN (2009) Construction of a *Monascus purpureus* mutant showing lower citrinin and higher production by replacement of ctnA with pks1 without using vector and resistance gene. J Agric Food Chem 57:9764–9768. doi:10.1021/jf9023504

Yang T, Liu J, Luo F, Lin Q, Rosol TJ (2014) Anticancer properties of *Monascus* metabolites. Anti-Cancer Drugs 25:735–744. doi:10.1097/CAD.0000000000000102

Zhang YQ, Brock M, Keller NP (2004) Connection of propionyl-CoA metabolism to polyketide biosynthesis in *Aspergillus nidulans*. Genet 168:785–794. doi:10.1534/genetics.104.027540s

Zhang X, Wang J, Chan M, Wang C (2013) Effect of nitrogen sources on production and photostability of *Monascus* pigments in liquid fermentation. IERI Procedia 5:344–350. doi:10.1016/j.ieri.2013.11.114

P.G.P. COLLEGE OF ARTS & SCIENCE NAMAKKAL 637 206

PRINCIPAL
PGP College of Arts and Science
Namakkal



Science Alert
scialert.net

HOME JOURNALS AUTHORS SUBSCRIBERS CONTACT US

Search

Journal of Applied Sciences

DOI: 10.3923/jas.2019.140.147

Identification of Antibacterial Compound from *Bacillus horikoshii*, Isolated from Rhizosphere Region of Alfalfa Plant

Nukarinkhan Nayak, R. Ramkumar, R. Mahesh, S. Saravanakumar, D. Vivekanandhan and S. Ramalingam

Abstract: Background and Objective: With increase in multiple drug resistance pathogens, it is necessary to look for new drug study compounds of microbial origin. Thus study was aimed to identify the rhizosphere microflora of unexplored alfalfa plant for new antimicrobials. **Materials and Methods:** Based on screening done, the isolates were subjected to antibacterial activity against selected bacteria. The isolate was mass cultured and secondary metabolites were extracted using ethyl acetate. The crude extracts collected were subjected to FTIR and GC-MS analysis. **Results:** Based on functional diversity analysis, the isolate subjected to anti-bacterial activity revealed significant activity against *Klebsiella* and *Staphylococcus aureus* with zone of inhibition in the range of 17-18 mm. Based on GC-MS analysis reports, six compounds were identified and 11-Octadecanal responsible for bio activity. FT

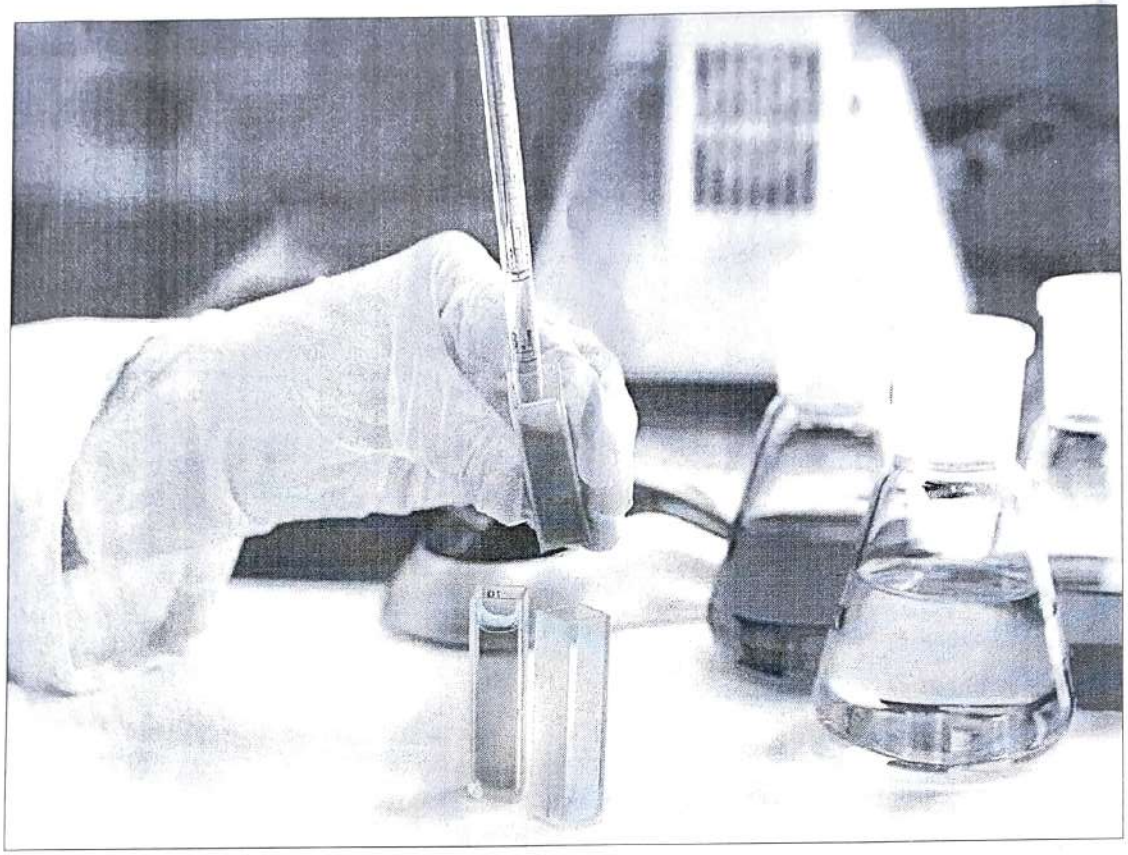
Navigation

- Online First
- Current Issue
- Previous Issues
- Editorial Board
- Submit a Manuscript
- Guide to Authors
- Subscribe to E-alerts

Indexed In

- ASFIS
- ASCI-Database
- Asian Digital Library
- Chemical Abstract Services

P.G. COLLEGE OF ARTS & SCIENCE
NAMAKKAL
637 206



Journal of Applied Sciences

ISSN 1812-5654

science alert

ANSInet
an open access publisher
http://ansinet.com

P.G.P. COLLEGE OF ARTS & SCIENCE
NAMAKKAL
637 206

OPEN ACCESS

Journal of Applied Sciences

ISSN 1812-5654
DOI: 10.3923/jas.2019.140.147

Research Article
Identification of Antibacterial Compound from *Bacillus horikoshii*, Isolated from Rhizosphere Region of Alfalfa Plant

[1]Nisha M. Nair, [2]R. Kanthasamy, [3]R. Mahesh, [4]S. Iruthaya Kalai Selvam and [1]S. Ramalakshmi

[1]Department of Microbiology, Karpagam Academy of Higher Education, 641 021 Coimbatore, Tamil Nadu, India
[2]PG and Research Centre of Botany, Rani Anna Govt. College for Women, 627 008 Tirunelveli, Tamil Nadu, India
[3]PG and Research Centre of Botany, South Travancore Hindu College, 629 002 Nagercoil, Kanyakumari District, Tamil Nadu, India
[4]PG and Research Centre of Zoology, Jayaraj Annapackiam College for Women (Autonomous), Periyakulam, 625 601 Theni District, Tamil Nadu, India

Abstract

Background and Objective: With increase in multiple drug resistance pathogens, it is necessary to look for new drug study compounds of microbial origin. Thus study was aimed to identify the rhizosphere microflora of unexplored alfalfa plant for new antimicrobials. **Materials and Methods:** Based on screening done, the isolates were subjected to antibacterial activity against selected bacteria. The isolate was mass cultured and secondary metabolites were extracted using ethyl acetate. The crude extracts collected were subjected to FTIR and GC-MS analysis. **Results:** Based on functional diversity analysis, the isolate subjected to anti-bacterial activity revealed significant activity against *Klebsiella* and *Staphylococcus aureus* with zone of inhibition in the range of 17-18 mm. Based on GC-MS analysis reports, six compounds were identified and 11-Octadecanal responsible for bio-activity. FT-IR results showed that N-H stretching functional group dominantly present in the extract. Molecular identification of the isolate by 16S rRNA sequencing showed the isolate as *Bacillus horikoshii*. **Conclusion:** The study results showed that the isolate *Bacillus horikoshii*, Gram-positive spore forming bacteria had wide antibacterial activity due to 11-Octadecanal. Thus Alfalfa plant rhizosphere region harbors antibacterial potential microbes.

Key words: Alfalfa plant, antibacterial activity, *Bacillus horikoshii*, gas chromatography-mass spectrometry, rhizosphere

Citation: Nisha M. Nair, R. Kanthasamy, R. Mahesh, S. Iruthaya Kalai Selvam and S. Ramalakshmi, 2019. Identification of antibacterial compound from *Bacillus horikoshii*, isolated from rhizosphere region of alfalfa plant. J. Applied Sci., 19: 140-147.

Corresponding Author: Ramalakshmi Subbiah, Department of Microbiology, Karpagam Academy of Higher Education, 641 021 Coimbatore, Tamil Nadu, India Tel: 8608000835, 9600202880

Copyright: © 2019 Nisha M. Nair *et al.* This is an open access article distributed under the terms of the creative commons attribution License, which permits unrestricted use, distribution and reproduction in any medium, provided the original author and source are credited.

Competing Interest: The authors have declared that no competing interest exists.

Data Availability: All relevant data are within the paper and its supporting information files.

P.G. COLLEGE OF ARTS & SCIENCE NAMAKKAL 637 205

INTRODUCTION

Alfalfa (*Medicago sativa*) means "father of all foods" belongs to Leguminosae family. It is a perennial herbaceous leguminous flowering plant known as Queen of Forage plant, lives upto 8 years. Due to its high protein content and fiber, they are cultivated worldwide and widely used as fodder for cows[1]. The crop is autorotated before reseeding due to its toxins having an allelopathic effect for other plants growth. The plant also has deep root system, thereby improving soil and water holding ability of plants. Alfalfa fixes high nitrogen than other plants due to its symbiotic association with microbes.

Medicago sativa, a therapeutic value plant has been reported for a number of phytopharmacological activities such as neuroprotective, hypocholesterolemic, antioxidant, antiulcer, antimicrobial, hypolipidemic, estrogenic and in the treatment of atherosclerosis, heart disease, stroke, cancer, diabetes[2] and menopausal symptoms in women[3-10].

The plant extract has been reported to possess bioactive compounds namely saponins, flavonoids, phytoestrogens, coumarins, alkaloids, amino acids, phytosterols, vitamins, digestive enzymes and terpenes[11-13].

Based on preliminary functional diversity studies carried (unpublished results) on the isolation of microbes from the rhizosphere of alfalfa plant. Out of 32 isolates, this isolate was selected for its amylase, cellulase, protease and phosphate solubilization activities. Thus the study was aimed at isolating the functionally diverse organism from rhizosphere soil region of Alfalfa plant (*Medicago sativa*) and identifying the bioactive compound responsible for antibacterial action.

MATERIALS AND METHODS

Sample collection: Soil sample was collected from the rhizosphere region of Alfalfa plant fields during June 2016 from Sulur, Coimbatore, Tamilnadu, India. Studies were carried out from June, 2016 to March, 2017 (Fig. 1).

Isolation and identification of micro-organism: One gram of the collected soil samples were used for serial dilution to isolate microbes by spread plate method. To the nutrient agar plates, 0.1 mL of serially diluted samples (10^{-1} to 10^{-7}) were plated, incubated at 37°C for 24-72 h. After incubation, bacterial isolates were checked for purity and preserved in glycerol stocks and as nutrient agar slants for further tests.

These colonies were observed for Gram's nature and morphological characters such as size, shape, color, texture,

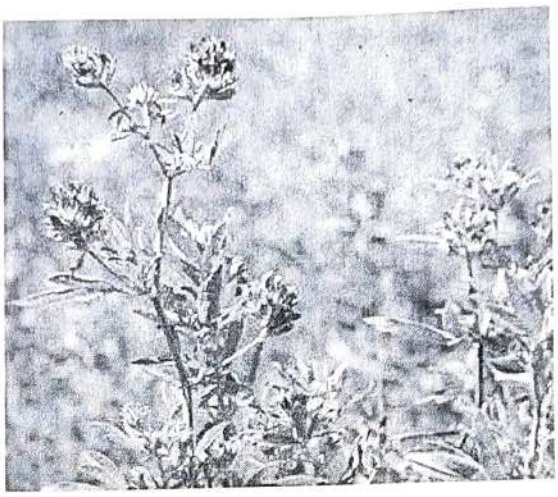


Fig. 1: Alfalfa plant (*Medicago sativa*)

opacity, elevation, margin and mobility. They were further identified using biochemical methods as stated in Bergey's manual for characterization which includes Indole, Methyl Red, VogesPrauskaeur, citrate, urease and TSI slants etc.

Antibacterial activity: The antimicrobial activities of crude extracts of all isolated bacteria were tested against bacterial pathogens by agar well diffusion method. Muller-Hinton agar (MHA) plates were prepared and the wells were made with sterile cork borer on the agar plates. The overnight grown nutrient broth cultures of all bacterial pathogens were uniformly swabbed on to the surface of MHA plates using sterile cotton swabs. Each 50 µL of cell free supernatants were aseptically incorporated into the well and the plates were incubated in an upright position at 37°C for 24 h. After incubation, the plates were observed for zone of inhibition.

Production and extraction of the bioactive compounds: For obtaining the large biomass, the active strain were inoculated into 1 L of nutrient agar medium and incubated in shaker at 30°C at 160 rpm for 36 h. After incubation, the media contents were centrifuged at 10,000 rpm for 10 min to obtain the cell free supernatant.

The cell free supernatant extracted with organic solvent-ethyl acetate and extraction carried out with 3 volume of solvent for 2 h by using rotary shaker supernatant fractions were flash evaporated at 45°C temperature to ensure complete removal of solvent and the extracts were evaporated to dryness. The resulting residues were dissolved in small amount of respective solvents and stored at -20°C until further purified.

P.G.P. COLLEGE OF ARTS & SCIENCE NAMAKKAL 637 206

Molecular identification and phylogenetic analysis of the bioactive compound

Genomic DNA isolation: DNA isolation from bacterial isolate performed according to the cold spring harbour lab protocol. Briefly, the isolates were grown in Nutrient Broth (Himedia, India) for 24 h days at 37°C, pelleted and washed in 1 mL Tris-EDTA (TE) buffer. The pellets were resuspended in 500 µL TE buffer containing 1 mg mL^{-1} lysozyme. After incubation at room temperature for 2 h, 75 µL of 10% Sodium Dodecyl Sulfate (SDS) and 125 µL of 5 M NaCl were added to this mixture. The samples were centrifuged (10,000 rpm for 10 min at room temperature) and incubated in ice cold ethanol (-70°C) for 3 min, later in a 65°C water bath for 3 min and on ice for 10 min. RNase (200 µg mL^{-1} of sample) added to the supernatant to remove RNA contamination and the mixture incubated at 37°C for 15 min.

Proteinase K (50 µg mL^{-1} of sample) added to content and the mixture was incubated at 37°C for 30 min. An equal volume of phenol/chloroform/isoamyl alcohol (25:24:1) with upper aqueous phase recovered after centrifugation (10,000 rpm for 10 min at room temperature). To this an equal volume of chloroform/isoamyl alcohol (24:1) added and upper aqueous phase transferred to a new microfuge tubes after centrifugation (10,000 rpm for 5 min at room temperature). The DNA precipitated by mixing the aqueous phase with 50 µL of 3 M sodium acetate, 300 µL of ice-cold isopropyl alcohol and incubated at -20°C for 20 min. The DNA pelleted and washed twice with 70% ethanol. The pellet blot dried and resuspended in 40 µL of TE buffer and stored at -20°C.

Amplification of 16S rRNA gene: 16S rRNA genes were amplified from the extracted genomic DNA using the 8 F and 1541 R universal eubacterial primers designed to target the conserved regions in the genomic DNA of the isolates and amplify approximately 1.4 kb length gene. The forward primer 5`-AGAGTTTGATCCTGGCTCAG-3` and reverse primer 5`-AAGGAGGTGATCCAGCCGCA-3` were used for amplification.

The PCR mix contained 5 µL of 25×PCR buffer, 4 µL of 25 mM $MgCl_2$, 5 µL of 5 µM 518 Forward Primer and 5 µL of 5 µM 800 Revers Primer, 5 µL of 1 mM dNTP's, 0.5 µL of *Taq* DNA polymerase (Thermo Scientific, India) and 2 µL of genomic DNA.

The reaction volume adjusted and made up to a final volume of 50 µL with sterile double-distilled water and amplified in an automated thermal cycler (Vapo protect Pro S, Eppendorf). The PCR conditions were an initial denaturation stage at 95°C for 2 min, followed by 35 cycles of denaturation at 94°C for 45 sec, annealing at 55°C for 60 sec, extension at 72°C for 60 sec and a final extension step at 72°C for 10 min. Negative controls with no DNA template were included in all PCR experiments.

16S rRNA gene sequencing: The Polymerase Chain Reaction (PCR) products were purified with a Montage PCR Clean up kit (Millipore) as per the manufacturer's instructions. The purified PCR products were then sequenced. Sequencing was performed by using Big Dye terminator cycle sequencing kit (Applied BioSystems, USA). Sequencing products were resolved on an Applied Biosystems model 3730XL automated DNA sequencing system (Xcelris Laboratories, India).

Phylogenetic analysis: The 16s rRNA sequence was blast using NCBI blast similarity search tool. The phylogeny analysis of query sequence with the closely related sequence of blast results performed followed by multiple sequence alignment. The program MUSCLE 3.7 used for multiple alignments of sequences. The resulting aligned sequences were cured using the program Gblocks 0.91b. This Gblocks eliminates poorly aligned positions and divergent regions (removes alignment noise). Finally, the program PhyML 3.0 aLRT used for phylogeny analysis and HKY85 as Substitution model.

FTIR analysis: The purified bacterial extract was subjected to FTIR spectroscopic analysis (Perkin Elmer Lambda), equipped with KBr beam splitter with DTGS (Deuterated triglycine sulfate) detector. The technique work on the fact that bonds and groups of bonds vibrate at characteristic frequencies. A molecule that is exposed to infrared rays absorbs infrared energy at frequencies, which are characteristic to that molecule.

GC-MS analysis: The Thermo MS DSQ II used for the analysis packed DB 35-MS capillary standard non-polar column and the components were separated using Helium as carrier gas at a flow of 1 mL min^{-1}. The injector temperature set at 260°C during the chromatographic run. The volume of sample injected 1 µL at an oven temperature of 70°C (6 min). Interpretations on mass spectrums of GC-MS were done using the database of National Institute Standard and Technology (NIST) having more than 62,000 patterns. The mass spectra of the unknown components will be compared with the spectrum of the known components stored in the NIST library. The name, molecular weight and structure of the components of the test materials will be ascertained.

PERIYAR COLLEGE OF ARTS & SCIENCE NAMAKKAL 637 206

RESULTS AND DISCUSSION

Antibacterial activity: The rhizosphere region of soil carries a heterogeneous group of microbial population which can play a vital role in soil function. The antibacterial activity of the crude extract of the isolate studied against 7 clinical pathogens (*P. aeruginosa*, *Klebsiella* sp, *S. aureus*, *Proteus vulgaricus*, *S. pneumonia*, *E. coli* and *B. cereus*). The isolate showed significant zone of inhibition against *Klebsiella* sp. and *S. aureus* (18 and 17 mm) (Fig. 2).

Similar reports by researchers showed that the microbes isolated form rhizosphere region possessed significant anti-microbial activity. Ramakrishnan *et al.*[14] reported the wide range of antibacterial activity of *Streptomycetes* sp. isolated from the rhizosphere soil of medicinal plants at Kolli hills of Tamil Nadu. Ryandini *et al.*[15] isolated *Streptomyces* sp. from mangrove rhizosphere mud of rhizophora mucronata from east Segara Anakan mud and reported significant activity on multiple drug resistant bacteria.

Also Rajalakshmi and Mahesh[16] reported antimicrobial activity of *Aspergillus terrus* isolated from rhizosphere region of medicinal plants in and around Kuttralam, Tirunelveli. Upon GC-MS analysis, ten compounds were identified and tetracontane was reported to be bioactive potential compound.

Molecular characterization of the isolates: The genomic DNA of the isolate isolated and subjected to 16S rRNA gene amplification for the species identification. PCR product of the length 1,400 bp purified and sequenced in Yaazhxenomics lab, Coimbatore. The 16S rRNA sequences of the isolate subjected to BLAST analysis using mega blast tool of GenBank (http://www.ncbi.nlm.n ih.gov/). Among different species comprising of closet neighbouring strains in NCBI-BLAST analysis used in the phylogenetic analysis. The phylogenetic trees were constructed based on the neighbour joining method and percentage differences in the genetic relationships between the neighbouring strains of the two samples were analyzed.

Results revealed that the 16S rRNA partial gene sequence of the isolate showed 97% similarity with *B. horikoshii* (Fig. 3, 4). The 16S rRNA gene sequence submitted to the Gene bank (NCBI, USA) and Genebank ID accession number MK226527 received.

FTIR analysis: Figure 5 depicted the FTIR analysis of the *B. horikoshii* extract showing strong peaks at 3417, 1643.35, 1097.5, 1658.78, 2926 and 715 cm^{-1}, respectively. Major group was found to be N-H stretching at 3417 cm^{-1} (Table 1). The FTIR results elucidated an array of functional groups at a frequency ranges indicating the presence of functional groups

Table 1: FTIR analysis of *B. horikoshii* extract

Peak	Corr. intensity	Corr. area	Functional group	Type of vibration
3417.86	70.60	346.46	N-H	Stretch
1643.35	55.86	59.91	C=C	Stretch
1097.5	30.93	30.24	C-O	Stretch
1411.89	13.97	4.61	-CH-	Bending
2802.57	13.67	11.38	O-H	Stretch
2877.79	11.97	2.29	O-H	Stretch

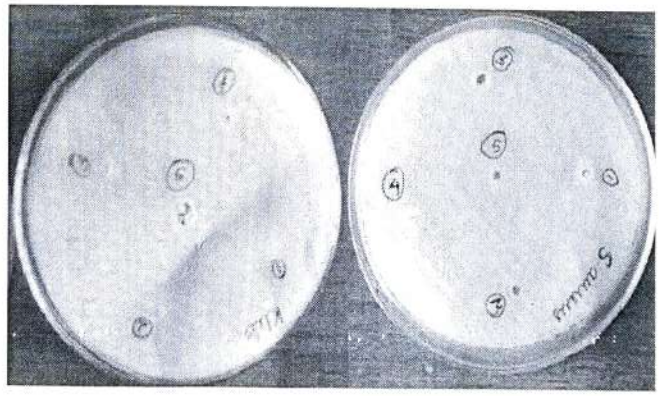


Fig. 2: Antibacterial activity of AL5 against *Klebsiella* and *S. aureus*

P.G.P. COLLEGE OF ARTS & SCIENCE NAMAKKAL 637 208

Table 2: GCMS analysis of compounds obtained from *B. horikoshii* extract

RT	Name of the compound	Molecular formula	MW	Peak area (%)
10.40	4-Cyano-2H-1-benzothiopyran	C10H7NS	173.00	8.12
15.49	Hexadecane	C16H34	226.00	4.89
19.59	1-Octadecene	C18H36	252.00	6.47
23.03	9,9-Dimethyl-8,10-dioxapentacyclo[5.3.0.0(2,5).0(3,5).0(3,6)]decane	C10H14O2	1663.75	
27.37	5-Octadecenal	C18H34O	226.00	3.73
36.19	11-Octadecenal	C18H34O	266.00	11.55

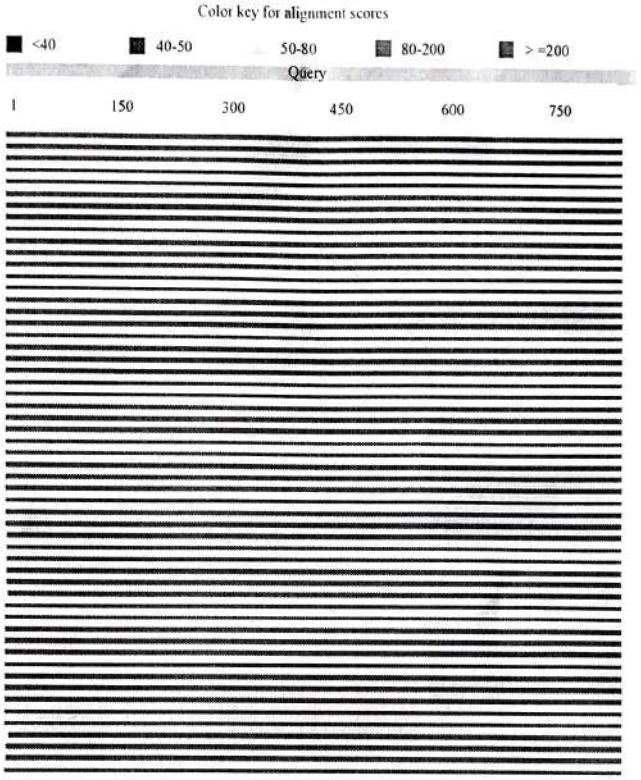


Fig. 3: Multiple alignment scores of *Bacillus horikoshii*

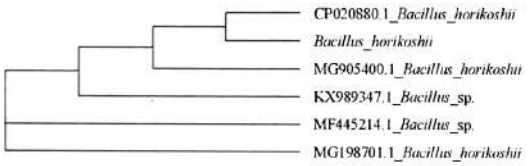


Fig. 4: Phylogenetic tree of *B. horikoshii* based on the 16S rRNA gene sequencing

corresponding to aromatic alkenes, aliphatic amines, compounds with aromatic rings, alkynes, amides, alcohols and phenols. The presence of such functional groups could be attributed to the bioactive nature of the partial fraction of *B. horikoshii* cell free supernatant.

GC-MS analysis: Figure 6 depicted the GC-MS analysis of *B. horikoshii* extract revealing presence of 31 peaks and 6 compounds were characterized and identified by comparison of the mass spectra of the constituents with the NIST library (Table 2, 3). The retention times (RT) are represented in minutes.

Stearyl alcohol, 11-octadecenal had highest intensity of 11.55% at retention time of 36.19 min. 11-Octadecenal has been reported to be present in essential oils from *Launaea resedifolia* L., possess antibacterial activity in range[17] of 11-37 mm. Similarly the presence of 9-octadecenal observed in marine red alga *Laurencia brandenii* showed various biological activities[18].

P.G. & R. COLLEGE OF ARTS & SCIENCE NAMAKKAL 637 206

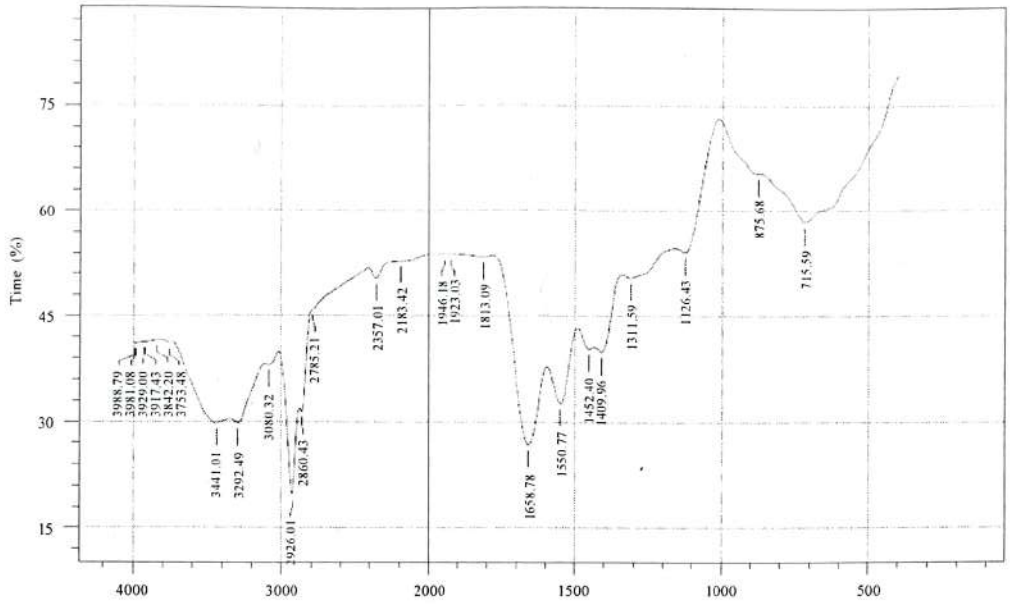


Fig. 5: FTIR spectrum of *B. horikoshii* extract

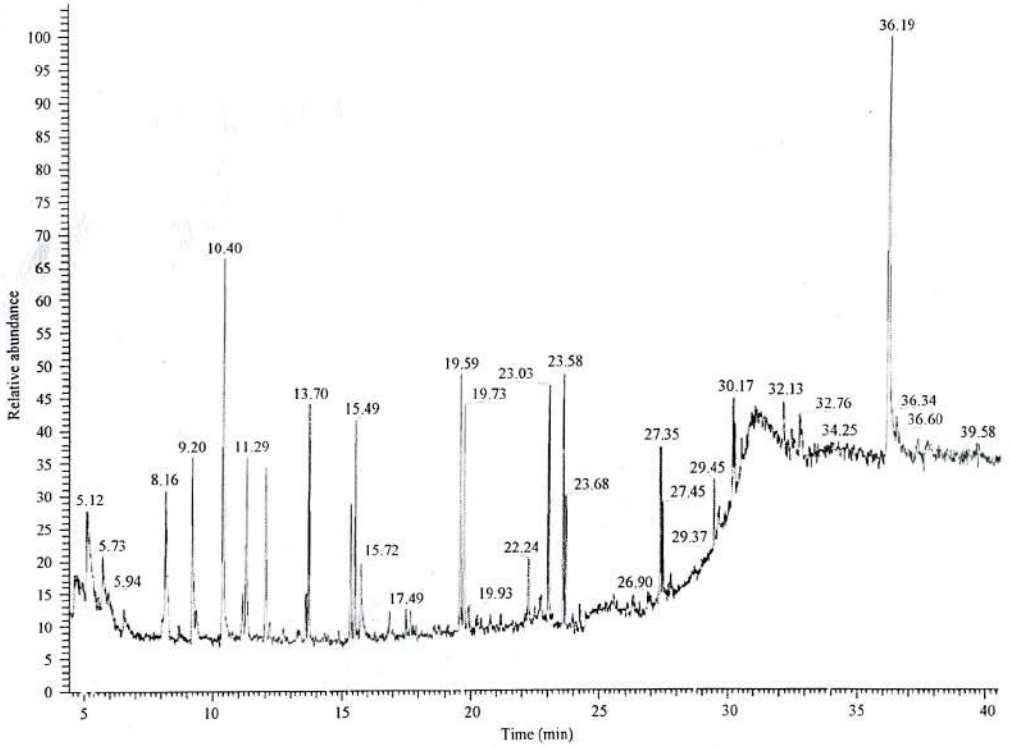


Fig. 6: GCMS spectrum analysis of *B. horikoshii* extract

145
NAMAKKAL
637 206

Table 3: Activity of compounds identified in *B. horikoshii* extract

RT	Name of the compound	Compound nature	Activity
10.40	4-Cyano-2H-1-benzothiopyran	Bicyclic benzene	Antibacterial activity Antimalarial Anti-coagulant
15.49	Hexadecane	Fatty alcohol	Emulsifier
19.59	1-Octadecene	Alkane hydrocarbon	Not reported
23.03	9,9-Dimethyl-8,10-dioxapentacyclo[5.3.0.0(2,5).0(3,5).0(3,6)]decane	Alkane	Not reported
27.37	5-Octadecenal	Stearyl alcohol	Lubricant
36.19	11-Octadecenal	Stearyl alcohol	lubricant

The next major constituent for *B. horikoshii* extract was found to be 4-Cyano-2H-1-benzothiopyran at retention time 10.4 min and intensity of 8.12%. 4-Cyano-2H-1-benzothiopyran, a bicyclic benzene reported to have antibacterial action, antimalarial and anti-tumor activities especially against colon cancer[19,20]. Fatty alcohol hexadecane with retention time of 15.49 min. The alkane hydrocarbon octadecane was found at the retention time of 19.59 min.

Similarly *Bacillus* strain isolated from the groundnut rhizosphere soil reported by Bharose and Gajera *et al.*[21] had biocontrol activity against aflatoxin producing *Aspergillus* strain. GCMS analysis of *Bacillus subtilis* revealed presence of 55 compounds, out of which 2-hydroxy-4-phenyl-6-phenethyl pyrimidine (10%) identified as bioactive compound responsible for anti-fungal action.

Saranya Devi and Mohan[22] studied the rhizosphere region of *Casuarina equisetifolia* and identified that *Bacillus pumilus* showed high inhibition against *Fusarium oxysporum*. The ethyl acetate extract of *Bacillus pumilus* on GC-MS analysis revealed presence of 19 compounds and Cis-3-chloro all alcohol and 9-octadecenamide as predominant bioactive compounds responsible for salt tolerance and antifungal activity.

CONCLUSION

Through this study we were able to isolate new antimicrobials against potent pathogens. Based on molecular identification the active isolate of rhizosphere region of Alfaalfa plant was identified as *Bacillus horikoshii*. The studies on the rhizosphere region isolate *Bacillus horikoshii* extract lead to identification of 11 volatile compounds and study on the antimicrobial activity showed that action to be due to presence of 11-octadecenal. Thus further *in vitro* and *in vivo* biological studies are required for anticancer medical applications in various fields.

REFERENCES

1. Frame, J., 2005. *Medicago sativa* L. FAO Grassland Index: A Searchable Catalogue of Grass and Forage Legumes, Crop and Grassland Service, Agriculture Department, Food and Agriculture Organization, Rome, Italy.
2. Gray, A.M. and P.R. Flatt, 1997. Pancreatic and extra-pancreatic effects of the traditional anti-diabetic plant, *Medicago sativa* (lucerne). Br. J. Nutr., 78: 325-334.
3. Story, J.A., S.L. LePage, M.S. Petro, L.G. West, M.M. Cassidy, F.G. Lightfoot and G.V. Vahouny, 1984. Interactions of alfalfa plant and sprout saponins with cholesterol *in vitro* and in cholesterol-fed rats. Am. J. Clin. Nutr., 39: 917-929.
4. Avato, P., R. Bucci, A. Tava, C. Vitali, A. Rosato, Z. Bialy and M. Jurzysta, 2006. Antimicrobial activity of saponins from *Medicago* sp.: Structure-activity relationship. Phytother. Res., 20: 454-457.
5. Zhang, L., D. Zhang and K. Feng, 2006. Inhibition of refined components of *Medicago sativa* polysaccharides to the activities of reverse transcriptase of HIV and protease of HIV. J. Chin. Inst. Food Sci. Technol., 6: 59-62.
6. Huyghe, C., E. Bertin and N. Landry, 2007. Medicinal and Nutraceutical Uses of Alfalfa (*Medicago sativa* L.): A Review. In: Advances in Medicinal Plant Research, Acharya, S.N. and J.E. Thomas (Eds.). Research Signpost, Trivandrum, Kerala, India, pp: 147-172.
7. Bora, K.S. and A. Sharma, 2011. Phytochemical and pharmacological potential of *Medicago sativa*: A review. Pharmaceut. Biol., 49: 211-220.
8. Bora, K.S. and A. Sharma, 2011. Evaluation of antioxidant and cerebroprotective effect of *Medicago sativa* Linn. against ischemia and reperfusion insult. Evidence-Based Complement. Altern. Med., Vol. 2011. 10.1093/ecam/neq019.
9. Krakowska, A., K. Rafinska, J. Walczak, T. Kowalkowski and B. Buszewski, 2017. Comparison of various extraction techniques of *Medicago sativa*: Yield, antioxidant activity and content of phytochemical constituents. J. AOAC Int., 100: 1681-1693.
10. Argentieri, M.P., T. D'Addabbo, A. Tava, A. Agostinelli, M. Jurzysta and P. Avato, 2008. Evaluation of nematicidal properties of saponins from *Medicago* spp. Eur. J. Plant Pathol., 120: 189-197.

11. El-Khrisy, E.A.M., O.M. Abdel Hafez, A.A. Khattab and K.M. Ahmed, 1994. Chemical constituents of *Medicago sativa* L. Bull. Natl. Res. Centre (Egypt), 19: 117-122.
12. Biagioni, M., A. Alpi and P. Picciarelli, 1990. Aminopeptidases (EC. 3.4.11) in alfalfa (*Medicago sativa* L.) leaves. J. Plant Physiol., 135: 559-564.
13. Bialy, Z., M. Jurzysta, W. Oleszek, S. Piacente and C. Pizza, 1999. Saponins in alfalfa (*Medicago sativa* L.) root and their structural elucidation. J. Agric. Food Chem., 47: 3185-3192.
14. Ramakrishnan, J., M. Shunmugasundaram and M. Narayanan, 2009. *Streptomyces* sp. SCBT isolated from rhizosphere soil of medicinal plants is antagonistic to pathogenic bacteria. Iran. J. Biotechnol., 7: 75-81.
15. Ryandini, D., O.K. Radjasa and Oedjijono, 2018. Isolate actinomycetes SA32 origin of Segara Anakan mangrove rhizosphere and its capability in inhibiting multi-drugs resistant bacteria growth. J. Microb. Biochem. Technol., 10: 1-7.
16. Rajalakshmi, S. and N. Mahesh, 2014. Production and characterization of bioactive metabolites isolated from *Aspergillus terreus* in rhizosphere soil of medicinal plants. Int. J. Curr. Microbiol. Applied Sci., 3: 784-798.
17. Zellagui, A., N. Gherraf, S. Ladjel and S. Hameurlaine, 2012. Chemical composition and antibacterial activity of the essential oils from *Launaea resedifolia* L. Org. Med. Chem. Lett., Vol. 2. 10.1186/2191-2858-2-2.
18. Manilal, A., S. Sujith, B. Sabarathnam, G. Kiran, J. Selvin, C. Shakir and A. Lipton, 2011. Biological activity of the red alga *Laurencia brandenii*. Acta Bot. Croatica, 70: 81-90.
19. Nakazumi, H., T. Ueyama and T. Kitao, 1985. Antimicrobial activity of 3-(substituted methyl)-2-phenyl-4*H*-l-benzothiopyran-4-ones. J. Heterocycl. Chem., 22: 1593-1596.
20. Abbas, E.M.H., S.M. Gomha and T.A. Farghaly, 2014. Multicomponent reactions for synthesis of bioactive polyheterocyclic ring systems under controlled microwave irradiation. Arabian J. Chem., 7: 623-629.
21. Bharose, A.A. and H.P. Gajera, 2018. Antifungal activity and metabolites study of bacillus strain against aflatoxin producing *Aspergillus*. J. Applied Microbiol. Biochem., Vol. 2, No. 2. 10.21767/2576-1412.100024.
22. Saranya Devi, K. and V. Mohan, 2017. Screening and molecular characterization of salt tolerant bio-control bacterial isolates from *Casuarina equisetifolia* rhizosphere soil. Asian J. Plant Pathol., 11: 156-166.

P.G.P. COLLEGE OF ARTS & SCIENCE NAMAKKAL 637 206

PRINCIPAL
PGP College of Arts and Science
Namakkal

Nano Biomedicine and Engineering

Development of Nanodrug for Treatment of Breast Cancer Using Mallotus Tetracoccus Leaves - Standardisation, Synthesis and Characterisation

Ramalaksmi Subolan, Krishnaswamy Muthuchelian

Views 2060

Abstract

In this study, an ecofriendly, green method for synthesis of silver nanoparticles (AgNPs) has been developed using *Mallotus tetracoccus* (VT) leaves as a reducing agent. The formation of AgNPs was standardised at pH 7 and 30°C. UV-visible spectroscopy showed the high peak of absorption band at 420 nm. By atomic force microscopic (AFM) and scanning electron microscopic (SEM) observations, the size of the silver nanoparticles was found to be in the range of 45 to 100 nm, with an average size of 73 nm. The energy dispersive x-ray spectroscopic (EDX) profile of silver nanoparticles showed typical optical absorption peak approximately at 3 keV. FTIR spectroscopic study revealed that hydroxyl groups of phenols and carboxylic acids were involved in the formation of AgNPs. Through MTT assay, the cytotoxicity results showed that AgNPs were highly effective on human ductal breast carcinoma cell lines (T47D) (76.8 to 84.9 %). Thus, the VT-synthesized NPs are said to possess significant anticancer activity on cancer cells and very less toxicity on normal cells, which suggests its further

...ating for enjoy tunes.

Nano Biomed Eng
2016, 8(2): 82-90. doi: 10.5101/nbe.v8i2.p82-90

GHOST

Research Article

Development of Nanodrug for Treatment of Breast Cancer Using *Mallotus Tetracoccus* Leaves-Standardisation, Synthesis and Characterisation

Ramalakshmi Subbiah[1,2], Krishnaswamy Muthuchelian[1]

[1]Department of Bioenergy, School of Energy, Environment and Natural Resources, Madurai Kamaraj University, Madurai – 625 021, India.
[2]Department of Agricultural Microbiology, Tamilnadu Agricultural University, Coimbatore-641003.

Corresponding author. Telephone: +91 452 2458020. E-mail: drchelian1960@yahoo.co.in

Received: May 13, 2016, **Accepted:** Jun. 15, 2016, **Published:** Jun. 20, 2016.

Citation: Ramalakshmi Subbiah, Krishnaswamy Muthuchelian, Development of Nanodrug for Treatment of Breast Cancer Using *Mallotus Tetracoccus* Leaves - Standardisation, Synthesis and Characterisation. *Nano Biomed. Eng.*, 2016, 8(2): 82-90.
DOI: 10.5101/nbe.v8i2.p82-90.

Abstract

In this study, an ecofriendly, green method for synthesis of silver nanoparticles (AgNP) has been developed using *Mallotus tetracoccus* (MT) leaves as a reducing agent. The formation of AgNPs was standardised at pH 7 and 60 °C. UV-visible spectroscopy showed the high peak of absorption band at 420 nm. By atomic force microscopic (AFM) and scanning electron microscopic (SEM) observations, the size of the silver nanoparticles was found to be in the range of 46 to 100 nm, with an average size of 73 nm. The energy dispersive x-ray spectroscopic (EDX) profile of silver nanoparticles showed typical optical absorption peak approximately at 3 keV. FTIR spectroscopic study revealed that hydroxyl groups of phenols and carboxylic acids were involved in the formation of AgNPs. Through MTT assay, the cytotoxicity results showed that AgNPs were highly effective on human ductal breast carcinoma cell lines (T47D) (76.8 to 84.9%). Thus, the MT-synthesized NPs are said to possess significant anticancer activity on cancer cells and very less toxicity on normal cells, which suggests its further applications in medicine.

Keywords: Nanodrug; *Mallotus tetracoccus*; Green synthesis; Silver nanoparticles; Anticancer activity

Introduction

Mallotus tetracoccus (Roxb.) Kurz. of family Euphorbiaceae, found in Western Ghats of India. The common names include *Thavatta*, *Vatta*, *Vatta kumbil*, *Vetta kumbil* (malayalam), *Uppale mara* (kannada) and "vatta kanni" in Tamil. Several species of the genus *Mallotus* are a rich source of biologically active compounds such as phloroglucinols, tannins, terpenoids, coumarins, benzopyrans and chalcones [1, 2]. The reported bioactivities of the extracts or the individual chemical constituents isolated from this genus include antipyretic [3], anti-inflammatory, hepatoprotective [4], antioxidant and radical scavenging activities [5].

The GC-MS analysis of *Mallotus tetracoccus* ethanolic leaf extract have revealed the presence of Bis (2-ethyl hexyl) phthalate (46.78 %), 3-methyl-2-(2-

P.G.P. COLLEGE OF ARTS & SCIENCE

oxypropyl) furan (13.31%), E-8-methyl-9-tetradecen-1-ol acetate (6.63 %), Octadecanoic acid, 2-oxo (4.46 %) and Longiborneol (2.39%) [6]. The bark of *M. tetracoccus* have been reported for high antioxidant and antibacterial activity [7]. Also, the bark extract studied for GC-MS showed presences of thiocyanic acid, furfural and 4H- Pyran-4 –one, 2, 3- Dihydro-3, 5- dihydroxy-6- methyl compounds. The bark extract showed significant cytotoxicity and phytotoxicity on radish seeds [8].

Thus, the leaves of MT have been used for synthesis of silver nanoparticles. Since time immemorial, silve has been used for curing various diseases due to its antibacterial properties. Recently, silver is gaining a role in development of nanoparticles for cancer therapy, biosensors, dressings, devices, formulations etc. [9]. The objective of this study was to characterize and study the anticancer potential of silver nanoparticles synthesized from MT leaf extract.

Materials and Methods

Plant material and preparation of the extract

Fresh and intermediate leaves of *Mallotus tetracoccus* (Roxb.) Kurz was collected from Agasthiar Malai Biosphere Forest, Western Ghats, collected plant materials were identified and authenticated by the Director, Centre for Biodiversity and Forest Studies (CBFS), MKU, and voucher specimens were deposited in the herbarium of CBFS of university (No. AM-02). The dry leaves was cut into small pieces and powdered finely. About 5 g of the leaf powder was boiled for 10 min in 100 ml sterile double distilled water and further filtered through Whatman No. 1 filter paper and used for the present study.

Synthesis of silver nanoparticles

Silver nitrate ($AgNO_3$) procured from Sigma-Aldrich (Bangalore, India) was used. For the synthesis of silver nanoparticles, $AgNO_3$ (2 mM) and aqueous plant extract (10 mg/ml) were mixed in different ratios. Briefly, 1 ml of plant extract was mixed with 9 ml of $AgNO_3$ (1:9 ratio). The subsequent mixtures were prepared by increasing plant extract and decreasing $AgNO_3$ volumes by 1 ml, until the final ratio of 9:1was attained. Furthermore, appropriate concentrations of $AgNO_3$ and plant extracts vice versa from 1 to 9 ratio mixed in a series of reactions for optimization of synthesis of silver nanoparticles, incubated overnight at room temperature in dark. The resultant yellowish brown solution indicated the formation of silver nanoparticles.

The above mentioned procedure was repeated for optimization of temperature and pH. The pH was studied in the range of 5, 6, 7, 8 and 9 by using 0.1 N HCl and 0.1 N NaOH respectively. The reaction temperature was studied at 30 °C to 70 °C.

Purification of silver nanoparticles

The broth containing nanoparticles was centrifuged at 15000 rpm for 15 min to obtain the pellet which was redispersed in sterile deionized water to get rid of any biological molecules. The process of centrifugation and redispersion in sterile deionized distilled water was repeated thrice to obtain better separation of entities from the metal nanoparticles. The purified pellet was then freeze dried using Lyophillizer (Micro Modulyo 230 freeze dryer, Thermo Electron Corporation, India).

UV–visible spectral analysis

The colour change was observed in the silver nitrate solution incubated with aqueous plant extract. The bioreduction of Ag nanoparticles was monitored by periodic sampling of aliquots (0.2 mL) of aqueous component and measuring the absorbance and spectrum of the solution in UV spectrophotometer (Shimadzu, UV 2500, Japan), at a resolution of 1 nm between 300 and 600 nm. The nanoparticle solution was diluted 20 times with deionized water to avoid errors due to high optical density of the solution.

Atomic force microscopy

A thin film of the sample was prepared on a cover slip by droping 0.1 ml of the sample on the slide, and allowed to dry for 30 minutes. The slide was then scanned with AFM (APE Research-model no: A100SGS). The AFM characterization was carried out in ambient temperature in non contact mode using silicon nitrate tips with varying resonance frequencies. These tips have spring constants of approximately 0.15 Nm-1 and are conical in shape with a cone angle of 20° and an effective radius of curvature at the tip of 10 nm.

Fourier transform infra-red (FTIR) spectroscopy

For FTIR measurements, bioreduced silver NP dried powder was analyzed using FTIR. The samples were

dried, grounded with KBr pellets and analyzed in a SHIZAMAZU model no 8400S spectrum instrument. A disk of 50mg of KBr was prepared with a mixture of 2% finely dried sample, and was then examined under IR-spectrometer. Infrared spectrum was recorded in the region of 500 to 4500 cm^{-1}.

Scanning electron microscopy (SEM) and energy dispersive X-ray analysis (EDX)

The lyophilized silver NPs were mounted on the copper stubs and the images were studied using scanning electron microscope (SEM). EDX analysis was done with (JEOL model-L6390) secondary electron detectors at an operating voltage of 30 kV.

Cytotoxic activity

Cell culture

Human ductal breast carcinoma cells (T47D) was obtained from the National Centre for Cell Science (NCCS), Pune, and maintained in Roswell Park Memorial Institute (RPMI) medium containing 10% fetal bovine serum (FBS). For evaluation of the cytotoxicity, cell was seeded on a 96 well plate with a density of 1×104 cells/cm^2. Normal cells of L929 (human fibroblast cell line) was maintained in MEM (minimum essential medium) containing 10% fetal bovine serum (FBS) provided by Promo Cell Germany.

Assessment of cytotoxicity

Cytotoxicity of NTR was evaluated by using the MTT [3-(4,5-dimethylthiazole-2-yl)-2,5-diphenyltetrazolium] assay. This colorimetric test is based on the selective ability of viable cells to reduce the tetrazolium component of MTT into purple coloured formazan crystals. Stock solution of the samples were freshly prepared (1 mg/1 mL) and diluted with cell culture medium to the desired concentrations (20, 50 and 100 mg). The compound with different concentration was added and incubated with phosphate buffer saline (PBS) resuspended cells, after attaining 90 % confluency. Cells in media devoid of compound acted as the negative control and wells treated with Triton X-100 as the positive control for a period of 48 hrs. 5 mg of MTT (Sigma) was dissolved in 1 ml of PBS and filter sterilized. 10 ml of MTT solution was further diluted to 100 ml with 90 ml of serum and phenol red free medium. 100 ml of the solubilisation solution (10 % Triton X-100, 0.1 N HCl and isopropanol) was added to each well and incubated at room temperature for 1 hr to dissolve the formazan crystals. The absorbance of the solution was measured at a wavelength of 570 nm using a Beckmann Coulter Elisa plate reader (BioTek Power Wave XS). Triplicate samples were analyzed for each experiment.

Statistical analysis

The values are presented as mean ± SD (standard deviation) of triplicate measurements.

Results and Discussion

Biosynthesis of silver nanoparticles

In this study, the AgNPs were rapidly formed soon after the addition of clear silver nitrate solution to the aqueous extract of MT leaves, which was indicated by the light yellowish color turning to the dark brown color after 24 hrs (Fig. 1). The UV-Vis spectroscopy examined the size and shape of nanoparticles at the range of 300–600 nm. Among the various combinations (Fig. 2(a), 2(b)) used for optimization of silver nanoparticle formation, the mixture of 6:4 (S6) of silver nitrate and plant extract gave the optimized absorption spectrum at 420 nm, which is

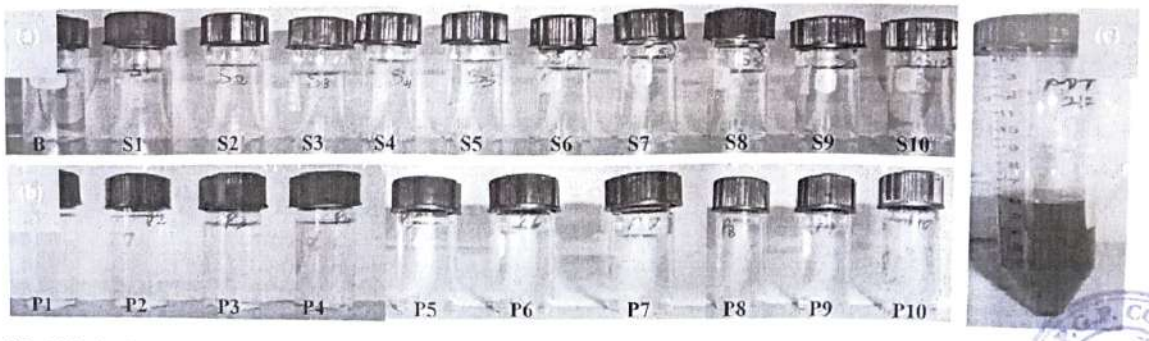


Fig. 1 The bottles containing silver nitrate solutions, plant extracts at different concentrations denoted as **(a)** S1-S10 and **(b)** P1-P10 respectively; **(c)** bottle containing purified, concentrated silver nanoparticles.

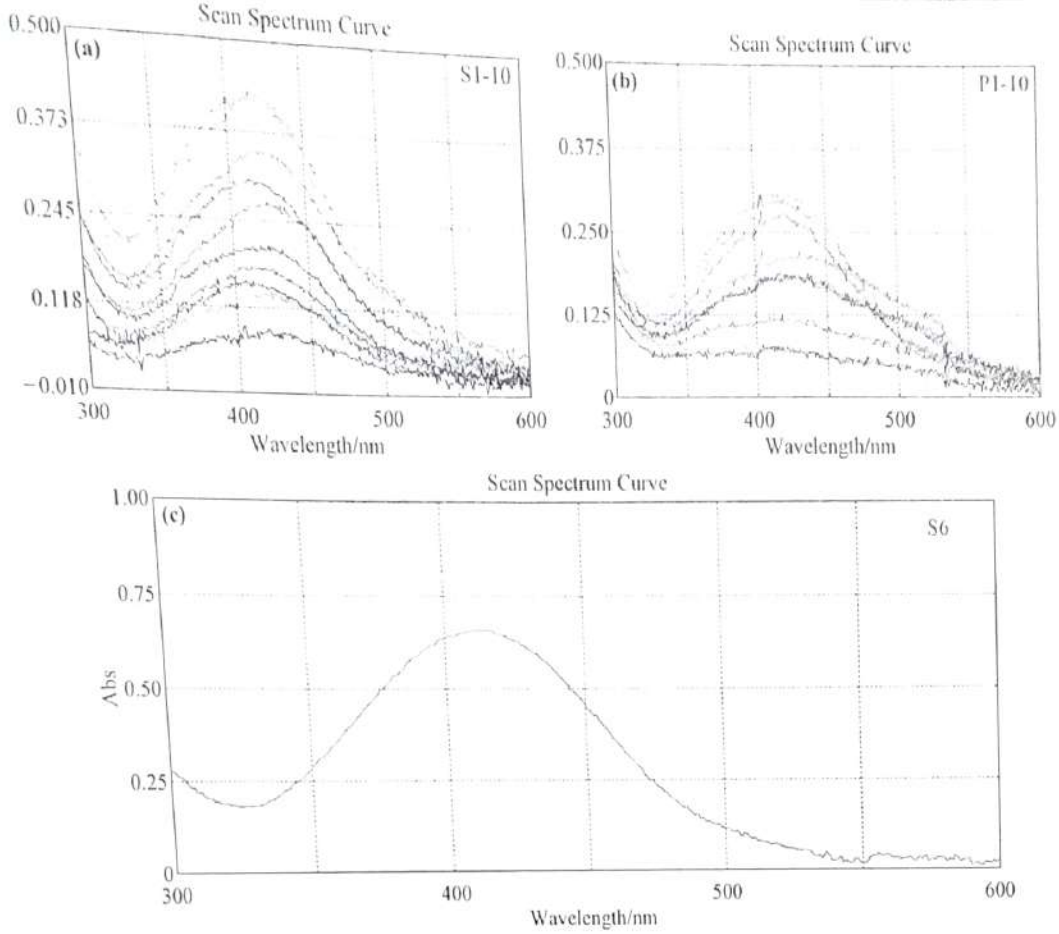


Fig. 2 (a) UV-visible spectrum of a mixture of solutions of silver nitrate S1-S10; **(b)** plant extracts P1-P10; **(c)** optimized silver nanoparticles synthesized using *Mallotus tetracoccus* leaves.

characteristic for surface plasmon resonance (SPR) of silver nanoparticles (Fig. 2(c)). Similar SPR of AgNPs synthesized by using seaweed *Padina tetrastromatica* showed an absorption peak at 424 nm (10). Here the biologically active molecules present in the leaf extract of MT have played a role in the reduction of silver nitrate to silver. The earlier investigations on the phytochemical constituents of *Mallotus tetracoccus* leaves revealed the presences of sugars, tannins, alkaloids, flavonoids, steroids, terpenoids and phenolic acids.

Optimization of physicochemical parameters for synthesis of silver nanoparticles

The formation of silver nanoparticles was optimized using different parameters: pH and temperature. PH and temperature play a very significant role in the synthesis of silver nanoparticles by controlling their shapes and sizes. The reaction medium was checked at different pH values for the production of optimized silver nanoparticles. PH 7 was said to give small, highly dispersed silver nanoparticles as indicated by their absorbance peaks at the nanometer scale, which was confirmed by the UV-Vis spectrum readings (Fig. 3). Among the different temperatures checked, the optimal production was observed at 60 °C, where high temperature favoured the synthesis (Fig. 3). Similar green synthesis of AgNPs was reported at the temperature of 60 °C using leaf extracts of *Tecomella undulata* (11).

Analysis of silver nanoparticles in AFM

The surface morphology of AgNPs synthesized using leaf extract of MT was studied by AFM. The obtained morphology revealed the fact that the synthesized silver nanoparticles were almost spherical in shape, which was confirmed by the absorbance spectrum (Fig. 4). The sizes of the silver nanoparticles as observed by AFM were found to be in the range of 46 to 100 nm, with an average size of 73 nm. The particles were polydispersed and agglomerated due to the binding of some stabilising and capping agents

http://www.nanobe.org

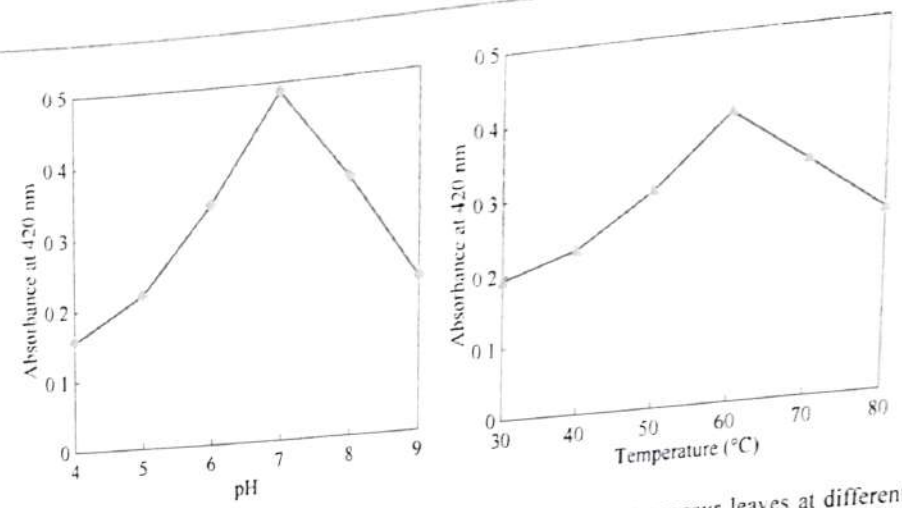


Fig. 3 Absorption spectrum for silver nanoparticles synthesized using *Mallotus tetracoccus* leaves at different pH values and temperatures.

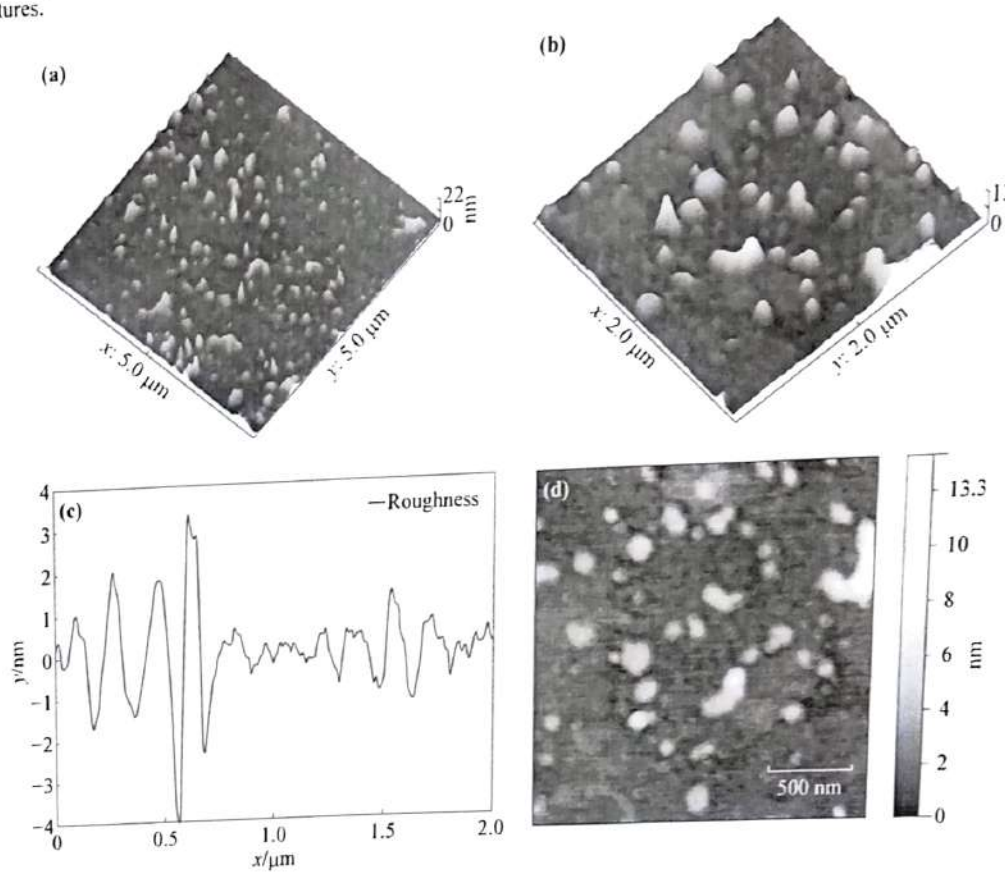


Fig. 4 AFM images obtained from the lyophilized sample of silver nanoparticles obtained from *Mallotus tetracoccus*, indicating the three dimensional images at the magnification of **(a)** 5 μm and **(b)** 2 μm; **(c)** roughness data of nanoparticles at 2 μm; **(d)** two dimensional image of nanoparticles with sizes in the range of 46 to 100 nm.

present in the MT extract. Figure 4 shows two and three dimensional views of the sample surface at the scan sizes of 2 μm×2 μm and 5 μm×5 μm, depicting the agglomerated, polydispersed distribution of silver nanoparticles.

Fourier transforms infrared spectroscopy (FTIR)

FTIR analysis gives an idea of the functional groups involved in reduction of silver nitrate to nanosilver. The FTIR spectrum of the silver nanoparticle showed bands at 3425, 2922, 2854, 2368, 1593, 1018, 667 and 609 cm^{-1}. Highly intense broad absorbance peak was observed at 3425 cm^{-1} characteristic of the O-H stretching of phenolic compounds (Fig. 5). The bands at 2922, 2854 represents the C-H stretch (alkane H)

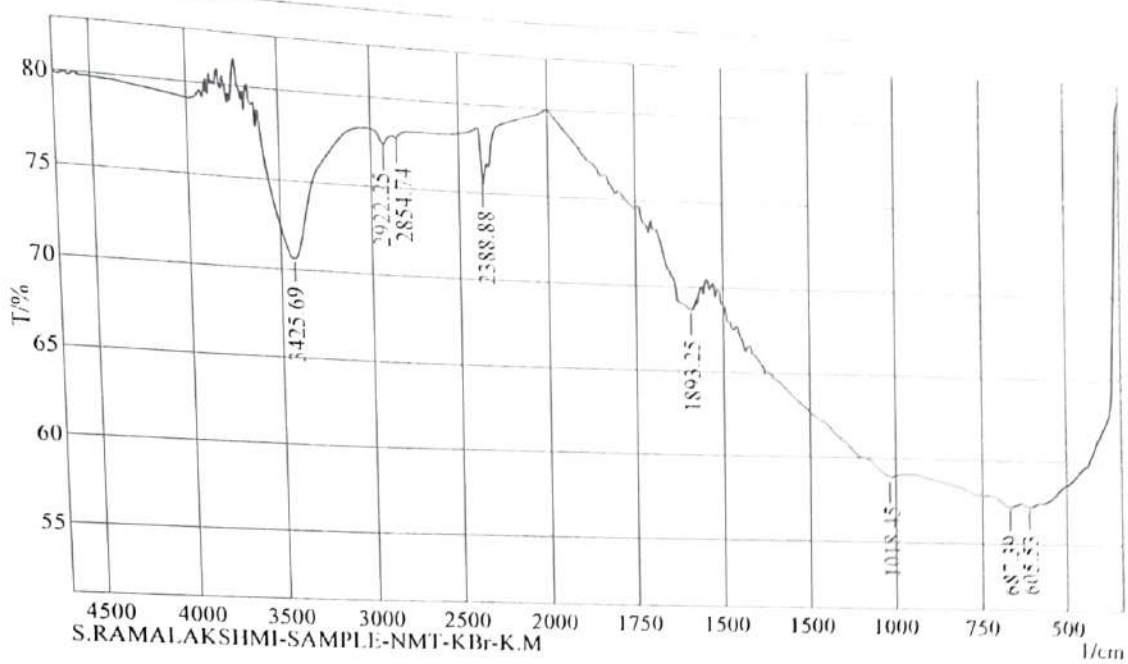


Fig. 5 FTIR spectrum for silver nanoparticles synthesized using *Mallotus tetracoccus* leaf extract.

O-H stretching in carboxylic acids and bands at 2368 and 1593 corresponds to C=O stretch in carboxylic acid respectively. Also the absorbance peak at 1018 cm^{-1} corresponds to the stretch vibration of C=C and C-N stretching vibrations of amine. Thus the silver nanoparticles are formed due to the interactions with the active compounds (secondary metabolites) of MT extract such as sugars, tannins, alkaloids, flavonoids, steroids, terpenoids and phenolic acids with silver nitrate to form nanoparticles. Thus the hydroxyl groups of phenols and carboxylic acids are involved in formation of AgNPs.

SEM and EDX profiles

SEM images were obtained from the lyophilised sample of silver nanoparticle synthesized from the leaf extract of MT (Fig. 6). Scanning electron microscope images of the silver nano powder showed spherical morphology with agglomeration. The obtained size distribution was similar to that found in AFM. The energy dispersive X-ray spectroscopy profile for silver nanoparticles showed strong silver signal along with signals for C and Mg, which may be due to the X-ray emission of the attached active molecules present on the surface of the silver nanoparticles (Fig. 7). Thus, the EDX reveals strong signal (78.38%) in the silver region, confirming the formation of silver nanoparticles. Metallic silver nanocrystals generally show typical optical absorption peak approximately at 3 keV due to surface plasmon resonance [12]. Various study reports on AgNp synthesized from plant extracts showed that several stabilizing agents act as capping agents and make the particles stable for a long time [13, 14].

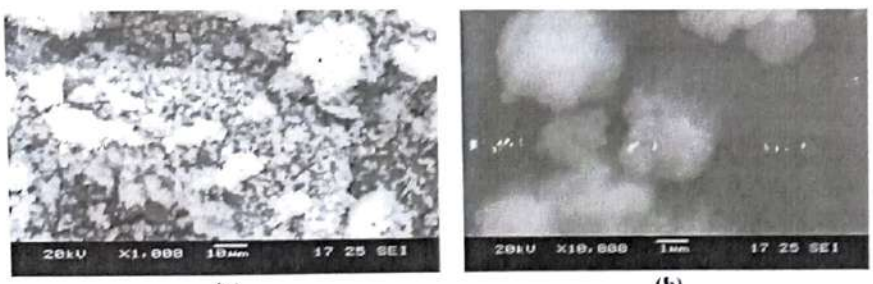
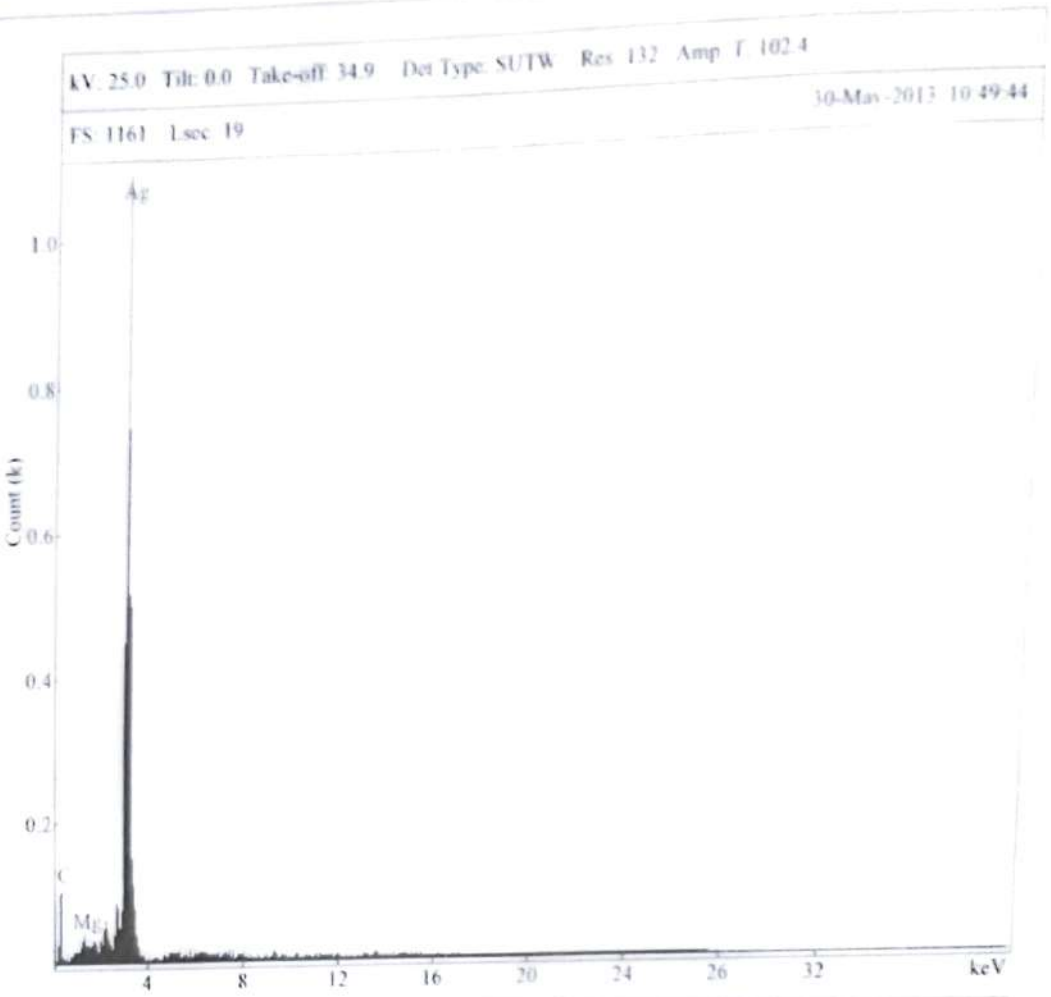


Fig. 6 SEM images of silver nanoparticles synthesized using *Mallotus tetracoccus* leaf extract at **(a)** 10 μm and **(b)** 1 μm magnifications.

P.G.P. COLLEGE OF ARTS & SCIENCE



EDAX ZAF Quantification (Standardless)
Element Normalized
SEC Table: Default

Element	wt%	at%	K-Ratio	Z	A	F
C K	20.04	67.83	0.1163	1.1897	0.4876	1.0000
MgK	1.58	2.64	0.0048	1.1250	0.2674	1.0036
AgL	78.38	29.54	0.7623	0.9220	1.0549	1.0000
Total	100.00	100.00				

Element	Net Inte.	Bkgd Inte.	Inte. Error	P/B
C K	27.58	0.61	4.39	45.25
MgK	10.51	2.13	8.24	4.93
AgL	510.01	2.34	1.00	218.28

Fig. 7 EDX images of silver nanoparticles synthesized using *Mallotus tetracoccus* leaf extract.

In vitro assessment of biosynthesized AgNPs cytotoxicity

Today, assays based on cell culture play an important role in the screening of compounds for various anticancer studies. Thus, the results of cytotoxicity study on normal human fibroblast cells (L929) and human ductal breast carcinoma cells (T47D) are given as cytotoxicity percentage. NMT showed very less toxicity on normal cells (4.4 to 10.6 %) at concentrations of 20 to 100 µg, whereas it exhibited highest cytotoxicity (76.8 to 84.9 %) on tumour cells (Fig. 8). Thus, the fact that AgNPs show higher cytotoxicity of 80-95 % at concentrations of 20 to 100 µg represents its potential to effectively kill cancer cells.

Similar study results from earlier researchers also show that silver nanoparticles synthesized from plants can effectively kill cancer cells at lower concentrations

COLLEGE OF ARTS & SCIENCE KANAKAL

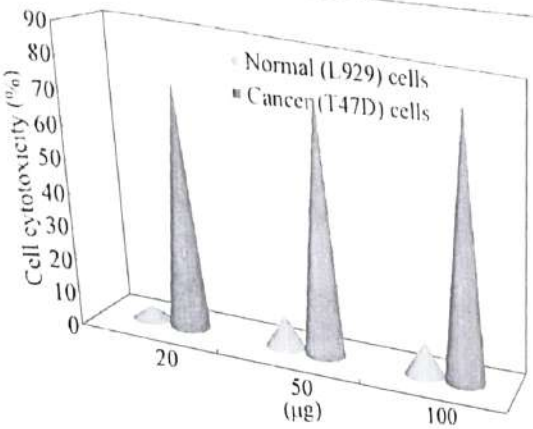


Fig. 8 MTT assay results confirm the *in vitro* cytotoxicity effect of AgNPs against the normal L929 cells and cancer T47D cells at 48 hrs.

[15]-[18]. The possible mode of the activity of silver nanoparticles on cancer cells has been reported by various researchers, that is, the created oxidative stress leads to depletion of GSH and induction of ROS, LPO, SOD and catalase in a dose dependent manner [16]-[18]. This stress causes interruption of ATP synthesis and mitochondrial damage, resulting in genotoxicity [22]. There is an interaction of AgNP with DNA, leading to cell cycle arrest in the G2/M phase [23]. There is also an increase in the activities of caspases, level of pro-inflammatory cytokines (interleukin-1b (IL-1b) and interleukin-6 (IL-6)) in the treated cancer cells [21]. Reports also show that there is the involvement of mitochondria-dependent jun-N terminal kinase (JNK) pathway in AgNP toxicity [24]. Finally the cancer cells undergo apoptosis.

Conclusions

This study reports the green synthesis of silver nanoparticles using *Mallotus tetracoccus* leaf extract. The synthesis of silver nanoparticles was standardised at pH 7 and the temperature of 60 °C. The silver nanoparticles were characterized using AFM, FTIR and SEM with EDX. FTIR analysis of the nanoparticle sample indicates the involvement of hydroxyl and carboxyl functional groups of phenols in the reduction of silver nitrate to silver nanoparticles. The nanoparticles showed a spherical morphology with the size range of 49 to 98 nm, and gave a strong silver signal in the EDX analysis. The AgNPs synthesized from MT leaf showed up to 85% cytotoxicity on cancer cells and very less toxicity on normal cells at the concentrations studied. Thus, further investigations are needed to prove its potential in *in vivo* studies for its application in cancer therapy.

Acknowledgements

The author Ramalakshmi Subbiah is thankful to University Grants Commission for providing meritorious fellowship (UGC-BSR) (Grant No. F.4-1/2006(BSR)/7-121/2007 (BSR)). The author is also thankful to USIC (University Science Instrumentation Centre), Dr. Suguna Shanmugasundram and Mr. K. Balachander, MKU for FTIR and AFM analysis.

References

[1] Y. Amakura, T. Yoshida. Tannins and related polyphenols of euphorbiaceous plants. 14. Euphorbin I, a new dimeric hydrolyzable tannin from *Euphorbia watanabei*. *Chem. Pharm. Bull.*, 1996, 44: 1293-1297.

[2] X.F. Cheng, Z.L. Chen, Two new diterpenoids from *Mallotus apelta* Muell. *Arg. J. Asian Nat. Prod. Res.*, 1999, 1: 319-325.

[3] D. Chattopadhyay, G. Arunachalam, A.B. Mandal, et al., Antimicrobial and anti-inflammatory activity of folklore *Mallotus peltatus* leaf extract. *J. Ethnopharmacol.*, 2002, 82: 229-237.

[4] H.S. Kim, H.K. Lim, M.W. Chung, et al., Antihepatotoxic activity of bergenin, the major constituent of *Mallotus japonicus*, on carbon tetrachloride-intoxicated hepatocytes. *J. Ethnopharmacol.*, 2000, 69: 79-83.

[5] M. Arfan, H. Amin, M. Karamac, et al., Antioxidant activity of extracts of *Mallotus philipensis* fruits and bark. *J. Food Lipids.*, 2007, 14: 280-297.

[6] S. Ramalakshmi, K. Muthuchelian, Anlaysis of bio-active constituents from the leaves of *Mallotus tetracoccus* (Roxb.) Kurz by gas chromatography-mass spectrometry. *I. J. Pharma. Sci. Res.*, 2011, 2(6): 1449-1454.

[7] S. Ramalakshmi, K. Muthuchelian, Evaluation of antioxidant potential and antimicrobial studies of bark extract of medicinal plant, *Mallotus tetracoccus* (Roxb.) Kurz. *J. Med. Plants. Res.*, 2012, 6(38): 5156-5165.

[8] S. Ramalakshmi, K. Muthuchelian, Studies on cytotoxic, phytotoxic and volatile profile of bark extract of important medicinal plant, *Mallotus tetracoccus* (Roxb.) Kurz. *Afr. J. Biotech.*, 2013, 12(43): 6176-6184.

[9] S. Prabhu, E.K. Poulose, Silver nanoparticles: mechanism of antimicrobial action, synthesis, medical applications, and toxicity effects. *I. Nano Letters*, 2012, 2.

[10] K.F. Princy, S. Manomi, R. Philip, et al., Antibacterial and catalytic efficacy of biosynthesized silver nanoparticles using marine seaweed *Padina tetrasromatica*. *Nano Biomed. Eng.*, 2016, 8(1): 16-23.

[11] S.K. Chaudhuri, S. Chandela and L. Malodia, Plant mediated green synthesis of silver nanoparticles using *Tecomella undulata* leaf extract and their characterization. *Nano Biomed. Eng.*, 2016, 8(1): 1-8.

[12] P. Magudapathi, P. Gangopadhyay, E.K. Panigrahi, et al., Electrical transport studies of silver nanoparticles embedded in glass matrix. *Physica B.*, 2001, 299: 142-146.

[13] J.Y. Song, B.S. Kim, Rapid biological synthesis of silver nanoparticles using plant leaf extracts. Bioprocess. *Biosyst. Eng.*, 2009, 32: 79-84.

[14] M. Singh, R.C. Kalaivani, M. Anand, et al., Rapid biomimetic synthesis of silver nanoparticles from Asiatic mangrove (*Rhizopora mucronata*) and its antimicrobial activity against clinically isolated pathogens. Proceedings of the International Conference on Nanoscience.

Engineering and Technology (ICONSET 2011). Kalpakkam, India, Nov. 28-30, 2011.

[15] R. Vivek, R. Thangam, K. Muthuchelian, et al., Green biosynthesis of silver nanoparticles from *Annona squamosa* leaf extract and its in vitro cytotoxic effect on MCF-7 cells. *Process Biochem.*, 2012, 47: 2405-2410.

[16] K. Renugadevi, D. Inbakandan, M. Bavanilatha, et al., *Cissus quadrangularis* assisted biosynthesis of silver nanoparticles with antimicrobial and anticancer potentials. *Int. J. Pharm. Bio. Sci.*, 2012, 3: 437-445.

[17] S. Das, J. Das, A. Samadder, et al., Biosynthesized silver nanoparticles by ethanolic extracts of *Phytolacca decandra, Gelsemium sempervirens, Hydrastis canadensis* and *Thuja occidentalis* induce differential cytotoxicity through G2/M arrest in A375 cells. *Colloids Surf B: Biointerf.*, 2013, 101: 325-336.

[18] K. Khanra, S. Panja, I. Choudhuri, et al., Bactericidal and cytotoxic properties of silver nanoparticle synthesized from root extract of *Asparagus racemosus*. *Nano Biomed. Eng*., 2016, 8(1): 39-46.

[19] S. Gurunathan, J.W. Hana, A.A. Dayem, et al., Green synthesis of anisotropic silver nanoparticles and its potential cytotoxicity in human breast cancer cells (MCF-7). *J. Ind. Eng. Chem.*, 2013, 19: 1600-1605.

[20] M. Jeyaraj, M. Rajesh, R. Arun, et al., An investigation on the cytotoxicity and caspase-mediated apoptotic effect of biologically synthesized silver nanoparticles using *Podophyllum hexandrum* on human cervical carcinoma cells. *Colloids Surf B*., 2013, 102: 708-717.

[21] A.O. Suliman, D. Ali, S. Alarifi, et al., Evaluation of cytotoxic, oxidative stress, proinflammatory and genotoxic effect of silver nanoparticles in human lung epithelial cells. *Environ Toxicol.*, 2013. DOI: 10.1002/tox.21880.

[22] R. Foldbjerg, D.A. Dang and H. Autrup, Cytotoxicity and genotoxicity of silver nanoparticles in the human lung cancer cell line, A549. *Arch. Toxicol.*, 2011, 85: 743-750.

[23] P.V. Asharani, G.L.K. Mun, M.P. Hande, et al., Cytotoxicity and genotoxicity of silver nanoparticles in human cells. *ACS Nano*, 2009,.3: 279–290.

[24] Y.H. Hsin, C.F. Chen, S. Huang, et al., The apoptotic effect of nanosilver is mediated by a ROS- and JNK-dependent mechanism involving the mitochondrial pathway in nih3t3 cells. *Toxicol. Lett.*, 2008, 179: 130-139.

Copyright© 2016 Ramalakshmi Subbiah, Krishnaswamy Muthuchelian. This is an open-access article distributed under the terms of the Creative Commons Attribution License, which permits unrestricted use, distribution, and reproduction in any medium, provided the original author and source are credited.



PRINCIPAL
PGP College of Arts and Science
Namakkal

Indian Journal of Applied Microbiology
(IJAM-Print ISSN : 2249-8400 Online ISSN : 2454-289X)

Authors are requested to submit the manuscripts only through IJAM web portal submission directly to journal then it will not be considered
IJAM is now a member of Crossref. Articles published from the year 2017 onwards are assigned a DOI
• Articles are invited for the first issue of the year 2022

Original Research Article

Studies on cytotoxic and phytotoxic potential of Mallotus tetracoccus (Roxb.) Kurz leaf extracts

Ramalakshmi Subbiah and Muthuchelian Krishnaswamy*
1.Department of Microbiology, Karpagam University, Coimbatore-641021
2. Department of Bioenergy, School of Energy, Environment and Natural Resources,Madurai Kamaraj University, Madurai – 625 021, India
Ind. J. Applied Microbiol. 2016, 19(2): 33-42
*Corresponding author

Abstract

The present study was aimed to investigate the cytotoxicity and phytotoxicity of various organic extracts from the leaves of medicinal plant Mallotus tetracoccus (Roxb.) Kurz (MT). The leaf powders of MT were extracted with different solvents such as petroleum ether (MT1), chloroform (MT2), ethyl acetate (MT3), acetone (MT4) and aqueous ethanol (MT5). The cytotoxicity of extracts was determined by using brine shrimp larvae. The phytotoxicity of plant extracts was assessed by using radish seeds (Raphanus sativus L.) by two methods, root shoot length inhibition and seed germination studies. The ethanolic extract showed significant cytotoxicity value of 6.33 ± 0.3 Smu;g/mL out of five extracts. The radish inhibition was observed in the order of

Print ISSN : 2249-8400
Online ISSN : 2454-289X
Issues : 3 per Year
Publisher : The Editor-in-Chief, IJAM
Email : ijamjournal@yahoo.co.in
Editor-in-chief : Prof. Dr Usha Anand Rao

• Download this Article
• PDF Full Text
• on Google
• Google Scholar

Useful Links

• Call for Papers

COLLEGE OF ARTS & SCIENCE
NAMAKKAL
637 209
P.G.P.

Indian Journal of Applied Microbiology
ISSN (Online): 2454-289X, ISSN (Print): 2249-8400
Copyright © 2016 IJAM, Chennai, India
Volume 19 Number 2
July - December 2016, pp. 33-42

Studies on cytotoxic and phytotoxic potential of *Mallotus tetracoccus* (Roxb.) Kurz leaf extracts.

Ramalakshmi Subbiah[a] and Muthuchelian Krishnaswamy[b*]

[a] Department of Microbiology, Karpagam University, Coimbatore-641021.

[b]Department of Bioenergy, School of Energy, Environment and Natural Resources, Madurai Kamaraj University, Madurai – 625 021, India.

Abstract: The present study was aimed to investigate the cytotoxicity and phytotoxicity of various organic extracts from the leaves of medicinal plant *Mallotus tetracoccus* (Roxb.) Kurz. (MT). The leaf powders of MT were extracted with different solvents such as petroleum ether (MT1), chloroform (MT2), ethyl acetate (MT3), acetone (MT4) and aqueous ethanol (MT5). The cytotoxicity of extracts was determined by using brine shrimp larvae. The phytotoxicity of plant extracts was assessed by using radish seeds (*Raphanus sativus L.*) by two methods: root, shoot length inhibition and seed germination studies. The ethanolic extract showed significant cytotoxicity value of 6.33 ± 0.8 µg/mL out of five extracts. The radish inhibition was observed in the order of MT3>MT2>MT4>MT5>MT1. There was considerable shoot length inhibition at 10,000 ppm for all MT extracts than root length. The radish seed germination rate for MT extracts was observed in the order of MT5>MT1>MT4>MT3>MT2. At 10,000 ppm, low germination index of 0.597 ± 0.089 and 0.769 ± 0.077 % were exhibited by ethyl acetate and chloroform extracts of MT. Thus the MT plant leaves in general was found to possess significant cytotoxic as well as allelopathic potential, which can be used as potential herbicide.

Key words: *Mallotus tetracoccus*, cytotoxicity, phytotoxicity, radish seed, *Artemia salina*.

Introduction

Medicinal plants are still used as radical scavengers to fight against many important diseases, such as cancer. The active phytochemical compounds present in the plants such as carotenoids, terpenoids, flavonoids, polyphenols, alkaloids, tannins, saponins possess various activities which

*Author for Correspondence. E-mail: drchelian1960@yahoo.co.in

COLLEGE OF ARTS & SCIENCE P.G.P.

help in scavenging the free radicals produced during initiation or progression of diseases [1]. *Mallotus tetracoccus* (Roxb.) Kurz. of family Euphorbiaceae, found in Western Ghats of India. The common names include *Thavatta, Vatta, Vatta kumbil, Vetta kumbil* (malayalam), *Uppale mara* (kannada) and "vatta kanni" in Tamil. Several species of the genus *Mallotus* are a rich source of biologically active compounds such as phloroglucinols, tannins, terpenoids, coumarins, benzopyrans and chalcones [2-5]. The reported bioactivities of the extracts or the individual chemical constituents isolated from this genus include antipyretic [6], anti-inflammatory, hepatoprotective [7], antioxidant and radical scavenging activities [8].

May and Ash has defined allelopathy as a mechanism in which allelochemicals produced by neighboring weeds for competition, may either have an inhibiting or stimulating effect on other plant growth [9], studied by observing the seed germination and plant growth. Weed species grow stronger, show competition on neighboring crops for light, water and nutrients, affecting the crop yields. In order to control weed growth application of chemical herbicides result in side effects affecting humans as well as causing environmental hazards, so herbicides from natural resources are preferred. Plants naturally produce a large amount of water-soluble toxins termed allelochemicals, released from leaves, flowers, seeds, stems and roots, to compete with other invaders present in their environment [10]. These chemical compounds are products of secondary metabolism of plants, such as alkaloids, phenols and terpenoids, affect the target plants seed germination, seedling growth, cell division and fungal activity [11]. Thus it is necessary to identify the compounds responsible for allelopathic effects which can be useful for developing green growth promoters [12].

The volatile compounds present in the MT leaf extract showed the presence of various chemical constituents such as bis (2-ethyl hexyl) phthalate (46.78 %), 3-methyl-2-(2-oxypropyl) furan (13.31 %), E-8-methyl-9-tetradecen-1-ol acetate (6.63 %), octadecanoic acid, 2-oxo (4.46 %) and longiborneol (2.39 %) analysed by GC-MS [13]. The bark extract of MT reported for higher phenolics, flavonoids and significant antioxidant potential [14]. Thus the objective was to study phytotoxicity using radish (*Raphanus sativus L.*) and cytotoxic studies using brine shrimps (*Artemia salina*) on different extracts of *Mallotus tetracoccus* leaves.

Materials and Methods

Collection of plant material

Healthy leaves of *Mallotus tetracoccus* were collected from Agasthiar Malai Reserve Forest, Western Ghats, South India, authenticated by the Director, Centre for Biodiversity and Forest Studies, Madurai Kamaraj University, and voucher specimens were deposited in the herbarium of Centre for Biodiversity and Forest Studies of our university (No.AM-03).

Extraction of plant material

The leaves were shade dried, powdered and packed in small packets and extracted successively with different solvents such as petroleum ether, chloroform, ethyl acetate, acetone and 70 % ethanol in the increasing order of polarity using soxhlet apparatus. The different solvent extracts

COLLEGE OF ARTS & SCIENCE P.G.P. NAMAKKAL 637 206

were filtered, concentrated, vacuum dried at 45°C for solvent removal and refrigerated in sterile bottles until use. The MT1, MT2, MT3, MT4 and MT5 indicate pet ether, chloroform, ethylacetate, acetone and aqueous ethanol extracts of MT respectively.

Cytotoxicity bioassay using brine shrimps

Brine shrimp cytotoxicity assay was performed according to the standard procedure described by McLaughlin, 1991 [15]. Brine shrimps (*Artemia salina*) were hatched using brine shrimp eggs in a conical flask(1L), filled with sterile artificial seawater (prepared using sea salt 38 g/L and adjusted to pH 8.5 using 1N NaOH) under constant aeration for 48 h. After hatching, active nauplii free from egg shells were collected from brighter portion of the hatching chamber and used for the assay. Twenty nauplii were drawn through a glass capillary and placed in each vial containing 4.5 ml of brine solution. In each experiment, 0.5 ml of the extract was added to 4.5 ml of brine solution and maintained at room temperature for 24 h under the light and surviving larvae were counted with a hand lens. Experiments were conducted along with control (vehicle treated), different concentrations (1-1000 µg/ml) of the test substances in triplicates.

Phytotoxicity studies using radish seeds

The phytotoxic properties of the various extracts of plant were evaluated using radish seed phytotoxicity assay [16, 17]. Two type of determination were done for this purpose:

Root Length Determination

Radish seeds were washed with distilled water and with 1 % mercuric chloride. Whatman #1 filter paper was kept on Petri dish and 5 ml of the plant extracts (100 ppm, 1000 ppm and 10,000 ppm) were added separately. Filter paper was dried at room temperature for reducing extra solvent. Five ml of double distilled water was added and then 20 radish seeds were placed on Petri dishes followed by tightly sealing and incubation at 23 ± 2°C. Root length was measured after 1, 3 and 5 days of interval. Only double distilled water containing Petri dish with seeds were used as control. Each assay was carried out in triplicates.

Seed Germination Determination

This part of the determination is similar to that of earlier determination except for the extract concentrations and number of seeds. Here two different concentrations (1000 ppm and 10,000 ppm) and 100 radish seeds were used. Germinated seeds were counted after every day up to 5 days. Each assay was carried out in triplicates.

Data analysis

The following parameters were adopted in this analysis to evaluate the conditions of seed germination: Relative germination rate and Germination Index. They were calculated based on the following equations according to previous reports [18]:

Relative germination rate = [Seeds germinated in test sample/Seeds germinated in control]*100

Relative root elongation = [Mean root length in test sample/Mean root length in control]*100

COLLEGE OF ARTS & SCIENCE NAMAKKAL 637 205

Germination Index = [Relative germination rate* Relative root elongation]/100.

Statistical analysis

The values are presented as mean ± SD (standard deviation) of triplicate measurements. Multiple comparisons between more than two groups were performed by one way ANOVA supplemented with Duncan's multiple range post hoc tests. Values at $P < 0.05$ were considered to indicate statistical significance.

Results

Brine shrimp cytotoxicity bioassay

Among the five extracts of *Mallotus tetracoccus*, all of them exhibited potent cytotoxicity against brine shrimp, where the LD_{50} values where less than 100 µg/mL. LD_{50} values for MT extracts were in the range of 6.33 ± 0.8 to 22.86 ± 1.658 µg/mL, where ethanolic extract showed noteworthy cytotoxicity value of 6.33 µg/mL (Table I). The MT ethyl acetate and acetone extracts showed almost similar LD_{50} value of 12.36 ± 1.643 and 13.17 ± 1.88 µg/mL respectively. The MT pet ether and chloroform extracts showed LD_{50} values of 22.86 ± 1.658 and 19.06 ± 1.259 µg/mL respectively. The results on brine shrimps assay indicate that the extracts had LC_{50} value lesser than 20 µg/ml; the recommended cutoff point for detecting cytotoxic activity [19].

Table I: Percentage (%) Mortality of brine shrimps at different concentrations of MT extracts and their respective LD_{50} value.

Extracts	Percentage (%) Mortality at different concentrations of the plant extracts							LD50 (µg/mL)
	1 (µg/mL)	5 (µg/mL)	10 (µg/mL)	50 (µg/mL)	100 (µg/mL)	500 (µg/mL)	1000 (µg/mL)	
MT1	16.67	26.67	40	53.33	66.67	96.67	100	22.86±1.658a
MT2	10	30	43.33	60	73.33	93.33	100	19.06±1.259b
MT3	13.33	36.67	53.33	70	96.67	100	100	12.36±1.643c
MT4	16.67	36.67	50	66.67	93.34	100	100	13.17±1.88c
MT5	26.67	46.67	60	76.67	90	100	100	6.33±0.8d

Each value represents the mean ± SD of three determinations. Means marked with different letters, within each column, are significantly different ($p < 0.05$).

Results for percentage mortality of brine shrimp indicates that highest percentage was observed at 500 µg/mL by most of the extracts tested. At a concentration of 10 µg/mL, only ethanolic and

COLLEGE OF ARTS & SCIENCE NAMAKKAL 637 206

ethyl acetate extracts of MT presented significant mortality values of 53.33 %; 60 % respectively (table 1).

Radish Seed Phytotoxicity Assay

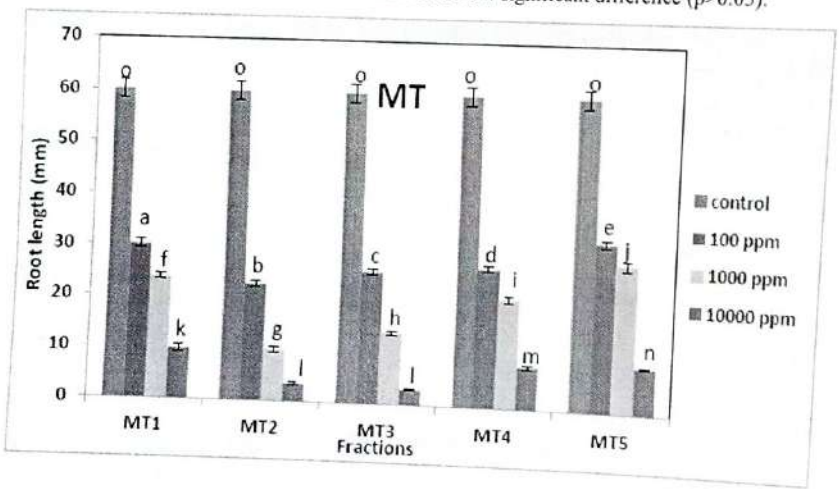
For radish (*Raphanus sativus L.*) seed germination, root, shoot length and percent of seed germination were determined. From the root length inhibition and seed germination percentage, germination index were calculated.

Radish seedling root length inhibition

The effect of three different concentrations (10,000, 1000 and 100 ppm) of the plant extracts were studied on root growth inhibition or stimulation of radish seedling. The radish root and shoot length at fifth day of study were observed.

All extracts of MT inhibited root growth at 10,000 ppm. The radish root length for MT extracts were observed in range of 22.85 ± 0.427 to 32.8 ± 0.681 mm for 100 ppm, 10.1 ± 0.486 to 28.7 ± 1.021 mm for 1000 ppm and 3.02 ± 0.176 to 9.9 ± 0.651 mm for 10,000 ppm when compared with control length of 60.07 ± 1.706 mm (Figure 1). At 100, 1000 ppm concentrations, all MT extracts exhibited inhibition in the range of 38.04 ± 0.711 to 54.55 ± 1.133 % and 16.79 ± 0.808 to 47.76 ± 1.7 % respectively. At 10,000 ppm concentration of plant extracts, the ethyl acetate and chloroform extracts showed root inhibition of 5.02 ± 0.292 and 5.66 ± 0.44 % respectively. Thus the radish inhibition were observed in the order of MT3>MT2>MT4>MT5>MT1 (Table II).

Figure I: Effect of different concentrations (100, 1000 and 10,000 ppm) of MT extracts on radish root length at fifth day. Values with similar letters don't show significant difference ($p>0.05$).



COLLEGE OF ARTS & SCIENCE NAMAKKAL 637 206

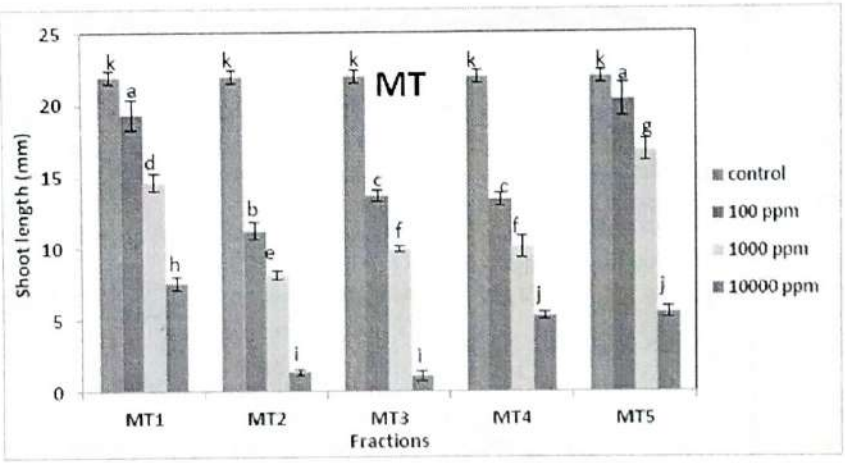
Table II: Percentage of radish root growth inhibition/stimulation at different concentrations of plant extracts.

	Root growth inhibition/stimulation at concentration (%)		
Extract	100 ppm	1000 ppm	10,000 ppm
MT1	50.25 ± 1.369^{a}	39.95 ± 0.999^{f}	16.43 ± 1.083^{k}
MT2	38.04 ± 0.711^{b}	16.79 ± 0.808^{g}	5.66 ± 0.44^{l}
MT3	42.98 ± 0.958^{c}	23.28 ± 0.636^{h}	5.022 ± 0.292^{l}
MT4	45.28 ± 1.04^{d}	35.54 ± 0.938^{i}	13.87 ± 0.585^{m}
MT5	54.55 ± 1.133^{e}	47.76 ± 1.7^{j}	15.29 ± 0.268^{n}

Each value represents the mean ± SD of three determinations. Means marked with different letters, within each column, are significantly different ($p < 0.05$).

Similarly the shoot length of radish seeds after five days were recorded. The radish shoot length for MT extracts were observed in range of 11.2 ± 0.643 to 20.3 ± 1.130 mm for 100 ppm, 8.1 ± 0.293 to 16.8 ± 0.765 mm for 1000 ppm and 1 ± 0.379 to 7.6 ± 0.493 mm for 10,000 ppm when compared with control length of 21.94 ± 0.487 mm. Thus there was high shoot length inhibition at 10,000 ppm for all MT extracts (Figure II).

Figure II: Effect of different concentrations (100, 1000 and 10,000 ppm) of MT extracts on radish shoot length at fifth day. Values with similar letters don't show significant difference ($p>0.05$).



Radish seed germination

The radish seed germination percentage of all the extracts were studied at two different concentrations 1000 and 10,000 ppm (Figure IIIa and IIIb). For 1000 ppm concentration of MT extracts tested, germination rate observed were in the range of 41.46 ± 0.604 to 72.47 ± 0.604 %.

P.G.P. COLLEGE OF ARTS & SCIENCE NAMAKKAL 637 206

At 10,000 ppm, lowest rates of 11.85 ± 1.207 and 13.59 ± 1.045 % were observed by ethyl acetate and chloroform extracts of MT. High germination was observed in MT ethanolic and petroleum ether extracts (62.02 ± 0.604 and 61.67 ± 1.045 % respectively). Thus the radish seed germination rate for MT extracts were observed in the order of MT5>MT1>MT4>MT>MT2 (Table III). At 1000 ppm, lowest and highest germination index of 6.96 ± 0.430 and 32.94 ± 0.810 % were exhibited by chloroform and ethanolic extracts of MT. At 10,000 ppm, low germination index of 0.597 ± 0.089 and 0.769 ± 0.077 % were exhibited by ethyl acetate and chloroform extracts of MT. Thus the germination index in the range of 0.597 ± 0.089 to 10.13 ± 0.768 % shows highest level of inhibition by the extracts at higher concentrations (Table III).

Figure III: Effect of different concentrations (a. 1000 ppm and b. 10,000 ppm) on seed germination of MT extracts at fifth day. Values with similar letters don't show significant difference ($p>0.05$).

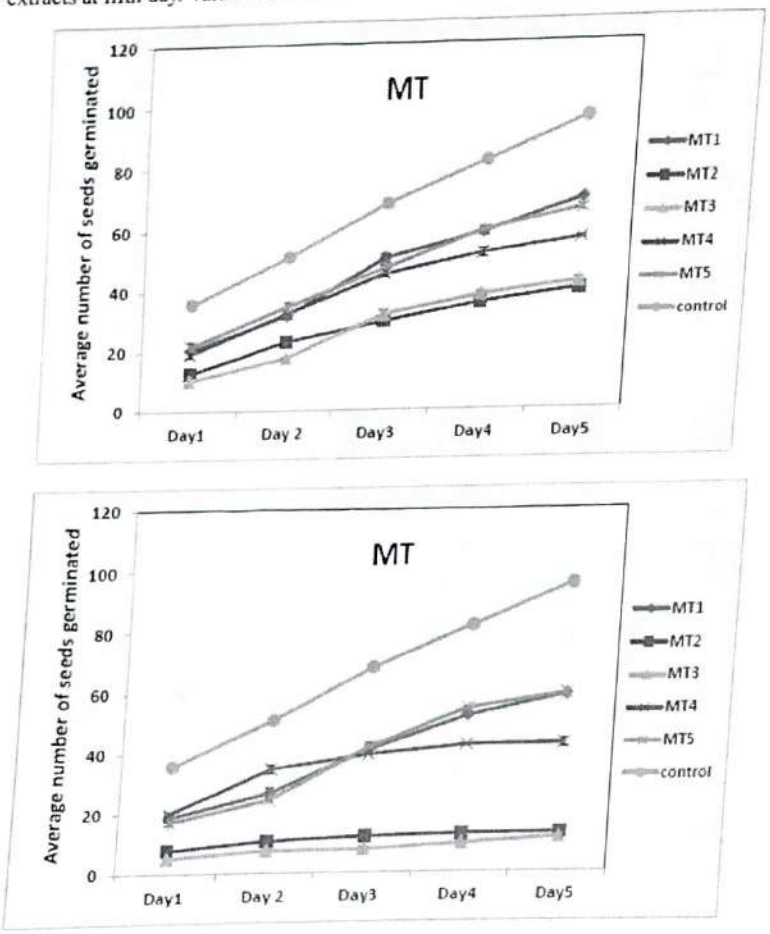


Table III: Effect of plant extracts on seed germination rate and germination index.

	Relative germination rate (%)		Germination index (%)	
Extract	1000 ppm	10,000 ppm	1000 ppm	10,000 ppm
MT1	72.47 ± 0.604^{a}	61.67 ± 1.045^{f}	28.96 ± 0.943^{a}	10.13 ± 0.768^{f}
MT2	41.46 ± 0.604^{b}	13.59 ± 1.045^{g}	6.96 ± 0.430^{b}	0.769 ± 0.077^{g}
MT3	43.90 ± 1.045^{c}	11.85 ± 1.207^{g}	10.22 ± 0.521^{c}	0.60 ± 0.089^{g}
MT4	58.89 ± 0.604^{d}	44.60 ± 1.597^{h}	20.93 ± 0.769^{d}	6.19 ± 0.410^{h}
MT5	68.99 ± 1.045^{e}	62.02 ± 0.604^{f}	32.94 ± 0.810^{e}	9.48 ± 0.077^{f}

Discussion

Brine shrimp cytotoxicity bioassay

Brine shrimp lethality bioassay (BSLT) is the general bioassay for detecting broad spectrum of bioactivity present in plant crude extracts [20]. The following study results on the extracts of *Mallotus tetracoccus* leaves showed that the ethanolic and ethyl acetate extracts revealed higher level of cytotoxicity when compared to other extracts. Similar study report by researchers also show that the polar fractions exhibited high cytotoxic activity than others. The methanolic extracts of *Physalis minima* and *Argemone Mexicana* showed LC_{50} values of 36.67 and 54.42 µg/mL [21]. The stem bark, leaf and root extracts of *Combretum adenogonium* showed LC_{50} values of 65.77, 76.97 and 110.04 µg/mL respectively [22]. The leaf extract of *Mesua ferrea* exhibited cytotoxicity value at doses of 500 ppm [23]. Five Bangladesh medicinal plants were studied for cytotoxicity, of which highest activity were observed only in *Curcuma longa* (26.63 µg/mL), whereas other plants *Curcuma zedoaria, Streblus asper, Enhydra fluctunas* and *Scoparia dulcis* exhibited activity at dose of >150 µg/mL [24]. Forty five Medicinal plants of Kenya possessing antimalarial activity were studied for cytotoxicity of which only 23 (51 %) plants showed activity at concentrations of 100 µg/mL [25]. Thirty one medicinal plants of eastern Nicaragna studied for cytotoxicity showed that only 4 (13%) plants exhibited activity at dose of <1000 µg/mL, whereas other 27 plants showed activity >1000 µg/mL [26]. On comparison of our study results with other research work, our extracts possessed significant cytotoxic activity at concentrations of <50 µg/mL.

Radish Seed Phytotoxicity Assay

Phytotoxicity is said to be an important attribute in determination of allelopathic potential of a plant species [27]. The phytotoxicity study on MT extracts showed that activity is found at higher concentrations. Our study reports are similar to study reports by other researchers too. The aqueous extracts of *Nicotiana glauca* Graham (stems, roots and fruits) were evaluated for phytotoxicity on two crops (lettuce and radish), where seed germination and root length inhibition was between 15 and 100 %, due to the presence of phenolics. Root length inhibition was more obvious than shoot length, which is an indicator of phytotoxicity [28].

P.G.P. COLLEGE OF ARTS & SCIENCE NAMAKKAL 637 206

The essential oils of *Salvia hierosolymitana* Boiss. and *Salvia multicaulis* Vahl. var. simplicifolia Boiss. studied for phytotoxic effects, showed that extracts inhibited and promoted radish seed germination at dose of 0.625 µg/mL and 0.24 µg/mL. Radical elongations of radish were inhibited significantly in response to 0.125 µg/mL and 1.25 µg/mL of *Salvia multicaulis* var. simplicifolia. Radical elongation seemed to be more affected than germination [29].

Thus the overall cytotoxic and phytotoxic activity of *Mallotus tetracoccus* extracts might be due to the presence of volatile terpenoid compounds such as longiborneol (2.39 %); p-menth-8(10)-en-9-ol (a terpene alcohol, 1.49 %) and fatty acid esters (48.11 %) such as bis (2-ethyl hexyl) phthalate (46.78 %); di-n-octyl phthalate (1.33 %) analysed by GC-MS [13]. The qualitative study on MT extract illustrated the presence of sugars, tannins, alkaloid, flavonoid, steroids, terpenoids and phenolic acids (unreported results). Recently the cytotoxic studies on nanodrug from MT leaf extract showed cytotoxicity upto 76.8 to 84.9 % at 20-100µL concentrations [30].

Conclusion

The different extracts of *Mallotus tetracoccus* leaves studied for cytotoxicity and phytotoxicity studies confirmed that ethanolic extract revealed cytotoxic activity and ethyl acetate extract demonstrated high phytotoxicity on radish seeds. Thus isolation of pure compounds from the ethanolic and ethyl acetate extracts can be studied for *in-vitro* and *in-vivo* studies for further application as herbicide.

Acknowledgment

The author Ramalakshmi Subbiah is grateful to University Grants Commission for providing meritorious fellowship (UGC-BSR) (Grant No. F.4-1/2006(BSR)/7-121/2007 (BSR)). The author is also thankful to the Dean and Management of Karpagam University, Coimbatore for the support and encouragement to publish the work.

References:

1. AI Adewale; MES Mirghani; SA Muyibi; JI Daoud and M.M. Abimbola. Plant. Adv Natural App Sci, 2012, 6, 583-587.
2. R Akter; MA Satter; MS Khan; MS Rahman; NU Ahmed. Bangladesh J Sci Ind Res,012, 47, 133-136.
3. Y Amakura; T Yoshida. Chem Pharm Bull, 1996, 44, 1293–1297.
4. M Arfan; H Amin; M Karamac; A Kosinska; R Amarowicz; F Shahidi. J Food Lipids, 2007, 14, 280–297.
5. D Chattopadhyay; G Arunachalam ; AB Mandal; TK Sur; SC Mandal; SK Bhattacharya. J Ethnopharmacol, 2002, 82, 229–237.
6. XF Cheng; ZL Chen. Arg J Asian Nat Prod Res, 1999, 1, 319–325.
7. FG Coe; DM Parikh; CA Johnson; GJ Anderson. Pharma Bio, 2012, 50, 384-392.

COLLEGE OF ARTS & SCIENCE NAMAKKAL 637 206

8. RI Geran; HM Greenberg; M McDonald; BJ Abbott. Cancer Chemoth Rep, 1972, 33,1–17.
9. AA Hamid; Z Shah Md; R Muse; Mohamed S. Food Chem, 2002, 77, 465–469.
10. KM Indergit; M Dakshini. J Bot. 1998, 76, 1317-21.
11. MS Islam; MM Akhtar; MM Rahman; MA Rahman; KK Sarker; MF Alam. Global J Pharma, 2009, 3, 99-106.
12. RA Khan; MR Khan; S Sahreen; J Bokhari; U Rashid; S Jan. African J Biotech. 2011, 10,5377-5380.
13. HS Kim; HK Lim; MW Chung; YC Kim. J Ethnopharmacol, 2000, 69, 79–83.
14. K Likhitwitayawuid; B Supudompol. Heterocycles, 2005, 65, 161–164.
15. MAK Lodhi. J Bot, 1976, 63, 1-8.
16. J Ma; SH Jones; SM Hecht. J Nat Prod, 2004, 67, 1614–1616.
17. E Mancini; NA Arnold; LD Martino; VD Feo; C Formisano; D Rigano; F Senatore. Molecules, 2009, 14, 4725-4736.
18. FE May; JE Ash. Aust J Bot, 1990, 38, 245-254.
19. JL McLaughlin. K Hostetsmann. Methods in Plant Biochemistry, Academic Press, London, 1991, 1–31.
20. NF Mushi; ZH Mbwambo; E Innocent; S Tewtrakul. BMC Comp Alt Med, 2012, 12, 163.
21. JM Nguta; JM Mbaria; DW Gakuya; PK Gathumbi; JD Kabasa; SG Kiama.). Drugs Therapy Studies, 2012, 2.
22. P Oudhia; SS Kolhe; RS Tripathi. Oryza, 1998, 35, 175-177.
23. R Ahsan Md; KM Islam; ME Haque; MA Mossaddik. World J A Sci, 2009, 5, 617-621.
24. S Ramalakshmi; K Muthuchelian. I J Pharma Sci Res, 2011, 2, 1449-1454.
25. S Ramalakshmi; K Muthuchelian. J Med Plants Res, 2012, 6, 5156-5165.
26. A Rinez; A Ladhari; F Omezzine; I Rinez; R Haouala. 3rd International Symposium on Weeds and Invasive Plants, October 2-7, 2011 in Ascona, Switzerland.
27. T Tanaka; T Ito; M Iinuma; Y Takahashi; H Naganawa. Phytochem, 1998, 48, 142–1427.
28. WH Thompson; PB Leege; PD Millner; ME Watson. Test methods for the examination of composting and compost, 2001, USCC, and USDA, Eds.
29. AU Turker; ND Camper. J. Ethnopharmacol, 2002, 82, 117-125.
30. S Ramalakshmi; K Muthuchelian. Nano Biomedicine engineering, 2016, 8(2), 82-90.

PRINCIPAL
PGP College of Arts and Science
Namakkal

P.G.P. COLLEGE OF ARTS & SCIENCE
NAMAKKAL
637 206